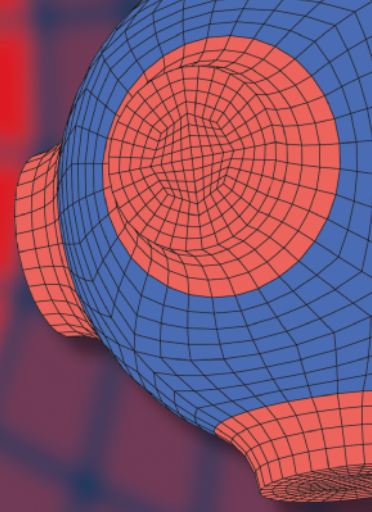


Advanced Structured Materials

Vladimir A. Polyanskiy
Alexander K. Belyaev *Editors*



Mechanics and Control of Solids and Structures

 Springer


Advanced Structured Materials

Volume 164

Series Editors

Andreas Öchsner, Faculty of Mechanical Engineering, Esslingen University of Applied Sciences, Esslingen, Germany

Lucas F. M. da Silva, Department of Mechanical Engineering, Faculty of Engineering, University of Porto, Porto, Portugal

Holm Altenbach , Faculty of Mechanical Engineering, Otto von Guericke University Magdeburg, Magdeburg, Sachsen-Anhalt, Germany

Common engineering materials reach in many applications their limits and new developments are required to fulfil increasing demands on engineering materials. The performance of materials can be increased by combining different materials to achieve better properties than a single constituent or by shaping the material or constituents in a specific structure. The interaction between material and structure may arise on different length scales, such as micro-, meso- or macroscale, and offers possible applications in quite diverse fields.

This book series addresses the fundamental relationship between materials and their structure on the overall properties (e.g. mechanical, thermal, chemical or magnetic etc.) and applications.

The topics of *Advanced Structured Materials* include but are not limited to

- classical fibre-reinforced composites (e.g. glass, carbon or Aramid reinforced plastics)
- metal matrix composites (MMCs)
- micro porous composites
- micro channel materials
- multilayered materials
- cellular materials (e.g., metallic or polymer foams, sponges, hollow sphere structures)
- porous materials
- truss structures
- nanocomposite materials
- biomaterials
- nanoporous metals
- concrete
- coated materials
- smart materials

Advanced Structured Materials is indexed in Google Scholar and Scopus.


More information about this series at <https://link.springer.com/bookseries/8611>


Vladimir A. Polyanskiy · Alexander K. Belyaev
Editors

Mechanics and Control of Solids and Structures

 Springer

Editors

Vladimir A. Polyanskiy 
Institute for Problems in Mechanical
Engineering
Russian Academy of Sciences
St. Petersburg, Russia

Alexander K. Belyaev 
Institute for Problems in Mechanical
Engineering
Russian Academy of Sciences
St. Petersburg, Russia

ISSN 1869-8433

ISSN 1869-8441 (electronic)

Advanced Structured Materials

ISBN 978-3-030-93075-2

ISBN 978-3-030-93076-9 (eBook)

<https://doi.org/10.1007/978-3-030-93076-9>

© The Editor(s) (if applicable) and The Author(s), under exclusive license to Springer Nature Switzerland AG 2022

This work is subject to copyright. All rights are solely and exclusively licensed by the Publisher, whether the whole or part of the material is concerned, specifically the rights of translation, reprinting, reuse of illustrations, recitation, broadcasting, reproduction on microfilms or in any other physical way, and transmission or information storage and retrieval, electronic adaptation, computer software, or by similar or dissimilar methodology now known or hereafter developed.

The use of general descriptive names, registered names, trademarks, service marks, etc. in this publication does not imply, even in the absence of a specific statement, that such names are exempt from the relevant protective laws and regulations and therefore free for general use.

The publisher, the authors and the editors are safe to assume that the advice and information in this book are believed to be true and accurate at the date of publication. Neither the publisher nor the authors or the editors give a warranty, expressed or implied, with respect to the material contained herein or for any errors or omissions that may have been made. The publisher remains neutral with regard to jurisdictional claims in published maps and institutional affiliations.

This Springer imprint is published by the registered company Springer Nature Switzerland AG
The registered company address is: Gewerbestrasse 11, 6330 Cham, Switzerland

Preface

The Institute for Problems in Mechanical Engineering of the Russian Academy of Sciences, abbreviated as IPME RAS, was established in September 1986 as the Leningrad branch of the Institute of Mechanical Engineering of the USSR Academy of Sciences named after academician A. A. Blagonravov.

In 1991, according to the Decree of the Presidium of the USSR Academy of Sciences, the Leningrad branch of the Blagonravov Institute of Mechanical Engineering of the USSR Academy of Sciences was renamed into the Institute for Problems in Mechanical Engineering of the USSR Academy of Sciences. This was the beginning of a new stage of the institute as an independent institution.

In Leningrad—St. Petersburg there were schools of scientists and engineers in mechanics, which originated from the Bernoulli brothers and Leonard Euler, who worked in St. Petersburg for a long time. In the 20th century, all these schools were at universities. The Institute for Problems of Mechanical Engineering of the Russian Academy of Sciences became the first scientific academic institute whose main activity was solving the fundamental problems of mechanics and engineering science.

The organizer and the first director of the IPME RAS from 1986 to 2002 was Doctor of Technical Sciences, Prof. Vladimir Pavlovich Bulatov.

From the very beginning of the foundation, the Institute was able to attract outstanding engineers and scientists with the closest ties to industry. The Institute laboratories were headed by the leading scientists, heads of the design calculation departments and research scientific departments of large industrial corporations who were also engaged in recruiting the scientific staff. As a result, a creative and truly innovative atmosphere was developed at the Institute, many original approaches to solving problems of theoretical and applied mechanics, engineering science and control in technical systems have been formulated.

Now the IPME RAS (also known as IPMash) includes 17 structural units:

1. Laboratory for Mathematical Modeling of Wave Processes (Head, Corresponding Member of RAS Dmitry A. Indeitsev).

2. Department of Extreme States of Materials and Structures (Head, Corresponding Member of the Russian Academy of Sciences Yuri V. Petrov).
3. Laboratory of Mechatronics (Head, Corresponding Member of the Russian Academy of Sciences Alexander K. Belyaev).
4. Laboratory "Discrete Models in Mechanics" (Head, Corresponding Member of the Russian Academy of Sciences Anton M. Krivtsov).
5. Laboratory of Mechanics of Nanomaterials and Theory of Defects (Head, Professor Mikhail Yu. Gutkin).
6. Laboratory of Mathematical Methods in Mechanics of Materials (Head, Professor Alexander B. Freidin).
7. Laboratory of Numerical Models of Mechanics of Materials and Structures (Head, Professor Sergei V. Petinov).
8. Laboratory of Micromechanics of Materials (Head, Professor Alexey V. Porubov).
9. Laboratory of Friction and Wear (Head, Professor Elena B. Sedakova).
10. Laboratory of Vibrational Mechanics (Head, Dr. Leonid I. Blekhman).
11. Laboratory of Physics of Fracture (Head, Professor Yuri I. Meshcheryakov).
12. Laboratory of Material Surfaces Modification (Head, Dr. Viacheslav G. Kuznetsov)
13. Laboratory of Structural and Phase Transformations in Condensed Matter (Head, Professor Sergey A. Kukushkin).
14. Laboratory for Control of Complex Systems (Head, Professor Alexander L. Fradkov).
15. Laboratory of Reliability Analysis Methods (Head, Professor Boris P. Kharlamov).
16. Laboratory of Intelligent Electromechanical Systems (Head, Professor Andrey E. Gorodetsky).
17. Laboratory for Applied Research (Head Dr. Yuri A. Yakovlev).

The advanced research areas of the institute include dynamics, strength and reliability of machines and structures, among them marine, arctic and underwater ones, operating in extreme conditions, as well as vibration and stability, wave and vibroimpact processes, theory and methods of control processes in complex physical and technical systems. Other directions are focused on mechanics of materials, thermodynamics and kinetics of transient processes in nanomaterials and smart materials, phase transitions and structural defects, nano- and microtribology, coupled problems of chemo-mechanics and interdisciplinary problems of mechanics.

In the framework of these directions the following approaches were developed:

- the experimental technique for visualizing kinematic modes of material deformation based on the use of liquid crystals.
- vibrational mechanics—a new branch of mechanics which offers a general mechanical and mathematical approach to describing the effect of vibration on nonlinear mechanical systems and media.
- mechanics of discrete media—a new branch of mechanics focusing on mechanical and physical phenomena for which discreteness of a medium is important.

- the hydrodynamic theory of friction during the ordering of the molecular structure of the lubricant on rubbing surfaces.
- new ion-plasma technologies for controlling the structure and physical-mechanical properties of materials for changing the surface properties of materials, creating superhard coatings, carbon nano- and microstructures and powdered composites.
- experimental and theoretical study of multiscale dynamic fracture of solids, shock-wave propagation in solids.
- the correlation method for determining the abrasive wear of a rubbing part which does not interfere with the operation of the machine.
- new algorithms for controlling transport robots in sliding modes, adaptive synchronization of interacting subsystems.
- mathematical models of wave processes in continuous media with inclusions.
- theoretical models of plasticity and fracture in nanostructured materials consisting of nanocrystallites and grain-boundary phase, which reveal the leading role of interfaces in the processes of inhomogeneous plastic deformation in ultra-strong nanostructured metals, ceramic and nanocomposites.
- new approaches to the description of phase transitions and stress-affected chemical reactions.
- the new method of growing defect-free nanoscale silicon carbide films on silicon proposed theoretically and implemented experimentally.
- the theory of condensation of multicomponent films from vapor and liquid phases, accompanying the growth of a new phase.
- the laboratory for the study of neuro-feedback processes.
- the platform-independent software environment for conducting experiments of any complexity in the electroencephalography paradigm of neuro-feedback. Clinical trials of software completed.
- the unique laboratory stand for development and research of algorithms for controlling electric power networks in normal operation and emergency situations.

The leading researchers of the institute are actively involved in the educational process, forming scientific schools at the universities of St. Petersburg, including: Faculty of Mathematics and Mechanics of St. Petersburg State University, Physics and Mechanics Institute of the Peter the Great St. Petersburg Polytechnic University, ITMO University, St. Petersburg State University of Aerospace Instrumentation, Baltic State Technical University and others.

The foundations laid in the creation of the IPME RAS allow our Institute to remain the center of attraction for scientists, to conduct a variety of scientific research in the most seemingly unrelated directions, but having common fundamental roots in natural sciences. This is evidenced by the book offered to the reader.

St. Petersburg, Russia
October 2021

Vladimir A. Polyanskiy
Alexander K. Belyaev

Contents

1	Mathematical Modeling of Some Diffusion and Thermomechanical Problems	1
	Andrei K. Abramian, Sergey A. Vakulenko, Dmitry A. Indeitsev, Mikhail V. Khovaiko, and Alexander S. Nemov	
1.1	Introduction	2
1.2	Statement of the Diffusion Problem	2
1.3	General Properties of Model	4
1.4	Particular Solutions	6
1.4.1	Reduction to Nonlinear Oscillator Equation	6
1.4.2	Analysis of Nonlinear Equation	6
1.5	Simplified Problem	8
1.6	Eigenfunctions of Linearized Problem	9
1.7	Fourier Decomposition	10
1.8	Peculiarities of the Interphase Boundary Movement in Thawing/Freezing Problems	11
1.9	Conclusion	20
	References	20
2	On an Attraction Basin of the Generalized Kapitza's Problem	23
	Alexander K. Belyaev, Nikita F. Morozov, Petr E. Tovstik, Tatiana M. Tovstik, and Tatiana P. Tovstik	
2.1	Introduction	23
2.2	Classical Model of the Kapitza's Pendulum	25
2.2.1	Stability of the Kapitza's Pendulum	25
2.2.2	Attraction Basin of the Solution of the Kapitza's Pendulum	26
2.2.3	Attraction Basins for Kapitza's Problem at Random Excitation	28
2.2.4	A Kapitza's Pendulum on the Flexible Support	32
2.3	Generalized Kapitza's Pendulum. Flexible Rod	33
2.3.1	Conditions of Stability of the Vertical Position	35

2.3.2	On the Attraction Basins for a Flexible Rod	37
2.3.3	Lagrange Equations of the Second Kind	39
2.3.4	Attraction Basins for Inextensible Rod	42
2.3.5	The Influence of Longitudinal Waves on Stability of the Vertical Position and Attraction Basins of the Extensible Rod	43
2.4	Discussion	45
2.4.1	Conclusions	47
	References	47
3	Application of Micropolar Theory to the Description of Ultrathin Liquid Layers	49
	Nikolay M. Bessonov and Ksenia P. Frolova	
3.1	Introduction	50
3.2	Viscosimetric Experiments	51
3.2.1	Squeeze of Liquid by Disks	51
3.2.2	Flow in Capillar	54
3.2.3	Blow of Liquid Layer Off Surface	55
3.2.4	Liquid Layer Between Two Moving Plates	57
3.3	Experiments and Development of Fluid Theory	58
3.4	Principles of Micropolar Fluid Theory	60
3.5	Boundary Conditions	62
3.6	Theory of Micropolar Fluid and Viscosimetric Experiments	64
3.6.1	Squeeze of Liquid by Disks	64
3.6.2	Flow in Capillar	66
3.6.3	Blow of Liquid Layer Off Surface	67
3.6.4	Liquid Layer Between Two Moving Plates	68
3.7	Conclusions	69
	References	72
4	Research on Vibration Processes and Devices: New Results and Applications	75
	Leonid I. Blekhman, Eugen B. Kremer, and Vladislav B. Vasilkov	
4.1	Introduction	76
4.2	Fundamental Principles of Research: Theoretical and Applied Developments	77
4.3	Development of Vibrational Mechanics and Vibrational Rheology Approaches	77
4.4	Studies on the Problem of Stochastic Resonance	79
4.5	Self-synchronization Phenomenon: Development of the Theory and New Applications	80
4.6	Vibrational Displacement: Theory, Applications, Energy Saving	81
4.7	New Nonlinear Vibration Effects: Research and Applications	83
4.8	New Ways of Damping Harmful Vibrations	87

4.9	Conclusions	88
	References	88
5	Micromechanics of Strength and Plasticity in Nanostructured Materials	91
	Sergey V. Bobylev, Mikhail Yu. Gutkin, Alexander G. Sheinerman, and Nikolay V. Skiba	
5.1	Introduction	91
5.2	Deviations from the Classical Hall-Petch Law	92
5.3	Homo- and Heterogeneous Nucleation of Dislocations in NCMs	94
5.4	Grain Boundary Sliding and Mechanisms of Its Accommodation	97
5.5	Rotational Deformation in NCMs	99
5.6	Deformation Twinning in UFG and NC Materials	100
5.7	Deformation-Induced Grain Growth and Refinement in UFG and NC Materials	101
5.8	Interaction Between Deformation and Fracture Processes in NCMs	104
5.9	Conclusions	107
	References	107
6	Solution of Dynamic Equations of Plane Deformation for Nonlinear Model of Complex Crystal Lattice	115
	Anatolii N. Bulygin and Yurii V. Pavlov	
6.1	Introduction	115
6.2	Basic Equations of Nonlinear Model	116
6.3	Solution of Dynamic Macrofield Equations	118
6.4	Complex Representation of General Solution of Macrofield Equations	121
6.5	Solution of Dynamic Microfield Equations	124
6.6	Uniform Movement of the Constant Localized Force Over the Surface of the Half-Space	126
	6.6.1 Subsonic Speed of Movement	126
	6.6.2 Transonic Speed of Movement	130
	6.6.3 Supersonic Speed of Movement	133
6.7	Conclusion	134
	References	135
7	Effective Directions of Development of the Method of Artificial Bases for Evaluating the Volumetric Wear Resistance of Materials	137
	Leonid V. Efremov	
7.1	Introduction	137
7.2	Determination of Linear Wear Resistance Based on the Formation of a Hole with a Simple and Precise Tool	138

7.3 Justification of Simplified Algorithms for Estimating Volumetric Wear Resistance 141

7.4 Modeling of the Dependence of Wear Parameters on the Hardness of the Material 145

References 148

8 Local, Modal and Shape Control Strategies for Active Vibration Suppression of Elastic Systems: Experiment and Numerical Simulation 151

Aleksandr V. Fedotov, Alexander K. Belyaev, Vladimir A. Polyanskiy, and Nina A. Smirnova

8.1 Introduction 152

8.2 Theoretical Background 153

8.2.1 Local Method 153

8.2.2 Modal Method 153

8.2.3 Shape Control Method 155

8.3 Experimental Setup 156

8.4 Sensor and Actuator Placement 157

8.4.1 Local and Modal Methods 157

8.4.2 Shape Control Method 158

8.5 Finite Element Modeling 160

8.6 Design of the Transfer Functions 161

8.7 Comparison of the Results 164

8.8 Conclusion 167

References 168

9 Speed-Gradient Method in Mechanical Engineering 171

Alexander L. Fradkov and Boris Andrievsky

9.1 Introduction 171

9.2 Speed-Gradient Method 172

9.3 Control of Energy and Nonlinear Vibrations 175

9.4 Control of Technical Systems 179

9.4.1 Control of Vibrating Machines 179

9.4.2 Control of Vehicles 181

9.4.3 Control of Power System 184

9.4.4 Control of Gyroscopes 185

9.4.5 Control of Induction Motors 187

9.5 Conclusions 190

References 190

10 FEM-simulations of a Chemical Reaction Front Propagation in an Elastic Solid with a Cylindrical Hole 195

Alexander B. Freidin, Igor K. Korolev, and Sergey P. Aleshchenko

10.1 Introduction 195

10.2 Chemical Affinity Tensor and Chemical Reaction Front Kinetics 197

10.3	Numerical Simulations	200
10.3.1	Axially Symmetric Problem	201
10.3.2	The Hole Under Uniaxial Tension or Compression	202
10.4	Conclusions	204
	References	207
11	Diffusion in Media with Spheroidal Pores	209
	Ksenia P. Frolova, Nikolay M. Bessonov, and Elena N. Vilchevskaya	
11.1	Introduction	209
11.2	Problem Statement	211
11.3	Effective Properties of a Porous Material	212
11.3.1	Effective Diffusivity Properties	212
11.3.2	Effective Elastic Properties	214
11.4	Diffusion Problem	215
11.4.1	Constitutive Equations for the Flux	215
11.4.2	Elasticity Problem Due to Mass Transport	217
11.5	Results	219
11.5.1	Diffusion Process in Material Initially Containing Inhomogeneities	219
11.5.2	Pore Formation During the Diffusion Process	221
11.6	Conclusions	223
	References	224
12	Divergence Method for Stability Study and Control of Dynamical Systems	227
	Igor B. Furtat and Pavel A. Gushchin	
12.1	Introduction	227
12.2	Instability Conditions	229
12.3	Extension of Bendixson and Bendixson–Dulac Theorems to n th Dimensional Systems	230
12.4	Stability Conditions	230
12.4.1	Stability of Linear Systems	233
12.5	Control Law Design	233
12.6	Conclusions	234
	References	235
13	Development of Situational Control Methods for a Group of Interacting Robots	237
	Andrey E. Gorodetskiy, Irina L. Tarasova, Vugar G. Kurbanov, Andrey Yu. Kuchmin, and Boris A. Kulik	
13.1	Logical and Mathematical Method of Making Behavioral Decisions	238
13.1.1	Stages of the Formation of Behavioral Decisions	238
13.1.2	Fuzzification Data and Forming Images	238
13.1.3	The Adoption of Reflective Solutions	242

- 13.1.4 Informed Decision-Making 244
- 13.2 Principles of Forming the Language of Sensation
for Decision-Making in the Central Nervous System
of SEMS 246
 - 13.2.1 Algorithm of Formation of the Language
of Sensations of the Robot 247
 - 13.2.2 Quantization of the Surrounding Space 248
 - 13.2.3 Fuzzification of Sensory Information 249
 - 13.2.4 Image Formation in the Display of the Surrounding
Space 251
 - 13.2.5 Formation of Images by Combining Images
from Different Senses 252
- 13.3 Problems with Secure Control of SEMS Group 253
 - 13.3.1 The Principles of Safe Control 254
 - 13.3.2 Managing the Safe Movement of the Group
Through the Intersection, Taking into Account
the Rules of Passage 256
 - 13.3.3 Control the Group’s Safe Movement Based
on Priorities 257
- 13.4 Using Binary Relationships in Decision-Making 258
 - 13.4.1 The Tasks of Situational Control of a Group
of Dynamic Objects 259
 - 13.4.2 Mathematical Methods for Using Binary Relations
in Decision 260
- References 263
- 14 Boundary-Value Problems for Defects in Nanoscale
and Nanocomposite Solids 267**

Mikhail Yu. Gutkin, Anna L. Kolesnikova, Alexey E. Romanov,
and Alexander G. Sheinerman

 - 14.1 Introduction 267
 - 14.2 The Method of Virtual Surface Defects in the Solution
of Boundary-Value Problems of the Theory of Defects 268
 - 14.3 Dislocations 269
 - 14.3.1 Straight Dislocations 269
 - 14.3.2 Dislocation Loops 276
 - 14.4 Disclinations 279
 - 14.5 Inclusions 281
 - 14.6 Conclusions 283
 - References 284
- 15 On Imbedded Alternating Renewal Process for a Diffusion
Semi-Markov Process on Interval with Unattainable
Boundaries 291**

Boris P. Harlamov

 - 15.1 Continuous Semi-Markov Processes 291

15.1.1	Space of Continuous Functions	292
15.1.2	Regeneration Times for a Family of Measures (P_x)	293
15.1.3	Semi-Markov Transition Generating Functions	294
15.2	Diffusion Semi-Markov Processes	295
15.2.1	Alternating Renewal Process	297
	References	301
16	On Dynamic Fracture of One-Dimensional Elastic Chain	303
	Nikita A. Kazarinov, Yuri V. Petrov, and Aleksey A. Gruzdkov	
16.1	Introduction	304
16.2	Static Preload with Abrupt Link Failure	304
16.2.1	Analytic Solution of the Chain Problem	304
16.2.2	Forced Chain Oscillations, Inhomogeneous System of Equations	308
16.3	Results. Comparison with Solutions for an Elastic Rod	311
16.4	Conclusion	313
	References	314
17	Vibrational Mechanics of Rotating Mechanisms: Modification of Low-Frequency Behaviour by High-Frequency Excitations	315
	Eugen B. Kremer	
17.1	Introduction	315
17.1.1	Motivation	316
17.1.2	Direct Simulation is Not Always the Best Way	317
17.1.3	Concept of Vibrational Mechanics	317
17.2	Rotating Mechanism with Fast Excitations	318
17.2.1	Kinematics of the Mechanism	319
17.2.2	Lagrange Equation	320
17.3	Vibro-Mechanical Transformation to the Slow System	321
17.3.1	Averaging	321
17.3.2	The Case of Periodical Excitation	322
17.3.3	The Case of Stochastic Excitation	323
17.3.4	Discussion	324
17.4	Low-Frequency Behaviour of Rotating Mechanisms	324
17.4.1	Equilibrium Position of the Slow Motion	324
17.4.2	Eigenfrequency of the Slow Motion Near an Equilibrium Position	325
17.4.3	Example of the Global Low-Frequency Behaviour of a Rotating Mechanism	326
17.5	Application to the Centrifugal Pendulum Absorber	329
17.6	Conclusion	332
	References	333

18 SiC/Si as a New Platform for Growth of Wide-Bandgap Semiconductors 335
 Sergey Kukushkin, Andrey Osipov, and Alexey Redkov

18.1 Introduction 335

18.2 Formation of SiC by the Method of Coordinated Substitution of Atoms 338

18.2.1 Growth Technique 338

18.2.2 Main Properties of the Obtained SiC Layers 339

18.2.3 Some Applications of the Method of Coordinated Substitution of Atoms for the Formation of Coatings on Various Materials (Porous Silicon, Al₂O₃, Graphite) 345

18.3 Growth of Thin Films and Heterostructures on SiC/Si Substrates 347

18.3.1 III-Nitrides (GaN, AlN, AlGaN) 348

18.3.2 Methods for Separating III-N Epitaxial Heterostructures from a Silicon Substrate 358

18.3.3 Growth of A^{II}B^{VI} and Other Semiconductor Compounds 358

18.4 Growth of Whisker Semiconductor Nanocrystals on SiC/Si Substrates 362

18.4.1 Arsenides (GaAs, AlGaAs, InGaAs, InAs) 362

18.4.2 III-Nitrides (GaN, InN) 364

18.5 Theoretical Approaches Developed to Describe the Growth of Multicomponent Semiconductor Compounds 365

18.5.1 Growth Mechanisms of Multicomponent Semiconductors 365

18.5.2 Growth Mechanisms and Formation of Pores in Multicomponent Crystals 366

18.6 Conclusion 367

References 367

19 Slushing in a Vertical Cylinder in the Presence of a Porous Layer 375
 Nikolay G. Kuznetsov and Oleg V. Motygin

19.1 Introduction 375

19.2 Statement of the Problem 376

19.3 Separation of Variables 379

19.4 Properties of the Eigenvalues ν_n and ω_n 380

19.5 Inverse Problems 383

19.6 Concluding Remarks 384

References 385

20 Global Stability Boundaries and Hidden Oscillations in Dynamical Models with Dry Friction 387
 Nikolay V. Kuznetsov, Elizaveta D. Akimova,
 Elena V. Kudryashova, Olga A. Kuznetsova,
 Mikhail Y. Lobachev, Ruslan N. Mokaev, and Timur N. Mokaev

20.1 Introduction 388
 20.2 Global Stability 388
 20.3 Oscillations 390
 20.4 Examples 393
 20.4.1 Watt Governor Model 393
 20.4.2 Keldysh Model with One Degree of Freedom 397
 20.4.3 Keldysh Model with Two Degrees of Freedom 399
 20.5 Conclusion 407
 References 408

21 Strain Behavior of Aluminum Alloys Under Dynamic Compression and Tensile 413
 Yuri I. Meshcheryakov, Grigory V. Konovalov,
 Natali I. Zhigacheva, Alexander K. Divakov,
 and Alexey F. Nechunaev

21.1 Introduction 414
 21.2 Experimental Technique 416
 21.3 Experimental Results and Analysis 427
 21.3.1 Structural Instability and Spall Strength 427
 21.3.2 Structural Instability and Penetration 431
 21.4 Spall Strength and Resistance to High Velocity Penetration 432
 21.5 Microstructural Investigations 434
 21.5.1 1561 Aluminum Alloy 434
 21.5.2 1565 Aluminum Alloy 435
 21.6 On the Resonance Excitation of Mesoscale 437
 21.7 Numerical Simulation 441
 21.8 Conclusion 447
 References 452

22 Equilibrium Structures and Flows of Polar and Nonpolar Fluids in Nanochannels 455
 Leonid V. Mirantsev and Andrei K. Abramyan

22.1 Introduction 456
 22.2 Simulation Details 458
 22.3 Results of Simulations and Discussion 461
 22.3.1 Equilibrium Structures Inside Carbon Nanotubes 461
 22.3.2 Fluid Flows Inside Carbon Nanotubes 470
 22.3.3 Equilibrium Fluid Structures Between Different Bounding Substrates 479

22.3.4 The Couette Flows of Polar Water Molecules and Nonpolar Argon Atoms Between Different Bounding Substrates 481

22.4 Conclusion 485

References 486

23 Fatigue Assessment of Structures—Problems in Current Methodology 489

Sergei V. Petinov and Ruslan V. Guchinsky

23.1 Introduction 489

23.2 Stress-Life Approaches 490

23.3 Strain-Life Criteria-Based Approach 495

23.4 Conclusions 499

References 499

24 Discrete Thermomechanics: From Thermal Echo to Ballistic Resonance (A Review) 501

Ekaterina A. Podolskaya, Anton M. Krivtsov, and Vitaly A. Kuzkin

24.1 Introduction 501

24.2 Nomenclature 503

24.3 Transient Processes 503

24.3.1 Infinite Harmonic Crystal 505

24.3.2 The Influence of Finiteness: Thermal Echo 511

24.3.3 The Influence of Dissipation on the Transition to Thermal Equilibrium 513

24.3.4 The Influence of Nonlinearity on Transient Thermal Processes 514

24.4 Heat Transfer 515

24.4.1 Scalar Lattices 517

24.4.2 Polyatomic Lattices 521

24.4.3 The Influence of Nonlinearity 523

24.5 Thermoelasticity: Ballistic Resonance in FPUT Chain 524

24.6 Concluding Remarks 528

References 529

25 Behavior of Pipeline Steels in Gaseous Hydrogen-Containing Mixtures 535

Vladimir A. Polyanskiy, Ksenia P. Frolova, Yulia S. Sedova, Yuriy A. Yakovlev, and Alexander K. Belyaev

25.1 Introduction 535

25.2 Experimental Methods 537

25.3 Influence of Hydrogen on the Mechanical Properties of Gas Pipelines Metals 538

25.3.1 Tensile Tests 539

25.3.2 Fractography Analysis 544

25.3.3 Fatigue Crack Growth Test 545

- 25.3.4 Fatigue Life 549
- 25.3.5 Indentation Tests 551
- 25.4 Conclusions 551
- References 552
- 26 Dynamic Model of Reliability and Survival in Big Data**
- Analysis** 557
- Vladimir A. Prourzin and Sofia S. Rasova
- 26.1 Introduction 558
- 26.2 Problem Statement 558
- 26.3 The Dynamic Reliability Model 560
 - 26.3.1 Example 1 561
 - 26.3.2 Example 2 562
 - 26.3.3 Self-similarity Property 562
 - 26.3.4 Model Equivalence and the Basic Dynamic Reliability Model 562
- 26.4 Multidimensional Models 564
 - 26.4.1 Example. The Model of Failure of Electrical Machines Owing to Heat Ageing of Insulation 565
- 26.5 Building a Dynamic Reliability Model Based on Experimental Data 566
 - 26.5.1 Example 3 568
- 26.6 Experimental Verification of the Dynamic Reliability Model 569
- 26.7 Conclusion 570
- References 571
- 27 Using the Wear Model of Polymer Composites Based on Polytetrafluoroethylene to Determine the Filling Efficiency of Matrix** 573
- Elena B. Sedakova and Yuri P. Kozyrev
- 27.1 Introduction 573
- 27.2 Structural Model of Polymer Composites Based on Polytetrafluoroethylene 574
- 27.3 Composites Wear Model 584
- References 587
- 28 Hydrodynamic Mechanism of Temperature Gradient Formation in Microfluidic Nematic Devices** 589
- Izabela Sliwa and Alex V. Zakharov
- 28.1 Introduction 589
- 28.2 Shear-Driven Flow Regimes in Microfluidic Nematic Devices: Tumbling and Laminar 592
 - 28.2.1 Formulation of the Balance of the Linear Momentum, Torque, and Conductivity Equations for Microsized Nematic Fluids 593

- 28.2.2 Numerical Results for the Relaxation Regimes
in HAN Channel 597
- 28.3 A Role of a Flow in a Temperature Gradient Formation
Across a HAN Channel 605
- 28.4 Conclusion 610
- References 610
- 29 Signatures of Transient Purely Ballistic Heat Conduction:
Theory and Experimental Investigation 613**
Aleksei A. Sokolov, Wolfgang H. Müller, Anton M. Krivtsov,
and Alexey V. Porubov
- 29.1 Introduction 613
- 29.2 Divergence of Heat Conductivity for Transient Purely
Ballistic Heat Conduction 616
- 29.3 Experimental Techniques 619
 - 29.3.1 Raman Thermometry 620
 - 29.3.2 Scanning Thermal Microscopy 625
- 29.4 Conclusions 630
- References 631
- 30 A Randomized Approach to Estimate Acoustic Strength
of Water 633**
Grigory A. Volkov, Aleksey A. Gruzdkov, and Yuri V. Petrov
- 30.1 Introduction 633
- 30.2 Pulse-Induced Cavitation 634
 - 30.2.1 Incubation Time Criterion 635
 - 30.2.2 Sign-Perturbed Sums Method 636
- 30.3 Ultrasonic Acoustic Cavitation 637
- 30.4 Conclusions 639
- References 639

Chapter 1

Mathematical Modeling of Some Diffusion and Thermomechanical Problems



Andrei K. Abramian, Sergey A. Vakulenko, Dmitry A. Indeitsev,
Mikhail V. Khovaiko, and Alexander S. Nemov

Abstract In this paper, we consider the mathematical methods which can be applied for the solution of two mechanical problems which have varying in space and time parameters, and some of them are described by the hyperbolic equations. The first problem is an interaction between the deformation waves and the diffusion process in a rigid solid. The main effect accompanying the transport of impurity in the material is a reduction of its initial rigidity parameters. Unlike the existing works, in our paper, an analytical approach is applied to the analysis. Considering the interaction of impurity waves and deformation waves, we obtained a number of solutions which can be used to develop acoustic diagnostics of defects in a material. For the one-dimensional case, analysis is given by taking into account the influence of a changing stress state of the environment. The second problem is a mathematical modeling of the thermomechanical processes in soils. We consider a plane thermal state of the soil surrounding the gas-main pipeline.

Keywords Thermodynamics · Phase transitions · Phase interface boundary · Permafrost · Enthalpy diagram · Finite element method · Mathematical modeling · Subsidence and heaving of soils

A. K. Abramian (✉) · S. A. Vakulenko
Institute for Problems in Mechanical Engineering RAS, V.O., Bolshoy pr., 61, St. Petersburg
199178, Russia
e-mail: vakulenfr@mail.ru

D. A. Indeitsev · M. V. Khovaiko · A. S. Nemov
Peter the Great St. Petersburg Polytechnic University, Politechnicheskaya, 29, St. Petersburg
195251, Russia
e-mail: hovajko_mv@spbstu.ru

A. S. Nemov
e-mail: nemov_as@spbstu.ru

1.1 Introduction

In this paper, we consider the mathematical methods which can be applied for the solution of two mechanical problems. Both problems are nonlinear. The first problem is an interaction between the deformation waves and diffusion process in a rigid solid. We continue the solution of diffusion problem in a strained material, which was presented in [1]. An analysis of that problem leads us to complicated systems of hyperbolic and parabolic nonlinear equations. The second problem is a mathematical modeling of the thermomechanical processes in soils. It is nonlinear because of the boundary conditions on the moving boundaries. In this problem, the behavior of the media near the moving wavefront or boundary is of special interest. Localized solutions for the first problem were studied in [1] and for similar hydroelastic problems in [2–4]. Our main results are as follows. By a new model of diffusion in a strained material, we find solutions describing the propagation of linear and periodic perturbations. The main effect accompanying the transport of impurity in material is a reduction of its initial rigidity parameters. Unlike the existing works, in our paper, an analytical approach is applied to the analysis. As a result, we obtained a number of solutions which can be used to develop acoustic diagnostics of defects in a material. For the one-dimensional case, analysis is given by taking into account the influence of a changing stress state of the environment. The interest in the second problem is caused by the fact that permafrost as a natural phenomenon is widespread in a large area of the globe, covering more than 60% of the territory of Russia. Recently, due to the active construction of buildings and structures in permafrost conditions, the problem of designing foundations and underground utilities has gained importance in view of the possible subsidence or heaving of the soil as a result of freezing or thawing [8–10]. Those phenomena are caused not only by the seasonal fluctuations in the temperature, depth of snow cover, and intensity of solar radiation, but also by the climatic changes and industrial human activities [11, 12]. Mathematical modeling of the thermomechanical processes in soils makes it possible to develop reliable and durable structures and to avoid the severe consequences of accidents. In view of the complexity of these thermomechanical calculations, it is advisable to use various computational methods [13–15]. The most perfect method for thermal state calculations of a solid is the finite element method [8, 13, 14]. The results of the application of this method are presented in this paper.

1.2 Statement of the Diffusion Problem

We will consider a solution of diffusion problem in a strained material which has two components. For example, the diffusing components can be solute atoms and vacancies. We introduce the one-dimensional model of two-component continuum, which allows us to describe both the hydrogen diffusion and its interaction with the

material, and therefore, to find the equation of state for hydrogen-containing media. The first component is represented by the crystal lattice of the initial material including stationary hydrogen atoms embedded (attached) in chemical bonds between atoms, the second component is represented by free mobile hydrogen atoms dissolved in the material. The specific feature of the model is that some of the hydrogen atoms are embedded in existing atomic bonds, breaking them and creating new bonds which are significantly less strong than the initial ones. In our paper, the problem of interference between the wave of deformation and wave of impurity has been considered and solved with the help of an analytical approach. For one-dimensional (1D) case, the solutions, which take into account possible variations of the strain state of the considered medium, have been found and analyzed. We establish the following basic relation: the deformation ϵ , induced by a localized perturbation of impurity density ρ_1 , is proportional to the product of the inverse speed V^{-1} of propagation of that impurity perturbation, the space derivative of logarithm of the impurity density ρ_1 and the diffusion coefficient of that impurity \bar{D} , i.e.

$$\epsilon = \bar{D}V^{-1} \frac{d \ln \rho_1}{dx}, \quad (1.1)$$

where for small concentrations ρ_1 the speed V is defined by the relation

$$V^2 \approx E_0(1 + \kappa \bar{R})^{-1}, \quad (1.2)$$

where $\kappa = (E_0/E_1 - 1)/m_1 > 0$

E_0 is Young's modulus of pure material in the absence of hydrogen, E_1 is Young's modulus of material with all bonds occupied by hydrogen, m_1 is the mass of embedded atoms; \bar{R} is the impurity perturbation. The velocity V is always less than the sound velocity in that material. So, finally, the problem can be described as follows:

$$\frac{\partial \sigma}{\partial x} = \frac{\partial^2 u}{\partial t^2}, \quad (1.3)$$

$$\sigma = \frac{E_0 \epsilon}{1 + \kappa \rho_1}, \quad (1.4)$$

$$\frac{\partial \rho_2}{\partial t} - \frac{\partial}{\partial x} \left[D(\epsilon) \left(\frac{\partial \rho_2}{\partial x} + \eta \rho_2 \frac{\partial^2 u}{\partial t^2} \right) - \rho_2 \frac{\partial u}{\partial t} \right] = -\alpha \rho_2, \quad (1.5)$$

$$\frac{\partial \rho_1}{\partial t} + \frac{\partial}{\partial x} \left[\rho_1 \frac{\partial u}{\partial t} \right] = \alpha \rho_2, \quad (1.6)$$

where

1. $\rho_1(x, t)$ is the density of impurity particles of the first component ($x \in [0, L]$ and $t \geq 0$) connected with the main structure;
2. $\rho_2(x, t)$ is the density of the second component;

3. $u(x, t)$ is the deviation of the first component;
4. $\epsilon = \frac{\partial u}{\partial x}$ is the deformation of the first component;
5. $J(x, t) = \alpha \rho_2(x, t)$ is the source term, which determines the exchange between the first and the second components. The constant α can have any sign.

Here, η, κ, E_0 are positive constant parameters. System (1.3)–(1.6) is complicated and we first consider particular solutions of that system describing propagating waves and periodic structures (patterns) in space. Below we assume that

$$D(\epsilon) = D_0 + D_1\epsilon,$$

where $D_0 > 0$, D_1 are constants, and ϵ is small, so, $D(\epsilon) > 0$ (to avoid negative diffusion coefficients). Equation (1.6) does not contain a diffusion term. To take into account diffusion effects, we can modify it as follows:

$$\frac{\partial \rho_1}{\partial t} + \frac{\partial}{\partial x} \left[\rho_1 \frac{\partial u}{\partial t} \right] = \bar{D} \frac{\partial^2 \rho_1}{\partial x^2} + \alpha \rho_2. \quad (1.7)$$

The system of Eqs. (1.3), (1.4), (1.5) and (1.7) should be complemented by the boundary conditions:

$$u(x, t)|_{x=0} = 0, \quad \sigma(x, t)|_{x=L} = g(t), \quad (1.8)$$

$$D(u_x) \left(\frac{\partial \rho_2}{\partial x} + \eta \rho_2 \frac{\partial^2 u}{\partial t^2} \right) - \alpha \rho_2|_{x=L} = 0, \quad (1.9)$$

$$\left(\frac{\partial \rho_1}{\partial x} \right)|_{x=0} = 0, \quad \left(\rho_1 \frac{\partial u}{\partial t} - \bar{D} \frac{\partial \rho_1}{\partial x} \right)|_{x=0, L}. \quad (1.10)$$

We set as well standard initial conditions at $t = 0$, however, we don't specify here the choice of these conditions. We also assume that at the initial moment of time, the density distribution is localized in a certain area, for example, it has the form of a Gaussian distribution.

1.3 General Properties of Model

The model is correctly posed, solutions exist for all $t > 0$. Moreover, they conserve positivity: if $\rho_1(x, 0) > 0$ and $\rho_2(x, 0) > 0$ then $\rho_1(x, t) > 0$ and $\rho_2(x, t) > 0$. It can be shown by the standard a priori estimates and the maximum principle [5–7]. Throughout below we suppose that $\rho_j(x, t) \geq 0$.

The total impurity masses M_j is defined by

$$M_j(t) = \int_0^L \rho_j(x, t) dx.$$

Let us compute dM_2/dt . By integrating (1.4) over x , we have

$$\frac{dM_2}{dt} = -\alpha M_2 + R(x, t)|_{x=0}^{x=L},$$

where

$$I(x, t) = D(u_x) \left(\frac{\partial \rho_2}{\partial x} + \eta \rho_2 \frac{\partial^2 u}{\partial t^2} \right).$$

We observe that $I(0, t) = 0$. In fact, condition (1.10) implies that $\frac{\partial \rho_2}{\partial x} = 0$ at $x = 0$ and (1.8) shows that $\frac{\partial^2 u(0, t)}{\partial t^2} = 0$ and thus $I(0, t) = 0$. Condition (1.9) gives that $I(L, t) = 0$. Therefore

$$\frac{dM_2}{dt} = -\alpha M_2. \quad (1.11)$$

In a similar way, one can show that

$$\frac{dM_1}{dt} = \alpha M_2. \quad (1.12)$$

Those two last relations show that the total mass $M = M_1 + M_2$ conserves:

$$M(t) = \text{const.}$$

This relation shows that the model is correct. Moreover, we observe the following. For $\alpha > 0$ one has $M_2(t) = M_2(0) \exp(-\alpha t)$ and thus since $\rho_2 \geq 0$, we have $\rho_2(x, t) \rightarrow 0$ as $t \rightarrow \infty$. This means that for large times our system can be simplified and it reduces to the following shorted system:

$$\frac{\partial \sigma}{\partial x} = \frac{\partial^2 u}{\partial t^2}, \quad (1.13)$$

$$\frac{\partial \rho_1}{\partial t} + \frac{\partial}{\partial x} \left[\rho_1 \frac{\partial u}{\partial t} \right] = \bar{D} \frac{\partial^2 \rho_1}{\partial x^2}. \quad (1.14)$$

For $\alpha < 0$, we have $M_2(t) \rightarrow \infty$ as $t \rightarrow \infty$. Therefore, in this case our model describes an instability.

1.4 Particular Solutions

1.4.1 Reduction to Nonlinear Oscillator Equation

We consider solutions of system (1.3)–(1.6), which have the form of propagating waves

$$u = U(z), \quad \rho_i = R_i(z), \quad z = x - Vt, \quad (1.15)$$

where V is the velocity, U, R_j are unknown functions. We assume that $x \in (-\infty, +\infty)$ and u, u_x are bounded as $|x| \rightarrow \infty$. Then by substituting relations (1.15) into system (1.3)–(1.6), we obtain that Eqs. (1.3) and (1.4) give

$$\frac{\partial}{\partial z} \left[\frac{E_0 u}{1 + \kappa \rho_1} \right] = V^2 \frac{\partial u}{\partial z} + \text{const}. \quad (1.16)$$

We suppose for simplicity that $\text{const} = 0$ and then

$$\rho_1 = (E_0 V^{-2} - 1) \kappa^{-1}. \quad (1.17)$$

Therefore, $V^2 < E_0$. We substitute that relation for ρ_1 in (1.5) and (1.6), which leads to the following differential equation of the second order:

$$V \epsilon_z + D(\epsilon)(\epsilon_{zz} - \eta V^2 \epsilon_z^2) - V \epsilon_z \epsilon - \alpha V \epsilon = C, \quad (1.18)$$

where $\epsilon_z = \frac{d\epsilon}{dz}$, $\epsilon_{zz} = \frac{d^2\epsilon}{dz^2}$ and C is a constant.

1.4.2 Analysis of Nonlinear Equation

The results of numerical solutions of the nonlinear equation are shown in Figs. 1.1, 1.2, and 1.3. Notice that the differential equation, boundary, and initial conditions can be transformed to a dimensionless form when we rescale the variables. All following results are presented in dimensionless form, in particular, $\bar{x} = x/L$, $\bar{z} = z/L$, where L is the characteristic size of the first component.

From the Fig. 1.1, it follows that in the case $D(\epsilon) = D_0 + D_1 \epsilon$ Eq. (1.18) has a family of linear solutions $\epsilon = az + b$. The blue line corresponds to $\alpha = 0.05$ and the red line to $\alpha = 0.1$. The constants a, b can be found directly from (1.18) for $D = D_0$. We obtain $a = \alpha/V$. The huge values of deformation correspond to the destruction of material. Equation (1.18) can be studied for small V , and $\alpha = O(1)$ (or, that is the same, for large α). We also assume that term $D_1 \epsilon$ is small, and thus we can use approximation

$$D(\epsilon)^{-1} = D_0^{-1} (1 - D_1/D_0 \epsilon).$$

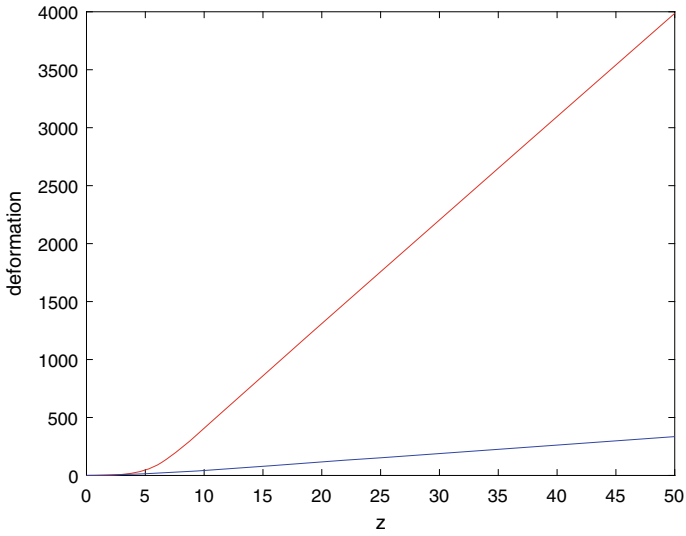


Fig. 1.1 This plot shows the linear solutions of Eq. (1.18); the blue line corresponds to the deformation for $\alpha = 0.1, V = 50$; the red curve to the deformation for $\alpha = 0.1, V = 8$

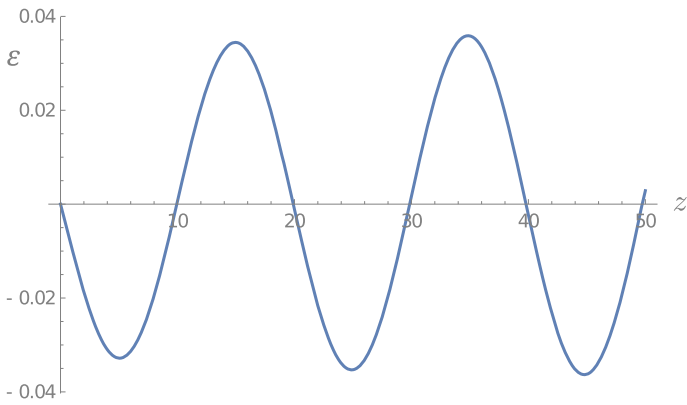


Fig. 1.2 This plot shows a periodic solution for $\alpha > 0$

Let ϵ_0 be the principal term and ϵ_1 be a correction, then the solution has the form

$$\epsilon = \epsilon_0 + V\epsilon_1 + \dots$$

Then the main terms give

$$D_0\epsilon_{0zz} - \alpha\epsilon_0 = C, \tag{1.19}$$

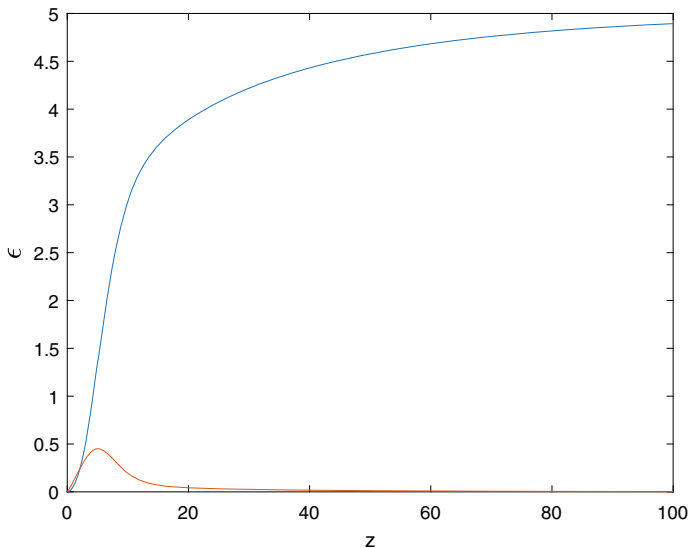


Fig. 1.3 This plot shows a solution of Eq. (1.18) in the case $D = D_0 + D_1\epsilon$. The parameters are $D_0 = 1$; $D_1 = 0$; $V = -0.2$; $\eta = 1$; $\alpha = 0.1$ and $C = 0.1$ —the blue line corresponds to the deformation, the red curve to the strain gradient

and the first corrections give

$$D_0\epsilon_{1zz} - \alpha\epsilon_1 = F, \quad (1.20)$$

where F is a given function of z .

For $\alpha < 0$, we obtain periodically oscillating solutions which can be seen in Fig. 1.2. For $\alpha = 0$, there are possible shock waves (see [1]). A typical result of the numerical simulations for $\alpha > 0$ is given in Fig. 1.3. The red curve corresponds to the strain gradient. To conclude this section, let us note that unbounded solutions can be interpreted as the destruction waves.

1.5 Simplified Problem

System (1.3)–(1.6) can be simplified for the case where D is a given function:

$$D(x) = D_0 + D_1 \sin(kx),$$

where $D(x)$ is a impurity diffusion coefficient depending on x periodically. Then this system can be reduced to the following hyperbolic equation:

$$\mu^{-1} \frac{\partial^2 \rho}{\partial t^2} + \frac{\partial \rho}{\partial t} - \frac{\partial}{\partial x} \left(D(x) \frac{\partial \rho}{\partial x} - v(x) \rho \right) = 0, \quad (1.21)$$

where $\rho(x, t)$ is a unknown impurity density, $t \geq 0$, $x \in [0, 1]$, and $\mu > 0$ is a parameter.

We set the boundary conditions

$$\frac{\partial \rho}{\partial x} \Big|_{x=0} = 0, \quad \left(D(x) \frac{\partial \rho}{\partial x} - v(x) \rho \right) \Big|_{x=1} = 0. \quad (1.22)$$

In the general case, Eq. (1.21) cannot be resolved analytically, however, we can find certain asymptotic solutions and investigate the large time behavior of the solutions.

The following case should be distinguished:

DD $\mu \gg 1$ (diffusion dominates);

DH $\mu \ll 1$ (the hyperbolic part of Eq. (1.21) dominates).

In the second case, we can expect wave propagation effects, and then diffusion works as a weak damping.

1.6 Eigenfunctions of Linearized Problem

In the case **DD**, the Fourier decomposition can be applied. Then Eq. (1.21) can be resolved by the Fourier method by substitution $u(x, t) = \psi(x) \exp(i\omega t)$. Let us consider the operator

$$\mathcal{L}\psi = \frac{\partial}{\partial x} \left(D(x) \frac{\partial \psi}{\partial x} - v(x) \psi \right), \quad (1.23)$$

and the eigenfunction problem

$$\mathcal{L}\psi_n = \lambda_n \psi_n, \quad (1.24)$$

where the functions ψ_n satisfy the boundary conditions (1.22). Solutions of that spectral problem can be found with the help of asymptotic methods. In certain cases the main contribution into ρ is given by the zero mode ψ_0 with $\lambda_0 = \min_n \lambda_n$. For self-adjoint operators L , without any loss of generality, we can assume that ψ_n form an orthonormal basis in $L_2([0, 1])$, and that λ_n are ordered as

$$\lambda_0 < \lambda_1 < \dots < \lambda_n < \dots$$

For non self-adjoint L , we use the bi-orthogonal system of functions ψ_n, ϕ_n such that

$$\langle \psi_m, \phi_n \rangle = \delta_{nm},$$

where δ_{nm} stands for Kronecker symbol and $\langle f, g \rangle = \int_0^1 f(x)g(x)dx$. It is easy to prove that for operator L , all eigenvalues are real numbers. In fact, by the substitution $\rho = \beta(x)\tilde{\rho}$, where

$$\ln \beta = \int_0^x \frac{D_x(s) - v(s)}{2D(s)} ds,$$

the operator L reduces to a self-adjoint operator H of Schrödinger type,

$$H = \frac{\partial^2}{\partial x^2}$$

with boundary conditions $\rho_x + a(x)\rho = 0$ at $x = 0, 1$. Therefore, all λ_n are real.

According to the Sturm–Liouville theory, the eigenfunction ψ_0 with the minimal $Re\lambda_n$ has no roots on $[0, 1]$ and physically it corresponds to an equilibrium density. If $v(0) = 0$ then

$$\psi_0(x) = \exp\left(\int_0^x D-1(s)v(s)ds\right). \quad (1.25)$$

The adjoint operator L^* has the form

$$L^*\phi = \frac{\partial}{\partial x}\left(D(x)\frac{\partial\phi}{\partial x}\right) - v(x)\frac{\partial\phi}{\partial x},$$

with the boundary conditions

$$\phi_x(x) = 0, \quad (x = 0, 1).$$

Therefore, $\phi_0(x) \equiv 1$.

1.7 Fourier Decomposition

By the eigenfunctions, ψ_n solutions of (1.21) can be represented in the form

$$\rho(x, t) = \sum_{n=0}^{\infty} c_n \exp(\theta_n t) \psi_n(x), \quad (1.26)$$

where

$$c_n = \int_0^1 \rho(x, 0) \phi_n = \langle \rho(\cdot, 0), \phi_n \rangle,$$

$$2\theta_n = \mu(-1 \pm \sqrt{1 - 4\lambda_n\mu^{-1}}).$$

The last relation shows that if $\lambda_n \leq 0$ then $\theta_n \geq 0$. According to (1.26), for large $t \gg 1$ the asymptotic of solutions ρ is defined by the main eigenfunction with the minimal $Re\lambda_n$:

$$\rho(x, t) = c_0 \exp(\theta_0 t) \psi_0(x) + O(\exp(-\delta t)), \quad t \rightarrow +\infty. \quad (1.27)$$

where $\delta > 0$. For λ_0 that asymptotic means that solution goes to an equilibrium density $\rho_{eq} = const \psi_0$.

1.8 Peculiarities of the Interphase Boundary Movement in Thawing/Freezing Problems

In this section, we start the investigation of the second mechanical problem which was mentioned in the Introduction. Mathematical modeling of the thermomechanical processes in soils makes it possible to develop reliable and durable structures and to avoid the severe consequences of accidents. In view of the complexity of these thermomechanical calculations, it is advisable to use various computational methods [13–15]. In particular, the finite element method is known as one of the most suited for the modeling of thermal state calculations of a solid [8, 13, 14]. The basic steps in finite element modeling for a given problem include construction of a computational domain, choice of constitutive equations, and identification of initial and boundary conditions. The first step, the correct definition of the boundaries of the computational domain, is often not obvious and may strongly affect the results when simulating thermomechanical processes in soils. Let us consider a plane thermal state of the soil surrounding the gas-main pipeline (Fig. 1.4). Constant positive temperatures are maintained at the upper boundary of the computational domain and inside the pipeline, while on the remaining boundaries zero heat flux is set (thermal insulation). The initial temperature of the soil is assumed to be -8°C . Two options for the vertical dimension of the computational domain are considered: 15 and 30 m. As a result of thermal calculations, we determine the distribution of temperature in the computational domain and the vertical dimension of the area in which the temperature exceeded 0°C . This dimension corresponds to the depth of the melt soil layer under the pipeline. Figure 1.5 shows the temperature distribution obtained as a result of transient finite element calculations for the two considered options of the domain geometry at the same time point. The area where temperatures exceed 0°C is shown with gray color.

As can be seen from the presented results, the depth of the thawed layer significantly (more than 1.5 times) differs depending on the depth of the soil layer included in the computational domain. A considerable difference is also observed in the temperature field—the minimum temperature values also differ by 1.5 times.

It was found that the difference in the depth of the melt soil layer increases as this area approaches the lower boundary of the computational domain, at which the

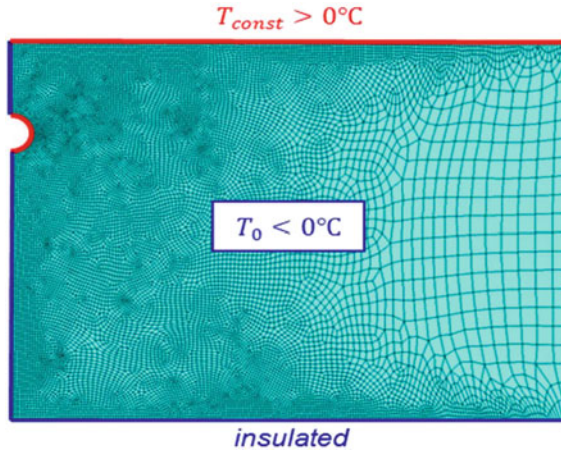


Fig. 1.4 Finite element model of the soil surrounding the gas-main pipeline

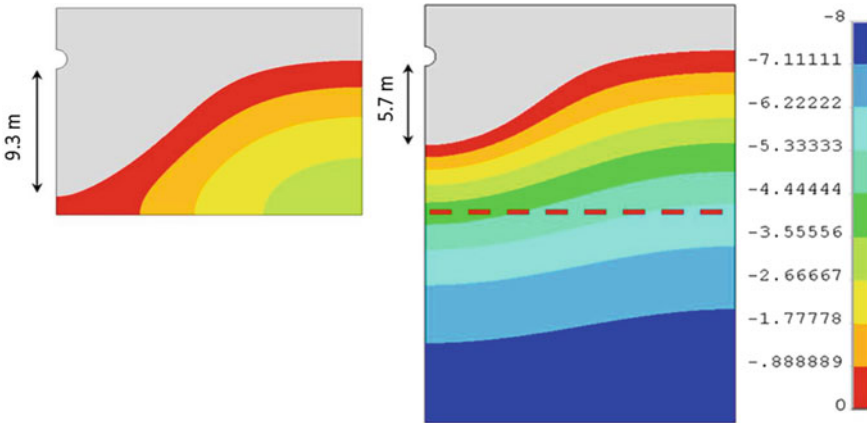


Fig. 1.5 Temperature distribution °C and the depth of the thawed soil layer for two options of the computational domain size

thermal insulation conditions are prescribed. A simplified model of the soil without pipeline is used to illustrate this effect (problem statement is similar to the one previously illustrated in Fig. 1.4). The position of the isotherm 0°C is denoted with ξ . As previously, two options are considered for the computational domain depth: 15 and 30 m (Fig. 1.6).

When the depth of the melted region reaches a certain value, we observe an increasing discrepancy in the size of the melted layer obtained for two considered options. In the considered example, this discrepancy reaches 2.2 m, which is approximately 15%. The results indicate that the speed at which 0°C isotherm is moving increases abruptly when it approaches the lower boundary of the model. Additionally, it was

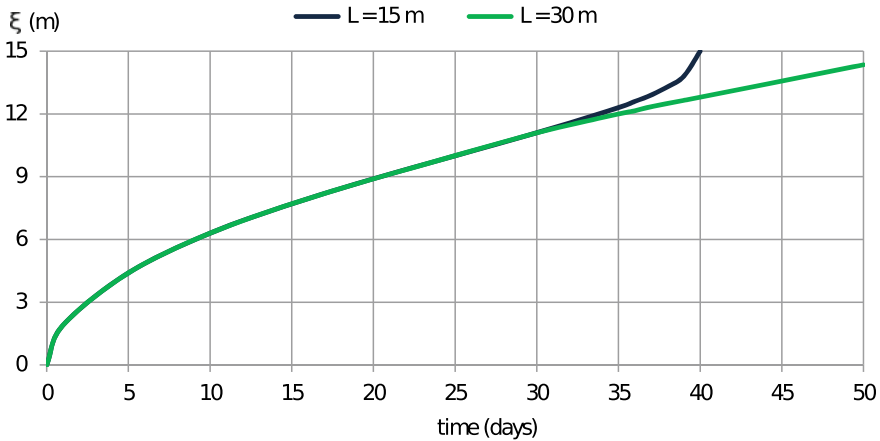


Fig. 1.6 Position of the 0°C isotherm versus time for two different options for the computational domain size

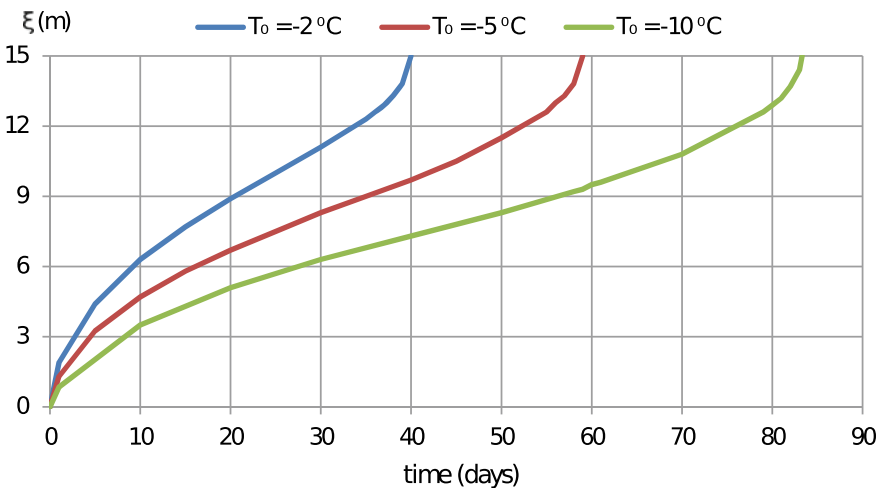


Fig. 1.7 Position of the 0°C isotherm versus time for different initial temperatures

found that this increase in the speed at which 0°C isotherm moves when it gets close to the lower boundary of the computational domain is observed regardless of the initial temperature of the soil. Figure 1.7 depicts results obtained for three different values of the initial temperature of the soil.

The statement of the problem considered above is of course a strongly simplified one. In particular, the assumption of a constant temperature at the upper boundary of the computational domain violated in most real situations. To make the statement slightly more realistic, we considered the case when the temperature prescribed at the upper boundary fluctuates with some amplitude ΔT . That change in the boundary

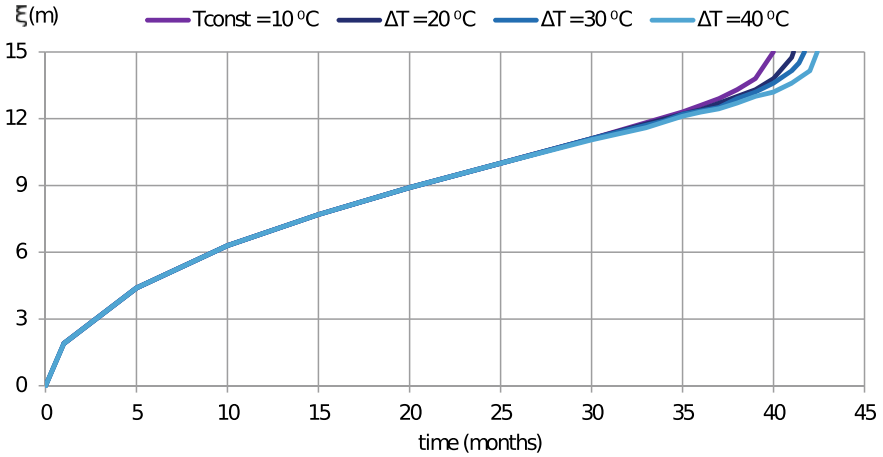


Fig. 1.8 Position of the 0°C isotherm versus time for different options of the boundary condition at the upper boundary of the computational domain: constant temperature $+10^{\circ}\text{C}$ and fluctuations of the prescribed temperature characterized by different amplitude ΔT

conditions affects the position of the 0°C isotherm in the results, but the effect of the increase in the speed at which this isotherm moves when approaching the insulated boundary remains; see Fig. 1.8.

The observed phenomenon of the increase in the speed at which 0°C isotherm (phase boundary) moves is clearly associated with the choice of the dimensions of the computational domain. In that sense, it can be considered as an error caused by computational assumptions and should be avoided as much as possible. An obvious way to eliminate this effect is to increase the computational area by placing the lower (insulated) boundary at a considerable distance from the area of interest. This approach, however, leads to an increase in the total number of degrees of freedom of the finite element model and, therefore, to the computational cost of the solution.

The objective of the presented research is to find ways to reduce the effect of increasing the speed of interphase boundary propagation without increasing the computational domain (the finite element model).

We first check whether the described phenomenon is only presented in the numerical solution, or it is a feature of the correct analytical solution of the boundary-value problem. The analytical solution for the problem of heat propagation in a rod of limited length is presented below.

Let us consider the heat conduction equation for a one-dimensional problem

$$\frac{\partial u}{\partial t} = a^2 \frac{\partial^2 u}{\partial x^2}, \quad (1.28)$$

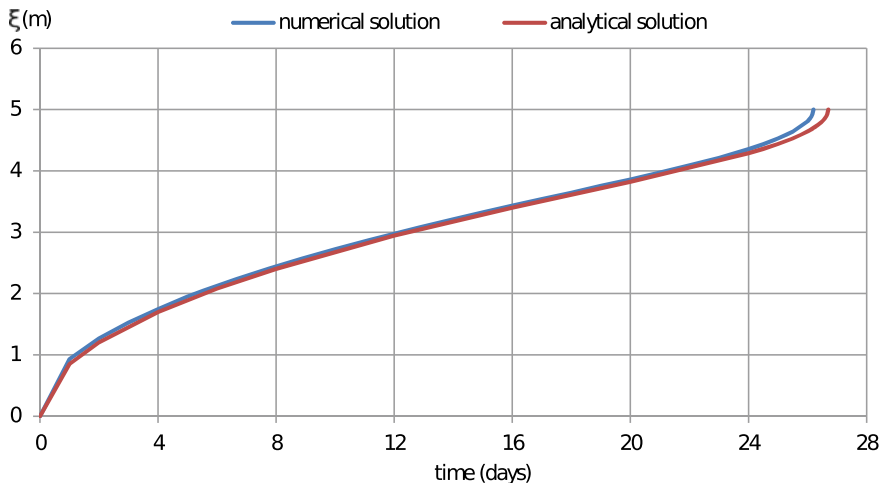


Fig. 1.9 Position of the 0°C isotherm versus time. Comparison of the analytical and numerical solutions

where a is the thermal diffusivity coefficient. We consider the following initial and boundary conditions: $u|_{t=0} = u_0$; $\frac{\partial u}{\partial x}|_{x=0} = 0$; $u|_{x=l} = \tilde{u}_l$ —prescribed temperature at the upper boundary.

The solution for the described problem can be expressed as follows [16]:

$$u = \tilde{u}_l + \frac{4(u_0 - \tilde{u}_l)}{\pi} \sum_{n=0}^{\infty} (-1)^n \frac{\cos \frac{(2n+1)\pi x}{2l}}{2n+1} e^{-\frac{(2n+1)^2 \pi^2 a^2 t}{4l^2}}. \tag{1.29}$$

The time-dependent position of the 0°C isotherm was calculated on the basis of the presented temperature distribution. Figure 1.9 depicts a comparison between the evolutions of the position of the isotherm calculated from the results of the analytical and numerical (finite element) solutions. It can be seen that the increase in the propagation speed of the 0°C isotherm near the heat-insulated boundary is predicted by the analytical solution also. The difference between numerical and analytical solutions does not exceed 5%.

Both numerical and analytical results presented above were obtained using a simplified statement of the problem, where we tracked the position of the 0°C isotherm, but the actual freezing and thawing processes happening at this temperature were neglected. When analyzing the real problem of freezing/thawing of soil, it is necessary to take into account different thermal parameters of the frozen and thawed soils, as well as the latent heat of the phase transition. A more elaborated statement of problem, which accounts for the phase transition processes, is considered below with the purpose to check whether the described above effect of the increase in speed of isotherm propagation is a consequence of the simplified statement.

In order to take into account the phase transition processes, we consider the classical Stefan problem

$$\begin{cases} \frac{\partial u_1}{\partial t} = a_1^2 \frac{\partial^2 u_1}{\partial x^2}, & 0 < x < \xi \\ \frac{\partial u_2}{\partial t} = a_2^2 \frac{\partial^2 u_2}{\partial x^2}, & \xi < x < l \end{cases} \quad (1.30)$$

with the initial and boundary conditions

$$u_2|_{t=0} = u_0; \left. \frac{\partial u_2}{\partial x} \right|_{x=0} = 0; u_1|_{x=l} = \tilde{u}_l,$$

and interphase boundary conditions:

$$\begin{aligned} u_1 = u_2 = 0, \quad x = \xi(t), \quad \xi(0) = 0, \\ k_1 \left. \frac{\partial u_1}{\partial x} \right|_{x=\xi} - k_2 \left. \frac{\partial u_2}{\partial x} \right|_{x=\xi} = \lambda \rho \frac{d\xi}{dt}. \end{aligned}$$

There are various methods for the numerical solution of this problem [17–20]. One possibility is to use the enthalpy form [17]:

$$\frac{\partial h}{\partial t} = \text{div}(\lambda \text{grad}(u)) \quad (1.31)$$

$$h(u) = \begin{cases} C_1(u - u_f), & u < u_f \\ \Phi, & u = u_f \\ \Phi + C_2(u - u_f), & u > u_f \end{cases} \quad (1.32)$$

where C_1 is the volumetric heat capacity of the frozen phase, C_2 is the volumetric heat capacity of the thawed phase, Φ is the volumetric heat of the phase transition, and u_f is the temperature of the phase transition. According to this model, thermal processes in all three phases (thawed, frozen and transition phase) are described by a single differential equation. Figure 1.10 shows the dependence of enthalpy on temperature for coarse soils, where all moisture is in a free state.

The numerical implicit solution of this problem is based on the method of “smearing the heat of the phase transition over temperature”, when the transition of phase is assumed to happen, not at a specific temperature, but within an interval Δu_f [10]. The heat conduction equation, which is common for both phases, has a clearly pronounced nonlinearity due to the rapid change of $C(u)$ within the interval Δu_f . In this case, the enthalpy is defined as

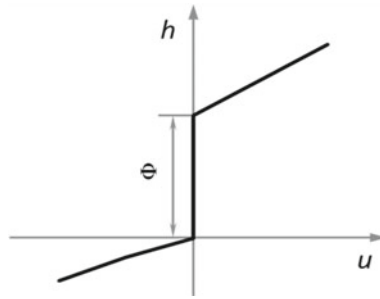


Fig. 1.10 Enthalpy versus temperature for coarse soils

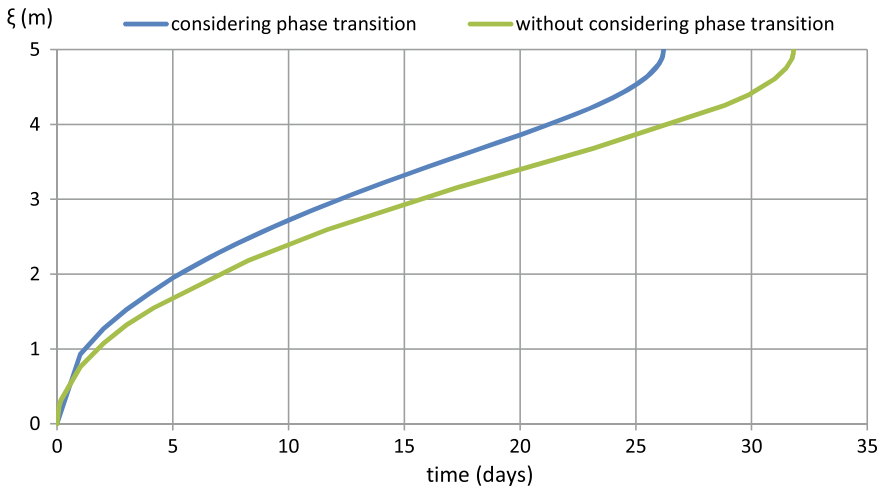


Fig. 1.11 Position of the 0°C isotherm versus time considering phase transition and without it

$$I(T) = \int_{T_0}^T (C(u) + \Phi \delta(u - u_f)) du \tag{1.33}$$

where δ is the Dirac delta function.

The dependence of the enthalpy on temperature is applied with the jump within the finite interval Δu_f in order to ensure the convergence of the iterative process of the nonlinear implicit solution.

Figure 1.11 shows a comparison of the position of the isotherm based on the results of the finite element solutions with accounting for the phase transition and without it.

Figure 1.11 illustrates that the increase in the speed of the interphase boundary propagation is also observed in the case when the heat of the phase transition is taken into account. It should be noted that similar phenomenon is also observed

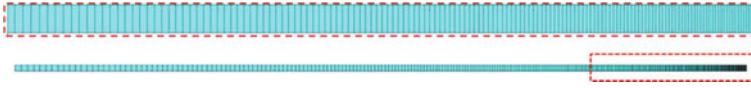


Fig. 1.12 Modified finite element mesh

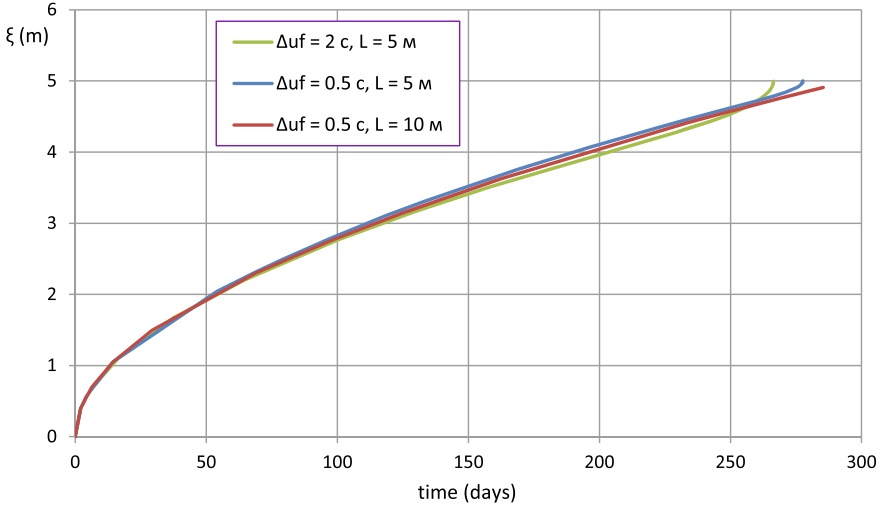


Fig. 1.13 Position of the phase interphase boundary versus time considering different enthalpy jump interval

when calculating the thermal state of a cylinder under external heating [21]. In that case, an increase in the speed of phase boundary propagation was detected near the center of the cylinder. However, in for the cylinder that effect has a simple geometrical explanation: the area on which the phase transition occurs is decreasing as the interphase boundary moves. It is necessary to note that the “smearing of the heat of the phase” method distorts the real temperature field, and the extent of that distortion depends on the chosen temperature interval Δu_f [10].

Thus, reduction of Δu_f is an important intermediate task. Convergence can be achieved by element size decreasing. Figure 1.12 shows a modified FE mesh, in which smaller element size is used near the thermally insulated boundary. The size of the computational domain in depth (L) is 5 m.

Adjusting the size of the finite element mesh and decreasing timesteps made it possible to reduce Δu_f interval from 2 to 0.5 °C. Figure 1.13 shows how the different values of Δu_f affect the propagation of the interphase boundary. The corresponding dependence for a model with an increased depth size ($L = 10$ m), is also presented in this figure. The boundary of the computational domain of this model does not affect the position of the interphase boundary in the investigated range.

Thus, the effect interphase boundary speed increase near the thermally insulated boundary of the computational region speed can be explained by the peculiarities of

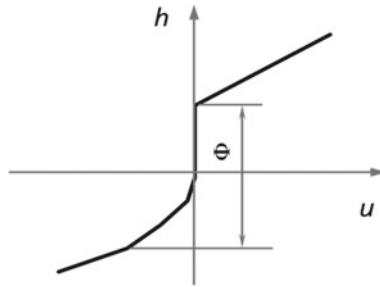


Fig. 1.14 Enthalpy versus temperature for finely dispersed soils

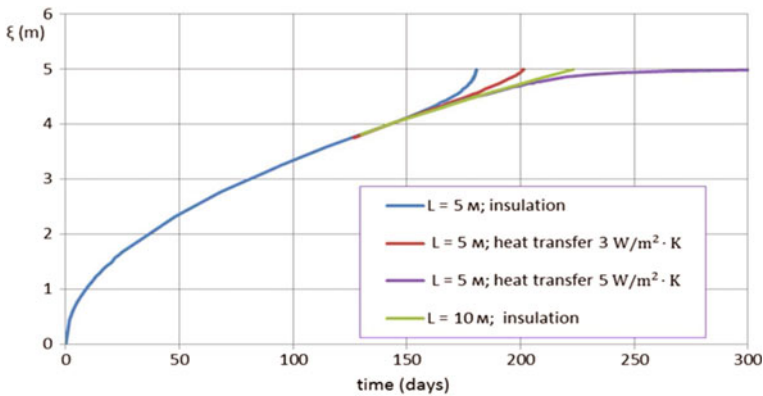


Fig. 1.15 Position of the interphase boundary versus time considering temperature fluctuations at the upper boundary

numerical problem statement. We demonstrated that this effect can be reduced by the refinement of the finite element mesh and by decreasing of the phase transition interval. The impact of these measures is, however, limited. In addition, for finely dispersed soils, the enthalpy function has a different character (Fig. 1.14), and the reduction of phase transition interval will not represent the real behavior of the soil. Therefore, it is desirable to find alternative ways to reduce the effect of the increase in the interphase boundary speed.

An alternative way to reduce the discussed effect may be adjusting the conditions at the lower boundary of the computational domain. We suggest using heat transfer according to Newton’s law convection boundary condition instead of thermal insulation conditions. Figure 1.15 shows the dependences of the interphase boundary motion on the condition prescribed at the lower boundary. The condition of heat transfer according to Newton’s law was considered with various values of the heat transfer coefficients. The initial computational statement with the thermal insulation condition applied at the lower boundary is presented in Fig. 1.15 for two options of

the computational domain size (5 and 10 m). It can be seen from the results presented that results obtained with heat transfer coefficients from 3 to W/m^2K are close to the ones obtained for a larger size of the computational domain.

1.9 Conclusion

In this paper, we first consider effects of impurity diffusion and convection in strained elastic materials. To describe those effects, we use the two-component continual model, taking into account the change in the rigid properties of the material, and prove that the model is mathematically well posed, its solutions exist and are unique. Moreover, we found a priori estimates of solutions and some asymptotic. The following conclusions can be drawn from the study:

- A phenomenon of an unrealistic increase in the propagation speed of the interphase boundary when it approaches the boundary of the computational domain was revealed in solution of the problem of soil freezing or thawing.
- It was proven that this phenomenon exists for various conditions of the phase transition, but its influence on the calculation result can be reduced by the refinement of the FE solution.
- It is possible to adjust the statement of the problem so as to reduce the effect of the phenomenon and obtain a more accurate solution without including larger region of the soil in the computational domain. In particular, using the convection boundary condition instead of thermal insulation may be an easy solution.

The results and recommendations obtained in this study can be helpful in solving various thermal problems for frozen and permafrost soils as well as in the design of foundations for buildings and underground pipelines.

References

1. Indeitsev, D., Vakulenko, S, Mochalova, Yu., Abramian, A.: Transport and deformation wave processes in solid. *Adv. Struct. Mater.* **114**, 83–94 (2019)
2. Maslov, V.P., Omel'yanov, G.A.: Asymptotic soliton-form solutions of equations with small dispersion. *Russ. Math. Surv.* **36**(3), 73–149 (1981)
3. Abramian, A.K., Vakulenko, S.A., Indeitsev, D.A.: Localized waves in a string of infinite length lying on a damaged elastic base under finitely many impacts. *Mech. Solids* **51**(5), 583–587 (2016)
4. Abramian, A.K., Indeitsev, D.A., Vakulenko, S.A.: Wave localization in hydroelastic systems. *Flow Turbul. Combust.* **61**, 1–20 (1999)
5. Abramian, A., Vakulenko, S.: Nonlinear Ritz method and motion of defects. *Theor. Math. Phys.* **155**(2), 678–688 (2008)
6. Friedman, A.: *Partial Differential Equations*. Holt, Rinehart and Winston, New York (1969)
7. Krylov, N.V.: *Nonlinear Elliptic and Parabolic Equations of the Second Order (Mathematics and its Applications)*. Springer, Berlin (1987)

8. Naumov, O., Moskvitin, G., Grigorieva, Y.: Influence processes freezing and thawing of permafrost soils on underground pipeline's stress-strain state. *Procedia Struct. Integr.* **20**, 53–56 (2019)
9. Yu, Q., Zhang, Z., Wang, G., Guo, L., Wang, X., Wang, P., Bao, Z.: Analysis of tower foundation stability along the Qinghai-Tibet Power Transmission Line and impact of the route on the permafrost. *Cold Reg. Sci. Technol.* **121**, 205–213 (2016)
10. Chen, J., Wu, Y., O'Connor, M., Bayani Cardenas, M., Schaefer, K., Michaelides, R., Kling, G.: Active layer freeze-thaw and water storage dynamics in permafrost environments inferred from InSAR. *Remote Sens. Environ.* **248**, 112007 (2020)
11. Yu, F., Qi, J., Lai, Y., Sivasithamparam, N., Yao, X., Zhang, M., Liu, Y., Wu, G.: Typical embankment settlement/heave patterns of the Qinghai-Tibethighway in permafrost regions: formation and evolution. *Eng. Geol.* **214**, 147–156 (2016)
12. Li, X., Jin, X., Wang, X., Jin, H., Tang, L., Li, X., He, R., Li, Y., Huang, C., Zhang, S.: Investigation of permafrost engineering geological environment with electrical resistivity tomography: a case study along the China-Russia crude oil pipelines. *Eng. Geol.* **291**, 106237 (2021)
13. Potts, D.M., Cui, W., Zdravkovic, L.: A coupled THM finite element formulation for unsaturated soils and a strategy for its nonlinear solution. *Comput. Geotech.* **136**, 104221 (2021)
14. Oclon, P.: The effect of soil thermal conductivity and cable ampacity on the thermal performance and material costs of underground transmission line. *Energy* **231**, 1208032 (2021)
15. Chen, Z., Guo, X., Shao, L., Li, S., Gao, L.: Sensitivity analysis of thermal factors affecting the nonlinearfreezing process of soil. *Soils Found.* **61**, 886–900 (2021)
16. Aramanovich, I.G., Levin, V.I.: *Uravneniya matematicheskoy fiziki (Equations of mathematical physics)*. Nauka, Moscow (1969)
17. Buchko, N.A.: Jentalpijnyj metod chislenogo reshenija zadach teploprovodnosti v promerzajushhih ili protaivajushhih gruntah (Enthalpy method of numerical solutions problems of heat conduction at freeze or thawing of soil). SPbGUNTiPT. http://refportal.com/upload/files/entalpiiny_metod_chislenogo_resheniya.pdf. Accessed 12 Feb (2016)
18. Xu, M., Akhtar, S., Zueter, A.F., Alzoubi, M.A., Sushama, L., Sasmito, A.P.: Asymptotic analysis of a two-phase Stefan problem in annulus: application to outward solidification in phase change materials. *Appl. Math. Comput.* **408**, 126343 (2021)
19. Voller, V., Cross, M.: An explicit numerical method to track a moving phase change point. *Int. J. Heat Mass Transf.* **26**, 147–150 (1983)
20. Ding, P., Liu, Z.: An explicit numerical method to track a moving phase change point. Accelerating phase-field modeling of solidification with a parallel adaptivecomputational domain approach. *Int. Commun. Heat Mass Transf.* **111**, 1044522 (2020)
21. Shubin, G.S.: Metod rascheta skorosti peremeshcheniya granitsy fazovogo perekhoda v protsessakh teplomassoperenosa v tverdykh dispersnykh materialakh (Method of calculation of the speed of displacement of the phase transition boundary in the processes of heat and mass transfer in solid dispersed materials). *Promyshlennaya teplotekhnika* **29**, 11–15 (2007)

Chapter 2

On an Attraction Basin of the Generalized Kapitza's Problem



Alexander K. Belyaev, Nikita F. Morozov, Petr E. Tovstik, Tatiana M. Tovstik, and Tatiana P. Tovstik

Abstract The problem of the generalized Kapitza pendulum on the stability of the vertical position of the rod under the vertical vibration of the support was studied in various settings. A vertical deformable rod with a free upper end and clamped or simply supported lower end under the action of harmonic or stationary random vibrations of the support is considered. We model the rod as a system with several degree of freedom. The conditions for stability of the upper vertical position of the pendulum are found. Both bending and longitudinal vibrations of the bar are taken into account. We found the attraction basin of the stable vertical position.

Keywords Kapitza's pendulum · Stability · Attraction basin · Two-scale asymptotic expansion · Harmonic and random vibrations · Flexible rod · Single mode approximation

2.1 Introduction

Interest in the problem of pendulum oscillations was born 300 years ago in the works of Galileo, who studied the periods of pendulum oscillations. It was A. Stephenson [12] who in 1908 first drew attention to one of the very interesting types of

A. K. Belyaev · T. P. Tovstik (✉)

Institute for Problems in Mechanical Engineering RAS, V.O., Bolshoy pr., 61, St. Petersburg 199178, Russia

e-mail: tovstik_t@mail.ru

A. K. Belyaev

e-mail: 13augen@mail.ru

N. F. Morozov · P. E. Tovstik · T. M. Tovstik

St. Petersburg State University, Universitetsky pr., 28, Stary Peterhof, St. Petersburg 198504, Russia

e-mail: morozov@nm1016.spb.edu

P. E. Tovstik

e-mail: peter.tovstik@mail.ru

© The Author(s), under exclusive license to Springer Nature Switzerland AG 2022

V. A. Polyanskiy and A. K. Belyaev (eds.), *Mechanics and Control of Solids and Structures*, Advanced Structured Materials 164,

https://doi.org/10.1007/978-3-030-93076-9_2

pendulum oscillations, namely, the stability of a pendulum in a gravity field in the upward position with vertical support vibrations.

With the development of high-energy physics, the problems involving oscillatory behaviour of objects with different time scales have received practical application and have attracted a vivid attention of researchers. In 1951 P.L. Kapitsa [7, 8] carried out various statements of theoretical and experimental studies of the oscillations of an inverted pendulum. It is known that the problems of oscillations of a pendulum with a vibrating support lead to the Mathieu equation which can be solved only in terms of elliptic functions. Kapitsa made an additional assumption of small oscillation amplitude of the support and considered a type of motion in which the period of the support oscillation is much less than the oscillation period of the pendulum itself. Under these assumptions, the pendulum can stand, without falling, in the upward position which was confirmed by a number of experiments described in the Kapitsa work. In the Kapitsa works one finds the theory of calculation of the pendulum oscillation period, the restoring moment acting on the pendulum deviated from the upper equilibrium position by a finite angle, as well as the equilibrium condition itself and an accuracy estimate under the assumption of small oscillation amplitude of the pivot point. The equilibrium condition occurs with sufficiently intense vibrations of the support.

The problem of the Kapitsa pendulum as well as similar beautiful and instructive phenomena of dynamic stability and instability associated with vibrations were included in the monographs by I.I. Blekhman [4, 5].

The present paper suggests the boundaries of the attraction basin of the upper stable position of the pendulum found by the method of two-scale asymptotic expansion. The solutions of the generalized problem of oscillations of the Kapitsa pendulum are investigated as they are important for practical application, too. Even P.L. Kapitsa in his work drew attention to the parameters of a pendulum suitable for practical experiments and predicted that bending vibrations at resonance frequencies can grow for a thin rod.

This paper gives attention to the generalized formulations of the problem in which the pendulum rod is not an absolutely rigid body. The flexible pendulum is assumed to be a homogeneous rod that obeys the hypotheses adopted for the Bernoulli - Euler beam. To analyze the solution of the problem, a series expansion in eigenforms of an auxiliary boundary value problem associated with free transverse vibrations of a rod compressed by a longitudinal force is used. Here the stability condition is found from the system of equations obtained by the method of two-scale asymptotic expansions.

A pendulum in the form of a vertical elastic rod is considered, which can be unstable not only in the case of a hinged support of the lower end, but also in the case of rigid fixation (provided that the rod is long enough). The influence of the propagation of longitudinal waves along the rod is investigated and the attraction basins are found [3].

The generalised Kapitsa problem is also considered in the case when the vibrations of the vertical support is a stationary random process [16]. As in the case of high vibration levels, the vertical position of the rod is stable and we determine the corresponding attraction basin.

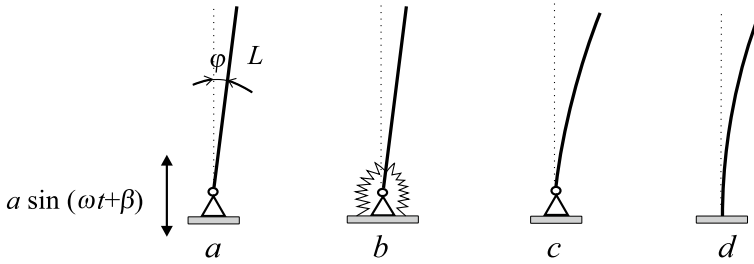


Fig. 2.1 The Kapitza's pendulum and its generalized models: **a** Classical model; **b** Flexible support; **c** Flexible rod with a hinged lower end; **d** Flexible rod with a clamped lower end

2.2 Classical Model of the Kapitza's Pendulum

2.2.1 Stability of the Kapitza's Pendulum

We consider a pendulum as a thin homogeneous rigid rod of length L , see Fig. 2.1a. Its motion in the movable co-ordinate system is described by the equation

$$J \frac{d^2\varphi}{d\tilde{t}^2} + n_1 \frac{d\varphi}{d\tilde{t}} - m \frac{L}{2} (g - a\omega^2 \sin(\omega\tilde{t} + \beta)) \sin\varphi = 0, \quad (2.1)$$

where $\varphi(\tilde{t})$ is the angle between a rod and a vertical axis; n_1 , $J = mL^2/3$, m , g are the damping coefficient, the inertia moment of a rod, its mass, and the gravitational acceleration; respectively, a , ω , β are the amplitude, frequency and initial phase of the support vibration.

The limitation of small amplitude $a \ll L$ of the support vibration is introduced. Additionally, it is known [7] that for the fixed values of L and a the stability condition for the Kapitza effect is fulfilled for the sufficiently high frequency $\omega \gg 1$. For this reason, for the following analysis is convenient to write down Eq. (2.1) to the dimensionless form:

$$\ddot{\varphi} + \varepsilon n \dot{\varphi} - (\varepsilon^2 q - \varepsilon \sin(t + \beta)) \sin\varphi = 0, \quad (2.2)$$

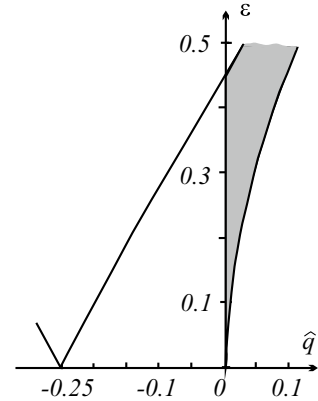
where

$$t = \omega\tilde{t}, \quad n = \frac{2n_1}{mLa\omega}, \quad q = \frac{2Lg}{3a^2\omega^2}, \quad \varepsilon = \frac{3\delta}{2}, \quad \delta = \frac{a}{L}. \quad (2.3)$$

Here q is the loading parameter, ε is the small parameter. A derivative with respect to time t is denoted by a dot. We introduce the relative acceleration of the support vibration κ as the critical parameter which ensures the pendulum stability

$$\kappa = \frac{a\omega^2}{g} = \frac{2}{3\delta q}. \quad (2.4)$$

Fig. 2.2 Part of the Anis-Strett diagram for the equation $\ddot{\varphi} - (\hat{q} - \varepsilon \sin t)\varphi = 0$



For small φ (namely, for $\sin \varphi \approx \varphi$) Eq. (2.2) is the Mathieu equation and for small $q > 0$ the solution $\varphi \equiv 0$ is stable under the condition [1] (see Fig. 2.2)

$$q < 1/2, \quad \kappa > \frac{4}{3\delta}. \quad (2.5)$$

2.2.2 Attraction Basin of the Solution of the Kapitza's Pendulum

Now we proceed to the attraction basin of this solution and consider the Cauchy problem consisting of Eq. (2.2) and the initial conditions

$$\varphi(0) = \varphi_0, \quad \dot{\varphi}(0) = 0. \quad (2.6)$$

We seek an asymptotic solution of Eq. (2.2) as a two-scale expansion [6]:

$$\varphi(t, \theta, \varepsilon) = \sum_{m=0}^{\infty} (U_m(\theta) + V_m(t, \theta))\varepsilon^m, \quad \int_0^{2\pi} V_m(t, \theta) dt = 0, \quad m = 0, 1, \dots, \quad (2.7)$$

where $\theta = \varepsilon t$ is the slow time and

$$\dot{\varphi} = \frac{\partial \varphi}{\partial t} + \varepsilon \frac{\partial \varphi}{\partial \theta}, \quad \ddot{\varphi} = \frac{\partial^2 \varphi}{\partial t^2} + 2\varepsilon \frac{\partial^2 \varphi}{\partial t \partial \theta} + \varepsilon^2 \frac{\partial^2 \varphi}{\partial \theta^2}. \quad (2.8)$$

An expansion of Eq. (2.2) in powers of ε yields consecutively

$$V_0(t, \theta) = 0, \quad V_1(t, \theta) = \sin U_0 \sin(t + \beta), \quad \frac{\partial^2 V_2}{\partial t^2} + H(\theta, t) = 0, \quad (2.9)$$

with

$$H = 2 \frac{\partial^2 V_1}{\partial t \partial \theta} + \frac{d^2 U_0}{d\theta^2} + n \frac{dU_0}{d\theta} - q \sin U_0 + (U_1 + V_1) \cos U_0 \sin(t + \beta). \quad (2.10)$$

According to (2.7) the average value in t of function $H(t, \theta)$ is to be equal zero that gives an equation for function $U_0(\theta)$

$$\frac{d^2 U_0}{d\theta^2} + n \frac{dU_0}{d\theta} + F(U_0) = 0, \quad F(U_0) = ((1/2) \cos U_0 - q) \sin U_0. \quad (2.11)$$

Due to relation $\dot{\varphi} = \varepsilon(dU_0/d\theta + \partial V_1/\partial t) + O(\varepsilon^2) = 0$, we solve Eq. (2.11) with initial conditions

$$U_0 = \varphi_0, \quad U'_0 = dU_0/d\theta = -\sin \varphi_0 \cos \beta \quad \text{for } \theta = 0. \quad (2.12)$$

The problem (2.11), (2.12) is the zero asymptotic approximation of the exact problem (2.2), (2.6).

For a definiteness we take $\alpha = 0.01$, $n = 0.1$ and for some values φ_0 and β we find $q_*(\varphi_0, \beta)$ such that for $q < q_*(\varphi_0, \beta)$ the limiting equality

$$\varphi(t) \rightarrow 0 \quad \text{at } t \rightarrow \infty, \quad (2.13)$$

is valid, whereas in the opposite case $q > q_*(\varphi_0, \beta)$ Eq. (2.13) is not fulfilled. The boundary $q_*(\varphi_0, \beta)$ depends on the initial phase β which is unknown in the general case. That is why we introduce two attraction basins in the plane of parameters (φ_0, q)

$$\begin{aligned} G_a(\varphi_0) : q < q_*^-(\varphi_0), \quad q_*^-(\varphi_0) &= \min_{\beta \in [0, 2\pi)} q_*(\varphi_0, \beta), \\ G_p(\varphi_0) : q_*^-(\varphi_0) < q < q_*^+(\varphi_0), \quad q_*^+(\varphi_0) &= \max_{\beta \in [0, 2\pi)} q_*(\varphi_0, \beta). \end{aligned} \quad (2.14)$$

see Fig. 2.3 Eq. (2.13) is fulfilled for all values β in basin G_a ; it is fulfilled only for some values β in basin G_p , and it is never fulfilled in part G_0 of plane (φ_0, q) .

The boundaries $q_*^-(\varphi_0)$ and $q_*^+(\varphi_0)$ are numerical solutions of the exact problem (2.2), (2.6). The approximate problem (2.11), (2.12) gives the close results (the corresponding curve $q_*^-(\varphi_0)$ in Fig. 2.3 is shown as a dashed line, and the difference between the exact and approximate curves is so small that it is impossible to see it in figure $q_*^+(\varphi_0)$).

Equation (2.11) is convenient for qualitative analysis in the phase plane (U_0, U'_0) . The trajectories $U_0(\theta)$, $U'_0(\theta)$ for $q = 0.3$, $n = 0$ are shown in Fig. 2.4. A bold curve separates the attraction basin while the possible values $|U'_0| \leq |\sin U_0|$ are marked by dashed lines.

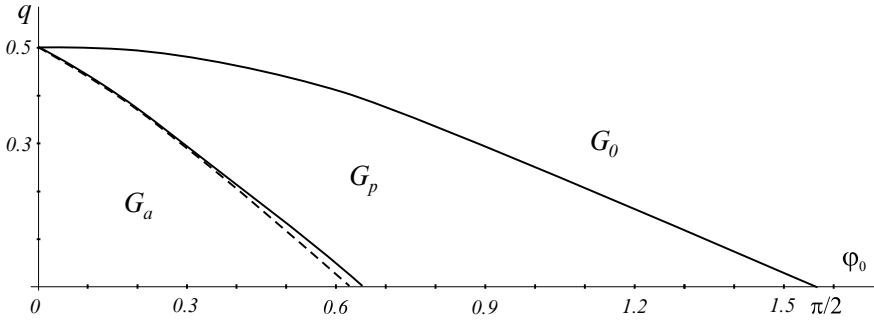
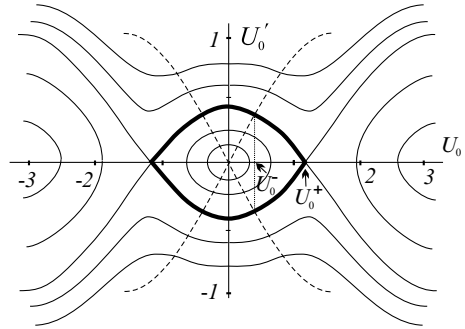


Fig. 2.3 The attraction basins

Fig. 2.4 The attraction basin in the phase plane (U_0, U'_0) at $q = 0.3$



2.2.3 Attraction Basins for Kapitza's Problem at Random Excitation

Let the vertical support vibration $x_e(t) = \xi(t)$ be random (Fig. 2.1a), and $\xi(t)$ be a stationary process with zero excitation and spectral density $S_\xi(\lambda)$. We consider the problems of Sect. 2.2 for the case of random excitation. Equation (2.1) reads as:

$$J \frac{d^2 \varphi}{d\tilde{t}^2} + n_1 \frac{d\varphi}{d\tilde{t}} - \frac{mL}{2} \left(g + \frac{d^2 \tilde{\xi}}{d\tilde{t}^2} \right) \sin \varphi = 0. \tag{2.15}$$

We rewrite Eq. (2.15) in the dimensionless form, relating time \tilde{t} to $1/\omega$ (ω is the typical frequency of vibration of support), and relating excitation $\tilde{\xi}(\tilde{t})$ to the average amplitude of support vibration $\sigma_{\tilde{\xi}}$:

$$\ddot{\varphi} + \varepsilon n \dot{\varphi} - (\varepsilon^2 q + \varepsilon \ddot{\xi}) \sin \varphi = 0, \tag{2.16}$$

where derivative with respect to t is denoted by a dot, and

$$t = \omega \tilde{t}, \quad \tilde{\xi}(\tilde{t}) = \sigma_{\tilde{\xi}} \xi(t), \quad \sigma_{\tilde{\xi}}^2 = \int_{-\infty}^{\infty} S_{\tilde{\xi}}(\tilde{\lambda}) d\tilde{\lambda}, \quad \varepsilon = \frac{3\sigma_{\tilde{\xi}}}{2L}, \quad q = \frac{3Lg}{2\sigma_{\tilde{\xi}}^2 \omega^2}. \quad (2.17)$$

Here ε is a small parameter that is proportional to the average amplitude of the support vibration $\sigma_{\tilde{\xi}}$ and $\xi(t)$ is the normalized process with a unit dispersion. The spectral densities and the dispersions of $\xi(t)$ and its derivatives are as follows:

$$S_{\tilde{\xi}}(\lambda) = \frac{S_{\tilde{\xi}}(\tilde{\lambda}\omega)}{\sigma_{\tilde{\xi}}^2}, \quad S_{\dot{\xi}}(\lambda) = \lambda^2 S_{\xi}(\lambda), \quad S_{\ddot{\xi}}(\lambda) = \lambda^4 S_{\xi}(\lambda), \quad (2.18)$$

$$\sigma_{\tilde{\xi}}^2 = \int_{-\infty}^{\infty} S_{\xi}(\lambda) \lambda^2 d\lambda.$$

We solve Eq. (2.16) with the initial conditions $\varphi(0) = \varphi_0$, $\dot{\varphi}(0) = 0$, and use two ways for solving the problem.

One of them is a statistical simulation [11, 15]. We model a random process $\xi(t)$ as a sum of harmonic summands with random amplitudes and phases. For this aim we choose Λ so that the part of frequencies $\lambda > \Lambda$ can be neglected and divide the interval $0 \leq \lambda \leq \Lambda$ by points λ_n , $n = 1, \dots, N$. Then the approximate realization of a random process $\xi(t)$ read as:

$$\xi(t) = \sum_{n=1}^N p_n (\eta_n \cos(\hat{\lambda}_n t) + \kappa_n \sin(\hat{\lambda}_n t)), \quad (2.19)$$

$$p_n = \sqrt{2S_{\xi}(\hat{\lambda}_n)(\lambda_n - \lambda_{n-1})}, \quad \hat{\lambda}_n = (\lambda_n + \lambda_{n-1})/2,$$

where η_n and κ_n are the random independent standard Gaussian numbers ($\mathbf{E}\eta_n = \mathbf{E}\kappa_n = 0$, $\mathbf{E}\eta_n^2 = \mathbf{E}\kappa_n^2 = 1$, and \mathbf{E} denotes expectation). Then a numerical solution of Eq. (2.16) with the initial conditions (2.6) gives a realization of a random process $\varphi(t)$.

As an example, we consider random process $\tilde{\xi}(\tilde{t})$ with the spectral density

$$S_{\tilde{\xi}}(\tilde{\lambda}) = \frac{\tilde{c}}{(\tilde{\lambda}^4 + 2(\tilde{\alpha}^2 - \omega^2)\tilde{\lambda}^2 + (\tilde{\alpha}^2 + \omega^2)^2)(\tilde{\lambda}^2 + \omega^2)}. \quad (2.20)$$

According to Eqs. (2.17), (2.18), for the dimensionless process $\xi(t)$ the spectral density reads as:

$$S_{\xi}(\lambda) = \frac{c}{(\lambda^4 + 2(\alpha^2 - 1)\lambda^2 + (\alpha^2 + 1)^2)(\lambda^2 + 1)}, \quad \lambda = \tilde{\lambda}/\omega, \quad \alpha = \tilde{\alpha}/\omega, \quad (2.21)$$

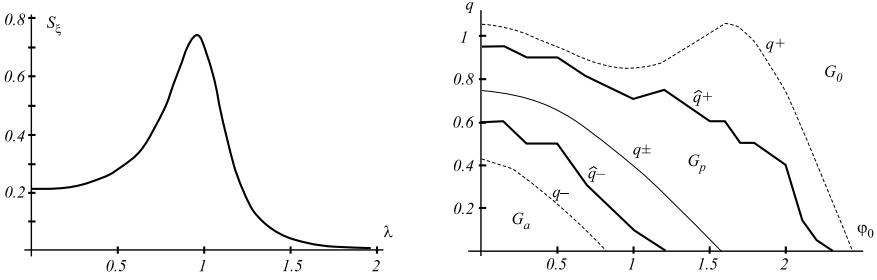


Fig. 2.5 Spectral density (left); Attraction basins (right)

where constant c is to be found from the condition $\sigma_\xi^2 = \int_{-\infty}^{\infty} S_\xi(\lambda) d\lambda = 1$. We find $\sigma_\xi^2 = (1 + \tilde{\alpha}^2)/(1 + 2\alpha)$. The constant \tilde{c} is introduced so that the value of σ_ξ^2 and small parameter ε can be taken arbitrary.

We take the following values: $\varepsilon = 0.01$, $n = 0.1$, $\alpha = 0.2$, $N = 200$ and consider the case $\varphi_0 > 0$. The spectral density $S_\xi(\lambda)$ of the normalized process $\xi(t)$ is plotted in Fig. 2.5. The maximum of $S_\xi(\lambda)$ is close to $\lambda = 1$ and $\sigma_\xi = 1$. The attraction basins G_a and G_p obtained by a numerical solution of Eq. (2.16) are shown in Fig. 2.5. In each numerical experiments we take 10 independent realizations of process $\varphi(t)$. A point (φ_0, q) is included in G_p if at least one realization converges to zero at $t \rightarrow \infty$, and at least one realization converges to $\pm\pi$. Hence in the areas G_p and G_0 all 10 realizations tends to zero and to $\pm\pi$ at $t \rightarrow \infty$, respectively. The boundaries of G_p are denoted by \hat{q}^- and \hat{q}^+ .

The second way of analysis of Eq. (2.16) is applying the two-scale expansion (2.7):

$$\varphi(t, \theta, \varepsilon) = U(\theta, \varepsilon) + V(t, \theta, \varepsilon), \quad (2.22)$$

$$U(\theta, \varepsilon) = \sum_{m=0}^{\infty} U_m(\theta) \varepsilon^m, \quad V(t, \theta, \varepsilon) = \sum_{m=0}^{\infty} V_m(t, \theta) \varepsilon^m,$$

where the average value V is equal to zero

$$\langle V \rangle = \frac{1}{T} \int_0^T V(t, \theta, \varepsilon) dt = 0, \quad T = O(\varepsilon^{-1}). \quad (2.23)$$

Repeating the calculations of Sect. 2.2.2, we successively obtain:

$$V_0(t, \theta) = 0, \quad V_1(t, \theta) = \xi(t) \sin U_0, \quad \frac{\partial^2 V_2}{\partial t^2} + H(t, \theta) = 0, \quad (2.24)$$

with

$$H = 2 \frac{\partial^2 V_1}{\partial t \partial \theta} + \frac{d^2 U_0}{\partial \theta^2} + n \frac{dU_0}{\partial \theta} - q \sin U_0 - (U_1 + V_1) \frac{d^2 \xi}{dt^2} \cos U_0. \quad (2.25)$$

The condition $\langle H \rangle = 0$ leads to equation for function $U_0(\theta)$

$$U_0'' + nU_0' + (\chi \cos U_0 - q) \sin U_0 = 0, \quad \chi = -\langle \xi(t) \ddot{\xi}(t) \rangle, \quad U_0(0) = \varphi_0, \quad (2.26)$$

The second initial condition $\dot{\varphi}(0) = 0$ due to Eqs. (2.8) and (2.24) yields

$$U_0'(0) = -\dot{\xi}(0) \sin \varphi_0. \quad (2.27)$$

The problem (2.26), (2.27) contains two random values: χ and $\dot{\xi}(0)$, and we use this problem to estimate the attraction basins. To construct them we note that for Gaussian values with a probability 0.95 the following inequalities are valid:

$$\mathbf{E}(\chi) - 2\sigma_\chi \leq \chi \leq \mathbf{E}(\chi) + 2\sigma_\chi, \quad -2(\mathbf{E}(\chi) - 2\sigma_\chi)^{1/2} \leq \dot{\xi}(0) \leq 2(\mathbf{E}(\chi) + 2\sigma_\chi)^{1/2}, \quad (2.28)$$

where $\mathbf{E}(\chi)$ is the expectation of χ and σ_χ is the root-mean-square.

For the taken values of the random process (2.19) we obtain

$$\mathbf{E}(\chi) \approx -\frac{1}{T} \int_0^T \xi(t) \ddot{\xi}(t) dt \approx \frac{1}{T} \int_0^T (\dot{\xi}(t))^2 dt \approx \sigma_\xi^2 = 0.743. \quad (2.29)$$

From Eq. (2.19) we have:

$$\chi \approx \frac{1}{2} \sum_{n=1}^N p_n \hat{\lambda}_n^2 (\eta_n^2 + \kappa_n^2). \quad (2.30)$$

Taking a large number (say, 10000) of random sets $(\eta_n, \kappa_n, n = 1, \dots, N)$ and using (2.30) we obtain the following value of root-mean-square $\sigma_\chi = 0.157$.

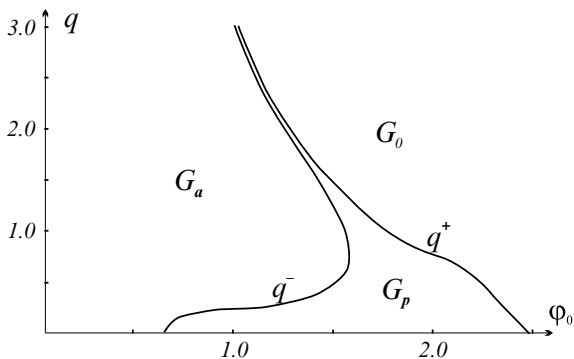
We put the upper and lower bounds of values of χ and $\dot{\varphi}(0)$ in Eq. (2.28) and obtain from Eq. (2.26) the boundaries $q^-(\varphi_0)$ and $q^+(\varphi_0)$ of attraction basins which are shown in Fig. 2.5. For comparison, curve $q^\pm(\varphi_0)$ corresponding to the values $\chi = \sigma_\chi^2$, $\dot{\xi}(0) = 0$ is also given there.

In particular, it follows from Eq. (2.26) that the vertical position (with a probability 0.95) is stable provided that

$$q < \sigma_\xi^2 - 2\sigma_\chi, \quad (2.31)$$

and for taken values if $q < 0.429$.

Fig. 2.6 Attraction basins in the plane (φ_0, q)



2.2.4 A Kapitza's Pendulum on the Flexible Support

Let us consider a rigid rod with an elastically supported lower end, see Fig. 2.1b. In terms of the dimensionless variables (2.3) the motion of rod on vibrating support is described by the equation

$$\ddot{\varphi} + n\alpha\dot{\varphi} + \alpha^2(b\varphi - q \sin \varphi) + \alpha \sin \varphi \sin(t + \beta) = 0, \quad b = \frac{4b_0L}{3ma^2\omega^2}. \quad (2.32)$$

In addition to Eq. (2.2) describing the classic Kapitza's pendulum, the bending support stiffness b_0 is introduced.

At $b < q$ and $a = 0$ the vertical rod position is unstable. The rod is stable at $\varphi = \varphi_0$, where φ_0 is the root of equation

$$b\varphi_0 = q \sin \varphi_0, \quad \text{or} \quad b = kq, \quad k = \frac{\sin \varphi_0}{\varphi_0} < 1. \quad (2.33)$$

Now we seek the conditions ensuring stable vertical position in the presence of support vibration.

We seek a solution of Eq. (2.32) satisfying the initial conditions $\varphi(0) = \varphi_0$, $\dot{\varphi}(0) = 0$. We assume that the angle $\varphi_0 < \pi$ is a leading parameter of problem, and a stiffness parameter $b = kq$. As in Sects. 2.2.2, and 2.2.3, we use two-scale expansions, that in the first approximation for a slowly changing function $U_0(\theta)$ lead to Cauchy problem:

$$U_0'' + nU_0' + F(U_0) = 0, \quad U_0(0) = \varphi_0, \quad U_0'(0) = -\sin \varphi_0 \sin \beta, \quad (2.34)$$

with $F(U_0) = kqU_0 + ((1/2) \cos U_0 - q) \sin U_0$. At $n > 0$, $q < q_*^+ = 1/(2(1-k))$ the solution $U_0(\theta) \equiv 0$ is asymptotically stable. As in Sect. 2.2.2, at $q < q_*^+$ we seek an attraction basin of this solution. A plane of parameters (φ_0, q) consists of three parts G_a, G_p, G_0 and for $\varepsilon = 0.01$, $n = 0.1$, $q \leq 3$ it is shown in Fig. 2.6. At $q > 3$ the boundaries q^- and q^+ coincide, and $q^- \approx q^+ \approx q_*^+$.

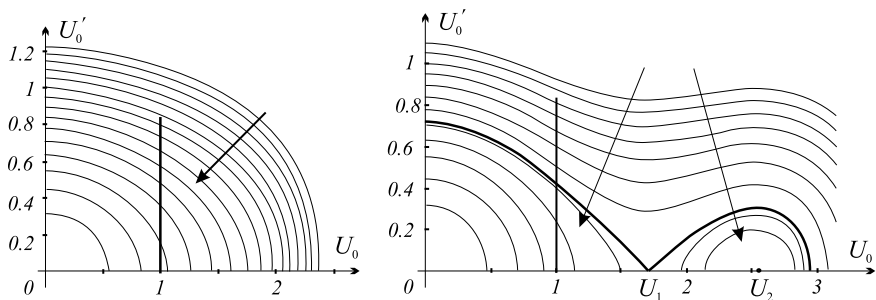


Fig. 2.7 A phase plane at $f_0 = 1$, and at $q = 1$ (left) and $q = 0.1$ (right)

At $n = 0$ the trajectories

$$\dot{U}_0^2 + 2 \int_0^{U_0} F(U) dU = C, \quad (2.35)$$

(with arbitrary constant C) in a phase plane (U_0, U'_0) are symmetric with respect to axes OU_0 and OU'_0 , and we consider a quarter part of plane $U_0, U'_0 \geq 0$. At $n > 0$ a point passes from one trajectory to another with the lower value of C . In Fig. 2.7 the phase planes for $\varphi_0 = 1$ and for two values $q = 1$ and $q = 0.1$ are shown. The direction of decreasing values of C is indicated by arrow. A set of possible values of $|U'_0|$ is marked by a vertical line. For $q = 1$ all $|U'_0|$ lie in the attraction basin of point $U_0 = U'_0 = 0$, therefore, for all values of the initial phase β Eq. (2.13) is fulfilled, and $(\varphi_0, q) \in G_a$. For $q = 0.1$ only a part of values $|U'_0|$ lie in the attraction basin of point $U_0 = U'_0 = 0$ (that is separated by a bold line), and as a result we have $(\varphi_0, q) \in G_p$.

2.3 Generalized Kapitza's Pendulum. Flexible Rod

We consider a flexible inverted pendulum in the case of a harmonic vertical vibration of the support $z_0(t) = a \sin(\omega t + \beta)$ (see also [2, 10]). Small transverse oscillations of a longitudinally compressed flexible rod of length L about the vertical position in the coordinate frame of the support are described by the equation

$$D \frac{\partial^4 w}{\partial x^4} + \frac{\partial}{\partial x} \left(P_s \frac{\partial w}{\partial x} \right) + \rho S \frac{\partial^2 w}{\partial t^2} = 0, \quad P_s = P_w(x) + P_v(x, t). \quad (2.36)$$

Here $w(x, t)$ is the deflection, $D = EI$ is the bending rigidity, ρ is the material density, S is the cross-sectional area. The upper end $x = L$ of the rod is free ($w_{xx} = w_{xxx} = 0$), and the lower end is clamped ($w = w_x = 0$).

The axial force P_s is assumed to have two summands: $P_w(x) = P(L - x)/L$ with $P = \rho gSL$ is caused by weight of the rod, and $P_v(x, t)$ is due to the support vibration. For the inextensible rod $P_v(x, t) = -\rho a \omega^2 S(L - x) \sin(\omega t + \beta)$, and for the extensible rod the axial force $P_v(x, t)$ is determined by the propagating longitudinal waves, see [2, 10] for detail:

$$P_v(x, t) = -ES \frac{\partial u}{\partial x} = -ES(a/v)(\cos v\hat{x} \operatorname{tg} v - \sin v\hat{x}) \sin(\omega t + \beta), \quad (2.37)$$

with $\hat{x} = x/L$, $v = L\omega/c$, $c^2 = E/\rho$. Here E , ρ , c , ω , v are the Young modules, the mass density, the sound velocity in the rod, the support frequency and the dimensionless frequency, respectively. For the inextensible rod $v = 0$.

The conditions for stability of the vertical position of the rod subjected to the support vibrations was found in [2, 10] for both inextensible and extensible flexible rods. Our aim is to obtain the attraction basin of this problem, but at first we repeat some results of papers [2, 10].

Equation (2.36) in the dimensionless form is given by:

$$\frac{\partial^4 w}{\partial \hat{x}^4} + P_* \frac{\partial}{\partial \hat{x}} \left((1 - \hat{x} - g_a p_v(\hat{x}) \sin(\hat{t} + \beta)) \frac{\partial w}{\partial \hat{x}} \right) + P_* g_L \frac{\partial^2 w}{\partial \hat{t}^2} = 0, \quad P_* = \frac{P_0 L^2}{D}, \quad (2.38)$$

with $\hat{t} = \omega t$, $g_a = a\omega^2/g$, $g_L = L\omega^2/g$. For an extensible rod $p_v(\hat{x}) = (\cos v\hat{x} \operatorname{tg} v - \sin v\hat{x})/v$, and for the inextensible rod $p_v(\hat{x}) = 1 - \hat{x}$. The last expression follows from the previous one at $v \rightarrow 0$.

In what follows we omit a sign $\hat{\cdot}$.

The solution of Eq. (2.38) is sought in the form of a series

$$w(x, t) = \sum_{k=1}^N \Psi_k(x) w_k(t), \quad (2.39)$$

where $\Psi_k(x)$ are eigenfunctions of the boundary-value problem

$$\frac{d^4 \Psi}{dx^4} + \lambda \frac{d}{dx} \left((1 - x) \frac{d\Psi}{dx} \right) = 0, \quad \Psi(0) = \Psi_x(0) = \Psi_{xx}(1) = \Psi_{xxx}(1) = 0. \quad (2.40)$$

This problem relates to the problem of static equilibrium bifurcation of a heavy rod with a free upper end and a clamped lower end. The solution of Eq. (2.40) may be expressed in terms of the Airy functions [1], and the first eigenvalues are $\lambda_1 = 7.8373$, $\lambda_2 = 55.98$, $\lambda_3 = 148.5$, $\lambda_4 = 285.4$. For $P_* > \lambda_1$ the rod buckles due to the gravity.

Due to the orthogonality relation $\int_0^1 (1 - x) \Psi'_k \Psi'_n dx = 0$ for functions $\Psi_k(x)$, we obtain the system for unknown functions $w_k(t)$:

$$\sum_{k=1}^N a_{nk} \frac{d^2 w_k}{dt^2} + \varepsilon \left(\frac{b_n}{g_a} \left(\frac{p_n}{P_*} - 1 \right) + c_n \sin(t + \beta) \right) w_n = 0, \quad n = 1, \dots, N,$$

$$\varepsilon = \frac{a}{L} \ll 1, \tag{2.41}$$

where $a_{kn} = \int_0^1 \Psi_k \Psi_n dx$, $b_n = \int_0^1 (1-x)(\Psi'_n)^2 dx$, $c_n = \int_0^1 p_v(x)(\Psi'_n)^2 dx$, and for the inextensible rod $c_n = b_n$.

The first coefficients are $a_{11} = 0.128$, $b_1 = 0.202$. For the extensible rod the coefficient c_1 depends on ν and $|c_1(\nu)|$ is plotted in Fig. 2.8. At $\nu = \pi/2 + n\pi$, $n = 0, 1, \dots$, the value $c_1(\nu) \rightarrow \infty$, that corresponds to resonances of longitudinal vibration of the rod.

2.3.1 Conditions of Stability of the Vertical Position

The introduced small parameter ε allows us to use two-scale expansions. We put $g_a = \zeta/\varepsilon$ and write Eq. (2.41) in the matrix form:

$$\mathbf{A} \cdot \frac{d^2 \mathbf{W}}{dt^2} + \frac{\varepsilon^2}{\zeta} \mathbf{P} \cdot \mathbf{W} + \varepsilon \mathbf{C} \cdot \mathbf{W} \sin t = 0, \tag{2.42}$$

where $\mathbf{W} = \{w_k\}_{k=1, N}^T$ is the vector of unknown functions, $\mathbf{A} = \{a_{kn}\}_{k, n=1, N}$ is the symmetric matrix, \mathbf{P} and \mathbf{C} are the diagonal matrices with elements $\{b_k(\lambda_k/P_* - 1)\}_{k=1, N}$ and $\{b_k\}_{k=1, N}$, respectively.

Similar to Sect. 2.2, we look for the unknown function $\mathbf{W} = \mathbf{W}(t, \theta, \varepsilon)$, $\theta = \varepsilon t$ in the form:

$$W(t, \theta, \varepsilon) = \sum_{m=0}^{\infty} (\mathbf{U}_m(\theta) + \mathbf{V}_m(t, \theta)) \varepsilon^m, \quad \int_0^{2\pi} \mathbf{V}_m(t, \theta) dt = 0, \quad m = 0, 1, \dots \tag{2.43}$$

Then from Eq. (2.42) we obtain consecutively:

$$\mathbf{V}_0(t, \theta) \equiv 0, \quad \mathbf{V}_1(t, \theta) = \mathbf{A}^{-1} \cdot \mathbf{C} \cdot \mathbf{U}_0 \sin t,$$

$$\mathbf{A} \cdot \frac{d^2 \mathbf{U}_0}{d\theta^2} + \mathbf{D} \cdot \mathbf{U}_0 = 0, \quad \mathbf{D} = \frac{\mathbf{P}}{\zeta} + \frac{1}{2} \mathbf{C} \cdot \mathbf{A}^{-1} \cdot \mathbf{C}. \tag{2.44}$$

It follows from Eq. (2.44) that the vertical position of rod is stable if matrix \mathbf{D} is positively definite that allows us to find the critical value ζ_* of the loading parameter $\zeta = a^2 \omega^2 / (Lg)$.

For the single mode approximation ($N = 1$)

$$\zeta_* = \frac{2a_{11}b_1}{c_1^2} \left(1 - \frac{\lambda_1}{P_*} \right) = \frac{0.0517}{c_1^2} \left(1 - \frac{7.84}{P_*} \right), \tag{2.45}$$

Fig. 2.8 Schematic of coefficient $|c_1(\nu)|$

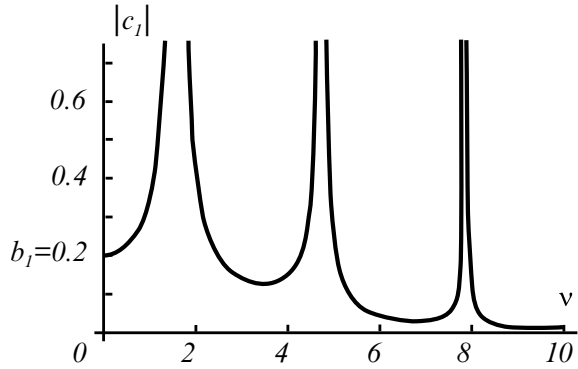


Table 2.1 Dependence of approximations $\zeta_*^{(1)}$ and $\zeta_*^{(2)}$ on P_*

P_*	$\leq \lambda_1$	8	10	25	50	100	∞
$\zeta_*^{(1)}$	0	0.02	0.27	0.87	1.06	1.16	1.26
$\zeta_*^{(2)}$	0	0.02	0.25	0.85	1.06	1.17	1.29

and for the inextensible rod

$$\zeta_* = \frac{2a_{11}}{b_1} \left(1 - \frac{\lambda_1}{P_*} \right) = 1.27 \left(1 - \frac{7.84}{P_*} \right). \tag{2.46}$$

Calculation of matrix **D** shows that the single mode approximation gives an acceptable accuracy for the critical value ζ_* . The single mode ($\zeta_*^{(1)}$) and the two-mode ($\zeta_*^{(2)}$) critical values of ζ are given for some values of P_* in Table 2.1 for the inextensible rod.

Remark 1 The hinged support ($w = w_{,xx} = 0$ at $x = 0$) of lower end is also studied in Refs. [2, 10]. In this case $\lambda_1 = 0$, $\lambda_2 = 25.64$, $a_{11} = 1/3$, $b_1 = 0.5$, and Eq. (2.46) gives $\zeta_* = 4/3$ independently of the value P_* that exactly corresponds to the critical value ($q = 1$) for a rigid rod (see Sect. 2.2). The higher approximations in Eq. (2.39) show that the value ζ_* slightly exceeds $\zeta_* = 4/3$, namely $\zeta_* = 1.37$ at $P_* = 120$. Dependence $\zeta_*(P_*)$ for the hinged and clamped lower end of rod are shown in Fig. 2.9.

For extensible rod, the inequality $|c_1(\nu)| > b_1$ is valid at some intervals of parameter ν (see Fig. 2.8 with $|c_1(0)| = b_1$), therefore according to Eqs. (2.45) and (2.46) the influence of longitudinal waves in the rod tends to decrease the critical level ζ_* of the support vibrations. A numerical example is presented in [10].

In Ref. [14], stationary positions were found and the stability was investigated for a flexible Chelomei pendulum under the support vibration and the used investigation methods were close to ours. However in contrast to Eq. (2.36), the axial compressive

Fig. 2.9 Functions $\zeta_*(P_*)$ for a hinged (1) and for a clumped (2) lower end of rod

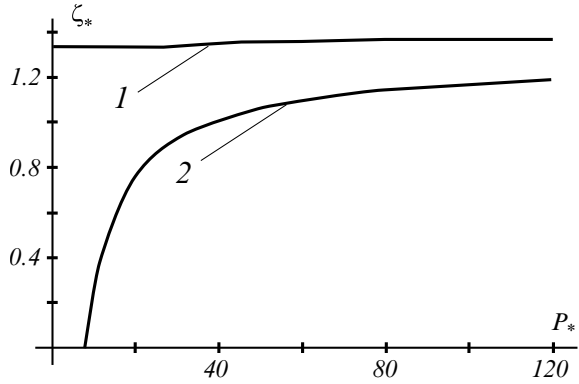
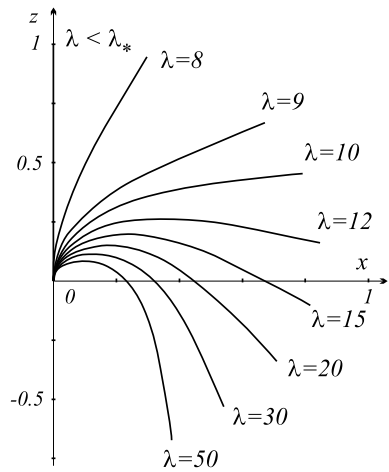


Fig. 2.10 Equilibrium forms of buckled rod



force caused by the rod weight is not taken into account when describing the flexural deformation of the rod. That is why no benchmark of the results was made.

2.3.2 On the Attraction Basins for a Flexible Rod

We consider a vertical flexible inextensible rod with a clamped lower end and a free upper end, cf. [9]. The long rod buckles under weight at $P_* > \lambda_* = 7.84$ (see Fig. 2.10), however the rod takes again the stable vertical position for high level of the support vibration, namely at $\zeta > \zeta_*$, see Eq. (2.45). Now we seek the attraction basin of this position.

Motion of the extensible rod under weight and vertical support vibrations is described by the equilibrium equations [13]:

$$\begin{aligned}
D \frac{\partial \varphi}{\partial s} &= M(s, t) = \int_s^L (F_x(s_1)(z(s_1) - z(s)) - F_z(s_1)(x(s_1) - x(s))) ds_1, \\
E e(s, t) &= \sin \varphi(s) \int_s^L F_x(s_1) ds_1 + \cos \varphi(s) \int_s^L F_z(s_1) ds_1,
\end{aligned} \tag{2.47}$$

where

$$\begin{aligned}
x(s) &= \int_0^s \sin \varphi(1 + e) ds, \quad z(s) = \int_0^s \cos \varphi(1 + e) ds, \\
F_x &= -S\rho \ddot{x}, \quad F_z = -S\rho(g + a\omega^2 \sin(\omega t + \beta) + \ddot{z}).
\end{aligned} \tag{2.48}$$

Here s ($0 \leq s \leq L$) is the length of arc of the rod axis, $\varphi(s, t)$ is the angle between tangent to the rod axis and the vertical and $e(s, t)$ is the longitudinal deformation of the rod axis.

For the inextensible rod $e = 0$.

In the static case (with $a = 0$) and for inextensible rod we can simplify Eq. (2.47) to obtain the boundary-value problem

$$\frac{d^2 \varphi}{ds^2} + P_*(1 - s) \sin \varphi = 0, \quad \varphi(0) = 0, \quad \varphi'(1) = 0, \tag{2.49}$$

where s is related to L . The forms of buckled rod shown in Fig. 2.10 are obtained from Eq. (2.49).

For the approximate analysis of attraction basin in the neighborhood of vertical position of the rod we use the single mode approximations for unknown functions $\varphi(s, t)$ and $e(s, t)$:

$$\begin{aligned}
\varphi(s, t) &= \Phi(s)u(t), \quad \Phi(s) = s - 0.200383s^2 - 0.81018s^3 + 0.457827s^4, \\
e(s, t) &= e(s)v(t), \quad e(s) = 1 - s, \quad 0 \leq s \leq 1.
\end{aligned} \tag{2.50}$$

Function $e(s) = 1 - s$ yields the first natural frequency 1.58 of longitudinal vibration instead of the exact value $\pi/2 = 1.57$. Function $\Phi(s)$ is close to the first eigenfunction $\Phi_1(x)$ of problem (2.40).

Table 2.2 displays the exact coordinates x^e, z^e of the rod end $s = 1$ obtained from Eq. (2.49). They are compared with the approximate values x^a, z^a from approximation (2.50) and shown in Fig. 2.10. Here u_* corresponds to the equilibrium state of vibration-free rod at given P_* . In what follows we will use approximation (2.50) at $|u| \leq 6$.

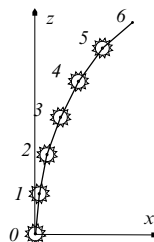
Remark 2 The other possibility, that is not used here, consists in replacing a flexible rod by a system of N rigid rods connected by elastic angular strings (Fig. 2.11). For the Kapitza problem the case $N = 1$ is considered in [9, 16] where an attraction basin is constructed.

Assumption (2.50) suggests the rod to be reduced to a system with two degrees of freedom, therefore we use the Lagrange equations of the second kind. We introduce

Table 2.2 Exact and approximate coordinates of the upper rod end

P_*	u_*	x^e	x^a	z^e	z^a
8	0.942	0.298	0.293	0.946	0.947
9	2.432	0.674	0.672	0.667	0.668
10	3.206	0.793	0.788	0.456	0.457
11	3.760	0.838	0.829	0.292	0.292
12	4.195	0.850	0.836	0.162	0.181
13	4.555	0.845	0.825	0.057	0.054
14	4.863	0.831	0.804	-0.030	-0.034
15	5.133	0.812	0.777	-0.102	-0.108

Fig. 2.11 Discrete model of a flexible rod



the designations

$$\{s, x, z, a\} = L\{\hat{s}, \hat{x}, \hat{z}, \varepsilon\}, \quad \omega t = \hat{t},$$

$$P_* = \frac{PL^2}{D}, \quad g_L = \frac{L\omega^2}{g}, \quad \hat{T} = \frac{T}{PL}, \quad \hat{\Pi} = \frac{\Pi}{PL}, \tag{2.51}$$

and then omit a sign $\hat{\cdot}$. Here T and Π are the kinetic and potential energy

$$T = \frac{gL}{2} \int_0^1 (\dot{x}^2 + (\dot{z} + \varepsilon \cos(t + \beta))^2) ds, \quad (')' = \frac{d(\cdot)}{du},$$

$$\Pi = \int_0^1 \left(\frac{(\varphi')^2}{2P_*} ds + z + \frac{c^2 e^2}{2gL} \right) ds. \tag{2.52}$$

where $x(s, t)$ and $z(s, t)$ are given by Eq. (2.48).

2.3.3 Lagrange Equations of the Second Kind

At first, we find from Eqs. (2.48) and (2.50)

$$x(s, t) = X(u, s) + vX_1(u, s), \quad z(s, t) = Z(u, s) + vZ_1(u, s) \quad (2.53)$$

with

$$X = \sum_{k=0}^K \frac{(-1)^k u^{2k+1} I_{2k+1}}{(2k+1)!}, \quad X_1 = \sum_{k=0}^K \frac{(-1)^k u^{2k+1} J_{2k+1}}{(2k+1)!}, \quad Z = \sum_{k=0}^K \frac{(-1)^k u^{2k} I_{2k}}{(2k)!},$$

$$Z_1 = \sum_{k=0}^K \frac{(-1)^k u^{2k} J_{2k}}{(2k)!}, \quad I_n(s) = \int_0^s \Phi^n(\sigma) d\sigma, \quad J_n(s) = \int_0^s \Phi^n(\sigma) e(\sigma) d\sigma.$$

and

$$\dot{x}(s, t) = (X'(u, s) + vX'_1(u, s))\dot{u} + X_1(u, s)\dot{v},$$

$$\dot{z}(s, t) = (Z'(u, s) + vZ'_1(u, s))\dot{u} + Z_1(u, s)\dot{v}.$$

Now the kinetic and the potential energy are as follows:

$$T = gL \left[\left(\frac{F_{00}}{2} + F_{01}v + \frac{F_{02}v^2}{2} \right) \dot{u}^2 + (F_{10} + F_{11}v)\dot{u}\dot{v} + \frac{F_{20}v^2}{2} + \varepsilon G \cos(t + \beta) \right],$$

$$G = (G_{00} + G_{01}v)\dot{u} + G_{10}\dot{v}, \quad (2.54)$$

$$\Pi = \frac{c_0 u^2}{2P_*} + \int_0^1 (Z + vZ_1) ds + \frac{c^2 v^2}{2gL} \int_0^1 e^2 ds, \quad c_0 = \int_0^1 (\Phi')^2 ds = 0.3184$$

with

$$F_{00} = \int_0^1 (X'^2 + Z'^2) ds, \quad F_{01} = \int_0^1 (X'X'_1 + Z'Z'_1) ds,$$

$$F_{10} = \int_0^1 (X'X_1 + Z'Z_1) ds, \quad F_{11} = \int_0^1 (X'_1X_1 + Z'_1Z_1) ds,$$

$$F_{02} = \int_0^1 (X_1'^2 + Z_1'^2) ds, \quad F_{20} = \int_0^1 (X_1^2 + Z_1^2) ds,$$

$$G_{00} = \int_0^1 Z' ds, \quad G_{01} = \int_0^1 Z'_1 ds, \quad G_{10} = \int_0^1 Z_1 ds.$$

The Lagrange equations read as:

$$\frac{d}{dt} \left(\frac{\partial \mathcal{L}}{\partial \dot{u}} \right) - \frac{\partial \mathcal{L}}{\partial u} = 0, \quad \frac{d}{dt} \left(\frac{\partial \mathcal{L}}{\partial \dot{v}} \right) - \frac{\partial \mathcal{L}}{\partial v} = 0, \quad \mathcal{L} = T - \Pi. \quad (2.55)$$

We seek solutions of Eq. (2.55) by using two-scale expansions, and we keep only the following first terms:

$$u(t) = U(\theta) + \varepsilon u_1(\theta, t) + \varepsilon^2 u_2(\theta, t), \quad v(t) = v_0(\theta) + \varepsilon v_1(\theta, t),$$

$$\langle u_1 \rangle = \langle u_2 \rangle = \langle v_1 \rangle = 0. \quad (2.56)$$

where $\theta = \varepsilon t$ is the slow time. Then the derivatives with respect to time are given by:

$$\dot{u} = \varepsilon \dot{u}_1 + \varepsilon U_{,\theta} + \varepsilon^2 \dot{u}_2 + O(\varepsilon^3), \quad \ddot{u} = \varepsilon \ddot{u}_1 + \varepsilon^2 U_{,\theta\theta} + \varepsilon^2 \ddot{u}_2 + 2\varepsilon^2 \dot{u}_{1,\theta} + O(\varepsilon^3).$$

Equations in (2.55) are cumbersome. In the first and second equations in Eq. (2.55) we omit the terms with orders smaller than ε^2 and ε , respectively. Then we have

$$\begin{aligned} g_L [F_{00} \ddot{u} + 2F_{01} (\dot{u}\dot{v} + \ddot{u}v) + F'_{00} \dot{u}^2/2 + F_{10} \ddot{v} - F'_{20} \dot{v}^2/2 - G_{00} \varepsilon \sin(t + \beta)] + \\ + \frac{c_0 u}{P_*} + G_{00} = 0, \\ g_L [F_{10} \ddot{u} + F_{20} \ddot{v} - G_{10} \varepsilon \sin(t + \beta)] + G_{10}(u) + \frac{c^2 v}{3gL} = 0. \end{aligned} \quad (2.57)$$

Here all the functions F_{ij} , G_{ij} depend on u .

We find $v_0 = -3gL/c^2 G_{10}(U_0)$ and put $u_1 = \hat{u}_1(\theta) \sin(t + \beta)$, $v_1 = \hat{v}_1(\theta) \sin(t + \beta)$. Then the terms of order ε in Eq. (2.57) give equations for functions $\hat{u}_1(\theta)$, $\hat{v}_1(\theta)$:

$$\begin{aligned} F_{00}(U) \hat{u}_1 + F_{10}(U) \hat{v}_1 + G_{00}(U) = 0, \\ v^2 (F_{10}(U) \hat{u}_1 + F_{20}(U) \hat{v}_1 + G_{10}(U)) - \hat{v}_1/3 = 0, \quad v = \frac{L\omega}{c}. \end{aligned} \quad (2.58)$$

In what follows the sign $\hat{}$ is omitted.

After time averaging the terms of order ε^2 in the first equation in Eq. (2.57) give the equation for function $U(\theta)$:

$$\begin{aligned} \zeta (F_{00} U_{,\theta\theta} + 1/2 F'_{00} (U_{,\theta}^2 - 1/2 u_1^2) - 1/2 F'_{10} u_1 v_1 - 1/4 F'_{20} v_1^2 - 1/2 G'_{00} u_1) + \\ + \frac{c_0 U}{P_*} + G_{00} = 0 \end{aligned} \quad (2.59)$$

with $\zeta = \varepsilon^2 g_L$. Here all the functions F_{ij} and G_{00} depend on U .

Equation (2.59) is the principle equation for following analysis of the attraction basin. We rewrite it in the form:

$$\begin{aligned} F_{00} U_{,\theta\theta} + 1/2 F'_{00} U_{,\theta}^2 + n U_{,\theta} + F(U) = 0, \\ F(U) = -1/4 F'_{00} u_1^2 - 1/2 F'_{10} u_1 v_1 - 1/4 F'_{20} v_1^2 - 1/2 G'_{00} u_1 + \zeta^{-1} \left(\frac{c_0 U}{P_*} + G_{00} \right), \end{aligned} \quad (2.60)$$

where the resistance term $nU_{,\theta}$ is introduced.

2.3.4 Attraction Basins for Inextensible Rod

For the inextensible rod we put $v = 0$, $v_1 = 0$, $u_1 = -G_{00}/F_{00}$ in the previous formulas, then Eq. (2.60) is as follows

$$F(U) = -1/4 F'_{00} u_1^2 - 1/2 G'_{00} u_1 + \zeta^{-1} \left(\frac{c_0 U}{P_*} + G_{00} \right) \quad (2.61)$$

with

$$\begin{aligned} F_{00}(u) &= 0.02565 - 0.000221u^2 + 0.00000117u^4, \\ G_{00}(u) &= -0.0406u + 0.00093u^3 - 0.00000736u^5. \end{aligned}$$

Function $F(U)$ is odd. Condition $F'(0) > 0$ yields the boundary of stability of the vertical position under the support vibration $\zeta_* = 1.26(1 - 7.84/P_*)$ which is very close to Eq. (2.46).

According to Eq. (2.8) the initial conditions for Eq. (2.60) are as follows

$$U = u_0, \quad \frac{dU}{d\theta} = -u_1(u_0) \cos \beta \quad \text{at } \theta = 0, \quad (2.62)$$

where β is the initial phase of vibration excitation.

For the inextensible rod the attraction basins are shown in Fig. 2.12 in plane $\{u_0, \zeta\}$ for various values of a weight-length parameter P_* . The resistance coefficient $n = 0.1$ is taken. For $P_* \leq 12$ the boundaries $\zeta_*(u_0)$ are approximately constant and do not depend on β . As a result, the absolute (G_a) and the partial (G_p) attraction basins coincide. For these values of P_* the equilibrium points u_* (see Table 2.2) marked by bold dots in Fig. 2.12 lie within the attraction basins. The case $P_* = 13$ is intermediate. For $P_* \geq 14$ the points u_* lie outside the attraction basins, and areas G_a and G_p differ from each other. The boundaries g^- of areas ($G_a : \zeta \geq \zeta_*(u_0)$) are pictured by continuous lines, and the boundaries g^+ of areas G_p are denoted by dashed lines.

For $P_* \geq 14$ the attraction basins lie at $u_0 < 6$, therefore the single mode approximation (2.50) is acceptable for their approximate construction.

For $P_* \leq 13$ the rod takes a curvilinear equilibrium position $u = u_*$ (see Fig. 2.10 with $\lambda = P_*$). For vibrations with $\zeta > \zeta_*$ the rod takes the vertical position. For $P_* \geq 14$, the initial condition $u_0 = u_*$ and under vibration the rod comes to another (non-vertical) position: $U(\theta) \rightarrow u_\infty$ at $\theta \rightarrow \infty$ with $F(u_\infty) = 0$. The stable vertical position can be achieved if the initial position u_0 of rod lies within the attraction basin (see the example below).

We consider, for example, the case $P_* = 15$, $\zeta = 0.7$. Then we have $u_* = 5.133$, $u_\infty = 3.157$, $u^- = 1.654$, $u^+ = 3.301$ where the points u^- and u^+ lie on the boundaries g^- and g^+ , respectively. At $\theta \rightarrow \infty$ the following limit relations are valid:

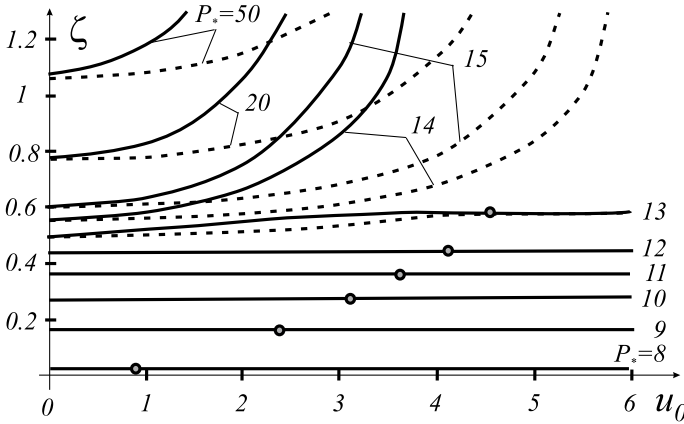


Fig. 2.12 Attraction basins for inextensible rod

$$\begin{aligned} \beta = 0 : \quad & U(\theta) \rightarrow 0 \text{ at } u_0 < u^-, \quad U(\theta) \rightarrow u_\infty \text{ at } u_0 > u^-, \\ \beta = \pi : \quad & U(\theta) \rightarrow 0 \text{ at } u_0 < u^+, \quad U(\theta) \rightarrow u_\infty \text{ at } u_0 > u^+. \end{aligned}$$

2.3.5 The Influence of Longitudinal Waves on Stability of the Vertical Position and Attraction Basins of the Extensible Rod

For study we use Eq. (2.60) in which functions $u_1(U)$ and $v_1(U)$ satisfy the linear system (2.58).

From Eq. (2.60) we obtain the condition for stability of the vertical position $F'(0) > 0$ or

$$F'(0) = -(1/2)F'_{10}u'_1v_1 - (1/4)F''_{20}v_1^2 - (1/2)G'_{00}u'_1 + \zeta^{-1} \left(\frac{c_0}{P_*} + G'_{00} \right) > 0, \quad (2.63)$$

where all functions are to be calculated at $U = 0$,

$$\begin{aligned} v_1(0) &= \frac{(5/2)v^2}{(5/2)-v^2}, \quad u'_1(0) = -\frac{F'_{10}(0)v_1(0)+G'_{00}(0)}{F_{00}(0)}, \\ v^2 &= f \zeta, \quad f = \frac{Lg}{c^2 \varepsilon^2} = \frac{L^3 g}{c^2 a^2}, \\ F_{00}(0) &= 0.02565, \quad F'_{10}(0) = -0.005847, \quad F''_{20}(0) = -0.00408, \quad G'_{00}(0) = -0.04062. \end{aligned} \quad (2.64)$$

The single mode approximation (2.50) $e(s, t) = (1 - s)v(t)$ is not sufficient for the complete analysis of extensible rod because higher longitudinal resonances (see Fig. 2.8) are not taken into account. We consider only the cases with $\nu \leq \pi$. For the

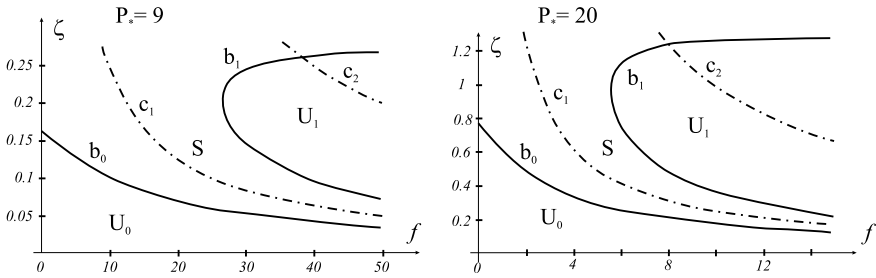


Fig. 2.13 Areas of the vertical position stability

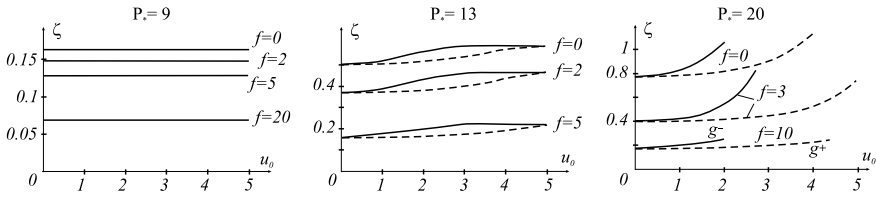


Fig. 2.14 Attraction basins for an extensible rod

fixed values of parameter f the inequalities

$$\zeta \leq \frac{\pi^2}{f} \quad \text{or} \quad \omega \leq \frac{\pi C}{L}. \tag{2.65}$$

are to be fulfilled.

Figure 2.13 displays the area of the vertical stability (area S between lines b_0 and b_1) under the support vibration for two values $P_* = 9$ and $P_* = 20$ of parameter P_* . The value $f = 0$ corresponds to the inextensible rod. The lower boundary decreases with growth of f . The lines c_1 and c_2 correspond to the first longitudinal resonance $\nu = \pi/2$ and curve $\nu = \pi$, respectively. The instability zone (U_1) is above line c_1 . As for the domain above c_2 , the results of the performed analysis are unreliable because the influence of second resonance is to be taken into account, see Fig. 2.8.

To construct the attraction basin of the vertical position we solve numerically the average equation (2.60), in which functions $u_1(U)$ and $v_1(U)$ are found from Eq. (2.58) with the initial conditions $U(0) = u_0$, $U_{,\theta}(0) = -u_1(u_0) \cos \beta$. For three values of parameter P_* the results are shown in Fig. 2.14. The results for the extensible rod basically repeat those for the inextensible rod (see Fig. 2.12), however there appears an additional parameter f describing extension. In all studied cases the boundaries g^- and g^+ decrease with growth of f . For small values of P_* (see $P_* = 9$ in Fig. 2.14) in the studied interval $0 \leq u_0 \leq 5$ the boundaries g^- and g^+ coincide and do not depend on u_0 . In the intermediate case $P_* = 13$ the influence of initial phase β is essential and $g^- \leq g^+$.

In the case $P_* = 20$ the attraction basins occupy areas smaller than $u_0 \leq 5$ because Eq. (2.60) has a singular point at resonance (at $\zeta = 2.5/f$). As a result, three various kinds of behavior of solution of Eq. (2.60) are possible depending upon the parameters $(P_*, f, \zeta, u_0, \beta)$:

- (i) $U(\theta) \rightarrow 0$ at $\theta \rightarrow \infty$, then the point lies in the attraction basin;
- (ii) $U(\theta) \rightarrow u_* \neq 0$ at $\theta \rightarrow \infty$ with $F(u_*) = 0$, $F'(u_*) > 0$, then the point comes to the equilibrium state $u = u_*$;
- (iii) $U(\theta) \rightarrow \infty$ at $\theta \rightarrow \theta_* < \infty$ then the point approaches the singular point of Eq. (2.60).

2.4 Discussion

Attraction basins of the vertical position for the Kapitza's pendulum under action of various types of support motion are constructed. A two-scale asymptotic expansion is used, and the average motion of pendulum is shown to depend on a slow time. A peculiarity of the problem is that the average motion of pendulum is sensitive to the initial (positive or negative at the initial time instant) impulse that depends on the initial phase of excitation. As a result, the attraction basin consists of two areas: in the so-called absolute area G_a the pendulum comes to vertical position for any initial phase, whereas in the so-called partial area G_p it comes to the vertical position only for a part of initial phases. The averaged system of equations by Blekhman [4, 5] obtained as a result of introduction of the vibrational force correctly determines the stability conditions, however, it does not allow one to construct the attraction basin because it does not account for the initial pulse generated by the initial phase of the disturbance.

Motion of the Kapitza's pendulum at random stationary vibration of support is basically similar to poly-harmonic vibrations with the following differences. The attraction basins obtained are not definite, and they can be described with some probability. Three kinds of attraction basins are constructed:

- (i) theoretical attraction basins. The study is based solely upon the properties of spectral density of excitation;
- (ii) attraction basins obtained by approximation of the random process by a sum of periodic terms with random amplitudes and phases. In the limit, (ii) tends to (i) in the mean-square sense with an unbounded increase in the number of terms. With a finite (albeit large) number of terms, the results differ markedly which is also mentioned in the present article;
- (iii) attraction basins obtained by a probabilistic elaboration of numerical solution of equations with this sum as excitation. The study is based on the numerical simulation of random variables included in the sum and the subsequent numerical solution of Eq. (2.15). The behavior of the solution with increasing time is revealed. This numerical simulation is repeated many times and the results are processed by methods of mathematical statistics. Particularly, in the present paper the results of ten simulations are processed to construct the attraction basin boundary.

Motion of a flexible rod with a clamped lower end and a free upper end subjected to harmonic vertical vibration of support is described by a system of non-linear integro-differential equations in partial derivatives. The exact solution is not constructed. We suggested an approximate model with two degrees of freedom which is acceptable if the rod inclination from the vertical position is not considerable and the excitation frequency is smaller than the second natural frequency of longitudinal vibrations of rod. The two-scale expansions are used to this approximate model, too.

For the inextensible rod the dimensionless equations contain a universal parameter P_* that depends on weight, length and bending stiffness of the rod. For $P_* < 7.84$ the vertical position of rod is stable (without the support vibration) thus the cases of $P_* > 7.84$ are of special interest. For the extensible rod an additional wave parameter f turns out to be important as it describes the influence of longitudinal vibration of the rod.

First we considered an inextensible rod. It is established that for $P_* \leq 13$ the rod with some initial static curvilinear equilibrium state (see Fig. 2.10) achieves the vertical position under the support vibration of high intensity ζ . In these cases the static equilibrium position lies within the attraction basin. At $P_* \geq 14$ the equilibrium lies outside the attraction basin, and the rod with the same initial conditions comes under vibration to another equilibrium of average motion. To obtain a vertical limit position it is necessary to shift the initial position of rod within the attraction basin more close to the vertical, see Fig. 2.12.

We studied the impact of longitudinal vibration of the extensible rod on its stability. The area of stable vertical position has the upper boundary that lies upper the first resonance of longitudinal vibrations of rod, cf. see Fig. 2.13. As for an inextensible rod, the lower boundaries g^- and g^+ of the attraction basins at $P_* \leq 13$ in the studied interval $0 \leq u_0 \leq 5$ weakly depend on u_0 and essentially depend on the wave parameter f (see Fig. 2.14). For both inextensible (Fig. 2.12) and extensible (Fig. 2.14) rods, at small weight parameter $P_* \leq 12$ the attraction basins occupy all studied interval of initial position $u_0 \leq 6$, while for $P_* \geq 14$ the right boundaries of attraction basins in plane (u_0, ζ) move left, close to the vertical position.

The level ζ of support vibrations bringing the rod to vertical position for the extensible rod is lower than that for the inextensible rod.

In order to demonstrate how broad can be the attraction basins we refer to Ref. [5] in which the theoretical analysis carried out in the present paper got an experimental confirmation. Book [5] reported the following experiment performed by V.B.Vasil'kov. A soft rope of ca. 10 cm length and 1 cm diameter is clamped at the lower end while the upper end is free. The rope has such a low bending rigidity that the upper end lies on the support. Under intensive vertical vibration of the support in some frequency band the rope takes stable upward position regardless of the initial shape. The theoretical study presented here explains existence of stable vertical position, however it is not capable to describe the rope motion from the initial state to the stable vertical position as our analysis is restricted to the case of small inclinations ($u \leq 6$) of the rope from the vertical.

2.4.1 Conclusions

We consistently considered the attraction basins of the upward vertical position of the pendulum which is known to be unstable without support vibration. The previously obtained areas of the attraction basins for the pendulum upward position are given for harmonic, polyharmonic and random vibration of the support. The attraction basins for a vertical flexible inextensible and extensible rod with a free upper end are constructed. The analytical solutions are constructed in the classical Kapitsa problem whereas for a flexible rod one has to restrict oneself to an approximate solution of systems with one or two degrees of freedom. The method of two-scale expansions is used. In all cases, the attraction basin consists of two parts: absolute and partial. In the first of them, the attraction takes place for all initial phases of the perturbation, while in the second one, only for some initial phases. For the sake of consistency, our previously published results are given, and the necessary references are made to them.

Acknowledgements Financial support of Russian Foundation for Basic Research is acknowledged, projects, 19-01-00208a, 20-51-S52001 MHT-a.

References

1. Abramovits, M., Stigan, I. (eds.): Handbook of Mathematical Functions. National Bureau of Standards. Applied mathematics series, vol. 55 (1964)
2. Belyaev, A.K., Morozov, N.F., Tovstik, P.E., Tovstik, T.P.: Stability of a flexible vertical rod on a vibrating support. Vestnik St. Petersburg University. Math. Mech. Astron. **51**(3), 296–304. Pleiades Publ., Ltd (2018)
3. Belyaev, A.K., Morozov, N.F., Tovstik, P.E., Tovstik, T.M., Tovstik, T.P.: Classical Kapitsa's problem of stability of an inverted pendulum and some generalizations. Acta Mechanica **232**, 1743–1759 (2021)
4. Blekhman, I.I.: Vibrational Mechanics. World Scientific, Singapore (2000)
5. Blekhman, I.I.: Vibrational Mechanics and Vibrational Reology. FIZMATLIT, Moscow (2018). [in Russian]
6. Bogoliubov, N.N., Mitropolski, Y.A.: Asymptotic Methods in the Theory of Non-Linear Oscillations. Gordon and Breach, New York (1961)
7. Kapitsa, P.L.: The pendulum in vibrating support. Uspekhi fizicheskikh nauk **44**(1), 7–20 (1951) [in Russian]
8. Kapitsa, P.L.: Collected papers of P.L.Kapitsa edited by D.TerHaar. Pergamon, no Y. 2, 714–726 (1965)
9. Kulizhnikov, D.B., Tovstik, P.E., Tovstik, T.P.: The Basin of Attraction in the Generalized Kapitsa Problem. Vestnik St.Petersburg University, Mathematics **52**(3), 309–316. Pleiades Publishing, Ltd (2019)
10. Morozov, N.F., Belyaev, A.K., Tovstik, P.E., Tovstik, T.P.: Stability of a vertical rod on a vibrating support. Dokl. Phys. **63**(9), 380–384 (2018) Pleiades Publ., Ltd
11. Pugachev, V.S.: Theory of Random Functions. Fizmatlit, Moscow (1960). [in Russian]
12. Stephenson, A.: On an induced stability. Phil. Mag. **15**, 233–236 (1908)
13. Svetlitsky, V.A.: Mechanics of Flexible Rods. Publ. MAI, Moscow (2001). [in Russian]
14. Thomsen, J.J., Tcherniak, D.M.: Chelomei's pendulum explained. R. Soc. <https://doi.org/10.1098/rspa.2001.0793>

15. Tovstik, P.E., Tovstik, T.P., Shekhovtsov, V.A.: Simulation of vibrations of a marine stationary platform under random excitation. *Vestnik St. Petersburg University* **1**(4) (2005) [in Russian]
16. Tovstik, T.M., Belyaev, A.K., Kulizhnikov, D.B., Morozov, N.F., Tovstik, P.E., Tovstik, T.P.: On an attraction basin of the generalized Kapitsa's problem. In: 7th ECCOMAS Thematic Conference on Computational Methods in Structural Dynamics and Earthquake Engineering (2019). <https://2019.compdyn.org/proceedings/>

Chapter 3

Application of Micropolar Theory to the Description of Ultrathin Liquid Layers



Nikolay M. Bessonov and Ksenia P. Frolova

Dedicated to the memory of Professor E.L. Aero

Abstract Experiments show that the coefficient of shear viscosity calculated by formulas of the classical theory of viscous fluid loses the sense of material constant when the thickness of the liquid flow becomes small enough. It becomes an effective quantity that changes significantly with decreasing flow thickness and takes a finite limit value on the wall. The limit (named the boundary viscosity) can be considered as the empirical material characteristic of given liquid–solid surface pair. This and many other facts indicate that the classical theory fails near a solid surface, that most real liquids (including usual water) form near solid surfaces a specific thin (\sim some μm and less) “subboundary” layer where new physical mechanisms of liquid flow become important. Modern experiments also show that the next specific ultrathin ($\sim 0.1 \mu\text{m}$ and less) layer is formed under subboundary layer. It consists of very orderly packed molecules of the liquid and flow does not take place in this “solid-like” layer. These fundamental effects have to be taken into account in the modern theory of fluid. It is especially important for the analysis of such problems as filtration, lubrication, flow of suspensions, polymer solutions, polar, and other real liquids. We show here that this aim can be achieved by combination of the Eringen-Aero theory of micropolar fluid and new generalized boundary conditions that take explicitly into account the existence of boundary viscosity and solid-like layer.

Keywords Micropolar fluid · Boundary viscosity · Solid-like layer · General boundary conditions

N. M. Bessonov · K. P. Frolova (✉)

Institute for Problems in Mechanical Engineering RAS, V.O., Bolshoy pr., 61, St. Petersburg 199178, Russia

© The Author(s), under exclusive license to Springer Nature Switzerland AG 2022
V. A. Polyanskiy and A. K. Belyaev (eds.), *Mechanics and Control of Solids and Structures*, Advanced Structured Materials 164,
https://doi.org/10.1007/978-3-030-93076-9_3

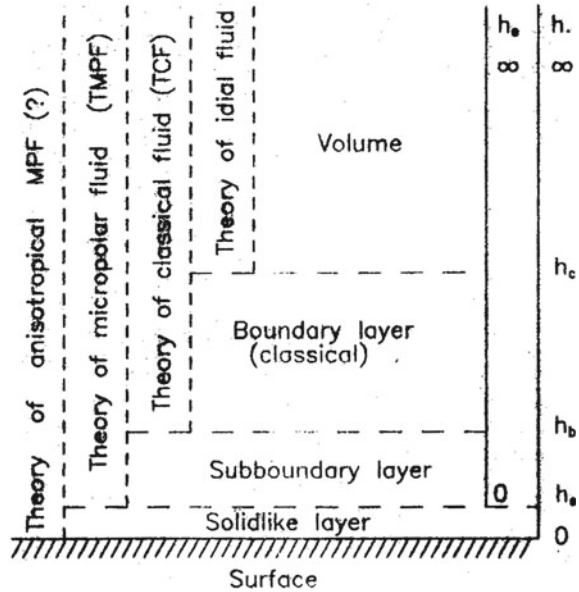
3.1 Introduction

The correct theoretical analysis of liquid flows is impossible without taking into account the influence of solid surface (further—surface) surrounding the flow. At large distances from the surface, the flow of real liquid is adequately described by the theory of ideal fluid and slip boundary condition. At approaching the surface, within classical boundary layer, one ought to use a more complex classical theory of viscous fluid (further—classical theory or TCF) and nonslip boundary condition directly on the surface. Experiments with thin layers of liquids flowing along or between surfaces show that the correct description of liquid flow at small distances h from the surface is impossible without further improvement of fluid theory [1–5]. At $h \leq h_b$ ($h_b \sim$ some μm and less) TCF does not agree any more with experiment. Here, the coefficient of dynamic shear viscosity μ (further—viscosity) calculated from experimental data by formulas of TCF loses the sense of fundamental material constant of the liquid. It becomes an “effective” viscosity μ_e depending on h . It decreases or increases efficiently in comparison with μ at decreasing of h and tends clearly to some finite limit named the “boundary” viscosity μ_b . The value of μ_b depends only on the nature of the liquid-surface system and can be considered as a new empirical material constant that has to be taken into account in fluid theory. Some earlier works [1, 2] and especially more modern experiments of J.N. Israelachvili and colleagues [6] show that at still less distances $h \leq h_s$ ($h_s \sim 0.1 \mu\text{m}$ and less), the next specific layer is formed directly on the surface. It consists of high orderly packed molecules of the liquid and manifests the properties of elasticity and plasticity. Flow on its usual sense cannot take place here.

Thus, one can distinguish in real liquids two specific near-the surface layers with different physical properties. Their existence has been established by not only viscosimetric, but also by optical, thermal, and other physical methods [3, 4]. Boundaries between the layers are smooth but their characteristic thicknesses can be estimated reliably by experimental data. The specific layer of thickness $h_s < h \leq h_b$ in which the liquid keeps fluidity and to which we shall pay here the most attention will be called further the “subboundary” layer. The layer of thickness $0 < h \leq h_s$, will be called further the “solid-like” layer. Evidently that TCF has to be modified at approaching to surface. The complete theory must describe the flow of real liquids at any distance from the surface. The arising situation is shown in Fig. 3.1. The situation will be yet discussed further.

In this work, we consider at first the empirical dependencies of effective viscosity μ_e on thickness h or on effective thickness $h_e = h - h_s$ of flowing layer, which were discovered by viscosimetric experiments. The numerical values of boundary viscosity μ_b and characteristic thicknesses h_b and h_s corresponding to these experiments for different liquids and surfaces are also discussed. We show then that all the diversity of empirical dependencies $\mu_e(h_e)$ can be described with the help of Eringen-Aero theory of micropolar fluid [7–9] and new boundary conditions. The Eringen-Aero theory of micropolar fluid (further—TMPF) is a generalization of TCF in which the rotational mobility of liquid microparticles and momental (orientational, rotational)

Fig. 3.1 States of real liquid and generalization of fluid theory at approaching to surface; h_e is an effective (mobile) part of fluid



interactions between them and with the surface are taken additionally into account. The new generalized boundary condition (further—GBC) proposed here takes into account the existence of the solid-like layer and boundary viscosity. GBC takes also into account all the possible variants of rotational interaction between the liquid microparticles and surface.

3.2 Viscosimetric Experiments

3.2.1 Squeeze of Liquid by Disks

Needs was the first who has determined reliably at what thicknesses and how the correspondence between TCF and experiment is lost [1]. He measured the velocity V of the approaching two parallel smooth steel disks of radius R , separated by a thin layer of liquid, under the dead load f . Carefully refined light oils were tested. It was discovered that at large thickness h of the oil layer the Stephan-Raynolds formula $\mu = 2fh^3/3\pi VR^4$ derived on the base of TCF, was kept accurately and gave the value of μ independent on h . But at small thicknesses $h \leq 2h_b$ ($h_b \sim$ some μm), the formula stopped working for most tested liquids except castor oil. Here, the combination of experimental data in the right part of the Stephan-Reynolds formula became some effective value μ_e with the dimensionality of viscosity but dependent on the thickness $\mu_e = \mu_e(h)$. The relative effective viscosity

$$\bar{\mu}_e = \mu_e/\mu = 2fh^3/3\pi\mu VR^4 \quad (\text{small gaps, } h \leq 2h_b) \quad (3.1)$$

was correspondingly not equal to unity and grow quickly with decreasing of h (according to $\bar{\mu}_e = 1$ for any $h!$). This fact is the direct evidence of the existence of subboundary layers of thickness h_b on the surfaces of both disks. Needs has also discovered that by decreasing the gap thickness to $h = 2h_s$, the movement of the disks stopped completely ($V = 0$), though the value h_s was certainly more than the zero reading of the instrument (the gap between dry disks). In this case, $\mu_e \rightarrow \infty$ according to Eq. (3.1). Needs positively said that it indicates the existence of solid-like layer of tested oil on the steel surfaces. He connected the effect of decreasing of h_s value at increasing of the load f and (or) temperature with the separation of oil molecules from the outer surface of solid-like layer due to the increasing radial flow velocity and (or) thermal movement of the molecules.

After Second World War Fuks has repeated experiments with disks, using more precise technique of h measuring and other liquids and materials of disks [2]. He proposed to take into account at calculations the effective thickness of the gap (the mobile part of the liquid) $h_e = h - 2h_s$. Then Eq. (3.1) converts into

$$\bar{\mu}_e = 2fh_e^3/3\pi\mu VR^4 \quad (3.2)$$

and $\bar{\mu}_e$ value remains finite at any velocity including the case $V = 0$. Experimental values of $\bar{\mu}_e$ calculated with the help of Eq. (3.2) from Needs data for olive oil are shown by triangles in Fig. 3.2 (experimental value of h_s was $0.31 \mu\text{m}$). According to Fig. 3.2, the equality for $\bar{\mu}_e$ following from TCF is kept only at $h_e > 3 \mu\text{m}$. Figure 3.2 shows also that the empirical dependence $\bar{\mu}_e(h_e)$ has two limit transitions. The first one

$$\bar{\mu}_e \rightarrow 1 \quad \text{at } h_e \rightarrow \infty \quad (3.3)$$

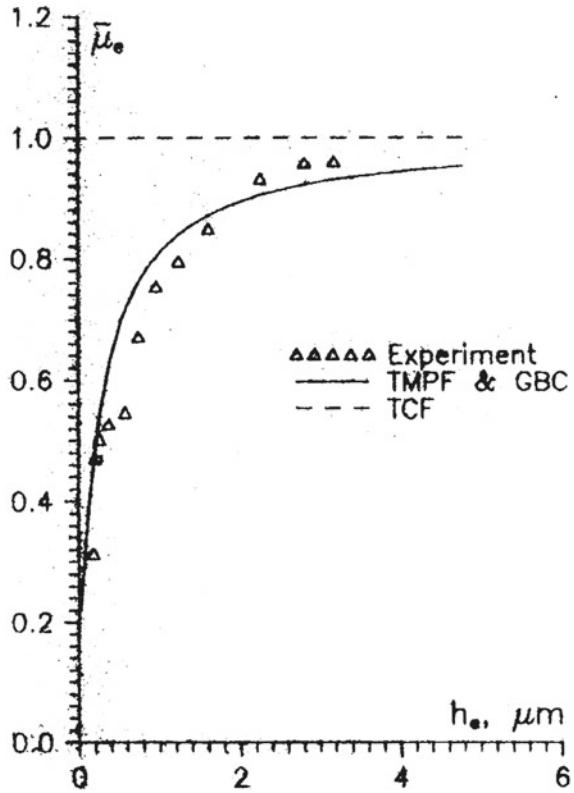
is the transition into the region of TCF applicability. The second one

$$\bar{\mu}_e \rightarrow \bar{\mu}_b \quad \text{at } h_e \rightarrow 0 \quad (3.4)$$

allows to introduce the concept of boundary viscosity $\bar{\mu}_b$ as an empirical material constant characterizing the liquid-surface pair. In the case of olive oil and steel $\bar{\mu}_b = 0.2$.

Theoretical dependencies $\bar{\mu}_e(h_e)$ are shown in Fig. 3.2 by solid (TMPF and GBC) and dotted (TCF) lines. Numerical values of $\bar{\mu}_b$, h_b and h_s calculated from experimental data of Needs and Fuks or quoted in their works are collected in Table 3.1. It gives the possibility to discuss more thoroughly the empirical characteristics of anomalous near the surface flow of real liquids. For castor oil, the condition $\bar{\mu}_e = 1$ was fulfilled at all gaps up to the least possible ones limiting by the roughness of disk surfaces, equal in practice to $\sim 0.1 \mu\text{m}$ or less. Therefore, the thickness of the subboundary layer of castor oil in steel is if the latter exists no more than $0.05 \mu\text{m}$. But both subboundary and solid-like layers were discovered for all other tested liquids (Table 3.1, rows 2 to 7). The values μ_b calculated by the limit transition (3.4) were

Fig. 3.2 Relative effective viscosity $\bar{\mu}_e$ of olive oil versus effective thickness h_e of gap between two steel disks. Treatment of experiments (Needs [1])



found to be 5–10 times less than the bulk shear viscosities μ of these liquids. We have calculated the mean radial velocity of flow $\langle v_r \rangle$ at $r = R$ for the moment when the thickness of the gap between approaching disks in Needs' and Fuks' experiments became equal to $1 \mu\text{m}$. The comparison of $\langle v_r \rangle$, h_b and h_s (Table 3.1, rows 2 to 7) shows that thicknesses of both specific subboundary and solid-like layers depend on the mean velocity of the liquid flow. The rough estimation of this dependence by these data shows that h_b and h_s decrease in proportion with $\lg \langle v_r \rangle$ and drop to zero at $\langle v_r \rangle \sim 200 \mu\text{m/s}$. In contrast with h_b and h_s , the value of boundary viscosity $\bar{\mu}_b$ does not practically depend on $\langle v_r \rangle$. Indeed all light oils on steel have $\bar{\mu}_b$ in interval between 0.12 and 0.2 at variation of $\langle v_r \rangle$ from 0.02 to $50 \mu\text{m/s}$; $\bar{\mu}_b$ of 0.01N water solution of NaCl changes in interval 0.06–0.08 at variation of $\langle v_r \rangle$ from 35 to $58 \mu\text{m/s}$ (Table 3.1, rows 2 to 5 and 6 and 7 correspondingly). These are the weighty arguments to consider the value $\bar{\mu}_b$ as the material constant of the liquid-surface pair.

Table 3.1 Collected results for tested liquids

	Liquid	Surface	$\langle v_r \rangle$, $\mu\text{m/s}$	h_b , $\mu\text{m/s}$	h_s , $\mu\text{m/s}$	$\bar{\mu}_b$	L , μm
	1	2	3	4	5	6	7
Squeeze by disks (Needs)							
1	Castor oil ^a	Steel	0.45	<0.05	–	–	–
2	Olive oil ^b	Steel	0.3	1.8	0.31	0.2	0.02
3	DTE light mineral oil	Steel	0.02	2.4	0.39	0.12	0.01
Squeeze by disks (Fucks)							
4	Transformer oil	Steel	30	0.6	0.07	0.18	0.006
5	Transformer oil	Steel	50	0.5	0.028	0.16	0.005
6	0.01N water solution of NaCl	Glass	35	0.8	0.06	0.06	0.003
7	0.01N water solution of NaCl	Glass	55	0.7	0.02	0.08	0.0035
Flow in capillar (Derjaguin)							
8	Benzene ^a	Glass	unknown	<0.05	–	–	–
9	CCl_4 ^a	Glass	unknown	<0.05	–	–	–
10	Water ^{b,c}	Glass	unknown	1	(a) 0	1.6	0.032
					(b) 0.02	0.09	0.003
Blowing-off (Derjaguin)							
11	PMS-70 ^b	Glass	unknown	0.03	–	2.2	0.02
12	PMS-70 ^b	Steel	unknown	0.004	–	0.15	0.02
13	Vaseline oil ^a	Steel	unknown	<0.001	–	–	–
Shear oscillations (Kondrashov and Marchasin)							
14	DBPh ^b	Glass	unknown	>5	0.4	0.2	0.6

^aAnomalous effects are absent

^bDependence $\mu_e(h_e)$ is shown in figure

^cExperiment shows only the possible interval $0 \leq h_s \leq 0.05 \mu\text{m}$

3.2.2 Flow in Capillar

In 70s, Derjaguin and colleagues have carried on the systematic investigation of the flow of low viscous liquids in superthin capillaries made of quartz glass [3]. They measured the liquid discharge Q at a constant longitudinal gradient of pressure dp/dz . Capillary diameters h were varied from 0.1 to 10 μm . Results of the experiments were treated by classical Poiseuille's formula that gave at large capillary diameters the "true" constant viscosity μ . But at small diameters, the same formula gave the effective viscosity dependent on h . The deviation of relative effective viscosity

$$\bar{\mu}_e = -\frac{\pi h^4}{128\mu Q} \frac{dp}{dz} \quad (\text{small diameters, } h \leq 2h_b) \quad (3.5)$$

from 1 allowed to determine the thickness h_b of subboundary layer. The experiments showed that in case of unpolar benzene and CCl_4 , the condition $\bar{\mu}_e = 1$ was kept at all capillar diameters up to the least ones $h \sim 0.1 \mu\text{m}$. Thus, if these liquids form subboundary layer on quartz glass, its thickness $h_b < 0.05 \mu\text{m}$ (Table 3.1, rows 8 and 9). For water (high polar liquid), the divergence of TCF and experiment began at capillar diameters $\sim 2 \mu\text{m}$ and became very significant at further decreasing of h . So the thickness of subboundary layer h_b was in this case $\sim 1 \mu\text{m}$. As water movement took place even in capillaries with the least diameters, the question about existence of the solid-like layer remains open. One can only affirm that its thickness is in the range $0 \leq h_s \leq 0.05 \mu\text{m}$. It is possible to take into account by analogy with the previous case (3.2) if one writes Eq. (3.5) as

$$\bar{\mu}_e = -\frac{\pi h_e^4}{128\mu Q} \frac{dp}{dz} \quad (3.6)$$

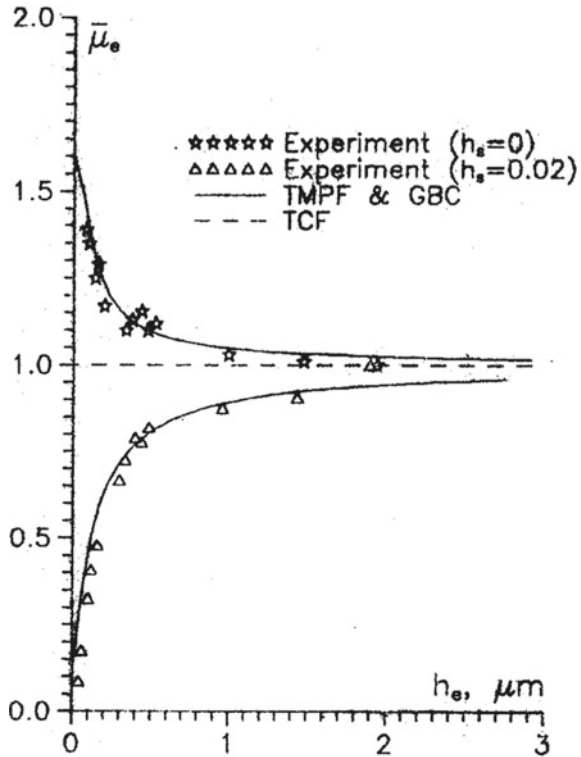
where $h_e = h - 2h_s$. The results of treatment of experimental data for water by Eq. 3.6 for two h_s values from the mentioned range (0 and $0.02 \mu\text{m}$) are shown in Fig. 3.3 and Table 3.1 (rows 10a and 10b). It is clear that indefinitely in estimation of h_s value can sufficiently change the form of dependence $\bar{\mu}_e(h_e)$ and $\bar{\mu}_b$ value.

Unfortunately, Derjaguin did not provide data on the values of mean flow rate in capillaries [3]. Nevertheless, if one proposes that the thickness of water solid-like layer on quartz glass in Derjaguin's experiments was equal to $0.02 \mu\text{m}$ (Table 3.1, row 10b), i.e., as in Fick's experiments with NaCl water solution on glass (Table 3.1, row 7), then the calculated values $\bar{\mu}_b$ are found to be very close (0.09 and 0.08 correspondingly). This estimation shows that the empirical dependence shown in Fig. 3.3 by triangles is more realistic.

3.2.3 Blow of Liquid Layer Off Surface

Above mentioned viscosimetric techniques give the integral value of the effective viscosity that characterizes the whole tested layer of the liquid. In the end of 40s, Derjaguin and colleagues have proposed the blow-off method that allows to determine directly the dependence of local effective viscosity on distance from surface [3]. In this method, the thin layer of tested nonvolatile liquid is applied on a flat smooth horizontal surface and its stationary movement along the surface is excited by the steady gas flow. The structure of the liquid flow reminds, in this case, the uniform shear of a paper ream. The front of the moving liquid film takes gradually the form of a very flat wedge. The profile of the wedge $h(x)$ (h —thickness, x —distance in flow direction) is measured by optical method. It is possible to calculate the velocity u of flow at different distances h from the surface. The working formula for calculation of local relative effective viscosity has the form

Fig. 3.3 Relative effective viscosity $\bar{\mu}_e$ of water versus effective diameter h_e of glass quartz capillary. Treatment of experiments (Derjaguin [3])

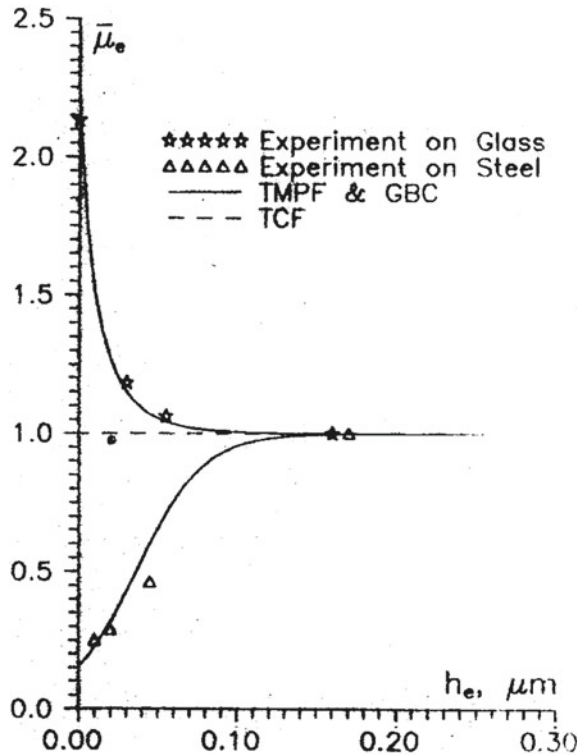


$$\bar{\mu}_e = \frac{dh/dx}{dh/dx|_{h \rightarrow \infty}} = \frac{du/dh|_{h \rightarrow \infty}}{du/dh} = \frac{du/dh_e|_{h_e \rightarrow \infty}}{du/dh_e}. \quad (3.7)$$

Rectilinear profile of the wedgelike front of vaseline oil film on steel manifested that the efficiency of TCF (condition $\bar{\mu}_e = 1$) is kept, in this case, up to the distance from surface $h \sim 0.001 \mu\text{m}$. The influence of surface nature on subboundary layer was discovered for polydimethylsiloxane liquids (PMS). Dependencies $\bar{\mu}_e(h_e)$ calculated by Eq. (3.7) from experimental data for the liquid PMS-70 on glass and steel are shown in Fig. 3.4 and in Table 3.1. There were no indications of solid-like layer in this case ($h_s = 0$, $h_e = h$). It is seen from the figure that deviations from TCF begin at $h_s \sim 0.1 \mu\text{m}$ but the character of the deviations is different for glass and steel. In the first case, $\bar{\mu}_e$ increases at decreasing of distance from the surface so that the relative boundary viscosity of PMS-70 on glass $\bar{\mu}_b > 1$. In the second case, $\bar{\mu}_e$ decreases at decreasing of h_e and $\bar{\mu}_b < 1$ for PMS-70—steel pair.

The blow-off method was applied to some other monomer and polymer liquids and, in most cases, the existence of subboundary layer of thickness $\sim 1 \mu\text{m}$ and less was discovered. Derjaguin connects the effects of changing of $\bar{\mu}_s$ value at approaching to surface with unfolding of polymer molecules and orientation of small asymmetric molecules under the action of surface and hydrodynamic field [3].

Fig. 3.4 Relative effective viscosity $\bar{\mu}_e$ of PMS-70 versus effective distance h_e from glass and steel flat surfaces at blowing-off. Treatment of experiments (Derjaguin [3])

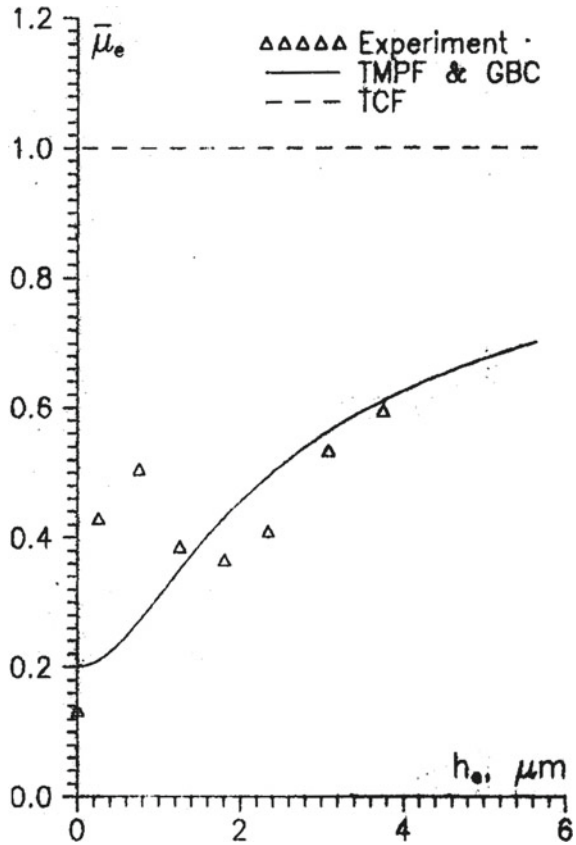


3.2.4 Liquid Layer Between Two Moving Plates

Derjaguin and colleagues have proposed the method of testing of viscoelastic properties of thin liquid layers between two flat smooth surfaces performing the relative plane-parallel oscillations [3]. The main idea of the method consists of measuring the resonant frequency of the system before and after entering the tested liquid between the plates. It allows to calculate the shear modulus and viscosity of the liquid using simple rheological models.

Kondrashov and Marchasin have investigated by this technique the changing of viscoelastic properties of dibutyl phthalate (DBPh) at variations of the gap thickness between two plates of quartz glass [10]. They discovered the existence of solid-like layer with thickness $h_s \sim 0.4 \mu\text{m}$. We used these data to calculate the dependence $\bar{\mu}_e(h_e)$ for DBPh. As it is seen from Fig. 3.5, all the experiments were realized in conditions when $\bar{\mu}_e \neq 1$ and the gap between plates was completely filled by closing subboundary layers. The thickness of the layers h_b has to be, according to Fig. 3.5, not less than $5 \mu\text{m}$. It is necessary to point out that DBPh manifested in these experiments not only viscous, but also to some extent elastic properties. Therefore, the calculated numerical values of \bar{h}_b and $\bar{\mu}_b$ (Table 3.1, row 14) are, in this case, not very reliable.

Fig. 3.5 Relative effective viscosity $\bar{\mu}_e$ of DBPh versus effective thickness h_e of gap between two glass flat surfaces at shear oscillations. Treatment of experiments (Kondrashov and Marchasin [10])



3.3 Experiments and Development of Fluid Theory

From today's point of view, the above discussed experimental works have certain limitations. The choice of tested liquids and surfaces was arbitrary. The comparison of numerous data from different works is possible only in rare cases. But one must not forget that only one general question arises there: if there are, then what are the peculiarities of the state and flow of real liquids near surfaces? And these works in total have given the clear answer: most of the real liquids form near surfaces two anomalous (from classical point of view) layers—subboundary and solid-like. The main physical properties of the liquids in these layers are known now quite reliably. Evidently these circumstances require the sufficient improvement of TCF. Otherwise, it is impossible to describe quantitatively the “anomalous” effects and solve the problems where near-wall flow is the dominant form of liquid movement.

Fluid theory has already been greatly improved to describe flows near the surface. At large distances from the surface, the real liquid flow is well described by the theory of ideal fluid. In this case, it is entirely sufficient to replace the solid surface with a

classical boundary layer and use the slip boundary condition at its outer surface. At smaller distances from the surface, in limits of the classical boundary layer, the theory of ideal fluid loses the accordance with experiment and is replaced by TCF. In TCF, the tangential viscous forces are introduced additionally. The influence of surface on fluid flow is taken into account by nonslip condition on the surface. It is clear now that this condition has to be referred to the outer surface of subboundary layer. However, the existence of this specific layer has no importance in many problems because of its extremely small thickness.

Two approaches are usually used in the improvement of fluid theory. In the first one, the basis of the theory (the fluid mathematical model) is not changed but some important conditions or postulates are additionally assumed to extend the field of the theory validity. The Kutta-Joukowski condition of attached vortex in dynamics of ideal fluid can be called as an example of such approach. The second approach is to revise the foundations of the theory in the transition from the theory of ideal fluid to TCF. The new theory (TCF) describes the liquid flow both within the classical boundary layer and far from it without additional assumptions.

Evidently that the correct description of liquid flow at micron and submicron distances from the surface is impossible without further improvement of fluid theory. In order to carry out such improvement, both the aforementioned approaches can be used. In the first approach, some empirical dependence of effective viscosity on distance $\bar{\mu}_e(h)$ may be introduced in TCF. This can help to solve a number of similar problems, but there is no guarantee that the accepted dependency $\bar{\mu}_e(h)$ is fit to any other ones. One may try also to use in TCF nonnewtonian rheological models consistent with real behavior of liquids in thin layers. But then the new theory will work only in limits of specific subboundary layer and the joining of two solutions based on newtonian and nonnewtonian models will be required on outer surface of the layer. The second approach consisting of improvement of the classical theory basis seems to be more reliable and universal. Of course, the efficiency of any new theory has to be tested with an experiment.

Some preliminary considerations of ways of TCF basis refinement can be done a priori. The fluid molecules are modeled in TCF by material points that interact one with another and with the surface by central forces and move only translationally. Accordingly, the fields of central forces and translation velocities are figured in the theory. As it works very well in and far off the classical boundary layer, the question of taking into account other physical properties of molecules than mass and translation velocity was not arisen. As was shown above, TCF loses the accordance with experiment at micron and less distances from surface, i.e., when the transverse dimension of the flow approaches to dimensions of microparticles in real liquids. It manifests that “anomalous” effects are connected first of all with interactions and movements which are characteristic of material objects of finite dimensions. In this case, not only translational movement, but rotational movement and not only central forces, but moments of forces have to be taken into account. Then it is reasonable to suppose that the formation of subboundary layer is connected just with the influence of the surface on rotational mobility of liquid microparticles exactly as the formation of classical boundary layer is connected with the influence of surface on translational

mobility. If so, then the theory that describes adequately the flow, both in classical and specific boundary layers, has to be sought among the theories of microstructural fluids where fields of moments and rotation velocities are certainly introduced in addition to fields of central forces and translation velocities.

3.4 Principles of Micropolar Fluid Theory

Eringen has proposed the very general theory of “micromorphous” fluid in which the motion of fluid microparticles is characterized by translation velocity \mathbf{v} as in classical theory and additionally by microrotation velocity $\boldsymbol{\omega}$ nonequal in general to $1/2\nabla \times \mathbf{v}$ [7]. The microparticles are considered to be deformable. But the practical application of the theory is complicated by great mathematical difficulties. The first rigorous and workable theory of fluid with microstructure has been proposed by Aero, Bulygin, and Kuvshinskii—the theory of “asymmetric” or “momental” fluid [8]. The analogous theory was proposed independently by Eringen [11]. He used the term “micropolar” fluid that has become most popular in science literature (see [12–14]). In the Eringen-Aero theory of micropolar fluid (further—TMPF), the fluid microparticles are considered to be nondeformable. The basic ideas of TMPF discussed below are given in accordance with two above mentioned fundamental works and the exhaustive review of Stokes [15].

The laws of conversation of mass, momentum, angular momentum, and energy E have in TMPF the following form:

$$\frac{d}{dt} \int_{\Omega} \rho d\Omega = 0, \quad (3.8)$$

$$\frac{d}{dt} \int_{\Omega} \mathbf{v} \rho d\Omega = \oint_s \mathbf{f} ds + \int_{\Omega} \mathbf{t} \rho d\Omega, \quad (3.9)$$

$$\frac{d}{dt} \int_{\Omega} (\mathbf{r} \times \mathbf{v} + \underline{I\boldsymbol{\omega}}) \rho d\Omega = \oint_s (\mathbf{r} \times \mathbf{f} + \underline{\mathbf{m}}) ds + \int_{\Omega} (\mathbf{r} \times \mathbf{t} + \underline{\mathbf{c}}) \rho d\Omega, \quad (3.10)$$

$$\frac{d}{dt} \int_{\Omega} E \rho d\Omega = \oint_s (\mathbf{v} \cdot \mathbf{f} + \underline{\boldsymbol{\omega} \cdot \mathbf{m}}) ds + \int_{\Omega} (\mathbf{v} \cdot \mathbf{t} + \underline{\boldsymbol{\omega} \cdot \mathbf{c}}) \rho d\Omega, \quad (3.11)$$

where ρ —density, Ω —region of space bounded by the surface s , \mathbf{t} , and \mathbf{c} —body force and body moment correspondingly, \mathbf{f} and \mathbf{m} —surface force and moment correspondingly, and I is moment of microinertia per mass unit. Terms underlined in Eqs. (3.8)–(3.11) show the contribution of microrotations and also surface and body moments (in the Appendix, we provide simple (not rigorous) but vivid derivation of

pre-imaged of TMPM conservation laws on the basis of the mechanics of material points).

In addition to usual tensor of force stresses \mathbf{F} , the tensor of moment stresses \mathbf{M} is introduced in TMPF and the following relations take place:

$$\mathbf{f} = \mathbf{e} \cdot \mathbf{F}, \quad \mathbf{m} = \mathbf{e} \cdot \mathbf{M}, \quad (3.12)$$

where \mathbf{e} —outer normal to s .

Substitution of Eq. (3.12) in conservation laws (3.8)–(3.11) allows to write the equations of motion in differential form (the case of incompressible fluid in the absence of external body forces and moments)

$$\nabla \cdot \mathbf{v} = 0, \quad (3.13)$$

$$\rho \frac{d\mathbf{v}}{dt} = \nabla \cdot \mathbf{F}, \quad (3.14)$$

$$\rho I \frac{d\boldsymbol{\omega}}{dt} = \mathbf{i} \times (\mathbf{i} \cdot \mathbf{F}) + \mathbf{j} \times (\mathbf{j} \cdot \mathbf{F}) + \mathbf{k} \times (\mathbf{k} \cdot \mathbf{F}) + \underline{\nabla \cdot \mathbf{M}}, \quad (3.15)$$

$$\rho \frac{dE}{dt} = \nabla \cdot (\mathbf{F} \cdot \mathbf{v}) + \underline{\nabla \cdot (\mathbf{M} \cdot \boldsymbol{\omega})}, \quad (3.16)$$

where t —time, \mathbf{i} , \mathbf{j} , and \mathbf{k} —unit vectors along coordinate axes. In TCF the fluid microparticles are regarded to be points. Therefore, the terms underlined in Eqs. (3.15) and (3.16) disappear. Then Eq. (3.15) gives the equalities for components of tensor \mathbf{F}

$$F_{23} = F_{32}, \quad F_{31} = F_{13}, \quad F_{12} = F_{21}, \quad (3.17)$$

that point to its symmetry in classical (“symmetrical”) hydrodynamics. In TMPF tensor, \mathbf{F} is asymmetrical (hence the term “asymmetrical” hydrodynamics).

The connection between kinematic and dynamic characteristics of fluid movement is set in TMPF by the following linear rheological relations

$$F_{nk} = -p\delta_{nk} + \mu (v_{n,k} + v_{k,n}) + \mu_r (v_{k,n} - v_{n,k} - 2\omega_q \epsilon_{qnk}), \quad (3.18)$$

$$M_{nk} = \gamma \omega_{k,n} + \lambda \omega_{n,k} + \vartheta \delta_{nk} \omega_{q,q}, \quad n, k, q = 1, 2, 3, \quad (3.19)$$

where μ_r —coefficient of microrotation viscosity, p —pressure, γ , λ , and ϑ —coefficients of dissipation in consequence of microrotation gradients, δ_{nk} and ϵ_{qnk} —Kronecker’s and permutation symbols correspondingly. Doubly repeated subscripts imply summation over the range 1, 2, 3, $v_{n,k} = \partial v_n / \partial x_k$, etc.

The basic thermodynamics laws are satisfied if all material constants in Eqs. (3.18) and (3.19) are nonnegative. The substitution of Eqs. (3.18) and (3.19) in Eqs. (3.13)–

(3.16) give the full system of TMPF equations of motion

$$\nabla \cdot \mathbf{v} = 0, \quad (3.20)$$

$$\rho \frac{d\mathbf{v}}{dt} = -\nabla p + \mu \nabla^2 \mathbf{v} + \mu_r \nabla \times (2\boldsymbol{\omega} - \nabla \times \mathbf{v}), \quad (3.21)$$

$$\rho I \frac{d\boldsymbol{\omega}}{dt} = \gamma \nabla^2 \boldsymbol{\omega} + (\lambda + \vartheta) \nabla (\nabla \cdot \boldsymbol{\omega}) - 2\mu_r (2\boldsymbol{\omega} - \nabla \times \mathbf{v}). \quad (3.22)$$

Let the scales of length, translation velocity, time, microrotation velocity, and pressure are taken to be h , U , h/U , U/h , and ρU^2 correspondingly, where h —transverse dimension of the flow region and U —characteristic velocity of the flow. Then the Eqs. (3.20)–(3.22) take the following nondimensional form:

$$\nabla \cdot \mathbf{v} = 0, \quad (3.23)$$

$$\frac{d\mathbf{v}}{dt} = -\nabla p + \frac{1}{Re} \nabla^2 \mathbf{v} + \frac{1}{Re_r} \nabla \times (2\boldsymbol{\omega} - \nabla \times \mathbf{v}), \quad (3.24)$$

$$\left(\frac{L_1}{h}\right)^2 Re \frac{d\boldsymbol{\omega}}{dt} = \left(\frac{L_2}{h}\right)^2 \nabla^2 \boldsymbol{\omega} + \left(\frac{L_3}{h}\right)^2 \nabla (\nabla \cdot \boldsymbol{\omega}) - \frac{2Re}{Re_r} (2\boldsymbol{\omega} - \nabla \times \mathbf{v}), \quad (3.25)$$

where $Re = \rho h U / \mu$, $Re_r = \rho h U / \mu_r$, $L_1 = I^{1/2}$, $L_2 = (\gamma / \mu)^{1/2}$, and $L_3 = ((\lambda + \vartheta / \mu))^{1/2}$. All nondimensional values in Eqs. (3.23)–(3.25) keep the same notations as the correspondent dimensional ones in Eqs. (3.20)–(3.22). The complexes L_1 , L_2 , and L_3 have the dimensions of length and play the role of inner linear scales of the liquid microstructure. The role of nonclassical terms in Eqs. (3.23)–(3.25) (in other words—the influence of fluid microstructure) grows with decreasing of the dimension h of the flow region. In contrast, when h becomes much bigger than L_1 , L_2 , and L_3 , Eq. (3.25) converts to the relation $\boldsymbol{\omega} = 1/2 \nabla \times \mathbf{v}$ and Eq. (3.24) transforms into the classical Navier–Stokes equation as the partial case.

3.5 Boundary Conditions

The question of boundary conditions is one of the central in any theory of fluid. TMPF needs in boundary condition for both \mathbf{v} and $\boldsymbol{\omega}$ [16]. The classical nonslip condition is used for translation velocity

$$\mathbf{v} = \mathbf{V} \quad \text{at } h = 0, \quad (3.26)$$

where \mathbf{V} —the surface velocity.

Other boundary conditions have to reflect the mechanism of the surface influence on the field of microrotations. In limit case when the fluid microparticles cannot rotate at all on the surface, the boundary condition for microrotation is written in the form

$$\boldsymbol{\omega} = 0 \quad \text{at } h = 0, \quad (3.27)$$

analogous to nonslip condition for \mathbf{v} given by Eq. (3.26). Thus, the simplest boundary condition is used in almost all works where TMPF is applied to practical problems [15]. Migun has proposed more general boundary condition [17]

$$\boldsymbol{\omega} = \frac{\alpha}{2} \nabla \times \mathbf{v} \quad \text{at } h = 0, \quad (3.28)$$

which admits the slip of microrotations on surface. The coefficient α in Eq. (3.28) characterizes the degree of microrotation slip and changes (as Migun has supposed apriori) in the range $0 \leq \alpha \leq 1$.

As it will be shown below, the boundary condition (3.28) and the more so (3.27) are not in full agreement with experimental results discussed above. The problem has been advanced by introducing the coefficient of empirical boundary viscosity μ_b into boundary conditions [18, 19]. But they were related as earlier to $h = 0$ ($h_s = 0$). Now we can consider the more general case $h_s \geq 0$ and relate the boundary conditions to outer surface of solid-like layer. According to Eq. (3.18), the friction force of micropolar fluid acting on the outer surface of solid-like layer is equal to

$$\mathbf{e}_n \left[-p\delta_{nk} + \mu (v_{n,k} + v_{k,n}) + \mu_r (v_{k,n} - v_{n,k} - 2\omega_q \epsilon_{qnk}) \right], \quad (3.29)$$

where \mathbf{e}_n —normal to surface. On the outer side, the same force can be determined with the help of empirical boundary viscosity μ_b as

$$\mathbf{e}_n \left[-p\delta_{nk} + \mu_b (v_{n,k} + v_{k,n}) \right]. \quad (3.30)$$

The combination of Eqs. (3.26), (3.29), and (3.30) gives the following general boundary conditions (further—GBC):

$$\begin{aligned} \mathbf{e}_n \left[(\mu - \mu_r - \mu_b) v_{n,k} + (\mu + \mu_r - \mu_b) v_{k,n} - 2\mu_r \omega_q \epsilon_{qnk} \right] &= 0, \\ \mathbf{v} = \mathbf{V} \quad \text{at } h_e = 0 \quad (h = h_s). \end{aligned} \quad (3.31)$$

In thin layer approximation, when the coordinate axes are directed along the surface, GBC take the following particular form:

$$\boldsymbol{\omega} = \frac{\mu + \mu_r - \mu_b}{2\mu_r} \nabla \times \mathbf{v}, \quad \mathbf{v} = \mathbf{V} \quad \text{at } h_e = 0, \quad (3.32)$$

It follows from Eq. (3.32) that the boundary condition (3.27) corresponds to the case $h_s = 0$ and $\mu_b = \mu + \mu_r$. It contradicts the experiment because we know now that μ_b depends on the properties of both the liquid and the surface (Table 3.1). The boundary condition (3.28) corresponds to the case $h_s = 0$ and $\mu \leq \mu_b \leq \mu + \mu_r$. But it is known now that the case $h_s \neq 0$ and $\mu_b < \mu$ is also possible (Table 3.1). Thus, GBC (3.32) have now the best experimental grounds.

3.6 Theory of Micropolar Fluid and Viscosimetric Experiments

TMPF and GBC are used below in derivation of theoretical dependencies $\bar{\mu}_e(h_e)$ corresponding to empirical ones obtained by different experimental techniques. Equations (3.20)–(3.22) are taken in thin layer approximation as the examined flows are laminar and slow [15, 20].

3.6.1 Squeeze of Liquid by Disks

The movement of the layer of micropolar fluid squeezing out of gap between two smooth disks is described in cylindrical coordinates (r, φ, z) by the following system of equations [21].

$$\begin{aligned} (\mu + \mu_r) \frac{\partial^2 v_r}{\partial z^2} - 2\mu_r \frac{\partial \omega_\varphi}{\partial z} &= \frac{dp}{dr}, \\ \gamma \frac{\partial^2 \omega_\varphi}{\partial z^2} - 2\mu_r \left(2\omega_\varphi - \frac{\partial v_r}{\partial z} \right) &= 0, \end{aligned} \quad (3.33)$$

where $\mathbf{v} = (v_r, 0, v_z)$, $\boldsymbol{\omega} = (0, \omega_\varphi, 0)$ and z axis is directed perpendicular to the disk surfaces. Prakash and Sinha have also given the general solution of Eq. (3.33) and solved them using the simplest boundary conditions (3.26) and (3.27) [21]. GBC (3.32) in this case have the following form:

$$\begin{aligned} v_r = 0, \quad v_z = 0, \quad \omega_\varphi &= \frac{\mu + \mu_r - \mu_b}{2\mu_r} \frac{\partial v_r}{\partial z} \quad \text{at } z = 0 \quad \text{and} \\ v_r = 0, \quad \theta_z = -V, \quad \omega_\varphi &= \frac{\mu + \mu_r - \mu_b}{2\mu_r} \frac{\partial v_r}{\partial z} \quad \text{at } z = h_e. \end{aligned} \quad (3.34)$$

The boundary conditions for pressure have the form

$$\frac{dp}{dr} = 0 \quad \text{at } r = 0 \quad \text{and} \quad p = 0 \quad \text{at } r = R. \quad (3.35)$$

The substitution of Eq. (3.34) in general solution of Eq. (3.33) allows to determine the analytical expression for the radial velocity v_r . The subsequent substitution of v_r in continuity equation

$$\frac{1}{r} \frac{\partial (rv_r)}{\partial r} + \frac{\partial v_z}{\partial z} = 0 \quad (3.36)$$

and integration of the latter with respect to z from 0 to h_e give the following equation for distribution of pressure between disks:

$$\frac{1}{r} \frac{d}{dr} \left(r \frac{dp}{dr} \right) = -\frac{12\mu\bar{\mu}_e V}{h_e^3}, \quad (3.37)$$

where

$$\bar{\mu}_e = \frac{1}{1 + 3K (1 - \bar{h}_e \coth \bar{h}_e) / \bar{h}_e^2}, \quad (3.38)$$

$$\bar{h}_e = h_e/L, \quad K = 1 - 1/\bar{\mu}_b, \quad \bar{\mu}_b = \mu_b/\mu, \quad L = [\gamma (1/\mu + 1/\mu_r)]^{1/2}. \quad (3.39)$$

The solution of Eq. (3.37) with respect to p at boundary condition (3.35) allows to determine the connection of the problem parameters with outer force f

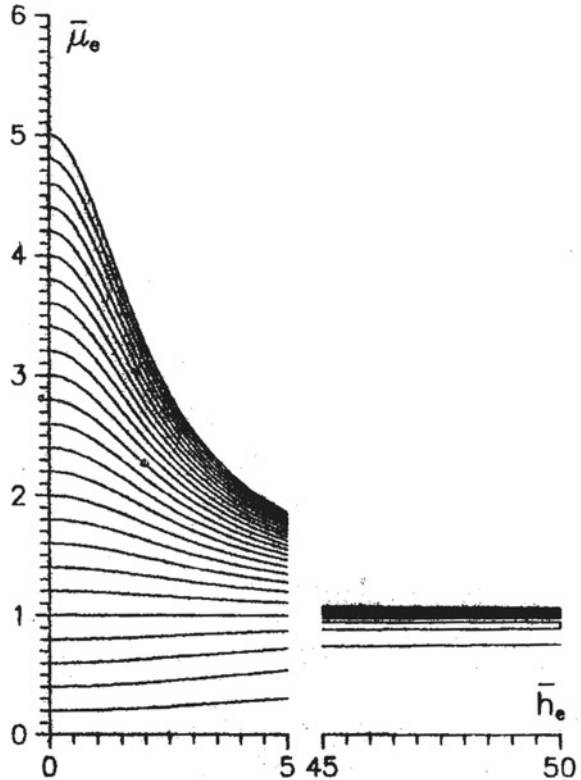
$$f = 2\pi \int_0^R pr dr = 3\pi\mu\bar{\mu}_e V R^4 / 2h_e^3, \quad (3.40)$$

and to receive the following formula for $\bar{\mu}_e$

$$\bar{\mu}_e = 2fh_e^3 / 3\pi\mu V R^4. \quad (3.41)$$

The comparison of Eqs. (3.40) and (3.2) shows that the relation (3.38) derived on the base of TMPF and GBC is just the theoretical dependence of relative effective viscosity $\bar{\mu}_e$ on effective gap thickness \bar{h}_e for the problem of two disks. Such dependencies at different $\bar{\mu}_b$ values are shown graphically in Fig. 3.6. It is seen that the sufficient deviation of $\bar{\mu}_e$ value from unity takes place when the effective thickness of gap h_e becomes comparable with the inner linear scale L of the liquid microstructure ($\bar{h}_e \leq 10$). Besides it is always $\bar{\mu}_e < 1$ at $\bar{\mu}_b < 1$ and $\bar{\mu}_e > 1$ at $\bar{\mu}_b > 1$. At large gaps ($\bar{h}_e > 10$) $\bar{\mu}_e \rightarrow 1$, and the classical case takes place. As it is shown in Fig. 3.2, the theory is in good accordance with experiment. The values of L calculated by fitting of theoretical curves and experimental data are given in the last column of Table 3.1.

Fig. 3.6 Theoretical dependencies of relative effective viscosity $\bar{\mu}_e$ of micropolar fluid on relative effective gap thickness \bar{h}_e . Value of $\bar{\mu}_b$ is varied from 0.2 to 5.0 in steps 0.2



3.6.2 Flow in Capillar

The problem of flow of micropolar fluid in cylindrical capillar comes to solution of the following equations

$$(\mu + \mu_r) \frac{d}{dr} \left(r \frac{dv_z}{dr} \right) + 2\mu_r \frac{d(r\omega_\varphi)}{dr} = r \frac{dp}{dz}, \tag{3.42}$$

$$\gamma \frac{d}{dr} \left[\frac{1}{r} \frac{d(r\omega_\varphi)}{dr} \right] - 2\mu_r \left(2\omega_\varphi + \frac{dv_z}{dr} \right) = 0, \tag{3.43}$$

where $\mathbf{v} = (0, 0, v_z)$, $\boldsymbol{\omega} = (0, \omega_\varphi, 0)$ and z axis is directed along the capillar axis. The continuity equation is satisfied here identically. Many authors, beginning from Eringen [11] solved the problem using the condition of full retardation of microrotations on surface (3.27). GBC (3.32) are written for the given problem as

$$\frac{dv_z}{dr} = 0, \quad \frac{d\omega_\varphi}{dr} = 0, \quad \text{at } r = 0$$

and $v_z = 0, \quad \omega_\varphi = -\frac{\mu + \mu_r - \mu_b}{2\mu_r} \frac{dv_z}{dr} \quad \text{at } z = h_e/2.$ (3.44)

The solution of Eqs. (3.42)–(3.43) in combination with conditions (3.44) allows to derive an equation for longitudinal velocity v_z and calculate the fluid discharge Q through the capillar by formula

$$Q = 2\pi \int_0^{h_e/2} v_z r dr = -\frac{\pi h_e^4}{128\mu\bar{\mu}_e} \frac{dp}{dz}, \quad (3.45)$$

where

$$\bar{\mu}_e = \frac{1}{1 - 4K I_2(\bar{h}_e) / (\bar{h}_e I_1(\bar{h}_e))}, \quad (3.46)$$

I_1 and I_2 —Bessel's functions. Comparison of Eqs. (3.6) and (3.45) shows that Eq. (3.46) is the theoretical dependence of the relative effective viscosity $\bar{\mu}_e$ determined by capillar on relative effective diameter \bar{h}_e . The form of dependence in Eq. (3.46) is quantitatively the same as that of analogous dependence for disks, shown in Fig. 3.6. It has also two limits transitions (3.3) and (3.4) and is easily fitted to the experimental curves as it is shown in Fig. 3.3.

3.6.3 Blow of Liquid Layer Off Surface

The stationary movement of the layer of micropolar fluid under action of steady gas flow along the surface is described by equations

$$(\mu + \mu_r) \frac{d^2 u}{dh_e^2} + 2\mu_r \frac{d\omega_z}{dh_e} = 0,$$

$$\gamma \frac{d^2 \omega_z}{dh_e^2} - 2m u_r \left(2\omega_z + \frac{du}{dh_e} \right) = 0, \quad (3.47)$$

where $\mathbf{v} = (u, 0, 0)$ and $\boldsymbol{\omega} = (0, 0, \omega_z)$. The general solution of the equations is analogous to the solution of Eq. (3.33). GBC (3.32) on outer surface of solid-like layer have the following form:

$$u = 0, \quad \omega_z = -\frac{\mu + \mu_r - \mu_b}{2\mu_r} \frac{du}{dh_e} \quad \text{at } h_e = 0. \quad (3.48)$$

The boundary conditions on the outer surface of the layer of the fluid can be written as

$$\frac{d\omega_z}{dh_e} = 0, \quad \frac{du}{dh_e} = \left. \frac{du}{dh_e} \right|_{h_e \rightarrow \infty} \quad \text{at } h_e \rightarrow \infty. \quad (3.49)$$

The solution of Eq. (3.47) with the boundary conditions (3.48) and (3.49) give the value u as

$$u = \left. \frac{du}{dh_e} \right|_{h_e \rightarrow \infty} L [\bar{h}_e - K [1 - \exp(-\bar{h}_e)]]. \quad (3.50)$$

As it follows from Eq. (3.50)

$$\bar{\mu}_e = \frac{du/dh_e}{\left. du/dh_e \right|_{h_e \rightarrow \infty}} = \frac{1}{1 - K \exp(-\bar{h}_e)}. \quad (3.51)$$

Comparison of Eqs. (3.51) and (3.7) shows that Eq. (3.51) is the theoretical formula for local effective viscosity. As it is seen from Fig. 3.4, TMPF and GBC are in good agreement with experiment.

3.6.4 Liquid Layer Between Two Moving Plates

The flow of the layer of micropolar fluid between two moving parallel plates is described by Eq. (3.47). GBC (3.32) have here the form

$$\begin{aligned} u = 0, \quad \omega_z = -\frac{\mu + \mu_r - \mu_b}{2\mu_r} \frac{du}{dy} \quad \text{at } y = 0 \\ \text{and } u = U, \quad \omega_z = -\frac{\mu + \mu_r - \mu_b}{2\mu_r} \frac{du}{dy} \quad \text{at } y = h_e. \end{aligned} \quad (3.52)$$

The solution of Eq. (3.47) with the boundary conditions (3.52) give the value of tangential stress acting on the plates from the fluid equal to $\mu \bar{\mu}_e U / h_e$, where

$$\bar{\mu}_e = \frac{1}{1 - (K \tanh \bar{h}_e) / \bar{h}_e}. \quad (3.53)$$

The theoretical formula for relative effective viscosity (3.53) can be again fitted with the correspondent experimental curves (Fig. 3.5).

3.7 Conclusions

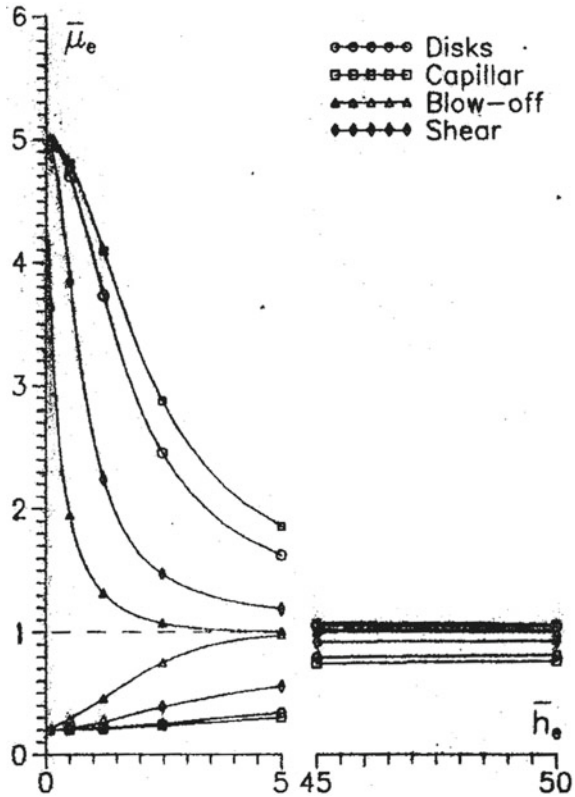
Independent viscosimetric experiments discussed above show ambiguously that most real liquids form near solid surfaces thin specific subboundary layer where the theory of classical fluid becomes unsuitable. Modern experiments also show that many liquids form directly on a solid surface the superthin solid-like layer where the liquids do not flow. The application of Eringen-Aero theory of micropolar fluid and new general boundary conditions to analyses of anomalous (from the classical point of view) effects in the flow of real liquids near solid surfaces has given good results. In all cases considered here (squeeze from gap, flow in thin capillaries, blow-off solid surface, and flow between moving plates), the full solutions of the correspondent hydrodynamic problems have been obtained. The theoretical dependencies of relative effective viscosity $\bar{\mu}_e$ on effective thickness h_e of flow derived here are fitted quite well with experimental dependencies (Figs. 3.2, 3.3, 3.4, and 3.5). Thus, we can conclude that the theory of micropolar fluid and new general boundary conditions allow to describe adequately the “anomalous” effects in subboundary layer and extend fluid theory up to the near most distances from solid surface, more exactly—to the other surface of solid-like layer, i.e., to 0.1 μm and less from the solid surface.

It is possible to make some additional remarks in connection with these conclusions. As was shown the empirical values of thicknesses of subboundary and solid-like layers (h_b and h_s in Table 3.1) depend on the mean velocity of the liquid flow. The empirical coefficient of boundary viscosity μ_b is determined by the nature of the system liquid-solid surface. These facts do not contradict the theory of micropolar fluid. According to this theory, the microstructure parameter L has to be dependent only on the liquid nature. The numerical values of L calculated from the condition of the best fitting of theoretical dependencies $\bar{\mu}_e(h_e)$ with the correspondent experimental ones are shown in Table 3.1. As it is seen (Table 3.1, rows 4 and 5; 6, 7 and 10b; 11 and 12) the calculations have given practically the same value of L for given liquid independently on conditions of experiment in all three cases pointed above. It is an objective argument in favor of the theory of micropolar fluid.

All theoretical dependencies of the relative effective viscosity $\bar{\mu}_e(\bar{h}_e)$ obtained above satisfy the necessary thermodynamic condition $\bar{\mu}_e \neq 0$ at $\bar{h}_e \neq 0$ and limit passes (3.3) and (3.4). These properties of the dependencies are visualized in Fig. 3.7. Figure 3.7 shows also that deviations from the classical condition $\bar{\mu}_e = 1$ begin at different distances from solid surface in different experimental situations. The biggest effect corresponds to flow in capillar when subboundary layer surrounds the flow from everywhere. The smallest effect corresponds to the blowing-off when there is only one solid boundary of the flow. So we can say that geometry of flow is the another important factor controlling the intensity of nonclassical near-the wall effects.

Though the calculations by the theory of micropolar fluid are in good accordance with experimental data, some quantitative deviations take place sometimes as seen in figures. The deviations can be provoked by both mistakes in measurements and in the completeness of calculations. One might notice that the theory of micropolar fluid permits if necessary the further generalizations by passing to nonlinear rheological

Fig. 3.7 Theoretical dependencies of relative effective viscosity $\bar{\mu}_e$ of micropolar fluid on relative effective distance \bar{h}_e from surface at different experimental conditions. Value of $\bar{\mu}_b$ is taken equal to 0.2 and 5.0



relations. But at first, all the possibilities of the linear theory of micropolar fluid that has already shown its effectiveness have to be utilized completely. And the most important (and difficult) problem is now the organization of systematic experiments to obtain the most reliable and full empirical data on near-the wall flows that can be analyzed theoretically without doubts. The chain of successive generalizations of fluid mathematical models: ideal fluid \rightarrow classical viscous fluid \rightarrow micropolar fluid is not finished now (Fig. 3.1). The existence of a specific solid-like layer prevents to use the theory of micropolar fluid (linear or not) directly up to the solid surface. The next step will be evidently the theory of micropolar viscoelastic fluid that has to take into account the properties of elasticity and plasticity which are manifested in solid-like layers of real liquids.

Appendix. Derivation of the Pre-images of TMPF Conversation Laws by Means of Particle System Mechanics

Let there is a system of particles (material points) with equal masses m . Let every Q neighboring particles are joined together in J equal rigid subsystems with constant mass $M = Qm$, $dM/dt = 0$. This rigid subsystems (further—bodies) are the pre-images of molecules or stable molecular aggregates. The radius vector \mathbf{r}_j and velocity \mathbf{v}_j of inertia center of the j -th body are equal to

$$\mathbf{r}_j = \left(\sum_{q=1}^Q \mathbf{r}_{qj} \right) / Q \quad \text{and} \quad \mathbf{v}_j = d\mathbf{r}_j/dt, \quad (3.54)$$

where \mathbf{r}_{qj} and $\mathbf{v}_{qj} = d\mathbf{r}_{qj}/dt$ —radius vector and velocity of the qj -th particle in motionless coordinate system $OXYZ$ correspondingly ($q = 1, 2, \dots, Q$; $j = 1, 2, \dots, J$). Let every j -th body is connected rigidly with mobile coordinate system $O'X'Y'Z'$ (with origin in inertia center of the body) rotating about axis $OXYZ$ with angular velocity $\boldsymbol{\omega}_j$. Then

$$\mathbf{r}_{qj} = \mathbf{r}_j + \mathbf{r}'_{qj} \quad \text{and} \quad \mathbf{v}_{qj} = \mathbf{v}_j + \boldsymbol{\omega}_j \times \mathbf{r}'_{qj}, \quad (3.55)$$

where \mathbf{r}_{qj} —radius vector of the qj -th particle in coordinate system $O'X'Y'Z'$.

Let inner paired central forces \mathbf{f} (\mathbf{f} type forces) act between all particles of the system. Then the following equalities take place for any particles a and b

$$\mathbf{f}_a = -\mathbf{f}_b, \quad \mathbf{r}_a \times \mathbf{f}_a = -\mathbf{r}_b \times \mathbf{f}_b, \quad \mathbf{r}'_a \times \mathbf{f}_a = -\mathbf{r}'_b \times \mathbf{f}_b. \quad (3.56)$$

Let \mathbf{f}_{qj} is the resultant of all \mathbf{f} type forces acting on the particle qj from all other particles. The outer forces as gravity, etc., with the resultant \mathbf{t}_{qj} (\mathbf{t} type forces) can also act. Then the Newton law for the qj -th particle is written as

$$m \frac{d\mathbf{v}_{qj}}{dt} = \mathbf{f}_{qj} + \mathbf{t}_{qj}. \quad (3.57)$$

The summation of Eq. (3.57) over all particles of the system gives

$$M \frac{d}{dt} \sum_{j=1}^J \mathbf{v}_j = \sum_{j=1}^J \mathbf{f}_j + \sum_{j=1}^J \mathbf{t}_j. \quad (3.58)$$

where $\mathbf{f}_j = \sum_{q=1}^Q \mathbf{f}_{qj}$, and \mathbf{t}_{qj} —the resultants of all correspondent forces acting on the j -th body. The left-hand side of Eq. (3.58) is the time derivation of the system momentum. The \mathbf{f} type forces between all particles of the system are mutually compensated according to Eq. (3.56). So the first sum in right-hand side of Eq. (3.58) contains in fact only \mathbf{f} type forces acting on the peripheral particles of the system

from outer ones. Therefore, the first sum may be named the “surface” sum. Thus, Eq. (3.58) is, up to notations, the full pre-image of momentum conservation law for micropolar fluid (3.9).

The vector multiplication of both sides of Eq. (3.57) on \mathbf{r}_{qj} and summation with respect to all particles give the following equation:

$$M \frac{d}{dt} \sum_{j=1}^J \left(\mathbf{r}_j \times \mathbf{v}_j + \underline{\mathbf{I}} \cdot \underline{\boldsymbol{\omega}}_j \right) = \sum_{j=1}^J \left(\mathbf{r}_j \times \mathbf{f}_j + \underline{\mathbf{m}}_j \right) + \sum_{j=1}^J \left(\mathbf{r}_j \times \mathbf{t}_j + \underline{\mathbf{c}}_j \right), \quad (3.59)$$

where $\underline{\mathbf{m}}_j = \sum_{q=1}^Q \mathbf{r}_{qj} \times \mathbf{f}_{qj}$, $\underline{\mathbf{c}}_j = \sum_{q=1}^Q \mathbf{r}_{qj} \times \mathbf{t}_{qj}$ are the resultant moments of correspondent forces acting on j -th body relatively its inertia center, $\underline{\mathbf{I}}$ —tensor of inertia moments of the bodies related to the mass unit. For rigid body of sphere symmetry $\underline{\mathbf{I}} = I\mathbf{E}$, where \mathbf{E} —unit tensor. The first sum in the right-hand side of Eq. (3.59) can be again named due to Eq. (3.56) the “surface” sum while the second sum remains “volume”. Thus, the Eq. (3.59) is, up to notations, the full pre-image of angular momentum conservation law for micropolar fluid (3.10). The change in full energy of any system is equal to the work of all outer forces acting on it. Therefore, one can write

$$M \frac{d}{dt} \sum_{j=1}^J E_j = \sum_{j=1}^J \left(\mathbf{v}_j \cdot \mathbf{f}_j + \underline{\boldsymbol{\omega}}_j \cdot \underline{\mathbf{m}}_j \right) + \sum_{j=1}^J \left(\mathbf{v}_j \cdot \mathbf{t}_j + \underline{\boldsymbol{\omega}}_j \cdot \underline{\mathbf{c}}_j \right), \quad (3.60)$$

where $E_j = \sum_{q=1}^Q E_{qj}$ —resultant energy of the j -th body.

As before, the first sum on the right-hand side of Eq. (3.60) is “surface” sum, while the second one is “volume”. It is clear that Eq. (3.60) is, up to notations, the full pre-image of energy conservation law for given volume of the micropolar fluid (3.11).

It should be noted that the only feature of the listed transformations in comparison with the usual ones is the division of the system of particles into equal subsystems of particles (solids) stationary relative to each other. When all subsystems contain only one particle ($Q = 1$), Eqs. (3.58), (3.59), and (3.60) transform into conservation laws for classical point continuum. Besides Eqs. (3.58), (3.59), and (3.60) contain velocities of subsystem inertia centers instead of velocities of particles as in classical case.

References

1. Needs, S.J.: Boundary film investigations. *J. Lubr. Technol.* **62**, 331–339 (1940)
2. Fuks, G.I: Investigation into boundary friction and adhesion for insight into the interaction of finely disperse particles. *Colloid J.* **20**, 748–758 (1958) (in Russian)

3. Derjaguin, B.V.: Surface forces in thin films and disperse systems. Selected works, 1. Prog. Surf. Sci. **40**, 1–465 (1992)
4. Aero, E.L., Bessonov, N.M.: Micromechanics of structural liquid layers between solids in contact. Advances in Science and Technology of VINITI. Series Mechanics of Fluids and Gases **23**, 237–315 (1989) (in Russian)
5. Kucaba-Piętal, A., Walenta, Z., Peradzyński, Z.: Molecular dynamics computer simulation of water flows in nanochannels. Bull. Pol. Acad. Sci. Tech. Sci. **57**(1), 55–61 (2009)
6. Israelachvili, J.N.: Intermolecular and Surface Forces, 2nd edn. Academic press, London (1991)
7. Eringen, A.C.: Simple microfluids. Int. J. Eng. Sci. **2**(2), 205–217 (1964)
8. Aero, E.L., Bulygin, A.N., Kuvshinskii, E.V.: Asymmetric hydromechanics. J. Appl. Math. Mech. **29**(2), 333–346 (1965) (in Russian)
9. Eringen, A.C.: Microcontinuum Field Theories: II. Fluent Media. Springer Science & Business Media (2001)
10. Kondrashov, O.F., Marchasin, I.L.: On morphology of subboundary layer of some individual substances. J. Phys. Chem. **52**, 1052–1054 (in Russian)
11. Eringen, A.C.: Theory of micropolar fluids. J. Math. Mech. **16**, 1–18 (1966)
12. Chen, J., Liang, C., Lee, J.D.: Theory and simulation of micropolar fluid dynamics. In: Proceedings of the Institution of Mechanical Engineers, Part N: Journal of Nanoengineering and Nanosystems, vol. 224, No. 1–2, pp. 31–39 (2010)
13. Lukaszewicz, G.: Micropolar Fluids: Theory and Applications. Springer Science & Business Media (1999)
14. Kucaba-Piętal, A.: Microchannels flow modelling with the micropolar fluid theory. Bull. Pol. Acad. Sci. Tech. Sci. 209–214 (2004)
15. Stokes, V.K.: Theories of Fluids with Microstructure: An Introduction. Springer, Berlin (1984)
16. Rickert, W., Vilchevskaia, E., Müller, W.: A note on Couette flow of micropolar fluids according to Eringen's theory. Math. Mech. Complex Syst. **7**(1), 25–50 (2019)
17. Migun, N.P.: On hydrodynamic boundary conditions for microstructural fluids. Rheologica Acta **23**(6), 575–581 (1984)
18. Bessonov, N.M.: A new generalization of the Reynolds equation for a micropolar fluid and its application to bearing theory. Tribol. Int. **27**(2), 105–108 (1994)
19. Bessonov, N.M.: Generalized Reynolds equation for micropolar fluid with microrotations near surface and its application to journal bearings. J. Tribol. **116**(3), 654–657 (1994)
20. Singh, C., Sinha, P.: The three-dimensional Reynolds equations for micropolar-fluid-lubricated bearings. Wear **76**, 199–209 (1982)
21. Prakash, J., Sinha, P.: Squeeze film theory for micropolar fluids. J. Lubr. Technol. **98**, 139–144 (1982)

Chapter 4

Research on Vibration Processes and Devices: New Results and Applications



Leonid I. Blekhman, Eugen B. Kremer, and Vladislav B. Vasilkov

Abstract This paper presents an overview of recent studies on the development of the theory of vibration processes and devices and on their industrial implementation. The work under consideration was completed by employees of the Laboratory of Vibrational Mechanics or with their participation. The fundamental principles of this work were established earlier due to the discovery and framing of the theory of self-synchronization of rotating bodies and the theory of vibrational displacement and to the development of new analytical approaches to studying the effect of vibration on nonlinear systems and media (vibrational mechanics and vibrational rheology). The work covered in this article provided a significant generalization and further development of these approaches. Their application allowed solving a large number of urgent applied problems in various fields of knowledge. As a significant recent achievement, a number of nonlinear vibration effects with a great potential for practical application have been discovered and studied. Moreover, new highly efficient vibration machines for the processing of natural and technogenic materials (crushers, screens, separators) and related laboratory and test vibration equipment are being designed, with the development of respective calculation methods.

Keywords Vibration · Nonlinear mechanics · Vibrational mechanics · Vibration technologies · Vibration machines

L. I. Blekhman (✉) · E. B. Kremer · V. B. Vasilkov
Institute for Problems in Mechanical Engineering RAS, V.O., Bolshoy pr., 61, 199178
St. Petersburg, Russia
e-mail: liblekhman@yandex.ru

E. B. Kremer
e-mail: ekr8576211@aol.com

V. B. Vasilkov
e-mail: vlvasilkov@yandex.ru

© The Author(s), under exclusive license to Springer Nature Switzerland AG 2022
V. A. Polyanskiy and A. K. Belyaev (eds.), *Mechanics and Control of Solids and Structures*, Advanced Structured Materials 164,
https://doi.org/10.1007/978-3-030-93076-9_4

4.1 Introduction

Processes in various industries, such as construction, mining, chemical, food manufacturing industry, etc., are associated with handling and processing of bulk masses of granular solids and multicomponent media. The effectiveness of vibration in these processes is due to the fact that vibration causes an apparent change in material properties (granular media and suspensions). In particular, a granular medium may behave like a solid, a viscous liquid, or a gas, depending on the vibration intensity. Under the influence of vibration, effective dry friction coefficients are reduced to zero and additional forces are generated (the so-called vibration forces), which may be utilized.

Vibration enhances the contrast between the properties of components in mixtures and ensures the separation of particles that have similar characteristics under normal conditions. The relative mobility of dissimilar particles under vibration intensifies the exchange processes, for example, by accelerating chemical reactions. Under certain conditions, vibration induces chaotic motions of the medium and its intensive mixing, which may be beneficial for a number of industrial processes. In other words, vibration makes it possible to change the natural behavior and optimize such processes. In many cases, vibration effects enable the design of environmentally friendly dry technologies and provide significant energy savings. When designing and improving vibration equipment and technology, a number of unique new problems of mechanics and the theory of nonlinear oscillations emerge. It becomes increasingly urgent to improve the analytical and numerical methods used to study the effects of vibration on various systems and media and to research respective vibration excitation methods and workflows.

This review examines the main recent developments in these areas. Many of the results described were obtained at the Laboratory of Vibrational Mechanics, a joint laboratory of the Institute for Problems in Mechanical Engineering of the Russian Academy of Sciences and Mekhanobr-Tekhnika Research and Engineering Corporation. The major contribution to this research was made by the long-standing leaders of the teams, the head of the Laboratory of Vibrational Mechanics, Professor Ilya Blekhman, and the scientific director of the Mekhanobr-Tekhnika Corporation, Academician Leonid Vaisberg. All colleagues, employees, and students will cherish their fond memories of these outstanding scientists.

Owing to the cooperation with the academic and scientific-industrial organizations, many developments have been completed to the full cycle: from the fundamental scientific research to the design of actual machines, development of applicable technologies, and their industrial implementation. The studies considered and their underlying work were conducted by an extensive team of scientists, whose contribution is partially reflected in the references below. The list is far from being exhaustive and starts with the monographs [1–25] by respective St. Petersburg scientists, covering the studies on vibration processes and machines. The collaboration with colleagues from academic and educational institutions in Russia and abroad has also been critical.

4.2 Fundamental Principles of Research: Theoretical and Applied Developments

The main theoretical achievements underlying the work of the recent years include:

- the development of the theory of vibrational displacement [1, 2];
- the discovery and framing of the theory behind the phenomenon of self-synchronization of rotating bodies (rotors) and the development of a new class of vibration machines and devices on this basis [3–6];
- the creation of new analytical approaches to studying the effects of vibration on nonlinear systems and media in the form of vibrational mechanics and vibrational rheology [7–14].

The studies and approaches listed are of a general mechanical nature and have effectively become new branches of the theory of oscillations and nonlinear dynamics. The approaches of vibrational mechanics and vibrational rheology are, in turn, a continuation of the classical studies on the theory of nonlinear oscillations based on the methods developed by A. Poincare, A.M. Lyapunov, N.M. Krylov, N.N. Bogolyubov, P.L. Kapitza, L.I. Mandelstam, N.D. Papaleksi, and other researchers.

The applied research basis is represented by the new class of highly efficient vibration machines designed in the recent decades (crushers, mills, screens, feeders, conveyors, separators, flotation machines [9, 10, 15–25]), as well as by the related process design and strength calculation methods [15–25] and by a set of laboratory and test vibration equipment. For many years, the universal vibration stand, designed using the phenomenon of self-synchronization, has been holding a special place among the equipment of the experimental base. Many of the new devices, technologies, and effects considered below have been tested using this setup. The main results of respective studies were reflected in the six-volume *Vibrations in Engineering handbook* [26] and in the monographs published in subsequent years. New advances, that build on these results, are discussed later in this overview (Sects. 4.3–4.8) and include, in particular, detection, theoretical substantiation, and analytical description of a number of nonlinear vibration effects and phenomena (vibratory injection, vibrational gradient segregation, abnormal segregation, vibrational maintenance and inhibition of rotation, abnormal behavior of solids and air bubbles in an oscillating fluid, vibrational rheological effects, including the formation of vibrational dynamic materials, stochastic resonance, etc.) [7–10].

4.3 Development of Vibrational Mechanics and Vibrational Rheology Approaches

1. Vibrational mechanics and vibrational rheology have been developed as the general analytical methods for studying the effect of vibration on nonlinear dynamic systems, as well as oscillatory strobodynamics as a generalization of these methods. The scientific foundations for these approaches, as set out in monographs

[9, 10], have been developed in the works by Sorokin [27] and Kremer [28] and publications by I. I. Blekhman and V. S. Sorokin in *Procedia IUTAM* 19 (2016, pp. 75–82) and *Nonlinear Dynamics* (2016, Vol. 83, Iss. 4, pp. 324–338), which also contain numerous examples of their practical use for solving relevant applied problems.

The oscillatory strobodynamics approach is presented and described in Chaps. 29–31 of the book [10], with the examples of use for solving problems from various fields of knowledge, indication of the main classes of problems, and an overview of the results. In particular, the impact on the following systems is considered:

- a Lorentz oscillator (chaos suppression);
- a Lotka-Volterra system ($\llcorner\llcorner$ predator/prey $\gg\gg$);
- a brusselator system, describing oscillatory chemical reactions;
- a Mathieu oscillator, describing the phenomenon of parametric resonance.

In all cases, it has been found that the oscillatory effect significantly affects the behavior of the system. The name of the approach is explained by the fact that it corresponds to the perception of system motion by an observer viewing the system in stroboscopic lighting.

2. The use of the oscillatory strobodynamics approach for solving applied problems may be illustrated by the study of the behavior of bound hydrogen in a rod under high-frequency pulsations [29]. It is known that accumulation of dissolved hydrogen can cause structural failure. When deriving the equations of hydrogen diffusion in a metal according to the general approach, a transition is made from the initial equations of the system to the equations describing only the slow component of the process ($\llcorner\llcorner$ vibration-transformed $\gg\gg$ equations). The slow component is usually of the main interest. In this case, an approximate solution to the problem shows that the dynamic effect leads to a redistribution of the hydrogen concentration and can affect the strength properties of the structure in different ways. In certain cases, the generalized stiffness of the rod decreases with higher cyclic load frequencies, which may lead to its failure. It is noteworthy that the equation describing slow changes in the average concentration of bound hydrogen differs significantly from the original equation, in particular, in that it has a higher order in spatial variables. A certain analogy with the problems of parametric excitation of a string or a rod, solved in a similar way [10], may be noted here. The tension pulsations lead, as it were, to the generation of additional bending stiffness. This explains the effect of the so-called Indian magic rope, which straightens and maintains an upright position when its lower end is under vibration. Vibration $\llcorner\llcorner$ turns a string into a rod and a rod into a beam $\gg\gg$ [10].
3. The vibrational mechanics approach has been extended to include systems with random effects. With regard to vibration machines, the practical significance of this generalization is due to the fact that the properties and composition of the medium (process load) in these machines tend to vary randomly. The results of respective studies are presented in the works by I. I. Blekhman, E. B. Kremer and V. S. Sorokin in *Journ. of Sound and Vibration* (2018, Vol. 437, pp. 422–436); *Nonlinear Dynamics* (2018, Vol. 93, Iss. 2, pp. 767–778); *European Journ.*

of Applied Mathematics (2019, Vol. 30, Iss. 5, pp. 986–1003) and Journ. of Mechanical Engineering Science. Part C (2019, Vol. 233, Iss. 23–24, pp. 7476–7488).

4. The idea of creating fundamentally new materials, the so-called dynamic materials and composites, has been put forward and developed by I. I. Blekhman and K. A. Lurie (2000) [9, 10, 30]. Dynamic materials refer to nonlinear media with their material parameters (density, rigidity, dissipative characteristics, self-induction, capacity, etc.) changing both in space and in time. Examples of dynamic materials are given in [10]. Vibratory dynamic materials and composites are an important class in this regard (2007) [9, 10]. Vibratory dynamic materials are materials, the parameters and properties of which with respect to relatively slow or static effects are significantly changed under the influence of vibration, i.e., relatively rapid impacts. Vibrational rheology lays down the theoretical basis for the creation of such materials.

4.4 Studies on the Problem of Stochastic Resonance

A series of studies have been completed on the problem of stochastic resonance, a fundamental physical phenomenon that manifests itself in a variety of nonlinear systems in different fields of science (geophysics, physics, biology, radio engineering, etc.). After the pioneering work by R. Benzi, A. Sutera, and A. Vulpiani [31], many other publications were released on this topic (by P. S. Landa, V. S. Anischenko, Cristina Stan, U.E. Vincent, P. V. E. McClintock, S. Rajasekar, I. A. Khovanov, etc.).

Since 2000, the team of the Laboratory of Vibrational Mechanics represented by I. I. Blekhman and then by E. B. Kremer, V. S. Sorokin, and later by I. V. Demidov joined the research on the stochastic resonance (largely under the influence of P. S. Landa). In previous studies, stochastic resonance was considered as a purely probabilistic phenomenon, requiring such approaches as, for example, a transition to the Fokker-Planck equations for its consideration. It has been shown in the Laboratory's work that the vibrational mechanics approach is a simple and effective way to mathematically study such phenomena. It has also been found that a phenomenon very similar to stochastic resonance can occur in a system under a deterministic rather than random high-frequency effect. In this regard, the term «vibrational resonance» has been established along with the term «stochastic resonance». While, under the stochastic approach, the resonant response of the system corresponds to a certain intensity of the random action, in vibrational resonance, it matches a certain amplitude of the high-frequency effect. In both cases, the resonant response of the system is caused by a change in the effective natural frequency of the system under the influence of a changing high-frequency effect rather than by the excitation frequency.

In recent years, the vibrational mechanics approach has been used to obtain new results and improve the understanding and mathematical description of the laws of stochastic resonance (see the references above in Sect. 4.3). The stochastic and vibrational resonance phenomena have been studied for a number of application-specific

nonlinear and parametrically excited systems. In addition to stochastic resonances, the improved understanding of the vibromechanical nature of stochastic resonance allowed identifying stochastic antiresonances in rotating mechanisms, which are critical for the design of dynamic vibration dampers.

Methods have also been developed for controlling vibration machines using the stochastic nature of the feedback caused by the chaotic effects of the medium being processed on the working body of the machine. A vibration machine control strategy has been proposed that maintains the resonant state and ensures energy-saving operation. The results obtained expand the possibilities of using the resonance phenomenon in vibration technology and materials processing technologies, where, in contrast to electrical and radio engineering, the applications of the resonance phenomenon are still very limited. This latter fact is largely due to the difficulties in controlling mechanical properties of materials.

The most recent results of the Laboratory's work in these areas were published in the form of three articles in the special issue of *Philosophical Transactions of the Royal Society A*. (2021), devoted to the problems of stochastic and vibrational resonance.

4.5 Self-synchronization Phenomenon: Development of the Theory and New Applications

1. A general overview of the problem of frequency self-synchronization (≪frequency attraction≫), a universal phenomenon characteristic of all processes, in which oscillations or rotations occur, is presented in [32]. The article was published in one of the issues of the *Avtomatika i Telemekhanika* (Automation and Telemechanics) journal dedicated to the 100th anniversary of the birth of Yuri Neimark, an outstanding scientist in the fields of mathematics, mechanics, and control theory. The active interest of Yu. I. Neimark and his substantial support for the research on frequency synchronization is noted in the introduction. The basic, not yet fully established, definitions and concepts of the theory of frequency synchronization are discussed in the article. Significant differences between the phenomena of synchronization, self-synchronization, and capture are described. It is noted that capture may be considered as an extreme special case of self-synchronization. The often-ignored affiliation of self-synchronization with the self-organization phenomena is emphasized. Certain relevant unsolved problems of the theory of frequency synchronization are listed. Among them, the question on the potential fundamental role of synchronization in the microworld is discussed in detail. An opinion is expressed on the advisability of attempting to describe the physical reality using the unified deterministic laws of physics, taking into account those listed in the work and other new achievements in nonlinear dynamics.

2. The possibilities of improving vibration machines with self-synchronizing inertial (unbalanced) vibration exciters operating at superresonance oscillation frequencies have been considered. One of them covers machine start-up regimes and the other ensures steady-state operation. The improvements proposed allow reducing the installed motor power, energy consumption, and dynamic loads in operation of the machines. Oscillations in drives of vibration machines with inertial (unbalanced) oscillation exciters have also been theoretically and experimentally studied; in these machines, the shafts of the electric motor and the exciter are coupled so as to enable relative displacement of the shafts (using an elastic coupling, V-belt drive, universal-joint shaft); see the works by N. P. Yaroshevich, written in collaboration with the team of the Laboratory of Vibrational Mechanics and published in the *Journ. of Machinery Manufacture and Reliability* (2013, Vol. 42, Iss. 3, pp. 192–195) and *Obogashchenie Rud* (*Mineral Processing Journ.*, 2017, Issue 4, pp. 20–25).
3. The paper [33] focuses on the possibility of using the phenomenon of self-synchronization of vibration exciters to design vibration machines with their vibration conditions changing throughout the operation cycle (adaptive vibration machines). Several possible dynamic layouts are provided for such devices. The practical significance of this work consists in the resulting ever-growing use of vibration machines with self-synchronizing vibration exciters. However, almost all existing types of vibration machines are limited to a certain type of oscillations. Meanwhile, a number of processes, in particular, screening and compaction of concrete mixtures, could be significantly intensified by changing the vibration conditions according to a certain pattern. In [33], this idea is illustrated using several classes of machines with self-synchronizing exciters. It is assumed that the program for changing the vibration conditions will be set by the process engineers. It may be expected that the above applications for the phenomenon of self-synchronization of vibration exciters will contribute to the design of new types of vibration machines, in particular, using the patterns suggested in this work.

4.6 Vibrational Displacement: Theory, Applications, Energy Saving

1. The works published in *Vibroengineering Procedia* (2020, Vol. 32, pp. 26–31) and *Obogashchenie Rud* (*Mineral Processing Journal*, 2020, No. 4, pp. 21–26) devoted to the average speed of vibrational transportation of piece goods and granular materials, which is a problem of significant interest for designers of vibration equipment and process engineers. The theory of vibrational displacement [1] is currently used for average speed calculations, presented in the form of a model based on the motion of a single particle (material point). This model is perfectly applicable under wide conditions. However, it may also require rather

complex calculations or the use of a series of graphs or special nomograms. The publications under consideration show that, in typical vibrational transportation conditions and process machines (conveyors, feeders, screens) and, namely, under the conditions with intensive material tossing, the vibrational transportation speed may be assessed using simple formulas that clearly reflect the dependence between the speed and the parameters. These formulas are obtained on the basis of respective physical considerations using only some of the fundamental provisions of the theory of vibrational displacement. Incidentally, an expression was obtained for the relative flight duration of the material, an important process quantity. The calculation results for the formulas proposed are in good agreement with the experimental data.

The research touches upon the issue of modeling dynamic systems with complex behavior. It is suggested that, in cases similar to the one considered, it is advisable to move to a simpler («crude») model or to a probabilistic description. With regard to the problem, this approach eliminates the need to design separate complex formulas for each of the many regimes predicted by the basic model.

2. Vibrational transportation of solid and granular bodies over a surface performing non-translational, in particular, rotary vibrations has been studied [34, 35]. Non-linear differential motion equations for the bodies on such a surface have been obtained. It has been shown that, for a case when the influence of the centrifugal and Coriolis forces of inertia may be ignored, the results of the existing theory may be used when finding the local average speed of vibrational transportation, provided that certain additional parameters are introduced. It has been found that, depending on the location of the vibrators relative to the center of gravity, the material may travel either in the direction of the plane of symmetry or in the opposite direction. This pattern has been confirmed experimentally using the vibration stand. The specific features of the emerging motion suggest that the results of these studies will allow developing new vibration devices for processing natural and technogenic materials. As an important by-product, recommendations were issued allowing to reduce the accident rate for vessels carrying granular materials and loose cargo under rolling conditions.
3. The main sources of energy consumption in vibrational transportation-based process machines, in particular, in screens, conveyors, and feeders, have been studied. The studies focus on the energy consumption in these machines that is required to ensure the vibration effect on the material being processed and to overcome the resistance forces in the drive. The power required to maintain the oscillatory motion in the steady state and the motor power required to start the machines are also considered. For machines driven by inertial unbalanced exciters, these are the power values required to lift the unbalanced loads and to overcome the resonant frequency during start-up. It is shown that these power values may be practically reduced to zero using relatively simple motor start control systems. Formulas have been obtained for estimating each type of energy consumption depending on the vibration parameters for the tossing regimes. The comparison of the calculated data against the technical specifications of actual machines indicates that, for example, the installed power of a number of screens may be

significantly reduced by reducing or eliminating the start-up consumption. The research results are published as a chapter in the monograph: Sapountzakis E. J., Banerjee M., Biswas P., Inan E. (eds) Proc. of the 14th Intern. Conf. on Vibration Problems. Lecture Notes in Mechanical Engineering. Springer, Singapore (2021), pp. 29–46.

4. The research presented in [36] (2020) is also directly related to the problems of energy saving in vibration machines. This work analyzes systems with amplitude and phase modulation and identifies the conditions for modifying their low-frequency behavior under this effect. In particular, it is shown that a vibration force may only emerge if at least one of the following conditions is met:

- the initial slow force is nonlinearly dependent on the speed;
- the amplitude modulation depends on the position of the system;
- the amplitude modulation is speed dependent;
- the phase modulation is speed dependent.

A comparison shows good agreement between the numerical and analytical results of the calculations. The practical significance of this work is to discover new possibilities for energy-efficient vibration control. In particular, vibration machines may be maintained near the resonance state as a result of a high-frequency modulated action rather than by the selection of proper rotation speeds, which is not always optimal. This opens up wide opportunities for the development of respective process solutions in mechatronics.

4.7 New Nonlinear Vibration Effects: Research and Applications

1. Theoretical and experimental studies of the unusual behavior of solid particles and air bubbles in a liquid under vibration have been carried out [9, 10, 37–40]. The main effects include the immersion of bubbles in an oscillating liquid deep into the vessel and, conversely, the floating of bodies with densities higher than that of the liquid. In particular, relations were obtained to establish the manifestation conditions for these effects. It has been confirmed, that the immersion of bubbles and light elastic particles and the floating of heavy bodies in an oscillating liquid are associated with the following two factors: with the acquisition of elastic properties by the gas-saturated layer of the liquid and with the elastic properties of each bubble. (Due to their own elasticity, bubbles can «sink» even in an incompressible liquid.) The speed of sound in the resulting gas-liquid medium is paradoxically low at approximately 20 m/s in a wide range of gas content values. A standing wave arises in the liquid with a node located at the bottom of the vessel. Depending on their compressibility (the size of the bubbles and the vibration frequency), the bubbles rush to the nodes or to the antinodes of the standing wave. Observations show that, with an increase in the vibration

intensity of the vessel holding the liquid, the bubbles are first captured by the turbulized surface layer of the liquid; this is followed by a gradual increase in the thickness of this layer, accompanied by a change in the size of the bubbles and the height of liquid splashes, a sharp («explosive») immersion of the bubbles and a transformation of the entire liquid into a gas-liquid medium, and then by the periodic formation at the bottom and floating of large air cavities. The results obtained may be used for process control and intensification.

2. The phenomenon of vibratory injection of gases into liquids has been discovered and studied [9, 10, 41]. This phenomenon is observed when air or gas is intensively sucked in the form of series of bubbles through the holes in the lower part of a vibrating vessel filled with liquid and the liquid flows out of the vessel in the form of drops. This effect may be used for processes intensification in mining and processing and other industries and makes it possible to improve various vibration devices, for example, for liquid dosing and aeration (Patents RU 2263883 and 2278738). It has been shown that vibratory injection and the previously known other nonlinear phenomenon of the vibrating-jet effect may be considered jointly as special cases of a more general theory. These effects are not only useful but have previously also caused accidents in the chemical industry and might have been the cause of a number of aviation accidents when, due to vibration, fuel supply from the gas tanks was cut off due to vibrational locking of the holes. Ways to suppress these undesirable phenomena have been developed.

New results of studying the phenomenon of vibratory injection were obtained in [42]. The calculations and experiments performed made it possible to clarify the specifics of the phenomenon and propose refined formulas for establishing the respective gas and liquid flow rates.

3. The wear of contacting nominally fixed machine parts operating under systematic vibration or shock effects (fretting wear) has been studied. The wear is due to micro- and sometimes macro-mobility of the joints. It occurs in bolted joints, seating surfaces of rolling bearings, shaft-sleeve joints, leaf springs, gears, couplings, and other devices. The same applies to hydraulic power units, construction and other machines. At the level of simple physical models, formulas for the wear rate have been obtained and recommendations have been developed on the design and operation of the corresponding equipment.

The relative shift (microslippage) of contacting bodies under high-frequency effects caused by shocks has also been theoretically and experimentally studied. The amount of the microslippage has been determined that allows estimating the wear rate and the trouble-free service life for the parts. Expressions for the effective coefficients of dry friction have been obtained, indicating a significant (down to zero) reduction of these coefficients under shock loads. The models considered are quite universal, may be used to explain and describe certain technogenic seismic phenomena and are applicable to the problem of increasing the efficiency of oil-bearing formations using vibration effects. These results were published in *Obogashchenie Rud (Mineral Processing Journ.):* 2011, Iss.

- 6, pp. 40–45; 2016, Iss. 6, pp. 32–39) and *Doklady Physics* (2017, Vol. 62, Iss. 5, pp. 253–256).
4. A series of studies have been carried out on the phenomenon of vibrational segregation of granular bodies, which underlies the processes of material separation by size, density, and shape [9, 10, 43–46].
 - a. Two types of the process have been established and studied. In the first case, segregation occurs in the direction of reduction of the potential energy of the system (normal segregation). In the second case, vice versa, the process occurs in the direction of increasing the potential energy, in particular, when large heavy particles float with fine and light particles (the Brazil nut effect). The latter is implemented in regular screens. It also forms the basis of the newly developed screenless wedge wire classifiers (Patent RU 2407600).
 - b. The effect referred to as vibrational diffusion (gradient) segregation has been discovered and studied [46]. It is observed when, under sufficiently intense vibration applied to a granular mixture, the particles of each specific size (fraction) slowly (as compared with the vibration rate) move in the direction of their lowest concentration, that is, in the direction opposite to the direction of the concentration gradient for this fraction. The motion of relatively fine particles in a vibrating granular medium is similar to the processes of matter propagation during diffusion and heat propagation. A significant result of these studies indicates that, with sufficiently intense vibration (up to 10g), the fines fraction is discharged more efficiently through inclined and, in particular, vertical screening surfaces of the tray than through the traditional bottom surfaces. Based on this effect, new high-performance screens have been developed and patented (Patent RU 2550607; Patent RU 155723, utility model).
 5. A group of vibration effects associated with the unusual behavior of a granular medium in communicating vibrating vessels is discussed in [10] (see Chap. 20). In addition to the phenomena studied earlier, the overview in [10] describes new and rather unexpected effects discovered for a case when one of the vessels has the shape of a tube. If a straight tube filled with material is immersed in a vessel with a granular material, the tube may quickly become empty when the vessel vibrates. If an empty tube with a slightly bent end is immersed in a vessel with a granular material, it is filled with material during vibration. That is, in one (the latter) case, the granular medium behaves like a liquid during vibration and, in the other case, it behaves differently. These effects are experimentally investigated and mathematically described using the methods of vibrational mechanics. The patterns considered enable classification of granular media during vibration as vibratory dynamic materials (see Sect. 4.3).
 6. The phenomenon of oscillation-induced suspension of a heavy body vibrating in a liquid near a solid wall has been investigated and explained. Suspension force expressions have been obtained for bodies of revolution of an arbitrary shape and the suspension height has been determined in [43]. The results may be used in the theory of suspension flows and the theory of vibration pumps to explain the paradox of «unsinkable» nodules and in other applications. The

general problem of the behavior of vibrating solid and deformable bodies near the interface between two media has been formulated. The increase in buoyancy of a vibrating body near the interface has been noted and investigated. The difference in the physical mechanisms of suspension for heavy bodies in a liquid and in a granular medium has been considered.

7. The effect of separation of particles in a fluidized state in magnetic and electrostatic fields has been studied analytically (Intern. Journ. of Engineering Science, 2019, Vol. 141, pp. 141–156). The study was carried out with respect to the design of improved separators for the processing of finely disseminated ores. A distinctive feature of these machines is the intense vibration effect on the feed material during its vibrational transportation and loading into the working area in a fluidized state. This effect eliminates the negative impact on the process generated by the forces of adhesive interaction between the finely ground particles. The results include an increase in the concentrate grade and higher recoveries. Such technologies may significantly reduce the consumption of water used as a dispersion medium for separation or, as in this case, completely eliminate water consumption through the principle of «vibration instead of water».
8. Generalization of the classical equation describing the motion of a complex actual machine using the vibrational mechanics approach to make it applicable to systems with several degrees of freedom. The equation is used in the analysis of resonances for vibration machine start-up and coasting (the Sommerfeld effect); see the works by I.I. Blekhman and E.B. Kremer (2017) in Journ. of Machinery Manufacture and Reliability (Vol. 46, Iss. 4, pp. 330–335), Journ. of Sound and Vibrations (Vol. 405, pp. 306–313) and Procedia Engineering (Vol. 199, pp. 3278–3283).
9. The effect of periodic energy ripples in common devices used for exciting useful vibration has been established and investigated [47]. It has been shown that the vibration frequency excited is not constant, but experiences periodic ripples with the same frequency and its multiple frequencies. As a result, oscillations are excited both with a certain vibration frequency and its multiple frequencies. The study was carried out both by solving nonlinear differential equations of motion and based on relevant energy considerations. The frequency ripple values are usually small, amounting to 10–15% of the nominal values, and may only reach 25% in special cases. The energy ripple is characterized by values that are twice as high. The energy and frequency ripple effects considered may cause undesirable phenomena in devices with inertial excitation of oscillations and, at the same time, serve as the basis for a number of applications, including those using the concept of vibrational resonance.
10. A cycle of theoretical and experimental studies has been carried out to develop measures to prevent or reduce the risk of accidents at industrial facilities, structures, and vehicles caused by non-linear oscillatory phenomena (see [9, 10, 41], as well as Sect. 4.2, 4.3, 4.7, 4.9 above and the references cited therein). The phenomena of vibrational braking and vibrational maintenance of rotation, the phenomenon that occurs when several unbalanced machines are installed on a single foundation (self-synchronization and in-phase operation), the phe-

nomenon of vibratory injection of gas into liquid, the associated phenomenon of liquid locks in holes of vibrating vessels, and the phenomenon of relative displacement of bodies in contact under the forces of dry friction due to weak vibration or shock effects have been studied. In particular, the mechanisms ensuring a significant reduction in the effective coefficient of dry friction under weak shock and vibration effects have been investigated. The magnitude of the resulting displacement of the bodies has been estimated. The following groups of accidents have been explained and described on this basis:

- the influence of technogenic factors on seismic phenomena;
- the impact of granular materials and loose cargo on the accident rate for vessels carrying such cargo under rolling conditions;
- the surface wear rate for nominally fixed machine parts in contact by means of dry friction forces;
- the manifestation mechanism of the Sommerfeld effect for irregular travel paths.

4.8 New Ways of Damping Harmful Vibrations

1. A method has been developed for damping harmful vibration, in which this vibration is simultaneously used for energy generation (Patent RU 2637156). This method is based on the use of the two physical phenomena associated with the behavior of an unbalanced rotor on a vibrating support [9, 10]: the phenomenon of vibrational maintenance of rotation and the phenomenon of vibrational capture of rotation of an unbalanced rotor. The advantages of this invention consist in the ease of its implementation and in the possibility to generate (mechanical or electrical) energy without significant heat losses. It is essential that the electricity generated is proportional to the cubed vibration frequency. This allows applying the proposed method at a low vibration frequency and makes it especially effective in the case of high-frequency vibration.
2. A fundamentally new method of vibration damping in elastic structural elements is proposed, for example, for rods, cables, plates, or enclosures (Patent RU 2678932). The method is based on a calculated periodic variation of an element's shape or material physical/mechanical properties along its spatial coordinates. In particular, the law of variation for a parameter of the element may be selected in the form of a harmonic standing wave of properties. This simplifies the design of vibration dampers, improves vibration damping, and increases operational reliability of external vibration damping devices.

4.9 Conclusions

This paper presents a brief and non-exhaustive overview of the results of recent years related to the problem of vibration effects on nonlinear systems and media. The results covered were mainly obtained by the Laboratory of Vibrational Mechanics (St. Petersburg). Analytical research methods have been developed, new peculiar vibration effects have been discovered and investigated, a number of urgent applied problems from various fields of knowledge have been solved, and new efficient vibration machines and technologies have been created. The results described have a great potential for further development and industrial use.

Acknowledgements The present work was supported by the Ministry of Science and Higher Education within the framework of the Russian State Assignment.

References

1. Blekhman, I.I., Dzhaneldidze, GYu.: Vibrational Displacement. Nauka, Moscow (1964)
2. Nagaev, R.F.: Periodic Regimes of Vibrational Displacement. Nauka, Moscow (1978)
3. Blekhman, I.I.: Synchronization of Dynamic Systems. Nauka, Moscow (1971)
4. Blekhman, I.I.: Synchronization in Science and Technology. ASME Press, New York (1988)
5. Nagaev, R.F., Guzev, V.V.: Self-Synchronization Inertial Vibration Exciters. Mashinostroenie (Mechanical Engineering), Leningrad (1990). (Biblioteka Inzhenera (Engineer's Library Series). Vibration Technology; Vol. 16)
6. Nagaev, R.F.: Quasi-Conservative Synchronizing Systems. Nauka, St.Petersburg (1996)
7. Blekhman, I.I.: Vibrational Mechanics. Nonlinear Dynamic Effects, General Approach, Applications. World Scientific, Singapore (2000) (Russian edition: Blekhman, I.I.: Vibrational Mechanics. Fizmatlit, Moscow (1994))
8. Selected Topics in Vibrational Mechanics (Series on Stability, Vibration and Control of Systems: Series A, Vol. 11). World Scientific, New Jersey (2004)
9. Blekhman, I.I.: Theory of Vibrational Processes and Devices. Vibrational Mechanics and Vibrational Rheology. Ore and Metals Publishing House, St. Petersburg (2013)
10. Blekhman, I.I.: Vibrational Mechanics and Vibrational Rheology (Theory and Applications). Fizmatlit, Moscow (2018)
11. Nagaev, R.F., Khodzhaev, KSh.: Oscillations of Mechanical Systems with Periodic Structure. FAN Publishing House, Tashkent (1973)
12. Nagaev, R.F.: Mechanical Processes with Repeated Attenuated Impacts. World Scientific Publishing Co Ltd., Singapore (1999)
13. Skubov, DYu., Khodzhaev, KSh.: Asymptotic Qualitative Methods in the Theory of Synchronous Electric Machines. Publishing House of Saint-Petersburg State Institute of Technology, St. Petersburg (1999)
14. Skubov, D., Khodzhaev, KSh.: Non-Linear Electromechanics. Springer, Berlin (2008)
15. Olevsky, V.A.: Designing and Calculation of Screens. Metallurgizdat, Moscow (1955)
16. Kizevalter, B.V.: Theoretical Basis of Gravity Beneficiation Processes. Nedra, Moscow (1979)
17. Vaisberg, L.A.: Design and Calculation of Vibrating Screens. Nedra, Moscow (1986)
18. Vaisberg, L.A., Rubisov, D.G.: Vibration Screening of Bulk Materials. Process Modeling and Technological Calculations for Screens. Mekhanobr, St.Petersburg (1994)
19. Vaisberg, L.A., Zarogatsky, L.P., Turkin, V.Ya.: Vibratory Crushers. Bases for Design, Engineering and Technological Applications. VSEGEI Publishing House, St.Petersburg (2004)

20. Ivanov, N.A.: The Inertial Cone Crusher. Operation. Ore and Metals, St.Petersburg, The Theory, Design, Calculation (2012)
21. Anakhin, V.D., Pliss, D.A., Monakhov, V.N.: Vibration Separators. Nedra, Moscow (1991)
22. Anakhin, V.D., Pliss, D.A.: On the Theory of Vibration Separators. Publishing House of Novosibirsk University, Novosibirsk (1992)
23. Vaisberg, L.A., Kartavy, A.N., Korovnikov, A.N.: Screening Surfaces of Screens, Application Experience, Designs, Materials. VSEGEI Publishing House, St.Petersburg (2005)
24. Arsentiev, V.A., Vaisberg, L.A., Zarogatsky, L.P., Shuloyakov, A.D.: The Production of Cuboid Crushed Stone and Building Sand Using Vibrating Crushers, 2nd edn. VSEGEI Publishing House, St.Petersburg (2008)
25. Kartavy, A.N.: Vibration Units for Processing Mineral and Technogenic Materials. Publishing House of the Moscow State Mining University, Moscow (2013)
26. Vibrations in Engineering: Handbook in 6 volumes. Ed. V.N. Chelomey. Mashinostroenie (Mechanical Engineering), Moscow (1978–1981)
27. Sorokin, V.S.: On the unlimited gain of a nonlinear parametric amplifier. Mech. Res. Commun. (2014). <https://doi.org/10.1016/j.mechrescom.2014.09.005>
28. Kremer, E.: Slow motions in systems with fast modulated excitation. J. Sound Vib. (2016). <https://doi.org/10.1016/j.jsv.2016.07.006>
29. Belyaev, A.K., Blekhman, I.I., Polyanskiy, V.A.: Equation for the evolution of trapped hydrogen in elastic rod subjected to high-frequency harmonic excitation. Acta Mech. (2016). <https://doi.org/10.1007/s00707-015-1505-1>
30. Lurie, K.A.: An Introduction to the Mathematical Theory of Dynamic Materials. Advances in Mechanics and Mathematics, vol. 15, 2nd edn. Springer, Cham (2017)
31. Benzi, R., Sutera, A., Vulpiani, A.: The mechanism of stochastic resonance. J. Phys. A (1981). <https://doi.org/10.1088/0305-4470/14/11/006>
32. Blekhman, I.: Frequency synchronization and its possible role in microworld phenomena. Autom. Remote Control (2020). <https://doi.org/10.1134/S0005117920080044>
33. Blekhman, I.I., Semenov, Y.A., Yaroshevych, M.P.: On the possibility of designing adaptive vibration machinery using self-synchronizing exciters. In: Misyurin, S., Arakelian, V., Avetisyan, A. (eds) Advanced Technologies in Robotics and Intelligent Systems. Mechanisms and Machine Science, vol 80. 231–236. Springer, Cham (2020). https://doi.org/10.1007/978-3-030-33491-8_28
34. Blekhman, I.I., Vasilkov, V.B., Semenov, Yu.A.: On vibrotransportation of a material on a surface performing rotary oscillations. Vibroengineering PROCEDIA (2019). <https://doi.org/10.21595/vp.2019.20745>
35. Blekhman, I.I., Vasilkov, V.B., Semenov, Yu.A.: Vibrotan sporting of bodies on a surface with non-translational rotational oscillations. J. Mach. Manuf. Reliab. (2020). <https://doi.org/10.3103/S1052618820040032>
36. Kremer, E.: Vibrational mechanics of systems with amplitude and phase modulation of excitation. In: Lacarbonara W., Balachandran B., Ma J., Tenreiro Machado, J., Stepan, G. (eds) Nonlinear Dynamics of Structures, Systems and Devices, vol. I, pp. 35–41. Springer, Cham (2020). https://doi.org/10.1007/978-3-030-34713-0_4
37. Blekhman, I.I., Blekhman, L.I., Vaisberg, L.A., Vasilkov, V.B., Yakimova, K.S.: «Anomalous» phenomena in fluid under the action of vibration. Dokl. Phys. (2008). <https://doi.org/10.1134/S1028335808100054>
38. Blekhman, I.I., Blekhman, L.I., Sorokin, V.S., Vasilkov, V.B., Yakimova, K.S.: Surface and Volumetric Effects in a Fluid Subjected to High-Frequency Vibration. Proc. Inst. J. Eng. Sci. C (2012). <https://doi.org/10.1177/0954406211433260>
39. Demidov, I.V., Sorokin, V.S.: Motions of deformable inclusions in a horizontally oscillating vessel with a compressible fluid. J. Sound Vib. (2016). <https://doi.org/10.1016/j.jsv.2016.07.034>
40. Blekhman, I.I., Blekhman, L.I., Vasilkov, V.B., Sorokin, V.S., Yakimova, K.S.: Motion of gas bubble in oscillating gas-saturated liquid. Obogashchenie Rud (Mineral Processing J.) **5**, 30–37 (2011)

41. Blekhman, I.I., Blekhman, L.I., Vaisberg, L.A., Vasilkov, V.B., Yakimova, K.S.: Nonlinear effects observed in the flow of a fluid out of vibrating vessels. *Dokl. Phys.* (2003). <https://doi.org/10.1134/1.1598246>
42. Demidov, I., Mikhailova, N., Yasinskaya, A., Samukov, A.: Development of the Theory of Vibratory Injection of Gas into Liquid. *Vibroengineering PROCEDIA* (2020). <https://doi.org/10.21595/vp.2020.21539>
43. Blekhman, L.I.: Oscillation-Induced Suspension of Solids in Fluid and Loose Media. *PNRPU Mechanics Bulletin*. Perm. PNRPU Publishing House (2013). <https://doi.org/10.15593/perm.mech/2013.2.52-83>
44. Blekhman, I.I., Vaisberg, L.A.: Toward a theory of vibrational segregation. *Obogashchenie Rud (Mineral Processing J.)* **5**, 35–40 (2014)
45. Vaisberg, L.A., Demidov, I.V., Ivanov, K.S.: Mechanics of granular media under vibration action: the methods of description and mathematical modeling. *Obogashchenie Rud (Mineral Processing J.)* (2015). <https://doi.org/10.17580/or.2015.04.05>
46. Blekhman, I.I., Blekhman, L.I., Vaisberg, L.A., Vasilkov, V.B., Yakimova, K.S.: On vibrational diffusion segregation in granular media. *Dokl. Phys.* (2016). <https://doi.org/10.1134/S1028335816010018>
47. Blekhman, I.I., Blekhman, L.I., Vaisberg, L.A., Vasilkov, V.B.: Energy and Frequency Ripple in Devices with Inertial Excitation of Oscillations. *Phil. Trans. R. Soc. A.* 3792020023320200233 (2021). <https://doi.org/10.1098/rsta.2020.0233>

Chapter 5

Micromechanics of Strength and Plasticity in Nanostructured Materials



Sergey V. Bobylev, Mikhail Yu. Gutkin, Alexander G. Sheinerman,
and Nikolay V. Skiba

Abstract A brief review of the research activity provided during the last three decades in the Laboratory of Mechanics of Nanomaterials and Theory of Defects at the Institute for Problems in Mechanical Engineering of Russian Academy of Sciences in the field of micromechanics of strength and plasticity in nanostructured materials is presented. It covers the works aimed at explanation and theoretical description of the following features in mechanical behavior of these materials: deviations from the classical Hall-Petch law, homo- and heterogeneous nucleation of dislocations, grain boundary sliding and mechanisms of its accommodation, rotational deformation, deformation twinning, deformation-induced grain growth and refinement, and interaction between deformation and fracture processes. Some most important and interesting results are discussed and compared with available data of experimental studies and computer simulations.

Keywords Micromechanics · Strength · Plasticity · Nanostructured materials · Hall-Petch law · Dislocations · Disclinations · Grain boundaries · Deformation twinning · Deformation-induced grain growth

5.1 Introduction

The present paper is a brief review of the research activity provided in the Laboratory of Mechanics of Nanomaterials and Theory of Defects, founded by Prof. I.A. Ovid'ko (1961–2017) in 1991 at the Institute for Problems in Mechanical Engineering of Russian Academy of Sciences (IPME RAS), in the field of micromechanics of strength and plasticity in nanostructured materials (NSMs) during the last three decades. This activity has concentrated at the development of theoretical models describing the physical mechanisms responsible for novel and often unpredictable phenomena in the mechanical behavior of such NSMs as nanocrystalline, ultrafine-

S. V. Bobylev · M. Yu. Gutkin (✉) · A. G. Sheinerman · N. V. Skiba
Institute for Problems in Mechanical Engineering RAS, V.O., Bolshoy pr., 61,
199178 St. Petersburg, Russia

© The Author(s), under exclusive license to Springer Nature Switzerland AG 2022
V. A. Polyanskiy and A. K. Belyaev (eds.), *Mechanics and Control of Solids and Structures*, Advanced Structured Materials 164,
https://doi.org/10.1007/978-3-030-93076-9_5

grained and nanocomposite metals, alloys and ceramics. In particular, the explanation and description of deviations in the dependence of the yield stress on the grain size from the classical Hall-Petch law (including the inverse Hall-Petch dependence), homo- and heterogeneous nucleation of dislocations, transition from translational to rotational plasticity, codevelopment and competing of different mechanisms of plasticity (dislocation glide, grain-boundary sliding, Coble creep, triple-junction creep, grain rotation, etc.), deformation twinning, stress-coupled migration of grain boundaries (GBs), pore and crack nucleation, fracture and toughening mechanisms have been in the focus of the studies. Most of these models were reviewed in more detail in parallel with work, experimental and theoretical, of other authors in monographs [1–5], textbook [6] and reviews [7–34]. It is also worth noting that elaboration of the majority of these models was initiated and guided by Prof. I. A. Ovid’ko who made a great contribution in the field. We devote this review to his memory as well as to the 30th anniversary of IPME RAS.

5.2 Deviations from the Classical Hall-Petch Law

The classical Hall-Petch law relates the yield stress σ_y of a polycrystalline solid with its average grain size d as follows [35, 36]:

$$\sigma_y = \sigma_0 + K d^{-1/2}, \quad (5.1)$$

where σ_0 and K are the material dependent constants; σ_0 is the friction stress required for dislocation glide in the single-crystalline material and K is just a slope of the linear dependence $\sigma_y(d^{-1/2})$. The physical interpretation of Eq. (5.1) may be given from different viewpoints (see, e.g., the reviews [37–39]), however, this law was treated as rather universal one until the invention of nanocrystalline metals (NCMs). In 1989, Chokshi et al. [40] first observed the inverse dependence of σ_y on $d^{-1/2}$ in nanocrystalline Cu, when σ_y decreased with grain refinement in the range from 16 to 8 nm, and explained this effect by Coble creep that is mass transfer along GBs. A bit later, Jang and Koch [41] reported on direct dependence $\sigma_y(d^{-1/2})$ similar to (5.1) in nanocrystalline Fe in the range from 11 to 6 nm, which however could also be well described by the Kocks relationship $\sigma_y \sim d^{-1}$ [42]. These controversial data stimulated extensive experimental and theoretical research in the following three decades (see, e.g., [1–4, 7, 8, 11, 31, 39, 43–47] for review).

One of the first theoretical models of such kind was suggested by Gryaznov et al. [48] who extended the ‘composite’ model of Kocks [42] to the case of NCMs. They represented an NCM as a composite material in which the intragrain material was treated as single-crystalline matrix while the GBs as inclusions in the shape of oblate ellipsoids randomly spaced and oriented with volume fraction $c \approx 3\delta/d$, where δ is the GB thickness. Using the rule of mixture for the effective shear modulus of such a composite [49] and assuming linear relationships of the shear moduli of the composite components and their yield stresses satisfying Eq. (5.1) with corre-

sponding constants for intragrain and GB phases, Gryaznov et al. [48] finally found the relationship

$$\sigma_y = (\sigma_{0m} + K_m d^{-1/2}) \left(1 - \frac{1 - q^2}{2q} \frac{3\delta}{d} \right), \quad (5.2)$$

where σ_{0m} and K_m are the constants of the matrix and q is the dimensionless constant smaller than 1, which characterizes the effect of GB porosity on the GB constants: $q \approx \sigma_{0GB}/\sigma_{0m} \approx K_{GB}/K_m$ with σ_{0GB} and K_{GB} attributed to the GB phase. The lower is the atomic density of the interface, the smaller is the values of q . When Eq. (5.2) is plotted as a dependence $\sigma_y(d^{-1/2})$, the straight line in the usual Hall-Petch law will remain straight only at large d or else as $q \rightarrow 1$. For $q < 1$, its slope will gradually decrease with decreasing d down to some critical size d_c , where the effective Hall-Petch factor will change sign. The critical size d_c is easily found from the condition $\partial\sigma_y/\partial(d^{-1/2}) = 0$. Gryaznov et al. [48] showed that it may be estimated as $d_c \approx 9\delta(1 - q^2)/(2q)$ in practically any nanocrystalline metal. They also demonstrated that the contradictions arising on comparison of experimental results obtained by Chokshi et al. [40] and Jang and Koch [41] can be resolved in the framework of this approach. It is worth noting that many similar models operating within the ‘rule-of-mixture’ approach have been later developed (see [3] for a review and references).

Another theoretical approach dealing with competition of different physical mechanisms of plasticity in intragrain and GB phases of NCMs, has been developed by many research groups. A great step ahead in this direction was done by Masumura et al. [50] who took into account the lognormal distribution of grain volumes in real NCMs. They assumed that, in larger nanograins, the plastic deformation is realized by the glide of lattice dislocations, which should lead to the classical Hall-Petch relationship (5.1), while in smaller grains, the Coble creep dominates, which results in the inverse Hall-Petch relationship like $\sigma_y \sim d^3$. As a result, the mean yield stress $\langle\sigma_y\rangle$, averaged over the sample volume, followed the classical Hall-Petch law, $\langle\sigma_y\rangle \sim \bar{d}^{-1/2}$, in the range of large average grain size ($\bar{d} > d^*$) and the inverse Hall-Petch law, $\langle\sigma_y\rangle \sim \bar{d}^3$, in the range of small average grain size ($\bar{d} < d^*$), where d^* is a grain size at which the classical Hall-Petch mechanism switches to the Coble creep mechanism [50].

In developing this approach, Gutkin et al. [51] suggested to replace the Coble creep mechanism by the GB sliding mechanism for NCMs produced by severe plastic deformation (SPD). In such NCMs, GBs are commonly in a non-equilibrium state due to some excess of extrinsic GB dislocations (GBDs) stored at the fabrication stage [52]. Some of these GBDs are capable to glide within GBs, thus providing the GB sliding [53, 54]. In this case, triple junctions of GBs serve as natural obstacles for the motion of gliding GBDs, and the critical stress, which is needed for the transfer of the GB sliding from one GB to other GBs in their triple junctions, can be treated as the yield stress for the NCMs produced by SPD. In the simplest model case, the yield stress is [51] $\sigma_y = p + q(l/d) + s(l/d)^2$, where $p (> 0)$, $q (> 0$ or

< 0) and s (> 0) are the material and structure dependent parameters of the model, and l is about of interatomic distance. By using the averaging procedure similar to that by Masumura et al. [50], Gutkin et al. [51] obtained significant deviation of the $\langle \sigma_y \rangle (\bar{d}^{-1/2})$ dependence from the classical Hall-Petch law (5.1). The Hall-Petch slope started to decrease for \bar{d} smaller than roughly 25 nm, in good accordance with experimental data obtained on as milled nanocrystalline NiAl powders [55]. However, this model gives no inverse Hall-Petch dependence. Interestingly, the measurements on heat treated nanocrystalline NiAl powders [55], in which the GB sliding had to be suppressed due to elimination of the excess density of extrinsic GBs, did show the inverse Hall-Petch dependence. Gutkin et al. [51] showed that it could be well described by the model of Masumura et al. [50] with account for the Coble creep contribution.

Fedorov et al. [56] extended the approach of Masumura et al. [50] by including the contribution of mass transfer along triple junctions of GBs. As with GB diffusion, triple junction diffusion is capable of playing a very important role in plastically deformed NCMs, where the volume fraction of triple junctions of GBs is extremely high. It was shown that the competition between conventional lattice dislocation glide, grain boundary diffusional creep and triple junction diffusional creep, which is characterized by the $\sigma_y \sim d^4$ dependence, may result in the inverse Hall-Petch dependence for the yield stress of NCMs with finest nanograins [56]. In the exemplary case of nanocrystalline Cu, this was expected for $\bar{d} < d^* \approx 18$ nm, in good accordance with experiments of Chokshi et al. [40].

Recently, the problem of the inverse Hall-Petch dependence interpretation has appeared for nanocrystalline ceramics (NCCs) as well [31]. As before for nanocrystalline metals, some authors have reported on their observations of the inverse Hall-Petch dependence in NCCs, while some others have not. To resolve the contradictions, Sheinerman et al. [57, 58] suggested two models describing the initial stage of plastic deformation in nanocrystalline ceramics. Within the first model, plastic deformation is realized via the thermally activated GB sliding, but without GB diffusion. Within the second model, plastic deformation occurs through the emission of lattice and GB dislocations from GBs and their triple junctions. Both models predict the transition from the direct to the inverse Hall-Petch dependence at some critical grain size. At the same time, the critical grain size for this transition can be smaller than the smallest grain size of the ceramic specimens fabricated in experiments. This explains the absence of the transition from the direct to the inverse Hall-Petch dependence in some experiments.

5.3 Homo- and Heterogeneous Nucleation of Dislocations in NCMs

The origin of lattice dislocations, which are carriers of plastic deformation in the internal regions of nanograins, is one of the most disputable questions in NCMs. The problem is that such well-known sources of dislocations as the Frank-Read

sources and the double-cross slip, which are responsible for dislocation nucleation and multiplication in conventional coarse-grained polycrystalline materials [59], are suppressed due to lack of space inside nanograins. On the other hand, many authors reported on experimental evidence of lattice dislocations, both perfect [60, 61] and partial [62–64], in NCMs. In the special case of shock-loaded nanocrystalline Ni, the density of observed dislocations was extremely high, $\sim 10^{16} \text{ m}^{-2}$ [65]. Molecular-dynamics computer simulations demonstrated the generation of partial and extended perfect dislocations by GBs and their triple junctions [66, 67].

In our lab, two types of theoretical models for dislocation generation in NCMs were elaborated. The models of the first type describe the homogeneous nucleation of glide dislocation loops, while those of the second type deal with heterogeneous nucleation of various dislocation configurations at GBs. The classical theory of dislocations predicts that lattice dislocations can nucleate homogeneously under an extremely high shear stress of the order of the theoretical shear strength of the material [59]. Analyzing the high-resolution transmission electronic microscopy (HRTEM) images of crystalline lattice in deformed multicomponent titanium alloys called Gum Metals, Gutkin et al. [68] noticed some characteristic nanoscale lattice disturbances which could be considered as precursors of dipoles of edge dislocations. They called these precursors ‘nanodisturbances’ and described them theoretically as finite-arm dislocation dipoles with variable Burgers vectors. According to this model, the nanodisturbances form randomly under local stress and thermal fluctuations. They have at once finite (nanoscopic) sizes and very small (smaller than the interatomic distance in the material) Burgers vectors, which both can increase under shear stress. Eventually nanodisturbances can gradually transform first to the dipole of conventional partial dislocations and then to the dipole of perfect dislocations. It was shown, that this process requires much smaller stress level than the classical model of homogeneous nucleation of dislocations. Experimental evidence of direct transformation of nanodisturbances to dislocation dipoles and reverse transformation of the latter to nanodisturbances was demonstrated by Cui et al. [69] in their HRTEM in situ observations of Gum Metal deformation under tension.

The initial idea of homogeneous nucleation of dislocation dipoles from nanodisturbances [68] was later extended to generation of glide dislocation loops in NCMs [70–72] and used in modelling of twinning, GB sliding and fracture of NCMs [73–76].

Regarding the heterogeneous nucleation of dislocations in NCMs, a number of different models were suggested to describe the decay of low-angle tilt GBs into lattice edge dislocations [77–79], the emission of partial and perfect dislocations by GBDs [78, 80–84], GB disclinations [85–89], GB triple junctions [54, 80–82, 90, 91] and GB pores [92]. In particular, Bobylev et al. [77–79] showed that the decay of low-angle GBs into ensemble of mobile lattice dislocations in mechanically loaded NCMs causes local plastic deformation in the grain where the decay takes place, as well as in neighboring grains. The decay of one low-angle GB can initiate a chain decay of neighboring GBs and the generation of a shear band (a narrow region where plastic deformation is localized). The critical stress τ_c of GB decomposition characterizes the initial stage of plastic deformation occurring via the development

of shear bands. For nanocrystalline Fe, the value of τ_c was estimated to vary from 0.5 GPa (for GB misorientation angle $\omega \sim 2^\circ$) to 2.5 GPa (for $\omega \sim 10^\circ$). Its average value $\langle \tau_c \rangle \sim 1.5$ GPa coincides with the experimentally measured value of the shear stress [93] at which shear bands are formed in nanocrystalline Fe.

Bobylev et al. [78] also proposed dislocation-based model describing emission of partial lattice dislocations from high-angle GBs nucleated on GBDs as well as experimentally observed effect of GB bowing. Through energetic description, both processes were found to be highly sensitive to applied mechanical stress and GB misorientation angle. The results of this theoretical model account for experimental observations of curved GBs [62] and emission of partial dislocations by GBs [62] in deformed NCMs.

Gutkin and Ovid'ko [80] considered the generation of rectangular lattice perfect, lattice partial and GB dislocation loops at similar pre-existent dislocation loops and showed that these modes of dislocation generation can effectively provide plastic flow transfer from grain to grain, from grain to GB, from GB to grain, and from GB to GB in deformed NCMs, depending on their geometric and material characteristics. Bobylev et al. [81, 82] further developed this approach and considered more general case of the generation of two (one after another) rectangular lattice partial dislocation loops at a pre-existent GB dislocation loop with these two new loops having arbitrary Burgers vectors making the gliding segments of the loops of either mixed (edge and screw) or screw types (before they were of the edge type only [80]). Three different dislocation slip systems typical for the face-centered cubic (FCC) crystalline lattice were considered and it was found that emission of the partial dislocation loops belonging to the 60° -I slip system is the most probable in nanocrystalline FCC metals. This model also allowed to establish that experimentally detected [64] anomalously wide stacking faults in nanocrystalline Al are caused by high stresses but not by small grain size as was initially believed [64, 94, 95].

In a similar manner, Bobylev et al. [96] considered the generation of lattice partial dislocations at amorphous GBs in NCCs. In contrast to conventional GBs that emit lattice dislocations due to transformations of pre-existing GBDs (see above), the micromechanism of emission from amorphous GBs is different. Within the framework of the model, a dipole of immobile non-crystallographic edge dislocations is generated at the triple junctions (at the ends of an amorphous GB) through local shear events in this GB. These dislocations can split resulting in emission of partial lattice dislocations into grain interior. It was concluded that this process is energetically favorable and can proceed in athermal way in nanocrystalline 3C-SiC. The critical stress required to carry out this process was found to decrease with an increase of the GB length (in fact, the grain size). In other words, the transition from intergranular slip to intragranular dislocation slip becomes more difficult as the grain size decreases.

Fedorov et al. [54] focused their attention on the emission of lattice dislocations from the head of a pile-up of GBDs pressed to a triple junction of GBs in a deformed NCM. They calculated the energy barriers, which lattice dislocations must overcome to be emitted, and concluded that this process of stress relaxation at the GBD pile-ups looks hardly realistic as compared with some other possibili-

ties such as emission of GBDs along the adjacent GBs. It is worth noting that this model has recently been used as a component of more general models aimed at the explanation and theoretical description of the effects of hardening by annealing and subsequent deformation-induced softening in ultra-fine grained (UFG) Al produced by high-pressure torsion [97–99].

Gutkin et al. [90, 91] analyzed in detail the emission of lattice dislocations from sessile GBDs which formed at triple junctions of GBs in the course of GB sliding during (super)plastic deformation of NCMs. In particular, they showed [90] that, in NCMs with FCC crystalline structure (Al, Cu and Ni), partial Shockley dislocations can be emitted from dislocated triple junctions to accommodate the GB sliding. In a similar way, the process of emission of perfect dislocations from dislocated triple junctions under superplastic deformation of NCMs was examined in [91]. The processes of accumulation of sessile GBDs at triple junctions and their further transformation through the emission of lattice dislocations were considered as mechanisms playing important roles in strengthening and softening of NCMs under superplastic deformation [91, 100].

Ovid'ko and Sheinerman [92] considered the emission of lattice and GB dislocations from nanovoids in single-phase and composite NCMs. They demonstrated that a GB nanovoid that serves as a sink for dislocations and therefore contains a dislocation with a large Burgers vector can emit lattice dislocations at room temperature. In contrast, the emission of lattice dislocations or lattice dislocation dipoles from a dislocation-free nanovoid is not realistic at room temperature. At the same time, a dislocation-free nanovoid at a GB can emit individual GB dislocations or GB dislocation dipoles. This provides a mechanism for void growth via GB dislocation emission in deformed NCMs.

5.4 Grain Boundary Sliding and Mechanisms of Its Accommodation

Among the modes of GB mediated plastic deformation, one of the key mechanisms is GB sliding. In particular, it has been experimentally proven that GB sliding processes dominate during superplastic deformation of NCMs and NCCs [1]. Computer simulations [101, 102] also confirm the key role of GB sliding in plastic deformation of NCMs, especially at high stresses and strain rates [103]. GB sliding is plastic shears localized within GBs and normally it creates defects – sources of internal stresses – in GB triple junctions [1, 104] capable of initiating the nucleation of nanocracks [1, 104] and subsequent brittle fracture of the nanomaterial [104]. However, in the material, in parallel with GB sliding, accommodation processes can develop, which transform defects produced by GB sliding severely reducing the level of internal stresses and increasing ductility and fracture toughness of the nanomaterial. Understanding the micromechanics of these accommodation processes provides key insight in the nature of superplastic deformation of NCMs and NCCs.

Typical GB sliding accommodation mechanisms include the emission of lattice dislocations from GB triple junctions [1, 54, 90, 91], diffusion [73, 105], and rotational deformation [106]. At the same time, some original approaches have been developed in our lab like accommodation via GB splitting and migration [107, 108]. In particular, Bobylev et al. [108] developed a theoretical model of the mechanism of cooperative action of GB sliding, GB splitting and GB migration, which plays the role of a special mode of plastic deformation in NCMs. It was shown that GB sliding and GB migration are able to effectively accommodate each other by transforming GB disclinations. It was shown theoretically (using nanocrystalline Ni as an example) that the ductility and fracture toughness of a material increases if the described cooperative mechanism dominates over pure GB sliding or cooperative GB sliding and migration (without GB splitting [107]). The results of theoretical analysis (in particular, the formation of nanograins in the vicinity of GB triple junctions) are consistent with experimental data [109, 110] and computer models [111, 112] on the observation of nano- and microscopic grain nucleation at triple junctions.

Accommodation of GB sliding affects not only ductility, but fracture toughness as well. Bobylev et al. [73] investigated fracture toughness enhancement by means of non-accommodated and accommodated GB sliding in NCMs at low and medium temperatures, respectively. In the case of non-accommodated GB sliding, immobile non-crystallographic Volterra dislocations are produced at GB triple junctions near crack tips at relatively low temperatures. For nanocrystalline Al, Ni, and 3C-SiC, using the force criterion of crack growth, it was calculated that the effective stress intensity factor K_{IC}^* (fracture toughness) increases by up to 30% due to the dislocation created by non-accommodated GB sliding. The effect is stronger when dislocation is closer to the triple junction. The sensitivity of the stress intensity factor to this distance correlates with the sensitivity to grain size, since the smaller the grain size, the greater the probability of detecting a triple junction near the crack tip. At higher temperatures, GB sliding is effectively accommodated by diffusion-controlled climb of GBDs and emission of lattice dislocations into the grain body. Accommodated GB sliding can lead to significant blunting of crack tips, which, in turn, significantly (from 1.1 to 3 times, depending on temperature) increases fracture toughness. This effect is most pronounced in nanomaterials with very small grain sizes and decreases significantly with increasing grain size as $K_{IC}^* \sim d^{-5/2}$.

Bobylev et al. [106] considered a special mechanism of transition from GB sliding into rotational deformation in NCMs. This transition is also a mechanism for the accommodation of GB sliding. The mechanism was effectively described through the formation of immobile wedge disclinations at GB triple junctions characterized by gradually increasing power. Calculations using Ni and α -Al₂O₃ as examples demonstrated that this mechanism is energetically favorable. Typical values of the equilibrium disclination power (which is equal to the angle of grain rotation) were found to be in the range from 3° to 7.5° in nanocrystalline Ni when applied shear stress $\tau = 0.5$ GPa, and from 4° to 11° in nanocrystalline α -Al₂O₃ when $\tau = 2$ GPa.

5.5 Rotational Deformation in NCMs

It is well known that the unique deformation behavior of NCMs is treated to be caused by suppression of conventional lattice dislocation slip and effective action of alternative deformation mechanisms occurring through generation, transformation and motion of GB defects. One of such defects are disclinations which are considered as carriers of rotational plastic deformation in solids [113, 114]. Experimental evidence of wedge disclinations in NCMs was demonstrated by Murayama et al. [115].

In the 1990s, the efforts of our lab were concentrated on theoretical description of transformation of wedge disclinations placed at GBs and their triple junctions as well as on crack generation in their vicinity. Gutkin and Ovid'ko [116] considered the splitting of a wedge triple-junction disclination of strength Ω into a circular periodic array of N similar disclinations of smaller strength Ω/N and related this process with solid-state amorphization of the triple junction. They showed that such a process can effectively compete with generation of microcracks at the GB triple junctions, thus making the material more ductile. Gutkin et al. [117–119] suggested similar models for linear splitting of GB disclinations.

In the early 2000s, the motion of dipoles of disclinations in NCMs was in the focus of research. Ovid'ko [120] and Gutkin et al. [88] considered deformation mechanism occurring through the motion of GB disclination dipoles as the mechanism of rotational deformation effectively contributing to the plastic flow in NCMs. As was assumed, the rotational deformation realized only due to movement of the GB disclination dipoles along parallel GB facets, accompanied by crystal lattice rotation between these facets. Gutkin et al. [121] analyzed the mechanisms of generation of mobile disclination dipoles from various (dipole and multipole) disclination configurations at the kinks, double kinks and triple junctions of GBs and related these models with generation and propagation of misorientation bands in poly- and nanocrystalline metals under severe plastic deformation. Mikaelyan et al. [122] clarified some details of the disclination dipole motion through accepting edge dislocations from the surrounding material by means of computer simulations using combined discrete dislocation-disclination dynamics.

In fact, GBs in NCMs are short and curved, and different deformation mechanisms strongly influence each other. For example, according to experimental data [123], GB sliding and rotational deformation are the key mechanisms of superplastic deformation in NCMs. Gutkin et al. [124] suggested a theoretical model describing the combined action of GB sliding and rotational deformation in NCMs, with focuses placed on the crossover from GB sliding to rotational deformation occurring at triple junctions of GBs. In the model [124], grain rotations occurred via the splitting of gliding GBDs at triple junctions into climbing GBDs which moved along GBs adjacent to the triple junction and caused crystal lattice rotation in the grain interior. It was shown that the splitting of the GBDs effectively occurs at triple junctions with large values of the triple junction angle. The experimentally detected [123] grain rotations in superplastically deformed nano- and microcrystalline materials, where GB sliding is the dominant deformation mechanism, support the theoretical model [124].

Recently, Borodin et al. [125] developed a coupled model for grain rotation, dislocation plasticity and GB sliding in UFG solids and NCMs under high-strain-rate deformation. They showed that competition between primal rotation caused by dislocation activity and inverse rotation provided by diffusional flux leads to the appearance of a critical grain size below which grains maintain their initial form in the course of deformation process. Under quasi-static deformation conditions, they obtained the critical grain size of NCMs, which is equal to just a few nanometers that is close to the experimentally found value of 6 nm [126]; the other value, of about 200 nm, was obtained for UFG metals, which is also in a good agreement with microstructural investigations [127]. For larger grains, dislocation kinetics fully determines the angle of rotation and accommodation of GB sliding. Borodin et al. [125] also estimated the maximum strain rate, below which equiaxed grains are still possible during the deformation process. For NC and UFG copper, their model predicted the values of 50 s^{-1} and 6 s^{-1} , respectively, for this maximum strain rate.

5.6 Deformation Twinning in UFG and NC Materials

One of the main specific deformation modes, which greatly contributes to plastic flow in NC and UFG materials, is deformation twinning (DT). Following numerous experimental data, computer simulations and theoretical models [64, 83, 128–133], nanoscale DT effectively operates in NCMs with various chemical compositions and structures. In contrast to coarse-grained polycrystals, in which deformation twins are typically generated within grain interiors, in NCMs under mechanical load, twins are often generated at GBs; see [130] and references therein. In order to explain this experimentally documented fact indicative of specific deformation behavior of NCMs, it was suggested that nanoscale DT occurs through consequent emission of partial dislocations from GBs [64, 128–130]. According to this explanation scheme, partial dislocations should either pre-exist at GBs on every slip plane or be resulted from transformations of pre-existent GBDs located on every slip plane to form a single twin through dislocation emission from the GB. However, it is practically impossible to have pre-existent GBDs or partial ones at a GB on every slip plane in real materials [64]. In order to avoid the discussed discrepancy, Zhu et al. [64] suggested that multiplication of partial dislocations can occur through dislocation reactions and cross-slip processes in deformed nanomaterials. As a result of such defect transformations, partial dislocations are capable of existing at a GB on every slip plane, in which case their consequent emission events provide a twin to grow continuously [64]. However, within this explanation, each dislocation reaction transforms a partial dislocation into two dislocations: a perfect dislocation and another partial dislocation. As a corollary, the dislocation reactions in question are characterized by very large energy barriers being of the order of the perfect dislocation energy. Such reactions can come into play, if only a very high level of the applied stress acts in a specimen. Therefore, multiplication of partial dislocations is hardly typical in

NCMs in wide ranges of their deformation parameters. This motivates search for new alternative explanations of twin generation at GBs in mechanically loaded NCMs.

Gutkin et al. [83] suggested a theoretical model of deformation twin formation from the region at a GB, which occurs in the local stress field created by a biaxial dipole of triple-junction wedge disclinations. Sequential emission of twinning Shockley partial Shockley dislocations under the combined action of the disclination and external shear stresses were modeled and analyzed in detail. It was shown that, in the exemplary cases of NC aluminum and copper with the average grain size of 30 nm, if the applied stress τ and disclination strength ω are high enough (but still realistic for NCMs), the DT generation is characterized by the absence of any energy barrier and the critical stress τ_c causing the emission of the first twinning dislocation is rather low, ~ 0.1 GPa and ~ 0.3 GPa, for Cu and Al, respectively, at $\omega = 0.5$. The generation of a thick DT lamella needs some increase in τ_c . That is, DT in NCMs is characterized by local strain hardening. Similar results were obtained by Gutkin et al. [131] when considering generation of deformation twin near the tip of a microcrack of mixed modes I and II in a sample of NCM under tension.

Within another approach described in theoretical works of Ovid'ko and Skiba [132, 133], nanoscale deformation twins are generated at locally distorted GBs that contain local, deformation-distorted fragments with GBDs located on every slip plane and produced by preceding deformation processes. The twinning mechanisms represent (i) the successive events of partial dislocation emission from GBs; (ii) the cooperative emission of partial dislocations from GBs; and (iii) the multiphase nanoscale shear generated at GBs. It was found that the deformation twinning mechanisms can operate in NC and UFG materials at rather high, but realistic levels of the stress. The suggested representations on generation of nanotwins at locally distorted GBs logically explains numerous experimental observations [64, 129] of generation of nanoscale twins at GBs in NC and UFG materials. These deformation twinning mechanisms illustrate complicated interactions between different deformation modes such as deformation twinning, GB sliding and GB dislocation climb.

5.7 Deformation-Induced Grain Growth and Refinement in UFG and NC Materials

UFG and NC structures are typically formed due to severe plastic deformation that causes grain refinement in initially coarse-grained structures. In order to control the final UFG and NC structures in severely deformed materials, it is important to understand and describe both the nature and micromechanisms of deformation-induced grain refinement. In these circumstances, of particular interest is the stress-driven GB migration which by definition represents a plastic deformation mode carried by migrating GBs [134]. It is conventionally treated that the stress-driven GB migration is responsible for both nanoscale plastic flow and grain growth [134].

A brief summary of early experimental observations of athermal stress-driven grain growth and GB migration is given in [135]. Gutkin and Ovid'ko [136] suggested probably the first simple analytical model to describe this phenomenon. They treated the migration of a tilt GB, characterized by the length $2a$ and the misorientation angle ω , over a distance d under an applied shear stress τ as an athermal process accompanied with generation of a quadrupole of partial wedge disclinations with strength ω and sizes $d \times 2a$. Analyzing the energy change caused by this process, they found two critical stress values: τ_{c1} which is necessary for starting the GB migration, and τ_{c2} which separate the stable and unstable regimes of the GB migration. These critical stresses are given by very simple formulas [135, 136]:

$$\tau_{c1} \approx \frac{D\omega b}{2a} \left(\ln \frac{2a}{b} + \frac{1}{2} \right), \quad \tau_{c2} \approx 0.8D\omega, \quad (5.3)$$

where $D = G/[2\pi(1 - \nu)]$, G is the shear modulus, ν is the Poisson ratio, and b is the interatomic distance. It was also shown that, if $\tau_{c1} \leq \tau < \tau_{c2}$, the equilibrium distance d_{eq} of the GB migration is determined from the following equation:

$$\tau = \frac{D\omega d_{eq}}{2a} \ln \left(1 + \frac{4a^2}{d_{eq}^2} \right). \quad (5.4)$$

If $\tau \geq \tau_{c2}$, the GB migration becomes unstable when the GB propagation does not depend on the value of τ . This model was later supported by computer simulations [137].

Gutkin et al. [135, 138] extended the model [136] to the case of cooperative migration of two neighboring GBs with opposite signs of misorientation angles. They showed that the elastic interaction of two migrating GBs leads to a decrease of the critical stress τ_{c1} . For GBs with misorientation angles of equal magnitude ω , the difference is $\Delta\tau_{c1} \approx 3D\omega b/4a$. In this case, the stress value τ_m , at which these GBs can meet, is given by $\tau_m \approx 1.6D\omega$. In general, it was shown that the stable migration of GBs at $\tau_{c1} \leq \tau \leq \tau_m$ leads to a decrease of the grain bounded by them at the cost of growth of the neighbor grains and can result in complete or partial annihilation of the GBs and the collapse of this grain. Unstable migration at $\tau > \tau_m$ can lead either to annihilation of GBs or to passage of them through each other, which can be considered as the disappearance of the grain and nucleation and growth of a new grain.

The models [135, 136, 138] described the GB migration in an infinite NCM. However, most of experiments on the stress-driven grain growth were done on thin films, either free standing or deposited on special substrates [134], in which case the role of free surface(s) could be important. To take this into account, Dynkin and Gutkin [139, 140] considered the migration of a tilt GB in a stretched ultrathin NC layer. In doing so, they suggested and analyzed two models. In the first model, the migrating GB emerges on the layer surface, while in the second it migrates in the bulk of the layer. It was shown that both the critical stresses, τ_{c1} and τ_{c2} , decrease with

decreasing GB misorientation angle ω and layer thickness h , and with increasing GB length $2a$. While a GB migrates in the stable regime, its equilibrium displacement d_{eq} increases with increasing τ and $2a$, and with decreasing ω , and practically does not depend on h . Thus, the least resistant to the stress-induced growth must be larger grains having low-angle GBs which are placed near free surfaces in the thinnest layers. The most advantageous case for athermal grain growth is that in which the migrating GB emerges on the layer surface.

Alternative role of stress-driven GB migration as a process responsible for nucleation of new nano-grains in NC and UFG materials (stress-induced grain refinement) has been suggested and investigated in a number of works [108, 109, 141–146] within our lab. The common approach employed in these works is a disclination description of stress-induced GB splitting and migration (modeled as splitting and movement of disclination dipoles) resulting in nucleation of new nanograins. First models using this method were developed by Bobylev and Ovid'ko [141, 142]. Within the framework of these models, nanograin nucleation occurs through splitting and migration of GBs containing disclination dipoles produced by GB sliding and/or lattice slip. It was shown that the nanograin nucleation is energetically favorable in mechanically loaded NC Al and α -Al₂O₃ in certain ranges of their parameters and the external stress levels.

Models [141, 142] considered simplified GB migration scenario producing rectangular nanograins. More realistic hexagonal grain shapes were considered by Bobylev et al. [108] in a similar manner. Further development of this approach included description [143] of nanograin nucleation near crack tips in NCMs, where GB splitting happened at a highly stressed, disclination-free region near a crack tip. The suggested theoretical models [108, 143] of plastic flow occurring through generation of nanograins at GBs in UFG materials were well consistent with the experimental observation [109] of nanograins generation at GBs in cobalt.

Morozov et al. [144] suggested a theoretical model which describes nanograin chain formation. In this model, the initial GB structure contained a quadrupole of disclinations located at GB junctions of a previously formed nanograin in a NC or UFG specimen. The final structure contained two neighboring nanograins which are elongated along the same direction and may serve as nuclei for experimentally observed [145] nanograin agglomerates (groups of nanograins with low-angle and/or special GBs within comparatively large grains having high-angle GBs) in NC and UFG materials.

Bobylev and Ovid'ko [146] extended description above on deformation-distorted GBs – non-equilibrium GBs containing trapped ensembles of lattice dislocations typical for NC and UFG materials produced by severe plastic deformation methods. It was concluded that the splitting processes in deformation-distorted GBs is specific to these GBs and do not have their analogs in the previously examined conventional, non-distorted GBs and lead to formation of new nanoscale (sub)-grains in nanomaterials. Thus, the stress-driven splitting of deformation-distorted GBs can effectively contribute to grain refinement in bulk metallic materials under severe plastic deformation.

Common feature of GB migration processes is the existence of unstable migration regime [108, 135–144, 146, 147] and corresponding critical stress τ_{c2} for its onset. When applied stress exceeds this critical stress, GB starts migrating uncontrollably until it is stopped at some obstacle or destroyed completely (which is the case with low-angle GBs). Bobylev and Ovid’ko [146, 147] assumed that this process is effectively controls grain refinement under SPD processing. It is known [148] that the grain size of metallic materials processed by SPD cannot be reduced below certain minimum value, i.e. there exists saturation of grain size. Indeed, grain refinement often occurs through formation and evolution of lattice dislocation cells [149]. In their turn, individual dislocations that form cell boundaries are generated at sources like Frank-Read ones. Thus, Bobylev and Ovid’ko [146, 147] assumed that saturation of grain size in metals under SPD occurs when the dislocation cell boundaries start intensively migrating (in unstable regime) under stress and saturated grain size can be estimated via the balance of the critical stress τ_{c2} and the stress of Frank-Read source operation. The following estimation for saturated grain size d_s was obtained:

$$d_s \approx \frac{15\pi(1-\nu)b}{2\omega}. \quad (5.5)$$

Using Eq. (5.5) in the case of dislocation cell misorientation $\sim 1^\circ\text{--}3^\circ$, Bobylev and Ovid’ko [146, 147] estimated $d_s \sim 78 - 233$ nm in Cu and $\sim 80 - 239$ nm in Ni. These estimates are well consistent with experiments showing $d_s \sim 200$ nm in Cu processed by equal-channel angular pressing [150], and $d_s \sim 50 - 200$ nm in Ni processed by high pressure torsion [151, 152].

5.8 Interaction Between Deformation and Fracture Processes in NCMs

Another research topic of our lab concerned the theoretical studies of the interaction between plastic deformation processes and fracture in deformed NCMs. The first work in this field [153] considered the generation of nanocracks in the stress field of dislocations with large Burgers vectors formed in triple junctions of GBs due to the coalescence of GBDs. This model [153] assumes that both GB sliding and conventional lattice dislocation slip cause plastic flow of a NC specimen. This means that when a mechanical load is applied to the specimen, mobile GBDs (with the Burgers vectors parallel to GB planes) move, causing GB sliding. These dislocations stop at triple junctions of GBs, where GB planes are curved and thereby dislocation movement is hampered. At some critical shear stress, GBDs merge at a triple junction, producing a sessile triple junction dislocation. This process is an elementary act of plastic deformation involving GB sliding. The process under consideration repeats and is accompanied by an increase of the Burgers vector magnitude of the sessile dislocation at each step. Within the model [153], a nanocrack at the triple junction is

generated to release the strain energy of the sessile triple junction dislocation. In this scenario, mobile GBDs that carry GB sliding also influence nanocrack generation.

The calculations [153] demonstrated that the triple junction nanocrack is characterized by the equilibrium length that corresponds to the stable, low-energy state of the nanocrack. The equilibrium nanocrack length is highly sensitive to the parameters characterizing the triple junction geometry, the specific energy of the nanocrack surface, and GBD storage at the triple junction. In particular, triple junction nanocracks nucleate and rapidly grow with rising the Burgers vectors of GBDs generated and accumulated at triple junctions due to GB sliding. More precisely, a stable nanocrack nucleates at a triple junction after just several (about 5) acts of the GBD coalescence at the triple junction.

The theoretical model suggested in [153] accounts for the experimental observation [154] of nanocracks nucleating at triple junctions during plastic deformation of nanocrystalline Ni samples exhibiting substantial ductility. Also, this model predicts a certain stability of triple junction nanocracks. This prediction is in agreement with experiments [154], in which good ductility of deformed NCMs and a non-catastrophic character of failure processes have been detected.

At the same time, at low strain rates and/or high enough temperatures, the process of dislocation accumulation at triple junctions and the resulting generation of nanocracks can be suppressed due to GB diffusion. GB diffusion can provide partial relaxation of the stress fields created by triple junction superdislocations and thereby hampers nanocrack generation at triple junctions. The theoretical study of the combined effect of GB sliding and GB diffusion [155] demonstrated that the intense generation of nanocracks occurs at some critical plastic strain, which depends on the strain rate and temperature. In particular, at high strain rate and low temperatures, when GB diffusion is low, the critical strain for the intense nanocrack generation is small. In contrast, at small strain rates and high enough temperatures, when GB diffusion is fast, the critical strain for nanocrack generation is large. In the latter case, during the extensive stage of (super)plastic deformation, the stress relaxation effect of GB diffusion is dominant, which causes suppression of nanocrack generation.

In addition to the formation of triple junction dislocations, GB sliding can also lead to the formation of another kind of defect – disclination dipoles [156]. The formation of disclination dipoles is related to the shift of triple junctions during GB sliding. If the formation of disclination dipoles is not accommodated by GB diffusion, the stress fields of these dipoles can result in strain hardening during plastic deformation of NCMs and, at the same time, can lead to the generation of nanocracks. The effects of such dislocation dipoles on strain hardening and nanocrack generation were theoretically analyzed in Refs. [156, 157]. It appeared that disclination dipoles can cause high strain hardening and, besides, lead to the formation of long enough nanocracks, whose equilibrium length can be comparable to the grain size. As a result, such nanocracks can merge, leading to the generation and growth of microcracks.

As in the case of triple junction dislocations, the stress fields of disclination dipoles produced due to GB sliding can be affected by GB diffusion. The study of the combined effects of GB sliding (accompanied by the formation of disclination dipoles) and GB diffusion [105] has demonstrated that the mechanical behavior of plastically

deformed NC specimens depends on strain rate and deformation temperature. At high strain rates and/or low temperatures, NCMs fail due to enhanced cracking. At high temperatures and/or low strain rates, they fail due to necking. In contrast, at intermediate strain rates and temperatures, NCMs can demonstrate good ductility. The region in the parameter space (strain rate, temperature) where NC specimens do not fail due to cracking or necking shrinks with an increase in the plastic strain, and at some critical plastic strain, NCMs fail at any strain rate and temperature.

Besides initiating the formation of new cracks, GB sliding can also affect the growth of existing cracks (see Sect. 5.4, the discussion of work by Bobylev et al. [73]).

As is indicated above, in addition to triple junction dislocations, GB sliding can also lead to the formation of disclination dipoles, which can also affect the growth of the existing cracks. The effect of the GB-sliding-induced disclination dipoles on the growth of existing cracks was analyzed in Ref. [158]. It was demonstrated that GB-sliding-induced disclination dipoles can increase the critical length for the catastrophic crack growth and thereby toughen NCMs. The increase in the critical nanocrack length is especially pronounced at very small grain sizes of NCMs and high misorientation angles of their GBs.

In parallel with GB sliding, other plastic deformation mechanisms also influence the fracture processes in NCMs. One such mechanism is the stress-driven GB migration, which can result in the formation of a quadrupole of wedge disclinations [135]. The effect of GB migration on the generation of nanocracks and the growth of pre-existent cracks in NCMs has been examined in Refs. [159, 160]. It was shown that, similar to GB sliding, GB migration can promote the generation of nanocracks in the stress fields of disclination quadrupoles and, at the same time, hinders the growth of the pre-existent cracks, leading to a small increase of the fracture toughness (by 10–15%).

Another example of a plastic deformation mechanism specific to NCMs is rotational deformation, which is accompanied by the rotation of crystal planes in a specified grain [30]. Such rotational deformation can lead to the formation of a wedge disclination dipole [30]. The effect of rotational deformation on the fracture toughness of NCMs was theoretically analyzed in Ref. [161]. It was shown [161] that rotational deformation can increase the fracture toughness by 10–15%.

In many cases, various plastic deformation mechanisms can be combined and accommodate each other in NCMs. An example is GB sliding accommodated by GB migration. Such mechanism was first suggested in Ref. [107]. The study of the effect of such deformation mechanism on the fracture toughness of NCMs [162] showed that this mechanism can dramatically increase the fracture toughness of NCMs (by a factor of 3 or more).

The importance of the above toughening mechanisms acting in NCMs is related to the low fracture toughness documented in these materials, which is much smaller than that of their coarse-grained counterparts. To explain the low fracture toughness of NCMs, the authors of Refs. [163, 164] considered the emission of dislocations from a tip of a large crack. Within the models [163, 164], the first emitted dislocation stops at a nearest GB. As a result, a pileup of dislocations is produced ahead of the crack tip, whose length decreases with a decrease in grain size. The emitted dislocations

can increase the fracture toughness in two ways: first, due to their stress fields that shield the crack tip, and, second, due to crack blunting. In coarse-grained metallic materials, the number of emitted dislocations can be large, and both toughening effects are strong. Therefore, such materials have high fracture toughness. In contrast, in NCMs, the length of dislocation pileups between the crack tip and the nearest GB is small. As a result, the number of dislocations emitted from a crack tip is also small, and their toughening effect is not essential. This explains the low fracture toughness of NCMs.

5.9 Conclusions

Thus, we gave a brief review of research efforts provided in our lab over almost 30 years on the development of theoretical models describing various aspects of mechanical behavior of nanostructured materials. As one could see, our contribution to the field has been rather extensive. In fact, our models have covered many important areas in micromechanics of plasticity of these materials with touching, although rather rarely, some problems of their fracture. In conclusion, we should say that nanostructured materials are specific solids in which plastic deformation develops through simultaneous action of various interacting physical mechanisms involving all elements of the defect structure, both in the bulk of nanograins and in their boundaries and triple junctions. These structural elements continuously change in the course of plastic deformation that makes their theoretical modeling rather difficult but very interesting for sure.

At present, some new topics are in focus of research in our lab, which we have not touched in this review. They concern theoretical modeling in the following areas: (i) plastic deformation and fracture in metal-graphene nanocomposites, (ii) fracture toughness of ceramic-graphene nanocomposites, (iii) mechanical behavior of monolithic nanoceramics, and (iv) evolution of structure and mechanical properties in ultra-fine grained aluminum and aluminum-based alloys in the process of thermal and mechanical treatment. We hope that, in the future, we will be capable to present an extended review of results obtained in these fields as well.

References

1. Gutkin, M.Yu., Ovid'ko, I.A.: Defekty i mehanizmy plastichnosti v nanostrukturnyh i nekristallicheskih materialah (Defects and mechanisms of plasticity in nanostructured and non-crystalline materials). Yanus, Saint-Petersburg (2001)
2. Gutkin, M.Yu., Ovid'ko, I.A.: Fizicheskaya mehanika deformiruemyh nanostruktur. T. 1. Nanokristallicheskie materialy (Physical mechanics of deformed nanostructures. Vol. 1. Nanocrystalline Materials). Yanus, Saint-Petersburg (2003)
3. Gutkin, M.Yu., Ovid'ko, I.A.: Plastic Deformation in Nanocrystalline Materials. Springer, Berlin, Heidelberg, New York (2004)

4. Koch, C.C., Ovid'ko, I.A., Seal, S., Veprek, S.: *Structural Nanocrystalline Materials: Fundamentals and Applications*. Cambridge University Press, Cambridge (2007)
5. Bobylev, S.V., Ovid'ko, I.A.: Granitsy zeren i plasticheskaya deformatsiya v nanomaterialah (Grain boundaries and plastic deformation in nanomaterials). Izd-vo Polytechn. un-ta, Saint-Petersburg (2016)
6. Ovid'ko, I.A., Semenov, B.N., Sheinerman, A.G.: *Mehanika deformiruemykh nanomaterialov: uchebnoe posobie* (Mechanics of deformable nanomaterials: textbook). Izd-vo S.-Peterb. un-ta, Saint-Petersburg (2013)
7. Gutkin, M.Yu., Ovid'ko, I.A., Pande, C.S.: Theoretical models of plastic deformation processes in nanocrystalline materials. *Rev. Adv. Mater. Sci.* **80**, 80–102 (2001)
8. Gutkin, M.Yu., Ovid'ko, I.A.: Yield stress and plastic deformation of nanocrystalline materials. *Usp. Mekh.* **2**, 68–125 (2003)
9. Gutkin, M.Yu., Ovid'ko, I.A.: Disclinations and rotational deformation in nanocrystalline materials. *Rev. Adv. Mater. Sci.* **4**, 79–113 (2003)
10. Ovid'ko, I.A.: Interfacial defects in nanostructures. In: Nalwa, H.S. (ed.) *Encyclopedia of Nanoscience and Nanotechnology*, vol. 4, pp. 249–265. American Scientific Publishers, Stevenson Ranch, CA (2004)
11. Gutkin, M.Yu., Ovid'ko, I.A., Pande, C.S.: Physical mechanisms of plastic flow in nanocrystalline materials. In: Nalwa, H.S. (ed.) *Nanoclusters and Nanocrystals*, pp. 225–252. American Scientific Publishers, Stevenson Ranch, CA (2003)
12. Ovid'ko, I.A.: Deformation and diffusion modes in nanocrystalline materials. *Int. Mater. Rev.* **50**, 65–82 (2005)
13. Ovid'ko, I.A.: Superplasticity and ductility of superstrong nanomaterials. *Rev. Adv. Mater. Sci.* **10**, 89–104 (2005)
14. Ovid'ko, I.A.: Defects and deformation mechanisms in nanostructured coatings. In: Cavaleiro, A., De Hosson, J.T.M. (eds.) *Nanostructured Coatings*, pp. 78–108. Springer, New York (2006)
15. Ovid'ko, I.A.: Review on the fracture processes in nanocrystalline materials. *J. Mater. Sci.* **42**, 1694–1708 (2007)
16. Ovid'ko, I.A.: Fracture processes in advanced nanocrystalline and nanocomposite materials. In: Shi, D. (ed.) *NanoScience in Biomedicine*, Chapter 21, pp. 537–567. Springer, Berlin, Heidelberg (2009)
17. Gutkin, M.Yu.: Elastic and plastic deformation in nanocrystalline metals. In: Whang, S.H. (ed.) *Nanostructured Metals and Alloys: Processing, Microstructure, Mechanical Properties and Applications*, Chapter 12, pp. 329–374. Woodhead Publishing Limited, Oxford, Cambridge, Philadelphia, New Delhi (2011)
18. Ovid'ko, I.A.: Enhanced ductility and its mechanisms in nanocrystalline metallic materials. In: Whang, S.H. (ed.) *Nanostructured Metals and Alloys: Processing, Microstructure, Mechanical Properties and Applications*, Chapter 14, pp. 430–458. Woodhead Publishing Limited, Oxford, Cambridge, Philadelphia, New Delhi (2011)
19. Ovid'ko, I.A., Sheinerman, A.G.: Micromechanisms for improved fracture toughness in nanoceramics. *Rev. Adv. Mater. Sci.* **29**, 105–125 (2011)
20. Ovid'ko, I.A., Sheinerman, A.G.: Fracture behavior of nanocrystalline ceramics. In: Li, J.C.M. (ed.) *Mechanical Properties of Nanocrystalline Materials*, Chapter 9, pp. 245–275. Pan Stanford Publishing Pte Ltd., New York (2011)
21. Ovid'ko, I.A.: Crack generation in nanomaterials at high-strain-rate and quasistatic regimes of deformation. *Mater. Phys. Mech.* **12**, 76–101 (2011)
22. Ovid'ko, I.A., Sheinerman, A.G., Aifantis, E.C.: Mechanics of crack growth processes in nanoceramics. *Mater. Phys. Mech.* **12**, 1–29 (2011)
23. Ovid'ko, I.A., Langdon, T.G.: Enhanced ductility of nanocrystalline and ultrafine-grained metals. *Rev. Adv. Mater. Sci.* **30**, 103–111 (2012)
24. Ovid'ko, I.A., Aifantis, E.C.: Nanocrystals & nanomechanics: mechanisms & models. A selective review. *Rev. Adv. Mater. Sci.* **35**, 1–24 (2013)
25. Ovid'ko, I.A.: Mechanics of fracturing in nanoceramics. *Phil. Trans. R. Soc. A* **373**, 20140129 (2015)

26. Bobylev, S.V., Ovid'ko, I.A.: Accommodation of grain boundary sliding and fracture toughness enhancement in deformed nanocrystalline materials. *Mater. Phys. Mech.* **29**, 43–70 (2016)
27. Ovid'ko, I.A., Sheinerman, A.G.: Plastic deformation and fracture processes in bulk nanotwinned materials and nanotwinned nanowires. In: Ebothe, J., Ahmed, W. (eds.) *Nanofabrication Using Nanomaterials*, pp. 46–64. One Central Press, Manchester, U.K. (2016)
28. Ovid'ko, I.A., Sheinerman, A.G.: Mechanical properties of nanotwinned metals: a review. *Rev. Adv. Mater. Sci.* **44**, 1–25 (2016)
29. Skiba, N.V., Bobylev, S.V.: Twinning mechanism and yield stress in nanotwinned materials. *Rev. Adv. Mater. Sci.* **51**, 86–89 (2011)
30. Ovid'ko, I.A., Valiev, R.Z., Zhu, Y.T.: Review on superior strength and enhanced ductility of metallic nanomaterials. *Prog. Mater. Sci.* **94**, 462–540 (2018)
31. Sheinerman, A.G., Gutkin, M.Yu.: Strengthening and softening of nanoceramics: A brief review. *Rev. Adv. Mater. Tech.* **1**, 46–53 (2019)
32. Skiba, N.V.: Review of mechanisms of nanograin generation. *Rev. Adv. Mater. Tech.* **1**, 62–68 (2019)
33. Skiba, N.V.: Mechanisms of deformation twin formation near crack tips in nanostructured materials. *Rev. Adv. Mater. Tech.* **2**, 56–63 (2020)
34. Sheinerman, A.G.: Plastic deformation of metal/graphene composites with bimodal grain size distribution: a brief review. *Rev. Adv. Mater. Tech.* **2**, 1–8 (2019)
35. Hall, E.O.: Deformation and ageing of mild steel. *Proc. Phys. Soc. Lond. B* **64**, 747–753 (1951)
36. Petch, N.J.: The cleavage strength of polycrystals. *J. Iron Steel Inst.* **174**, 25–28 (1953)
37. Lasalmonie, A., Strudel, J.L.: Influence of grain size on the mechanical behavior of some high strength materials. *J. Mater. Sci.* **21**, 1837–1852 (1986)
38. Armstrong, R.W.: 60 years of Hall-Petch: Past to present nano-scale connections. *Mater. Trans.* **55**, 2–12 (2014)
39. Cordero, Z.C., Knight, B.E., Schuh, C.A.: Six decades of the Hall-Petch effect - a survey of grain-size strengthening studies on pure metals. *Int. Mater. Rev.* **61**, 495–512 (2016)
40. Chokshi, A.H., Rosen, A., Karch, J., Gleiter, H.: On the validity of the Hall-Petch relationship in nanocrystalline materials. *Scripta Metall.* **23**, 1679–1684 (1989)
41. Jang, J.S.C., Koch, C.C.: The Hall-Petch relationship in nanocrystalline iron produced by ball milling. *Scripta Metall. Mater.* **24**, 1599–1604 (1990)
42. Kocks, U.F.: The relation between polycrystal deformation and single crystal deformation. *Metal. Trans.* **1**, 1121–1143 (1970)
43. Malygin, G.A.: Plasticity and strength of micro- and nanocrystalline materials. *Phys. Solid State* **49**, 1013–1033 (2007)
44. Pande, C.S., Cooper, K.P.: Nanomechanics of Hall-Petch relationship in nanocrystalline materials. *Prog. Mater. Sci.* **54**, 689–706 (2009)
45. Hahn, E.N., Meyers, M.A.: Grain-size dependent mechanical behavior of nanocrystalline metals. *Mater. Sci. Eng., A* **646**, 101–134 (2015)
46. Kozlov, E.V., Glezer, A.M., Koneva, N.A., Popova, N.A., Kurzina, I.A.: *Osnovy plasticheskoi deformatsii v nanostrukturnykh materialakh (Fundamentals of Plastic Deformation of Nanostructured Materials)*. Fizmatlit, Moscow (2016)
47. Naik, S.N., Walley, S.M.: The Hall-Petch and inverse Hall-Petch relations and the hardness of nanocrystalline metals. *J. Mater. Sci.* **55**, 2661–2681 (2020)
48. Gryaznov, V.G., Gutkin, M.Yu., Romanov, A.E., Trusov, L.I.: On the yield stress of nanocrystals. *J. Mater. Sci.* **28**, 4359–4365 (1994)
49. Christensen, R.M.: *Mechanics of Composite Materials*. Wiley, New York (1979)
50. Masumura, R.A., Hazzledine, P.M., Pande, C.S.: Yield stress of fine grained materials. *Acta Mater.* **46**, 4527–4534 (1998)
51. Gutkin, M.Yu., Ovid'ko, I.A., Pande, C.S.: Yield stress of nanocrystalline materials: Role of grain boundary dislocations, triple junctions and Coble creep. *Philos. Mag.* **84**, 847–863 (2004)

52. Nazarov, A.A., Romanov, A.E., Valiev, R.Z.: On the structure, stress fields and energy of nonequilibrium grain boundaries. *Acta Metall. Mater.* **41**, 1033–1040 (1993)
53. Hahn, H., Mondal, P., Padmanabhan, K.A.: Plastic deformation of nanocrystalline materials. *Nanostruct. Mater.* **9**, 603–606 (1997)
54. Fedorov, A.A., Gutkin, M.Yu., Ovid'ko, I.A.: Transformations of grain boundary dislocation pile-ups in nano- and polycrystalline materials. *Acta Mater.* **51**, 887–898 (2003)
55. Volpp, T., Göring, E., Kuschke, W.-M., Arzt, E.: Grain size determination and limits to Hall-Petch behavior in nanocrystalline NiAl powders. *Nanostruct. Mater.* **8**, 855–865 (1997)
56. Fedorov, A.A., Gutkin, M.Yu., Ovid'ko, I.A.: Triple junction diffusion and plastic flow in fine-grained materials. *Scripta Mater.* **41**, 51–55 (2002)
57. Sheinerman, A.G., Castro, R.H.R., Gutkin, M.Yu.: A model for direct and inverse Hall-Petch relation for nanocrystalline ceramics. *Mater. Lett.* **260**, 126886 (2020)
58. Sheinerman, A.G., Gutkin, M.Yu.: The role of grain boundaries and their triple junctions in strengthening and softening of nanocrystalline ceramics. *Lett. Mater.* **10**, 547–550 (2020)
59. Hirth, J., Lothe, L.: *Theory of Dislocations*. Wiley, New York (1982)
60. Wu, X.L., Ma, E.: Dislocations in nanocrystalline grains. *Appl. Phys. Lett.* **88**, 231911 (2006)
61. Wu, X.L., Ma, E.: Accommodation of large plastic strains and defect accumulation in nanocrystalline Ni grains. *J. Mater. Res.* **22**, 2241–2253 (2007)
62. Liao, X.Z., Zhou, F., Lavernia, E.J., Srinivasan, S.G., Baskes, M.I., He, D.W., Zhu, Y.T.: Deformation mechanism in nanocrystalline Al: Partial dislocation slip. *Appl. Phys. Lett.* **83**, 632–634 (2003)
63. Wu, X., Zhu, Y.T., Chen, M.W., Ma, E.: Twinning and stacking fault formation during tensile deformation of nanocrystalline Ni. *Scripta Mater.* **54**, 1685–1690 (2006)
64. Zhu, Y.T., Wu, X.L., Liao, X.Z., Narayan, J., Mathaudhu, S.N., Kecskés, L.J.: Twinning partial multiplication at grain boundary in nanocrystalline fcc metals. *Appl. Phys. Lett.* **95**, 031909 (2009)
65. Wang, Y.M., Bringa, E.M., McNaney, J.M., Victoria, M., Caro, A., Hodge, A.M., Smith, R., Torralva, B., Remington, B.A., Schuh, C.A., Jamarkani, H., Meyers, M.A.: Deforming nanocrystalline nickel at ultrahigh strain rates. *Appl. Phys. Lett.* **88**, 061917 (2006)
66. Yamakov, V., Wolf, D., Phillpot, S.R., Gleiter, H.: Deformation twinning in nanocrystalline Al by molecular-dynamics simulation. *Acta Mater.* **50**, 5005–5020 (2002)
67. Van Swygenhoven, H.: Footprints of plastic deformation in nanocrystalline metals. *Mater. Sci. Eng., A* **483–484**, 33–39 (2008)
68. Gutkin, M.Yu., Ishizaki, T., Kuramoto, S., Ovid'ko, I.A.: Nanodisturbances in deformed Gum Metal. *Acta Mater.* **54**, 2489–2499 (2006)
69. Cui, J.P., Hao, Y.L., Li, S.J., Sui, K.L., Li, D.X., Yang, R.: Reversible movement of homogeneously nucleated dislocations in a β -titanium alloy. *Phys. Rev. Lett.* **102**, 045503 (2009)
70. Gutkin, M.Yu., Ovid'ko, I.A.: Special mechanism for dislocation nucleation in nanomaterials. *Appl. Phys. Lett.* **88**, 211901 (2006)
71. Gutkin, M.Yu., Ovid'ko, I.A.: Homogeneous nucleation of glide dislocation loops in nanoceramics. *Phys. Solid State* **50**, 655–664 (2008)
72. Gutkin, M.Yu., Ovid'ko, I.A.: Homogeneous nucleation of dislocation loops in nanocrystalline metals and ceramics. *Acta Mater.* **56**, 1642–1649 (2008)
73. Bobylev, S.V., Mukherjee, A.K., Ovid'ko, I.A., Sheinerman, A.G.: Effects of intergrain sliding on crack growth in nanocrystalline materials. *Int. J. Plast.* **26**, 1629–1644 (2010)
74. Ovid'ko, I.A., Sheinerman, A.G.: Deformation twinning through nanoscale ideal shears in nano- and polycrystalline materials at ultra high stresses. *Rev. Adv. Mater. Sci.* **27**, 189–194 (2011)
75. Morozov, N.F., Ovid'ko, I.A., Sheinerman, A.G., Skiba, N.V.: Formation of deformation twins through ideal nanoshear events near crack tips in deformed nanocrystalline materials. *Rev. Adv. Mater. Sci.* **32**, 75–81 (2012)
76. Ovid'ko, I.A., Sheinerman, A.G.: Crack generation initiated by nanoscale ideal shear in crystalline, nanocrystalline and metal-ceramic nanocomposite solids. *Rev. Adv. Mater. Sci.* **39**, 84–91 (2014)

77. Bobylev, S.V., Gutkin, M.Yu., Ovid'ko, I.A.: Decay of low-angle tilt boundaries in deformed nanocrystalline materials. *J. Phys. D Appl. Phys.* **37**, 269–272 (2004)
78. Bobylev, S.V., Gutkin, M. Yu., Ovid'ko, I.A.: Transformations of grain boundaries in deformed nanocrystalline materials. *Acta Mater.* **52**, 3793–3805 (2004)
79. Bobylev, S.V., Gutkin, M.Yu., Ovid'ko, I.A.: Chain decay of low-angle tilt boundaries in nanocrystalline materials. *Phys. Sol. State* **46**, 2053–2057 (2004)
80. Gutkin, M.Yu., Ovid'ko, I.A.: Generation of dislocation loops in deformed nanocrystalline materials. *Phil. Mag.* **86**, 1483–1511 (2006)
81. Bobylev, S.V., Gutkin, M.Yu., Ovid'ko, I.A.: Partial and split dislocation configurations in nanocrystalline metals. *Phys. Rev. B* **73**, 064102 (2006)
82. Bobylev, S.V., Gutkin, M.Yu., Ovid'ko, I.A.: Generation of gliding semi-loops of split dislocations by grain boundaries in nanocrystalline Al. *Phys. Sol. State* **48**, 1495–1505 (2006)
83. Gutkin, M.Yu., Ovid'ko, I.A., Skiba, N.V.: Generation of deformation twins in nanocrystalline metals: theoretical model. *Phys. Rev. B* **74**, 172107 (2006)
84. Gutkin, M.Yu., Ovid'ko, I.A., Skiba, N.V.: Mechanism of deformation-twin formation in nanocrystalline metals. *Phys. Sol. State* **49**, 874–882 (2007)
85. Gutkin, M.Yu., Kolesnikova, A.L., Ovid'ko, I.A., Skiba, N.V.: Rotational deformation in fine-grained materials prepared by severe plastic deformation. *J. Metastab. Nanocryst.* **12**, 47–57 (2002)
86. Gutkin, M.Yu., Ovid'ko, I.A., Skiba, N.V.: Changes in the grain boundary misorientation caused by the emission of dislocation pairs. *Tech. Phys. Lett.* **28**, 437–438 (2002)
87. Gutkin, M.Yu., Ovid'ko, I.A., Skiba, N.V.: Transformations of grain boundaries due to disclination motion and emission of dislocation pairs. *Mater. Sci. Eng., A* **339**, 73–80 (2003)
88. Gutkin, M.Yu., Kolesnikova, A.L., Ovid'ko, I.A., Skiba, N.V.: Disclinations and rotational deformation in fine-grained materials. *Phil. Mag. Lett.* **82**, 651–657 (2002)
89. Gutkin, M.Yu., Ovid'ko, I.A., Skiba, N.V.: Emission of partial dislocations by grain boundaries in nanocrystalline metals. *Phys. Sol. State* **46**, 2042–2052 (2004)
90. Gutkin, M.Yu., Ovid'ko, I.A., Skiba, N.V.: Emission of partial dislocations from triple junctions of grain boundaries in nanocrystalline materials. *J. Phys. D Appl. Phys.* **38**, 3921–3925 (2005)
91. Gutkin, M.Yu., Ovid'ko, I.A., Skiba, N.V.: Grain boundary sliding and lattice dislocation emission in nanocrystalline materials under plastic deformation. *Phys. Sol. State* **47**, 1662–1674 (2005)
92. Ovid'ko, I.A., Sheinerman, A.G.: Dislocation emission from nanovoids in single-phase and composite nanocrystalline materials. *Rev. Adv. Mater. Sci.* **11**, 46–55 (2006)
93. Wei, Q., Jia, D., Ramesh, K.T., Ma, E.: Evolution and microstructure of shear bands in nanostructured Fe. *Appl. Phys. Lett.* **81**, 1240–1242 (2002)
94. Bobylev, S.V., Ovid'ko, I.A.: Partial and split dislocations in deformed nanocrystalline metals. *Rev. Adv. Mater. Sci.* **7**, 75–82 (2004)
95. Zhu, Y.T., Liao, X.Z., Srinivasan, S.G., Zha, Y.H., Baskes, M.I., Zhou, F., Lavernia, E.J.: Nucleation and growth of deformation twins in nanocrystalline aluminum. *Appl. Phys. Lett.* **85**, 5049–5051 (2004)
96. Bobylev, S.V., Mukherjee, A.K., Ovid'ko, I.A.: Emission of partial dislocations from amorphous intergranular boundaries in deformed nanocrystalline ceramics. *Scripta Mater.* **60**, 36–39 (2009)
97. Orlova, T.S., Skiba, N.V., Mavlyutov, A.M., Murashkin, M.Yu., Valiev, R.Z., Gutkin, M.Yu.: Hardening by annealing and implementation of high ductility of ultra-fine grained aluminum: experiment and theory. *Rev. Adv. Mater. Sci.* **57**, 224–240 (2018)
98. Gutkin, M.Yu., Latynina, T.A., Orlova, T.S., Skiba, N.V.: Mechanism of hardening of ultrafine-grained aluminum after annealing. *Phys. Solid State* **61**, 1790–1799 (2019)
99. Skiba, N.V., Orlova, T.S., Gutkin, M.Yu.: Mechanism of implementation of high ductility in ultrafine-grained aluminum after annealing and subsequent deformation. *Phys. Solid State* **62**, 2094–2100 (2020)

100. Gutkin, M.Yu., Ovid'ko, I.A., Skiba, N.V.: Strengthening and softening mechanisms in nanocrystalline materials under superplastic deformation. *Acta Mater.* **52**, 1711–1720 (2004)
101. Van Swygenhoven, H., Derlet, P.A.: Grain-boundary sliding in nanocrystalline fcc metals. *Phys. Rev. B* **64**, 224105 (2001)
102. Monk, J., Hyde, B., Farkas, D.: The role of partial grain boundary dislocations in grain boundary sliding and coupled grain boundary motion. *J. Mater. Sci.* **41**, 7741–7746 (2006)
103. Wolf, D., Yamakov, V., Phillpot, S.R., Mukherjee, A.K., Gleiter, H.: Deformation of nanocrystalline materials by molecular-dynamics simulation: relationship to experiments? *Acta Mater.* **53**, 1–40 (2005)
104. Morozov, N.F., Ovid'ko, I.A., Petrov, Yu.V., Sheinerman, A.G.: Generation and convergence of nanocracks in nanocrystalline materials deformed by grain boundary sliding. *Rev. Adv. Mater. Sci.* **19**, 63–72 (2009)
105. Ovid'ko, I.A., Sheinerman, A.G.: Enhanced ductility of nanomaterials through optimization of grain boundary sliding and diffusion processes. *Acta Mater.* **57**, 2217–2228 (2009)
106. Bobylev, S.V., Mukherjee, A.K., Ovid'ko, I.A.: Transition from plastic shear into rotation deformation mode in nanocrystalline metals and ceramics. *Rev. Adv. Mater. Sci.* **19**, 103–113 (2009)
107. Bobylev, S.V., Morozov, N.F., Ovid'ko, I.A.: Cooperative grain boundary sliding and migration process in nanocrystalline solids. *Phys. Rev. Lett.* **105**, 055504 (2010)
108. Bobylev, S.V., Morozov, N.F., Ovid'ko, I.A.: Cooperative grain boundary sliding and nanograin nucleation process in nanocrystalline, ultrafine-grained, and polycrystalline solids. *Phys. Rev. B* **84**, 094103 (2011)
109. Wu, X., Tao, N., Hong, Y., Liu, G., Xu, B., Lu, J., Lu, K.: Strain-induced grain refinement of cobalt during surface mechanical attrition treatment. *Acta Mater.* **53**, 681–691 (2005)
110. Miura, H., Sakai, T., Andiarwanto, S., Jonas, J.J.: Nucleation of dynamic recrystallization at triple junctions in polycrystalline copper. *Philos. Mag.* **85**, 2653–2669 (2002)
111. Demkowicz, M.J., Argon, A.S., Farkas, D., Frary, M.: Simulation of plasticity in nanocrystalline silicon. *Philos. Mag.* **87**, 4253–4271 (2007)
112. Cao, A., Wei, Y.: Atomistic simulations of crack nucleation and intergranular fracture in bulk nanocrystalline nickel. *Phys. Rev. B* **76**, 024113 (2007)
113. Romanov, A.E., Vladimirov, V.I.: Disclinations in crystalline solids. In: Nabarro, F.R.N. (ed.) *Dislocations in Solids*, vol. 9, pp. 191–402. North-Holland, Amsterdam (1992)
114. Romanov, A.E., Kolesnikova, A.L.: Application of disclination concept to solid structures. *Prog. Mater. Sci.* **54**, 740–769 (2009)
115. Murayama, M., Howe, J.M., Hidaka, H., Takaki, S.: Atomic-level observation of disclination dipoles in mechanically milled, nanocrystalline Fe. *Science* **295**, 2433–2435 (2002)
116. Gutkin, M.Yu., Ovid'ko, I.A.: Disclinations, amorphization and microcrack generation at grain boundary junctions in polycrystalline solids. *Philos. Mag. A* **70**, 561–575 (1994)
117. Gutkin, M.Yu., Mikaelyan, K.N., Ovid'ko, I.A.: Linear splitting of disclinations in polycrystalline and nanocrystalline solids. *Sov. Phys.-Solid State (USA)* **37**, 300–301 (1995)
118. Gutkin, M.Yu., Ovid'ko, I.A., Mikaelyan, K.N.: On role of disclinations in relaxation and deformation processes in nanostructured materials. *NanoStruct. Mater.* **6**, 779–782 (1995)
119. Gutkin, M.Yu., Mikaelyan, K.N., Ovid'ko, I.A.: Low-energy disclination structures at grain boundaries in polycrystalline and nanocrystalline solids. *Phys. Status Solidi A* **153**, 337–346 (1996)
120. Ovid'ko, I.A.: Deformation of nanostructures. *Science* **295**, 2386 (2002)
121. Gutkin, M.Yu., Mikaelyan, K.N., Romanov, A.E., Klimanek, P.: Disclination models of misorientation band generation and propagation. *Phys. Status Solidi A* **193**, 35–52 (2002)
122. Mikaelyan, K.N., Seefeldt, M., Gutkin, M.Yu., Klimanek, P., Romanov, A.E.: Simulation of the dynamics of a two-dimensional dislocation-disclination ensemble. *Phys. Solid State* **45**, 2104–2109 (2003)
123. Mukherjee, A.K.: An examination of the constitutive equation for elevated temperature plasticity: *Mater. Sci. Eng. A* **322**, 1–22 (2002)

124. Gutkin, M.Yu., Ovid'ko, I.A., Skiba, N.V.: Crossover from grain boundary sliding to rotational deformation in nanocrystalline materials. *Acta Mater.* **51**, 4059–4071 (2003)
125. Borodin, E.N., Mayer, A.E., Gutkin, M.Yu.: Coupled model for grain rotation, dislocation plasticity and grain boundary sliding in fine-grained solids. *Int. J. Plasticity* **134**, 102776 (2020)
126. Han, X., Wang, L., Yue, Y., Zhang, Z.: In situ atomic scale mechanical microscopy discovering the atomistic mechanisms of plasticity in nano-single crystals and grain rotation in polycrystalline metals. *Ultramicroscopy* **151**, 94–100 (2015)
127. Belyakov, A., Sakai, T., Miura, H., Tsuzaki, K.: Grain refinement in copper under large strain deformation. *Phil. Mag.* **81**, 2629–2643 (2001)
128. Chen, M., Ma, E., Hemker, K.J., Sheng, H., Wang, Y., Cheng, X.: Deformation twinning in nanocrystalline aluminum. *Science* **300**, 1275–1277 (2003)
129. Wu, X.-L., Ma, E.: Dislocations and twins in nanocrystalline Ni after severe plastic deformation: The effects of grain size. *Mater. Sci. Eng., A* **483–484**, 84–86 (2008)
130. Zhu, Y.T., Liao, X.Z., Wu, X.-L.: Deformation twinning in nanocrystalline materials. *Prog. Mater Sci.* **57**, 1–62 (2012)
131. Gutkin, M.Yu., Ovid'ko, I.A., Skiba, N.V.: Crack-stimulated generation of deformation twins in nanocrystalline metals and ceramics. *Phil. Mag.* **88**, 1137–1151 (2008)
132. Ovid'ko, I.A., Skiba, N.V.: Generation of nanoscale deformation twins at locally distorted grain boundaries in nanomaterials. *Int. J. Plast* **62**, 50–71 (2014)
133. Ovid'ko, I.A., Skiba, N.V.: Nanotwins induced by grain boundary deformation processes in nanomaterials. *Scripta Mater.* **71**, 33–36 (2014)
134. Rupert, T.J., Gianola, D.S., Gan, Y., Hemker, K.J.: Experimental observations of stress-driven grain boundary migration. *Science* **326**, 1686–1690 (2009)
135. Gutkin, M.Yu., Mikaelyan, K.N., Ovid'ko, I.A.: Grain growth and collective migration of grain boundaries under plastic deformation of nanocrystalline materials. *Phys. Solid State* **50**, 1216–1229 (2008)
136. Gutkin, M.Yu., Ovid'ko, I.A.: Grain boundary migration as rotational deformation mode in nanocrystalline materials. *Appl. Phys. Lett.* **87**, 251916 (2005)
137. Sansoz, F., Dupont, V.: Grain growth behavior at absolute zero during nanocrystalline metal indentation. *Appl. Phys. Lett.* **89**, 111901 (2006)
138. Gutkin, M.Yu., Mikaelyan, K.N., Ovid'ko, I.A.: Athermal grain growth through cooperative migration of grain boundaries in deformed nanomaterials. *Scripta Mater.* **58**, 850–853 (2008)
139. Dynkin, N.K., Gutkin, M.Yu.: Migration of grain boundaries in free-standing nanocrystalline thin films. *Scripta Mater.* **66**, 73–75 (2012)
140. Gutkin, M.Yu., Dynkin, N.K.: Dislocation-disclination models of grain boundary migration in ultra-thin nanocrystalline films. *Phys. Solid State* **54**, 798–807 (2012)
141. Bobylev, S.V., Ovid'ko, I.A.: Nanograin nucleation initiated by intergrain sliding and/or lattice slip in nanomaterials. *Appl. Phys. Lett.* **92**, 081914 (2008)
142. Bobylev, S.V., Ovid'ko, I.A.: Nanograin nucleation through splitting and migration of grain boundaries in deformed nanomaterials. *Rev. Adv. Mater. Sci.* **17**, 76–89 (2008)
143. Ovid'ko, I.A., Skiba, N.V., Mukherjee, A.K.: Nucleation of nanograins near cracks in nanocrystalline materials. *Scripta Mater.* **62**, 387–390 (2010)
144. Morozov, N.F., Ovid'ko, I.A., Skiba, N.V.: Stress-driven formation of nanograin chains in nanocrystalline and ultrafine-grained materials. *Rev. Adv. Mater. Sci.* **29**, 180–186 (2011)
145. Champion, Y., Langlois, C., Guerin-Mailly, S., Langlois, P., Bonnetien, J.-L., Hytch, M.: Near-perfect elastoplasticity in pure nanocrystalline copper. *Science* **300**, 310–311 (2003)
146. Bobylev, S.V., Ovid'ko, I.A.: Stress-driven migration of deformation-distorted grain boundaries in nanomaterials. *Acta Mater.* **88**, 260–270 (2015)
147. Bobylev, S.V., Ovid'ko, I.A.: On minimum grain size in ultrafine-grained materials and Gummets processed by severe plastic deformation. *Mater. Phys. Mech.* **29**, 17–23 (2016)
148. Pippin, R., Scheriau, S., Taylor, A., Hafok, M., Hohenwarter, A., Bachmaier, A.: Saturation of fragmentation during severe plastic deformation. *Ann. Rev. Mater. Res.* **40**, 319–343 (2010)

149. Estrin, Y., Vinogradov, A.: Extreme grain refinement by severe plastic deformation: a wealth of challenging science. *Acta Mater.* **61**, 782–817 (2013)
150. Dalla Torre, F., Lapovok, R., Sandlin, J., Thomson, P.F., Davies, C.H.J., Pereloma, E.V.: Microstructures and properties of copper processed by equal channel angular extrusion for 1–16 passes. *Acta Mater.* **52**, 4819–4832 (2004)
151. Zhang, H.W., Huang, X., Hansen, N.: Evolution of microstructural parameters and flow stresses toward limits in nickel deformed to ultrahigh strains. *Acta Mater.* **56**, 5451–5465 (2008)
152. Schafner, E., Pippan, R.: Effect of thermal treatment on microstructure in high pressure torsion (HPT) deformed nickel. *Mater. Sci. Eng., A* **387–389**, 799–804 (2004)
153. Ovid'ko, I.A., Sheinerman, A.G.: Triple junction nanocracks in deformed nanocrystalline materials. *Acta Mater.* **52**, 1201–1209 (2004)
154. Kumar, K.S., Suresh, S., Chisholm, M.F., Horton, J.A., Wang, P.: Deformation of electrodeposited nanocrystalline nickel. *Acta Mater.* **51**, 387–405 (2003)
155. Ovid'ko, I.A., Sheinerman, A.G.: Suppression of nanocrack generation in nanocrystalline materials under superplastic deformation. *Acta Mater.* **53**, 1347–1359 (2005)
156. Ovid'ko, I.A., Sheinerman, A.G.: Special strain hardening mechanism and nanocrack generation in nanocrystalline materials. *Appl. Phys. Lett.* **90**, 171927 (2007)
157. Ovid'ko, I.A., Sheinerman, A.G.: Generation of disclination dipoles and nanoscopic cracks in deformed nanoceramic materials. *Phys. Solid State* **50**, 1044–1049 (2008)
158. Ovid'ko, I.A., Skiba, N.V., Sheinerman, A.G.: Influence of grain boundary sliding on cracking resistance of nanocrystalline ceramics. *Phys. Solid State* **50**, 1261–1265 (2008)
159. Ovid'ko, I.A., Sheinerman, A.G., Aifantis, E.C.: Stress-driven migration of grain boundaries and fracture processes in nanocrystalline ceramics and metals. *Acta Mater.* **56**, 2718–2727 (2008)
160. Morozov, N.F., Ovid'ko, I.A., Sheinerman, A.G., Aifantis, E.C.: Effect of grain boundary migration on the fracture toughness of nanocrystalline materials. *Mater. Phys. Mech.* **8**, 155–164 (2009)
161. Morozov, N.F., Ovid'ko, I.A., Sheinerman, A.G., Aifantis, E.C.: Special rotational deformation as a toughening mechanism in nanocrystalline solids. *J. Mech. Phys. Solids* **58**, 1088–1099 (2010)
162. Ovid'ko, I.A., Sheinerman, A.G., Aifantis, E.C.: Effect of cooperative grain boundary sliding and migration on crack growth in nanocrystalline solids. *Acta Mater.* **59**, 5023–5031 (2011)
163. Ovid'ko, I.A., Sheinerman, A.G.: Grain size effect on crack blunting in nanocrystalline materials. *Scripta Mater.* **60**, 627–30 (2009)
164. Ovid'ko, I.A., Sheinerman, A.G.: Ductile vs brittle behavior of pre-cracked nanocrystalline and ultrafine-grained materials. *Acta Mater.* **58**, 5286–5294 (2010)

Chapter 6

Solution of Dynamic Equations of Plane Deformation for Nonlinear Model of Complex Crystal Lattice



Anatolii N. Bulygin and Yurii V. Pavlov

Abstract Solutions of dynamic equations of plane deformation for a nonlinear model of complex crystal lattice are obtained. Crystalline media of cubic symmetry are considered. Macrofield vector \mathbf{U} (acoustic mode) and microfield vector \mathbf{u} (optical mode) describe the deformation of the medium in the nonlinear model. In the case of plane deformation, the vectors \mathbf{U} and \mathbf{u} can be found from a system of four related nonlinear equations. A complex representation of the general solution of macrofield equations is given. Macrostress tensor σ_{ij} and vector \mathbf{U} are expressed through a function $Q(t, x, y)$, which is a dynamic analogue of the Airy function. A general solution of the microfield equations was found.

Keywords Nonlinear model · Crystal lattice · Plane deformation · Dynamic equations

6.1 Introduction

Materials with internal nanostructure play an important role in modern materials science. Technologies are being developed to produce such materials from amorphous and crystalline solids. As a rule, materials with internal nanostructure are produced under the influence of intensive external effects. In this case, the structure and properties of the initial material undergo profound changes. The cell of the crystalline medium is fundamentally changing, singular defects such as micropores, microseals, trunk cracks, dislocations, etc. are forming. Potential barrier of interaction of atoms is reduced, switching of interatomic bonds is realized, and phase transitions of martensitic type occur. The problem of developing scientific foundations of technology for

A. N. Bulygin (✉) · Yu. V. Pavlov
Institute for Problems in Mechanical Engineering RAS, V.O., Bolshoy pr., 61,
St. Petersburg 199178, Russia
e-mail: bulygin_an@mail.ru

Yu. V. Pavlov
e-mail: yuri.pavlov@mail.ru

obtaining materials with nanostructure becomes urgent. It was necessary to create an analytical model that adequately describes both the physical and mechanical processes that are implemented in the processes of obtaining materials with the required nanostructure, as well as the behavior of new materials in the operating conditions (deformation, aging, fatigue, and destruction). Nonlinear model of deformation of crystalline bodies with complex lattice was proposed in works [1, 2] and developed in [3, 4].

6.2 Basic Equations of Nonlinear Model

Let us limit ourselves to the consideration of crystal media of cubic symmetry consisting of two sublattices. In this case, the medium deformation is described by the macroshift vector \mathbf{U} (acoustic mode) and the microshift vector \mathbf{u} (optical mode) [1, 2]. They satisfy the equations of motion that are derived from the Lagrange variation principle

$$\rho \frac{\partial^2 U_i}{\partial t^2} = \sigma_{ij,j}, \quad (6.1)$$

$$\mu_0 \frac{\partial^2 u_i}{\partial t^2} = \chi_{ij,j} - R \frac{\partial \Phi(u_s)}{\partial u_i}. \quad (6.2)$$

Here ρ , μ_0 are average and specific mass densities of atoms; σ_{ij} and χ_{ij} are macro- and microstress tensors, respectively,

$$\sigma_{ij} = \lambda_{ijmn} e_{mn} - s_{ij} \Phi(u_s), \quad e_{mn} = \frac{U_{m,n} + U_{n,m}}{2}, \quad (6.3)$$

$$\chi_{ij} = k_{ijmn} \varepsilon_{mn}, \quad \varepsilon_{mn} = \frac{u_{m,n} + u_{n,m}}{2}, \quad (6.4)$$

λ_{ijmn} , k_{ijmn} are macro- and microelasticity tensors, s_{ij} is the tensor of nonlinear striction. The index after the comma denotes the partial derivative with respect to corresponding variable. The multiplier before function $\Phi(u_s)$ in Eq. (6.2)

$$R = p - s_{ij} e_{ij} \quad (6.5)$$

is an effective interatomic barrier—the energy of activation of communications. Here p is half of the activation energy of the rigid shift of sublattices.

The function $\Phi(u_s)$ describes the energy of the interaction of sublattices. By physical meaning, it must be an even function invariant to Bravais sublattice translations

along the direction of vectors $(\mathbf{b}_1, \mathbf{b}_2, \mathbf{b}_3)$ elementary cell. In pioneer work [5] and in most modern works [6], it is accepted that

$$\Phi(u_s) = 1 - \cos u_s. \quad (6.6)$$

The argument is

$$u_s = \mathbf{B}\mathbf{u}. \quad (6.7)$$

Here \mathbf{B} is vector of inverse lattice [7].

In the case of spatial problems Eqs. (6.1)—(6.4) are rather complex system of six connected nonlinear equations. For this reason, we will make simplifying assumptions. Below we will consider the plane deformation of crystalline media of cubic symmetry with weak anisotropy

The deformed state of the medium will be called the state of plane deformation, parallel to the axis OZ , if

$$\begin{aligned} U_x &= U_x(t, x, y), & U_y &= U_y(t, x, y), & U_z &= 0, \\ u_x &= u_x(t, x, y), & u_y &= u_y(t, x, y), & u_z &= 0. \end{aligned} \quad (6.8)$$

Then the motion Eqs. (6.1), (6.2) take the form

$$\rho \frac{\partial^2 U_x}{\partial t^2} = \sigma_{xx,x} + \sigma_{xy,y}, \quad (6.9)$$

$$\rho \frac{\partial^2 U_y}{\partial t^2} = \sigma_{yx,x} + \sigma_{yy,y}, \quad (6.10)$$

$$\mu_0 \frac{\partial^2 u_x}{\partial t^2} = \chi_{xx,x} + \chi_{xy,y} - R \frac{\partial \Phi(u_s)}{\partial u_x}, \quad (6.11)$$

$$\mu_0 \frac{\partial^2 u_y}{\partial t^2} = \chi_{yx,x} + \chi_{yy,y} - R \frac{\partial \Phi(u_s)}{\partial u_y}. \quad (6.12)$$

If one uses symbols

$$\lambda_{1122} = \lambda_{12} = \lambda, \quad \lambda_{1212} = \lambda_{44} = \mu, \quad k_{1122} = k_{12}, \quad k_{1212} = k_{44}, \quad (6.13)$$

for macro- and microelastic modules, then material relations (6.3), (6.4) are written as

$$\sigma_{xx} = \lambda(U_{x,x} + U_{y,y}) + 2\mu U_{x,x} - s\Phi(u_s), \quad (6.14)$$

$$\sigma_{yy} = \lambda(U_{x,x} + U_{y,y}) + 2\mu U_{y,y} - s\Phi(u_s), \quad (6.15)$$

$$\sigma_{xy} = \mu(U_{x,y} + U_{y,x}), \quad (6.16)$$

$$\chi_{xx} = 2k_{44}u_{x,x} + k_{12}(u_{x,x} + u_{y,y}), \quad (6.17)$$

$$\chi_{yy} = 2k_{44}u_{y,y} + k_{12}(u_{x,x} + u_{y,y}), \quad (6.18)$$

$$\chi_{xy} = k_{44}(u_{x,y} + u_{y,x}). \quad (6.19)$$

The relations (6.14)–(6.19) take into account that $s_{ij} = s \delta_{ij}$, $\lambda_{11} - \lambda_{12} = 2\lambda_{44}$, $k_{11} - k_{12} = 2k_{44}$ and for isotropic medium $\lambda_{44} = 0 = k_{44}$.

6.3 Solution of Dynamic Macrofield Equations

Let's differentiate Eq. (6.9) with respect to x , Eq. (6.10) with respect to y and find the difference of derivatives

$$\rho \frac{\partial^2}{\partial t^2} (U_{x,x} - U_{y,y}) = \sigma_{xx,xx} - \sigma_{yy,yy}. \quad (6.20)$$

From Eqs. (6.14), (6.15), we find

$$2\mu(U_{x,x} - U_{y,y}) = \sigma_{xx} - \sigma_{yy}. \quad (6.21)$$

Taking into account (6.21) Eq. (6.20) takes form

$$\left(\frac{\partial^2}{\partial x^2} - \frac{1}{2V_2^2} \frac{\partial^2}{\partial t^2} \right) \sigma_{xx} = \left(\frac{\partial^2}{\partial y^2} - \frac{1}{2V_2^2} \frac{\partial^2}{\partial t^2} \right) \sigma_{yy}, \quad (6.22)$$

where

$$V_2 = \sqrt{\frac{\mu}{\rho}} \quad (6.23)$$

is velocity of shift. Equation (6.22) describes the distortion of the medium without changing the volume. In seismology, this wave is called a secondary wave or S -wave. Equation (6.22) allows us to express stress tensor components σ_{xx} , σ_{yy} through some function $Q(t, x, y)$

$$\sigma_{xx} = \left(\frac{\partial^2}{\partial y^2} - \frac{1}{2V_2^2} \frac{\partial^2}{\partial t^2} \right) Q, \quad (6.24)$$

$$\sigma_{yy} = \left(\frac{\partial^2}{\partial x^2} - \frac{1}{2V_2^2} \frac{\partial^2}{\partial t^2} \right) Q, \quad (6.25)$$

$$\sigma_{xx} + \sigma_{yy} = \left(\Delta - \frac{1}{V_2^2} \frac{\partial^2}{\partial t^2} \right) Q, \quad \Delta = \frac{\partial^2}{\partial x^2} + \frac{\partial^2}{\partial y^2}. \quad (6.26)$$

If one differentiates Eqs. (6.9), (6.10) with respect to y and x , respectively, take into account (6.16), (6.26), then for the sum of derivatives, one finally gets

$$\left(\Delta - \frac{1}{2V_2^2} \frac{\partial^2}{\partial t^2}\right) \left(\sigma_{xy} + \frac{\partial^2 Q}{\partial x \partial y}\right) = 0. \quad (6.27)$$

Equation (6.27) allows us to express the tensor component σ_{xy} through the sought function $Q(t, x, y)$. The function $Q(t, x, y)$ must satisfy the equation that follows from compatibility conditions for macrodeformations [8] (Saint-Venant condition). One compatibility condition

$$e_{xx,yy} + e_{yy,xx} = 2e_{xy,xy} \quad (6.28)$$

remains for the case of plane deformation. Equation (6.28) can be written as Beltrami–Michell condition [8] for stress tensor, if one expresses the component of deformation tensor (e_{xx} , e_{yy} , e_{xy}) using (6.3) and (6.14)–(6.16) through the components of stress tensor (σ_{xx} , σ_{yy} , σ_{xy})

$$\begin{aligned} e_{xx} &= \frac{\sigma_{xx}}{2\mu} - \frac{\lambda(\sigma_{xx} + \sigma_{yy})}{4\mu(\lambda + \mu)} + \frac{s\Phi(u_s)}{2(\lambda + \mu)}, \\ e_{yy} &= \frac{\sigma_{yy}}{2\mu} - \frac{\lambda(\sigma_{xx} + \sigma_{yy})}{4\mu(\lambda + \mu)} + \frac{s\Phi(u_s)}{2(\lambda + \mu)}, \\ e_{xy} &= \frac{\sigma_{xy}}{2\mu}. \end{aligned} \quad (6.29)$$

Substituting (6.29) in (6.28), we find

$$\sigma_{xx,yy} + \sigma_{yy,xx} - 2\sigma_{xy,xy} = \Delta \left[\frac{\lambda}{2(\lambda + \mu)} (\sigma_{xx} + \sigma_{yy}) - \frac{\mu}{(\lambda + \mu)} s\Phi(u_s) \right]. \quad (6.30)$$

Left side of equality (6.30) can be written as follows:

$$\begin{aligned} \sigma_{xx,yy} + \sigma_{yy,xx} - 2\sigma_{xy,xy} &= \\ \sigma_{xx,yy} + \sigma_{xx,xx} + \sigma_{yy,xx} + \sigma_{yy,yy} - \sigma_{xx,xx} - \sigma_{yy,yy} - 2\sigma_{xy,xy} &= \\ \Delta(\sigma_{xx} + \sigma_{yy}) - (\sigma_{xx,xx} + \sigma_{yy,yy} + 2\sigma_{xy,xy}). \end{aligned} \quad (6.31)$$

From the equations of motion (6.9), (6.10), one obtains

$$\rho \frac{\partial^2 U_{x,x}}{\partial t^2} = \sigma_{xx,xx} + \sigma_{xy,xy}, \quad (6.32)$$

$$\rho \frac{\partial^2 U_{y,y}}{\partial t^2} = \sigma_{yx,xy} + \sigma_{yy,yy}, \quad (6.33)$$

$$\sigma_{xx,xx} + \sigma_{yy,yy} + 2\sigma_{xy,xy} = \rho \frac{\partial^2}{\partial t^2} (U_{x,x} + U_{y,y}). \quad (6.34)$$

From the material relations (6.14), (6.15), we find

$$U_{x,x} + U_{y,y} = \frac{1}{2(\lambda + \mu)} (\sigma_{xx} + \sigma_{yy} + 2s\Phi(u_s)). \quad (6.35)$$

That is why

$$\sigma_{xx,xx} + \sigma_{yy,yy} + 2\sigma_{xy,xy} = \frac{\rho}{2(\lambda + \mu)} \frac{\partial^2}{\partial t^2} (\sigma_{xx} + \sigma_{yy} + 2s\Phi(u_s)) \quad (6.36)$$

and

$$\sigma_{xx,yy} + \sigma_{yy,xx} - 2\sigma_{xy,xy} = \left(\Delta - \frac{\rho}{2(\lambda + \mu)} \frac{\partial^2}{\partial t^2} \right) (\sigma_{xx} + \sigma_{yy}) - \frac{\rho s}{\lambda + \mu} \frac{\partial^2 \Phi(u_s)}{\partial t^2}. \quad (6.37)$$

Taking into account (6.37) the Beltrami–Michell condition (6.30) takes the form

$$\left(\Delta - \frac{1}{V_1^2} \frac{\partial^2}{\partial t^2} \right) (\sigma_{xx} + \sigma_{yy}) + \frac{2s\mu}{\lambda + 2\mu} \left(\Delta - \frac{1}{V_2^2} \frac{\partial^2}{\partial t^2} \right) \Phi(u_s) = 0, \quad (6.38)$$

$$V_1 = \sqrt{\frac{\lambda + 2\mu}{\rho}}. \quad (6.39)$$

Here V_1 is velocity of a longitudinal wave. It describes the condensation–rarefaction of the medium with volume change. In seismology, this wave is called *P*-wave. If taking into account Eq. (6.26) in the condition (6.38), then one gets equation for finding the function $Q(t, x, y)$

$$\left(\Delta - \frac{1}{V_2^2} \frac{\partial^2}{\partial t^2} \right) \left[\left(\Delta - \frac{1}{V_1^2} \frac{\partial^2}{\partial t^2} \right) Q + 2s \frac{V_2^2}{V_1^2} \Phi(u_s) \right] = 0. \quad (6.40)$$

From (6.40), one can see that the function $Q(t, x, y)$ is a dynamic equivalent of the Airy function which is introduced to solve static problems of classical plane deformation. Unlike the classical Airy function, the function $Q(t, x, y)$ satisfies non-uniform dynamic biharmonic equation. The function $\Phi(u_s)$ plays the role of the potential for volume sources of macrostresses.

6.4 Complex Representation of General Solution of Macrofield Equations

Generally, a solution to Eq. (6.40) can be represented as the sum of two functions

$$Q(t, x, y) = F(t, x, y) + Q_0(t, x, y), \quad (6.41)$$

where the function $F(t, x, y)$ satisfies the homogeneous biharmonic equation

$$\left(\Delta - \frac{1}{V_1^2} \frac{\partial^2}{\partial t^2}\right) \left(\Delta - \frac{1}{V_2^2} \frac{\partial^2}{\partial t^2}\right) F = 0, \quad (6.42)$$

and $Q_0(t, x, y)$ is a partial solution to non-uniform equation

$$\left(\Delta - \frac{1}{V_1^2} \frac{\partial^2}{\partial t^2}\right) Q_0 + 2s \frac{V_2^2}{V_1^2} \Phi(u_s) = 0. \quad (6.43)$$

Instead of independent variables t, x, y , we will introduce new variables

$$\xi = x + C_1 t, \quad \eta = y + C_2 t. \quad (6.44)$$

Here C_1, C_2 are arbitrary velocities. In the new variables, one has

$$\frac{\partial}{\partial x} = \frac{\partial}{\partial \xi}, \quad \frac{\partial}{\partial y} = \frac{\partial}{\partial \eta}, \quad \frac{\partial}{\partial t} = C_1 \frac{\partial}{\partial \xi} + C_2 \frac{\partial}{\partial \eta}, \quad (6.45)$$

$$\frac{\partial^2}{\partial x^2} + \frac{\partial^2}{\partial y^2} - \frac{1}{V_1^2} \frac{\partial^2}{\partial t^2} = \left(1 - \frac{C_2^2}{V_1^2}\right) D_1 D_2, \quad (6.46)$$

$$\frac{\partial^2}{\partial x^2} + \frac{\partial^2}{\partial y^2} - \frac{1}{V_2^2} \frac{\partial^2}{\partial t^2} = \left(1 - \frac{C_2^2}{V_2^2}\right) D_3 D_4. \quad (6.47)$$

Here D_1, D_2, D_3, D_4 are differential operators

$$D_1 = \frac{\partial}{\partial \eta} - \mu_1 \frac{\partial}{\partial \xi}, \quad D_2 = \frac{\partial}{\partial \eta} - \bar{\mu}_1 \frac{\partial}{\partial \xi}, \quad (6.48)$$

$$D_3 = \frac{\partial}{\partial \eta} - \mu_2 \frac{\partial}{\partial \xi}, \quad D_4 = \frac{\partial}{\partial \eta} - \bar{\mu}_2 \frac{\partial}{\partial \xi}, \quad (6.49)$$

$$\mu_1 = \frac{C_1 C_2}{V_1^2 - C_2^2} (1 + i\beta_1), \quad \mu_2 = \frac{C_1 C_2}{V_1^2 - C_2^2} (1 + i\beta_2), \quad (6.50)$$

$$\beta_1 = \frac{V_1}{C_2} \sqrt{\frac{V_1^2}{C_1^2} - \frac{C_2^2}{C_1^2}} - 1, \quad \beta_2 = \frac{V_2}{C_2} \sqrt{\frac{V_1^2}{C_1^2} - \frac{C_2^2}{C_1^2}} - 1. \quad (6.51)$$

Here and further, the line over denotes complex conjugation.

Taking into account (6.45), Eqs. (6.42) and (6.43) are written as

$$D_1 D_2 D_3 D_4 F = 0, \quad (6.52)$$

$$D_1 D_2 Q_0 = -2s \frac{V_2^2}{V_1^2 - C_2^2} \Phi(u_s). \quad (6.53)$$

The solution to Eq. (6.52) is expressed through two functions $F_1(z_1)$, $F_2(z_2)$ and the functions complex conjugate to their

$$F = F_1(z_1) + \bar{F}_1(\bar{z}_1) + F_2(z_2) + \bar{F}_2(\bar{z}_2) = 2\text{Re} [F_1(z_1) + F_2(z_2)], \quad (6.54)$$

$$z_1 = \xi + \mu_1 \eta, \quad z_2 = \xi + \mu_2 \eta.$$

Through the functions $F_1(z_1)$ and $F_2(z_2)$, one can represent the stress tensor (σ_{xx} , σ_{yy} , σ_{xy}) and the macrovector (U_x , U_y) if using the following derivatives:

$$\begin{aligned} \frac{\partial^2 F}{\partial x^2} &= \frac{\partial^2 F}{\partial \xi^2} = F_1'' + \bar{F}_1'' + F_2'' + \bar{F}_2'', \\ \frac{\partial^2 F}{\partial y^2} &= \frac{\partial^2 F}{\partial \eta^2} = \mu_1^2 F_1'' + \bar{\mu}_1^2 \bar{F}_1'' + \mu_2^2 F_2'' + \bar{\mu}_2^2 \bar{F}_2'', \\ \frac{\partial^2 F}{\partial x \partial y} &= \frac{\partial^2 F}{\partial \xi \partial \eta} = \mu_1 F_1'' + \bar{\mu}_1 \bar{F}_1'' + \mu_2 F_2'' + \bar{\mu}_2 \bar{F}_2''. \end{aligned} \quad (6.55)$$

Here, the prime denotes the derivative with respect to corresponding argument. Taking into account (6.24)–(6.26) and (6.55), one has

$$\sigma_{xx} = \text{Re} \{ [a_{11} - (1 - \mu_1^2)] F_1'' - (1 - \mu_2^2) F_2'' \} + L_{11} Q_0, \quad (6.56)$$

$$\sigma_{yy} = \text{Re} \{ [a_{11} + (1 - \mu_1^2)] F_1'' + (1 - \mu_2^2) F_2'' \} + L_{22} Q_0, \quad (6.57)$$

$$\sigma_{xx} + \sigma_{yy} = 2 \text{Re} (a_{11} F_1'') + (L_{11} + L_{22}) Q_0, \quad (6.58)$$

where

$$a_{11} = \left(1 - \frac{C_2^2}{V_2^2}\right) (\mu_1 - \mu_2)(\mu_1 - \bar{\mu}_2) = \left(1 - \frac{V_1^2}{V_2^2}\right) (1 + \mu_1^2), \quad (6.59)$$

$$L_{11} = \frac{\partial^2}{\partial y^2} - \frac{1}{2V_2^2} \frac{\partial^2}{\partial t^2}, \quad L_{22} = \frac{\partial^2}{\partial x^2} - \frac{1}{2V_2^2} \frac{\partial^2}{\partial t^2}. \quad (6.60)$$

Using the functions $F_1(z_1)$, $F_2(z_2)$, one can also write the components of the macroshift vector taking into account (6.56), (6.57) in the relations (6.29):

$$\mu U_x = \operatorname{Re} \left[a_1 F_1' - \frac{1}{2} (1 - \mu_2^2) F_2' \right] - \frac{1}{2} \frac{\partial Q_0}{\partial x}, \quad (6.61)$$

$$\mu U_y = \operatorname{Re} \left[a_2 F_1' - \frac{1}{2\mu_2} (1 - \mu_2^2) F_2' \right] - \frac{1}{2} \frac{\partial Q_0}{\partial y}, \quad (6.62)$$

where

$$a_1 = \frac{1}{2} \left[\frac{V_2^2 a_{11}}{V_1^2 - V_2^2} - (1 - \mu_1^2) \right], \quad a_2 = \frac{1}{2\mu_1} \left[\frac{V_2^2 a_{11}}{V_1^2 - V_2^2} + (1 - \mu_1^2) \right]. \quad (6.63)$$

Using the relations (6.61), (6.62), and (6.15), one can express tangent component of the microstress tensor through the functions $F_1(z_1)$ and $F_2(z_2)$

$$\sigma_{xy} = \operatorname{Re} \left[a_{12} F_1'' + \frac{1}{2\mu_2} (1 - \mu_2^2) F_2'' \right] - \frac{\partial^2 Q_0}{\partial x \partial y}, \quad (6.64)$$

where

$$a_{12} = a_1 \mu_1 + a_2.$$

The found representations of macrostress tensor $(\sigma_{xx}, \sigma_{yy}, \sigma_{xy})$ and macroshift vector (U_x, U_y) through arbitrary analytical functions $F_1(z_1)$ and $F_2(z_2)$ give a general solution to dynamic equations of macrofield for plane deformation in nonlinear model.

If we limit ourselves to solving dynamic problems for a semi-infinite body $y > 0$ (axis y is directed inside the body) and accept that the optical mode is not excited ($u_s = 0$), and the perturbation of the acoustic mode propagates at speed C_1 parallel to the axis x , i.e., accept that $C_2 = 0$. Then, we have

$$\begin{aligned} \mu_1 &= i\beta_{10}, \quad \mu_2 = i\beta_{20}, \quad \beta_{10}^2 = 1 - \frac{C_1^2}{V_1^2}, \quad \beta_{20}^2 = 1 - \frac{C_1^2}{V_2^2}, \\ C_{12} &= -i\beta_{10}, \quad a_1 = -1, \quad a_2 = -i\beta_{10}, \quad a_{11} = \left(1 - \frac{V_1^2}{V_2^2} \right) \frac{C_1^2}{V_1^2}, \end{aligned} \quad (6.65)$$

and formulas (6.56)–(6.58), (6.61), and (6.62) become the solutions of the dynamic plane deformation equations of classical elasticity theory which were received by Sneddon [9] and later by Radok [10].

Note that in the present work, the general solution of the equations of the nonlinear dynamic model is found for the case of $C_1 \neq 0$ and $C_2 \neq 0$. Therefore, with $u_s = 0$, we obtain a solution of the dynamic equations of the classical theory of elasticity in a more general case compared to solutions [9, 10]. Solutions [9, 10] are

obtained by additionally assuming that $C_2 = 0$. This means that the solution obtained in the present work allows to solve boundary problems when external disturbances propagate not only parallel to the OX axis, but also along the OY -axis.

6.5 Solution of Dynamic Microfield Equations

The microfield Eqs. (6.11), (6.12) taking into account (6.17)–(6.19) can be represented in the form

$$\begin{aligned} \mu_0 \frac{\partial^2 u_x}{\partial t^2} &= k_{44} \Delta u_x + (k_{12} + k_{44})(u_{x,xx} + u_{y,xy}) + \\ &\quad (k_{11} - k_{12} - 2k_{44})u_{x,xx} - \frac{R}{b} \sin u_s, \\ \mu_0 \frac{\partial^2 u_y}{\partial t^2} &= k_{44} \Delta u_y + (k_{12} + k_{44})(u_{x,xy} + u_{y,yy}) + \\ &\quad (k_{11} - k_{12} - 2k_{44})u_{y,yy} - \frac{R}{b} \sin u_s. \end{aligned} \quad (6.66)$$

Instead of the components (u_x, u_y) , one can use the values u_s and $u_m = (u_x - u_y)/b$. Then for the sum and difference of Eqs. (6.66), we get

$$\begin{aligned} 2\mu_0 \frac{\partial^2 u_s}{\partial t^2} &= (k_{11} + k_{44}) \Delta u_s + 2(k_{12} + k_{44})u_{s,xy} + \\ &\quad (k_{11} - k_{44})(u_{m,xx} - u_{m,yy}) - \frac{4R}{b^2} \sin u_s, \\ 2\mu_0 \frac{\partial^2 u_m}{\partial t^2} &= (k_{11} + k_{44}) \Delta u_m - 2(k_{12} + k_{44})u_{m,xy} + \\ &\quad (k_{11} - k_{44})(u_{s,xx} - u_{s,yy}). \end{aligned} \quad (6.67)$$

In moving coordinate system $(\xi = x + ct, y)$, Eqs. (6.67) are written as follows:

$$\begin{aligned} (k_{11} + k_{44}) \left[\left(1 - \frac{c^2}{v_1^2}\right) \frac{\partial^2 u_s}{\partial \xi^2} + \frac{\partial^2 u_s}{\partial y^2} + 2k_0 \frac{\partial^2 u_s}{\partial \xi \partial y} \right] + \\ + (k_{11} - k_{44})(u_{m,\xi\xi} - u_{m,yy}) - \frac{4R}{b^2} \sin u_s = 0, \\ (k_{11} + k_{44}) \left[\left(1 - \frac{c^2}{v_1^2}\right) \frac{\partial^2 u_m}{\partial \xi^2} + \frac{\partial^2 u_m}{\partial y^2} - 2k_0 \frac{\partial^2 u_m}{\partial \xi \partial y} \right] + \\ + (k_{11} - k_{44})(u_{s,\xi\xi} - u_{s,yy}) = 0, \end{aligned} \quad (6.68)$$

where

$$v_1^2 = \frac{k_{11} + k_{44}}{2\mu_0}, \quad k_0 = \frac{k_{12} + k_{44}}{k_{11} + k_{44}}. \quad (6.69)$$

One can see that Eqs. (6.68) are coupled. They are separated if $k_{11} = k_{44}$. We accept this condition and instead of variables (ξ, y) enter

$$q_1 = L_1(\xi + \alpha y), \quad q_2 = L_2(\xi - \alpha y), \quad \alpha = \sqrt{1 - \frac{c^2}{v_1^2}},$$

$$L_1 = \frac{1}{b} \sqrt{\frac{2p}{(k_{11} + k_{44})\alpha(\alpha + k_0)}}, \quad L_2 = \frac{1}{b} \sqrt{\frac{2p}{(k_{11} + k_{44})\alpha(\alpha - k_0)}}. \quad (6.70)$$

In the new variables, Eqs. (6.68) take the form

$$\frac{\partial^2 u_s}{\partial q_1^2} + \frac{\partial^2 u_s}{\partial q_2^2} = \frac{R}{p} \sin u_s, \quad (6.71)$$

$$\omega^2 \frac{\partial^2 u_m}{\partial q_1^2} + \frac{\partial^2 u_m}{\partial q_2^2} = 0, \quad \omega = \sqrt{\frac{\alpha - k_0}{\alpha + k_0}}. \quad (6.72)$$

Thus, the solution of the dynamic equations of the microfield is reduced to the solution of the nonlinear Eq. (6.71) and the linear Eq. (6.72). Equation (6.71) differs from the classical dynamic sine-Gordon equation in that R/p is not a constant value, but a function of (t, x, y) .

Solution of Eq. (6.71) is determined by amplitude R/p . From relations (6.5)–(6.7), (6.29), we find

$$\frac{R}{p} = P_1 + 2P_2 \cos u_s, \quad P_1 = 1 - P_2 \left[2 + \frac{1}{s}(\sigma_{xx} + \sigma_{yy}) \right], \quad P_2 = \frac{s^2}{2p(\lambda + \mu)}. \quad (6.73)$$

Taking into account (6.73), Equation (6.71) takes the form

$$\frac{\partial^2 u_s}{\partial q_1^2} + \frac{\partial^2 u_s}{\partial q_2^2} = P_1 \sin u_s + P_2 \sin 2u_s. \quad (6.74)$$

In Eq. (6.74) $P_2 = \text{const}$ and P_1 is a function of (t, x, y) . In this way, it differs from the classical double sine-Gordon equation. There are no analytical methods for solving such equation in the literature. For this reason, we make assumptions that convert (6.74) to equations that have analytical solutions. We assume that in the studied domain $(\sigma_{xx} + \sigma_{yy})$ changes smoothly, then it can be assumed that $P_1 = \text{const}$ and Eq. (6.74) will become the classical double sine-Gordon equation.

For case $s = 0$, Equation (6.74) becomes the classical sine-Gordon equation

$$\frac{\partial^2 u_s}{\partial q_1^2} + \frac{\partial^2 u_s}{\partial q_2^2} = \sin u_s. \quad (6.75)$$

The condition $s = 0$ means that the nonlinear model does not take into account the influence of stressed state on the activation energy of the rigid shift of the sublattices. Equation (6.75) is obtained under a weaker assumption, namely, $P_2 \ll 1$. For $s^2 \ll 2p(\lambda + \mu)$ and $s \approx |\sigma_{xx} + \sigma_{yy}|/2p(\lambda + \mu)$, Eq. (6.74) takes the form of a sine-Gordon equation with variable amplitude

$$\frac{\partial^2 u_s}{\partial q_1^2} + \frac{\partial^2 u_s}{\partial q_2^2} = p(q_1, q_2) \sin u_s, \quad (6.76)$$

$$p(q_1, q_2) = 1 - \frac{s(\sigma_{xx} + \sigma_{yy})}{2p(\lambda + \mu)}. \quad (6.77)$$

The sine-Gordon equation and the double sine-Gordon equation are well researched in the literature [11, 12]. For the sine-Gordon equation with variable amplitude (6.76), solutions are constructed only for a some type of functions $p(q_1, q_2)$ [13–17].

The found general macro- and microfield solutions allow to set and solve the concrete dynamic boundary problems on basic of nonlinear model.

6.6 Uniform Movement of the Constant Localized Force Over the Surface of the Half-Space

Let the localized force uniformly movement with a speed C on the surface of the half-space. Force is directed normal to the surface and creates a constant localized stress G . To solve this problem, we use the moving coordinate system $(\xi = x + Ct, y)$ associated with the force. In the moving coordinate system, Eq. (6.42) takes the form

$$\left[(1 - M_1^2) \frac{\partial^2}{\partial \xi^2} + \frac{\partial^2}{\partial y^2} \right] \left[(1 - M_2^2) \frac{\partial^2}{\partial \xi^2} + \frac{\partial^2}{\partial y^2} \right] F = 0, \quad (6.78)$$

$$M_1 = \frac{C}{V_1}, \quad M_2 = \frac{C}{V_2}.$$

The solutions of Eq. (6.78) are determined by the speed C .

6.6.1 Subsonic Speed of Movement

We will call the speed of movement subsonic, if

$$M_1 < 1, \quad M_2 < 1. \quad (6.79)$$

In this case, the solution (6.78) will be

$$F = F_1(z_1) + \bar{F}_1(\bar{z}_1) + F_2(z_2) + \bar{F}_2(\bar{z}_2), \quad (6.80)$$

$$z_1 = \xi + \mu_1 y, \quad \mu_1 = i\sqrt{1 - M_1^2}, \quad z_2 = \xi + \mu_2 y, \quad \mu_2 = i\sqrt{1 - M_2^2}. \quad (6.81)$$

Here $F_1(z_1)$ and $F_2(z_2)$ are arbitrary analytical functions of the corresponding complex variables, and a line from above denotes complex conjugation.

In our case, the following conditions must be met on the surface of the half-space

$$\sigma_{xy}|_{y=0} = 0, \quad \sigma_{yy}|_{y=0} = -G \delta(\xi), \quad G = \text{const}. \quad (6.82)$$

Here $\delta(\xi)$ is Dirac delta-function. In addition, we will assume that $(v_x, v_y, \sigma_{xx}, \sigma_{xy}, \sigma_{yy})$ are decreasing when $|x|, |y| \rightarrow \infty$. Macrostress tensor components $(\sigma_{xx}, \sigma_{xy}, \sigma_{yy})$ can be expressed through functions F_1, F_2 and Q_0 . To do this, the representation (6.80) must be substituted in (6.24), (6.25), (6.64) and taking into account (6.41), (6.65), we get

$$\sigma_{xx} = -(M_2^2 - 2M_1^2 + 2) \text{Re } F_1'' + (M_2^2 - 2) \text{Re } F_2'' + L_{11}(Q_0), \quad (6.83)$$

$$\sigma_{yy} = -(M_2^2 - 2)(\text{Re } F_1' + \text{Re } F_2') + L_{22}(Q_0), \quad (6.84)$$

$$\sigma_{xy} = 2\sqrt{1 - M_1^2} \text{Im } F_1'' + \frac{(M_2^2 - 2)^2}{2\sqrt{1 - M_2^2}} \text{Im } F_2'' - \frac{\partial^2 Q_0}{\partial x \partial y}. \quad (6.85)$$

Components of macroshifts vector are found from (6.61), (6.62) with taking into account (6.65)

$$\mu U_x = -\text{Re } F_1' + \frac{1}{2}(M_2^2 - 2) \text{Re } F_2' - \frac{1}{2} \frac{\partial Q_0}{\partial x}, \quad (6.86)$$

$$\mu U_y = \sqrt{1 - M_1^2} \text{Im } F_1' - \frac{M_2^2 - 2}{2\sqrt{1 - M_2^2}} \text{Im } F_2' - \frac{1}{2} \frac{\partial Q_0}{\partial y}. \quad (6.87)$$

The found representation of the macrostress tensor allows to write boundary conditions that functions F_1, F_2 , and Q_0 must satisfy. Substituting Eqs. (6.84) and (6.85) into (6.82), one has

$$\left(2\sqrt{1 - M_1^2} \text{Im } F_1'' + \frac{1}{2} \frac{(M_2^2 - 2)^2}{\sqrt{1 - M_2^2}} \text{Im } F_2'' \right) \Big|_{y=0} = \frac{\partial^2 Q_0}{\partial x \partial y} \Big|_{y=0}, \quad (6.88)$$

$$(M_2^2 - 2) [\operatorname{Re} F_1'' + \operatorname{Re} F_2'']_{y=0} = G \delta(\xi) + L_{22}(Q_0) \Big|_{y=0}. \quad (6.89)$$

The ratios (6.88) and (6.89) can be integrated over x . Then the boundary conditions will take the form

$$\left(2\sqrt{1 - M_1^2} \operatorname{Im} F_1' + \frac{1}{2} \frac{(2 - M_2^2)^2}{\sqrt{1 - M_2^2}} \operatorname{Im} F_2' \right) \Big|_{y=0} = \frac{\partial Q_0}{\partial y} \Big|_{y=0}, \quad (6.90)$$

$$(M_2^2 - 2) [\operatorname{Re} F_1' + \operatorname{Re} F_2']_{y=0} = G H(\xi) + \int L_{22}(Q_0) dx \Big|_{y=0}, \quad (6.91)$$

where

$$H(\xi) = \begin{cases} 1, & \xi \geq 0, \\ 0, & \xi < 0, \end{cases}$$

and the integration constant is omitted due to the accepted behavior of the macrostress tensor at infinity.

From the boundary conditions (6.90) and (6.91), one can see that in a nonlinear model the deformation and stress states of the medium are determined by both external influences and gradients of the optical mode. The latter play the role of volumetric sources of macrodeformations and macrostresses. For the analysis of the deformed and stress states of the medium, it is advisable to separate these components. For this purpose, the functions F_1' and F_2' are represented as the sum of two terms

$$F_1' = F_{11}' + F_{12}', \quad F_2' = F_{21}' + F_{22}' \quad (6.92)$$

and we will require that the functions F_{11}' and F_{21}' satisfy the boundary conditions

$$\left(2\sqrt{1 - M_1^2} \operatorname{Im} F_{11}' + \frac{1}{2} \frac{(2 - M_2^2)^2}{\sqrt{1 - M_2^2}} \operatorname{Im} F_{21}' \right) \Big|_{y=0} = 0, \quad (6.93)$$

$$(M_2^2 - 2) [\operatorname{Re} F_{11}' + \operatorname{Re} F_{21}']_{y=0} = G H(\xi), \quad (6.94)$$

and for the functions F_{12}' and F_{22}'

$$\left(2\sqrt{1 - M_1^2} \operatorname{Im} F_{12}' + \frac{1}{2} \frac{(2 - M_2^2)^2}{\sqrt{1 - M_2^2}} \operatorname{Im} F_{22}' \right) \Big|_{y=0} = \frac{\partial Q_0}{\partial y} \Big|_{y=0}, \quad (6.95)$$

$$(M_2^2 - 2) [\operatorname{Re} F_{12}' + \operatorname{Re} F_{22}']_{y=0} = \int L_{22}(Q_0) dx \Big|_{y=0}. \quad (6.96)$$

With this separation, the functions F'_{11} and F'_{21} will describe the contribution to the deformation and stress of the medium due to external impact, and the functions F'_{12} and F'_{22} determine the contribution to the same values from the optical mode. Condition (6.93) remains valid if $\text{Im } F'_{11}$ is replaced by $\text{Re } F'_{11}$, and $\text{Im } F'_{21}$ is replaced by $\text{Re } F'_{21}$. This statement becomes apparent if one makes Hilbert transformation [18] for Condition (6.93). So

$$\text{Re } F'_{11}|_{y=0} = -\frac{4\sqrt{(1-M_1^2)(1-M_2^2)}}{(2-M_2^2)^2} \text{Re } F'_{21}|_{y=0}. \quad (6.97)$$

Substitution (6.97) in (6.94) reduces the finding of the function F'_{11} and F'_{21} to the solution of the Dirichlet problem

$$\begin{aligned} \text{Re } F'_{11}|_{y=0} &= G_{11} G H(\xi), \quad G_{11} = \frac{M_2^2 - 2}{(M_2^2 - 2)^2 - 4\sqrt{(1-M_1^2)(1-M_2^2)}}, \\ \text{Re } F'_{21}|_{y=0} &= G_{12} G H(\xi), \quad G_{12} = \frac{-4\sqrt{(1-M_1^2)(1-M_2^2)}}{(M_2^2 - 2)^2 - 4\sqrt{(1-M_1^2)(1-M_2^2)}}. \end{aligned} \quad (6.98)$$

The functions F'_{11} and F'_{21} are found using the Poisson formula for half-plane [19]

$$F'_{11}(z_1) = G_{11} \left(\frac{i}{\pi} \ln z_1 + 1 \right), \quad (6.99)$$

$$F'_{21}(z_2) = G_{12} \left(\frac{i}{\pi} \ln z_2 + 1 \right). \quad (6.100)$$

The functions F'_{11} and F'_{21} allow to calculate the components of the macrostress tensor and the components of the macroshift vector that are due to external influences on the medium. To do this, in solutions (6.83)–(6.87), one needs to leave the terms

$$\begin{aligned} \text{Re } F'_{11} &= G_{11} \left(1 - \frac{\theta_1}{\pi} \right), \quad \text{Im } F'_{11} = G_{11} \frac{1}{\pi} \ln r_1, \\ \text{Re } F'_{21} &= G_{12} \left(1 - \frac{\theta_2}{\pi} \right), \quad \text{Im } F'_{21} = G_{12} \frac{1}{\pi} \ln r_2, \\ \text{Re } F''_{11} &= G_{11} \frac{\sin \theta_1}{\pi r_1}, \quad \text{Im } F'_{11} = G_{12} \frac{\cos \theta_1}{\pi r_1}, \\ \text{Re } F''_{21} &= G_{11} \frac{\sin \theta_2}{\pi r_2}, \quad \text{Im } F'_{21} = G_{12} \frac{\cos \theta_2}{\pi r_2}, \end{aligned} \quad (6.101)$$

where

$$r_1 = |z_1| = \sqrt{(x + Ct)^2 + (1 - M_1^2)y^2}, \quad \theta_1 = \arctan \frac{\sqrt{1 - M_1^2}y}{x + Ct},$$

$$r_2 = |z_2| = \sqrt{(x + Ct)^2 + (1 - M_2^2)y^2}, \quad \theta_2 = \arctan \frac{\sqrt{1 - M_2^2}y}{x + Ct}.$$

6.6.2 Transonic Speed of Movement

We will call the speed of movement transonic, if

$$M_1 < 1, \quad M_2 > 1. \quad (6.102)$$

In this case, solution (6.78) will be

$$F = F_1(z_1) + \bar{F}_1(\bar{z}_1) + \Phi_2(\zeta_2). \quad (6.103)$$

Here $\Phi_2(\zeta_2)$ are arbitrary functions of $\zeta_2 = \xi - \sqrt{M_2^2 - 1}y$. The components of the macrostress tensor and the components of the macroshift vector are expressed through the functions F_1 and Φ_2 as follows:

$$\begin{aligned} \sigma_{xx} &= -(M_2^2 - 2M_1^2 + 2) \operatorname{Re} F_1'' + \frac{1}{2}(M_2^2 - 2)\Phi_2'' + L_{11}(Q_0), \\ \sigma_{yy} &= -(M_2^2 - 2) \operatorname{Re} F_1'' - \frac{1}{2}(M_2^2 - 2)\Phi_2'' + L_{22}(Q_0), \\ \sigma_{xy} &= 2\sqrt{1 - M_1^2} \operatorname{Im} F_1'' - \frac{1}{4} \frac{(M_2^2 - 2)^2}{\sqrt{M_2^2 - 1}} \Phi_2'' - \frac{\partial^2 Q_0}{\partial x \partial y}, \end{aligned} \quad (6.104)$$

$$\begin{aligned} \mu U_x &= -\operatorname{Re} F_1' + \frac{1}{4}(M_2^2 - 2)\Phi_2' - \frac{1}{2} \frac{\partial Q_0}{\partial x}, \\ \mu U_y &= \sqrt{1 - M_1^2} \operatorname{Im} F_1' + \frac{M_2^2 - 2}{4\sqrt{M_2^2 - 1}} \Phi_2' - \frac{1}{2} \frac{\partial Q_0}{\partial y}. \end{aligned} \quad (6.105)$$

According to (6.82), the functions F_1 and Φ_2 must satisfy boundary conditions

$$\left(2\sqrt{1 - M_1^2} \operatorname{Im} F_1' - \frac{1}{4} \frac{(M_2^2 - 2)^2}{\sqrt{M_2^2 - 1}} \Phi_2' \right) \Big|_{y=0} = - \frac{\partial Q_0}{\partial y} \Big|_{y=0}, \quad (6.106)$$

$$(M_2^2 - 2) \left(\operatorname{Re} F_1' + \frac{1}{2} \Phi_2' \right) \Big|_{y=0} = G H(\xi) + \int L_{22}(Q_0) dx \Big|_{y=0}. \quad (6.107)$$

From (6.106), (6.107), we find a boundary condition for the function F_1

$$\left(4\sqrt{(1 - M_1^2)(M_2^2 - 1)} \operatorname{Im} F_1' + (M_2^2 - 2) \operatorname{Re} F_1' \right) \Big|_{y=0} = (M_2^2 - 2) [G H(\xi) + A(\xi)], \quad (6.108)$$

$$A(\xi) = \left[\int L_{22}(Q_0) d\xi + 2 \frac{\sqrt{M_2^2 - 1}}{M_2^2 - 2} \frac{\partial Q_0}{\partial y} \right]_{y=0},$$

and function Φ_2

$$\Phi_2' \Big|_{y=0} = \frac{8\sqrt{(1 - M_1^2)(M_2^2 - 1)}}{(M_2^2 - 2)^2} \left[\operatorname{Im} F_1' - \frac{1}{2\sqrt{1 - M_1^2}} \frac{\partial Q_0}{\partial y} \right]_{y=0}. \quad (6.109)$$

From (6.108), one can see that function F_1 is the solution of Riemann–Hilbert problem [18, 19]. However, condition (6.108) can be converted to Dirichlet condition. To do this, instead of F_1' , we enter the function Ψ_1'

$$F_1'(z_1) = (G_{21} + i G_{22}) \Psi_1'(z_1). \quad (6.110)$$

Here G_{21} and G_{22} are constants

$$G_{21} = \frac{(M_2^2 - 2)^3}{16(1 - M_1^2)(M_2^2 - 1) + (M_2^2 - 2)^4},$$

$$G_{22} = \frac{4\sqrt{(1 - M_1^2)(M_2^2 - 1)}(M_2^2 - 2)}{16(1 - M_1^2)(M_2^2 - 1) + (M_2^2 - 2)^4}. \quad (6.111)$$

For the function Ψ_1' , the ratio (6.108) becomes the Dirichlet condition

$$\operatorname{Re} \Psi_1' \Big|_{y=0} = G H(\xi) + A(\xi). \quad (6.112)$$

The functions Ψ_1' and Φ_2' are represented as the sum of two terms

$$\Psi_1' = \Psi_{11}' + \Psi_{12}', \quad \Phi_2' = \Phi_{21}' + \Phi_{22}', \quad (6.113)$$

satisfying boundary conditions

$$\operatorname{Re} \Psi'_{11}|_{y=0} = G H(\xi), \quad (6.114)$$

$$\operatorname{Re} \Psi'_{12}|_{y=0} = A(\xi), \quad (6.115)$$

$$\Phi'_{21}|_{y=0} = \frac{8\sqrt{(1-M_1^2)(M_2^2-1)}}{(M_2^2-2)^2} \left[G_{21} \frac{1}{\pi} \ln r_1 + G_{22} H(\xi) \right]_{y=0} G, \quad (6.116)$$

$$\Phi'_{22}|_{y=0} = \frac{8\sqrt{(1-M_1^2)(M_2^2-1)}}{(M_2^2-2)^2} \left[G_{21} \operatorname{Im} \Psi'_{12} + G_{22} \operatorname{Re} \Psi'_{12} - \frac{1}{2\sqrt{1-M_1^2}} \frac{\partial Q_0}{\partial y} \right]_{y=0}. \quad (6.117)$$

Boundary conditions (6.114) and (6.116) are satisfied by functions

$$\Psi'_{11}(z_1) = \left(\frac{i}{\pi} \ln z_1 + 1 \right) G, \quad (6.118)$$

$$\Phi'_{21}(\zeta_2) = \frac{8\sqrt{(1-M_1^2)(M_2^2-1)}}{(M_2^2-2)^2} \left[G_{21} \frac{1}{\pi} \ln |\zeta_2| + G_{22} H(\zeta_2) \right] G. \quad (6.119)$$

The functions Ψ'_{11} and Φ'_{21} allow to find deformations and stresses that are caused by external influences on the medium. To do this, in solutions (6.104), (6.105), it needs to leave the terms that are determined by the functions Ψ'_{11} and Φ'_{21}

$$\begin{aligned} \operatorname{Re} \Psi'_{11} &= \left[G_{21} H(z_1) - G_{22} \frac{1}{\pi} \ln |z_1| \right] G, \\ \operatorname{Im} \Psi'_{11} &= \left[G_{21} \frac{1}{\pi} \ln |z_1| + G_{22} H(z_1) \right] G, \\ \operatorname{Re} \Psi''_{11} &= \left[G_{21} \frac{\sin \theta_1}{r_1} - G_{22} \frac{\cos \theta_1}{r_1} \right] \frac{G}{\pi}, \\ \operatorname{Im} \Psi''_{11} &= \left[G_{21} \frac{\cos \theta_1}{r_1} + G_{22} \frac{\sin \theta_1}{r_1} \right] \frac{G}{\pi}, \\ \Phi''_{21} &= \frac{8\sqrt{(1-M_1^2)(M_2^2-1)}}{(M_2^2-2)^2} \left[G_{21} \frac{1}{\pi \zeta_2} + G_{22} \delta(\zeta_2) \right] G. \end{aligned} \quad (6.120)$$

The function Φ'_{21} describes the deformation and stress that are caused by the external influence on the medium and the function Φ'_{22} describes the deformation

and stress that are caused by optical mode. The functions Φ'_{21} and Φ'_{22} are known solutions to boundary problems for the two-dimensional hyperbolic equation [20].

6.6.3 Supersonic Speed of Movement

We will call the speed of movement supersonic, if

$$M_1 > 1, \quad M_2 > 1. \quad (6.121)$$

For supersonic speed of motion, the solution to Eq. (6.78) is a function

$$F = \Phi_1(\zeta_1) + \Phi_2(\zeta_2), \quad \zeta_1 = x + Ct - \sqrt{M_1^2 - 1}y, \quad (6.122)$$

where $\Phi_1(\zeta_1)$ and $\Phi_2(\zeta_2)$ are arbitrary functions of arguments ζ_1 and ζ_2 . The macrostress tensor and the components of the macroshift vector are written through the functions $\Phi_1(\zeta_1)$ and $\Phi_2(\zeta_2)$ as follows:

$$\begin{aligned} \sigma_{xx} &= -\frac{1}{2}(M_2^2 - 2M_1^2 + 2)\Phi_1'' + \frac{1}{2}(M_2^2 - 2)\Phi_2'' + L_{11}(Q_0), \\ \sigma_{yy} &= -\frac{1}{2}(M_2^2 - 2)(\Phi_1'' + \Phi_2'') + L_{22}(Q_0), \\ \sigma_{xy} &= \sqrt{M_2^2 - 1}\Phi_1'' - \frac{1}{4}\frac{(M_2^2 - 2)^2}{\sqrt{M_2^2 - 1}}\Phi_2'' - \frac{\partial^2 Q_0}{\partial x \partial y}, \end{aligned} \quad (6.123)$$

$$\begin{aligned} \mu U_x &= -\frac{1}{2}\Phi_1' + \frac{1}{4}(M_2^2 - 2)\Phi_2' - \frac{1}{2}\frac{\partial Q_0}{\partial x}, \\ \mu U_y &= \frac{1}{2}\sqrt{M_2^2 - 1}\Phi_1' + \frac{M_2^2 - 2}{4\sqrt{M_2^2 - 1}}\Phi_2' - \frac{1}{2}\frac{\partial Q_0}{\partial y}. \end{aligned} \quad (6.124)$$

According to (6.82), the functions Φ_1 and Φ_2 must satisfy boundary conditions

$$\left(\sqrt{M_1^2 - 1}\Phi_1' - \frac{(M_2^2 - 2)^2}{4\sqrt{M_2^2 - 1}}\Phi_2' \right) \Big|_{y=0} = -\frac{\partial Q_0}{\partial y} \Big|_{y=0}, \quad (6.125)$$

$$\frac{1}{2}(M_2^2 - 2)(\Phi_1' + \Phi_2') \Big|_{y=0} = G H(\xi) + \int L_{22}(Q_0) d\xi \Big|_{y=0}. \quad (6.126)$$

From (6.124) and (6.125), we find boundary conditions separately for functions Φ_1 and Φ_2

$$\Phi_1' \Big|_{y=0} = G_{31} \left[G H(\xi) + \int L_{22}(Q_0) d\xi + \frac{2\sqrt{M_2^2 - 1}}{M_2^2 - 2} \frac{\partial Q_0}{\partial y} \right]_{y=0}, \quad (6.127)$$

$$\Phi_2' \Big|_{y=0} = G_{32} \left[G H(\xi) + \int L_{22}(Q_0) d\xi - \frac{(M_2^2 - 2)}{2\sqrt{M_1^2 - 1}} \frac{\partial Q_0}{\partial y} \right]_{y=0}, \quad (6.128)$$

where

$$G_{31} = \frac{2(M_2^2 - 2)}{4\sqrt{(M_1^2 - 1)(M_2^2 - 1)} + (M_2^2 - 2)^2},$$

$$G_{32} = \frac{8\sqrt{(M_1^2 - 1)(M_2^2 - 1)}}{(M_2^2 - 2) \left[4\sqrt{(M_1^2 - 1)(M_2^2 - 1)} + (M_2^2 - 2)^2 \right]}.$$

The functions Φ_1' and Φ_2' are solutions to boundary problems for the two-dimensional hyperbolic equation. They are found in the same way as Φ_{21}' and Φ_{22}' .

6.7 Conclusion

General solutions of dynamic equations for plane deformation of nonlinear model are constructed. The found solutions allow you to set and solve specific boundary dynamic problems based for the nonlinear model, such as press die movement on semi-space surface, crack propagation, diffraction problems, etc. The solution of these problems based on the equations of linear theory of elasticity is obtained by many authors and is well studied. However, linear theory does not describe the occurrence of structural features such as cracks in an initially homogeneous environment, formation of nanostructures, phase transitions, dislocations, etc. Linear theory only describes the strain–stress state of the medium in which these structural features are introduced.

The nonlinear model, unlike a linear model, describes the occurrence of these structural defects. They can be found from solutions to nonlinear equations. This allows you to establish the conditions for the occurrence of these structural features depending on the external effects and properties of the medium, as well as describe the stress–strain state of the medium with these structural defects. The solution of these problems has both fundamental and practical interests. In modern technologies for the production of solid materials with an internal nanostructure, physical and

mechanical phenomena and structural features are realized, which are described by the nonlinear model. It is hoped that the nonlinear model will be used both in the development of mathematical models and as the scientific foundation of modern technologies for the production of solid materials with an internal structure.

The solutions found relate to the case when the external influence propagates with a speed that is less than the longitudinal wave velocity V_1 . The proposed method is easily generalized for the case of any speed of propagation of external perturbations.

References

1. Aero, E.L.: Microscale deformations in a two-dimensional lattice: structural transitions and bifurcations at critical shear. *Phys. Solid State* **42**, 1147–1153 (2000). <https://doi.org/10.1134/1.1131331>
2. Aero, E.L.: Micromechanics of a double continuum in a model of a medium with variable periodic structure. *J. Eng. Math.* **55**, 81–95 (2006). <https://doi.org/10.1007/s10665-005-9012-3>
3. Aero, E.L., Bulygin, A.N., Pavlov, Yu.V.: Nonlinear model of deformation of crystal media with complex lattice: mathematical methods of model implementation. *Math. Mech. Solids* **21**, 19–36 (2016). <https://doi.org/10.1177/1081286515572243>
4. Aero, E.L., Bulygin, A.N., Pavlov, Yu.V.: Nonlinear deformation model of crystal media allowing martensite transformations: solution of static equations. *Mech. Solids* **53**, 623–632 (2018). <https://doi.org/10.3103/s0025654418060043>
5. Frenkel, J., Kontorova, T.: On the theory of plastic deformation and twinning. *Acad. Sci. U.S.S.R. J. Phys.* **1**, 137–149 (1939)
6. Braun, O.M., Kivshar, Y.S.: *The Frenkel–Kontorova Model. Concepts, Methods, and Applications*, Springer, Berlin (2004)
7. Shaskol'skaya, M.P.: *Crystallography* [In Russian], Vysshaya Shkola, Moscow (1984)
8. Muskhelishvili, N.I.: *Some Basic Problems of the Mathematical Theory of Elasticity*. Springer, Dordrecht (1977)
9. Sneddon, I.N.: The stress produced by a pulse of pressure moving along the surface of a semi-infinite solid. *Rend. Circ. Mat. Palermo* **1**, 57–62 (1952). <https://doi.org/10.1007/BF02843720>
10. Radok, J.R.M.: On the solution of problems of dynamic plane elasticity. *Quart. Appl. Math.* **14**, 289–298 (1956). <https://doi.org/10.1090/qam/81075>
11. Dodd, R.K., Eilbeck, J.C., Gibbon, J.D., Morris, H.C.: *Solitons and Nonlinear Wave Equations*. Academic Press, New York (1982)
12. Bullough, R.K., Caudry, P.J.: *Solitons*. Springer, Berlin (1980)
13. Aero, E.L., Bulygin, A.N., Pavlov, Yu.V.: Functionally invariant solutions of nonlinear Klein–Fock–Gordon equation. *Appl. Math. Comput.* **223**, 160–166 (2013). <https://doi.org/10.1016/j.amc.2013.07.088>
14. Aero, E.L., Bulygin, A.N., Pavlov, Yu.V.: Solutions of the sine-Gordon equation with a variable amplitude. *Theor. Math. Phys.* **184**, 961–972 (2015). <https://doi.org/10.1007/s11232-015-0309-8>
15. Aero, E.L., Bulygin, A.N., Pavlov, Yu.V.: Exact analytical solutions for nonautonomic nonlinear Klein–Fock–Gordon equation. In: dell'Isola F., Eremeyev, V.A., Porubov, A. (eds.) *Advances in Mechanics of Microstructured Media and Structures*. *Advanced Structured Materials*, vol. 87, pp. 21–33. Springer, Cham, Switzerland (2018). https://doi.org/10.1007/978-3-319-73694-5_2

16. Bulygin, A.N., Pavlov, Yu.V.: Methods of finding of exact analytical solutions of nonautonomous nonlinear Klein–Fock–Gordon equation. In: Altenbach, H., et al. (eds.) *Dynamical Processes in Generalized Continua and Structures*. *Advanced Structured Materials*, vol. 103, pp. 147–161. Springer, Cham, Switzerland (2019). https://doi.org/10.1007/978-3-030-11665-1_8
17. Bulygin, A.N., Pavlov, Y.V.: Some solutions of dynamic and static nonlinear nonautonomous Klein–Fock–Gordon equation, In: Altenbach, H., et al. (eds.) *Nonlinear Wave Dynamics of Materials and Structures*. *Advanced Structured Materials*, vol. 122, pp. 107–120. Springer, Cham, Switzerland (2020). https://doi.org/10.1007/978-3-030-38708-2_7
18. Gakhov, F.D.: *Boundary Value Problems*. Pergamon Press, Oxford (1966)
19. Lavrentev, M.A., Shabat, B.V.: *Methods of the Theory of Complex Variable Functions* [In Russian]. Nauka, Moscow (1973)
20. Tikhonov, A.N., Samarskii, A.A.: *Equations of Mathematical Physics*. Dover Publications Inc., New York (1990)

Chapter 7

Effective Directions of Development of the Method of Artificial Bases for Evaluating the Volumetric Wear Resistance of Materials



Leonid V. Efremov

Abstract This article presents some results of our work on improving the original version of the artificial bases method in the following areas. Determination of linear wear resistance based on the formation of a hole with a simple and precise tool is given. Justification of simplified algorithms for evaluating the volumetric wear resistance in testing materials is done. The “block-on-ring” method for evaluating the volumetric wear resistance taking into account the level of hardness of the material is applied.

Keywords Wear · Wear resistance · Sample · Evaluation · Segment · Testing · Friction · Chord · Block-on-ring

7.1 Introduction

In the science of tribology, the use of the artificial bases method, proposed in the last century by Professor M. M. Khrushchev, is of great importance in testing materials for wear [1]. Recognizing the originality of the idea of this method, it should be noted that it does not provide for an assessment of the volumetric wear resistance and requires its adjustment in accordance with the current level of control and measuring devices and software.

This article presents some results of our work on improving the original version of this method in the following areas:

1. Determination of linear wear resistance based on the formation of a hole with a simple and precise tool.
2. Justification of simplified algorithms for evaluating the volumetric wear resistance in testing materials.

L. V. Efremov (✉)

Institute for Problems in Mechanical Engineering RAS, V.O., Bolshoy pr., 61,
St. Petersburg 199178, Russia
e-mail: levlefr@mail.ru

3. Application of the “block-on-ring” method for evaluating the volumetric wear resistance, taking into account the level of hardness of the material.

7.2 Determination of Linear Wear Resistance Based on the Formation of a Hole with a Simple and Precise Tool

The tests were initiated by testing the indentation method with an indenter in the form of a ball with a diameter of 10 mm by striking with a hammer. This operation confirmed the formation of a small swelling around the print and its different sizes depending on the direction of the friction path. Therefore, this method is not recommended for practical use, as well as the use of a diamond prism of a Vickers hardness tester. It was decided to form holes only by cutting or scraping.

Based on control tests of more than 10 cutting tools, it was found that the main tool should be taken as a conventional drill according to GOST 10902-77 with a diameter of 6–10 mm with a sharpening angle of 118^0 (Fig. 7.1d).

The advantages of this method in comparison with the manufacture of a complex device according to the rules of the original version of the artificial bases method are as follows:

- Incommensurably lower tool cost.
- Easy function of the depth of the hole from its diameter (Fig. 7.1e).
- High accuracy and quality of the formation of a round hole (Fig. 7.1c) with a diameter of up to 5 mm and a depth of up to 1.5 mm due to the factory production of the cutting part of the drill with a sharpening angle of 118^0 and a strictly vertical tool feed on the drilling machine (Fig. 7.1b).
- Use of a low-cost modern digital microscope with a built-in image recognition program to accurately determine the diameter and depth of the hole (Fig. 7.1a).

$$\begin{aligned}\mu &= \operatorname{tg}(\varphi/2)/2 = \operatorname{tg}(118^0/2)/2 = 0.3 \\ h &= \mu d = 0.3d\end{aligned}\quad (7.1)$$

Figure 7.2 shows a screenshot of the estimation of the diameter of a round hole using the image recognition microscope program, which consists of the following operations:

- Photographing an enlarged hole—(a)
- Image scale calibration—(b), (c), and (d)
- Measurement of the hole diameter—(e) and (f)
- Image recognition software IMAGEJ—(g)

These procedures are performed at the end of each test session or in total for the total test time.

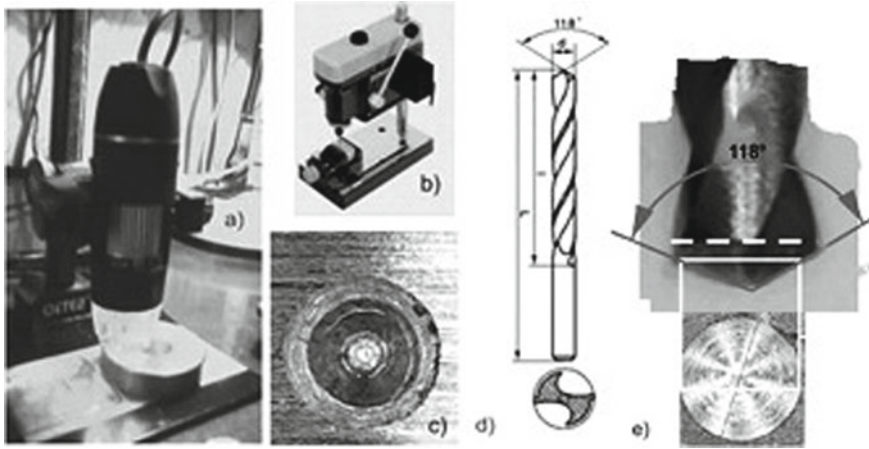


Fig. 7.1 Tools for forming and measuring the diameter of a round hole in order to accurately assess the wear of the sample

Initially, the method of artificial bases is designed to determine the linear wear resistance ϵ_L km/mm or the wear intensity $J_L = 1/\epsilon_L$ mm/km of the material.

In the case of a friction pair consisting of a rotating disc (the element to be sewn) and a pad (counterbody), the following parameters are the constant initial data for their determination:

d and $r = 500d$ are diameter and radius of the disk, n is the disk speed (rpm). The speed of friction on the disk V (km/min) is

$$V = 2\pi rn/10^6 \tag{7.2}$$

Diameter of the first hole when cutting with a drill before testing is d_0 .

The source data variables include: session number i , $i = 1 \dots k$, operating time value t_i min and the results of diameter measurements d_i for each i th session, well depth h_i according to the formula (7.1), wear Δh_i and friction path S_i according to formulas (7.3) and (7.4) during the session

$$\Delta h_i = h_{i-1} - h_i \tag{7.3}$$

$$S_i = Vt_i \tag{7.4}$$

Thus, all the initial data for calculating ϵ_L and J_L according to formulas (7.5) and (7.6) for each session are obtained. For the total estimation of these parameters, the formulas (7.8)–(7.10) should be used. The latter option is used for comparative tests of materials with a constant test duration.

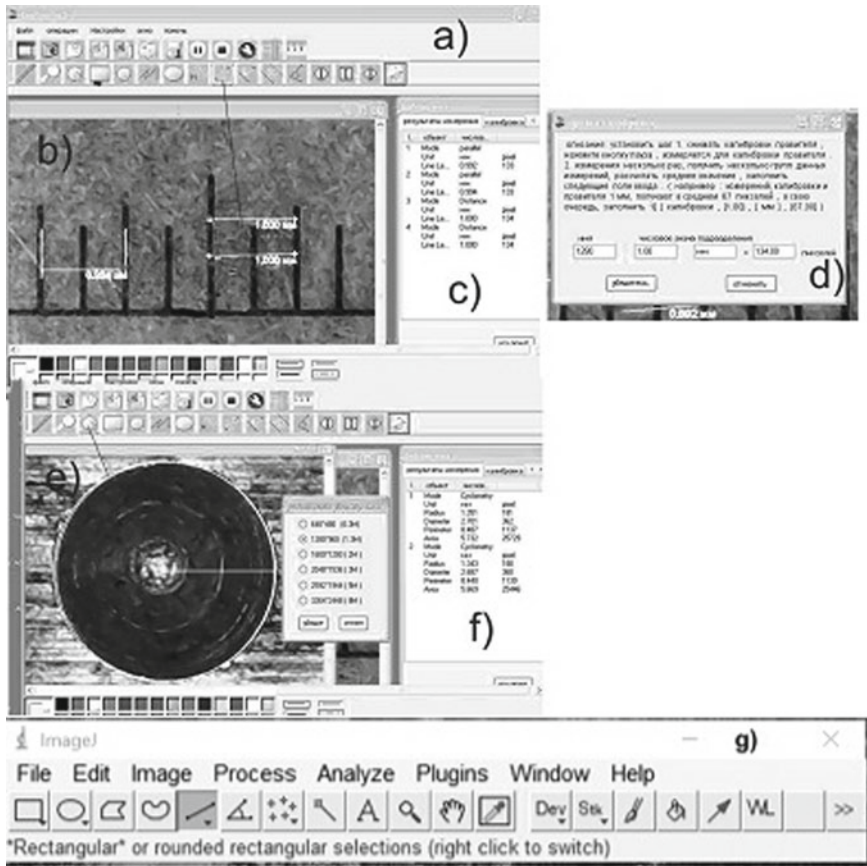


Fig. 7.2 Software for measuring the diameter of a round hole on a digital microscope

$$\varepsilon_{L_i} = S_i / \Delta h_i \tag{7.5}$$

$$t = \sum_1^k t_i \tag{7.6}$$

$$\Delta h_i = \mu (d_{i-1} - d_i) \tag{7.7}$$

$$\Delta h = \mu (d_0 - d_k) \tag{7.8}$$

$$S = Vt \tag{7.9}$$

$$\varepsilon_L = S / \Delta h \tag{7.10}$$

The described method is completely suitable for any methods of forming holes. For example, the zero size of the length of a slit-shaped hole 10 mm, similar to the one created in [2], can be instantly cut out by a mini-disk with a radius $r = 12$ mm.

And then the wear of Δh_i for the i -th session will be equal to (7.12)

$$\mu = 1/8r \quad (7.11)$$

$$\Delta h_i = \mu (l_0^2 - l_i^2) \quad (7.12)$$

Further calculations are performed according to the formulas (7.5)–(7.10).

7.3 Justification of Simplified Algorithms for Estimating Volumetric Wear Resistance

The main purpose of testing sliding friction pairs for wear by the artificial bases method is to evaluate the linear wear resistance of materials that have an inverse relationship with the intensity of linear wear $J_L = 1/\varepsilon_L$ mm/km. The application of an accurate and simple tool and the algorithm to solve this problem were shown above.

However, when testing materials for friction and wear, the evaluation of the volumetric wear resistance ε_W nm/mm³ and the intensity $J_W = 1/\varepsilon_W$ mm³/nm is becoming increasingly common. This is usually due to the application of the method of weighing small samples. Some test standards only require the determination of volumetric wear resistance. This applies to the “block on ring” method in accordance with the international standard ASTM G77, which will be considered, in particular, because it has a variable specific pressure. Next, we will perform the original proof of the universal algorithm of the ε_W function, taking into account the following obvious dependencies. If the contact spot area s_k can be determined, then the volume of wear products $W = s_k \Delta h$, and the specific pressure is determined by the formula (7.13). From this we obtain the function ε_W (7.14), taking into account the formula (7.10) for estimating ε_L .

For the first time, this expression was proved in a more complex way in our work [8].

$$P = F/s_k \quad (7.13)$$

$$\varepsilon W = FS/W = FS/s_k \Delta h = 1000 P \varepsilon_L \quad (7.14)$$

To confirm the universality of function (7.14), we consider models of friction pairs in order to simplify the algorithms for estimating W and s_k with an acceptable error. It is advisable to start the problem by considering the models of friction pairs in Fig. 7.3 with a conditionally constant specific pressure P MPa, due to the constant contact spot area s_k mm² and the load F H during wear. This can be seen from Eq. (7.13).

The simplest way to solve this problem is to use it for the popular model 3a to wear out the end of a small sample 2 in the process of rubbing it against the plane of the disk 1 at a distance of the friction path r mm from the center. The sample

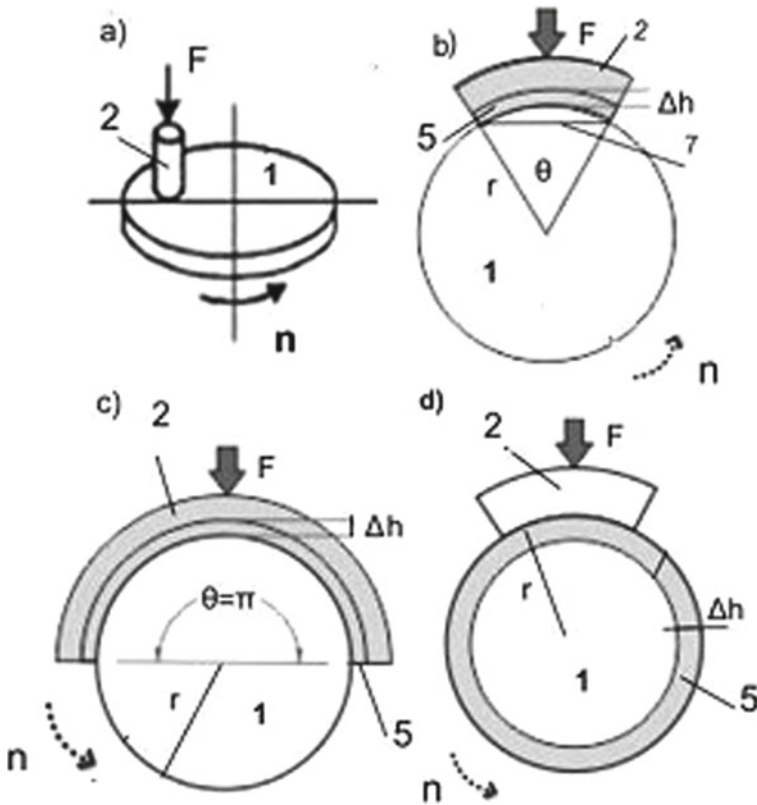


Fig. 7.3 Models of friction pairs with constant pressure

has a contact area of s_k mm² under load F N at a speed of n rpm. The method of determining s_k is simple and does not matter. The standard test session time is t min. The wear mass in mg is determined from the ratio (7.15) by weighing the sample on an accurate balance at a known material density of γ mg/mm³

$$W = G/\gamma \quad (7.15)$$

$$\Delta h = W/s_k \quad (7.16)$$

$$\varepsilon_L = S/(10^6 \Delta h) \quad (7.17)$$

$$\varepsilon_W = FS/W = FS/(s_k \Delta h) = 1000 P \varepsilon_L \quad (7.18)$$

Based on calculations and formulas (7.15)–(7.18) it can be concluded that the last formula exactly corresponds to the standard (7.14).

Further, it is advisable to confirm the universality of expression (7.14) by the example of three more models in Fig. 7.3, operating at a constant specific pressure on the friction machine.

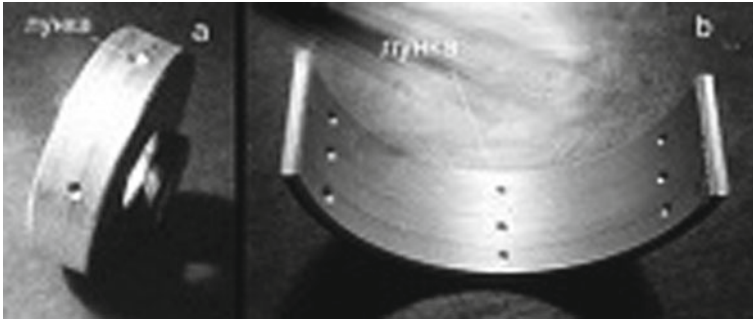


Fig. 7.4 Examples of samples for measuring wear: a—disk, b—sliding bearing

Model 3b—wear pads standard machine Tre-tion angle θ with radius $= \pi/4$ when the diameter of the disk is $r = 25$ mm and with a maximum wear of 1 mm,

Model 3c—wear markup sliding bearing with angular radius $\theta = \pi$ when the diameter of the disk is $r = 25$ mm and with a maximum wear of 1 mm,

3d model—wear of the end face of the disk with an angle of radius $\theta = 2\pi$ with a diameter $r = 25$ mm and with a wear of up to 1 mm.

Figure 7.4 shows a photo of the 3d (disc) and 3c (sub-pin) models with cut-out holes in the wear holes.

The calculated version of determining the volume W with the simplification of formula (7.19) for models 3b and 3c, as well as formula (7.20) for the 3d model, is considered. Simplification (7.22) with an error of 2% is achieved by neglecting the small value of the ratio $\Delta h/r = 0.04$ in the sum $(2 \mp \Delta h/r)$.

The wear value Δh included in the formulas is preliminarily determined by the method of artificial bases (7.8), which allows us to estimate the contact spot area $s_k = W/(\Delta h)$ for each model of the friction pair:

$$s_k = 0.25\pi r H_k \text{ for model 3b pad wear,}$$

$$s_k = \pi r H_k \text{ for model 3c bearing wear,}$$

$$s_k = 2\pi r H_k \text{ for 3d disc model wear.}$$

Since the friction path is known for all models, we can confirm the expression (7.14) by calculating (7.21).

$$\begin{aligned} W &= \frac{\theta}{2} ((r + \Delta h)^2 - r^2) H_k = \frac{\theta}{2} (r^2 - r^2 + 2\Delta hr + \Delta h^2) = \\ &= \frac{\theta}{2} \left(2 + \frac{\Delta h}{r} \right) r \Delta h H_k \approx \theta r \Delta h H_k = s_k \Delta h \end{aligned} \tag{7.19}$$

$$\begin{aligned} W &= \pi (r^2 - (r - \Delta h)^2) H_k = \pi (r^2 - r^2 + 2\Delta hr - \Delta h^2) H_k \\ &= \pi \left(2 - \frac{\Delta h}{r} \right) r \Delta h H_k \approx 2\pi r \Delta h H_k \approx s_k \Delta h \end{aligned} \tag{7.20}$$

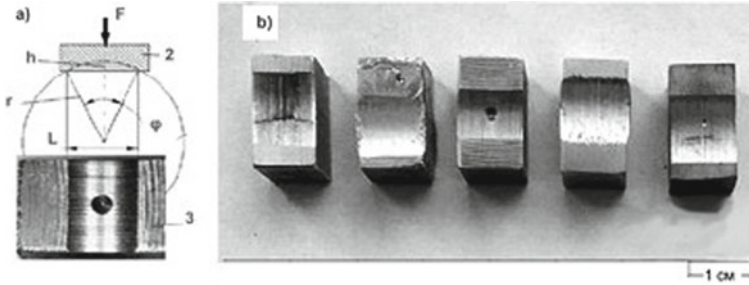


Fig. 7.5 Formation of the chord of the embedding of the disc—**a**, examples of wear of samples of materials—**b**

$$\varepsilon_W = FS/W = FS/(s_k \Delta h) = 1000P\varepsilon_L \quad (7.21)$$

$$\Delta = \frac{(2 \pm \Delta h/r) - 2}{(2 \pm \Delta h/r)} = \frac{\pm \Delta h/r}{(2 \pm \Delta h/r)} = \frac{|0.04|}{2.04} = 0.02 = 2\% \quad (7.22)$$

Thus, the error of the e_W estimation for all the considered models does not exceed 2%.

Features of the “block on the ring” method.

As previously noted, the “block on ring” method according to the international standard ASTM G77 is widely used in the testing of materials for wear. This method is one of the most effective ways of testing materials for wear by the method of artificial bases [1–7]. As shown in Fig. 7.5a the test friction pair consists of a ring (or disk) 1 with a radius of p and a rectangular flat bar (block) with a width of $2h$, into the flat surface of which the disk cuts, forming a wear mass in the form of a segment (in contrast to the layout 3b). This method is called the chord method in our works, since all the parameters under study are a function of the L mm chord formed due to the disk embedding in the sample. The value of L can be easily and accurately measured in tests (Fig. 7.5b). Since it increases with the wear of the sample, this method is characterized by a variable specific pressure, unlike the models in Fig. 7.3.

The algorithm for estimating linear and volumetric wear resistance by this method consists of the formulas (7.23)—(7.26), while (7.26) is the desired expression for evaluating ε_W in terms of linear wear resistance e_L and specific load P .

Note that, in contrast to the previously published simplified functions of the product volume W mm³ and the value Δh mm of wear, the analysis of the Taylor series takes into account not one of its first terms $L^2/(12r)$, but two of its first terms, $L^2(1 + 0.075L^2/r^2)/(12r)$ which reduced the calculation error from 5 to 1% with a maximum chord of $L = 20$ mm. As the chord decreases, the error decreases.

$$W = \left[r^2 \arcsin \left(\frac{L}{2r} \right) - \frac{L}{2} \sqrt{r^2 - \left(\frac{L}{2} \right)^2} \right] H_L \rightarrow \quad (7.23)$$

$$\left(\frac{L^3}{12r} + \frac{L^5}{160r^3} + \frac{3L^7}{3584r^5} + \dots \right) H_L \approx H_L \frac{L^3}{12r} \left(1 + 0.075 \frac{L^2}{r^2} \right) \Rightarrow \Delta \leq 1$$

$$\Delta h = W/LH_L \approx \frac{L^2}{12r} \left(1 + 0.075 \frac{L^2}{r^2} \right) \Rightarrow \Delta \leq 1 \quad (7.24)$$

$$P = \frac{F}{LH_L}$$

$$\varepsilon_L = \frac{S}{\Delta h} \quad (7.25)$$

$$\varepsilon_W = \frac{FS_L}{W} = \frac{FS}{H_L \frac{L^3}{12r} \left(1 + 0.075 \frac{L^2}{r^2} \right)} =$$

$$= \frac{FS}{LH_L \frac{L^2}{12r} \left(1 + 0.075 \frac{L^2}{r^2} \right)} = \frac{FS}{LH_L \Delta h} = 1000P\varepsilon_L \quad (7.26)$$

Based on the consideration of the formulas for all models of friction pairs, the universality of the function (7.14) and its suitability for assessing the wear resistance and wear intensity of any friction pairs in Fig. 7.3 can be considered proven with an error of no more than 2%.

To confirm the effectiveness of the simplified “block-on-ring” version, comparative wear tests were performed on 14 samples of various materials in a wide range of their hardness [6–8]. Their wear tests were carried out on the SMC-2 friction machine under the following conditions: $r = 25$ mm, $H_L = 10$ mm, $F = 200$ N, $n = 100$ rpm, $t = 10$ min and $cv = nt = 1000$ cycles, which are further considered as model cycles. This solution is related to the alignment of all the hardness functions under these conditions.

The first four samples (steel, cast iron, copper, and aluminum) were tested for abrasive wear from the P600 abrasive skin glued to the disc. The remaining nine samples from various materials were worn by boundary friction on the smooth surface of the disk with grease. It is proved that for the same material, the chord length at abrasive friction is about three times greater than at boundary friction. This should be taken into account when proceeding to the calculation in accordance with the boundary friction test rules.

7.4 Modeling of the Dependence of Wear Parameters on the Hardness of the Material

In conclusion, we will consider the original justification for the dependence of the wear characteristics on the hardness level of various materials on the Mohs scale. A nomogram of the hardness scales was found on the Internet, which allowed us to find a correlation between the Mohs and Brinell HB scales.

According to the test results of 14 samples, 6 materials were selected, tested at the boundary friction with the lubricant, having a hardness close to the recommended ones.

As the research experience in [9] shows, it is most likely that these functions have the power form $y(x) = a \cdot x^b$. Then the constants a and b can be determined by the least squares method (OLS) using the logarithm, for example, $X = \lg(\theta)$ and $Y = \lg(HB)$. In the Mathcad editor, when using OLS, complex calculations of the constants c_0 and c_1 are performed using a simple operator $c = \text{line}(X, Y) = \begin{vmatrix} c_0 \\ c_1 \end{vmatrix}$, followed by $a = 10^{c_0}$ and $b = c_1$.

For the correlation analysis of the dependence of hardness on the Mohs scale and wear parameters, Table 7.1 is obtained.

The described method is completely suitable for any methods of forming holes. For example, the zero size of the length of a slit-shaped hole 10 mm, similar to the one created in [2], can be instantly cut out by a mini-disk with a radius $r = 12$ mm.

Further, it is advisable to consider working algorithms for assessing wear resistance in production conditions, taking into account the level of hardness of materials.

To do this, it is recommended to equip the SMC-2 friction machine with a “block-on-ring” device with suitable disc and rod sizes. For example, [10] uses a disk with a radius of 20 mm and a width of 10 mm and a rod with a length of 30 mm and a width of 7 mm. This allows you to increase the permissible chord to 26–28 mm, compared to 15–16 mm for the length of the rod 2 with a length of 18 mm, shown in Fig. 7.1.

The values of the load F , the speed n , the measurement time t and the number of cycles $cv = nt$ are set depending on the choice of test options, which are characterized by a constant value of β according to the formula

$$\beta = \frac{r H_L \sqrt{cv}}{F}. \tag{7.27}$$

The input measured parameter can be either the chord length L or the mass of the wear products G , if it is determined by weighing the sample before and after the test session.

This method is used to justify the following correlation functions (7.28)–(7.34):

$$HB(\theta) = 4, 32\theta^{2.63} \tag{7.28}$$

$$\theta = \left(\frac{r\sqrt{cv}}{20L} \right)^{1/2} = \left(\frac{\beta}{604I_w} \right)^{1/6} \tag{7.29}$$

$$L(\theta) = \frac{r\sqrt{cv}}{20\theta^2} = \frac{\beta F}{20 H_L \theta^2} \tag{7.30}$$

$$h(\theta) = \frac{L(\theta)^2}{12r} = \frac{rcv}{4800\theta^4} \tag{7.31}$$

$$P(\theta) = \frac{F}{L(\theta)H_L} = \frac{20\theta^2}{\beta} \tag{7.32}$$

Table 7.1 Baseline data for hardness function evaluation

Material	Hardness Indicator					
	θ	HB , MPa	L , mm	ε_L , km/mm	P , MPa	$\varepsilon_W/1000$, Nm/mm ³
Tin O1	1.8	20	12.6	0.327	1.67	0.55
Copper M3r	3.0	100	4.1	2.5	4.93	12.3
Steel 40	4.0	200	2.53	6.68	7.53	50.3
Steel 08H18N10T	5.0	300	1.5	21.4	13	278.2
VK6 Alloy	6.0	500	1.11	37.7	17.88	674.1
Si ₂ O ₃ Ceramic	8.0	1000	0.63	121	32.05	3878

$$\varepsilon_L(\theta) = \frac{2\pi r_{cv}4800\theta^4}{10^6 r_{cv}} = 0,0302\theta^4 \tag{7.33}$$

$$\varepsilon_W(\theta) = 1000P(\theta)\varepsilon_L(\theta) = \frac{604\theta^6}{\beta} \tag{7.34}$$

If the tests are carried out at any initial data (Table 7.2), the calculated value of θ will not coincide with the reference hardness. In this case, it is suggested to call it the level of hardness. The possibility of reducing this value to the model hardness is shown in the studied version of the evaluation of wear parameters.

Based on the initial data and the results of research by scientists of the People’s Republic of China [1] on various properties of a polytetrafluoroethylene (PTFE) composite, taking into account the filling with ultrafine diamond (UFD), a new method for evaluating wear parameters has been developed. The “block-on-ring” method was used to determine the volumetric wear rate of both pure PTFE and its composite with different concentrations of UFD filler as a percentage. The wear of the polished surfaces of the disc and rod was measured during dry sliding under conditions of formation of a polymer transfer film on the disc, which acts as a lubricant.

The following test modes are specified as the initial data in [10]: $F = 200$ N, $n = 200$ rpm, and $t = 120$ min;

The results of calculating the wear rate I_W are given: $626 \cdot 10^{-6} \pm 124 \cdot 10^{-6}$ for pure PTFE and $26 \cdot 10^{-6} \pm 5 \cdot 10^{-6}$ for a composite with a UVD of 5%.

Two-hour test sessions are used to study not only wear but also the dynamics of changes in the coefficient of friction, temperature, material structure depending on the percentage of UFD, etc. Unfortunately, [10] does not provide the results of measurements of the initial chord length L or the mass of wear products G , as well as the method for calculating the parameters: h , P , ε_L and ε_W .

This problem is solved using the algorithms discussed above, and the results are shown in Table 7.2. It follows from Table that the chord length L should formally be used as the initial parameter, but it is unknown. This parameter is obtained as follows:

Table 7.2 Results of wear resistance assessment

	The set parameters			The set parameters								
	F , N	n , rpm	t , m	$L(\theta)$, mm	$h(\theta)$, mm	$P(\theta)$, MPa	$\varepsilon_L(\theta)$, km/mm	$\varepsilon_W(\theta)$, Nm/mm ³ × 10 ⁻³	I_W , mm ³ /Nm × 10 ⁻⁶	β , mm/N	θ	HB , MPa
1	200	200	120	23.4	2.28	1.22	1.32	1.60	626	108	2.57	52
2				8.14	0.28	3.51	10.94	38.5	26	108	4.36	208
3	200	100	10	8.4	0.24	2.38	0.67	1.60	626	39.5	2.17	33
4				2.9	0.028	6.88	5.6	38.5	26	39.5	3.69	134

The constant β is determined by the formula (7.27) and the hardness level θ (7.29), taking into account the known wear intensity I_W ;

Calculate the chord length $L(\theta)$ (7.30); $h(\theta)$, $P(\theta)$, $\varepsilon_L(\theta)$ and $\varepsilon_W(\theta)$ according to the formulas (7.31)–(7.34) and $I_W = 1/\varepsilon_W(\theta)$.

Due to the significant difference between the input parameters n and t from the sample values (Table 7.2) the hardness level θ may be slightly higher than the reference value. This can be seen from the recalculation of the hardness on the Mohs scale θ in the lines of materials 3 and 4 according to the formula (7.10) at the model values of F and cv and at a given volumetric wear intensity I_W . The Brinell hardness HB is determined by the formula (7.8). The obtained conditional Brinell hardness of PTFE before and after the introduction of the filler (33 and 134 MPa) is in good agreement with the reference data.

Note. Material: 1, 2-values for pure PTFE and composite; 3, 4-sample values.

This leads to the conclusion that the pure PTFE composite has a relatively low hardness, which increases by a factor of 4 when 5% of the UFD filler is added.

Acknowledgements The present work was supported by the Ministry of Science and Higher Education within the framework of the Russian State Assignment under contract No. FFNF-2021-0006.

References

1. Lai, S.-Q., Yueb, L., Li, T.-S., Zhi-Meng, H.: The friction and wear properties of polytetrafluoroethylene filled with ultrafine diamond. *Wear* **260**, 462–468 (2006)
2. Khrushchev, M.M. (ed.): *Methods of wear testing: proceedings of the meeting held on December 7–10, 1960*. Publishing House of the USSR Academy of Sciences (1962)
3. Wang, B., Lv, Q., Hou, G.: Tribological behavior of Nano-Al₂O₃ and PEEK reinforced PTFE composites. In: *AIP Conference Proceedings*, vol. 1794. AIP Publishing LLC (2017)
4. Musalimov, V.M., Valetov, V.A.: *Dynamics of Frictional Interaction*. St. Petersburg State University ITMO, St. Petersburg (2006)
5. Musalimov, V.M., Nuzhdin, K.A.: Modelling of external dynamics of frictional interaction using the elastic system stability theory. *J. Frict. Wear* **40**, 51–57 (2019)
6. Ginzburg, B.M., Tochilnikov, D.G.: The influence of fullerene-containing additives to fluorolayers on their bearing capacity under friction. *J. Tech. Phys.* **71**, 120–124 (2001)

7. Efremov, L.V., Tikalov, A.V.: Algorithms for estimating the linear, volumetric (weight) intensity of wear of materials on a friction machine. *Izv. vuzov. Speed control* **63**(4), 291–299 (2020)
8. Efremov, L.V., Tikalov, A.V.: Modeling of the wear process of flat samples of materials on a friction machine. *Izv. vuzov. Instrumentation* **63**(2), 163–169 (2020)
9. Efremov, L.V., Tikalov, A.V.: Evaluation of the wear resistance of materials on a friction machine with a decrease in the specific pressure on a flat sample. *J. Instrum. Eng.* **620203**(1), 157–166 (2020) (in Russian)
10. Efremov, L.V.: *Problems of Management of Reliability-Oriented Technical Operation of Machines*. Art-Xpress, St. Petersburg (2015)

Chapter 8

Local, Modal and Shape Control Strategies for Active Vibration Suppression of Elastic Systems: Experiment and Numerical Simulation



Aleksandr V. Fedotov, Alexander K. Belyaev, Vladimir A. Polyanskiy, and Nina A. Smirnova

Abstract The problem of active vibration suppression of the distributed elastic system is considered in the example of a slender metal beam undergoing bending vibrations. Control systems include piezoelectric sensors and actuators. Three different strategies for vibration suppression are considered: local, modal and shape control strategy. The local approach means that each feedback loop includes only one sensor–actuator pair placed at specific location on the beam, while the modal strategy implies that each feedback loop corresponds to a specific vibration mode of the object. The shape control method is based on the compensation of known distribution of the external excitation using only one feedback loop with all available sensors and actuators. First, experimental results are obtained for the local and the modal control systems using the same two sensor–actuator pairs, and then the transfer functions in feedback loops for these systems are improved as the result of numerical modeling. After that, the modal method is compared numerically with the shape control strategy. The results show that the modal method is the most effective if it is needed to suppress several vibration modes of the object.

Keywords Modal control · Shape control · Feedback control · Active vibration suppression · Piezoelectric sensors and actuators · Distributed elastic systems

A. V. Fedotov (✉) · A. K. Belyaev · V. A. Polyanskiy
Institute for Problems in Mechanical Engineering RAS, V.O., Bolshoy pr., 61, St. Petersburg
199178, Russia
e-mail: alvafed@yandex.ru

A. K. Belyaev
e-mail: vice.ipme@gmail.com

V. A. Polyanskiy
e-mail: vapol@mail.ru

N. A. Smirnova
Peter the Great St. Petersburg Polytechnic University, Polytechnicheskaya, 29, St. Petersburg
195259, Russia
e-mail: nina-mpu@mail.ru

8.1 Introduction

Undesirable vibrations can be dangerous for mechanical systems and cause failure, damage and unwanted noise, while the resonance vibrations are especially harmful. Active vibration control is a modern method of vibration attenuation, which is developing rapidly due to advances in digital signal processing and sensor and actuator technology. The presence of the infinite number of eigenmodes and resonance frequencies complicates the active vibration control of the elastic systems with distributed parameters and leads to reduced accuracy and stability of the control systems.

Piezoelectric materials give wide opportunities for control and monitoring of elastic systems, since these are smart materials, which combine two physical fields: mechanical and electrical. On one hand, sensor networks can be used for health monitoring and damage detection in engineering structures [1]. On the other hand, actuators allow one to control the stress–strain state of structures by applying electrical voltage, which helps to realize not only the displacement tracking but also the stress control in order to protect the structure or the piezoelectric actuator itself from damage and destruction [2]. The joint use of sensors and actuators allows one to organize the feedback control of elastic systems. This raises the following questions: how to locate the piezoelectric elements on the object, how to process the sensor signals, how to arrange the feedback loops and which control laws in these loops to specify. There are several strategies to control the elastic objects, which give different answers to the aforementioned questions.

The most simple is the local approach [3]: sensors and actuators are placed in pairs at several locations on the object, and each feedback loop includes only one sensor–actuator pair. The second method is modal and it accounts for the dynamics of the object: each control loop corresponds to a specific vibration mode of the object and uses all sensors to measure this mode and all actuators to affect it [4]. The third approach under consideration is the shape control strategy [5]. This strategy was originally formulated as a method to fully compensate the external excitation on the elastic object with known spatial distribution provided that the disturbance is known and the appropriate control capabilities are available. In real cases, the time variation of the external excitation may be not given, which makes it necessary to use feedback control. The shape control method can be used if the spatial distribution of the disturbance is known in advance and does not vary in time. The control action is distributed on the object in the way that allows one to compensate this disturbance, while sensor and actuator systems are collocated and form a single feedback loop.

The objective of the present study is to compare the three mentioned strategies for the problem of active vibration suppression of a slender metal beam using piezoelectric sensors and actuators. The previous work of the authors [6] provides the experimental comparison of local and modal approaches, and in the present study, control systems obtained previously are improved by means of numerical modeling, and their results are compared with the numerically obtained results for the shape control strategy.

8.2 Theoretical Background

This section presents the basic theoretical information and schemes for the three control strategies under consideration.

8.2.1 Local Method

Figure 8.1 shows the scheme of the local control system with two sensor–actuator pairs. In the scheme, y_i are the sensor signals, and u_i are the control actions on the actuators. After attaching sensors and actuators to the control object, it is necessary to specify the transfer function for each feedback loop $R_i(s)$. The drawback of this approach is that different feedback loops are not independent, because they are connected through the elastic object and can strongly influence each other.

8.2.2 Modal Method

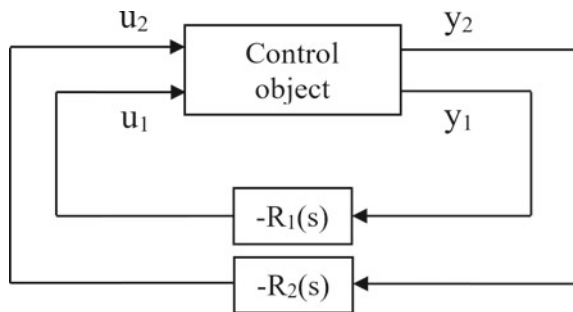
Modal control of flexible structures is also called independent modal space control (IMSC). This approach was first formulated by Gould and Murray-Lasso [4] and further developed by Meirovitch [7].

Let us consider a thin metal beam undergoing bending vibrations. Consider the equation of motion of the beam in spectral decomposition, assuming that n eigenmodes are enough to describe the motion of the beam:

$$w(x, t) = \sum_{i=1}^n w_i(x)q_i(t), \tag{8.1}$$

where w is the displacement, w_i is the i th bending mode of the beam, and q_i is the i th generalized coordinate. The matrix equation of motion for the vibration modes

Fig. 8.1 Scheme of the local control system



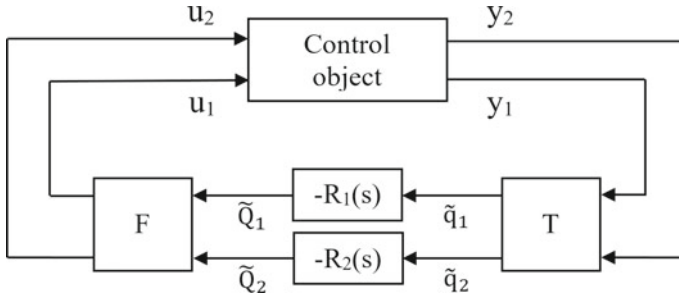


Fig. 8.2 Scheme of the modal control system

will have the following form:

$$\ddot{q} + 2\xi\Omega\dot{q} + \Omega^2q = Q^d + Q^c, \quad (8.2)$$

where q is the vector of generalized coordinates, ξ is the diagonal damping matrix, Ω is the diagonal matrix of eigenfrequencies, Q^d is the vector of external excitation and Q^c is the vector of control actions on the modes.

The scheme of the modal control system is given in Fig. 8.2. For simplicity, we consider a system with two sensors, two actuators and two modal control loops. In the scheme \tilde{q}_i are the estimates of the first and the second generalized coordinates, \tilde{Q}_i are the desired generalized forces acting on the first and the second modes, T is the mode analyzer matrix, used to estimate the generalized coordinates, and F is the mode synthesizer matrix, used to generate proper control actions.

Let us introduce the excitation matrix θ^a and the measurement matrix θ^s . The excitation matrix θ^a shows how strong is the influence of each actuator on each eigenmode of the object, and the measurement matrix θ^s shows how strong is the influence of each eigenmode on each sensor:

$$Q^c = \theta^a u = \theta^a F \tilde{Q}, \quad (8.3)$$

$$\tilde{q} = T y = T \theta^s q. \quad (8.4)$$

It is obvious that the correspondence between eigenmodes of the object and the modal control loops requires that the modal matrices T and F have the following form:

$$F = (\theta^a)^{-1}, T = (\theta^s)^{-1}. \quad (8.5)$$

Then, the single equation from the system (8.2) for i th eigenmode of the beam takes the following form:

$$\ddot{q}_i + 2\xi_i\Omega_i\dot{q}_i + \Omega_i^2q_i = Q^d - R_i(s)q_i. \quad (8.6)$$

This means that one can control each mode individually by setting the corresponding transfer function $R_i(s)$ and thus realize the independent modal space control. Of course, all these derivations are valid only if the matrices θ^a and θ^s are square and have the size $n \times n$, which means, that there are enough sensors and actuators in the control system and no higher modes are active. In real problems, the presence of higher, uncontrolled modes always complicates the overall situation: for example, some higher modes can become unstable. This is called the spillover effect, which can be minimized by increasing the number of sensors and actuators.

8.2.3 Shape Control Method

Originally, the notion *shape control* was first mentioned in a study by Haftka and Adelman [8], where the problem of minimizing static distortion of large space structures using thermal control elements was considered. Then, the shape control method was further developed by Austrian researchers from Johannes Kepler University Linz. The review of shape control is given in [9]. Paper [5] presents the theory of dynamic shape control of beams by piezoelectric actuation and sensing. The presented method allows one to eliminate force-induced vibrations of a beam by the use of piezoelectric actuators attached to the structure.

As stated in [5], in order to fully compensate the deformations of the beam, the actuation bending moment M^t should be opposite to the statically admissible bending moment $M^{q \cdot p_z}$ produced by the distributed forces p_z :

$$M^{q \cdot p_z}(x, t) + M^t(x, t) = 0. \quad (8.7)$$

Thus, in order to compensate the external disturbance by the piezoelectric actuation, the distribution of this disturbance should be known in space and time, and the needed actuation should be available. However, usually in real problems, the possibilities of actuation are limited: for example, often only finite set of rectangular piezoelectric actuators is available. In these cases, the desired distribution of the actuation moment should be approximated by discrete step functions corresponding to separate piezoelectric patches [10]. In the present study, the deflection of the beam with applied actuation is analyzed directly, and the condition of minimization of the maximum deflection is applied in order to find positions and actuation intensity for discrete piezoelectric actuators.

Classic example of feedback control within the framework of shape control strategy in application to bending vibrations of a beam is given in the book of Nader [10]. The following control scheme is used: all the actuators and all the sensors form a single control loop, which means that \tilde{q} and \tilde{Q} in the scheme in Fig. 8.3 are scalars, and vectors f^s and f^a are used instead of matrices T and F in the modal system. Moreover, the design of the sensor system completely repeats the design of the actuator system (sensors are located symmetrically to the actuators at the opposite side

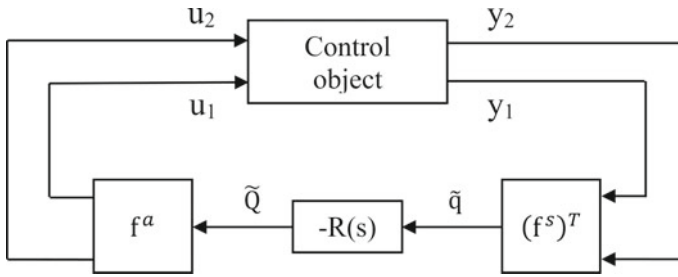


Fig. 8.3 Scheme of the shape control system

of the beam), that is, the sensor and the actuator systems are collocated. Therefore, vectors of weighting factors f^s and f^a are equal:

$$f^s = f^a. \quad (8.8)$$

8.3 Experimental Setup

The first part of the study is the experimental investigation and comparison of local and modal approaches to active vibration suppression of a metal beam, which is described in detail in the paper [6]. The second part of the study is the numerical modeling of the same system and the synthesis of more efficient control laws [11]. At the final stage of the study, the shape control systems are synthesized and compared to the previously obtained local and modal systems.

The experimental setup is shown in Fig. 8.4. The control object is an aluminum beam 70 cm long with the cross-section of 3×35 mm. It is disposed vertically and fixed at one point 10 cm far from the lower end. The external excitation is the base vibration. It is applied by means of a piezoelectric stack actuator, which is a part of the fixation that connects the beam to the massive basement. Axial displacement of the stack actuator causes bending vibration of the beam. The control system includes PI Ceramic DuraAct patch transducers P-876.A15, which are used as sensors and actuators. They consist of rectangular PZT plates with dimensions $50 \times 30 \times 0.5$ mm, thin metal electrodes and the polymer coating. Actuators and sensors are connected through a digital controller dSPACE DS1103 PPC Controller Board. Apart from this, feedback loops also contain low-pass-filters (LPF) and a signal amplifier, which also gives contribution to the frequency characteristics of the object.

The purpose of the control system is to reduce forced vibrations of the beam in the frequency range containing the first and the second resonance frequencies. The first and the second bending modes are shown in Fig. 8.4. Two sensor–actuator pairs are located on the beam on both sides at the beginning of the experiment and hold the same positions for all tested local and modal control systems. In order to monitor

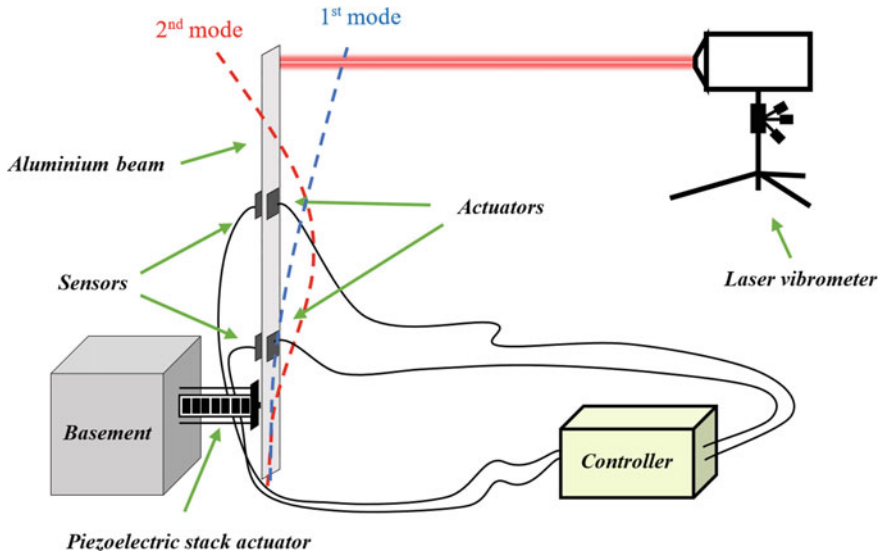


Fig. 8.4 Experimental setup

the control efficiency, the vibration amplitude of the upper endpoint of the beam is measured by the laser Polytec Scanning Vibrometer PSV-400. The choice of this point is caused by the fact that the amplitude of its vibration is the highest among all points of the beam for the first and the second vibration modes.

8.4 Sensor and Actuator Placement

In this section, we consider a problem of sensor and actuator placement on the beam for each control strategy and choosing proper matrices T and F for the modal control systems and vectors f^a and f^s for the shape control systems.

8.4.1 Local and Modal Methods

First, we need to define the positions of the piezopatches on the beam for the experimental study of local and modal methods. This process is described in the paper [6]. The positions of sensors and actuators in the framework of the numerical investigation are the same as for the experimental research. These positions are obtained as a result of analyzing the first and the second bending modes of the beam. Sensors and actuators should be placed in those locations where the curvature $w''(x)$ of these modes gets maximum values: in this case, they can excite and measure these modes

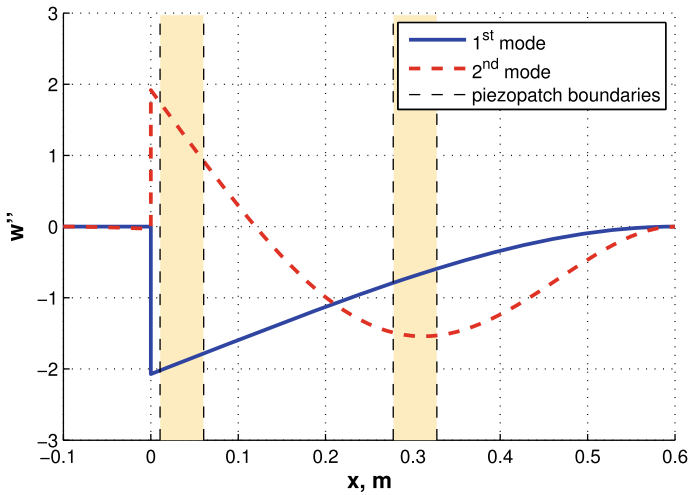


Fig. 8.5 Curvature of the first and the second bending modes of the beam with the piezopatch locations

most effectively. The curvature of the first and the second modes with the chosen positions of two sensor–actuator pairs is shown in Fig. 8.5. The coordinates of the centers of the piezopatches are the following: $x_1 = 0.0355$ m, $x_2 = 0.3025$ m.

The matrices T and F (mode analyzer and synthesizer) for the experimental study are obtained using the identification procedure described in detail in [12]. As the result, these matrices are defined in the following way:

$$T^{(exp)} = \begin{pmatrix} 0.99 & 1.03 \\ -0.49 & 1.53 \end{pmatrix}, \quad (8.9)$$

$$F^{(exp)} = \begin{pmatrix} 0.98 & -0.49 \\ 1.02 & 1.51 \end{pmatrix}. \quad (8.10)$$

8.4.2 Shape Control Method

Here, we need to specify the positions for sensors and actuators and define the vectors of weighting factors f^a and f^s for the numerical study of the shape control method. As stated before, sensor and actuator systems are collocated; therefore, $f^a = f^s$. We consider a system with either two or five sensor–actuator pairs. Thus, we need to define the positions of the piezopatches and the weighting factors, that is, the actuation moments for each actuator, from the condition of the best compensation of the external excitation.

We know the form of the external excitation: it is the transverse vibration of the support, which is equivalent to the transversal inertia force uniformly distributed

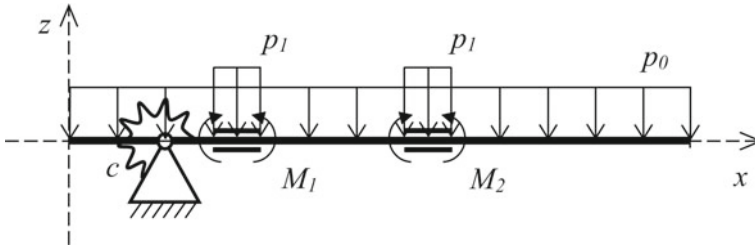


Fig. 8.6 Beam with two sensor–actuator pairs

over the whole beam as shown in Fig. 8.6. Here, the model of the beam from the experimental setup shown in Fig. 8.4 is presented. We use for calculations the value of the distributed load $p_0 = 1 \text{ N/m}$. In the case of using sensors and actuators, the load is not uniform: the control elements present an additional mass, therefore, the distributed load at the corresponding locations slightly increases (the resulting load is denoted as p_1). The fixation is modeled by the torsional spring with the stiffness $c = 400 \text{ N} \cdot \text{m/rad}$ (this model is verified in [6] and [11]). We choose the locations of the piezopatches and actuation moments M_i from the condition of the minimization of the maximum deflection of the beam in the static case. We also require that the deflection at the right endpoint of the beam is zero, because the efficiency of the obtained control systems is defined using the deflection at this point.

As a result of the investigation, two configurations of shape control systems were obtained, differing in the number of sensor–actuator pairs. The beam deflection corresponding to these two systems in the static case with feedforward control is shown in Fig. 8.7. The black curve corresponds to the system with two sensor–actuator pairs, and the red curve corresponds to the system with five pairs of piezopatches. The maximum deflection of the beam without control (not displayed in the figure) is 3.2 mm, while for the systems with two and five sensor–actuator pairs this value equals to 0.044 mm and 0.012 mm, respectively. For the system with two pairs of piezopatches, the maximum deflection cannot be smaller because the actuators on the right side of the beam do not influence the deflection of the left side. For the system with five sensor–actuator pairs, the maximum deflection cannot be smaller because the piezopatches technically cannot be located closer than 10 mm to the fixation point due to the presence of a nut, which fixates the beam. For the first system, the coordinates of the centers of the piezopatches are the following: $x_1 = 0.048 \text{ m}$, $x_2 = 0.237 \text{ m}$, and the actuation moments are: $M_1 = 0.835 \text{ N} \cdot \text{m}$, $M_2 = 0.603 \text{ N} \cdot \text{m}$. For the second system, the coordinates are: $x_1 = -0.035 \text{ m}$, $x_2 = 0.035 \text{ m}$, $x_3 = 0.1345 \text{ m}$, $x_4 = 0.235 \text{ m}$, $x_5 = 0.363 \text{ m}$, and the moments are: $M_1 = -0.22 \text{ N} \cdot \text{m}$, $M_2 = 0.622 \text{ N} \cdot \text{m}$, $M_3 = 0.354 \text{ N} \cdot \text{m}$, $M_4 = 0.267 \text{ N} \cdot \text{m}$, $M_5 = 0.1603 \text{ N} \cdot \text{m}$.

Thus, the vectors of the weighting factors for the shape control systems with two or five pairs of piezopatches are defined, since they are taken equal to the actuation moments:

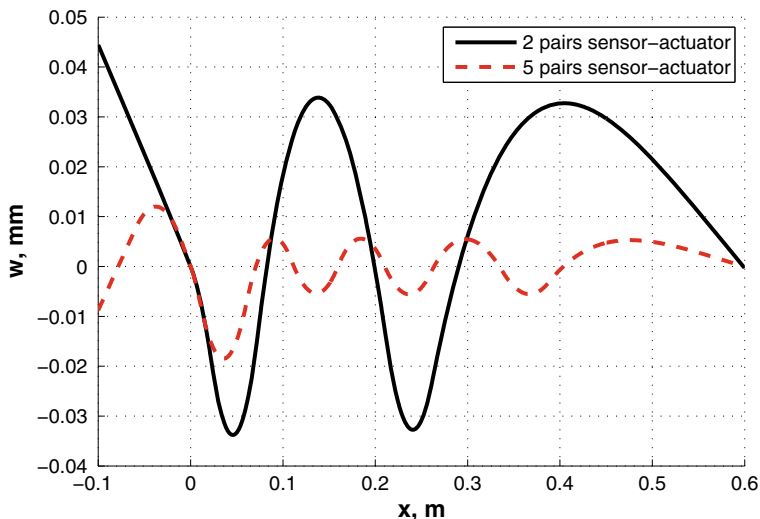


Fig. 8.7 Compensation of the external excitation with two or five sensor–actuator pairs

$$f^{a(2)} = f^{s(2)} = (0.835 \ 0.603)^T, \quad (8.11)$$

$$f^{a(5)} = f^{s(5)} = (-0.22 \ 0.622 \ 0.354 \ 0.267 \ 0.1603)^T. \quad (8.12)$$

8.5 Finite Element Modeling

Before the synthesis of the transfer functions in the feedback loops of the control systems, one needs to obtain the frequency response functions (FRFs) of the beam. In order to obtain FRFs of the beams with piezopatches and without piezopatches for reference, the finite element (FE) models of these beams are created in ANSYS software. The choice of this software is caused by the fact that it can give precise results for a wide range of eigenmodes of the beam, while the numerical simulation of the beam dynamics in MATLAB software resulted in errors for the higher vibration modes. The previous numerical research in MATLAB for the beam with different boundary conditions (simply supported beam) has shown the importance of taking into account the influence of piezopatches on the beam eigenmodes during the modeling of beam dynamics [13, 14].

Two types of FE models of the system were created: the first one (Fig. 8.8a) constructed of three-dimensional elements (Solid186 for ordinary materials and Solid226 for piezoelectric materials), and the second one (Fig. 8.8b) constructed of one-dimensional elements Beam189. At first, both models were created for the system with two sensor–actuator pairs constructed within the experimental study, and both were verified using the experimental data [11]. These models differ greatly in



Fig. 8.8 Finite element models of the beam

complexity: the first contains 3534 elements and 21088 nodes, and the second—only 161 element and 283 nodes. Moreover, in the 3D model, the fixation construction is modeled entirely with the stack actuator and additional elements, and the piezoelectric effect is modeled directly, while in the 1D model the beam fixation is modeled by two springs (longitudinal and torsional), and the piezoelectric effect in this model is absent. Instead of this, the actuator excitation is specified by an application of corresponding forces and moments, and the sensor signal is calculated from the longitudinal deformation of the piezoelectric material.

The modeling has shown no big difference in the results for two described FE models. Therefore, for testing local and modal control systems, the 3D model was used as more precise one, and for the subsequent calculations (shape control systems and the beam without piezopatches for reference) for simplicity, the 1D model was used. Figure 8.8b shows the 1D model of the system with five sensor–actuator pairs created for the testing of the shape control strategy.

In order to obtain FRFs of the beams, the harmonic analysis is performed in the frequency range from 1 to 2000 Hz, where a harmonic excitation is applied either to the beam support or to the actuators. The measured values are the sensor signals and the deflection of the right endpoint of the beam. In all models, the same damping coefficient $\xi = 0.002$ is used for all vibration modes; this choice is justified in [15].

In order to obtain the mode analyzer and synthesizer for the modal control system in the framework of the numerical study, the FRFs of the beam with piezopatches are analyzed. The height of the resonance peaks in the FRFs allows one to determine the matrices θ^a and θ^s . It is important to mention here that the rows of matrix θ^a and the columns of matrix θ^s , therefore, the rows of matrix T and the columns of matrix F are defined up to a constant. The matrices T and F are calculated from the matrices θ^a and θ^s using Eq. (8.5). The results are the following:

$$T = F^T = \begin{pmatrix} 1.01 & 0.96 \\ -0.49 & 1.49 \end{pmatrix}. \quad (8.13)$$

8.6 Design of the Transfer Functions

Within the experimental study, the transfer functions for local and modal strategies were designed using the frequency response design method [16, 17]. In order to do this, FRFs of the beam were previously measured for two variants of excitation (each of two actuators) and two variants of measured signal (each of two sensors) in the

frequency range from 1 to 2000 Hz. After that, the designed control systems were tested experimentally. The optimization criterion was the height of the resonance peaks in the FRF showing the vibration amplitude of upper endpoint of the beam under the excitation of the fixation point at the first and the second resonances of the beam. As a result, three most efficient control systems were obtained: the first local system is designed to work at the first resonance, the second local system—at the second resonance, and the modal system with two feedback loops is effective at both resonances. These results are presented in the paper [6], and they are also included in Table 8.1.

At the next stage of the investigation, the designed transfer functions for local and modal systems were improved in the framework of the numerical simulation. During this process, the FRFs of the beam were used that were obtained not experimentally, but numerically by means of FE modeling (Sect. 8.5). In order to calculate the FRF of the beam under feedback control with two loops using only existing FRFs of the beam without control and the control laws, the mathematical procedure is used described in [11, 15].

The main advantage of the numerical simulation is that it is so fast and precise, that it is possible to realize the numerical optimization of the designed transfer functions. Thus, the special optimization procedure was realized in MATLAB [11]. This algorithm optimizes parameters of different filters composing the transfer function of selected feedback loop and its gain value and ensures the stability of the closed-loop system. Let us consider this procedure in more detail.

First of all, each transfer function is constructed from the finite number of special filters. The first one is an inverse notch filter, which raises the phase of the control signal in the working frequency domain near to the resonance to be controlled so that the control action has the opposite phase with the external excitation and can effectively compensate it. The second one is a low-pass filter, which reduces the amplitude of the signal at high frequencies and thus increases the stability of the closed-loop system. The third one is optional—it is a notch filter, which reduces the amplitude of the signal at one of the higher resonances where the risk of instability is the greatest, and thus allows one to raise the overall gain value. The transfer function of the designed feedback loop is obtained by multiplying the transfer functions of the individual filters. The described procedure calculates the control results for different variants of filter parameters from the specified range, finds the optimal gain value for each variant of the control law, compares the control results and finds the best combination of parameters, which provides the most effective vibration suppression and at the same time does not cause instability in the closed-loop system.

With the help of the described algorithm, the control loops were optimized for local, modal and shape control strategies. The results are presented in Sect. 8.7. Here as an example, the control laws and the Bode diagrams are presented for the most efficient of the created control systems—namely, the modal control system with two feedback loops. Mode analyzer and synthesizer for this system are given in Sect. 8.5. The transfer functions in the feedback loops are the following:

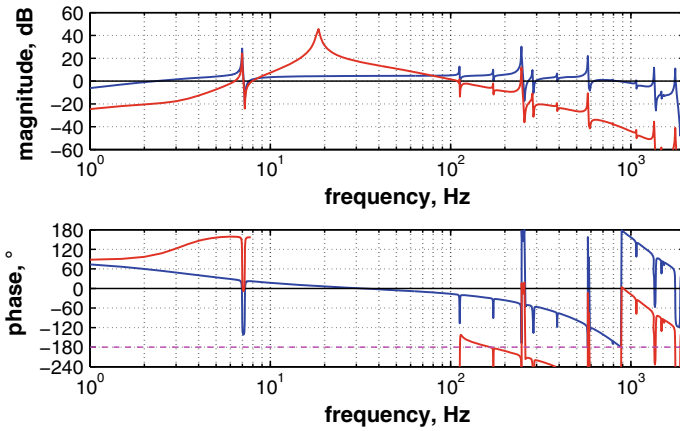


Fig. 8.9 Bode diagram for the first loop of the modal control system (blue lines—control object, red lines—open-loop system)

$$R_1(s) = (3.07 \cdot 10^5 s^4 + 9.84 \cdot 10^6 s^3 + 1.52 \cdot 10^{11} s^2 + 2.74 \cdot 10^{12} s + 6.14 \cdot 10^{13}) / (s^6 + 572 s^5 + 5.99 \cdot 10^5 s^4 + 2.79 \cdot 10^8 s^3 + 4.48 \cdot 10^{10} s^2 + 3.72 \cdot 10^{12} s + 4.83 \cdot 10^{14}), \quad (8.14)$$

$$R_2(s) = \frac{2.17 \cdot 10^5 s^2 + 3.61 \cdot 10^6 s + 3.43 \cdot 10^7}{s^4 + 414 s^3 + 5.57 \cdot 10^5 s^2 + 7.65 \cdot 10^7 s + 6.13 \cdot 10^{10}}. \quad (8.15)$$

The Bode diagrams for both loops of the modal control system are given in Figs. 8.9, 8.10. Here, the blue lines correspond to the control object, and the red lines

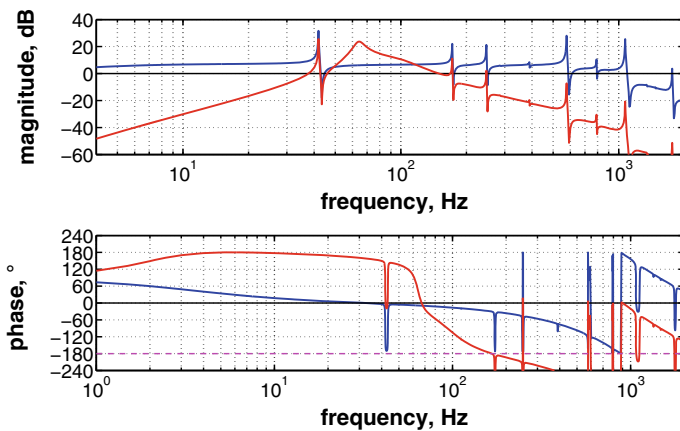


Fig. 8.10 Bode diagram for the second loop of the modal control system (blue lines—control object, red lines—open-loop system)

—to the open-loop system. In the used FRFs of the control object, the characteristics of the low-pass filters and the amplifier, which are included in the control loop, are also taken into account. These characteristics were measured during the experimental part of the investigation [6].

8.7 Comparison of the Results

In this section, the control results for all designed systems are summarized. In Figs. 8.11, 8.12, 8.13 and 8.14, the resulting FRFs of the beam with control showing the vibration amplitude of upper endpoint of the beam under the excitation of the fixation point in the vicinity of the first and the second resonances are shown in comparison with the FRF of the beam without piezopatches. Then, the difference in the level of endpoint vibrations of the beam at both resonances for each control system compared to the level of vibrations without control is given in Table 8.1. Figures show only results obtained numerically, while the experimental results for tested earlier local and modal systems are presented in the table. In the table, Δw_1 and Δw_2 are the change in the magnitude of endpoint vibrations at the first and the second resonances, respectively.

First, three local and three modal control systems were obtained (Figs. 8.11, 8.12). In the first local system, both loops were designed to work at the first resonance of the beam, and in the second system—at the second resonance. In the third local system, the first feedback loop (lower sensor–actuator pair) was designed to suppress

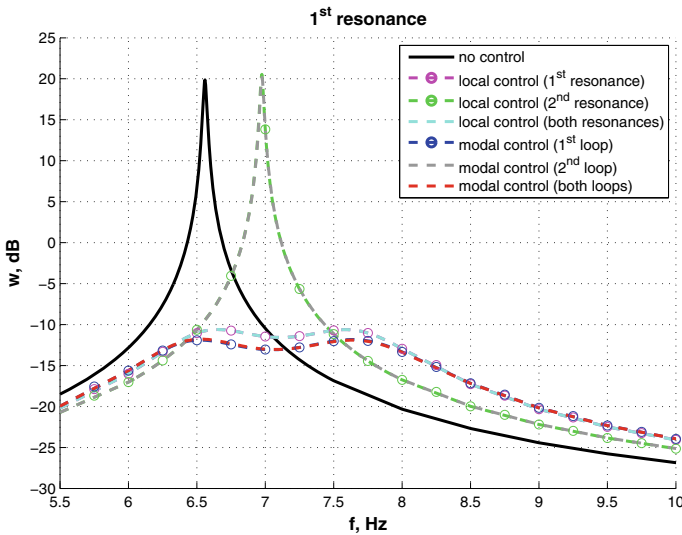


Fig. 8.11 Compensation of the first resonance of the beam with local and modal control systems

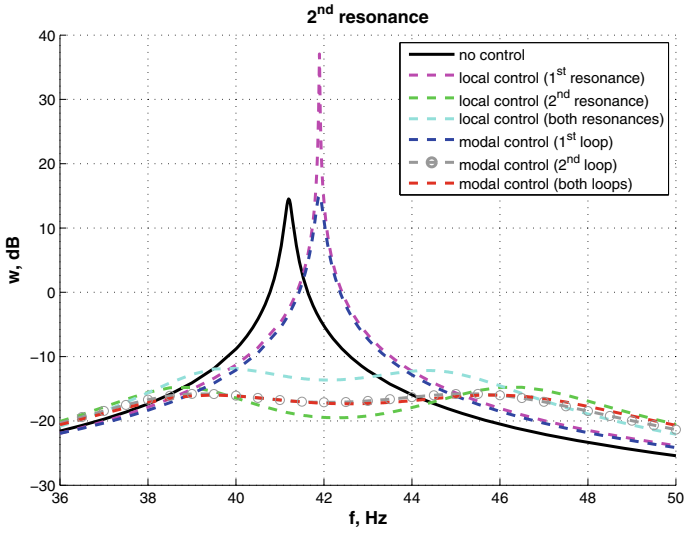


Fig. 8.12 Compensation of the second resonance of the beam with local and modal control systems

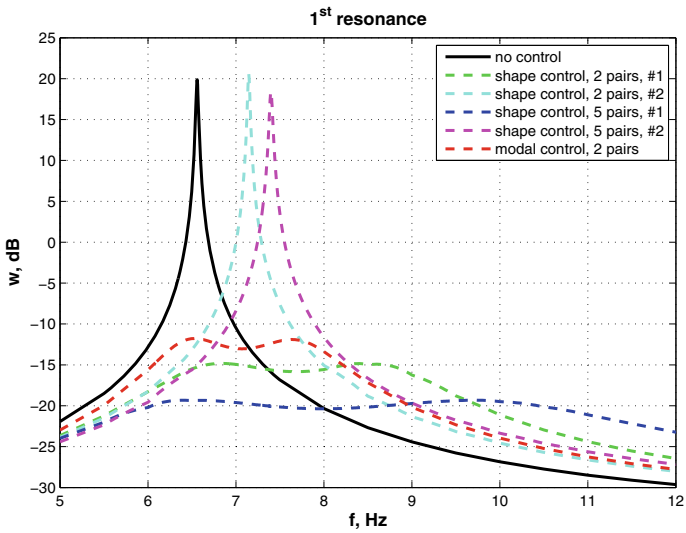


Fig. 8.13 Compensation of the first resonance of the beam with modal and shape control systems

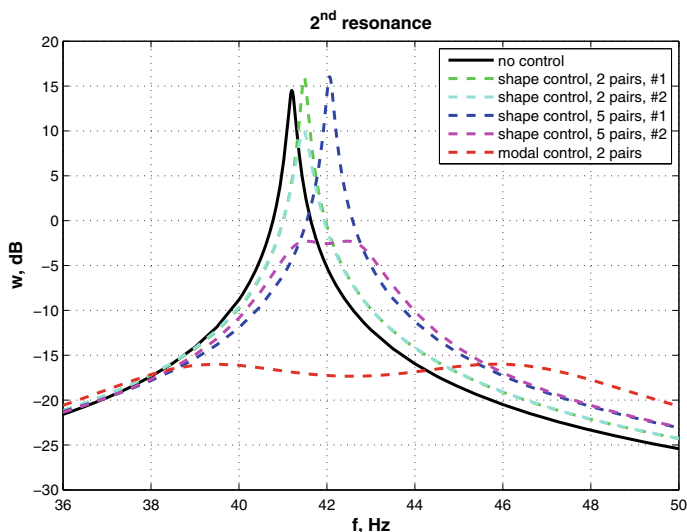


Fig. 8.14 Compensation of the second resonance of the beam with modal and shape control systems

the first resonance, and the second loop (upper sensor–actuator pair)—the second resonance. The first and the second modal systems have only one active feedback loop—either the first (corresponding to the first bending mode of the beam) or the second (corresponding to the second bending mode), while in the third system both loops are active.

After that, four shape control systems were obtained (Figs. 8.13, 8.14). The first and the second variants of the shape control system with two sensor–actuator pairs were designed to suppress the first and the second resonances of the beam, respectively, and the same is true for the systems with five sensor–actuator pairs. The results for these four systems are compared to the results for the modal control system with two feedback loops.

The results of all the obtained control systems are summarized in Table 8.1. As can be seen from the table, the local and modal systems tested experimentally are much less effective than the systems obtained numerically. This result emphasizes the effectiveness of the optimization procedure used to design the latter systems. The second conclusion is that the modal system with two loops is the most efficient at both resonances among all local and modal systems. The local system №3 is works also very well at both resonances, but its efficiency is lower compared to the modal system. The results of the local system №1 is close to the local system №3 at the first resonance, and the same holds for local systems №2 and №3 at the second resonance. Similarly, the results of the modal system with two loops practically repeat the individual results of the modal systems with only one loop at corresponding resonances. This means that two loops almost do not interfere with each other not only in the modal system, but, surprisingly, in the local system too.

Table 8.1 Change in the level of endpoint vibrations of the beam at the first and the second resonances for different control systems (experiment and simulation)

Control system	Δw_1 , dB	Δw_2 , dB
Local control, №1 (exp.)	-12.7	4.8
Local control, №2 (exp.)	-5.2	-18.9
Modal control, both loops (exp.)	-15.7	-17.9
Local control, №1	-30.48	22.55
Local control, №2	0.67	-29.29
Local control, №3	-30.47	-26.37
Shape control, two pairs, №1	-34.69	1.42
Shape control, two pairs, №2	0.72	-4.57
Shape control, five pairs, №1	-39.19	1.51
Shape control, five pairs, №2	-1.47	-15.82
Modal control, first loop	-31.7	0.57
Modal control, second loop	0.31	-30.33
Modal control, two loops	-31.65	-30.5

It can also be seen that the first variants of the shape control systems work only at the first resonance, while the second variants of the shape control systems suppress vibrations only at the second resonance. At the same time, the shape control systems with five sensor–actuator pairs are more efficient than the similar systems with two pairs, what is expected. At the first resonance, the shape control systems are more effective than the modal system; on the contrary, at the second resonance, the modal system with two sensors and two actuators is much more effective even than the shape control system with five sensor–actuator pairs. Therefore, the modal control strategy is preferable compared to the shape control strategy in the cases, where it is necessary to suppress vibrations at several resonance frequencies.

8.8 Conclusion

Within the present study, the problem of active suppression of forced bending vibrations of a thin metal beam was analyzed experimentally and numerically. The purpose of the designed control systems was to suppress forced vibrations in the frequency range containing the first and the second eigenfrequencies of bending vibrations of the beam. Different control systems based on each of the three strategies (local, modal and shape control strategy) were tested and compared to each other. All considered systems contained piezoelectric sensors and actuators, but the number of piezopatches and feedback loops in these systems was different. The local and modal systems included two sensor–actuator pairs and two feedback loops, while

in the shape control systems either two or five pairs of piezopatches integrated into only one control loop were used.

The results of the investigation show that local and modal systems can demonstrate effective vibration suppression at both resonances together, and the efficiency of the modal system is higher than the local one (more than 30 dB resonance amplitude suppression for the systems under consideration). It should be noted that the experimental results for local and modal systems were significantly improved by the numerical optimization procedure. At the same time, the efficiency of the shape control systems at the first resonance is much greater than at the second resonance (for the system with five sensor–actuator pairs, the results are, respectively, 39 dB and 16 dB). This can be explained by the fact that the distribution of the control action of the shape control system is designed to compensate the static disturbance, which causes the deflection of the beam close to the first bending eigenmode. Therefore, the influence of the control loop of this system on the second eigenmode of the beam is rather small. On the contrary, in the modal system, each control loop corresponds to the particular bending mode of the beam. The lower result of the modal control system at the first resonance compared to the shape control systems can be explained by the fact that the distribution of the control action in the first control loop of the modal system is specified not to compensate the first mode most effectively, but it is specified from the condition of not affecting the second mode (in order to separate the modes).

In summary, the shape control strategy is the best choice if it is needed to suppress vibrations only at the first resonance of the beam, but not at the higher resonances. In the cases, where it is necessary to suppress vibrations at several resonance frequencies, the modal control strategy gives the best result.

Acknowledgements This work was supported by the Ministry of Science and Higher Education of the Russian Federation (Project Number 075-15-2021-573).

References

1. Krommer, M., Zellhofer, M., Irschik, H.: Structural health monitoring of multi-storey frame structures using piezoelectric incompatibility filters: theory and numerical verification. *J. Appl. Comp. Mech.* (2021). <https://doi.org/10.22055/JACM.2020.33246.2186>
2. Schoeftner, J., Brandl, A., Irschik, H.: Stress control of a piezoelectric lumped-element model - theoretical investigation and experimental realization. *J. Appl. Comp. Mech.* (2021). <https://doi.org/10.22055/JACM.2020.33327.2203>
3. Kim, S.-M., Elliott, S.J., Brennan, M.J.: Decentralized control for multichannel active vibration isolation. *IEEE Trans. Cont. Syst. Tech.* **9**, 93–100 (2001)
4. Gould, L.A., Murray-Lasso, M.A.: On the modal control of distributed parameter systems with distributed feedback. *IEEE Trans. Autom. Cont.* **11**, 729–737 (1966)
5. Irschik, H., Krommer, M., Pichler, U.: Dynamic shape control of beam-type structures by piezoelectric actuation and sensing. *Int. J. Appl. Electromagn. Mech.* **17**, 251–258 (2003)
6. Belyaev, A.K., Fedotov, A.V., Irschik, H., Nader, M., Polyanskiy, V.A., Smirnova, N.A.: Experimental study of local and modal approaches to active vibration control of elastic systems. *J. Struct. Control Health Monit.* (2018). <https://doi.org/10.1002/stc.2105>

7. Meirovitch, L.: Dynamics and Control of Structures. Wiley, New York (1990)
8. Haftka, R.T., Adelman, H.M.: An analytical investigation of shape control of large space structures by applied temperatures. *AIAA J.* **23**, 450–457 (1985)
9. Irschik, H.: A review on static and dynamic shape control of structures by piezoelectric actuation. *Eng. Struct.* **24**, 5–11 (2002)
10. Nader, M.: Compensation of Vibrations in Smart Structures: Shape Control, Experimental Realization and Feedback Control. Trauner Verlag, Linz (2008)
11. Fedotov, A.V.: Active vibration suppression of Bernoulli-Euler beam: experiment and numerical simulation. *Cyber. Phys.* **8**, 228–234 (2019)
12. Belyaev, A.K., Polyanskiy, V.A., Smirnova, N.A., Fedotov, A.V.: Identification procedure in the modal control of a distributed elastic system. *St. Petersburg Polytech. Univ. J. Phys. Math.* (2017). <https://doi.org/10.1016/j.spjpm.2017.06.004>
13. Polyanskiy, V.A., Belyaev, A.K., Smirnova, N.A., Fedotov, A.V.: Influence of sensors and actuators on the design of the modal control system. In: Matveenko, V., Krommer, M., Belyaev, A., Irschik, H. (eds.) *Dynamics and Control of Advanced Structures and Machines*, pp. 127–135. Springer, Cham (2019)
14. Fedotov, A.V.: Applicability of simplified models of piezoelectric elements in the problem of active vibration damping. *J. Instr. Eng.* (2020) (in Russian). <https://doi.org/10.17586/0021-3454-2020-63-2-126-132>
15. Fedotov, A.V.: The damping of the distributed system vibrations using piezoelectric transducers: simulation. *St. Petersburg Polytech. Univ. J. Phys. Math.* (2019). <https://doi.org/10.18721/JPM.12112>
16. Dorf, R.C., Bishop, R.H.: *Modern Control Systems*, 12th edn. Prentice Hall, New Jersey (2011)
17. Franklin, G.F., Powell, J.D., Emami-Naeini, A.: *Feedback Control of Dynamic Systems*, 5th edn. Prentice Hall, New Jersey (2006)

Chapter 9

Speed-Gradient Method in Mechanical Engineering



Alexander L. Fradkov and Boris Andrievsky

Abstract The paper is devoted to development of the speed-gradient method in the IPME RAS in 1986–2021 and its applications to the problems of mechanical engineering.

Keywords Speed gradient · Mechanical engineering · Nonlinear dynamics · Control · Adaptation · Identification · Energy · Oscillations

9.1 Introduction

Control problems in mechanics and mechanical engineering are characterized by complex, nonlinear dynamics, and high-dimensional models of controlled systems. This often leads to the need to create new, specific control algorithms for each new control object and each new control problem. Therefore, of particular interest are schemes and methods for synthesizing algorithms that allow a unified approach to solving various control problems. One of these methods is the so-called speed-gradient method, which appeared back in the 1970s [1, 2], and has been intensively developed in relation to mechanical objects at the IPME RAS and other organizations since the early 1990s [3–14]. This article provides a brief overview of the applications of the velocity gradient method in mechanics and technical problems. Section 9.2 gives a short description of the method, following [15]. Section 9.3 describes approaches to the problem of controlling energy and other properties

A. L. Fradkov · B. Andrievsky (✉)

Institute for Problems in Mechanical Engineering RAS, 61 Bolshoy prospekt, V.O., 199178 St. Petersburg, Russia
e-mail: fradkov@mail.ru

St. Petersburg State University, 28 Universitetsky prospekt, 198504 Peterhof, St. Petersburg, Russia

of nonlinear oscillations. Section 9.4 gives examples of applying the SG method to solving control problems in technical systems. The description of some examples follows the survey [16].

9.2 Speed-Gradient Method

A continuous-time counterpart of the gradient method is the so-called *speed-gradient (SG) method*. Like the gradient method for discrete-time systems, SG method is intended for control problems where control goal is specified by means of a goal function.

Consider a nonlinear time-varying system

$$\dot{x} = F(x, u, t) \quad (9.1)$$

and control goal

$$\lim_{t \rightarrow \infty} Q(x(t), t) = 0, \quad (9.2)$$

where $Q(x, t) \geq 0$ is a smooth goal function.

In order to design control algorithm the scalar function $\dot{Q} = \omega(x, u, t)$ is calculated that is the speed (rate) of changing $Q_t = Q(x(t), t)$ along trajectories of (9.1): $\omega(x, u, t) = \partial Q(x, t) / \partial t + (\nabla_x Q(x, t))^T F(x, u, t)$. Then it is needed to evaluate the gradient of $\omega(x, u, t)$ with respect to input variables: $\nabla_u \omega(x, u, t) = (\partial \omega / \partial u)^T = (\partial F / \partial u)^T \nabla_x Q(x, t)$. Finally, the algorithm of changing $u(t)$ is determined according to the differential equation

$$\frac{du}{dt} = -\Gamma \nabla_u \omega(x, u, t), \quad (9.3)$$

where $\Gamma = \Gamma^T > 0$ is a positive-definite gain matrix, e.g., $\Gamma = \text{diag} \{\gamma_1, \dots, \gamma_m\}$, $\gamma_i > 0$. The algorithm (9.3) is called *speed-gradient (SG) algorithm*, since it suggests to change $u(t)$ proportionally to the gradient of the speed of changing Q_t .

The origin of the algorithm (9.3) can be explained as follows. In order to achieve the control goal (9.2), it is desirable to change $u(t)$ in the direction where $Q(x(t), t)$ decrease. However, it may be a problem since $Q(x(t), t)$ does not depend on $u(t)$ directly. Instead one may try to decrease \dot{Q} , in order to achieve the inequality $\dot{Q} < 0$, which implies decrease of $Q(x(t), t)$. The speed $\dot{Q} = \omega(x, u, t)$ generically depends on u explicitly which allows to write down (9.3). The speed-gradient algorithm can be also interpreted as a continuous-time counterpart of the gradient algorithm, since for small sampling step size the direction of the gradient is close to the direction of the speed gradient.

Let us illustrate speed-gradient design methodology for a class of tracking control problems for controlled systems linear in the inputs:

$$\dot{x} = A(x, t) + B(x, t)u, \quad (9.4)$$

where $x(t) \in \mathbb{R}^n$ is the state vector, $u(t) \in \mathbb{R}^m$ is vector of controlling variables (inputs) which may be either physical quantities or adjustable parameters, $A(x, t)$ is n -vector, and $B(x, t)$ is $n \times m$ -matrix. Let the control goal have the form

$$\lim_{t \rightarrow \infty} (y(t) - y_*(t)) = 0, \quad (9.5)$$

where $y(t) = h(x(t)) \in \mathbb{R}^l$ is l -vector of regulated variables (outputs) and $y_*(t) \in \mathbb{R}^l$ is the goal trajectory (desired trajectory) of the outputs. It is clear that the goal (9.5) has equivalent form (9.2) if the goal function $Q(x, t)$ is chosen as follows:

$$Q(x, t) = \frac{1}{2}(y - y_*(t))^T P(y - y_*(t)), \quad (9.6)$$

where P is symmetric positive-definite $l \times l$ -matrix.

For the purpose of control algorithm design, rewrite Eq. (9.4) in the form

$$\dot{x} = A(x, t) + \sum_{i=1}^m B_i(x, t)u_i, \quad (9.7)$$

where u_i are components of the vector $u \in \mathbb{R}^m$ and $B_i(x, t) \in \mathbb{R}^n$ are columns of the matrix $B(x, t)$. Then the rate (speed) of changing $Q(x(t), t)$ along trajectories of the system (for constant u) is as follows:

$$\omega(x, u, t) = (y - y_*(t))^T P(CA(x, t) + CB(x, t)u - \dot{y}_*(t)), \quad (9.8)$$

where $C = C(x, t) = \partial G(x, t)/\partial x$. Taking the gradient of (9.8) in u , we obtain the speed gradient and the speed-gradient algorithm in the following form:

$$\nabla_u \omega(x, u, t) = B(x, t)^T C^T P(y - y_*(t)), \quad (9.9)$$

$$\frac{du}{dt} = -\Gamma B(x, t)^T C^T P(y - y_*(t)). \quad (9.10)$$

To simplify design, the gain matrix Γ is often chosen as diagonal matrix ($\Gamma = \text{diag}\{\gamma_i\}$) or scalar matrix ($\Gamma = \gamma I$) where γ_i, γ are positive numbers. For special case of the system linear in inputs, the algorithm (9.10) is nothing but the classical *integral control law*.

In a similar way, the so-called speed-gradient algorithm in finite form is designed

$$u(t) = u_0 - \Gamma \nabla_u \omega(x(t), u(t), t), \quad (9.11)$$

where u_0 is some initial value of control variable, e.g., $u_0 = 0$). Algorithm (9.11) is a generalization of classical *proportional control law*.

More general form of speed-gradient algorithms is sometimes useful:

$$u(t) = u_0 - \gamma \psi(x(t), u(t), t), \quad (9.12)$$

where $\gamma > 0$ is the scalar gain parameter and vector function $\psi(x, u, t)$ satisfies the so-called *pseudogradient condition*

$$\psi(x, u, t)^\top \nabla_u \omega(x, u, t) \geq 0 \quad (9.13)$$

for all x, u, t . Special case of (9.12) is called *sign-like* or *relay-like* algorithm:

$$u(t) = u_0 - \gamma \operatorname{sign} \nabla_u \omega(x(t), u(t), t), \quad (9.14)$$

where *sign* of a vector is understood component-wise: for a vector $z = \operatorname{col}(z_1, \dots, z_m)$ $\operatorname{sign} z$ is defined as $\operatorname{sign} z = \operatorname{col}(\operatorname{sign} z_1, \dots, \operatorname{sign} z_m)$.

In order to make a reasonable choice of the control algorithm parameters the applicability conditions should be verified. The main conditions are convexity of the function $\omega(x, u, t)$ in u and existence of “ideal” control u_* such that $\omega(x, u_*, t) \leq 0$ for all x (attainability condition). More precise formulations can be found in [17, 18].

The speed-gradient algorithms can be modified to take into account constraints. For example, let the equality constraint be given

$$g(x(t), u(t), t) = 0, \quad (9.15)$$

where g is a smooth scalar function, and a scalar control function $u(t)$ is to be chosen such that (9.15) is satisfied for all $t \geq 0$. The modified (constrained) SG algorithm in differential form is as follows:

$$\dot{u}(t) = -\gamma \nabla_u \omega(x(t), u(t), t) - \lambda(t) \nabla_u g(x(t), u(t), t), \quad (9.16)$$

where the Lagrange multiplier $\lambda(t)$ is chosen to satisfy condition $\dot{g} = 0$, that is,

$$\lambda(t) = \frac{-\gamma \nabla_u \omega(x(t), u(t), t) + \nabla_x g^\top F(x(t), u(t), t) + \partial g / \partial t}{|\nabla_u g(x(t), u(t), t)|^2}. \quad (9.17)$$

Initial condition $u(0)$ should satisfy constraint too: $g(x(0), u(0), t) = 0$. The case of SG algorithms in finite form and the case of inequality constraints are considered in a similar way.

The speed-gradient algorithm is tightly associated to the concept of Lyapunov function $V(x)$ —a function of the system state nonincreasing along its trajectories. Lyapunov function is an abstraction for such physical characteristics as energy and

entropy. It is important that Lyapunov function can be used not only for analysis but also for system design. In particular, for the speed-gradient algorithms in the finite form, the goal function itself may serve as the Lyapunov function: $V(x) = Q(x)$. The Lyapunov function for differential form of SG algorithms is as follows: $V(x, u) = Q(x) + 0.5(u - u_*)^T \Gamma^{-1}(u - u_*)$, where u_* is the desired “ideal” value of controlling variables. Note that in order to justify discrete-time gradient algorithm one may use Lyapunov function as square distance between the current and the “ideal” controlling variables $V(u) = |u - u_*|^2$.

9.3 Control of Energy and Nonlinear Vibrations

In the development of the speed-gradient (SG) method in the 1990s, two important milestones can be subdivided. Firstly, it was possible to systematize on the basis of the SG algorithms [3] the methods of adaptive control of mechanical systems, including robotic manipulators, based on the passivity concept [19–22].

Secondly, it was proposed to design control algorithms for the excitation of oscillations of Hamiltonian systems based on the SG using objective functions that depend on the Hamiltonian (the energy) of a free system. In particular, for a controllable Hamiltonian system with the Hamiltonian $H(q, p) = H_0(q, p) + H_1(q, p)u$, where $q \in \mathbb{R}^n$ is the vector of generalized coordinates, $p \in \mathbb{R}^n$ is a vector of generalized momenta, u is a scalar control action, $H_0(q, p)$ is the Hamiltonian of a free system, and $H_1(q, p)u$ is an interaction Hamiltonian, the following control goal is posed:

$$H_0(q(t), p(t)) \rightarrow H^* \text{ as } t \rightarrow \infty, \quad (9.18)$$

where H^* is the desired value of the system energy. Choosing the objective function in the form of $Q(x) = 1/2(H_0(x) - H^*)^2$, one obtains the SG algorithm in the form

$$u = -\gamma(H_0 - H^*)p, \quad (9.19)$$

where $\gamma > 0$ is the gain [4, 23–25]. The results obtained were summarized in the books [17, 18] and became the basis for the synthesis of control algorithms in numerous problems of oscillation control in systems and networks. In [3, 4, 25], these methods were extended to systems in more general form than Hamiltonian ones. The conditions for the applicability of the SG method for controlling invariants of a wide class of nonlinear systems were also obtained.

The concept of the “swinging control” is introduced, ensuring achievement of an arbitrarily large level of the objective function using an arbitrarily small control level. The existence of a swinging control is established for Hamiltonian systems. The simulation results of swinging up a pendulum are presented. The results further are developed in [25], where the method of synthesis of control of oscillatory nonlinear systems is extended to the problems with several objective functionals under

constraints. For the first time, an approach based on the SG method to the problem of controlling the passage through resonant zones is proposed.

In [26], the method is proposed for using the SG approach to controlling the synchronization of two oscillators, using the example of two pendulums weakly coupled by a spring. In this case, the equation of the controlled system has the form

$$\begin{cases} \ddot{\varphi}_1 + \rho\dot{\varphi}_1 + \omega^2 \sin \varphi_1 = k(\varphi_2 - \varphi_1) + u, \\ \ddot{\varphi}_2 + \rho\dot{\varphi}_2 + \omega^2 \sin \varphi_2 = k(\varphi_1 - \varphi_2), \end{cases} \quad (9.20)$$

where $\varphi_i = \varphi_i(t)$ are the angles of rotation of the pendulums ($i = 1, 2$); $u = u(t)$ denotes the external moment (control action) acting on the first pendulum; ω, k, ρ are the system parameters: ω is the frequency of natural oscillations of small amplitude, k is the coupling coefficient between pendulums (for example, the coefficient of elasticity of a spring), and ρ is the damping factor.

The objective function is taken in the following form:

$$Q(x) = \alpha Q_\varphi(\dot{\varphi}_1, \dot{\varphi}_2) + (1 - \alpha) Q_H(x), \quad (9.21)$$

where $x = [\varphi_1, \varphi_2, \dot{\varphi}_1, \dot{\varphi}_2]^T$ is the system state vector,

$$Q_\varphi(\dot{\varphi}_1, \dot{\varphi}_2) = \frac{1}{2} \delta_\varphi^2, \quad Q_H(x) = \frac{1}{2} (H(x) - H_*)^2, \quad (9.22)$$

$$H(x) = \frac{1}{2} \dot{\varphi}_1^2 + \omega^2(1 - \cos \varphi_1) + \frac{1}{2} \dot{\varphi}_2^2 + \omega^2(1 - \cos \varphi_2) + \frac{k}{2}(\varphi_1 - \varphi_2)^2 \quad (9.23)$$

stands for the total energy of the system, $\delta_\varphi = \dot{\varphi}_1 - \dot{\varphi}_2$ is the synchronization error, H_* is the desired energy value, and $\alpha > 0$ is the weight coefficient. Obviously, the minimum (zero) value of the objective function corresponds to the synchronous movement of the pendulums at a given level of the entire system oscillations energy.

The SG algorithm in the *final form*, designed for such an objective function, has the form

$$\begin{aligned} u(t) &= -\gamma(\alpha\delta_\varphi(t) + (1 - \alpha)\delta_H(t)\dot{\varphi}_1(t)), \\ \delta_\varphi(t) &= \dot{\varphi}_1(t) - \dot{\varphi}_2(t), \\ \delta_H(t) &= H(x(t)) - H_*, \end{aligned} \quad (9.24)$$

where $\gamma > 0$ is the gain.

The simulation results show that the SG algorithm (9.24) creates a synchronous regime in the system with two degrees of freedom (two coupled pendulums), and at a low friction coefficient $\rho > 0$, an energy close to the specified H_* can be achieved at a low gain $\gamma > 0$, i.e., the system exhibits the feedback resonance effect.

A similar problem is considered in [27], where the control law is synthesized by the SG method with an energy goal functional. The analysis of the system is carried out according to a simplified model of its dynamics. The results of both computer simulation and experiments on the laboratory setup demonstrated the efficiency of the adopted control method.

The problem of raising the Furuta pendulum up is analyzed in [28] by comparing the results obtained using the traditional Åström–Furuta strategy based on a model of dimension two with a new strategy, based on the SG law on a manifold of dimension three. A counterexample is given where the new law works well but the old one does not. The problem of bringing the Furuta pendulum to the top position is usually solved by a hybrid controller, in which the global problem is divided into two stages. First, the pumping of energy brings the pendulum to a vertical position. The pendulum then stabilizes in this position. In [29], different control strategies for both problems are analyzed both by simulation and using a real laboratory pendulum. The problem of raising the Furuta pendulum is solved in [30] by applying the SG method to a model of a system with dimension four. The new law is compared to the traditional Åström–Furuta strategy based on a two-dimensional model. The results of a comparative analysis, including modeling and experiments, which show the advantages and efficiency of the proposed swinging law, are presented.

The problem of stabilizing the vertical position of a spherical pendulum is discussed in detail in [31]. This problem is reduced to stabilization of the stable manifold Ω_{st} of the vertical position of a free spherical pendulum. It is shown that for any smooth feedback control obtained using the SG algorithm to stabilize Ω_{st} , the closed-loop system has a limit cycle Γ that does not belong to the desired attractor Ω_{st} .

In [32], the available results on the stabilization of invariant sets for nonlinear systems based on the SG method and the notion of V -detectability are generalized and extended. The results on the control of oscillations of a pendulum, a pendulum on a trolley, and a spherical pendulum are presented. The algorithm providing the global attractiveness of the vertical (unstable) equilibrium position of the pendulum, based on the discontinuous version of the SG energy method, is obtained in [33]. It is shown that global attractiveness cannot be obtained using continuous static state feedback. A detailed global analysis of the transient behavior of a closed-loop system is presented. In addition, it is shown that the global attractiveness of the vertical equilibrium position can be achieved by applying an arbitrarily small control action.

In [34], the problem of numerical computation of the *excitability index* for oscillatory systems is considered. It is shown that excitation by the SG method provides an exact solution to the problem of achieving the maximum energy for a second-order linear oscillator over an infinite time interval. The upper and lower limits of the total energy of the system in the steady oscillations mode and the excitability index were estimated. The exact value of the available energy of the system is found for the harmonic excitation case.

SG algorithm for control of nonlinear oscillations of a dynamical system for the regulation and tracking problems is presented in [35]. The *Colpitts oscillator*, see [36], which has a chaotic behavior, is taken as an example. The algorithm uses only

structural information about the dynamic model to designing the control law and can globally asymptotically converge to the given regular orbits or fixed points.

In [37], the problems of excitation and synchronization of oscillations in a double-coupled double pendulum mechatronic system are considered. Hardware, communication interface, and software for laboratory experiments and control are described. The pulse-modulated control law for excitation/synchronization of oscillations is obtained by means of the SG method. Laboratory experiments were performed to check and evaluate the parameters of the adopted mathematical model. The comparison results of simulation and laboratory experiments for excitation and synchronization analysis are presented.

The authors of [38] have used adaptive gain tuning in time-delayed feedback for improving the control quality. The adaptive controller proposed in [38] is used to stabilize an unstable fixed point and an unstable periodic orbit built into a chaotic attractor. The adaptation algorithm is designed by means of the SG method. Computer simulations presented in [38] show that the adaptation algorithm can find a suitable feedback gain for single and multiple delays. In addition, the [38] method is shown to be robust against noise and variations of the initial conditions.

The problem of adaptive synchronization of two connected non-identical models of Hindmarsh–Rose neurons is considered in [39]. It is shown that the use of the developed controller based on the SG method ensures achievement of the synchronous behavior of the systems under study. The results obtained are mathematically verified and illustrated by the simulations.

The problem of controlling pendulum mechanisms is discussed in [40]. The Hamiltonian formalism is used to describe the pendulum's dynamics. An algorithm for achieving equal energy values of oscillating pendulums by means of feedback control based on the SG method is proposed. The conditions for the attainability of the control goal are obtained. A connection has been established between the synchronization of energy and the frequency of oscillations. The results of computer simulations are presented, demonstrating the control goal achievement and showing the dynamic properties of a closed-loop system.

In [41], the problem of controlling the energy of a pendulum in the presence of an irregular input disturbance is considered. The feedback control law based on the SG method is designed. The main result is the precise estimates for the initial set and the final set (attractor), as well as conditions guaranteeing that all solutions starting in the initial set reach the attractor in a finite time.

Using the example of controlling the pendulum energy, in [42], the problem of controlling a nonlinear system on an invariant manifold using quantized state feedback is considered. A SG feedback control law is employed. The main result of [42] is an accurate description of the limits of the allowable quantization error and the resulting limits of the energy deviation.

In [43], the problems of energy control for the Frenkel–Kontorova model are posed and their connection with the control of pendulum chains is discussed. An energy control algorithm based on the SG method is proposed and analyzed. Simulation results are presented, illustrating the proposed algorithm convergence.

9.4 Control of Technical Systems

9.4.1 Control of Vibrating Machines

In [44, 45], the problem of controlled passage through the resonance zone for mechanical systems with several degrees of freedom is investigated. In [44], a control algorithm has been developed based on the SG method and the estimation of the slow motion frequency near resonance (“*Blechman frequency*”). The simulation results of two-rotor flexible vibrating plants are presented, demonstrating the efficiency of the proposed algorithms and the fractal dependence of the transient time on the initial conditions. A feature of the research given in [45] is the study of the operation of a closed-loop system, taking into account the dynamics of an electric drive. It was found that the time of passage through the resonance zone may turn out to be shorter than for the simplified model without taking into account the dynamics of the electric drive. Research was continued in [46]. It is noted that the existing control algorithms based on the SG method require measuring the full state vector of the system. To eliminate this drawback, a control algorithm based on a partial observer has been developed to estimate the vertical velocity of the supporting body. The proposed observer is based on a simplified nonlinear model of a two-mass oscillatory system. The efficiency of controlled passage through the resonance zone with a control algorithm based on the proposed observer is analyzed using computer simulations for a complete model of a mechanical system.

The work [47] is devoted to the control of vibrations of mechanical systems during start-up and passing through resonant modes. In both cases, the control algorithm is based on the SG method with energy-based objective functions. It is shown that for Hamiltonian systems with one degree of freedom, in the general case, it is possible to move the system from any initial state to any final state using a control force of arbitrarily low intensity. A controlled passage through resonance on a vibration machine with five degrees of freedom with the presence of friction forces is investigated. Simulations have shown that the use of feedback control makes it possible to pass through a lower resonance with a lower control intensity compared to passing through a resonance with a constant control torque. A feature of [47] is the consideration of the case when constant control torques do not allow the rotors to even start rotating. The use of closed-loop control allows the rotors to overcome gravity and start rotating. In [47], a comparison of the simulation results with the experimental ones obtained on the SV-2M double-rotor laboratory mechatronic setup of the Institute for Problems in Mechanical Engineering of the Russian Academy of Sciences (IPME RAS), which includes unbalanced vibration exciters installed on a spring-loaded platform, sensors, electric motors, control computer, interface for data exchange, cf. [48–51], is presented. Most of the results are in qualitative agreement, which confirms the adopted model adequacy.

Results of an experimental study of the phenomenon self-synchronization and Sommerfeld effect [52, 53] in both open and closed control loops are presented in [49]. Experiments were performed on a multiresonant mechatronic laboratory setup

SV-2M. It is shown that closed-loop control based on the SG method allows more accurate stabilization of the rotation speed than the open-loop control of motors usually used in vibration technology. Some additional effects such as low-frequency self-oscillation may appear due to the integral (I) component feedback control signal.

In [54], the synchronization of a controlled unbalanced rotor with a viscoelastic base and force excitation is studied. By the method of direct separation of motion, the conditions for the existence and stability of the synchronous mode of motion are derived for the general control law. Then, using the SG method, a control law is developed to transfer the maximum energy from the excitation to the rotor. The free parameters of the control law are derived in such a way that the controlled synchronization is stable at the bound of its existence.

The authors of [55] consider the problem of controlling the number of the electric machine rotor cycles slipping using the influence of an external moment using a simple mathematical model as an example. To solve the problem, the SG method was used with an objective function determined by the function of the vibration energy. A feature of this approach is the possibility of using a sufficiently small control, which contributes to energy conservation. An algorithm for controlling the oscillations of the rotor of an electric machine is designed, using which a given number of cycle slips occurs. In [56], the use of the SG and relay algorithms is compared. In the simulation, the task is to perform the desired number of cycle slips at the beginning, and then excite the rotor oscillations with a constant amplitude. The simulation results showed the efficiency of the proposed algorithms.

In [57], the adaptive estimation of unknown parameters and states of a spherical robot with a pendulum drive is considered. For this purpose, the following generalized problem is considered: for a nonlinear plant model in the form $\dot{x} = f(x, p, u)$, where $x \in \mathbb{R}^n$, $p \in \mathbb{R}^k$, find the estimate $\hat{x} = f(\hat{x}, \hat{p}, u)$ for ensuring the goal condition $\lim_{t \rightarrow \infty} |p - \hat{p}(t)| = 0$. To use the SG method, the following objective functional

is introduced: $J(x, \hat{x}) = \frac{1}{2} \sum_{i=1}^n w_i e_i^2$, where $e_i = \hat{x}_i - x_i$, w_i are the weight coefficients chosen by the developer; $i = 1, \dots, n$. The SG design method leads to the following expressions: $\dot{J} = \frac{\partial J}{\partial t} + \hat{f}(\hat{x}, \hat{p}, u)^T \nabla_{\hat{x}} J = \sum_{i=1}^n w_i e_i \left(\dot{e}_i + \hat{f}_i(\hat{x}, \hat{p}, u) \right) = \sum_{i=1}^n w_i e_i \left(2\hat{f}_i(\hat{x}, \hat{p}, u) - f_i(x, p, u) \right)$. The result is the following SG estimation law:

$$\dot{\hat{p}} = -\Gamma \nabla_{\hat{p}} \left(\sum_{i=1}^n w_i e_i \hat{f}_i(\hat{x}, \hat{p}, u) \right). \quad (9.25)$$

Algorithm (9.25) is applied in [57] for real-time estimation of states and unknown parameters of a spherical robot for various values of the step length and the initial conditions. For adaptive adjustment of this gain, a heuristic fuzzy-logic controller is used. The simulation results presented in [57] show that the proposed approach is quite encouraging to identify this nonlinear chaotic system, even if the initial conditions change and the level of uncertainty increases.

9.4.2 Control of Vehicles

9.4.2.1 Regulation of the Speed of Heavy Vehicles.

Authors [58] consider the problem of longitudinal speed control of heavy vehicles equipped with variable compression brakes. Nonlinear controllers have been developed that perform both non-critical and critical maneuvers. The design technique is based on the SG method. The nominal objective function is selected to solve the speed control problem, and then it is modified accordingly by introducing the barrier functions to meet the critical requirements of the maneuver. In order to perform more aggressive (critical) braking maneuvers or to control the vehicle speed during large slope changes, the compression brake should be matched with the gear ratio control and the friction brakes. Two ways of controlling under the condition of the road slope uncertainty are discussed: by using the integral action of the SG controller for constant (but unknown) slopes and by using an additional differential action for various slopes.

9.4.2.2 Controlling the Operation of Gasoline Engines with Direct Injection Stratified Charge.

The SG method is used in [59] to develop a law for coordinated air-to-fuel ratio control and torque control in *direct injection stratified charge gasoline engines* (DISCE). The method is based on dynamic minimization of the objective function.

The following process model is used in [59]:

$$\dot{x} = f(x) + g(x)u, \tag{9.26}$$

where the state vector $x = [p_m, W_f, \delta]^T$ and the control vector $u = [u_{th}, u_f, u_\delta]^T$ are the sum of the pressure in the intake manifold p_m , the effective flow area of the throttle valve u_{th} , the flow through the throttle W_f , and ignition time δ . For introducing the integral action into the control law, it is assumed that W_f and δ are governed by the following equations: $\dot{W}_f = u_f, \dot{\delta} = u_\delta$.

For the controller design, the objective function $Q = Q_p + Q_b$ is used, where

- Q_p is *transient penalty*—squared deviations the moment of braking of the motor, the flow through the cylinders, and the ignition time from their settings;
- Q_b is a *penalty for violating the constraint* $\lambda \in [\lambda_{\min}, \lambda_{\max}]$, where $\lambda(t)$ is the air-to-fuel ratio inside the cylinder.

The control goal is to stabilize the desired equilibrium state $x = x_d$ so that $f(x_d) + g(x_d)u_d = 0$, minimizing $Q(x(t))$ to ensure $\dot{Q}(x(t)) \rightarrow 0$.

For the selected objective function Q , the speed gradient is $\omega(x) \equiv \nabla_u \dot{Q}(x(t), u) = \left(\frac{\partial Q_p}{\partial x} g(x)\right)^T + \left(\frac{\partial Q_b}{\partial x} g(x)\right)^T$. Then, for the considered objective function, the SG method leads to the following control law:

$$u = u_d - \Gamma\omega(x). \quad (9.27)$$

In [59], the numerical procedure that can be used in practice to test the stability conditions of the considered feedback system is proposed.

9.4.2.3 Adaptive Control of an Autonomous Underwater Manipulation Robot.

Papers [35, 60, 61] are devoted to the adaptive control of an autonomous underwater vehicle (AUV) with a manipulator. In [35, 60, 61], a nonlinear adaptive AUV control system with six degrees of freedom based on the SG method has been developed. Based on the adaptive approach, the problems of positioning and kinematic tracking are solved together. To develop a control algorithm, no prior knowledge of the parameters of the dynamics and hydrodynamics of the AUV is required, except for the dynamics of the engine. The adaptation was carried out using a nonlinear adaptive SG control law. The design takes into account the dynamics of the motors using the method of reverse dynamics and observation of the state/disturbance.

In [60], a class of fully controlled AUVs with two planes of symmetry and six degrees of freedom is considered. The AUV dynamics model is based on the results of [62, 63] and has the following form:

$$M\dot{\mathbf{v}} = -C(\mathbf{v})\mathbf{v} - D(|\mathbf{v}|)\mathbf{v} + \mathbf{F}_b(\eta) + \mathbf{F}_c + \mathbf{F}_t, \quad (9.28)$$

$$\dot{\eta} = J(\eta)\mathbf{v} \quad (9.29)$$

with system matrices $M(t) = M_b(t) + M_a(t)$, $C(t, \mathbf{v}) = C_b(t, \mathbf{v}) + C_a(t, \mathbf{v})$, where M_b is the inertia matrix of the body, M_a denotes the matrix of added masses (mass of the surrounding fluid), and $C_b(t, \mathbf{v})$, $C_a(t, \mathbf{v})$ are Coriolis and centripetal matrices, $D(|\mathbf{v}|) = D_l + D_q \text{diag}(|\mathbf{v}|)$. The following generalized coordinates and velocities are introduced into (9.28), (9.29): $\eta = [x, y, z, \varphi, \theta, \psi]^T$ is the generalized position in the frame of reference fixed to the Earth, $\mathbf{v} = [u, v, w, p, q, r]^T$ is the vector of the generalized velocity on the trajectory of the AUV in the body reference frame, $J(\eta)$ is the rotation matrix with Euler angles (φ, θ, ψ) , \mathbf{F}_b stands for the pure buoyancy force, \mathbf{F}_c is the rope reaction force, and \mathbf{F}_t denotes the generalized thrust.

From (9.29), it follows that $\mathbf{v} = J(\eta)^{-1}\dot{\eta}$. With the substitution of this relation in (9.28), the AUV model takes the form

$$M_\eta(\eta)\ddot{\eta} + \frac{1}{2}\dot{M}_\eta(\eta)\dot{\eta} + D_\eta(\mathbf{v}, \eta)\dot{\eta} + g_\eta(\eta) = \tau_\eta, \quad (9.30)$$

where τ_η is the generalized controlling torque. By introducing the orientation and speed errors as $\tilde{\eta}(t) = \eta(t) - \eta^*(t)$, $\tilde{\mathbf{v}}(t) = \mathbf{v}(t) - \mathbf{v}^*(t)$ in [60] the following tracking problem is posed: to ensure the limiting relations $\lim_{t \rightarrow \infty} \tilde{\eta}(t) = 0$, $\lim_{t \rightarrow \infty} \tilde{\mathbf{v}}(t) = 0$.

To solve this problem in [60], the *energy estimation functional* $Q(\tilde{\eta}, \tilde{\mathbf{v}}) = \frac{1}{2} \tilde{\eta}^T \tilde{\eta} + \frac{1}{2} \tilde{\mathbf{v}}^T M \tilde{\mathbf{v}}$ is employed and the following control aim is chosen: $Q(\tilde{\eta}, \tilde{\mathbf{v}}) \rightarrow 0$ for $t \rightarrow \infty$. The SG design procedure consists of the following steps: $\dot{Q}(\eta, \mathbf{v})$, therefore $\nabla_{\tau} \dot{Q}(\eta, \mathbf{v})$, and finally the SG control law has the form $\tau(\eta, \mathbf{v}, \tilde{\eta}, \tilde{\mathbf{v}})$.

Due to the AUV parameters uncertainty, the following SG adaptive control law was used

$$\dot{U}_i = -\Gamma_i \frac{\partial \dot{Q}(U_i)}{\partial U_i}, \quad i = 1, \dots, 6, \tag{9.31}$$

where U_i are the matrix controller parameters and $\Gamma_i = \Gamma_i^T > 0$ are the adaptation gains. In [60, 61], the simulation results are presented which demonstrate the features of the proposed approach.

The approach to direct adaptive control and the development of a fast navigation system for 3D tracking of all-wheel drive remote controlled vehicles is presented in [64], where the SG algorithm is combined with the time-optimal tracking law.

9.4.2.4 Neural Network Control System for Underwater Robot

Works [65–67] are devoted to the design of control systems for an underwater robot based on an intelligent neural network. A new learning algorithm for an intelligent controller is obtained using the SG method. The proposed systems provide robot dynamics close to the desired one.

Let us present the results of [67] in more detail. As an initial model of an underwater robot (UR), [67] uses its standard description in the form of a set of kinematic and dynamic equations [68]

$$\dot{q}_1 = J(q_1)q_2, \tag{9.32}$$

$$D(q_1)\dot{q}_2 + B(q_1, q_2)q_2 + G(q_1, q_2) = U, \tag{9.33}$$

where J denotes the kinematic matrix; q_1, q_2 are the vectors of generalized coordinates and velocities of UR in the body-frame reference system; U is the vector of control forces and moments; D is the matrix of inertia taking into account the added mass of water; B denotes the matrix of Coriolis and centrifugal forces; and G is the vector of generalized forces and moments of gravity, buoyancy, and non-linear damping. In [67], it is proposed to overcome the existing incompleteness of a priori information about the parameters of the UR model based on intelligent neural network (NN) control.

The problem is to track the UR of a given trajectory $q_1^*(t), q_2^*(t)$. Tracking the velocities $q_2^*(t)$ is discussed first. Tracking error $e_2(t) = q_2^*(t) - q_2(t)$ is introduced, with respect to which the following local goal functional is constructed

$$Q = \frac{1}{2} e_2^T D e_2 \quad (9.34)$$

with some matrix $D(t) = D(t)^T > 0$. Following the SG method, the derivative \dot{Q} is calculated by virtue of system (9.34):

$$\dot{Q} = e_2^T D \dot{e}_2 + \frac{1}{2} e_2^T \dot{D} e_2, \quad (9.35)$$

whence, after substitutions, one obtains

$$\dot{Q} = e_2^T (D(q_1) \dot{q}_2^* + B(q_1, q_2) q_2^* + G(q_1, q_2) - U). \quad (9.36)$$

It is proposed to implement the UR control law using a two-layer NN [69], i.e., as

$$U = W f(w, x), \quad (9.37)$$

where W is the matrix of the transfer coefficients from the neurons of the inner (hidden) layer to the output neurons, $f(\cdot)$ are the activation functions of the neurons of the hidden layer, and w is the matrix of the transfer gains from the input neurons to the neurons of the hidden layer.

Expressions (9.36), (9.37) lead to the following formula for the derivative of the objective function rate of change with respect to the coefficients of matrix W :

$$\frac{\partial \dot{Q}}{\partial W} = -e_2 f^T(w, x). \quad (9.38)$$

The neuron activation functions are taken in the exponential form $f(w, x) = 1/(1 + e^{-\tau w x})$ with some $\tau > 0$.

Paper [67] is illustrated by the computer simulation results.

9.4.3 Control of Power System

The problem of controlled synchronization of a multi-machine power system with losses is considered in [70], where conditions for the existence of invariants in the system are obtained and a synchronization algorithm based on the SG method is developed for the objective function penalizing for deviations from the existing invariant. The quality evaluation of the closed-loop system is made based on the simulation results.

Works [71, 72] present an inverse optimal neural controller according to the SG method for nonlinear systems with discrete time in the presence of external disturbances and parameter uncertainties for a power system with various types of

faults in transmission lines, including the load fluctuations. The controller is based on a discrete-time recurrent high-order neural network (RHONN) trained using an algorithm based on the extended Kalman filter (EKF). In [72], a simplified neural model of a synchronous machine to stabilize a nine-bus system in the presence of a fault in three different cases on the transmission lines is proposed.

The problem of increasing the stability and quality of operation of electrical networks using control is considered in [73]. In this work, the approach based on the use of an invariant function depending on system variables and the SG method for control synthesis, proposed in [70], has been expanded. Namely, changes have been made to the algorithm of [70] for more flexibility in the control system design. The stability and performance of a closed-loop system for a network consisting of three generators has been studied. The simulation results are presented to illustrate the system dynamics.

9.4.4 Control of Gyroscopes

Works [74, 75] are devoted to the control of nonlinear oscillations of an annular vibrating microgyroscope, the resonator of which is a thin elastic ring of thickness h connected to the base by means of eight semicircular spokes [76, 77]. The center line of the resonator in the undeformed state has the form of a circle of radius R . Its oscillations are excited and recorded by the system of control and measuring electrodes. In [74, 75], the errors of a vibrating microgyroscope arising from the nonlinear elastic properties of the ring resonator material are studied. The aim of [74, 75] is to synthesize the control law for resonator oscillations to reduce the effect of nonlinear elasticity of the ring material on the gyroscope errors. Using the SG method, a control law of the potentials of the electrodes is designed, which allows maintaining a given amplitude of the normal deflection of the resonator and parrying gyroscope errors arising from the nonlinear elastic properties of the material.

For describing the resonator dynamics, the quantities v , w are introduced, which stand for the elastic displacements of the resonator ring element in the circumferential and radial directions, respectively. To simplify the solution, a single-mode approximation is used, i.e., it is assumed that $w = f \sin(n\varphi) + g \cos(n\varphi)$, where n is the number of the oscillation mode of the resonator; $f = f(\tau)$, $g = g(\tau)$ are functions of dimensionless time $\tau = \omega_n t$, determined by a system of two nonlinear differential equations of the second order obtained from the equation of normal deflection using the Bubnov–Galerkin procedure. The right-hand sides of the equations for $f(\tau)$, $g(\tau)$ contain the control voltages \tilde{U}_1 (for f) and \tilde{U}_2 (for g), which are taken in the form

$$\tilde{U}_1 = u_1 \sin \tau + u_2 \cos \tau, \quad (9.39)$$

$$\tilde{U}_2 = u_3 \sin \tau + u_4 \cos \tau, \quad (9.40)$$

where u_1, \dots, u_4 are the slowly changing control actions.

For studying the system by the Krylov–Bogolyubov averaging method [78], the following change of variables was performed:

$$f = p_1 \sin \tau + q_1 \cos \tau, \quad g = p_2 \sin \tau + q_2 \cos \tau, \quad (9.41)$$

where slowly changing variables p_1, q_1, p_2, q_2 are introduced.

Further, the equations of the system are represented in the Hamiltonian form:

$$q_i = \varepsilon \left(\frac{\partial H}{\partial p_i} - \frac{1}{2} \gamma q_i \right), \quad p_i = \varepsilon \left(\frac{\partial H}{\partial q_i} - \frac{1}{2} \gamma p_i \right), \quad i = 1, 2 \quad (9.42)$$

with the Hamilton function

$$H = -1/2v(p_2q_1 - p_1q_2) - 1/8\xi(p_2q_1 - p_1q_2)^2 + 3/32\xi(q_1^2 + p_1^2 + q_2^2 + p_2^2)^2 + 1/2(p_2u_1 + q_1u_2 + p_2u_3 + q_2u_4). \quad (9.43)$$

Coefficient γ in (9.42) corresponds to the system damping (the energy dissipation). In [74, 75], it is shown that in the absence of damping ($\gamma = 0$), functions

$$G_1 = q_1^2 + p_1^2 + q_2^2 + p_2^2, \quad G_2 = p_2q_1 - p_1q_2 \quad (9.44)$$

are the first integrals of system (9.42), which makes it possible to reduce the problem of nonlinear oscillations of a ring resonator to quadratures.

The considered problem of excitation and stabilization of oscillations of a ring resonator is formalized in [74, 75] using scalar objective functions G_1, G_2 , while the control goal is set as reaching the limit equality

$$\lim_{t \rightarrow \infty} G_i = G_i^*, \quad i = 1, 2, \quad (9.45)$$

where $G_1^* = r_\infty^2, G_2^* = 0$.

For exciting and maintaining a given amplitude of the resonator oscillations in the form of a standing wave, the following quadratic objective function is introduced

$$V = 0.5(\zeta(G_1 - G_1^*)^2 + (1 - \zeta)G_2^2), \quad (9.46)$$

where $0 \leq \zeta \leq 1$ is the weight coefficient chosen during the synthesis.

The control algorithm is derived based on the SG method. For this, the time derivative \dot{V} of function (9.46) is calculated

$$\dot{V} = \zeta(G_1 - G_1^*)\dot{G}_1 + (1 - \zeta)G_2\dot{G}_2, \quad (9.47)$$

where the derivatives of functions G_i due to (9.42) have the form

$$\begin{aligned} \dot{G}_i &= \varepsilon(-\gamma G_i + \mathbf{u}^T \{\bar{\mathbf{H}}, G_i\}), \quad i = 1, 2, \\ \bar{\mathbf{H}} &= 1/2(p_1, q_1, p_2, q_2)^T, \quad \mathbf{u} = (u_1, u_2, u_3, u_4)^T, \end{aligned} \tag{9.48}$$

where \mathbf{u} is the control vector and $\{\bar{\mathbf{H}}, G_i\}$ is the column vector of Poisson brackets [79].

For objective function (9.46), the following SG algorithm in the final form is derived

$$\mathbf{u} = -\eta (\zeta (G_1 - G_1^*) \{\bar{\mathbf{H}}, G_1\} + (1 - \zeta) G_2 \{\bar{\mathbf{H}}, G_2\}), \tag{9.49}$$

where $\eta > 0$ is the control gain.

Further, in [74, 75], an analysis of the properties of a closed-loop system with SG algorithm is performed. To this end, the influence of gain η on the form of phase trajectories and on the location of singular points in the space (G_1, G_2) is examined, and the relations for choosing weight coefficient ζ in (9.46) are found, which provide the highest degree of damping of oscillations depending on the model parameters.

9.4.5 Control of Induction Motors

9.4.5.1 Starting Induction Squirrel-Cage Motor

Paper [80] is devoted to the problem of soft start of an induction electric motor (IM) with a squirrel-cage rotor. An unsatisfactory dynamics of the starting processes of the IM was noted, which is especially pronounced in electric drives with frequent starts or operating in intermittent mode. To improve the starting processes of the IM, one can use a soft starter, i.e., a special starter based on power semiconductor devices. In [80], the control law is proposed for smooth start of IM based on the SG method based on the assumption that at a constant frequency of the supply voltage, the starting device is capable of changing its amplitude at an infinitely high speed.

To describe the starting process in [80], the following model of a generalized two-phase electric machine is used, written for the coordinate system x - y , rotating synchronously with the stator voltage vector:

$$\dot{x} = A(x) + B(x)u, \tag{9.50}$$

where

$$A(x) = \begin{bmatrix} -\frac{R_1}{L_1}\psi_{1x} + \frac{R_1}{L_1}k_2\psi_{2x} + \omega_0\psi_{1y} \\ -\frac{R_1}{L_1}\psi_{1y} + \frac{R_1}{L_1}k_2\psi_{2y} + \omega_0\psi_{1x} \\ -\frac{R_2}{L_2}\psi_{2x} + \frac{R_2}{L_2}k_1\psi_{1x} + (\omega_0 - p\omega)\psi_{2y} \\ -\frac{R_2}{L_2}\psi_{2y} + \frac{R_2}{L_2}k_1\psi_{1y} - (\omega_0 - p\omega)\psi_{2x} \\ \frac{1}{J}(M - M_c) \end{bmatrix}, \quad B = \begin{bmatrix} 1 \\ 0 \\ 0 \\ 0 \\ 0 \end{bmatrix}, \quad (9.51)$$

$u = U_m$, $x = [\psi_{1x} \ \psi_{1y} \ \psi_{2x} \ \psi_{2y} \ \omega]^T$ are the components of stator (index 1) and rotor (index 2) flux linkages; R_1, R_2, L_1, L_2 are active resistances and total inductances of the stator and rotor, respectively; ω_0, ω are frequencies of the field and rotor rotation, respectively; p is the number of pole pairs; $M = c(\psi_{1y}\psi_{2x} - \psi_{1x}\psi_{2y})$ denoted the electromagnetic torque developed by the motor; M_c is the moment of resistance; J stands for the moment of inertia of the electric drive; $k_1 = L_m/L_1$; $k_2 = L_m/L_2$; L_m is the inductance of the magnetizing circuit.

Two control objectives are posed: stabilization of the torque and stabilization of the flux linkage vector modulus. The first goal is aimed at minimizing the pulsations of the electromagnetic moment, and the second is to exclude saturation of the magnetic system. These control goals are expressed by means of the local goal functional

$$Q(x, t) = \frac{1}{2}(y - y^*)^T H(y - y^*), \quad (9.52)$$

where $y = [M \ \psi_1^2]^T$ is the vector of controlled quantities; $y^* = [M^* \ \psi_1^{*2}]^T$ is the vector of reference actions; H denotes the unit matrix of order 2; $\psi_1^2 = \psi_{1x}^2 + \psi_{1y}^2$ is the square of the modulus of the stator flux linkage vector; and M^*, ψ_1^{*2} are the desired values of the electromagnetic moment and the squared modulus of the stator flux linkage vector, respectively.

The controlled plant (9.51) is affine in input, and therefore the SG algorithm in the integral form is as follows:

$$u = \int (-\Gamma B(x)^T C^T H(y - y^*)) dt, \quad (9.53)$$

where $\Gamma = \Gamma^T > 0$, $C = \frac{\partial y(x)}{\partial x}$ is the Jacobi matrix for the vector of controlled variables. Taking into account (9.50), (9.52), the following control algorithm is derived:

$$U_m = -\gamma \int (2\psi_{1x}(\psi_1^2 - \psi_1^{*2}) - \psi_{2y}(MM^*)) dt, \quad (9.54)$$

where $\gamma > 0$ is the selected control gain.

In [80], the proposed control algorithm was simulated for induction motor 4A80A4U3. The results showed that when using the (9.54) algorithm, the time histories of the electromagnetic torque and flux linkage module have much less ripple than when starting by direct connection to the power network.

9.4.5.2 Multi-motor Drive Control

The task of controlling a multi-motor induction drive is discussed in [81]. The problem is posed to ensure the coordination of the values of the electromagnetic torque developed by each of the n IM, maintaining the value of the total torque M_Σ at the required level. In addition, it is required to maintain the values of each IM at a given level.

Paper [81] uses the following mathematical model of the set of induction motors working on one shaft:

$$\dot{x} = A(x, t) + B(x, t)u, \quad (9.55)$$

where $x = \text{col}\{x_1, \dots, x_i, \dots, x_n\}$ is a column vector composed of the state vectors of each motor $x_i = [\psi_{1\alpha,i}, \psi_{1\beta,i}, \psi_{2\alpha,i}, \psi_{2\beta,i}, \omega]^T$, $i = 1, \dots, n$, ψ denote components of the stator and rotor flux linkage vectors, ω is the rotor angular velocity, and $u_i = [u_{1,\alpha}, u_{1,\beta}]^T$ are the components of the voltage vector supplied to the IM stator in a fixed coordinate system $\alpha\text{--}\beta$ (control vector). The matrix A has a block form. The vector of deviations of the controlled variables $[y(t) - y^*(t)]$ is introduced, where its individual components are as follows:

$$[y(t) - y^*(t)] = \begin{bmatrix} [p_i \sigma_i L_{12,i} (\psi_{1\beta,i} \psi_{2\alpha,i} - \psi_{1\alpha,i} \psi_{2\beta,i}) - M_i^*(t)] \\ [\psi_{1\alpha,i}^2 + \psi_{1\beta,i}^2 - \psi_{1,i}^{*2}] \end{bmatrix}, \quad (9.56)$$

where $L_1 = L_{12} + L_{\sigma 1}$, $L_2 = L_{12} + L_2$ are the total stator and rotor inductances, respectively; $\sigma = 1/(L_1 L_2 - L_{12}^2)$ denotes the engine dissipation factor; p is the number of pole pairs; and M^* is the desired electromagnetic torque of the motor.

For designing the control algorithm, a following local goal functional is introduced:

$$Q(x, t) = 0.5(y(t) - y^*(t))^T H(y(t) - y^*(t)). \quad (9.57)$$

Applying the SG method for goal functional (9.57), expressions were found for the components of the voltage vector at the output of the frequency converter, which ensure the achievement of the posed control goal. It is noted that the obtained expressions are computationally laborious, and also require information on the components of the flux linkage vectors of the rotor of each IM in real time, and therefore it is difficult to apply the obtained SG algorithm in practice. To avoid these disadvantages, following [82], in [81], a number of assumptions are made, taking into account which law of torque control of a multi-motor induction drive takes the form:

$$\begin{aligned}
 u_{1\alpha} &= -\gamma \int \left(\sum_{i=1}^n \left(h_i \left(\frac{-M_i - M_i^*}{M_{Hi}} \psi_{1\beta,i} + \frac{|\psi_{1,i}|^2 - \psi_{1,i}^{*2}}{\psi_{1H,i}^2} \psi_{1\alpha,i} \right) \right) \right) dt, \\
 u_{1\beta} &= -\gamma \int \left(\sum_{i=1}^n \left(h_i \left(\frac{-M_i - M_i^*}{M_{Hi}} \psi_{1\alpha,i} + \frac{|\psi_{1,i}|^2 - \psi_{1,i}^{*2}}{\psi_{1H,i}^2} \psi_{1\beta,i} \right) \right) \right) dt. \quad (9.58)
 \end{aligned}$$

Checking the functionality of the proposed control law is performed by computer simulation for explosion-proof asynchronous electric motors DKV355L4, operating on one shaft and controlled by a single frequency converter. As a result of research, it has been shown that using (9.58) for multi-motor ID drives with group connection of motors to a frequency converter, it is possible to achieve high-quality control of the total torque of the drive with a spread of ID parameters in a wide range.

9.5 Conclusions

In the paper, the main statements of the speed-gradient method with the focus on mechanical engineering problems are presented. Such directions of the SG method applications in the fields as the problem of controlling energy and other properties of nonlinear oscillations, control of car engines, adaptive control of autonomous underwater vehicles, and identification of spherical robot parameters are reviewed. It is demonstrated that the SG method is a useful and an efficient tool for solving a wide range of engineering problems, confirming that it “enables a transparent trade-off between control performance and design parameters. Furthermore the steps for controller design results in general simple ...it has become widespread in other multiple successful applications in adaptive control mainly in Physics and Mechanics” [60]. Recent research on [83] shows that this method can also serve as a bridge between control theory and the field of machine learning, revealing the commonality of many approaches in these areas.

Acknowledgements This work was supported by the Ministry of Science and Higher Education of the Russian Federation (Project No. 075-15-2021-573 and by the grant of SPbSU No. 84912397).

References

1. Fradkov A.L.: Speed-gradient scheme and its application in adaptive control problems. *Autom. Remote Control* **40**(9), 1333–1342 (1980) (Translated from *Avtomat. i Telemekh.*, 1979, issue 9, 90–101)
2. Fomin, V.N., Fradkov, A.L., Yakubovich, V.A.: *Adaptive control of dynamical plants*, Nauka, M. (1981), (in Russian)
3. Fradkov, A.L., Stotsky A.: Speed gradient adaptive control algorithms for mechanical systems. *Int. J. Adapt. Control Signal Process.* **6**(3), 211–220 (1992). <http://dx.doi.org/10.1002/acs.4480060309>

4. Andrievskij, B., Guzenko, P., Fradkov, A.L.: Control of nonlinear oscillations in mechanical systems by the steepest gradient method. *Autom. Remote Control* **57**(4), 456–467 (1996)
5. Andrievsky, B., Konoplev, V., Koniukhov, A., Fradkov, A.L.: Control, state estimation and laboratory experiments with oscillatory mechanical system. *IFAC Proc. Vol.* **31**(17), 735–738 (1998). <https://www.sciencedirect.com/science/article/pii/S1474667017404265>
6. Fradkov, A.L., Evans, R.J., Andrievsky, B.R.: Control of chaos: methods and applications in mechanics. *Phil. Trans. R. Soc. A.* 3642279–2307 (2006). <https://doi.org/10.1098/rsta.2006.1826>
7. Efimov, D., Panteley, E., Loria, A., Fradkov, A.: Switched mutual-master-slave synchronisation: Application to mechanical systems. *IFAC Proc. Vol.* **41**(2), 11508–11513 (2008)
8. Ananyevskiy, M.S., Fradkov, A.L., Nijmeijer, H.: Control of mechanical systems with constraints: Two pendulums case study. *IFAC Proc. Vol.* **41**(2), 7690–7694 (2008)
9. Fradkov, A.L., Andrievskiy, B., Evans, R.: Hybrid quantized observer for multi-input-multi-output nonlinear systems. In: Leonov, G., Nijmeijer, H., Pogromsky, A., Fradkov, A.L. (eds.) *Dynamics and Control of Hybrid Mechanical Systems*. World Scientific Series on Nonlinear Science, Series B, vol. 14, pp. 89–102. World Scientific, Singapore (2010)
10. Fradkov, A.L., Tomchina, O.P., Tomchin, D.A.: Controlled passage through resonance in mechanical systems. *J. Sound Vib.* **330**(6), 1065–1073 (2011). <https://doi.org/10.1016/j.jsv.2010.09.031>
11. Ananyevskiy, M.S., Fradkov, A.L.: Speed-gradient control of mechanical systems with constraint. In: Belyaev, A.K., Irschik, H., Krommer, M. (eds.) *Mechanics and Model-Based Control of Advanced Engineering Systems*, pp. 21–29. Springer, Wien (2014)
12. Fradkov, A.L., Tomchin, D.A., Tomchina, O.P.: Controlled passage through resonance for two-rotor vibration unit. In: Belyaev, A.K., Irschik, H., Krommer, M. (eds.) *Mechanics and Model-Based Control of Advanced Engineering Systems*, pp. 95–102. Springer, Wien (2014)
13. Porubov, A.V., Antonov, I.D., Fradkov, A.L., Andrievsky, B.: Control of localized non-linear strain waves in complex crystalline lattices. *Int. J. Non-Linear Mech.* **86**, 174–184 (2016). <https://doi.org/10.1016/j.ijnonlinmec.2016.09.002>
14. Porubov, A., Antonov, I., Indeitsev, D., Fradkov, A.L.: Mechanical system allowing distributive control with feedback. *Mech. Res. Commun.* **93** (2018) 124–127. <http://dx.doi.org/10.1016/j.mechrescom.2017.07.014>
15. Fradkov, A.L.: *Cybernetical Physics: From Control of Chaos to Quantum Control*. Springer, Berlin-Heiderlberg (2007)
16. Andrievsky, B.R., Fradkov, A.L.: Method of speed-gradient and its applications. *Autom. Remote Control.* **9**, 5–78 (2021)
17. Fradkov, A.L., Miroshnik, I., Nikiforov, V.: *Nonlinear and Adaptive Control of Complex Systems*. Kluwer, Dordrecht (1999)
18. Fradkov, A.L., Pogromsky, A.Y.: *Introduction to Control of Oscillations and Chaos*. World Scientific Publishers, Singapore (1998)
19. Dunsakaya, N., Pyatnitskii, E.: Stabilization of mechanical and electromechanical systems. *Autom. Remote Control* **49**(12), 1565–1574 (1988)
20. Ortega, R., Spong, M.W.: Adaptive motion control of rigid robots: A tutorial. *Automatica.* **25**, 877–888 (1989)
21. Andrievsky, B.R., Churilov A.N., Fradkov A.L.: Feedback Kalman-Yakubovich lemma and its applications to adaptive control. In: *Proceedings of 35th IEEE Conference on Decision and Control, CDC'96*, pp. 4537–4542 (1996)
22. Slotine, J., Li, W.: *Applied Nonlinear Control*. Prentice-Hall, Englewood Cliffs, NJ (1990)
23. Fradkov, A.L.: Nonlinear adaptive control: Regulation-tracking-oscillations. *IFAC Proc. Vol.* **27**(11), 385–390 (1994). [https://doi.org/10.1016/S1474-6670\(17\)47680-4](https://doi.org/10.1016/S1474-6670(17)47680-4)
24. Fradkov, A.L.: Swinging control of nonlinear oscillations. *Int. J. Control.* **64**(6), 1189–1202 (1996). <https://doi.org/10.1080/00207179608921682>
25. Fradkov, A.L., Makarov, I.A., Shiriaev, A.S., Tomchina, O.P.: Control of oscillations in Hamiltonian systems. In: *Proceedings of European Control Conference, ECC'97*, 1243–1248 (1997)

26. Andrievsky, B., Fradkov, A.L.: Feedback resonance in single and coupled 1-DoF oscillators. *Int. J. Bifurcat. Chaos Appl. Sci. Eng.* **9**(10), 2047–2057 (1999). <https://doi.org/10.1142/S0218127499001486>
27. Kumon, M., Washizaki, R., Sato, J., Kohzawa, R., Mizumoto, I., Iwai, Z.: Controlled synchronization of two 1-DoF coupled oscillators. *IFAC Proc. Vol. (IFAC-PapersOnline)*. **15**(1), 109–114 (2002)
28. Acosta, J., Gordillo, F., Aracil, J.: Swinging up the Furuta pendulum by the speed gradient method. In: *Proceedings of European Control Conference, ECC 2001*, pp. 469–474 (2001)
29. Acosta, J., Aracil, J., Gordillo, F.: Nonlinear control strategies for the Furuta pendulum. *Control Intell. Syst.* **29**(3), 101–107 (2001)
30. Gordillo, F., Acosta, J., Aracil, J.: A new swing-up law for the Furuta pendulum. *Int. J. Control.* **76**(8), 836–844 (2003). <https://doi.org/10.1080/0020717031000116506>
31. Ludvigsen, H., Shiriaev, A., Egeland, O.: Stabilization of stable manifold of upright position of the spherical pendulum. *Model. Identif. Control.* **22**(1), 3–14 (2001). <https://doi.org/10.4173/mic.2001.1.1>
32. Shiriaev, A., Fradkov, A.L.: Stabilization of invariant sets for nonlinear systems with applications to control of oscillations. *Int. J. Robust Nonlinear Control.* **11**(3), 215–240 (2001). <https://doi.org/10.1002/rnc.568>
33. Shiriaev, A., Egeland, O., Ludvigsen, H., Fradkov, A.L.: VSS-version of energy-based control for swinging up a pendulum. *Syst. Control Lett.* **44**(1), 45–56 (2001). [https://doi.org/10.1016/S0167-6911\(01\)00124-4](https://doi.org/10.1016/S0167-6911(01)00124-4)
34. Andrievsky, B.: Computation of the excitability index for linear oscillators. In: *Proceedings of 44th IEEE Conference on Decision and Control, and the European Control Conference, CDC-ECC '05*, vol. 2005, pp. 3537–3540 (2005). <https://doi.org/10.1109/CDC.2005.1582710>
35. Jordán, M., Bonitatus, J.: Speed-gradient control with non-linearity in the parameters for a chaotic Colpitts oscillator. In: *Proc. Int. Conf. on Physics and Control, PhysCon 2005*, vol. 2005, pp. 266–271 (2005). <https://doi.org/10.1109/PHYCON.2005.1513991>
36. Kennedy, M.: Chaos in the Colpitt's oscillator. *IEEE Trans. Circuits Syst. I* **41**(11), 771–774 (1994)
37. Fradkov, A.L., Andrievsky, B., Boykov, K.: Control of the coupled double pendulums system. *Mechatronics*. **15**(10), 1289–1303 (2005). <https://doi.org/10.1016/j.mechatronics.2005.03.008>
38. Lehnert, J., Hövel, P., Flunkert, V., Guzenko, P., Fradkov, A.L., Schöll, E.: Adaptive tuning of feedback gain in time-delayed feedback control. *Chaos*. **21**(4) (2011). <https://doi.org/10.1063/1.3647320>
39. Semenov, D., Fradkov, A.L.: Adaptive synchronization of two coupled non-identical hindmarsh-rose systems by the speed gradient method. *IFAC-PapersOnLine*. **51**(33), 12–14 (2018). <https://doi.org/10.1016/j.ifacol.2018.12.077>
40. Fradkov, A.L., Lashkov, S., Andrievsky, B.: Energy synchronization of pendulum mechanisms. In: *Proceedings of 5th International Conference on Control, Automation, Robotics and Vision, ICARCV 2018*, pp. 1257–1262 (2018). <https://doi.org/10.1109/ICARCV.2018.8581308>
41. Seifullaev, R., Plotnikov, S.: Attractor estimates for an energy-controlled pendulum in presence of irregular bounded disturbance. *IFAC-PapersOnLine*. **51**(33), 132–137 (2018). <https://doi.org/10.1016/j.ifacol.2018.12.106>
42. Seifullaev, R., Fradkov, A.L., Liberzon, D.: Energy control of a pendulum with quantized feedback. *Automatica*. **67**, 171–177 (2016). <https://doi.org/10.1016/j.automatica.2016.01.019>
43. Fradkov, A.L., Usik, E., Andrievsky, B.: Simple energy control in Frenkel–Kontorova model. *Advanced Structured Materials*, vol. 103, pp. 209–222. Springer Nature, Switzerland (2019). https://doi.org/10.1007/978-3-030-11665-1_11
44. Tomchin, D., Tomchina, O., Fradkov, A.L.: Controlled passage through resonance for flexible vibration units. *Math. Prob. Eng.* (2015). <https://doi.org/10.1155/2015/839105>
45. Gorlatov, D., Tomchin, D.A., Tomchina, O.: Controlled passage through resonance for two-rotor vibration unit: Influence of drive dynamics. *IFAC-PapersOnLine*. **48**(11), 313–318 (2015). <https://doi.org/10.1016/j.ifacol.2015.09.204>

46. Fradkov, A.L., Tomchina, O., Tomchin, D., Gorlatov, D.: Time-varying observer of the supporting body velocity for vibration units. *IFAC-PapersOnLine*. **49**(14), 18–23 (2016). <https://doi.org/10.1016/j.ifacol.2016.07.967>
47. Fradkov, A.L. Gorlatov, D., Tomchina, O., Tomchin, D.: Control of oscillations in vibration machines: Start up and passage through resonance. *Chaos*. **26**(11) (2016). <https://doi.org/10.1063/1.4966632>
48. Andrievskii, B., Blekhman, I., Blekhman, L., Boikov, V., Vasil'kov, V., Fradkov, A.: Education and research mechatronic complex for studying vibration devices and processes. *J. Mach. Manuf. Reliab.* **45**(4), 369–374 (2016). <https://doi.org/10.3103/S1052618816030031>
49. Boikov, V., Andrievsky, B., Shiegin, V.: Experimental study of unbalanced rotors synchronization of the mechatronic vibration setup. *Cybern. Phys.* **5**(1), 5–11 (2016)
50. Andrievsky, B., Boikov, V.: Experimental study of multiresonance mechatronic vibrational laboratory set-up. *Cybern. Phys.* **6**(1), 5–12 (2017)
51. Andrievsky, B., Fradkov, A.L., Tomchina, O.P., Boikov, V.I.: Angular velocity and phase shift control of mechatronic vibrational setup. *IFAC-PapersOnLine*. **52**(15), 436–441 (2019). <https://doi.org/10.1016/j.ifacol.2019.11.714>
52. Sommerfeld, A.: Beitrage zum dynamischen ausbau der festigkeitslehre. *Z. Ver. Deut. Ing.* **46**, 391–394 (1902). (in German)
53. Blekhman, I.I.: *Vibrational Mechanics: Nonlinear Dynamic Effects, General Approach, Applications*. World Scientific, Singapore (2000)
54. Bartkowiak, R.: Controlled synchronization at the existence limit for an excited unbalanced rotor. *Int. J. Non-Linear Mech.* **91**, 95–102 (2017). <https://doi.org/10.1016/j.ijnonlinmec.2017.02.012>
55. Plotnikov, S., Fradkov, A.L., Shepeljavyi, A.: The speed-gradient algorithm in the inverse stoker problem for a synchronous electric machine. *Vestnik St. Petersburg Univ.: Math.* **51**(1), 82–86 (2018). <https://doi.org/10.3103/S1063454118010089>
56. Plotnikov, S., Shepeljavyi, A.: Energy control of electric machine: Inverse stoker problem. *IFAC-PapersOnLine*. **51**(33), 22–26 (2018). <https://doi.org/10.1016/j.ifacol.2018.12.079>
57. Roozegar, M., Mahjoob, M., Ayati, M.: Adaptive estimation of nonlinear parameters of a nonholonomic spherical robot using a modified fuzzy-based speed gradient algorithm. *Regul. Chaotic Dyn.* **22**(3), 226–238 (2017)
58. Druzhinina, M., Stefanopoulou, A., Moglegaard, L.: Speed gradient approach to longitudinal control of heavy-duty vehicles equipped with variable compression brake. *IEEE Trans. Contr. Syst. Technol.* **10**(2), 209–220 (2002). <https://doi.org/10.1109/87.987066>
59. Kolmanovsky, I., Druzhinina, M., Sun, J.: Speed-gradient approach to torque and air-to-fuel ratio control in disc engines. *IEEE Trans. Contr. Syst. Technol.* **10**(5), 671–678 (2002). <https://doi.org/10.1109/TCST.2002.801803>
60. Jordán, M., Bustamante, J.: A speed-gradient adaptive control with state/disturbance observer for autonomous subaquatic vehicles. In: *Proceedings of 45th IEEE Conference on Decision and Control, CDC 2006*, pp. 2008–2013 (2006)
61. Jordán, M., Bustamante, J.: A totally stable adaptive control for path tracking of time-varying autonomous underwater vehicles. *IFAC Proc. Vol. (IFAC-PapersOnline)* **17**(1). <https://doi.org/10.3182/20080706-5-KR-1001.3693>
62. Fossen, T.: *Guidance and Control of Ocean Vehicles*. Wiley, Chichester, UK (1994)
63. Kreuzer, E., Pinto, F.: Controlling the position of a remotely operated underwater vehicle. *App. Math. Comput.* **78**, 175–185 (1996)
64. Jordán, M., Bustamante, J.: An adaptive control system for perturbed ROVs in discrete sampling missions with optimal-time characteristics. In: *Proceedings of IEEE Conference on Decision and Control, CDC 2007*, pp. 1300–1305 (2007). <https://doi.org/10.1109/CDC.2007.4434786>
65. Dyda, A., Os'kin, D.: Underwater robot intelligent control based on multilayer neural network. *IFAC Proc. Vol. (IFAC-PapersOnline)*. **43**(20), 179–183 (2010). <https://doi.org/10.3182/20100915-3-DE-3008.00082>
66. Oskin, D., Dyda, A.: Underwater robot intelligent control based on multilayer neural network. In: *Proceedings of 2013 IEEE 7th International Conference on Intelligent Data Acquisition*

- and Advanced Computing Systems, IDAACS 2013, vol. 2, pp. 921–924 (2013). <https://doi.org/10.1109/IDAACS.2013.6663061>
67. Dyda, A., Oskin, D., Dyda, P.: An application of speed gradient method to neural network control for underwater robot. In: CEUR Workshop Proceedings, vol. 1623, pp. 689–700 (2016)
 68. Fossen, T.I.: Marine Control Systems: Guidance, Navigation and Control of Ships. Rigs and Underwater Vehicles. Marine Cybernetics, Trondheim, Norway (2002)
 69. Dyda, A.: Adaptive and Neural Network Control of Complex Dynamical Plants. Dalnauka, Vladivostok (2007). (in Russian)
 70. Pchelkina, I., Fradkov, A.L.: Combined speed-gradient controlled synchronization of multi-machine power systems. IFAC Proc. Vol. (IFAC-PapersOnline). **5**(1), 59–63 (2013). <https://doi.org/10.3182/20130703-3-FR-4039.00034>
 71. Lastire, E., Alanis, A., Sanchez, E.: Inverse optimal neural control with speed gradient for a power electric system with changes in loads. In: Proceedings of 9th International Conference on Electrical Engineering, Computing Science and Automatic Control, CCE 2012 (2012). <https://doi.org/10.1109/ICEEE.2012.6421116>
 72. Alanis, A., Lastire, E., Arana-Daniel, N., Lopez-Franco, C.: Inverse optimal control with speed gradient for a power electric system using a neural reduced model. Math. Prob. Eng. (2014). <https://doi.org/10.1155/2014/514608>
 73. Furtat, I., Tergoev, N., Tomchina, O., Kazi, F., Singh, N.: Speed-gradient-based control of power network: Case study. Cybern. Phys. **5**(3), 85–90 (2016)
 74. Gavrilenko, A., Merkurjev, I., Podalkov, V.: Algorithms for the control of oscillations of the wave solid-state gyroscope resonator. In: Proceedings of 15th Saint Petersburg International Conference on Integrated Navigation Systems, ICINS 2008, pp. 34–36 (2008)
 75. Martynenko, Y., Merkurjev, I., Podalkov, V.: Control of nonlinear vibrations of vibrating ring microgyroscope. Mech. Solids. **43**(379), 379–390 (2008). <https://doi.org/10.3103/S0025654408030102>
 76. Putty, M., Najafi, K.: A micromachined vibrating ring gyroscope. In: Proceedings of Digest, Solid-State Sensors and Actuators Workshop, Hilton Head, SC, pp. 213–220 (1994)
 77. Ayazi, F., Najafi, K.: A HARPSS polysilicon vibrating ring gyroscope. J. Microelectromech. Syst. **10**(2), 169–179 (2001)
 78. Bogoliubov, Y.A., Mitropolsky, N.N.: Asymptotic Methods in the Theory of Nonlinear Oscillations. Gordon and Breach, London (1961)
 79. Landau, L.D., Lifshitz, E.M.: Mechanics: Volume 1 (Course of Theoretical Physics), 3rd edn. Elsevier Ltd. (1976)
 80. Kashirskih, V.G., Zav'jalov, V.M., Pereverzev, S.S.: Formation of the control algorithm for the smooth start of an induction electric motor based on the speed-gradient method. Vestnik KuzGTU **2**, 7–9 (2005). (in Russian)
 81. Semykina, I.J., Zav'jalov, V.M., Glazko, M.A.: Gradient control of multi-motor induction electric drive. Izv. Tomskogo Politehn. Un-ta. **315**(4), 65–69 (2009) (in Russian)
 82. Zav'jalov, V.M.: Reduction of Dynamic Loads in Transmissions of Mining Machines. KuzGTU, Kemerovo (2008). (in Russian)
 83. Boffi, N., Slotine, J.: Implicit regularization and momentum algorithms in nonlinearly parameterized adaptive control and prediction. Neural Comput. **33**, 590–673 (2021). https://doi.org/10.1162/neco_a_01360

Chapter 10

FEM-simulations of a Chemical Reaction Front Propagation in an Elastic Solid with a Cylindrical Hole



Alexander B. Freidin, Igor K. Korolev, and Sergey P. Aleshchenko

Abstract The influence of a stress concentrator on a chemical reaction front propagation in a solid is investigated for the reaction between diffusing and deformable solid constituents. A kinetic equation is used in a form of the dependence of the reaction front velocity on the normal component of the chemical affinity tensor which in turn depends on the mechanical stresses. A plane problem for a linear-elastic body with a cylindrical hole as a concentrator is studied using numerical FEM-simulations. An analytical solution of the axially symmetric problem is used for the verifications of the numerical procedure. Then reaction front propagation in the vicinity of the hole is studied for all-round and uniaxial external loadings.

Keywords Mechanochemistry · Chemical affinity tensor · Reaction front · Stress analysis · FEM-simulations · Coupled problems

10.1 Introduction

The present paper considers a chemical reaction between diffusing and deformable solid constituents and continues studies of the propagation of chemical reaction fronts in solids which were started in [9, 11, 12] for elastic solids in the case of small strains and were extended for finite strains in nonlinear viscoelastic solids [31] and composite materials [32, 42] and were applied for modeling intermetallic phase growth in lead-free solders [29, 30]. Modeling the front propagation is based on the concept of a chemical affinity tensor. The expression of the chemical affinity tensor was derived in [8, 10] for the case of a reaction between a diffusing constituent and deformable solid of an arbitrary rheology from the analysis of fundamental laws and the entropy inequality (see also Appendix in [9], and a review [13] where a state of the art and references are also presented). Earlier the chemical affinity tensor was derived for the case of nonlinear reaction constituents in [7] similar to how it was

A. B. Freidin (✉) · I. K. Korolev · S. P. Aleshchenko
Institute for Problems in Mechanical Engineering RAS, V.O., Bolshoy pr., 61,
St. Petersburg 199178, Russia

done for nonlinear-elastic phases in the case of propagating interface in the case of stress-induced phase transformations [19].

It was shown that the energy dissipation due to the propagation of a chemical reaction front equals to the product of the reaction rate at the oriented surface element by the normal component of a tensor that was naturally to call a chemical affinity tensor. Tensorial nature of the chemical affinity, analogously to the tensorial nature of a chemical potential (see discussions of a chemical potential tensor in [16]), can be explained by the fact that the reaction in a deformable solid takes place not just in a point but at an oriented surface element. Tensorial nature of the chemical potential and affinity was also pointed out in [37, 38].

The expression of the dissipation gave a hint for formulating the kinetic equation in a thermodynamically consistent form of the dependence of the reaction rate and, thus, the reaction front velocity on the normal component of the affinity tensor. This, in turn, allowed to include the influence of stress-strain state on the reaction rate through the affinity tensor.

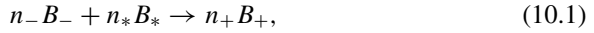
Note other approaches to the description of the influence of stresses on the reaction front propagation. Stresses may affect the reaction rate via stress-dependent diffusion coefficient, e.g., [18, 39], concentration-volumetric expansion due to diffusion [35, 36] or/and additional stress-dependent driving force in the diffusion equation [20, 21]. Another group of models includes the influence of stresses on the diffusion flux and the chemical reaction rate via a scalar chemical potential that depends not only on the concentration but also on the stresses [1–5, 20–25]. As an alternative to considerations of the transformation front as a sharp interface, phase field models have been developed, e.g., [40].

In the present paper we consider the chemical reaction front as a sharp interface across which corresponding strain compatibility conditions are satisfied. Recognizing the influence of stresses on diffusion, we focus on the stress effects via the tensorial affinity only and accept the simplest Fick's law of the diffusion. Note that even in this case stresses affect the diffusion via the boundary condition for the diffusion flux at the reaction front. This leads to coupling of stress, diffusion, and mechanochemistry problems. Since analytical solutions of the coupled boundary value problems "diffusion–chemistry–mechanics" can be obtained only for simplest cases, the problems of the chemical reaction front propagation stimulated the development of the numerical simulation methods. For example, in [14, 36], along with a development of the theoretical approach, the integral numerical methods and gradient FEM were used for the problems with the unknown internal boundary. XFEM procedure was used in [6, 43]; CutFEM approach [33] and isogeometric analysis [26, 27] were tried for problems with moving interfaces.

In the present paper we utilize the concept of the chemical affinity tensor developing a numerical procedure based on FEM and, in this sense, continue studies presented in [11, 28, 30, 32], focusing on the reaction front propagation in the vicinity of a stress concentrator, namely, in the vicinity of a cylindrical hole in a plane strain statement.

10.2 Chemical Affinity Tensor and Chemical Reaction Front Kinetics

We consider a chemical reaction of the following type:



where B_- , B_+ and B_* are the chemical formulae of the reacting constituents, B_- and B_+ are the initial and transformed deformable solid constituents, B_* is the diffusing constituent, n_{\pm} and n_* are the stoichiometric coefficients.

The following assumptions are accepted:

1. The reaction is localized at the reaction front and is sustained by the diffusion of the diffusing constituent B_* through the transformed material B_+ .
2. The diffusing constituent is completely consumed by the reaction at the front.
3. The Fick's diffusion law with stress independent diffusivity coefficient is accepted.
4. In comparison with the reaction front propagation, the diffusion is fast enough to consider a steady-state diffusion process.
5. The transformed material is considered as a solid skeleton for the diffusing constituent, i.e., the diffusing constituent does not induce additional strains in the solid constituent.
6. The reaction front is coherent: the displacement in solid phases is continuous across the front.
7. The influence of the pressure produced by the diffusing constituent on the stress state is neglected.
8. The temperature effects of the reaction are neglected.
9. A small strains approach and quasi-static case are considered.

In [8, 10] it was derived that the energy dissipation due to the chemical reaction front propagation takes the form

$$\text{Dis} = \omega(\mathbf{n}) A_{nn} = \frac{\rho_-}{n_- M_-} A_{nn} W, \quad (10.2)$$

where ρ_- is the mass density of the initial material, $\omega(\mathbf{n})$ is the reaction rate at the front surface element with the normal \mathbf{n} , W is the normal component of the reaction front velocity, $A_{nn} = \mathbf{n} \cdot \mathbf{A} \cdot \mathbf{n}$ is the normal component of the chemical affinity tensor which is defined in a quasi-static case by the formula

$$\mathbf{A} = n_- M_- \mathbf{M}_- + n_* M_* \mu_* \mathbf{I} - n_+ M_+ \mathbf{M}_+, \quad (10.3)$$

where M_{\pm} and M_* are the molar masses of the solid and diffusing constituents, \mathbf{I} is the unit tensor, μ_* is the chemical potential of the diffusing constituent, \mathbf{M}_{\pm} are the Eshelby energy-momentum tensors divided by the reference mass densities of the solid constituents. Note the similarity between (10.2), (10.3) and the classical

expression of the dissipation $\text{Dis} = A\omega$ with the reaction rate ω in a point, the scalar chemical affinity $A = -\sum n_k M_k \mu_k$ and the scalar chemical potentials μ_k , where the stoichiometric coefficients n_k ($k = 1, 2, \dots$) are substituted into the sum with the sign “+” if the k th constituent is produced in the reaction and with the sign “-” otherwise [34].

Further we suppose that the solid constituents are linear-elastic, and take μ_* in the form

$$M_* \mu_* = \eta_*(T) + R_g T \ln \frac{c}{c_*}, \quad (10.4)$$

where R_g is the universal gas constant, c is the molar concentration of B_* , c_* is the reference concentration of B_* taken as the solubility of B_* in B_+ , T is the temperature, $\eta_*(T)$ is the reference free energy of B_* . Then the normal component of the chemical affinity tensor can be written in a form [9–11]:

$$A_{nn} = \frac{n_- M_-}{\rho_-} \left\{ \gamma(T) + \frac{1}{2} \boldsymbol{\varepsilon}_- : \boldsymbol{\sigma}_- - \frac{1}{2} \boldsymbol{\sigma}_+ : (\boldsymbol{\varepsilon}_+ - \boldsymbol{\varepsilon}^{ch}) + \boldsymbol{\sigma}_- : (\boldsymbol{\varepsilon}_+ - \boldsymbol{\varepsilon}_-) \right\} + n_* R_g T \ln \frac{c}{c_*}, \quad (10.5)$$

where $\boldsymbol{\varepsilon}_\pm$ are the strain tensors of the solid constituents, $\boldsymbol{\varepsilon}^{ch}$ is the transformation strain, $\boldsymbol{\sigma}_- = \mathbf{C}_- : \boldsymbol{\varepsilon}_-$ and $\boldsymbol{\sigma}_+ = \mathbf{C}_+ : (\boldsymbol{\varepsilon}_+ - \boldsymbol{\varepsilon}^{ch})$ are the Cauchy stress tensors, \mathbf{C}_\pm are the elasticity tensors. The temperature-dependent energy parameter γ is the combination of the chemical energies η_0^\mp of the solid constituents B_\mp (Helmholtz free energies of solids in stress-free states) and the reference energy of B_* :

$$\gamma = \eta_0^- - \eta_0^+ + \frac{\rho_-}{n_- M_-} n_* \eta_*. \quad (10.6)$$

Note that mechanical stresses affect the front propagation only if the input of the strain energy is comparable with γ .

Following [8, 9], we formulate the kinetic equation for the reaction rate $\omega(\mathbf{n})$ by replacing the scalar chemical affinity in a known formula (e.g., [15]) for the reaction rate in a point by the normal component of the chemical affinity tensor, as

$$\omega(\mathbf{n}) = k_* c \left\{ 1 - \exp \left(-\frac{A_{nn}}{R_g T} \right) \right\}, \quad (10.7)$$

where k_* is the reaction constant. Then from the mass balance it follows that the normal component of the reaction front velocity is defined by the formula:

$$W = \frac{n_- M_-}{\rho_-} k_* c \left\{ 1 - \exp \left(-\frac{A_{nn}}{R_g T} \right) \right\}. \quad (10.8)$$

The stresses can be found from the equilibrium equations

$$\nabla \cdot \boldsymbol{\sigma} = 0 \quad (10.9)$$

with the boundary conditions and traction and displacement continuity conditions across the reaction front.

The concentration of the diffusing constituent is found from the diffusion problem which, in accordance with the assumptions, includes the Laplace equation

$$\Delta c = 0 \quad (10.10)$$

and the boundary conditions

$$c|_{\Omega_+} = c_* \quad \text{or} \quad D \frac{\partial c}{\partial n} \Big|_{\Omega_+} - \alpha (c_* - c(\Omega_+)) = 0, \quad (10.11)$$

$$D \frac{\partial c}{\partial n} \Big|_{\Gamma} + n_* \omega(\mathbf{n}) = 0, \quad (10.12)$$

where Ω_+ is the part of the outer surface of the body through which the diffusion flux is supplied, Γ is the reaction front, c_* is the given concentration or solubility of B_* in the material B_+ , α is the mass transfer coefficient. Without loss of generality, one may take c_* also as the reference volume density in Eqs. (10.4), (10.5).

Kinetic equations (10.7), (10.8) can be rewritten in terms of the equilibrium concentration c_{eq} [8, 9], introduced such that

$$A_{nn}(c = c_{eq}) = 0. \quad (10.13)$$

By the solid skeleton approach the mechanical part in (10.5) does not depend on the concentration and, therefore, A_{nn} can be rewritten as

$$A_{nn} = n_* R_g T \ln \frac{c}{c_{eq}}. \quad (10.14)$$

Further, the stoichiometric coefficients are normalized by n_* :

$$n_- \rightarrow n_-/n_*, \quad n_+ \rightarrow n_+/n_*, \quad n_* \rightarrow 1.$$

Then, by (10.7), (10.8) and (10.14), the reaction rate and reaction front velocity are expressed through the current concentration of the diffusing constituent and the equilibrium concentration corresponding to the stresses and strains at the front (see, e.g., [11]):

$$\omega(\mathbf{N}) = k_* (c(\Gamma) - c_{eq}), \quad W = \frac{n_- M_-}{\rho_-} k_* (c(\Gamma) - c_{eq}), \quad (10.15)$$

where c_{eq} is determined by Eq. (10.13). The boundary condition (10.12) takes the form

$$D \frac{\partial c}{\partial n} \Big|_{\Gamma} + k_* (c(\Gamma) - c_{eq}) = 0, \quad (10.16)$$

In such a representation stresses and strains affect the reaction rate via the equilibrium concentration, and the front may propagate only if $c(\Gamma) > c_{eq}$.

10.3 Numerical Simulations

The formulated coupled problem can be solved analytically only in simple cases. Thus, using the subroutine written in ANSYS internal programming language, we develop a numerical approach for the modeling localized chemical reactions in deformable solids. The finite-element modeling in the case of elastic solid constituents includes the following steps:

1. Choose the initial layer of the transformed material.
2. Calculate stresses at the reaction front.
3. Find the equilibrium concentration of the diffusing constituent for stresses at the reaction front.
4. Find the current concentration of the diffusing constituent at the reaction front.
5. Calculate the normal component of the reaction front velocity W .
6. Give the increment $\Delta s = W\tau$ to each reaction front point and find the new front position. Here τ is a time increment.
7. Repeat the procedure from the Step 2 for the new reaction front position.

The developed subroutine allows to simulate the reaction front propagation in a fully automatic mode. As an output, the position and the velocity of the every reaction front point as well as the stresses and strains are found in dependence of time. The diffusion problem is solved using thermo-diffusion analogy. This allows us easily switch between the mechanical and diffusion problems, thus the automatic operation of the whole subroutine is provided. An additional subroutine is developed to avoid any kind of reaction front intersection during propagation, which can cause the numerical problems.

10.3.1 Axially Symmetric Problem

To verify the numerical model we compare finite-element results and analytical solution of the axially symmetric plane problem for the front propagation in the vicinity of a cylindrical hole under all-round external tension σ_0 . The reaction starts at the inner surface of the hole, and the material B_* forms the cylindrical layer of a thickness h round the hole (Fig. 10.1). For the sake of simplicity, we suppose that the concentration c_* of the diffusing constituent is constant inside the hole.

In cylindrical coordinates (r, φ, z) , the radial displacements u_{\pm} in domains occupied by the materials B_+ and B_- are given by the Lamé solution:

$$u_{\pm} = A_{\pm}r + D_{\pm}/r, \quad (10.17)$$

where A_{\pm} , D_{\pm} are found from the boundary conditions and from displacement and traction continuity across the reaction front.

The stresses and strains are given by formulae:

$$\begin{aligned} \varepsilon_r^{\pm} &= A_{\pm} - D_{\pm}/r^2, & \varepsilon_{\varphi}^{\pm} &= A_{\pm} + D_{\pm}/r^2 \\ \sigma_r^{\pm} &= 2K_{\pm}(A_{\pm} - \varepsilon_{\pm}^{ch}) - 2\mu_{\pm}D_{\pm}/r^2, \\ \sigma_{\varphi}^{\pm} &= 2K_{\pm}(A_{\pm} - \varepsilon_{\pm}^{ch}) + 2\mu_{\pm}D_{\pm}/r^2, \end{aligned} \quad (10.18)$$

where $\varepsilon_-^{ch} = 0$, $\varepsilon_+^{ch} = \varepsilon^{ch}$, the constants A_{\pm} and D_{\pm} can be easily found from the boundary and interface conditions. Then the stress-strain dependent part in the expression (10.5) of A_{nn} can be written in an explicit form as the function of the reaction front radius and external stress, and the equilibrium concentration c_{eq} at the reaction front can be found from Eq. (10.13).

To find the concentration of the diffusing constituent at the reaction front one have to solve the diffusion equation

$$\frac{\partial^2 c}{\partial r^2} + \frac{1}{r} \frac{\partial c}{\partial r} = 0, \quad (10.19)$$

Fig. 10.1 The axially symmetric problem (all-round tension)

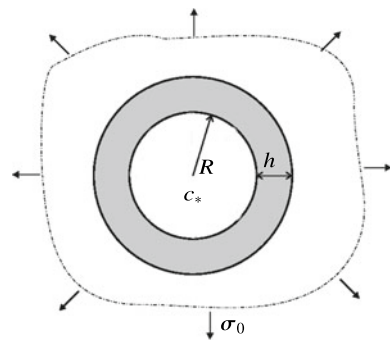


Table 10.1 The material parameters

The parameter	The component B_-	The component B_+
Young modulus, E (GPa)	163	60
Poisson's ration, ν	0.23	0.17
Transformation strain, ε^{ch}	—	0.015
ρ/M (Mol/m ³)	$8.29 \cdot 10^4$	$3.66 \cdot 10^4$

with the boundary conditions:

$$c|_{r=R} = c_*, \quad D \frac{\partial c}{\partial r} \Big|_{r=R+h} + k_* (c - c_{eq}) \Big|_{r=R+h} = 0, \quad (10.20)$$

where h is the thickness of the transformed material layer.

Finally, the expression (10.15) of the reaction front velocity $W = \dot{h}$ can be written down and then integrated.

The numerical simulation is carried out for material parameters given in Table 10.1. The energy parameter $\gamma = 9.6 \cdot 10^7$ J/Mol. The results are shown in Fig. 10.2. Due to the symmetry, only a quarter of the model is pictured.

One can see that the reaction front remains cylindrical and keeps axial symmetry. We emphasize that the front velocity was independently calculated in every point of the front from the local numerical values of stresses and concentration, and axial symmetry was not assumed during the simulation but was obtained. The results of the numerical simulation are compared with the analytical solution in Fig. 10.3 and 10.4 where the dependencies of the reaction front position on time and the front velocity on the front position are shown. The square dots correspond to the numerical simulation, and the dashed line represents the analytical solution. One can observe a good agreement between analytical results and numerical simulations.

10.3.2 The Hole Under Uniaxial Tension or Compression

Figure 10.5 demonstrates the reaction front kinetics near the cylindrical hole under uniaxial tension and uniaxial compression in the horizontal direction. The detailed front kinetics through the time dependencies of the position of points A (the pole of the hole) and B (the “equator” of the hole) is presented in Fig. 10.6, 10.7 for various types of external loading. One can see that the stress-strain state affects the chemical reaction front propagation, and in the vicinity of the hole the tensile stress concentration increases the reaction front velocity, while compressive stresses near the hole retard the front.

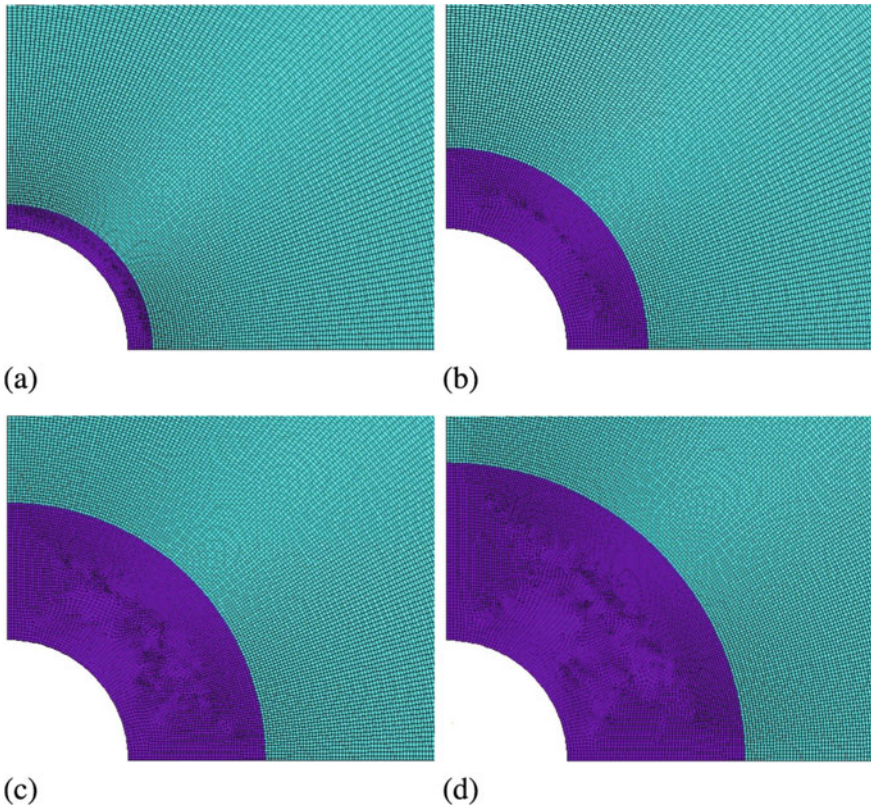


Fig. 10.2 The reaction front kinetics in the vicinity of the hole at all-round tension $\sigma_0 = 400$ MPa: (a) $t = \tau$, (b) $t = 8\tau$, (c) $t = 15\tau$, (d) $t = 19\tau$

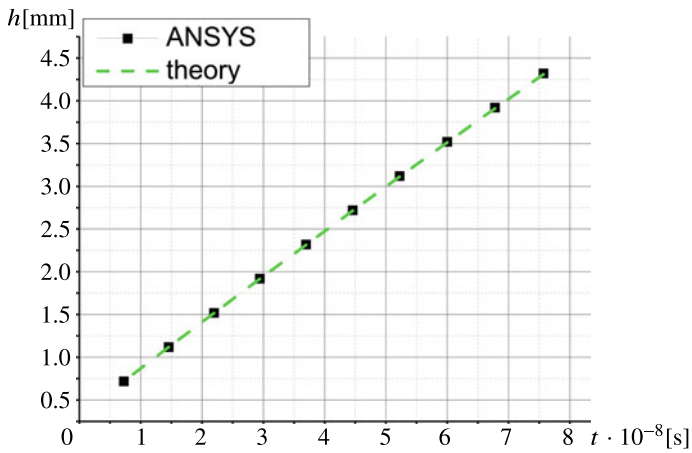


Fig. 10.3 Comparing numerical and analytical results: the reaction front position vs time at all-round tension

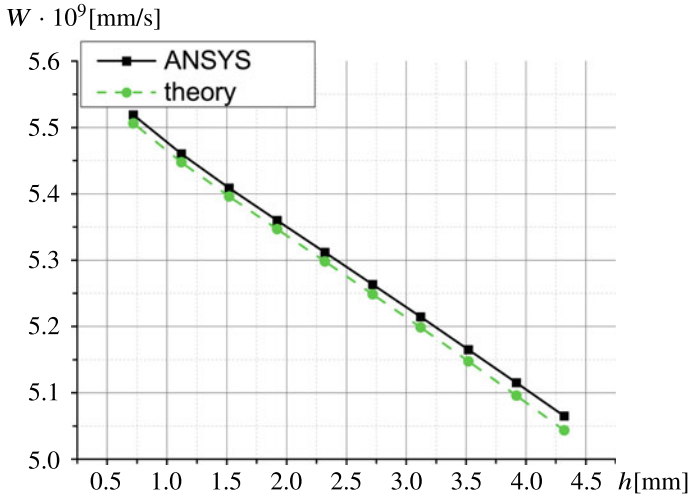


Fig. 10.4 Comparing numerical and analytical results: the reaction front velocity vs reaction front position at all-round tension

10.4 Conclusions

This paper is devoted to the modeling the influence of a stress-state on the chemical reaction front kinetics. The theoretical approach to the solution of a coupled problem “diffusion–chemistry–mechanics” is based on the chemical affinity tensor concept which puts the problem into the framework of the mechanics of configuration forces. Numerical simulations allow to investigate complicate problems of the chemical reaction front propagation. In the present paper an example of the procedure is given for the case of linear-elastic solid reaction constituents and quasi-stationary diffusion, which includes the FEM software development, analytical solution of a simple problem which is used for the verification of the procedure, and finally the use of the procedure for the solution of a problem that cannot be solved analytically. A reaction in the vicinity of a stress concentrator was chosen as a trial problem. For the simplicity sake, only the case of linear-elastic solid constituents was considered, and the transformation strain was taken small for the consistency with a small strain approach. Nevertheless the results obtained give understanding of the influence of stress concentrators on the chemical reaction front propagation.

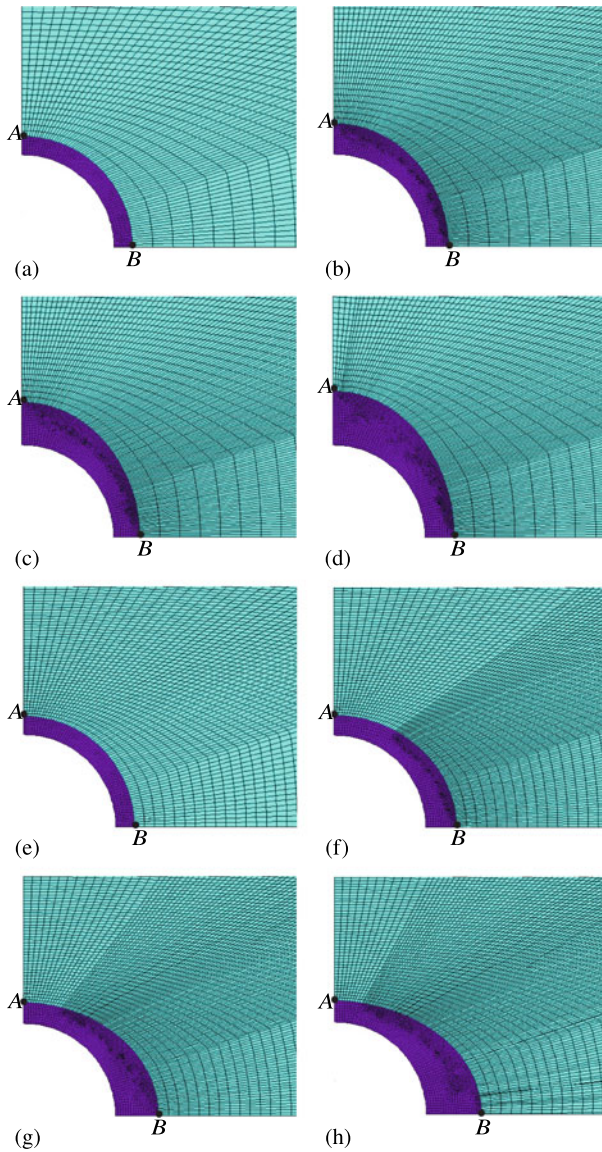


Fig. 10.5 The chemical reaction front kinetics: **a–d** at horizontal uniaxial tension $\sigma_0 = 400$ MPa, **e–h** at uniaxial horizontal compression $\sigma_0 = -400$ MPa, **a, e** $t = \tau$, **b, f** $t = 4\tau$, **c, g** $t = 8\tau$, **d, h** $t = 12\tau$

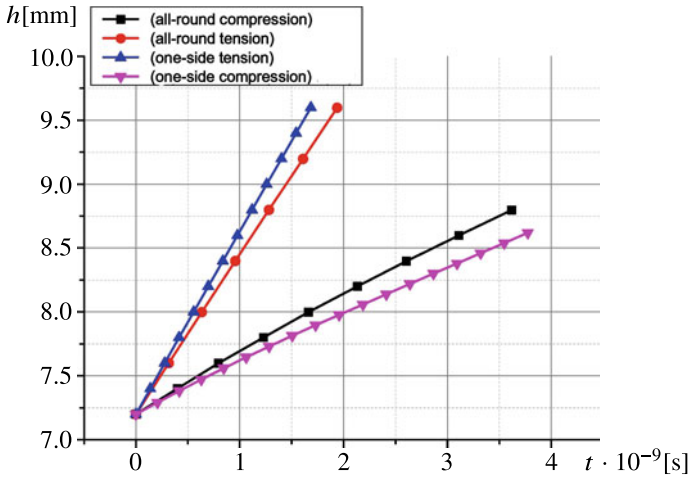


Fig. 10.6 The reaction front position vs time for point A at all-round and uniaxial tension/compression

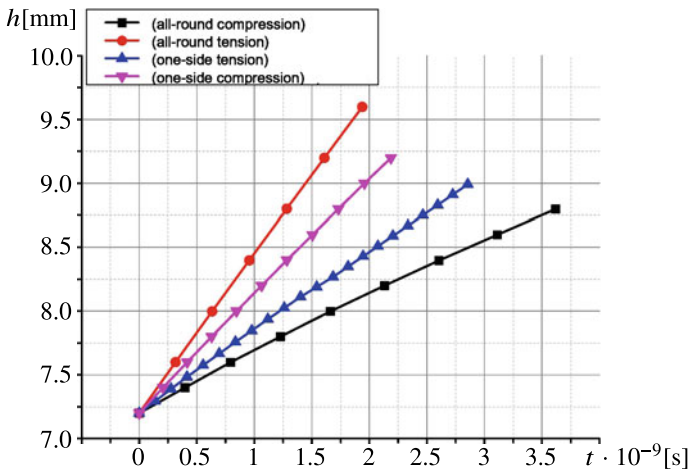


Fig. 10.7 The reaction front position vs time for point B at all-round and uniaxial tension/compression

Acknowledgements The authors greatly appreciate the financial support of the Russian Science Foundation (Grant No. 19-19-00552).

References

1. Bower, A.F., Guduru, P.R., Sethuraman, V.A.: A finite strain model of stress, diffusion, plastic flow, and electrochemical reactions in a lithium-ion half-cell. *J. Mech. Phys. Solids* **59**(4), 804–828 (2011)
2. Bower, A.F., Guduru, P.R., Chason, E.: Analytical solutions for composition and stress in spherical elastic-plastic lithium-ion electrode particles containing a propagating phase boundary. *Int. J. Solids Struct.* **69–70**, 328–342 (2015)
3. Brassart, L., Suo, Z.: Reactive flow in solids. *J. Mech. Phys. Solids* **61**(1), 61–77 (2013)
4. Cui, Z., Gao, F., Qu, J.: Interface-reaction controlled diffusion in binary solids with applications to lithiation of silicon in lithium-ion batteries. *J. Mech. Phys. Solids* **61**, 93–310 (2013)
5. Dal, H., Miehe, C.: Computational electro-chemo-mechanics of lithium-ion battery electrodes at finite strains. *Comput. Mech.* **55**(2), 303–325 (2015)
6. Duddu, R., Chopp, D.L., Voorhees, P., Moran, B.: Diffusional evolution of precipitates in elastic media using the extended finite element and the level set methods. *J. Comput. Phys.* **230**, 1249–1264 (2011)
7. Freidin, A.B.: On chemical reaction fronts in nonlinear elastic solids. In: Indeitsev, D., Krivtsov, A.M. (eds.) *Proceedings of the XXXVII Summer School–Conference Advanced Problems in Mechanics (APM 2009)*, St. Petersburg (Repino), June 30–July 5, 2009, pp. 231–237. Institute for Problems in Mechanical Engineering of Russian Academy of Sciences (2009)
8. Freidin, A.B.: Chemical affinity tensor and stress-assist chemical reactions front propagation in solids. In: *Proceedings of the ASME 2013 International Mechanical Engineering Congress and Exposition*, vol. 9, p. V009T10A102. American Society of Mechanical Engineers (2013)
9. Freidin, A.B., Vilchevskaya, E.N., Korolev, I.K.: Stress-assist chemical reactions front propagation in deformable solids. *Int. J. Eng. Sci.* **83**, 57–75 (2014)
10. Freidin, A.B.: On a chemical affinity tensor for chemical reactions in deformable solids. *Mech. Solids* **50**(3), 260–285 (2015)
11. Freidin, A.B., Korolev, I.K., Aleshchenko, S.P., Vilchevskaya, E.N.: Chemical affinity tensor and chemical reaction front propagation: theory and FE-simulations. *Int. J. Fract.* **202**(2), 245–259 (2016)
12. Freidin, A.B., Morozov, N.F., Petrenko, S.E., Vilchevskaya, E.N.: Chemical reactions in spherically-symmetric problems of mechanochemistry. *Acta Mech.* **227**(1), 43–56 (2016)
13. Freidin, A.B., Vilchevskaya, E.N.: Chemical affinity tensor in coupled problems of mechanochemistry. In: Altenbach, H., Öchsner, A. (eds) *Encyclopedia of Continuum Mechanics*. Springer, Berlin, Heidelberg (2020)
14. Garikipati, K., Rao, V.S.: Recent advances in models for thermal oxidation of silicon. *J. Comput. Phys.* **174**, 138–170 (2001)
15. Glandsdorff, P., Prigogine, I.: *Thermodynamic Theory of Structure, Stability and Fluctuations*. Wiley, New York (1971)
16. Grinfeld, M.: *Thermodynamic Methods in the Theory of Heterogeneous Systems*. Longman, New York (1991)
17. Kao, D., McVitie, J., Nix, W., Saraswat, K.: Two dimensional thermal oxidation of silicon-I. Experiments. *IEEE Trans. Electron Devices* **ED-34**, 1008–1017 (1987)
18. Kao, D., McVitie, J., Nix, W., Saraswat, K.: Two dimensional thermal oxidation of silicon-II. Modeling stress effect in wet oxides. *IEEE Trans. Electron Devices* **ED-35**, 25–37 (1988)
19. Knowles, J.K.: On the dissipation associated with equilibrium shocks in finite elasticity. *J. Elast.* **9**, 131–158 (1979)
20. Knyazeva, A.: Cross effects in solid media with diffusion. *J. Appl. Mech. Tech. Phys.* **44**, 373–384 (2003)
21. Knyazeva, A.: Application of irreversible thermodynamics to diffusion in solids with internal surfaces. *J. Non-Equilib. Thermodyn.* **45**(4), 401–418 (2020)
22. Levitas, V., Attariani, H.: Anisotropic compositional expansion and chemical potential for amorphous lithiated silicon under stress tensor. *Sci. Rep.* **3**(1), 1–5 (2013)

23. Levitas, V., Attariani, H.: Anisotropic compositional expansion in elastoplastic materials and corresponding chemical potential: Large-strain formulation and application to amorphous lithiated silicon. *J. Mech. Phys. Solids* **69**, 84–111 (2014)
24. Loeffel, K., Anand, L.: A chemo-thermo-mechanically coupled theory for elastic-viscoplastic deformation, diffusion, and volumetric swelling due to a chemical reaction. *Int. J. Plast.* **27**, 1409–1431 (2011)
25. Loeffel, K., Anand, L.: On modeling the oxidation of high-temperature alloys. *Acta Mater.* **61**, 399–424 (2013)
26. Morozov, A., Khakalo, S., Balobanov, V., Freidin, A.B., Müller, W.H., Niiranen, J.: Modeling chemical reaction front propagation by using isogeometric analysis. *Tech. Mech.* **38**, 73–90 (2018)
27. Morozov, A., Freidin, A., Müller, W.H., Hauck, T., Schmadlak, I.: Modeling reaction front propagation of intermetallic compounds by using isogeometric analysis. In: 2018 19th International Conference on Thermal, Mechanical and Multi-Physics Simulation and Experiments in Microelectronics and Microsystems (EuroSimE), pp. 1–10 (2018). <https://doi.org/10.1109/EuroSimE.2018.8369860>
28. Morozov, A.V., Freidin, A.B., Müller, W.H.: Stability of chemical reaction fronts in the vicinity of a blocking state. *PNRPU Mech. Bull.* **2019**(3), 58–64 (2019). <https://doi.org/10.15593/perm.mech/2019.3.06>
29. Morozov, A., Freidin, A., Müller, W.H. *et al*: Modeling temperature dependent chemical reaction of intermetallic compound growth. In: 2019 20th International Conference on Thermal, Mechanical and Multi-Physics Simulation and Experiments in Microelectronics and Microsystems (EuroSimE), pp. 1–8 (2019). <https://doi.org/10.1109/EuroSimE.2019.8724531>
30. Morozov, A., Freidin, A., Klinkov, V., et al.: Experimental and theoretical studies of Cu-Sn intermetallic phase growth during high-temperature storage of eutectic SnAg interconnects. *J. Elec. Mater.* **49**(12), 7194–7210 (2020)
31. Poluektov, M., Freidin, A.B., Figiel, L.: Modelling stress-affected chemical reactions in non-linear viscoelastic solids with application to lithiation reaction in spherical Si particles. *Int. J. Eng. Sci.* **128**, 44–62 (2018)
32. Poluektov, M., Freidin, A.B., Figiel, L.: Micromechanical modelling of mechanochemical processes in heterogeneous materials. *Model. Simul. Mater. Sci. Eng.* **27**, 084005 (2019)
33. Poluektov, M., Figiel, L.: A numerical method for finite-strain mechanochemistry with localised chemical reactions treated using a Nitsche approach. *Comput. Mech.* **63**, 885–911 (2019)
34. Prigogine, I., Defay, R.: *Chemical Thermodynamics*. Longmans, Green, London (1954)
35. Rao, V.S., Hughes, T.J.R.: On modelling thermal oxidation of silicon. I: Theory. *Int. J. Numer. Meth. Eng.* **47** 341–358 (2000)
36. Rao, V.S., Hughes, T.J.R., Garikipati, K.: On modelling thermal oxidation of silicon ii: Numerical aspects. *Int. J. Numer. Meth. Eng.* **47**359–377 (2000)
37. Rusanov, A.I.: Surface thermodynamics revisited. *Surf. Sci. Rep.* **58**, 111–239 (2005)
38. Rusanov, A.I.: *Thermodynamic Foundations of Mechanochemistry*. Nauka, Saint-Petersburg (2006).(in Russian)
39. Sutardja, P., Oldham, W.G.: Modeling of stress effects in silicon oxidation. *IEEE Trans. Electron Devices* **36**(11), 2415–2421 (1988)
40. Svendsen, B., Shanthraj, P., Raabe, D.: Finite-deformation phase-field chemomechanics for multiphase, multicomponent solids. *J. Mech. Phys. Solids* **112**, 619–636 (2018)
41. Vilchevskaya, E.N., Freidin, A.B.: On kinetics of chemical reaction fronts in elastic solids. In: Altenbach, H., Morozov, N. (eds.) *Surface Effects in Solid Mechanics*, pp. 105–117. Springer, Berlin-Heidelberg (2013)
42. Vilchevskaya, E.: Modeling stress-affected chemical reactions in composite materials *Z. Angew. Math. Mech.* **101**(4), e202000281 (2021). <https://doi.org/10.1002/zamm.202000281>
43. Zhao, X.J., Bordas, S.P.A., Qu, J.M.: Equilibrium morphology of misfit particles in elastically stressed solids under chemo-mechanical equilibrium conditions. *J. Mech. Phys. Solids* **81**, 1–21 (2015)

Chapter 11

Diffusion in Media with Spheroidal Pores



Ksenia P. Frolova, Nikolay M. Bessonov, and Elena N. Vilchevskaya

Abstract The chapter describes the diffusion process in a composite material with non-uniformly distributed isolated spheroidal pores. The pores are assumed to present in the material initially or to form during the mass transport. The influence of the segregation effect, shape of pores, and its orientation scatter on the distribution of impurity is discussed. Various constitutive equations for the diffusion flux are compared. Consideration of Fick's first law allows to account for effective diffusion properties of material with microstructure. Consideration of the constitutive equation introducing chemical potential allows to account for effective diffusion and effective elastic properties of a porous material.

Keywords Effective properties · Effective diffusivity · Segregation effect · Homogenization methods · Chemical potential

11.1 Introduction

The diffusion process is largely determined by the microstructure of the material. Usually, the diffusion coefficient along grain boundaries is several times higher than the one for the bulk diffusion [1]. Impurity can be partially trapped inside vacancies, voids, and microcracks [2–4]. In addition, the mobility of impurity can be changed by a stress field [5] that depends not only on strains, but also on the stiffness of a heterogeneous solid.

A detailed examination of the surface layer of a uniform monocrystal shows that there are voids near the boundary [6]. Subsurface regions of the metal specimens can contain vacancies [7]. In some cases accumulation of impurity within grain boundaries can initiate intergranular microcracks. A non-uniform distribution of microstructural defects can affect the distribution of impurity in a host material. Sometimes, a local increase of impurity can change the properties and behavior

K. P. Frolova (✉) · N. M. Bessonov · E. N. Vilchevskaya
Institute for Problems in Mechanical Engineering RAS, V.O., Bolshoy pr., 61, St. Petersburg
199178, Russia

of material [8]. For this reason, a realistic picture of the distribution of impurity concentration in material with microcracks must be drawn.

The dependence of the diffusion process on the microstructure of material can be accounted for in a mathematical expression for the diffusion flux. The last one can be defined in different ways in accordance with various constitutive equations. According to the classical Fick's first law, matter flows from regions of high concentration to regions of low concentration, with a magnitude that is proportional to the concentration gradient. This law allows for the introduction of the dependence of the diffusion coefficient on the microstructure of a host material. Fick's first law is sometimes referred to as local law since it relates the local flux to the local concentration gradient. This local law may be amended to include local gradients of other field variables through the introduction of a chemical potential that makes the law non-local [9–11]. In general, the chemical potential is a sum of the stress-independent and stress-dependent parts. In this case, the dependence of diffusivity and the dependence of stiffness on the microstructure of a solid can be introduced.

Effective properties of heterogeneous materials can be determined by different methods. A detailed review of the history of various methods can be found in [12], whereas the current state of knowledge of the problem is described in [13]. Elastic and conductivity properties have been determined for various composites. A number of approximate schemes were rewritten in [14] for diffusivity on the basis of similarity between governing equations in the diffusivity and conductivity problems. However, a principal difference between the two problems is that temperature is a continuous function across the phase boundaries, while concentration is usually not. Therefore, the segregation effect should be taken into account [15]. Typical micromechanical models were rewritten for diffusivity in [1] to calculate the effective diffusion coefficient of a polycrystalline material accounting for the isotropic distribution of spheroidal inhomogeneities over orientation. In [16] we rewrote Maxwell's homogenization scheme for a transversely isotropic material accounting for various orientation distributions of spheroidal inhomogeneities.

The present paper is concerned with modeling of mass transport process in transversely isotropic composite material consisting of grains, grain boundaries, and non-uniformly distributed isolated pores. Impurity is assumed to diffuse along grain boundaries and fill the pores. A composite consisting of grains and grain boundaries is represented here by a homogenized background matrix with a known diffusivity calculated in [1]. Pores are considered as embedded inhomogeneities. Two different processes are considered:

1. Diffusion process in material initially containing unevenly distributed spheroidal pores. The effect of oblate and prolate spheroidal pores, as well as spherical ones, is investigated. The following orientation distribution of inhomogeneities is considered: arbitrary orientation distribution, orientational scatter of pores about a preferential orientation, arbitrary orientation distribution of rotational axes of spheroidal pores in one plane.

2. Diffusion process accounting for the pore formation during the mass transport. The effect of oblate spheroidal pores modeling intergranular microcracks is investigated. An arbitrary orientation distribution is considered since the external loading that could lead to a specific orientation distribution is absent.

11.2 Problem Statement

The modeling of the mass transport process in a porous material consists of two stages. At the first stage, the effective properties of a composite are calculated. Effective diffusivity of a material containing spheroidal pores with different orientation distribution corresponding to the transversally isotropic material was calculated in our paper [16] using Maxwell's homogenization scheme. Inhomogeneities with diffusion coefficient D_1 were embedded in a solid with much lower diffusion coefficient D_0 ($\alpha = D_0/D_1 = 0.05$). We assumed continuity of the normal component of the solute flux across the matrix (denoted by "+")/pore (denoted by "-") interface and a constant jump in impurity concentration, c , described by the segregation factor, s , as follows

$$c(x)|_{x \rightarrow \partial V_+} = sc(x)|_{x \rightarrow \partial V_-} \quad (11.1)$$

When concentration is a continuous function across the phase boundaries, there is no segregation effect and $s = 1$. The presence of the segregation effect leads to a fundamental distinction of the diffusion process from that of conductivity. In the present paper, we assume that impurity can be partially trapped inside the pores that mean $s \leq 1$. The effect of the segregation factor on the concentration profiles is investigated.

Effective elastic properties of composite materials consisting of pores with compliance $\mathbf{S}_1 \rightarrow \infty$ and matrix with compliance \mathbf{S}_0 were calculated in a large number of works using various homogenization schemes (in particular, Maxwell's homogenization scheme), see [12, 13] for details. Effective elastic properties can be also calculated by means of effective diffusivity properties on the base of the cross-property connections that interrelate the changes in different physical properties caused by a certain microstructure. Explicit connections between effective elastic and conductive properties of materials were established in [17, 18]. In a similar way, we obtained explicit connections between the effective elastic moduli and diffusion coefficient of a two-phase material with isolated inhomogeneities identical in shape in [19].

At the second stage of modeling, a diffusion problem is solved for a long cylinder. For simpleness, in the case of initially unevenly distributed spheroidal pores in a matrix we consider only a stress-free diffusion following classical Fick's first law. Hence, only effective diffusion coefficients are introduced. In the case of pore formation directly during the mass transport, we assume that stresses and strains may appear due to the inhomogeneous distribution of impurity. We consider a stress-free and stress-induced diffusion that allows for investigating the influence of effective diffusion coefficients on the concentration profiles and the joint influence of effective

diffusivity and compliance on the distribution of impurity. A linear dependence of the volume fraction of pores on concentration is considered.

We now discuss two stages of modeling.

11.3 Effective Properties of a Porous Material

This section provides the main ideas and results of calculation effective diffusivity and elastic properties of material with spheroidal pores.

11.3.1 Effective Diffusivity Properties

In the present research, we refer to our results obtained in [16] for effective diffusivity of a composite material containing isolated pores. Let us briefly recall the main ideas.

Following [13, 20], we use property contribution tensors to express the effect of a given inhomogeneity on the properties of interest. Their sums are proper microstructural parameters that reflect contributions of individual inhomogeneities to the overall effective properties.

To explain the influence of an isolated inhomogeneity on the process of the mass transport we use the second-rank diffusivity contribution tensor, \mathbf{H}^D , and resistance contribution tensor, \mathbf{H}^{DR} . In the case of spheroidal inhomogeneity with the isotropic diffusivity tensor $\mathbf{D}_1 = D_1 \mathbf{I}$ embedded in a matrix with $\mathbf{D}_0 = D_0 \mathbf{I}$, property contribution tensors are as follows

$$\mathbf{H}^D = -D_0^2 \mathbf{H}^{DR} = [B_1 \boldsymbol{\theta} + B_2 \mathbf{nn}], \quad (11.2)$$

where $\boldsymbol{\theta} = \mathbf{I} - \mathbf{nn}$, \mathbf{I} is the second-rank unit tensor, \mathbf{n} is a unit vector along the axis of symmetry of spheroidal inhomogeneity, and

$$B_1 = \frac{1 - s\alpha}{s\alpha + (1 - s\alpha) f_0}, \quad B_2 = \frac{1 - s\alpha}{1 - 2(1 - s\alpha) f_0}. \quad (11.3)$$

Here the shape function $f_0 = f_0(\gamma)$ depends on the aspect ratio of the spheroidal inhomogeneity γ ($\gamma < 1$, $\gamma = 1$, and $\gamma > 1$ correspond respectively to an oblate spheroid, sphere, and prolate spheroid). Hence, functions $B_1 = B_1(s, \alpha, \gamma)$ and $B_2 = B_2(s, \alpha, \gamma)$ depend on the segregation factor, contrast in diffusivity of the matrix and inhomogeneity and shape of the inhomogeneity.

To solve the homogenization problem for a composite material with multiple inhomogeneities we use formulation of Maxwell's homogenization scheme in terms of diffusivity (resistivity) contribution tensors [21, 22]. According to Maxwell's idea, it is necessary to evaluate far-field perturbations due to inhomogeneities in two different ways and equate the results. The first way is to evaluate this field as

the one generated by some homogenized region possessing (yet) unknown effective properties. This field can be expressed in terms of the property contribution tensor of the domain denoted by \mathbf{Q}^* . The second way is based on consideration of the sum of far fields generated by all the individual inhomogeneities within this domain (treated as non-interacting ones). Equating the results yields the effective diffusion properties in the form

$$(\mathbf{D}^{eff})^{-1} = \frac{1}{D_0} \mathbf{I} + \left\{ \left[\frac{1}{V} \sum_k V_k \mathbf{H}_k^{DR} \right]^{-1} - \mathbf{Q}^* \right\}^{-1} \quad (11.4)$$

in terms of the resistivity and

$$\mathbf{D}^{eff} = D_0 \mathbf{I} + \left\{ \left[\frac{1}{V} \sum_k V_k \mathbf{H}_k^D \right]^{-1} - \mathbf{P}^* \right\}^{-1} \quad (11.5)$$

in terms of diffusivity. Here \mathbf{P}^* and $\mathbf{Q}^* = [\mathbf{D}_0 - \mathbf{D}_0 \cdot \mathbf{P}^* \cdot \mathbf{D}_0]$ are the second-rank Hill's tensors that reflect the shape of the homogenized spheroidal domain and take into account interactions between the inhomogeneities. The first Hill's tensor \mathbf{P}^* can be expressed in terms of derivatives of Green's function G for concentration as

$$\mathbf{P}^* = \left(\nabla \int_{V_1} \nabla' G(x - x') dx' \right)^S.$$

In the absence of \mathbf{P}^* and \mathbf{Q}^* , Maxwell's scheme coincides with the non-interaction approximation.

In [16] we obtained the following expression for the effective diffusion coefficient of a composite material with an arbitrary orientation distribution of spheroidal pores:

$$\frac{D^{eff}}{D_0} = \frac{3 + 2\phi(2B_1/3 + B_2/3)}{3 - \phi(2B_1/3 + B_2/3)}. \quad (11.6)$$

In the case of orientational scatter of pores about a preferential orientation, Eqs. (11.4), (11.5) reduced to

$$\frac{D_{11}^{eff}}{D_0} = \frac{D_{22}^{eff}}{D_0} = \left(1 + \frac{\phi(B_1(1-g_1) + B_2g_1)}{1 - \phi f_0(\gamma^*)(B_1(1-g_1) + B_2g_1)} \right), \quad (11.7)$$

$$\frac{D_{33}^{eff}}{D_0} = \left(1 + \frac{\phi(B_1(1-g_2) + B_2g_2)}{1 - \phi(1-2f_0(\gamma^*))(B_1(1-g_2) + B_2g_2)} \right), \quad (11.8)$$

where $g_1 = g_1(\bar{\lambda})$, $g_2 = g_2(\bar{\lambda})$ are functions of the scatter parameter $\bar{\lambda}$ that appears in the expression for the probability density function introduced in [21]. The scatter parameter varies in the range from zero to infinity that corresponds to fully random and strictly parallel orientations of pores, respectively.

In the case of arbitrary orientation distribution of rotational axes of spheroidal pores in one plane, Eqs. (11.4), (11.5) took the form

$$\frac{D_{11}^{eff}}{D_0} = \frac{D_{22}^{eff}}{D_0} = \left(1 + \frac{\phi (B_1 + B_2)}{2 - \phi f_0 (\gamma^*) (B_1 + B_2)} \right), \quad (11.9)$$

$$\frac{D_{33}^{eff}}{D_0} = \left(1 + \frac{\phi B_1}{1 - \phi (1 - 2f_0 (\gamma^*)) B_1} \right). \quad (11.10)$$

Note that Maxwell's scheme formulated in terms of diffusivity and resistivity contribution tensors led to the same result.

11.3.2 Effective Elastic Properties

Effective elastic properties can be determined in a similar way by means of Maxwell's homogenization scheme in terms of fourth-rank compliance contribution tensor \mathbf{H} describing extra strain occurring over a reference volume due to the presence of the isolated inhomogeneity or in terms of fourth-rank stiffness contribution tensor \mathbf{N} describing extra stress [13]. Property contribution tensors of a spheroidal inhomogeneity embedded in an isotropic matrix are transversely isotropic and can be expressed as linear combinations of the tensor basis elements

$$\begin{aligned} \mathbf{T}_1 &= \boldsymbol{\theta}\boldsymbol{\theta}, & \mathbf{T}_2 &= \frac{1}{2} \left((\boldsymbol{\theta}\boldsymbol{\theta})_{(1,4)}^T + (\boldsymbol{\theta}\boldsymbol{\theta})_{(2,4)}^T - \boldsymbol{\theta}\boldsymbol{\theta} \right), & \mathbf{T}_3 &= \boldsymbol{\theta}\mathbf{nn}, & \mathbf{T}_4 &= \mathbf{nn}\boldsymbol{\theta} \\ \mathbf{T}_5 &= \frac{1}{4} \left(\mathbf{n}\boldsymbol{\theta}\mathbf{n} + (\mathbf{n}\boldsymbol{\theta}\mathbf{n})_{(1,2),(3,4)}^T + (\boldsymbol{\theta}\mathbf{nn})_{(1,4)}^T + (\boldsymbol{\theta}\mathbf{nn})_{(2,3)}^T \right), & \mathbf{T}_6 &= \mathbf{nnnn}, \end{aligned}$$

so

$$\mathbf{H} = \sum_{k=1}^6 h_k \mathbf{T}_k, \quad \mathbf{N} = \sum_{k=1}^6 n_k \mathbf{T}_k. \quad (11.11)$$

When inhomogeneities have a spherical shape, the composite material is isotropic, and Maxwell's homogenization scheme results in the following expressions for the effective bulk modulus K^{eff} and effective shear modulus G^{eff} [13]:

$$\frac{K^{eff}}{K_0} = \frac{1 - 3K_0\alpha_K\phi A}{1 + 3K_0(1 - \alpha_K)\phi A}, \quad (11.12)$$

$$\frac{G^{eff}}{G_0} = \frac{1 - 2G_0\alpha_G\phi B}{1 + 2G_0(1 - \alpha_G)\phi B}, \quad (11.13)$$

where

$$\alpha_K = \frac{2(1-2\nu_0)}{(1-\nu_0)}, \quad \alpha_G = \frac{(7-5\nu_0)}{15(1-\nu_0)},$$

$$A = \frac{20h_1 + 10(h_3 + h_4) + 5h_6}{15}, \quad B = \frac{2h_1 + 6h_2 - 2(h_3 + h_4) + 3h_5 + 2h_6}{15},$$

ν_0 is the Poisson's ratio of the matrix.

In [19] we calculated effective elastic properties by means of effective diffusivity properties on the base of the cross-property connections. Two main assumptions were used in the course of deriving the connections: inhomogeneities are spheroidal and effective properties are determined in the framework of the non-interaction approximation [17, 18]. Establishing explicit connections between the effective elastic and diffusion properties is possible if they are expressed in terms of the same microstructural parameters. To this end, an approximate expression for the effective compliance (stiffness) tensor introduced in [17, 18] must be used. These expressions coincide with the exact ones only in the case when inhomogeneities have a spherical shape. In the case of spheroidal inhomogeneities with an arbitrary orientation distribution, the explicit connections obtained in [19] lead to the following expressions for the effective Young's modulus E^{eff} and shear modulus G^{eff} :

$$\frac{E^{eff}}{E_0} = \left[1 + \frac{3(s_1 + s_2) + s_3 + s_4}{2B_1 + B_2} \left(\frac{D^{eff}}{D_0} - 1 \right) \right]^{-1}, \quad (11.14)$$

$$\frac{G^{eff}}{G_0} = \left[1 + \frac{3s_2 + s_4}{2(1+\nu_0)(2B_1 + B_2)} \left(\frac{D^{eff}}{D_0} - 1 \right) \right]^{-1}, \quad (11.15)$$

where $s_i = s_i(h_k)$ ($i = 1..6, k = 1..6$) are coefficients of the approximate fourth-order effective compliance tensor obtained in [17, 18]. The effective bulk modulus can be calculated as

$$K^{eff} = \frac{E^{eff}G^{eff}}{3(3G^{eff} - E^{eff})}. \quad (11.16)$$

11.4 Diffusion Problem

We now turn to the diffusion problem and introduce equations describing the mass transport of impurity in a host material.

11.4.1 Constitutive Equations for the Flux

Following linear non-equilibrium thermodynamics we define the diffusion flux \mathbf{J} as

$$\mathbf{J} = -Mc\nabla\mu, \quad (11.17)$$

where $M = D/RT$ is the impurity mobility (D is the diffusion coefficient, $R = 8.31455 \text{ J}/(\text{mol}\cdot\text{K})$ is the universal gas constant, T is the absolute temperature), c is concentration and μ is the chemical potential.

The chemical potential of the impurity/host material system may contain the stress-independent part μ_0 and stress-dependent part μ_S :

$$\mu = \mu_0 + \mu_S. \quad (11.18)$$

We take the stress-independent part in the form of the chemical potential of the ideal gas

$$\mu_0 = \mu_0^0 + RT \ln c, \quad (11.19)$$

where μ_0^0 is a constant that represents the chemical potential at a standard state.

The stress-dependent part of the chemical potential is proportional to the trace of the Eshelby energy-momentum tensor Σ [10]:

$$\mu_S = m_S \left(f_S^0 + \frac{\bar{\alpha}}{\rho} \text{tr} \Sigma \right), \quad (11.20)$$

where m_S is a molar mass of the solid host material, f_S^0 is the free energy density of the solid in a stress-free state, $\bar{\alpha}$ is a linear expansion coefficient, ρ is the initial density of impurity/host material system (we assume that $\rho \approx \rho_S$, where ρ_S is the initial density of the host material).

The Eshelby energy-momentum tensor is defined by [23]

$$\Sigma = W \mathbf{I} - \mathbf{P} \cdot \mathbf{F}, \quad (11.21)$$

where W the strain energy density per initial volume, $\mathbf{P} = \det \mathbf{F} \mathbf{F}^{-1} \cdot \boldsymbol{\sigma}$ is the Piola stress tensor ($\boldsymbol{\sigma}$ is the Cauchy stress tensor), $\mathbf{F} = \mathbf{r} \overset{\circ}{\nabla}$ is the deformation gradient (\mathbf{r} is the position occupied at the current time, operator $\overset{\circ}{\nabla}$ is defined in the initial configuration).

In conjunction with Eq. (11.21),

$$\text{tr} \Sigma = 3W - \det \mathbf{F} \text{tr} \boldsymbol{\sigma}. \quad (11.22)$$

If the host material is linearly elastic, one has

$$W = \det \mathbf{F} w, \quad \det \mathbf{F} = 1 + \text{tr} \boldsymbol{\epsilon}, \quad w = \frac{1}{2} \boldsymbol{\epsilon}^{el} \cdot \cdot \cdot \mathbf{C} \cdot \cdot \boldsymbol{\epsilon}^{el}, \quad (11.23)$$

where $\boldsymbol{\epsilon}$ are strains, $\boldsymbol{\epsilon}^{el}$ are elastic strains.

Therefore, in the case of linear elasticity, Eq. (11.22) reduces to

$$\text{tr} \Sigma = 3w - (1 + \text{tr} \boldsymbol{\epsilon}) \text{tr} \boldsymbol{\sigma} \quad (11.24)$$

and the constitutive equation (11.17) takes the form

$$\mathbf{J} = -D \left(\nabla c + \frac{c}{RT} \frac{m_s \bar{\alpha}}{\rho} \nabla (3w - (1 + \text{tr} \boldsymbol{\epsilon}) \text{tr} \boldsymbol{\sigma}) \right). \quad (11.25)$$

Neglecting the influence of the stress-dependent part of the chemical potential, Eq. (11.25) reduces to Fick's first law

$$\mathbf{J} = -D \nabla c. \quad (11.26)$$

11.4.2 Elasticity Problem Due to Mass Transport

We now identify the stress-strain state of material due to inhomogeneous distribution of impurity by using the balance of linear momentum, which in the absence of body forces can be written in a local form as

$$\nabla \cdot \boldsymbol{\sigma} = 0. \quad (11.27)$$

We assume that impurity leads to dilatation only. Therefore, the eigenstrain tensor of the host material due to impurity is spherical, $\boldsymbol{\epsilon}^* = \bar{\alpha} c \mathbf{I}$, and the stresses satisfy the Duhamel-Neumann relations

$$\boldsymbol{\sigma} = (\lambda \text{tr} \boldsymbol{\epsilon} - 3K \bar{\alpha} c) \mathbf{I} + 2G \boldsymbol{\epsilon}, \quad (11.28)$$

where λ , G and K are elastic moduli; $\lambda = K - 2G/3$.

The linear strain tensor can be introduced as follows:

$$\boldsymbol{\epsilon} = \frac{1}{2} (\nabla \mathbf{u} + \mathbf{u} \nabla), \quad (11.29)$$

where \mathbf{u} is a displacement.

The system of elasticity equations supplements with the mass balance equation for impurity

$$\frac{\partial c}{\partial t} = -\nabla \cdot \mathbf{J}. \quad (11.30)$$

To solve a boundary-value problem, we consider a long circular cylindrical specimen of radius r_0 in a cylindrical coordinate system (r, φ, z) . The displacement u_φ is absent due to the axial symmetry. We neglect the influence of the end faces of the cylinder and assume the cross-sections to be under the same conditions so that they remain flat. Hence, the radial displacement depends only on the radial coordinate, $u_r = u_r(r)$, and the axial displacement depends only on the axial coordinate, $u_z = u_z(z)$ [24].

Substitution of the constitutive equations (11.28) into the balance (11.27) leads to the following differential equations for the displacements:

$$\begin{aligned} \frac{\partial^2 u_r}{\partial r^2} + \frac{1}{r} \frac{\partial u_r}{\partial r} - \frac{u_r}{r^2} &= \bar{\alpha} \frac{3K}{K + 4G/3} \frac{\partial c}{\partial r}, \\ \frac{\partial u_z}{\partial z} &= \text{const} \quad (\epsilon_{zz} = \text{const}). \end{aligned} \quad (11.31)$$

Substitution of the constitutive equation for the flux into the mass balance (11.30) results in

$$\frac{\partial c}{\partial t} = \frac{1}{r} \frac{\partial}{\partial r} \left[r D \left(\frac{\partial c}{\partial r} + c P \right) \right], \quad (11.32)$$

where P is equal to

$$P = \frac{1}{RT} \frac{m_S \bar{\alpha}}{\rho} \frac{\partial}{\partial r} \left(\frac{3}{2} (\epsilon - 3\bar{\alpha}c) \cdot \cdot^4 \mathbf{C} \cdot \cdot (\epsilon - 3\bar{\alpha}c) - (1 + \text{tr}\epsilon) \text{tr}\sigma \right) \quad (11.33)$$

if one uses the constitutive equation (11.25) or

$$P = 0 \quad (11.34)$$

if one uses Fick's first law (11.26).

In linear elasticity, $W \ll \text{tr}\sigma$ when only normal stresses occur in material or when normal components of the stress tensor exceed shear stresses. Since impurity is assumed to lead to dilatation only, only normal components of the stress tensor are non-zero in the considered problem. Hence, Eq. (11.33) can be simplified as

$$P = -\frac{1}{RT} \frac{m_S \bar{\alpha}}{\rho} \frac{\partial \text{tr}\sigma}{\partial r}. \quad (11.35)$$

The boundary conditions in the elasticity problem due to mass transport are as follows:

$$u_r|_{r=0} < \infty, \quad \sigma_{rr}|_{r=r_0} = 0. \quad (11.36)$$

According to Saint-Venant's principle, the stress-strain state in a long cylinder loaded at its end faces is practically independent on the distribution of the surface forces acting on the end cross-sections [25]. At a certain distance from the end faces the stress state is determined only by the principal force, and boundary conditions on the end faces can be replaced by the integral relationship. The end faces are assumed to be free of loads, so

$$\int_0^{r_0} T_{zz} r dr = 0. \quad (11.37)$$

We assume that a constant concentration is maintained on the lateral surface of the cylinder, so the boundary conditions for the diffusion problem are as follows:

$$\left. \frac{\partial c}{\partial r} \right|_{r=0} = 0, \quad c|_{r=r_0} = c_0. \quad (11.38)$$

11.5 Results

We seek a numerical solution of the mass transport problem accounting for the microstructure and stress-strain state of the host material. To this end, an implicit finite difference method was applied. The Thomas algorithm was realized with C++. Concentration and displacement components were specified in mesh nodes, whereas diffusion coefficient, deformations, stresses (and, therefore, chemical potential) were specified in mesh cells.

To be specific, we investigate distribution of impurity in aluminum with elastic moduli $\mu_0 = 27$ GPa and $E_0 = 70$ GPa, molar mass $m_S = 0.027$ kg/mol and density $\rho = 2700$ kg/m³. The diffusion problem is solved at room temperature $T = 293$ K, the concentration is determined after 50 h. We assume that the linear expansion coefficient of the impurity in aluminum $\bar{\alpha} = 0.03$, constant diffusion coefficient $D_0 = 1 \cdot 10^{-12}$ m²/s. Note that the choice of the solid host material and impurity should not affect the solution qualitatively.

11.5.1 Diffusion Process in Material Initially Containing Inhomogeneities

We start with a discussion of the results of modeling the diffusion process in the material containing non-uniformly distributed spheroidal pores. To be specific, we introduce an exponential function

$$\phi = 0.1e^{-\frac{r_0-r}{r_0}},$$

here the volume fraction of pores takes its maximum value on the outer border.

Oblate spheroidal pores with $\gamma = 0.1$, prolate spheroidal pores with $\gamma = 10$ and spherical pores with $\gamma = 1$ are considered. Diffusion flux follows Fick's first law.

The concentration profiles corresponding to the diffusion problem with effective diffusion coefficient $D^{eff}(\phi)$ at various values of the segregation factor are shown in Figs. 11.1, 11.2. We compare the results with the solution of a diffusion problem with a constant diffusion coefficient D_0 (black dashed line). An arbitrary orientation distribution of oblate and prolate spheroidal pores is considered in Fig. 11.1. According to the results, the segregation factor affects the distribution of impurity. Increasing

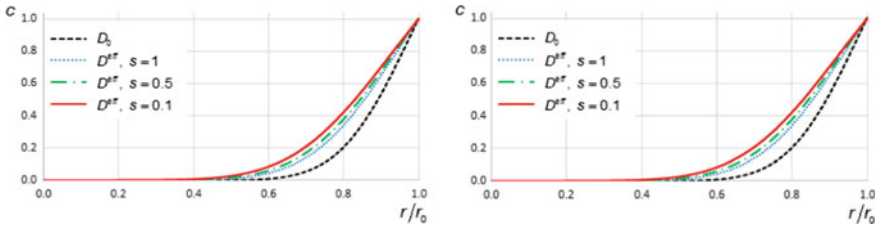
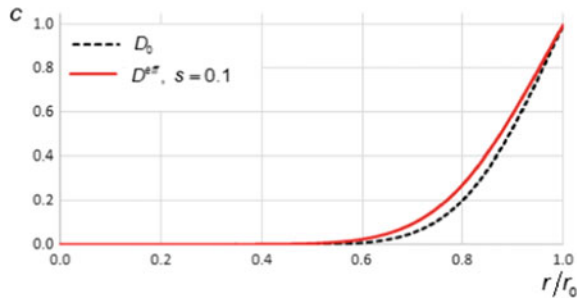


Fig. 11.1 Concentration profiles at different values of the segregation factor: material with oblate spheroidal pores (left) and prolate spheroidal pores (right)

Fig. 11.2 Concentration profiles: material with spherical pores



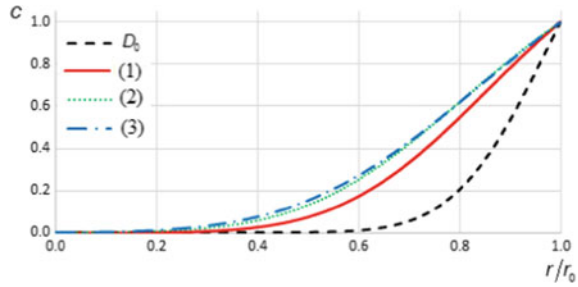
the jump in the concentration of particles at the matrix/pore interface (decreasing of s) results in deeper penetration of the solute. The distribution of spherical pores is considered in Fig. 11.2. The solution of the problem with the effective diffusion coefficient was found to be close to the one obtained at a constant diffusion coefficient at any s . The maximum difference was at the least value of the segregation factor $s = 0.1$, the corresponding concentration profile is shown. Prolate spheroidal pores with $\gamma = 10$ have a greater influence on the distribution of impurity than oblate spheroidal pores with $\gamma = 0.1$ and spherical pores.

Consideration of orientation scatter of oblate spheroidal pores about a preferential orientation \mathbf{e}_z or \mathbf{e}_φ , as well as arbitrary orientation distribution of rotational axes of oblate spheroidal pores in the plane normal to \mathbf{e}_r lead to results close to the ones shown in Fig. 11.1 (left). Consideration of other orientation scatters (when \mathbf{n}_i are preferentially oriented along \mathbf{e}_r or when \mathbf{n}_i are distributed in the plane normal to \mathbf{e}_z or to \mathbf{e}_φ) leads to the concentration dependencies that coincide with the one obtained at a constant value of the diffusion coefficient. At the same time, consideration of

1. arbitrary orientation distribution of prolate pores,
2. arbitrary orientation distribution of rotational axes of prolate spheroidal pores in one plane normal to \mathbf{e}_z or to \mathbf{e}_φ ,
3. orientational scatter of prolate spheroidal pores about a preferential orientation \mathbf{e}_r (the scatter parameter $\lambda = 100$)

results in different distributions of impurity. Figure 11.3 compares the results. The deepest penetration of impurity takes place in material with pores that have a prefer-

Fig. 11.3 Concentration profiles: different orientation scatter of prolate pores (see discussion in the text)



ential orientation (blue dot-dashed line). Note that consideration of other orientation scatter (when \mathbf{n}_i are preferentially oriented along \mathbf{e}_z or \mathbf{e}_φ , as well as when \mathbf{n}_i are distributed in the plane normal to \mathbf{e}_r) leads to the dependencies of concentration that coincide with the one obtained at a constant value of the diffusion coefficient.

Consideration of material containing non-uniformly distributed spheroidal pores allows to conclude that the difference between solutions obtained at D^{eff} and D_0 can be significant. It depends on the segregation factor, shape of pores, and its distribution over orientations.

11.5.2 Pore Formation During the Diffusion Process

We now turn to the problem of pore formation during the diffusion process and introduce a linear dependence of the volume fraction of pores on concentration in the form $\phi = 0.1c$. An arbitrary orientation distribution of oblate spheroidal pores with $\gamma = 0.1$ is considered, the segregation factor $s = 0.1$.

Let us first assume the diffusion flux to follow Fick's first law ($P = 0$). In this case, equations in the elasticity problem due to mass transport are partially coupled: the displacement field depends on the concentration distribution, whereas concentration is independent on the stress-strain state of the host material.

The concentration profile corresponding to the diffusion problem with effective diffusion coefficient $D^{eff}(\phi(c))$ is shown in Fig. 11.4 (red solid line). We compare the result with the solution of a diffusion problem with a constant diffusion coefficient D_0 (black dashed line). If pore formation is accounted for, a deeper impurity penetration results.

Let us account for the chemical potential in the constitutive equation for the diffusion flux (P is given by Eq. (11.35)). In this case, equations in the elasticity problem due to mass transport are fully coupled and there is a reason to account for the effective diffusion coefficient $D^{eff}(\phi(c))$ and effective elastic moduli $K^{eff}(\phi(c))$, $G^{eff}(\phi(c))$. Concentration profiles are shown in Fig. 11.5. We compare the solutions of four problems:

- Constant diffusion coefficient and constant elastic moduli, see black dashed line,

Fig. 11.4 Concentration profiles: diffusion flux follows classical Fick’s law

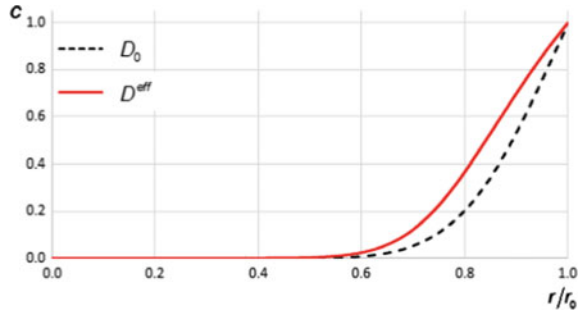
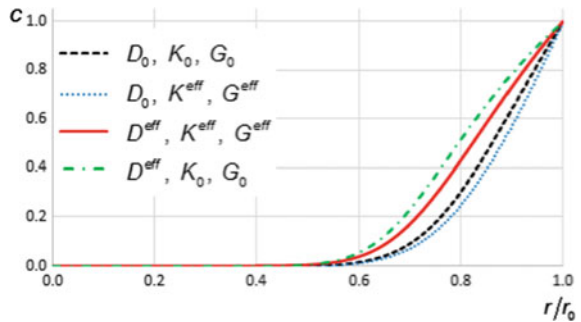


Fig. 11.5 Concentration profiles: diffusion flux accounts for chemical potential. Solutions of four problems are compared (see discussion in the text)

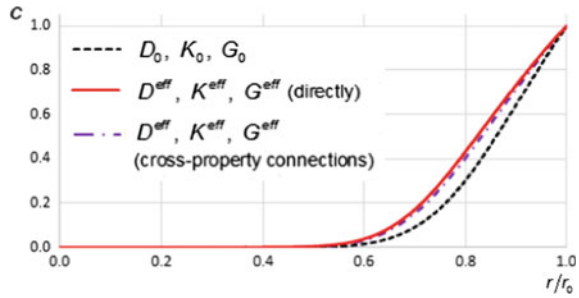


- Effective diffusion coefficient and constant elastic moduli, see green dot-dashed line,
- Effective diffusion coefficient and effective elastic moduli, see red solid line,
- Constant diffusion coefficient and effective elastic moduli, see blue dotted line.

Accounting for the effective diffusion coefficient only increases concentration excessively, whereas accounting both for effective diffusion coefficient and effective elastic moduli leads to a more accurate result (see red solid line and green dash-dotted line). Accounting only for effective elastic moduli, in turn, underestimates the result (see blue dotted line). The reason is that pore formation increases the diffusion coefficient of composite material and, vice versa, decreases its elastic moduli. As a result, the stresses and chemical potential decrease. For this reason, it is necessary to account for changes in different physical properties caused by a certain microstructure.

As it was discussed above, the effective elastic moduli can be calculated directly on the base of the homogenization scheme, or by means of effective diffusivity properties on the base of the cross-property connections. Figure 11.6 displays the concentration profiles corresponding to these two methods. The difference is insignificant in the case of the considered host material. Therefore, it is not necessary to apply homogenization methods to find all physical properties. It is enough to estimate only one type of properties. However, further investigations are necessary for materials with other physical properties/microstructure.

Fig. 11.6 Concentration profiles obtained by various methods of calculating effective elastic moduli (see discussion in the text)



Comparison of the results accounting for the microstructure (red solid lines on Figs. 11.4, 11.5, 11.6) with the results obtained at constant values of the diffusion coefficient and elastic moduli (black dashed lines on Figs. 11.4, 11.5, 11.6) allows one to conclude that the difference can be significant for specific materials and specific impurities. An observed increase of impurity concentration can affect the material behavior when it is “sensitive” to low concentrations of the dissolved flux (in particular, to low concentrations of hydrogen in the context of the problems of hydrogen degradation). Additionally, it is shown that introduction of the chemical potential in the equation for the diffusion flux results in higher concentration.

11.6 Conclusions

The chapter describes the diffusion process in material with non-uniformly distributed isolated pores. The main focus is on the influence of microstructure on the distribution of impurity in a host material. Initial non-uniform distribution of pores is commonly observed in experiments since subsurface layers usually contain microcracks and discontinuities. Pore formation can be also caused directly by impurity. Both mentioned cases are modeled. Diffusion flux in media with initial non-uniform distribution of inhomogeneities follows Fick’s first law, effective diffusion coefficient is introduced in the model. Diffusion flux accompanied by pore formation follows non-local Fick’s law including chemical potential. The corresponding model introduces effective diffusion coefficient and effective elastic moduli. It is shown that it is necessary to account for changes in all material parameters entering the diffusion equation.

Accounting for the effective properties of material in mass transport models can change the result significantly. On the one hand, the degree of influence depends on the segregation factor, shape of pores, and its distribution over orientations. On the other hand, it depends on the nature of the interaction between the host material and impurity. For example, metals are “sensitive” to low concentrations of hydrogen, whereas other impurities may not affect steels at low concentrations.

Acknowledgements Support of this work by a grant No. 18-19-00160 from the Russian Science Foundation is gratefully acknowledged.

References

1. Knyazeva, A.G., Grabovetskaya, G.P., Mishin, I.P., Sevostianov, I.: On the micromechanical modelling of the effective diffusion coefficient of a polycrystalline material. *Philos. Mag.* **95**(19), 2046–2066 (2015)
2. Mehrer, H.: *Diffusion in Solids: Fundamentals, Methods, Materials, Diffusion-Controlled Processes*, vol. 155. Springer Science & Business Media (2007)
3. Nair, S.V., Jensen, R.R., Tien, J.K.: Kinetic enrichment of hydrogen at interfaces and voids by dislocation sweep-in of hydrogen. *Metall. Mater. Trans. A* **14**(2), 385–393 (1983)
4. Pressouyre, G.M.: A classification of hydrogen traps in steel. *Metall. Mater. Trans. A* **10**(10), 1571–1573 (1979)
5. Shewmon, P.: *Diffusion in Solids*. Springer (2016)
6. Steffens, Th., et al.: Transmission electron microscopy study of the stacking-fault energy and dislocation structure in CuMn alloys. *Philos. Mag. A* **56**(2), 161–173 (1987)
7. Hadam, U., Zakroczyński, T.: Absorption of hydrogen in tensile strained iron and high-carbon steel studied by electrochemical permeation and desorption techniques. *Int. J. of Hydrog. Energy* **34**(5), 2449–2459 (2009)
8. Konopel'ko, L.A., et al.: New metrological support for measurements of the concentration of hydrogen in solid samples. *Meas. Tech.* **60**(12), 1222–1227 (2018)
9. Larché, F.C., Cahn, J.W.: Overview no. 41 the interactions of composition and stress in crystalline solids. *Acta metall.* **33**(3), 331–357 (1985)
10. Wu, Ch.H.: The role of Eshelby stress in composition-generated and stress-assisted diffusion. *J. Mech. Phys. Solids* **49**(8), 1771–1794 (2001)
11. Cui, Z., Gao, F., Qu, J.: A finite deformation stress-dependent chemical potential and its applications to lithium ion batteries. *J. Mech. Phys. Solids* **60**(7), 1280–1295 (2012)
12. Markov, K.Z.: Elementary micromechanics of heterogeneous media. In: *Heterogeneous Media*, pp. 1–162. Birkhäuser, Boston, MA (2000)
13. Kachanov, M., Sevostianov, I.: *Micromechanics of materials, with applications*. In: *Solid Mechanics and Its Applications*, vol. 249. Springer, Cham (2018)
14. Barrer R.M.: Diffusion and permeation in heterogeneous media. *Diffusion in Polymers*, pp. 165–217 (1968)
15. Kaur I., Mishin Y., Gust W.: *Fundamentals of Grain and Interphase Boundary Diffusion*. Wiley (1995)
16. Frolova, K.P., Vilchevskaya, E.N.: Effective diffusion coefficient of a porous material applied to the problem of hydrogen damage. In: Polyansky, V.A, Belyaev, A.K (eds.) *Advances in Hydrogen Embrittlement Study Advanced Materials Research*, vol. 143, pp. 113–130. Springer (2021)
17. Sevostianov, I., Kachanov, M.: Explicit cross-property correlations for anisotropic two-phase composite materials. *J. Mech. Phys. Solids* **50**(2), 253–282 (2002)
18. Sevostianov, I., Kachanov, M.: Connections between elastic and conductive properties of heterogeneous materials. In: van der Aref, H., Giessen, E. (eds.) *Advances in Applied Mechanics*, vol. 42, pp. 69–252. Elsevier, USA (2009)
19. Frolova, K.P.: Cross-property connections between Young's modulus and diffusion coefficient of two-phase composite. *St. Petersburg Polytechnical State University J. Phys. Math.* **14**(1), 177–189 (2021)
20. Kachanov, M., Sevostianov, I.: On quantitative characterization of microstructures and effective properties. *Int. J. Solids Struct.* **42**(2), 309–336 (2005)

21. Sevostianov, I.: On the shape of effective inclusion in the Maxwell homogenization scheme for anisotropic elastic composites. *Mech. Mater.* **75**, 45–59 (2014)
22. Sevostianov, I., Giraud, A.: Generalization of Maxwell homogenization scheme for elastic material containing inhomogeneities of diverse shape. *Int. J. Eng. Sci.* **64**, 23–36 (2013)
23. Eshelby, J.D.: The elastic energy-momentum tensor. *J. Elast.* **5**(3–4), 321–335 (1975)
24. Knyazeva, A.: *Thermophysical Foundations of Modern High-Temperature Technologies*. Publishing house of Tomsk Polytechnic University, Tomsk (2009). (in Russian)
25. Lurie, A.: *Teoriya uprugosti [theory of elasticity]*. Izdatel'stvo Nauka, M (1970)

Chapter 12

Divergence Method for Stability Study and Control of Dynamical Systems



Igor B. Furtat and Pavel A. Gushchin

Abstract A novel method of instability and stability of equilibrium points of autonomous dynamical systems using a flow and divergence of the vector field is proposed. A relation between the method of Lyapunov functions, Gauss (Ostrogradsky) and Chetaev theorems with the divergence conditions is established. The generalizations of Bendixon and Bendixon–Dulac theorems about a lack of periodic solutions in arbitrary order systems are considered. The state feedback control law design is proposed based on new divergence conditions. Examples illustrate the efficiency of the proposed method and the comparison with some existing ones.

Keywords Divergence stability conditions · Control law design · Lyapunov method · Gauss's theorem · Asymptotic stability

12.1 Introduction

The method of Lyapunov functions is a widely used approach to instability/stability study of system equilibrium points and the control law design [1]. However, a search of Lyapunov functions may be a rather difficult problem and sometimes it may be not feasible. In the present paper, we consider another method based on properties of the vector field divergence for stability/instability study of system equilibrium points and the control law design. The first instability conditions for arbitrary order systems and the stability conditions for the second-order systems are proposed in [2–7]. These conditions are improved for instability study in [8, 9] and stability study of the second-order systems in [10]. Differently from [10], the asymptotic stability and the convergence of almost all solutions of arbitrary order systems are considered in [11, 12]. Unlike [2–7], the improved stability/instability conditions [8–12] are obtained by using the positive definite auxiliary (density) function. In [11, 12], the

I. B. Furtat (✉) · P. A. Gushchin

Institute for Problems in Mechanical Engineering RAS, V.O., Bolshoy pr., 61, St. Petersburg 199178, Russia
e-mail: cainenash@mail.ru

control law design based on divergence conditions is considered. Currently, method [11, 12] has been extended to various kind of dynamical systems, see, i.e. [13–16].

However, necessary stability and sufficient instability conditions [8, 9] remain rough in some cases. The sufficient stability condition [10] is proposed only for second-order systems. The method [11, 12] guarantees the convergence of almost all solutions, but not all solutions, or ensure asymptotic stability only.

Recently, a new divergent method is proposed in [17, 18] for stability study of equilibrium points of autonomous dynamical systems. The necessary stability conditions in the integral form [17, 18] improve results [2–9]. Differently from [10–12], the sufficient stability conditions [17, 18] allow to study both stability and asymptotic stability of equilibrium points of arbitrary order systems.

Inspired by an idea from [17, 18], we obtain new results of instability/stability of equilibrium points, lack of periodic solutions and control law design. Thus, the main contributions of the present paper are as follows:

- (i) we propose new improved instability conditions, where the auxiliary (density) function can be not positive definite, and instability may be established in a part of the domain. It significantly extends a class of investigated systems in comparison with [8, 9];
- (ii) we obtain new improved stability conditions and new conditions of the control law design in comparison with [10–12, 17, 18]. We simplify results [17, 18] in equilibrium points. It is shown that the necessary stability conditions have the form of a continuity equation. Thus, the proposed results can be applied in tasks of fluid dynamics, electromagnetism, energy conservation and quantum mechanics;
- (iii) based on the proposed divergence conditions, we generalize Bendixon and Bendixon–Dulac theorems (about lack of periodic solutions, see [1, 19]) to systems with arbitrary order.

The paper is organized as follows. Section 12.2 describes instability conditions. Section 12.3 contains an extension of Bendixon and Bendixon–Dulac theorems. Section 12.4 describes new necessary and sufficient stability conditions. Section 12.5 describes methods for designing the state feedback control law. Also, Sects. 12.2, 12.4 and 12.5 present the numerical examples and the comparisons with the methods from [8, 10–12]. Finally, Sect. 12.6 collects some conclusions.

Notations. In the paper, the superscript T stands for matrix or vector transposition; \mathbb{R}^n denotes the n dimensional Euclidean space with the vector norm $|\cdot|$; $\mathbb{R}^{n \times m}$ is the set of all $n \times m$ real matrices; $\nabla\{W(x)\} = \left[\frac{\partial W}{\partial x_1}, \dots, \frac{\partial W}{\partial x_n} \right]^T$ is a gradient of the scalar function $W(x)$; $\nabla \cdot \{h(x)\} = \frac{\partial h_1}{\partial x_1} + \dots + \frac{\partial h_n}{\partial x_n}$ is a divergence of the vector field $h(x) = [h_1(x), \dots, h_n(x)]^T$. We mean that the zero equilibrium point is stable (unstable) if it is Lyapunov stable (unstable) [1].

12.2 Instability Conditions

Consider an autonomous dynamical system in the form

$$\dot{x}(t) = f(x(t)), \quad (12.1)$$

where $x = [x_1, \dots, x_n]^T$ is the state, $f = [f_1, \dots, f_n]^T : D \rightarrow \mathbb{R}^n$ is the continuously differentiable function in $D \subset \mathbb{R}^n$. The set D contains the origin and $f(0) = 0$. Assume that the domain of attraction D_A of the point $x = 0$ coincides with the domain D . However, all obtained results are valid if $D_A \subset D$ or $D_A = \mathbb{R}^n$. Denote by \bar{D} a boundary of the domain D .

The first instability condition in the form $\nabla \cdot \{f(x)\} > 0$ in $x \in D \setminus \{0\}$ is considered in [2–6, 8]. The improved condition $\nabla \cdot \{\rho(x)f(x)\} > 0$ in $x \in D \setminus \{0\}$ [9] extends a class of investigated systems in comparison with [2, 5] through the use of the positive definite continuously differentiable function $\rho(x)$.

Differently from [2–6, 8, 9], we propose a new instability condition, where the function $\rho(x)$ can be not a positive definite in D and instability may be established in a part of the domain $x \in D$. It significantly extends a class of investigated systems in comparison with [2–6, 8, 9].

Let us formulate the instability conditions of (12.1) in the following theorem.

Theorem 12.1 *Let $\rho(x) : D \rightarrow \mathbb{R}$ be a continuously differentiable function, $\rho(0) = 0$ and $\rho(x_0) > 0$ for some x_0 with arbitrary small $\|x_0\|$. Denote by $B = \{x \in \mathbb{R}^n : \|x\| \leq r, r > 0\} \subset D$ and $U = \{x \in B : \rho(x) > 0\}$. The equilibrium point $x = 0$ of the system (12.1) is unstable, if at least one of the following conditions holds for any $x \in U$:*

- (i) $\nabla \cdot \{\rho(x)f(x)\} > \rho(x)\nabla \cdot \{f(x)\}$;
- (ii) $\nabla \cdot \{\rho^{-1}(x)f(x)\} < 0$ and $\nabla \cdot \{f(x)\} \geq 0$;
- (iii) $\nabla \cdot \{\rho(x)f(x)\} > \beta(x)\rho^2(x)\nabla \cdot \{\rho^{-1}(x)f(x)\}$, where $\beta(x) > 1$ and $\nabla \cdot \{f(x)\} \geq 0$ or only $\beta(x) = 1$;
- (iv) $\nabla \cdot \{\rho(x)f(x)\} > 0$ and $\nabla \cdot \{\rho^{-1}(x)f(x)\} < 0$.

Proof According to Chetaev theorem [1], if $\nabla\{\rho(x)\}f(x) > 0$ for $x \in U$, then the equilibrium point $x = 0$ is unstable.

From the relation $\nabla \cdot \{\rho(x)f(x)\} = \nabla\{\rho(x)\}^T f(x) + \nabla \cdot \{f(x)\}\rho(x)$ implies that if $\nabla \cdot \{\rho(x)f(x)\} > \nabla \cdot \{f(x)\}\rho(x)$ for $x \in U$ (see case (i)), then $\nabla\{\rho(x)\}^T f(x) > 0$ for $x \in U$.

Consider expression $\nabla\{\rho(x)\}^T f(x) = \rho(x)\nabla \cdot \{f(x)\} - \rho^2(x)\nabla \cdot \{\rho^{-1}(x)f(x)\}$. If $\nabla \cdot \{\rho^{-1}(x)f(x)\} < 0$ and $\nabla \cdot \{f(x)\} > 0$ (see case (ii)), then $\nabla\{\rho(x)\}^T f(x) > 0$ for $x \in U$.

Consider relation $(1 + \beta(x))\nabla\{\rho(x)\}^T f(x) = \nabla \cdot \{\rho(x)f(x)\} - \beta(x)\rho^2(x)\nabla \cdot \{\rho^{-1}(x)f(x)\} + (\beta(x) - 1)\rho(x)\nabla \cdot \{f(x)\}$. If $\nabla \cdot \{\rho(x)f(x)\} > \beta(x)\rho^2(x)\nabla \cdot \{\rho^{-1}(x)f(x)\}$ for $\beta(x) = 1$ or $\beta(x) > 1$ and $\nabla \cdot \{f(x)\} > 0$ for $x \in U$ (see case (iii)), then $\nabla\{\rho(x)\}^T f(x) > 0$ for $x \in U$.

Consider equality $2\nabla\{\rho(x)\}^T f(x) = -\rho^2(x)\nabla \cdot \{\rho^{-1}(x)f(x)\} + \nabla \cdot \{\rho(x)f(x)\}$. If $\nabla \cdot \{\rho(x)f(x)\} > 0$ and $\nabla \cdot \{\rho^{-1}(x)f(x)\} < 0$ for $x \in U$ (see case (iv)), then $\nabla\{\rho(x)\}^T f(x) > 0$ for $x \in U$. Theorem 12.1 is proved. \square

12.3 Extension of Bendixson and Bendixson–Dulac Theorems to n th Dimensional Systems

The lack of periodic solutions in a simply connected domain in \mathbb{R}^2 can be established by Bendixson and Bendixson–Dulac theorems [1, 19]. We generalize these theorems to the n th dimensional systems.

Theorem 12.2 *Let $D \subseteq \mathbb{R}^n$ is a simply connected domain. If $\nabla \cdot \{f(x)\}$ does not change the sign for all $x \in D$ (except possibly in a set of measure 0), then the system (12.1) has no invariant closed subset with a positive measure in D .*

Proof Denote by Γ the closed invariant subset with a positive measure in D , $\bar{\Gamma}$ is the boundary of Γ , $int\{\Gamma\}$ is the interior of Γ , $V = \bar{\Gamma} \cup int\{\Gamma\}$, and \bar{V} is a volume of V . According to Liouville’s theorem and [20, Theorem 1 in p. 69], $d\bar{V}/dt = \int_V \nabla \cdot \{f(x)\}dV = 0$, i.e. the volume of a closed invariant subset does not change at any time t . If $\nabla \cdot \{f(x)\}$ does not change the sign in D , then the value of $d\bar{V}/dt$ has a negative or a positive value, i.e. the volume \bar{V} is decreased or increased. We have a contradiction except possibly in a set of measure 0, where $\nabla \cdot \{f(x)\}$ can be zero. Thus, system (12.1) has no invariant closed subset with a positive measure in D . Theorem 12.2 is proved. \square

Theorem 12.3 *Let $D \subseteq \mathbb{R}^n$ is a simply connected domain. If there exists the continuously differentiable function $\rho(x)$ such that $\nabla \cdot \{\rho(x)f(x)\}$ does not change the sign for all $x \in D$ (except possibly in a set of measure 0), then the system (12.1) has no invariant closed subset with a positive measure in D .*

Proof Let $\Gamma = \{x \in D : S(x) = C\}$ be an invariant closed subset, \bar{V} be a phase volume of $V = \{x \in D : S(x) \leq C\}$ and $\rho(x) = \phi(x)|\nabla\{S(x)\}|$, where $\phi(x)$ is a continuously differentiable function. If $\nabla \cdot \{\rho(x)f(x)\} \neq 0$, then $\int_V \nabla \cdot \{\rho(x)f(x)\}dV \neq 0$. Considering Divergence theorem, we have $\int_V \nabla \cdot \{\rho(x)f(x)\}dV = \int_\Gamma \phi(x)\nabla\{S(x)\}^T f(x)d\Gamma \neq 0$. If system (12.1) has an invariant closed subset with a positive measure, then $\nabla\{S(x)\}^T f(x) = 0$ and $\int_\Gamma \phi(x)\nabla\{S(x)\}^T f(x)d\Gamma = 0$. We have a contradiction except possibly in a set of measure 0, where $\nabla\{S(x)\}^T f(x)$ can be zero. Thus, system (12.1) has no invariant closed subset with a positive measure in D . Theorem 12.2 is proved. \square

12.4 Stability Conditions

Let us formulate necessary stability conditions in the following theorem.

Theorem 12.4 *Let $x = 0$ be an asymptotically stable equilibrium point of the system (12.1). Then there exist twice differentiable functions $\phi(x)$ and $S(x)$ such that $S(x) > 0$ and $\phi(x) > 0$ for any $x \in D \setminus \{0\}$, $S(0) = 0$ and $\phi(0) \geq 0$, $S(x) \rightarrow \infty$ for $x \rightarrow \bar{D}$, $|\nabla\{S(x)\}| \neq 0$ for any $x \in D \setminus \{0\}$ and at least one of the following conditions holds:*

- (i) *the function $\text{div}\{\rho(x)f(x)\}$ is integrable in the domain $V = \{x \in D : S(x) \leq C\}$ and $\int_V \nabla \cdot \{\rho(x)f(x)\}dV < 0$ for all $C > 0$, where $\rho(x) = \phi(x)|\nabla\{S(x)\}|$;*
- (ii) *the function $\nabla \cdot \{\rho^{-1}(x)f(x)\}$ is integrable in the domain $V_{inv} = \{x \in D : S^{-1}(x) \geq C\}$ and $\int_{V_{inv}} \nabla \cdot \{\rho^{-1}(x)f(x)\}dV_{inv} > 0$ for all $C > 0$, where $\rho^{-1}(x) = \phi^{-1}(x)|\nabla\{S^{-1}(x)\}|$.*

Proof Denote by F_1 the flow of the vector field $\rho(x)f(x)$ through the surface $\Gamma = \{x \in D, t \geq 0 : S(x) = C\}$ with the unit normal vector $\frac{1}{|\nabla\{S(x)\}|}\nabla\{S(x)\}$. Additionally, denote by F_2 the flow of the vector field $\rho^{-1}(x)f(x)$ through the surface $\Gamma_{inv} = \{x \in D, t \geq 0 : S^{-1}(x) = C\}$ with the unit normal vector $\frac{1}{|\nabla\{S^{-1}(x)\}|}\nabla\{S^{-1}(x)\}$. According to [1], if $x = 0$ is an asymptotically stable equilibrium point of the system (12.1), then there exists a continuously differentiable positive definite function $S(x)$ such that $S(x) \rightarrow \infty$ for $x \rightarrow \bar{D}$, $\text{grad}\{S(x)\}^T f(x) < 0$ for any $x \in D \setminus \{0\}$ and $\text{grad}\{S(x)\}^T f(x)\Big|_{x=0} = 0$. If $D = \mathbb{R}^n$, then the function $S(x)$ is radially unbounded. Next, we consider two cases separately which correspond to the functions $S(x)$ and $S^{-1}(x)$.

Case (i). If $\nabla\{S(x)\}^T f(x) < 0$, then $\frac{1}{|\nabla\{S(x)\}|}\nabla\{S(x)\}^T \rho(x)f(x) < 0$. Therefore, we have $F_1 = \oint_{\Gamma} \frac{1}{|\nabla\{S(x)\}|}\nabla\{S(x)\}^T \rho(x)f(x)d\Gamma < 0$. Using Divergence theorem (or Gauss theorem), one gets $F_1 = \int_V \nabla \cdot \{\rho(x)f(x)\}dV < 0$.

Case (ii). If $\nabla\{S(x)\}^T f(x) < 0$, then $\nabla\{S^{-1}(x)\}^T \phi^{-1}(x)f(x) = -S^{-2}(x)\text{grad}\{S(x)\}^T \phi^{-1}(x)f(x) > 0$. Also, $\text{grad}\{S^{-1}(x)\}^T \phi^{-1}(x)f(x) = \frac{1}{|\text{grad}\{S^{-1}(x)\}|}\nabla\{S^{-1}(x)\}^T \rho^{-1}(x)f(x)$. Therefore, the following relation $F_2 = \oint_{\Gamma_{inv}} \frac{1}{|\nabla\{S^{-1}(x)\}|}\nabla\{S^{-1}(x)\}^T \rho^{-1}(x)f(x)d\Gamma_{inv} > 0$ is satisfied. According to Divergence theorem, we get $F_2 = \int_{V_{inv}} \nabla \cdot \{\rho^{-1}(x)f(x)\}dV_{inv} > 0$. Theorem 12.4 is proved. \square

Remark 12.1 The relation $\rho(0) = 0$ is required in [17, 18], whereas $\rho(0) \geq 0$ is used in Theorem 12.4. Therefore, the proposed results extend a class of investigated system through the use of a more general function $\rho(x)$, than in [17, 18].

Remark 12.2 The integrability of $\nabla \cdot \{\rho^{-1}(x)f(x)\}$ and the positivity of $\nabla \cdot \{\rho^{-1}(x)f(x)\}$ are required in [12] for convergence of almost all solutions of (12.1). Thus, the results of [12] are particular case in Theorem 12.4, case (ii).

Remark 12.3 Consider the physical interpretation of Theorem 12.4. Rewriting the integral inequalities as $\int_V \nabla \cdot \{\rho(x)f(x)\}dV = -\Sigma$ or $\int_{V_{inv}} \nabla \cdot \{\rho^{-1}(x)f(x)\}dV_{inv} = \Sigma$, $\Sigma \geq 0$, one gets the integral forms of stationary continuity equation with the sources (the flux is directed inward) located in the equilibrium points [20]. In particular, one has the continuity equation:

- (a) in fluid dynamics [21], where $\rho(x)$ or $\rho^{-1}(x)$ is fluid density and $f(x)$ is a flow velocity of the vector field;

- (b) in electromagnetic theory [22], $\rho(x)f(x)$ or $\rho^{-1}(x)f(x)$ means the current density and $\rho(x)$ is a charge density;
- (c) in the form of energy conservation [21], $\rho(x)f(x)$ or $\rho^{-1}(x)f(x)$ is a vector energy flux and $\rho(x)$ is local energy density;
- (d) in quantum mechanics [23], $\rho(x)$ is the probability density function and $\rho(x)f(x)$ or $\rho^{-1}(x)f(x)$ is a probability current.

If $\nabla \cdot \{\rho(x)f(x)\}$ or $\nabla \cdot \{\rho^{-1}(x)f(x)\}$ are integrable and $\nabla \cdot \{\rho(x)f(x)\} = -\sigma$ or $\nabla \cdot \{\rho^{-1}(x)f(x)\} = \sigma$, $\sigma > 0$ holds for $x \in D \setminus \{0\}$, then one gets corresponding stationary differential forms of continuity equation [20–23].

Now let us formulate a sufficient stability condition.

Theorem 12.5 *Let $\rho(x)$ be a positive definite continuously differentiable function in D . The equilibrium point $x = 0$ of the system (12.1) is stable, if at least one of the following conditions holds:*

- (i) $\nabla \cdot \{\rho(x)f(x)\} \leq \rho(x)\nabla \cdot \{f(x)\}$ for any $x \in D$;
- (ii) $\nabla \cdot \{\rho^{-1}(x)f(x)\} \geq 0$ and $\nabla \cdot \{f(x)\} \leq 0$ for any $x \in D \setminus \{0\}$;
- (iii) $\nabla \cdot \{\rho(x)f(x)\} \leq \beta(x)\rho^2(x)\nabla \cdot \{\rho^{-1}(x)f(x)\}$, where $\beta(x) > 1$ and $\nabla \cdot \{f(x)\} \leq 0$ or only $\beta(x) = 1$ for any $x \in D \setminus \{0\}$;
- (iv) $\nabla \cdot \{\rho(x)f(x)\} \leq 0$ and $\nabla \cdot \{\rho^{-1}(x)f(x)\} \geq 0$ for any $x \in D \setminus \{0\}$.

If the inequalities are strict in the cases (i)–(iv) in $x \in D \setminus \{0\}$, then $x = 0$ is asymptotically stable.

Proof We consider the proof of stability. The proof of asymptotic stability is omitted because it is similar to the stability proof, but taking into account the sign of a strict inequality. Also, according to Lyapunov theorem [1], the system (12.1) is stable, if $\nabla\{\rho(x)\}^T f(x) \leq 0$ in D .

Case (i). From the relation $\nabla \cdot \{\rho(x)f(x)\} = \nabla\{\rho(x)\}^T f(x) + \nabla \cdot \{f(x)\}\rho(x)$ implies that if $\nabla \cdot \{\rho(x)f(x)\} \leq \nabla \cdot \{f(x)\}\rho(x)$, then $\nabla\{\rho(x)\}^T f(x) \leq 0$ in D . Therefore, the system (12.1) is stable.

Case (ii). From the expression $\nabla \cdot \{\rho^{-1}(x)f(x)\} = \nabla\{\rho^{-1}(x)\}^T f(x) + \nabla \cdot \{f(x)\}\rho^{-1}(x)$ it follows that $\nabla\{\rho(x)\}^T f(x) = \rho(x)\nabla \cdot \{f(x)\} - \rho^2(x)\nabla \cdot \{\rho^{-1}(x)f(x)\}$. If $\nabla \cdot \{\rho^{-1}(x)f(x)\} \geq 0$ and $\nabla \cdot \{f(x)\} \leq 0$, then $\nabla\{\rho(x)\}^T f(x) \leq 0$ in $D \setminus \{0\}$. Thus, the system (12.1) is stable.

Case (iii) is a combination of the cases (i) and (ii). Summing $\beta(x)\text{grad}\{\rho(x)\}^T f(x) = \beta(x)\rho(x)\nabla \cdot \{f(x)\} - \beta(x)\rho^2(x)\text{div}\{\rho^{-1}(x)f(x)\}$ and $\nabla\{\rho(x)\}^T f(x) = \nabla \cdot \{\rho(x)f(x)\} - \nabla \cdot \{f(x)\}\rho(x)$, we get $(1 + \beta(x))\nabla\{\rho(x)\}^T f(x) = \nabla \cdot \{\rho(x)f(x)\} - \beta(x)\rho^2(x)\nabla \cdot \{\rho^{-1}(x)f(x)\} + (\beta(x) - 1)\rho(x)\nabla \cdot \{f(x)\}$. If $\nabla \cdot \{\rho(x)f(x)\} \leq \beta(x)\rho^2(x)\nabla \cdot \{\rho^{-1}(x)f(x)\}$ for $\beta(x) = 1$ or $\beta(x) > 1$ and $\nabla \cdot \{f(x)\} \leq 0$, then $\nabla\{\rho(x)\}^T f(x) \leq 0$ in $D \setminus \{0\}$. Therefore, the system (12.1) is stable.

Case (iv). The case (iii) is satisfied if $\nabla \cdot \{\rho(x)f(x)\} \leq 0$ and $\nabla \cdot \{\rho^{-1}(x)f(x)\} \geq 0$ in $D \setminus \{0\}$. Theorem 12.5 is proved. \square

Remark 12.4 Differently from [17, 18], we have simplified the cases (i)–(iii) at the equilibrium point and have proposed the additional case (iv) in Theorem 12.5. Further, these cases will allow one to get new conditions for the stability study of linear systems and a new method for the control law design.

The result of [8, 10] is applicable only to second-order systems. Next, we consider an illustration of the proposed results for third-order systems and compare the obtained results with ones from [12].

12.4.1 Stability of Linear Systems

Theorem 12.6 *Given $\alpha > 0$. The linear system $\dot{x} = Ax$, $x \in \mathbb{R}^n$, $A \in \mathbb{R}^{n \times n}$ is stable if at least one of the following conditions holds:*

- (i) $A^T P + PA - \frac{1}{\alpha} \frac{\beta-1}{\beta+1} \text{trace}(A)P < 0$ for $\beta = 1$ or for $\beta > 1$ and $\text{trace}(A) \leq 0$;
- (ii) $A^T P + PA - \frac{1}{\alpha} \text{trace}(A)P < 0$ and $A^T P + PA + \frac{1}{\alpha} \text{trace}(A)P < 0$.

Proof Let $\rho(x) = (x^T P x)^\alpha$. According to Theorem 12.5 (case (iii)), the relation $\nabla \cdot \{\rho(x)f(x)\} - \beta\rho^2(x)\nabla \cdot \{\rho^{-1}(x)f(x)\} = \alpha(1 + \beta)(x^T P x)^{\alpha-1}x^T[A^T P + PA - \frac{1}{\alpha} \frac{\beta-1}{\beta+1} \text{trace}(A)P]x < 0$ is satisfied, if $A^T P + PA - \frac{1}{\alpha} \frac{\beta-1}{\beta+1} \text{trace}(A)P < 0$ holds for $\beta = 1$ or for $\beta > 1$ and $\text{trace}(A) \leq 0$.

Considering Theorem 12.5 (case (iv)), the relations $\nabla \cdot \{\rho(x)f(x)\} = \alpha(x^T P x)^{\alpha-1}x^T[A^T P + PA + \frac{1}{\alpha} \text{trace}(A)P]x < 0$ and $\nabla \cdot \{\rho^{-1}(x)f(x)\} = -\alpha(x^T P x)^{-\alpha-1}x^T[A^T P + PA - \frac{1}{\alpha} \text{trace}(A)P]x > 0$ are satisfied, if $A^T P + PA + \text{trace}(A)P < 0$ and $A^T P + PA - \text{trace}(A)P < 0$ simultaneously hold. Theorem 12.6 is proved. \square

As a result, the matrix inequality in Theorem 12.6 (case (i)) simultaneously includes Lyapunov inequality (for $\beta = 1$) and inequality from [12] (for $\beta > 1$). In Theorem 12.6 (case (ii)), the matrix inequality $A^T P + PA - \text{trace}(A)P < 0$ from [12] is complemented by a new inequality $A^T P + PA + \text{trace}(A)P > 0$. The sum of the inequalities from Theorem 12.6 (case (ii)) gives Lyapunov inequality.

12.5 Control Law Design

Consider a dynamical system in the form

$$\dot{x} = \xi(x) + g(x)u(x), \quad (12.2)$$

where $x \in D \subset \mathbb{R}^n$, $u(x) \in \mathbb{R}^m$ is the control signal, the functions $\xi(x)$, $g(x)$ and $u(x)$ are continuously differentiable in D , $\xi(0) + g(0)u(0) = 0$, and the system (12.2) is stabilizable in D .

Theorem 12.7 *Let $\rho(x)$ be a positive definite continuously differentiable function in $x \in D$. The closed-loop system is stable if the control law $u(x)$ is chosen such that at least one of the following conditions holds:*

- (i) $\nabla \cdot \{\rho(x)(\xi(x) + g(x)u(x))\} \leq \rho(x)\nabla \cdot \{\xi(x) + g(x)u(x)\}$ for any $x \in D$;
- (ii) $\nabla \cdot \{\rho^{-1}(x)(\xi(x) + g(x)u(x))\} \geq 0$ and $\nabla \cdot \{\xi(x) + g(x)u(x)\} \leq 0$ for any $x \in D \setminus \{0\}$;
- (iii) $\nabla \cdot \{\rho(x)(\xi(x) + g(x)u(x))\} \leq \beta(x)\rho^2(x)\nabla \cdot \{\rho^{-1}(x)(\xi(x) + g(x)u(x))\}$, where $\beta(x) > 1$ and $\nabla \cdot \{\xi(x) + g(x)u(x)\} \leq 0$ or only $\beta(x) = 1$ for any $x \in D \setminus \{0\}$;
- (iv) $\nabla \cdot \{\rho(x)(\xi(x) + g(x)u(x))\} \leq 0$ and $\nabla \cdot \{\rho^{-1}(x)(\xi(x) + g(x)u(x))\} \geq 0$ for any $x \in D \setminus \{0\}$.

If the inequalities are strict in the cases (i)–(iv) in $x \in D \setminus \{0\}$, then the closed-loop system is asymptotically stable.

Since system (12.2) is stabilizable in D , the proof of Theorem 12.7 is similar to the proof of Theorem 12.5 (denoting by $f(x) = \xi(x) + g(x)u(x)$).

Remark 12.5 Differently from [17], we have modified cases (i)–(iii) at the equilibrium point and have proposed the additional case (iv) in Theorem 12.7.

Remark 12.6 If the control law design is based on the method of Lyapunov functions, then it is required to solve the algebraic inequality $\nabla\{V\}(f + gu) < 0$. According to Theorem 12.7, the control law is chosen from the feasibility of differential inequality. This gives new opportunities for the control law design.

12.6 Conclusions

A new method of stability and instability study of dynamical systems using the properties of the flow and divergence of the vector field is proposed. To study the stability and instability, the existence of a certain type of integration surface or the existence of an auxiliary scalar function is required. Necessary and sufficient stability and instability conditions are proposed. The generalization of Bendixon and Bendixon–Dulac theorems for n th dimensional systems is given. The relation between the necessary condition and the continuity equation is shown.

The obtained results are applied to the synthesis of the state feedback control law. It is shown that the control law is found as a solution of a differential inequality, while the control law based on the method of Lyapunov functions is found as a solution of an algebraic inequality.

Acknowledgements The results were developed under support of Russian Science Foundation (grant 18-79-10104, <https://rscf.ru/en/project/18-79-10104/>) in IPME RAS.

References

1. Khalil, H.K.: *Nonlinear Systems*. Prentice Hall (2002)
2. Zaremba, S.K.: Divergence of vector fields and differential equations. *Am. J. Math.* **LXXV**, 220–234 (1954)
3. Fronteau, J.: *Le théorème de Liouville et le problème général de la stabilité*. CERN, Genève (1965)
4. Brauchli, H.I.: *Index, Divergenz und Stabilität in Autonomen Equations*. Abhandlung Verlag, Zürich (1968)
5. Zhukov, V.P.: On one method for qualitative study of nonlinear system stability. *Autom. Remote Control* **39**(6), 785–788 (1978)
6. Zhukov, V.P.: On the method of sources for studying the stability of nonlinear systems. *Autom. Remote Control* **40**(3), 330–335 (1979)
7. Krasnoselsky M.A., Perov A.I., Povolotsky A.I., Zabreiko, P.P.: *Vector fields on the plane*. Fizmatlit, Moscow (1963, in Russian)
8. Shestakov, A.A., Stepanov, A.N.: Index and divergent signs of stability of a singular point of an autonomous system of differential equations. *Differ. Equ.* **15**(4), 650–661 (1978)
9. Zhukov, V.P.: Necessary and sufficient conditions for instability of nonlinear autonomous dynamic systems. *Autom. Remote Control* **51**(12), 1652–1657 (1990)
10. Zhukov, V.P.: On the divergence conditions for the asymptotic stability of second-order nonlinear dynamical systems. *Autom. Remote Control* **60**(7), 934–940 (1999)
11. Rantzer, A., Parrilo, P.A.: On Convexity in Stabilization of Nonlinear Systems. In: *Proceedings of the 39th IEEE Conference on Decision and Control, Sydney, Australia (CDC2000)*, pp. 2942–2946 (2000)
12. Rantzer, A.: A dual to Lyapunov’s stability theorem. *Syst. Control Lett.* **42**, 161–168 (2001)
13. Monzon, P.: On necessary conditions for almost global stability. *IEEE Trans. Autom. Control* **48**(4), 631–634 (2003)
14. Loizou, S.G., Jadbabaie, A.: Density functions for navigation-function-based systems. *IEEE Trans. Autom. Control* **53**(2), 612–617 (2008)
15. Casta A., ñeda, Robledo, G. Differentiability of Palmer’s linearization theorem and converse result for density functions. *J. Differ. Equ.* **259**(9), 4634–4650 (2015)
16. Karabacak, O., Wisniewski, R., Leth, J.: On the almost global stability of invariant sets. In: *Proceedings of the 2018 European Control Conference (ECC 2018)*, Limassol, Cyprus, 1648–1653 (2018)
17. Furtat, I.B.: Divergent stability conditions of dynamic systems. *Autom. Remote Control* **81**(2), 247–257 (2020)
18. Furtat, I.B., Gushchin, P.A.: Divergence conditions for stability study of autonomous nonlinear systems. *IFAC-PapersOnLine* **53**(2), 6317–6320 (2020)
19. Guckenheimer, J., Holmes, P.: *Nonlinear Oscillations, Dynamical Systems, and Bifurcations of Vector Fields*. Springer, New York (1983)
20. Arnold, V.I.: *Mathematical Methods of Classical Mechanics*, 2nd edn. Springer (1989)
21. Pedlosky, J.: *Geophysical Fluid Dynamics*. Springer, New York (1979)
22. Griffiths, D.J.: *Introduction to Electrodynamics* (4th ed.). Cambridge University Press (1981)
23. McMahon, D.: *Quantum Mechanics Demystified* (2nd edn.). McGraw-Hill Education (2013)

Chapter 13

Development of Situational Control Methods for a Group of Interacting Robots



Andrey E. Gorodetskiy, Irina L. Tarasova, Vugar G. Kurbanov,
Andrey Yu. Kuchmin, and Boris A. Kulik

Abstract Recently, there has been a tendency to use parallel structures in the design of intelligent robots. In particular, such structures are used in the smart electromechanical systems (SEMS) proposed by the IEMS laboratory. This is one of the variants of cyber physical systems (CPhS). Cyber physical systems the ability to integrate computing, communication, and storage of information, monitoring, and control of the physical world objects. The main tasks in the field of theory and practice CPhS are to ensure the efficiency, reliability, and safety of functioning in real time. It is important to keep in mind that the behavior of the system is based on making decisions based on information received from the sensors of the Central nervous system (CNS) about the environment and its own state. The task of making a decision about the behavior of SEMS in a group interaction of several SEMS is much more complicated, since in this case additional information about the planned behavior of other members of the group is necessary.

Keywords Situation control · SEMS groups · Selection environment · Fuzzy mathematical models · Making decisions · Formation of images · Safe control

A. E. Gorodetskiy (✉) · I. L. Tarasova · V. G. Kurbanov · A. Yu. Kuchmin · B. A. Kulik
Institute for Problems in Mechanical Engineering RAS, V.O., Bolshoy pr., 61, St. Petersburg
199178, Russia
e-mail: g27764@yandex.ru

I. L. Tarasova
e-mail: g17265@yandex.ru

A. Yu. Kuchmin
e-mail: radiotelescope@yandex.ru

B. A. Kulik
e-mail: ba-kulik@yandex.ru

13.1 Logical and Mathematical Method of Making Behavioral Decisions

The functioning of the automatic control system (ACS) of the robot relies on information from sensor systems regarding the environment and the state of the robot itself. However, in order for robots created on the basis of SEMS modules to be able to independently formulate tasks and perform them successfully, without human intervention, they must be equipped not only with more advanced sensory sensors (sensors), but also have the ability to understand the language of sensations. That is, to have feelings such as “friend–alien”, “dangerous–safe”, “loved–unloved”, and “pleasant–unpleasant”. In the presence of such abilities in the central nervous system of the robot (CNSR), it becomes possible to independently decision-making regarding expedient behavior [1]. In particular, as a result of solving systems of logical equations formed on the basis of the language of sensations, robots can acquire the ability for reflexive and conscious reasoning.

13.1.1 Stages of the Formation of Behavioral Decisions

After collecting numerical information from the sensor system of the robot, it becomes possible to proceed to the formation of the language of sensations of the robot. In this case, it is necessary to perform the following steps (operations), which are included in the software of the robot:

- Fuzzification of numerical data received from the sensor system, i.e., obtaining high-quality data of a logical type;
- Selection of images based on the combination of quality data using logical inference rules;
- Formation of binary evaluations of images of the type “dangerous–not dangerous”, “strong–weak”, “bad–good”, etc. on the basis of solving systems of logical equations that form binary relations;
- Formation of reflective reasoning based on logical analysis of binary evaluations of images in the environment of the robot;
- Formation of goals for the functioning of the robot based on the choice of reflective reasoning corresponding to the maxima (minima) of the used quality criteria;
- Decision-making about expedient behavior to achieve the formed goals based on solving optimization problems with constraints.

13.1.2 Fuzzification Data and Forming Images

Operation fuzzification numerical data is widely used in intelligent control systems, [2] and in the intelligent robot control systems. For example, when forming databases

of expert regulators. After performing the fuzzification operation, sets X_i are formed for each sensor measuring channel, containing sets of logical variables x_{ij} . For example, for the channel for measuring the brightness of the image, you can obtain the following logical variables: x_{11} – “very dark”, x_{12} – “dark”, x_{13} – “semi-dark”, x_{14} – “semi-light”, x_{15} – “light”, x_{16} – “semi-bright”, x_{17} – “bright”, x_{18} – “very bright”. The obtained logical variables for various points of the space surrounding the robot can be true ($x_{ijk} = 1$) or false ($x_{ijn} = 0$). In this case, often there may be a situation where when fuzzification numerical data about the truth or falsity of the received one or other logical variables can only say with some confidence. In this case, each obtained logical variable x_{ijk} is supplied with a corresponding attribute in the form of probability values $P\{x_{ijk} = 1\}$ or membership function $\mu(x_{ijk})$ [3], which are stored in the database along with them. In addition, together with logical variables are stored in the database the coordinates of points of the surrounding space of the robot corresponding to each logical variable.

Fuzzification of data coming through the sensory information channels of the CNSR from various sensors is an important operation for further logical constructions when decision-making. After fuzzification data possible imaging to select the environment and their classification.

The operation of selecting images in the space surrounding the robot is widely used in the systems of technical vision of intelligent robots. In this setting, this operation, in the simplest case, is reduced to combining into one set M_i those points in space that have the same set of logical variables with the same attributes and provided that the distance to the nearest neighboring point with the same parameters does not exceed some predetermined value. In this case, the coordinates of the center of gravity of the obtained images are also determined. After combining points into sets, the latter can obtain additional qualitative parameters in the form of logical variables y_{ij} obtained after, for example, analyzing the geometric parameters of these images (areas, volumes, contours, etc.). These additional parameters: y_{11} – “large volume”, y_{21} – “smooth contour”, etc. are entered into the database in the section “set of images” together with other logical parameters of sets and coordinates of their centers of gravity. The contents of this section of the database are also updated when changing the environment of the robot. When situations of incomplete certainty arise in the process of combining points in space into a set (image) due to, for example, the probabilistic attributes of logical variables, it is necessary, in addition to geometric measures of proximity of points, to introduce additional measures of proximity, such as the admissible spread of values of the probability of logical variables in neighboring points.

Formation of binary estimates of images is carried out by logical analysis of the parameters of images. To do this, you first need to draw up rules, such as “if – then”, assigning a given image of one or another binary assessment. For example, if the image is very bright, large and quickly moves toward the robot, then this image (object) is very dangerous. The system of such rules is entered into the CNSR knowledge base at the stage of robot creation. In some cases, it can be corrected during the operation of the robot through training or self-learning [4]. With a large number of such rules, it is advisable to reduce them to a system of algebraic equations

modulo two or to the algebra of Zhegalkin's logic [5]. In this case, we obtain matrix equations, the solution of which is easily parallelized by matrix processors. The latter allows you to dramatically speed up the logical analysis of the parameters of images.

However, this approach will usually be obtained matrix system is very large dimension. In a real CNSR, not all components of logical equations (not all combinations of logical variables) are physically realizable and can be discarded. As a result of such a reduction, we obtain a matrix system of equations mod 2 of a lower dimension [3]:

$$C^*R = G, \quad (13.1)$$

where $C \subset A$, $R \subset F$, $G \subset B$, B is a binary vector of dimension n , F is a fundamental vector of a logical system of dimension n , built from combinations of logical variables obtained during fuzzification of sensory data, and supplemented by 1 in place of the last element, A is a rectangular binary matrix of dimension $[n, m]$.

In addition, not every solution obtained from (13.1) a specific robot is feasible in the current environment (the state of functioning of the environment). This means that the solution obtained by the CNSR from (13.1) must satisfy the constraints, which can also be expressed in the form of systems of logical equations [5]:

$$C_i^*R_i = H, \quad (13.2)$$

$$C_j^*R_j = D, \quad (13.3)$$

where: C_i and C_j are constraint matrices obtained by analogy with the matrix C , H and D are binary vectors obtained by analogy with the vector G , $R_i \subset F_i$ and $R_j \subset F_j$.

Many solutions obtained by the CNSR when solving Eqs. (13.1)–(13.3) will naturally lead to ambiguity in the behavior of the robot. A person in this situation behaves expediently or purposefully intuitively, relying on his own experience, or a genetically inherent behavioral stereotype. Therefore, the procedure for pattern recognition in the case of their representation in algebra modulo 2 requires the setting of rules or algorithms for processing the linguistic attribute part that characterizes logical variables when performing addition and multiplication operations on them mod 2.

Linguistic attributes characterizing images form non-metrizable sets B_i . In this case, during recognition, the choice of the best class from the set of alternative ones can be based on the procedure for finding binary relations $B_i g B_j$. Where B_{cj} is a set characterizing an ideal image from the class $C_j m$ under consideration, to which we want to get as close as possible, and g is a two-place predicate on the analyzed sets, which can be given. For example, by specifying the formulas of a logical-mathematical language or by specifying a formalized linguistic expression [2]. In this case, the problem of identifying the best approximation is reduced to two tasks. The first is the task of obtaining the sets B_i , B_{cj} , and the second is the construction of an optimal procedure g that allows one to obtain a quantitative estimate of the proximity of B_i to B_{cj} .

It is advisable to start creating the initial base for constructing g by selecting metrizable subsets in each of the compared sets (for example, subsets of decision probabilities), for whose elements relations and numerical measures of proximity can be specified. The next, most difficult step is to order the elements of non-metrizable subsets. It is very likely that to solve this problem, you will need to build a new system of logical equations, the solution of which will lead either to metrizable sets, or to ordered ones. In the first case, we immediately get numerical measures of proximity. In the second case, these measures will have to be built anew. As possible numerical estimates, the cardinality of sets, the number of matching elements, the number of groups of matching elements, and so on can be used. Any recommendations on the choice of these or other estimates cannot be recommended at present due to the lack of knowledge of such models. Therefore, if it is impossible to order non-metrizable sets, the decision about the greatest proximity of any set to the standard should be made by the developer or operator himself, based on their preferences, experience and intuition [3].

The most commonly used and easily constructed binary functional relationships include the following:

- estimation by the maximum deviation of power sets:

$$\sum_i x_i - \sum_i y_i = \Delta, \quad (13.4)$$

where $x_i = 1$ and $y_i = 1$ for non-zero (non-empty) elements of the compared sets and, respectively, $x_i = 0$ and $y_i = 0$ for zero (empty) elements of the compared sets, and Δ is the numerical proximity estimate.

- estimation based on the standard deviation of set capacities:

$$\sqrt{\left(\sum_i x_i\right)^2 - \left(\sum_i y_i\right)^2} = \delta, \quad (13.5)$$

where δ is the numerical estimate of proximity.

- probabilistic estimation based on the maximum deviation of power sets:

$$\sum_i P(x_i = 1) x_i - \sum_i P(y_i = 1) y_i = \Delta_p, \quad (13.6)$$

where $P(\cdot)$ is the probability, and Δ_p is the numerical probability estimate of proximity.

- probabilistic estimation based on the standard deviation of set capacities:

$$\sqrt{\left(\sum_i P(x_i = 1) x_i\right)^2 - \left(\sum_i P(y_i = 1) y_i\right)^2} = \delta_p, \quad (13.7)$$

where δ_p is a numerical probability estimate of proximity.

Using these binary functional relationships makes it easy to rank B_i images by their proximity to B_{ej} standards, and at the same time allows you to enter a numerical proximity score.

13.1.3 *The Adoption of Reflective Solutions*

The robot's reflexive reasoning can be formed on the basis of logical analysis of binary evaluations of images in its environment. To do this, you need to create rules of the "if – then" type of reaction to a particular binary evaluation of the image, taking into account its location and the state of the robot itself. For example,

1. if the image is very dangerous and is located nearby, the robot must move away from it;
2. if the image is very dangerous, is nearby and there is a large good image nearby, the robot must hide behind it.

These rules are compiled and entered into the knowledge base at the stage of creating the robot. There can be a lot of them and they can be adjusted during operation. At the same time, it is also advisable to bring them to the system of algebraic equations modulo two or to the algebra of logic Zhegalkin for parallelization of calculations. The program for translating a system of rules into algebraic equations modulo two should be included in the mathematical support of the CNSR.

The formation of robot functioning goals based on the choice of reflexive reasoning obtained after analyzing binary evaluations of images surrounding the robot is a complex problem associated with solving poorly formalized multi-criteria optimization problems [6]. In this case, it is often necessary to choose not one specific goal, but a sequence of consecutive goals when the previous goals are successfully completed. At the design stage of the robot, it is impossible to foresee all the situations that the robot may be in when making a decision about choosing the purpose of functioning. Therefore, the robot's memory is filled with possible situations based on the expected operating conditions and the corresponding possible goals with an index of their effectiveness. Then the CNSR should have such software that could, by evaluating acceptable reflexive reasoning and available suitable most effective goals for functioning in a given situation, create a sequence of goals that would provide the maximum (minimum) quality criteria expressed numerically. The formation of such a quality criterion is a complex and time-consuming task, the solution of which is primarily associated with the formation and solution of a number of logical problems that lead to the formula for calculating the quality criterion [6].

When choosing optimal reflexive reasoning described by systems of logical equations in the Zhegalkin algebra, it is necessary to solve optimization problems with restrictions. In this case, the simplest solutions will be those where it is possible to build a scalar quality criterion, including from attributes of logical variables. In

this case, the optimal search can be reduced to mathematical programming (MP) problems [7].

In the MP problem, we need to calculate an n -dimensional vector X that optimizes (converts to a maximum or minimum, depending on the content of the problem) the quality criterion of the solution $f_0(x)$, subject to the restrictions $f_j(x) \leq u_j$, $j = 1, 2, \dots, r$, $x \in G$, where f_j —known scalar functional, u_j —given numbers, G —a predetermined set of n -dimensional space R^n .

Thus, the MP task has the form:

$$f_0(X) \rightarrow \text{extr}/f_j(x) \leq u_j, \quad j = 1, 2, \dots, r, \quad x \in G \subseteq R^n. \quad (13.8)$$

For the probabilistic attribute part of logical variables in the specified systems of equations [8], the optimization goal can be to search for those identification rows of the matrix of the system of logical equations describing the solution that give the true values of logical functions y_i with the maximum values of probabilities $P\{y_i = 1\}$. Then the quality criterion can be expressed as follows:

$$f_0(Y) = \sum_{i=1}^n P\{y_i = 1\} \rightarrow \max. \quad (13.9)$$

The probability values $P\{y_i = 1\}$ can be calculated approximately using the algorithm described in [6].

If the analysis of a complex CNSR reveals that the influence of certain components of y_i on its behavior is different, then the quality criterion (13.9) should be given the form:

$$f_0(Y) = \sum_{i=1}^n \beta_i P\{y_i = 1\} \rightarrow \max, \quad (13.10)$$

where β_i is the assigned weight coefficients.

If the attribute part of logical variables in the specified systems of equations [6] contains membership functions, the optimization goal may be to search for those identification rows of the matrix of the system of logical equations describing the solution that give values of logical functions y_i with the maximum values of their membership functions $\mu(y_i)$. Then the quality criterion can be expressed as follows:

$$f_0(Y) = \sum_{i=1}^n \mu(y_i) \rightarrow \max. \quad (13.11)$$

The values of the membership functions $\mu(y_i)$ can be calculated using the algorithms described in [6].

If the analysis of a complex CNSR reveals that the influence of certain components of y_i on its behavior is different, then the quality criterion (13.11) should be given the form:

$$f_0(Y) = \sum_{i=1}^n \beta_i \mu(y_i) \rightarrow \max, \quad (13.12)$$

where β_i is the assigned weight coefficients.

If the attribute part of logical variables in the specified systems of equations [6] contains intervals $[a_{ji}, b_{ji}]$, then the following scalar functional can be used:

$$J_1 = \sum_j^m \sum_i^n k_{ji} (b_{ji} - a_{ji}) \rightarrow \min, \quad (13.13)$$

$$J_2 = \sum_j^m \sum_i^n [k_{ji} (b_{ji} - a_{ji}) - c_{ji}]^2 \rightarrow \min, \quad (13.14)$$

$$J_3 = \sum_j^m \sum_i^n k_{ji} [(b_{ji} - a_{ji}) - (b_{ji}^0 - a_{ji}^0)]^2 \rightarrow \min, \quad (13.15)$$

$$J_4 = \sum_j^m \sum_i^n [k_{ji}^b (b_{ji} - b_{ji}^0)^2 + k_{ji}^a (a_{ji} - a_{ji}^0)^2] \rightarrow \min, \quad (13.16)$$

where: k_{ji} , k_{ji}^b , k_{ji}^a —coefficients of preference of the decision-maker (DM) on optimality, c_{ji} —the desired DM interval width, b_{ji}^0 , a_{ji}^0 —the desired DM interval boundaries.

However, the recommendations available in various literatures [8–10] for calculating integrals of complex logical functions with known intervals of logical variables are still very contradictory and may give completely unacceptable results. This issue is discussed in more detail in [10]. The most acceptable results in solving this problem can be obtained using multi-step generalized programming [11] and software environments such as A-life [12].

13.1.4 Informed Decision-Making

After completing the formation of a sequence of goals for the robot's functioning, it is necessary to make a decision about the appropriate behavior to achieve the formed goals. The task of providing robots with appropriate behavior skills is still at an early stage. Currently, the most fully studied problems of choosing optimal solutions in conditions of incomplete certainty of interval, probabilistic, or linguistic type [6]. The process of making a decision about appropriate behavior can be significantly accelerated by recognizing the formed M_i images, i.e., assigning them to certain classes of C_{jm} images containing the so-called ideal M_i^* images, for which the

previously accepted optimal solutions are known ($M_i^* \in C_{jm}$). In this case, you can use the method of the situation of familiarity [13] (analogous to intuition in humans), i.e., replace the desired solution with an analog.

A person in the process of thinking and making decisions based on the processing of available information usually adheres to one of two styles of deductive or inductive. There is also a third, poorly studied and rarely encountered type of thinking—the abductive. When using such approaches in the CNSR, it is necessary to solve a number of optimization problems with restrictions. The basis for solving these problems can be various methods of mathematical programming, mathematical programming in ordinal scales, generalized mathematical programming and multi-step generalized mathematical programming [7, 11]. A number of new approaches to solving optimization problems with interval uncertainty are described in [10]. When solving such optimization problems of solutions described by systems of equations in algebra modulo two, decisions about optimality can be made based on the concept of sequential preference of one of the compared options to another. When using this approach in the CNSR, it is advisable to set the acceptable set of alternatives not by inequalities, but by certain conditions of preference for the selected options. To solve such problems, you can generalize the scheme of mathematical programming, moving from quantitative scales to ordinal ones, i.e., moving from models that require the assignment of functions that define the goals and limitations of the problem to models that take into account the preferences of the persons involved in choosing the solution. This extends the range of applications of the theory of extreme problems and can be useful in a number of choice situations [2, 14]. The transition to problems of mathematical programming in ordinal scales, generalized mathematical programming, and multi-step generalized mathematical programming is described in more detail in [3]. In this case, when choosing the optimal solution to a system of logical equations, part of the attributes of logical variables can be linguistic expressions that describe preferences in the form of, for example, score ratings formed based on the analysis of the opinions of decision-makers. Moreover, there is a fundamental possibility of ordering preferences.

In deductive decision-making, the process of thinking in the Central Nervous System begins at the global level and then moves down to the local level [15]. The technical equivalent of this type of thinking can be the optimization process, when first the best possible solution is found based on the available information, and then the solution is corrected by checking all the restrictions based on the available information. In this case, after calculating the quality criteria for all possible solutions, all the solutions found are ranked. The solutions are then checked for compliance with the restrictions, starting with the first one that has the highest quality criteria. In this case, the first of the tested solutions that meet the restrictions is considered optimal.

In inductive decision-making, the process of thinking in the Central nervous system begins with the analysis of individual decisions and then the search for a common, global conclusion [15]. The technical equivalent of this type of thinking can be the optimization process, when first all solutions are checked for the feasibility of type

constraints based on available information, and then the best solution is found out of all possible solutions based on type criteria.

In abduction decision-making according to *Peirce*, cognitive activity in the Central nervous system is an interaction of induction, deduction and abduction [16]. In this case, abduction makes the acceptance of plausible hypotheses by explaining the facts, with the help of induction, testing of the hypotheses put forward is implemented, and by deduction, consequences are deduced from the accepted hypotheses. A technical analogue of this type of thinking can be the process of searching for an optimal solution by analogy, when from all possible solutions, the solutions that are closest to the existing solutions stored in the CNSR database and that gave good results in the past are first selected using image recognition methods [17]. Then you can use deductive and/or inductive decision-making methods to select the best quality criteria.

Comparing the described decision-making methods, we can conclude that the abduction method is the fastest by analogy with intuition, but its reliability depends on the completeness of the database of good decisions from past experience, i.e., it strongly depends on the time of operation of similar robots in similar environments. The deductive method is faster than the inductive method for a large number of constraints, since it does not require checking the constraints for all solutions. With complex quality criteria and a small number of restrictions, the inductive method can give a faster result, since it will reject the search for solutions based on complex quality criteria for solutions that are unacceptable by restrictions.

13.2 Principles of Forming the Language of Sensation for Decision-Making in the Central Nervous System of SEMS

The development of modern robots is closely connected with the creation of their languages of sensations, on the basis of which a figurative representation of the environment and the intellectual interaction of robots between themselves and with the human operator is possible. In this area, many developments are devoted to the control of robots in different conditions. For example, in [18], a spoken language is proposed as a convenient interface (ELI- Extensible Language Interface) for controlling a mobile robot. It is designed to interpret speech commands to perform the tasks of extracting and transmitting information for use in specific, narrow tasks, such as caring for the elderly. In order to use it effectively, a number of basic terms must be associated with perception and motor skills. Therefore, at present there is a wide range of tasks for which the robot using the ELI cannot be pre-programmed. For example, such as the nature of specific tasks in the household that he may be asked to perform. In [19], an algorithm is proposed for teaching the robot to see various objects. Developed robotic vision systems are based on what animals are supposed to see as developers. That is, they use the concept of layers of neurons, as in the

brain of animals. Engineers program the structure of the system, but do not develop an algorithm that works in this system.

Since the 1970s, robotics engineers have been thinking about reducing information for displaying images in a computer's memory, using the features of images. These can be lines or points of interest, such as angles or certain textures. Algorithms are created for finding these functions and tracking them from the image frame to the image frame in the video stream. This significantly reduces the amount of data from millions of pixels in an image to several hundred or thousands of objects. Then the engineers think about how the robot can realize what they saw and what it will need to do. They write software that recognizes patterns in images to help the robot understand what's around it.

It should be noted that certain specific tasks have been solved for the processing and comprehension of the sensory information of robots, but there is no integral algorithm that takes into account all the organs of the robot's sense: organs of sight, hearing, smell, taste, touch, etc. no. Therefore, in order that intelligent robots could independently, go without human intervention, formulate tasks and successfully accomplish them, they must not only be equipped with sensation sensors (sensors), but also have the ability to understand the language of sensations, i.e., have sensations such as "yours is alien", "dangerous – safe", "beloved – unloved", "pleasantly – unpleasantly", etc., formed as a result of solving systems of logical equations describing the environment in the language of feelings. For this, it is possible to use logical inference systems, which in intellectual systems are associated with solving systems of logical equations [2]. They may have a higher dimension. The number of variables usually exceeds the number of equations, which leads to non-uniqueness of the solution. Using the Zhegalkin algebra [20] allows one to perform algebraization of the problem, so that the Euclidean norm can serve as a scalar measure of the quality of the solution. At the same time, to solve it, you can use a method similar to the Gauss elimination method when solving linear systems of algebraic equations with real numbers. This technique can be the basis for providing the robot with the ability to form a sensation language in the database of the "Central Nervous System of the Robot" (CNSR). In this case, the robot has the opportunity to make independent decisions regarding expedient behavior [21].

13.2.1 Algorithm of Formation of the Language of Sensations of the Robot

The central nervous system of a robot is built by analogy with the central nervous system of a person who has sensory organs that perceive information about the environment and their own state. Therefore, the solution to the problem of creating a central nervous system of a robot is reduced, first of all, to research and development of circuits of the type of the following circuit (consisting of approximately seven blocks): 1 – (robot sensors) → 2 – (signal receiving channel), 3 – (primary pro-

cessing of measuring signals) \rightarrow 4 – (combining signals, fuzzification, recognition, classification, decision-making) \rightarrow 5 – (transmission channel of control signals), 6 – (transformation and formation of a control action) \rightarrow 7 – (moving, stretching, and other actions of the working parts of the robot).

The description of all CNSR blocks is described in detail in [22]. It should be noted that one of the most promising options for the mathematical implementation of the fuzzification block is a logical-mathematical model for the formation of behavioral processes based on the analysis of sensations in the form of signals from the robot's sensory system. To do this, the robot's sensor system collects environmental information from various sensors and transmits it to the CNSR. Next, the measurement signal preprocessing unit and the fuzzification, recognition, and decision-making unit [23] of the CNSR processor form the robot's sensory language using the following algorithm:

1. Quantization of the surrounding space in the visibility zone of the robot's sensor system with the assignment of the resulting pixels a value in the form of a pixel number.
2. Fuzzification of the robot's sensory information for each pixel of the surrounding space and the formation in the memory of the CNSR of the display of the surrounding space in the form of pixels with their coordinates and fused data.
3. The formation of images in the display of the surrounding space for each sense organ of the robot.
4. Formation of images by combining images from different senses.
5. Assigning names to images in the form of words of the English language.
6. Write words in the form of a combination of letters of the English language.
7. If for any images there was no suitable word of the English language, then such images can be combined with others in various combinations until all possible combinations have been used.
8. If any combination finds the appropriate words of the English language, then these names are assigned to these combinations of images.
9. If after the completion of operation (8) any images cannot be found suitable words, such images are given a name in the form of a new word from a combination of English letters and the corresponding message is transmitted to the robot community to legitimize a new reference word and the corresponding image. English language and the corresponding message is transmitted to the community of robots to legitimize the new reference word and the corresponding image.

Let us consider in more detail the basic operations of this algorithm.

13.2.2 Quantization of the Surrounding Space

The center of gravity of the robot is placed in the center of the Euclidean space E^3 . The boundaries of the sensitivity zones (intervals) of the sensor system are determined: $[-X, +X]$, $[-Y, +Y]$, $[-Z, +Z]$. The result is a three-dimensional

subspace $C \subset E^3$. This subspace is divided into quanta along the X axis with a step h_x , along the Y axis with a step h_y , and along the Z axis with a step h_z . The quanta in $[-X, +X]$, $[-Y, +Y]$, $[-Z, +Z]$ are assigned numbers i, j, k , respectively. As a result, the entire subspace C will be divided into many pixels p_{ijk} . Each p_{ijk} pixel will correspond to information measured by the CNSR sensor system on sensations of the organs of vision, hearing, smell, taste, touch, etc.

13.2.3 Fuzzification of Sensory Information

A very important operation for forming the language of sensations is fuzzification of sensory data assigned to pixels and recorded in the CNSR database. To do this, first of all, it is necessary to combine the sensory information of each pixel p_{ijk} into groups that form, like a person, the following senses of the robot: vision in the form of the set E ; hearing in the form of the set R ; sense of smell in the form of the set S ; taste in the form of a set U ; the sense of V .

In each of the introduced sets, it is possible to distinguish the subsets forming them that characterize the properties of the observed pixel (object):

$$E_i \subset E, \quad R_i \subset R, \quad S_i \subset S, \quad U_i \subset U, \quad V_i \subset V.$$

The set of such subsets depends on the set of sensors that form the sensory organs of a particular robot. For example, for vision, the following subsets can be introduced: E_1 —image brightness; E_2 —image color; E_3 —flashing frequency; E_4 —rate of change of brightness; E_5 —speed of color change, etc.

For hearing, the following subsets can be introduced: R_1 —sound power; R_2 is the key; R_3 is the interval; R_4 —rate of change of volume; R_5 —rate of change of tonality; R_6 —interval change rate, etc.

For the sense of smell, the following subsets can be introduced: S_1 —type of smell; S_2 —odor intensity; S_3 is the rate of rise or fall of the odor; S_4 is the rate of change of the type of smell; S_5 - odor interval, etc.

For taste, the following subsets can be introduced: U_1 —type of taste; U_2 is the power of taste; U_3 —rate of change in taste, etc.

For touch, the following subsets can be entered: V_1 —flatness of the surface; V_2 —dry surface; V_3 —surface temperature, etc.

The data forming these subsets are extracted from signals from sensors of the senses of robots by their fuzzification [22]. This data can be of logical, logical-probabilistic, or logical-linguistic types.

Data of a logical type is formed from data or signals from sensors of the sense organs of robots by quantizing the entire range of a specific sensor and assigning Δ_n , (where $n = 1, 2, \dots, N$ is the number of a quantum), the names of logical variables that take values: true (1) or false (0). For example, logical variables are formed by quantizing the entire range of the acoustic sensor and assigning the obtained Δ_n quanta to the names of logical variables that take the value true (1) or false (0).

Then, if the range of the sound intensity sensor lies in the range from 0dB to 80dB, then by entering a quantum of 20dB, you can divide the entire range of the change in sound intensity into four quanta $\Delta_1 = [0, 20]$, $\Delta_2 = [20, 40]$, $\Delta_3 = [40, 60]$, $\Delta_4 = [60, 80]$. Then, the quantum Δ_1 can be given the name R_{r1} very weak sound, the quantum Δ_2 should be given the name R_{r2} weak sound, the quantum Δ_3 should be given the name R_{r3} strong sound, and the quantum Δ_4 should be given the name R_{r4} very strong sound. In particular, if, for example, the sensor shows the sound intensity $r = 50dB$, then after fuzzification, the following values of the logical variables $R_{r1} = 0$, $R_{r2} = 0$, $R_{r3} = 1$, $R_{r4} = 0$ and the corresponding intervals described above will be entered into the CNSR database as attributes of these logical variables.

When receiving data of a logical-probabilistic type, the probabilities $P(r_i)$ are additionally added to the attributes, which can be determined under the normal law of the distribution of sound strength as follows:

$$P(r_n) = 2 \left(\Phi(3) - \Phi \left(\frac{|r_n - m|}{\sigma} \right) \right),$$

where: a is the lower boundary of the quantum, b is the upper boundary of the quantum, $m = (b - a)/2$ is the expected value and $\sigma = (b + a)/6$ is the standard deviation, $\Phi(\cdot)$ —Gaussian standard distribution function, which corresponds to the simplest normal law with parameters $m = 0$, $\sigma = 1$ and whose values are known.

Naturally, for logical variables corresponding to quanta, which do not include sensor readings, the probabilities will be zero.

In particular, if the sensor shows the sound strength $r = 50dB$, then after fuzzification, the following values of the logical variables $R_{r1} = 0$, $R_{r2} = 0$, $R_{r3} = 1$, $R_{r4} = 0$ and the following attributes corresponding to them will be entered into the CNSR database: for R_{r1} —interval $[0; 20]$ and the probability $P(r_1) = 0$; for R_{r2} , the interval $[20; 40]$ and the probability $P(r_2) = 0$; for R_{r3} , the interval $[40; 60]$ and the probability $P(r_3) = 1$; for R_{r4} , the interval $[60; 80]$ and $P(r_4) = 0$.

It should be noted that in the formation of logical-probabilistic variables, the quantization of the sensor range can be carried out with overlap. For example, if the range of the sound intensity sensor lies in the range from 0dB to 75dB, then by entering a quantum value of 30dB, you can break the entire range of sound strength into the following four quanta: $[0; 30]$; $[15; 45]$; $[30; 60]$; $[45; 75]$. Then, if the sound intensity sensor shows $r = 50dB$, then after fuzzification, the following values of the logical variables $R_{r1} = 0$, $R_{r2} = 0$, $R_{r3} = 1$, $R_{r4} = 1$ and the following attributes corresponding to them will be entered into the CNSR database: for R_{r1} —the interval $[0; 30]$ and the probability $P(r_1) = 0$; for R_{r2} , the interval $[15; 45]$ and the probability $P(r_2) = 0$; for R_{r3} , the interval $[30; 60]$ and the probability $P(r_3) = 0.12$; for R_{r4} , the interval $[45; 75]$ and the probability $P(r_4) = 0.12$.

When receiving data of a logical-probabilistic type and with a uniform law of the distribution of sound strength, the probabilities $P(r_n)$ are additionally added to the attributes, which can be determined as follows:

$$P(r_n) = \left\{ \begin{array}{ll} \frac{2(b-r_n)}{b-a}, & \text{if } r_n \geq m \\ \frac{2(r_n-a)}{b-a}, & \text{if } r_n < m \end{array} \right\}.$$

In this case, for the above example, after fuzzification, the following values of the logical variables $R_{r_1} = 0$, $R_{r_2} = 0$, $R_{r_3} = 1$, $R_{r_4} = 1$ and the following attributes corresponding to them will be entered into the CNSR database: for R_{r_1} , the interval [0; 30] and the probability $P(r_1) = 0$; for R_{r_2} , the interval [15; 45] and the probability $P(r_2) = 0$; for R_{r_3} , the interval [30; 60] and the probability $P(r_3) = 0.25$; for R_{r_4} , the interval [45; 75] and $P(r_4) = 0.25$.

When receiving data of a logical-linguistic type, the membership functions are additionally added to the attributes, which can be determined in the triangular form of the function as follows:

$$\mu(r_n) = \left\{ \begin{array}{ll} \frac{2(b-r_n)}{b-a}, & \text{if } r_n \geq \frac{a+b}{2} \\ \frac{2(r_n-a)}{b-a}, & \text{if } r_n < \frac{a+b}{2} \end{array} \right\}.$$

In this case, for the above example, after fuzzification, the following values of the logical variables $R_{r_1} = 0$, $R_{r_2} = 0$, $R_{r_3} = 1$, $R_{r_4} = 1$ and the following attributes corresponding to them will be entered into the CNSR database: for R_{r_1} , the interval [0; 30] and the value of the membership function $\mu(r_1) = 0$; for R_{r_2} , the interval [15; 45] and the value of the membership function $\mu(r_2) = 0$; for R_{r_3} , the interval [30; 60] and value of the membership function $\mu(r_3) = 0.25$; for R_{r_4} , the interval [45; 75] and $\mu(r_4) = 0.25$.

Thus, after fuzzification of sensory data in the database for each pixel there will be a set of logical, logical-probabilistic, and logical-linguistic variables. The next step in creating a robot sensation language will be the task of forming images in the surrounding space for each sensory organ.

13.2.4 Image Formation in the Display of the Surrounding Space

The formation of images is performed for the display of the surrounding space for each sensory organ individually. In particular, for the view there will be a display of the surrounding space $C_E \subset C$, for hearing $C_R \subset C$, for the sense of smell $C_S \subset C$; for the taste of $C_U \subset C$ and for the sense of $C_V \subset C$. In each of these mappings, adjacent pixels with equal values of logical variables and close values of their attributes can be combined. Then in the spaces of the sense organs C_E , C_R , C_S , C_U and C_V we get sets of images Im_E , Im_R , Im_S , Im_U , Im_V with certain contours. Since attributes of logical variables can be intervals, probabilities, membership functions,

etc., for each type of attribute it is necessary, accordingly, to introduce a measure of proximity δ_Δ , δ_P , δ_μ .

After the operation of combining pixels into image sets $Im_E(i)$, $Im_R(i)$, $Im_S(i)$, $Im_U(i)$, $Im_V(i)$, in each space of the sensory organs C_E , C_R , C_S , C_U and C_V , one can depict image contours and give each circuit a name. As a result, there will be five cards K_E , K_R , K_S , K_U and K_V with sets of image contours $Im_E(i)$, $Im_R(i)$, $Im_S(i)$, $Im_U(i)$, $Im_V(i)$, where $i = 1, 2, \dots$

It should be noted that, when processing two images, a preliminary analysis is first performed (spectral and correlation analysis), which includes the selection and application of the most suitable filter (linear filtering), on the basis of which contour representations (polygonal contours) are formed.

13.2.5 *Formation of Images by Combining Images from Different Senses*

Typically, the formation of images from images consists in operations on images such as intersection, union, or symmetric difference of ordered sets and assigning the result to one or another reference image stored in the database. If there is not a single suitable image in the database, then such a combination of images is given the name of the new image, which is placed in the database for temporary storage. When this new image is repeated many times during the operation of the robot, this image becomes a reference image and is given a permanent name.

To assign a combination of images to a particular standard, it is necessary to introduce a measure of proximity of ordered sets. Among the most well-known proximity measures (criterion), the following can be distinguished [24]: estimation by the maximum deviation of cardinalities of sets; estimate of the standard deviation of the cardinality of sets; probabilistic assessment of the maximum deviation of cardinalities of sets; probabilistic estimate of the standard deviation of cardinalities of sets. Using these criteria allows you to rank combinations of images according to their proximity to the reference image and at the same time allows you to enter a numerical estimate of proximity.

The process of forming images based on information from the senses of the robot is carried out in the following sequence.

First, we look for the presence of images that are close to the database standards in each of the K_E , K_R , K_S , K_U , and K_V cards. The found images are assigned the names of the standards. They are recorded in the observable data base of the central nervous system together with their coordinates and are excluded from the corresponding maps.

Then a sequential pairwise overlay of cards is performed on each other with the operation of intersecting the sets K_E , K_R , K_S , K_U , and K_V . Similarly, three (four, five) cards are superimposed on top of each other. At each intersection of images, the presence of images close to the database standards is searched for. The

found intersections of the images are assigned the names of the standards. They are recorded in the observable data base of the central nervous system together with their coordinates and excluded from the corresponding map intersections. Therefore, in each subsequent intersection, the maps corrected by the results of deletions are involved.

If any images appear in the corrected intersection, then new names are assigned to them. They are also recorded with their coordinates in the observational database of the central nervous system.

At the last stage, in the symmetric differences of the sets from the maps K_E , K_R , K_S , K_U , and K_V , the presence of images close to the standards in the databases is searched. Moreover, it is similar at first by the operation of the symmetric difference of two sets, then three, four, and five. The found symmetrical differences of the images are assigned the names of the standards. They are recorded in the database of observable data of the Central nervous system together with their coordinates and are excluded from the respective map associations. Therefore, in each subsequent association, cards corrected by the results of deletions are involved.

Thus, semantic data about the space surrounding the robot are generated in the central nervous system database, based on which the robot makes behavioral decisions [23] using standard behavioral algorithms stored in the robot knowledge base. These algorithms are recorded in the knowledge base of the robot at the stage of its creation, based on its purpose. Therefore, such algorithms will be called genetic. However, after the formation of the semantic database of the space surrounding the robot, it may turn out that two or more images are partially or completely present in the same place in space. Therefore, it is necessary to adjust the semantic database in order to exclude detected collisions. Such adjustment is closely related to the formation of semantic data - pragmatic, corresponding to the problem being solved by the robot at the moment.

13.3 Problems with Secure Control of SEMS Group

To create a future of humanity that will be literally filled with robots and all sorts of “smart” systems, it is required that these robots and artificial intelligence systems have “instincts” that allow them to avoid collisions with obstacles and with each other while driving. However, if these instincts are too strong, the robots will be too slow, which will negatively affect the effectiveness of their actions. To solve this problem, we need to develop algorithms that constantly strive to find the optimal balance between speed and safety, which will allow robots to always act with high efficiency.

Collision avoidance is the main aspect of the systems of all vehicles and other robotic devices that can move completely independently, in automatic mode. Some of the developers of control systems for robot cars deliberately allow them to commit minor traffic violations in the event of a collision hazard.

In addition, the task of managing a group of robots has an additional complexity due to the need to ensure coordination between robots. In complex robotic systems, each robot must satisfy its own kinematic equations, as well as existing phase constraints, including dynamic constraints that ensure that there are no collisions between robots.

13.3.1 *The Principles of Safe Control*

Safe control is closely related to survivability control, algorithms that are included in the mathematical support of intelligent robots. In this case, the behavior of SEMS can be adjusted due to the flexible response of the automatic survivability control system included in the automatic control system (ACS) to sudden changes in time of external conditions and the internal state of the SEMS itself. The most studied and frequently encountered tasks of survivability control are adaptation, hot redundancy, compensation, and borrowing [25]. Less studied and less common is the problems of stress and stupor or switching on emergency mode. In the process of development of robot ACS and their intellectualization, new modes of their functioning began to appear. In particular, robots created on the basis of SMS are able to work as part of a group of robots under the control of an operator or a higher level ACS [26]. In this case, there may be situations when the operator's instructions and/or higher level ACS will contradict the internal state of the SEMS itself. Another, no less difficult task is to build algorithms for checking the feasibility of conditions. They should probably rely on simulating the behavior of SEMS when executing the proposed operator instructions and/or top-level control system instructions. At the same time, it is desirable that the created algorithms can take into account the possible rapid degradation of SEMS and include survivability control mechanisms in advance with the output of messages to the upper level of group control about the undesirability or danger of the proposed behavior instructions.

When forming a set of acceptable controls (SEMS behavior instructions), it is first necessary to identify and write to the SEMS ACS database the acceptable values of parameters of individual group members, as well as their static and dynamic characteristics. Then, based on the purpose of a particular SEMS, you need to make a list of possible $U_{ki}(t)$ instructions. Next, you need to identify a set of acceptable $Y_d(t)$ behavior instructions by mathematical and computer modeling of the dynamic configuration space. The task is divided into two stages.

At the first stage, for example, using computer simulations of SEMS, invalid $U_{ki}^*(t)$ instructions are identified among possible $U_{ki}(t)$ instructions, which lead to the output of certain parameters and characteristics beyond the acceptable limits:

$$U_{ki}^*(t) \subseteq U_{ki}(t).$$

These instructions should be excluded from the possible:

$$U_{ki}^d(t) = U_{ki}(t)/U_{ki}^*(t).$$

At the second stage, dangerous instructions are identified among $U_{ki}^d(t)$ instructions, i.e., those $U_{ki}^o(t)$ whose frequent repetition leads to rapid degradation of SEMS with subsequent failures and breakdowns. In this case, logical-probabilistic and logical-linguistic modeling of SEMS degradation is required [27, 28] with analysis of degradation time. If the degradation time of the t_{di} system during repeated application of any $U_{ki}^d(t)$ instruction is less than the permissible t_{dop} ($t_{di} < t_{dop}$), then these instructions are classified as dangerous $U_{ki}^d(t)$ and they are excluded from the possible ones. Therefore:

$$Y_d(t) = (U_{ki}^d(t)/U_{ki}^o(t)).$$

Next, among the $Y_d(t)$ instructions, we identify those $U_{ki}^c(t)$ that can lead to collisions. They are also excluded from the possible ones. As a result, the safe control instructions will be

$$U_s(t) = (Y_d(t)/U_{ki}^c(t)).$$

In some cases, when implementing group control systems for robots, some instructions issued by the top-level ACS (coordinator-planner ACS) may not be clear to the SEMS ACS, although they were considered acceptable by the simulation results. This, for example, may be due to incomplete adequacy of the models used. You can partially remove such instructions from acceptable ones by semantic analysis of instructions for correctness and non-inconsistency, and by organizing a dialogue between interacting SEMS ACS.

In order to achieve a specific goal for a group of robots, each robot can perform a pre-defined sequence of actions without collisions in the case of a deterministic environment. In the case of a nondeterministic environment, this sequence must be found by the control system of a group of robots in the process of achieving the goal. At the same time, you first need to synthesize a single control system to stabilize the robot relative to a certain point in the state space with phase constraints. Then you need to look for optimal robot trajectories in the form of points in the state space for robots to move from different initial conditions to the specified end positions.

First, we solve the problem of choosing the optimal route for all members of the group without intersections. If the routes of the group members do not intersect and the time to reach the goal of moving the group does not exceed the required time, then the solution to the task is found, otherwise they move on to the next stage.

At this stage, the task of driving group members in the case of possible intersections of traffic routes is solved. If the time to reach the goal of moving the group, taking into account the passage of intersections without collisions, does not exceed the required time, then the solution to the task is found, otherwise they proceed to the next stage.

At this stage, the problem of safe traffic with the crossing of the trajectories and dynamics of movements with delays at the intersections to avoid collisions, applying the rules of journey of intersections or prioritization of journey of intersections of members of the group.

13.3.2 *Managing the Safe Movement of the Group Through the Intersection, Taking into Account the Rules of Passage*

In this case, in the vicinity of the intersection, the surrounding space L^3 is allocated with the dimension L_x, L_y, L_z along the $X, Y,$ and Z axes. It is divided at the beginning of control t_0 into cells $e_q(t_0)$ with constant steps h_x, h_y, h_z on the X, Y, Z axes. Robot cars $A = \{a_1, a_2, \dots, a_n\}$ are located at points $S = \{s_1, s_2, \dots, s_n\}$ of the surrounding space L^3 and in their corresponding cells. Each of them is characterized by the speed of movement, acceleration, and target points $F = \{f_1, f_2, \dots, f_n\}$ of this space. They need to arrive at the time t_f in the minimum time T . Moreover, the number of possible collisions of robot cars must satisfy the inequality:

$$\sum_{i,j} m_{ij}(t_k) \leq M, \quad (13.17)$$

where: M —the maximum allowed number of collisions, i, j —robot numbers from numbers from 1 to n ($i \neq j$), k —the number of the moment of collision time from the time interval T , the value $m_{ij}(t_k)$ is determined from the logical expression:

“If at time t_k the trajectory r_i of the robot a_i intersects the trajectory r_j of the robot a_j , that is, $r_i \cap r_j \neq \emptyset$, then $m_{ij}(t_k) = 1$, otherwise $m_{ij}(t_k) = 0$.”

Cell sizes (steps h_x, h_y, h_z) are selected larger than the dimensions of the largest robot car. Each $e_q(t_k)$ cell is characterized by the presence or absence of a_i robot cars and $B_i(t_k)$ obstacles. In addition, each cell is characterized by the interaction of the robot car with the environment in the form of matrices $G(t_k) = \{G_1(t_k), G_2(t_k), \dots, G_n(t_k)\}$, describing the effect of the cell environment (road surface, humidity, temperature, etc.) on the dynamic state of the robot. In the linear formulation, these are the transfer functions of the work-car perturbation.

If rules are used, the set of cells is characterized by $R_m(t_k)$ traffic rules through an intersection of the type: if-then. These rules are determined by the type of intersection. For example:

When passing through an intersection:

If: There are no traffic lights and no additional signs and Each street has 1 lane of traffic

then: necessary to turn to the right.

If: There is a robot car in front of the intersection and It moves at a speed greater than controlled

then: the controlled robot car continues to the intersection (moves to the next cell) without braking.

The selection environment $O(t)$ containing cells and robot cars changes over time t , i.e., it is dynamic. It can be split into $O(t_k)$ layers with some constant or variable h_k step depending on the dynamic properties of robot cars and the disturbing properties of the cell environment. Then, taking into account restrictions of type (13.1) and other logical, logical-probabilistic, and logical-linguistic restrictions, such as the type of intersection rules, the optimization problem will be

$$T = t_f - t_0 \rightarrow \min,$$

where: t_f is the end time of the group's movement, and t_0 is the start time of the movement.

This problem can be solved sequentially for each layer of the $O(t)$ selection environment. However, this approach does not guarantee that the entire group of vehicles $A = \{a_1, a_2, \dots, a_n\}$ will pass through the intersection, since the selection environment at each subsequent step depends on the decisions made in the previous steps and may change over time. Therefore, it is necessary to solve this problem using forecasting and modeling sequences of situations during the transition from one layer to another before reaching the final goal.

13.3.3 Control the Group's Safe Movement Based on Priorities

Using the well-known potential field control method to solve this problem is inefficient, since it is essentially kinematic and may not be acceptable for fast-moving SEMS. An example of another approach to solving the problem of safe management of a group of SEMS with priority setting can be the problem of interaction in the warehouse of robot forklifts built on the basis of SEMS modules. In this task, you need to move three robots from the specified points (areas) to the end points (a rectangular storage room) without colliding with the set robot priority values: P_{R1} —for robot R_1 , P_{R2} —for robot R_2 , and P_{R3} —for robot R_3 , for example, as numbers 1, 2, 3.

In addition, priorities can be determined during the movement of robots in the event of a dangerous situation (possible collision). For this purpose, robot parameters can be compared. For example, if the size of the i -th robot is larger than the j -th, then its priority is greater ($P_{Ri} > P_{Rj}$). Other robot parameters can also be used (speed, proximity to an intersection, weight, destination, etc.). More fine-grained prioritization will be used when comparing several robot parameters at once, especially taking into account their significance by introducing significance coefficients:

$$P_{Ri} = \sum_{n=1}^N p_{in} k_{in},$$

where: p_{in} is the n -th parameter of the i -th robot, and k_{in} is the coefficient of significance of this parameter.

Algorithms for controlling these robots at each step of the movement, i.e., when moving from one cell $e_q(t_i)$ of the configuration space to an adjacent one, $e_{q+1}(t_{i+1})$ determines the possibility of a collision ($r_i \cap r_j \neq 0$, then $m_{ij}(t_k) = 1$, otherwise $m_{ij}(t_k) = 0$). If $m_{ij}(t_k) = 1$, the control algorithm determines the robot that has the highest priority and gives it a command to pass the intersection and gives the other robot a command to delay the passage for the time when the first robot passes the intersection, taking into account the maximum braking time, depending on the speed and road conditions.

Building such an optimal algorithm is a difficult task, since some of the parameters of control objects and the environment, taking into account possible obstacles on traffic routes, are not fully defined. They can be described as logical-probabilistic and/or logical-linguistic expressions [3]. To solve such problems, it is necessary to use multi-step generalized mathematical programming [11] and software tools of the A-life type [12]. The solution can be significantly simplified by reducing logical-probabilistic and logical-linguistic expressions to logical-interval expressions [29]. In this case, the group's travel time will be slightly longer, but the safety is higher.

13.4 Using Binary Relationships in Decision-Making

Decision-making on control the behavior of a group of interacting SEMS as dynamic objects is determined by structural approaches to organizing situational control of a group of robots and the methods of situational control used [30]. In this case, control consists in making control decisions as problems arise when solving a group task in a dynamically changing environment of choice [31]. Such control can be attributed to the optimization problems of situational control [32, 33].

The quality of situational control in solving various problems of group control depends on the structural organization of control and on decision-making methods. Among the control structures, the following can be distinguished: decentralized without the allocation of a robot leader; decentralized with a leader, centralized with an operator, combined with an operator and without a leader and combined with an operator and a leader [34].

The choice of control type is determined by the available technical means and the type of group task to be solved. Moreover, the choice of a decision-making method for situational control of a SEMS group largely depends on the type of group control scheme.

13.4.1 The Tasks of Situational Control of a Group of Dynamic Objects

A typical task of situational control is the problem of the optimal transition of a group of controlled objects from a certain initial variety of points of space to a finite variety, and the dimensions of these varieties can be arbitrary if the phase spaces of the controlled objects themselves are taken into account. It is completely obvious that in technical systems not only control parameters, but also the coordinates of control objects must obey certain physical restrictions.

Traditionally, under optimal control, such objects control problems are considered: problems when each object can be described by a system of ordinary differential equations [6]; problems of optimal hit of objects in moving points of space, tasks when the movement of pursued objects (moving points of space) is not known in advance, and information about them comes only with time; tasks when the pursued objects are controllable and their movement is described by a system of differential equations [35, 36].

Finally, in situational control of intelligent systems with appropriate behavior, which include smart electromechanical systems SEMS [37], control can consist in choosing the best solution from a variety of alternative solutions with a fuzzy and not necessarily probabilistic or statistical description of the dynamics of control objects and the environment, and also with a non-scalar indicator of the quality of the control system. Such problems relate to decision theory [11], i.e., decision-making problems on the optimality of the system. For cases where it is possible to indicate a scale—the objective function, the value of which determines the solution, the theory and methods of mathematical programming are known and well developed [7], which allow for a qualitative and numerical analysis of the clear-cut solution optimization problems that arise in this case. Taking into account the uncertainties that may arise when solving decision problems with a fuzzy mathematical description of complex systems, including the SEMS group operating in a poorly formalized environment; it is possible to use these mathematical programming methods with more or less success in these cases [38].

In the simplest decision-making situation, the Decision-Maker (DM) pursues a single goal and this goal can be formally defined as a scalar function, i.e., quality criterion of choice. In this case, the values of the quality criterion can be obtained for any admissible set of argument values. It is also assumed that the domain of determination of the selection parameters is known, i.e., component of the selected vector, or, in any case, for any given point, it can be established whether it is an acceptable choice, i.e., Does it belong to the domain of determining the quality criterion for a solution. In such a situation, the problem of choosing a solution can be formalized and described by a Mathematical Programming model (MP). In other cases, one should use Mathematical Programming in Ordinal Scales (MPOS), Generalized Mathematical Programming (GMP), or Multi-step Problems of Generalized Mathematical Programming (MsPGMP) [6].

13.4.2 *Mathematical Methods for Using Binary Relations in Decision*

In the process of searching for the best decision to be made using binary relations, it is necessary to consistently solve the following basic mathematical problems, namely, determining the adequacy of mathematical models of control objects and the environment, constructing a set of accepted O_i , and reference O_s decisions, constructing a set of binary relations δ_{ij} and calculating values characterizing these binary relations.

When constructing a mathematical model, the researcher usually takes into account only the most significant factors for achieving the set control goals. At the same time, the adequacy of the model depends on the control goals and control quality criteria adopted for optimization. Building a perfectly adequate model is fundamentally impossible due to the practical impossibility of taking into account the infinite number of parameters of the original object.

As a rule, the behavior of the SEMS group in the environment of choice is not fully defined. Therefore, when searching for optimal or best solutions for situational management of the SEMS group, fuzzy mathematical models of dynamic objects and functioning environments are usually used, among which one can distinguish: Logical-Interval (LIM), Logical-Probabilistic (LPM) and Logical-Linguistic (LLM) [3]. Moreover, their logical and mathematical part can be written in the following form [39]:

$$\left. \begin{aligned} X(t+1) &= A \otimes x(t) \oplus B \otimes u(t) \oplus r \\ Y(t) &= C \otimes x(t) \oplus D \otimes u(t) \oplus h \end{aligned} \right\}, \quad (13.18)$$

where: $X(t)$ is the extended binary state vector, $u(t)$ —input vector; $Y(t)$ —output vector; r, h —0, 1 vectors; A, B, C, D —0, 1 matrices, \otimes —multiplication according to mod 2, \oplus —addition according to mod 2.

Moreover, each component x_i, u_j, y_k of vectors X, u, Y should be characterized by the corresponding values of their probabilities or membership functions or intervals, the calculations of which are described in detail in [3].

The process of assessing the adequacy of such models of complex systems in general form can be reduced to solving the problem of finding a binary relation g_i , which is an element or a subset of the set G ($g_i \subseteq G$) and which corresponds to the relation $I_i g_o I_s$ when the constraints $I_i q_i U_i$ and $I_s q_i U_i$ ($q_i \subseteq Q, i = 1, 2, m$), where I_i and I_s are mathematical models or images of the estimated i -th and reference model, G and Q are some fixed compact sets, g_o is the best binary ratio, and U_i are the models or images given a priori restrictions. In this case, we can assume that the plans or strategies and tactics of building a model are admissible by the i -th constraint if the pair $(I_i, U_i) \in q_i$ and the pair $(I_s, U_i) \in q_i$, and the plan or strategy and tactics of building the model are optimal if the pair $(I_i, I_s) \in g_o$, g_o is the preference of the decision-maker, the cardinality of the set g_o is minimal and the elements of the set are ordered according to some feature.

The relations g and q can be expressed as a system of logical equations [6]:

$$CG = E \quad (13.19)$$

or

$$DQ = Y \quad (13.20)$$

Vectors G and Q have dimension N and in the most general case can have $N = 2n - 1$ component of the form:

$$\langle g_1, g_2, \dots, g_n, g_1g_2, \dots, g_{n-1}g_n, g_1g_2g_3, \dots, g_{n-2}g_{n-1}g_n, \dots, g_1g_2 \dots g_{n-1}g_n \rangle,$$

$$\langle q_1, q_2, \dots, q_n, q_1q_2, \dots, q_{n-1}q_n, q_1q_2q_3, \dots, q_{n-2}q_{n-1}q_n, \dots, q_1q_2 \dots q_{n-1}q_n \rangle.$$

The components g_i of the vector G is logical variables that characterize the proximity of the objects and relations of the constructed model I_i to the elements and relations of the ideal model I_3 . The q_i components of the Q vector are logical variables that characterize the correspondence of objects and relations of the constructed model I_i to the elements and relations of the U_i constraint model.

Matrices C and D consist of identification strings c_i and d_i having the dimension of vectors G and Q and containing elements 0 and 1 in the specified order. For example,

$$c_1 = (0011 \dots 01).$$

Vector E has the dimension of vector G , its e_i components can take the value 1 with some probabilities $P_i(e_i)$. The vector Y has the dimension of the vector Q and its y_i components can take the value 1 with some probabilities $P_i(y_i)$. The values of these probabilities are calculated using the probabilities of the g_i and q_i components. In this case, the probability values can be calculated approximately according to the algorithm described in [40].

Mathematical methods for solving problems of determining g_o are described in detail in [6]. After choosing an adequate model, it is necessary to start calculating the quantities characterizing the binary relations g_{ij} . In the process of solving this problem for SEMS group control systems, in which control objects are described by LPM, LLM, or LIM, measures of the quality of decisions made are also set in the form of binary relations describing the preferences of the decision-maker, in the form of, for example, point scores formed on the basis of analysis of the opinion of experts in a given area. Then the estimation of the proximity of the decision to the reference (optimal) one is reduced to the problem of mathematical programming in ordinal scales [11].

In contrast to the MPOS problem, optimization by the Generalized Mathematical Programming method corresponds to the choice of the decision to be made based on comparing its characteristics with the characteristics of an ideal solution, and not their parameters [11]. Mathematical methods for solving these problems are also described in detail in [6]. At the same time, the search for the optimal solution can be automated by artificial intelligence software.

Appendix

The stages of forming decision-making in CNSR based on the use of systems of equations modulo two or systems of logical equations in the Zhegalkin algebra are considered. The features of pattern recognition described by systems of equations in algebra modulo two are described. The effectiveness of using the method of the usual situation in the CNSR, which is an analog of human intuition and allows you to replace the desired solution with an analog, is shown. This dramatically increases the speed of forming reflexive reasoning. When choosing the optimal reflexive reasoning described by systems of logical equations in the Zhegalkin algebra, as well as when making optimal decisions about the appropriate behavior to achieve the formed goals, it is desirable to reduce the search for the optimum to well-studied problems of mathematical programming. If some of the attributes of logical variables in the CNSR system of equations are linguistic expressions, then a more natural way to choose the optimal solution is to switch to the concept of consistently preferring one of the compared options to another. To solve such problems, you can generalize the scheme of mathematical programming, moving from quantitative scales to ordinal ones, i.e., moving from models that require the assignment of functions that determine the goals and limitations of the problem, to models that take into account the preferences of the persons involved in choosing the solution.

The proposed principles of deductive, inductive and inductive decision-making based on information from the central nervous system using algebraization and matrix solution of systems of logical equations are effectively used in the formation of strategies and tactics for controlling intelligent robots in conditions of incomplete certainty. In this case, the fastest decision-making will be when using the principle of abduction, which includes elements of deductive and inductive thinking. The reliability and reliability of decision-making with this approach can be improved during the operation of the robot, if you include elements of self-learning in the control system, adding to the database selected good solutions that gave the right decisions in the past.

The article proposes an algorithm for the formation of the robot's language of sensations, which allows robots to provide the possibility of reflexive and reasoned reasoning. To do this, the following procedures are proposed: quantization of the surrounding space, blurring of sensory information, image formation when displaying the surrounding space, image formation by combining images from different sensory organs and assigning words to the generated language.

In the considered principles and decision-making stages for control the safe movement of a group of robots built on the basis of SEMS modules, it is assumed that when forming a set of acceptable controls (SEMS behavior instructions), it is first of all advisable to identify and record the acceptable values of the parameters of individual members of the group, as well as their static and dynamic characteristics in the SEMS ACS database. The next step is to determine a set of acceptable behavior instructions for group members by mathematical and computer simulations of the dynamic configuration.

The article describes the mathematical formulation of the problem of controlling the safe movement of a group through an intersection, taking into account the rules of passage. It is proposed to solve this problem by predicting and modeling sequences of situations during the transition from one layer to another before reaching the final goal.

When solving problems of making decisions on the safe management of the movement of a group of robots based on their priorities, the construction of an algorithm for controlling the movement of a group of robots should begin with determining each step of movement, the possibility of a collision, and the robot with a higher priority should be given a command to pass the intersection, and the other robot should be given a command to delay the passage at the moment of passing the intersection by the first robot with the maximum braking time, depending on speed and road conditions. To solve such problems, you can use multi-stage generalized mathematical programming and software tools such as A-life. In this case, the quality of optimization will be mainly determined by the correctness of constructing a binary relation describing the measure of proximity of the designed SEMS control system to the ideal one. This can be a time-consuming and complex task, often involving solving a number of logical problems. The quality of setting and solving these tasks depends on the experience and skill of the developer as a decision-maker. To increase the objectivity of the optimality assessment, it is advisable to make the decision-making collective with the involvement of the customer in the work on building binary relations.

References

1. Akoff, R., Emeri, F.: O celestremlennyh sistemah [On purposeful systems]. Sov. Radio Publ, Moscow (1974). (In Russian)
2. Gorodetskiy, A.: Osnovy teorii intellektual'nykh sistem upravleniya [Fundamentals of the theory of intelligent control systems]. LAP LAMBERT Academic Publishing GmbH & Co., KG (2011)
3. Gorodetskiy, A.E., Tarasova, I.L.: Nechetkoye matematicheskoye modelirovaniye plokhoy formalizuyemykh protsessov i sistem. [Fuzzy Mathematical Modeling of Poorly Formalized Processes and Systems]. Polytechnic. University Publ., St. Petersburg (2010) (In Russian)
4. Nikolenko, S.I., Tulup'ev, A.L.: Samoobuchaiushchiesya sistemy [Self-Learning Systems], Izdatel'stvo (Moskovskii tsentr nepreryvnogo matematicheskogo obrazovaniya), MTsNMO (2009) (In Russian)
5. Gorodetskiy, A.E., Dubarenko, V.V., Erofeev, A.A.: Algebraicheskiy podkhod k resheniyu zadach logicheskogo upravleniya [Algebraic approach to the solution of tasks of logical control]. *Avtomatika i telemekhanika/Autom. Telemekh.* **61**(2), 295–305 (2000) (In Russian)
6. Gorodetskiy, A.E., Kurbanov, V.G., Tarasova, I.L.: Methods of Synthesis of Optimal Intelligent Control Systems SEMS. In: Gorodetskiy, A.E. (ed.) *Smart Electromechanical Systems*. Springer International Publishing (2016). <https://doi.org/10.1007/978-3-319-27547-5>
7. Tabak, D., Kuo, B.: Optimal'noye upravlenie i matematicheskoye programmirovaniye [Optimal Control and Mathematical Programming]. Nauka Publ, Moscow (1975). (In Russian)
8. Levin, V.I.: Nepreryvnaia logika i ee primeneniye [Continuous logic and its application]. *Informatsionnyye tekhnologii / Inf. Technol.* **1**, 17–21 (1997). (In Russian)
9. Alefel'd, G., Khertsberger, I.: Vvedeniye v interval'nyye vychisleniya [Introduction to the Interval Calculation]. Mir Publ, Moscow (1987). (In Russian)

10. Kuchmin, A. Y.: Ob odnom metode nelineinogo programmirovaniia s proizvol'nymi ogranicheniiami [A method for nonlinear programming with arbitrary constraints]. *Informatsionno-upravliaiushchie sistemy/Inf. Control Syst.* **2**, 2–9 (2016) (In Russian)
11. Iudin, D.B.: Vychislitel'nye metody teorii priiniatii reshenii [Computational Methods of Decision Theory]. Nauka Publ, Moscow (1989). (In Russian)
12. Gorodetskiy, A.E., Dubarenko, V.V., Tarasova, I.L., Shereverov, A.V.: Programmnye sredstva intellektual'nykh sistem [Software Intelligent Systems]. Izdatel'stvo SPbGTU, St. Petersburg (2000). (In Russian)
13. Gorodetskiy, A.E.: Fuzzy decision making in design on the basis of the habituality situation application. In: Reznik, L., Dimitrov, V., Kacprzyk, J. (eds.) *Fuzzy Systems Design. Social and Engineering Applications*, pp. 63–73. Physica-Verlag, A Springer Company, New York (1998)
14. Gorodetskiy, A.E., Kurbanov, V.G., Tarasova, I.L.: Ergaticheskie metody analiza processov ekspluatsii i prinyatiya reshenij pri povrezhdeniyah i avariayah energoob'ektov [Ergatic methods of analysis of exploitation processes and decision-making in case of damage and accidents of power facilities]. *Informatsionno-upravliaiushchie sistemy/Inf. Control Syst.* **67**(6), 29–36 (2013) (In Russian)
15. Kondakov, N.I.: *Logicheskii slovar'-spravochnik* [Logical Dictionary-Reference Book]. Nauka Publ, Moscow (1975). (In Russian)
16. Vagin, V.N., Golovina, E.Yu., Zagoryansky, A.A., Fomin, M.V.: Dostoverniy i pravdopodobnyy vyvod v intellektual'nykh sistemakh [Reliable and plausible conclusion in intelligent systems]. In: Vagin, V.N., Pospelov, D.A. (eds.) 2nd Edition Revised and Enlarged, FIZMATLIT Publ., p. 712 (2008) (In Russian)
17. Gorodetskiy, A.E.: Ob ispol'zovanii situatsii privychnosti dlya uskoreniya prinyatiya resheniya v intellektual'nykh informatsionno-izmeritel'nykh sistemakh [The use of a situation accustomed to accelerate the adoption of intellectual solutions in information and measuring systems]. In: *Physical Metrology: Theoretical and Applied Aspects*. KN Publ., St. Petersburg, pp. 141–151 (1996) (In Russian)
18. Connell, J.: Robots that Talk and Listen. In: Markowitz, J. (ed.) *De Gruyter* (2014)
19. [Theconversation.com/how-do-robots-see-the-world-51205](https://www.theconversation.com/how-do-robots-see-the-world-51205)
20. Zhegalkin, I.I.: Arifmetizatsiya simvolicheskoy logiki. [Arithmetization symbolic logic]. *Matematicheskii sbornik* [Math. Collect.] **35**(3–4), 335 (1928) (In Russian)
21. Dobrynin, D.A.: Intellectual Robots yesterday, today, tomorrow. In: *Proceedings of the X National Conference on Artificial Intelligence with International Participation KII-2006* Moscow, Fizmatlit Publish, vol. 2, pp. 20–32 (2006) (In Russian)
22. Gorodetskiy, A.E., Tarasova, I.L., Kurbanov, V.G.: Challenges related to development of central nervous system of a robot on the bases of SEMS modules. In: Gorodetskiy, A.E., Kurbanov, V.G. (eds.) *Smart Electromechanical Systems: The Central Nervous System, Studies in Systems, Decision and Control*, vol. 95, pp. 3–17 (2017). https://doi.org/10.1007/978-3-319-53327-8_1
23. Gorodetskiy, A.E., Kurbanov, V.G., Tarasova, I.L.: Decision-making in central nervous system of a robot. *Inf. Control Syst.* **1**, 21–30 (2018). <https://doi.org/10.15217/issnl684-8853.2018.1.21> (In Russian)
24. Gorodetskiy, A.E., Tarasova, I.L., Kurbanov, V.G.: Behavioral decisions of a robot based on solving of systems. In: Gorodetskiy, A.E., Kurbanov, V.G. (eds.) *Smart Electromechanical Systems: The Central Nervous System, Studies in Systems, Decision and Control*, vol. 95, pp. 61–71 (2017). https://doi.org/10.1007/978-3-319-53327-8_5
25. Gorodetskiy, A.E., Tarasova, I.L.: *Upravlenie i neyronnye seti* [Control and neural networks]. Polytechnic. University Publ, St. Petersburg (2005). (In Russian)
26. Gorodetskiy, A.E., Tarasova, I.L.: *Smart Electromechanical Systems. Group Interaction. Studies in Systems, Decision and Control*, vol. 174. Springer International Publishing (2018). <https://doi.org/10.1007/978-3-319-99759-9>
27. Ziniakov, V.Y., Gorodetskiy, A.E., Tarasova, I.L.: Control of vitality and reliability analysis. In: Gorodetskiy, A.E. (eds.) *Smart Electromechanical Systems*, pp. 193–204. Springer International Publishing (2016). https://doi.org/10.1007/978-3-319-27547-5_18

28. Ziniakov, V.Y., Gorodetskiy, A.E., Tarasova, I.L.: System failure probability modelling. In: Gorodetskiy, A.E. (eds.) *Smart Electromechanical Systems*, pp. 25–44. Springer International Publishing (2016). https://doi.org/10.1007/978-3-319-27547-5_4
29. Gorodetskiy, A.E., Tarasova, I.L., Kurbanov, V.G.: Reduction of logical-probabilistic and logical-linguistic constraints to interval constraints in the synthesis of optimal SEMS. In: Gorodetskiy, A.E., Tarasova, I.L. (eds.) *Smart Electromechanical Systems. Group Interaction*, pp. 77–90. Springer International Publishing (2018). https://doi.org/10.1007/978-3-319-99759-9_7
30. Gorodetskiy, A.E., Tarasova, I.L.: Situational control a group of robots based on SEMS. In: Gorodetskiy, A.E., Tarasova, I.L. (eds.) *Smart Electromechanical Systems. Group Interaction*, pp. 9–18. Springer International Publishing (2018). https://doi.org/10.1007/978-3-319-99759-9_2
31. Gorodetskiy, A.E., Kurbanov, V.G., Tarasova, I.L.: Decision-making in central nervous system of a robot. *Inf. Control Syst.* **1**, 21–30 (2019). <https://doi.org/10.15217/issnl684-8853.2018.1.21>
32. Pospelov, D.A.: *Situacionnoe upravlenie: Teoriya i praktika [Situation Control: Theory and Practice]*. Nauka Publ, Moscow (1986). (In Russian)
33. Kunc, G., O Donnel, S.: *Upravlenie: sistemnyj i situacionnyj analiz upravlencheskih funkcij [Control: System and Situation Analysis of Control Functions]*. Progress Publ., Moscow (2002) (In Russian)
34. Gorodetskiy, A.E., Tarasova, I.L., Kurbanov, V.G.: Situational control of the group interaction of mobile robots. In: Gorodetskiy, A.E., Tarasova, I.L. (eds.) *Smart Electromechanical Systems. Situational Control*, pp. 91–101. Springer International Publishing (2020). https://doi.org/10.1007/978-3-030-32710-1_7
35. Vajsbord, E.M., Zhukovskij, V.I.: *Vvedenie v differencial'nye igry neskol'kih lic i ih prilozhenie [Introduction to the Differential Game of Several Persons and Their Application]*. Sov. Radio Publ, Moscow (1980). (In Russian)
36. Ajzeks, R.: *Differencial'nye igry [Differential Games]*. Mir Publ, Moscow (1967). (In Russian)
37. Gorodetskiy, A.E.: Smart electromechanical systems modules. In: Gorodetskiy, A.E. (eds.) *Smart Electromechanical Systems*, pp. 7–15. Springer International Publishing (2016). https://doi.org/10.1007/978-3-319-27547-5_2
38. Gorodetskiy, A.E.: The principles of situational control SEMS group. In: Gorodetskiy, A.E., Tarasova, I.L. (eds.) *Smart Electromechanical Systems. Situational Control*, pp. 3–13. Springer International Publishing (2020). https://doi.org/10.1007/978-3-030-32710-1_1
39. Gorodetskiy, A.E., Tarasova, I.L., Shkodyrev, V.P.: *Matematicheskoe modelirovanie intellektual'nyh sistem upravleniya: Modelirovanie determinirovannyh intellektual'nyh sistem upravleniya [Mathematical Modeling of Intelligent Control Systems: Modeling of Deterministic Intelligent Control Systems]*. Polytechnic. University Publ, St. Petersburg (2016). (In Russian)
40. Gorodetskiy, A.E., Dubarenko, V.V.: A combinatorial method for the evaluation of probabilities of complex Boolean functions. *Comput. Math. Math. Phys.* **39**(7), 1201–1203 (1999) (In Russian)

Chapter 14

Boundary-Value Problems for Defects in Nanoscale and Nanocomposite Solids



Mikhail Yu. Gutkin, Anna L. Kolesnikova, Alexey E. Romanov,
and Alexander G. Sheinerman

Abstract A brief review of solutions of boundary-value problems in the theory of elasticity for defects in nanoscale and nanocomposite solids, which were found during the last three decades in the Laboratory of Mechanics of Nanomaterials and Theory of Defects at the Institute for Problems in Mechanical Engineering of Russian Academy of Sciences, is presented. It covers the elastic behavior of dislocations, disclinations, and inclusions near free surfaces and interfaces in such inhomogeneous nanostructures as composite nanolayers, core-shell nanowires and nanoparticles, quantum dots and wires in subsurface layers, etc. Some relevant works dealing with application of the solutions found to the theoretical models describing the nucleation and development of different defect structures in the process of crystal growth and misfit stress relaxation in advanced composite nanostructures which are highly promising for use in modern electronics, optoelectronics and photonics, are also briefly reviewed.

Keywords Boundary-value problems · Theory of elasticity · Dislocations · Disclinations · Inclusions · Interfaces · Composite nanostructures · Misfit stress · Stress relaxation

14.1 Introduction

In the present paper, we give a brief review of solutions of boundary-value problems in the theory of elasticity for defects in nanoscale and nanocomposite solids, which were found and used during the last three decades in the Laboratory of Mechanics of Nanomaterials and Theory of Defects at the Institute for Problems in Mechanical Engineering of Russian Academy of Sciences (IPME RAS). These solutions were given within isotropic elasticity for straight dislocations and disclinations, circular

M. Yu. Gutkin (✉) · A. L. Kolesnikova · Alexander G. Sheinerman
Institute for Problems in Mechanical Engineering RAS, V.O., Bolshoy pr., 61, St., Petersburg
199178, Russia

A. E. Romanov
ITMO University, Kronverkskiy pr., 49, St., Petersburg 197101, Russia

© The Author(s), under exclusive license to Springer Nature Switzerland AG 2022
V. A. Polyanskiy and A. K. Belyaev (eds.), *Mechanics and Control of Solids and Structures*, Advanced Structured Materials 164,
https://doi.org/10.1007/978-3-030-93076-9_14

and rectangular dislocation loops, circular disclination loops, inclusions of different shapes, sharp and diffuse interfaces in elastic solids bounded by planar, cylindrical, and spherical free surfaces, and in inhomogeneous elastic solids with planar, cylindrical, and ellipsoidal interfaces. The results normally included the displacement and stress fields of the defects, their strain energies and sometimes the interaction energies of the defects, and elastic image forces acting on the defects from the free surfaces and/or interfaces. These results were extensively applied to theoretical models describing misfit strain/stress relaxation and defect generation in various solid-state micro- and nanoheterostructures which are the basis of advanced structural and functional materials. Some of these solutions and results were reviewed in more detail in monographs [1, 2] and reviews [3–10]. In most cases, our results were obtained within the classical theory of elasticity and this will not be specially noted anymore, although sometimes the gradient elasticity and the surface/interface elasticity were used as well. In both the latter cases, we will specially announce about. We devote this brief review to the 30 anniversary of IPME RAS.

14.2 The Method of Virtual Surface Defects in the Solution of Boundary-Value Problems of the Theory of Defects

Elasticity boundary-value problems for defects of different dimensionality, i.e., for point, line, surface, and volume defects, with prescribed geometrical characteristics, e.g., configuration of dislocation line, or inclusion shape, located in the bodies with various geometries, were solved analytically both by standard methods of mathematical physics and theory of elasticity (see, e.g., [11, 12]) and by a new method of virtual surface defects (MVSD) that were advanced for the solution of such problems.

In the framework of the MVSD, which is further development of surface straight-linear dislocation–disclination technique [13–17], virtual defect types are chosen according to the symmetry of the boundary-value problem for real defect under consideration. Virtual defects are then continuously distributed on free surfaces or/and interfaces in such a way that their elastic field together with the field of the real defect satisfy the imposed boundary conditions. In works [18–20], defect loops (including Volterra and Somigliana ring dislocations) were proposed as virtual defects for solving elasticity boundary-value problems with axial symmetry. Defect ring loops were defined as planar defects with the *eigenstrain* prescribed in the part of the plane bounded by a circle [21, 22].¹ A characteristic feature of the elastic fields of the circular (ring) loops is a possibility to express their fields through Lipschitz–Hankel integrals [23] that is extremely convenient because of separation of axial and radial variables.

¹ Note that only Volterra dislocations, i.e., translation (ordinary) dislocations and disclinations, can be considered as linear (1D) defects as a degenerate case of more general class of surface (2D) defects—Somigliana dislocations [22].

Boundary conditions accounting for the distributed virtual loops acquire the form of integral equations for unknown distribution functions which are solved by the integral transformations. For the case of the planar boundaries, Hankel–Bessel transform is used, see, e.g. [24, 25]; for the case of cylindrical boundaries—Fourier transform [25, 26]; and for the case of spherical surfaces, the expansion of the elastic field components of virtual defect loops in the series with Legendre polynomials is used [27]. When discussing below the results of our studies, MVSD is presented in necessary details and variety.

14.3 Dislocations

General reviews on the boundary-value problems for dislocations in the classical theory of elasticity were given by Dundurs [28], Eshelby [29], Lothe [30], and Belov [31]. A great number of more recent solutions are spread over original papers, from which we will consider the works of our lab only.

14.3.1 *Straight Dislocations*

14.3.1.1 **Edge Dislocations**

Gutkin and Romanov [32, 33] considered an edge dislocation parallel to the surfaces in a thin two-layer film with different elastic moduli. The solution was obtained in the integral form using a modernized MVSD, i.e., using the fields of both the considered dislocation and virtual surface dislocations, which satisfy the boundary conditions on the interface [32]. It was shown [33] that the dislocation may have from one to five equilibrium (stable and unstable) positions in the film interior, depending on the Burgers vector orientation and the ratio between elastic moduli of the layers. These results were later applied to some related problems, the first of which were the models of misfit dislocations (MDs) in similar systems with lattice mismatch of the layers [34, 35]. The strain energy of the dislocation found in [33] allowed to define the critical conditions for nucleation of MDs and their stable positions near the interface. It was shown that, depending on the parameters of the two-layer film, a MD may occupy the stable equilibrium position in the softer layer (the so-called ‘stand-off position’) or directly in the interface. More recently, the stress fields and strain energy found in [33, 34] have been used in the models describing the critical conditions for the formation of MDs in core-shell nanoparticles (NPs) [36]; the glide of circular prismatic [37, 38], and mixed [39, 40] dislocation loops along the interface between straight [37, 38] or Y-shaped [39, 40] nanotubes (NTs) and ceramic matrix at the bridging [37, 38] or pull-out [39, 40] stages of fracture in ceramic nanocomposites; and the emission of dislocation dipoles from an edge of a long prismatic nanowire (NW) of rectangular cross-sectional embedded in a free-standing nanolayer [41].

Using Romanov's [42] solution for the Airy stress function of an edge dislocation (as a limiting case of a bi-axial dipole of wedge disclinations) in an elastic cylinder, Gutkin et al. [43] for the first time considered the generation of a straight edge MD in a core-shell NW. The formation of the MD in such a NW was assumed to be driven by the misfit stresses associated with the mismatch of the lattice parameters of the core and the shell. It was shown that the generation of the MD decreases the strain energy of the system and can be realized at some ranges of parameters (misfit, core radius, and shell thickness). To calculate the conditions for the formation of a straight MD parallel to the NW axis, Gutkin et al. [43] first calculated the misfit stresses and then cast the conditions at which the MD generation is energetically beneficial. It appeared that the MD generation is favored if the thicknesses of both NW phases (the core and the shell) are not too small. Also, according to [43], the generation of an MD requires that the misfit should be large enough and the core radius and shell thickness should be not too different. The calculations [43] also predict that a decrease in the core radius makes the generation of a straight MD more difficult. This situation is similar to the case of MDs in films on planar substrates, where a decrease in the substrate thickness also hinders the formation of MDs at or near the film/substrate interface [44, 45].

The theoretical analysis of MD formation in NWs was complemented by the analysis of their generation in uncapped islands and NWs on the surface of a thick substrate or on the surface of a thin film layer located on a substrate. For example, theoretical models describing the formation of partial, split, and delocalized dislocations in NWs on the substrate surface were suggested in Refs. [46–48]. The first of these models [46] considers a composite solid consisting of a semi-infinite crystalline substrate and a pyramidal crystalline island modeled as a triangular NW. In this case, the author approximated the self-strain energies and the interaction energies of MDs by the solutions found for edge dislocations parallel to the flat free surface of a half-space [28, 29]. In contrast, in Refs. [47, 48], the substrate and the island were modeled as cylindrical segments that together composed a cylinder, in which case the authors used the Airy stress function [42] as the departure point. As with model [46], 2D models [47, 48] describe dislocations in a 2D NW. However, their results can be extended to the case of 3D islands.

The calculations performed in Ref. [47] demonstrated that near an island edge the most energetically favorable dislocation structure is a single partial MD. During the motion of this MD inside the island, the nucleation of a second partial MD at the island edge and its motion along the substrate-island interface become favorable. The motion of partial MDs may happen until they have reached their equilibrium positions located symmetrically at opposite sides from the island base center. In parallel with localized dislocations, the formation of dislocations delocalized over a strip of a certain width can occur in islands [48]. The calculations [48] showed that the energy of a delocalized dislocation in an island is always smaller than the energy of a localized one. As a result, the nucleation of a delocalized dislocation in an island may occur even in small islands, where the formation of conventional localized dislocations is energetically unfavorable.

Recently, Smirnov et al. [49] have used the solution [42] for an edge dislocation in a cylinder for analyzing the mechanisms of misfit stress relaxation in core-shell NWs, in which the cores had the shape of long prisms of square cross sections. In particular, they have shown that the emission of dipoles of partial and perfect dislocations by edges of the cores are the most energetically favorable relaxation mechanisms in relatively thin and thick NWs, respectively.

Besides the solutions obtained within the classical theory of elasticity, some boundary-value problems were also solved for edge dislocations within the gradient elasticity [50] and the surface/interface elasticity [52–56]. Mikaelyan et al. [50] used one of the early versions of the stress/strain-gradient elasticity, first suggested by Ru and Aifantis [51], to obtain a solution of the boundary-value problem for a straight edge dislocation parallel to the planar interface between two elastic isotropic media with different elastic constants and different gradient coefficients. The main difference of this gradient solution from the classical one [11] is that the dislocation stress field has no singularities on the dislocation line and remains continuous at the interface, while the classical solution is singular at the dislocation line and allows a discontinuity of two stress components at the interface. The gradient solution also removes the classical singularity of the image force for the dislocation on the interface. Moreover, an additional elastic image force associated with the difference in the gradient coefficients of contacting phases was determined. It was shown that this force, which has a short range and a maximum at the interface, expels the edge dislocation into the material with a smaller gradient coefficient.

The surface/interface elasticity was used to reveal new nanoscopic peculiarities in elastic behavior of edge dislocations inside the wall of a nanotube [52], near an elliptical nano-inhomogeneity [53], in a core-shell NW embedded to an infinite matrix [54] as well as in the shell of a free-standing core-shell NW [55]. Based on the results of these work, one can conclude that there is no special need to use the more complicated surface elasticity theory for describing the dislocation fields and behavior in the bulk of a nanoscale solid at distances larger than about 1 nm from the free surface or the interface. When studying the situation near the free surface or the interface, the choice between the classical and surface theories of elasticity depends on the values of surface elastic moduli. On the other hand, the non-classical effects in nanoscale solids can be very impressive. For example, in the case of an edge dislocation placed in the shell of a core-shell NW, these effects are [55]: (i) the stress oscillations along the shell surface and core-shell interface for negative values of the surface/interface elastic moduli; (ii) a strong dependence of image forces on the core size; (iii) extra repelling (attraction) of the dislocation from (to) the shell surface and core-shell interface characterized by positive (negative) interface modulus; and (iv) a decrease of the dislocation strain energy in the central region of the shell and its local increase with an extra maximum in the vicinity of the shell surface for negative values of the surface/interface elastic moduli. Moreover, the study of the surface/interface effects on the formation of MDs in a core-shell NW showed [39] that these effects are significant for fine cores of radius smaller than roughly 20 interatomic distances. The positive and negative surface/interface Lamé constants mostly make the generation of the MD easier and harder, respectively. The positive

(negative) residual surface/interface tensions mostly make the generation of the MD harder (easier).

14.3.1.2 Screw Dislocations

For screw dislocations, a number of boundary-value problems have been solved in our lab within the classical, gradient, and surface/interface theories of elasticity. Some of these problems concern “normal” screw dislocations with full cores, while the others deal with “abnormal” hollow-core screw dislocations which are commonly referred to as “micropipes” (MPs). First, we will consider the solutions done for normal screw dislocations, and then turn to MPs.

Gutkin et al. [57] solved the problem of a screw dislocation placed near a triple junction of flat interfaces separating phases with different elastic moduli. In doing so, they used the modernized MVSD similar to that suggested by Gutkin and Romanov [32]. The exact analytical expressions for the dislocation stress fields were found in the Mellin space in the general integral form. For the limiting case, when the interphase boundaries contacted under right angles, the Mellin transforms for the functions of distribution of virtual surface dislocations were represented in the closed explicit form.

Gutkin and Sheinerman [58] analyzed the elastic behavior of a screw dislocation in the wall of a hollow NT. They used the method of infinite image-dislocation rows [59] and represented their solutions for the stress fields, strain energy, and image force by infinite series convenient for numerical analysis. The internal space of the NT was shown to cause (i) a change in the sign of stress-tensor components near the inner NT surface, (ii) a high stress concentration, and (iii) a strong stress gradient at this surface. It was also shown that the dislocation has one position of unstable equilibrium in the NT wall, which is always shifted toward the inner NT surface. As the internal-space radius increases, the dislocation energy decreases, and the position of its equilibrium shifts toward the outer NT surface; in the limiting case of a flat layer, it reaches the center of the layer.

The technique of infinite arrays of image dislocations was also used [60] to calculate the stress field and strain energy of a screw dislocation in an elastically isotropic solid containing two cylindrical voids. Based on the solution derived, the image force exerted by the two voids on a screw dislocation was also calculated and studied. As a limiting case of the solution obtained, the authors derived the stress field of a screw dislocation in a half-space containing a cylindrical void. It was shown, in particular, that, if the void radii are smaller than their spacing from the dislocation, the voids significantly influence the dislocation stress fields at the distances of several void radii from the void surfaces.

Kolesnikova et al. [61] solved the boundary-value problems for screw dislocations normally piercing two-layer flat film and two-layer hollow sphere. The analytical solutions were found by the MVSD. Elastic fields of the dislocation in the film were presented in the form of integrals with Bessel functions, while those of the dislocation in the hollow sphere in the form of series with Legendre polynomials. The stress fields

were analyzed by stress maps which allowed to reveal some peculiarities in stress distribution in dependence of the geometric and elastic parameters of the systems. It was demonstrated that in the limiting cases of a homogeneous plate and a half-space, the solutions for a screw dislocation coincide with the solutions found by the authors earlier [18, 19], as well as with the solutions the first given by Eshelby and Stroh (plate) [62] and Yoffe (half-space) [63] and found with other techniques. When passing from a two-phase spherical layer to a solid sphere, the fields of a screw dislocation become fields first derived by Polonsky et al. [64], and after that recalculated with the MVSD [27].

Gutkin et al. [65, 66] found the solution for a screw dislocation parallel to the planar interface between two elastic isotropic media with different elastic constants and different gradient coefficients within the stress/strain-gradient elasticity [51]. The principal differences from the well-known classical solution [28] are practically the same as in the case of an edge dislocation (see above Sect. 14.3.1.1).

Shodja et al. [67] used the simplest strain-gradient elasticity theory [68] to analyze the displacement and strain fields of a screw dislocation in a free-standing NW. They showed that these fields do not contain classical jumps and singularities at the dislocation line. Moreover, the maximum values of the displacement and elastic strain strongly depend on both the dislocation position and NW radius, thus demonstrating a non-classical size effect.

Davoudi et al. [69, 70] considered the cases of a screw dislocation inside [69] and near [70] an embedded NW within the gradient elasticity theory suggested in [51]. In both the cases, the classical stress singularity was removed from the solutions and all stress components were continuous and smooth across the interface, in contrast with the results obtained within the classical theory of elasticity [28]. As a result, the image force exerted on the dislocation due to the differences in elastic and gradient constants of the matrix and NW, remained finite when the dislocation approaches the interface. The maximum magnitude of dislocation stress greatly depended on the dislocation position, the NW size, and the ratios of shear moduli and gradient coefficients of the matrix and NW materials.

The surface/interface effects on elastic behavior of a screw dislocation in finite-size and inhomogeneous nanostructures were studied in Refs. [71–73]. Shodja et al. [71] studied the same case of a screw dislocation inside the wall of a NT as Gutkin and Sheinerman [58] within the classical elasticity. The non-classical results demonstrated [71] that in tiny NTs with wall thickness in the order of a few nanometers, the surface stresses noticeably affect the bulk stress fields over the NT's cross section, while in coarser NTs, the surface stress effect is negligibly small. Further, a screw dislocation was repelled by the inner and outer free surfaces, which is an atypical behavior in the context of classical elasticity. Thus, a screw dislocation had one unstable equilibrium position in the bulk of the NT wall, as is also the case with the classical elasticity [58], and additionally two stable equilibrium positions in close vicinity of the free surfaces. However, this non-classical effect was strictly localized in atomically thin subsurface layers. It was also shown that the image force strongly depends on the NT radii and elastic characteristics of the surfaces.

Ahmadzadeh-Bakhshayesh [72] analyzed the surface/interface effects for a screw dislocation in an eccentric core-shell NW. They showed that (i) near the free surface and the interface, the stress fields considerably differ from the classical ones, while this difference practically vanishes in the bulk of the NW; (ii) the surface with positive (negative) shear modulus applies an extra non-classical repelling (attracting) image force to the dislocation, which can change the nature of the equilibrium positions depending on the system parameters; (iii) the non-classical surface/interface effect has a short-range character and becomes more pronounced when the nanowire diameter is smaller than 20 nm.

Shodja et al. [73] considered the interface effect on the critical condition for the formation of a screw misfit dislocation dipole (MDD) at the interface between an embedded NW with uniform shear eigenstrain field and surrounding matrix. The critical radius of the NW corresponding to the MDD generation was shown to decrease with the increase in the uniform shear eigenstrain inside the NW as well as when the stiffness of the NW increases with respect to the matrix, and to strongly depend on the non-classical interface parameter.

In addition to boundary-value problems for full-core screw dislocations, the studies of our lab included the investigations of the elastic behavior of MPs which are in fact hollow-core superscrew dislocations with giant Burgers vectors often observed in some crystals with hexagonal crystalline lattice, for example, in silicon carbide [74]. The first of these works [75] considered the elastic interaction of a dislocated MP with a screw dislocation or another dislocated MP. For the analysis of the elastic interaction between MPs, the stress field of a dislocated MP in the solid containing another MP was derived using the technique of infinite arrays of image dislocations [59]. The stress field, strain energy, and the force of interaction of two MPs, the parameter regions where they are attracted or repelled were determined. It was demonstrated that at distances large as compared to the radii of the MPs, the presence of MP free surfaces can be neglected, and the interaction force between MPs approaches that of two dislocations in an infinite medium. That is, in this case, the MPs with opposite-sign Burgers vectors attract each other, while those with same-sign Burgers vectors repel each other. At the same time, when the distances between the MPs are short enough, the contribution of the MP free surfaces to the interaction force may dominate. As a consequence, for same-sign MPs, there exists a parameter region where they attract each other. The attraction area for such MPs exists if the ratios of their radii and Burgers vectors magnitudes are sufficiently different.

Using the expression for the energy of a pair of MPs, the criterion for MP split into two smaller MPs has been derived [76]. With the assumption that the split is possible if the energy of MPs after the split is smaller than the energy of the initial MP, it was shown that the MP split is energetically favorable in a certain parameter region if the MPs are of the same sign. The parameter region comprises the normalized magnitudes of the Burgers vectors as well as the radii of the initial and split MPs. This region expands if the radius of the initial MP rises. The split of an MP into two smaller ones is possible if the radius of the initial MP exceeds the equilibrium radius and the total MP surface energy decreases due to the split. The MP split also requires

that the ratio of the split MP radii should be close to that of the magnitudes of the MP Burgers vectors.

In works [75, 76], it was supposed that the MPs are situated in an infinite medium. However, the split of an MP is also likely to happen at the crystal growth front. For example, in work [77] the split of a MP into another MP and a full-core screw dislocation has been proposed to occur through the lateral motion of the surface step produced by the MP. In terms of the dislocation theory, the split of an MP at or near the crystal growth front may be considered as the formation of a glide dislocation semi-loop. Since such a split occurs near the crystal free surface, its theoretical analysis required preliminary solving a number of boundary-value problems for the MPs terminated at the free crystal surface.

The first of these problems was the problem about an MP perpendicular to a free crystal surface [78]. The exact analytic solution of this problem was obtained with an account for both the cylindrical surface of the MP and its perpendicular flat crystal surface. The displacement, strain, and stress fields of the MP in a half-space were calculated in [78] through distributing virtual twist disclination loops over the MP surface. As a result, it was demonstrated, in particular, that the rigorous account for the boundary conditions at the cylindrical MP surface considerably influences the stress field of the MP. The region of strong influence is situated around the MP at the distance of the order of the MP radius. In this region, the elastic strains may reach high enough values of several tenths of a percent.

Another boundary-value problem whose solution is necessary for the analysis of the MP split near the crystal free surface is the problem on glide rectangular dislocation loops that are perpendicular to a free surface. The energy of such dislocation loops was calculated in [77] using the Green function method.

Using the obtained solutions of the boundary-value problems for the MP and dislocation loops perpendicular to a free surface, Gutkin and Sheinerman [77] carried out a theoretical analysis of the MP split into a smaller MP and a dislocation semi-loop. The calculations demonstrated the existence of the MP attraction zone (with the width of several hundredths to tenths of MP radius) and the flat crystal surface attraction zone (with the width of several MP radii), which the semi-loop has to overcome before its expansion becomes energetically favorable. The semi-loop can pass over the flat crystal surface attraction zone owing to the crystal growth, while going through the MP attraction zone requires the presence of an external perturbation or a stress source. After the semi-loop has left the attraction zones, it becomes stable, and the MP split becomes irreversible. Thus, a fast crystal growth may get it easier for the semi-loop to pass over the attraction zone and thereby promote the split of an MP (provided that the split has already been initiated due to an external perturbation or a stress source). Therefore, one may suppose that MPs are most likely to split and be overgrown if the crystal growth rate is sufficiently high.

Gutkin and Sheinerman [77] also theoretically showed that the most expectable trajectory of the semi-loop central point goes rather closely to the MP in such a manner that the shape of the semi-loop becomes strongly elongated along the MP. Therefore, the new MP, which may be formed around the semi-loop line, has to lie

just near the initial MP. This conclusion is in good agreement with the experimental observations of ramifying MPs in silicon carbide [76].

Another boundary-value problem solved for the MPs concerns the calculation of the elastic fields of MPs with axially symmetric steps [79]. The evidence of such steps is clearly demonstrated by scanning electron microscopy observations of MPs appearing at the free surface of a crystal (see, for example, [76]). In view of the presence of the sharp step edge, such a problem cannot be solved using traditional methods of dislocation theory. However, its approximate but fully analytical solution was obtained [79] using the method [80] for studying the effect of stress concentration near rough surfaces. Gutkin and Sheinerman [79] considered separately MPs that lie in an infinite medium and MPs perpendicular to a planar free surface. For both the cases, they calculated the thermodynamic forces acting on the steps. For MPs in an infinite medium, the force of interaction between their steps was also found. For an MP with a step, perpendicular to a free surface, the equilibrium position of the step was estimated. It was shown that subsurface MP steps repulse from the free surface if they result in decreasing the MP radius. This means that, in vicinity of the free surface, the MP radius may reduce compared to its radius far from the free surface if the energetic barrier for the generation of subsurface steps is overcome. It was also shown that same-sign steps attract each other (at least, as long as they are small), and so the formation of large enough steps at the MP surface is possible.

It is worth noting in conclusion that the solution for a screw dislocation interacting with two cylindrical voids [60] was used to describe the effect of contact-less reaction of two MPs by exchange of full-core screw dislocations that should lead to diminishing the radii of reacting MPs and potentially to their healing in the growing crystal [81, 82]. This theoretical model was supported by experimental observations combined with computer simulation of the phase contrast images of MPs obtained in X-ray synchrotron radiation [81, 82].

14.3.2 Dislocation Loops

In real materials and solid-state structures, dislocations often form closed loops of various shapes [59]. Dislocation loops are of special interest for theoretical models dealing with nucleation and multiplication of dislocations. In our lab, a number of boundary-value problems have been solved for circular and rectangular dislocation loops with some application to the models of MD generation in core-shell NPs and NWs, quantum dots (QDs), and stress relaxation in pentagonal NPs and whiskers.

For example, the problem of a circular prismatic dislocation loop (CPDL; “prismatic” means that the Burgers vector of the loop is normal to its plane, in contrast to “glide” dislocation loop with its Burgers vector parallel to the loop plane [59]) placed in the axisymmetric position in the cross section of a long elastic circular cylinder was solved independently by Ovid’ko and Sheinerman [83], Aifantis et al. [84], and Chernakov et al. [85]. The authors used different techniques and found different mathematical forms for their solution, however the aim was in general the same: to

analyze the critical conditions for the generation of MDs in core-shell NWs. Indeed, besides the formation of straight MDs, the relaxation of misfit stresses in core-shell NWs is possible via the formation of MD loops at the NW cross sections. It was found that the formation of a CPDL is energetically favored if the misfit exceeds a critical value. This critical misfit decreases with an increase in the core radius or shell thickness, similar to the case of the nucleation of a straight MD. For a specified misfit, the formation of a CPDL in a core-shell NW is beneficial if the core radius and the shell thickness are not too small. Chernakov et al. [85] also calculated the energy of elastic interaction between two similar CPDLs and used this result to determine the equilibrium density of such CPDLs in a core-shell NW. In the special case of the InAs-GaAs core-shell NW of diameter 100 nm and core-shell radii ratio ~ 0.7 , experimentally grown and studied by Popovitz-Biro et al. [86], the authors [85] showed that the calculated equilibrium spacing of misfit CPDLs 8.35–9.05 nm was in good agreement with their experimentally observed spacing 7.0–8.5 nm. The relative energy gain caused by such partial misfit stress relaxation was estimated as roughly 31%.

Another research topic of the lab comprised the analysis of dislocation behavior in nanocomposites containing capped or uncapped islands (QDs) or NWs. One such a model considered a misfit CPDL around a subsurface cylindrical QD [87]. Such a QD represented an inclusion in the form of a finite-height cylinder situated in a film on a semi-infinite substrate. The flat facet of the QD was supposed to enter a surface of a semi-infinite matrix. To calculate the conditions for the CPDL formation, the authors used the well-known strain energy of the CPDL near a flat free surface and its stress fields [88] for finding the energy of elastic interaction of the CPDL and the QD. Their theoretical analysis [87] demonstrated that the formation of a CPDL around a subsurface cylindrical QD of a specified height is easiest if the diameter of this QD is approximately equal to its height and becomes more difficult with an increase of the absolute difference between the QD diameter and its height.

In the work [20], Kolesnikova and Romanov presented elastic fields of CPDL located parallel to the free surfaces of a flat plate. This solution was found using MVSD, in which two types of circular loops were chosen as virtual defects: CPDLs and the radial Somigliana dislocation ring loops [18–20].

Kolesnikova et al. [89] solved the boundary-value problem for an axially symmetric CPDL in an elastic hollow sphere. They calculated the stress fields and the strain energy of the CPDL and showed that the CPDL stress and dilatation fields are strongly screened and distorted by the free surfaces of the sphere as compared with the case of a CPDL in an infinite medium. Moreover, they revealed some interesting qualitative peculiarities in the distribution of the elastic fields, which would be impossible to predict based on the infinite-medium solution. This mainly concerns the CPDL dilatation which can change its sign in the subsurface layers of the particle, near the cavity and in the shell. In the case of an interstitial CPDL, some regions of 3D stretching appear near the free surfaces where the conditions favorable for surface nucleation of vacancies are formed. These vacancies are stimulated to migrate to the interstitial CPDL, accommodate the compression near it and annihilate with the interstitials forming the CPDL. As a result, the CPDL can be kinetically unstable

in the systems under discussion. On the other hand, the interstitials and impurities having the atomic size larger than that of the parent atoms, are stimulated to migrate to the stretched regions and form their surface segregations or even second phases. The strain energies of CPDLs were shown to strongly depend on their radii and positions in particles and shells, or near cavities. In particles and shells, the strain energy reaches its maximum when a CPDL lies in the equatorial planes and has the radius of roughly 0.8 of the particle radius or outer radius of the shell, if the latter is several times larger than the inner radius of the shell. For a cavity, the strain energy of a CPDL increases with its radius and its shift from the equatorial plane.

The solution [89] was extensively used in recent years for theoretical modeling of stress relaxation in bulk [90, 91] and hollow [91, 92] core-shell NPs, icosahedral [93] and decahedral [94] small particles, decahedral core-shell NPs [95] and core-shell nanoparticles with truncated spherical cores [96]. Moreover, Krasnitskii et al. [97] utilized this solution to calculate the energy of elastic interaction of two coaxial CPDLs in an elastic hollow sphere. They showed that the interaction energy of CPDLs is strongly screened by free spherical surfaces when at least one of the CPDLs is localized near the surface. The outer free surface makes a greater effect on the interaction energy than the inner free surface. In particular, there is a region near the equator and the outer free surface, where the interaction energy changes its sign. The inner free surface does not give such effect.

Besides the CPDLs, the rectangular prismatic dislocation loops (RPDLs) have also been in the focus of research in our lab. For example, Gutkin et al. [98] analyzed the critical conditions for the formation of various misfit defects at the interface between subsurface NWs of rectangular cross section, which were parallel to a free surface, and surrounding semi-infinite matrix. It was supposed that the accommodation of the misfit stresses in such a system might occur through the generation of either RPDLs, or dislocation semi-loops, or dipoles of straight MDs. The defects were supposed to form if their generation was energetically favorable. For the calculation of the strain energy of the RPDL, the authors applied the Green function method. The calculations [98] demonstrated that taking into account of the NW shape anisotropy and the presence of a free surface nearby significantly alters the critical conditions for defect formation in a NW. In contrast to cylindrical NWs and spherical QDs in an infinite medium, an increase of one of the sizes of a subsurface rectangular NW does not always reduce the critical misfit for the formation of RPDLs, although it decreases the critical misfit for the formation of MD dipoles at the NW-matrix interface. The presence of a matrix free surface may either increase or decrease the critical misfits for the nucleation of RPDLs and MD dipoles.

The strain energy of a RPDL placed normally to a close flat free surface, found in [98], were recently used in theoretical models of initial stages of misfit stress relaxation in various composite nanostructures of spherical (bulk [91, 99, 101] and hollow [91, 100, 101] core-shell NPs), cylindrical (bulk [100–104] and hollow [100, 101] core-shell NWs) and flat (bi- and tri-nanolayers [100, 101]) geometry. Based on the strained states in the misfitting nanostructures, the authors quantitatively estimated changes in their energies, which accompany the generation of RPDLs in them, revealed places of the energetically more favorable generation of the RPDLs

in these nanostructures and determined optimum shape of the RPDLs. By comparing the critical conditions for appearance of the most energetically favorable RPDLs in the different composite nanostructures, Gutkin and Smirnov [100, 101] ranged the relative stabilities of these nanostructures against generation of RPDLs. In particular, they showed that the hollow nanostructures are always more stable than their bulk counterparts, the cylindrical nanostructures are more stable than the symmetric flat tri-nanolayers, the spherical nanostructures are more stable than the cylindrical ones, and the flat bi-nanolayers are the most stable composites among those under investigation.

14.4 Disclinations

For disclinations, quite a limited number of boundary-value solutions have been found in our lab, although some earlier solutions were used in theoretical modeling. In particular, in parallel with MDs, other misfit defects can nucleate in core-shell NWs. An example is wedge disclinations (WDs) that can form at the junctions of twin or grain boundaries in poly- and nanocrystalline solids [9, 28, 105]. The elastic solutions, found by Romanov [42] for WDs in elastic cylinder, were applied by Sheinerman and Gutkin [106] to examine the critical conditions of the formation of individual misfit WDs, their dipoles, and arrays in core-shell NWs. In considering individual misfit WDs, the authors showed that their appearance at the core-shell interface is energetically favored if their strength is smaller than a critical strength. In contrast, the formation of a WD dipole, with one WD at the core-shell interface and another inside the shell, is beneficial if the disclination strength exceeds another critical strength. Similar to individual misfit WDs, the formation of a periodic array of misfit WDs at the core-shell interface is favorable if the disclination strength is below some critical strength that depends on the core to NW radii ratio, misfit, and the number of misfit WDs in the array.

Another example is the solution for a bi-axial dipole of WDs in a thin elastic layer [16], which was used by Dynkin and Gutkin in their models of stress-coupled migration of grain boundaries in ultra-thin nanocrystalline films under tension [107, 108].

New solutions were found by Shodja et al. [109] for a bi-axial dipole of WDs in an embedded NW and by Rezazadeh-Kalehbasti et al. [110] for a bi-axial dipole of WDs and an individual WD in the shell of a free-standing core-shell NW. In both the cases, the surface/interface elasticity was used. Shodja et al. [109] showed that the positive interface modulus leads to increased strain energy and extra repulsive forces on the WD dipole. The noticeable effect of the negative interface modulus is the non-classical oscillations in the stress field of the WD dipole and an extra attractive image force on it. Rezazadeh-Kalehbasti et al. [110] demonstrated that the stresses are rather inhomogeneous across the NW cross section, change their signs and reach local maxima and minima far from the WD lines in the bulk or on the surface of the NW. For negative values of the surface/interface modulus and relatively small values

of the ratio of the shell and core shear moduli, the surface/interface effect manifests itself through non-classical stress oscillations along the shell free surface in the case of a WD dipole and core-shell interface in both the cases of a WD dipole and an individual WD. The non-classical solution for the strain energy deviates from the classical solution with different effects caused by the surface/interface moduli on the WD dipole and an individual WD. When the core is softer than the shell, the dipole with radial orientation of its arm has an unstable equilibrium position in the shell. In general, if the surface/interface modulus is positive, the surface/interface effects are rather weak; however, if it is negative, the effect can be very strong, especially near the shell surface.

Solution for the dipole of WDs whose lines are perpendicular to the free surfaces of the flat plate of finite thickness is given in the works [18, 19].

Within the classical theory of elasticity, Kolesnikova et al. [111] solved a new boundary-value problem for a WD axially piercing a hollow sphere. The displacements, the stresses, and the dilatation of the WD were represented in the form of series with Legendre polynomials and analyzed in detail. The related problems of WDs axially piercing a bulk elastic sphere and a spherical pore in an elastic medium were addressed as well. The authors concluded that the divergence of the WD elastic fields was eliminated everywhere in the elastic bodies with the exception of the WD line. The hollow and bulk spheres are the most screening systems for the WD in comparison with the flat layer [16] and the infinite cylinder [42] considered earlier. The distribution and the magnitude of the WD elastic fields in spherical bodies strongly depend on the presence and the size of the inner cavity. Nevertheless, the regions adjacent to the lines of positive (negative) WDs are always hydrostatically compressed (stretched), while the regions distant from these lines are always hydrostatically stretched (compressed). The formal solution for a WD axially piercing a spherical pore in an infinite elastic medium is inapplicable for analyzing the elastic fields of the WD. To get their realistic description, it is necessary to strictly take into account the boundary conditions on remote external boundaries of the body containing the WD. For example, the solution of the problem of a WD, axially piercing a sufficiently thick spherical layer, is suitable for analyzing the case of a spherical pore on the WD line.

The elastic fields found by Kolesnikova et al. [111] were used in theoretical models which described the fracture of hollow decahedral particles under chemical etching [112], the elastic strains in homogeneous [94] and core-shell [95] decahedral NPs and their relaxation through generation of CPDLs. In these models, the positive partial WD of strength $+7^{\circ}20'$ lies along the axis of five-fold symmetry in a decahedral particle, which axis coincides with the line of junction of five twin domains [113]. The solution by Kolesnikova et al. [111] allowed to consider the decahedral particle as an elastic sphere (either hollow [112], or bulk [94], or composite [95]) axially pierced by the WD and to calculate the initial (unrelaxed) strain-stress states within these models.

We also mention a number of boundary-value problems solved for a circular twist disclination loop, the Frank vector of which is perpendicular to the plane of the loop. Solutions for elastic fields and energy of the twist loop in a finite thickness flat plate,

near a free surface and an interface are given in the Refs. [18, 19]. In the cylinder, solid sphere and for the loop circling the spherical hole, the solutions for the twist loops can be found in the Refs. [20, 114] and [27], respectively.

14.5 Inclusions

The boundary-value problems for inclusions have been solved in our lab with the aim to use these solutions mainly for studying the misfit stress distribution in various composite nanostructures. Some of these results were found from more general solutions by simple limiting transitions. For example, Malyshev et al. [115] solved the problem for a dilatational inclusion in the shape of a long prism of rectangular cross-sectional (rectangular inclusion) embedded to a thin elastic layer in such a way that the edges of the inclusion and two its faces were parallel to the layer free surfaces. Mikaelyan et al. [41] reproduced this solution and used it to analyze the model of dislocation emission from the edge of such an inclusion embedded in a free-standing nanolayer. With a limiting transition from the nanolayer to a semi-infinite medium, Gutkin et al. [98] found an explicit analytical solution for a similar inclusion in an elastic half-space and applied it to modeling the misfit stress relaxation in misfitting NWs embedded to a half-space (see also Sect. 14.3.2).

Gutkin et al. [116–118] considered a similar rectangular inclusion with antiplane eigenstrain as a model for polytype inclusions in growing crystals of silicon carbide. With using this model, they gave a theoretical description for the elastic interaction of these inclusions with MPs (see Sect. 14.3.1.2) and showed that MPs must be attracted to the boundaries of the inclusion and agglomerate there with formation of elongated pores, as was revealed by their own direct experimental observations. In doing so, they solved a boundary-value problem for the rectangular inclusion interacting with the free cylindrical surface of an MP [117] and demonstrated that the equilibrium positions of MPs lie at the inclusion boundaries. Moreover, Gutkin et al. [118] found the solution for the stress field of a similar inclusion containing an elliptic pore on its boundary. The analysis of the forces exerted on MPs by the inclusion and elliptic pore showed that the pore attracts MPs until their number reaches a critical value. After that, the MPs absorbed by the pore produce a repulsion zone for new MPs, and pore growth stops. The critical pore size is determined by the values of inclusion plastic distortions. At their small values, isolated MPs form at the inclusion/matrix interface; at medium values MPs coalesce to form a pore of a certain size; at large values the pore occupies the whole inclusion boundary.

The spherical dilatational inclusion embedded in the flat finite thickness plate was considered in [20], and the related boundary-value problem was solved using MVSD.

A number of boundary-value problems have been solved for the inclusions that play the role of cores in core-shell NWs and NPs. First, infinite cylindrical inclusions with 3D dilatational eigenstrains were considered as cores in elastically homogeneous [43, 119, 120] and inhomogeneous [84] cylindrical core-shell NWs. Enze-

vae et al. [56] solved a similar elastically inhomogeneous problem within the surface/interface elasticity.

Gutkin et al. [121] constructed the model of a cylindrical core with axial 1D dilatational eigenstrain and finite length in a cylindrical NW. The stress fields of this finite-length core were found through continuous distribution of virtual CPDLs with infinitesimal Burgers vectors over the side boundary of the core and integration of stress fields of these virtual CPDLs over the core length. The authors analyzed two possible ways of stress relaxation in such a composite NW – by misfit CPDLs and by mode I penny-shaped cracks. It was shown that the first way is more preferable than the second one for almost all possible real cases. The elastic solution of Gutkin et al. [121] was then used by Gutkin and Panpurin [122, 123] to study the spontaneous formation and equilibrium distribution of axial cylindrical QDs in atomically inhomogeneous pentagonal NWs.

Krasnitckii et al. solved a number of boundary-value problems for faceting cores in core-shell NWs, including the cases of axial prismatic cores of square [104, 124, 125], triangle [104, 125] and hexagonal [103, 104, 125] cross sections, and eccentric prismatic cores of rectangular [126] and trapezoidal [125] cross sections. They used these solutions for comparative analysis of critical conditions for nucleation of RPDLs (see Sect. 14.3.2) at the initial stages of misfit stress relaxation in such NWs [102–104, 125]. For example, Krasnitckii et al. [104] considered different sites of RPDL nucleation in the NWs with hexagonal, square and triangular shapes of the core cross section. The energy change caused by the RPDL nucleation was calculated for every case under the assumption that the shell thickness is much smaller than the core size. The corresponding critical values of the misfit parameter for the RPDL nucleation were determined and compared with each other. According to this comparison, the most favorable sites in the core-shell NWs and the optimal shapes of the RPDLs were defined. NWs with round, hexagonal, square, and triangle shapes of the core cross section were ranged with respect to their stability to RPDL nucleation.

The inclusion problem for bulk spherical cores in spherical core-shell NPs was solved many years ago [127, 128] and extensively used in theoretical modeling of mechanisms of misfit stress relaxation in these systems [90, 91, 95, 129]. Gutkin et al. [92] considered the case of hollow spherical cores in spherical core-shell NPs and applied its solution to modeling of misfit CPDL generation in such NPs [91, 92]. Kolesnikova et al. [130] suggested the elastic models for finite cylindrical and truncated spherical inclusions in an infinite medium as well as for a truncated spherical inclusion in an elastic sphere [131]. As a limiting case of the latter problem, a spherical Janus particle (composed of two semispheres of different materials) was considered as well [131]. The solution for a truncated spherical dilatational inclusion in an elastic sphere [131] was also used in studying the critical conditions for the formation of misfit CPDLs in core-shell NPs with truncated spherical cores [96].

In addition, spherical two-phase inclusion in the infinite matrix as a model of the core-rim structured carbide grain in the cermet, was considered in Ref. [132].

Romanov et al. [133, 134] considered a number of boundary-value problems for flat sharp and diffusive interfaces in axially inhomogeneous NWs. These interfaces

were normal to the NW axes and separated the NWs onto cylindrical segments of different misfitting materials.

The authors presented a general solution of the isotropic elasticity problem for the sandwiched inclusion in an elastic cylinder and having axially varying eigenstrain. The technique of the solution and the results for the elastic fields and energies of dilatational inclusions with different distribution of eigenstrain, namely, constant, trapezoidal, and diffusion-like, along the axis of the cylinder, were given in full details. The technique explored the axial superpositions of infinitely thin dilatation disks inserted in the cylinder, the elastic fields of which were found in analytical form. In addition, the energies of interfaces separated domains with constant eigenstrains in the cylinder were given. It was demonstrated that the blurring of the eigenstrain in the transition region leads to a decrease in interface energy.

In the works [135, 136], a finite element method was used to calculate the elastic fields and total displacements in a surface QD and an adjusted region of the substrate. The effects of QD form factor and aspect ratio δ on QD elastic properties were analyzed. A quasilinear dependence of radial displacements on radial coordinate for spherical, elliptical, and truncated spherical QDs was demonstrated. It has been found that the displacement field does not depend on the shape and aspect ratio for QDs with $\delta > \delta_{c1}$, and the upper part of a QD remains practically undistorted for QDs with $\delta \geq \delta_{c2}$. For InSb/InAs heterosystem these critical values are $\delta_{c1} \sim 0.13$ and $\delta_{c2} \sim 0.33$. The total displacements were used for computation of TEM diffraction contrast associated with QDs [135, 136].

Along with solutions of the boundary-value problems for defects that are internal sources of elastic fields, the complete analytical solution for the plane elasticity problem of a concentrated force acting on a half-space weakened by a circular hole was found [137, 138]. The solution is based on the algorithm proposed by Jeffery [139] for elasticity problems and treated in detail by Uflyand [12] using bipolar coordinates to characterize the geometry of the problem. Earlier, this problem was solved correctly by applying numerical methods and extended to the case with an elliptical hole (see, e.g., Ref. [140]). We found the biharmonic stress function describing stresses and strains in the half-space and the associated biharmonic function that allows determining the displacement field. Both functions were given in the form of Fourier series with quite compact coefficients. The stresses were written and plotted. Particular attention was paid to the displacements at the surface of the half-space. It was speculated how these displacements could be used in an inverse procedure for the identification of a circular hole diameter and position in the solid by the measurements of surface displacements induced by a concentrated force.

14.6 Conclusions

Thus, we have given a brief review of boundary-value problems in the theory of elasticity, which have been solved for various defects (dislocations, disclinations, and inclusions) in our lab during the last three decades. We have also touched some

relevant works dealing with application of the solutions found to our theoretical models describing the nucleation and development of different defect structures in the process of crystal growth and misfit stress relaxation in advanced composite nanostructures which are highly promising for use in modern electronics, optoelectronics, photonics, etc.

Based on these studies, we can conclude that theoretical description of elastic behavior of defects near inner and outer boundaries of solids within the classical theory of elasticity gives rather reliable results that in a set of cases are in good accordance with available experimental data. Although the use of more extended versions of the elasticity theory (as, for example, the strain/stress gradient elasticity and the surface/interface elasticity) looks much more attractive when dealing with nanostructures, it was demonstrated that in reality they give new important results in close vicinity (not farther than ~ 1 nm) of surfaces/interfaces and lines of defects.

Among the problems that seem to be of special interest in the nearest future, we can notice the following areas of research:

- boundary-value problems for defects in faceted core-shell NWs and NPs;
- boundary-value problems for inhomogeneous nanostructures with diffuse interfaces;
- theoretical models describing the elastic behavior of defects in inhomogeneous nanostructures with diffuse interfaces.

The statement and solution of the above problems will allow to get new results which are expected to better reflect the behavior of defects and related phenomena in real device nanostructures.

References

1. Gutkin, M.Yu., Ovid'ko, I.A.: *Physical Mechanics of Deformed Nanostructures, vol. II. Nanolayered Structures*, Yanus, Saint-Petersburg (2005) (in Russian)
2. Ovid'ko, I.A., Sheinerman, A.G.: *Mechanics of Nanowires and Nanostructured Films*. Exlibris-Nord, Saint-Petersburg (2011) (in Russian)
3. Gutkin, M.Yu., Kolesnikova, A.L., Romanov, A.E.: Misfit dislocations and other defects in thin films. *Mater. Sci. Eng. A* **164**(1–2), 433–437 (1993)
4. Gutkin, M.Yu.: Nanoscopies of dislocations and disclinations in gradient elasticity. *Rev. Adv. Mater. Sci.* **1**, 27–60 (2000)
5. Ovid'ko, I.A., Sheinerman, A.G.: Elastic fields of inclusions in nanocomposite solids. *Rev. Adv. Mater. Sci.* **9**, 17–33 (2005)
6. Gutkin, M.Yu.: Elastic behavior of defects in nanomaterials. I. Models for infinite and semi-infinite media. *Rev. Adv. Mater. Sci.* **13**, 125–161 (2006)
7. Ovid'ko, I.A., Sheinerman, A.G.: Misfit dislocations in nanocomposites with quantum dots, nanowires and their ensembles. *Adv. Phys.* **55**(7–8), 627–689 (2006)
8. Gutkin, M.Yu., Sheinerman, A.G., Argunova, T.S.: Development of defect structures in silicon carbide growing crystals. *Phys. Status Solidi C* **6**(8), 1942–1947 (2009)
9. Romanov, A.E., Kolesnikova, A.L.: Application of disclination concept to solid structures. *Prog. Mater. Sci.* **54**, 740–769 (2009)

10. Romanov, A.E., Kolesnikova, A.L., Aifantis, E.C.: Disclinations and materials structure. In: Merson, D.L. (ed.) *Advanced Materials, Tutorial*, vol. 4, pp. 251–316. TSU, Togliatti (2011) (in Russian)
11. Lurie, A.I.: *Spatial Problems of Theory of Elasticity*. State Publishing House of Scientific and Technical Literature, Moscow (1955) (in Russian)
12. Uflyand, J.S.: *Bipolar Coordinates in the Theory of Elasticity*. State Publishing House of Scientific and Technical Literature, Moscow (1950) (in Russian)
13. Louat, N.: Solution of boundary problems in plane strain. *Nature (London)* **196**(4859), 1081–1082 (1962)
14. Marcinkowski, M.J.: *Unified Theory of the Mechanical Behavior of Matter*. Wiley, New York (1979)
15. Romanov, A.E., Vladimirov, V.I.: Straight disclinations near a free surface. I. Stress fields. *Phys. Status Solidi A* **63**(1), 109–118 (1981)
16. Vladimirov, V.I., Kolesnikova, A.L., Romanov, A.E.: Wedge disclinations in an elastic plate. *Phys. Metals Metallograp.* **60**(6), 58–67 (1985)
17. Belov, A.J., Chamrov, V.A., Indenbom, V.L., Lothe, J.: Elastic fields of dislocations piercing the interface of an anisotropic bicrystal. *Phys. Status Solidi B* **119**(2), 565–578 (1983)
18. Kolesnikova, A.L., Romanov, A.E.: Circular dislocation–disclination loops and their application to boundary problem solution in the theory of defects. Preprint No. 1019, Ioffe Institute, Leningrad (1986) (in Russian)
19. Kolesnikova, A.L., Romanov, A.E.: Dislocation and disclination loops in the virtual-defect method. *Phys. Solid State* **45**, 1706–1718 (2003)
20. Kolesnikova, A.L., Romanov, A.E.: Virtual circular dislocation-disclination loop technique in boundary value problems in the theory of defects. *J. Appl. Mech.* **71**, 409–417 (2004)
21. Kolesnikova, A.L., Soroka, R.M., Romanov, A.E.: Defects in the elastic continuum: classification, fields and physical analogies. *Mater. Phys. Mech.* **17**, 71–91 (2013)
22. Kolesnikova, A.L., Gutkin, M.Yu., Romanov, A.E.: Elastic models of defects in 3D and 2D crystals. *Rev. Adv. Mater. Sci.* **51**(2), 130–148 (2017)
23. Eason, G., Noble, B., Sneddon, I.N.: On certain integrals of Lipschitz-Hankel type involving products of Bessel functions. *Philos. Trans. R. Soc. London, Ser. A* **247**(935), 529–551 (1955)
24. Bateman, H., Erdelyi, A.: *Tables of Integral Transforms*, vol. 2. Mc Graw-Hill Book Company Inc, New York (1953)
25. Uflyand, J.S.: *Integrals Transforms in the Problems of the Theory of Elasticity*. Nauka, Leningrad (1967) (in Russian)
26. Bateman, H., Erdelyi, A.: *Tables of Integral Transforms*, vol. 1. Mc Graw-Hill Book Company Inc, New York (1953)
27. Kolesnikova, A.L., Romanov, A.E.: Representation of elastic fields of circular dislocation and disclination loops in terms of spherical harmonics and their application to various problems of the theory of defects. *Int. J. Solids Struct.* **47**, 58–70 (2010)
28. Dundurs, J.: Elastic interaction of dislocations with inhomogeneities. In: Mura, T. (ed.) *Mathematical Theory of Dislocations*, pp. 70–115. A.S.M.E, New York (1969)
29. Eshelby, D.J.: Boundary problems. In: Nabarro, F.R.N. (ed.) *Dislocations in Solids*, vol. 1, pp. 167–221. North-Holland, Amsterdam (1979)
30. Lothe, J.: Dislocations interacting with surfaces, interfaces or cracks. In: Indenbom, V.L., Lothe, J. (eds.) *Elastic Strain Fields and Dislocation Mobility*, pp. 329–389. North-Holland, Amsterdam (1992)
31. Belov, A.Yu.: Dislocations emerging at planar boundaries. In: Indenbom, V.L., Lothe, J. (eds.) *Elastic Strain Fields and Dislocation Mobility*, pp. 391–446. North-Holland, Amsterdam (1992)
32. Gutkin, M.Yu., Romanov, A.E.: Straight edge dislocations in a thin two-phase plate. I. Elastic stress fields. *Phys. Stat. Sol. (a)* **125**(1), 107–125 (1991)
33. Gutkin, M.Yu., Romanov, A.E.: Straight edge dislocations in a thin two-phase plate. II. Impurity-vacancy polarization of plate, interaction of a dislocation with interface and free surfaces. *Phys. Stat. Sol. (a)* **129**(2), 363–377 (1992)

34. Gutkin, M. Yu., Romanov, A.E.: Misfit dislocations in a thin two-phase heteroepitaxial plate. *Phys. Stat. Sol. (a)* **129**(2), 117–126 (1992)
35. Gutkin, M. Yu., Romanov, A.E.: On the stand-off positions of misfit dislocations. *Phys. Stat. Sol. (a)* **144**(1), 39–57 (1994)
36. Gutkin, M. Yu.: Misfit stress relaxation in composite nanoparticles. *Int. J. Eng. Sci.* **61** (Special Issue), 59–74 (2012)
37. Gutkin, M. Yu., Ovid'ko, I.A.: Glide of hollow fibers at the bridging stage of fracture in ceramic nanocomposites. *Scripta Mater.* **59**(3), 368–371 (2008)
38. Gutkin, M. Yu., Ovid'ko, I.A.: Dislocation mechanism of hollow fiber sliding during ceramic nanocomposite fracture. *Phys. Solid State* **50**(11), 2053–2061 (2008)
39. Gutkin, M. Yu., Ovid'ko, I.A.: Effect of Y-junction nanotubes on strengthening of nanocomposites. *Scripta Mater.* **61**(12), 1149–1152 (2009)
40. Gutkin, M. Yu., Ovid'ko, I.A.: Effect of triple joints of nanotubes on strengthening and fracture toughness of ceramic nanocomposites. *Phys. Solid State* **52**(7), 1397–1403 (2010)
41. Mikaelyan, K.N., Gutkin, M. Yu., Borodin, E.N., Romanov, A.E.: Dislocation emission from the edge of a misfitting nanowire embedded in a free-standing nanolayer. *Int. J. Solids Struct.* **161**, 127–135 (2019)
42. Romanov, A.E.: Boundary-value problems in the theory of elasticity for disclinations. In: Vladimirov, V.I. (ed) *Experimental Investigation and Theoretical Description of Disclinations*, pp. 110–135. Ioffe Institute, Leningrad (1984) (in Russian)
43. Gutkin, M. Yu., Ovid'ko, I.A., Sheinerman, A.G.: Misfit dislocations in wire composite solids. *J. Phys.: Cond. Matter* **12**, 5391–5401 (2000)
44. Lo, Y.H.: New approach to grow pseudomorphic structures over the critical thickness. *Appl. Phys. Lett.* **59**, 2311–2313 (1991)
45. Huang, F.Y.: Effect of strain transfer on critical thickness for epitaxial layers grown on compliant substrates. *Appl. Phys. Lett.* **76**, 3046–3048 (2000)
46. Ovid'ko, I.A.: Relaxation mechanisms in strained nanoislands. *Phys. Rev. Lett.* **88**, 046103 (2002)
47. Ovid'ko, I.A., Sheinerman, A.G.: Perfect, partial and split dislocations in quantum dots. *Phys. Rev. B* **66**, 245309 (2002)
48. Ovid'ko, I.A., Sheinerman, A.G.: Delocalized dislocations in quantum dots. *JETP* **98**, 334–337 (2004)
49. Smirnov, A.M., Krasnitskii, S.A., Gutkin, M. Yu.: Generation of misfit dislocations in a core-shell nanowire near the edge of prismatic core. *Acta Mater.* **186**, 494–510 (2020)
50. Mikaelyan, K.N., Gutkin, M. Yu., Aifantis, E.C.: Edge dislocations near phase boundaries in the gradient theory of elasticity. *Phys. Solid State* **42**(9), 1659–1667 (2000)
51. Ru, C.Q., Aifantis, E.C.: Some studies on boundary value problems in gradient elasticity. Preprint of the MTU Report, Houghton, MI (1993)
52. Moeni-Ardakani, S.S., Gutkin, M. Yu., Shodja, H.M.: Elastic behavior of an edge dislocation inside the wall of a nanotube. *Scripta Mater.* **64**(8), 709–712 (2011)
53. Shodja, H.M., Ahmadzadeh-Bakhshayesh, H., Gutkin, M. Yu.: Size-dependent interaction of an edge dislocation with an elliptical nano-inhomogeneity incorporating interface effects. *Int. J. Solids Struct.* **49**(5), 759–770 (2012)
54. Gutkin, M. Yu., Enzevae, C., Shodja, H.M.: Interface effects on elastic behavior of an edge dislocation in a core-shell nanowire embedded to an infinite matrix. *Int. J. Solids Struct.* **50**(7–8), 1177–1186 (2013)
55. Gutkin, M. Yu., Rezaezadeh-Kalehbasti, S., Shodja, H.M.: Surface/interface effects on elastic behavior of an edge dislocation in the shell of a core-shell nanowire. *Eur. J. Mech. – A/Solids* **41**, 86–100 (2013)
56. Enzevae, C., Gutkin, M. Yu., Shodja, H.M.: Surface/interface effects on the formation of misfit dislocation in a core-shell nanowire. *Phil. Mag.* **94**(5), 492–519 (2014)
57. Gutkin, M. Yu., Romanov, A.E., Aifantis, E.C.: Screw dislocation near a triple junction of phases with different elastic moduli. I. General solution. *Phys. Stat. Sol. (a)* **153**(1), 65–75 (1996)

58. Gutkin, M.Yu., Sheinerman, A.G.: Elastic behavior of a screw dislocation in the wall of a hollow nanotube. *Phys. Sol. State* **49**(9), 1672–1679 (2007)
59. Anderson, P.M., Hirth, J.P., Lothe, J.: *Theory of Dislocations*. Cambridge University Press, New York (2017)
60. Gutkin, M.Yu., Sheinerman, A.G., Smirnov, M.A.: Elastic behavior of screw dislocations in porous solids. *Mech. Mater.* **41**(8), 905–918 (2009)
61. Kolesnikova, A.L., Gutkin, M.Yu., Romanov, A.E.: Threading screw dislocations in a two-phase plate and a two-phase sphere. *Rev. Adv. Mater. Sci.* **55**, 102–116 (2018)
62. Eshelby, J.D., Stroh, A.N.: Dislocations in thin plates. *Phil. Mag.* **42**(335), 1401–1405 (1951)
63. Yoffe, E.H.: A dislocation at a free surface. *Phil. Mag.* **6**(69), 1147–1155 (1961)
64. Polonsky, I.A., Romanov, A.E., Gryaznov, V.G., Kaprelov, A.M.: Screw dislocation in an elastic sphere. *Czechoslovak J. Phys.* **41**, 1249–1255 (1991)
65. Gutkin, M.Yu., Mikaelyan, K.N., Aifantis, E.C.: Screw dislocation near interface in gradient elasticity. *Scripta Mater.* **43**(6), 477–484 (2000)
66. Gutkin, M.Yu., Mikaelyan, K.N., Aifantis, E.C.: Behavior of screw dislocations near phase boundaries in the gradient theory of elasticity. *Phys. Solid State* **42**(9), 1652–1658 (2000)
67. Shodja, H.M., Davoudi, K.M., Gutkin, M.Yu.: Analysis of displacement and strain fields of a screw dislocation in a nanowire using gradient elasticity theory. *Scripta Mater.* **59**(3), 368–371 (2008)
68. Altan, S.B., Aifantis, E.C.: On the structure of the mode III crack-tip in gradient elasticity. *Scr. Metall. Mater.* **26**, 319–324 (1992)
69. Davoudi, K.M., Gutkin, M.Yu., Shodja, H.M.: Analysis of stress field of a screw dislocation inside an embedded nanowire using strain gradient elasticity. *Scripta Mater.* **61**(4), 355–358 (2009)
70. Davoudi, K.M., Gutkin, M.Yu., Shodja, H.M.: A screw dislocation near a circular nanoinhomogeneity in gradient elasticity. *Int. J. Solids Struct.* **47**(6), 741–750 (2010)
71. Shodja, H.M., Gutkin, M.Yu., Moeini-Ardakani, S.S.: Effect of surface stresses on elastic behavior of a screw dislocation inside the wall of a nanotube. *Phys. Stat. Sol. (b)* **248**(6), 1437–1441 (2011)
72. Ahmadzadeh-Bakhshayesh, H., Gutkin, M.Yu., Shodja, H.M.: Surface/interface effects on elastic behavior of a screw dislocation in an eccentric core-shell nanowire. *Int. J. Solids Struct.* **49**(13), 1665–1675 (2012)
73. Shodja, H.M., Enzevae, C., Gutkin, M.Yu.: Interface effect on the formation of a dipole of screw misfit dislocations in an embedded nanowire with uniform shear eigenstrain field. *Eur. J. Mech. - A/Solids* **51**(1), 154–159 (2015)
74. Huang, X.R., Dudley, M., Vetter, W.M., Huang, W., Wang, S., Carter, C.H.: Direct evidence of micropipe-related pure superscrew dislocations in SiC. *Appl. Phys. Lett.* **74**, 353–355 (1999)
75. Gutkin, M.Yu., Sheinerman, A.G.: Elastic interaction of micropipes in crystals. *Phys. Stat. Sol. (b)* **231**, 356–372 (2002)
76. Gutkin, M.Yu., Sheinerman, A.G., Argunova, T.S., Je, J.H., Kang, H.S., Hwu, Y., Tsai, W.-L.: Ramification of micropipes in SiC crystals. *J. Appl. Phys.* **92**, 889–894 (2002)
77. Gutkin, M.Yu., Sheinerman, A.G.: Split and sealing of dislocated pipes at the front of a growing crystal. *Phys. Stat. Sol. (b)* **241**, 1810–1826 (2004)
78. Sheinerman, A.G., Gutkin, M.Yu.: Elastic fields of a screw superdislocation with a hollow core (pipe) perpendicular to the free crystal surface. *Phys. Solid State* **45**, 1694–1700 (2003)
79. Gutkin, M.Yu., Sheinerman, A.G.: Dislocated micro- and nanopipes with surface steps. *Phys. Stat. Sol. (b)* **241**, 797–817 (2004)
80. Husu, A.P., Vittenberg, Yu.R., Palmov, V.A.: *Roughness of Surfaces: Theoretical Probabilistic Approach*. Nauka, Moscow (1975) (in Russian)
81. Gutkin, M.Yu., Sheinerman, A.G., Smirnov, M.A., Kohn, V.G., Argunova, T.S., Je, J.H., Jung, J.W.: Correlated reduction in micropipe cross sections in SiC growth. *Appl. Phys. Lett.* **93**(15), 151905 (2008)
82. Gutkin, M.Yu., Sheinerman, A.G., Kohn, V.G., Argunova, T.S., Smirnov, M.A., Je, J.H.: Contact-free reactions between micropipes in bulk SiC growth. *Phys. Stat. Sol. (a)* **209**(8), 1432–1437 (2012)

83. Ovid'ko, I.A., Sheinerman, A.G.: Misfit dislocation loops in composite nanowires. *Phil. Mag.* **84**, 2103–2118 (2004)
84. Aifantis, K.E., Kolesnikova, A.L., Romanov, A.E.: Nucleation of misfit dislocations and plastic deformation in core/shell nanowires. *Philos. Mag.* **87**, 4731–4757 (2007)
85. Chernakov, A.P., Kolesnikova, A.L., Gutkin, M.Yu., Romanov, A.E.: Periodic array of misfit dislocation loops and stress relaxation in core-shell nanowires. *Int. J. Eng. Sci.* **156**, 103367 (2020)
86. Popovitz-Biro, R., Kretinin, A., Von Huth, P., Shtrikman, H.: InAs/GaAs core-shell nanowires. *Crystal Growth & Design* **11**, 3858–3865 (2011)
87. Ovid'ko, I.A., Sheinerman, A.G.: Misfit dislocation loops in cylindrical quantum dots. *J. Phys.: Condens. Matter* **16**, 7225–7232 (2004)
88. Dundurs, J., Salamon, N.J.: Circular prismatic dislocation loop in a two-phase material. *Phys. Status Solidi (b)* **50**, 125–133 (1972)
89. Kolesnikova, A.L., Gutkin, M.Yu., Krasnitckii, S.A., Romanov, A.E.: Circular prismatic dislocation loops in elastic bodies with spherical free surfaces. *Int. J. Solids Struct.* **50**(10), 1839–1857 (2013)
90. Gutkin, M.Yu., Kolesnikova, A.L., Krasnitckii, S.A., Romanov, A.E.: Misfit dislocation loops in composite core-shell nanoparticles. *Phys. Solid State* **56**(4), 723–730 (2014)
91. Gutkin, M.Yu., Krasnitckii, S.A., Smirnov, A.M., Kolesnikova, A.L., Romanov, A.E.: Dislocation loops in solid and hollow semiconductor and metal nanoheterostructures. *Phys. Solid State* **57**(6), 1177–1182 (2015)
92. Gutkin, M.Yu., Kolesnikova, A.L., Krasnitckii, S.A., Romanov, A.E., Shalkovskii, A.G.: Misfit dislocation loops in hollow core-shell nanoparticles. *Scripta Mater.* **83**(1), 1–4 (2014)
93. Gutkin, M.Yu., Kolesnikova, A.L., Krasnitckii, S.A., Dorogin, L.M., Serebryakova, V.S., Vikarchuk, A.A., Romanov, A.E.: Stress relaxation in icosahedral small particles via generation of circular prismatic dislocation loops. *Scripta Mater.* **105**, 10–13 (2015)
94. Krauchanka, M.Yu., Krasnitckii, S.A., Gutkin, M.Yu., Kolesnikova, A.L., Romanov, A.E., Aifantis, E.C.: Generation of circular prismatic dislocation loops in decahedral small particles. *Scripta Mater.* **146**, 77–81 (2018)
95. Krauchanka, M.Yu., Krasnitckii, S.A., Gutkin, M.Yu., Kolesnikova, A.L., Romanov, A.E.: Circular loops of misfit dislocations in decahedral core-shell nanoparticles. *Scripta Mater.* **167**, 81–85 (2019)
96. Gutkin, M.Yu., Kolesnikova, A.L., Mikheev, D.S., Romanov, A.E.: Misfit stresses and their relaxation by misfit dislocation loops in core-shell nanoparticles with truncated spherical cores. *Eur. J. Mech./A Solids* **81**, 103967 (2020)
97. Krasnitckii, S.A., Smirnov, A.M., Gutkin, M.Yu.: Pair interaction of coaxial circular prismatic dislocation loops in elastic solids with spherical surfaces. *Mater. Phys. Mech.* **44**(1), 116–124 (2020)
98. Gutkin, M.Yu., Ovid'ko, I.A., Sheinerman, A.G.: Misfit dislocations in composites with nanowires. *J. Phys.: Condens. Matter* **15**, 3539–3554 (2003)
99. Gutkin, M.Yu., Smirnov, A.M.: Generation of rectangular prismatic dislocation loops in shells and cores of composite nanoparticles. *Phys. Solid State* **56**(4), 731–738 (2014)
100. Gutkin, M.Yu., Smirnov, A.M.: Initial stages of misfit stress relaxation in composite nanostructures through generation of rectangular prismatic dislocation loops. *Acta Mater.* **88**, 91–101 (2015)
101. Gutkin, M.Yu., Smirnov, A.M.: Initial stages of misfit stress relaxation through the formation of prismatic dislocation loops in GaN-Ga₂O₃ composite nanostructures. *Phys. Solid State* **58**(8), 1611–1621 (2016)
102. Krasnitckii, S.A., Kolomoetc, D.R., Smirnov, A.M., Gutkin, M.Yu.: Misfit stress relaxation in composite core-shell nanowires with parallelepipedal cores by rectangular prismatic dislocation loops. *J. Phys.: Conf. Ser.* **993**, 012021 (2018)
103. Krasnitckii, S.A., Smirnov, A.M., Mynbaev, K.D., Zhigilei, L.V., Gutkin, M.Yu.: Axial misfit stress relaxation in core-shell nanowires with hexagonal core via nucleation of rectangular prismatic dislocation loops // *Mater. Phys. Mech.* **42**(6), 776–783 (2019)

104. Krasnitckii, S.A., Smirnov, A.M., Gutkin, M.Yu.: Axial misfit stress relaxation in core-shell nanowires with polyhedral cores through the nucleation of misfit prismatic dislocation loops. *J. Mater. Sci.* **55**, 9198–9210 (2020)
105. Romanov, A.E., Vladimirov, V.I.: Disclinations in crystalline solids. In: Nabarro, F.R.N. (ed.) *Dislocations in Solids*, vol. 9, pp. 191–402. North-Holland, Amsterdam (1992)
106. Sheinerman, A.G., Gutkin, M.Yu.: Misfit disclinations and dislocation walls in a two-phase cylindrical composite. *Phys. Stat. Sol. A* **184**, 485–505 (2001)
107. Dynkin, N.K., Gutkin, M.Yu.: Migration of grain boundaries in free-standing nanocrystalline thin films. *Scripta Mater.* **66**(2), 73–75 (2012)
108. Gutkin, M.Yu., Dynkin, N.K.: Dislocation-disclination models of grain boundary migration in ultra-thin nanocrystalline films. *Phys. Solid State* **54**(4), 798–807 (2012)
109. Shodja, H.M., Rezaazadeh-Kalehbasti, S., Gutkin, M.Yu.: Wedge disclination dipole in an embedded nanowire within the surface/interface elasticity. *J. Mech. Behav. Mater.* **22**(5–6), 161–168 (2013)
110. Rezaazadeh-Kalehbasti, S., Gutkin, M.Yu., Shodja, H.M.: Wedge disclinations in the shell of a core-shell nanowire within the surface/interface elasticity. *Mech. Mater.* **68**(1), 45–63 (2014)
111. Kolesnikova, A.L., Gutkin, M.Yu., Proskura, A.V., Morozov, N.F., Romanov, A.E.: Elastic fields of straight wedge disclinations axially piercing bodies with spherical free surfaces. *Int. J. Solids Struct.* **99**, 82–96 (2016)
112. Gutkin, M.Yu., Kolesnikova, A.L., Yasnikov, I.S., Vikarchuk, A.A., Aifantis, E.C., Romanov, A.E.: Fracture of hollow multiply-twinned particles under chemical etching. *Eur. J. Mech./A Solids* **6**, 133–139 (2018)
113. De Wit, R.: Partial disclinations. *J. Phys. C: Solid State Phys.* **5**, 529–534 (1972)
114. Kolesnikova, A.L., Romanov, A.E.: Twist disclination loop in an elastic spheroid. *Tech. Phys. Lett.* **35**, 985–989 (2009)
115. Malyshev, K.L., Gutkin, M.Yu., Romanov, A.E., Sitnikova, A.A., Sorokin, L.M.: Dislocation models and diffraction contrast of rod-like defects in silicon. Preprint No.1109, A.F. Ioffe Physico-Technical Institute, Leningrad (1987) (in Russian)
116. Gutkin, M.Yu., Sheinerman, A.G., Argunova, T.S., Yi, J.M., Kim, M.U., Je, J.H., Nagalyuk, S.S., Mokhov, E.N., Margaritondo, G., Hwu, Y.: Interaction of dislocated micropipes with polytype inclusions in SiC. *J. Appl. Phys.* **100**(9), 093518 (2006)
117. Gutkin, M.Yu., Sheinerman, A.G., Argunova, T.S., Yi, J.M., Je, J.H., Nagalyuk, S.S., Mokhov, E.N., Margaritondo, G., Hwu, Y.: Role of micropipes in the formation of pores at foreign polytype boundaries in SiC crystals. *Phys. Rev. B* **76**(6), 064117 (2007)
118. Gutkin, M.Yu., Sheinerman, A.G., Smirnov, M.A., Argunova, T.S., Je, J.H., Nagalyuk, S.S., Mokhov, E.N.: Micropipe absorption mechanism of pore growth at foreign polytype boundaries in SiC crystals. *J. Appl. Phys.* **106**(12), 123515 (2009)
119. Dorogin, L.M., Vlassov, S., Kolesnikova, A.L., Kink, I., Löhmus, R., Romanov, A.E.: Crystal mismatched layers in pentagonal nanorods and nanoparticles. *Phys. Stat. Solidi (b)* **247**(2), 288–298 (2010)
120. Dorogin, L.M., Kolesnikova, A.L., Vlassov, S., Kink, I., Löhmus, R., Romanov, A.E.: Pentagonal nanorods and nanoparticles with mismatched shell layer. *J. Nanosci. Nanotechnol.* **10**, 6136–6143 (2010)
121. Gutkin, M.Yu., Kuzmin, K.V., Sheinerman, A.G.: Misfit stresses and relaxation mechanisms in a nanowire containing a coaxial cylindrical inclusion of finite length. *Phys. Stat. Sol. (b)* **248**(7), 1651–1657 (2011)
122. Gutkin, M.Yu., Panpurin, S.N.: Spontaneous formation and equilibrium distribution of cylindrical quantum dots in atomically inhomogeneous pentagonal nanowires. *J. Macromol. Sci. B: Phys.* **52**(12), 1756–1769 (2013)
123. Gutkin, M.Yu., Panpurin, S.N.: Equilibrium ensembles of quantum dots in atomically inhomogeneous pentagonal nanowires. *Phys. Solid State* **56**(6), 1187–1194 (2014)
124. Krasnitckii, S.A., Smirnov, A.M., Gutkin, M.Yu.: Misfit stresses in a core-shell nanowire with core in the form of long parallelepiped. *J. Phys.: Conf. Ser.* **690**, 012022 (2016)

125. Krasnitckii, S.A.: Dislocation mechanisms of residual stress relaxation in low-dimensional heterogeneous nanostructures. Ph.D. Thesis. Peter the Great St. Petersburg Polytechnic University, St. Petersburg (2019) (in Russian)
126. Krasnitckii, S.A., Kolomoetc, D.R., Smirnov, A.M., Gutkin, M.Yu.: Misfit stresses in a composite core-shell nanowire with an eccentric parallelepipedal core subjected to one-dimensional cross dilatation eigenstrain. *J. Phys.: Conf. Ser.* **816**, 012043 (2017)
127. Teodosiu, C.: *Elastic Models of Crystal Defects*. Springer, Berlin (1982)
128. Trusov, L.I., Tanakov, M.Yu., Gryaznov, V.G., Kaprelov, A.M., Romanov, A.E.: Relaxation of elastic stresses in overlaid microcrystals. *J. Cryst. Growth* **114**, 133–140 (1991)
129. Gutkin, M.Yu.: Misfit stress relaxation in composite nanoparticles. *Int. J. Eng. Sci.* **61** (Special Issue), 59–74 (2012)
130. Kolesnikova, A.L., Gutkin, M.Yu., Romanov, A.E.: Analytical elastic models of finite cylindrical and truncated spherical inclusions. *Int. J. Solids Struct.* **143**, 59–72 (2018)
131. Kolesnikova, A.L., Gutkin, M.Yu., Krasnitckii, S.A., Smirnov, A.M., Dorogov, M.V., Serebryakova, V.S., Romanov, A.E., Aifantis, E.C.: On the elastic description of a spherical Janus particle. *Rev. Adv. Mater. Sci.* **57**(1/2), 246–256 (2018)
132. Hussainova, I., Kolesnikova, A., Hussainov, M., Romanov, A.: Effect of stressed state on erosive performance of cermets with core-rim structured ceramic grains. *Wear* **267**(1–4), 177–185 (2009)
133. Romanov, A.E., Kolesnikova, A.L., Gutkin, M.Yu., Dubrovskii, V.G.: Elasticity of axial nanowire heterostructures with sharp and diffuse interfaces. *Scripta Mater.* **176**(2), 42–46 (2020)
134. Romanov, A.E., Kolesnikova, A.L., Gutkin, M.Yu.: Elasticity of a cylinder with axially varying dilatational eigenstrain. *Int. J. Solids Struct.* **213**, 121–134 (2021)
135. Bert, N.A., Freidin, A.B., Kolesnikova, A.L., Korolev, I.K., Romanov, A.E.: On strain state and pseudo moiré TEM contrast of InSb quantum dots coherently grown on InAs surface. *Phys. Stat. Solidi (a)* **207**, 2323–2326 (2010)
136. Bert, N.A., Kolesnikova, A.L., Korolev, I.K., Romanov, A.E., Freidin, A.B., Chaldyshev, V.V., Aifantis, E.C.: Elastic fields and physical properties of surface quantum dots. *Phys. Solid State* **53**, 2091–2102 (2011)
137. Proskura, A.V., Freidin, A.B., Kolesnikova, A.L., Morozov, N.F., Romanov, A.E.: Identification of defects in a solid body on the base of surface displacements. *Mater. Phys. Mech.* **15**, 9–25 (2012)
138. Proskura, A.V., Freidin, A.B., Kolesnikova, A.L., Morozov, N.F., Romanov, A.E.: Plane elasticity solution for a half-space weakened by a circular hole and loaded by a concentrated force. *J. Mech. Behav. Mater.* **22**(1–2), 11–25 (2013)
139. Jeffery, G.B.: Plane stress and plane strain in bipolar co-ordinates. *Philos. Trans. R. Soc. Lond. A* **221**, 265–293 (1921)
140. Kosmodamianskii, A.S.: *Stress State of Anisotropic Media with Holes*. Publishing Association “Vishcha School”, Kiev, Donetsk (1976) (in Russian)

Chapter 15

On Imbedded Alternating Renewal Process for a Diffusion Semi-Markov Process on Interval with Unattainable Boundaries



Boris P. Harlamov

Abstract A diffusion semi-Markov process on a bounded interval range of values with unattainable boundaries is considered. It is supposed that the process does not have any infinite-value interval of stop. So unattainability of the boundaries is provided only because of changing the coefficient of shift. A limit theorem of the alternating renewal process is used to derive a limit distribution of this diffusion semi-Markov process.

Keywords Regeneration time · Continuous semi-Markov process · Diffusion semi-Markov process · Regular and unattainable boundaries · Alternating renewal process

15.1 Continuous Semi-Markov Processes

A one-dimension diffusion semi-Markov process (see, for example, [1], p. 137) is the main objective of this investigation. Sample trajectories of such a process (unlike a diffusion Markov process) may contain finite intervals of constancy, which, in some applications, have quite pithy interpretations. For example, such a time is that of chromatographic particles location in absorbed position (see [2]), or time of unexpected trading discontinuances on a stock, and so on. We think that the existence of random intervals of constancy can be explained for any applications of random processes.

Statistical consideration of such a property leads to constructing a model of continuous semi-Markov processes [1] as a generalization of Markov processes. Applications of Markov processes are well known in physics, chemistry, biology, geology, sociology and so on. Continuous semi-Markov models could supplement the list of these applications taking into account more real process properties than the traditional Markov model.

B. P. Harlamov (✉)

Institute for Problems in Mechanical Engineering RAS, V.O., Bolshoy pr., 61,
St. Petersburg 199178, Russia

Along with an extended region of applications, the continuous semi-Markov processes have some lacks comparatively with Markov processes. For example, the formers do not have distribution formulae for fixed time moments. In this article, it is shown how one can do without these formulae deriving limit distributions of one-dimensional diffusion semi-Markov processes on an interval with unattainable boundaries.

15.1.1 Space of Continuous Functions

We will consider a one-dimensional continuous random process \mathcal{X} on the interval $[0, \infty)$. A mathematical description of the process begins from that of corresponding measurable space with a probability measure.

Let \mathcal{C} be the standard metric space of continuous functions ξ , determining on the interval $[0, \infty)$ with values from \mathbb{R} (sample trajectories of the process), \mathcal{F} be a subset sigma-algebra of \mathcal{C} and P be a probability measure on \mathcal{F} . This triple characterizes completely the continuous random process of general view. Sometimes, it is more convenient to consider a coordinated family of probability measures than one that.

Further, we use some attributes of the measurable space $(\mathcal{C}, \mathcal{F})$.

Let X_t ($t \geq 0$) be a function with a parameter t on \mathcal{C} , determined by the equality $X_t(\xi) = \xi(t)$ (one-coordinate projection), and θ_t be the shift operator on \mathcal{C} , where $\theta_t(\xi) \in \mathcal{C}$ and $X_s(\theta_t(\xi)) = \xi(t + s)$ holds for any $s \geq 0$.

We will use also a class \mathcal{T} of measurable maps τ , where $0 \leq \tau(\xi) \leq \infty$ holds for any ξ (random times admitting infinite means). On the set $\{\xi : \tau(\xi) < \infty\}$, we determine a functional X_τ and an operator θ_τ with the random parameter, where

$$X_\tau(\xi) \equiv X_{\tau(\xi)}(\xi), \quad \theta_\tau(\xi) \equiv \theta_{\tau(\xi)}(\xi).$$

As a rule, a set $S \subset \mathcal{C}$ is given by some description for its element properties. For example, $S = \{\xi \in \mathcal{C} : \tau(\xi) < \infty\}$. Further instead of the full description of a set, we will write only description itself omitting argument ξ . In this example, $S = \{\tau < \infty\}$, and $E(f; \tau < \infty)$ for expectation of a function f on the set S , corresponding to a measure P .

Let us denote $f_2 \circ f_1 \equiv f_2(f_1)$ (superposition of two functions). Note that substitution of an argument ξ into this construction must be done from the right to the left.

Using these denotations on set

$$\{\tau_1 < \infty, \tau_2 \circ \theta_{\tau_1} < \infty\} \equiv \{\tau_1 < \infty\} \cap \{\tau_2 \circ \theta_{\tau_1} < \infty\}$$

one can write

$$X_{\tau_2} \circ \theta_{\tau_1} \equiv X_{\tau_2}(\theta_{\tau_1}) = X_{\tau_3}, \tag{15.1}$$

and also

$$\theta_{\tau_2} \circ \theta_{\tau_1} \equiv \theta_{\tau_2}(\theta_{\tau_1}) = \theta_{\tau_3}, \tag{15.2}$$

where $\tau_3 \equiv \tau_1 + \tau_2 \circ \theta_{\tau_1} < \infty$ and it is so called addition with shift. Further, we will denote

$$\tau_1 + \tau_2 \circ \theta_{\tau_1} \equiv \tau_1 \dot{+} \tau_2,$$

which is the map, determined on the set $\tau_1 < \infty$. Note that the operation $\dot{+}$ is associative but not commutative.

So we have

$$X_{\tau_1 \dot{+} \tau_2} = X_{\tau_2} \circ \theta_{\tau_1},$$

$$\theta_{\tau_1 \dot{+} \tau_2} = \theta_{\tau_2} \circ \theta_{\tau_1}.$$

From the last expression, it follows

$$\theta_{\tau_1 \dot{+} \dots \dot{+} \tau_n} = \theta_{\tau_n} \circ \dots \circ \theta_{\tau_1}. \tag{15.3}$$

15.1.2 Regeneration Times for a Family of Measures (P_x)

Let \mathcal{F}_t be standard sigma-algebra of events (subsets), “preceding” to time $t \geq 0$, and τ be standard Markov time relating to $(\mathcal{F}_t)_{t \geq 0}$ (which call to be natural filtration). Let \mathcal{F}_τ be standardly defined sigma-algebra of events presiding to the Markov time τ . It lets us to investigate regeneration times.

We will denote P_x a probability measure on the measurable space $(\mathcal{C}, \mathcal{F})$ with the property $P_x(X_0 = x) = 1$. Also, we assume (without discussing details), what for any measurable set S the function $P_x(S)$ as a function of x is measurable on \mathbb{R} .

Markov time τ_1 is called to be **regeneration time** for the family of measures (P_x) ($x \in \mathbb{R}$), if for any x , \mathcal{F}_{τ_1} -measurable function f_1 , and \mathcal{F} -measurable function f_2 the equality

$$E_x(f_1 \cdot (f_2 \circ \theta_{\tau_1}); \tau_1 < \infty, \tau_2 \circ \theta_{\tau_1} < \infty) = E_x(f_1 \cdot E_{X(\tau_1)}(f_2; \tau_2 < \infty); \tau_1 < \infty)$$

holds. Here, $E_x(g; S)$ is integral of a function g corresponding to measure P_x on set S .

Further, we call a family of measures (P_x) to be coordinated if it has even one nontrivial regeneration time.

For to write formulae more compact, we will sometimes write a subscript (parameter) of the function X_t as an argument (in parentheses); for example, $X_{\sigma_\Delta} \equiv X(\sigma_\Delta)$.

15.1.3 Semi-Markov Transition Generating Functions

Let us denote σ_Δ the time of the first exit of trajectory from interval Δ :

$$\sigma_\Delta(\xi) = \inf(t \geq 0 : \xi(t) \notin \Delta)$$

assuming $\sigma_\Delta \xi = 0$, if $\xi(0) \notin \Delta$, and also $\sigma_\Delta \xi = \infty$, if $\xi(t) \in \Delta$ for any $t \geq 0$. It is known (see [5], c. 194), what σ_Δ is a Markov time relative to the natural filtration. Evidently that from condition $\Delta_1 \subset \Delta_2$, it follows $\sigma_{\Delta_1} \leq \sigma_{\Delta_2}$.

The random process \mathcal{X} is determined by a coordinated family of probability measures (P_x) is called to be **continuous semi-Markov process**, if for any interval Δ the Markov time σ_Δ is regeneration time of this family.

The boundary a of an interval (a, b) is called to be **regular** for a continuous semi-Markov process if

$$P_x(\sigma_{(a,b)} < \infty, X(\sigma_{(a,b)}) = a) > 0$$

for any $x \in (a, b)$. The boundary a of the interval (a, b) is called to be **unattainable** for a continuous semi-Markov process if

$$P_x(\sigma_{(a,b)} < \infty, X(\sigma_{(a,b)}) = a) = 0$$

for any $x \in (a, b)$.

Regularity and unattainability of the right boundary of interval (a, b) are determined analogously.

From here, it follows the determination: both boundaries of the interval (a, b) are unattainable for a continuous semi-Markov process if

$$P_x(\sigma_{(a,b)} < \infty) = 0$$

for any $x \in (a, b)$.

Let $x \in (a, b)$ be a starting point of a continuous semi-Markov process \mathcal{X} , and boundaries of (a, b) are regular points for this process.

Let us consider functions

$$g_{(a,b)}(\lambda, x) \equiv E_x(\exp(-\lambda\sigma_{(a,b)}); \sigma_{(a,b)} < \infty, X_{\sigma_{(a,b)}} = a), \tag{15.4}$$

$$h_{(a,b)}(\lambda, x) \equiv E_x(\exp(-\lambda\sigma_{(a,b)}); \sigma_{(a,b)} < \infty, X_{\sigma_{(a,b)}} = b), \tag{15.5}$$

where $\lambda \geq 0$. We call these functions as semi-Markov transition generating functions of the process. They determine the semi-Markov process completely (to within distribution of its starting point).

Note that for a semi-Markov process usual Markov transition functions like $P_x(X_t \in S)$, where S is a measurable subset of \mathbb{R} are determined too. However,

these functions are useless because fixed (non-random) times are not regeneration times for continuous semi-Markov processes (unlike that of Markov processes).

From the definition of semi-Markov transition generating functions, it follows that the most simple continuous semi-Markov process is monotone one. For to construct a non-decreasing process, it is sufficient to consider a homogeneous process with independent positive increments \mathcal{Y} which has the Levy presentation (see [6], p. 49) without a linear component (for example, gamma process), and to construct \mathcal{X} with property $(\sigma_{(0,t)})_{t>0} \equiv (Y_t)_{t>0}$, where $(Y_t)_{t>0}$ is a family of one-coordinate maps of the process \mathcal{Y} relative to its coordinated family of probability measures. It is so-called inverse process with independent positive increments. Evidently that such a process has continuous non-decreasing trajectories. For this process, the functions defined above are such that

$$g_{(a,b)}(0, x) = 0$$

for any (a, b) , and $x \in (a, b)$. A continuous semi-Markov process with non-increasing trajectories is constructed analogously. For such a process

$$h_{(a,b)}(0, x) = 0$$

for any (a, b) , and $x \in (a, b)$.

Sample trajectories of these processes have exotic view like the famous Cantor curve. In common case, trajectories of such a process consist of random finite intervals of constancy positioned like a “ladder”.

15.2 Diffusion Semi-Markov Processes

It is interesting to consider a class of processes with the property: for any $x \in (a, b)$ boundaries of the interval (a, b) are regular, and both values $g_{(a,b)}(0, x)$ and $h_{(a,b)}(0, x)$ are positive.

Let $\Delta_r \equiv (x - r, x + r)$, $\Delta_r \subset (a, b)$, where $r > 0$, and $x \in (a, b)$ be a starting point of a continuous semi-Markov process \mathcal{X} , and both boundaries of the interval (a, b) be regular for this process.

Let us consider a decomposition by powers of $r \rightarrow 0$ for functions $g_{\Delta_r}(\lambda, x)$ and $h_{\Delta_r}(\lambda, x)$.

$$g_{\Delta_r}(\lambda, x) = C_1(\lambda, x) + A_1(\lambda, x)r + B_1(\lambda, x)r^2 + o(r^2),$$

$$h_{\Delta_r}(\lambda, x) = C_2(\lambda, x) + A_2(\lambda, x)r + B_2(\lambda, x)r^2 + o(r^2),$$

where A_i are continuously differentiable, B_i and C_i are continuous functions, and $C_i > 0$.

Let this asymptotic be homogeneous with respect to x on every finite interval. Due to properties of Laplace transformation in the book [1], pp. 141–149 it is proved that

$$A_1(\lambda, x) + A_1(\lambda, x) = 0, \quad A_i \text{ do not depend on } \lambda,$$

$$B_1(\lambda, x) = B_2(\lambda, x) < 0,$$

$$C_1(\lambda, x) = C_2(\lambda, x) = \frac{1}{2}.$$

Further, we will denote $A_1(x) \equiv -\frac{1}{2}A(x)$ and $B_1(\lambda, x) = B_2(\lambda, x) \equiv -\frac{1}{2}B(\lambda, x)$. From here if $r \rightarrow 0$:

$$g_{\Delta_r}(\lambda, x) = \frac{1}{2}(1 - A(\lambda, x)r - B(\lambda, x)r^2) + o(r^2), \tag{15.6}$$

$$h_{\Delta_r}(\lambda, x) = \frac{1}{2}(1 + A(\lambda, x)r - B(\lambda, x)r^2) + o(r^2). \tag{15.7}$$

Note that the process does not have an infinite interval of constancy. From here, it follows that $B(0, x) = 0$. Besides from Laplace transformation property to be decreasing with respect to $\lambda > 0$, it follows that $B'_\lambda(0, x) \geq 0$. These properties of the coefficient $B(\lambda, x)$ will be used below while evaluating the expectations of the first exits.

Further from the definition of the continuous semi-Markov process (for which σ_{Δ_r} is a regeneration time), it follows equations:

$$g_{\Delta}(\lambda, x) = g_{\Delta_r}(\lambda, x)g_{\Delta}(\lambda, x - r) + h_{\Delta_r}(\lambda, x)g_{\Delta}(\lambda, x + r), \tag{15.8}$$

$$g_{\Delta}(\lambda, x) = g_{\Delta_r}(\lambda, x)h_{\Delta}(\lambda, x - r) + h_{\Delta_r}(\lambda, x)h_{\Delta}(\lambda, x + r). \tag{15.9}$$

Substituting into these equations, the above asymptotical decompositions (15.6) and (15.7) we obtain both functions $g_{\Delta}(\lambda, x)$ and $h_{\Delta}(\lambda, x)$ satisfying on Δ the same differential equation

$$\frac{1}{2}u'' + A(x)u' - B(\lambda, x)u = 0. \tag{15.10}$$

But boundary conditions of these two solutions are different:

$$g_{\Delta}(\lambda, a) = h_{\Delta}(\lambda, b) = 1, \quad g_{\Delta}(\lambda, b) = h_{\Delta}(\lambda, a) = 0,$$

if $\Delta \equiv (a, b)$.

Continuous semi-Markov process is called to be diffusion one on the interval (a, b) , if its semi-Markov transition generating functions satisfy the differential Eq. (15.10) with above boundary conditions.

Note that with $\lambda = 0$, Eq. (15.10) turns to the equation

$$\frac{1}{2}u'' + A(x)u' - B(0, x)u = 0,$$

where solutions do not depend on λ . It is well known (see, for example, [4], p. 15) that the case $B(0, x) \equiv 0$ corresponds to Markov diffusion process without break. This property holds for the semi-Markov diffusion process without an infinite interval of constancy (it means without “forever”).

We are interested in the diffusion semi-Markov process with interval region (a_0, b_0) for which both boundaries are unattainable.

In work [3], conditions of unattainability in terms of coefficients $A(x)$ were investigated for a diffusion semi-Markov process corresponding to the Eq. (15.10) without the member $B(\lambda, x)u$. Necessary and sufficient conditions for boundaries unattainability were proved. In this work, we study the limit distribution of the diffusion semi-Markov process without stopping forever given on a finite interval with unattainable boundaries.

15.2.1 Alternating Renewal Process

For to find the limit distribution, we use the results of the renewal theory.

The renewal process is called to be a random piecewise constant process \mathcal{Z} with non-decreasing trajectories such that interval lengths between jumps are independent positive random values (independence is supposed to be relative to some probability measure).

Alternating renewal process \mathcal{Z} is called to be a renewal process for which all odd intervals between jumps have the same distribution function F_1 , and all even intervals between jumps have the same distribution function F_2 , where in common case $F_1 \neq F_2$ (terms odd and even correspond to the jump sequence of \mathcal{Z}). See, for example, [7].

Let $a_0 < a < b < b_0$, and $(\Delta_n)_{n=1}^\infty$ be a sequence of intervals, where $\Delta_n \subset (a_0, b_0)$. This sequence generates a set of non-decreasing sequences $(T_k^n)_{n=1}^\infty$, ($1 \leq k \leq n$) points on time axis where

$$T_1^1 = \sigma_{\Delta_1}, \quad T_k^{n+1} = T_k^n \dot{+} \sigma_{\Delta_{n+1}}.$$

From here:

$$T_k^n = \sigma_{\Delta_k} \dot{+} \sigma_{\Delta_{k+1}} \dot{+} \dots \dot{+} \sigma_{\Delta_n}.$$

Also we determine $T_k^{k-1} = 0$.

Let (t_n) be an arbitrary sequence of numbers ($t_n \in \mathbb{R}$). Let us consider the sequence of random values $(S_k^n)_{k=1}^n$, where

$$S_k^n = t_k \sigma_{\Delta_k} + S_{k+1}^n \circ \theta_{\sigma_{\Delta_k}}.$$

Also we determine $S_{n+1}^n = 0$. From here, we obtain

$$S_k^n = \sum_{m=k}^n t_m \sigma_{\Delta_m} \circ \theta_{T_k^{m-1}},$$

hence

$$S_1^n = t_1 \sigma_{\Delta_1} + \sum_{k=2}^n t_k \sigma_{\Delta_k} \circ \theta_{T_1^{k-1}}.$$

Let $\Delta_n = (a_0, b)$ if n odd, and $\Delta_n = (a, b_0)$ if n even.

Condition A. $P_x(\sigma_{(a_0, b_0)} < \infty) = 0$, and $P_x(\sigma_{\Delta} < \infty) = 1$ for any interval Δ , where $\Delta \subset (a_0, b_0)$ and $\Delta \neq (a_0, b_0)$, and $x \in \Delta$.

From this condition and definition of unattainability of boundaries, it follows that with P_a -probability one $X_{T_1^n} = b$ if n odd, and $X_{T_1^n} = a$ if n even.

Besides from condition A, it follows that $P_x(T_k^n < \infty) = 1$ and also $E_x(f; T_k^n < \infty) = E_x(f)$ for any $n \geq 1$ and $1 \leq k \leq n$.

Lemma 15.1 *Let a be the starting point of the process \mathcal{X} on the interval (a_0, b_0) with unattainable boundaries. If Condition A is fulfilled then for any $n \geq 2$ random values $T_1^1, T_1^2 - T_1^1, \dots, T_1^n - T_1^{n-1}$ are mutually independent random values with respect to the measure P_a .*

Proof Until the end of the proof to simplify notation, we will denote

$$\tau_k \equiv \sigma_{\Delta_k}; \quad \beta_k \equiv \theta_{\tau_k}; \quad \phi_k \equiv t_k \tau_k,$$

and also we will omit the symbol “ \circ ” between operators where it does not induce doubt.

In these denotations

$$S_k^n = \phi_k + S_{k+1}^n \beta_k,$$

where $T_1^1 = \tau_1, T_1^0 = 0$, and also θ_0 is the identify mapping (i.e. $\theta_0(\xi) = \xi$).

By the method of inverse mathematical induction we obtain

$$S_k^n = \sum_{m=k}^n \phi_m \theta_{T_k^{m-1}}. \tag{15.11}$$

From Condition A, it follows that

$$E_a(\exp(i S_1^n); T_1^{n-1} < \infty) = E_a(\exp(i S_1^n)),$$

where $i \equiv \sqrt{-1}$ (imaginary one).

Due to the semi-Markov property, we obtain

$$E_a(\exp(iS_1^n)) = E_a(\exp(i\phi_1))E_b(\exp(iS_2^n)).$$

Because of measurability of a constant function (for example $f \equiv 1$) relative to any sigma-algebra, we have

$$E_b(\exp(iS_2^n)) = E_a(\exp(iS_2^n\beta_1)).$$

Consequently

$$\begin{aligned} E_a(\exp(iS_1^n)) &= E_a(\exp(i\phi_1))E_a(\exp(iS_2^n\beta_1)) = \\ &= E_a(\exp(i\phi_1))E_a(\exp(i\phi_2\beta_1))E_a(\exp(i\phi_3\beta_2\beta_1)) \dots E_a(\exp(i\phi_n\beta_{n-1} \dots \beta_1)) = \\ &= E_a(\exp(i\phi_1))E_a(\exp(i\phi_2\theta_{T_1}))E_a(\exp(i\phi_3^n\theta_{T_1^2})) \dots E_a(\exp(i\phi_n\theta_{T_1^{n-1}})) = \\ &= E_a(\exp(it_1\tau_1))E_a(\exp(it_2\tau_2\theta_{T_1}))E_a(\exp(it_3\tau_3\theta_{T_1^2})) \dots E_a(\exp(it_n\tau_n\theta_{T_1^{n-1}})). \end{aligned}$$

On the other hand

$$S_1^n = t_1\tau_1 + t_2\tau_2\theta_{T_1} + t_3\tau_3\theta_{T_1^2} + \dots + t_n\tau_n\theta_{T_1^{n-1}}.$$

From here and from well-known theorem about multi-dimension characteristic functions (see, for example, [8], p. 304), it follows that random values

$$\tau_1, \tau_2\theta_{T_1}, \tau_3\theta_{T_1^2}, \dots, \tau_n\theta_{T_1^{n-1}}$$

are mutually independent random values respectively to measure P_a .

From definition of T_1^n and from the associative property of the operation $\dot{+}$, it follows that $T_1^n - T_1^{n-1} = \tau_n\theta_{T_1^{n-1}}$ where $n \geq 1$.

Lemma is proved.

From Lemma 15.1, it follows that a point process $\mathcal{Z} \equiv \mathcal{Z}(a, b)$, determined by the sequence of time points T_1^n , is an alternating process with distribution functions $F_1(t) \equiv P_a(\sigma_{(a_0, b)} < t)$ for odd intervals, and $F_2(t) \equiv P_b(\sigma_{(a, b_0)} < t)$ for even intervals.

Let us determine $N_t(a, b)$ an event that at time t the random value X_t belongs to some odd (“left”) interval of the process $\mathcal{Z}(a, b)$ (alternating process corresponding to the pare of points $\{a, b\}$). And let $M_t(a, b)$ be corresponding denotation for even (“right”) intervals.

Then corresponding to [7], p. 98

$$\lim_{t \rightarrow \infty} P_a(N_t(a, b)) = \frac{m_{(a_0, b)}(a)}{m_{(a_0, b)}(a) + l_{(a, b_0)}(b)},$$

$$\lim_{t \rightarrow \infty} P_b(M_t(a, b)) = \frac{l_{(a, b_0)}(b)}{m_{(a_0, b)}(a) + l_{(a, b_0)}(b)},$$

where

$$m_{(a, b)}(x) \equiv E_x(\sigma_{(a, b)}; \sigma_{(a, b)} < \infty, X(\sigma_{(a, b)}) = b),$$

$$l_{(a, b)}(x) \equiv E_x(\sigma_{(a, b)}; \sigma_{(a, b)} < \infty, X(\sigma_{(a, b)}) = a),$$

hence

$$m_{(a_0, b)}(x) \equiv E_x(\sigma_{(a_0, b)}),$$

$$l_{(a, b_0)}(x) \equiv E_x(\sigma_{(a, b_0)}).$$

Evidently that event $N_t(a, b)$ equals to event $\{X_t \in (a_0, b)\}$ which implies

$$\lim_{t \rightarrow \infty} P_a(X_t \in (a_0, b)) = \frac{m_{(a_0, b)}(a)}{m_{(a_0, b)}(a) + l_{(a, b_0)}(b)}.$$

The same fulfils for event $M_t(a, b)$, which equals to event $\{X_t \in (a, b_0)\}$. Hence

$$\lim_{t \rightarrow \infty} P_b(X_t \in (a, b_0)) = \frac{l_{(a, b_0)}(b)}{m_{(a_0, b)}(a) + l_{(a, b_0)}(b)}.$$

We see that the first limit represents the value of some distribution function K_a with parameter a at the point $b \in (a, b_0)$ relative to probability measure P_a . The second limit represents the value of some function p_b with parameter b at the point $a \in (a_0, b)$.

It is possible to extend the domain of definition for the distribution function K_a at the expense of choice another parameter nearer to the boundary a_0 . But in this case, the measure P_a has another meaning. It does not correspond to our aim to express the limit distribution function of the process \mathcal{X} as $t \rightarrow \infty$ in terms of the initial probability measure P_a where a is the starting point of the process.

To obtain the corresponding left part of definition domain for the distribution function K_a , we consider an auxiliary point process $\mathcal{Z}(c, d)$ with the starting point d , where $a_0 < c < d < b_0$. Corresponding sequence of time intervals begins from interval $(0, \sigma_{(c, b_0)})$ (the first odd interval). Event $M_t(c, d)$ that point t belongs to some odd interval of this sequence has probability $P_d(M_t(c, d)) = P_d(X_t \in (c, b_0))$, which tends to the limit

$$\lim_{t \rightarrow \infty} P_d(M_t(c, d)) = \frac{l_{(c, b_0)}(d)}{m_{(a_0, d)}(c) + l_{(c, b_0)}(d)}.$$

Now let $d=a$. Then $c < a$ and

$$\lim P_a(M_t(c, a)) = \frac{l_{(c, b_0)}(a)}{m_{(a_0, a)}(c) + l_{(c, b_0)}(a)}.$$

This is the meaning of the function $p_b \equiv 1 - K_a$ on interval (a_0, a) . Hence

$$K_a(c) = 1 - \frac{l_{(c, b_0)}(a)}{m_{(a_0, a)}(c) + l_{(c, b_0)}(a)} = \frac{m_{(a_0, a)}(c)}{m_{(a_0, a)}(c) + l_{(c, b_0)}(a)}.$$

So we prove the next theorem

Theorem 15.1 *The limit distribution function of the diffusion semi-Markov process $X(t)$ with probability measure P_a on a finite interval range (a_0, b_0) as $t \rightarrow \infty$ is the function*

$$K_a(x) = \begin{cases} \frac{m_{(a_0, x)}(a)}{m_{(a_0, x)}(a) + l_{(a, b_0)}(x)}, & x \in (a, b_0), \\ \frac{m_{(a_0, a)}(x)}{m_{(a_0, a)}(x) + l_{(x, b_0)}(a)}, & x \in (a_0, a). \end{cases}$$

References

1. Harlamov, B.P.: Continuous Semi-markov Processes. ISTE, Wiley, London (2008)
2. Harlamov, B.P.: Stochastic model of gas capillary chromatography. Commun. Stat.-Simul. Comput. **41**, 1023–1031 (2012)
3. Harlamov, B.P.: On unattainable boudary of a diffusion process range: semi-Markov approach. J. Math. Sci. **244**, 912–924 (2020)
4. Dynkin, E.B.: Markov Processes. Fyzmatgiz, Moscow (1963) (in Russian)
5. Gihman, I.I., Skorohod, A.V.: Theory of random processes, vol. 2. Nauka, Moscow (1973) (in Russian)
6. Ito, K., Makkin, G.: Diffusion Processes and Their Trajectories. Mir, Moscow (1968) (in Russian)
7. Cox, D., Smith, V.: Renewal Theory. Soviet radio, Moscow (1967) (in Russian)
8. Shiryayev, A.N.: Probability. Nauka, Moscow (1980) (in Russian)

Chapter 16

On Dynamic Fracture of One-Dimensional Elastic Chain



Nikita A. Kazarinov, Yuri V. Petrov, and Aleksey A. Gruzdkov

Abstract Dynamic fracture of a one-dimensional chain of identical linear oscillators (masses connected by springs) is regarded in the work. The considered system consists of arbitrary but finite number of links and the first mass is supposed to be fixed. Two types of load are discussed: free oscillations of the initially uniformly stretched chain and loading the chain with a short deformation pulse. Both problems are solved analytically for an arbitrary number of links. The obtained solutions are investigated, and a dynamic fracture effect related to the discreteness of the system is discussed: a deformation wave travelling through the chain is distorted and some links may be subjected to critical deformation. The obtained solutions for the chain are compared to the solutions of analogous problems stated for an elastic rod—a continuum counterpart of the considered discrete system. It is shown that the discussed fracture effect is not observed in a continuous system.

Keywords Dynamic fracture · Oscillator chain · Analytic solution

N. A. Kazarinov (✉)

Emperor Alexander I Saint Petersburg State Transport University, Moskovsky av., 9, St. Petersburg 190031, Russia

Institute of Problems in Mechanical Engineering RAS, V.O., Bolshoy pr., 61, St. Petersburg 199178, Russia

Y. V. Petrov

Institute for Problems in Mechanical Engineering RAS, V.O., Bolshoy pr., 61, St. Petersburg 199178, Russia

A. A. Gruzdkov

Saint Petersburg State University of Technology, Moskovsky av., 26, St. Petersburg 190013, Russia

e-mail: gruzdkov@mail.ru

16.1 Introduction

Mass-spring models are a common tool in mechanics due to their simplicity and ability to address rather complicated phenomena. For example, in work [1], the oscillator model is coupled with finite element method to address the acoustic emission studies of rocks.

Oscillator chains were considered in works by L. Slepyan and his co-workers [2]; however, this approach considers infinite oscillator chains. Moreover, the chain models are successfully used to study peculiar heat conduction effects in crystals. Two-dimensional models have been also used to address the effects encountered in dynamic crack propagation problems. For example, in work [3], the crack velocity oscillations are explained using a lattice model, while in [4], a bi-material model is studied in order to investigate various regimes of the interface crack propagation. The chain models have been also used to address martensitic phase transformations as seen from work [5].

Simple mass-spring models have been effectively applied to study rate sensitivity of materials and inverse rate sensitivity in particular [6].

In this paper, dynamic fracture effects related to discreteness of the oscillator chain system are discussed. First, an analytic solution for the system of differential equations governing the chain movement is obtained. This solution is then compared to the solution of a one-dimensional wave equation, which describes wave propagation in an elastic rod—a continuous analogue of the oscillator chain.

16.2 Static Preload with Abrupt Link Failure

16.2.1 Analytic Solution of the Chain Problem

Consider a uniformly deformed chain consisting of $N + 1$ equal linear oscillators with both ends fixed.

If the masses are taken equal m , stiffnesses of the springs- c , the following system of differential equations coupled with initial conditions describes the chain motion:

$$\begin{aligned} \mathbf{M} \ddot{\mathbf{Q}} + \mathbf{C} \mathbf{Q} &= \mathbf{0} \\ q_i(t=0) - q_{i-1}(t=0) &= l_c \\ \dot{q}_i(t=0) &= 0 \\ q_0(t) &= 0 \end{aligned} \tag{16.1}$$

where $\mathbf{Q} = (q_1, q_2, \dots, q_N)$ is a vector containing relative mass displacements, \mathbf{M} is the mass matrix and \mathbf{C} is a stiffness matrix and l_c is critical link deformation. Moreover, it is supposed that link with number $N + 1$ (dashed link in Fig. 16.1) does not bear this load and breaks abruptly at $t = 0$ initiating a release wave. The

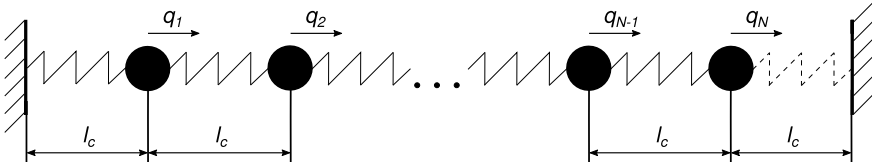


Fig. 16.1 Uniformly deformed chain with an abruptly failing link

following fracture conditions are used: $|q_i - q_{i-1}| > l_c, \quad i = 1 \dots N$. Matrices \mathbf{M} and \mathbf{C} read as (\mathbf{E} is identity matrix):

$$\mathbf{M} = m\mathbf{E}; \mathbf{C} = c \begin{pmatrix} 2 & -1 & \dots & 0 & 0 \\ -1 & 2 & -1 & \dots & 0 \\ & \ddots & \ddots & \ddots & \\ 0 & & -1 & 2 & -1 \\ 0 & 0 & \dots & -1 & 1 \end{pmatrix} = c\mathbf{K}'. \quad (16.2)$$

One of the chain ends remains fixed, and therefore $q_0(t) = 0 \forall t$. The substitution $t' = t\sqrt{c/m}$ yields the dimensionless problem with the mass matrix equaling identity matrix and the stiffness matrix $\mathbf{K}' = \frac{1}{c}\mathbf{C}$ from Eq. 16.2. Additionally, normalized deformations of the chain links are introduced according to equation $u_i = q_i - q_{i-1}/l_c, \quad i = 1 \dots N$ resulting in a modified stiffness matrix $\mathbf{K} = \mathbf{S}\mathbf{K}'\mathbf{S}^{-1}$ with \mathbf{S} being a matrix of coordinates transformation. The fracture condition has the form: $|u_i(t)| > 1, \quad i = 1 \dots N$. This way, the following problem is solved if vector $\mathbf{U} = (u_1, u_2, \dots, u_N)$ is introduced:

$$\begin{aligned} \ddot{\mathbf{U}} + \mathbf{K}\mathbf{U} &= \mathbf{0} \\ u_i(t=0) &= 1 \\ \dot{u}_i(t=0) &= 0 \\ u_0(t) &= 0 \\ |u_i(t)| &> 1. \end{aligned} \quad (16.3)$$

Solution of the system Eq. 16.3 is sought in form

$$\mathbf{U}(t) = \sum_{j=1}^n c_j \mathbf{R}_j \cos(\omega_j t) \quad (16.4)$$

where ω_j are the system eigenfrequencies, $\mathbf{R}_j = (r_1^{(j)}, r_2^{(j)}, \dots, r_N^{(j)})^T$ are corresponding eigenvectors and c_j is the set constants evaluated using the initial conditions.

The eigenfrequencies are calculated from eigenvalues λ_j of the system stiffness matrix \mathbf{K} : $\omega_j = \sqrt{\lambda_j}$. The eigenvalues of \mathbf{K} are calculated from equation

$$Det(\mathbf{K} - \lambda\mathbf{E}) = Det(\mathbf{K}' - \lambda\mathbf{E}) = 0. \tag{16.5}$$

If we put $\alpha = 2 - \lambda$, (5) can be rewritten explicitly in the following way:

$$\begin{vmatrix} \alpha & -1 & \dots & 0 & 0 \\ -1 & \alpha & -1 & \dots & 0 \\ & & \ddots & \ddots & \ddots \\ 0 & & & -1 & \alpha & -1 \\ 0 & 0 & \dots & -1 & \alpha & -1 \end{vmatrix} = D_N = 0. \tag{16.6}$$

In Eq. 16.6, D_N is determinant of order N . One may note that a recursive equation can be composed for a determinant of order k :

$$D_k = \alpha D_{k-1} - D_{k-2} \tag{16.7}$$

and the following relations hold: $D_0 = 1$, $D_1 = \alpha - 1$. Equation 16.7 is reduced to a quadratic equation $p^2 - \alpha p + 1 = 0$ with roots $p_{1,2}$ using substitution $D_k = p^k$. This way the following expression is obtained:

$$D_N = b_1 p_1^N + b_2 p_2^N = 0 \tag{16.8}$$

where b_1 and b_2 are constants to be evaluated using conditions $D_0 = 1$, $D_1 = \alpha - 1$ and substitution $\alpha = 2\cos(\theta)$. Equation 16.8 yields the following formula for eigenvalues of the stiffness matrix:

$$\lambda_k = 2 - 2\cos\left(\frac{\pi(2k - 1)}{2N + 1}\right), \quad k = 1 \dots N \tag{16.9}$$

and thus, we obtain the formula for eigenfrequencies of the studied system:

$$\omega_k = 2\sin\left(\frac{\pi(2k - 1)}{4N + 2}\right), \quad k = 1 \dots N. \tag{16.10}$$

For components of the eigenvectors of matrix \mathbf{K} the following equation holds:

$$r_i^j = P_{i-1}(x_j) - P_{i-2}(x_j) \tag{16.11}$$

where $x_j = (2 - \lambda_j) / 2$ and $P_k(x)$ is a k -order Chebyshev polynomial of second kind, which can be expressed in the following way:

$$P_k(y) = \frac{\sin((k + 1)\arccos(y))}{\sin(\arccos(y))}. \tag{16.12}$$

Thus, the following expression can be obtained for the components of eigenvectors \mathbf{R}_j :

$$r_i^j = \frac{\cos\left(\frac{\pi(2i-1)(2j-1)}{4N+2}\right)}{\cos\left(\frac{\pi(2j-1)}{4N+2}\right)}, \quad i = 1 \dots N. \quad (16.13)$$

In order to evaluate constants c_j to satisfy the initial conditions the following system should be solved accounting for Eq. 16.11:

$$\begin{aligned} & \begin{pmatrix} P_0(x_1) & P_0(x_2) & \dots & P_0(x_N) \\ P_1(x_1) - P_0(x_1) & P_1(x_2) - P_0(x_2) & \dots & P_1(x_N) - P_0(x_N) \\ \vdots & \vdots & \vdots & \vdots \\ P_{N-1}(x_1) - P_{N-2}(x_1) & P_{N-1}(x_2) - P_{N-2}(x_2) & \dots & P_{N-1}(x_N) - P_{N-2}(x_N) \end{pmatrix} \begin{pmatrix} c_1 \\ c_2 \\ \vdots \\ c_N \end{pmatrix} = \\ & = \begin{pmatrix} 1 \\ 1 \\ \vdots \\ 1 \end{pmatrix} = \begin{pmatrix} P_0(1) \\ P_1(1) - P_0(1) \\ \vdots \\ P_{N-1}(1) - P_{N-2}(1) \end{pmatrix}. \end{aligned} \quad (16.14)$$

If the second-order Chebyshev polynomials are explicitly written and elementary matrix operations are performed, the system Eq. 16.14 is reduced to the system with a Vandermonde matrix:

$$\begin{pmatrix} 1 & 1 & \dots & 1 \\ x_1 & x_2 & \dots & x_N \\ \vdots & \vdots & \vdots & \vdots \\ x_1^{N-1} & x_2^{N-1} & \dots & x_N^{N-1} \end{pmatrix} \begin{pmatrix} c_1 \\ c_2 \\ \vdots \\ c_N \end{pmatrix} = \begin{pmatrix} 1 \\ 1 \\ \vdots \\ 1 \end{pmatrix}. \quad (16.15)$$

Constants c_j can be evaluated from Eq. 16.15 using Cramer rule and formula for the determinant of the Vandemonde matrix:

$$c_j = \frac{(1-x_1) \dots (1-x_{j-1})(1-x_{j+1}) \dots (1-x_N)}{(x_j-x_1) \dots (x_j-x_{j-1})(x_j-x_{j+1}) \dots (x_j-x_N)}. \quad (16.16)$$

Let's put $M_N(x) = 2^N \prod_{k=1}^N (x-x_k)$. Then Eq. 16.16 can be rewritten:

$$c_j = \frac{M_N(1)}{M_N'(x_j)(1-x_j)}. \quad (16.17)$$

Considering the fact that $M_N(x)$ has zeros at points x_j and multiplier 2^N , one may conclude that $M_N(x) = P_N(x) - P_{N-1}(x)$ and thus one can deduce formula for constants c_j taking into account that $M_N(1) = 1$:

$$c_j = \frac{(-1)^{j+1} 2 \sin\left(\frac{\pi(2j-1)}{2n+1}\right) \cos\left(\frac{\pi(2j-1)}{4n+2}\right)}{(2n+1) \left(1 - \cos\left(\frac{\pi(2j-1)}{2n+1}\right)\right)}. \tag{16.18}$$

Now general solution of the problem Eq. 16.3 is the following:

$$u_i(t) = \frac{2}{(2N+1)} \sum_{j=1}^n \frac{(-1)^{j+1} \sin(\beta_j) \cos\left(\frac{\beta_j}{2}(2i-1)\right)}{(1 - \cos(\beta_j))} \cos(\omega_j t) \tag{16.19}$$

$$\beta_j = \frac{\pi(2j-1)}{2N+1}.$$

In Eq. 16.19, $u_i(t)$ stands for deformation of the chain link with number i .

16.2.2 Forced Chain Oscillations, Inhomogeneous System of Equations

The following problem is considered: a chain of oscillators with N links and a fixed end is loaded with an arbitrary force $f(t)$ applied to the chain free end (Fig. 16.2).

The system of dimensionless equations describing deformation of the chain links is the following:

$$\begin{aligned} \ddot{\mathbf{U}} + \mathbf{K}\mathbf{U} &= \mathbf{F}(t) = (0, 0, \dots, f(t))^T \\ u_i(t=0) &= 0 \\ \dot{u}_i(t=0) &= 0 \\ u_0(t) &= 0. \end{aligned} \tag{16.20}$$

In Eq. 16.20, $\mathbf{U} = (u_1, u_2, \dots, u_N)$ and $i = 1 \dots N$. In order to solve system Eq. 16.20, an auxiliary homogeneous system of differential equations with modified initial conditions is introduced and solved following Duhamel’s method (system inhomogeneity is transferred to the initial conditions [7]):

$$\begin{aligned} \ddot{\mathbf{W}} + \mathbf{K}\mathbf{W} &= \mathbf{0} \\ w_i(t=0) &= 0 \\ \dot{w}_i(t=0) &= 0 \\ w_N(t=0) &= f(p) \\ w_0(t) &= 0. \end{aligned} \tag{16.21}$$

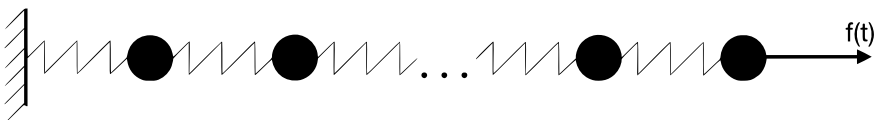


Fig. 16.2 Chain loaded with an arbitrary force $f(t)$

In Eq. 16.21, $\mathbf{W} = (w_1, w_2, \dots, w_N)$ and $i = 1 \dots N$ and p is an arbitrary real number. Systems, Eqs. 16.20 and 16.21, share stiffness matrix \mathbf{K} with the system solved in the previous section. Solution of Eq. 16.20 is further obtained using solution of Eq. 16.21.

Solution steps for Eq. 16.21 are similar to those for Eq. 16.3. The general solution is sought in form

$$\mathbf{W}(t) = \sum_{j=1}^N a_j \mathbf{R}_j \sin(\omega_j t) \quad (16.22)$$

where eigenfrequencies and eigenvectors ω_j and \mathbf{R}_j are evaluated according to formulas Eqs. 16.10 and 16.13. In order to obtain the solution, constants a_j should be calculated satisfying the initial conditions. Let's put $b_j = a_j \omega_j$. Then the system for b_j reads as:

$$\begin{pmatrix} P_0(x_1) & P_0(x_2) & \cdots & P_0(x_N) \\ P_1(x_1) - P_0(x_1) & P_1(x_2) - P_0(x_2) & \cdots & P_1(x_N) - P_0(x_N) \\ \vdots & \vdots & \vdots & \vdots \\ P_{N-1}(x_1) - P_{N-2}(x_1) & P_{N-1}(x_2) - P_{N-2}(x_2) & \cdots & P_{N-1}(x_N) - P_{N-2}(x_N) \end{pmatrix} \cdot \begin{pmatrix} b_1 \\ b_2 \\ \vdots \\ b_N \end{pmatrix} = \begin{pmatrix} 0 \\ 0 \\ \vdots \\ f(p) \end{pmatrix} \quad (16.23)$$

In Eq. 16.23 $x_j = (2 - \lambda_j) / 2$ and $P_k(x)$ is a k -order Chebyshev polynomial of second kind. As in the previous case, Eq. 16.23 is reduced to a system with a Vandermonde matrix:

$$\begin{pmatrix} 1 & 1 & \cdots & 1 \\ x_1 & x_2 & \cdots & x_N \\ \vdots & \vdots & \vdots & \vdots \\ x_1^{N-1} & x_2^{N-1} & \cdots & x_N^{N-1} \end{pmatrix} \begin{pmatrix} b_1 \\ b_2 \\ \vdots \\ b_N \end{pmatrix} = \begin{pmatrix} 0 \\ 0 \\ \vdots \\ f(p) / 2^{N-1} \end{pmatrix} \quad (16.24)$$

If the Cramer's rule is applied and function $M_N(x) = 2^N \prod_{k=1}^N (x - x_k)$ is introduced, the following formula holds:

$$b_j = \frac{2f(t)}{M'_N(x_j)}. \quad (16.25)$$

Thus, if $M_N(x)$ is expressed using $P_k(x)$, final formula for the constants a_j can be written:

$$b_j = \frac{(-1)^{j+1} 4 \cos^2 \left(\frac{\pi(2j-1)}{4N+2} \right) f(t)}{(2N+1)}. \quad (16.26)$$

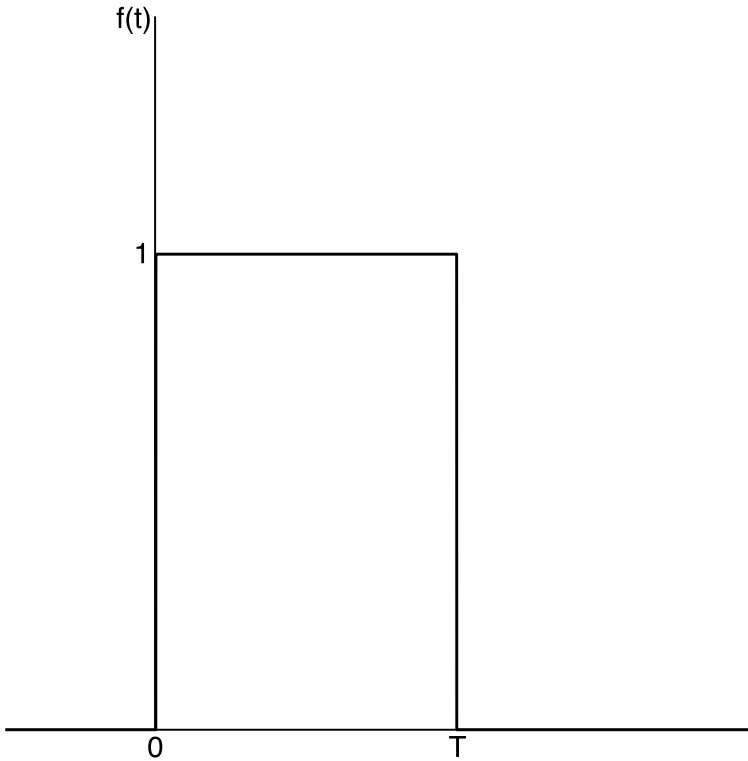


Fig. 16.3 Loading function: pulse with duration T

Since the auxiliary system is explicitly solved, solution to the initial system Eq. 16.20 can be written:

$$U(t) = \sum_{j=1}^N a_j R_j \int_0^t \sin(\omega_j(t-s)) f(s) ds. \quad (16.27)$$

The considered loading function $f(t)$ is shown in Fig. 16.3.

Then Eq. 16.27 is transformed into the following expression:

$$U(t) = \begin{cases} \sum_{j=1}^N \frac{a_j R_j}{\omega_j} (1 - \cos(\omega_j t)), & t < T \\ \sum_{j=1}^N \frac{a_j R_j}{\omega_j} (\cos(\omega_j(t-T)) - \cos(\omega_j t)), & t \geq T \end{cases}. \quad (16.28)$$

Thus, Eq. 16.28 is a formula for the deformation of links of the chain subjected to pulse load.

16.3 Results. Comparison with Solutions for an Elastic Rod

In this section formulas, Eqs. 16.19 and 16.28 will be used to evaluate deformations in particular chain links. Moreover, these solutions will be compared to deformations of an elastic rod, subjected to similar loads. The rod can be regarded as a continuous counterpart of the chain.

A prestressed elastic rod is a complete analogue of the chain problem considered in 2.1. A release wave propagation in the homogeneously deformed elastic rod of length l with model material parameters (elastic modulus and density equal 1) is considered. If displacements of the rod points are described by function $U(x, t)$ and deformations by $\varepsilon(x, t)$ and sealing of the rod end $x = 0$ is supposed, the following initial boundary value problem can be stated:

$$\begin{aligned} \frac{\partial^2 U(x,t)}{\partial x^2} &= \frac{\partial^2 U(x,t)}{\partial t^2} \\ U(x, 0) &= x \Rightarrow \varepsilon(x, t) = 1 \\ \frac{\partial U(x,t)}{\partial t} \Big|_{t=0} &= 0 \\ U(0, t) &= 0 \\ \frac{\partial U(x,t)}{\partial x} \Big|_{x=l} &= H(-t) \end{aligned} \quad . \quad (16.29)$$

Additionally, the following fracture condition is set: fracture takes place if $|\varepsilon(x, t)| > 1$. Solution of Eq. 16.29 can be obtained as a combination of travelling and reflected waves. In Fig. 16.4, deformation of the first link and deformation of the rod sealing are shown. It is clear that deformations of the elastic rod never exceed the initial value 1 and thus fracture never takes place, while deformation of the first link of the chain exceeds critical value by about 50% leading to the system failure. This way, equal loading conditions result in fracture for the discrete system, while its continuous analogue remains intact.

Now the rod is supposed to be loaded by a deformation pulse. Model material is used and the rod is supposed to be sealed from one end. Thus, the initial boundary value problem reads as:

$$\begin{aligned} \frac{\partial^2 \varepsilon(x,t)}{\partial x^2} &= \frac{\partial^2 \varepsilon(x,t)}{\partial t^2} \\ \varepsilon(x, 0) &= 0 \\ \frac{\partial \varepsilon(x,t)}{\partial t} \Big|_{t=0} &= 0 \\ U(0, t) &= 0 \\ \varepsilon(l, t) &= f(t) = H(t) - H(t-T) \end{aligned} \quad . \quad (16.30)$$

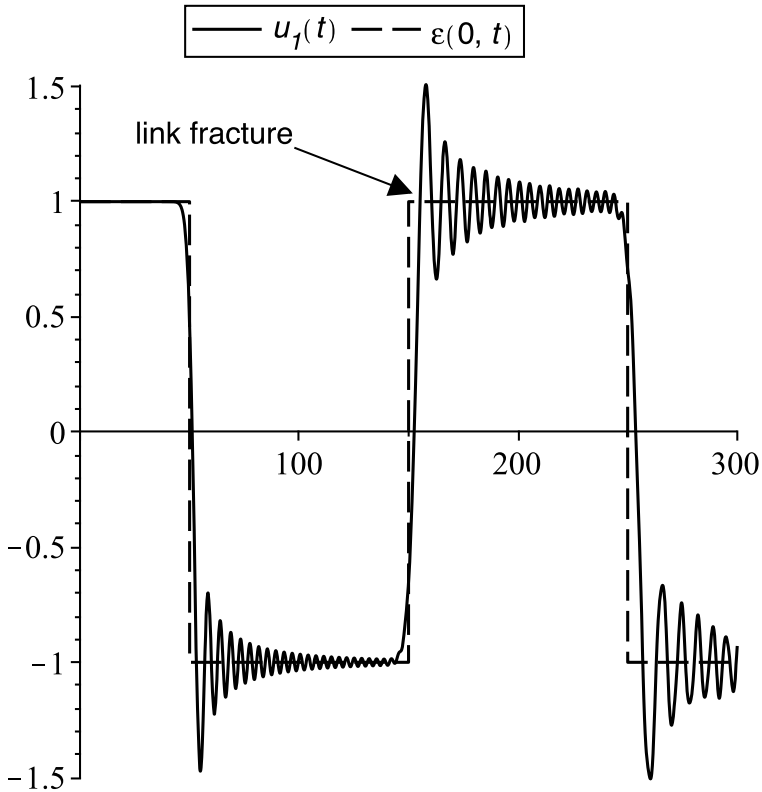


Fig. 16.4 Deformation of the first chain link (solid line) and deformation of rod in a sealed point (dashed line). Arrow indicates the link fracture. Results for 50 links and a rod with length $l = 50$ are shown

If d'Alembert method is applied, one can find that an undistorted deformation pulse $f(t)$ travels through the rod and no fracture occurs, since $|\varepsilon(x, t)| > 1$ fracture condition is considered. On the contrary, solution for the chain shows distortion of the pulse, which leads to failure of the link with number N . This phenomenon is shown in Fig. 16.5 for a chain consisting of 100 links, pulse duration $T = 10$ and rod with length $l = 100$.

This way pulse load applied to a discrete system may lead to failure, while the continuous system remains intact for the identical load.

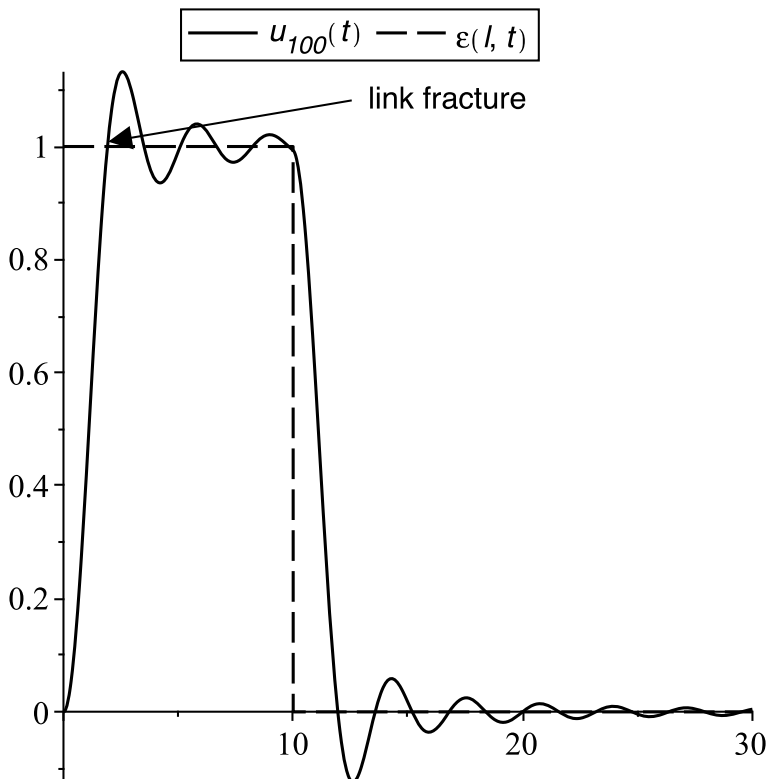


Fig. 16.5 Deformation of the chain link with number N (solid line) and rod deformation at point $x = l$ (dashed line). Link fracture is indicated by an arrow. In this case number of links $N = 100$ and rod length $l = 100$

16.4 Conclusion

Dynamic fracture of linear oscillator chains is considered in the work. In particular, the effect related to discreteness of the system is studied. Two load cases are considered: abrupt release of a prestressed chain and pulse loading of an undeformed chain. For both cases, analytical solutions for the chain link deformations are obtained. These solutions are compared to the results for a continuous analogue of chain—elastic rod. It is demonstrated that the wave travelling through a chain (resulting either from abrupt release or from deformation pulse applied) is distorted comparing to an elastic rod, which can result in fracture. On the contrary, such effect is not possible for the continuous system.

This effect can be accounted for when structures with explicit discreteness and periodicity are designed and studied, e.g. construction facilities in civil engineering. A railway train could serve as another example of possible application of the studied

discrete problem. A railway train moving with a constant velocity can be modelled by a statically uniformly deformed chain of oscillators. Thus, a sudden break of a damaged or worn coupling device can potentially lead to the failure of normally functioning coupling devices.

Acknowledgements The work was supported by Russian Foundation for Basic Research (grants 19-31-60037 and 20-01-00291).

References

1. Ngo, D.T., Pellet, F.L.: On modeling the dynamic response induced by fracturing brittle materials. *Eng. Fract. Mech.* **224**, 106802 (2020)
2. Slepyan, L.I., Troyankina, L.V.: Fracture wave in a chain structure. *J. Appl. Mech. Techn. Phys.* **25**, 921–927 (1984)
3. Marder, M., Gross, S.: Origin of crack tip instabilities. *J. Mech. Phys. Solids* **43**(1), 1–48 (1995)
4. Gorbushin, N., Mishuris, G.: Dynamic fracture of a dissimilar chain. *Phil. Trans. R. Soc. A.* **377**, 20190103 (2019)
5. Truskinovsky, L., Vainchtein, A.: Kinetics of martensitic phase transitions: lattice model. *SIAM J. Appl. Math.* **66**(2), 533–553 (2005)
6. McNelley, T.R., Gates, S.F.: Inverse strain-rate sensitivity and the Portevin - Le Chatelier effect. *Acta Metallurgica.* **26**, 1605–1614 (1978)
7. Epstein, M.: *Partial Differential Equations: Mathematical Techniques for Engineers (Mathematical Engineering)*, 1st edn. Springer, Berlin (2017)

Chapter 17

Vibrational Mechanics of Rotating Mechanisms: Modification of Low-Frequency Behaviour by High-Frequency Excitations



Eugen B. Kremer

Abstract In the frame of the concept of vibrational mechanics, a rotating multi-mass mechanism with high-frequency periodic or stochastic excitation is considered, and the general equation for the averaged motion of such mechanisms is obtained (the equation of vibrational mechanics). The equation of vibrational mechanics has the same structure as the original Lagrange equation without excitation, but has a modified inertial coefficient and dissipative function, depending on the intensity of the excitation. As a result of this difference, the equilibrium position and eigenfrequency depend on the intensity of high-frequency excitation. As an example of modification of the global behaviour of a rotation mechanism, a centrifugal analogue of the Stephenson–Kapitsa pendulum is considered. The theory is applied also to the analysis of the centrifugal pendulum absorber with a complex kinematics. The sensitivity of the pendulum order deviation from the nominal order due to high-frequency excitation is studied. It is shown that the own rotation angle of the pendulum as a function of its position has a significant impact on this sensitivity.

Keywords Vibrational mechanics · Rotating mechanisms · Stochastic excitation · Stephenson–Kapitsa pendulum · Centrifugal pendulum absorber

17.1 Introduction

In this paper, the approach of vibrational mechanics is applied to rotating mechanisms whose low-frequency behaviour is affected by high-frequency periodic or stochastic oscillations in the angular velocity of the carrier disc. These oscillations can be caused by impacts in gearboxes, processed material, higher harmonics of engine torque, etc. The effects connected with these excitations are especially important for technical applications, where the frequency characteristics of the mechanism play a key role in

E. B. Kremer (✉)

Institute for Problems in Mechanical Engineering RAS, V.O., Bolshoy pr., 61,
St. Petersburg 199178, Russia
e-mail: keb@ipme.ru; ekr8576211@aol.com

© The Author(s), under exclusive license to Springer Nature Switzerland AG 2022
V. A. Polyanskiy and A. K. Belyaev (eds.), *Mechanics and Control of Solids and Structures*, Advanced Structured Materials 164,
https://doi.org/10.1007/978-3-030-93076-9_17

315

its function. Among these mechanisms are torsional vibration dampers, centrifugal regulators and absorbers, inertial vibrators, etc.

In this paper, the equations of vibrational mechanics for such mechanisms are obtained in a general form. The effectiveness of these equations is demonstrated by examples of their application to some rotating pendulum mechanisms.

17.1.1 Motivation

For many processes and systems with periodic or stochastic excitations, the most interesting is the averaged motion, and the details of the high-frequency oscillations caused by these excitations are not important themselves. However, these high-frequency oscillations cannot simply be neglected, although they have a zero mean (Fig. 17.1).

The effect of these oscillations on the averaged motion is often significant and can lead to qualitative differences from the situation without excitations.

Well-known practical important examples of such systems are: vibro-transportation of materials, in which a periodic zero mean action causes one-directional motion of particles [1, 2]; and the synchronisation of rotors, the effect of high-frequency interaction of rotors through the supporting body on their slow dynamics, which manifests itself in synchronising the averaged phases [3].

The effect of high-frequency oscillations on the low-frequency behaviour takes place also for the case of stochastic excitation [4–11]. A known example is so-called stochastic resonance—a resonance-like response of a system to the level of a random

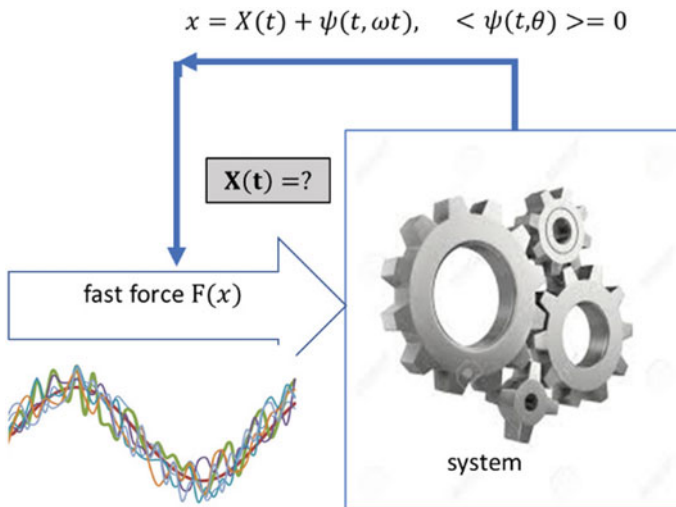


Fig. 17.1 Schematic representation of the averaging problem

excitation. This effect was originally discovered in climatology [6] and later applied in many fields of natural sciences and engineering [7].

How should such processes and systems be analysed?

17.1.2 Direct Simulation is Not Always the Best Way

One of the possibilities is direct numerical simulations of the complete motion and averaging of the results. In the case of stochastic excitation, it can be done on the basis of the Monte Carlo method, which consists of many single simulations with time averaging and subsequent averaging of the single results over the ensemble of realisations. However, this is not very efficient for many practical applications, because most of the information obtained in these simulations is just the details of high-frequency oscillations which are no longer needed after the averaging. This approach can be especially time-consuming if a parameter study or bifurcation analysis for the averaged solution is needed, not simply a single calculation (Figs. 17.2 and 17.3).

17.1.3 Concept of Vibrational Mechanics

Another, in most cases, much more effective approach for such systems is offered by the concept of vibration mechanics. This concept was proposed by Professor I. I. Blekhman [12–14] and developed by his collaborators in the Joint Laboratory

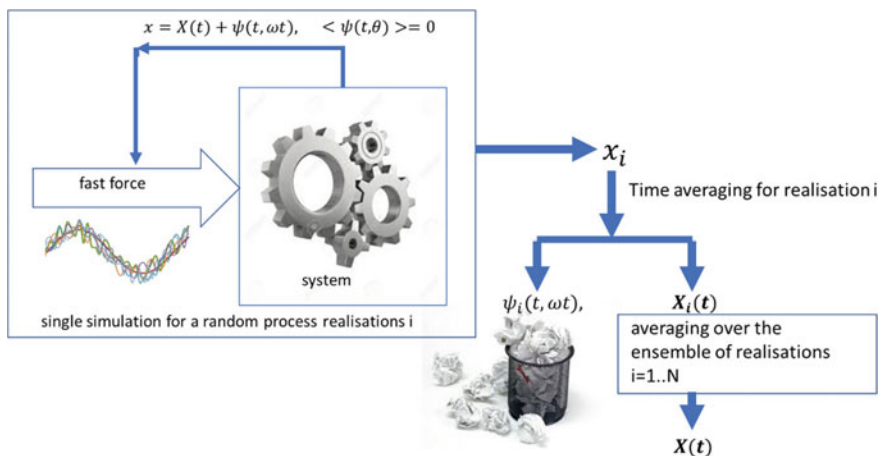


Fig. 17.2 Schematic representation of the solution with direct numerical simulations

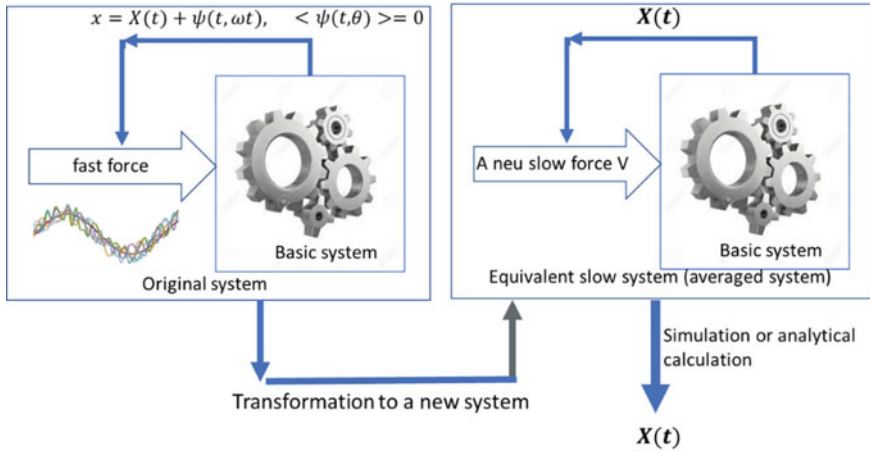


Fig. 17.3 Schematic representation of the approach of vibrational mechanics

of Vibrational Mechanics of IPME RAS and REC Mekhanobr-tekhnika, as well as by his followers in many institutions and countries [15–21].

The approach of vibrational mechanics not only has theoretical value but also provides engineers with very efficient calculation techniques. The application of this approach has allowed the development of many essential new solutions in vibration technology and the improvement of a number of processes and machines [22, 23].

In this approach of vibrational mechanics, an equivalent slow system instead of the original system with fast motion is considered. The motion of this slow system is equal to the average motion of the original system. It is provided by additional slow forces instead of high-frequency interactions in the original system.

These forces are called vibrational forces [12] and are calculated with the method of direct separation of motions originally developed by Professor I. I. Blekhman [14]. In the further development of vibrational mechanics in relation to modulated and stochastic systems, a modification of this method by using small parameters and some elements of the multiple scales technique was proposed [18–21]. In relation to stochastic system. In earlier works, stochastic resonance was considered as a purely stochastic phenomenon and only for the systems with two-well potential. Further development made it clear that this effect is relevant for a wider class of dynamical systems and that it can be effectively considered within the frame of vibrational mechanics.

17.2 Rotating Mechanism with Fast Excitations

A rotating mechanism with one degree of freedom ψ is considered, consisting of n kinematically coupled solids performing a flat motion relative to the rotating disc.

17.2.1 Kinematics of the Mechanism

The kinematics of the mechanism is illustrated in Fig. 17.4. Here, one of the bodies of the mechanism with number j is depicted in two positions: the initial ($\psi = 0$) and the current with the generalised coordinate ψ .

The disc rotates with an angular velocity Ω , which oscillates periodically or stochastically with an average value Ω_0 . The frequencies of these oscillations are assumed to be significantly higher than the rotation frequency. Thus, we use for the angular velocity Ω the following representation:

$$\Omega = \Omega_0(1 + \xi(t)). \tag{17.1}$$

In the case of periodic excitation of the disc, the function $\xi(t)$ can be described as

$$\xi(t) = \lambda \sin(q\Omega_0 t), \tag{17.2}$$

which corresponds to a kinematic excitation with amplitude $\Omega_0\lambda$ and frequency $q\Omega_0$. In the case of stochastic excitation, the function $\xi(t)$ represents a stochastic process described by its canonical expansion [5, 6]:

$$\xi = \int_{\omega_0}^{\infty} (\xi_s(\omega) \sin\omega t + \xi_c(\omega) \cos\omega t) d\omega. \tag{17.3}$$

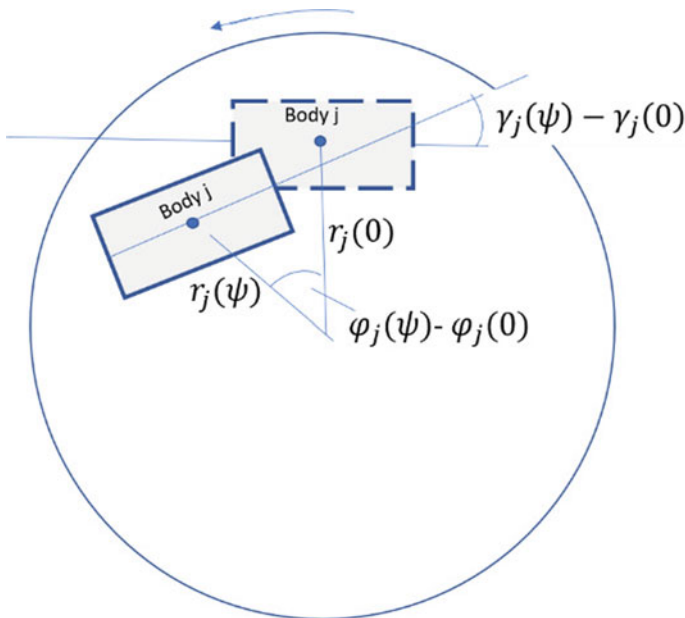


Fig. 17.4 The kinematics of the rotating mechanism

Here, $\xi_s(\omega)$ and $\xi_c(\omega)$ are mutually independent and stochastically orthogonal random functions. They have the following properties:

$$\begin{aligned} E(\xi_s(\omega)) &= E(\xi_c(\omega)) = 0 & E(\xi_s(\omega)\xi_c(\omega)) &= 0 \\ E(\xi_s(\omega_i)\xi_s(\omega_j)) &= E(\xi_c(\omega_i)\xi_c(\omega_j)) = S(\omega_i)\delta(\omega_i-\omega_j). \end{aligned} \quad (17.4)$$

Here, E denotes the mathematical expectation, $\delta(\omega)$ is the δ -function, and $S(\omega)$ is the spectral density of the process. It is assumed that the spectrum of the random process ξ does not contain frequencies lower than $\omega_0 = \Omega_0 q$ with $q \gg 1$. Therefore, any realisation of this random process can be considered subsequently as a function of only a fast time $\theta = \omega_0 t$.

17.2.2 Lagrange Equation

The kinetic energy of the system is calculated as

$$T = \frac{1}{2}A\dot{\psi}^2 + B\dot{\psi}\Omega + \frac{1}{2}C\Omega^2, \quad (17.5)$$

where the point means differentiation by dimensionless time $\tau = \Omega_0 t$, and the values A , B , and C are functions of the generalised coordinate ψ , which are calculated as follows:

$$\begin{aligned} A &= \sum_{j=1}^n (m_j (r_j'^2 + \varphi_j'^2 r_j^2) + J_j \gamma_j'^2), \\ B &= \sum_{j=1}^n (m_j \varphi_j' r_j^2 + J_j \gamma_j'), \\ C &= \sum_{j=1}^n (m_j r_j^2 + J_j), \end{aligned} \quad (17.6)$$

where m_j and J_j are masses and central moments of inertia, $r_j(\psi)$ and $\varphi_j(\psi)$ are polar coordinates of the gravity centres of the bodies in the rotating reference system, and $\gamma_j(\psi)$ is the rotation angle of the bodies relative to the rotating disc. The bar denotes differentiation by the generalised coordinate ψ .

The potential energy $\Pi(\psi)$ as a function of the generalised coordinate ψ and the dissipative function $\Phi(\dot{\psi})$ are assumed to be predetermined, and the complete motion of the system is described by the Lagrange equation

$$A\ddot{\psi} + \frac{1}{2}A'\dot{\psi}^2 + B\Omega_0\dot{\xi} - \frac{1}{2}C'\Omega_0^2(1+\xi)^2 + \Pi'(\psi) - \frac{\partial\phi}{\partial\dot{\psi}} = 0. \quad (17.7)$$

In particular, in the case of periodic excitation in accordance with Eq. (17.2), this equation takes the form

$$A\ddot{\psi} + \frac{1}{2}A'\dot{\psi}^2 + B\lambda q \cos(q\tau) - \frac{1}{2}C'(1+\lambda \sin(q\tau))^2 + \frac{1}{\Omega_0^2} \left(\Pi(\psi) - \frac{\partial\phi}{\partial\dot{\psi}} \right) = 0. \quad (17.8)$$

17.3 Vibro-Mechanical Transformation to the Slow System

In this section, the equations of vibrational mechanics for a rotating mechanism with periodic or stochastic excitation will be derived, which correspond to the original Lagrange equations Eqs. (17.8) and (17.7), respectively.

17.3.1 Averaging

Assuming that $q \gg 1$ and following the concept of vibration mechanics, we consider the generalised coordinate ψ as depending on slow time τ and fast time $=q\tau$. Further, it can be presented as $\psi(\tau, \theta) = \Psi(\tau) + \zeta(\tau, \theta)$, where Ψ is the result of averaging ψ over the fast time θ , and ζ is the high-frequency part of ψ with a zero mean:

$$\Psi(\tau) = \langle \psi \rangle = \frac{1}{2\pi} \int_0^{2\pi} \psi(\tau, \theta) d\theta, \quad \langle \zeta \rangle = \frac{1}{2\pi} \int_0^{2\pi} \zeta(\tau, \theta) d\theta = 0. \quad (17.9)$$

These expressions correspond to the usual definition of the averaging assumed in vibrational mechanics and are valid in the case of periodic excitation.

Some modification of this definition for stochastic excitation was introduced in [21]. The averaging, generalised to stochastic systems, is also denoted by $\langle \dots \rangle$, but it is understood that it means the successive application of the usual averaging over the fast time $\theta = \omega_0 t$ on a period equal to 2π and calculating the mathematical expectation. Thus, for some function f is introduced

$$\langle f \rangle = \frac{1}{2\pi} E \left(\int_0^{2\pi} f d(\theta) \right) = \frac{1}{2\pi} \int_0^{2\pi} E(f) d(\theta). \quad (17.10)$$

In accordance with this definition, $\langle \zeta \rangle = 0$.

The aim of the study is to obtain the equation for the averaged variable $\Psi(t) = \langle \psi \rangle$.

17.3.2 The Case of Periodical Excitation

The vibro-mechanical transformation of the original Eq. (17.8) to the equation for slow motion in the case of periodic excitation is based on the method of direct separation of motions by Professor I. I. Blekhman [12]. This method was modified in [20] for modulated periodic excitation depending on the coordinate and velocity. It was done by using small parameters and some elements of the multiple scales technique. The results of this paper provide us with the ready-made analytical expressions for the equation

$$\ddot{\psi} = F(\psi, \dot{\psi}) + B_c(\psi, \dot{\psi})\cos(\theta) + B_s(\psi, \dot{\psi})\sin(\theta) + B_{2c}(\psi, \dot{\psi})\cos(2\theta) \tag{17.11}$$

with arbitrary analytical functions F, B_c, B_s and B_{2c} . The vibrational transformed equation corresponding to Eq. (17.11) has the form

$$\ddot{\Psi} = F(\Psi, \dot{\Psi}) + V(\Psi, \dot{\Psi}). \tag{17.12}$$

This equation corresponds to the concept of vibrational mechanics. Here the first term is the force in the absence of the high-frequency excitation. The second term is a slow *vibrational force*, which replaces the terms with high-frequency excitation of the original Eq. (17.11). In accordance with [20], the expression for V with an error of the order of $\frac{1}{q^2}$ can be presented in the form

$$V = -\frac{1}{4q^2} \left(\frac{\partial^2 F}{\partial \dot{\psi}^2} \left(B_s^2 + B_c^2 + \frac{1}{4} B_{2c}^2 \right) - \left(B_s^2 + B_c^2 + \frac{1}{4} B_{2c}^2 \right)' \right). \tag{17.13}$$

For the considered Lagrange equation (17.8), we have

$$F = \frac{1}{A} \left(-\frac{1}{2} A' \dot{\psi}^2 + \frac{1}{2} C' \left(1 + \frac{1}{2} \lambda^2 \right) - \frac{1}{\Omega_0^2} \left(\Pi(\psi) - \frac{\partial \phi}{\partial \dot{\psi}} \right) \right) \\ B_c = -\frac{Bq\lambda}{A}, B_s = \frac{\lambda C'}{A}, B_{2c} = -\frac{\lambda^2 C'}{4A}. \tag{17.14}$$

Substituting the functions F, B_c, B_s and B_{2c} from (17.14) in (17.13), we obtain the following concretisation of Eq. (17.12) for the rotating mechanism with periodic high-frequency excitation:

$$A \ddot{\Psi} + \frac{1}{2} A' \dot{\Psi}^2 - \frac{1}{2} C'_{eff} \Omega_0^2 + \Pi' - \frac{\partial \phi_{eff}}{\partial \dot{\Psi}} = 0 \tag{17.15}$$

with

$$C_{eff} = C + \frac{\lambda^2 (CA - B^2)}{2A}, \quad \Phi_{eff} = \Phi + \lambda^2 \Omega_0^2 \frac{d^2 \Phi}{d\dot{\psi}^2} B^2 / (4A^2). \tag{17.16}$$

17.3.3 The Case of Stochastic Excitation

The generalisation of the method of direct separation of motions for the stochastic excitation was given in [21]. Instead of Eq. (17.11), the following equation was considered:

$$\ddot{\psi} = F(\psi, \dot{\psi}) + B_1(\psi, \dot{\psi})\xi_1 + B_2(\psi, \dot{\psi})\xi_2 + B_3(\psi, \dot{\psi})\xi_3, \quad (17.17)$$

where ξ_1 , ξ_2 and ξ_3 are mutually independent and stochastically orthogonal random functions. In this case, the vibro-mechanical transformed equation for the slow motion has the same form of Eq. (17.12) as for the case of periodic excitation, but with another expression for the vibrational force V :

$$V = \frac{1}{2} \left(\frac{\partial^2 F}{\partial \dot{\psi}^2} (\kappa_1 B_1^2 + \kappa_2 B_2^2 + \kappa_3 B_3^2) - (\kappa_1 B_1^2 + \kappa_2 B_2^2 + \kappa_3 B_3^2)' \right). \quad (17.18)$$

Here, the values κ_j ($j = 1, 2, 3$) are integral characteristics of the stochastic processes ξ_1, ξ_2, ξ_3 which are calculated from their spectral density S_j as

$$\kappa_j = \int_{\omega_0}^{\infty} S_j(k) k^{-2} dk. \quad (17.19)$$

In accordance with the original Eq. (17.7) for the case of stochastic excitation, the values F , B_1 , B_2 , B_3 , ξ_1 , ξ_2 and ξ_3 have the following specification:

$$F = \frac{1}{A} \left(-\frac{1}{2} A' \dot{\psi}^2 + \frac{1}{2} C' \Omega_0^2 (1 + \langle \xi^2 \rangle) - i \Pi'(\psi) + \frac{\partial \phi}{\partial \dot{\psi}} \right),$$

$$\xi_1 = \dot{\xi}, \quad \xi_2 = \xi, \quad \xi_3 = \xi^2 - \langle \xi^2 \rangle$$

$$B_1 = -\frac{B \Omega_0}{A}, \quad B_2 = \frac{\Omega_0^2 C'}{A}, \quad B_3 = \frac{\Omega_0^2 C'}{2A}. \quad (17.20)$$

Substituting the functions F , B_1 , B_2 and B_3 from Eq. (17.20) in Eq. (17.18), we obtain the following specification of Eq. (17.12) for the slow motion:

$$\ddot{\psi} = \frac{1}{A} \left(-\frac{1}{2} A' \dot{\psi}^2 + \frac{1}{2} C' \Omega_0^2 (1 + \langle \xi^2 \rangle) - \Pi(\psi) + \frac{\partial \phi}{\partial \dot{\psi}} \right) + V \quad (17.21)$$

with

$$V = \frac{\Omega_0^2}{2A} \left(H \frac{\partial^3 \phi}{\partial \dot{\psi}^3} - (AH)' \right), \quad (17.22)$$

$$H = \frac{1}{A^2} \left(\kappa_1 B^2 + \Omega_0^2 (\kappa_2 + \kappa_3/4) C'^2 \right). \quad (17.23)$$

Since $q \gg 1$, it is possible to limit the expression (17.21) to the first member with sufficient precision:

$$H \approx \frac{\kappa_1 B^2}{A^2}. \quad (17.24)$$

The averaged Eqs. (17.19)–(17.21) can also be presented in the form of Eq. (17.15) with

$$C_{eff} = C (1 + \langle \xi^2 \rangle) - AH, \quad \Phi_{eff} = \Phi + \frac{1}{2} \Omega_0^2 \frac{d^2 \Phi}{d\dot{\psi}^2} H. \quad (17.25)$$

17.3.4 Discussion

We see that the Eq. (17.15) of vibrational mechanics with the averaged coordinate Ψ is similar to the Eq. (17.7) of the complete motion with the original fast variable ψ for both periodic and stochastic high-frequency excitation. In both cases, the equation of vibrational mechanics (17.15) differs from the original Eq. (17.7) by replacing the oscillating angular velocity Ω with its mean value Ω_0 , and by introducing the values C_{eff} and Φ_{eff} instead of C and Φ . The effective characteristics of the slow dynamics \tilde{N}_{eff} and Φ_{eff} are calculated with Eqs. (17.16) and (17.25) in the cases of periodic and stochastic excitation, respectively, and differ from the original inertial coefficient C and the dissipative function Φ by the terms, which consider the effect of high-frequency excitation on the slow motion.

17.4 Low-Frequency Behaviour of Rotating Mechanisms

As a result of this difference, the equilibrium position, eigenfrequency, dissipation and sometimes the global behaviour of the system depend on the intensity of the high-frequency excitation.

These effects, which will be considered in this section, are of special interest for the different pendulum-type systems used as vibration absorbers adapting to the rotation speed [24, 25] because the operating performance of such mechanisms is sensitive to misalignment in their eigenfrequency. Focusing on this class of applications, we will further restrict ourselves to considering the case of the pure inertial rotating mechanism ($\Pi' \equiv 0$) without dissipation ($\Phi = 0$).

17.4.1 Equilibrium Position of the Slow Motion

The position of the relative equilibrium in the absence of the high-frequency periodic or stochastic excitation is assumed to correspond to $\psi = 0$. This can always

be provided by the corresponding definition of this generalised coordinate. From Eqs. (17.7) and (17.8), it follows with $\Pi' \equiv 0$ that without excitation ($\xi = 0$)

$$C'(0) = 0. \quad (17.26)$$

The position of the relative equilibrium for the slow motion $\Psi = \Psi_0$ is defined for both periodic and stochastic excitation from Eq. (17.15):

$$C'_{eff}(\Psi_0) = 0 \quad (17.27)$$

and can differ in general from 0. The value of Ψ_0 for small relative amplitude of the angular velocity λ can be obtained approximately as

$$\Psi_0 = \lambda^2 \frac{2B(0)B'(0)A(0) - B^2(0)A'(0)}{2C''(0)A^2(0)} \quad (17.28)$$

for periodic excitation and

$$\Psi_0 = \kappa_1 \frac{2B(0)B'(0)A(0) - B^2(0)A'(0)}{(1 + \langle \xi^2 \rangle) C''(0)A^2(0)} \quad (17.29)$$

for stochastic excitation.

These expressions are obtained from Eq. (17.27) after its linearisation by Ψ_0 , considering Eqs. (17.16) and (17.25), respectively.

This vibro-mechanical modification of the equilibrium position due to the high-frequency excitation needs some asymmetry of the system relative to the point $\psi = 0$. In other words, it needs that $B'(0) \neq 0$ or $A'(0) \neq 0$.

17.4.2 Eigenfrequency of the Slow Motion Near an Equilibrium Position

Another effect is the shift of the eigenfrequency due to the high-frequency excitation. This effect takes place also for the symmetric pendulum systems, for which $B(\psi) = B(-\psi)$, $A(\psi) = A(-\psi)$, or, as is equivalent, if

$$B'(0) = 0, \quad A'(0) = 0. \quad (17.30)$$

Then $\Psi_0 = 0$. We consider the effect of the shift of the eigenfrequency just for this case for two reasons. First, it is of most interest for the practice. Second, it gives the most transparent and compact expression, which, nonetheless, matches the more sophisticated result for a non-symmetrical system with an accuracy of the order of magnitude λ^2 .

The eigenfrequency ω is obtained from Eq. (17.15), which, after its linearisation, has the form

$$\ddot{\Psi} + \omega^2 \Psi = 0 \tag{17.31}$$

with

$$\omega = \omega_0 \sqrt{\frac{C''_{eff}(0)}{C''(0)}}. \tag{17.32}$$

Here, ω_0 is the eigenfrequency of the original system without high-frequency excitation, which is calculated as

$$\omega_0 = \Omega_0 \sqrt{-\frac{C''(0)}{2A(0)}}. \tag{17.33}$$

The expression (17.32) can also be presented in the form

$$\omega = \omega_0 \sqrt{1 - \eta} \tag{17.34}$$

with a dimensionless parameter η , which determines the effect of high-frequency excitation on the eigenfrequency of the slow motion. The parameter η is calculated as

$$\eta = \frac{\lambda^2 \Omega_0^2 (C''(0) A^2(0) - 2B''(0) B(0) A(0) + B^2(0) A''(0))}{4\omega_0^2 A^3(0)} \tag{17.35}$$

for periodic excitation and

$$\eta = (A''(0)H(0) + H''(0)A(0)) / C''(0) - \langle \xi^2 \rangle \tag{17.36}$$

for stochastic excitation. The last expression can also be presented in the form

$$\eta = \frac{\kappa_1 B(0)}{2Q_0^2 A^3(0)} (A''(0) B(0) - 2B''(0) A(0)) + 4Q_0^2 \Omega_0^2 (\kappa_2 + \kappa_3 / 4) - \langle \xi^2 \rangle. \tag{17.37}$$

17.4.3 Example of the Global Low-Frequency Behaviour of a Rotating Mechanism

As an example in which the global behaviour of a rotating mechanism is modified by the high-frequency excitation, we consider a system that may be called a Stephenson–Kapitsa centrifugal pendulum. We will limit ourselves to studying the case of the periodic excitation, but very similar results can be obtained for stochastic excitation.

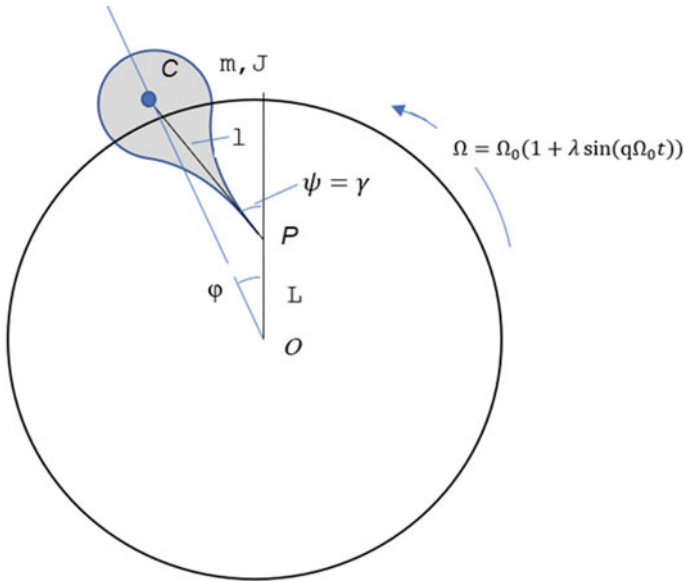


Fig. 17.5 Stephenson–Kapitsa centrifugal pendulum

The Stephenson–Kapitsa pendulum commonly refers to a pendulum with a vertically oscillating suspension point [12]. We use the term *Stephenson–Kapitsa centrifugal pendulum* for its centrifugal analogue, a pendulum hinged to a rotating disc, the angular velocity of which makes high-frequency oscillations near some mean value. This system is shown in Fig. 17.5.

Here, a pendulum with mass m and central moments of inertia J is pivotally mounted at the point P located at a distance L from the centre of rotation O of the carrier disc. The distance between the pivot and the centre of gravity of the pendulum is l .

The angular velocity of the disc oscillates in accordance with Eq. (17.1). Thus, there are variations in the centrifugal force, which here plays the same role as the gravity force in the classic Stephenson–Kapitsa pendulum. This analogy suggests that the behaviour of the Stephenson–Kapitsa centrifugal pendulum with increasing excitation amplitude is similar to the behaviour of the classical pendulum with a vertical vibrating pivot point. This means:

- the natural frequency of oscillations near the initial equilibrium position is expected to increase;
- the bifurcation at some amplitude of excitation is expected to stabilise the inverted equilibrium position without changing the stability of the initial equilibrium position.

As we will see, the behaviour of the centrifugal pendulum differs from this scenario.

To study the global low-frequency behaviour of the system, we concretise Eq. (17.8) by taking the rotation angle γ as the generalised coordinate ψ and considering the following geometrical relationships for the polar coordinates r and φ of the centre of gravity of the pendulum:

$$r = \sqrt{L^2 + l^2 + 2Ll \cos \psi}, \quad \tan \varphi = \frac{l \sin \psi}{L + l \cos \psi}. \quad (17.38)$$

Thus, the functions A , B and C take the form

$$A = ml^2 + J, \quad B = ml(l + L \cos \psi) + J, \quad C = m(l^2 + L^2 + 2Ll \cos \psi) + J \quad (17.39)$$

and after some routine transformations, we have, in accordance with Eq. (17.16),

$$C'_{eff} = -2mLl \sin \psi + \frac{\lambda^2}{2} \frac{m^2 l^2 L^2}{ml^2 + J} \sin 2\psi. \quad (17.40)$$

Correspondingly, Eq. (17.15) takes the form

$$\ddot{\Psi} + \omega_0^2 \sin(\Psi) \left(1 - \frac{1}{2} \left(\frac{\lambda \omega_0}{\Omega_0} \right)^2 \cos(\Psi) \right) = 0. \quad (17.41)$$

Here, in accordance with Eq. (17.33), the value ω_0^2 is proportional to Ω_0^2 and connected with the parameters of the pendulum as follows:

$$\omega_0^2 = \Omega_0^2 \frac{mL}{ml^2 + J}. \quad (17.42)$$

From Eq. (17.41), it is clear that the eigenfrequency near the equilibrium point $\Psi = 0$ is equal to

$$\omega^2 = \omega_0^2 \left(1 - \frac{1}{2} \left(\frac{\lambda \omega_0}{\Omega_0} \right)^2 \right). \quad (17.43)$$

(The same result can be obtained directly from Eqs. (17.34) and (17.35) considering Eq. (17.39).)

Expression (17.43) shows that the eigenfrequency of the low-frequency oscillations near the initial equilibrium point $\Psi = 0$ does not increase with an increase in the excitation amplitude λ , but decreases. This is the first difference from the classic Stephenson–Kapitsa pendulum.

The second difference concerns the bifurcation which takes place with increasing λ when $1 - \frac{1}{2} \left(\frac{\lambda \omega_0}{\Omega_0} \right)^2 = 0$, i.e. at

$$\lambda = \lambda_{cr} = \frac{\Omega_0}{\omega_0} \sqrt{2}. \quad (17.44)$$

For the classic Stephenson–Kapitsa pendulum, a similar bifurcation leads to stability of the upper equilibrium point $\Psi = \pi$ without changing the stability of the initial equilibrium position $\Psi = 0$. Unlike this, the initial equilibrium position of the centrifugal Stephenson–Kapitsa pendulum $\Psi = 0$ becomes unstable at $\lambda > \lambda_{cr}$ while the upper equilibrium point $\Psi = \pi$ remains ever unstable.

At the same time, the bifurcation at $\lambda = \lambda_{cr}$ creates a doublet of stable equilibrium positions:

$$\Psi_{12} = \pm \arccos(\lambda_{cr}^2 / \lambda^2)$$

between the unstable upper ($\Psi = \pi$) and lower ($\Psi = 0$) equilibrium positions.

17.5 Application to the Centrifugal Pendulum Absorber

The obtained results can be applied to the centrifugal pendulum absorber with bifilar hanging, which is described, for example, in Den Hartog's classic textbook [24]. This absorber has been used effectively since the 1930s, first in aircraft and in recent years in the automotive industry [25]. This type of absorber allows us to provide its eigenfrequency proportional to the rotational speed and thus to keep it equal to the frequency of the torque irregularity of a reciprocating engine, whose frequency also increases linearly with engine speed with a factor which is called the excitation order. The coefficient of proportionality between the engine speed and the eigenfrequency of the absorber is known as the centrifugal pendulum order.

Thus, the pendulum should be so designed that its order is equal to the excitation order as accurately as possible. One of the factors that lead to the violation of this equality is high-frequency excitation. This problem was first addressed in [28] for the case of stochastic excitation caused, for example, by impact in gearboxes. It was shown that both stochastic resonance and stochastic anti-resonance are possible in the centrifugal pendulum absorber. Now, we consider another aspect of the problem: the case of periodic high-frequency excitation caused by higher engine orders.

The considered pendulum can have a rather complex kinematics, as shown in Fig. 17.4. In the case of the centrifugal pendulum absorber, it can be achieved due to a special design of the pendulum hanging even for a one-mass pendulum. The goal of considering this is to understand how the kinematic characteristics affect the sensitivity of the pendulum order to the high-frequency excitation.

In the case of the centrifugal pendulum absorber, one can take the angle of the relative rotation γ as the generalised coordinate ψ . Then $\gamma' = 1$, and the following formulae are valid for $A(0)$, $B(0)$, $A''(0)$, $B''(0)$ and $C''(0)$ in accordance with Eq. (17.6):

$$A(0) = m\dot{\varphi}^2(0)r^2(0) + J,$$

$$B(0) = m\dot{\varphi}'(0)r^2(0) + J,$$

$$\begin{aligned}
 A''(0) &= 2m \left(r''^2(0) + r(0)r''(0)\varphi'^2(0) + \varphi'(0)\varphi'''(0)r^2(0) \right) \\
 B''(0) &= 2mr(0)\varphi'(0)r''(0) + mr^2(0)\varphi'''(0) \\
 C''(0) &= 2mr(0)r''(0).
 \end{aligned}
 \tag{17.45}$$

Here, for the single mass, the index j in Eq.(17.6) is omitted. It is also taken into account that Eq. (17.30) is equivalent here to the conditions

$$r'(0) = 0, \varphi'(0) = 0. \tag{17.46}$$

Now we are obtaining the coefficient η as a function of $r(0)$, $\varphi'(0)$ and $\varphi'''(0)$.

From Eqs. (17.33) and (17.45), the second derivative of r can be presented as

$$r''(0) = -r(0) \frac{\omega_0^2}{\Omega_0^2} \left(\varphi'^2(0) + H_p \right) \tag{17.47}$$

with $H_p = \frac{J}{mr^2(0)}$.

Substitution of $A(0)$, $B(0)$, $A''(0)$, $B''(0)$ and $C''(0)$ from Eq.(17.45) into Eq. (17.35), while considering Formula (17.47) for $r''(0)$, gives the following expression for the coefficient η in Eq. (17.34), which characterises the sensitivity of the eigenfrequency to the vibro-mechanical effect of the high-frequency excitation: $\eta = \frac{K\lambda^2}{4}$ with

$$\begin{aligned}
 K &= 2 \left(\frac{\omega_0^2}{\Omega_0^2} \left(\varphi'^2(0) + H_p \right)^2 \left(\varphi'(0) + H_p \right)^2 - H_p^2 \left(\varphi'^2(0) + H_p \right) \left(1 - \varphi'(0) \right)^2 \right. \\
 &\quad \left. + \frac{\Omega_0^2}{\omega_0^2} H_p \left(\varphi'(0) - 1 \right) \left(\varphi'(0) + H_p \right) \varphi'''(0) \right) \left(H_p + \varphi'^2(0) \right)^{-3}.
 \end{aligned}
 \tag{17.48}$$

Figures 17.6 and 17.7 show the corresponding characteristic diagrams for K as a function of H_p and $\varphi'(0)$ at $\frac{\omega_0}{\Omega_0}$ equal to 2 and 3 correspondingly and $\varphi'''(0) = 0$.

The diagrams show that positive values of the coefficient K prevail in the parameter space. This means that a reduction of the eigenfrequency of the pendulum is typical due to an additional high-frequency oscillation. Especially, the simple formulae for η correspond to the most practically interesting cases. These are the classical pendulum without relative rotation for which $\varphi'(0) = \infty$, and the pendulum with $\varphi'(0) = 1$, which has some special design advantages [25]. For these two types of pendulum, Eq. (17.24) gives correspondingly $\eta = 2 \frac{\omega_0^2}{\Omega_0^2}$ and $= 2(1 + H_p)$. In both cases, $\eta > 0$.

It is worth noting that only in the second case, the coefficient K is maximal (see Figs. 17.1 and 17.2).

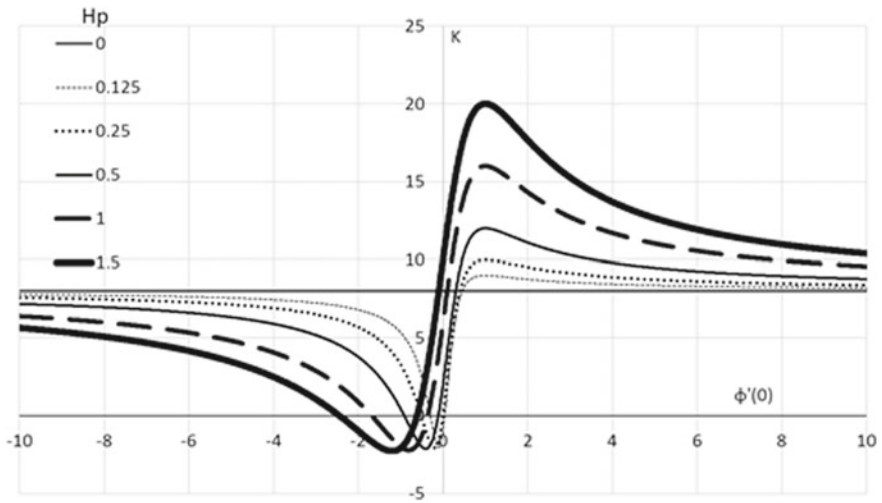


Fig. 17.6 Characteristic diagrams for the coefficient K as a function of $\phi'(0)$ at $\frac{\omega_0}{\Omega_0} = 2$, $\phi'''(0) = 0$ and H_p equal to 0, 0.125, 0.25, 0.5, 1 and 1.5

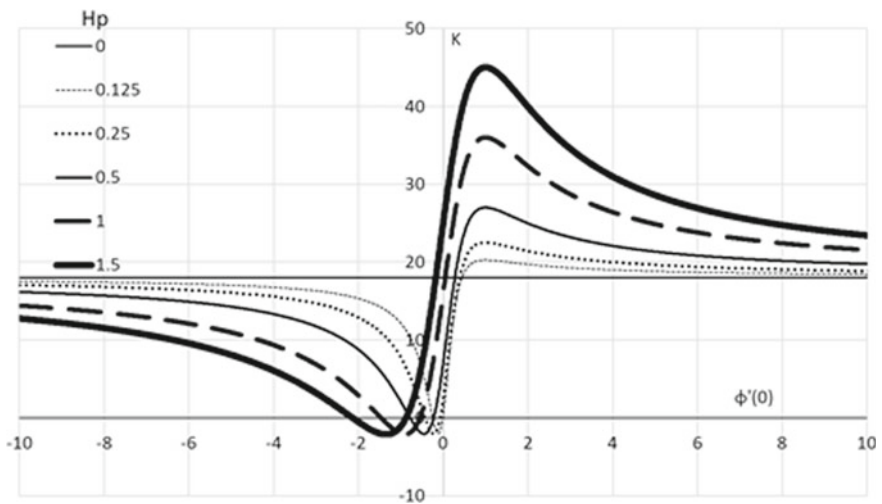


Fig. 17.7 Characteristic diagrams for the coefficient K as a function of $\phi'(0)$ at $\frac{\omega_0}{\Omega_0} = 3$, $\phi'''(0) = 0$ and H_p equal to 0, 0.125, 0.25, 0.5, 1 and 1.5

We see that the own rotation angle of the pendulum as a function of its position has a significant impact on this sensitivity. This kinematic characteristic determines even the sign of the order deviation, which is caused by additional high-frequency excitation. It can qualitatively affect the behaviour of the absorber, as follows from the results presented in [26].

17.6 Conclusion

The main results of the work are as follows:

- In the frame of the concept of vibrational mechanics, a rotating multi-mass mechanism with high-frequency periodic or stochastic excitation was considered, and the general equation for the averaged motion of such mechanisms has been obtained (the equation of vibrational mechanics).
- The equation of vibrational mechanics has the same structure as the original Lagrange equation without excitation, but has a modified inertial coefficient and dissipative function, depending on the intensity of the excitation.
- As a result of this difference, the equilibrium position and eigenfrequency depend on the intensity of high-frequency excitation. The corresponding calculation expressions have been obtained, in general, for the cases of periodic and stochastic excitation.
- As an example of modification of the global behaviour of a rotation mechanism, a centrifugal analogue of the Stephenson–Kapitsa pendulum was considered. Unlike a classical pendulum with an oscillating point of suspension, the centrifugal Stephenson–Kapitsa pendulum has the following peculiarities:
 - Its natural frequency near the initial position of equilibrium drops with an increase in the excitation amplitude and, at some value of this amplitude, loses its stability.
 - A pair of new stable equilibrium positions appears next to the original equilibrium position, and the inverted equilibrium position always remains unstable.
- The theory was applied to the analysis of the centrifugal pendulum absorber with a complex kinematics provided by a special design of hanging. The sensitivity of the pendulum order deviation from the nominal order due to high-frequency excitation was studied. It has been shown that the own rotation angle of the pendulum as a function of its position has a significant impact on this sensitivity. This kinematic characteristic even determines the sign of the deviation, which can qualitatively affect the behaviour of the absorber.

References

1. Blekhman, I.I., Dzanelidze, G.Y.: *Vibrational Displacement*. Nauka, Moscow (1964) (in Russian)
2. Blekhman, I., Blekhman, L., Vasilkov, V.: Engineering model of the vibrational transportation process. *Vibroeng. Procedia* **32**, 26–31 (2020)
3. Blekhman, I.I.: *Synchronization in Science and Technology*. ASME Press, New York (1988)
4. Uchechukwu, E.V., McClintock, P.V.E., Khovanov, I.A., Rajasekar, S.: Vibrational and stochastic resonance in driven nonlinear systems (part 1). *Phil. Trans. R. Soc. A* **379**, 20200242 (2021)
5. Blekhman, I., Kremer, E.: Stochastic resonance as the averaged response to random broadband excitation and its possible applications. *Proc. IMechE. Pt. C J. Mech. Eng. Sci.* **233**(23–24), 7445–7446 (2019)
6. Benzi, R., Sutera, A., Vulpiani, A.: The mechanism of stochastic resonance. *J. Phys. A* **14**, 453–457 (1981)
7. Gammaitoni, L., Hänggi, P., Jung, P.: Stochastic resonance. *Rev Mod Phys.* **70**(1), 223–287 (1998). <https://doi.org/10.1103/RevModPhys.70.223>
8. Sorokin, V.S.: Vibrations of a nonlinear stochastic system with a varying mass under near resonant excitation. *J. Vib. Control* **26**, 17–18 (2020). <https://doi.org/10.1177/1077546319898304>
9. Blekhman, I.I., Landa, P.S.: Conjugate resonances and bifurcations in nonlinear systems under biharmonic excitation. *Int. J. Nonlinear Mech.* **39**, 421–426 (2004)
10. Landa, P.S., McClintock, P.: Vibrational resonance. *J. Phys. A: Math. Gen.* **33**, 433–438 (2000)
11. Kremer, E.: The effect of high-frequency stochastic actions on the low-frequency behaviour of dynamic systems. *Phil. Trans. R. Soc. A* **379**, 20200242 (2021). <https://doi.org/10.1098/rsta.2020.0242>
12. Blekhman, I.: *Vibrational Mechanics: Nonlinear Dynamic Effects, General Approach, Applications*. World Scientific, Singapore (2000)
13. Blekhman, I.I.: *Vibrational Mechanics and Vibrational Rheology (Theory and Applications)*. FIZMATLIT, Moscow (2018) (in Russian)
14. Blekhman, I.: Method of direct motion separation in problems of vibration acting on nonlinear mechanical systems. *Mech. Solids* **11**, 7–19 (1976)
15. Blekhman, I. (ed.): *Selected Topics in Vibrational Mechanics (Series on Stability, Vibration and Control of Systems. Series A. Volume 11)*. World Scientific, Singapore (2004)
16. Fidlin, A.: *Nonlinear Oscillations in Mechanical Engineering*. Springer, Berlin (2006)
17. Thomsen, J.: *Vibrations and Stability - Advanced Theory, Analysis, and Tools*. Springer, Berlin (2013)
18. Blekhman, I.I., Sorokin, V.S.: Extension of the method of direct separation of motions for problems of oscillating action on dynamical systems. *Procedia IUTAM* **19**, 75–82 (2016)
19. Blekhman, I., Sorokin, V.: On the separation of fast and slow motions in mechanical systems with high-frequency modulation of the dissipation coefficient. *J. Sound Vib.* **329**, 4936–4949 (2010)
20. Kremer, E.: Slow motions in systems with fast modulated excitation. *J. Sound Vib.* **383**, 295–308 (2016)
21. Kremer, E.: Low-frequency dynamics of systems with modulated high-frequency stochastic excitation. *J. Sound Vib.* **437**, 422–436 (2018)
22. Blekhman, I., Vaisberg, L., Indeitsev, D.: Theoretical and experimental basis of advanced vibrational technologies. In: *Vibration Problems ICOVP 2011* (2011). https://doi.org/10.1007/978-94-007-2069-5_18
23. Vaisberg, L.: Vibration technology research achievements of the Mekhanobr scientific school and their practical implementation. *Vibroeng. PROCEDIA* **25**, 76–82 (2019). <https://doi.org/10.21595/vp.2019.20820>
24. Den Hartog, J.P.: *Mechanical Vibrations*. McGraw-Hill, New York (1956)

25. Dresig, H., Fidlin, A.: Schwingungen mechanischer Antriebssysteme: Modellbildung, Berechnung, Analyse, Synthese, 4th edn. Springer, Vieweg (2020)
26. Kremer, E.: Stochastic resonances and antiresonances in rotating mechanisms. In: Lacarbonara, W., Balachandran, B., Leamy, M.J., Jun Ma, J., Machado, J.A., Stepan, G. (eds.): Advances in Nonlinear Dynamics - Proceedings of the Second International Nonlinear Dynamics, Conference (NODYCON 2021), vol. 1. Springer, Cham (2021) (in press)

Chapter 18

SiC/Si as a New Platform for Growth of Wide-Bandgap Semiconductors



Sergey Kukushkin, Andrey Osipov, and Alexey Redkov

Abstract The review provides a short list of the latest scientific achievements of the Laboratory of Structural and Phase Transformations in Condensed Matter, Institute for Problems in Mechanical Engineering (IPME RAS). We present the results on the developed growth method of thin silicon carbide films on silicon by coordinated atomic substitution, the properties of the obtained SiC/Si layers, and the prospects for their use as substrates for the growth of thin films of various materials. Special attention is paid to the experimental results on the deposition on SiC/Si substrates of various promising wide-bandgap semiconductors, such as aluminum nitride AlN, gallium nitride GaN, and their solid solutions. Data on the growth of the A^{II}B^{VI} semiconductor compounds are presented. The possibility of using SiC/Si substrates for deposition of nanocrystals is discussed. A number of theoretical results devoted to the description of the growth mechanisms of these semiconductors are outlined.

Keywords Silicon carbide · Silicon · Atomic substitution · Wide-bandgap · Semiconductors · Electronics · Gallium nitride · Aluminum nitride LED

18.1 Introduction

Silicon is one of the key materials on the basis of which most modern electronic devices, computers, communication facilities, sensors, transmitting and reproducing equipment operate. This material has both a number of advantages and some significant disadvantages. One of the important advantages of silicon is its availability: the production of silicon wafers for chips and microcircuits, their polishing, cleaning, and cutting are well mastered all over the world. Therefore, the devices based on silicon wafers are relatively cheap. Despite this, silicon-based devices have a number of limitations. So, with an increase in the ambient temperature, its semiconductor properties deteriorate greatly, there is an instability in the operation of devices, mal-

S. Kukushkin (✉) · A. Osipov · A. Redkov
Institute for Problems in Mechanical Engineering RAS, V.O., Bolshoy pr., 61, St., Petersburg
199178, Russia

functions. Silicon cannot operate stably under high-radiation conditions, for example, in space and in nuclear reactors. It also has a number of other fundamental defects. In this regard, it has now become clear that for some applications it is necessary to use other materials that are capable of replacing silicon at least partially if not completely. Such semiconductor materials include wide-bandgap semiconductors [1]: silicon carbide (SiC), gallium nitride (GaN), aluminum nitride (AlN), their solid solutions, and a number of other materials. In addition to the fact that these semiconductors have excellent electrical characteristics, they can ensure the operation of modern electronic and optoelectronic devices under conditions of high temperatures and high radioactive radiation.

To gradually replace silicon with wide-bandgap semiconductors, the production cost of the latter must approach the cost of silicon production, which is unattainable for the currently existing growth technologies. Since there are no native substrates for homoepitaxy of these materials, at present, completely different approaches and substrates are used for their growth, starting from specially grown substrates with a given coefficient of thermal expansion [2], and ending with pendeo-epitaxy [3], the ELO method [4] or growing a large number of intermediate layers. All these methods, although they make it possible to grow sufficiently high-quality thin films, are too complicated for mass production of products and devices based on wide-bandgap semiconductors. Therefore, in industrial production, mainly sapphire, silicon carbide, or silicon substrates [5] are used. Each of these substrates has advantages and disadvantages. Sapphire has insufficiently good thermal conductivity and is a dielectric, which significantly limits the applicability of devices and complicates the process of their production. Its lattice parameter and thermal expansion coefficient differ significantly from the analogous parameters of III-nitrides, which causes difficulties in the growth of high-quality dislocation-free thin films and heterostructures. Silicon carbide, although much better suited in terms of its parameters for the growth of GaN and AlN, is currently too expensive. In addition, silicon carbide plates of large diameter (8–10 inches) are not commercially available. Silicon, although it is the most accessible, cheap, and technologically advanced material, but, like sapphire, has lattice parameters different from III-nitrides, which causes a low quality of growing heterostructures and a high dislocation density. Nevertheless, the growth of wide-bandgap semiconductors on silicon substrates is of greatest interest in connection with the prospect of integrating gallium nitride and silicon electronics, the possibility of using large-diameter substrates, their low cost, and good electrical and thermal conductivity. Currently, the largest electronic companies in the world are dealing with this problem. However, a satisfactory solution to this problem has not yet been found due to the huge difference in the lattice parameters of silicon and gallium nitride (~17%).

A fundamentally new method of chemical substitution of atoms was developed at the Laboratory of Structural and Phase Transformations of Institute of Problems of Mechanical Engineering (IPME RAS), which makes it possible to grow thin SiC films directly from silicon [6, 7]. The proposed method for the topochemical conversion of the upper Si layer into an epitaxial SiC film as a result of the coordinated substitution of half of the Si atoms by carbon C atoms makes it possible to almost completely

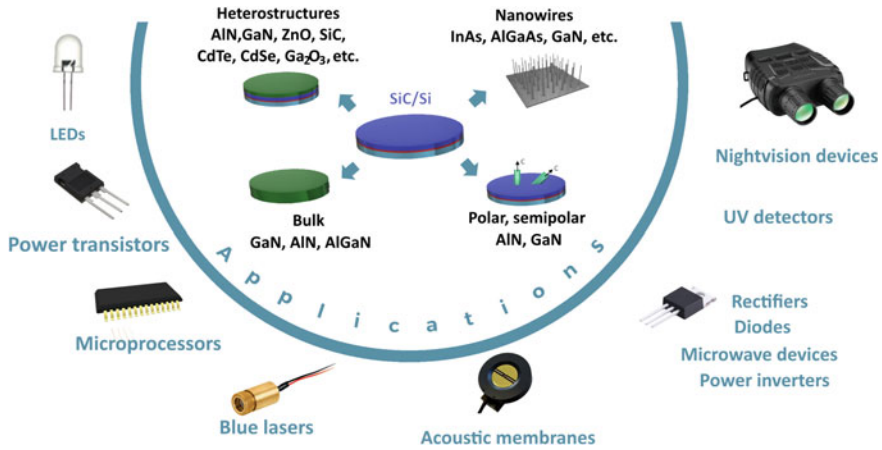


Fig. 18.1 Possible application fields of SiC/Si films, as well as III-nitride semiconductor heterostructures grown on these substrates

eliminate mechanical stresses in the film. The term “coordinated” means that new Si–C chemical bonds are formed simultaneously and consistently with the destruction of old Si–Si bonds. In this case, the pores at the boundary of the film with the substrate are formed by themselves as a result of natural processes of relaxation of the stress–strain state, such as the process of reducing the volume of the initial Si layer into a smaller volume of denser and harder SiC. This method, in contrast to traditional epitaxy, can also be used to obtain hexagonal SiC polytypes, since the transformation of Si into SiC passes through an intermediate metastable state saturated with point defects in the crystal.

SiC/Si substrates obtained by this method combine the advantages of both materials (SiC and Si) and eliminate the disadvantages, the cost of their production is close to the cost of silicon wafers, while the SiC surface layer, mechanically detached from silicon through a porous layer, provides a good matching of lattice parameters during the growth of III-nitride heterostructures.

In connection with the fabrication of the new nano-SiC/Si material, several large fields of their application in the electronics industry have arisen and, as a consequence, several independent research areas, which are currently being developed in Laboratory of Structural and Phase Transformations of IPME RAS (see Fig. 18.1).

This review briefly lists the main results in all of the fields noted above, namely, on the use of SiC/Si substrates for the growth of thin films and heterostructures of wide-bandgap semiconductors and other materials; obtaining AlN, GaN, AlGaN bulk layers (thickness more than 100 μm); growing whiskers of various semiconductors. In addition, the review presents some of the theoretical approaches developed by the authors to describe the growth and formation of pores in such multicomponent systems.

The review is organized as follows. The first part of the review is devoted to the SiC growth on Si substrates by the method of coordinated atomic substitution, its features, and a brief description of the resulting SiC layers. Then the structure and properties of the porous layer under the SiC layer are discussed, and its role in the subsequent growth of thin films of other materials. It also presents possible applications of the method of coordinated atomic substitution for deposition of SiC layers on other substrates (including graphite, sapphire, profiled silicon).

The next part of the review discusses the results on the growth of wide-gap semiconductors such as gallium nitride, aluminum nitride, and AlGaN solid solutions by various methods, including chloride–hydride, molecular beam, and metal–organic epitaxy. Data on the growth of both thin films and heterostructures and bulk layers of these materials of different polarities are presented. The influence of the deposition method and the substrate on the polarity of the growing film is discussed. It is shown that the specific features of the porous buffer layer make it possible to separate the grown heterostructures from the silicon substrate rather quickly and simply from the technological point of view. A separate subsection is devoted to the growth of other materials on SiC/Si substrates, such as ZnO, CdTe, CdSe, CdS, Ga₂O₃, etc.

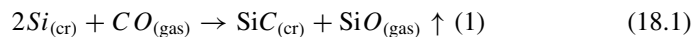
The third part of the review presents the results on the growth of whisker nanocrystals (NW) of various semiconductor compounds on SiC/Si substrates, including GaN, GaAs, InN, their solutions, as well as some phenomena that occur during the growth of NWCs on SiC/Si substrates and their theoretical explanation.

The final section is devoted to various theoretical models developed by the authors to describe the growth and evolution of crystals and pores in such complex crystalline compounds as wide-gap semiconductors.

18.2 Formation of SiC by the Method of Coordinated Substitution of Atoms

18.2.1 Growth Technique

The method of coordinated substitution of atoms [6, 7], theoretically predicted and subsequently experimentally confirmed in the Laboratory of Structural and Phase Transformations of IPME RAS, is based on the use of a chemical reaction:



for self-consistent conversion of the near-surface layer of a silicon substrate into a thin single-crystal silicon carbide layer. The term “coordinated” means that new chemical bonds in SiC are formed simultaneously and consistently with the destruction of old bonds in Si. The method is realized as follows. The initial prepared and cleaned silicon plate is placed in a vacuum oven and kept in an atmosphere of carbon monoxide with the addition of silane gas at temperatures of 900–1300 °C and a pressure of

1–5 Torr. As a result, a thin single-crystal SiC layer with a thickness of several tens to several hundred nanometers is formed on the surface, depending on the chosen growth conditions. During synthesis, a porous layer is formed under the surface of the SiC layer, which consists of a mixture of silicon carbide, voids, and a silicon substrate. This layer has a thickness varying from several hundred nanometers to several microns. A detailed description of the growth process of a SiC film is given in reviews [6, 7], which also contain a description of both theoretical and experimental results on growth process, and a detailed description of the setup in which the growth of SiC is carried out. These works also describe a number of purely technological methods necessary to fabricate SiC layers with a high degree of crystalline perfection, of various thicknesses and polytypes. The main properties of silicon carbide were also discussed in detail there.

18.2.2 Main Properties of the Obtained SiC Layers

Since this review is mainly devoted to the growth of layers and thin films of various semiconductors on a SiC substrate, the properties of the SiC buffer layer, which are important in the context of the growth of subsequent layers: structure, type of crystal lattice, defect content, elastic characteristics, ability to damp elastic stress, and hold the main interest. In addition, the properties that affect various characteristics of the resulting heterostructures are also of importance. This section briefly summarizes studies of the properties of SiC films synthesized under various conditions.

18.2.2.1 Polytype Composition, Structure, Stoichiometry

Since a detailed description of the properties of the obtained SiC films is presented in reviews [6, 7], we will restrict ourselves to only listing the main characteristics. So, one of the key properties of the crystal structure of SiC is its polytype (3C, 2H, 4H, 6H, and others). In [8], the properties of SiC/Si films grown by the method of coordinated substitution of atoms on silicon substrates of various crystallographic orientations were investigated by the method of ultraviolet ellipsometry. An ellipsometric model was selected (see Fig. 18.2a) that best describes the film structure. The model is a simple set of three layers on a substrate, in which the silicon concentration decreases stepwise from the substrate to the surface. In this model, layer 3 with silicon vacancies is an effective medium, i.e., a mixture of SiC and equal volume fractions of voids and crystalline carbon (pyrocarbon), since the removal of a Si atom from SiC leaves excess carbon and leads to the formation of carbon-vacancy structures. Note that point dilatation defects (vacancy Si–interstitial C) in an anisotropic SiC crystal strongly interact with each other along certain crystallographic directions, and this leads to a significant decrease in the total energy. Probably, this is the reason for the presence of residual silicon vacancies in the upper SiC layer. Analysis of ellipsometric curves showed that silicon carbide grown on Si (111) is predominantly cubic, while SiC

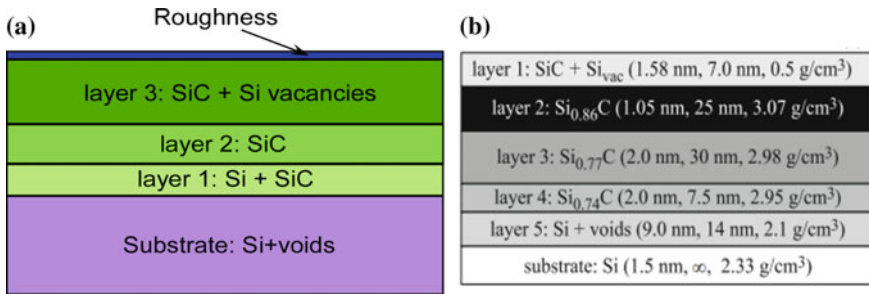


Fig. 18.2 Ellipsometric model from [8], which best describes the structure of SiC/Si layers (a). The Si concentration in the layers decreases in a stepwise way in the direction from the substrate to the surface. Layer 3 is an anisotropic effective medium. **b**—model of the SiC/Si structure obtained by X-ray reflectometry in [9]. Reprinted by permission from Springer Nature

on Si (110) is predominantly hexagonal (with an admixture of cubic polytype). SiC grown on Si (100) has a mixed polytype composition.

Note that due to the peculiarities of growth by the method of coordinated substitution of atoms, SiC films of mixed polytypes are a “pie” in which one polytype dominates in the near-surface region (for example, 3C), and other polytypes appear when moving deeper in the sample.

Other possible factors influencing the violation of stoichiometry of the SiC upper layer, in particular, the mechanochemical effect of Gorskii, were considered in [10]. As a result of this effect, larger Si atoms will be pushed onto the surface of the SiC layer under the influence of the inevitably arising gradient of elastic stresses, forming vacancies in the silicon sublattice. As a result, atoms are redistributed over the film thickness. Si atoms released from the SiC film onto its surface will evaporate and interact with CO according to reaction (1), again forming SiC (however, it is no longer so ordered). In the same work, a method was proposed for reducing the excess of silicon vacancies by adding trichlorosilane gas to the gas mixture. Additional elastic stress and the manifestation of the Gorsky effect are also possible upon cooling of the SiC/Si wafer after growth.

Quantum-chemical calculations have shown that at temperatures above 1100 °C, the carbon atom closest to the silicon vacancy jumps to the place of the missing silicon atom, forming an almost flat cluster of four carbon atoms (see Fig. 18.3). And the absence of a carbon atom in the right place leads to the appearance of two new voids with a radius of 2.1 Å. As a result, instead of a simple silicon vacancy, a carbon-vacancy structure is formed, which consists of an almost flat cluster of four C atoms and two voids below it (Fig. 18.3). Studies have shown that these carbon-vacancy structures largely determine the electrical and magnetic properties of SiC obtained by the method of coordinated substitution of atoms, in particular, provide n-type conductivity of SiC.

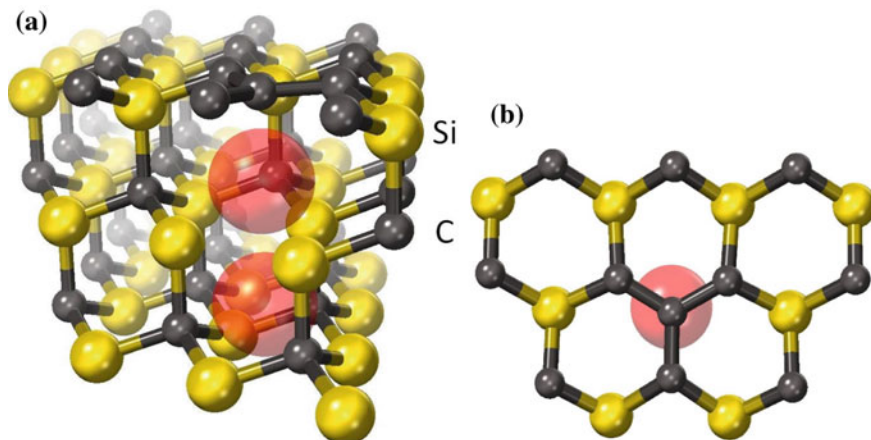


Fig. 18.3 Carbon-vacancy structure formed from a silicon vacancy at temperatures above 1100 °C (a); b—the same structure, top view. Yellow balls are Si atoms, black balls are C atoms, red spheres are voids with a radius of 2.1 Å

In [9, 11], the structure of SiC/Si films grown by coordinated substitution of atoms was studied by various methods, including X-ray reflectometry. As a result, a SiC/Si structural model was proposed according to which the silicon carbide film consists of a series of layers parallel to the substrate. The composition and thickness of each layer included in the structure of the film were determined experimentally (see Fig. 18.2b). The results obtained in [9], as well as the data from ellipsometry [8], also confirmed the presence of stoichiometric carbon in the near-surface region of the film and the presence of silicon vacancies. Note, however, that the structure of carbon is significantly different for the samples synthesized at temperatures of 1250 and 1330 °C, respectively. In the first case, the film surface is saturated with silicon vacancies and carbon in a structurally loose form, resembling pyrocarbon. In SiC/Si films grown at 1330 °C, carbon has a dense structure with a density close to diamond.

In [12], a study of SiC/Si films was carried out by infrared spectroscopy. The band at 960 cm^{-1} was found both in the absorption and transmission spectra. Note that, according to [12, 13], this band corresponds to the vibration energy of C–C bonds in the carbon-vacancy structure (Fig. 18.3). This band is always present in SiC films grown in an atmosphere of pure carbon monoxide (CO) or in a mixture of CO with silane (SiH_4) on Si substrates of different orientations, levels and types of conductivity, which also confirms their invariable presence of dilatation dipoles during the transformation of Si into SiC. Note, however, that the very type of conductivity of the initial silicon also affects the growth of SiC. It was found in [14] that the mechanism of atomic substitution is different in the case of n- and p-conductivity of the Si substrate; this difference has been confirmed experimentally and its nature has been theoretically examined. It is shown that the surface of a SiC film synthesized on p-type Si (100) substrates, tilted by 4° toward $\langle 110 \rangle$, consists of faces coated with

the hexagonal SiC polytype. The planes of the hexagonal faces can have orientations $(1\bar{1}02)$, $(2\bar{2}00)$, $(2\bar{2}02)$, which can further ensure the growth of high-quality epitaxial semipolar films of hexagonal AlN and GaN by the HVPE method. At the same time, the surface of a SiC film synthesized on a similar n-type substrate does not contain such faces and contains a cubic 3C-SiC polytype. Such a surface can serve as a good buffer layer on Si for the growth of semiconductors crystallizing in a cubic crystal symmetry.

Paper [15] is devoted to micro-mapping of the near-surface region of SiC/Si films by confocal Raman spectroscopy. In this paper, the polytypic composition of films growing under various conditions, mentioned in the previous sections, has been confirmed. In addition, judging by the significant increase in the Raman signal measured in the pores, it was concluded that the pore walls are also coated with silicon carbide. The mapping of elastic stresses in the film and substrate, calculated from the shifts of the Raman lines of silicon and SiC, respectively, indicates that the pores in the substrate cause relaxation of the elastic stress caused by the lattice mismatch between SiC and Si. A study of the properties of this porous layer and its effect on the elastic properties of the SiC/Si structure is given in the next section.

18.2.2.2 Microporous Layer in the SiC/Si Structure, Damping Elastic Stresses

Note that one of the key features of SiC/Si films grown by the atomic substitution method is a microporous layer, which is inevitably formed as a result of volume relaxation during the transformation of Si into SiC (the volumes of their crystal unit cells differ by almost a factor of 2 [6]). The porous layer, depending on the growth conditions and growth time, has a thickness varying from several tens of nanometers to several micrometers [6, 16]. Figure 18.4 shows SEM-images of thin and thick SiC layers obtained under various processing conditions, in which the porous layer under the SiC layer is clearly visible. It lies on the silicon like a “bridge on piles”.

The porous layer plays an important role in the growth of subsequent layers above the silicon carbide surface. Due to the presence of pores, the effective contact area between SiC and the initial silicon substrate is significantly reduced. As a result, the difference in the thermal expansion coefficients and lattice parameters of the layers growing above SiC and the original silicon substrate plays a much smaller role. Note that the degree of damping strongly depends on the thickness of the porous layer, the volume fraction of pores in it, their shape, and many other factors. Therefore, it is important to understand the mechanisms of the layer formation. In [17], the temporal evolution of the porous layer during the synthesis was experimentally investigated. It was found that the formation of a porous layer includes several characteristic stages: the appearance of single pores directly under the SiC surface, their growth with the formation of dendrite-like structures, and subsequent merger into a continuous layer. In [17], all stages are considered successively, and a model is constructed that describes the dependence of the thickness of the porous layer on time. It is shown that the average thickness h of the porous layer at the initial stages of growth is

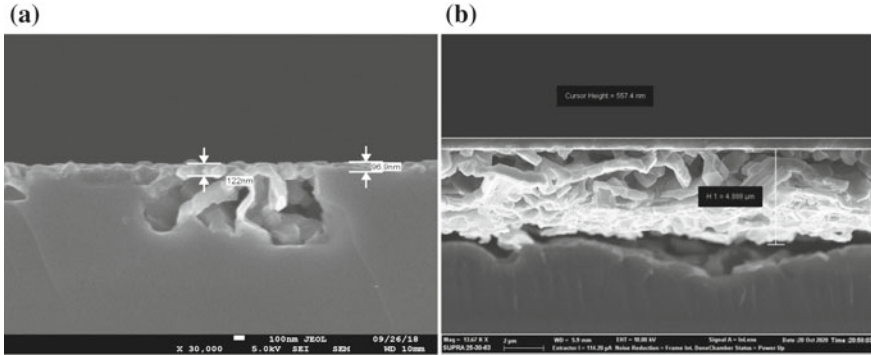


Fig. 18.4 SEM-images of a cleavage of SiC/Si films grown under various conditions: **a** a thin SiC layer (~50 nm) practically without a porous layer; **b** a thick SiC layer (~700 nm) with a porous sublayer ~5 μm thick

proportional to the cubic root of the time $h(t) \sim \sqrt[3]{t}$, but as the pores merge into a single layer, this dependence turns into $h(t) \sim \sqrt{t}$.

In [18], the authors studied the effect of the size and volume fraction of pores in a porous layer on the elastic and thermomechanical characteristics of the SiC/Si substrate as a whole by means of numerical simulation by the finite element method. It was shown that an increase in porosity leads to a gradual decrease in elastic moduli. The results presented in [18] can be used to determine the elastic properties of SiC/Si substrates of various orientations containing a porous layer. In particular, Young's modulus along the [111] direction changes according to the formula:

$$E_{[111]} = 187.9 - 215.96\varphi \text{ (GPa)}$$

where φ is the volume fraction of pores in the porous layer. Note that this result is in good agreement with the values obtained experimentally by nanoindentation of SiC/Si samples with different porosities in [19]. In this paper, the thickness of the SiC layer, the thickness of the porous layer, and the mechanical characteristics of the substrate were compared.

18.2.2.3 Electrical, Optical, Magnetic Properties

Since one of the main purposes of SiC/Si is the use of various types of sensors in heterostructures for electronic and optoelectronic applications, it is important to understand what properties the SiC/Si structure has in this respect. For example, hexagonal polar polytypes of silicon carbide exhibit spontaneous polarization and hence pyroelectric properties. In [20], the electrical response to light irradiation of SiC nanostructures formed on Si substrates with different types of conductivity was investigated. Irradiation was carried out in the visible and near-infrared spectral

range (400–980 nm). Analysis of the photosensitivity showed that the activation energy of radiation at all investigated wavelengths is less than the bandgap of silicon carbide. In this case, photoconductivity in the SiC layer can arise only due to impurity donor–acceptor levels located in the bandgap and localized near defects or pores. Such defects can be carbon atoms, oxygen vacancies, etc. The energy of absorbed photons of light is spent either on the transfer of electrons from donor levels to the conduction band, or from the valence band to acceptor levels. It has been shown that the electrical response is photovoltaic in nature. The mechanisms of its occurrence, apparently, are associated with a barrier at the SiC/Si interface, the presence of which confirms the jumps in the capacitance on the current–voltage characteristics. Additional non-stationary responses were also found, indicating several mechanisms for their occurrence, however, they need further study.

In [21, 22], the photoelectric properties and I–V characteristics of SiC/Si structures grown at different synthesis times (which, among other things, determines the concentration of dilatation dipoles) and on substrates of different orientations, were investigated. It was found that the higher the concentration of dilatation dipoles, the higher the conversion efficiency of sunlight with Si/SiC heterojunctions. A one-to-one correspondence has been established between the synthesis time of SiC films, the maximum density of dipoles, and the efficiency of sunlight conversion into electrical energy. It was also determined that the maximum conversion efficiency of sunlight by a silicon–silicon carbide (silicon carbide–silicon) heterojunction is 5.4%. Also in [21], a theory was proposed that explains the mechanism of the formation of an electric barrier at the silicon–silicon carbide interface.

In the paper [23] devoted to the study of SiC/Si thin films of the cubic polytype by UV ellipsometry, it was found that the dielectric constant of a thin intermediate layer formed at the 3C–SiC (111)/Si (111) interface is more characteristic of a semimetal than for a semiconductor. This result was confirmed by quantum-chemical modeling of the properties of the 3C–SiC (111)/Si (111) heterointerface, which showed that the conductivity of this intermediate layer is associated with the p-electrons of the Si atoms most distant from the silicon substrate. The authors of [24] have performed an analysis of the field dependences of the static magnetic susceptibility in SiC/Si samples grown on silicon of various orientations: (100), (110), and (111). It was found that in the SiC/Si (111) and SiC/Si (110) samples, two quantum effects are observed in weak magnetic fields at room temperature. The first effect is the hysteresis of the static magnetic susceptibility, and the second one is the generation of the Aharonov–Bohm oscillations on its field dependences. The first effect is associated with the Meissner–Ochsenfeld effect, while the manifestation of the second one is caused by the presence of microdefects in the form of nanotubes and micropores formed during the synthesis of structures in them under the SiC layer. In SiC/Si (100) structures, these effects do not manifest themselves, which is associated with a different mechanism of the formation of SiC on the Si (100) surface.

18.2.3 Some Applications of the Method of Coordinated Substitution of Atoms for the Formation of Coatings on Various Materials (Porous Silicon, Al₂O₃, Graphite)

Recent works [25, 26] have shown that the atomic substitution method can be successfully applied to deposition of silicon carbide coatings not only on flat polished silicon substrates. Due to the fact that SiC is formed in the near-surface region, and is not deposited from above, as it happens in the usual gas-phase growth methods, it becomes possible to use it when deposited on micro- and mesoporous or specially profiled silicon substrates for pendeo-epitaxy or other applications. Also, using two-stage techniques of silicon deposition with its subsequent transformation into SiC, the method of substitution of atoms can be applied to SiC on other materials, for example, a sapphire substrate, or even as a functional (protective) layer on a graphite surface. This subsection provides information on the results obtained by the Laboratory of Structural and Phase Transformations in Condensed Matter of the IPME RAS in this direction.

18.2.3.1 SiC Coating Deposition on Microporous and Profiled Silicon

In [25, 26], studies were carried out on the formation of silicon carbide layers by the method of atomic substitution on macro- and mesoporous silicon (100) substrates of p- and n-type. To obtain porous silicon structures, the technique of photolithography was used together with etching and subsequent anodizing. After the deposition of a silicon carbide layer on the resulting structure, the samples were investigated by various methods and it was revealed that in the presence of micropores on the surface, silicon is completely transformed into silicon carbide to a depth corresponding to the depth of the original pores. SEM images of the sample before and after the SiC/Si film deposition are shown in Fig. 18.5. Raman and X-ray diffraction analyses confirm that the entire surface layer to a depth corresponding to the pore depth consists of cubic silicon carbide. Polycrystalline 3C-SiC films were formed on mesoporous Si (100) substrates, in which the crystallite size, determined from X-ray diffraction patterns, was 27.5 nm.

Note that this technique makes it possible to obtain surface nano- and microstructures from silicon carbide on silicon in a fairly simple way, using only equipment and reagents designed for working with silicon. At the first stage, the required structure, which is a workpiece, is applied to the surface of a silicon sample using photolithography and etching methods. The sample is then processed in carbon monoxide using the atomic substitution method. As a result, the initial workpiece, either in whole or in part (depending on the processing conditions), is converted into silicon carbide. Thus, a method of SiC layer deposition on a profiled Si surface, which completely retains the initial morphology of the Si surface without geometric distortions, has

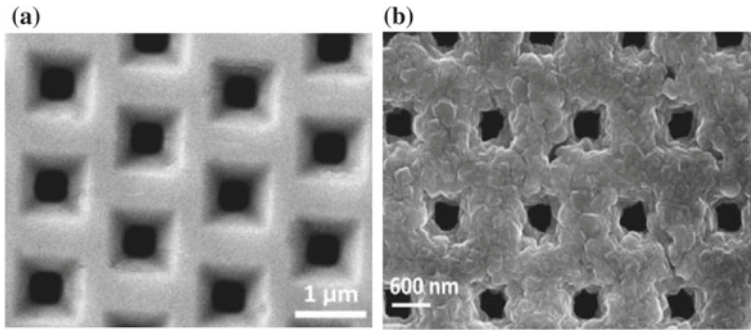


Fig. 18.5 SEM images of the microporous silicon surface before (a) and after (b) deposition of silicon carbide by atomic substitution. Reproduced from [26]

been realized in [27, 28]. In these works, a thin layer of silicon carbide was deposited on a silicon surface, which is a system of pointed “hills” being emitters.

18.2.3.2 A New Method for the Synthesis of Epitaxial Silicon Carbide Films on Other Materials

In [29, 30], a fundamentally new approach was proposed, which makes it possible to deposit thin epitaxial silicon carbide layers not only on silicon but also on any other high-temperature materials, including single-crystal sapphire substrates. To implement the method, a layer of epitaxial silicon with a thickness of up to 400 nm and different orientations (100) and (111) was preliminarily deposited on a sapphire substrate by the method of chemical vapor deposition. Then, the sample was processed according to reaction (1) in order to transform the deposited epitaxial film into a SiC film (see Fig. 18.6). As a result of the experiments, it was shown that, under certain conditions, a high-quality layer of epitaxial SiC of various polytypes can be formed on the sapphire surface. Note that the proposed approach to deposition of silicon carbide coatings on high-temperature materials can find its application not only in semiconductor technology but also for creating a new class of composite, heat-resistant, and other hard coatings.

In [31], the atomic substitution method was used to deposit silicon carbide coatings on graphite samples. To deposit the coating, the graphite surface was brought into contact with a silicon melt in a CO gas atmosphere. The process consists of two simultaneous reactions, one of which is reaction (1), which describes the interaction of molten Si with carbon monoxide (CO), and the second one is the reaction of gaseous silicon monoxide (SiO) with graphite. As a result, the entire surface region of graphite, which has absorbed a silicon melt like a sponge, is transformed into silicon carbide. The thickness of the coatings obtained was up to 1 mm. Note that the deposition of the coating led to a significant hardening of the material: the hardness

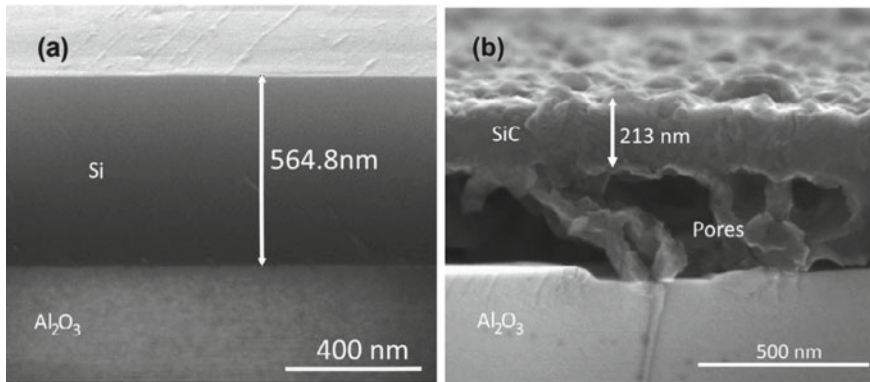


Fig. 18.6 SEM image of the cleaved Si/Al₂O₃ structure before (a) and after (b) the deposition of the SiC layer. Reproduced from [29] by permission from De Gruyter

of the initial material (graphite) and the coated material measured by nanoindentation differed by more than 250 times.

18.2.3.3 Two-Stage Transformation of Silicon into Nanostructured Carbon by the Method of Coordinated Atomic Substitution

In [32], a fundamentally new two-stage method was developed for obtaining epitaxial layers of nanostructured carbon on silicon substrates. At the first stage of conversion, the first half of silicon atoms are consistently replaced by carbon atoms according to reaction (1), during which an epitaxial layer of cubic silicon carbide SiC–3C is obtained. During the second stage, the principle of atomic substitution is also activated, but now the SiC film itself reacts with a reagent gas, as a result of which silicon atoms are replaced by carbon atoms while keeping the original lattice. Tetrafluoromethane CF₄ was used as a reagent gas in [32]. In such a reaction, depending on the initial orientation of silicon and growth conditions, carbon structures with different properties appear on the SiC/Si substrate surface after the synthesis process, such as nanodiamonds, carbon nanotubes, and other carbon nanostructures.

18.3 Growth of Thin Films and Heterostructures on SiC/Si Substrates

Note that the atomic substitution method makes it possible to grow epitaxial nanolayers of silicon carbide with a thickness of 60–100 nm, which is practically not subject to elastic stress, on silicon substrates, despite the ~20% difference in their crystal lattice parameters. The existence of a SiC buffer layer with a porous sublayer makes it

possible to grow high-quality epitaxial layers of wide-bandgap semiconductors, gallium nitrides (GaN), aluminum nitrides (AlN), and their solid solutions, on SiC/(111) Si substrates. This is due to the fact that the lattice parameters of III-nitrides differ by less than a few percent from the corresponding lattice parameters of SiC.

This section presents the latest results on the growth of thin and thick layers and heterostructures of wide-bandgap semiconductors and some other semiconductor compounds on SiC/Si substrates by various methods, including molecular beam epitaxy (MBE), metal–organic epitaxy (MOCVD), and chloride–hydride epitaxy (MBE). Some effects caused by the presence of the SiC buffer layer and the possibilities for the growth of semipolar layers of III-nitrides are discussed.

18.3.1 III-Nitrides (GaN, AlN, AlGaN)

18.3.1.1 Hydride Vapor Phase Epitaxy

One of the most promising methods for the growth of thick layers of III-nitrides, in addition to the ammonothermal method [33], is hydride vapor phase epitaxy (HVPE) [34], which allows the layers to be grown at a high speed, on the order of 60–100 $\mu\text{m}/\text{h}$. In this regard, a significant part of the laboratory's research was aimed at studying the growth mechanisms of GaN and AlN by this method. For growth, a horizontal HVPE setup with a quartz tube diameter of 76 mm and resistive heating was used. For epitaxy, we used SiC/Si substrates grown by the method of atomic substitution with different orientations: SiC/Si (111), SiC/Si (110), and SiC/Si (100). During the deposition of AlN, AlGaN, and GaN, the temperature in the growth zone was 1050 °C, and in the source zone, from 600 to 850 °C. The reagents were hydrogen chloride (HCl) and ammonia (NH₃). High-purity argon (Ar) was used as the transport gas. Metallic gallium (Ga) and aluminum (Al) were used as sources of elements that immediately participated in a chemical reaction. A series of experiments was carried out on the growth of thin and thick layers under various conditions and the mechanisms of growth of III-nitrides, the effect of the substrate on the growth process, and also many properties of the layers obtained were investigated in detail.

Thus, in a series of works [35–37], methods were developed for the growth of thin layers of gallium nitride, aluminum nitride, and AlGaN on the SiC/Si surface. In [35], a three-layer heterostructure was grown, consisting of AlN, AlGaN, and GaN layers (see Fig. 18.7), and the possibility of HVPE growth of A^{III}B^V semiconductor compound films at a high rate was demonstrated ($\sim 66 \mu\text{m}/\text{h}$) without cracks and with small residual elastic stresses ($\sim 160 \text{ MPa}$).

In [36, 37], a new method for the synthesis of semipolar layers of gallium nitride and aluminum nitride on SiC/Si substrates was proposed and implemented, and it was shown that the use of SiC and AlN buffer layers makes it possible to form epitaxial layers of semipolar gallium nitride with a deviation from the polar axis \mathbf{c} of the crystal at an angle of 48–51°. The samples obtained had the minimum X-ray diffraction rocking curve half-width $\omega(\theta) \sim 24'$. In [37], the authors showed that the formation

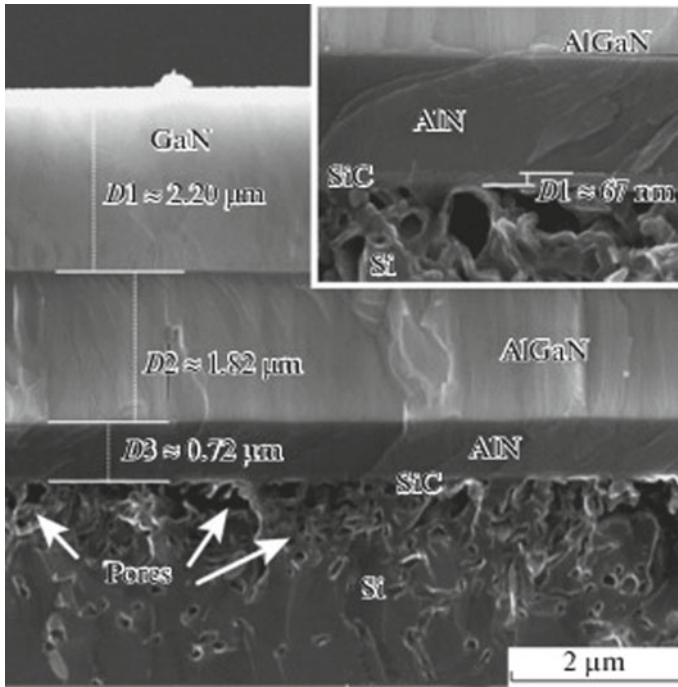


Fig. 18.7 SEM image of the cleaved GaN/AlGaN/AlN/SiC/Si structure. Reproduced from [35] by permission from Springer Nature

of a specially oriented SiC seed layer with subsequent epitaxy of the AlN layer by the HVPE method and low rates ensures the growth of aluminum and gallium nitrides in the semipolar direction. In [38], this technique was developed, and the possibility of obtaining bulk semipolar AlN films on SiC/Si (001) was demonstrated. In the same work, the authors compared the growth of AlN on Si (100) and SiC/Si (100) substrates and showed that an AlN layer grown on a Si substrate is stretched, while an AlN layer grown on a hybrid SiC/Si substrate, on the contrary, experiences compressive loads. The limiting (critical) thickness of the semipolar AlN layer on the Si (100) substrate was determined to be $\sim 7.5 \mu\text{m}$, after which cracking and delamination from the substrate occurred. Note that it was possible to grow semipolar AlN films with a thickness of more than $40 \mu\text{m}$ on SiC/Si substrates without cracking and exfoliation from the substrate.

In [39], the main features of the growth of bulk AlN, AlGaN and GaN with a thickness of $100 \mu\text{m}$ and more were outlined (see Fig. 18.8), and it was also shown that in some cases their natural exfoliation from the substrate is possible in order to transfer to others (for example, heat sink) substrates. A number of structural, physical, and chemical features of the SiC/Si film are discussed in comparison with SiC layers grown on Si by standard methods, and it is shown that these features provide the possibility of growing thick AlN, AlGaN, and GaN layers with their subsequent

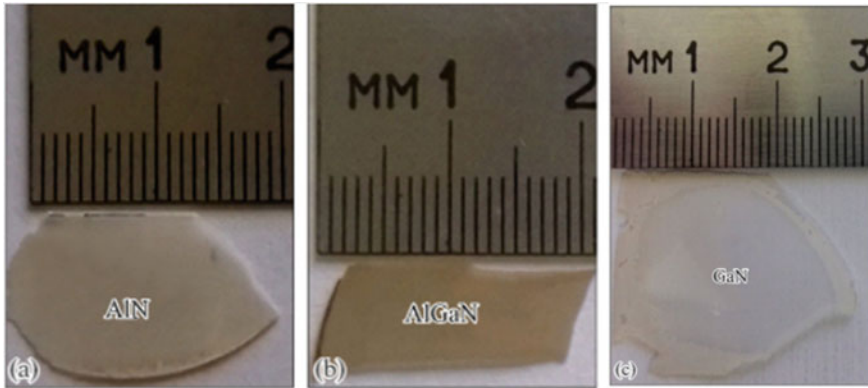


Fig. 18.8 Bulk layers of III-nitrides grown on the SiC/Si surface and separated from the substrate. **a**—AlN, **b**—AlGaN, **c**—GaN. Reproduced from [39] by permission from Springer Nature

exfoliation from the substrate. As a result, the authors obtained and investigated single-crystal AlN layers without cracks up to 300 μm thick, AlGaN layers up to 400 μm thick, GaN layers up to 200 μm thick, and semipolar (11 $\bar{2}$ 4) GaN films with thickness up to 30 μm .

Note that, the growth of $\text{Al}_x\text{Ga}_{1-x}\text{N}$ solid solutions was found to be accompanied by the phenomenon of self-organized composition change in composition at different depths. For example, it was found in [40] that the growth of $\text{Al}_x\text{Ga}_{1-x}\text{N}$ layers with a low (about 11–24%) Al content gives rise to interlayers or domains consisting of AlGaN of stoichiometric composition. In [40], this phenomenon was explained by two processes: the first process is the competition of two chemical reactions for the formation of GaN and AlN, proceeding at different rates; the second process, closely related to the first one, is the appearance and relaxation of elastic stresses as $\text{Al}_x\text{Ga}_{1-x}\text{N}$ films grow on SiC/Si (111). Both processes influence each other, which leads to a complex pattern of aperiodic composition changes along the film layer thickness.

Note that the mechanism of the formation of III-nitride thin films on the SiC surface substantially depends on the SiC surface structure, which, in turn, is determined by the type of doping (see Sect. 18.2.2.1). In this regard, the mechanisms of growth and the structure of epitaxial layers of semipolar AlN and GaN grown on a SiC/Si substrate with initial Si of various conductivity types (n- and p-type) were investigated in [41]. The authors showed experimentally that the mechanisms of growth of AlN and GaN layers on n- and p-type substrates are fundamentally different: an epitaxial structure grows on a SiC/p-Si (100) substrate, whereas on a SiC/Si (100) substrate, the nucleation of a polycrystal is more probable.

In [42], the authors investigated the growth mechanisms of GaN films on SiC/Si at various levels of supersaturation. Growth regimes were found in which both spiral and stepwise growth of this material is realized (see Fig. 18.9). The realization of both regimes was considered theoretically (see Sect. 18.5), and the dependences of

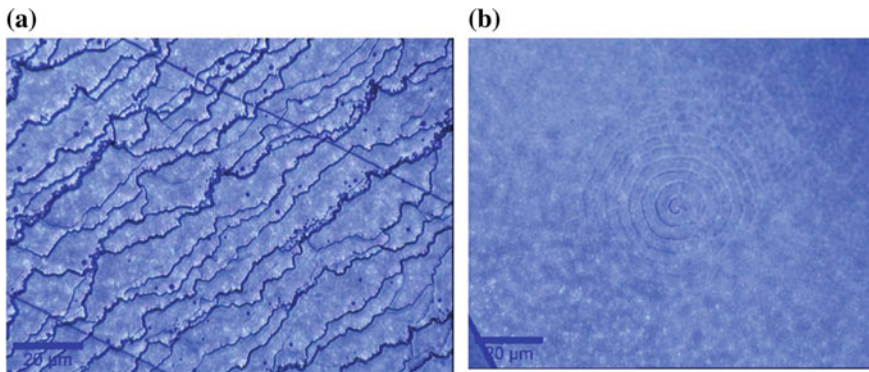


Fig. 18.9 Layer-by-layer growth and step-bunching (a) as well as helical growth (b) of a GaN crystal during HVPE growth. Reproduced from [42]

the crystal growth rate on the growth conditions in these regimes were found. The elastic stresses in a thin GaN film were also estimated using Raman spectroscopy, which gave a value of the order of 100–200 MPa.

In a series of works [43–45], detailed studies of defects in GaN and AlN layers were carried out by the method of high-resolution transmission electron microscopy. In these works, thick semipolar GaN layers (up to 15 μm) grown on SiC/Si (100) substrates with a deviation from the basal plane by angles of 4° and 7° were investigated, and it was revealed that defects in the semipolar layer are asymmetric. The authors showed that the main type of defects in the GaN layer are stacking faults in the basal plane and partial dislocations bounding them. The deviation of the c axis of the GaN layer from the axis of the intermediate AlN layer (epitaxial tilt) was also found and explained. In [44], the authors studied dislocation reactions in semipolar layers of gallium nitride, in particular, the interaction of $a + c$ and a -dislocations, and showed that the propagation of an a -type dislocation half-loop with the Burgers vector $\mathbf{b} = 1/3 \langle 1\bar{2}10 \rangle$ at cooling can be blocked due to its reaction with an $a+c$ dislocation with the Burgers vector $\mathbf{b} = 1/3 \langle 1\bar{2}1\bar{3} \rangle$ resulting in formation of a dislocation segment of the c -type with the Burgers vector $\mathbf{b} = \langle 0001 \rangle$. In [45], the authors investigated the phenomenon of a change in the propagation direction of misfit dislocations during the growth of a GaN layer on the surface of the AlN/SiC/Si (111) structure. This phenomenon manifests itself when gallium nitride reaches a certain thickness of ~ 300 nm. In this case, the misfit dislocations oriented along the growth axis of the layer stop and begin to propagate in the direction perpendicular to the growth axis. A theoretical model of the nucleation of AlN and GaN on the (111) SiC/Si face explaining this effect was constructed. The effect of a change in the film growth mechanism from the nucleation of islands for AlN on SiC/Si (111) to a layer-by-layer one for a GaN layer growing on an AlN/SiC/Si surface was also theoretically predicted and experimentally observed. Studies have shown that a SiC/Si substrate with an AlN buffer layer makes it possible to grow low-defect unstressed GaN layers, and its structure

resembles the foundation of a house built on soft soil or permafrost. This foundation adapts to external conditions, while maintaining an almost unstressed, ordered structure. Some of the stresses that remain in some cases can relax by various mechanisms. Thus, in [46], the stress relaxation and the conditions for the formation of dislocations, cracks and bulges in the epitaxial AlN (0001)/SiC/Si (111) heterostructure were studied in detail. It also proposed a method for assessing the imperfection and defect content in the grown thin films by measuring the temperature dependence of the curvature of the substrate with the grown heterostructure, and calculated the criteria for the formation and preferred orientation of defects (dislocations, cracks, delamination, bulges) in AlN/SiC/Si films.

Note that to reduce elastic stresses during the growth of heterostructures, pendeo-epitaxy [3] and growth on porous substrates are used, which makes it possible to reduce the contact between the substrate and the growing film, and, as a consequence, to reduce the propagation of dislocations initially present in the substrate into the film. Similar studies were carried out for SiC/Si substrates. Thus, in [47], a new approach to the pendeo-epitaxy of unstressed AlN films was developed. For the synthesis of AlN, a SiC/Si substrate was used, on which a two-dimensional array of “wells” ~200 nm in diameter, 400 nm period, and ~70 nm deep (smaller than the SiC layer thickness) was formed. On this substrate, in one process of hydride-chloride epitaxy, an AlN film was grown both in the area with “wells” and in the smooth areas. As a result of studies of the grown film by various methods, including Raman spectroscopy, it was shown that the part grown on the “wells” is subject to lower elastic stresses than the part grown on the smooth region of the SiC/Si substrate. In turn, the mechanisms of growth of GaN films on porous SiC/Si substrates were studied in [48]. In this case, however, a slightly different approach to pore deposition was used. An array of micro- and mesopores was initially formed in silicon (see Sect. 18.2.3). Then, SiC was deposited on the surface of porous silicon by the method of atomic substitution, and after that, an AlN buffer layer 500 nm thick was grown on the surface of the obtained SiC/Si samples. The next step was the deposition of a 5 μm thick GaN layer. Studies have shown that the pores introduced into the initial silicon, although they make a large contribution to the relaxation of mechanical stress in GaN films grown on Si, are themselves a source of various defects, as a result of which dislocations and etching pits are formed in GaN. The results obtained indicate that it is better to form an ensemble of pores not on the initial Si surface, but on the surface of the formed SiC layer, as was done in the AlN pendeo-epitaxy [47]. Thus, for additional relaxation of elastic stresses during the growth of GaN and AlN films on SiC/Si, it is preferable to form an array of shallow pores (that do not penetrate into the silicon matrix) already on the formed SiC layer, rather than to form pores in the initial silicon prior to SiC deposition.

Since aluminum nitride layers are of considerable interest in the field of infrared technology and micromechanics (MEMS), a series of works [49–51] was carried out to study their dielectric and pyro properties. For example, in [51], the results of pyro- and piezoelectric studies of AlN films grown on SiC/Si substrates by both HVPE and MBE are presented. It was found that the vertical component of the piezoresponse in AlN films grown by the HVPE method is more spatially uniform than in AlN films

grown by the MBE method. However, the signal from the AlN films synthesized by the MBE method turned out to be stronger. It was found experimentally that the polar axis in films grown by the MBE method is directed from the free surface of the film to the Si substrate, while in HVPE films, the polarization vector, on the contrary, is directed toward the free surface. Thus, polarization vector is highly dependent on the deposition method.

In [49], a dynamic pyroelectric response of the AlN layer was found. The kinetics of the pyroelectric current was analyzed in the frequency range 10–1000 Hz, and the calculated pyroelectric coefficient was about $9 \cdot 10^{-10}$ C/(cm²K). Note that this value practically corresponds to the pyroelectric coefficient characteristic of textured hexagonal AlN films grown directly on Si substrates. In [50], the effect of the initial orientation of a silicon substrate on the properties of AlN films was studied. In the experiments, we used SiC films grown on the surfaces of Si (100), (110), and (111) substrates, as well as on vicinal surfaces (100), (110), and (111) deviated from these basic orientations by 2°. 10°. The results of studying the polar properties by two independent methods, i.e. dynamic pyroelectric effect and force microscopy of the piezoresponse, show that the use of a SiC buffer layer significantly improves the polar properties of a thin layer of aluminum nitride. In [52], the piezoelectric properties of AlN crystals grown by sublimation and HVPE on SiC/Si substrates were investigated and compared. The calculated piezoelectric coefficient for the AlN/SiC/Si d₃₁ crystal was determined to be of the order of $1.6 \cdot 10^{-12}$ m/V.

In [53, 54], the structural and mechanical characteristics of GaN and AlN films grown on SiC/Si substrates were studied. The Young's modulus of the GaN and AlN epitaxial layers on SiC/Si, determined using the nanoindentation method are 265 GPa and 223 GPa, respectively. Note that the AlN film, according to ellipsometry data, contained 1.5% excess aluminum.

18.3.1.2 Organometallic Epitaxy

Organometallic epitaxy (MOCVD), due to the rather high growth rates, on the one hand, and the possibility of more precise control of thickness and uniformity than HVPE, is widely used for the growth of device heterostructures. This section presents the results on the deposition of III-nitride films on SiC/Si substrates by the MOCVD method. Note that although the SiC buffer layer was mainly referred to as a layer that allows one to reduce elastic stress in growing films, it also plays another important role. Namely, SiC acts as a chemical shield for the Si substrate. It prevents the silicon of the substrate from interacting with gallium remaining in the reactor after previous growth cycles on the walls. When growth is carried out on clean silicon substrates, this phenomenon can lead to the appearance of additional defects in the growing layers and the appearance of V-defects on the surface of the GaN films.

Another “chemical” problem that arises during growth on pure silicon is the interaction of ammonia with Si, leading to the formation of an amorphous SiN layer at the AlN/Si interface [55]. The most common way to avoid SiN formation is to use Al pre-precipitation, but in some cases this is not sufficient and a reduction in the

initial growth temperature is also necessary [56]. The use of SiC/Si films can help overcome these problems at the initial stage of growth. The SiC layers are stable under typical MOCVD conditions, therefore, no other chemical reactions can occur at the interface besides the epitaxial growth of AlN.

To test this hypothesis, experiments on the growth of AlGa_N heterostructures on SiC/Si substrates were carried out in [57]. TEM study of the grown samples showed clear crystalline interfaces with an epitaxial ratio between the SiC/Si and AlN/SiC layers, without the presence of amorphous regions. Thus, it was confirmed that the SiC layer also protects the Si surface from residual metal particles in the reactor chamber at the initial stage of growth. It was found that the surface roughness of SiC, which is mainly determined by the total pressure and the CO/SiH₄ ratio in the gas phase during SiC synthesis, strongly affects the density of pits (V-defects) in the upper GaN layers. By optimizing the morphology and thickness of the AlN and SiC seed layer, we determined the conditions under which GaN layers grow without V-defects on the surface.

Note that as was found in [57], the doping degree of the initial silicon affects the final density of V-defects. As a result the following conclusions were drawn: the quality and structure of the SiC layer have a significant effect on the density of defects and, first of all, on the density of dislocations in the GaN layers; the formation of V-defects, as a rule, occurs at the grain boundaries, where a bundle of dislocations is formed. Besides, a decrease in the thickness of the AlN layer leads to two effects: a decrease in the dislocation density in the AlGa_N layer and a sharp (up to complete disappearance) decrease in the density of V-defects in the GaN layer. And finally, a decrease in the dislocation density in the AlGa_N layer does not affect the change in the dislocation density in the bulk of the GaN layer. For all studied structures on SiC/Si, a decrease in the dislocation density at the AlGa_N/GaN interface was observed in comparison with the samples grown on pure silicon.

One of the explanations for the latter fact may be that aluminum-containing layers grow by the mechanism of three-dimensional growth (islands, columns), and the growth of further structures is partially similar to the ELOG process (epitaxial lateral growth), in which the dislocation density is often significantly lower; the creation of a low-temperature AlN insert with a simultaneous decrease in the thickness of the AlN layer to values no more than 50 nm makes it possible to almost completely prevent the formation of V defects in the GaN layer. In this case, the density of screw and mixed dislocations in the studied GaN layers was in the range from $5 \cdot 10^9$ to $1 \cdot 10^{10} \text{ cm}^{-2}$.

In [58], a method was proposed for the growth of semipolar gallium nitride by the MOCVD method using a specially profiled silicon substrate with a characteristic element size of about 100 nm. Figure 18.10 schematically shows the growth mechanisms of a GaN film on such a substrate.

The experiments showed that the deposition of 3C-SiC and AlN buffer layers makes it possible to form a semipolar GaN layer (10–11), characterized by an X-ray diffraction rocking curve with FWHM $\omega(\theta) \approx 45^\circ$. To describe this process, a model was proposed based on the anisotropic nucleation of the AlN buffer layer on a profiled substrate.

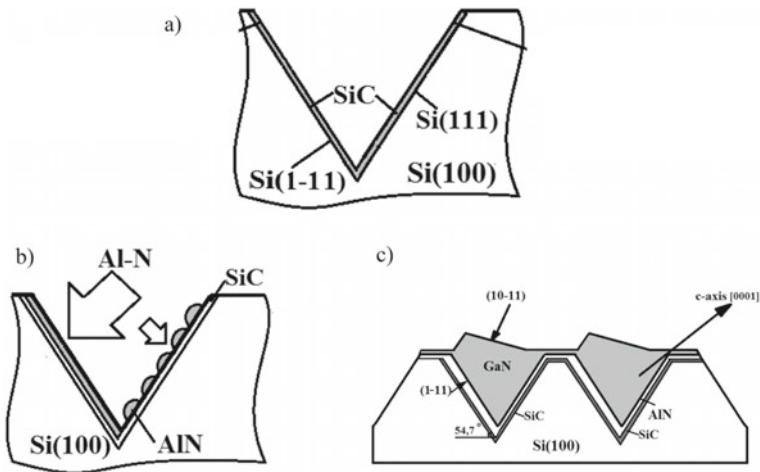


Fig. 18.10 Schematic mechanism of GaN growth on a profiled substrate with a SiC/Si layer: **a** formation of thin SiC film on profiled Si; **b** formation of thin AlN layer; **c** growth of GaN on top of profiled AlN/SiC/Si. Reproduced from [58] by permission from John Wiley and Sons

In [59], the mechanical properties and mechanisms of cracking of a gallium nitride thin film grown on SiC/Si were studied by the nanoindentation method. Using confocal Raman microscopy, the authors constructed three-dimensional maps of residual elastic stresses, mechanical stresses and crystal quality of both GaN and silicon near the indentation for different indentation depths. The obtained values of the hardness and Young's modulus of GaN were $H = 21.1$ GPa, $E = 317$ GPa, respectively, which is close to the values for a high-quality GaN crystal. Note that the elasticity modulus of MOCVD-GaN was found to be higher than that of HVPE-GaN (see the section above). The fairly good quality of the GaN film is also confirmed by the small FWHM (~ 10 arcmin) of the X-ray diffraction rocking curve and the FWHM (3.65 cm^{-1}) of the 568 cm^{-1} Raman line.

18.3.1.3 Molecular Beam Epitaxy

In a series of experiments on the growth of gallium nitride on SiC/Si substrates by the MBE method with plasma activation of nitrogen (NPA-MBE), a number of features were also found due to the presence of the SiC buffer layer. Thus, in [60, 61], gallium nitride films were grown in a single growth process both on SiC/Si substrates and on silicon substrates without buffer layers (see Fig. 18.11). Comparison of the GaN samples showed that an N-polar film grows on the SiC/Si (111) substrate, while the formation of a Ga-polar film is observed on Si. It was found that GaN films grown on a SiC buffer layer have a higher crystal quality and a lower FWHM ($36'$) of the X-ray rocking curve, while for the GaN/Si (111) sample this value was $53'$. The

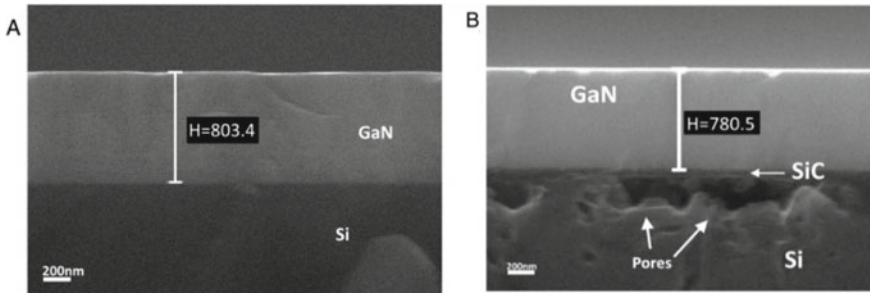


Fig. 18.11 SEM image of a cleaved GaN/Si (111) (a) and GaN/SiC/Si (111) samples grown by the PA-MBE method. Reproduced from [60] by permission from Elsevier

evaluation of the mechanical stress gave a tensile stress of 150 MPa in a GaN/Si (111) sample and a compressive stress of 190 MPa in a GaN/SiC/Si (111) sample. The formation of triangular-shaped GaN islands on the sample surface is revealed, and it is shown that islands are formed on the Si substrate more actively than on the SiC/Si substrate. Note that the goal of [60] was to show the phenomenon of a GaN polarity reversal upon adding a SiC buffer layer, and the quality of the growing GaN films could be much higher, and the mechanical stresses could be lower if we used an additional AlN buffer layer deposited on SiC/Si, as shown in the previous sections. Nevertheless, the experimental results obtained [60] indicate a positive effect of the SiC buffer layer on the quality of GaN thin films grown using NPA-MBE.

Developing these results, the authors of [62] proposed a method for controlling the polarity of gallium nitride layers during their epitaxial synthesis. The method includes two stages: at the first stage, a transitional N-polar GaN layer is grown on the SiC/Si (111) surface by MBE with plasma activation of nitrogen. At the second stage, two layers are grown on the obtained N-polar GaN layer by HVPE: an intermediate AlN layer, and then a GaN layer, which at this stage grows already in a polar Ga-orientation.

In [63], the process of nitridation of the Si (111) and SiC/Si (111) surfaces was studied. Photoelectron spectroscopy revealed that the film obtained by nitriding a silicon substrate at a high temperature (840 °C) has a stoichiometry of Si_3N_4 . It was found that nitriding of the SiC surface also leads to the formation of a surface layer of silicon nitride. However, the SiCN layer consists of both stoichiometric silicon nitride (Si_4^+) and other subnitrides (at least Si_3^+).

In the experiments on GaN growth by the NPA-MBE method [60–63], the following results were obtained. First, the plasma activation of the surface of the SiC/Si (111) and Si (111) samples makes it possible to remove parts of the defective surface layer of SiC (111). In addition, the carbon-vacancy structures are also partially removed. Second, it was shown that high-temperature nitridization of substrates with subsequent growth of GaN in two stages makes it possible to obtain stoichiometric, continuous, and smooth GaN layers both on hybrid SiC/Si (111) and Si (111) substrates. The conditions for such growth were also identified. In the first stage,

the growth of the seed low-temperature GaN layer must be carried out at a substrate temperature $T_S = 650^\circ\text{C}$ and flux densities $F_{Ga} = F_N = 0.1 \mu\text{m/h}$, and in the second stage (at the GaN growth stage), it is necessary to maintain the substrate temperature $T_S = 730^\circ\text{C}$ and the flux density $F_{Ga} = 0.6 \mu\text{m/h}$ and $F_N = 0.1 \mu\text{m/h}$. Third, experiments have confirmed that the structural quality of the GaN layer grown on a SiC/Si substrate (111), much higher than the GaN layer on the Si (111) substrate. Fourth, it was found that the GaN-SiC interface is smoother than GaN-Si and contains a 10 nm thick layer being a solid solution of SiC and GaN.

The experimental study and comparison of the photoelectric properties of GaN layers on the Si (111) and SiC/Si (111) substrates mentioned above has been performed in [64]. The authors have revealed a significant effect of carbon-vacancy structures contained in the SiC layer on the subsequent growth of gallium nitride and its properties. Measurements have shown that the GaN/SiC/Si (111) sample has a higher photosensitivity than GaN/Si (111). In GaN/SiC/Si (111), the coexistence of two oppositely directed p-n junctions was found, one of which is formed at the SiC/Si interface, and the other at the GaN/SiC interface. In this sample, the effect of inversion of the forward and reverse I-V characteristics is observed under illumination with light with a wavelength $\lambda \leq 350 \text{ nm}$. In the spectral range $\lambda \geq 380 \text{ nm}$, the GaN layer does not absorb, and the photosensitivity is determined by the SiC/Si (111) heterojunction. At $\lambda \leq 350 \text{ nm}$, the GaN/SiC heterojunction becomes active and determines the photosensitivity of the sample. In turn, an analysis of the I-V characteristics of the GaN/Si (111) heterostructure confirmed the absence of a p-n junction in this sample.

In [64], the electronic and photoemission properties of GaN/SiC/Si (111) layers were studied. The authors investigated the electronic structure of the GaN surface and an ultrathin Li/GaN interface using various Li submonolayer coatings. Based on the analysis of the evolution of the spectra of surface states and the spectra of core levels, the activity of the N and Ga dangling bonds on the GaN surface was discovered and investigated.

In a series of works [65, 66], the effect of a mesoporous layer introduced into the initial silicon before the SiC growth on the properties of gallium nitride films obtained by the NPA-MBE method was also studied. The authors found that the introduction of a porous silicon layer Si into a SiC/Si substrate provides unambiguous advantages over standard silicon substrates. In particular, this approach allows one to reduce the stress level in the crystal lattice of the epitaxial GaN layer by about 90% and to reduce the proportion of vertical dislocations in the GaN layer. It was found for the first time that the use of a porous layer leads to the formation of a qualitatively more uniform GaN layer without visible extended defects. It was found that the growth by the NPA-MBE method makes it possible to obtain a GaN film of a higher structural and optical quality at a lower growth temperature compared to the growth on porous Si substrates, for example, by the HVPE method (see Sect. 18.3.1.1).

18.3.2 *Methods for Separating III-N Epitaxial Heterostructures from a Silicon Substrate*

Note that new-generation heterostructures and devices based on III-nitrides are capable of operating at significantly higher frequencies, currents, voltages, and temperatures than conventional silicon. This requires to dissipate large heat powers. One of the advantages of SiC/Si substrates grown by the atomic substitution method is the possibility of efficient separation of the grown III-nitride heterostructures from the substrate by chemical etching without the use of complex methods (laser cutting, etc.). This makes it possible to transfer the working heterostructure to other substrates, in particular, for better heat dissipation.

To date, two separation technologies have been developed. The first of them is described in papers [67, 68]. They present a chemical etching method for separating GaN and AlN epitaxial heterostructures grown on SiC/Si. For this purpose, GaN/AlN/SiC/Si and AlN/SiC samples 2.5 μm and 18 μm thick were subjected to chemical etching in a solution containing a mixture of nitric and hydrofluoric acids and water in a ratio of 4: 1: 5, respectively. This mixture effectively removes silicon. Etching was carried out for 15–20 min at a temperature of 20 °C, after which the heterostructure was completely detached from the substrate without cracking or other defects. This fast and efficient chemical etching is due to the pore system under the SiC surface in the silicon substrate. Through this system of pores, the etchant quickly penetrates under the entire area of the heterostructure and eliminates all places of contact between the Si substrate and the heterostructure (see Figs. 18.12 and 18.13a). Note that, after removing the substrate, the mechanical stresses in the free heterostructure decrease almost to zero, as confirmed by the Raman spectroscopy.

The second separation technology is presented in [62] and patent [69], and consists in the effect of anisotropic etching of GaN layers of different polarity. For example, in Sect. 18.3.1.3 we wrote that during the three-stage growth of GaN/ AlN/GaN on a SiC/Si substrate by NPA-MBE (first layer) and HVPE (AlN layer and second GaN layer), GaN polarity inversion occurs: the first layer has one polarity, and the other is oriented in the opposite direction. If such a sample is etched in a KOH solution, then, due to the anisotropy, KOH will etch only the first N-polar GaN layer, which will eventually lead to its complete dissolution. At the same time, the Ga-polar layer does not react with KOH. Thus, after etching, only the main Ga-polar layer will remain, and GaN will completely separate from the SiC/Si (111) substrate (see Fig. 18.13b)

18.3.3 *Growth of $A^{\text{II}}B^{\text{VI}}$ and Other Semiconductor Compounds*

Since not only III-nitrides are used in modern electronics, but also some other promising semiconductor compounds, for example, gallium oxide Ga_2O_3 , $A^{\text{II}}B^{\text{VI}}$ semiconductors (ZnO, CdSe, CdTe, CdS) and others, a cycle of experiments on the growth of

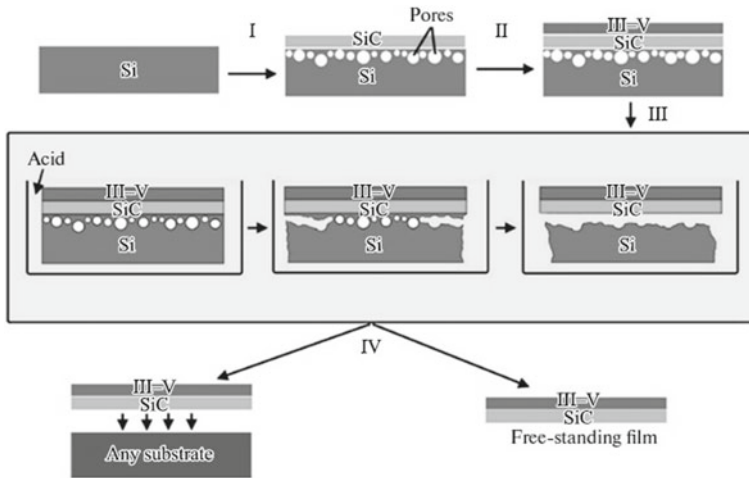


Fig. 18.12 Scheme of separation of the heterostructure from the substrate by chemical etching. Reproduced from [67] by permission from Springer Nature

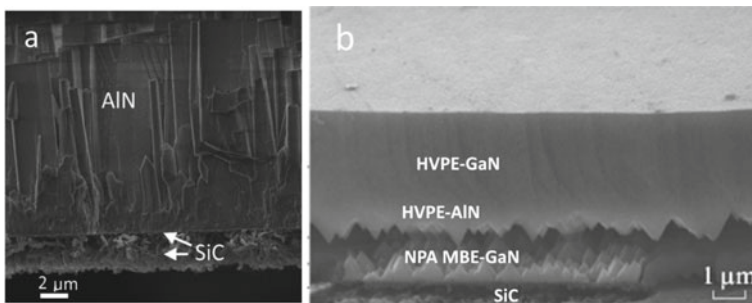


Fig. 18.13 SEM images of a cleavage of a columnar AlN/SiC/Si structure separated from the Si substrate by etching in HNO₃ and HF (a), and a GaN/AlN heterostructure separated from the GaN/SiC/Si substrate as a result of two-stage growth (MBE + HVPE) and a subsequent etching in KOH. Figures are reproduced from [62, 67] by permission from Springer Nature

such materials on SiC/Si substrates was carried out in the Laboratory of Structural and Phase Transformations. This section provides information about these studies.

18.3.3.1 Zinc Oxide ZnO

Zinc oxide ZnO is a direct gap semiconductor with a bandgap of 3.4 eV. In recent years, the interest of researchers in ZnO has significantly increased due to the prospect of its use in thin-film transistors, LEDs, lasers, photodetectors, and other devices. In [70], ZnO films were grown for the first time on SiC/Si substrates by the atomic layer deposition (ALD) method. The films were grown on Si (100) wafers at a temperature

of $T = 250^\circ\text{C}$. The authors showed that the use of SiC as a buffer layer significantly improves the quality of ZnO, providing stoichiometric and epitaxial growth. Ellipsometric analysis showed exceptional uniformity of the ZnO layer thickness, a direct bandgap of ~ 3.4 eV, and almost complete absence of impurities that absorb light at energies below the bandgap. Raman spectroscopy data and electron diffraction analysis showed a high structural perfection of the ZnO layer. The absence of a polycrystalline phase makes this method promising for the growth of ZnO layers on silicon with an intermediate SiC layer. It was found in [71] that the mechanism of formation of epitaxial ZnO textures depends on the substrate conductivity type (n- or p-type). Consequently, a theoretical model was proposed to explain the effect of texture formation and its dependence on the type of conductivity. The effect is associated with the transformation of vicinal Si (100) surfaces into SiC surfaces during its synthesis by atomic substitution. Significant differences were found between the structure and growth mechanisms of ZnO layers on SiC/Si (111) and SiC/Si (100) substrates. The experimental results on the zinc oxide growth by the method of ion-plasma high-frequency magnetron sputtering are presented in [72]. This method also made it possible to obtain epitaxial ZnO films of a sufficiently high crystal quality. In [73], the optical constants of this layer were studied by the ellipsometry method, and one of the main features of the obtained samples was discovered, namely the light absorption in the range of 2.0–3.3 eV, which was explained by elastic stresses in the zinc oxide layer.

18.3.3.2 Cadmium Selenides, Sulfides and Tellurides

Cadmium sulfide (CdS) is a direct bandgap semiconductor with a bandgap of ~ 2.4 eV, which is used in many microelectronic applications including solar cells, photovoltaic converters, lasers, and others. When cadmium sulfide grows on silicon, the problem arises of the chemical interaction of CdS with Si accompanied by the amorphous silicon sulfide (SiS) formation, which greatly worsen the semiconducting properties of growing structures. In [74], the epitaxial growth of cadmium sulfide films in the metastable cubic phase by the ALD method on SiC/Si substrates at a low temperature ($\sim 180^\circ\text{C}$) has been developed. In [75], another growth method was used, namely the method of evaporation and condensation in a closed volume, which also made it possible to obtain epitaxial CdS layers up to 300 nm thick.

Cadmium selenide (CdSe) has a slightly narrower bandgap (1.70 eV in cubic CdSe and 1.73 eV in hexagonal CdSe) and is also of interest in electronic applications being a direct bandgap material. In [76], epitaxial cubic CdSe layers of ~ 350 nm thick were grown for the first time on SiC/Si substrates by the method of evaporation and condensation in a quasi-closed volume, mentioned above. It was found that in this method the optimum substrate temperature is 590°C , the evaporator temperature is 660°C , and the growth time is 2 s. Analysis of the thin film by various methods showed a high structural perfection of the CdSe layer and the absence of a polycrystalline phase in it. In [77], a kinetic model of the growth of CdSe films on SiC/Si substrates was constructed within the framework of the nucleation theory, and two

growth mechanisms were considered: 2D growth (nucleation of disk-shaped nanoislands) and 3D growth (nucleation of hemispherical nanoislands). This model made it possible to estimate the growth conditions (substrate and evaporator temperatures, as well as partial pressures) which determine the dominating growth mechanism.

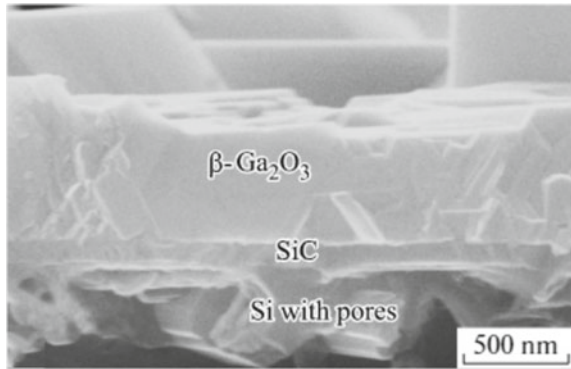
Cadmium telluride (CdTe) is also a direct bandgap (1.49 eV) semiconductor and has applications in solar cells, ionizing radiation detectors, and photodetectors. In [78, 79], epitaxial cadmium telluride films of 1–3 μm thick were grown on SiC/Si substrates. It was found that the optimum substrate temperature is 500 °C at an evaporator temperature of 580 °C, and the growth time is 4 s. Ellipsometric, Raman, X-ray structural and electron diffraction analyzes have shown a high structural perfection of the CdTe layer and the absence of a polycrystalline phase in it. We also performed a theoretical study of the initial stages of nucleation of CdTe films on SiC/Si taking into account the mechanical stresses caused by the lattice mismatch and the difference in the thermal expansion coefficients of the CdTe film and the substrate. The influence of the growth conditions on the nucleation mechanism and the kinetics of the initial stages of growth was estimated, and the optimal conditions were found. Note that the elastic stresses in the CdTe/SiC/Si structure are approximately three times lower than the elastic stresses in a CdTe film coherently grown on a Si substrate without a SiC buffer layer. This leads to a large difference in the rate of nucleation of CdTe films on the SiC/Si substrate and the Si substrate.

18.3.3.3 Gallium Oxide (Ga_2O_3)

Gallium oxide is a promising wide-bandgap semiconductor ($E_g \approx 4.9$ eV) which is currently poorly studied. This material has a number of physical properties that make it quite competitive with silicon carbide and III-nitrides. First of all, it is transparent in the ultraviolet spectrum region and has a high breakdown voltage (8 MV/cm). In addition, Ga_2O_3 is easily doped, which makes it possible to obtain highly conductive layers of this material. In [80], well-textured gallium oxide (β - Ga_2O_3) layers with a thickness of about 1 μm were grown on SiC/Si substrates by the HVPE method (see Fig. 18.14). Studies have shown that the films have a texture close to epitaxial and consist of pure β -phase Ga_2O_3 with orientation (2 $\bar{2}$ 01). In [81, 82], the structural and mechanical properties of gallium oxide films grown on SiC/Si substrates of various orientations (111), (100), (110) were studied experimentally and by simulated numerically using quantum chemistry methods. The following parameters were established: tensile strength, hardness, elastic stiffness constants, elastic compliance constants, Young's modulus, linear compressibility, shear modulus, Poisson's ratio and a number of other characteristics of Ga_2O_3 . It is shown that all these properties of gallium oxide are substantially anisotropic. It was also found that a gallium oxide crystal is an auxetic since Poisson's ratio takes negative values for some stretching directions.

The experimentally determined hardness values of Ga_2O_3 according to Vickers and Young's modulus turned out to be the following: for $\text{Ga}_2\text{O}_3/\text{SiC/Si}$ (001), $H = 11 \pm 1$ GPa, $E = 215 \pm 15$ GPa; for $\text{Ga}_2\text{O}_3/\text{SiC/Si}$ (011), $H = 10 \pm 2$ GPa, $E = 185$

Fig. 18.14 SEM image of a cleaved $\text{Ga}_2\text{O}_3/\text{SiC}/\text{Si}$ film. Reproduced from [81] by permission from Springer Nature



± 25 GPa; for $\text{Ga}_2\text{O}_3/\text{SiC}/\text{Si}$ (111), $H = 9 \pm 2$ GPa, $E = 120 \pm$ GPa. The calculated values are in quantitative agreement with the experimental data. As follows from the results, the orientation of the initial substrate significantly affects the orientation and properties of the grown Ga_2O_3 film.

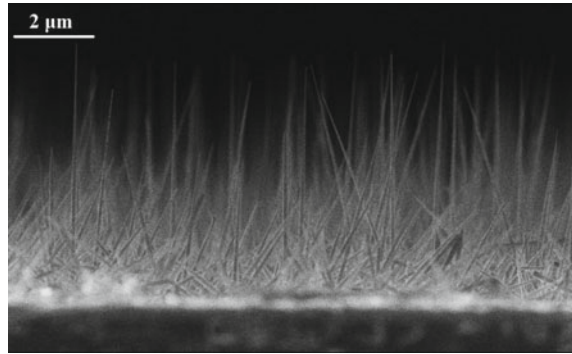
18.4 Growth of Whisker Semiconductor Nanocrystals on SiC/Si Substrates

Whisker nanocrystals (NWCs) usually have a cross-sectional size of the order of 10–100 nm, and their length exceeds the diameter by an order of magnitude or more. Semiconductor NWs are promising from the point of view of their application in microelectronics and optoelectronics as well as in many other fields, for example, as cantilevers of probe microscopes, in gas analyzers, etc. On the basis of such NWs, it is possible to create field-effect transistors, photovoltaic cells, light-emitting elements, and other functional nanodevices. This section presents the results on the growth of whisker nanocrystals of various semiconductor compounds on SiC/Si substrates. The main attention is paid to such semiconductor compounds as GaAs, InAs, GaN, InN, InGaAs, AlGaAs.

18.4.1 Arsenides (*GaAs, AlGaAs, InGaAs, InAs*)

In [83–85], the principal possibility of growing GaAs, AlGaAs (see Fig. 18.15) and InAs NWs on SiC/Si substrates was demonstrated for the first time. Studies have shown that the diameter of NWs growing on SiC/Si is smaller than the diameter of similar NWs grown on a silicon substrate. Thus, for InAs NWs, the minimum diameter was less than 10 nm. In addition, based on photoluminescence measurements, the authors suggested that for AlGaAs NWs grown on SiC/Si substrates a complex

Fig. 18.15 SEM image of AlGaAs/SiC/Si (111) whiskers. Reproduced from [84]



structure is formed due to the self-organized formation of AlGaAs quantum dots, in which the proportion of aluminum differs from that in other sample regions. Note that a similar self-organization phenomenon was also noted in growing AlGaN films (see Sect. 18.3.1.1).

In [85], the growth features and physical properties of small GaAs segments in AlGaAs NWs, growing both on SiC/Si and Si substrates by MBE using gold (Au) droplets were also studied. The influence of the growth conditions of nanowires on their structural and optical properties has been studied in detail. It is shown that, by varying the growth parameters, it is possible to form quantum dot-type structures emitting in a wide wavelength range. In [6, 86], such a combination of a quantum dot and an NWC on a SiC/Si substrate was investigated by the photoluminescence method and was shown that it can be used as single-photon sources.

In [87], InGaAs NWs with different molar fractions of indium were grown by MBE on SiC/Si substrates, and their structural properties depending on the composition were studied. In [88], a new technique was proposed for preparing the substrate to increase the number of vertical InAs NWs growing perpendicular to the substrate, which made it possible to achieve a significantly larger proportion of such NWs in comparison with previous works on the growth of NWs on SiC/Si. Typical length and diameter of NWs were 2 μm and 15–20 nm, respectively, with a surface density of $5 \times 10^8 \text{ cm}^{-2}$. It was shown theoretically that despite the low growth temperature ($\sim 270^\circ\text{C}$) it is possible to grow NWs in the vapor-solid-solid (VSS) mode. In addition, the authors were the first to establish that the presence of elastic stresses due to the lattice mismatch between the solid catalyst particle and the NWC material also affects its growth rate. This phenomenon was also investigated for GaAs NWs in [89, 90] where it was theoretically shown that the intensity of nucleation of coherent islands during the VSS growth can be higher than the intensity of nucleation in the case of vapor-liquid-solid mode growth since in coherent solid-solid pairing the interfacial surface energy can be less. In [91], a theoretical model was constructed to describe the growth of GaAs NWs, which includes the kinetics of material transfer inside a catalyst droplet. The model made it possible to describe the nucleation and growth of 2D islands on the upper face of an NW and to obtain analytical expressions for the

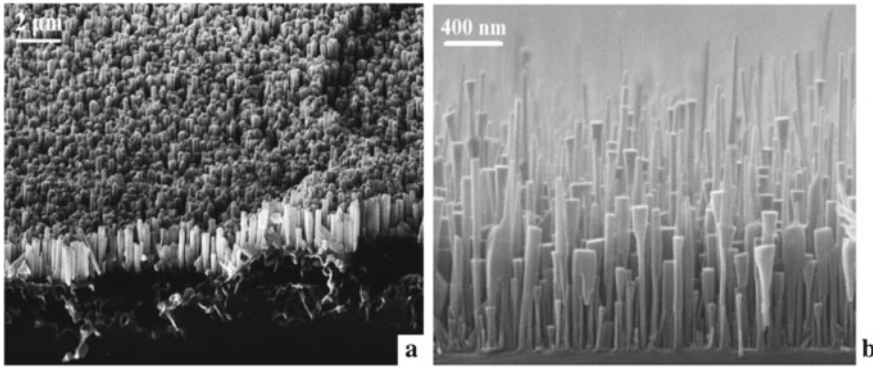


Fig. 18.16 SEM images of GaN **a** and InN **b** NWs grown on SiC/Si substrates. Reproduced from [94]

growth rate of a GaAs disk island due to bulk diffusion of particles in a droplet and for the rate of attachment of GaAs pairs to a critical island. Note that the simulation results are in good agreement with the experimental data and the obtained equations can be applied to simulate the growth of other $A^{III}B^V$ compounds on SiC/Si substrates (and not only on these substrates) using a catalyst.

18.4.2 III-Nitrides (GaN, InN)

In a series of works [92–94], the fundamental possibility of growing GaN NWs and InGaN nanostructures of branched morphology on SiC/Si substrates by MBE method was demonstrated for the first time (see Fig. 18.16). The obtained NWC samples were also compared with similar NWCs on pure silicon substrates, and it was shown that the SiC/Si substrate provides better structural perfection of NWCs as compared to silicon. It is found that the intensity of the photoluminescence spectrum of GaN NWs on a SiC/Si (111) substrate is, as a whole, more than 2 times higher than that of the best GaN NW structures without a silicon carbide buffer layer. InGaN nanostructures turned out to be optically active at room temperature and have a wide visible radiation range.

In [95], a new mechanism of embedding silicon in GaN NWs was discovered and explained, which can provide silicon concentrations in NWs higher than the solubility limit of Si in GaN. The mechanism takes place during growth on misoriented SiC/Si substrates containing groups of steps. The study of the samples by various methods confirmed the high concentration of silicon and even the possibility of the formation of a Ga(Si)N solid solution. This phenomenon can be caused by ascending diffusion due to the mechanochemical effect whereupon the energy-beneficial silicon atoms move into the less stressed NWs.

The authors of [96] investigated the properties of a solar cell based on an array of GaN NWs grown on SiC/Si by MBE. A study of the spectral and current-voltage characteristics of n-GaN/SiC/p-Si with different thicknesses of the SiC diffusion buffer layer showed that buffer layers with a thickness of more than 100 nm provide an increase in the open-circuit voltage and efficiency of the solar cell in comparison with the n-GaN/p-Si heterostructure without a buffer layer.

18.5 Theoretical Approaches Developed to Describe the Growth of Multicomponent Semiconductor Compounds

When studying the growth of thin films of semiconductor compounds, such as GaN, with the crystal unit cell consisting of two different types of atoms, one needs a deep understanding of growth processes and mechanisms as well as phenomena that are caused by the presence of more than one type of atoms. Thus, Fig. 18.9 shows a number of growth mechanisms by which GaN grows under different conditions: layer-by-layer and spiral. To determine the dependence of the growth rate of such a two-component crystal on the growth conditions, a number of problems were solved. Thus, the growth theories, developed to describe the growth of one-component systems by various mechanisms from their own vapors, were extended to the multicomponent case. In particular, models were considered when various types of atoms enter the crystal surface due to chemical reactions. In addition, the mechanisms of the growth and porosity development in crystals under the influence of elastic stresses occurring in films or, for example, in the near-surface region of SiC/Si were studied in detail. This section summarizes the results obtained.

18.5.1 Growth Mechanisms of Multicomponent Semiconductors

In a series of works [97–99] the classical Burton–Cabrera–Frank growth theory has been successively extended to the growth of a single-component crystal due to a chemical reaction [98]; multicomponent crystal from its own vapors [99]; multicomponent crystal due to a chemical reaction [97]. Expressions were found for the movement speed of a single step, a group of equidistant steps, and a step formed by a screw dislocation. It was shown that these processes can be described by the same formulas as in the one-component case, if the averaged values determined by the properties of individual crystal components and their surface concentrations are used for the diffusion coefficient. Estimates are made for the averaged growth rates of GaN. Some features of multicomponent systems with chemical reactions are revealed, such as the dependence of the growth rate at a fixed supersaturation on the

chemical reaction rate, as well as the dependence of the mean free path of adatoms on the absolute pressure in the system. In [100], similar calculations were performed for crystal growth according to the Chernov mechanism [101].

Papers [102, 103] are devoted to the study of the precipitation process of individual component islands on the multicomponent crystal surface during its growth. This phenomenon is often observed when GaN grows in an excess of gallium. In this case, Ga islands are observed on the terraces. Expressions determining the conditions, under which the nucleation of such islands is possible, are derived. The interaction of an individual island and a step on the surface of a multicomponent crystal is investigated, and a calculation is performed for the modes of interaction of a gallium island with a step on the GaN surface. The phenomena considered in [103] can be used for the formation of ordered nanostructures both in the bulk and on the surface of the crystal, including for the self-organized formation of ordered arrays of NWs. In a series of works [104, 105], the phenomenon of morphological instability of a spherical particle or flat surface of GaN, growing in the system by chemical reactions, was investigated. It was shown that the shape instability, i.e. spontaneous self-increasing geometry distortion of the growing crystal can be caused by fluctuations in elastic stresses. Criteria were found for the corresponding shape stability, linking the affinity of a chemical reaction and elastic stresses, and the growth of GaN films on sapphire was analyzed. Note that an analysis of the results in the context of the growth of GaN films showed that growth in an excess of gallium leads to the formation of smoother films, whereas in an excess of nitrogen a characteristic roughness of the order of the free path of gallium atoms may appear.

18.5.2 Growth Mechanisms and Formation of Pores in Multicomponent Crystals

In a series of papers [106–108], the results on the growth mechanisms and morphological instability of multicomponent crystals, using GaN as an example, described in the previous section were extended to the case of vacancy growth of faceted pores in a crystal. They developed the previously proposed approach [109], when a faceted pore is regarded as a crystal of “void” growing due to the diffusion of excess vacancies that arise in the crystal under the influence of elastic loads. In these studies, formulas were found for the dependence of the pore growth rate on the applied load or vacancy concentration. It is shown that in a certain range of small tensile loads, the rate has a quadratic dependence on the load whereas at high loads it is linear. The authors also showed that impurities introduced into the crystal can affect the kinetics of pore growth by these mechanisms. In [108], all the results obtained are extended to a multicomponent system, and the main differences of multicomponent systems from single-component ones as well as from real crystals are given. The theory and approaches proposed in [108] can be used to create porous crystals or crystalline substrates with a given pore distribution, as well as to predict the material lifetime before fracture if it is caused by the growth of faceted pores and their percolation.

18.6 Conclusion

This review reflects the main results obtained after 2015 by the Laboratory of Structural and Phase Transformations using the technology of growing SiC on Si by the method of coordinated substitution of atoms. The physicochemical properties of SiC/Si structures are briefly described, as well as some applications of the atomic substitution method for the deposition of thin films and coatings of SiC on other materials, such as sapphire, graphite, or profiled silicon. Experimental results on the growth of wide-bandgap III-N semiconductors (GaN, AlN, AlGaIn) on SiC/Si substrates needed in the fabrication of new-generation electronic devices are presented. We present also the results on the growth and study of a number of other semiconductor compounds on SiC/Si substrates, such as CdSe, CdTe, CdS, ZnO, Ga₂O₃. In addition, the review describes experiments on the growth of nanocrystals of A³B⁵ group compounds (GaAs, InAs, GaN, InGaIn, AlGaAs), and it is shown that in a number of cases the use of SiC/Si substrates leads to an improvement in the characteristics and the appearance of new effects due to the properties substrate. In the last sections of the review, theoretical results obtained by the laboratory are presented for describing the growth of crystalline multicomponent films (and in particular, GaN) as well as pores in crystals.

Note that to date, working blue and white LEDs based on III-N/SiC/Si heterostructures and various pyro- and piezoelectric sensors have already been manufactured, and work has begun on the creation of transistors with high electron mobility. The studies performed show that the proposed technology for growing SiC/Si substrates, which has already been brought to a semi-industrial scale, is one of the possible ways for the further integration of traditional silicon electronics with technologies based on wide-gap semiconductors and can become a platform for new generations of devices.

Acknowledgements A.V. Redkov expresses gratitude for the support of this work to the Council on Grants of the President of the Russian Federation (Grant No. MK-201.2021.1.2). This work was supported by the Ministry of Science and Higher Education in the framework of the state assignment of the IPME RAS (FFNF-2021-0001). The research was carried out using the equipment of the unique scientific installation “Physics, chemistry and mechanics of crystals and thin films” FSUE IPME RAS (St. Petersburg).

References

1. Takahashi, K., Yoshikawa, A., Sandhu, A. (eds.): Wide Bandgap Semiconductors. Fundamental Properties. Springer, Berlin (2007)
2. Wang, W., Yan, T., Yang, W., Zhu, Y., Wang, H., Li, G., Ye, N.: Epitaxial growth of GaN films on lattice-matched ScAlMgO₄ substrates. *Cryst. Eng. Commun.* **18**(25), 4688–4694 (2016)
3. Zheleva, T.S., Smith, S.A., Thomson, D.B., Linthicum, K.J., Rajagopal, P., Davis, R.F.: Pendeo-epitaxy: a new approach for lateral growth of gallium nitride films. *J. Electron. Mater.* **28**(4), L5–L8 (1999)

4. Beaumont, B., Vennéguès, P., Gibart, P.: Epitaxial lateral overgrowth of GaN. *Physica Status Solidi (b)* **227**(1), 1–43 (2001)
5. Kukushkin, S.A., Osipov, A.V., Bessolov, V.N., Medvedev, B.K., Nevolin, V.K., Tcarik, K.A.: Substrates for epitaxy of gallium nitride: new materials and techniques. *Rev. Adv. Mater. Sci.* **17**(1), 1–32 (2008)
6. Kukushkin, S.A., Osipov, A.V.: Theory and practice of SiC growth on Si and its applications to wide-gap semiconductor films. *J. Phys. D Appl. Phys.* **47**(31), 313001 (2014)
7. Kukushkin, S.A., Osipov, A.V., Feotistov, N.A.: Synthesis of epitaxial silicon carbide films through the substitution of atoms in the silicon crystal lattice: a review. *Phys. Solid State* **56**(8), 1507–1535 (2014)
8. Kukushkin, S.A., Osipov, A.V.: Determining polytype composition of silicon carbide films by UV ellipsometry. *Tech. Phys. Lett.* **42**(2), 175–178 (2016)
9. Kukushkin, S.A., Nussupov, K.K., Osipov, A.V., Beisenkhanov, N.B., Bakranova, D.I.: X-ray reflectometry and simulation of the parameters of SiC epitaxial films on Si (111), grown by the atomic substitution method. *Phys. Solid State* **59**(5), 1014–1026 (2017)
10. Kukushkin, S.A., Osipov, A.V.: The Gorsky effect in the synthesis of silicon-carbide films from silicon by topochemical substitution of atoms. *Tech. Phys. Lett.* **43**(7), 631–634 (2017)
11. Kukushkin, S.A., Nussupov, K.K., Osipov, A.V., Beisenkhanov, N.B., Bakranova, D.I.: Structural properties and parameters of epitaxial silicon carbide films, grown by atomic substitution on the high-resistance (111) oriented silicon. *Superlattices Microstruct.* **111**, 899–911 (2017)
12. Grudinkin, S.A., Golubev, V.G., Osipov, A.V., Feoktistov, N.A., Kukushkin, S.A.: Infrared spectroscopy of silicon carbide layers synthesized by the substitution of atoms on the surface of single-crystal silicon. *Phys. Solid State* **57**(12), 2543–2549 (2015)
13. Kukushkin, S.A., Osipov, A.V.: Mechanism of formation of carbon-vacancy structures in silicon carbide during its growth by atomic substitution. *Phys. Solid State* **60**(9), 1891–1896 (2018)
14. Kukushkin, S.A., Osipov, A.V., Soshnikov, I.P.: Growth of epitaxial SiC layer on Si (100) surface of n- and p-type of conductivity by the atoms substitution method. *Rev. Adv. Mater. Sci.* **52**, 29–42 (2017)
15. Perova, T.S., Wasyluk, J., Kukushkin, S.A., Osipov, A.V., Feoktistov, N.A., Grudinkin, S.A.: Micro-Raman mapping of 3C-SiC thin films grown by solid-gas phase epitaxy on Si (111). *Nanoscale Res. Lett.* **5**(9), 1507–1511 (2010)
16. Grashchenko A., Kukushkin S., Osipov A., Redkov A.: Vacancy growth of monocrystalline SiC from Si by the method of self-consistent substitution of atoms. *Catalysis Today*. In press
17. Redkov, A.V., Grashchenko, A.S., Kukushkin, S.A., Osipov, A.V., Kotlyar, K.P., Likhachev, A.I., Nashchekin, A.V., Soshnikov, I.P.: Studying evolution of the ensemble of micropores in a SiC/Si structure during its growth by the method of atom substitution. *Phys. Solid State* **61**(3), 299–306 (2019)
18. Koryakin, A.A., Ereemeev, Y.A., Osipov, A.V., Kukushkin, S.A.: The influence of the porosity of silicon layer on the elastic properties of hybrid SiC/Si substrates. *Tech. Phys. Lett.* **47**(2), 126–129 (2021)
19. Grashchenko, A.S., Kukushkin, S.A., Osipov, A.V.: Study of elastic properties of SiC films synthesized on Si substrates by the method of atomic substitution. *Phys. Solid State* **61**(12), 2310–2312 (2019)
20. Sergeeva, O.N., Solnyshkin, A.V., Nekrasova, G.M., Senkevich, S.V., Pronin, I.P., Kukushkin, S.A.: Microstructure and electrical response of thin SiC films on Si substrates of p- and n-types. *Ferroelectrics* **542**(1), 52–57 (2019)
21. Grashchenko, A.S., Feoktistov, N.A., Osipov, A.V., Kalinina, E.V., Kukushkin, S.A.: Photoelectric characteristics of silicon carbide-silicon structures grown by the atomic substitution method in a silicon crystal lattice. *Semiconductors* **51**(5), 621–627 (2017)
22. Grashchenko, A.S., Kukushkin, S.A., Osipov, A.V., Feoktistov, N.A.: Dependencies of photoelectric properties of SiC/Si structures grown by the method of atoms substitution on synthesis time. *J. Phys: Conf. Ser.* **872**(1), 012030 (2017)

23. Kukushkin, S.A., Osipov, A.V.: The optical properties, energy band structure, and interfacial conductance of a 3C-SiC (111)/Si (111) heterostructure grown by the method of atomic substitution. *Tech. Phys. Lett.* **46**(11), 1103–1106 (2020)
24. Bagraev, N.T., Kukushkin, S.A., Osipov, A.V., Romanov, V.V., Klyachkin, L.E., Malyarenko, A.M., Khromov, V.S.: Magnetic properties of thin epitaxial SiC layers grown by the atom-substitution method on single-crystal silicon surfaces. *Semiconductors* **55**(2), 137–145 (2021)
25. Kidalov, V.V., Kukushkin, S.A., Osipov, A.V., Redkov, A.V., Grashchenko, A.S., Soshnikov, I.P., Dyadenchuk, A.F.: Properties of SiC films obtained by the method of substitution of atoms on porous silicon. *ECS J. Solid State Sci. Technol.* **7**(4), 158 (2018)
26. Kidalov, V.V., Kukushkin, S.A., Osipov, A.V., Redkov, A.V., Grashchenko, A.S., Soshnikov, I.P., Boiko, M.E., Sharkov, M.D., Diadenchuk, A.F.: Growth of SiC films by the method of substitution of atoms on porous Si (100) and (111) substrates. *Mater. Phys. Mech.* **36**, 39–52 (2018)
27. Grashchenko, A.S., Kukushkin, S.A., Osipov, A.V.: A new method for creating nanoprofiled epitaxial silicon carbide surfaces on silicon. *J. Phys: Conf. Ser.* **1695**(1), 012005 (2020)
28. Grashchenko, A.S., Kukushkin, S.A., Osipov, A.V.: Coating of a nanostructured profiled Si surface with a SiC layer. *Tech. Phys. Lett.* **46**(10), 1012–1015 (2020)
29. Kukushkin, S.A., Osipov, A.V., Redkov, A.V., Grashchenko, A.S., Feoktistov, N.A., Fedotov, S.D., Statsenko, V.N., Sokolov, E.M., Timoshenkov, S.P.: A new Method for synthesis of epitaxial films of silicon carbide on sapphire substrates ($\alpha - Al_2O_3$). *Rev. Adv. Mater. Sci.* **57**(1), 82–96 (2018)
30. Grashchenko, A.S., Kukushkin, S.A., Osipov, A.V., Lukjanov, A.V., Feoktistov, N.A., Redkov, A.V., Svyatets, G.V., Fedotov, S.D., Patent No RU 2684128: “Article with silicon carbide coating and method for manufacturing of article with silicon carbide coating” from 06.04.2018
31. Grashchenko A.S., Kukushkin S.A., Osipov A.V., Redkov A.V., Feoktistov N.A., Patent No RU 2695423: “Article from graphite with modified near-surface layer and method of modification of article surface, having base from graphite” from 26.02.2018
32. Kukushkin, S.A., Osipov, A.V., Feoktistov, N.A.: Two-stage conversion of silicon to nanostructured carbon by the method of coordinated atomic substitution. *Phys. Solid State* **61**(3), 456–463 (2019)
33. Grabianska, K., Kucharski, R., Puchalski, A., Sochacki, T., Bockowski, M.: Recent progress in basic ammonothermal GaN crystal growth. *J. Cryst. Growth* **547**, 125804 (2020)
34. Bockowski, M., Iwinska, M., Amilusik, M., Fijalkowski, M., Lucznik, B., Sochacki, T.: Challenges and future perspectives in HVPE-GaN growth on ammonothermal GaN seeds. *Semicond. Sci. Technol.* **31**(9), 093002 (2016)
35. Sharofidinov, S.S., Kukushkin, S.A., Red'kov, A.V., Grashchenko, A.S., Osipov, A.V.: Growing III-V semiconductor heterostructures on SiC/Si substrates. *Tech. Phys. Lett.* **45**(7), 711–713 (2019)
36. Bessolov, V.N., Konenkova, E.V., Kukushkin, S.A., Myasoedov, A.V., Osipov, A.V., Rodin, S.N., Shcheglov, M.P., Feoktistov, N.A.: Epitaxy of semipolar GaN on a Si (001) substrate with a SiC buffer layer. *Tech. Phys. Lett.* **40**(5), 386–388 (2014)
37. Bessolov, V., Kalmykov, A., Konenkova, E., Kukushkin, S., Myasoedov, A., Poletaev, N., Rodin, S.: Semipolar AlN and GaN on Si (100): HVPE technology and layer properties. *J. Cryst. Growth* **457**, 202–206 (2017)
38. Kukushkin, S.A., Osipov, A.V., Redkov, A.V., Sharofidinov, S.S.: Epitaxial Growth of Bulk Semipolar AlN Films on Si (001) and Hybrid SiC/Si (001) Substrates. *Tech. Phys. Lett.* **46**(6), 539–542 (2020)
39. Kukushkin, S.A., Sharofidinov, S.S.: A new method of growing AlN, GaN, and AlGaIn bulk crystals using hybrid SiC/Si substrates. *Phys. Solid State* **61**(12), 2342–2347 (2019)
40. Kukushkin, S.A., Sharofidinov, S.S., Osipov, A.V., Grashchenko, A.S., Kandakov, A.V., Osipova, E.V., Kotlyar, K.P., Ubyivovk, E.V.: Self-organization of the composition of $Al_xGa_{1-x}N$ films grown on hybrid SiC/Si substrates. *Phys. Solid State* **63**(3), 442–448 (2021)

41. Bessolov, V.N., Grashchenko, A.S., Konenkova, E.V., Myasoedov, A.V., Osipov, A.V., Red'kov, A.V., Rodin, S.N., Rubetz, V.P., Kukushkin, S.A.: Effect of the n and p-type Si (100) substrates with a SiC buffer layer on the growth mechanism and structure of epitaxial layers of semipolar AlN and GaN. *Phys. Solid State* **57**(10), 1966–1971 (2015)
42. Sharofidinov, S.S., Redkov, A.V., Osipov, A.V., Kukushkin, S.A.: GaN growth via HVPE on SiC/Si substrates: growth mechanisms. *J. Phys: Conf. Ser.* **917**(3), 032028 (2017)
43. Sorokin, L.M., Myasoedov, A.V., Kalmykov, A.E., Kirilenko, D.A., Bessolov, V.N., Kukushkin, S.A.: TEM investigation of semipolar GaN layers grown on Si (001) offcut substrates. *Semicond. Sci. Technol.* **30**(11), 114002 (2015)
44. Sorokin, L.M., Gutkin, M.Y., Myasoedov, A.V., Kalmykov, A.E., Bessolov, V.N., Kukushkin, S.A.: Dislocation reactions in a semipolar gallium nitride layer grown on a vicinal Si (001) substrate using aluminum nitride and 3C-SiC buffer layers. *Phys. Solid State* **61**(12), 2316–2320 (2019)
45. Kukushkin, S.A., Osipov, A.V., Bessolov, V.N., Konenkova, E.V., Panteleev, V.N.: Misfit dislocation locking and rotation during gallium nitride growth on SiC/Si substrates. *Phys. Solid State* **59**(4), 674–681 (2017)
46. Telyatnik, R.S., Osipov, A.V., Kukushkin, S.A.: Pore-and delamination-induced mismatch strain relaxation and conditions for the formation of dislocations, cracks, and buckles in the epitaxial AlN (0001)/SiC/Si (111) heterostructure. *Phys. Solid State* **57**(1), 162–172 (2015)
47. Bessolov, V.N., Karpov, D.V., Konenkova, E.V., Lipovskii, A.A., Osipov, A.V., Redkov, A.V., Soshnikov, I.P., Kukushkin, S.A.: Pendeo-epitaxy of stress-free AlN layer on a profiled SiC/Si substrate. *Thin Solid Films* **606**, 74–79 (2016)
48. Kukushkin, S.A., Sharofidinov, S.S., Osipov, A.V., Redkov, A.V., Kidalov, V.V., Grashchenko, A.S., Soshnikov, I.P., Dydenchuk, A.F.: The mechanism of growth of GaN films by the HVPE method on SiC synthesized by the substitution of atoms on porous Si substrates. *ECS J. Solid State Sci. Technol.* **7**(9), 480 (2018)
49. Sergeeva, O.N., Solnyshkin, A.V., Kukushkin, S.A., Osipov, A.V., Sharofidinov, S., Kaptelov, E.Yu., Senkevich, S.V., Pronin, I.P.: New semipolar aluminum nitride thin films: growth mechanisms, structure, dielectric and pyroelectric properties. *Ferroelectrics* **544**(1), 33–37 (2019)
50. Sergeeva, O.N., Solnyshkin, A.V., Kiselev, D.A., Il'ina, T.S., Kukushkin, S.A., Sharofidinov, S.S., Kaptelov, E.Yu., Senkevich, S.V., Pronin, I.P.: Influence of orientation of a silicon substrate with a buffer silicon carbide layer on dielectric and polar properties of aluminum nitride films. *Phys. Solid State* **61**(12), 2386–2391 (2019)
51. Kukushkin, S.A., Osipov, A.V., Sergeeva, O.N., Kiselev, D.A., Bogomolov, A.A., Solnyshkin, A.V., Kaptelov, E.Yu., Senkevich, S.V., Pronin, I.P.: Pyroelectric and piezoelectric responses of thin AlN films epitaxy-grown on a SiC/Si substrate. *Phys. Solid State* **58**(5), 967–970 (2016)
52. Sergeeva, O.N., Solnyshkin, A.V., Kukushkin, S.A., Sharofidinov, S.S., Kazarova, O.P., Mohov, E.N., Kaptelov, E.Yu., Senkevich, S.V., Pronin, I.P.: Dielectric and polar properties of aluminum nitride single crystals. *Ferroelectrics* **576**(1), 55–61 (2021)
53. Grashchenko, A.S., Kukushkin, S.A., Osipov, A.V.: Elastic properties of GaN and AlN films formed on SiC/Si hybrid substrate, a porous basis. *Mech. Solids* **55**(2), 157–161 (2020)
54. Grashchenko, A.S., Kukushkin, S.A., Osipov, A.V.: Strength and structural properties of AlN films grown on SiC/Si substrates synthesized by atomic substitution. *J. Phys: Conf. Ser.* **1410**(1), 012003 (2019)
55. Radtke, G., Couillard, M., Botton, G.A., Zhu, D., Humphreys, C.J.: *Appl. Phys. Lett.* **100**, 011910 (2012)
56. Lahreche, H., Vennegues, P., Tottereau, O., Laugt, M., Lorenzini, P., Leroux, M., Beaumont, B., Gibart, P.: *J. Cryst. Growth* **217**, 13 (2000)
57. Rozhavskaya, M.M., Kukushkin, S.A., Osipov, A.V., Myasoedov, A.V., Troshkov, S.I., Sorokin, L.M., Brunkov, P.N., Baklanov, A.V., Telyatnik, R.S., Juluri, R.R., Pedersen, K., Popok, V.N.: Metal organic vapor phase epitaxy growth of (Al) GaN heterostructures on SiC/Si (111) templates synthesized by topochemical method of atoms substitution. *Phys. Status Solidi (a)* **214**(10), 1700190 (2017)

58. Bessolov, V., Zubkova, A., Konenkova, E., Konenkov, S., Kukushkin, S., Orlova, T., Smirnov, V.: Semipolar GaN (10 $\bar{1}$ 1) Epitaxial Layer Prepared on Nano-Patterned SiC/Si (100) Template. *Phys. Status Solidi (b)* **256**(2), 1800268 (2019)
59. Grashchenko, A.S., Kukushkin, S.A., Osipov, A.V., Redkov, A.V.: Nanoindentation of GaN/SiC thin films on silicon substrate. *J. Phys. Chem. Solids* **102**, 151–156 (2017)
60. Kukushkin, S.A., Mizerov, A.M., Osipov, A.V., Redkov, A.V., Timoshnev, S.N.: Plasma assisted molecular beam epitaxy of thin GaN films on Si (111) and SiC/Si (111) substrates: effect of SiC and polarity issues. *Thin Solid Films* **646**, 158–162 (2018)
61. Kukushkin, S.A., Mizerov, A.M., Osipov, A.V., Redkov, A.V., Telyatnik, R.S., Timoshnev, S.N.: Effect of SiC buffer layer on GaN growth on Si via PA-MBE. *J. Phys: Conf. Ser.* **917**(3), 032038 (2017)
62. Mizerov, A.M., Kukushkin, S.A., Sharofidinov, S.S., Osipov, A.V., Timoshnev, S.N., Shubina, K.Y., Berezovskaya, T.N., Mokhov, D.V., Buravlev, A.D.: Method for controlling the polarity of gallium nitride layers in epitaxial synthesis of GaN/AlN heterostructures on hybrid SiC/Si substrates. *Phys. Solid State* **61**(12), 2277–2281 (2019)
63. Timoshnev, S.N., Mizerov, A.M., Lapushkin, M.N., Kukushkin, S.A., Bouravleuv, A.D.: Electronic structure of SiN layers on Si (111) and SiC/Si (111) substrates. *Semiconductors* **53**(14), 1935–1938 (2019)
64. Timoshnev, S.N., Mizerov, A.M., Benemanskaya, G.V., Kukushkin, S.A., Buravlev, A.D.: Photoemission studies of the electronic structure of GaN grown by plasma assisted molecular beam epitaxy. *Phys. Solid State* **61**(12), 2282–2285 (2019)
65. Seredin, P.V., Goloshchapov, D.L., Zolotukhin, D.S., Lenshin, A.S., Khudyakov, Y.Y., Mizerov, A.M., Kukushkin, S.A.: Influence of a nanoporous silicon layer on the practical implementation and specific features of the epitaxial growth of GaN Layers on SiC/por-Si/c-Si templates. *Semiconductors* **54**, 596–608 (2020)
66. Seredin, P.V., Goloshchapov, D.L., Zolotukhin, D.S., Lenshin, A.S., Mizerov, A.M., Timoshnev, S.N., Kukushkin, S.A.: Optical properties of GaN/SiC/por-Si/Si (111) hybrid heterostructures. *Semiconductors* **54**, 417–425 (2020)
67. Kukushkin, S.A., Osipov, A.V., Red'kov, A.V.: Separation of III-N/SiC epitaxial heterostructure from a Si substrate and their transfer to other substrate types. *Semiconductors* **51**(3), 396–401 (2017)
68. Redkov, A.V., Osipov, A.V., Mukhin, I.S., Kukushkin, S.A.: Separation of stress-free AlN/SiC thin films from Si substrate. *J. Phys: Conf. Ser.* **741**(1), 012034 (2016)
69. Buravlev A.D., Kukushkin S.A, Osipov A.V., Lukyanov A.V., Mizerov A.M., Svyatets G.V., Sobolev M.S., Timoshnev S.N., Sharofidinov Sh. Sh., Patent No RU 2683103: “Method for producing plates of gallium nitride monocrystal” from 06.06.2018
70. Kukushkin, S.A., Osipov, A.V., Romanychev, A.I.: Epitaxial growth of zinc oxide by the method of atomic layer deposition on SiC/Si substrates. *Phys. Solid State* **58**(7), 1448–1452 (2016)
71. Kukushkin, S.A., Osipov, A.V., Kasatkin, I.A., Mikhailovskii, V.Y., Romanychev, A.I.: Formation of ordered ZnO structures grown by the ALD method on hybrid SiC/Si (100) substrates. *Mater. Phys. Mech.* **42**(1), 30–39 (2019)
72. Osipov, A., Kukushkin, S.A., Feoktistov, N.A., Osipova, E., Venugopal, N., Verma, G.D., Gupta, B.K., Mitra, A.: Structural and optical properties of high quality ZnO thin film on Si with SiC buffer layer. *Thin Solid Films* **520**(23), 6836–6840 (2012)
73. Kukushkin, S.A., Osipov, A.V., Osipova, E.V., Razumov, S.V., Kandakov, A.V.: The optical constants of zinc oxide epitaxial films grown on silicon with a buffer nanolayer of silicon carbide. *J. Opt. Technol.* **78**(7), 440–443 (2011)
74. Kukushkin, S.A., Osipov, A.V., Romanychev, A.I., Kasatkin, I.A., Loshachenko, A.S.: Low-temperature growth of the CdS cubic phase by atomic-layer deposition on SiC/Si hybrid substrates. *Tech. Phys. Lett.* **46**(11), 1049–1052 (2020)
75. Antipov, V.V., Kukushkin, S.A., Osipov, A.V.: Epitaxial growth of cadmium sulfide films on silicon. *Phys. Solid State* **58**(3), 629–632 (2016)

76. Antipov, V.V., Kukushkin, S.A., Osipov, A.V., Rubets, V.P.: Epitaxial growth of cadmium selenide films on silicon with a Silicon carbide buffer layer. *Phys. Solid State* **60**(3), 504–509 (2018)
77. Koryakin, A.A., Kukushkin, S.A., Redkov, A.V.: Nucleation of CdSe thin films: the kinetic model *J. Phys.: Conf. Ser.* **1124**(2), 022044 (2018)
78. Antipov, V.V., Kukushkin, S.A., Osipov, A.V.: Epitaxial growth of cadmium telluride films on silicon with a buffer silicon carbide layer. *Phys. Solid State* **59**(2), 399–402 (2017)
79. Koryakin, A.A., Kukushkin, S.A., Redkov, A.V.: Nucleation and growth mechanisms of CdTe thin films on silicon substrates with silicon carbide buffer layers. *Mat. Phys. Mech.* **32**(3) (2017)
80. Kukushkin, S.A., Nikolaev, V.I., Osipov, A.V., Osipova, E.V., Pechnikov, A.I., Feoktistov, N.A.: Epitaxial gallium oxide on a SiC/Si substrate. *Phys. Solid State* **58**(9), 1876–1881 (2016)
81. Osipov, A.V., Grashchenko, A.S., Kukushkin, S.A., Nikolaev, V.I., Osipov, A.V., Pechnikov, A.I., Soshnikov, I.P.: Structural and elastoplastic properties of $\beta - Ga_2O_3$ films grown on hybrid SiC/Si substrates. *Continuum Mech. Thermodyn.* **30**(5), 1059–1068 (2018)
82. Grashchenko, A.S., Kukushkin, S.A., Nikolaev, V.I., Osipov, A.V., Osipova, E.V., Soshnikov, I.P.: Study of the anisotropic elastoplastic properties of $\beta - Ga_2O_3$ films synthesized on SiC/Si substrates. *Phys. Solid State* **60**(5), 852–857 (2018)
83. Reznik, R.R., Kotlyar, K.P., Shtrom, I.V., Soshnikov, I.P., Kukushkin, S.A., Osipov, A.V., Cirlin, G.E.: MBE growth of ultrathin III-V nanowires on a highly mismatched SiC/Si (111) substrate. *Semiconductors* **51**(11), 1472–1476 (2017)
84. Reznik, R.R., Shtrom, I.V., Soshnikov, I.P., Kukushkin, S.A., Zeze, D.A., Cirlin, G.E.: MBE growth of thin AlGaAs nanowires with a complex structure on strongly mismatched SiC/Si (111) substrate. *J. Phys: Conf. Ser.* **1038**(1), 012063 (2018)
85. Cirlin, G.E., Reznik, R.R., Shtrom, I.V., Khrebtov, A.I., Soshnikov, I.P., Kukushkin, S.A., Leandro, L., Kasama, T., Akopian, N.: AlGaAs and AlGaAs/GaAs/AlGaAs nanowires grown by molecular beam epitaxy on silicon substrates. *J. Phys. D: Appl. Phys.* **50**(48), 484003 (2017)
86. Cirlin, G.E., Reznik, R.R., Shtrom, I.V., Khrebtov, A.I., Samsonenko, Y.B., Kukushkin, S.A., Kasama, T., Akopian, N., Leonardo, L.: Hybrid GaAs/AlGaAs nanowire-quantum dot system for single photon sources. *Semiconductors* **52**(4), 462–464 (2018)
87. Reznik, R.R., Kotlyar, K.P., Soshnikov, I.P., Kukushkin, S.A., Osipov, A.V., Cirlin, G.E.: MBE growth and structural properties of InAs and InGaAs nanowires with different mole fraction of In on Si and strongly mismatched SiC/Si (111) substrates. *Semiconductors* **52**(5), 651–653 (2018)
88. Koryakin, A.A., Kukushkin, S.A., Kotlyar, K.P., Ubyivovk, E.D., Reznik, R.R., Cirlin, G.E.: A new insight into the mechanism of low-temperature Au-assisted growth of InAs nanowires. *Cryst. Eng. Commun.* **21**(32), 4707–4717 (2019)
89. Koryakin, A.A., Kukushkin, S.A., Sibirev, N.V.: On the mechanism of the vapor-solid-solid growth of Au-catalyzed GaAs nanowires. *Semiconductors* **53**(3), 350–360 (2019)
90. Koryakin, A.A., Kukushkin, S.A.: Influence of elastic stresses on the vapor-solid-solid growth mechanism of Au-catalyzed GaAs nanowires. *J. Phys: Conf. Ser.* **1124**(2), 022036 (2018)
91. Koryakin, A.A., Kukushkin, S.A. (2021). Self-consistent modeling of nucleation and growth of 2D islands on the top facet of self-catalyzed GaAs nanowires. *Phys. Status Solidi (b)* **258**(6) 2000604 (2021)
92. Reznik, R.R., Kotlyar, K.P., Khrebtov, A.I., Kukushkin, S.A., Kryzhanovskaya, N.V., Cirlin, G.E.: MBE synthesis and properties of GaN NWs on SiC/Si substrate and InGaN nanostructures on Si substrate. *J. Phys: Conf. Ser.* **1537**(1), 012003 (2020)
93. Reznik, R.R., Kotlyar, K.P., Ilkiv, I.V., Khrebtov, A.I., Soshnikov, I.P., Kukushkin, S.A., Osipov, A.V., Nikitina, E.V., Cirlin, G.E.: MBE growth and optical properties of GaN, InN, and Al_{0.3}B_{0.7} nanowires on SiC/Si (111) hybrid substrate. *Adv. Cond. Matter Phys.* **2018**, 1040689 (2018)

94. Reznik, R.R., Kotlyar, K.P., Il'kiv, I.V., Soshnikov, I.P., Kukushkin, S.A., Osipov, A.V., Nikitina, E.V., Cirlin, G.E.: Growth and optical properties of filamentary GaN nanocrystals grown on a hybrid SiC/Si (111) substrate by molecular beam epitaxy. *Phys. Solid State* **58**(10), 1952–1955 (2016)
95. Talalaev, V.G., Tomm, J.W., Kukushkin, S.A., Osipov, A.V., Shtrom, I.V., Kotlyar, K.P., Mahler, F., Schilling, J., Reznik, R.R., Cirlin, G.E.: Ascending Si diffusion into growing GaN nanowires from the SiC/Si substrate: up to the solubility limit and beyond. *Nanotechnology* **31**(29), 294003 (2020)
96. Shugurov, K.Y., Reznik, R.R., Mozharov, A.M., Kotlyar, K.P., Koval, O.Y., Osipov, A.V., Fedorov, V.V., Shtrom, I.V., Bolshakov, A.D., Kukushkin, S.A., Mukhin, I.S., Cirlin, G.E.: Study of SiC buffer layer thickness influence on photovoltaic properties of n-GaN NWs/SiC/p-Si heterostructure. *Mat. Sci. Semicond. Proc.* **90**, 20–25 (2019)
97. Redkov, A.V., Kukushkin, S.A.: Development of Burton-Cabrera-Frank theory for the growth of a Non-Kossel crystal via chemical reaction. *Crystal Growth Des.* **20**(4), 2590–2601 (2020)
98. Redkov, A.V., Kukushkin, S.A., Osipov, A.V.: Spiral growth of a crystal due to chemical reaction. *J. Phys. Conf. Ser.* **1124**(2), 022006 (2018)
99. Redkov, A.V., Kukushkin, S.A., Osipov, A.V.: Spiral growth of a multicomponent crystal from vapor of its components. *J. Cryst. Growth* **548**, 125845 (2020)
100. Redkov, A.V., Kukushkin, S.A., Osipov, A.V.: Growth of a multicomponent crystal via Chernov's mechanism. *J. Phys. Conf. Ser.* **1410**(1), 012039 (2019)
101. Chernov, A.A.: *Modern Crystallography III: Crystal Growth*, vol. 36. Springer, Berlin (1984)
102. Redkov, A.V., Kukushkin, S.A.: Nucleation of nano-islands of pure components during growth of a multicomponent crystal via step-flow mode. *J. Phys.: Conf. Ser.* **1695**(1), 012003 (2020)
103. Redkov, A., Kukushkin, S.: Dynamic interaction of steps and nanoislands during growth of a multicomponent crystal. *Crystal Growth Des.* (2021). <https://doi.org/10.1021/acs.cgd.1c00349>
104. Redkov, A.V., Osipov, A.V., Kukushkin, S.A.: Stability of the surface of an elastically strained multicomponent film in a system with chemical reactions. *Phys. Solid State* **57**(12), 2524–2531 (2015)
105. Kukushkin, S.A., Osipov, A.V., Redkov, A.V.: Morphological stability criterion for a spherical crystallization front in a multicomponent system with chemical reactions. *Phys. Solid State* **56**(12), 2530–2536 (2014)
106. Redkov, A.V., Kukushkin, S.A., Osipov, A.V.: Vacancy growth of a faceted pore in a crystal via Chernov mechanism. *Mech. Solids* **55**(1), 77–83 (2020)
107. Red'kov, A.V.: Growth of faceted pores in a crystal by the Burton-Cabrera-Frank mechanism. *Phys. Solid State* **61**(12), 2392–2396 (2019)
108. Redkov, A.V., Kukushkin, S.A., Osipov, A.V.: Growth of faceted pores in a multi-component crystal by applying mechanical stress. *Cryst. Eng. Commun.* **22**(32), 5280–5288 (2020)
109. Kukushkin, S.A.: Nucleation of pores in brittle solids under load. *J. Appl. Phys.* **98**(3), 033503 (2005)

Chapter 19

Sloshing in a Vertical Cylinder in the Presence of a Porous Layer



Nikolay G. Kuznetsov and Oleg V. Motygin

Abstract An eigenvalue problem for a pair of harmonic functions is considered; it contains a spectral parameter in the Steklov condition on a part of the boundary. This problem concerns eigenvalues of fluid's free oscillations in a vertical, cylindrical container; its cross-section is arbitrary, whereas a porous medium occupies a bottom-adjacent layer. Assuming the fluid to be inviscid, incompressible and heavy, properties of its eigensolutions are investigated.

Keywords Sloshing problem · Fluid in a vertical-walled container · Bottom-adjacent porous layer · Time-periodic motion · Potential theory · Eigenvalues of fluid's free oscillations · Dependence of spectrum on parameters · Damping

19.1 Introduction

Linear theory of water waves is a common tool for studies of sloshing in containers occupied by a fluid of constant density. The corresponding problem involves the homogeneous Neumann condition on the rigid part of container's boundary and the Steklov condition on the free surface of fluid, which contains a spectral parameter depending on the frequency of fluid's oscillations. This problem has been the subject of a great number of papers over more than two centuries; a historical review can be found, for example, in [1], and the classical results are described by Lamb [2]. During the past two decades, at least three books on this topic were published. Two of them, [3, 4], are of interest primarily to engineers; the same concerns the recent survey article [5] containing an extensive bibliography. On the other hand, the comprehensive monograph [6] based on spectral theory of operators in Hilbert

N. G. Kuznetsov · O. V. Motygin (✉)
Institute for Problems in Mechanical Engineering RAS, V.O., Bolshoy pr., 61, St. Petersburg
199178, Russia
e-mail: mov@ipme.ru

© The Author(s), under exclusive license to Springer Nature Switzerland AG 2022
V. A. Polyanskiy and A. K. Belyaev (eds.), *Mechanics and Control of Solids and Structures*, Advanced Structured Materials 164,
https://doi.org/10.1007/978-3-030-93076-9_19

375

space is addressed to mathematicians, both pure and applied. Thus, many aspects of sloshing are studied in great detail.

However, there remain some questions on which our understanding of this phenomenon is still far from complete. According to [5] (especially, see Sect. 4), one of the most important challenges is damping; the latter concerns such characteristics as frequencies and amplitudes of oscillations. The list of references cited in [5] contains a number of related items; also, the results obtained in [7] should be mentioned in this connection. In the latter paper dating back to 1967, Miles investigated the damping of waves in closed basins by means of capillarity and various forms of viscous dissipation. Nevertheless, the question of using a layer of porous material as a means for the sloshing damping has received, to the authors' best knowledge, no attention at all. This looks strange because the propagation of gravity waves over a porous bed accompanied by damping was considered in [8, 9] to mention just a couple of papers.

Thus, the aim of the present paper is to fill in this gap at least partially by studying the modified sloshing problem that involves two extra coupling conditions imposed on the interface between fluid and porous medium. In our study of this problem, we restrict ourselves to the following simple geometry: a vertical-walled cylinder of constant depth and of arbitrary cross-section. This allows us to apply the approach similar to that used in the recent paper [10], where sloshing in a two-layer fluid was investigated under the following assumptions. In an open bounded container, the upper fluid occupies a layer with the free surface on top, whereas below this layer borders with a fluid of greater density. Despite the apparent similarity between these two sloshing problems (both include a pair of coupling conditions on an interface), there is an essential difference; indeed, the problem considered in [10] is self-adjoint, unlike that to be studied here.

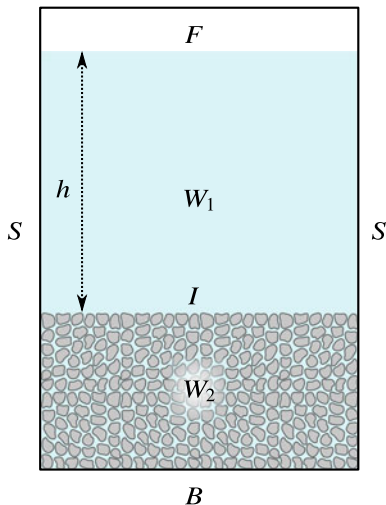
19.2 Statement of the Problem

Let W be a vertical, cylindrical container of constant depth with rigid walls and bottom. We suppose that a layer of porous medium having a constant thickness is adjacent to the bottom, whereas an inviscid, incompressible, heavy fluid, say water, occupies the other part of W as well as gaps in the porous medium. Let the Cartesian coordinates (x_1, x_2, y) be chosen so that the origin lies in the mean free surface of water and the y -axis is directed upwards. Without loss of generality, we use dimensionless variables (the container's depth serves for this purpose and also the acceleration of gravity is taken equal to one), in which case

$$W = \{x = (x_1, x_2) \in D, y \in (-1, 0)\},$$

where D is a bounded, two-dimensional domain with a piecewise-smooth boundary without cusps. Thus,

Fig. 19.1 A sketch of geometry and notation



$$S = \partial D \times (-1, 0), \quad B = \{x \in D, y = -1\} \quad \text{and} \quad F = \{x \in D, y = 0\}$$

are the vertical container’s side-wall, its horizontal bottom and the free surface of water, respectively. Let $I = \{x \in D, y = -h\}$, $h \in (0, 1)$, be the interface, separating

$$W_1 = W \cap \{y \in (-h, 0)\} \quad \text{and} \quad W_2 = W \cap \{y \in (-1, -h)\}$$

occupied by the water and the mixture of water and porous medium, respectively; notation is shown in Fig. 19.1.

In the absence of porous medium, the sloshing is treated as an irrotational, time-periodic motion of water in W with the angular frequency ω , whereas the corresponding velocity field is given by the gradient of the velocity potential

$$\Phi(x, y; t) = \text{Re}\{\phi(x, y) e^{i\omega t}\},$$

where ϕ is harmonic in the water domain W , satisfies the Steklov spectral condition on F and the homogeneous Neumann condition elsewhere on ∂W . In the case under consideration, this remains valid for $\Phi^{(1)}$ defined on $\overline{W_1}$ by the above formula with the superscript added; the only exception is the interface I , where the so-called coupling conditions must hold.

In the porous medium, domain W_2 , the motion of water is also described by the velocity potential $\Phi^{(2)}$ of the same form as $\Phi^{(1)}$, which must satisfy a pair of interface conditions coupling these potentials. The latter conditions involve the characteristics of the porous medium: the porosity ϵ , the linear friction factor f_0 and the inertial term s_0 ; all of them are taken here to be non-negative constants. (The statement in use originates from [11], later adopted in many investigations; see, e.g., [12, 13].)

So, summing up, we seek two velocity potentials

$$\Phi^{(j)}(x, y; t) = \text{Re}\{\phi^{(j)}(x, y) e^{i\omega t}\}, \quad j = 1, 2, \tag{19.1}$$

both belonging to $C(\mathbb{R}; H^1(W_j))$ (the Sobolev space $H^1(W_j)$ is relevant in view of no energy influx). The complex-valued functions $\phi^{(j)}$ must satisfy the coupled boundary value problem:

$$\phi_{x_1x_1}^{(j)} + \phi_{x_2x_2}^{(j)} + \phi_{yy}^{(j)} = 0 \quad \text{in } W_j, \quad j = 1, 2, \tag{19.2}$$

$$\phi_y^{(1)} = \nu \phi^{(1)} \quad \text{on } F, \tag{19.3}$$

$$\phi_y^{(2)} = 0 \quad \text{on } B; \tag{19.4}$$

$$\partial u^{(j)} / \partial n = 0 \quad \text{on } S_j = S \cap \partial W_j, \quad j = 1, 2, \tag{19.5}$$

$$\phi_y^{(1)} = \epsilon \phi_y^{(2)} \quad \text{on } I, \tag{19.6}$$

$$\phi^{(1)} = (s_0 - i f_0) \phi^{(2)} \quad \text{on } I. \tag{19.7}$$

Here ν is the spectral parameter equal to ω^2 and \mathbf{n} is the unit normal to S . The conditions (19.6) and (19.7) mean continuity of normal velocity and pressure, respectively.

By introducing $\bar{\phi}^{(2)}(x, y) = \epsilon \phi^{(2)}(x, y)$, we replace the conditions on the interface I by the following ones:

$$\phi_y^{(1)} = \bar{\phi}_y^{(2)} \quad \text{on } I, \tag{19.8}$$

$$\phi^{(1)} = (s - i f) \bar{\phi}^{(2)} \quad \text{on } I, \tag{19.9}$$

where we thus reduce the number of material parameters of the problem to two:

$$f = f_0/\epsilon, \quad s = s_0/\epsilon.$$

Further, we will assume $\epsilon = 1$ and use notation $\phi^{(2)}$ for $\bar{\phi}^{(2)}$.

According to the first Green's formula for the Laplacian, we have that

$$\int_{\partial W_k} \frac{\partial \phi^{(k)}}{\partial n} dS = 0, \quad k = 1, 2,$$

where dS is the area element on ∂W_k . Then (19.4), (19.5) (with $j = 2$) and (19.8) yield that

$$\int_I \phi_y^{(2)} dx = 0, \quad \text{and so} \quad \int_I \phi_y^{(1)} dx = 0$$

in view of (19.8). Now, the last equality, (19.5) with $j = 1$ and (19.3) imply that the orthogonality condition

$$\int_F \phi^{(1)} dx = 0 \tag{19.10}$$

must hold. Thus, we have problem (19.2)–(19.5), (19.8), (19.9), (19.10) for determining sequences of sloshing eigenvalues $\{v_n\}$ and eigenvectors $\{(\phi_n^{(1)}, \phi_n^{(2)})\}$.

19.3 Separation of Variables

For a homogeneous fluid occupying W , the sloshing problem is equivalent to the free membrane problem. Indeed, let us separate variables as follows:

$$\phi(x, y) = v(x) \cosh k(y + 1).$$

Then problem (19.2)–(19.5) for ϕ complemented by the orthogonality condition (19.10) reduces to the following spectral problem:

$$\nabla_x^2 v + k^2 v = 0 \text{ in } D, \quad \partial v / \partial n_x = 0 \text{ on } \partial D, \quad \int_D v \, dx = 0, \quad (19.11)$$

where $\nabla_x = (\partial/\partial x_1, \partial/\partial x_2)$ and n_x is the unit normal to ∂D in \mathbb{R}^2 . It is clear that \hat{v} is an eigenvalue of the problem for ϕ , if and only if $k^2 > 0$ is an eigenvalue of (19.11) and

$$\hat{v} = k \tanh k. \quad (19.12)$$

It is well known that problem (19.11) has a sequence of positive eigenvalues $\{k_n^2\}_1^\infty$, usually arranged in the increasing order with each eigenvalue repeated according to its multiplicity. The corresponding eigenfunctions $\{v_n\}_1^\infty$ form a complete system in $H^1(D)$. Furthermore, $k_n^2 \rightarrow \infty$, or more precisely, $k_n^2 = 4\pi|D|^{-1}n + o(n)$ as $n \rightarrow \infty$ (see, for example, [14], Chap. VI, Sect. 4). Here $|D|$ is the Lebesgue measure of D .

Let us apply the same reduction procedure in the case when $W = W_1 \cup I \cup W_2$ and W_2 is occupied by porous medium. Putting

$$\phi_n^{(1)}(x, y) = v_n(x) [A_n \cosh k_n y + B_n \sinh k_n y], \quad (19.13)$$

$$\phi_n^{(2)}(x, y) = v_n(x) C_n \cosh k_n(y + 1), \quad (19.14)$$

where $A_n, B_n, C_n \in \mathbb{C}$ and $k_n > 0$ is defined by the n th eigenvalue of problem (19.11), one reduces (19.2)–(19.5), (19.8), (19.9), (19.10) to a linear algebraic system for these coefficients. Thus, v_n is an eigenvalue of this sloshing problem if and only if v_n is a zero of the system's determinant.

For the sake of brevity, we denote $\Lambda_n = \tanh k_n h$ and $V_n = \tanh k_n(1 - h)$. Straightforward calculation, following the outlined scheme, yields that

$$v_n = k_n \frac{(s - if)\Lambda_n + V_n}{s - if + \Lambda_n V_n}. \quad (19.15)$$

To obtain an eigenvector $\{(\phi_n^{(1)}, \phi_n^{(2)})\}$ corresponding to v_n , one has to substitute the following coefficients

$$A_n = c k_n, \quad B_n = c v_n, \quad C_n = \frac{c k_n \operatorname{sech} k_n h \operatorname{sech} k_n (1-h)}{s - i f + \Lambda_n V_n}$$

into (19.13) and (19.14); here $c \in \mathbb{C}$ is arbitrary, but non-zero.

19.4 Properties of the Eigenvalues v_n and ω_n

We start noting some properties of the dependencies of $\operatorname{Re} v_n$ and $\operatorname{Im} v_n$ on the parameters f and s . Using (19.15), we write

$$\operatorname{Re} v_n = k_n \frac{(f^2 + s^2 + V_n^2) \Lambda_n + s(1 + \Lambda_n^2) V_n}{f^2 + (s + \Lambda_n V_n)^2}, \quad \operatorname{Im} v_n = k_n \frac{f(1 - \Lambda_n^2) V_n}{f^2 + (s + \Lambda_n V_n)^2}$$

and find

$$(\operatorname{Re}\{v_n\})'_f = (\operatorname{Im}\{v_n\})'_s = -2f k_n \frac{V_n(1 - \Lambda_n^2)(s + \Lambda_n V_n)}{[f^2 + (s + \Lambda_n V_n)^2]^2}.$$

Hence, it is easy to note that the function $\operatorname{Re}\{v_n\}$ ($\operatorname{Im}\{v_n\}$) decreases monotonically in f (in s).

Analogously, we have

$$(\operatorname{Im}\{v_n\})'_f = -(\operatorname{Re}\{v_n\})'_s = k_n \frac{V_n(1 - \Lambda_n^2)([s + \Lambda_n V_n]^2 - f^2)}{[f^2 + (s + \Lambda_n V_n)^2]^2}.$$

The only positive zero of $(\operatorname{Im}\{v_n\})'_f$ as a function of f is attained at

$$f = s + \Lambda_n V_n.$$

Since $\operatorname{Im}\{v_n\} = 0$ when $f = 0$ and $f \rightarrow \infty$, the latter displayed formula defines maximum of $\operatorname{Im}\{v_n\}$ as a function of f . We have

$$v_n^0 := v_n|_{f=0} = k_n \Lambda_n + \frac{k_n V_n(1 - \Lambda_n^2)}{s + \Lambda_n V_n}, \quad v_n^\infty := v_n|_{f \rightarrow \infty} = k_n \Lambda_n. \quad (19.16)$$

At the point of maximum

$$v_n|_{f=s+\Lambda_n V_n} = k_n \Lambda_n + \frac{(1+i)k_n V_n(1 - \Lambda_n^2)}{2[s + \Lambda_n V_n]} = \frac{1+i}{2} v_n^0 + \frac{1-i}{2} v_n^\infty.$$

Despite of the similarity between the problem considered in [10] and problem (19.2)–(19.5), (19.8), (19.9), (19.10), properties of spectra can be essentially different (presumably, due to the problem in question being non-self-adjoint). In particular, Proposition 1 in [10] proves that the fundamental frequency for a two-layer fluid in a container is smaller than that for the same container filled in with homogeneous fluid. At the same time, we can show that it is possible that

$$|v_n|^2 > \hat{v}_n^2, \quad n = 1, 2, \dots \tag{19.17}$$

where \hat{v}_n are the eigenvalues (19.12) for a homogeneous fluid occupying W .

In view of (19.15), we write

$$\frac{|v_n|^2}{k_n^2} = \frac{\Lambda_n^2(f^2 + s^2) + 2s\Lambda_n V_n + V_n^2}{f^2 + (s + \Lambda_n V_n)^2}.$$

Equating the denominator and the numerator, we get the equation

$$\Lambda_n^2(f^2 + s^2) + V_n^2 = f^2 + s^2 + \Lambda_n^2 V_n^2,$$

which is reduced to $V_n^2 = f^2 + s^2$. So, it is easy to note that the inequality

$$f^2 + s^2 < V_n^2 \tag{19.18}$$

guarantees that

$$|v_n|^2 > k_n^2 > \hat{v}_n^2,$$

and so the inequality (19.17) is satisfied. It is important to note that the right-hand side of (19.18) depends on the geometry of D (through the eigenvalue k_n) and on the depth $1 - h$ of the porous layer. It is also to note that since $V_1 \leq V_2 \leq V_3 \leq \dots$, the inequality $f^2 + s^2 < V_1^2$ guarantees that $|v_n|^2 > \hat{v}_n^2$ for all $n = 1, 2, \dots$

Consider another condition guaranteeing (19.17). In view of (19.16), it is easy to note that $v_n^\infty < \hat{v}_n$. At the same time, the equation $v_n^0 = \hat{v}_n$ is reduced to $s = 1$. (We also use the relationship $\tanh(k_n) = (\Lambda_n + V_n)/(1 + \Lambda_n V_n)$.) So, due to monotonicity of $\text{Re } v_n$ as a function of f , for $s > 1$ we have $\text{Re } v_n < \hat{v}_n$ for any $f > 0$. But for any $s \in [0, 1)$ there exists a unique solution

$$f = f_n^*(s) = \sqrt{1 - s} \sqrt{s + \Lambda_n V_n}$$

of $\text{Re } v_n = \hat{v}_n$, such that

$$\begin{aligned} \text{Re } v_n < \hat{v}_n & \text{ for } f \in (f_n^*, +\infty), \\ \text{Re } v_n > \hat{v}_n & \text{ for } f \in [0, f_n^*). \end{aligned}$$

Since $\operatorname{Re} \nu_n \leq |\nu_n|$, the condition (19.17) is satisfied for all $n = 1, 2, \dots$ in the set of parameters $\{(f, s) : s \in [0, 1), f \in [0, \sqrt{1-s} \sqrt{s + \Lambda_1 V_1}]\}$.

Now, we present the expressions for ω_n , corresponding to the eigenvalues ν_n , and find parameters maximizing damping for particular eigenmodes. We remind that $\omega_n = \sqrt{\nu_n}$, where the branch is chosen so that $\operatorname{Im} \omega_n \geq 0$. We find

$$\begin{aligned} \operatorname{Re} \omega_n &= \sqrt{k_n} \frac{\sqrt{\varpi_2 + \sqrt{\varpi_1^2 + \varpi_2^2}}}{\sqrt{2} \sqrt{f^2 + (s + \Lambda_n V_n)^2}}, \\ \operatorname{Im} \omega_n &= \sqrt{k_n} \frac{\varpi_1}{\sqrt{2} \sqrt{f^2 + (s + \Lambda_n V_n)^2} \cdot \sqrt{\varpi_2 + \sqrt{\varpi_1^2 + \varpi_2^2}}}, \end{aligned} \tag{19.19}$$

where

$$\varpi_1 = f V_n (1 - \Lambda_n^2), \quad \varpi_2 = f^2 \Lambda_n + (s \Lambda_n + V_n) (s + \Lambda_n V_n).$$

Turning to the ansatz (19.1), we observe the decay of the solution in time due to the factor $\exp\{-t \operatorname{Im} \omega\}$. So, with the purpose to maximize damping of oscillations in time for the eigenmode having the number n , we seek a maximum of $\operatorname{Im} \omega_n$, considered as a function of f . From (19.19), we have

$$(\operatorname{Im} \omega_n)'_f = \frac{\varpi_1 \left(\varpi_1^2 \varpi_4 + 2\varpi_5 \left(\varpi_2 + \sqrt{\varpi_1^2 + \varpi_2^2} \right) \right)}{2\sqrt{2} f \varpi_3^{3/2} \sqrt{\varpi_1^2 + \varpi_2^2} \left(\varpi_2 + \sqrt{\varpi_1^2 + \varpi_2^2} \right)^{3/2}}, \tag{19.20}$$

where

$$\begin{aligned} \varpi_3 &= f^2 + (s + \Lambda_n V_n)^2, \\ \varpi_4 &= -f^2 + (s + \Lambda_n V_n)^2, \\ \varpi_5 &= -f^4 \Lambda_n + (s \Lambda_n + V_n) (s + \Lambda_n V_n)^3. \end{aligned}$$

Define

$$f_n^\diamond = \frac{(s + \Lambda_n V_n) (3V_n + 4s \Lambda_n + \Lambda_n^2 V_n)^{1/2}}{(V_n + 4s \Lambda_n + 3\Lambda_n^2 V_n)^{1/2}}.$$

Substituting $f = f_n^\diamond$ into (19.20), it is not difficult to check that

$$(\operatorname{Im} \omega_n)'_f = 0 \text{ for } f = f_n^\diamond.$$

Besides, we have

$$(\text{Im } \omega_n)''_f \Big|_{f=f_n^\diamond} = - \frac{V_n (1 - \Lambda_n^2) (4s \Lambda_n + V_n (3 + \Lambda_n^2)) (4s \Lambda_n + V_n (1 + 3\Lambda_n^2))^3}{32\sqrt{2} (s + \Lambda_n V_n)^{5/2} (2s \Lambda_n + V_n (1 + \Lambda_n^2))^{9/2}}.$$

Since the latter expression for the second derivative of $\text{Im } \omega_n$ at $f = f_n^\diamond$ is negative, we have established that $f = f_n^\diamond$ corresponds to a maximum of $\text{Im } \omega_n$. We also note that

$$\begin{aligned} \text{Im } \omega_n \Big|_{f=0} &= \text{Im } \omega_n \Big|_{f \rightarrow \infty} = 0, \\ \text{Im } \omega_n \Big|_{f=f_n^\diamond} &= \frac{V_n (1 - \Lambda_n^2)}{2\sqrt{2} (s + \Lambda_n V_n)^{1/2} (2s \Lambda_n + V_n (1 + \Lambda_n^2))^{1/2}}. \end{aligned}$$

So, by this choice of the parameter $f = f_n^\diamond$, we can achieve rapid time-decaying of the n th eigenmode.

19.5 Inverse Problems

In this section, we discuss a possibility to recover parameters of the problem from the known spectral data. Assume that the eigenvalue ν_1 of the problem (19.2)–(19.5), (19.8), (19.9), (19.10) is found to be equal to $\hat{\nu}_1$ (say, measured experimentally). Then, using the formula (19.15), we find solutions of the equations $\text{Re } \nu_1 = \text{Re } \hat{\nu}_1$, $\text{Im } \nu_1 = \text{Im } \hat{\nu}_1$ as follows:

$$\begin{aligned} s &= \frac{\Lambda_1 V_1 (k_1^2 + |\hat{\nu}_1|^2) + k_1 V_1 (1 + \Lambda_1^2) \text{Re } \hat{\nu}_1}{\Lambda_1^2 k_1^2 - 2\Lambda_1 k_1 \text{Re } \hat{\nu}_1 + |\hat{\nu}_1|^2}, \\ f &= \frac{k_1 V_1 (1 - \Lambda_1^2) \text{Im } \hat{\nu}_1}{\Lambda_1^2 k_1^2 - 2\Lambda_1 k_1 \text{Re } \hat{\nu}_1 + |\hat{\nu}_1|^2}. \end{aligned}$$

Substituting these solutions to (19.15), we obtain the following expression for ν_n , $n = 2, 3, \dots$, in terms of $\hat{\nu}_1$ instead of s and f :

$$\begin{aligned} \text{Re } \nu_n &= k_n \frac{(\zeta_1 \Lambda_n V_1^2 + \zeta_2 \Lambda_n V_n^2 - \zeta_3 V_1 V_n (1 + \Lambda_n^2))}{\zeta_1 V_1^2 + \zeta_2 \Lambda_n^2 V_n^2 - 2\zeta_3 V_1 V_n \Lambda_n}, \\ \text{Im } \nu_n &= k_n \text{Im } \hat{\nu}_1 \frac{k_1 V_1 V_n (1 - \Lambda_1^2) (1 - \Lambda_n^2)}{\zeta_1 V_1^2 + \zeta_2 \Lambda_n^2 V_n^2 - 2\zeta_3 V_1 V_n \Lambda_n}, \end{aligned} \tag{19.21}$$

where

$$\begin{aligned} \varsigma_1 &= \Lambda_1^2 |\dot{v}_1|^2 + k_1^2 - 2\Lambda_1 k_1 \operatorname{Re} \dot{v}_1, \\ \varsigma_2 &= |\dot{v}_1|^2 + \Lambda_1^2 k_1^2 - 2\Lambda_1 k_1 \operatorname{Re} \dot{v}_1, \\ \varsigma_3 &= \Lambda_1 (|\dot{v}_1|^2 + k_1^2) - k_1 (1 + \Lambda_n^2) \operatorname{Re} \dot{v}_1. \end{aligned}$$

Assume that the eigenvalue v_2 of the problem (19.2)–(19.5), (19.8), (19.9), (19.10) is also known and it is equal to \dot{v}_2 . We can use the relationship

$$\frac{\dot{v}_n}{k_n} = \tanh k_n = \frac{\Lambda_n + V_n}{1 + \Lambda_n V_n},$$

to write

$$\Lambda_n = \frac{V_n k_n - \dot{v}_n}{V_n \dot{v}_n - k_n}.$$

Substituting the expressions of Λ_1 and Λ_2 and values $\operatorname{Re} v_2 = \operatorname{Re} \dot{v}_2$, $\operatorname{Im} v_2 = \operatorname{Im} \dot{v}_2$ into (19.21) for $n = 2$, we get two equations for finding V_1 and V_2 . Further, from the transcendental equation

$$h = 1 - \frac{\operatorname{arctanh} V_1}{k_1},$$

we can find the depth h , where the interface between two layers is located.

19.6 Concluding Remarks

The sloshing problem has been considered, in which a fluid occupies an open vertical-walled cylinder of constant depth with a bottom-adjacent porous layer covered by fluid having a free surface. The model under consideration is based on the theory developed in [11], where the nonlinear drag in porous structures was linearized by applying the Lorentz principle of virtual work. In the problem of fluid's free oscillations, they are described by two velocity potentials, which must satisfy a pair of interface conditions, and a spectral parameter is contained in the Steklov condition on free surface of the upper fluid.

The approach similar to that used in [10] for investigation of sloshing in a two-layer fluid has been applied. The separation of variables allows us to obtain expressions for the sequences arising in the spectral problem: eigenvalues and eigensolutions. The elements of these sequences are expressed in terms of eigenvalues for the Neumann Laplacian in the two-dimensional domain, which is a horizontal cross-section of the container.

The behaviour of sloshing eigenvalues as functions of parameters of the problem (the porosity, the linear friction factor and the inertial term) has been analyzed. Inequalities between the eigenvalues for the case under consideration and for the

problem of sloshing in the same container without the porous material are obtained. In particular, these results show that, despite the obvious similarity between the problem in question and the problem studied in [10], there is significant difference in the properties of the spectra.

In the present study, the question of maximizing damping in time of the free oscillations is of special interest; it can be achieved by choosing physical parameters of the porous layer. Expressions for angular frequencies ω_n , corresponding to the eigenvalues are obtained. To ensure rapid decay in time of the n th eigenmode, the expression for the optimal value of the linear friction factor is found; it guarantees that the maximum of $\text{Im } \omega_n$ is attained.

Inverse sloshing problem is formulated as the problem of finding characteristics of the porous layer and the depth of the interface from eigenvalues measured by observing them at the free surface. It is demonstrated that for determining two characteristics of the porous layer, one has to measure the smallest sloshing eigenfrequency. Knowledge of the two smallest eigenfrequencies also allows us to find the depth of the interface.

References

1. Fox, D.W., Kuttler, J.R.: Sloshing frequencies. *ZAMP* **34**, 668–696 (1983)
2. Lamb, H.: *Hydrodynamics*. Cambridge University Press, Cambridge (1932)
3. Faltinsen, O.M., Timokha, A.N.: *Sloshing*. Cambridge University Press, New York (2009)
4. Ibrahim, R.A.: *Liquid Sloshing Dynamics*. Cambridge University Press, New York (2005)
5. Lukovsky, I.A., Timokha, A.N.: Multimodal method in sloshing. *J. Math. Sci.* **220**, 239–253 (2017)
6. Kopachevsky, N.D., Krein, S.G.: *Operator Approach to Linear Problems of Hydrodynamics*. Birkhäuser, Basel (2001)
7. Miles, J.W.: Surface-wave damping in closed basins. *Proc. R. Soc. Lond. A.* **297**, 459–475 (1967)
8. Packwood, A.R., Peregrine, D.H.: The propagation of solitary waves and bores over a porous bed. *Coast. Eng.* **3**, 221–242 (1979)
9. Hunt, J.N.: On the damping of gravity waves propagated over a permeable surface. *J. Geophys. Res.* **64**, 437–442 (2012)
10. Kuznetsov, N.: On direct and inverse spectral problems for sloshing of a two-layer fluid in an open container. *Nanosyst.: Phys. Chem. Math.* **7**, 854–864 (2016)
11. Sollitt, C.K., Cross, R.H.: Long-wave transmission through porous break-waters. In: *Proceedings 13th Coastal Engineering Conference*, ASCE, New York, vol. 3, pp. 1827–1846 (1972)
12. Dalrymple, R.A., Losada, M.A., Martin, P.A.: Reflection and transmission from porous structures under oblique wave attack. *J. Fluid Mech.* **224**, 625–644 (1991)
13. Behera, H., Sahoo, T.: Gravity wave interaction with porous structures in two-layer fluid. *J. Eng. Math.* **87**(1), 73–97 (2014)
14. Courant, R., Hilbert, D.: *Methods of Mathematical Physics*, vol. 1. Interscience, New York (1953)

Chapter 20

Global Stability Boundaries and Hidden Oscillations in Dynamical Models with Dry Friction



Nikolay V. Kuznetsov, Elizaveta D. Akimova, Elena V. Kudryashova, Olga A. Kuznetsova, Mikhail Y. Lobachev, Ruslan N. Mokaev, and Timur N. Mokaev

Abstract In this chapter, the issues of global stability, bifurcations, and emergence of nontrivial limiting dynamic regimes in systems described by differential equations with discontinuous right-hand sides are considered within the framework of the theory of hidden oscillations. Such systems are important in the problems of mechanics, engineering, and control, and arise both a priori and as a result of idealization of some characteristics included in real physical systems. Determining the boundaries of global stability, scenarios of its violation, as well as identifying all arising limiting oscillations are the key challenges in the design of real systems based on mathematical modeling. While the self-excitation of oscillations can be effectively investigated numerically, the identification of hidden oscillations requires special analytical and numerical methods. The analysis of hidden oscillations is necessary to determine the exact boundaries of global stability, to estimate the gap between the necessary and sufficient conditions of global stability, and their convergence. This work presents a number of theoretical results and engineering problems in which hidden oscillations (their absence or presence and location) play an important role.

Keywords Control theory · Differential inclusions · Global stability · Hidden attractors · Periodic oscillations · Theory of hidden oscillations

N. V. Kuznetsov (✉)

Institute for Problems in Mechanical Engineering RAS, V.O., Bolshoy pr., 61, St. Petersburg 199178, Russia

N. V. Kuznetsov · E. D. Akimova · E. V. Kudryashova · O. A. Kuznetsova · M. Y. Lobachev · R. N. Mokaev · T. N. Mokaev
St. Petersburg State University, University Embankment, 7/9, St Petersburg 199034, Russia

N. V. Kuznetsov · E. D. Akimova · M. Y. Lobachev
LUT University, Lappeenranta, Yliopistonkatu 34, 53850 Lappeenranta, Finland

© The Author(s), under exclusive license to Springer Nature Switzerland AG 2022
V. A. Polyanskiy and A. K. Belyaev (eds.), *Mechanics and Control of Solids and Structures*, Advanced Structured Materials 164,
https://doi.org/10.1007/978-3-030-93076-9_20

387

20.1 Introduction

Development of the theory of differential inclusions and the theory of discontinuous systems is connected to the studies of particular mechanical and engineering problems. One of the first such problems is associated with the law of dry friction that was introduced by C.A. de Coulomb more than 200 years ago [1]. In the 1930s–1940s, the first steps toward the rigorous analysis of the mathematical peculiarities of discontinuous dynamical models were taken on the examples of mechanical models in the works of J.D. Hartog, A.A. Andronov, N.N. Bautin, and M.V. Keldysh [2–4]. Further development of the theory is related to various studies by S.V. Emelyanov, A.S. Poznyak, V.I. Utkin, and others [5–8]. That is to say, along with general considerations and attempts to understand how the notion of derivative is introduced for differential inclusions, there were other trends, related to particular needs of applied problems. For instance, various electronic systems are described by mathematical models with discontinuous nonlinearities (see, e.g., [9, 10]).

20.2 Global Stability

Consider a system of ordinary differential equations

$$\dot{x} = f(x), \quad f : \mathbb{R}^n \rightarrow \mathbb{R}^n \quad (20.1)$$

and suppose that, for any initial state x_0 , there exists a unique solution $x(t, x_0) : x(0, x_0) = x_0$, defined on $[0, +\infty)$.

Now we consider system (20.1) where f is a piecewise-continuous function with the set of discontinuity points of zero Lebesgue measure. As it was mentioned before, discontinuous right-hand side of system (20.1) caused a problem of defining a solution of (20.1) at the discontinuity points. Thus, it was suggested to consider the solutions as absolutely continuous functions satisfying the following differential inclusion (see, e.g., [11–13]):

$$\dot{x} \in F(x). \quad (20.2)$$

Here, a set $F(x)$ equals to $f(x)$ at continuity points of function f . At discontinuity points $F(x)$ is defined in a special way. In this chapter, we consider solutions of differential inclusions in the Filippov sense [11].

Definition 20.1 ([11]) Vector function $x(t)$ defined on an interval (t_1, t_2) is called a solution of (20.2) if it is absolutely continuous and for almost all $t \in (t_1, t_2)$ vector $\dot{x}(t)$ is within a minimal closed convex set, which contains all $f(t, x')$, when x' is within almost all δ -neighborhoods of the point $x(t) \in \mathbb{R}^n$ (for the fixed t), i.e.,

$$\dot{x} \in \prod_{\delta > 0} \prod_{\mu N = 0} \text{conv} f(t, U(x(t), \delta) - N).$$

Filippov's approach proved to be convenient from a theoretical point of view as it provided the necessary theorems for qualitative analysis of solutions, however, from a computational point of view it is often more convenient to use different approaches to define solutions of differential inclusions. One of the first popular ones was Aizerman–Pyatnitsky approach [14], the popularity of which is due to the ability to use various methods for numerical analysis of ODEs. Also, numerical modeling approaches that incorporate Filippov's definition of the solution of discontinuous systems appeared (see, e.g., [15]).

The definition of the solution to equations with discontinuous right-hand side proposed by M.A. Aizerman and E.S. Pyatnitsky makes it possible to use the ordinary definition of derivative. We consider their approach in a special case when $f(t, x)$ is discontinuous on a surface Σ . Now consider a sequence of continuous vector-functions $f_\varepsilon(t, x)$ that coincides with $f(t, x)$ outside of ε -neighborhood of the surface Σ , and tends to $f(t, x)$ as $\varepsilon \rightarrow 0$ at every point that does not belong to Σ . Let $x_\varepsilon(t)$ be a solution of the system

$$\dot{x} = f_\varepsilon(t, x). \quad (20.3)$$

Definition 20.2 ([14]) A solution to system (20.3) in the Aizerman–Pyatnitsky sense is said to be the limit of any uniformly converging subsequence of solutions $x_\varepsilon(t)$:

$$x_\varepsilon(t) \rightrightarrows x(t).$$

In general, there may exist more than one such limit.

It is known that both Filippov and Aizerman–Pyatnitsky approaches coincide for various classes of discontinuous systems (see, e.g., [13, 16, 17]).

If any trajectory of system (20.1) tends to the stationary set, then we call such system *globally stable* [18].¹ At first, global stability analysis of low-order discontinuous systems was done via rigorous analysis of the phase space of a system [2, 19]. However, it turned out that even for systems of the third order this approach required a lot of complex calculations and was quite cumbersome. For example, rigorous analysis of the Watt governor model carried out by A.A. Andronov and A.G. Mayer [20–22], took more than 40 pages. Therefore, it became apparent that general methods for global stability analysis were required. The development of such methods was connected to the generalization of the Lurie–Postnikov approach and the Barbashin–Krasovsky theorem [23] on global stability via Lyapunov functions for autonomous systems of ODEs.

Theorem 20.1 (see, e.g., [13, 18]) *Let a continuous function $V(x)$ defined in \mathbb{R}^n have the following properties:*

¹ We use the term “global stability” for simplicity of further presentation, while in the literature there are used different terms like “globally asymptotically stable” [35, p. 137], [36, p. 144], “gradient-like” [13, p. 56], [37, p. 2], “quasi-gradient-like” [13, p. 56], [37, p. 2], and others, reflecting the features of the stationary set and the convergence of trajectories to it.

1. $V(x(t))$ is nonincreasing in t for any solution $x(t)$ of (20.2);
2. if the identity $V(x(t)) = \text{const}$ is valid for all $t \in \mathbb{R}$ and for some solution $x(t)$ bounded when $t \in \mathbb{R}$, then the solution $x(t)$ is a stationary vector;
3. $V(x) \rightarrow +\infty$ as $\|x\| \rightarrow +\infty$.

Then differential inclusion (20.2) is globally stable.

As it will be shown later, applying ideas of Theorem 20.1, it is also possible to use discontinuous Lyapunov functions for global analysis [24] (see also [25, 26]).

In general, construction of such Lyapunov functions is a challenging task and a number of constructive frequency theorems was introduced over the years. For Lurie systems with smooth nonlinearities, an effective method to obtain sufficient conditions of global stability was developed by V.M. Popov, V.A. Yakubovich and R.E. Kalman (see [18, 27–32]) and was later generalized for discontinuous systems by Gel'fand and Leonov [33, 34] in 196x–197x. These theorems provide sufficient conditions of global stability, which in many cases give significantly conservative estimates and are not efficient from a practical point of view. Therefore, it gives a rise to the problem of analysis of the global stability boundaries, which are connected to the onset of oscillations in the phase space of a system.

20.3 Oscillations

Within the framework of global stability study, it is natural to classify oscillations in control systems as *self-excited*, either *hidden* [38–41]. Basin of attraction of a hidden oscillation in the phase space does not intersect with a vicinity of any equilibria, whereas a self-excited oscillation is excited from an unstable equilibrium. A self-excited oscillation is a nontrivial one if it does not approach the stationary states (i.e., ω -limit set of corresponding trajectory does not contain an equilibrium). The loss of global stability may occur by appearance of either nontrivial self-excited oscillation (see, e.g., [42]), or a hidden one. A nontrivial self-excited oscillations can be visualized numerically by a trajectory starting from a point in a neighborhood of unstable equilibrium. However, the revealing of hidden oscillations and obtaining initial data for their computation are challenging problems. These problems are studied in the theory of hidden oscillations [43–47], that represents the genesis of the modern era of Andronov's theory of oscillations.

The most important problem nowadays revolves around finding the exact boundary of global stability in the parameter space of the system. An outer estimate of the global stability boundary in the parameter space of the system and the birth of self-excited oscillations in the phase space can be obtained by the linearization around equilibria and the analysis of local bifurcations. An inner estimate of the global stability boundary can be obtained by sufficient criteria of global stability for discontinuous systems discussed above [18, 24]. In the gap between outer and inner estimates, the exact boundary of global stability can be studied numerically. For some discontinuous systems the global stability boundary may include both *trivial* and *hidden* parts.

Trivial part of the boundary is defined by local bifurcations, however, hidden part is not defined by local behavior in the vicinity of equilibria and its study requires analysis of nonlocal bifurcations and the birth of hidden oscillations [39, 48]. Let us also note that practical boundary of global stability (in dissipative systems) is defined by the birth of nontrivial attractor, therefore, methods for localization of oscillations can be used to refine the global stability boundary. One of the first examples of the nontriviality of this problem was the Kapranov conjecture [49] on determining the global stability boundary in the two-dimensional PLL model by self-excitation of oscillations, which was later disproved in [50–53] by showing the existence of hidden parts of the global stability boundary.

Among engineers, one of the most widely used methods for searching and analyzing oscillations in nonlinear control systems is the harmonic balance method (HBM). It was developed in the 1920s–1930s in the works of van der Pol [54], Krylov and Bogolyubov [55] (see also [56, 57]). It is known [40] that the harmonic balance method is an approximate method for determining the existence of periodic solutions. Later, different extensions of the harmonic balance method for Lurie systems with relay nonlinearities were introduced, namely, the Tsytkin method [58] and the locus of a perturbed relay systems approach (the LPRS method) [59]. They made it possible in many cases to refine the results, obtained by the harmonic balance method (e.g., see [60]).

Consider the following Lurie system [61, 62]:

$$\dot{x} = Ax + B\varphi(\sigma), \quad \sigma = Cx \tag{20.4}$$

where $x \in \mathbb{R}^n$ is a state vector, $\sigma \in \mathbb{R}^1$, $A \in \mathbb{R}^{n \times n}$, $B \in \mathbb{R}^{n \times 1}$, $C \in \mathbb{R}^{1 \times n}$ are matrices, all quantities are real. The linear part of system (20.4) can be represented by the following transfer function:

$$W(s) = C(A - Is)^{-1}B. \tag{20.5}$$

The harmonic balance method is as follows: suppose there is a periodic solution $a \cos(\omega_0 t)$ of system (20.4), then frequency ω_0 can be found from

$$\text{Im } W(j\omega_0) = 0 \tag{20.6}$$

where $W(s)$ is from (20.5) and j is an imaginary unit. Amplitude a can be found from harmonic balance equation

$$\int_0^{\frac{2\pi}{\omega_0}} \varphi(a \cos(\omega_0 t)) \cos(\omega_0 t) dt = ak \int_0^{\frac{2\pi}{\omega_0}} (\cos(\omega_0 t))^2 dt, \tag{20.7}$$

where k is a linearization coefficient:

$$k = -(\operatorname{Re} W(j\omega_0))^{-1}. \tag{20.8}$$

For relay systems with nonlinearity $\varphi(\sigma) = \operatorname{sign}(\sigma)$ this method allows to calculate amplitude analytically:

$$a = \frac{4}{\pi k}. \tag{20.9}$$

Although the classical harmonic balance method is approximate, its various developments have shown to be effective in localization of periodic as well as chaotic oscillations² (see, e.g., [40, 63]).

Now we consider two effective methods for finding periodic oscillations that are applicable to an important class of systems in control theory, namely, discontinuous systems with one scalar nonlinearity. In 1955, Ya. Z. Tsytkin published his famous book [58], where he further developed the ideas of harmonic balance method for design and analysis of relay control systems. Consider his approach on the example of a relay system in Lurie form (20.4) with $\varphi(\sigma) = \operatorname{sign}(\sigma)$ nonlinearity (i.e., an ideal relay). For that, we have to construct a special function $J_{\text{Tsytkin}}(\omega)$ which is as follows:

$$J_{\text{Tsytkin}}(\omega) = \frac{4}{\pi} \left(\sum_{l=1}^{\infty} \operatorname{Re} W(j(2l-1)\omega) \right) + j \sum_{l=1}^{\infty} \frac{1}{2l-1} \operatorname{Im} W(j(2l-1)\omega). \tag{20.10}$$

In case of ideal relay (no hysteresis, delay, or a dead zone), frequencies of periodic oscillations can be found from the equations:

$$\begin{cases} \operatorname{Im} J_{\text{Tsytkin}}(\omega_0) = 0, \\ \operatorname{Re} J_{\text{Tsytkin}}(\omega_0) < 0. \end{cases} \tag{20.11}$$

In 2008, the locus of a perturbed relay system (LPRS) method was introduced in [59], which can be considered as a further development of Tsytkin’s ideas on analysis of relay control systems. Consider this method on the example of its application to a relay system in Lurie form (20.4) with $\varphi(\sigma) = \operatorname{sign}(\sigma)$ nonlinearity. For this system, following a matrix state-space description approach we construct LPRS function $J_{\text{LPRS}}(\omega)$ which is as follows³:

² In some cases, the use of HBM makes it possible to accurately identify all periodic orbits in a system. For example, for a system described by the equation $\ddot{x} + x - b\dot{x} \cos(x) = 0$ (see, e.g., [64, 65]), this method predicts an infinite number of periodic orbits in the form $x^{\text{hbm}}(t) = a_0^i \sin(t)$, where $\{a_0^i\}_{i=1}^{\infty}$ are zeros of the Bessel function: $J_1(a_0^i) = \frac{1}{\pi} \int_0^\pi \cos(\tau - a_0^i \sin \tau) d\tau = 0$.

³ Without limiting the generality of the foregoing, suppose that $\det A \neq 0$.

$$\begin{aligned}
 J_{\text{LPRS}}(\omega) = & -0.5 C \left[A^{-1} + \frac{2\pi}{\omega} (I - e^{\frac{2\pi}{\omega} A})^{-1} e^{\frac{\pi}{\omega} A} \right] B + \\
 & + j \frac{\pi}{4} C (I + e^{\frac{\pi}{\omega} A})^{-1} (I - e^{\frac{\pi}{\omega} A}) A^{-1} B.
 \end{aligned}
 \tag{20.12}$$

Suppose we have computed the LPRS of a given system. Then there is a finite number of points of intersection of the LPRS and the horizontal axis. The following equation defines frequencies ω_0 of symmetric periodic solutions:

$$\text{Im } J_{\text{LPRS}}(\omega_0) = 0.
 \tag{20.13}$$

Therefore, an actual periodic motion can be found only among these candidate points. Note that formula (20.13) is a necessary condition for the existence of the frequency of symmetric periodic motion in the system (the actual existence of a periodic motion depends on a number of other factors (see, e.g., [60])).

20.4 Examples

20.4.1 Watt Governor Model

In 1877, I.A. Vyshnegradsky published his famous work on the Watt governor [66] (see Fig. 20.1)) where he considered the following nonlinear dynamical model of the governor:

$$\ddot{x} + \beta \dot{x} + \alpha x = y - \frac{1}{2} \text{sign}(\dot{x}), \quad \dot{y} = -x,
 \tag{20.14}$$

where α and β are positive parameters. System (20.14) can be rewritten in Lurie form (20.4) with

$$A = \begin{pmatrix} 0 & 0 & 1 \\ -1 & 0 & 0 \\ -\alpha & 1 & -\beta \end{pmatrix}, \quad B = \begin{pmatrix} 0 \\ 0 \\ -1 \end{pmatrix}, \quad C = \begin{pmatrix} 0 \\ 0 \\ 1 \end{pmatrix}^T, \quad \varphi(\sigma) = \frac{1}{2} \text{sign}(\sigma).
 \tag{20.15}$$

Vyshnegradsky performed ‘linearization’ (by discarding sign nonlinearity) in a vicinity of working regime, analyzed its local stability, and obtained the following conditions:

$$\alpha > 0, \beta > 0, \alpha\beta > 1.
 \tag{20.16}$$

Vyshnegradsky conjectured that these conditions of local stability would also imply the global stability.

However, nontrivial oscillating periodic working regimes (later called *limit cycles* [67]) were discovered by Leaute in [68] in a similar regulation system with dry friction. Later on, N.Ye. Zhukovsky criticized Vyshnegradsky approach and posed a

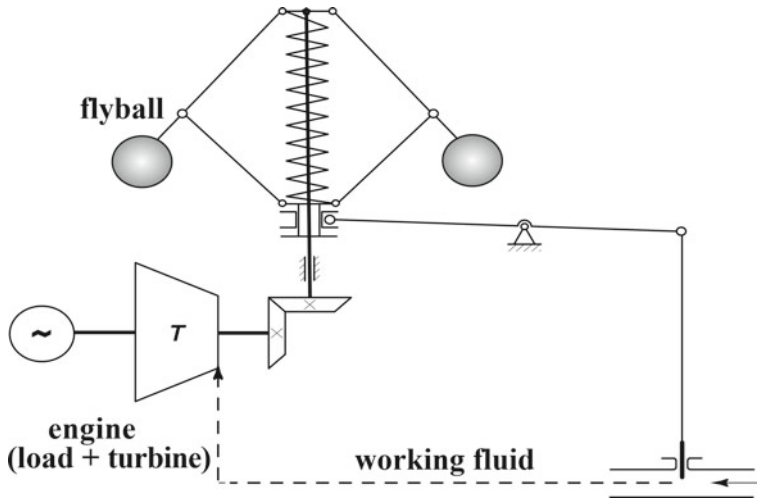


Fig. 20.1 Scheme of the Watt governor

problem of rigorous justification of the conditions obtained by Vyshnegradsky [69]. In 1944, Andronov and Mayer [20] applied the point-mapping method and solved the Zhukovsky problem concerned with rigorous proof of the Vyshnegradsky conjecture.

The global analysis carried out by Andronov and Mayer involved rather difficult and lengthy reasoning. However, recent developments of global stability theory for discontinuous systems [13, 18, 24, 33] made it possible to analyze system (20.14) by constructing a discontinuous Lyapunov function.

Theorem 20.2 *System (20.14) is globally stable if $\alpha > 0$, $\beta > 0$, $\alpha\beta > 1$.*

Proof Let us consider the following discontinuous Lyapunov function:

$$V(x) = \frac{\alpha}{2} \left(\frac{1}{\alpha}x_1 + x_3 \right)^2 + \frac{1}{2} (\alpha x_1 - x_3 + \psi(x))^2 + \frac{1}{\alpha}x_3\psi(x) - \frac{1}{\alpha} \int_0^{x_3} \left(\frac{\alpha\beta - 1}{\alpha}s + \varphi(s) \right) ds \geq 0 \quad (20.17)$$

where

$$\psi(x) = \begin{cases} \frac{\alpha\beta-1}{\alpha}x_3 + \varphi(x_3), & \text{if } x_3 \neq 0, \\ \frac{1}{2}, & \text{if } x_3 = 0, x_2 - \alpha x_1 > \frac{1}{2}, \\ -\frac{1}{2}, & \text{if } x_3 = 0, x_2 - \alpha x_1 < -\frac{1}{2}, \\ x_2 - \alpha x_1, & \text{if } x_3 = 0, |x_2 - \alpha x_1| \leq \frac{1}{2}. \end{cases}$$

The corresponding discontinuity surface, sliding mode band, and a rest segment take the form

$$S = \{(x_1, x_2, x_3) \in \mathbb{R}^3 | x_3 = 0\}, \tag{20.18}$$

$$D = \left\{ (x_1, x_2, x_3) \in \mathbb{R}^3 | x_3 = 0, -\frac{1}{2} \leq x_2 - \alpha x_1 \leq \frac{1}{2} \right\}, \tag{20.19}$$

$$\Lambda = \left\{ (x_1, x_2, x_3) \in \mathbb{R}^3 | x_1 = x_3 = 0, -\frac{1}{2} \leq x_2 \leq \frac{1}{2} \right\}. \tag{20.20}$$

Outside of the discontinuity surface S , Lyapunov function (20.17) is smooth and has the form

$$V(x) = \frac{\alpha}{2} \left(\frac{1}{\alpha} x_1 + x_3 \right)^2 + \frac{1}{2} \left(\alpha x_1 - x_2 + \frac{\alpha\beta - 1}{\alpha} x_3 + \varphi(x_3) \right)^2 + \frac{\alpha\beta - 1}{2\alpha^2} x_3^2 \geq 0. \tag{20.21}$$

Its derivative along the trajectories of system (20.14) is equal to

$$\dot{V}(x) = - \left(\frac{\alpha\beta - 1}{\alpha} + \varphi'(x_3) \right) (-\alpha x_1 + x_2 - \beta x_3 - \varphi(x_3))^2. \tag{20.22}$$

The form of system (20.14) implies that $V(x(t_1)) < V(x(t_2))$ for all $t \in (t_1, t_2) : x_3(t) \neq const$.

For the trajectories with initial data $x_0 = (x_{01}, x_{02}, 0) \in D$, where D is the sliding mode band (20.19), function $V(x)$ has the form

$$V(x(t)) = \frac{\alpha}{2} \left(\frac{1}{\alpha} x_1(t) \right)^2 + \frac{1}{2} (\alpha x_1(t) - x_2(t) + \psi(x))^2 \equiv \frac{1}{2\alpha} x_{01}^2. \tag{20.23}$$

In this case, if the trajectory leaves D after time t , continuity holds:

$$V(x(t)) \equiv \frac{1}{2\alpha} x_{01}^2 = \lim_{t^+ \rightarrow t} V(x(t^+)).$$

The crossing of the discontinuity surface S occurs for

$$x_3 = 0, \quad |x_2 - \alpha x_1| > \frac{1}{2} = \varphi(0+).$$

At the moment of intersection t , for the vector field, we have

$$\begin{aligned} \dot{x}_1(t) &= 0, \\ \dot{x}_2(t) &= -x_1(t), \\ \begin{cases} \dot{x}_3(t) > 0, & x_2 - \alpha x_1 > \varphi(0+) \geq 0, \\ \dot{x}_3(t) < 0, & x_2 - \alpha x_1 < -\varphi(0+) \leq 0. \end{cases} \end{aligned}$$

Then for $t \in (t^-, t^+)$, the following relations hold:

$$\begin{aligned}
 x_2(t) - \alpha x_1(t) &> \varphi(0+) \geq 0, \\
 \lim_{t^- \rightarrow t} V(x(t^-)) &= \frac{\alpha}{2} \left(\frac{1}{\alpha} x_1(t) \right)^2 + \frac{1}{2} (\alpha x_1(t) - x_2(t) + \varphi(0-))^2 \geq \\
 &\geq \frac{\alpha}{2} \left(\frac{1}{\alpha} x_1(t) \right)^2 + \frac{1}{2} (\alpha x_1(t) - x_2(t) + \varphi(0+))^2 = \lim_{t^+ \rightarrow t} V(x(t^+)); \\
 x_2 - \alpha x_1 &< \varphi(0+) \leq 0, \\
 \lim_{t^- \rightarrow t} V(x(t^-)) &= \frac{\alpha}{2} \left(\frac{1}{\alpha} x_1(t) \right)^2 + \frac{1}{2} (\alpha x_1(t) - x_2(t) + \varphi(0+))^2 \geq \\
 &\geq \frac{\alpha}{2} \left(\frac{1}{\alpha} x_1(t) \right)^2 + \frac{1}{2} (\alpha x_1(t) - x_2(t) + \varphi(0-))^2 = \lim_{t^+ \rightarrow t} V(x(t^+)).
 \end{aligned}$$

It follows from the above that the function $V(x)$ possesses the properties:

1. For any trajectory $x(t, y_0)$, function $V(x(t, y_0))$ is a nonincreasing function of t ;
2. It follows from $V(x(t, x_0)) = \text{const}$ at $t \geq 0$ that $x(t, x_0) \in D$ for $t \geq 0$.

Following [33], let us take a trajectory $x(t, y_0)$ and let x_0^ω be an arbitrary ω -limit point $x(t, y_0)$. Suppose that $x_0^\omega \in D$. Then, taking advantage of the continuity of function $V(x)$ outside of D and property (1), we arrive at

$$\lim_{t \rightarrow +\infty} V(x(t, y_0)) = V(x_0^\omega). \tag{20.24}$$

Point x_0^ω is visited by a trajectory $x(t, x_0^\omega)$ that consists of the ω -limit points of the trajectory $x(t, y_0)$. For each ω -limit point x_0^ω , there exists a subsequence $t_k \rightarrow +\infty$ such that $x(t_k, y_0) \rightarrow x_0^\omega$. Hence, Eq. (20.24) implies the equality $V(x(t, x_0^\omega)) \equiv V(x_0^\omega)$. The above and property (2) imply that $x_0^\omega \in D$. Thus, all ω -limit points of system (20.14) are situated in D and, therefore, are ω -limit points of the system

$$\dot{x}_1 = 0, \quad \dot{x}_2 = -x_1, \quad \dot{x}_3 = 0, \tag{20.25}$$

describing the evolution of the trajectories in D . However, the set of ω -limit points of (20.25) belonging to D coincides with the rest segment Λ of (20.14). Therefore, for all initial points y_0 , we have

$$\lim_{t \rightarrow \infty} \min_{u \in \Lambda} \|x(t, y_0) - u\| = 0$$

and function $V(x)$ have the following property:

3. $V(x) = 0$ for $x \in \Lambda$ and $V(x) > 0$ for $x \notin \Lambda$. □

In 194x, the only available general analytical method for the analysis of oscillations in nonlinear systems with one scalar nonlinearity was the harmonic balance method. Applying it to (20.14), we get the frequency of the periodic oscillation

$\omega = \sqrt{\alpha}$ and the amplitude $a = \frac{4\alpha}{\pi(1-\alpha\beta)}$. It is clear that for the amplitude to be positive, conditions (20.16) must be met. Results of the application of the harmonic balance method to (20.14) are in line with the global analysis carried out by Andronov and Mayer: the periodic solutions are nonexistent under conditions (20.16). Similarly, the application of the Tsytkin and LPRS methods to system (20.14) with parameters satisfying (20.16) coincides with global analysis. It is clear that, in case of system (20.14), global stability conditions (20.16) provided by the Lyapunov function (20.17) coincide with the conditions of absence of oscillations. Even so, in many cases the global stability boundary estimate obtained through the Lyapunov function may be significantly conservative, while the application of the harmonic balance method leads to erroneous conclusions about stability or presence of oscillations. Both these scenarios will be investigated on the example of two- and four-dimensional Keldysh models.

The works by Vyshnegradsky [66], Andronov-Mayer [20], and Lurie-Postnikov [61] led to the problem of describing a class of Lurie systems for which necessary conditions of stability (i.e., stability of a linearized model) coincide with sufficient ones (i.e., global stability of a nonlinear model). The history of attempts to solve this problem is connected with the Aizerman [40] and Kalman [70] conjectures on global stability of Lurie systems with nonlinearity satisfying generalized Routh-Hurwitz criterion. It is known [71] that Kalman conjecture is valid for two- and three-dimensional cases (while Aizerman conjecture is valid only for two-dimensional case [72–74]) but it becomes incorrect when another dimension is added.⁴ This gives a rise to certain difficulties connected to the theory of hidden oscillations and numerical modeling. Such problems arise when studying more practical models including Watt governor, for example, Watt governor with servomotor that is obtained by adding fourth equation to (20.15). Note that such problems still remain relevant for modern turbine regulators, as shown by the recent accident at the Sayano-Shushenskaya hydroelectric power station and an analysis of its possible causes [76–78]. However, we will illustrate these difficulties with another classical example that is the four-dimensional Keldysh model.

20.4.2 Keldysh Model with One Degree of Freedom

In 1944, M.V. Keldysh studied various flutter suppression models for aircraft controls including a dry friction hydraulic damper [4], and used the harmonic balance method for analysis of oscillations and stability of the rest segment. Keldysh wrote: “*we do not give a rigorous mathematical proof ..., we construct a number of conclusions on intuitive considerations ...*”. Before studying the four-dimensional model, Keldysh analyzed a simplified two-dimensional model, on the example of which he described the main difficulties, before moving on to investigate the full model. Note that while

⁴ Further research in this field led to the onset of several conjectures on global stability of various classes of nonlinear systems (see, e.g., [75]).

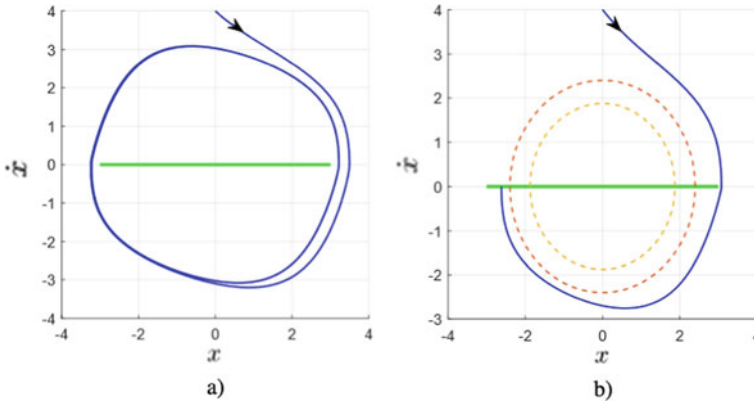


Fig. 20.2 Numerical analysis of the Keldysh system (20.26) with one degree of freedom and $\Phi = 3, \kappa = 1$. **a** $\mu = -3.85792$: outer trajectory attracts to the limit cycle around rest segment; **b** $\mu = -3.6287$: limit cycle ‘disappeared’

in control theory the problem of suppressing of all oscillations is often formulated, Keldysh in his works admitted the operation of the regulation system in bounded region of stability of the operating regime (and the possibility of coexistence of undesirable limiting regimes, which turned out to be hidden attractors) due to the design features of the regulator.

Using the models considered in Keldysh’s paper, we show the limitations of the harmonic balance method. First, we consider the Keldysh model with one degree of freedom in Lurie form (20.4), which is as follows:

$$A = \begin{pmatrix} 0 & 1 \\ -1 & -\mu \end{pmatrix}, \quad B = \begin{pmatrix} 0 \\ -1 \end{pmatrix}, \quad C = \begin{pmatrix} 0 \\ 1 \end{pmatrix}^T, \quad (20.26)$$

$$\varphi(\sigma) = (\Phi + \kappa\sigma^2) \text{sign}(\sigma).$$

Using the harmonic balance method, Keldysh formulated the following result: *if*

$$-2.08\sqrt{\Phi\kappa} < \mu, \quad (20.27)$$

then all trajectories of (20.26) converge to the rest segment; if

$$\mu < -2.08\sqrt{\Phi\kappa}, \quad (20.28)$$

then there are two periodic trajectories (limit cycles).

Figure 20.2 shows the bifurcation of collision of the external limit cycle and the stationary segment. In this numerical experiment, both limit cycles have disappeared, while Keldysh’s estimate (20.28) holds.

A rigorous study of the Keldysh model (20.26) was performed in [79, 80]. It was shown that $S = \{x : x_2 = 0\}$ is a discontinuity manifold, $\Lambda = \{-\Phi/k \leq x_1 \leq \Phi/k, x_2 = 0\}$ is a stationary segment. System (20.26) was re-written to study the following differential inclusion:

$$\dot{x} \in Ax + B\psi(\sigma), \quad \sigma = Cx, \quad \psi(\sigma) = \begin{cases} \varphi(\sigma), & \sigma \neq 0, \\ [-\Phi, \Phi], & \sigma = 0. \end{cases} \quad (20.29)$$

Application of Lyapunov function $V(x_1, x_2) = \frac{1}{2}(kx_1^2 + J^{-1}x_2^2)$ and Theorem 20.1 leads to the global stability condition:

$$\lambda - h > -2\sqrt{\Phi\kappa}.$$

20.4.3 Keldysh Model with Two Degrees of Freedom

The opposite effect can be observed in the Keldysh system [4, Eq. (2), p. 34], [43, 79], of flutter suppression with two degrees of freedom:

$$A = \begin{pmatrix} 0 & 1 & 0 & 0 \\ -(m_1^2 + \beta^2) & -2\beta & 0 & -\lambda \\ 0 & 0 & 0 & 1 \\ 0 & 1 & -(m_2^2 + \beta^2) & -2\beta \end{pmatrix}, \quad B = \begin{pmatrix} 0 \\ -1 \\ 0 \\ 0 \end{pmatrix}, \quad C = \begin{pmatrix} 0 \\ 0 \\ 0 \\ 1 \end{pmatrix}^T, \quad (20.30)$$

$$\varphi(\sigma) = \text{sign}(\sigma)$$

where λ is a linear parameter of a damper. Throughout this paper we will consider the following values of the parameters m_1, m_2, β :

$$m_1 = 0.9, \quad m_2 = 1.1, \quad \beta = 0.01. \quad (20.31)$$

Transfer function of the linear part of system (20.4), (20.30), (20.31) is

$$W(s) = \frac{s^2}{s^4 + a_3s^3 + (a_2 + \lambda)s^2 + a_1s + a_0} \quad (20.32)$$

where $a_0 = (m_1^2 + \beta^2)(m_2^2 + \beta^2), a_1 = 2\beta(m_1^2 + m_2^2 + 2\beta^2), a_2 = m_1^2 + m_2^2 + 6\beta^2, a_3 = 4\beta$ and the rest segment is

$$\Lambda = \{(x_1, x_2, x_3, x_4) \in \mathbb{R}^4 \mid x_2 = x_3 = x_4 = 0, -\frac{1}{a_0} \leq x_1 \leq \frac{1}{a_0}\}. \quad (20.33)$$

Applying the Routh-Hurwitz criterion to find a stability sector of system (20.30) with nonlinearity $\varphi(\sigma) = \text{sign}(\sigma)$ we get

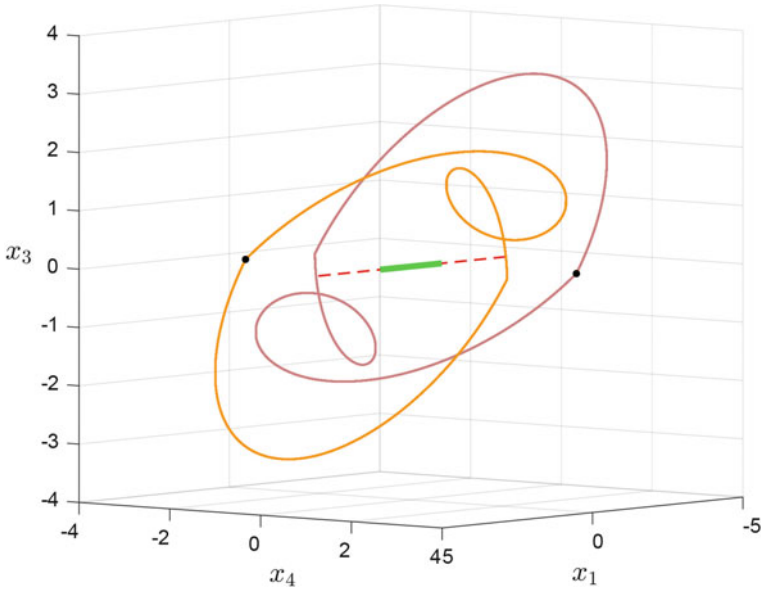


Fig. 20.3 Two self-excited asymmetric periodic solutions of system (20.4), (20.30), (20.31) with $\lambda = -0.041$ in subspace (x_1, x_3, x_4) . These solutions cannot be found by the harmonic balance method

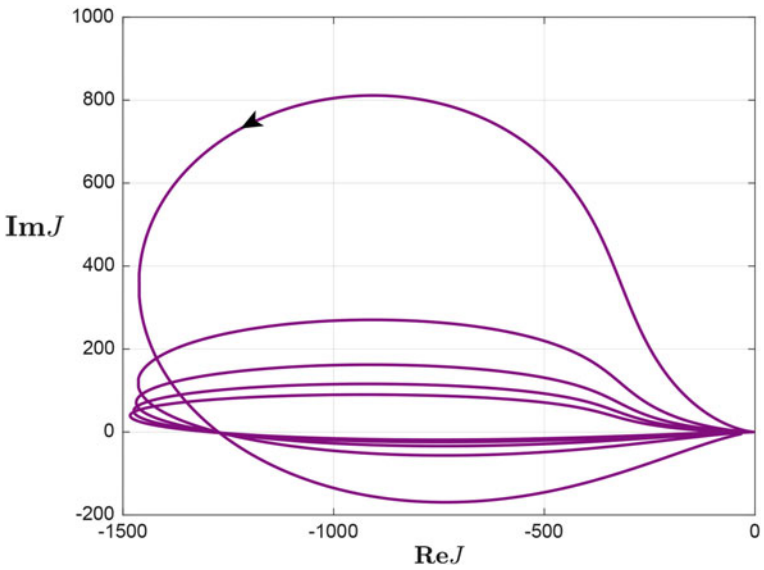


Fig. 20.4 The Tsytkin locus of system (20.4), (20.30), (20.31) with $\lambda = -0.041$ and $\omega \in [0.1, 1.1]$

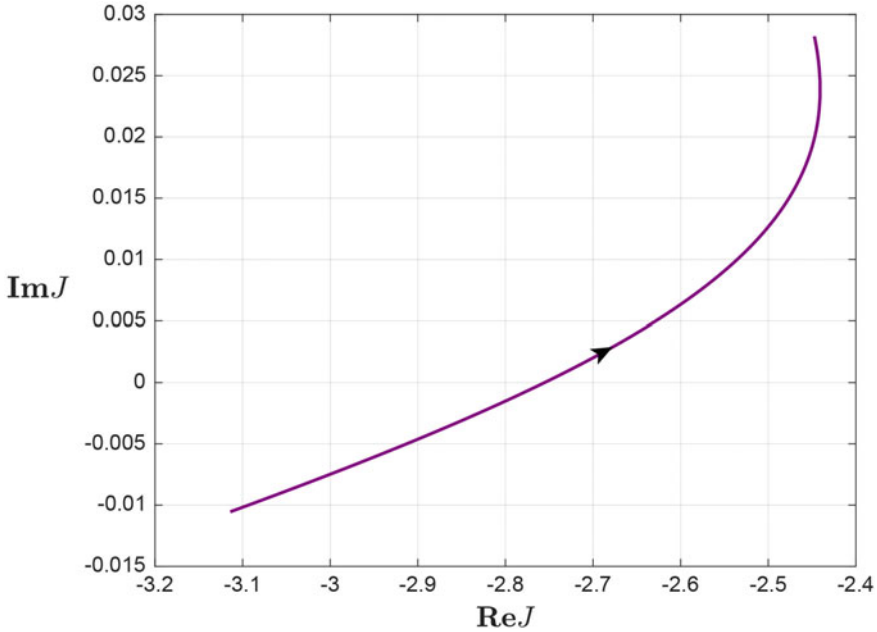


Fig. 20.5 The Tsytkin locus of system (20.4), (20.30), (20.31) with $\lambda = -0.041$ and $\omega \in [0.5, 0.6]$

$$\left(-4\beta^2 - \lambda - \frac{(m_1^2 - m_2^2)^2}{2(m_1^2 + m_2^2 + 2\beta^2)}, +\infty \right). \tag{20.34}$$

Firstly, consider system (20.4), (20.30), (20.31) with

$$\lambda = -0.041, \tag{20.35}$$

then the sector of stability becomes $(0.000999960, +\infty)$.

According to the harmonic balance method, this system has only one unstable periodic solution with frequency $\omega_{unst} = 1.005037312$ (see (20.6)). However, using numerical integration [15] with initial data in the vicinity of rest segment (20.33), we can localize two additional asymmetric periodic solutions (see Fig. 20.3), which are self-excited with respect to the rest segment. According to the Tsytkin and the LPRS methods, that are known to give more accurate results than the harmonic balance method, system (20.30) with parameters (20.35) has two unstable symmetric periodic solutions $\omega_{unst_1} = 0.52533579$ and $\omega_{unst_2} = 1.005037302$, which can be seen by visualizing corresponding functions (20.10) and (20.12) (see Figs. 20.4, 20.5, 20.6).

Visualization of these periodic solutions is presented in Fig. 20.7. Now consider system (20.4), (20.30), (20.31) with $\lambda = 0.01$. According to the harmonic balance method this system has no periodic solutions ($a < 0$), but using the Tsytkin method

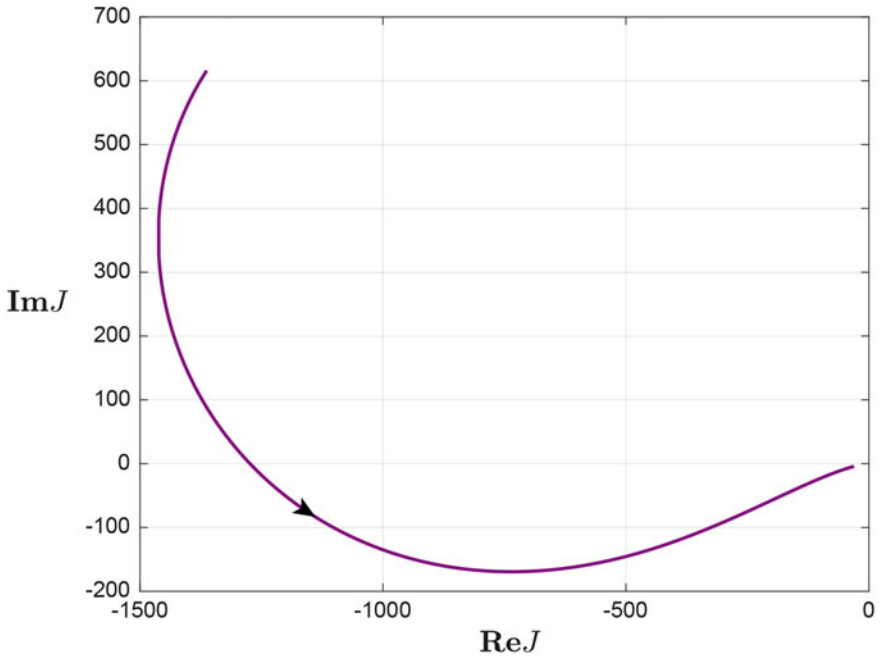


Fig. 20.6 The Tsytkin locus of system (20.4), (20.30), (20.31) with $\beta = 0.01$ and $\lambda = -0.041$ and $\omega \in [1, 1.1]$

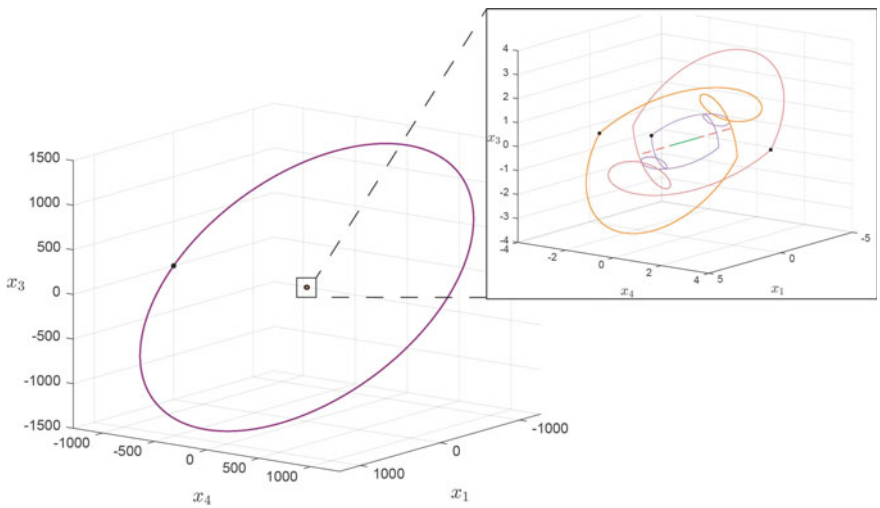


Fig. 20.7 Two symmetric unstable periodic solutions of system (20.4), (20.30), (20.31) with $\lambda = -0.041$ in subspace (x_1, x_3, x_4) coexist with two stable hidden asymmetric periodic solutions

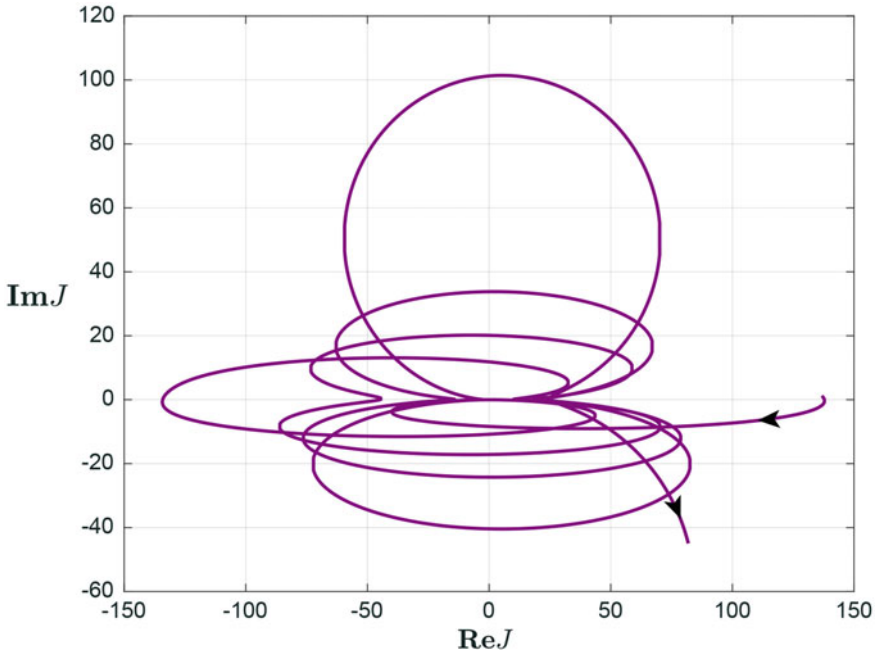


Fig. 20.8 The Tsyarkin locus of system (20.30) with $\beta = 0.01$ and $\lambda = 0.01$ and $\omega \in [0.1, 1.1]$

Table 20.1 Initial data for visualization of two stable hidden asymmetric periodic solutions of system (20.4), (20.30), (20.31) with $\lambda = 0.01$

x_1	± 0.983749160399365
x_2	± 3.665119741559401
x_3	0.0
x_4	∓ 3.395816595914568

and the LPRS method it is possible to find a stable symmetric periodic solution with two relay switches (see Figs. 20.8 and 20.9).

Using special approaches of localization of hidden oscillations (see, e.g., [40]), it is possible to visualize two stable asymmetric periodic solutions (see initial data in Table 20.1) and one more stable symmetric periodic solution (see initial data in Table 20.2). Mutual disposition of these solutions can be seen in Fig. 20.10.

Finally, we consider system (20.30) with $\beta = 0.01$ and $\lambda = 2$. As in the previous case ($\lambda = 0.01$), there are no periodic solutions according to the harmonic balance method. Using the Tsyarkin method and the LPRS method, one can obtain the frequency of a stable symmetric periodic solution with two relay switches (see Fig. 20.11) with initial data given in Table 20.3. Further numerical analysis of the phase space of the system shows that there are at least two more solutions: a stable periodic solution with six relay switches (initial data given in Table 20.4) and

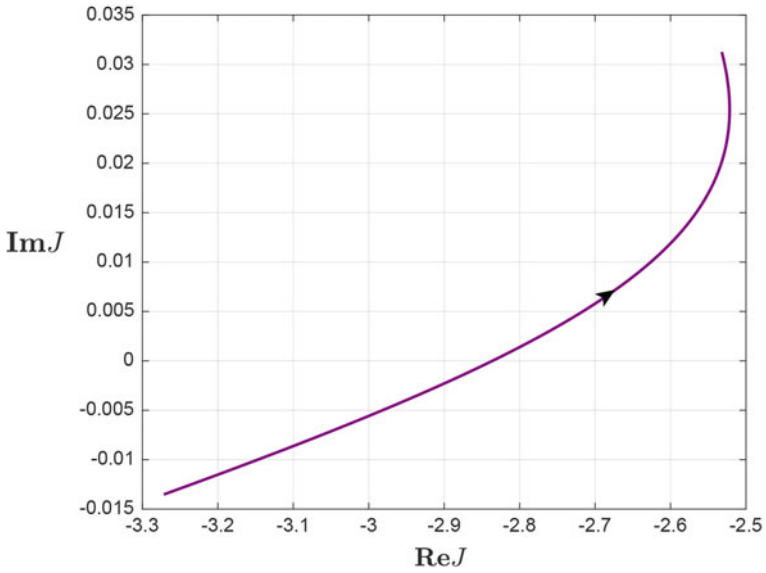


Fig. 20.9 The Tsytkin locus of system (20.30) with $\beta = 0.01$ and $\lambda = 0.01$ and $\omega \in [0.5, 0.6]$

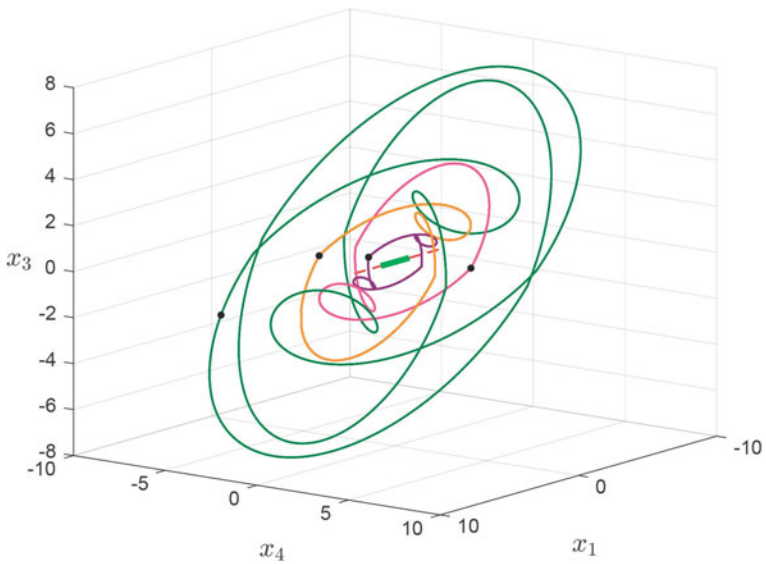


Fig. 20.10 Two stable hidden asymmetric periodic solutions of system (20.4), (20.30), (20.31) with $\lambda = 0.01$ coexist with two stable (one self-excited and the other one is hidden) symmetric periodic solutions in subspace (x_1, x_2, x_3) . None of these solutions can be found by the harmonic balance method

Table 20.2 Initial data for visualization of stable hidden symmetric periodic solution of system (20.4), (20.30), (20.31) with $\lambda = 0.01$

x_1	4.605660036110889
x_2	5.921019580311663
x_3	-2.298040698707351
x_4	-6.019404471999593

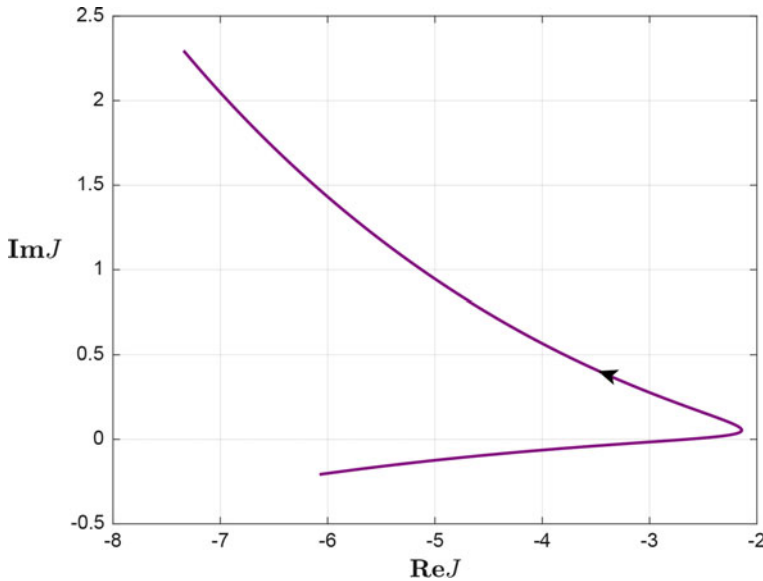


Fig. 20.11 The Tsytkin locus of system (20.30) with $\beta = 0.01$ and $\lambda = 2$ and $\omega \in [0.4, 0.5]$

Table 20.3 Initial data for visualization of symmetric periodic solution of system (20.4), (20.30), (20.31) with $\lambda = 2$ with two relay switches

x_1	-0.203592844886790
x_2	1.863854848726598
x_3	0.0
x_4	-1.130138381086802

a chaotic solution (see Fig. 20.12). Note that chaotic solution could not be found neither using the harmonic balance method (or its extensions on relay systems), nor using point-mapping method [81]. Whereas further developments of Tsytkin and LPRS methods may allow to find the solution with six relay switches.

Notice that if the Aizerman–Pyatnitsky approach to the numerical modeling by smoothing the discontinuous nonlinearity is applied, a series of counterexamples to the Kalman conjecture can be obtained.

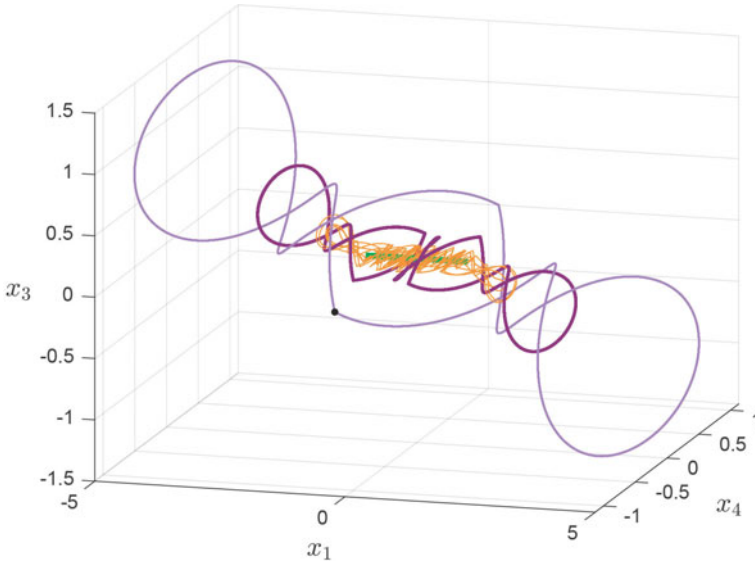


Fig. 20.12 Two stable hidden symmetric periodic solutions of system (20.4), (20.30), (20.31) with $\lambda = 2$ coexist with a self-excited chaotic solution. None of these solutions can be found by harmonic balance method

Table 20.4 Initial data for visualization of symmetric periodic solution of system (20.4), (20.30), (20.31) with $\lambda = 2$ with six relay switches

x_1	1.030891111160810
x_2	-0.840369003270022
x_3	-0.169868291721377
x_4	0.232271927066882

The Kalman conjecture Consider Lurie system (20.4) where φ is a smooth scalar function with $\varphi(0) = 0$ satisfying the condition

$$k_1 < \varphi'(\sigma) < k_2, \sigma \in (-\infty, +\infty), \tag{20.36}$$

where k_1 is a number or $-\infty$, and k_2 is a number or $+\infty$. If the linear system $\dot{x} = Ax + kBCx$, with $k \in (k_1, k_2)$ is asymptotically stable, then system (20.4) is globally stable. \square

Consider system (20.30) with smooth nonlinearity $\varphi(\sigma) = \tanh(100\sigma)$. The sector of linear stability (20.34) of system (20.4), (20.30), (20.31) with \tanh nonlinearity is infinite for all of the considered values of parameters and $\varphi'(\sigma)$ lies in the considered sector. Therefore, the Kalman conjecture conditions are met. However, the attractors that were localized in system (20.4), (20.30), (20.31) with sign nonlinearity and $\lambda = 0.01$ (see Fig.20.10) retain in the phase space of sys-

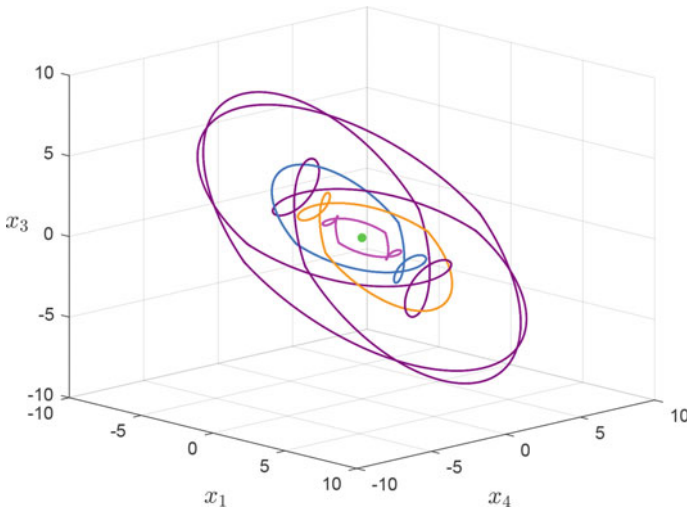


Fig. 20.13 Two stable hidden asymmetric periodic solutions of system (20.30) with $\beta = 0.01$ and $\lambda = 0.01$ coexist with two stable hidden symmetric periodic solutions. None of these solutions can be found by the harmonic balance method

tem (20.4), (20.30), (20.31) with \tanh nonlinearity and $\lambda = 0.01$ (see Fig. 20.13), while equilibrium point is stable. Hence, a new counterexample to the Kalman conjecture with hidden oscillations is obtained.

20.5 Conclusion

This chapter is devoted to the theory of hidden oscillations and its relevant applications, such as the Andronov–Vyshnegradsky problem on the nonlinear analysis of the Watt governor, the Keldysh problem on the nonlinear analysis of flutter suppression systems and the Aizerman and Kalman conjectures on the global stability of control systems. To conduct reliable mathematical modeling of technical systems, it is important to pay special attention to the rigorous derivation of the mathematical models used and the consideration of the limits of their applicability, the development of effective analytical and numerical methods for studying dynamics, taking into account the possibilities and limitations of the existing analytical methods for studying the stability and the occurrence of oscillations.

Acknowledgements The work is supported by the Leading Scientific Schools of Russia Project NSh-2624.2020.1, NSh-4196.2022.1.1, St.Petersburg State University grant Pure ID 75207094 (section 1), and Team Finland Knowledge Programme (163/83/2021)

References

1. Coulomb, C.A.: *Théorie des machines simples*. Mèm. Math. et Phys. l'Acad. Sci. **10**, 161–331 (1785)
2. Hartog, J.D.: *Forced vibrations with combined viscous and Coulomb damping*. Lond. Edinb. Dubl. Philos. Mag. J. Sci. **9**(59), 801 (1930)
3. Andronov, A., Bautin, N.: *Dvizhenie nejtral'nogo samoleta, snabzhenogo avtopilotom, i teoriya tochechnyh preobrazovanij poverhnostej* (Motion of a neutral aeroplane supplied with an automatic pilot and the theory of pointwise transformations of surfaces). Dokl. Akad. Nauk SSSR **43**(5), 197 (1944)
4. Keldysh, M.: *O dempferakh s nelinejnoj kharakteristikoj* (On dampers with a nonlinear characteristic). TsAGI Tr. **557**, 26 (1944)
5. Bennett, S.: *A history of control engineering 1930–1955*. IET (1993)
6. Emelyanov, S.: *Sistemy avtomaticheskogo upravleniya s peremennoj strukturoj* (Automatic control systems with variable structure). Nauka (1967)
7. Poznyak, A., Yu, W., Sanchez, E., Perez, J.: *Nonlinear adaptive trajectory tracking using dynamic neural networks*. IEEE Trans. Neural Networks **10**(6), 1402–1411 (1999)
8. Utkin, V., Poznyak, A.: *Adaptive sliding mode control with application to super-twist algorithm: equivalent control method*. Automatica **49**(1), 39–47 (2013)
9. Best, R.E., Kuznetsov, N.V., Leonov, G.A., Yuldashev, M.V., Yuldashev, R.V.: *Tutorial on dynamic analysis of the Costas loop*. IFAC Annu. Rev. Control **42**, 27–49 (2016)
10. Kuznetsov, N.V., Kuznetsova, O.A., Leonov, G.A., Yuldashev, M.V., Yuldashev, R.V.: *A short survey on nonlinear models of QPSK Costas loop*. IFAC-PapersOnLine **50**(1), 6525–6533 (2017)
11. Filippov, A.: *Differencial'nye uravneniya s razryvnoj pravoj chast'yu* (Differential equations with discontinuous right-hand side). Mat. Sb. (N.S.) **51**(1), 99–128 (1960)
12. Ważewski, T.: *Sur une condition équivalente à l'équation au contingent*. Bull. Acad. Polon. Sci. Sér. Sci. Math. Astronom. Phys. **9**, 865–867 (1961)
13. Gelig, A.K., Leonov, G.A., Yakubovich, V.A.: *Ustojchivost' nelinejnyh sistem s needinstvennym sostoyaniem ravnowesiya* (Stability of Nonlinear Systems with Nonunique Equilibrium). Nauka (1978) [English transl: *Stability of Stationary Sets in Control Systems with Discontinuous Nonlinearities*. World Scientific (2004)]
14. Aizerman, M.A., Pyatnitskii, E.S.: *Foundations of a theory of discontinuous systems. I*. Autom. Remote Control **35** 1066–1079 (1974)
15. Piironen, P.T., Kuznetsov, Yu.A.: *An event-driven method to simulate Filippov systems with accurate computing of sliding motions*. ACM Trans. Math. Softw. (TOMS) **34**(3), 13 (2008)
16. Kiseleva, M., Kuznetsov, N.: *Coincidence of Gelig-Leonov-Yakubovich, Filippov, and Aizerman-Pyatnitskii definitions*. Vestn. St. Petersburg Univ. Math. **48**(2), 66–71 (2015)
17. Cortes, J.: *Discontinuous dynamical systems*. IEEE Control Syst. **28**(3), 36–73 (2008)
18. Kuznetsov, N.V., Lobachev, M.Y., Yuldashev, M.V., Yuldashev, R.V., Kudryashova, E.V., Kuznetsova, O.A., Rosenwasser, E.N., Abramovich, S.M.: *The birth of the global stability theory and the theory of hidden oscillations*. In: 2020 European Control Conference (ECC), pp. 769–774 (2020)
19. Andronov, A.A., Vitt, E.A., Khaikin, S.E.: *Teoriya kolebanij* (Theory of Oscillators). ONTI NKTP SSSR (1937). [English transl.: Pergamon Press (1966)]
20. Andronov, A.A., Maier, A.G.: *Zadacha Mizesa v teorii pryamogo regulirovaniya i teoriya tochechnyh preobrazovanij poverhnostej* (The Mizes problem in the theory of direct control and the theory of point transformations of surfaces). Dokl. Akad. Nauk SSSR **43**(2), 58–60 (1944)
21. Andronov, A.A., Maier, A.G.: *Zadacha Vyshnegradskogo v teorii pryamogo regulirovaniya. I* (The problem of Vyshnegradsky in the theory of direct regulation). Avtomat. Telemekh. **8**(5), 314–335 (1947)

22. Andronov, A.A., Maier, A.G.: Zadacha Vyshnegradskogo v teorii pryamogo regulirovaniya. I (The problem of Vyshnegradsky in the theory of direct regulation). *Avtomat. Telemekh.* **15**(5), 505–530 (1953)
23. Barbashin, E.A., Krasovsky, N.N.: Ob ustojchivosti dvizheniya v celom (On the stability of a motion in the large). *Dokl. Akad. Nauk SSSR* **86**(3), 453–456 (1952)
24. Leonov, G.A., Kuznetsov, N.V., Kiseleva, M.A., Mokaev, R.N.: Global problems for differential inclusions. Kalman and Vyshnegradskii problems and Chua circuits. *Differ. Equ.* **53**, 1671–1702 (2017)
25. Polyakov, A., Fridman, L.: Stability notions and Lyapunov functions for sliding mode control systems. *J. Franklin Inst.* **351**(4), 1831–1865 (2014)
26. Polyakov, A.: Discontinuous Lyapunov functions for nonasymptotic stability analysis. *IFAC Proc. Vol.* **47**(3), 5455–5460 (2014)
27. Popov, V.M.: Criterii de stabilitate pentru sistemele neliniare de reglare automata, bazate pe utilizarea transformatei Laplace. *Studii Cercet. Energ.* (in Romanian) **9**(1), 119–135 (1959)
28. Popov, V.M.: Criterion of quality for non-linear controlled systems. *IFAC Proc. Vol.* **1**(1), 183–187 (1960)
29. Popov, V.M.: Absolute stability of nonlinear systems of automatic control. *Autom. Remote Control* **22**(8), 857–875 (1961)
30. Yakubovich, V.A.: Reshenie nekotoryh matrichnyh neravenstv, vstrechayushchihsvya v teorii avtomaticheskogo regulirovaniya (The solution of certain matrix inequalities in automatic control theory). *Dokl. Akad. Nauk SSSR* **143**(6), 1304–1307 (1962) [English transl: *Soviet Math. Dokl.* (1962)]
31. Kalman, R.E.: Lyapunov functions for the problem of Lur'e in automatic control. *Proc. Natl. Acad. Sci. U.S.A.* **49**(2), 201 (1963)
32. Barabanov, N.E., Gelig, A.Kh., Leonov, G.A., Likhtarnikov, A.L., Matveev, A.S., Smirnova, V.B., Fradkov, A.L.: The frequency theorem (the Yakubovich-Kalman lemma) in control theory. *Autom. Remote Control* **10**(9), 3–40 (1996)
33. Leonov, G.A.: Concerning stability of nonlinear controlled systems with non-single equilibrium state. *Autom. Remote Control* **32**(10), 1547–1552 (1971)
34. Gelig, A.Kh.: Investigations of stability of nonlinear discontinuous automatic control systems with a nonunique equilibrium state (transl.). *Avtomat. Remote Control* **25**, 141–148 (1964)
35. Vidyasagar, M.: *Nonlinear Systems Analysis*. Prentice-Hall (1978)
36. Haddad, W.M., Chellaboina, V.S.: *Nonlinear Dynamical Systems and Control: A Lyapunov-Based Approach*. Princeton University Press (2011)
37. Leonov, G.A., Reitmann, V., Smirnova, V.B.: *Nonlocal Methods for Pendulum-like Feedback Systems*. Teubner Verlagsgesellschaft, Stuttgart-Leipzig (1992)
38. Bragin, V.O., Vagaitsev, V.I., Kuznetsov, N.V., Leonov, G.A.: Algorithms for finding hidden oscillations in nonlinear systems. The Aizerman and Kalman conjectures and Chua's circuits. *J. Comput. Syst. Sci. Int.* **50**(4), 511–543 (2011)
39. Kuznetsov, N.: Theory of hidden oscillations and stability of control systems. *J. Comput. Syst. Sci. Int.* **59**(5), 647–668 (2020)
40. Leonov, G.A., Kuznetsov, N.V.: Hidden attractors in dynamical systems. From hidden oscillations in Hilbert-Kolmogorov, Aizerman, and Kalman problems to hidden chaotic attractors in Chua circuits. *Int. J. Bifurc. Chaos Appl. Sci. Eng.* **23**(1), 1330002 (2013)
41. Kuznetsov, N.V., Leonov, G.A.: Hidden attractors in dynamical systems: systems with no equilibria, multistability and coexisting attractors (survey lecture, 19th IFAC World Congress). *IFAC Proc. Vol.* **47**, 5445–5454 (2014)
42. Bautin, N.N.: *Povedenie dinamiceskikh sistem vblizi granic ustojchivosti* (The Behaviour of Dynamical Systems close to the Boundaries of a Stability Domain). Gostekhizdat, Leningrad, Moscow (1949)
43. Kuznetsov, N.V.: Plenary lecture “Theory of hidden oscillations”. In: 5th IFAC Conference on Analysis and Control of Chaotic Systems (2018)
44. Kuznetsov, N.V.: Plenary lecture “Theory of hidden oscillations”. In: 11th Russian Multiconference on Control Problems. Proceedings, pp. 41–54 (2018)

45. Kuznetsov, N.V.: Teoriya skrytykh kolebaniy (Theory of hidden oscillations). In: XIII All-Russian Meeting on Control Problems. Proceedings, pp. 103–107 (2019)
46. Kuznetsov, N.V.: Plenary lecture “Theory of hidden oscillations and stability of control systems”. In: International Conference “Stability, Control, Differential Games” Devoted to the 95th Anniversary of Academician N.N. Krasovskiy (Yekaterinburg), pp. 201–204 (2019)
47. Kuznetsov, N.V.: Invited lecture “Theory of hidden oscillations and stability of control systems”. In: XII All-Russian Congress on Fundamental Problems of Theoretical and Applied Mechanics (UFA, Russia) (2019). <https://www.youtube.com/watch?v=843m-rl5nTM>
48. Kuznetsov, N., Mokaev, T., Kuznetsova, O., Kudryashova, E.: The Lorenz system: hidden boundary of practical stability and the Lyapunov dimension. *Nonlinear Dyn.* **102**, 713–732 (2020)
49. Kapranov, M.: Locking band for phase-locked loop. *Radiofizika* **11**(12), 37–52 (1956)
50. Kuznetsov, N.V., Leonov, G.A., Yuldashev, M.V., Yuldashev, R.V.: Hidden attractors in dynamical models of phase-locked loop circuits: limitations of simulation in MATLAB and SPICE. *Commun. Nonlin. Sci. Numer. Simulat.* **51**, 39–49 (2017)
51. Kuznetsov, N. et al.: Comments on van Paemel’s mathematical model of charge-pump phase-locked loop. *Differentsialnie Uravneniya i Protsesy Upravleniya* **1**, 109–120 (2019). <https://diffjournal.spbu.ru/pdf/19107-jdec-p-kuznetsov.pdf>
52. Kuznetsov, N., Matveev, A., Yuldashev, M., Yuldashev, R., Bianchi, G.: Stability of charge-pump phase-locked loops: the hold-in and pull-in ranges. *IFAC-PapersOnLine*, **53**(2), 2022–2026 (2020). IFAC World Congress
53. Gubar’, N.A.: Issledovanie odnoj kusochno-lineynoy dinamicheskoy sistemy s tremya parametrami (Investigation of a piecewise linear dynamical system with three parameters). *Prikl. Mat. i Mekh.* **25**(6), 1011–1023 (1961)
54. Van der Pol, B.: A theory of the amplitude of free and forced triode vibrations. *Radio Rev.* **1**, 701–710 (1920)
55. Krylov, N.M., Bogolyubov, N.N.: *Vvedenie v nelinejnyuyu mekhaniku* (Introduction to nonlinear mechanics. AN USSR, Kiev (1937) [English transl: Princeton University Press (1947)])
56. Goldfarb, L.S.: O nekotorykh nelinejnostyakh v sistemah regulirovaniya (Certain nonlinearities in control systems). *Autom. Telemekh.* **8**(5), 349–383 (1947)
57. Khalil, H.K.: *Nonlinear Systems*. Prentice Hall, N.J (2002)
58. Tsytkin, Y.Z.: *Teoriya relejnykh sistem avtomaticheskogo upravleniya*. In: *Theory of Relay Control Systems*. Moscow, Gostekhizdat (1955)
59. Boiko, I.: *Discontinuous control systems: frequency-domain analysis and design*. Springer Science & Business Media (2008)
60. Akimova, E.D., Boiko, I.M., Kuznetsov, N.V., Mokaev, R.N.: Analysis of oscillations in discontinuous Lurie systems via LPRS method. *Vibroengineering PROCEDIA* **25**, 177–181 (2019)
61. Lurie, A.I., Postnikov, V.N.: K teorii ustojchivosti reguliruemykh sistem (To the stability theory of controlled systems). *Prikl. Mat. Mekh.* **8**(3), 246–248 (1944)
62. Lurie, A.I.: *Nekotorye nelinejnye zadachi teorii avtomaticheskogo regulirovaniya* (Some Nonlinear Problems in the Theory of Automatic Control), Gostekhizdat (1951) [English transl: H.M. Stationery Office, London (1957)]
63. Boiko, I.M., Kuznetsov, N.V., Mokaev, R.N., Akimova, E.D.: On asymmetric periodic solutions in relay feedback systems. *J. Franklin Inst.* **358**(1), 363–383 (2021)
64. Kahn, P.B., Zarmi, Y.: *Nonlinear Dynamics. Exploration through normal forms*, Wiley, New York (1998)
65. Sprott, J.C., Jafari, S., Khalaf, A.J.M., Kapitaniak, T.: Megastability: coexistence of a countable infinity of nested attractors in a periodically-forced oscillator with spatially-periodic damping. *Eur. Phys. J. Spec. Top.* **226**(9), 1979–1985 (2017)
66. Vyshnegradskiy, I.A.: O regulyatorah pryamogo dejstviya (On regulators of direct action). *Izv. St. Petersburg Technol. Inst.* **1** (1877)
67. Poincare, H.: *Les methodes nouvelles de la mecanique celeste*. Gauthiers-Villars, Paris **13** (1892, 1893, 1899). [English transl. edited by D. Goroff: American Institute of Physics, NY (1993)]

68. Léauté, M.H.: Mémoire sur les oscillations à longue période dans les machines actionnées par des moteurs hydrauliques et sur les moyens de prévenir ces oscillations. *J. de l'école Polytech.* **55**, 1–126 (1885)
69. Zhukovsky, N.Y.: *Teoriya regulirovaniya hoda mashin (Theory of regulation of the course of machines)*. Tipo-litgr. T-va I. N. Kushnerev and Co. (1909)
70. Kalman, R.E.: Physical and mathematical mechanisms of instability in nonlinear automatic control systems. *Trans. ASME* **79**(3), 553–566 (1957)
71. Leonov, G., Ponomarenko, D., Smirnova, V.: *Frequency-Domain Methods for Nonlinear Analysis. Theory and Applications*, World Scientific, Singapore (1996)
72. Erugin, N.P.: Ob odnoj zadache teorii ustojchivosti sistem avtomaticheskogo regulirovaniya (A problem in the theory of stability of automatic control systems). *Prikl. Mat. Mekh.* **5**, 620–628 (1952)
73. Malkin, I.G.: Ob ustojchivosti sistem avtomaticheskogo regulirovaniya (On the stability of automatic control systems). *Prikl. Mat. Mekh.* **16**(4), 495–499 (1952)
74. Krasovsky, N.N.: Teoremy ob ustojchivosti dvizhenij, opredelyaemyh sistemoj dvuh uravnenij (Theorems on the stability of motions determined by a system of two equations). *Prikl. Mat. Mekh.* **16**(5), 547–554 (1952)
75. Kuznetsov, N.V., Lobachev, M.Y., Yuldashev, M.V., Yuldashev, R.V.: The Egan problem on the pull-in range of type 2 PLLs. *IEEE Trans. Circuits Syst. II Express Briefs* **68**(4), 1467–1471 (2021)
76. Leonov, G.A., Kuznetsov, N.V., Andrievsky, B.R., Yuldashev, M.V., Yuldashev, R.V.: Mathematical modeling of transients of the hydraulic unit of the Sayano-Shushenskaya HPP. *Differencialnie Uravnenia i Protsesy Upravlenia (Differential Equations and Control Processes)* **4**, 80–106 (2018)
77. Leonov, G.A., Kuznetsov, N.V., Solovyeva, E.P.: Mathematical modeling of vibrations in turbo-generator sets of Sayano-Shushenskaya hydroelectric power station. *Dokl. Phys.* **61**(2), 55–60 (2016)
78. Kuznetsov, N.V., Yuldashev, M.V., Yuldashev, R.V.: Analytical-numerical analysis of closed-form dynamic model of Sayano-Shushenskaya hydropower plant: stability, oscillations, and accident. *Commun. Nonlinear Sci. Numer. Simul.* **93**, 105530 (2021)
79. Leonov, G.A., Kuznetsov, N.V.: On flutter suppression in the Keldysh model. *Dokl. Phys.* **63**(9), 366–370 (2018)
80. Kudryashova, E.V., Kuznetsov, N.V., Kuznetsova, O.A., Leonov, G.A., Mokaev, R.N.: Harmonic balance method and stability of discontinuous systems. In: Matveenko, V.P., et al. (eds.) *Dynamics and Control of Advanced Structures and Machines*, pp. 99–107. Springer Nature, Switzerland (2019)
81. Kuznetsov, N.V., Kuznetsova, O.A., Koznov, D.V., Mokaev, R.N., Andrievsky, B.R.: Counterexamples to the Kalman conjectures. *IFAC-PapersOnLine* **51**(33), 138–143 (2018)

Chapter 21

Strain Behavior of Aluminum Alloys Under Dynamic Compression and Tensile



Yuri I. Meshcheryakov, Grigory V. Konovalov, Natali I. Zhigacheva, Alexander K. Divakov, and Alexey F. Nechunaev

Abstract Two kinds of aluminum alloy, 1561 and 1565 alloys, were tested within impact velocity range of 241.9–744.8 m/s in two schemes of shock loading: (i) under uniaxial strain conditions and (ii) in high-velocity penetration. Combination of load regimes allows a formation of multiscale structure to be retraced. Formation of mesoscale-1 in form of micro-shears of 3–10 mkm is found to be identical for both kinds of alloy. As for the mesoscale-2 (50–150 mkm), the formation of dynamic structures for two kinds of alloy is of different nature. In 1565 alloy the transition from mesoscale-1 to mesoscale-2 occurs in form of structural instability whereas in 1561 alloy this transition happens gradually. In 1561 alloy the mesoscale-2 structural elements are elongated plights and ellipsoids whereas in 1565 alloy the mesoscale-2 structures are the fault cells at the boundary of penetration cavern. Affect of transition from mesoscale-1 to mesoscale-2 in both aluminum alloys turns out to opposite: in 1561 alloy the transition on to mesoscale-2 decreases the resistance to high-velocity penetration whereas in 1565 alloy the formation of mesoscale-2 structures increases the resistance to penetration. Numerical simulation of impact aluminum mm-size projectile in same aluminum target with speeds ~ 300 m/s in the moment ~ 240 nanoseconds after the beginning of interaction at mesoscale-2 shown turbulization of particle motion of the environment at their movement in close proximity to target axis of gravity. Numerical researches demonstrated that transition of material to the structural and unstable state has the local and kinetic nature of impact damage material.

Keywords Aluminum alloys · Spallation · Penetration · Structure-unstable state

Y. I. Meshcheryakov (✉) · G. V. Konovalov · N. I. Zhigacheva · A. K. Divakov · A. F. Nechunaev
Institute for Problems in Mechanical Engineering RAS, V.O., Bolshoy pr., 61, St. Petersburg
199178, Russia
e-mail: ym38@mail.ru

© The Author(s), under exclusive license to Springer Nature Switzerland AG 2022
V. A. Polyanskiy and A. K. Belyaev (eds.), *Mechanics and Control of Solids and Structures*, Advanced Structured Materials 164,
https://doi.org/10.1007/978-3-030-93076-9_21

413

21.1 Introduction

Further developing of the mechanics of deformed solid supposes the incorporating of multiscale mechanisms of deformation and fracture. The multiscale mechanics implies a formation of intermediate scales between macroscale and microscale followed by transient non-equilibrium processes. At least three scale levels of deformation have been recognized for over several decades: dislocation scale, mesoscale, and macroscale. The modern approaches to dynamic mesoscale assume a subdividing the mesoscale by two sublevels—the mesoscale-1 (1–10 mkm) and mesoscale-2 (50–500 mkm) [1–4]. Herewith, the elementary carriers of dynamic deformation at the mesoscale-1 are found to be the short-living (150–200 ns) single-sign dislocation groups [5–7]. The process of collectivization and motion of dislocations results in particle velocity fluctuations, which is registered in the form of particle velocity distribution at the mesoscale-1 [8, 9] (Fig. 21.1a).

In parallel, the shock-wave experiments under uniaxial strain conditions with the LINE-VISAR registration reveal the velocity fluctuations at the mesoscale-2 for tantalum [10], boron ceramics [11], and sugar [12] (Fig. 21.1b).

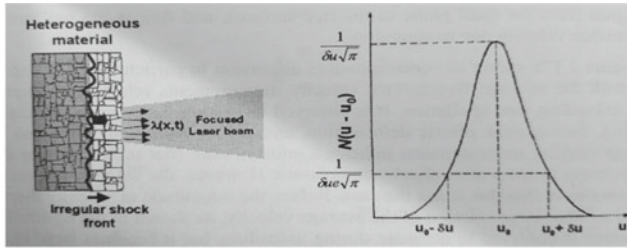
Specifically, experiments with tantalum revealed a direct coupling of the particle velocity distribution at the mesoscale-2 with the mechanism of spallation [10].

Simulation of “wavy-wave” shock-wave propagation with taking into account the particle velocity distribution at the mesoscale has been conducted in [13–15]. Evolution of the particle velocity distribution function as far as propagating of the shock wave through the target is shown in Fig. 21.2.

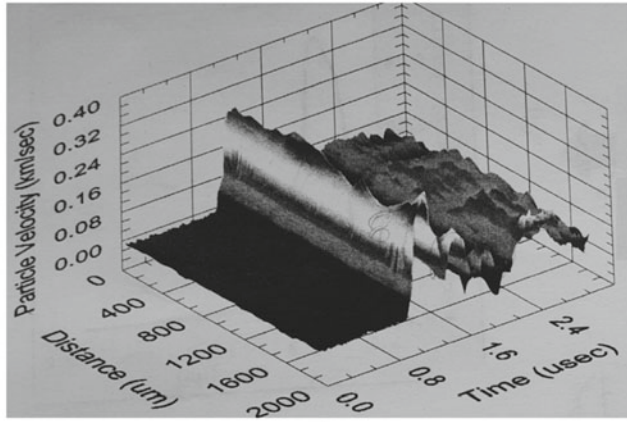
The significant result of simulation of [14] is a discovery of threshold particle velocity at what the material (polycrystalline copper) transits into structure-unstable state whereas the mechanism of dynamic deformation changes from uniform to turbulent.

In this paper, in order to identify the successive stages of developing the hierarchy of multiscale mechanisms of dynamic deformation, the formation of mesostructure is studied in combined experiments. A critical step in having an efficient picture of multiscale processes is the parallel tests in two schemes of shock loading. The first scheme is the test under uniaxial strain conditions whereas the second scheme is the high-velocity penetration of elongated rigid rod. By using the combine technique of shock loading, an attempt is made to visualize the processes of the multiscale structure formation.

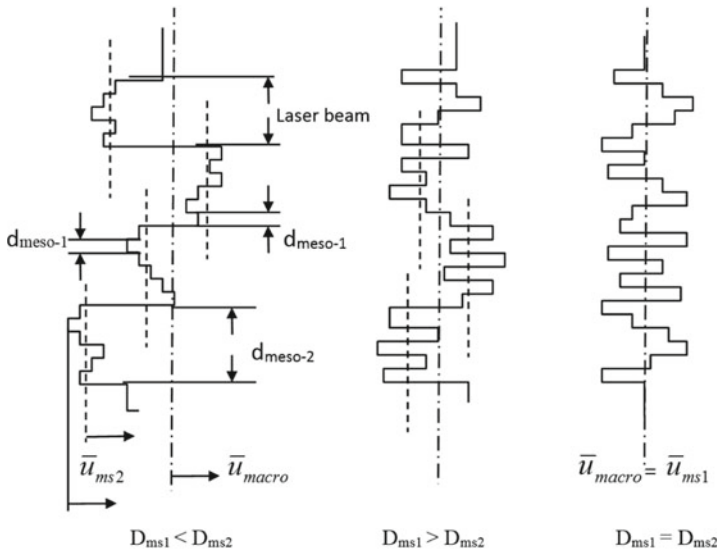
Two kinds of materials—1561 and 1565 aluminum alloys—were subjected to dynamic tests in order to show different mechanisms of transition from one scale to another depending on the chemical composition and initial morphology of material. The first kind of alloy has previously been tested under identical loading conditions without comparative analysis of results [16]. In present study, the results of tests for both materials are provided in order to show the difference in coupling the multiscale mechanisms of dynamic deformation and dynamic plasticity and strength of material.



a)



b)



c)

Fig. 21.1 a—Qualitative pattern of laser beam and free surface of target interaction at the mesoscale-1 (after [1]), b—at the mesoscale-2 (after [1]); c—U-L velocity-space configurations of shock front for different relations between velocity dispersions at mesoscale-1 and mesoscale-2

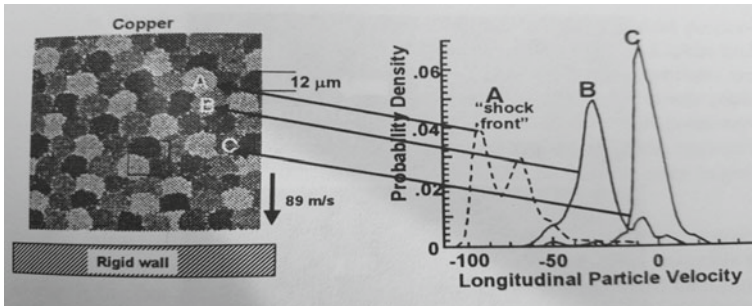


Fig. 21.2 Evolution of the mesoparticle velocity distribution function as far as propagating through the target (after [14])

21.2 Experimental Technique

Shock tests under uniaxial strain conditions were conducted with one-stage light gas gun of 37 mm barrel diameter. Functional scheme of equipment for tests under uniaxial strain conditions and constructions of impactors for plane collision and for penetration tests are presented in Fig. 21.3. Plane targets were the discs of 52 mm in diameter and 7 mm thick. Data on dynamic strength and plasticity of material, including dynamic yield limit, spall strength and threshold of structural instability and particle velocity distribution are inferred from the temporal profiles of the free surface velocity, $u_{fs}(t)$, registered with two-channel velocity interferometer.

Detailed analysis of the velocity interferometer is given in [17]. The coupling between mean particle velocity $u(t)$ and number of fringe signal beats, $N(t)$, takes the form:

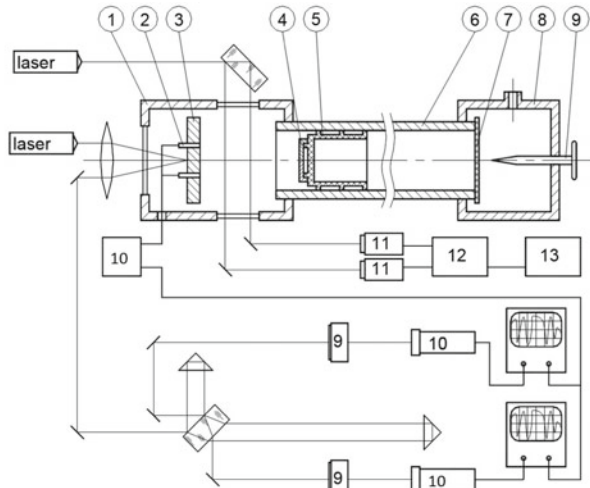
$$u(t) = \frac{\lambda_0}{2\tau_d} N(t) \tag{21.1}$$

Here $U_{int} = \lambda_0/2\tau_d$ is the interferometer constant which is determined by the wave length of laser radiation λ_0 and τ_d is the time delay of laser radiation in delay shoulder of interferometer. In [8, 9] the additional relationship which ties the contrast of fringe signal K and particle velocity dispersion, D , is obtained for the case of the particle velocity distribution:

$$K = \exp \left[-\frac{1}{2} \frac{\pi^2 D^2}{U_{int}^2} \right] \tag{21.2}$$

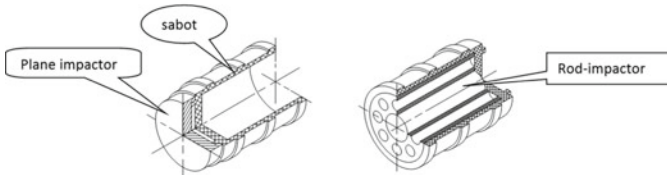
The number of fringe signal beats is seen to be determined by the mean particle velocity, $u(t)$, (Eq. (21.1)) whereas the amplitude of fringe beats and accordingly, interference contrast, K , are determined by the particle velocity dispersion D^2 , Eq. (21.2). The current values of both characteristics can be registered during the single action of shock loading.

Expressions for mean particle velocity (21.1) and for the velocity dispersion (21.2) have been verified with the set of targets manufactured from different materials such

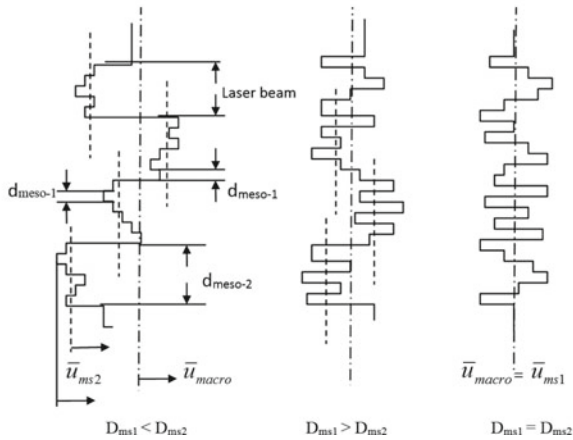


1 – vacuum chamber, 2 – pins, 3 – target, 4 – projectile, 5 – sabot, 6 – barrel, 7 – membrane, 8 – high pressure chamber, 9 – polaroid, 10 - photo detectors, 11-12 – amplifiers, 13 – equipment for measuring the time intervals

a)



b)



c)

Fig. 21.3 a—functional scheme of facility for the shock tests under uniaxial strain conditions; b—poly-vinyl-carbonate sabot and plane and rod projectiles

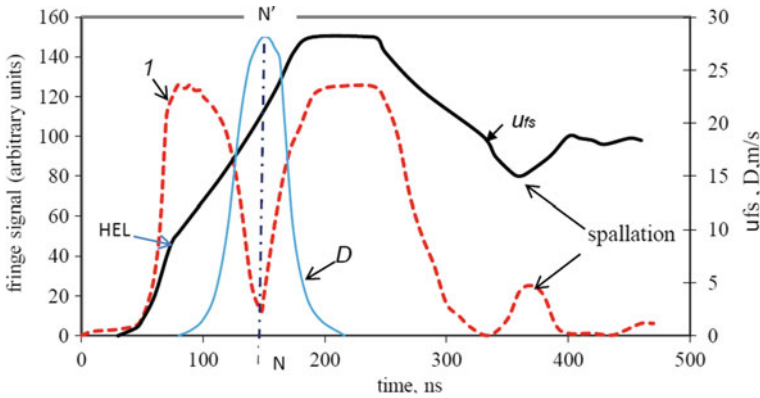


Fig. 21.4 Fringe signal, deciphered free surface velocity profile, u_{fs} , and velocity variance, D , for steady wave in 5 mm steel target loaded at the impact velocity of 150 m/s

as aluminum and titanium alloys, steels, copper, and other materials. These materials are of different degree of heterogeneity which creates the different particle velocity distribution and, accordingly, different velocity dispersion. One of the examples of interferogram registered with interferometer for 5 mm 28Cr3NiMoV steel target is provided in Fig. 21.4. The number of fringe signal beats at the forehead front of compressive pulse equal 1.5. If the interferometer constant equals $U_{int} = 100$ m/s per one beat, the maximum free surface velocity at the plateau of compressive pulse equals 150 m/s, which coincides with the velocity of projectile $U_{pj} = 150$ m/s. This satisfies to well-known rule for the velocity redoubling when shock wave comes to the free surface of target [18]:

$$u_{fs} = 2u_p = U_{pj} \tag{21.3}$$

where u_{fs} is the free surface velocity and u_p is the particle velocity inside the target; U_{pj} is the velocity of projectile.

It can be seen that amplitude of fringe signal decreases in the middle of forehead front (line $N'N$) and again restored up to the maximum value to plateau of pulse. This means that the velocity distribution is widen to the middle of plastic front and then again narrowed at the plateau of pulse up to δ -function. The value of fringe signal contrast in the middle of plastic front equals $K = 0,727$. In accordance with Eq. (21.2), the velocity variance equals:

$$D = \frac{U_{int}}{\pi} \sqrt{-2\ln K} = \frac{100}{\pi} \sqrt{-2\ln 0,727} = \frac{100}{\pi} \sqrt{-2\ln 0,727} = 21,2 \text{ m/s.}$$

Here the velocity variance D corresponds to width of the velocity distribution in the middle of plastic front. Presented in Fig. 21.4 example reflects the situation

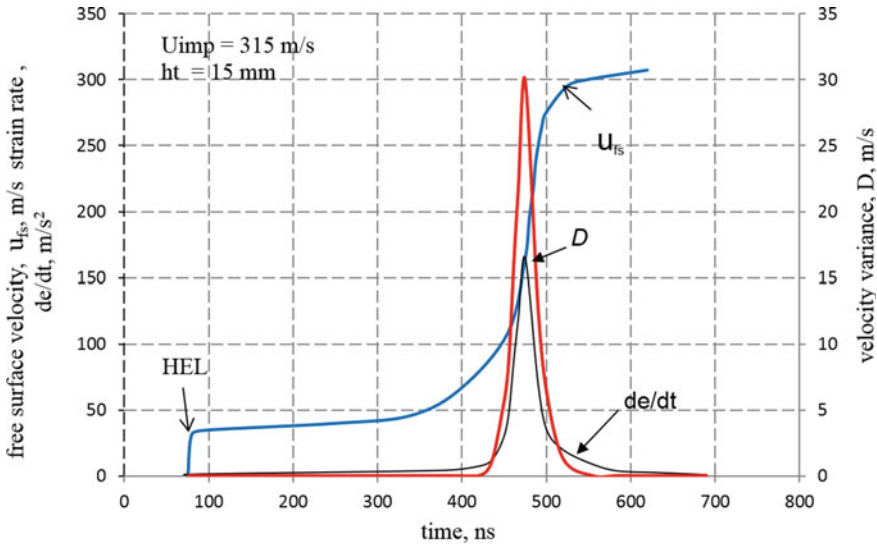


Fig. 21.5 Dependencies of the velocity variance, D , strain rate, $d\epsilon/dt$, and free surface velocity profile for steady situation in 15 mm D16 aluminum alloy target loaded at the impact velocity of 315 m/s

when the velocity distribution is maximum in the middle of plastic front. In the steady shock-wave velocity variance, maximum strain rate coincide with the middle of shock front [19] (see Fig. 21.5)

If, however, the plastic front has no time to become steady, amplitude of fringe signal continues to decrease up to plateau of pulse. It, in turn, means that the velocity dispersion grows along the plastic wave. Typical example of change of the free surface velocity for the non-steady plastic wave is presented in Fig. 21.6 where the fringe signal, deciphered free surface profile and velocity variation are provided together for shock loading of 5 mm 30CrNi4Mo steel target loaded at the impact velocity of 320 m/s. It is clearly seen that amplitude of fringe signal has no time to restore upto maximum value during the plastic front. The contrast of fringe signal continues to decrease so just before pulse plateau velocity variance equals 34 m/s. This means that shock wave has no time to come on the steady regime.

In our experiments, the laser beam of interferometer at the free surface of target is focused up to 60–70 μm , so the registered free surface profile corresponds to single element of mesoscale-2 (50–500 μm). In this situation, the registered mean particle velocity concerns the motion of single element of mesoscale-2. At the same time, within single structural element of mesoscale-2 there are a lot of structural elements of mesoscale-1 (1–10 μm) (see Fig. 21.1a), so the interferometer registers the velocity distribution of the elementary carriers of deformation of mesoscale-1 inside the single structural element of mesoscale-2. To obtain the mean macroscopic free surface response of target on impact, one has to average the mesoscale-2 responses over target. The free surface velocity profile in 1565 aluminum alloy target shown in

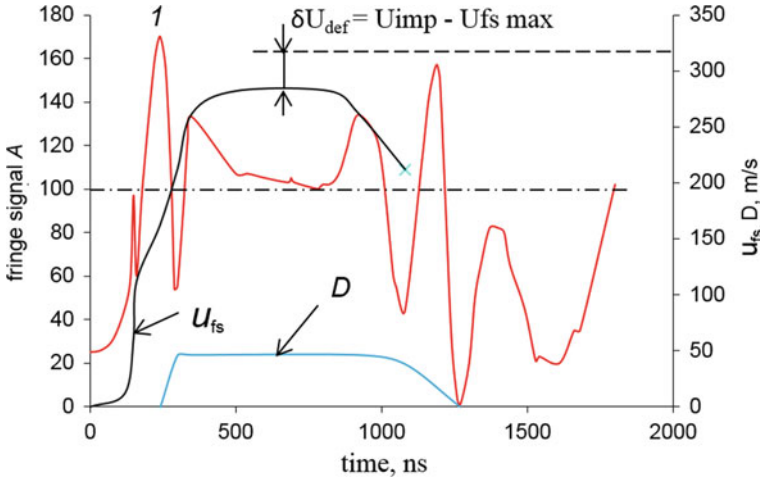


Fig. 21.6 Fringe signal, deciphered free surface velocity profiles, u_{fs} , and velocity variance, D , for unsteady wave in 5 mm steel target loaded at the impact velocity of 320 m/s

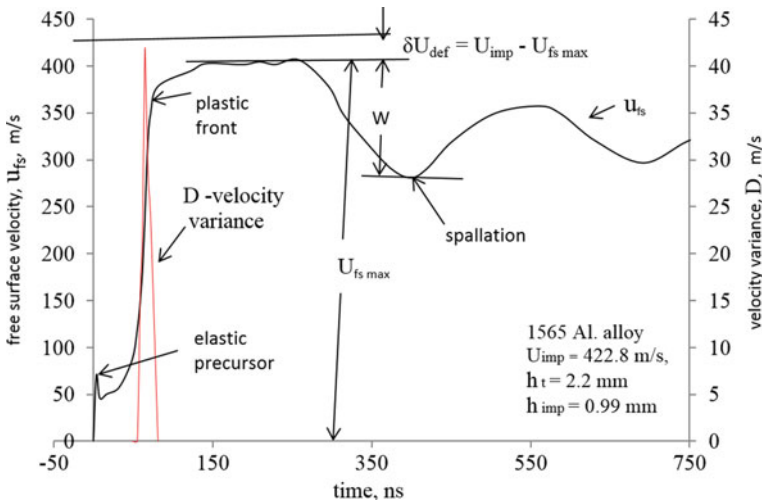


Fig. 21.7 Free surface velocity profile, $u_{fs}(t)$, and particle velocity variance profile, $D(t)$, for steady wave at the mesoscale-2 in 1565 aluminum alloy target at the impact velocity of 442.8 m/s

Fig. 21.7 is a typical response of single structural element of mesoscale-2. This profile provides the information on mean free surface velocity, $u_{fsm2}^{fv}(t)$ at the mesoscale-2 and velocity variance, $D(t)$ (square root of the particle velocity dispersion), at the mesoscale-1 (1–10 mkm). This is the main distinction of our diagnostic approach as compared to that based on VISAR instrumentation which registers only the mean free surface velocity over the target [20].

The velocity defect δU_{def} quantitatively characterizes the intensity of macro-meso momentum exchange. In the case of shock-wave experiments, determination of velocity defect is based on independent measuring the impact velocity U_{pj} under symmetrical collision of impactor and target and maximum free surface velocity U_{fsmax} at the plateau of compressive. According to the free surface approximation, in the case of symmetrical collision of projectile and target ($\rho_{\text{pj}}C_{\text{pj}} = \rho_{\text{tag}}C_{\text{tag}}$), the particle velocity equals to half of impact velocity, i.e., $u_p = \frac{1}{2}U_{\text{pj}}$. On the other hand, when the shock wave comes to the free surface of target, the mean velocity is redoubled. In this case, the impact velocity equals to the free surface velocity, i.e., $U_{\text{pj}} = U_{\text{fsmax}}$. Specifically, in the case of shock loading of iron, this equality has been experimentally studied in detail and confirmed in [21].

The specifics of used diagnostics is in focusing the laser beam of interferometer up to 50–70 mkm. In this case, the mean particle velocity corresponds to motion of single mesoscale-2 structural element whereas the velocity dispersion corresponds to velocity distribution of mesoscale-1 structural elements inside the mesoscale-2 element. The time of relaxation of the particle velocity distribution function from non-equilibrium state to equilibrium that for different scales may differ by orders. This means that particle velocity distribution function for mesoscale-1 may be equilibrium whereas for mesoscale-2 it may be far from equilibrium. The situation shown in Fig. 21.7 presents the steady shock front in 2.2 mm 1565 aluminum alloy target.

In this investigation, the processes of dynamic deformation are considered from the position of physical kinetics [4]. In the frame of this approach, the dynamic deformation, instead of dislocation mechanisms of deformation, is considered to be the motion of elementary carriers of deformation at the mesoscale (motion of mesoparticles). In accordance with the mesomechanics, the mesoparticles are the positive and negative dislocation groups which suffer two kinds of interaction: (i) the long-range mutual interaction and (ii) interaction with the medium where they move. From the position of physical kinetics, the motion of mesoparticles can be characterized by the particle velocity distribution function $f(\mathbf{r}, \mathbf{v}, t)$ and/or its statistical moments. In the case of quasi-equilibrium situation, the mean particle velocity, $u(\mathbf{x}, t)$, and particle velocity dispersion, $D^2(\mathbf{x}, t)$, are the first and second statistical moments of the particle velocity distribution function:

$$u(\mathbf{x}, t) = \int \mathbf{v} f(\mathbf{x}, \mathbf{v}, t) d\mathbf{v}$$

$$D^2(\mathbf{x}, t) = \int (\mathbf{v} - u)^2 f(\mathbf{x}, \mathbf{v}, t) d\mathbf{v} \quad (21.4)$$

In this situation, the propagation of shock wave in heterogeneous medium may be presented as a superposition of two modes—propagation of approximately rectilinear front with mean particle velocity $u(\mathbf{x}, t)$, and random motions around mean velocity as a result of fluctuative strain fields induced by the random internal stresses. It is fortunate, the parameters of dynamic deformation can be registered with interference technique of shock waves diagnostics in real time. Principles of measuring the particle

velocity variation, D (square root of the particle velocity dispersion, D^2) and mean particle velocity, $u(x, t)$, are in detail discussed everywhere [8, 9].

In the case of shock loading of heterogeneous solids, the equality $U_{\text{imp}} = U_{\text{fs max}}$ is not accomplished. If the strain rate is higher the critical value of strain rate corresponding to the threshold of structural instability, the velocity defect emerges, so $\delta U_{\text{def}} = (U_{\text{imp}} - U_{\text{fs max}}) \neq 0$ (Fig. 21.6). This phenomenon allows to reveal the principally new mechanism of structural instability. As distinct from the heat mechanism of [22, 23], the new mechanism of structural instability is found to be of kinetic nature.

Development of structural instability turns out to occur at the critical relation between rate of change of the velocity dispersion at the mesoscale-1 and velocity defect for the mesoscale-2. Scenario for developing the kinetic structural instability includes the following stages.

1. Formation of totality of mesoscale-1 structural elements as collectives of single-sign dislocations.
2. Chaotisation of mesoscale-1 structural elements.
3. Threshold transition into structural-unstable state and turbulization of meso-1 particles within meso-2 volume. Condition for transition into structural-unstable state is the avalanche-like growth of the velocity dispersion at the mesoscale-1.
4. Decrease of mean velocity of meso-2 structural element and appearance of the velocity defect at the meso-2 scale.

Above scenario is proper for the non-equilibrium processes at which the mesoparticle velocity distribution function is not symmetrical. For the non-symmetrical particle velocity distribution function, the number of particles with the velocities smaller the mean particle velocity is greater than number of particles with the velocities greater the mean particle velocity. In this case, the so-called “Landau decay” takes place [24, 25], which is registered as a decrease, or defect, of mean velocity. Experiments show (i) the local values of the velocity defect can reach large values, up to hundred meters per second, whereas the mean velocity defect over the target surface can be very small or absent at all, (ii) as distinct from the dissipation, this kind of decay (Landau decay) is reversible, it disappears when the mesoparticle velocity distribution function tends to equilibrium state. In the frame of physical kinetics approach, dynamic deformation presents the motion of mesoparticles as self-sufficient objects, which play a role of elementary carriers of deformation. The dislocations provide only formation of mesoparticles at the initial stage of deformation process. In this approach, dynamic deformation can be quantitatively characterized by two statistical moments of the mesoparticle velocity distribution function—mean mesoparticle velocity, $u(t)$, and mesoparticle velocity dispersion, $D^2(t)$ determined in accordance with Eq. (21.4).

Three dynamic characteristics considered in our investigation are used in present analysis. One of the basic characteristics of dynamic deformation which reflects a transition of material into structure-unstable state and provides the quantitative data on energy and momentum exchange between scales is the *defect of particle velocity*, δU_{def} .

In non-equilibrium stochastic systems, such as a dynamically deformed medium, the mean particle velocity, $u(t)$, velocity defect, δU_{def} and particle velocity dispersion, $D^2(t)$ are not independent. There is a following relationship between particle velocity dispersion, velocity defect, and mean particle velocity [3, 4].

$$\delta u_{\text{def}}(x, t) = u(x_0, t) - u(x, t) = \frac{1}{2} \frac{d(D^2)}{du} \quad (21.5)$$

Here $u(x, t)$ is a current value of the particle velocity and $u(x_0, t)$ is a referent value of particle velocity. $\delta u_{\text{def}}(x, t)$ is the current value of the velocity defect which determines a change of particle velocity resulting from the interscale momentum exchange. Right-hand side of Eq. (21.5) characterizes the intensity of interscale momentum exchange which equals to rate of change of the particle velocity dispersion in the velocity space. Physically, the right-hand side of Eq. (21.5) determines the change of mean particle velocity due to change of the intensity of velocity fluctuations at the mesoscale.

The second important relationship which has previously been found in our experiments ties the particle velocity variance, D , and strain rate [19]:

$$D = R \frac{d\varepsilon(t)}{dt} \quad (21.6)$$

Here D is the velocity variance which is the quantitative characteristic of the intensity of the particle velocity chaotic pulsations in dynamically deformed solid, $\frac{d\varepsilon}{dt}$ is the strain rate and R is the proportionality coefficient. An analogous relationship is known to exist in turbulence where the intensity of turbulent pulsations is proportional to particle acceleration [26]. Equations (21.5) and (21.6) determine the character of coupling between macroscopic and mesoscopic scales of dynamic straining. Multiplying the left- and right-hand sides of Eq. (21.6) by ρC_p yields

$$\rho C_p D = \rho C_p R \frac{d\varepsilon}{dt} \quad (21.7)$$

The left-hand side of Eq. (21.7) is the spherical component of stress initiated by random velocity pulsations at the mesoscale [5–7]. Quantitative characteristics of the pulsations is the particle velocity dispersion D^2 (in West scientific literature, the variance of particle velocity at the mesoscale calls the “Granular temperature”). The right-hand side of Eq. (21.7) is the viscous component of stress. In this equation, the value $\eta_{\text{ms}} = \rho C_p R$ has a meaning of mesoscale viscosity. The interscale momentum exchange law in the form of Eq. (21.5) has been found in experiments on shock loading of copper [3]. It became possible owing to simultaneous registration of both the mean particle velocity $u(t)$ and particle velocity dispersion $D^2(t)$. If the particle velocity is measured at the plateau of compressive pulse, the left-hand side of Eq. (21.5) equals:

$$\delta U_{\text{def}} = (U_{\text{imp}} - U_{\text{fs max}}) \quad (21.8)$$

On the other hand, Eq. (21.5) can be written in the form:

$$\delta U_{\text{def}} = D \frac{dD/dt}{du/dt} \quad (21.9)$$

When the rate of change of velocity variance equals to the rate of change of mean particle velocity

$$\frac{dD}{dt} = \frac{du}{dt} \quad (21.10)$$

the velocity defect equals to the particle velocity variance

$$\delta U_{\text{def}} = D \quad (21.11)$$

In the case of uniaxial straining, Eq. (21.9) can be written in the terms of strain and strain rate:

$$\frac{\delta U_{\text{def}}}{C_0} = \frac{D}{C_0} \frac{\dot{D}/C_0}{\dot{u}/C_0} \quad (21.12)$$

or

$$\Delta \varepsilon_{\text{mc}} = \varepsilon_D \frac{E_D}{E_{\text{mc}}} \quad (21.13)$$

Here $\Delta \varepsilon_{\text{mc}}$ is a part of macroscopic deformation resulted from the meso-macro interscale momentum exchange, ε_D and E_D are the strain and strain rate at the mesoscale, ε_{mc} and E_{mc} are the strain and strain rate at the macroscale. If the strain rate at the mesoscale equals to the macroscopic strain rate

$$E_{\text{mc}} = E_D, \quad (21.14)$$

the change of deformation at the macroscale resulted from interscale momentum exchange is determined by the value of deformation at the mesoscale

$$\Delta \varepsilon_{\text{mc}} = \varepsilon_D \quad (21.15)$$

where ε_D is the dynamic deformation at the mesoscale. In shock experiments, the directly registered characteristics are the free surface velocity, $u_{\text{fs}}(t)$, velocity defect, δU_{def} , and velocity variance, D . At the same time, physical meaning of the processes may also be understood from the Eq. (21.14) which implies the equality of strain rate at the mesoscale and macroscale.

Equation (21.5) reflects a current character of interscale momentum exchange. However, a swinging of the velocity pulsations requires a time. Even so, one can introduce an averaging of interscale momentum exchange in the form:

$$\int_{t-\tau_i}^t \left(\frac{1}{2} \frac{dD^2}{du} \right) ds \leq \delta U_{def} \tau_i \tag{21.16}$$

where τ_i is the time of averaging which can be considered as ‘‘incubation time’’ for interscale momentum exchange. Right-hand side is the displacement resulted from the velocity pulsations for incubation time. In the case of equilibrium regime of interscale momentum exchange, when condition (21.10) is fulfilled, the criterion (21.16) is transformed into the form:

$$\int_{t-\tau_i}^t (D(s)) ds \leq \delta U_{def} \tau_i \tag{21.17}$$

where $\delta U_{def}^{cr} = D$ is the critical value of velocity defect which corresponds to displacement $\delta U_{def}^{cr} \tau_i$. The multiplying of both sides of Eq. (21.16) by acoustic impedance ρC_0 yields

$$\rho C_0 \int_{t-\tau_{ms}}^t D(s) ds \leq \sigma \tau_i \tag{21.18}$$

where right-hand side

$$\sigma \tau_i = \rho C_0 \delta U_{def}^{cr} \tau_i \tag{21.19}$$

is the elementary momentum transferred from mesoscale to macroscale. Dynamic plastic deformation is controlled in a complex way by both pre-existing non-uniformity of material and dynamic effects although the velocity distribution behavior at the modest strain levels may indicate that dynamic effects are dominant. This means that the particle velocity variance is not determined only by the pre-existing non-uniformity of material, but rather, by the dynamic non-linear features of material. Equations (21.16) and (21.17) are the integral criteria for transition of solid into structural-unstable state which is determined by the kinetics of elementary carriers of deformation at the mesoscale.

The threshold of structural instability characterizes the beginning of shock-induced structural heterogenization of material. Experimentally, this characteristic can be obtained upon the series of the free surface velocity profiles registered under uniaxial strain conditions over the impact velocity range. The method for determination of instability threshold is explained in Fig. 21.8 where the dependence of maximum free surface velocity on the impact velocity is provided. In order to determine the instability threshold, a set of identical targets of 1565 aluminum alloy targets were loaded within impact velocity range of 241.9–744.8 m/s. The maximum free surface velocity $U_{fs \max} = f(U_{imp})$ at what the velocity defect begins to increase drastically is defined as the **threshold of structural instability**, U_{inst} , the second strength-characteristic of dynamic deformation. Aluminum 1565 suffers two thresholds of structural instability: (i) $U_{imp} = 435$ m/s corresponds to the free surface velocity of 370 m/s and (ii) $U_{imp} = 625.3$ m/s corresponds to maximum free surface velocity of $U_{inst} = 588.7$ m/s (indicated by symbols *). After transition into structure-unstable state, beginning from $U_{imp} = 625,5$ m/s, the free surface velocity

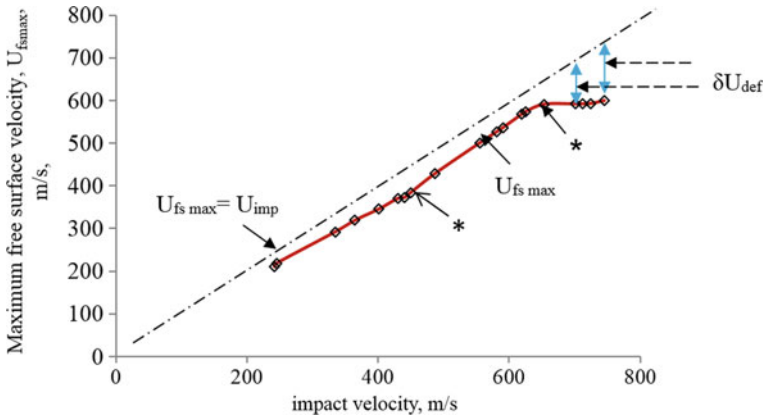


Fig. 21.8 Maximum free surface $U_{fs\ max}$ versus impact velocity for 1565 aluminum alloy

is constant. The dotted line corresponds to equality of maximum free surface velocity and impact velocity: $U_{fs\ max} = U_{imp}$.

Lastly, the third dynamic strength-characteristic determined in tests under uniaxial strain conditions is the *spall strength* [27]. In the form of the so-called “pull-back velocity” the spall strength is defined as difference between maximum value of the free surface velocity at the plateau of compressive pulse and first minimum of the free surface velocity at the back front of pulse.

The high-velocity penetration tests were conducted by using the same facility as for the tests under uniaxial strain conditions. To provide the perpendicularity relatively plane target, the rod of 20 mm in length and 5 mm in diameter is mounted into polyvinyl-carbonate sabot. The conditions for “rigid rod and target” [28] are provided by using the high-strength 02Cr18Co9Mo5-VI maraging steel as a material for rod. During the shock loading, sabot stopped just before the target whereas the rod-impactor continues to move up to collision with the target. The typical penetration cavern in 1561 aluminum alloy target is shown in Fig. 21.9.

The tests under uniaxial strain conditions provide an information on the character of spall fracture whereas the tests on penetration allow to tie the resistance penetration with the evolution of microstructure depending on the impact velocity. In our experiments, the post-shocked targets cut along the impact direction and after polishing, etching in concentrated mixture of sulphuric and nitrogen asides were investigated with optical microscope Axio-Observier Z-1m. The quasistatic mechanical characteristics of materials are provided in Table 21.1.

Fig. 21.9 Penetration cavern in 1561 aluminum alloy at the impact velocity of 577 m/s

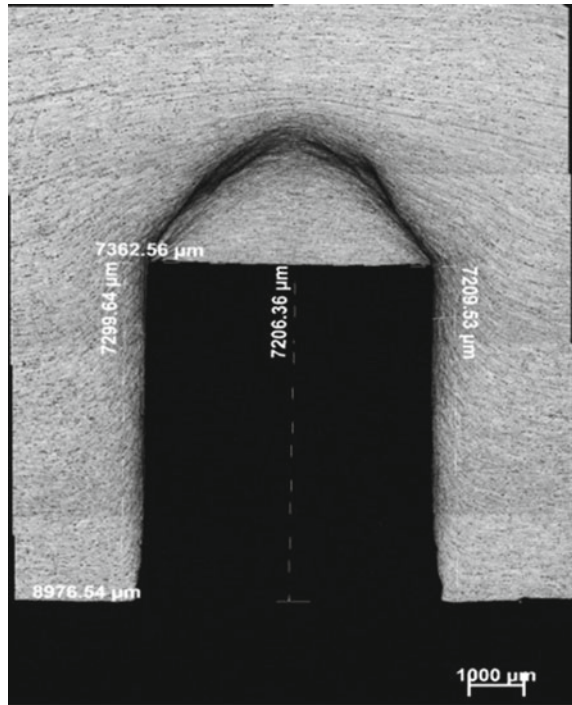


Table 21.1 Mechanical characteristics of 1565 and 1561 aluminum alloys

Alloy	Target thickness, mm	σ_b , MPa	σ_{02} , MPa	δ , %
AL 1565	7	363	221	15.8
AL 1561	7	353–354	217–224	17.8–18.8

21.3 Experimental Results and Analysis

21.3.1 Structural Instability and Spall Strength

To reveal the influence of initial property of material on the threshold of structural instability, a series of shocks under uniaxial strain conditions within impact velocity range of 241.9–744.8 m/s was performed for both alloys. In Fig. 21.10 the dependencies of maximum free surface velocity, $U_{fs\ max}$, for 1561 and 1565 aluminum alloys are plotted together as functions of impact velocity. In 1561 aluminum alloy dependence of maximum free surface velocity presents a smooth curve without breaks, which supposes the absence of transition into structure-unstable state. In 1565 aluminum alloy, the structural instability thresholds occur at the impact velocities of

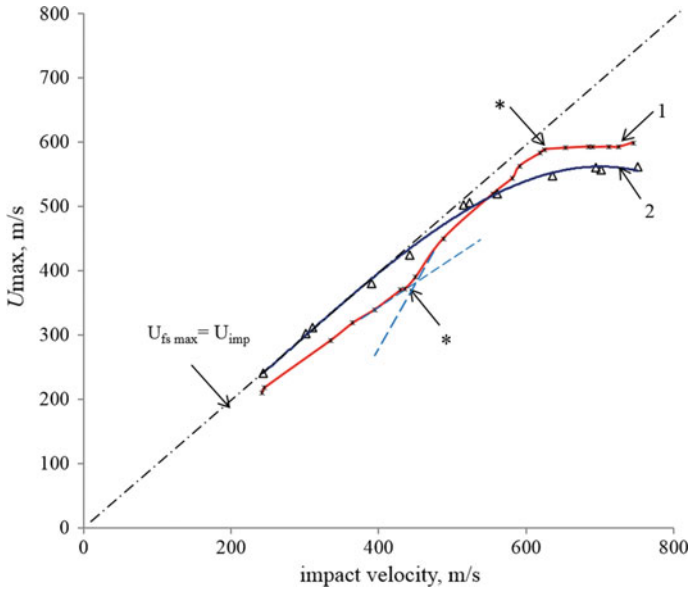


Fig. 21.10 Dependencies of maximum free surface velocity on impact velocity for 1565 aluminum alloy and 1561 aluminum alloy

$U_{pj} = 435 \text{ m/s}$ ($U_{inst} = 370 \text{ m/s}$) and $U_{pj} = 625.5 \text{ m/s}$ ($U_{inst} = 588.7 \text{ m/s}$). Thus, the dependence $U_{fs \max} = f(U_{imp})$ turns out to be very sensitive characteristics defining the shock-induced structural transitions in material (Fig. 21.10).

It is of interest to compare the plastic front velocity behavior for both alloys below and beyond of instability threshold. The value of plastic front velocity is determined from the free surface velocity profile as

$$C_p = ht / (ht/C_1 - \Delta t)$$

where ht is the target thickness, C_p is the velocity of plastic front, C_e is the longitudinal elastic velocity, Δt is the delay of plastic front relatively elastic precursor. In Fig. 21.11 the dependencies of plastic front velocities on impact velocity for both alloys are plotted together. For both alloys the plastic front velocity stops to grow just after transition of material into structure-unstable state.

In Fig. 21.12 the dependencies of maximum free surface velocity at the plateau of compression pulse, $U_{fs \max}$, and pull-back velocity (spall strength), W , on the impact velocity for 1565 aluminum alloy are plotted together. While the threshold of structural instability characterizes the dynamic strength of material under compression, the spall strength is the tensile strength-characteristic. The breaks at both curves happen at the identical impact velocities (dotted lines NN' and MM'), which means that the internal processes responsible for dynamic deformation and strength for both deformation processes in 1565 aluminum alloy are mutual related. All region of impact velocities is subdivided into three zones.

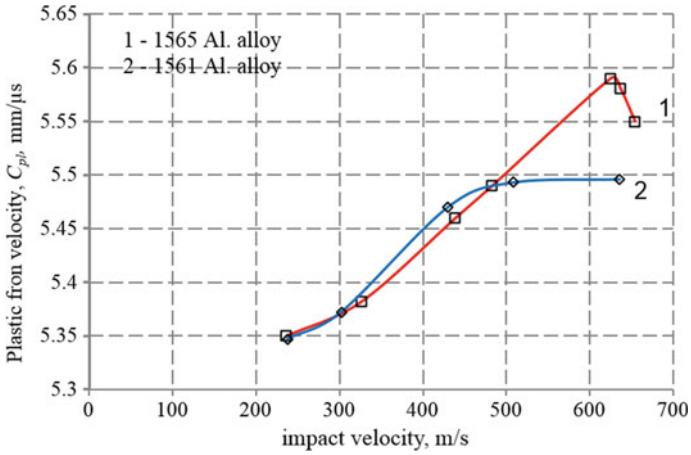


Fig. 21.11 Dependencies of plastic front velocities on the impact velocity for 1565 and 1561 aluminum alloys

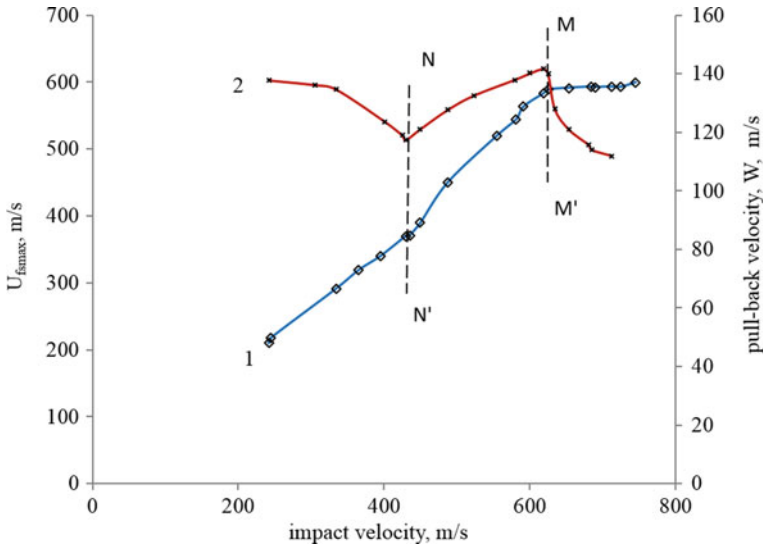


Fig. 21.12 Dependencies of maximum free surface velocity, $U_{fs\ max}$ and pull-back velocity, W , on the impact velocity for 1565 aluminum alloy

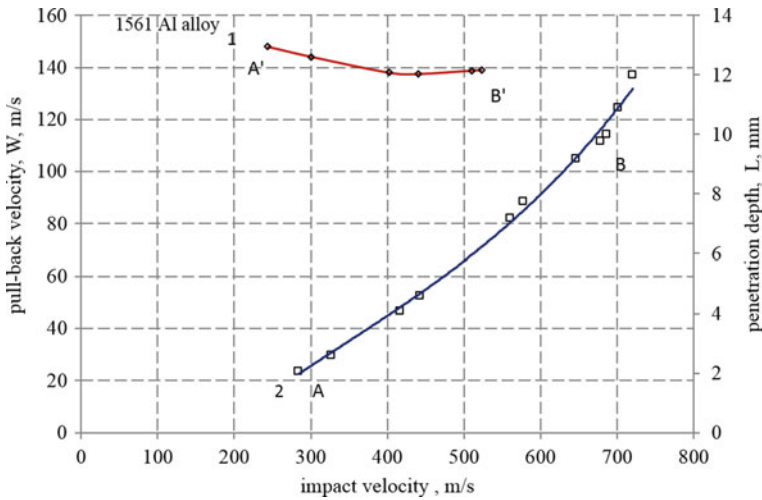


Fig. 21.13 Maximum free surface velocity, $U_{fs\ max}$, and pull-back velocity, W , versus impact velocity for 1561 Al alloy

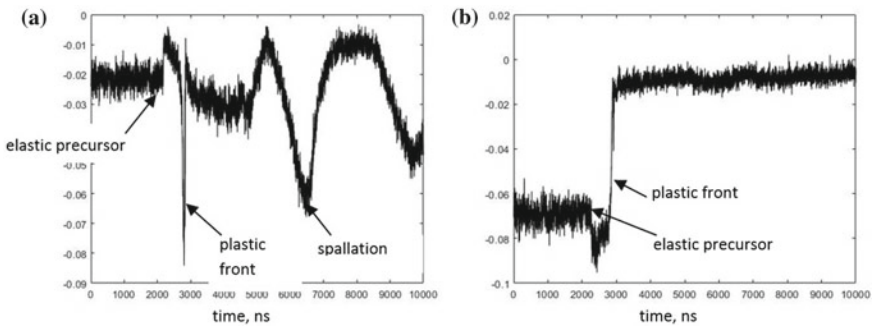


Fig. 21.14 Fringe signals for 1565 **a** and 1561 alloy **b** loaded at the impact velocity of ~ 650 m/s

For the 1561 Al alloy, the dependence $W = f(U_{imp})$ could be built up to impact velocity of 522.9 m/s (Fig. 21.13). At higher impact velocities, the laser beam of interferometer reflected from the free surface of target is deviated, so the fringe signal disappears. In Fig. 21.14 the fringe signals for both kinds of alloys are provided. According to working principle of the interferometer, irreversible displacement of fringe signal to upper level of interference pattern means a loss of intensity of laser beam reflected from the free surface of target.

The reason for loss of fringe signal for the 1561 aluminum alloy target becomes clear after comparison of dependencies for pull-back velocity, $W = f(U_{imp})$, maximum free surface velocity (Fig. 21.13), fringe signal (Fig. 21.14), and data on microstructural investigations of post-shocked specimens (Fig. 21.15). Point B' in Fig. 21.13 indicates the maximum impact velocity at what the pull-back velocity

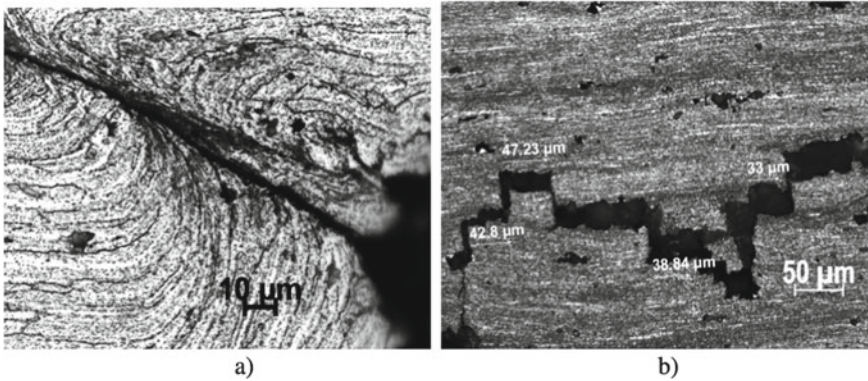


Fig. 21.15 Morphology of spall zone in 1561 **a** and 1565 **b** aluminum alloy targets

could be registered for 1561 alloy. In Fig. 21.15a the spall crack for 1561 alloy demonstrates a rotation motion material, which results in deviation of laser beam and loss of the fringe signal. As for the 1565 aluminum alloy, dynamic deformation flows in form of translational motion of structural elements of mesoscale-2 (Fig. 21.15b). In this case, the deviation of laser beam at the free surface of target doesn't occur and free surface velocity profile can be registered within overall range of impact velocities. Such behavior of inner structure of 1565 alloy is related to texture of material which prevents to rotational motion of structural elements.

21.3.2 Structural Instability and Penetration

Resistance to high-velocity penetration is characterized by the value of penetration depth and by the slope of curve $L = f(U_{imp})$ —the smaller the slope of curve, the higher the resistance to penetration. The penetration curve for 1561 aluminum alloy does not suffer the brakes. One can see that resistance to penetration for 1561 alloy gradually decreases (Figs. 21.16 and 21.17).

At the regions A'B' and C'D' the resistance to penetration turns out to be higher than that in the region of B'C'—at upper region of impact velocities C'D', the dynamic strength of 1565 alloy increases whereas that value for 1561 alloy decreases.

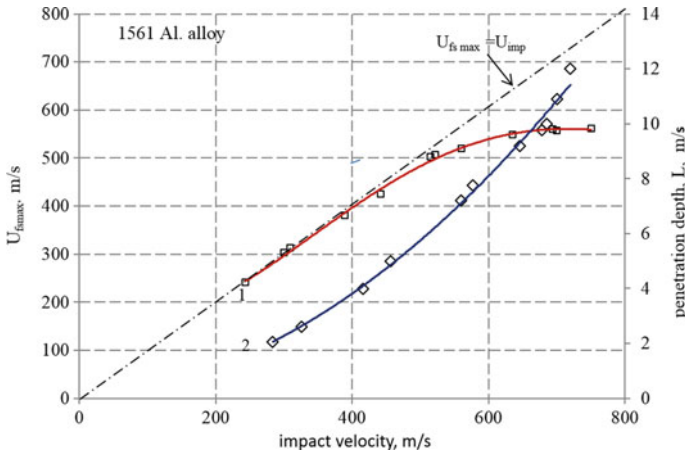


Fig. 21.16 Dependence of maximum free surface velocity, $U_{fs\ max}$, and penetration depth, L , on the impact velocity for 1561 aluminum alloy

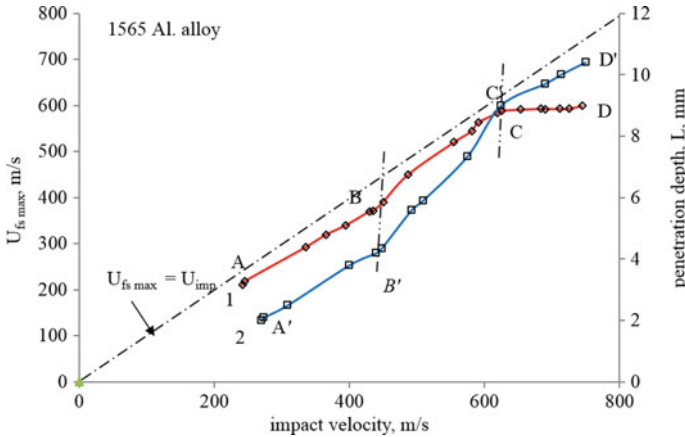


Fig. 21.17 Dependence of maximum free surface velocity, $U_{fs\ max}$, and penetration depth, L , on the impact velocity for 1565 aluminum alloy

21.4 Spall Strength and Resistance to High Velocity Penetration

It is thought to be very interesting to compare the resistance to spallation and resistance to penetration in different regions of impact velocities for both alloys. In Fig. 21.18 the penetration depth curve $L = f(U_{imp})$ for 1565 alloys is plotted together with the dependence for pull-back velocity $W = f(U_{imp})$. Comparison of curves shows the correlation between these processes. The curve $W = f(U_{imp})$ determined on the basis of tests under uniaxial strain conditions suffers two breaks: at the

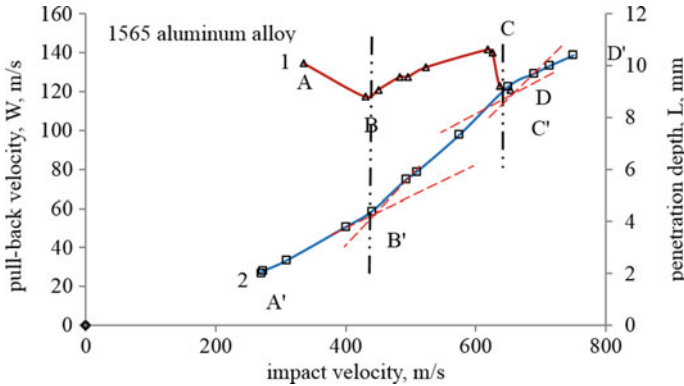


Fig. 21.18 Dependence of pull-back velocity, W , and penetration depth, L , on the impact velocity for 1565 aluminum alloy

impact velocities of 440 and 625.5 m/s. The dependence of penetration depth curve $L = f(U_{imp})$ also suffers two breaks: at the impact velocities of 440 and 608 m/s. The critical changes of penetration dependence slope happen approximately at the strain rates where the first break for dependence $W = f(U_{imp})$ occurs (dash lines in Fig. 21.18). Such behavior of curves evidences the common mechanism of interaction of impactor and structure of target both in tests under uniaxial strain conditions and high-velocity penetration. The breaks at high region of impact velocities in both loading schemes also happen at close impact velocities: 625.5 m/s in plane tests and 608 m/s in penetration tests. This means that both breaks are of the same nature—strength behavior of that material under dynamic compression and dynamic tension is identical.

Now let us consider in details a correlation between spall strength and resistance to penetration for 1565 aluminum alloy. Within pieces $A'B'$ and $B'C'$ of penetration depth of curve in Fig. 21.18, the first break at curve occurs in point B' : $\frac{dL_{A'B'}}{dU_{imp}} < \frac{dL_{B'C'}}{dU_{imp}}$. The resistance to penetration within impact velocity region $A'B'$ of curve is seen to be higher as compared to that for piece $B'C'$. At the same time, the spall strength of curve within the same impact velocity region shows the opposite trend. Within the piece AB the pull-back velocity decreases from 137.8–117.3 m/s. After point B , within piece BC $\frac{dW_{BC}}{dU_{imp}} > \frac{dW_{AB}}{dU_{imp}}$, which means that pull-back velocity increases with the impact velocity increasing. Thus, the critical changes in both curves happen within impact velocity range of 430–440 m/s. Analogous situation is seen after the second critical impact velocity of ~ 608 m/s—within piece $C'D'$ of penetration curve the slope of decreases: $\frac{dL_{C'D'}}{dU_{imp}} < \frac{dL_{B'C'}}{dU_{imp}}$, i.e., the resistance to penetration within region $C'D'$ increases. Thus, within impact velocity range of 241.9–744.8 m/s the strength behavior of 1565 aluminum alloy in two schemes of shock loading proves to be opposite—when resistance to penetration increases, the spall strength decreases.

Dependencies $L = f(U_{pj})$ and $W = f(U_{pj})$ for 1561 alloy are presented in Fig. 21.19. Within overall range of impact velocities, the resistance to penetration gradually

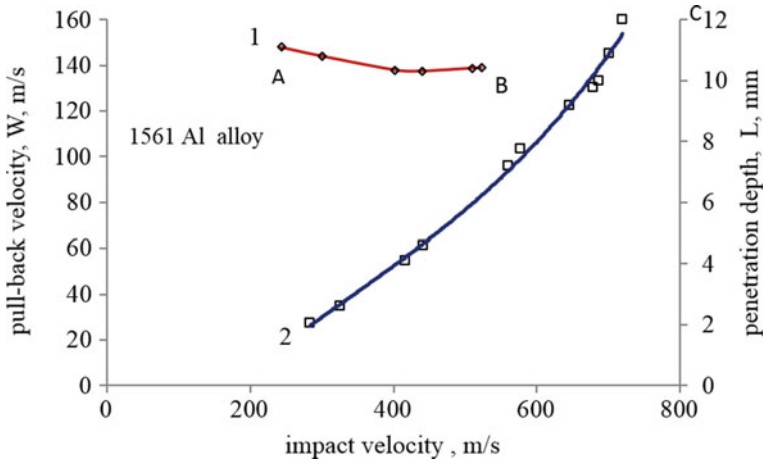


Fig. 21.19 Dependencies of pull-back velocity, W , and penetration depth, L , on the impact velocity for 1561 aluminum alloy

decreases. As for the pull-back velocity, within piece AB of curve it is practically constant and after point B of curve, the pull-back velocity for the single structural element of mesoscale-2 cannot be determined since the material transits into unstable state whereas the mesoscale-2 element begins to rotate. On the basis of above analysis it may be concluded that behavior of spall strength and resistance to penetration for 1561 aluminum alloy turns out to be different as compared to that for 1565 aluminum alloy.

21.5 Microstructural Investigations

21.5.1 1561 Aluminum Alloy

To understand the multiscale mechanisms of strength behavior of 1565 aluminum alloy in different regions of impact velocities it thought to be appropriately to compare the microstructural data for different regions of impact velocity with the dependence of penetration. The inner structure is seen to consist of equal-axis grains with the seldom inclusions of intermetallides. In Fig. 21.20b the morphology of lateral region of cavern in 1561 alloy target loaded at the impact velocity of 328 m/s is shown. The numerous micro-shears oriented along the direction of impact are clearly seen.

Formation of meso-shears is a typical dynamic effect [30, 31]. The micro-shears are the result of the particle velocity distribution at the mesoscale-1. The interferometer registers the velocity distribution in the form of the particle velocity variance at the mesoscale-1 (1–10 mkm). According to [5–7], the random motions of structural

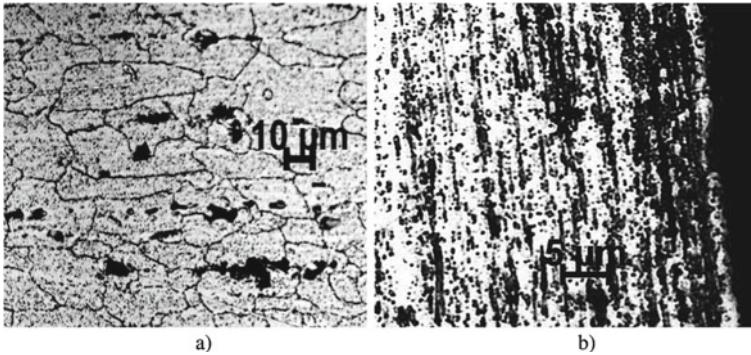


Fig. 21.20 **a**—initial structural states of 1561 aluminum alloy; **b**—morphology of lateral region of cavern at the impact velocity of 328 m/s

elements initiate the short-living particle velocity pulsations, the living time for similar pulsations equals approximately $\Delta t = 150\text{--}200$ ns. The maximum value of the velocity variance at the plastic front in 1565 aluminum alloy equals $D = 4.0 \cdot 10^3$ m/s (see Fig. 21.7), from where the mean displacement caused by the pulsations equals:

$$L = D \cdot \Delta t = 4.0 \cdot 10^3 \cdot 2 \cdot 10^{-7} = 8 \cdot 10^{-4} \text{ cm} = 8 \text{ mkm}$$

In vicinity of side wall of cavern, the distance between micro-shears decreases. The thickness of region consisting of micro-shears increases with the increase of impact velocity from ~ 40 mkm at the impact velocities of 284—m/s to ~ 100 mkm at the velocity of 667 m/s (Fig. 21.21a, b).

With the increasing of impact velocity, the micro-shears are seen to unite into large-scale formations in the form of elongated plaits and ellipsoids of (50×150) mm in size. With the increasing of impact velocity, the region occupied by large-scale formations increases from 328.65 to 580 mkm (Fig. 21.21a, b). Comparison of the penetration depth curve with the structural patterns allows to conclude: within overall region of impact velocities the resistance to penetration decreases.

21.5.2 1565 Aluminum Alloy

In Fig. 21.23 three states of structure for different impact velocities for 1565 aluminum alloy are presented. The specific feature of post-shocked 1565 aluminum is the presence of the regular fault-structures at the edge of cavern. Where observed, the fault-structures are nucleated in regions AB and CD (Fig. 21.23).

Simultaneously, the resistance to penetration increases (see Fig. 21.18). At the same time, the regular faults are absent within range of BC where the structure is uniform whilst the resistance to penetration increases. From the point of view of resistance to penetration, the 1565 aluminum alloy turns out to be more preferable

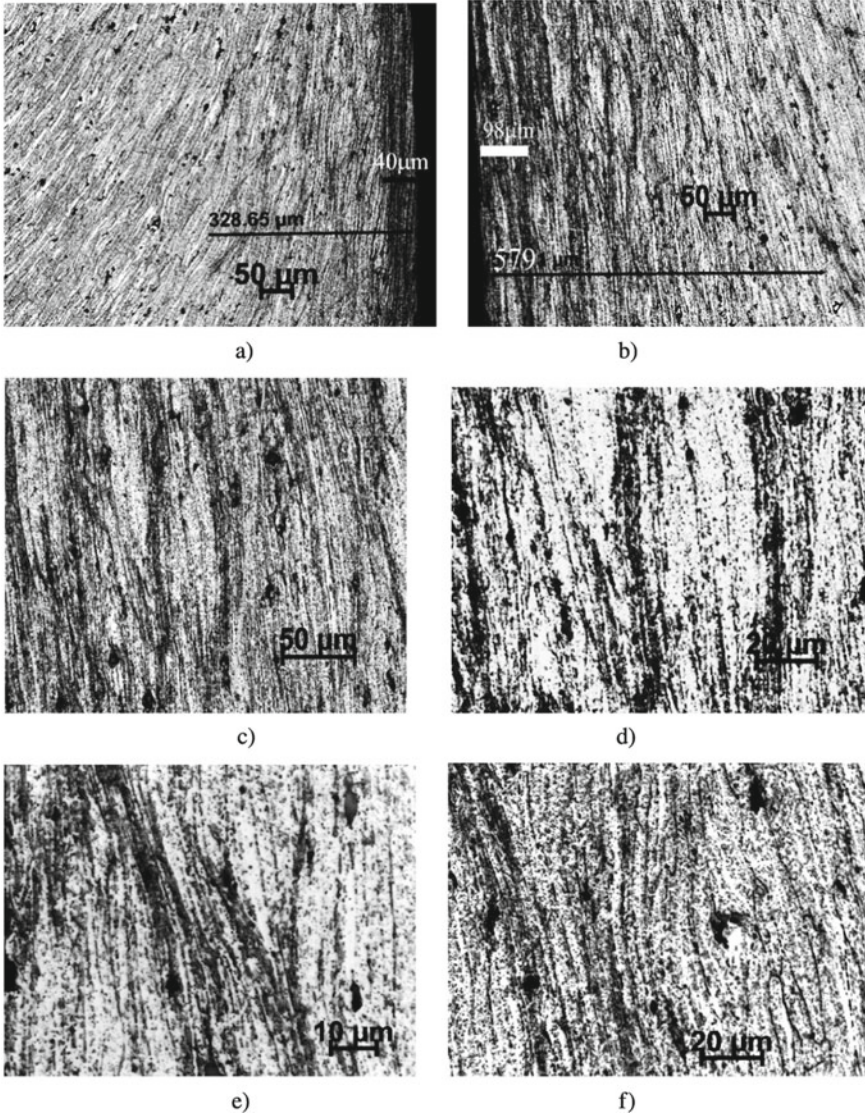


Fig. 21.21 The structured regions in 1561 Al. alloy for different impact velocities: **a** $U_{\text{imp}} = 284 \text{ m/s}$; **b-f** $U_{\text{imp}} = 677 \text{ m/s}$

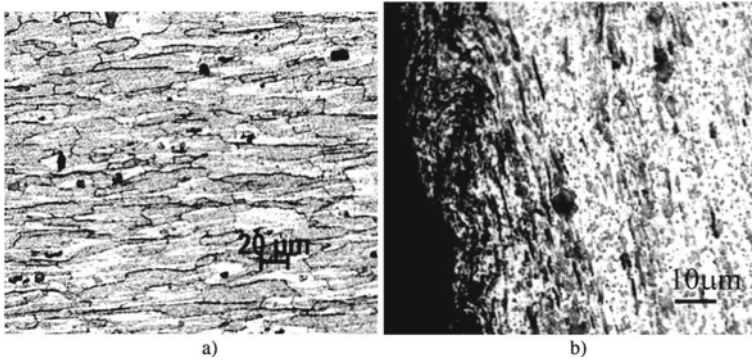


Fig. 21.22 Initial structural states **a** and micro-shears **b** in 1565 aluminum alloy

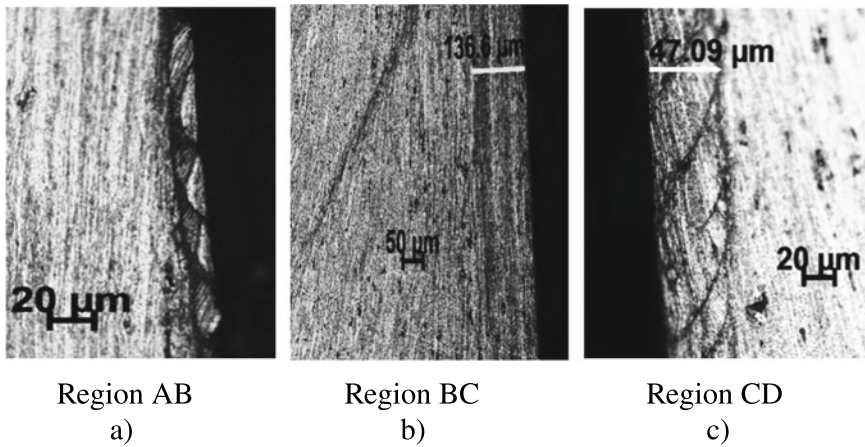


Fig. 21.23 Three regions of lateral structure in 1565 aluminum alloy after penetration

at upper region of impact velocities as compared to 1561 alloy where the decrease of resistance to penetration at high region of impact velocities is seen.

21.6 On the Resonance Excitation of Mesoscale

In the light of the above experimental results, three questions arise: (i) what is the physical mechanism responsible for nucleation of fault-structures, (ii) what parameters of shock wave determine the dimensions of fault-structures, (iii) what is the physical mechanism for transition from one scale to another. To answer the questions we consider propagation of plane shock wave in a relaxing medium. In the case of

a steady shock wave, two important relationships have previously been found. The first of them ties the particle velocity variance, D , and strain rate [19].

In the case of one-dimensional propagation of shock wave, the balance equations for momentum conservation and medium continuity take the form

$$\rho u_t - \sigma_x = 0; \quad (21.20)$$

$$u_x - \varepsilon_t = 0. \quad (21.21)$$

The constitutive equation for a relaxing medium introduced by Duvall [32] and Taylor [33]:

$$\sigma - \rho C_l^2 \varepsilon = -2\mu \varepsilon^p \quad (21.22)$$

or in differential form

$$\sigma_t - \rho C_l^2 \varepsilon_t = -F. \quad (21.23)$$

Here C_l is the longitudinal sound velocity, μ is the shear modulus, and the relaxation function

$$F = 2\mu \frac{\partial \varepsilon^p}{\partial t} \quad (21.24)$$

is determined through the plastic strain rate which, in turn, is determined by Orowan's equation for density and velocity of dislocations $\frac{d\varepsilon^p}{dt} = bN_d V_d$. As distinct from Duvall-Taylor approach, in the present investigation the stress relaxation in the dynamically deformed medium is accepted to be realized only through the motion of elementary carriers of deformation at the mesoscale. Dislocations and other carriers of the deformation of atom-dislocation scale provide the formation and motion of mesoparticles whereas the mesoparticles it selves play a role of self-consistent carriers of deformation. In this situation, the stress relaxation is determined only by the velocity defect.

The advantage of such an approach is that the relaxation model doesn't incorporate the parameters of dislocations, such as density and velocity of dislocations which cannot be controlled under conditions of dynamic straining. As distinct from the dislocation structure, defect of particle velocity can be registered in real time. In this case, the relaxation function takes the form:

$$F = \frac{2\mu}{C_l} \frac{d(u_{\text{def}})}{dt}. \quad (21.25)$$

The equation system can be reduced to second-order differential equation

$$\rho \varepsilon_{tt} - \sigma_{xx} = 0. \quad (21.26)$$

Substitution of into yields

$$\frac{d\varepsilon^p}{dt} = (R^2/C_1^2) \frac{d^2\varepsilon}{dt^2}. \quad (21.27)$$

Then Eq. (21.26) is reduced to

$$\varepsilon_{tt} - \rho C_1^2 \varepsilon_{xx} - 2(\mu R^2 / \rho C_1^2) \varepsilon_{xxtt} = 0. \quad (21.28)$$

For the case of the steady propagation of shock wave, the single variable $\zeta = x - C_p t$ can be used. Equation (21.28) takes the form:

$$(C_1^2 - C_p^2) \varepsilon_{\zeta\zeta} + 2(\mu R^2 / \rho C_1^2) \varepsilon_{\zeta\zeta\zeta\zeta} = 0. \quad (21.29)$$

Exchanging $\varepsilon_{\zeta\zeta} = \psi$ leads to the equation for an oscillator:

$$(C_1^2 - C_p^2) \psi + 2(\mu R^2 / \rho C_1^2) \Psi_{\zeta\zeta} = 0 \quad (21.30)$$

The frequency of oscillations equals

$$\omega = \frac{1}{2} \frac{\rho C_1^2 (C_1^2 - C_p^2)}{\mu R^2} \quad (21.31)$$

Physically, the oscillatory regime of shock-wave propagation is a sequence of *positive back coupling* provided by united solution of the Eqs. (21.5) (21.6) (21.20)–(21.21). The temporal resolution of experimental diagnostics (0.6–1.0 ns), allows registering the fine structure of plastic wave including the high-frequency oscillations at the mesoscale-2. Where observed, the oscillations are excited at the top of the plastic front. Figure 21.24 demonstrates the velocity oscillations in 7 mm 1565 aluminum alloy target loaded at the impact velocity of 636.5 m/s. The oscillations are seen at the impact velocity which are higher than the threshold of structure-unstable transition, U_{inst} . The space period of oscillations equals ~ 50 mkm, which coincides with the mean size fault-structures (40–50 mkm). Thus, while the mesoscale-1 structures are nucleated owing to particle velocity pulsations, the fault-structures of mesoscale-2 are initiated due to resonance interaction of mesoscale-1 structures with the plastic front oscillations, which, in turn, result from positive back coupling between mesoparticle velocity dispersion and velocity defect.

Although oscillations are initiated due to the interaction of stochastic features of dynamically deformed structure in form of particle velocity pulsations, the transition itself happens *due to swinging* the high-frequency oscillations of mesostructure. Thus, it should be underlined that the meso-macro transition is *not a direct transition from chaotic motion of structural elements to translation motion* at the next scale level

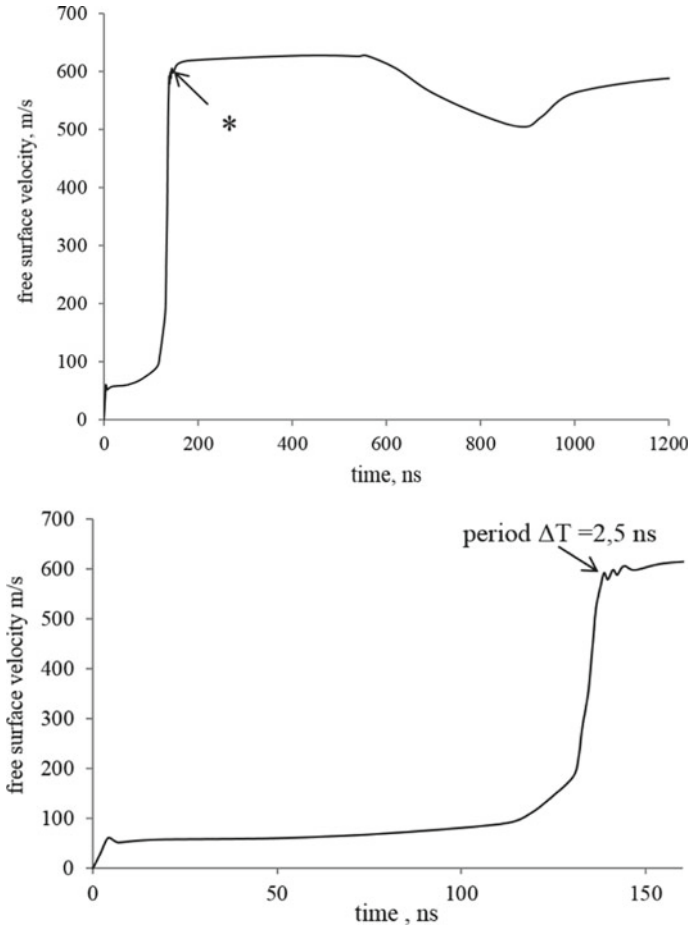


Fig. 21.24 Free surface velocity profiles, ufs, for 7 mm 1565 aluminum alloy target loaded at the impact velocity of 636.5 m/s (the oscillations are indicated by symbol *)

as “noise-induced transition” [34]. This transition is thought to be realized through the oscillation regime of straining at the mesoscale.

Below the dimensions of fault-structures are calculated for regions AB and CD. The experimental free surface profiles are used for calculation of parameters of shock waves.

Region AB

1. Impact velocity $U_{imp} = 335$ m/s.
2. Velocity variance $D = 22$ m/s.
3. Velocity of plastic front $C_p = 5.478 \cdot 10^5$ cm/s.
4. Longitudinal sound velocity $C_l = 6.387 \cdot 10^5$ cm/s.

5. Strain rate $\frac{d\varepsilon}{dt} = 7.79 \cdot 10^5 \text{c-1}$.
6. Shear modulus $\mu = 2.7 \cdot 10^{11} \frac{\text{dyn}\cdot\text{cm}}{\text{cek}^2}$.
7. Density $\rho = 2.7 \text{g/cm}^3$.

From Eq. (21.6) $R = \frac{D}{d\varepsilon/dt} = 28 \times 10^{-4} \text{cm}$ and from Eq. (21.31) $\omega = 2.35 \times 10^8 \text{s}^{-1}$ or $f = \omega/2\pi = 0.374 \times 10^8 \text{s}^{-1}$ which corresponds to period of oscillations: $T = \frac{1}{f} = 2.672 \times 10^{-8} \text{s}$. Then the space period of cell-structures in region AB equals: $\lambda = T \times U_{\text{imp}} = 2.672 \times 10^{-8} \text{s} \times 3.35 \times 10^4 \text{cm/s} = 8.95 \times 10^{-4} \text{cm}$. The obtained value for space period of oscillations coincides with the dimensions of fault-structures shown in Fig. 21.23a.

Region CD

1. Impact velocity $U_{\text{imp}} = 653.7 \text{m/s}$.
2. Velocity variance $D = 52 \text{m/s}$.
3. Velocity of plastic front $C_p = 5.66 \times 10^5 \text{cm/s}$.
4. Longitudinal sound velocity $C_l = 6.387 \times 10^5 \text{cm/s}$.
5. Strain rate $\frac{d\varepsilon}{dt} = 5 \times 10^6 \text{s}^{-1}$.
6. Shear modulus $\mu = 2.7 \times 10^{11} \frac{\text{dyn}\times\text{cm}}{\text{sec}^2}$.
7. Density $\rho = 2.7 \text{g/cm}^3$.

From Eq. (21.6) $R = \frac{D}{d\varepsilon/dt} = 10.36 \times 10^{-4} \text{cm}$ and from Eq. (21.31) $\omega = 1.84 \times 10^8 \text{s}^{-1}$ or $f = \omega/2\pi = 0.29 \times 10^8 \text{s}^{-1}$ which corresponds to the time period of oscillations $T = \frac{1}{f} = 2.35 \times 10^{-8} \text{s}$. Then the dimension of fault-structures in region CD equals $\lambda = T \times U_{\text{imp}} = 2.35 \times 10^{-8} \times 6.637 \times 10^4 = 47 \times 10^{-4} \text{cm}$.

The obtained value for space period of oscillations coincides with the dimensions of fault-structures for region CD shown in Fig. 21.23c.

21.7 Numerical Simulation

In this investigation the impact of aluminum cylinder provided Al2024 alloy and having the characteristic sizes $\sim 1 \text{mm}$ in the next cylinder provided the same material and having the same characteristic sizes was modeled by numerical simulation. At the solution of this problem the new high-allowing computing method in mechanics—the method of smoothed particles was used (in English scientific literature in abbreviated form of SPH-Smoothed Particle Hydrodynamics). This method is intended for numerical simulation not only at low impact velocities (100–1000 m/s), it is also applied with great accuracy for hypervelocity impact [37]. The main equations on which the specified method leans and also algorithms at calculation are considered in [41, 42]. Well-known software LS-DYNA/ANSYS was used in this investigation. When developing approaches to the solution of the task, the following methodology was accepted: in order that the scale of numerical simulation corresponded with experimental investigation of development of instability, the numerical experiment

is made from the very beginning at the meso-2 with the elementary carriers of deformation corresponding to meso-1. For this purpose in the macroscopic sample the material volume corresponding to one building block meso-2 is chosen. Shock loading of such building block is carried out by means of projectile which also have the sizes of the building meso-2. The spatio-temporal trajectories of all particles of large-scale level are traced meso-1 in limits it is large-scale meso-2.

The length of projectile and target was 1 mm. Diameter of projectile and target was 1 mm too. Initial conditions: speed of interaction of projectile with the target was 300 m/s. Boundary conditions were set full of reflection of the wave from the surface which the wave reaches. The size of 1 particle of SPH in the dimensional equivalent was 10 μ. The gap between projectile and target was 0.1 mm before start numerical solver (Fig. 21.30).

The number of projectile’s SPH was 1061880. The number of SPH in target was also 1061880. The total quantity of particles of SPH participating in the considered task—2.12 million SPH about.

The Johnson-Cook constitutive relationship is intended to characterize material response under various loading conditions using material model [35]. In this model, von Mises flow stress is calculated as a function of strain, strain rate, and temperature in the form:

$$\sigma_y = (A + B\epsilon^n)(1 + C \ln \dot{\epsilon}^*)(1 - T^{*m}) \tag{21.32}$$

where ϵ is the equivalent plastic strain, $\dot{\epsilon}^*$ is a dimensionless plastic strain rate, T^* is the homologous temperature, and the constants A, B, C, m and n are material specific (Table 21.2). These coefficients were taken from those presented by Johnson and Cook in 1983 [39]. A path dependent fracture model that can be used in conjunction with the stress model has also been developed to characterize material failure, taking into account the effect of equivalent stress, pressure, strain rate, and temperature [35]. Material damage is accumulated locally using a damage parameter, calculated:

$$D = \sum_{t=0} \frac{\Delta\epsilon}{\epsilon_{JC}^f} \tag{21.33}$$

where $\Delta\epsilon$ is the incremental strain and ϵ_{JC}^f is the equivalent failure strain. The value of ϵ_{JC}^f is recalculated using Eq. (21.34) each time step giving the damage parameter its dependency.

$$\epsilon_{JC}^f = [D_1 + D_2 \exp D_3 \sigma^*][1 + D_4 \ln \dot{\epsilon}^*][1 + D_5 T^*] \tag{21.34}$$

Here, $\sigma^* = p/\sigma$, where p is the pressure and σ is the von Mises equivalent stress. The material constants D_1, D_2, D_3, D_4, D_5 with their presence, the collective motion of the SPH-particles was observed in the opposite direction of the impact, is in the Table 21.1. These damage material coefficients were taken from [40].

In this numerical simulation was used *MAT_JOHNSON_COOK (*MAT_015 model of material [36]) and *EOS_GRUNEISEN for equation of state. The

Table 21.2 Material constants and parameters

Parameter	Unit	Projectile Al-2024	Target Al-2024
Density ρ	kg/m^3	2710	2710
Modulus of shearing G	Pa	$25.9 \cdot 10^9$	$25.9 \cdot 10^9$
Yield stress A	Pa	$2.65 \cdot 10^8$	$2.65 \cdot 10^8$
Material hardening B	Pa	$4.26 \cdot 10^8$	$4.26 \cdot 10^8$
Exponent n	–	0.34	0.34
Johnson-Cook constant C		0.015	0.015
Thermodynamic parameter m		1.0	1.0
Testing temperature	K	293	293
Melting temperature	K	893	893
Testing strain rate	1/s	1	1
Specific heat capacity c_p	$\text{J}/(\text{kg} \cdot \text{K})$	910	910
Damage Johnson-Cook parameters			
D_1		0.13	0.13
D_2		0.13	0.13
D_3		-1.5	-1.5
D_4		0.011	0.011
D_5		0	0

Table 21.3 Mie-Gruneisen of state coefficients

C_0 , m/s	S_1	S_2	S_3	a	E_0	Γ_0	V_0
3935	1.578	0	0	0	0	1.69	1

Gruneisen equation of state with cubic shock-velocity as a function of particle velocity $v_s(v_p)$ defines pressure for compressed material as

$$p = \frac{\rho_0 C^2 \mu \left[1 + \left(1 - \frac{\gamma_0}{2} \right) \mu - \frac{a}{2} \mu^2 \right]}{\left[1 - (S_1 - 1) \mu - S_2 \frac{\mu^2}{\mu+1} - S_3 \frac{\mu^3}{(\mu+1)^2} \right]^2} + (\gamma_0 + a \mu) E \quad (21.35)$$

and for expanded materials as

$$p = \rho_0 C^2 \mu + (\gamma_0 + a \mu) E \quad (21.36)$$

In Eq. (21.36) C is the intercept of $v_s(v_p)$ curve (in velocity units); S_1 , S_2 and S_3 are the unitless coefficients of the slope of the $v_s(v_p)$ curve; γ_0 is the unitless Gruneisen gamma; a is the unitless, first order volume correction to γ_0 ; E is the internal energy, which is increased according to an energy deposition rate as function of time curve. The coefficient for Gruneisen equation of state is in Table 21.3. These coefficients were taken from [43]. The multiplier μ in Eqs. (21.35) and (21.36) is

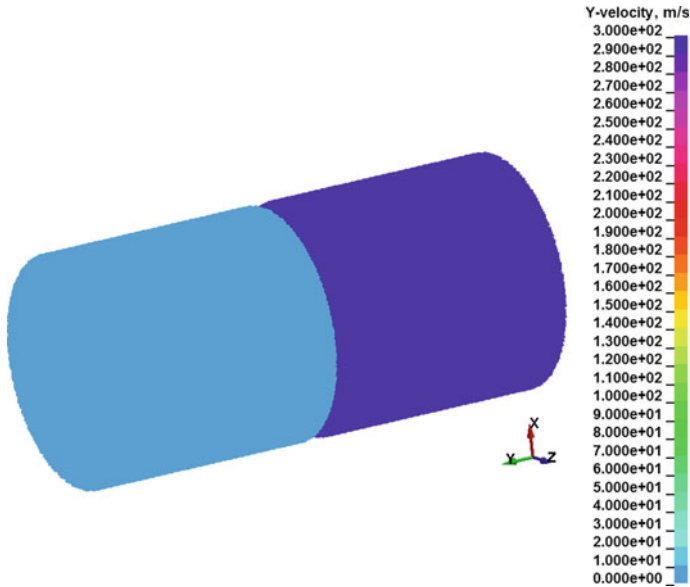


Fig. 21.25 Numerical simulation of impact aluminum 2024 alloy cylinder mm-size at the same one. Initial problem

$$\mu = \frac{\rho}{\rho_0} - 1 \tag{21.37}$$

In Figs. 21.25, 21.26, 21.27, 21.28, 21.29, 21.30, 21.31, 21.32 and 21.33 shown results of numerical simulation—the diagram of speeds of particles are reported for several time moments. In scientific literature, there are group diagrams of the velocities of the SPH, which are given by a series of lines [38], but besides the group diagrams of the velocities of the SPH, generated in the form of particle array, displayed on a color palette of velocities, are no less useful for consideration than the above-mentioned ones. Figure 21.34 shows the choice of the region A for detailed studying of speed’s vectors of the same kind of SPH-particles.

The chart of vectors of joint speeds of particles (total components from V_x, V_y, V_z) in the considered region is presented on Figs. 21.35 and 21.36. Figure 21.35 shows the total vectors of particle velocities, the distance between the particles is $10\ \mu\text{m}$, when the number of particles along the X-axis was taken from region A (Fig. 21.34). Figure 21.36 is an enlarged fragment of Fig. 21.35. The figure shows that the total of the velocity vector of SPH-particles have both positive and negative directions (vectors are shown in blue).

Numerical simulation shows that in the time moment about 250 ns (Fig. 21.33) are observed rudiments of turbulence at the movement of particles in close proximity to axis of impact. Origin of three-dimensional turbulence is observed at the initial speed of blow of $V = 300\ \text{m/s}$.

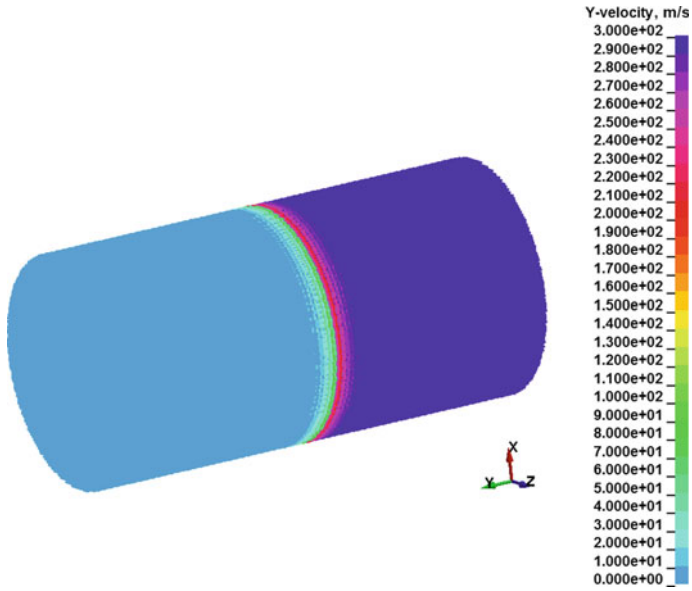


Fig. 21.26 The first moment of impact touch, $t = 0.32$ mks from numerical process start

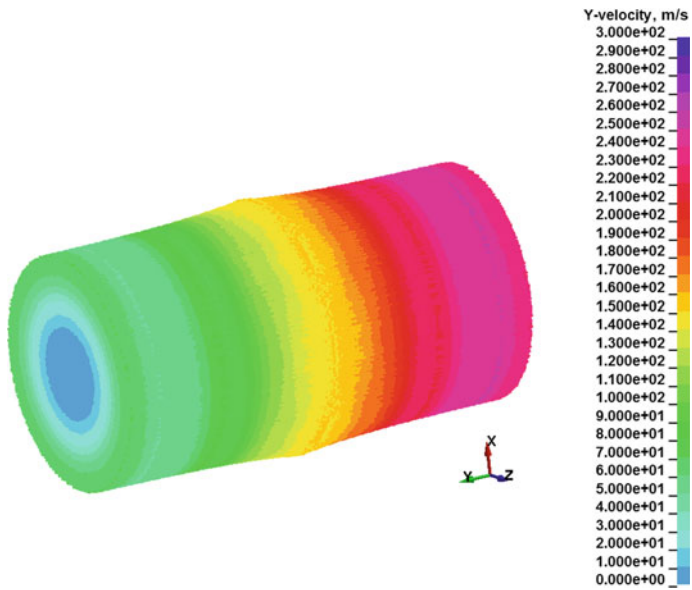


Fig. 21.27 Moment of the time $t = 0.6$ mks from numerical process start

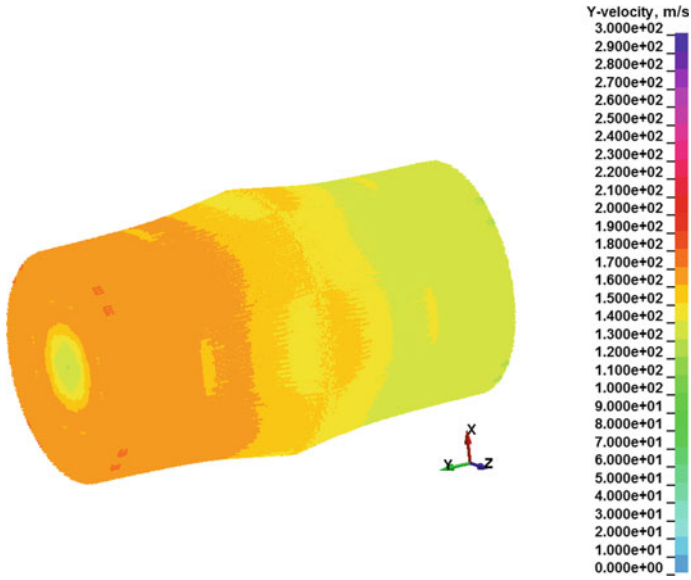


Fig. 21.28 Moment of the time $t = 1.0$ mks from numerical process start

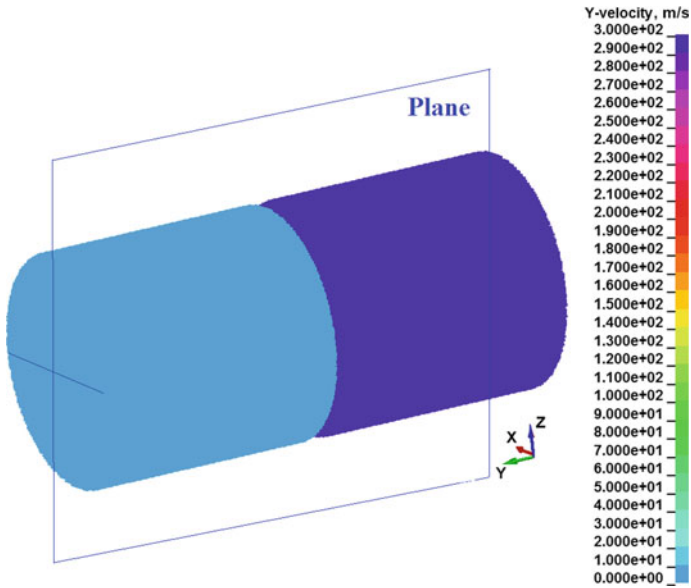


Fig. 21.29 The preparation of axial plane section

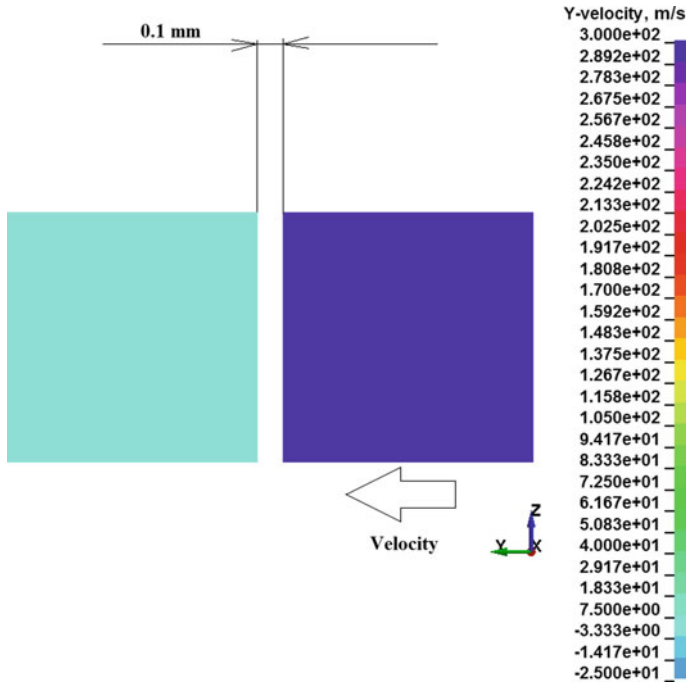


Fig. 21.30 Axial plane section—projection on Y-Z plane. Start simulation view

21.8 Conclusion

–New kinetic criterion for the shock-induced structural instability and localization of dynamic deformation is suggested. The transition into structure-unstable state happens when rate of change of the mesoparticle velocity dispersion at the mesoscale becomes higher than the rate of change of mean particle velocity.

–Shock tests of two kinds of aluminum alloy in two schemes of loading reveal different mechanisms of mesostructure formation:

(1) Mechanisms of nucleation of mesoscale-1 formations in form of micro-shears of (1–10 mkm) for both alloy are identical—mesoscale-1 structures are nucleated due to shock-induced velocity pulsations resulted from the collectivization of single-sign dislocations.

(2) Mechanisms of nucleation of mesoscale-2 formations for both kinds of alloy are different: (i) in 1561 aluminum alloy the formation of mesoscale-2 flows by means of uniting the mesoscale-1 micro-shears into plaits and ellipsoids of (150 × 50 mkm) elongated along the shock loading direction; (ii) in 1565 alloy the mesoscale-2 formations are the fault-structures at the banks of penetration cavern.

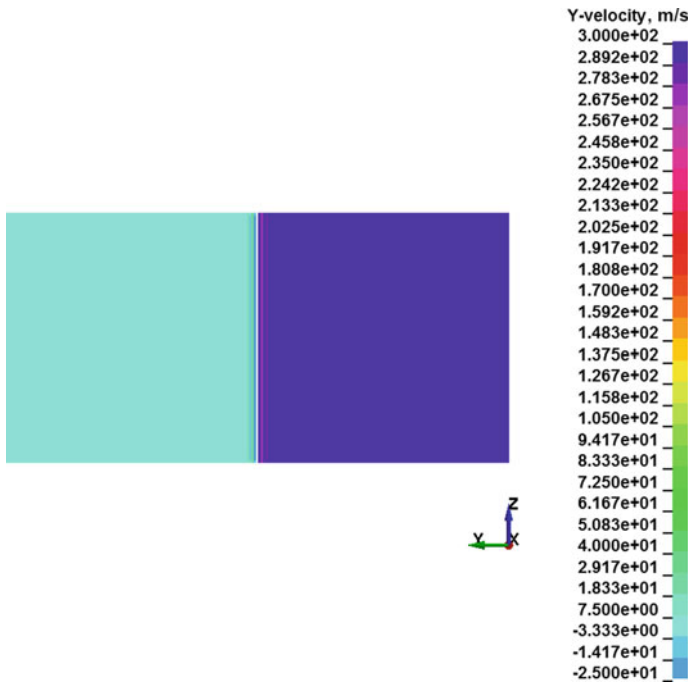


Fig. 21.31 The first moment of impact touch, $t = 0.31\text{--}0.32$ mks

(3) The mesoscale-2 structures are nucleated due to resonance interaction of mesoscale-1 structures with the plastic front oscillations, which, in turn, result from positive back coupling between mesoparticle velocity dispersion and velocity defect.

(4) Affect of transition from mesoscale-1 to mesoscale-2 in both aluminum alloys turns out to opposite: in 1561 alloy the transition on mesoscale-2 decreases the resistance to high-velocity penetration whereas in 1565 alloy the formation of mesoscale-2 structures increases the resistance to penetration.

–There is full correlation between response of material on impact at the mesoscale-2 and microstructural patterns of post-shocked samples: (i) in 1561 aluminum alloy the gradual decreasing of resistance to penetration with the increasing of impact velocity corresponds to gradual joining of micro-shears into elongated plaits and ellipsoids; (ii) in 1565 aluminum alloy the greatest resistance to penetration corresponds to formation of fault-structures at the bank of penetration cavern.

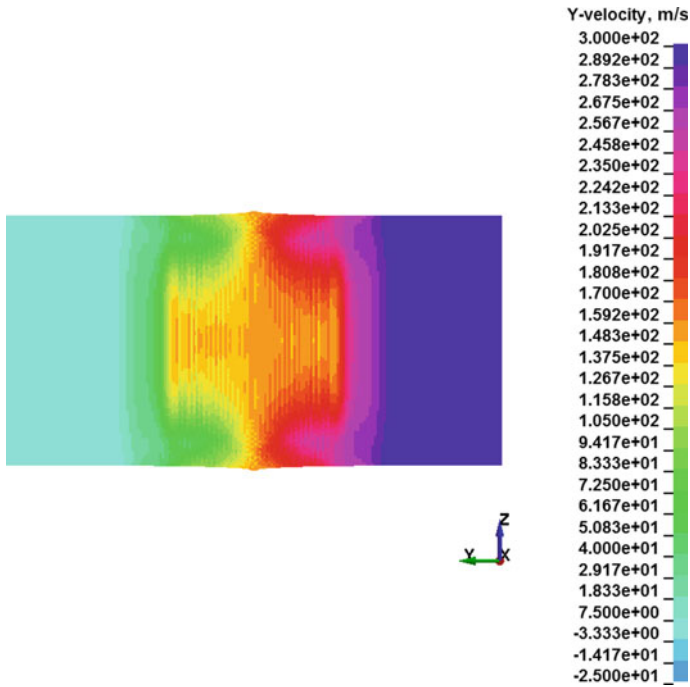


Fig. 21.32 Moment of the time $t = 0.41$ mks

–Numerical simulation of impact aluminum mm-size projectile in same aluminum target with speeds ~ 300 m/s in the moment ~ 240 ns after the beginning of interaction at mesoscale-2 shown turbulization of particle motion of the environment at their movement in close proximity to target axis of gravity. Numerical researches demonstrated that the transition of material to the structural and unstable state has the local and kinetic nature of impact damage material.

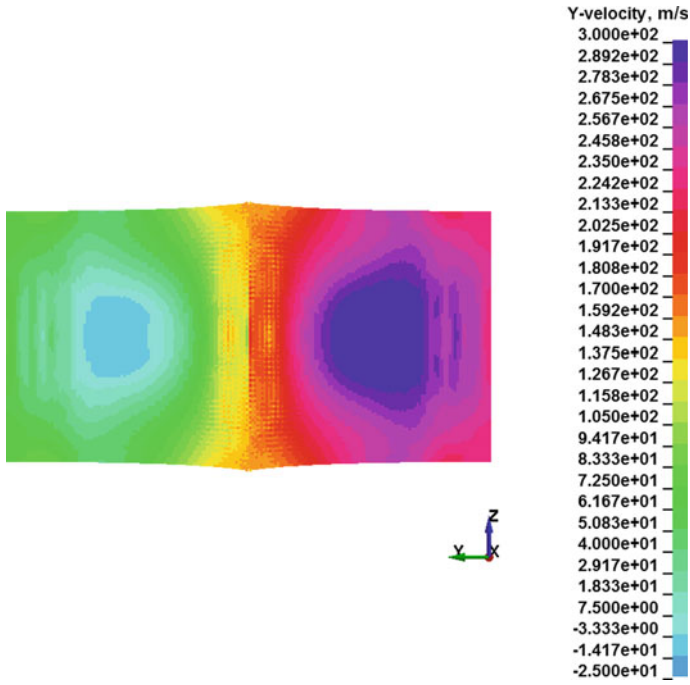


Fig. 21.33 Moment of the time $t = 0.55$ mks

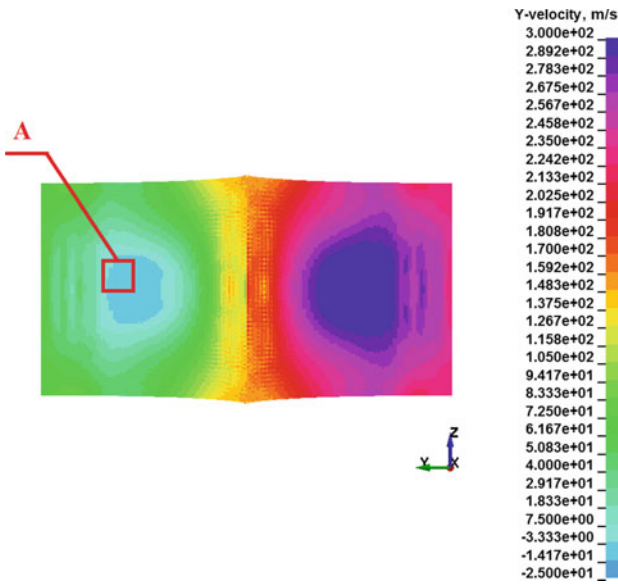


Fig. 21.34 Numerical simulation of impact aluminum 2024 alloy cylinder mm-size at the same one. Selection of region A of SPH-array

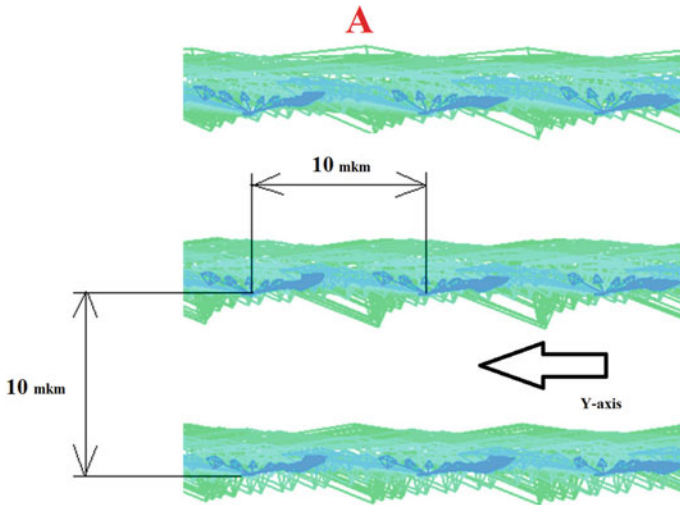


Fig. 21.35 Numerical simulation of impact aluminum 2024 alloy cylinder mm-size at the same one. Region A of SPH-array. Total velocity vector (blue color) of line SPH along X-axis (total of X, Y, Z—velocity projections)

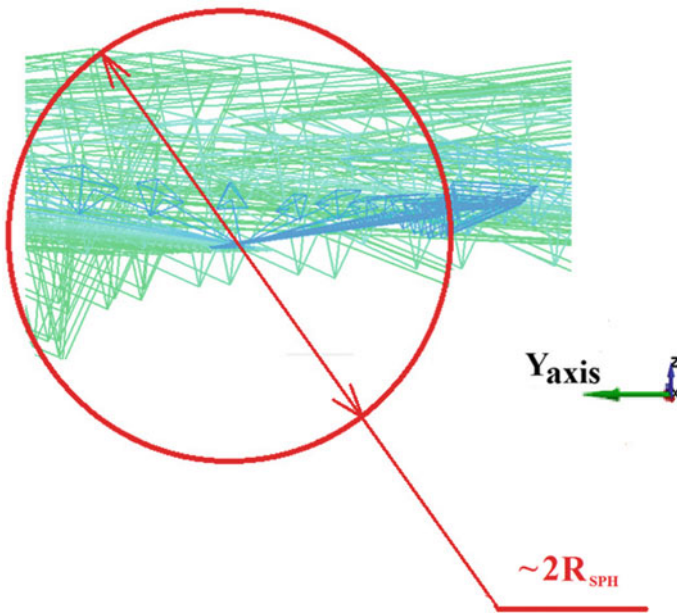


Fig. 21.36 Total velocity vector (blue color) of line SPH along X-axis (total of X, Y, Z—velocity projections)

References

1. Asay, J.R., Chhabildas, L.C.: Paradigms and challengers in shock wave research. In: High-Pressure Shock Compression of Solids VI, pp. 57–119. Springer, N.Y.
2. Baer, M.R.: Computational modeling of heterogeneous reactive materials at the mesoscale. In: Furnish, M.D., Chhabildas, L.C., Nixon, R.S. (eds.) Shock Compression of Condensed Matter-1999, The APS Proceedings, N.Y. pp. 27–33
3. Meshcheryakov, Y.I., Divakov, A.K., Zhigacheva, N.I., Makarevich, I.P.: Dynamic structures in shock-loaded copper. *Phys. Rev. B*, **78**, 64301–64316. <https://doi.org/10.1103/PhysRevB.78.064301>
4. Meshcheryakov, Y.I.: Meso-macro energy exchange in deformed and fractured solids. In: Paradigms and Challengers in Shock Wave Research. High-Pressure Shock Compression of Solids VI. Springer, N.Y. pp. 57–119
5. Prokuratova, E.I., Indeitzev, D.I.: The conditions for the dislocation distribution localization under dynamic loading. *Dymat. J.* **VI**(3/4), 229–233
6. Meshcheryakov, Y.I., Prokuratova, E.I.: Kinetic theory of continuously distributed dislocations. *Int. J. Solids Struct.* **3**, 1711–1726
7. Meshcheryakov, Y.I.: Kinetic theory of dislocations and mesoscale formation in dynamically deformed solids. In: Generalized Continua and Structures. Advanced Structured Materials. Springer Nature, Switzerland, AG. https://doi.org/10.1007/978-3-030-11665-1_22
8. Asay, J.R., Barker, L.M.: Interferometric measurements of shock-induced internal particle velocity and spatial variation of particle velocity. *J. Appl. Phys.* **45**, 2540–2546
9. Meshcheryakov, Y.I., Divakov, A.K.: Multiscale kinetics of microstructure and strain- rate dependence of materials. *Dymat. J.* **1**, 271–287
10. Chhabildas, L.C., Trott, W.M., Reinhart, W.D., Cogar, I.R., Mann, G.A.: Incipient spall structures in tantalum—microstructural effects. In: Furnish, M.D., Thadani, N.N., Horie, Y.-Y. (eds.) Shock Compression of Condensed Matter M.A. ed Meyers Matter-2001, pp. 483–486. Atlanta 24–29 June 2001
11. Vogler, T.J., Reinhart, W.D., Chhabildas, L.C.: Dynamic behavior of boron carbide. *J. Appl. Phys.* **95**, 4173–4183
12. Baer, M.R., Trott, W.M.: Mesoscale description of shock loaded heterogeneous porous materials. *Bull. Am. Phys. Soc.* **46**, 102
13. Meyers, M.A., Murr, L.E.: Shock waves and defects of crystalline structure. In: M.A. Meyers, M.A., Murr L.E. (eds.) Shock Waves and High-Strain-Rate Phenomena in Metals: Concepts and Applications. Plenum Publishing Corporation, N.Y
14. Yano, K, Horie Y.: Discrete-element modeling of shock compression of polycrystalline copper. *Phys. Rev. B* **59**, 13672–13680
15. Case, S., Horie, Y.: Discrete element simulation of shock wave propagation in polycrystalline copper. *J. Mech. Phys. Solids* **55**, 389–514
16. Meshcheryakov, Y.I., Zhigacheva, N.I., Divakov, A.K., Kononov, G.V, Osokin, E.P.: Multiscale mesostructure formation under impact loading. *Phys. Mesomech.* **23**, 231–240. <https://doi.org/10.1134/S1029959920030078>
17. Barker, L.M.: Fine structure of compressive and release wave shape in aluminum measured by the velocity interferometer technique. In: Symposium on High Dynamic Pressure, pp. 369–382. Paris
18. Grady, D.E.: Steady rise-time and spall measurement on Uranium (3–16 GPa). In: Murr, L.E., Staudhammer, K.R., Meyers, M.A. (eds.) Metallurgical Applications of Shock-Wave and High-Strain-Rate Phenomena' (Explomet-85), pp. 763–780. Marcel Dekker, N.Y.
19. Indeitzev, D.A., Meshcheryakov, Y.I., Kuchmin, A.Y., Vavilov, D.S.: Multiscale model of steady-wave shock in a medium with relaxation. *Acta Mech.* **226**, 917–925. <https://doi.org/10.1007/s00707-014-1231-0>
20. Barker, L.M., Hollenbach, R.E.: Laser interferometer for measuring high velocities of any reflecting surface. *J. Appl. Phys.* **43**, 4669–4679

21. Barker, L.M., Hollenbach, R.E.: Shock wave study of alpha-epsilon phase transition in iron. *J. Appl. Phys.* **45**(11), 4872–4887 (1974)
22. Grady, D.E., Asay, J.R.: Calculation of thermal trapping in shock deformation of aluminum. *J. Appl. Phys.* **83**, 7350–7354
23. Grady, D.E., Kipp, M.E.: The growth of unstable thermoplastic shear with application to steady wave compression of solid. *J. Mech. Phys. Solids* **35**, 95–119
24. Landau, L.D.: *J. Exp. Theor. Phys.* *JETP* **16**, 574
25. Spitzer, L.: *Physics of fully ionized gases*, 209 p. Wiley, N.Y. London
26. Hintze, J.O.: *Turbulence*, 680 p. Graw Hill Inc., New York (1959)
27. Grady, D.E.: The spall strength of condensed matter. *J. Mech. Phys. Solids* **36**, 353–384
28. Rosenberg, Z., Dekel, E.: *Terminal Ballistics*. Springer, Heidelberg, London New York (2012) <https://doi.org/10.1007/978-3-642-25305-8>
29. Asay, J.R., Chhabildas, C.: Determination of the shear strength of shock compressed 6061-T6 aluminum. In: Meyers, M.A., Murr, L.E. (eds.) *Shock Waves and High-Strain-Rate Phenomena in Metals: Concepts and Applications*. Plenum Publishing Corporation, N.Y
30. Murr, L.E., Esquivel, E.V.: Review observation of common microstructural issues associated with dynamic deformation phenomena: twins, microbands, grain size effects, shear bands and dynamic deformation recrystallization. *J. Mater. Sci.* **39**, 1153–1168
31. Swan, G.W., Duvall, G.E., Thornhill, C.K.: *J. Mech. Physocs Solids* **21**, 215
32. Duvall, G.E.: Propagation of plane shock waves in a stress-relaxing medium. In: Kolsky, H., Prager, W. (eds.) *Stress Waves in Inelastic Solids*, pp. 20–32. Springer, Berlin
33. Taylor, J.W.: Dislocation dynamics and dynamic yielding. *J. Appl. Phys.* **36**, 3146–3155
34. Horsthemke, W., Lefever, R.: *Noise-induced transitions*, 480 p. Springer, N.Y
35. Kupchella, R., Stowe, D., Xiao, X., Algosio, A., Cogar, J.: Incorporation of material variability in the Johnson-Cook model. *Procedia Eng.* **103**, 318–325 (2015)
36. LS-DYNA. Keyword user's manual. Volume II. Material Models. Livermore Software Technology (LST), An Ansys Company. 05/27/21 (r:13775). LS-DYNA Dev
37. Silnikov, M.V., Guk, I.V., Mikhaylin, A.I., Nechunaev, A.F., Rummyantsev, B.V.: Numerical simulation of hypervelocity impacts of variously shaped projectiles with thin bumpers. *Mater. Phys. Mech.* **42**(1), 20–29 (2019). https://doi.org/10.18720/MPM.4212019_3
38. Silnikov, M., Guk, I., Mikhaylin, A., Nechunaev, A.: Efficiency of needle structure at hypervelocity impact. *Acta Astronaut.* **150**, 73–80 (2018). <https://doi.org/10.1016/j.actaastro.2017.10.026>
39. Johnson, G.R., Cook, W.H.: A constitutive model an data for metals subjected to large strains, high strain rates and high temperatures. In: *Proceedings of the 7th International Symposium on Ballistic*, vol. 21, pp. 541–547 (1983)
40. Senthil, K., Arindam, B., Mittal, R., Iqbal, M.A., Gupta, N.K.: Numerical investigations on the impact of hemi spherically tipped projectiles on thin plates. *Procedia Eng.* **173**, 1926–1931 (2017). <https://doi.org/10.1016/j.proeng.2016.12.254>
41. Liu, M.B., Liu, G.R.: Smoothed particle hydrodynamics (SPH): an overview and recent developments. *Arch. Comput. Methods Eng.* **17**, 25–76 (2010)
42. Liu, M.B., Liu, G.R.: *Smoothed Particle Hydrodynamics A Meshfree Particle Method*. World Scientific Publishing, Singapore (2003)
43. Silnikov, M.V., Guk, I.V., Nechunaev, A.F., Smirnov, N.N.: Numerical simulation of hypervelocity impact problem for spacecraft shielding elements. *Acta Astronaut.* **150**, 56–62 (2018). <https://doi.org/10.1016/j.actaastro.2017.08.030>

Chapter 22

Equilibrium Structures and Flows of Polar and Nonpolar Fluids in Nanochannels



Leonid V. Mirantsev and Andrei K. Abramyan

Abstract Molecular dynamics (MD) simulations of equilibrium structures and flows of polar water, nonpolar argon and methane, and mixtures of water and methane confined by single-walled carbon nanotubes (SWCNTs) with different cross sections have been performed. The results of these simulations show that equilibrium structures and flows of all confined fluids significantly depend not only on the shape of the SWCNT's rectangular cross sections but also on the types of liquids inside SWCNTs. The cross sections of equilibrium structures of all confined fluids resemble replicas of cross sections of corresponding SWCNTs. In addition, the equilibrium structures formed by nonpolar argon atoms are most spatially ordered whereas nonpolar water molecules form the least spatially ordered equilibrium structures. It has been found that, for nonpolar methane flows through SWCNTs with rectangular cross sections, there are critical values f_{xc} of the external driving force below which an average flow velocity is equal to nearly zero and above f_{xc} methane molecules can flow. It has been also found that, for a sufficiently large value of the external driving force, the liquid argon flow through SWCNT with rectangular cross section with the ratio between its sides 1:4 demonstrates the ballistic frictionless regime. MD simulations of equilibrium structures and Couette flows of polar water molecules and nonpolar argon atoms between bounding carbon substrates disposed at the distance $h = 1.5$ nm from each other have been also performed. Two symmetric configurations when both substrates have similar, either graphene-like crystalline or amorphous structures, and one asymmetric configuration consisted of one substrate with graphene-like crystalline structure and another substrate with amorphous structure have been considered. It has been found that, in all configurations under consideration, the Couette flow velocity profiles depend strongly on polarity of fluid particles confined between bounding substrates. In has been also found that, for substrates with different structures, the Couette flows depend strongly on which of the substrate is moving and which is fixed.

L. V. Mirantsev (✉) · A. K. Abramyan
Institute for Problems in Mechanical Engineering RAS, V.O., Bolshoy pr., 61, St. Petersburg
199178, Russia
e-mail: miran@mail.ru

© The Author(s), under exclusive license to Springer Nature Switzerland AG 2022
V. A. Polyanskiy and A. K. Belyaev (eds.), *Mechanics and Control of Solids and Structures*, Advanced Structured Materials 164,
https://doi.org/10.1007/978-3-030-93076-9_22

455

Keywords Nanochannel · Carbon nanotube · Polar fluid · Nonpolar fluid · Structure · Flow

22.1 Introduction

During last few decades, behavior of fluids inside nanochannels and carbon nanotubes (CNTs) is a subject of intensive experimental and theoretical investigations. An interest to this behavior is caused by its fundamental and technological importance for chemistry, biology, material science, and nanoscience [1–7]. From the fundamental point of view, behavior of fluids confined to nanochannels is of prime importance because such fluids demonstrate properties strongly different from those of the bulk liquid phase. In addition, nanochannel-liquid systems could have a wide scope of application in nanofluidics, including sensors, filters, and gating devices. In addition, carbon nanotubes also can be used as molecular transporters of various cargoes across cellular membranes that could give rise to a new route for drug delivery and, hence, to a novel mechanism for cancer therapy [8]. Therefore, an effective design of nanofluidic devices is very important, and it requires a deep and complete understanding of behaviors of equilibrium structures and flows of different fluids inside nanochannels [9].

As said above, experimental investigations and computer simulations revealed considerable differences between behaviors of different fluids inside nanochannels and those in corresponding bulk phases [10–16]. For example, the pressure drop-driven Poiseuille fluid flows through carbon nanotubes are much faster than the flows predicted by the classic hydrodynamics [10, 11, 17–21]. In addition, the recent studies [22] revealed a significant enhancement of the axial and radial diffusion rates of water molecules near the boundary walls. These remarkable phenomena were explained on the basis of depletion of hydrogen bonds, weak carbon–water interactions and water orientations near the bounding surface of CNTs. However, there is a very strong variation in experimental data on flow rates obtained from different experiments on the fluid flows through nanochannels. An interpretation of these data based on the slip-modified Hagen–Poiseuille equation [23] gives values of slip lengths which vary from several nanometers [24] to 54μ [11]. This fact suggests that there are several factors determining the fluid flow through nanochannels which are not completely understood by now. One of this factors is a structure of bounding walls. The interactions between fluid atoms (molecules) and boundary wall atoms depend on positions of latter in the space. The randomly distributed boundary wall atoms should give a contribution to the total interaction with fluid particles different from that given by atoms located in the sites of a regular crystalline lattice. Thus, behavior of fluids in nanochannels with amorphous bounding walls should differ from that of the fluids in nanochannels with crystalline bounding walls. Another factor that should influence the behavior of fluids in nanochannels is their polarity. For polar fluids composed of molecules possessing permanent dipole moments, in addition to short-range intermolecular interactions, such as van der Waals ones, the

long-range dipole–dipole interactions should be also considered. Since the strength of these long-range interactions may be comparable or even stronger than that of the short-range interactions, behavior of polar fluids in nanochannels can be significantly different from the behavior of nonpolar ones. In addition to the Poiseuille flow caused by an external pressure drop, there is the Couette flow in the space between two parallel surfaces, one of which is moving relative to the other [25]. Using molecular dynamic (MD) simulations, the Couette flows were investigated for various nanochannels [27–33] with distances between bounding surfaces ranging from ~ 16 to ~ 40 atomic (molecular) sizes. The fluid flow velocity profiles obtained from these simulations recovered the flow behavior expected from continuum hydrodynamics [26] with boundary conditions involving varying degrees of the slip. The slip lengths L_s obtained in [26–32] depend on the strength of interaction between liquid particles and bounding wall atoms and densities of the bounding walls. These lengths varied from a few atomic molecular sizes σ to several tens of σ . However, recent techniques, which were developed a few years ago [33, 34], allow to create artificial flat channels with graphite substrates having heights down to an atomic (molecular) size. It has been found in previous papers [34–36] that inside such channels fluid atoms (molecules) form spatially ordered structures which could have a strong effect on the Couette flow. In addition, the techniques developed in [33, 34] allow to create artificial flat channels with top and bottom substrates having different structures. The Couette flow between such different substrates has not yet been simulated at all. In the present paper, using molecular dynamics (MD) simulations, we study equilibrium structures and Poiseuille flows of polar and nonpolar fluids and their mixtures through single-walled CNTs (SWCNTs) with circular cross-sectional boundary walls having the perfect graphene structure, SWCNTs with the same bounding wall but with various rectangular cross sections, and SWCNTs with both circular and rectangular cross sections but with amorphous bounding wall consisting of randomly distributed carbon atoms. A possibility of existence of CNTs with rectangular cross sections was discussed in [38], and it was reported in [39] that such carbon nanotubes can be really formed. All these nanotubes have the same length and the cross-sectional area. The polar fluid confined by the abovementioned SWCNTs is water, and the methane and argon in their liquid phases are considered as nonpolar ones. It has been found that equilibrium structures of all confined fluids depend strongly on the shape of the cross section of SWCNT, whereas the structure of its bounding wall has a minor influence on these structures. On contrary, the external pressure-driven fluid flows through abovementioned SWCNTs depend significantly on both the shape of their cross sections and the structure of their bounding walls. We also study equilibrium structures and Couette flows of polar water molecules and nonpolar argon atoms between two carbon substrates separated from each other by a distance $h = 1.5$ nm. We consider two symmetric systems when both substrates have either graphene-like crystalline or amorphous structures and one asymmetric system consisting of one substrate with crystal graphene-like structure and another substrate with amorphous structure. It has been found that, for two first systems, both the fluid velocity profiles and the average flow velocities depend strongly on both the polarity of fluid particles

and the structure of the boundary substrates. For the third asymmetric system, the fluid flows depend also on which of the substrate is moving and which is at the rest.

22.2 Simulation Details

As said above, using MD simulations, we investigate static and dynamic behavior of polar and nonpolar model fluids and their mixtures confined by carbon nanotubes with circular and rectangular cross sections. As in our previous paper [40], we use a very simple model of polar fluid in which molecules are assumed to be point-like particles possessing a permanent dipole moment. These particles interact with each other via the short-range Lennard-Jones (LJ) pairwise potential

$$U_{LJ}(r_{ij}) = 4\epsilon_{ij} \left[\left(\sigma_{ij}/r_{ij} \right)^{12} - \left(\sigma_{ij}/r_{ij} \right)^6 \right], \quad (22.1)$$

where ϵ_{ij} and σ_{ij} are the strength and characteristic length, respectively, for the LJ interaction between i -th and j -th molecules, and r_{ij} is the distance between them, and the dipole–dipole interaction potential

$$U_{dd}(r_{ij}) = (\mathbf{d}_i \cdot \mathbf{d}_j)/r_{ij}^3 - 3(\mathbf{d}_i \cdot \mathbf{r}_{ij})(\mathbf{d}_j \cdot \mathbf{r}_{ij})/r_{ij}^5, \quad (22.2)$$

where \mathbf{d}_i is the dipole moment of the i -th molecule. Since the polar molecules are considered as the water ones, the LJ interaction constants ϵ_{ij} and σ_{ij} in Eq. (22.1) should be similar to those for the LJ interactions between oxygen atoms of the i th and j th water molecules. These constants, ϵ_{H_2O} and σ_{H_2O} , are taken from the well-known model for water molecules [42, 43], and they are equal to $\epsilon_{H_2O} = 1.083 \times 10^{-14}$ erg and $\sigma_{H_2O} = 3.166\text{\AA}$, respectively. As in [41], an effective dipole moment of the water molecule is set $d_w = 1.89 \times 10^{-18} \text{ g}^{1/2}\text{cm}^5/2\text{s}^{-1}$. An interaction between water molecules and carbon atoms of SWCNTs is described by the LJ potential similar to Eq. (22.1) in which the interaction constants ϵ_{H_2O} and σ_{H_2O} are replaced by ϵ_{CH_2O} and σ_{CH_2O} , respectively. All these constants are taken from [42]. As for nonpolar argon atoms and methane molecules, they are described in framework of the united atom model of methane [21] and the well-known model of argon atoms [43]. According to this model, the argon atoms Ar and the methane molecules CH_4 also interact with each other and with carbon atoms of SWCNTs via the LJ potential (1). The corresponding interaction constants for methane ϵ_{CH_4} , σ_{CH_4} , ϵ_{CCH_4} , and σ_{CCH_4} are taken from [22], and the constants ϵ_{Ar} , σ_{Ar} for argon atoms are taken from [43]. As for interactions between argon and carbon atoms, the corresponding constants ϵ_{CAr} and σ_{CAr} are determined by means of the Lorentz–Berthelot rules [44]. The total force \mathbf{F}_i and the total torque $\boldsymbol{\tau}_i$ acting on the i -th fluid molecule due to interactions with other molecules, and equations of motion of this molecule are given by Eqs. (3)–(8) in [36]. All simulations are performed in the NVT ensembles, and, at each time step, the equations of motion of fluid molecules are solved numerically by the standard method described in [44]. The temperatures of the systems under consideration are

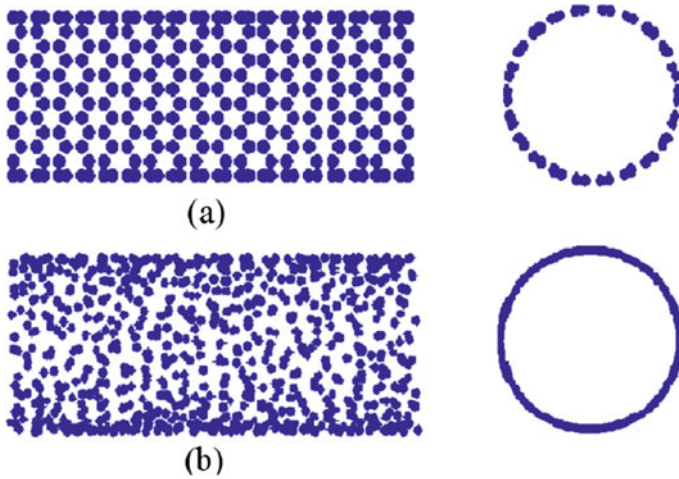


Fig. 22.1 The lateral projections and cross sections of SWCNTs with circular cross sections used in our MD simulations. **a**—SWCNT with boundary wall having the perfect graphene structure; **b**—SWCNT with amorphous bounding wall consisting of randomly distributed carbon atoms

kept constant ($T = 300K$ for water and its mixture with methane, $T = 108K$ for liquid phase of methane, and $T = 85K$ for liquid phase of argon) by employment of the Berendsen thermostat [45].

As said above, we studied static and dynamic behavior of polar and nonpolar model fluids and their mixtures confined by carbon nanotubes with circular and various rectangular cross sections. The lateral projection and cross section of SWCNT with circular cross section and boundary wall having the perfect graphene structure are shown in Fig. 22.1a, whereas Fig. 22.1b demonstrates lateral projection and cross section of analogous SWCNT but with amorphous bounding wall consisting of randomly distributed carbon atoms. The lateral projections and cross sections of SWCNT with square cross section, SWCNT with rectangular cross section and with the ratio between its sides 1 : 2, SWCNT with rectangular cross section and with the ratio between its sides 1 : 4 are shown in Fig. 22.2a, b, and c, respectively. One can see that these tubes with rectangular cross sections have boundary walls with the perfect graphene structure. We also studied behavior of polar and nonpolar model fluids and their mixtures confined by analogous rectangular SWCNTs with amorphous bounding walls.

All abovementioned carbon nanotubes have the same length $L = 3.8\text{ nm}$ and the cross-sectional area $S = 1.77\text{ nm}^2$. Since the carbon atoms in these CNTs are connected to each other with very strong covalent bonds [46] with the interaction constants much larger than the LJ interaction constants ϵ_{CH_2O} , ϵ_{CAr} , and ϵ_{CCH_4} , these atoms are considered to be fixed at their equilibrium sites. This approximation

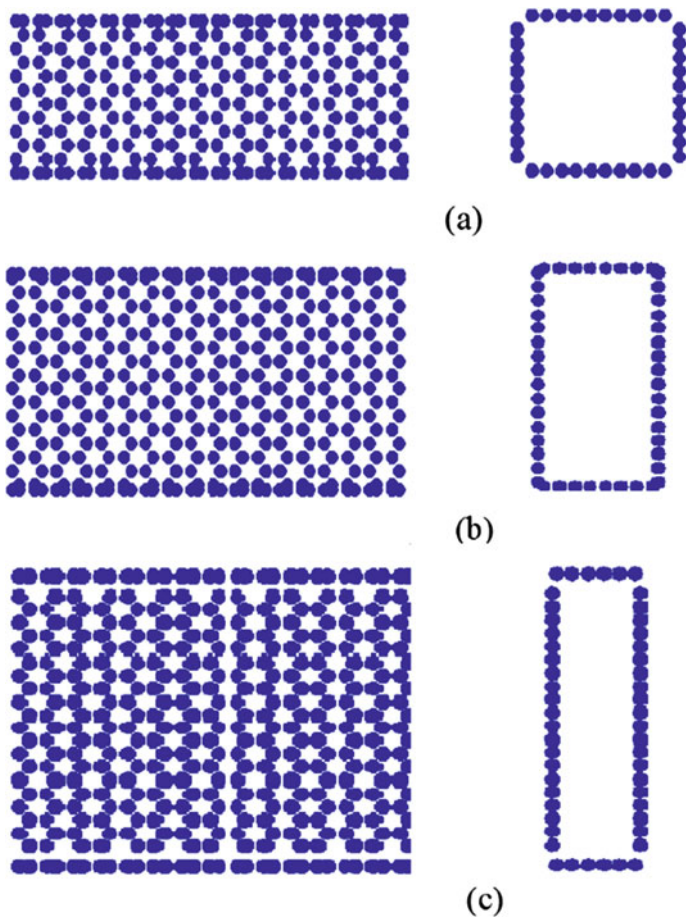


Fig. 22.2 The lateral projections and cross sections of SWCNTs with rectangular cross sections used in our MD simulations. **a**—SWCNT with square cross section; **b**—SWCNT with rectangular cross section and with the ratio between its sides 1:2; **c**—SWCNT with rectangular cross section and with the ratio between its sides 1:4

is also supported by estimations of thermal vibrations of SWCNTs performed in [47]. According to these estimations, average amplitudes of such vibrations are of the order of ~ 0.01 nm that is significantly smaller than typical molecular sizes.

22.3 Results of Simulations and Discussion

22.3.1 Equilibrium Structures Inside Carbon Nanotubes

In order to obtain equilibrium static structures of the water, argon, methane, and the mixture of the water and methane molecules inside SWCNTs under consideration, we performed MD simulations of free (without an external pressure drop) permeations of particles of all fluids into these SWCNTs. These simulations started from the initial configuration schematically depicted in Fig. 22.3a. This configuration is made as follows: initially, we have two reservoirs of fluid particles separated from each other by the wall consisting of carbon atoms. Then, we make a channel in this wall and insert the corresponding SWCNT into the channel. Now, this SWCNT connects two reservoirs with each other and fluid atoms (molecules) can freely permeate into the SWCNT without any external action. For the mixture of the water and methane molecules, both reservoirs contain initially equal numbers of the water and methane molecules. After running during about 100000 time steps (one time step was equal to 0.001 ps), one can reach the equilibrium configuration schematically shown in Fig. 22.3b.

During simulation processes, the system under consideration is placed within the parallelepiped simulation box of $6.332 \times 6.332 \times 6.332 \text{ nm}^3$ in size, and the periodic boundary conditions [44] are imposed on the system in x -, y -, and z -directions.

Figures 22.4 and 22.5 demonstrate cross sections of equilibrium configurations of water and methane molecules inside SWCNTs with circular cross sections. If we look at these figures, it is easily seen that, despite the strong difference in the structures of their bounding walls, the equilibrium structures of polar water and

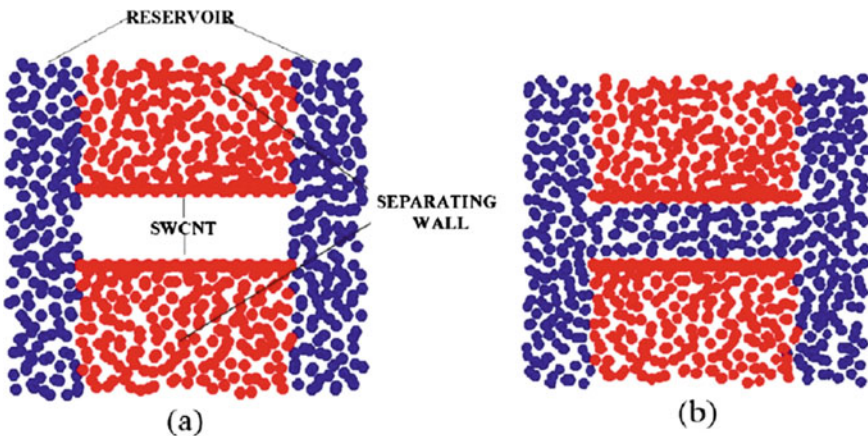


Fig. 22.3 The lateral projection of initial and final equilibrium configurations considered in our MD simulations. **a**—initial configuration; **b**—final equilibrium configuration. Blue circles are fluid atoms (molecules) and red ones are carbon atoms

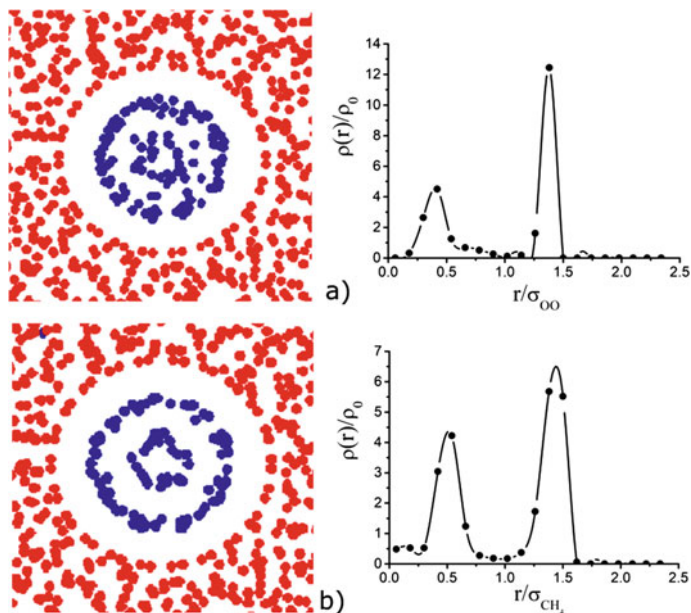


Fig. 22.4 Cross sections of equilibrium water and methane structures (left panels) and corresponding density profiles (right panels) inside SWCNTs with circular cross sections and bounding walls with regular graphene structure. **a**—water; **b**—methane. ρ_0 is the density of number of water (methane) molecules inside SWCNT

nonpolar methane inside SWCNTs with circular cross sections are very similar (see left panels in Figs. 22.4a, b, 22.5a, b). From these figures, one can conclude that both polar water and nonpolar methane molecules are mainly placed inside such SWCNTs on two coaxial cylindrical surfaces. The corresponding density profiles (right panels in these figures) demonstrate two maxima disposed at similar distances equal to about σ_{OO} and $\sigma_{CH_4CH_4}$, respectively. It can be easily understood because both polar water and nonpolar methane molecules interact with each other via LJ potentials (22.1) with characteristic interaction lengths σ_{OO} and $\sigma_{CH_4CH_4}$, respectively. The polar water molecules also interact via Coulomb-like dipole–dipole potential (22.2), but this long-range interaction does not possess any characteristic interaction length. Thus, the characteristic lengths σ_{OO} and $\sigma_{CH_4CH_4}$, respectively, are the only lengths which have an influence on the water and methane equilibrium structures inside the abovementioned SWCNTs.

From these figures, one can conclude that both polar water and nonpolar methane molecules are mainly placed inside such SWCNTs on two coaxial cylindrical surfaces. The corresponding density profiles (right panels in these figures) demonstrate two maxima disposed at similar distances equal to about σ_{OO} and $\sigma_{CH_4CH_4}$, respectively. It can be easily understood because both polar water and nonpolar methane molecules interact with each other via LJ potentials (22.1) with characteristic interac-

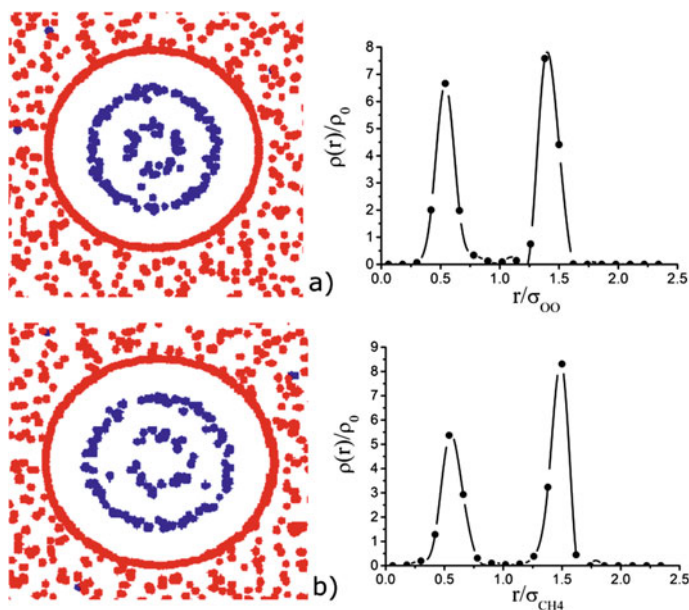


Fig. 22.5 Cross sections of equilibrium water and methane structures (left panels) and corresponding density profiles (right panels) inside SWCNTs with circular cross sections and bounding walls with amorphous structure. **a**—water; **b**—methane

tion lengths σ_{OO} and $\sigma_{CH_4CH_4}$, respectively. The polar water molecules also interact via Coulomb-like dipole–dipole potential (22.2), but this long-range interaction does not possess any characteristic interaction length. Thus, the characteristic lengths σ_{OO} and $\sigma_{CH_4CH_4}$, respectively, are the only lengths which have an influence on the water and methane equilibrium structures inside the abovementioned SWCNTs.

Figure 22.6a–l demonstrates cross sections of equilibrium configurations of water molecules (Fig. 22.6a–c), argon atoms (Fig. 22.6d–f), methane molecules (Fig. 22.6g–i), and mixture of water and methane molecules (Fig. 22.6j–l) inside SWCNTs with the described above rectangular cross sections shown in Fig. 22.2a, b, and c.

The corresponding density profiles along z (vertical) and y (lateral) directions perpendicular to the tube x -axes are shown in Figs. 22.7, 22.8, 22.9, and 22.10. If we look at Fig. 22.6a–l, it is clearly seen that, for all types of liquid atoms (molecules), the main features of the corresponding equilibrium structures are similar, and these features are defined by the shapes of SWCNT cross sections. For example, all liquid atoms (molecules) inside SWCNTs with square cross sections form structures with square-like cross sections which are reduced replicas of the SWCNTs ones (see Fig. 22.6a, d, g, j). All liquid atoms (molecules) inside SWCNTs with rectangular cross sections having the ratio 1 : 2 between their sides form equilibrium structures consisting of two planes parallel to the vertical bounding walls (see Fig. 22.6b, e, h, k). Finally, all liquid atoms (molecules) inside SWCNTs with rectangular cross

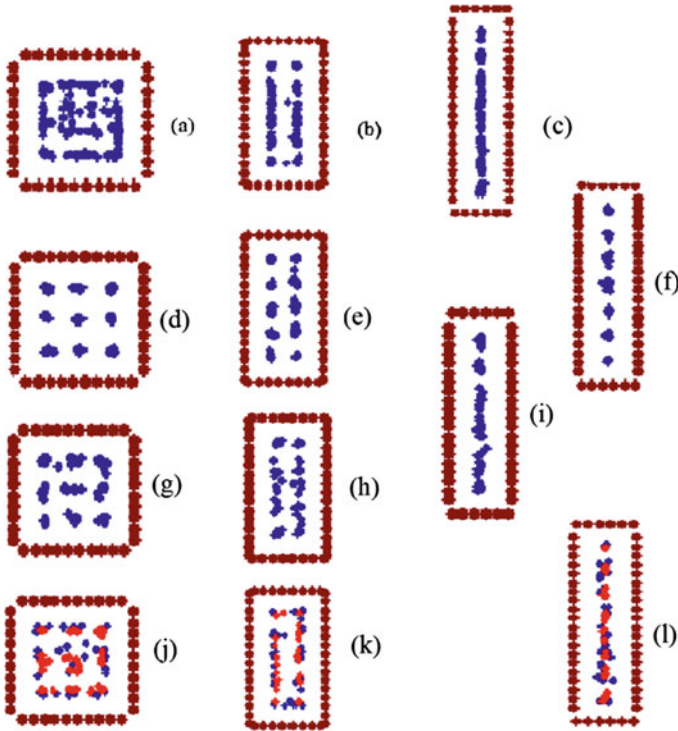


Fig. 22.6 Cross sections of equilibrium structures of water molecules (a–c), argon atoms (d–f), methane molecules (g–f), and the mixture of the water and methane molecules (j–l) inside SWCNTs with rectangular cross sections depicted in Fig. 22.2a–c. In all figures, brown circles denote the bounding wall carbon atoms. In a–i, blue circles denote liquid atoms (molecules). In j–l, blue and red circles denote the water and methane molecules, respectively. The equilibrium ratios between the water and methane molecules are 43 : 59, 52 : 49, and 43 : 46 for SWCNTs with rectangular cross sections with ratios between their sides equal to 1 : 1, 1 : 2, and 1 : 4, respectively

sections having the ratios 1 : 4 between their sides form equilibrium 2D structures in a form of the plane parallel to the vertical bounding walls (see Fig. 22.6c, f, i, l). Thus, the shape of the rectangular SWCNT cross sections plays a dominant role in the formation of equilibrium structures of liquid atoms (molecules) inside SWCNTs.

It is simultaneously seen that the equilibrium structures depicted in Fig. 22.6a–l demonstrate certain additional features depending on characteristics of concrete liquid atoms (molecules) under consideration. It is easily seen that, inside all SWCNTs, liquid structures formed by argon atoms are most ordered. For example, argon atoms inside SWCNT with square cross section form nine well-ordered chains parallel to the tube axis (see Fig. 22.8d). One of these chains coincides with the tube axis, and other eight chains are disposed on bounding surfaces of imaginable parallelepiped inside this SWCNT. Simultaneously, methane molecules inside the same SWCNT form similar structure but with more smeared chains (see Fig. 22.6g). This fact is

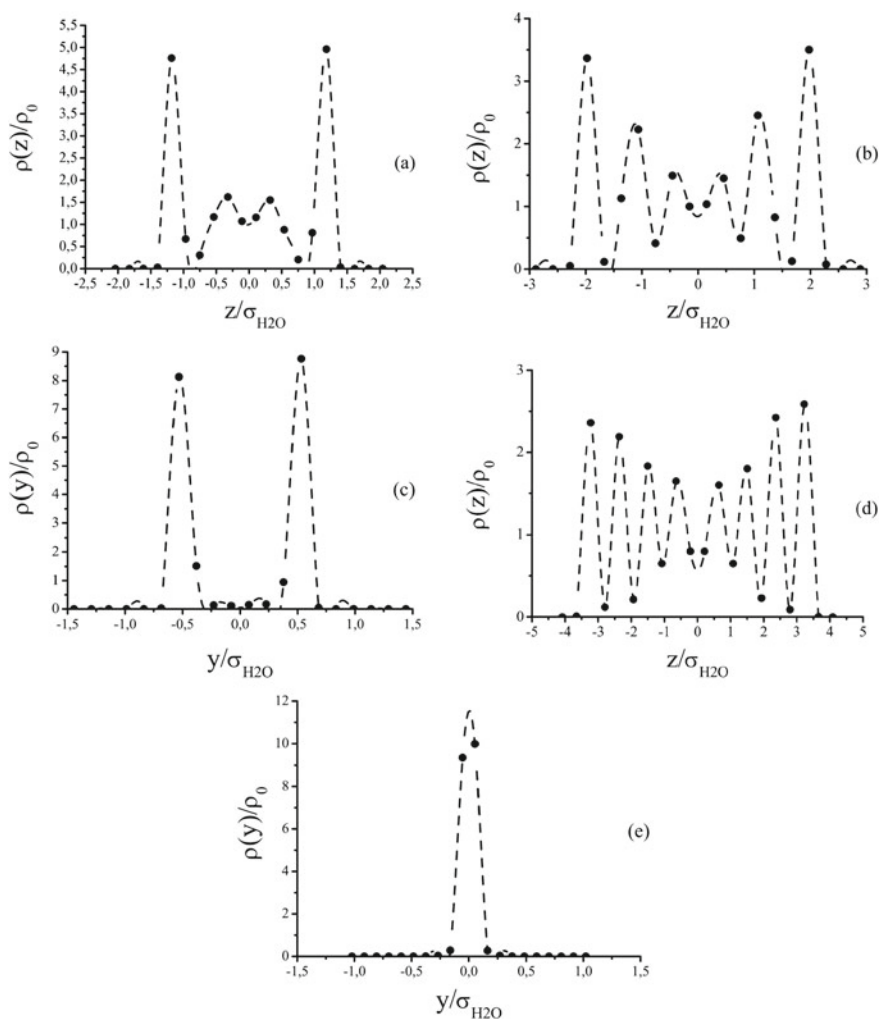


Fig. 22.7 Equilibrium density profiles for the water inside SWCNTs with different rectangular cross sections. **a**—The density profile along z -axis for SWCNT with square cross section. For symmetry reasons, the analogous profile along y -axis should be similar. $\rho_0 = 0.61745$ is the average density in the tube in reduced MD units. **b**—The analogous profile for SWCNT with rectangular cross section having the ratio between its sides 1 : 2. **c**—The density profile along y -axis for the same SWCNT. $\rho_0 = 0.5996$. **d**—The density profile along z -axis for SWCNT with rectangular (cross section having the ratio between its sides 1 : 4. **e**—The density profile along y -axis for the same SWCNT. $\rho_0 = 0.44619$

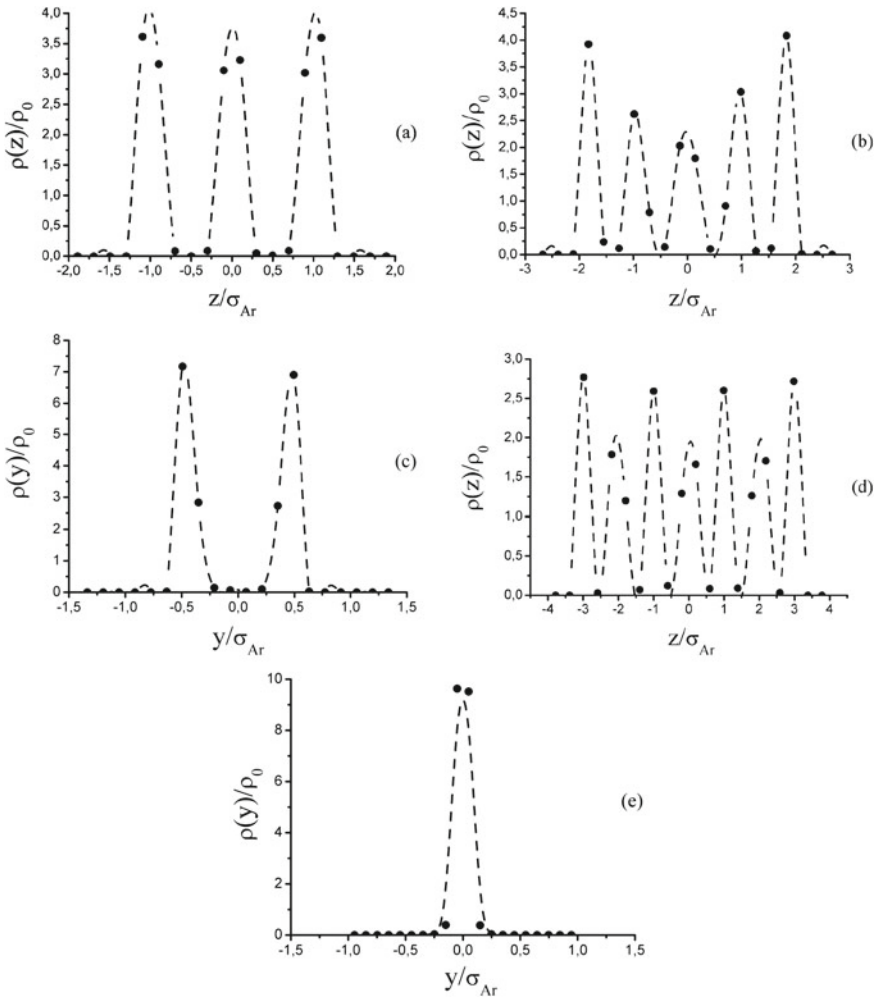


Fig. 22.8 Equilibrium density profiles for argon atoms inside SWCNTs with different rectangular cross sections. **a**—The density profile along z -axis for SWCNT with square cross section. $\rho_0 = 0.53368$. **b**—The analogous profile for SWCNT with rectangular cross section having the ratio between its sides 1 : 2. **c**—The density profile along y -axis for the same SWCNT. $\rho_0 = 0.52252$. **d**—The density profile along z -axis for SWCNT with rectangular cross section having the ratio between its sides 1 : 4. **e**—The density profile along y -axis for the same SWCNT. $\rho_0 = 0.41445$

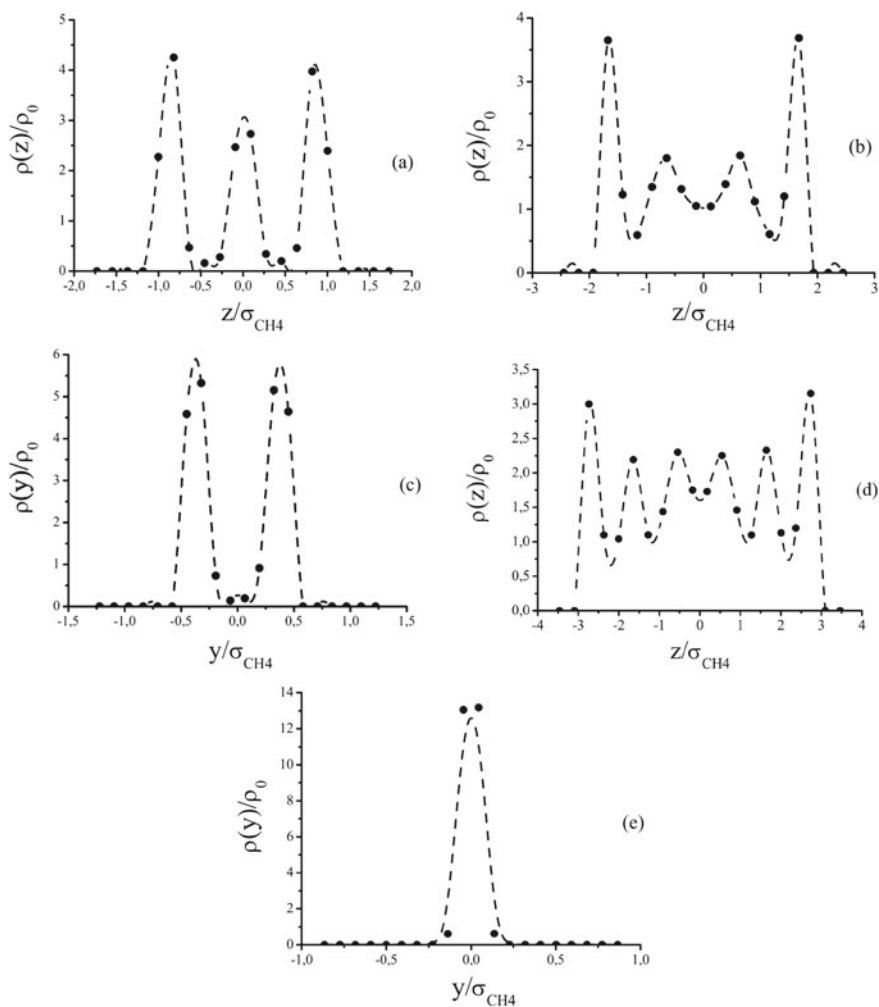


Fig. 22.9 Equilibrium density profiles for methane molecules inside SWCNTs with different rectangular cross sections. **a**—The density profile along z -axis for SWCNT with square cross section. $\rho_0 = 0.51835$. **b**—The analogous profile for SWCNT with rectangular cross section having the ratio between its sides 1 : 2. **c**—The density profile along y -axis for the same SWCNT. $\rho_0 = 0.38506$. **d**—The density profile along z -axis for SWCNT with rectangular cross section having the ratio between its sides 1 : 4. **e**—The density profile along y -axis for the same SWCNT. $\rho_0 = 0.25177$

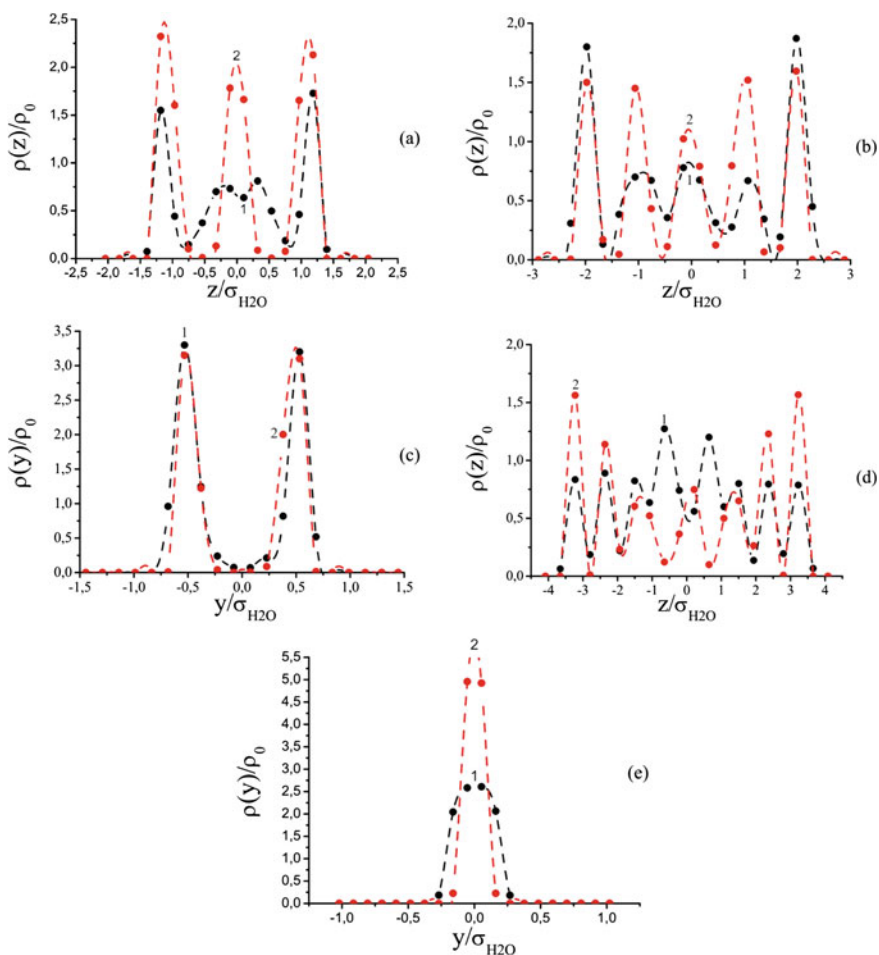


Fig. 22.10 Equilibrium density profiles for mixtures of water and methane molecules inside SWCNTs with different rectangular cross sections, 1—the water profiles, 2—the methane profiles. **a**—The density profile along z -axis for SWCNT with square cross section. $\rho_0 = 0.4597$. **b**—The analogous profile for SWCNT with rectangular cross section having the ratio between its sides 1 : 2. **c**—The density profile along y -axis for the same SWCNT. $\rho_0 = 0.45357$. **d**—The density profile along z -axis for SWCNT with rectangular cross section having the ratio between its sides 1 : 4. **e**—The density profile along y -axis for the same SWCNT. $\rho_0 = 0.40112$

also reflected in Fig. 22.8a and Fig. 22.9a, which demonstrate the density profiles along z -axis for argon atoms and methane molecules inside the same SWCNT with square cross section. One can see that the density profile for argon atoms exhibits three peaks having almost the same height and width equal to about $0.6 \sigma_{Ar}$. The analogous profile for methane molecules has also three peaks, but the central one is noticeably lower than two others, and the width of these peaks is about $0.6 \sigma_{CH_4}$ that is about 10% larger than that of the analogous peaks in the density profile for argon atoms. If we look at Fig. 22.3a which exhibits the cross section of the equilibrium water structure inside the SWCNT with the square cross section and at Fig. 22.4a demonstrating the corresponding density profile along z -axis, then we find that this structure is much more disordered relative to those depicted in Fig. 22.6d and g for argon atoms and methane molecules, respectively. Perhaps, it is due to the Coulomb-like dipole–dipole interactions between polar water molecules which do not occur in ensembles of nonpolar argon atoms and methane molecules. According to the Earnshaw theorem [48], an ensemble of particles interacting via Coulomb-like forces cannot be maintained in a stable stationary equilibrium configurations. Thus, the well-ordered structures of water molecules inside SWCNTs cannot exist for sufficiently long times. If we look at Fig. 22.6j, which demonstrates the cross section of the equilibrium structure formed by the mixture of water and methane molecules inside SWCNT with square cross section, we can find that this structure resembles the abovementioned structure formed by the pure methane inside the same SWCNT. This fact is also confirmed by the density profiles for methane and water molecules depicted in Fig. 22.10a. The density profile for methane molecules (curve 2) exhibits three well-developed peaks of almost similar height, whereas the analogous profile for water molecules (curve 1) demonstrates two well-developed peaks at the edges and the strongly smeared central one. This fact can be explained by that the interaction constants ϵ_{CH_4} and ϵ_{CCH_4} for interactions between methane molecules and those between methane molecules and boundary wall carbon atoms, respectively, are significantly larger than analogous interaction constants ϵ_{H_2O} and ϵ_{CH_2O} for water molecules. So, if we look at Fig. 22.6b, c, e, f, h, i, k, l, which demonstrate equilibrium structures formed by water molecules, argon atoms, methane molecules, and the mixture of water and methane molecules inside SWCNTs with rectangular cross sections having the ratios between their sides 1 : 2 and 1 : 4, and at Fig. 22.7b–e, Fig. 22.8b–e, Fig. 22.9b–e, Fig. 22.10b–e demonstrating the corresponding equilibrium density profiles, we can conclude that the said above for equilibrium structures inside SWCNT with square cross section is valid for equilibrium structures in all SWCNTs with rectangular cross sections. The most ordered structures are exhibited by argon atoms, whereas water molecules form most disordered structures, and the positional order of structures formed by methane molecules and the mixtures $H_2O + CH_4$ has an intermediate positional order.

It should be also noted that the shape of the SWCNT's cross section and the interaction constants ϵ and σ play very important role not only in equilibrium structures and average liquid densities inside SWCNTs but also in a compositions of the mixture of water and methane molecules inside different SWCNTs. For example, inside SWCNT with square cross section, the ratio between numbers of water

and methane molecules is equal to 43:59, whereas inside SWCNTs with rectangular cross sections these molecules occur in almost equal proportions, namely, 52:49 for SWCNT with ratio between its sides 1:2 and 43:46 for SWCNT with the side ratio 1:4. This result can be qualitatively explained as follows. In the case of SWCNT with square cross section, the distance between bounding walls is large enough for both water and methane molecules. Therefore, the strengths of interactions between liquid molecules and bounding walls, ϵ_{CH_2O} and ϵ_{CCH_4} , play a main role in their penetration into SWCNTs, and the effective sizes of these molecules, σ_{H_2O} and σ_{CH_4} , play a minor role. Since the interaction constant ϵ_{CCH_4} for the interaction between methane molecules and bounding wall carbon atoms is noticeably larger than the analogous interaction constant ϵ_{CH_2O} for the water molecules, then the number of methane molecules penetrating into SWCNT with square cross section is larger than that of water molecules. For SWCNTs with rectangular cross sections having ratios between their sides equal to 1:2 and 1:4, respectively, the distances between lateral bounding walls along y-direction become sufficiently small for larger methane molecules and not so small for smaller water molecules (effective diameter σ_{CH_4} of the methane molecule is about 10% larger than the analogous diameter σ_{H_2O} of the water molecule). Thus, for these SWCNTs, a competition between interactions of different liquid molecules with bounding wall atoms and their molecular sizes occurs, and these competition equalizes concentrations of water and methane molecules inside such SWCNTs.

22.3.2 Fluid Flows Inside Carbon Nanotubes

Now, let us turn to results of MD simulations of polar water and nonpolar methane and argon Poiseuille flows through the abovementioned SWCNTs under action of the external pressure drop across these nanotubes. To simulate these flows, in the equilibrium configurations depicted in Fig. 22.3b, we removed the liquid reservoirs and applied periodic boundary conditions to edges of SWCNTs. The external pressure drop across nanotubes was mimicked by the external force $f_{x0} = 0.2$ (in MD units [44]) acting on each liquid particle inside SWCNTs. The fluid flow velocity profiles obtained from our simulations of fluid flows through SWCNTs with circular cross sections are shown in Figs. 22.11 and 22.12 for the polar water and nonpolar methane, respectively.

One can see that, for both the polar water and nonpolar methane (see Figs. 22.11a and 22.12a), the fluid flow velocity profiles for SWCNTs with circular cross section and bounding walls with regular graphene structures demonstrate two sufficiently sharp maxima separated from each other by the gaps with widths equal to about σ_{OO} and $\sigma_{CH_4CH_4}$, respectively. One can also see that, for both the water and methane, these two maxima have similar heights. It means that, inside SWCNTs with circular cross sections and bounding walls with regular graphene structure, both polar water and nonpolar methane molecules move along two coaxial cylindrical surfaces depicted in Fig. 22.4a and b with similar velocities. Figures 22.11b and 22.12b

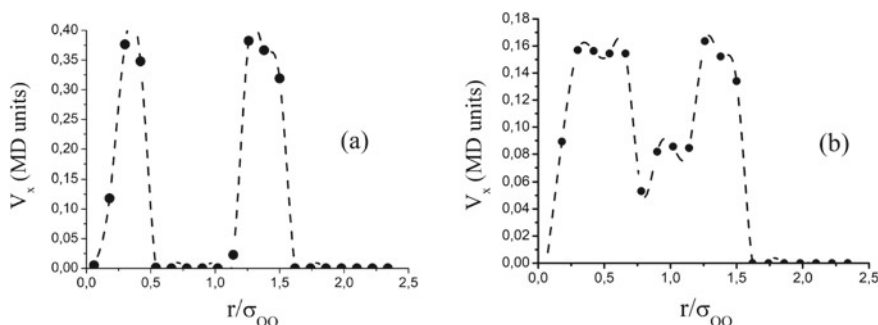


Fig. 22.11 The water flow velocity profiles for SWCNTs with circular cross section and with bounding walls having regular graphene and amorphous structures. **a**—velocity profile for SWCNT with circular cross section and bounding wall with regular graphene structure; **b**—velocity profile for SWCNT with circular cross section and bounding wall amorphous structure

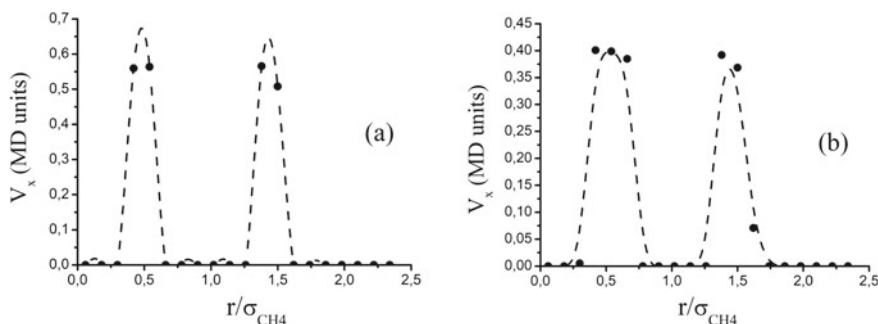


Fig. 22.12 The methane flow velocity profiles for SWCNTs with circular and cross section and with bounding walls having regular graphene and amorphous structures. **a**—velocity profile for SWCNT with circular cross section and bounding wall with regular graphene structure; **b**—velocity profile for SWCNT with circular cross section and bounding wall amorphous structure

demonstrate analogous velocity profiles for the polar water and nonpolar methane flows, respectively, through SWCNTs with circular cross section and bounding walls with random (amorphous) distributions of carbon atoms. One can see that, for the nonpolar methane, the fluid flow velocity profile (see Fig. 22.12b) also demonstrates two maxima separated from each other by the gap with width equal to about σ_{CH4CH4} . The analogous polar water flow velocity profile depicted in Fig. 22.11b also have two maxima of similar height, but these maxima are much wider than those shown in Fig. 22.12b and they are not separated from each other by the gap seen in Fig. 22.12b. It means that, inside SWCNT with circular cross section and amorphous bounding wall, nonpolar methane molecules move along coaxial cylindrical surfaces similar to those in the case of SWCNTs with circular cross section and bounding wall with regular graphene structure of carbon atoms. As for the motion of polar water molecules through similar SWCNT, one can conclude from the velocity profile in Fig. 22.11b

that this motion is less regular than that through SWCNT with circular cross section and bounding wall with regular graphene structure of carbon atoms. For both the polar water and nonpolar methane, the fluid flows through SWCNTs with circular cross section and bounding wall with regular graphene structure are noticeably more intensive than those through analogous SWCNTs with bounding walls having amorphous distribution of carbon atoms. The ratios between corresponding intensities are equal to about 3:1 for the polar water and about 1.3:1 for the nonpolar methane. This fact can be qualitatively understood if we assume that, during the fluid flow through SWCNTs with bounding walls having regular graphene structure of carbon atoms, the fluid molecules can find more or less “easy” trajectories for their motion, whereas, for SWCNTs with bounding walls with amorphous distribution of carbon atoms, such “easy” trajectories are absent.

Now, let us turn to results of MD simulations of Poiseuille flows of the polar water, nonpolar methane and argon, and the mixture of the water and methane through the abovementioned SWCNTs with rectangular cross sections under action of the external pressure drops across these nanotubes. The external pressure drop across such nanotubes is also mimicked by the external force f_{x0} acting on each liquid particle inside SWCNTs. In order to calculate velocity profiles, we divide the space inside these carbon nanotubes into very thin sublayers parallel to the top and bottom bounding walls and calculate average molecular velocities inside these sublayers as a function of z -coordinates of their centers. These fluid flow velocity profiles obtained from our simulations are shown in Fig. 22.13a–c for the polar water, the nonpolar argon, and the mixture of the water and methane, respectively. The profiles for the water and argon flows are obtained for the external force equal to $f_{x0} = 0.05$ (in reduced MD units [44]), and for the flow of the mixture of the water and methane $f_{x0} = 0.1$. The nonpolar methane flow through all rectangular SWCNTs under consideration at these values of f_{x0} is absent. This case will be discussed below.

One can see from Fig. 22.13a–c that fluid flows through SWCNTs with rectangular cross sections depend strongly on both the type of the fluid inside the tube and the shape of its cross section. For example, it is easily seen that, for the polar water, the average flow velocity v_x^{aver} should have a maximum value for SWCNT having rectangular cross section with the ratio between its side 1 : 4 ($v_x^{aver} = 1.15$ in MD units). The intermediate value $v_x^{aver} = 0.97$ corresponds to the water flow through SWCNT having rectangular cross section with the ratio between its side 1:2, and the minimum value $v_x^{aver} = 0.28$ exhibits the water flow through SWCNT with square cross section. For nonpolar argon, the average fluid flow velocity has also the minimum value $v_x^{aver} = 0.08$ in the case of SWCNT with square cross section but the results for two SWCNTs with other rectangular cross sections change places: the maximum average flow velocity $v_x^{aver} = 1.2$ corresponds to SWCNT with the rectangular cross section with the ratio between sides 1:2, and the fluid flow through other SWCNT with rectangular cross section has the intermediate average fluid flow velocity $v_x^{aver} = 0.7$. Finally, for the mixture of polar water and nonpolar methane, we have the maximum value $v_x^{aver} = 0.8$ in the case of SWCNT with the square cross section, the minimum value $v_x^{aver} = 0.03$ for SWCNT having the rectangular

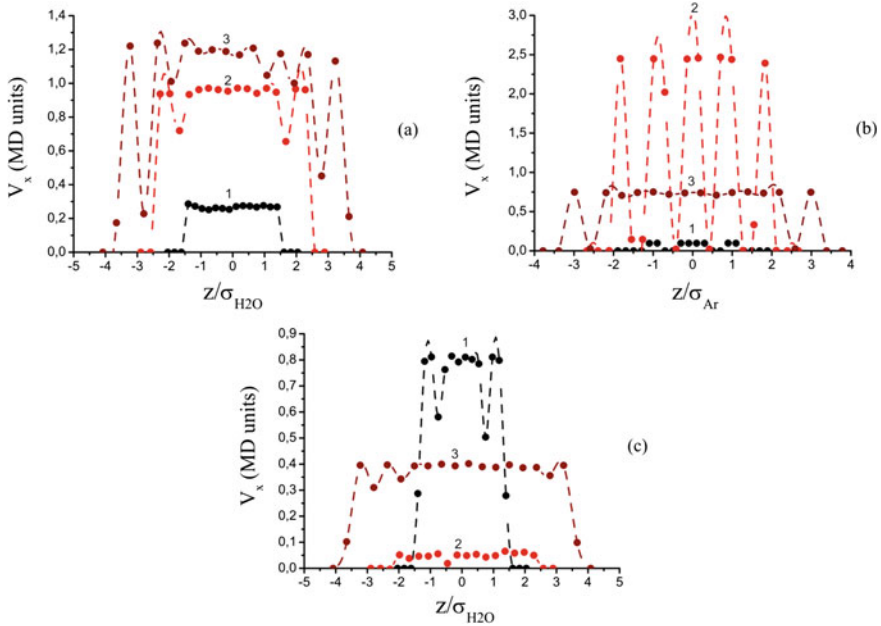


Fig. 22.13 The fluid flow velocity profiles for flows of polar water molecules, nonpolar argon atoms, and mixtures of water and methane molecules through SWCNTs with different rectangular cross sections. **a**—fluid flow velocity profiles for water molecules, **b** and **c**—analogous profiles for argon atoms and mixtures of water and methane molecules, respectively. $f_{x0} = 0.05$ for 13a and 13b, and $f_{x0} = 0.1$ for 13c. Curves 1 in all figures correspond to SWCNT with square cross section; curves 2 and 3 correspond to SWCNTs with rectangular cross sections having the ratio between their sides 1:2 and 1:4, respectively

cross section with the ratio between sides 1:2, and the intermediate average fluid flow velocity $v_x^{aver} = 0.4$ corresponds SWCNT with other rectangular cross section. At first glance, it is not easy to give a plausible explanation of these somewhat intricate results. However, the following qualitative considerations can be made.

It is clear that the flow of liquid particles through SWCNTs is governed by the external force f_{x0} , which is a given constant, and by certain retarding forces due to the interactions between liquid atoms (molecules) and bounding wall carbon atoms. It is also clear that the stronger these interactions the stronger retarding forces, and, hence, the slower the fluid flow. In our simulations, the interactions between liquid atoms (molecules) and the bounding wall carbon atoms are modeled by means of the LJ pairwise potentials which are characterized by the abovementioned interaction constants ϵ_{CH2O} , ϵ_{CCH4} , ϵ_{CAr} , and characteristic lengths σ_{CH2O} , σ_{CCH4} , σ_{CAr} . It is also well known that these LJ potentials have the minimum disposed at the distance r^* to a given carbon atom equal to $r^* = 2^{1/6}\sigma$, and, at this minimum, the force acting on the liquid particle is equal to zero. When the distance between the liquid particle and the carbon atom is less than r^* this force is repulsive, and for distances larger

than r^* it is attractive. When we study the flow of the same liquid particles through different SWCNTs, the interaction constant ϵ for LJ interactions between liquid particles and bounding wall carbon atoms is the same for all SWCNTs, and only distances between wall atoms and liquid particles define a difference in their flows. Let us consider the water flows through different rectangular SWCNTs. It is easy to calculate average minimum distances d_{min}^{aver} from water molecules to the bounding wall carbon atoms corresponding to equilibrium structures of water molecules inside these SWCNTs depicted in Fig. 22.6a–c. These distances are equal to $1.0223\sigma_{H_2O}$ for SWCNT with square cross section, $1.03\sigma_{H_2O}$ for SWCNT with rectangular cross section with the ratio between its sides 1:2, and $1.064\sigma_{H_2O}$ for SWCNT with other rectangular cross section with analogous ratio equal to 1:4. The distance r^* for LJ interactions between water molecules and bounding wall carbon atoms is equal to $r^* = 1.131\sigma_{H_2O}$. One can see that, for all these SWCNTs, d_{min}^{aver} is smaller than r^* , and, therefore, inside these nanotubes, the forces acting on water molecules from bounding wall carbon atoms are repulsive. In addition, the larger difference between r^* and d_{min}^{aver} the stronger these forces. Hence, these forces are strongest for SWCNT with square cross section, they are weakest for SWCNT with rectangular cross section having the ratio between its sides 1:4, and for other SWCNT with rectangular cross section we have an intermediate value for the force between water molecules and bounding wall carbon atoms. So, one can conclude that the water flow through SWCNT with rectangular cross section having the ratio between its sides 1:4 should be fastest, for water flow through SWCNT with square cross section should be slowest, and the water flow through SWCNT with other rectangular cross section should have intermediate average liquid flow velocity. These speculations are in a qualitative agreement with the velocity profiles depicted in Fig. 22.8a. One can repeat such qualitative analysis for the flow of argon atoms through the abovementioned SWCNTs with rectangular cross sections. For equilibrium structures of argon atoms inside these nanotubes depicted in Fig. 22.3d–f, we obtain the values of d_{min}^{aver} equal to $0.96\sigma_{Ar}$, $0.98\sigma_{Ar}$, and $0.97\sigma_{Ar}$ for SWCNTs having rectangular cross sections with the ratios between their sides equal to 1:1, 1:2, and 1:4, respectively, and r^* for LJ interactions between argon and carbon atoms equal to $r^* = 1.089\sigma_{Ar}$. Therefore, inside all these SWCNTs, argon atoms are subjected to repulsive forces from the bounding wall carbon atoms, and these forces are strongest for SWCNT with square cross section, weakest for SWCNT with rectangular cross section with the ratio between its sides 1:2, and they have an intermediate value for other SWCNT with rectangular cross section. Then, the argon flow should be fastest for SWCNT having the rectangular cross section with the ratio between its sides 1:2, the average fluid flow velocity should be lowest for SWCNT with square cross section, and the argon flow through SWCNT having rectangular cross section with the ratio between its sides 1:4 should have an intermediate value of the average fluid flow velocity. The results of this analysis are also in a qualitative agreement with the fluid flow profiles depicted in Fig. 22.13b.

As said above, for the external forces equal to $f_{x0} = 0.05$ and $f_{x0} = 0.1$, the flow of methane molecules through all SWCNTs under consideration is absent. Therefore, we increased little by little the external force f_{x0} and found that there are

certain threshold or critical values of f_{x0} , f_{x0}^c , above which methane molecules can flow through SWCNTs with rectangular cross sections. These critical values, which can be considered as certain strengths of breakaway, depend strongly on the shape of SWCNT cross sections. We found that, for SWCNT with the square cross section, $f_{x0}^c = 0.275$ (in reduced MD units), for SWCNT with the rectangular cross section with the ratio between its sides 1:2, $f_{x0}^c = 0.15$, and, for SWCNT having the rectangular cross section with the ratio between its sides 1:4, $f_{x0}^c = 0.8$. The following questions arise: (i) why the liquid methane flows through SWCNTs with rectangular cross sections demonstrate an existence of strengths of breakaway that is absolutely not inherent to flows of ordinary liquids?; (ii) why we do not observe such strengths of breakaway for the water and argon flows through the same SWCNTs?; and (iii) how can we explain the abovementioned dependence of f_{x0}^c on the shape of the SWCNT cross sections?. The answer to the first question seems to be sufficiently obvious. If we look at Fig. 22.6a–i, which exhibit equilibrium structures of argon atoms and water and methane molecules inside SWCNTs under consideration, we can see an occurrence of different types of positional order which is not inherent to an ordinary liquid phase. Thus, fluid atoms (molecules) inside our SWCNTs form solid-like structures, and, as is well known, the strength of breakaway is a typical phenomenon for sliding a solid along a solid surface.

The answer to the second question is also simple enough. The interaction constant ϵ_{CCH_4} , which defines a strength of interaction between methane molecules and bounding wall carbon atoms, is considerably larger than analogous constants ϵ_{CH_2O} and ϵ_{CAr} which define strengths of interactions between bounding wall carbon atoms and water molecules and argon atoms, respectively. In addition, the effective size of methane molecules, σ_{CH_4} , is larger than effective sizes of argon atoms σ_{Ar} and water molecules σ_{H_2O} . Therefore, the interaction between methane molecules and bounding wall carbon atoms is significantly stronger than analogous interactions of water molecules and argon atoms. Perhaps, their flows through SWCNTs under consideration could also exhibit certain strengths of breakaway, but these strengths are much lower than the force f_{x0} used to drive argon atoms and water molecules.

In order to answer to the third question, we should, as we made above, calculate average minimum distances d_{min}^{aver} between methane molecules and bounding wall carbon atoms for equilibrium structures formed by methane molecules inside SWCNTs under consideration. Our calculations give $d_{min}^{aver} = 0.94\sigma_{CH_4}$ for SWCNT with square cross section, $d_{min}^{aver} = 0.95\sigma_{CH_4}$ for SWCNT having rectangular cross section with the ratio between its sides 1 : 2, and $d_{min}^{aver} = 0.89\sigma_{CH_4}$ for SWCNT with other rectangular cross section. We also obtain $r^* = 1.055\sigma_{CH_4}$ for LJ interactions between methane molecules and bounding wall carbon atoms. Repeating the above reasoning about relationship between difference $r^* - d_{min}^{aver}$ and the strength of interactions between liquid particles and bounding wall carbon atoms, one can conclude that such interaction between methane molecules and carbon atoms should be strongest for SWCNT having rectangular cross section with the ratio between its sides 1:4, weakest for SWCNT with other rectangular cross section, and intermediate for SWCNT with square cross section. Thus, one can explain why the strength of breakaway should be highest for SWCNT with rectangular cross section with the

ratio between its sides 1:4, lowest for SWCNT with other rectangular cross section, and intermediate for SWCNT with square cross section.

The qualitative explanation of velocity profiles for the flows of the mixture H₂O + CH₄ through SWCNTs with different rectangular cross sections depicted in Fig. 22.13c can be obtained by means of similar analysis. Since in this mixture, methane molecules are characterized by largest constant ϵ_{CCH_4} for LJ interactions of these molecules with bounding wall carbon atoms, they are subjected to strongest retarding forces from bounding walls. The stronger these forces the slower the fluid of water and methane molecules through SWCNT and vice versa. Therefore, we should calculate d_{min}^{aver} for methane molecules in equilibrium structures formed by the mixture H₂O + CH₄ inside SWCNTs with different rectangular cross sections (see Fig. 22.3j–l) and compare these values with r^* for LJ interactions between methane molecules and bounding wall carbon atoms. Such calculations give $d_{min}^{aver} = 1.097\sigma_{H_2O}$ for SWCNT with the square cross section, $d_{min}^{aver} = 1.069\sigma_{H_2O}$ for SWCNT with the rectangular cross section with the ratio between its sides 1:2, and $d_{min}^{aver} = 1.075\sigma_{H_2O}$ for SWCNT with other rectangular cross sections. r^* for LJ interactions between methane molecules and carbon atoms is equal to $r^* = 1.089\sigma_{H_2O}$. Then, one can see that the value d_{min}^{aver} for SWCNT with the square cross section is closest to r^* , d_{min}^{aver} for SWCNT with rectangular cross section with the ratio between sides is most different from r^* , and d_{min}^{aver} for SWCNT with other rectangular cross section has an intermediate value between two abovementioned ones. Then, one can conclude that the flow of the mixture H₂O + CH₄ through SWCNT with the square cross section should be fastest, the flow of this mixture through SWCNT with the rectangular cross section with the ratio between its sides 1:2 should be slowest, and the flow of such mixture through SWCNT with other rectangular cross section should have an intermediate average flow velocity. It is easily seen that these conclusions are in a qualitative agreement with the velocity profiles depicted in Fig. 22.13c.

By analogy with previous papers devoted to investigation of fluid flows through carbon nanotubes [10, 49] we can calculate the so-called enhancement factor for fluid flows through CNTs, i.e., the ratio between average fluid flow velocities obtained from our MD simulations and those given by classic Hagen–Poiseuille equation for flows of similar fluids through the round nanopore with the same length and the cross-sectional area [25]. If we remember that the reduced MD unit of the velocity is equal to $V_{MD} = (\epsilon/m)^{1/2}$, we can obtain for water molecules $V_{MDH_2O} = 1.9 \times 10^4$ cm/s and for argon atoms $V_{MDAr} = 1.57 \times 10^4$ cm/s. The expression for the MD unit of the force $f_{MD} = \epsilon/\sigma$ gives $f_{MDH_2O} = 3.42 \times 10^{-7}$ dyn and $f_{MDAr} = 4.85 \times 10^{-7}$ dyn. Then, taking into account that the pressure gradient along nanotube $\Delta P/\Delta L$ can be calculated as $\Delta P/\Delta L = f_{x0}n_{tube}$, where n_{tube} is the average particle number density inside nanotube, and that the macroscopic viscosities of water (at 300 K) and liquid argon (at 85 K) are equal to 10^{-2} [43] and 2.78×10^{-3} g/cm s, respectively, we can obtain the following enhancement factors Q for abovementioned rectangular SWCNTs at $f_{x0} = 0.05$: $Q_{H_2O}(rect1 : 4) = 2850$; $Q_{H_2O}(rect1 : 2) = 1990$; $Q_{H_2O}(square) = 695$; $Q_{Ar}(rect1 : 4) = 299$; $Q_{Ar}(rect1 : 2) = 513$; and $Q_{Ar}(square) = 34$. For a comparison, we also calculated the analogous enhancement factors for SWCNT with the same length and circular cross section. This calcu-

lation gives $Q_{H_2O}(circular) = 922$ and $Q_{Ar}(circular) = 269$. From these results, one can conclude that the enhancement factor for the polar water flows for all nanotubes under consideration is significantly larger than that for the nonpolar argon flows. In addition, the enhancement factor for both polar and nonpolar liquid flows through SWCNTs with rectangular cross sections is larger than that for SWCNT with circular cross section whereas the enhancement factor for flows through SWCNT with square cross section is smaller than that through SWCNT with circular one.

As said above, for external driving force $f_{x0} = 0.05$, argon atoms and water molecules flow through SWCNTs with different rectangular cross sections with steady and finite average flow velocities v_x^{aver} . It means that, since the external force f_{x0} is switched on, liquid particles begin to move along the tube axis with certain accelerations until the average fluid flow velocity achieves the steady value v_x^{aver} . This is a quite expected behavior of fluid flows through SWCNTs. However, when the external driving force is two times larger, $f_{x0} = 0.1$, the situation changes radically, and one can observe two drastically different behaviors that depend on types of fluid particles and the shapes of rectangular sections of SWCNTs. In the case of the water flows through SWCNTs with different rectangular cross sections, one can observe again the flows with steady average flow velocities v_x^{aver} , which are higher than those for $f_{x0} = 0.05$, but remain finite. For argon atom flows through SWCNTs with square cross section and rectangular cross section with the ratio between its sides 1:2, one can observe the similar fluid flows with steady and finite flow velocities (see curves 1 and 2 in Fig. 22.14a). This figure exhibits time dependences of v_x^{aver} averaged over subsequent time intervals with a duration equal to 100 MD time units (symbols on these curves correspond to central points of such time intervals). One can see that, for argon flows through SWCNTs with such rectangular cross sections, the fluid flow velocities averaged over subsequent time intervals first grow with time and then reach saturation at certain steady and finite values. However, for argon flow through SWCNT with the rectangular cross section with the ratio between its sides 1:4, the fluid flow velocity averaged over abovementioned subsequent time intervals exhibits an unlimited growth with no signs of saturation. Moreover, if we then switch off the external force ($f_{x0} = 0$), the average flow velocity remains constant with no signs of decay (curve 4 in Fig. 22.14a).

In order to understand such extraordinary behavior of argon flows through SWCNTs with different rectangular cross sections, we must analyze a time dependence of all forces acting on argon atoms during their flows through SWCNTs. Each atom (molecule) inside SWCNT is subjected to two forces directed along the tube axis, namely, the external driving force f_{x0} and retarding force f_{rx} due to interactions between a given atom (molecule) and bounding wall carbon atoms. The external driving force f_{x0} is constant, and typical time dependence of instant value of f_{rx} is shown in Fig. 22.14b. It is easily seen that this time dependence has a stochastic-like character, and we must perform time averaging of this force over the abovementioned subsequent time intervals. The results of such time averaging for argon flows through SWCNTs with different rectangular cross sections are shown in Fig. 22.14c, which exhibits time dependences of the ratio $|f_{rx}|/f_{x0}$, where $|f_{rx}|$ is the absolute value of the time-averaged retarding force f_{rx} (if f_{x0} is positive f_{rx} after time averaging is

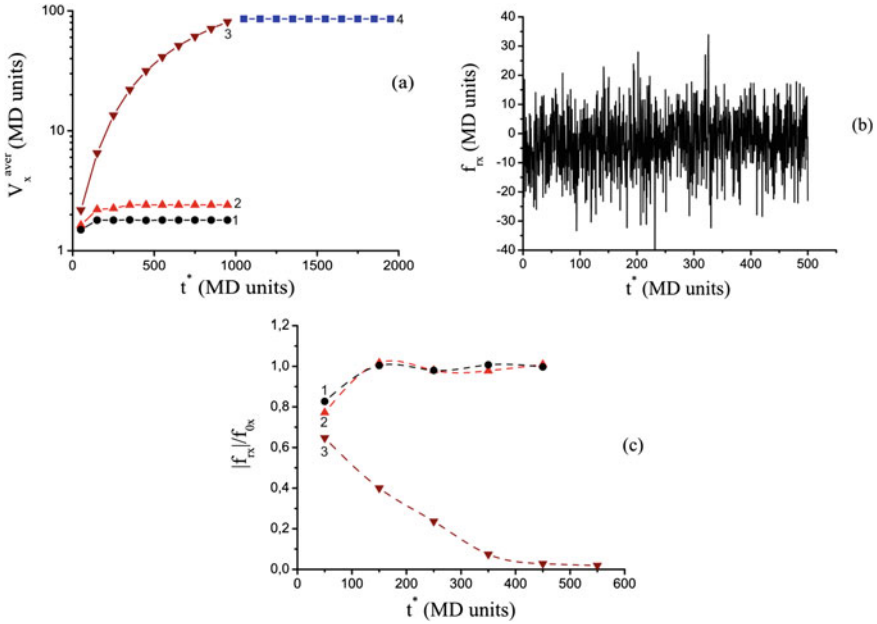


Fig. 22.14 Time dependences of average argon flow velocities v_x^{aver} through SWCNTs with different rectangular cross sections and analogous dependences for retarding forces acting on argon atoms from bounding wall carbon ones. **a**—time dependence of v_x^{aver} averaged over subsequent time intervals with duration equal to 100 reduced MD units. **b**—typical time dependence of instant retarding force f_{rx} acting on argon atoms from bounding wall carbon atoms during argon flow through SWCNT with rectangular cross section with the ratio between its sides 1 : 4. **c**—time dependences of the ratios $|f_{rx}|/f_{x0}$ averaged over above subsequent time intervals during the argon atom flows through SWCNTs with different rectangular cross sections. In 8a and 8c curve 1 corresponds to SWCNT with square cross section; curves 2 and 3 correspond to SWCNTs with rectangular cross sections having the ratios between their sides 1:2 and 1:4, respectively. For all figures $f_{x0} = 0.1$

always negative) for argon flows through SWCNTs with different rectangular cross sections. One can see from this figure that for argon flows through SWCNTs with square cross section and rectangular cross section with the ratio between its sides 1 : 2, the ratios $|f_{rx}|/f_{x0}$ first grow with time and then reach saturation at the steady value equal to nearly 1 (curves 1 and 2). It means that the absolute value of the time-averaged retarding force f_{rx} becomes equal to the external driving force f_{x0} , but it has an opposite sign. As a result, the total force acting on carbon atoms during their flows through SWCNTs vanishes, and they move with certain constant time-averaged velocities. One can also see from this figure (curve 3) that, for argon flow through SWCNT with rectangular cross section having the ratio between its sides 1:4, the ratio $|f_{rx}|/f_{x0}$ decays with time to nearly zero, and argon atoms begin to move along tube axis in a ballistic regime. This fact can explain the unlimited growth of the average fluid velocity during argon flow through SWCNT with such rectangular cross section under action of the external driving force $f_{x0} = 0.1$. It should be

noted that qualitatively similar phenomenon, namely, ballistic frictionless gas flow through two-dimensional channels made from graphene or boron nitride has been experimentally observed [34].

At first glance, this phenomenon seems to be somewhat similar to the superfluidity that occurs, for example, in helium-4 near the absolute zero [25]. However, there are several principal differences between well-known regular classic superfluidity and our results on argon flow through SWCNT with one of the abovementioned rectangular cross sections. First of all, the regular classic superfluidity is the macroscopic quantum phenomenon whereas our MD simulations are based on the usual classic mechanics. Secondly, our “pseudo-superfluidity” depends on the shape of the cross section of SWCNT, whereas the “true” superfluidity is independent of shapes of channels. Thirdly, when the external driving force is equal to $f_{x0} = 0.05$, the average fluid argon flow velocity through our SWCNT is finite, whereas disappearance of viscosity of helium-4 depends only on its temperature and does not depend on the external driving forces. Thus, the results of our simulations on the liquid argon flows through SWCNTs with rectangular cross sections have nothing to do with the classic superfluidity. Perhaps, these results are due to a combination of several factors, namely, the equilibrium structure formed by argon atoms inside SWCNT with the rectangular cross section with the ratio between its sides 1:4, and the time averaging of retarding forces acting on argon atoms from bounding wall carbon atoms. May be, the analysis of the time dependence of the instant retarding force f_{rx} depicted in Fig. 22.9b will allow us to elucidate this challenge.

22.3.3 *Equilibrium Fluid Structures Between Different Bounding Substrates*

We also studied equilibrium static structures of the polar water molecules and non-polar argon atoms between different carbon substrates mentioned in Introduction. All these carbon substrates have the same length in x-direction $L_x = 3.96$ nm, the width in y-direction $L_y = 4.1$ nm, and the distance between them in z-direction is equal to $h = 1.5$ nm. Though some of these substrates have the graphene-like crystalline structure, and others are formed by randomly distributed carbon atoms, the total numbers of carbon atoms inside these substrates are the same and equal to 1090. As said above, carbon atoms in such bounding substrates are also connected to each other with very strong covalent bonds with the interaction constants much larger than the LJ interaction constants ϵ_{CH_2O} and ϵ_{CAr} , and these atoms are considered to be fixed at their equilibrium sites. In order to obtain equilibrium static structures formed by the water molecules and argon atoms between the abovementioned substrates, we also performed MD simulations of free permeations of water molecules and argon atoms into the space between these substrates, and these simulations also started from the initial configurations similar to those depicted in Fig. 22.3a in which two reservoirs of water molecules or argon atoms are separated from each other by the

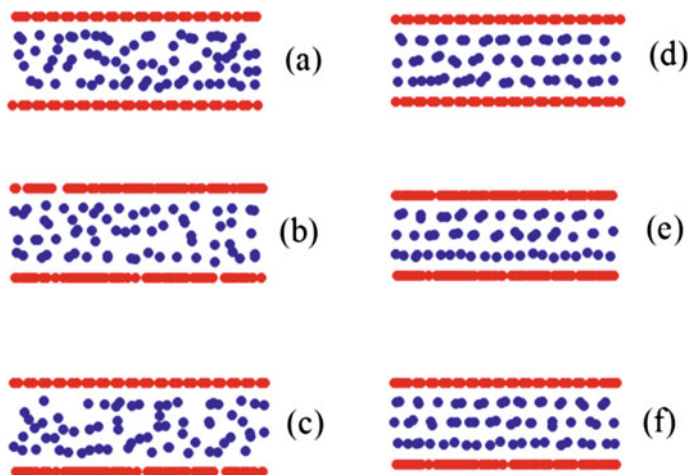


Fig. 22.15 a, b, and c demonstrate the lateral (xz) projections of equilibrium structures formed by water molecules between two similar substrates with graphene-like crystalline structures, two similar amorphous substrates, and one top substrate with graphene-like crystalline structure and another bottom substrate with amorphous structure. d, e, and f demonstrates the lateral projections of equilibrium structures formed by argon atoms between the same substrates

wall consisting of carbon atoms and connected with a channel containing the corresponding substrates. After running during about 100000 time steps (one time step was equal to 0.001 ps), one can reach the equilibrium configurations formed by the water molecules and argon atoms between bounding substrates. During simulation processes, the system under consideration is placed within the cubic simulation box of $6.332 \times 6.332 \times 6.332 \text{ nm}^3$ in size, and the periodic boundary conditions [44] are imposed on the system in x -, y -, and z -directions.

Figure 22.15a, b, c demonstrates the lateral (x, z) projections of equilibrium configurations formed by water molecules between two carbon substrates with graphene-like crystalline structure, between two carbon substrates with amorphous structure, and between one substrate with graphene-like crystalline structure and other substrate with amorphous structure, respectively, and Fig. 22.16a, b, c demonstrates the corresponding density profiles along z -axis. Figure 22.15d, e, f demonstrates equilibrium structures formed by argon atoms between abovementioned substrates, and Fig. 22.17a, b, c demonstrates the corresponding density profiles. One can see that, for all cases under consideration, argon atoms form very similar layered structures, and the corresponding density profiles demonstrate three sufficiently sharp peaks. At the same time, for all configurations under consideration, water molecules form structures with more or less developed layers near substrates and spatially disordered formations in the middle. The corresponding density profiles demonstrate two peaks disposed near substrates and the bell-like dependencies between them. Thus, one can conclude that water molecules disposed between bounding substrates form structures spatially less ordered than analogous structures formed by argon atoms.

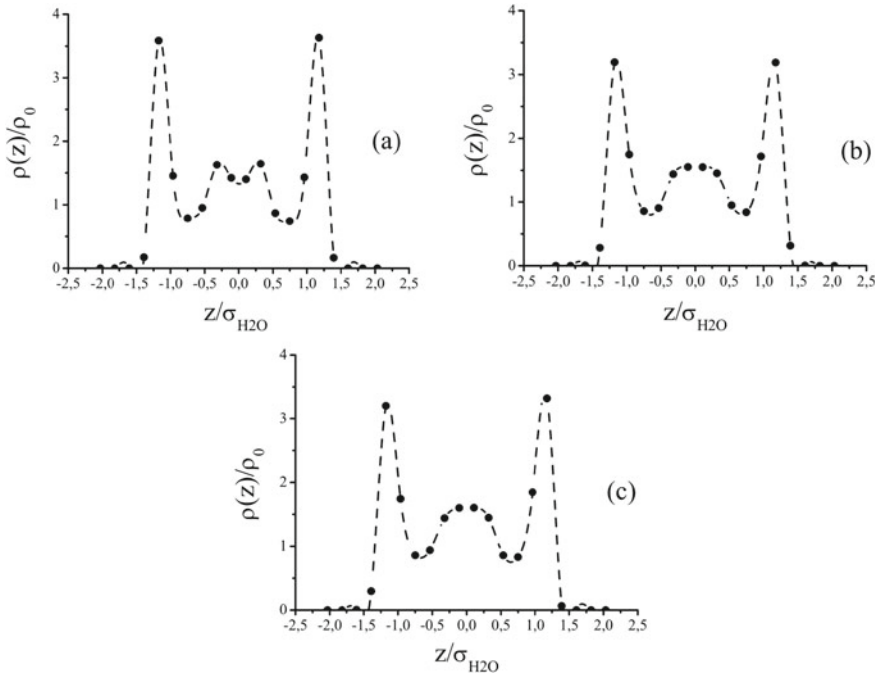


Fig. 22.16 The density profiles corresponding to equilibrium structures depicted in Fig. 22.15a, b, c

As said above, it may be due to the Coulomb-like interactions between polar water molecules which do not occur in ensembles of nonpolar argon atoms. According to the abovementioned Earnshaw theorem [48], an ensemble of particles interacting via Coulomb-like forces cannot be maintained in a stable stationary equilibrium configurations, and, hence, the well-ordered structures of water molecules between bounding substrates cannot exist for sufficiently long times.

22.3.4 *The Couette Flows of Polar Water Molecules and Nonpolar Argon Atoms Between Different Bounding Substrates*

Now, let us turn to results of MD simulations of Couette flows of polar water molecules and nonpolar argon atoms between abovementioned bounding substrates. To simulate these flows, in the above equilibrium configurations, we remove the liquid reservoirs and all particles outside the space confined by the bounding substrates. Then we apply periodic boundary conditions to edges of these substrates and give a constant velocity V_{x0} along the x-axis to all carbon atoms of one of them. We

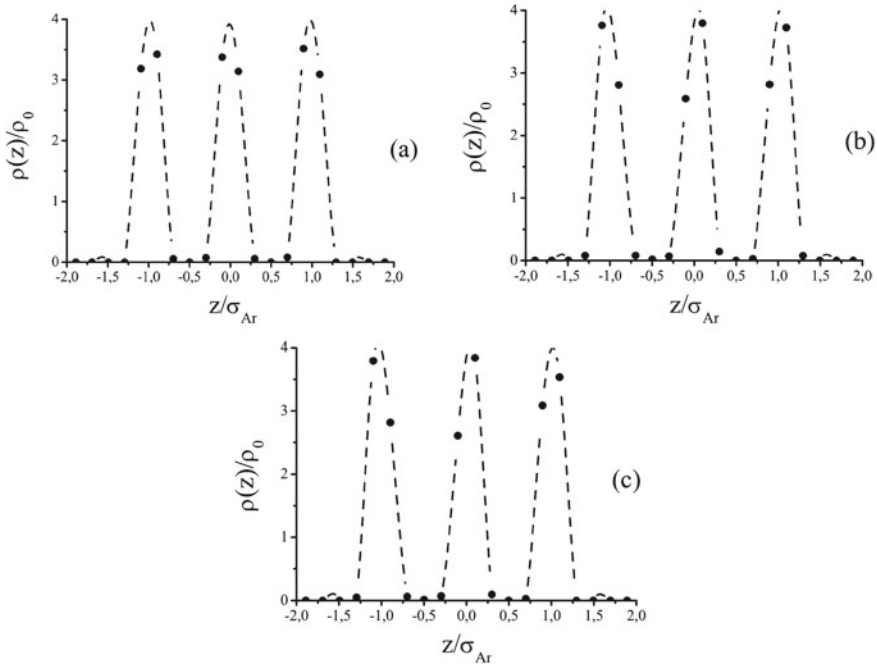


Fig. 22.17 The density profiles corresponding to equilibrium structures depicted in Fig. 22.15d, e, f

set $V_{x0} = 0.5$ (in reduced MD units [44]). After running during about 100000 time steps, we reach equilibrium Couette flows, and then during the next 500000 time steps we calculate their equilibrium velocity profiles. In order to calculate these velocity profiles, we divide the space between bounding substrates into very thin sublayers parallel to the top and bottom substrates and calculate average atomic (molecular) velocities inside these sublayers as a function of z -coordinates of their centers.

The fluid flow velocity profiles obtained from our simulations are shown in Fig. 22.18 for the polar water, and in Fig. 22.19 for the nonpolar argon. One can see that, for water molecules, the velocity profiles for similar substrates with graphene-like crystalline structures and amorphous structures are qualitatively similar (curves 1 and 2, respectively). Both profiles exhibit moderate enough decay with approaching the bottom fixed substrate. Nevertheless, the average flow velocity in the case of substrates with graphene-like structure is about 18 percent higher than that for the carbon substrates with amorphous structure. As for the case of two substrates with different structures, the corresponding velocity profiles and average flow velocities depend strongly on which of the substrates is moving and which is at the rest. When the substrate with graphene-like crystalline structure is moving and the substrate with amorphous structure is fixed, the resulting Couette flow is very weak (curve 3), and the corresponding average flow velocity is more than ten times lower than the

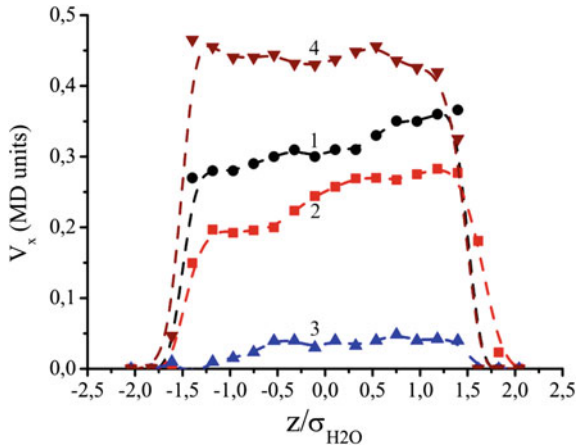
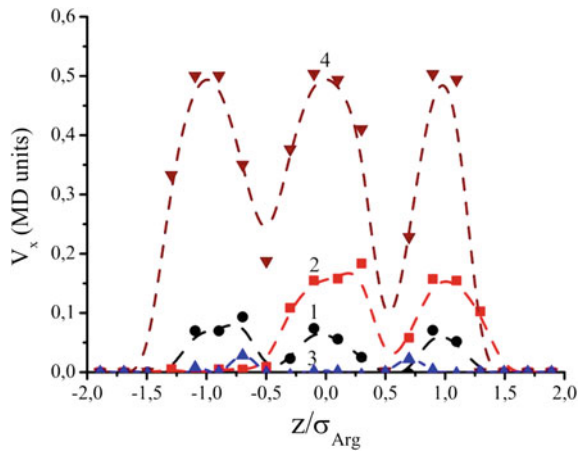


Fig. 22.18 The fluid velocity profiles for the Couette flows of water molecules between different bounding substrates. 1—both substrates have graphene-like crystalline structures, 2—both substrates have amorphous structures, 3—the top substrate with crystalline-like structure is moving whereas the bottom substrate with amorphous structure is fixed, 4—the opposite case when the bottom substrate with amorphous structure is moving whereas the top substrate with graphene-like crystalline structure is fixed

Fig. 22.19 The Couette flow velocity profiles for argon atoms analogous to those depicted in Fig. 22.18



velocity V_{x0} of the moving top substrate with graphene-like crystalline structure. In the opposite case, when the carbon substrate with amorphous structure is moving (curve 4), the velocity profile exhibits a very weak decay with approaching the fixed top substrate, and the average flow velocity is only about ten percent lower than V_{x0} . In addition, in this case, the average flow velocity is significantly higher than those for the Couette flows between similar top and bottom substrates.

The results obtained could be qualitatively explained as follows. The motion of the substrate relative to fluid particles is equivalent to the motion of fluid particles relative to the substrate in an opposite direction. In our previous paper [37], it was shown that the time-averaged force acting on a moving fluid particle from the carbon surface with graphene-like crystalline structure should be much weaker than the analogous force from the carbon surface with amorphous structure. Therefore, when two bounding substrates have similar structure, the driving and retarding forces acting on fluid particles from moving and fixed substrates, respectively, should be similar. When the bounding substrates have different structures and the moving substrate has graphene-like crystalline structure whereas the fixed substrate has amorphous structure, the retarding force should be stronger than the driving one. On the contrary, when the moving substrate has amorphous structure and the fixed substrate has graphene-like crystalline structure, the driving force should be stronger than the retarding one. This speculation could, in principle, explain at the qualitative level why the Couette flow of water molecules is strongest for the configuration with different bounding substrates when the moving substrate has amorphous structure. The same speculation could explain why the Couette flow is weakest for the configuration with different bounding substrates when the moving substrate has graphene-like crystalline structure.

The velocity profiles for the Couette flows of nonpolar argon atoms depicted in Fig. 22.19 are strongly different from the abovementioned profiles for polar water molecules. It is easily seen that these profiles have shapes of either sharp enough (curve 4) or sufficiently smooth (curves 1 and 2) peaks due to the layered structures formed by argon atoms between the bounding substrates (see Fig. 22.15a, b, c). Nevertheless, as in the case of polar water molecules, the Couette flow velocities for similar bounding substrates have sufficiently moderate values. The average flow velocity for substrates with graphene-like crystalline structure is about 0.07, and, for the substrates with amorphous structure, this velocity is about 0.1. For the Couette flows between bounding substrates with different structures, one can see a drastic difference between two abovementioned cases of flow (see curves 3 and 4). When the top substrate with graphene-like structure is moving and the bottom substrate with amorphous structure is fixed, the Couette flow is practically absent, whereas in opposite case, when the bottom substrate is moving, the average flow velocity is almost equal to the velocity $V_{x,0}$ of the moving substrate. The explanation of this fact is similar to the abovementioned explanation for the Couette flows of water molecules between bounding substrates with different structures. It should be noted that, for argon atom flows between such bounding substrates, the difference between two cases of flow, i.e., when the top substrate is moving and the bottom substrate is fixed and vice versa, is more pronounced than for the same flows of water molecules. Perhaps, this is due to the fact that argon atoms form between bounding substrates more spatially ordered structures than the water molecules.

22.4 Conclusion

We performed MD simulations of equilibrium structures and flows of polar water, nonpolar argon and methane, and mixtures of water and methane confined by SWCNTs with circular and different rectangular cross sections having the same area, and bounding walls with regular graphene structure and random (amorphous) distribution of carbon atoms. The results of our simulations show that equilibrium structures of all confined fluids depend mainly on the shape of the SWCNT's cross sections, namely, the cross sections of these structures resemble replicas of those of SWCNTs. Nevertheless, the types of fluids confined by abovementioned SWCNTs also have some influence on their equilibrium structures. For example, the results of performed MD simulations revealed that nonpolar argon atoms form inside all SWCNTs the most spatially ordered equilibrium structures, whereas polar water molecules form the least spatially ordered ones. As for the external pressure-driven flows of all abovementioned fluids through SWCNTs with different cross sections, these flows depend strongly on both the shapes of cross sections and the type of the confined fluids. Our MD simulations revealed that, for nonpolar methane inside SWCNTs with different rectangular cross sections, there are critical values f_{xc} of the external driving force below which the average flow velocity is nearly zero, and above which the liquid methane flow occurs. Our simulations also revealed that these critical values depend strongly on the shape of rectangular cross sections of our SWCNTs. Perhaps, this phenomenon, which is absolutely not inherent to flows of ordinary fluids, is due to a certain spatial order formed by argon and methane atoms inside SWCNTs with rectangular cross sections. Another interesting phenomenon was revealed from our MD simulations of the liquid argon flows through SWCNTs with rectangular cross sections. It was found that, for a sufficiently large value of the external driving force, the liquid argon flow through SWCNT with rectangular cross section with the ratio between its sides 1 : 4 demonstrates the ballistic frictionless regime when the fluid flow velocity-averaged over consecutive time intervals exhibit an unlimited growth with no signs of saturation. Moreover, if we then switch off the external driving force the average flow velocity remains constant with no signs of decay. Though this phenomenon seems to be similar to the "classic" superfluidity that occurs, for example, in helium-4 near the absolute zero, there are several principal differences between this "true" superfluidity and our results on argon flow through SWCNT with the abovementioned rectangular cross section. The main difference is that the regular classic superfluidity is the macroscopic quantum phenomenon whereas our MD simulations are based on the usual classic mechanics. In addition, our "pseudo-superfluidity" depends on the shape of the cross section of SWCNT and on the value of the external driving force whereas the "true" superfluidity is independent of these parameters and depends only on temperature. Thus, the abovementioned phenomenon found in our simulations on the liquid argon flows through SWCNTs with rectangular cross sections has nothing to do with the classic superfluidity. Perhaps, this phenomenon is caused by a combination of several factors and its elucidation requires further investigations.

We also performed MD simulations of equilibrium structures and Couette flows of polar water molecules and nonpolar argon atoms between bounding carbon substrates disposed at the distance $h = 1.5$ nm from each other that is much shorter than analogous distances considered in previous papers [35–37]. We considered two symmetric configurations when both substrates have similar, either graphene-like crystalline or amorphous structures, and one asymmetric configuration consisted of one substrate with graphene-like crystalline structure and another substrate with amorphous structure. It was found that, in all cases under consideration, the Couette flow velocity profiles depend strongly on polarity of fluid particles confined between bounding substrates, and that these profiles are significantly different from those found in previous papers [35–37] for larger distances between substrates. In addition, it was found that, for the abovementioned asymmetric configuration, the fluid flows depend strongly also on which of the substrate is moving and which is fixed. When the substrate with graphene-like crystalline structure is moving, the Couette flow of water molecules is very weak and the Couette flow of argon atoms is practically absent. On the contrary, when the amorphous substrate is moving, the Couette flows of both water molecules and argon atoms are sufficiently strong, and, for argon atoms, the average flow velocity is very close to the velocity V_{x0} of the moving substrate. We suppose it would be interesting to test these simulation results in an experiment.

References

1. Rostami, A.A., Mujumdar, A.S., Saniei, N.: Flow and heat transfer for gas flowing in microchannels: a review. *Heat Mass Transf.* **38** 359–367 (2002)
2. Darhuber, A.A., Troian, S.M.: Principles of microfluidic actuation by modulation of surface stresses. *Annu. Rev. Fluid Mech.* **37**, 425–455 (2005)
3. Zuo, G.C., Shen, R., Ma, S.J., Guo, W.L.: Transport properties of single-file water molecules inside a carbon nanotube biomimicking water channel. *ACS Nano*. **4**, 205–210 (2010)
4. Kofinger, J., Hummer, G., Dellago, C.: Macroscopically ordered water in nanopores. *Proc. Natl. Acad. Sci. USA* **105**, 13218–13222 (2008)
5. Alexiadis, A., Kassinos, S.: Molecular simulation of water in carbon nanotubes. *Chem. Rev.* **108**, 5014–5034 (2008)
6. Kalra, A., Garde, S., Hummer, G.: Osmotic water transport through carbon nanotube membranes. *Proc. Natl. Acad. Sci. USA* **100**, 10175–10180 (2003)
7. Ghosh, S., Sood, A.K., Kumar, N.: Carbon nanotube flow sensors. *Science* **299**, 1042–1044 (2003)
8. Kam, N.W.S., O’Connell, M., Wisdom, J.A., Dai, H.J.: Carbon nanotubes as multifunctional biological transporters and near-infrared agents for selective cancer cell destruction. *Proc. Natl. Acad. Sci. USA*. **102**, 11600–11605 (2005)
9. Karniadakis, G., Beskok, A., Aluru, N.: *Microflows and Nanoflows: Fundamentals and Simulations*. Springer, New York (2005)
10. Holt, J.K., Park, H.G., Wang, Y.M., Stadermann, M., Artyukhin, A.B., Grigoropoulos, C.P., Noy, A., Bakajin, O.: Fast mass transport through sub-2-nanometer carbon nanotubes. *Science* **312**, 1034–1037 (2006)
11. Majumder, M., Chopra, N., Andrews, R., Hinds, B.J.: Nanoscale hydrodynamics: enhanced flow in carbon nanotubes. *Nature* **438**, 930 (2005)

12. Beckstein, O., Biggin, P.C., Sansom, M.S.P.: A hydrophobic gating mechanism for nanopores. *J. Phys. Chem. B.* **105**, 12902–12905 (2001)
13. Hummer, G., Rasaiah, J.C., Noworyt, J.P.: Water conduction through the hydrophobic channel of a carbon nanotube. *Nature* **414**, 188–190 (2001)
14. Mashl, R.J., Joseph, S., Aluru, N.R., Jakobsson, E.: Anomalous immobilized water: a new water phase induced by confinement in nanotubes. *Nano Lett.* **3**(5), 589–592 (2003)
15. Maibaum, L., Chandler, D.: A coarse-grained model of water confined in a hydrophobic tube. *J. Phys. Chem. B.* **107**, 1189–1193 (2003)
16. Chandler, D.: Interfaces and the driving force of hydrophobic assembly. *Nature* **437**, 640–647 (2005)
17. Majumder, S.R., Choudhury, N., Ghosh, S.K.: Enhanced flow in smooth single-file channel. *J. Chem. Phys.* **127**, 054706 (2007)
18. Choudhury, N., Pettitt, B.M.: Dynamics of water trapped between hydrophobic solutes. *J. Phys. Chem. B.* **109**, 6422–6429 (2005)
19. Mukherjee, B., Maiti, P.K., Dasgupta, C., Sood, A.K.: Strong correlations and Fickian water diffusion in narrow carbon nanotubes. *J. Chem. Phys.* **126**, 124704 (2007)
20. Melillo, M., Zhu, F., Snyder, M.A., Mittal, J.: Water transport through nanotubes with varying interaction strength between tube wall and water. *J. Phys. Chem. Lett.* **2**, 2978–2983 (2011)
21. Chopra, M., Choudhury, N.: Comparison of structure and dynamics of polar and nonpolar fluids through carbon nanotubes. *J. Phys. Chem. C.* **117**, 18398 (2013)
22. Farimani, A.B., Aluru, N.R.: Spatial diffusion of water in carbon nanotubes: from Fickian to ballistic motion. *J. Phys. Chem. B.* **115**, 12145 (2011)
23. Thomas, J.A., McGaughey, A.J.H.: Reassessing fast water transport through carbon nanotubes. *Nano Lett.* **8**, 2788–2793 (2008)
24. Sinha, S., Rossi, M.P., Mattia, D., Gogotsi, Y., Bau, H.H.: Induction and measurement of minute flow rates through nanopipes. *Phys. Fluids.* **19**, 013603 (2007)
25. Landau, L.D., Lifshitz, E.M.: *Fluid Mechanics*. Pergamon Press, Oxford (1959)
26. Thomson, P.A., Troian, S.M.: A general boundary condition for liquid flow at solid surfaces. *Nature* **389**, 360–362 (1997)
27. Priezjev, N., Troian, S.M.: Influence of periodic wall roughness on the slip behaviour at liquid/solid interfaces: molecular-scale simulations versus continuum predictions. *J. Fluid Mech.* **554**, 25–46 (2006)
28. Priezjev, N.: Rate-dependent slip boundary conditions for simple fluids. *Phys. Rev. E.* **75**, 051605 (2007)
29. Priezjev, N.: Molecular dynamics simulations of oscillatory Couette flows with slip boundary conditions. *Microfluid. Nanofluidics* **14**, 225–233 (2013)
30. Yong, X., Zhang, L.T.: Slip in nanoscale shear flow: mechanisms of interfacial friction. *Microfluid. Nanofluid.* **14**, 299–308 (2013)
31. Zhang, C., Chen, Y.: Slip behavior of liquid flow in rough nanochannels. *Chem. Eng. Proc. Proc. Intens.* **85**, 203–208 (2014)
32. Esmaeilzadeh, H., Su, J., Su, C., Sun, H.: Molecular dynamic simulation of Couette flow of liquid argon in nanochannel. *Proc. ASME. FEDSM* **2016**, 7917 (2016)
33. Radha, B., Esfandiari, A., Wang, F.C., Rooney, A.P., Gopinadhan, K., Keerthi, A., Mishchenko, A., Janardanan, A., Blake, P., Fumagalli, L., Lozada-Hidalgo, M., Garaj, S., Haigh, S.J., Grigorieva, I.V., Wu, H.A., Geim, A.K.: Molecular transport through capillaries made with atomic-scale precision. *Nature* **538**, 222–225 (2016)
34. Keerthi, A., Geim, A.K., Janardanan, A., Rooney, A.P., Esfandiari, A., Hu, S., Dar, S.A., Grigorieva, I.V., Haigh, S.J., Wang, F.C., Radha, B.: Ballistic molecular transport through two-dimensional channels. *Nature* **558**(7710), 420–424 (2018)
35. Abramyan, A.K., Bessonov, N.M., Mirantsev, L.V., Reinberg, N.A.: Influence of liquid environment and bounding wall structure on fluid flow through carbon nanotubes. *Phys. Lett. A.* **379**, 1274–1282 (2015)
36. Abramyan, A.K., Bessonov, N.M., Mirantsev, L.V., Chevrychkina, A.A.: Equilibrium structures and flows of polar and nonpolar liquids in different carbon nanotubes. *Eur. Phys. J. B.* **91**, 48 (2018)

37. Mirantsev, L.V.: Superfluidity inside carbon nanotubes. *Phys. Rev. E* **100**, 023106 (2019)
38. Autreto, P.A.S., Legoas, S.B., Flores, M.Z.S., Galvao, D.S.: Carbon nanotube with square cross-section: an ab initio investigation. *J. Chem. Phys.* **133**, 124513 (2010)
39. Mizutani, K., Kohno, H.: Multi-walled carbon nanotubes with rectangular or square cross-section. *Appl. Phys. Lett.* **108**, 263112 (2016)
40. Mirantsev, L.V., Lyra, M.L.: Nonpolar and polar fluid flow through flat nanochannels with amorphous and crystalline walls. *Phys. Lett. A* **380**, 1318–1323 (2016)
41. Teleman, O., Jonsson, B., Engstrom, S.: A molecular dynamics simulation of a water model with intramolecular degrees of freedom. *Mol. Phys.* **60**, 193–203 (1987)
42. Walther, J.H., Jaffe, R., Halicioglu, T., Koumoutsakos, P.: Carbon nanotubes in water: structural characteristics and energetics. *J. Phys. Chem. B* **105**, 9980–9987 (2001)
43. Barker, J.A., Fisher, R.A., Watts, R.D.: Liquid argon: Monte Carlo and molecular dynamics calculations. *Mol. Phys.* **21**, 657–673 (1971)
44. Allen, M.P., Tildesly, D.J.: *Computer Simulations of Liquids*. Clarendon Press, Oxford (1989)
45. Berendsen, H.J., Postma, J.P.M., van Gunsteren, W.F., DiNola, A., Haak, J.R.: Molecular dynamics with coupling to an external bath. *J. Chem. Phys.* **81**, 3684–3690 (1984)
46. Tersoff, J.: New empirical approach for the structure and energy of covalent systems. *Phys. Rev. B* **37**, 6991–7000 (1988)
47. Wang, L., Hu, H.: Thermal vibration of single-walled carbon nanotubes with quantum effects. *Proc. Math. Phys. Eng. Sci.* **470**, 20140087 (2014)
48. Tamm, I.E.: *Fundamentals of the Theory of Electricity*. Nauka, Moscow (1989)
49. Qin, X., Yuan, Q., Zhao, Y., Xie, S., Liu, Z.Z.: *Z. Nano Lett.* **11**, 2173–2177 (2011)

Chapter 23

Fatigue Assessment of Structures—Problems in Current Methodology



Sergei V. Petinov and Ruslan V. Guchinsky

Abstract Presently in rules for fatigue assessment of steel and steel welded structures in different technologies subjected to intensive alternating service loading, the stress-life (S-N) criteria are recommended in several versions of approaches. The criteria and approaches are addressed at assessment of fatigue properties of structures; however, the procedures are accompanied with a series of approximations and uncertainties. The nature of drawbacks of the S-N criteria and approaches is commented and feasible means of improvement of the fatigue criteria evaluation and applications in fatigue assessment procedures are proposed.

Keywords Fatigue · Fracture · Crack · Welded joint · FEA · S-N curve · Damage accumulation · Strain-life criterion

23.1 Introduction

The stress-life (S-N) criteria are recommended presently in rules for fatigue assessment of structures subjected to intensive alternating service loading in versions (approaches) differing mostly by the procedure of considering effects of stress concentration in critical locations [1–3], etc. The approaches are supplemented with the linear damage summation rule to consider random character of service loading in fatigue analysis of structures. The criteria and approaches were derived aimed at a non-complicated application in practical problems; however, a series of drawbacks and inaccuracies of those was being noted.

S. V. Petinov

Institute for Problems in Mechanical Engineering RAS, V.O., Bolshoy pr., 61, St. Petersburg 199178, Russia

R. V. Guchinsky (✉)

TMH Engineering Ltd, Institute for Problems in Mechanical Engineering RAS, V.O., Bolshoy pr., 61, St. Petersburg 199178, Russia
e-mail: ruslan239@mail.ru

© The Author(s), under exclusive license to Springer Nature Switzerland AG 2022
V. A. Polyanskiy and A. K. Belyaev (eds.), *Mechanics and Control of Solids and Structures*, Advanced Structured Materials 164,
https://doi.org/10.1007/978-3-030-93076-9_23

489

Firstly, the experimentally obtained database—S-N curves—providing evaluation of fatigue properties of structures was collected by testing “classed” specimens (including typified welded joints, as in the case of the nominal stress approach [2] under cyclic loading terminated at almost complete failure (“separation in two parts”). This was leading to uncertainties in considering fatigue properties of materials in welded joints, effects of residual welding stress, definition of the state of damage in structural components, and crack size corresponding exhaustion of fatigue life. Further, recommendations for testing specimens comprising typified welded joints which were aimed at considering effects of materials of the joint (weld material, material of fusion zone, etc.), of residual welding stress, implemented in the database did not provide identity of fatigue damage between specimens and structural details. Partly, it was because of diversity of geometry of structural details comprising “typified” joints, which was recognized decades ago.

Substantial uncertainty introduces into fatigue design of structural components the current definition of expected service loading. Although the random nature of service loading is well understood for long (Palmgren, 1924) and respective recommendations are given in the rules, it depends on non-controllable factors (weather changes, economic factors, etc.) resulting in rather conditional standardization of loading (description and parameters of statistical and power spectra data) in different technologies, e.g., [2, 3]. In the following by the mentioned reasons specifics of the loading histories (programs) is not commented.

Development of the finite-element analysis (FEA) facilities allowed analyzing the stress field in actual structural details, in particular, stress at critical locations. These facilities [4] and experience of strain measurement in welded components [5] were used to derive the hot-spot stress approach (HSS) [1, 2], etc. The approximate estimation of the local stress caused by the particulars of the stress flow at the welded joint in HSS, necessity to account for the effects of geometry of the weld itself, resulted lately in development of the notch-stress approach [6], etc. Assessment of local stress causing the damage process allowed reducing the range of the design S-N curves to those presenting properties of the base and weld material only.

However, apart from solving the problem of effects of geometry of structural detail on the damage process, the abovementioned disadvantages were not corrected.

The above criteria and approaches are commented in more detail in the below focused on problems of practical application and certain remedial actions are proposed.

23.2 Stress-Life Approaches

The current S-N (stress-life) approaches to fatigue analysis and design of structures, e.g., [3], are based on assumption of elastic behavior of the structure material in service loading conditions. Respectively, in the range of fatigue lives (the left-hand side is related to the above statement, and the right-hand one corresponds to the long-established practice of assessment of the fatigue limit stress in mechanical

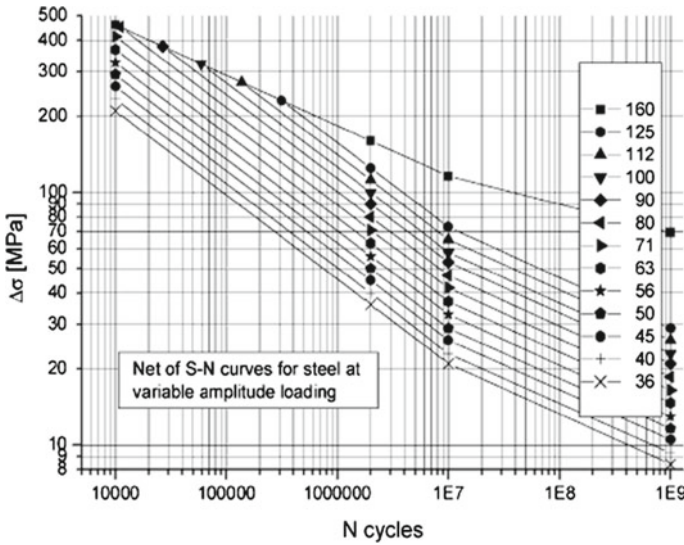


Fig. 23.1 IIW classed S-N curves for structural steels [3]

engineering) the S-N curve is usually approximated in logarithmic coordinates by the straight line equation which is given by Basquin’s formula (1910):

$$N(S) = C/S^m, \tag{23.1}$$

where S is the stress range, C and m are the “material constants”, and m is the S-N curve “slope parameter”. The range of endurance of the design S-N curves is limited from the left side, as said, by the number of cycles prior to failure equal to $N = 10^4$, which approximately corresponds to the nominal stress amplitude around the yield stress.

Presently in rules for fatigue design of steel structures (steels of 235–390 grades) the S-N curves are indicated and obtained in air and in corrosive media, for parent material and welded joints, in certain applications, fatigue rules (e.g., Fig. 23.1 [4]) ranged for different types of welded joints.

Damaging effects of stress amplitudes below the conventional fatigue limit stress (attributed to $N = 10^7$ cycles) in service irregular loading histories are considered by the “two-slope” shape of S-N curves and by introducing the “cut-off” fatigue limit stress, substantially lower than the conventional one, Fig. 23.1.

The mechanics of fatigue damage of welded joint materials is implied (not definitely specified) as built into the design S-N curves based on analysis of results of fatigue testing of specimens comprising the typified (classed) welded joints, e.g., Fig. 23.2.

The numbers in the right-hand column (Fig. 23.1) indicate so-called “FAT-Classes” of the welded joint types (in this figure—in air environment). The base and

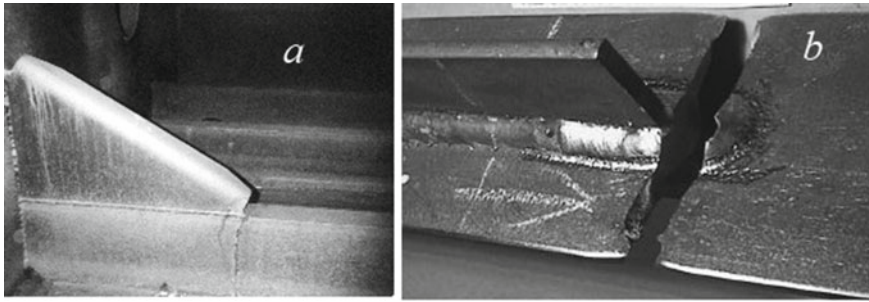
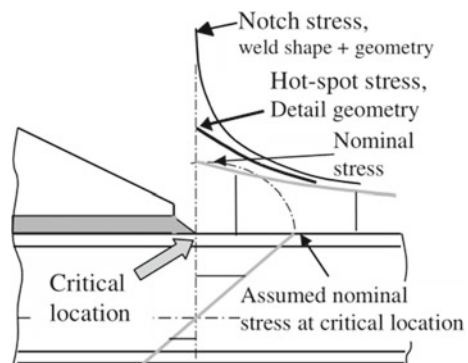


Fig. 23.2 a—Crack in a ship structural detail identified as FAT63 (Courtesy B. Purtle, Lloyd’s Register of Shipping, UK) b—Fractured specimen, FAT63 Class (Fig. 23.1)

weld material mechanical properties are not specified, and the S-N curves uniquely represent fatigue properties of the indicated range of structural steels supporting the so-called “Nominal stress approach”, as shown in Fig. 23.1. Whereas it is known that fatigue strength of steels is approximately proportional to the ultimate strength [7], although resistance of welded joints may depend substantially on the mechanical properties of the electrode material. The scheme of evaluation of the nominal stress in example of a bracket welded to the flange of stiffener in ship structure (Fig. 23.2) is shown in Fig. 23.3.

Specific of the testing specimens procedure is automated termination of test when initiated and growing fatigue crack notably affects the specimen compliance preceding complete fracture in two parts. Therefore, the test result, the number of cycles by the test completion includes a portion of life until the macroscopic crack origination and a part when crack propagates from the origination site. It means that the stress limits in the phase of crack origination remain unchanged, but in the crack growth phase rapidly increase. If fatigue properties of the statically determinate structure detail are to be assessed, the test results might be regarded appropriate; however, the state of damage, corresponding a crack size, would occur uncertain what attracted

Fig. 23.3 Assessment of characteristic stress for fatigue analysis of structural details



attention of experts (e.g., [6, 8, 9]). What is important, fatigue tests of typified welded joints at cyclic loading were (and are) being carried up with positive load ratio (ratio of the minimum to the maximum load in the cycle) to avoid buckling in the compressive part of the load cycle. This means the design S-N curves are related to the mentioned type of loading. Lately, attempts were made to consider in fatigue analysis of structural detail effects of different loading conditions [3]. Meanwhile, loading asymmetry plays secondary role in the crack initiation phase which is controlled almost completely by the stress ranges, excursions causing slip processes in material microstructure [7, 10], etc. When the macroscopic crack is initiated its further extensions substantially depend on the tensile part of alternating loading. In the load-control testing, the nominal stress in the affected cross section of specimen increases and does not fit the assumed test conditions. Respectively, since a substantial portion of fatigue life of specimens represents the crack growth, it introduces as mentioned above, additional uncertainty into the results of fatigue analysis of structural details.

When fatigue life of a non-redundant structure detail is analyzed by the means of the finite-element modeling, application of the classed S-N data would be incorrect by the mentioned specifics of the testing procedure. Moreover, if the detail is a part of substantially redundant structure the testing of specimens should be carried out at the displacement of the testing machine frame control (strain limits of the work part of specimen).

The briefly mentioned in above disadvantages of the nominal stress approach promoted development and application in practice of the hot-spot stress (HSS) [1, 2], etc., and later of the notch-stress approach (NS) [5, 6], etc. These approaches are supported by respective stress-life criteria, addressed to avoiding ambiguity in establishing the identity between classed welded joints and actual structural details, and providing considering effects of stress concentration in structural details by the means of finite-element detail modeling. With regard to the principles of the HSS and the NS approaches the set of design S-N curves is reduced to those of the base material and material of welded joint (butt-welded joint), completed with the design curves for details in corrosive environment (e.g., [12]).

In HSS approach, the stress at a critical location, typically at the weld toe, shown as arrows in Fig. 23.2, has to be found by extrapolating stress in element centroid toward the weld toe, Fig. 23.3; by this the stress raise is assumed to be caused by the shape of structural detail and the role of the weld bead geometry is related to properties of the respective S-N curve (class D curve, butt-welded joint).

Substantially fine meshing of the welded detail model in the NS approach allows obtaining local stress at the weld toe considering both effects of the detail and the weld bead geometry, as schematically shown in Fig. 23.3; at the same time, it is assumed that at the weld toe there is a smooth, radiused, transition from the parent to the weld material [6]. Such assumption is based on physics of liquid metal contact with the solid one where meniscus appears.

So far, effects of stress concentration in critical locations of structure in the HSS and NS approaches are considered by multiplying the nominal stress range by the respective stress concentration factors or calculation local stress using, as said, the finite-element technique.

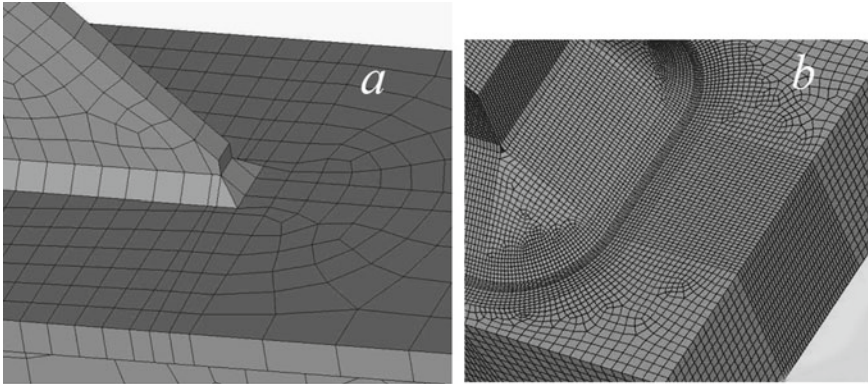


Fig. 23.4 Examples of FE meshes designed for application of the HSS (a) and the NS (b) approaches

Figure 23.4 shows the types of meshing of the bracket ending in ship structure (Fig. 23.2a) designed for application of the mentioned approaches. The mesh type in Fig. 23.4a is attributed to the hot-spot stress approach; its design follows the principle “ $t \times t$ ”, t is the flange thickness and the size of finite elements at the bracket ending [13]. Another mesh, Fig. 23.4b, fits the requirements of the FE modeling when the notch stress has to be applied; the element size at the weld toe is 0.2 of the assumed weld toe radius [6].

It should be emphasized that assessment of the local stress in these approaches is based on assumed linear elastic material behavior in critical locations. Referring further the characteristic stress to the classed S-N curve makes rather an illusion of proper assessment of damage.

In fact, it means evaluation of the damage with uncertainty, although somewhat on the conservative side. In the high-stress range of the service loading, the input of this over-estimation of fatigue damage in the total sum might be regarded insignificant due to stochastic properties of excitation and relatively infrequent intensive loading of structures. Whereas at the moderate service loading, in the high-cycle regime, which provides the predominant damage, the above approaches neglecting the effects of material microplasticity at critical locations may substantially over-estimate the damage.

Comparative analysis of fatigue properties of ship structural detail shown in Fig. 23.2, “Post-Liberty” dry cargo ship, nonspecified wave climate, and upper deck structure amidships [13], resulted in substantially differing values of fatigue damage related to 20 years of ship service. Application of the HSS approach indicated the damage index $D = 1.24$, whereas the notch-stress approach use had shown the damage index as $D = 0.54$, and the strain-life approach, where the inelastic behavior of material was accounted for, resulted in $D = 0.35$.

The mentioned comparative study just illustrated the problem; perhaps, a comprehensive analysis might be needed.

The feasible means of improvement the principles of assessment the fatigue properties of structural details might be as the following.

The reduction of the mentioned uncertainty effects in the current techniques of fatigue assessment of steel welded structures based on application of the S-N criteria might be achieved by a series of corrections.

As it concerns the hot-spot stress technique, the improvement of it is barely feasible, since the elastic-plastic properties of the joint materials, residual welding stress effects, and the crack size cannot be considered.

The notch-stress approach application, as we see it, would need in correction of the fatigue failure criteria implied, as briefly discussed in above:

–The procedure of evaluation of S-N criteria fatigue testing of specimens should be carried out until the macroscopic crack origination. The methods and techniques of the macroscopic crack identification are known, and the testing procedure should be, respectively, changed.

–Inelastic cyclic straining of material at critical locations of a structure may be approximately considered by applying the “notch factor” (Peterson [14]):

$$K_f = 1 + (K_t - 1)/(1 + g/r), \quad (23.2)$$

where K_t is the theoretical stress concentration factor (local stress accordingly the approach is calculated assumed elastic ones), r is the notch root radius, g is “structural parameter” of the material; according to [15] this parameter for structural steels of the 235–390 grades may be approximated as $g = 0.38(350/\sigma_u)^{1.16}$, where σ_u is the ultimate strength of steel (in the case the crack origination is expected in the weld area, the proper value is necessary).

–Within the macroscopic crack origination phase in the “critical location” the residual welding stress relaxation may be considered due to cyclic elastic-plastic straining of material.

The notch-stress technique, in principle, addressed to assessment of the crack initiation at the stress concentration may be complemented with the crack extension calculation technique based on the damage accumulation approach, as shown in [16, 17], etc. Elements of the technique were suggested in [1], etc.

Concluding it may be stated that for fatigue analysis of the redundant steel welded structures testing of specimens (standard IIW) should preferably be carried out at the strain limits (displacements of the loading frame of a testing machine) and the respective criteria be applied.

23.3 Strain-Life Criteria-Based Approach

The strain-life approach considered in the present rules as optional is being developed since mid-60s of the last century. It may be regarded a more accurate than above techniques for fatigue analysis and design of structures by the following reasons. The current damage in load cycles is characterized by the cyclic plastic strain range

in Coffin's criterion [18], lately complemented with the elastic strain component as proposed by Manson [19], in criterion:

$$\Delta\varepsilon = \Delta\varepsilon_p + \Delta\varepsilon_e = CN^{-\alpha} + BN^{-\beta}, \quad (23.3)$$

where $\Delta\varepsilon$ is the total, plastic plus elastic, strain range, C , B , α and β are the empirical constants, criterion parameters for a given material.

The parameters are obtained through the cyclic testing at the strain range control conditions. This allows considering the loading specifics of the stress concentration areas at nominally elastic behavior of the structure. The criteria parameters are defined for particular structural materials (e.g., [10, 11], etc.), and in the case of welded structures, the base and weld material properties can also be obtained and distinguished in failure criteria [15].

Fatigue testing of specimens is terminated when the ascending stress-strain diagram branch (tensile part of the cycle) would be distorted due to the early crack origination. This makes predictions of the fatigue life of structural details more realistic than by using the S-N criteria.

Application of a strain-life criterion in fatigue assessment of a structural detail needs in evaluation of the local (elastic-plastic) strain at a notch root under applied nominal stress. The local cyclic strain can be obtained by means of Neuber's heuristic formula [22], empirical relationships [15], or by applying the elastic-plastic cyclic finite-element software, e.g., [15]. In order of considering effect of stress concentration in the high-cycle component of the criterion (23.3), it can be approximated as [14]

$$\Delta\varepsilon = \Delta\varepsilon_p + \Delta\varepsilon_e = CN^{-\alpha} + 2\beta\sigma_f K_t / EK_f, \quad (23.4)$$

where σ_f is the fatigue limit stress of the appropriate joint zone [23]; $\beta \leq 0.55$ is the correction for decreasing fatigue resistance under irregular loading [2]; K_t is the theoretical ("elastic") stress concentration factor (SCF); and K_f is the fatigue notch factor [14].

The above criteria (23.3), (23.4) with reasonably fine meshing in the finite-element modeling of critical locations and expected crack extensions in structural details allow carrying out analysis of fatigue process covering the very initiation of service loading and the crack nucleation and growth until the onset of a critical state of a structure, e.g., until the through crack in a tubular structure, Fig. 23.5 ([16], etc.). The elements in the mesh at expected critical locations ("material elements") should be small enough to provide the necessary resolution of the stress field, but at the same time fitting the format of continua mechanics.

In example (Fig. 23.5), it was assumed that at the inner surface of cylindrical shell there is a chain of defects of material microstructure along the generating line. Respectively, in criterion (23.4) for the finite elements of the above chain the second term was assumed smaller than that for surrounding elements.

The procedure of analysis is as follows. At initiation of cyclic loading of the model in elements assumed affected the damage accumulation is estimated accordingly the Palmgren-Miner rule. Initially, the cyclic strain-stress field is calculated in elements

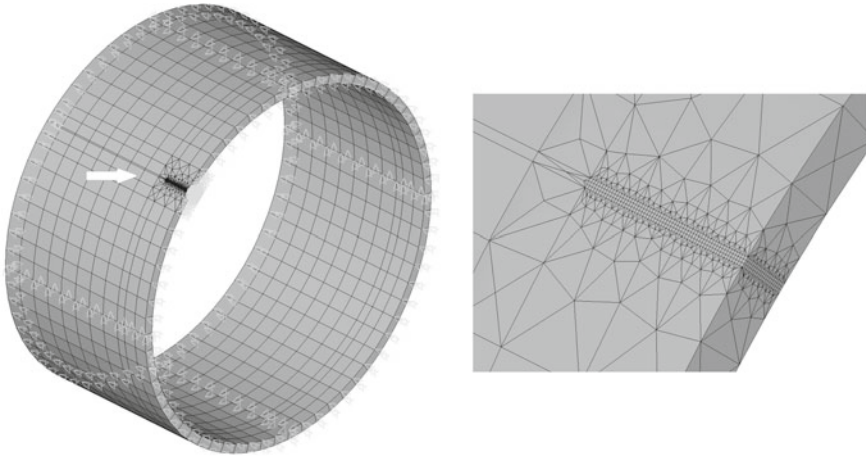


Fig. 23.5 FE model of a pipeline designed for the crack growth analysis [16]

located at the crack initiation and extensions. Then, applying criterion, e.g., (23.4), respective life of affected (“ i ”) elements at the first procedure step, N_i^1 , should be found, and then the damage in elements at failure of the most stressed element:

$$d_{initial,i} = \min\{n_i^1\}/N_i^1. \quad (23.5)$$

Further, the sequential strain-stress field is calculated and the number of loading cycles should be found in elements considering the damage accumulated by the failure of the most affected element (elements). Criterion for failure of the following elements, again, is found from the linear damage summation procedure:

$$d_i^j = d_{initial,i} + \sum_j \min\{n_i^j\}/N_i^j, \quad (23.6)$$

where $\min\{n_i^j\}$ is the number of load cycles up to failure of the “weak-most” element at the j th step of the crack extensions and N_i^j is the number of load cycles until failure of the i th element at the j th step of the crack growth found from the (6) criterion.

Figure 23.6 [17] shows several steps in progress of the crack originated at the inner surface toward the outer surface of the pipeline when the crack becomes the through-the-shell (the instable failure of the shell was not assumed; the limited extension of the crack along the generating line of the shell depends in the example on the properties of the FE mesh).

It should be noted that in this problem and in other, addressed to fatigue analysis, the consecutive re-design of the mesh may be reasonable on condition that the information on the accumulated damage would be retained in material as said in above.

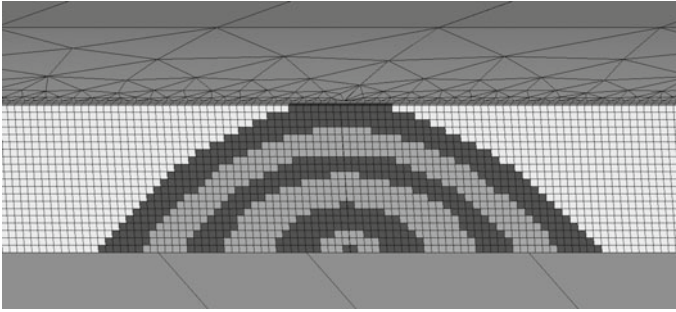
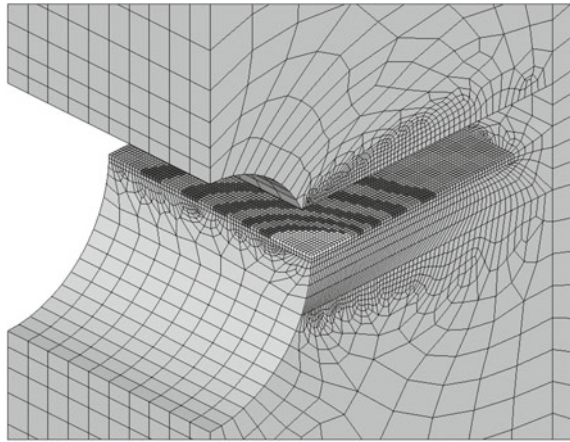


Fig. 23.6 Modeling of the crack extensions toward the outer surface of the pipeline

Fig. 23.7 The crack front evolution found by the damage accumulation technique [17]



Another example of application of the strain-life criterion and FE technique in modeling fatigue crack initiation and extensions is shown in Fig. 23.7 [17]. Shown is a steel plate with semi-circular notches subjected to cyclic tensile-compressive loading, and crack initiated at the notch root.

When the fatigue process is analyzed in a welded joint, especially when the crack origination is expected at the weld toe, the properties of the critical location, fusion zone material, barely can be obtained by fatigue testing of standard (“strain-life”) specimens—mechanical homogeneity of the joint may be assumed [15]. The residual welding stress cannot be retained in standard test (hour-glass) specimens, but it may be assumed the tensile stress part relaxation due to the cyclic plasticity of material at a critical location accentuated by the stress concentration. Examples of the strain-life approach application, infrequent though, show reasonable agreement of the life estimated and experimentally obtained, e.g., [15, 17], etc.

23.4 Conclusions

The stress-life (S-N) criteria applied in the nominal stress approach, hot-spot stress, and notch-stress approach provide assessment of fatigue properties of structures accompanied with a series of approximations and uncertainties. The most substantial drawbacks of the S-N criteria-based techniques of fatigue analysis are seen when the damage progress in details of redundant structures is assessed where loading of critical locations is rather provided under the strain range control, uncertainty of the crack size corresponding completion of estimated fatigue life of a structural component, etc. Several means of improvement of the notch-stress approach and respective S-N criteria are suggested proved by results of a series of studies. Specifics of the strain-life application in problems of crack initiation and propagation are briefly discussed and illustrated .

References

1. Niemi, E., Fricke, W., Maddox, S.J.: Structural Hot-spot Stress Approach to Fatigue Analysis of Welded Components. In: Designers' Guideline International Institute of Welding, IIW-Doc. XIII-WG3-31r1-14 2015. p. 49. Cambridge, Abington (2015)
2. EUROCODE 3: Design of Steel Structures. Part 1-9: Fatigue. BS EN 1993-1-9 (2014)
3. IACS Common Structural Rules for Bulk Carriers and Oil Tankers.: CSR-H 01. Part 1, Chap. 9 Fatigue, 519–625 (2019)
4. Marshall, P.W.: Basic Considerations for Tubular Joint Design in Offshore Construction. WRC Bulletin 193, New York (1974)
5. Haibach, E.: Die Schwingfestigkeit von Schweiß Verbindungen aus der Sicht einer Örtlichen Beanspruchungsmessung. Ber. FB-77. Darmstadt: Lab. f. Betriebsf (1968)
6. Fricke, W.: Guideline for the Fatigue Assessment by Notch Stress Analysis for Welded Structures, IIW-Doc. XIII-2240r1-08/XV-1289r1-08. Cambridge, Abington (2008)
7. Frost, N.E., Marsh, K.J., Pook, L.P.: Metal Fatigue. Clarendon Press, Oxford (1974)
8. Petinov, S.V., Thayamballi, A.K.: The application of S-N curves considering mismatch of stress concentration between test specimen and structure. *J. Ship Res.* **42**(1), 68 (1998)
9. Petinov, S.V., Reemsnyder, H.S., Thayamballi, A.K.: The Similitude of Fatigue Damage Principle: Application in S-N Curves-based Fatigue Design. In: Marquis, G., Solin, J. (eds.) *Fatigue Design and Reliability*, pp. 219–228.ESIS Publication 23. Elsevier Science Ltd., (1999)
10. Ivanova, V.S., Terentiev, V.F.: Physical Basics of Fatigue of Metals. Metallurgia, Moscow (1975)
11. Petinov, S.V., Melnikov, B.E.: Mean stress evolution in irregular cyclic loading of aluminium alloy. In: The XLIII International Summer School-Conference APM-2015, SPb, IPME RAS-SPbPU, p. 81. Abstracts (2015)
12. Det Norske Veritas.: Fatigue Assessment of Ship Structures. Classification Notes no 30.7. Hovik, Norway (2014)
13. Petinov, S.V., Afanasyeva, I.M.: Fatigue Assessment of Structures in High-cycle Segment: Technique and Problems. In: Proceedings, The XXXVII International Summer School—Conference Advanced Problems in Mechanics APM-2010, SPb-Repino, pp. 519–525 (2010)
14. Peterson, R.E.: Stress Concentration Factors. A Handbook, Wiley, New York (1977)
15. Petinov, S.V.: In-Service Fatigue Reliability of Structures. Springer International Publishing (2018)

16. Petinov, S.V., Guchinsky, R.V.: Fatigue assessment of tubular structures. *Mag. Civ. Eng.* **1**(36), 39–47 (2013)
17. Guchinsky, R.V., Petinov, S.V.: Surface fatigue crack growth simulation based on the finite-element aided damage accumulation procedure. *J. Sib. Fed. Univ. Eng. Technol.* **8**(7), 890–900 (2015)
18. Coffin, L.F., Tavernelli, J.F.: Experimental support for generalized equation predicting low-cycle fatigue. *Trans. ASME. Ser. D.* **4**, 533–545 (1962)
19. Manson, S.S.: Fatigue: a complex subject—some simple approximations. *Exp. Mech.* **7**, 193–225 (1965)
20. Hatanaka, K.: Cyclic stress-strain response and low-cycle fatigue life in metallic materials. *JSME Int. J.* **33**(1), 13–25 (1990)
21. Makhutov, N.A., Burak, M.I., Gadenin, M.M.: *Mechanics of Low Cycle Fatigue Failure*. Nauka, Moscow (1986)
22. Neuber, H.: Theory of stress concentration for shear-strained prismatic bodies with arbitrary nonlinear stress-strain law. *J. Appl. Mech.* **28**(4), 544–550 (1961)
23. Yassni, P.V., Troshchenko, V.T.: Fatigue crack growth: a model of the sub-critical growth. *Probl. Strength* **11**, 46–51 (1989)

Chapter 24

Discrete Thermomechanics: From Thermal Echo to Ballistic Resonance (A Review)



Ekaterina A. Podolskaya, Anton M. Krivtsov, and Vitaly A. Kuzkin

Abstract We present a review of the results in the field of discrete thermomechanics that have been achieved in the Institute for Problems in Mechanical Engineering RAS over the past decade. The focus is set on the novel approach for analytical description of non-equilibrium thermomechanical processes in crystalline solids. One, two, and three-dimensional perfect crystals with arbitrary harmonic and weakly anharmonic interactions are considered. The discussed topics cover three major areas: transition to thermal equilibrium, ballistic heat transfer, and thermoelasticity. The analysis reveals and elucidates such phenomena as thermal waves, heat flow from “cold” to “hot”, the existence of several kinetic temperatures, thermal echo, and ballistic resonance.

Keywords Ballistic heat transport · Ballistic resonance · Transient processes · Thermal waves · Kinetic temperature

24.1 Introduction

One of the topical problems of solid mechanics is the calculation of thermoelastic fields in materials and structures under various external influences. The continuum linear thermoelasticity theory provides an adequate and consistent description of the behavior of materials at the macro level. In particular, the problem of determining the temperature field causing thermoelastic stresses at the macro level is usually successfully solved using the Fourier law. The law describes the diffusive transfer of thermal energy, which is typical for macroscopic systems. However, the recent experiments reported in the works of Zettl [14], Maznev and Huberman [41], Nelson [49], Rogers [101], etc. indicate that at the micro- and nanoscale levels the

E. A. Podolskaya (✉) · A. M. Krivtsov · V. A. Kuzkin
Institute for Problems in Mechanical Engineering RAS, V.O., Bolshoy pr., 61,
St. Petersburg 199178, Russia
e-mail: akrivtsov@bk.ru

Peter the Great St. Petersburg Polytechnic University, Polytekhnicheskaya, 29,
St. Petersburg 195259, Russia

thermal energy can spread in a wave manner. In particular, it is shown that in many materials, including nanowires, carbon nanotubes, graphene, silicon membranes, etc., significant deviations from the Fourier law are observed. Theoretical investigation of this issue is addressed worldwide by Chen [15], Dhar [18, 19, 50], Gendelman and Savin [26, 27, 104, 105], Hemmer [34], Kosevich [58], Lebowitz [12, 50, 78, 100], Lepri, Livi and Politi [81–83], Lukkarinen [33], Mielke [90], Slepyan [108], Spohn [109], and many other authors. In such context, the development of mechanical models describing the thermoelastic behavior of solids, taking into account the ballistic transfer of thermal energy, becomes relevant. This goal is essential in connection with the development of microprocessor technology and the problem of heat removal from processors. In the Institute for Problems in Mechanical Engineering of the Russian Academy of Sciences (IPME RAS), the comprehensive study in this field was initiated by our research group in the works of Krivtsov [60, 61], followed by a series of papers, for example, [8, 23–25, 62–66, 70–77, 80, 85, 86, 91, 96, 111–113].

Anomalous heat transfer is closely connected with more general problems of non-equilibrium thermomechanical behavior of materials. This topic is considered in the works of Allen [2], Belyaev and Indeitsev [43, 44], Dmitriev [103], Dudnikova [20], Fortov [3, 45], Gavrilov [24, 25], Guzev [32], Ivanova [48], Krivtsov [60, 61, 64], Kukushkin [68, 69], Kuzkin [73, 75], Lurie [87, 88], Muratkov [92], Müller [62, 111], Petrov [45], Prigogine [98], Vilchevskaya [112], etc. At thermal equilibrium, the kinetic energy is usually equally distributed among the degrees of freedom. This fact makes it possible to describe the thermal state of an elementary volume of a material using a single scalar parameter – *kinetic temperature* proportional to the energy of chaotic thermal motion of atoms. Far from thermal equilibrium, the kinetic energies corresponding to the different degrees of freedom can differ significantly. As a result, it is necessary to introduce several temperatures. In particular, it is known that the lattice and electron subsystem temperatures in laser exposed solids may vary [43]. Multiple temperatures are also found in molecular dynamics simulations of shock waves [3, 35] and simulations of heat propagation in polyatomic crystal lattices [74]. It is often necessary to describe the process of energy equilibration, corresponding to different degrees of freedom. To describe this transient process within multicomponent continuum mechanics models, the construction of appropriate constitutive equations is required.

Discrete models of solids can be effectively used to simulate the thermomechanical behavior of materials at the micro- and nanoscale and construct continuum constitutive equations, e.g., referred to in the papers by Abramian et al. [1], Belyaev et al. [97], Dmitriev [7], Fortov [3, 45], Goldstein and Morozov [28], Golovneva et al. [29, 30], Ivanova [46, 47], Korobeynikov [56], Krivtsov [59], Norman [67, 93], Psakhie [99], and other authors. In particular, different variations of the particle method, such as the method of molecular dynamics [2] or the method of movable cellular automata [99], have become widely used.

The main objective of the present work is to provide a review of methods for *analytical* description of thermomechanical processes in crystalline solids that have been developed at IPME RAS over the past few years. After a brief notation outline

in Sect. 24.2, the paper is organized as follows. In Sect. 24.3, the so-called “fast” processes, i.e., energy equilibration and redistribution among the degrees of freedom, are considered. Next, Sect. 24.4 addresses the “slow” process (ballistic heat transfer). The paper is concluded by Sect. 24.5, where the conversion of thermal energy into mechanical energy and vice versa is considered.

24.2 Nomenclature

We use lower-case letters in boldface for vectors, either upper-case letters or Greek letters in boldface for tensors, and italic for scalars. The following notation is used:

- $d = 1, 2, 3$ is the space dimension;
- m and C are the particle mass and bond stiffness; C_1 is the substrate stiffness;
- $\omega_e = \sqrt{C/m}$ is the characteristic frequency, $\tau_e = 2\pi/\omega_e$ is the characteristic period of oscillations, and $c = \omega_e a$ is the characteristic velocity;
- η is damping coefficient, $\widehat{\omega}_e = 1/4\sqrt{16\omega_e^2 - \eta^2}$ is the characteristic frequency for non-conservative problems;
- \mathbf{r} is the position vector of a particle (or a unit cell—see Sects. 24.3.1.3 and 24.4.2);
- \mathbf{a}_α is the vector connecting this particle (or unit cell—see Sects. 24.3.1.3 and 24.4.2) with neighboring particle/cell number α ; $a_\alpha \equiv |\mathbf{a}_\alpha|$, $\mathbf{e}_\alpha \equiv \mathbf{a}_\alpha/a_\alpha$;
- $\mathbf{u}(\mathbf{r})$ and $\mathbf{v}(\mathbf{r})$ are the displacement and velocity of a particle (or columns, consisting of components of displacements and velocities of particles from unit cell—see Sects. 24.3.1.3 and 24.4.2);
- $\mathbf{u}_0(\mathbf{r})$ and $\mathbf{v}_0(\mathbf{r})$ are the initial displacement and velocity of a particle (or the respective columns—see Sects. 24.3.1.3 and 24.4.2);
- $\xi(\mathbf{r}_i, \mathbf{r}_j) = \langle \mathbf{u}(\mathbf{r}_i)\mathbf{u}(\mathbf{r}_j) \rangle$ and $\varkappa(\mathbf{r}_i, \mathbf{r}_j) = \langle \mathbf{v}(\mathbf{r}_i)\mathbf{v}(\mathbf{r}_j) \rangle$ are the tensor covariances of displacements and velocities for a pair of particles i and j ; brackets $\langle \rangle$ denote the mathematical expectation; $\mathbf{u}(\mathbf{r}_i)\mathbf{u}(\mathbf{r}_j)$ is the tensor product of the respective displacements;
- \mathbf{D} is the tensor difference operator, D is the respective scalar difference operator;
- \mathbf{K} , $\mathbf{\Pi}$, and \mathbf{L} are generalized (non-local) kinetic energy, potential energy, and Lagrangian;
- $\mathbf{T}(\mathbf{r})$ is the tensor temperature, and $T \equiv \text{tr}\mathbf{T}/d$ is the kinetic temperature;
- $J_k(\tau)$ is the Bessel function of the first kind;
- \mathbf{k} is the wave vector, $\omega(\mathbf{k})$ is the dispersion relation, and $\mathbf{c} = d\omega/d\mathbf{k}$ is the group velocity vector.

24.3 Transient Processes

The solution of problems of thermomechanics for materials in a highly non-equilibrium state is one of the topical questions of solid mechanics. At thermal equilibrium, the kinetic energy is conventionally accepted to be equally distributed

among the degrees of freedom. This fact follows from the equipartition theorem [38, 119]. This theorem allows us to describe the thermal state of the system using a single scalar parameter of kinetic temperature proportional to the energy of chaotic thermal motion of the atoms. As mentioned above, the kinetic energies corresponding to various degrees of freedom can differ significantly far from thermal equilibrium, so in many works several temperatures are introduced [11, 31, 44, 45]. For example, in papers [36, 37, 116] it is shown that the kinetic energies (temperatures) corresponding to the motions of atoms along and across the direction of shock wave propagation can differ almost by a factor of two near its front. In [50, 51] the heat propagation in a diatomic one-dimensional harmonic chain placed between two thermal reservoirs with different temperatures was considered. It was shown that the temperatures of the sublattices in the non-equilibrium stationary state are different. A similar effect observed for unsteady heat transfer is demonstrated in Sect. 24.3.1.1 [74].

In the absence of any external influences, the non-equilibrium system tends to thermal equilibrium. The transition to thermal equilibrium is accompanied by several processes:

- The velocity distribution function tends to Gaussian [20, 34, 52, 78, 109];
- The total energy is redistributed among kinetic and potential forms [2, 52, 108] (also described below following [5, 60, 71]);
- The kinetic energy is redistributed among the degrees of freedom (addressed below following [71, 73]);
- The energy is redistributed among the system's eigenmodes [98].

These processes, except for the last one, occur both in linear (harmonic) and nonlinear systems [2, 20, 52, 60, 71, 78, 109]. In harmonic crystals, the energies of the eigenmodes are constant in time. However, the kinetic temperature field in infinite harmonic crystals tends to become spatially homogeneous and constant in time [34, 72, 109]. Therefore, the concept of thermal equilibrium has been widely applied to harmonic crystals [10, 20, 42, 78, 109, 114].

The transition to thermal equilibrium is considered in many works, and such aspects of this process as the existence of an equilibrium state [78], ergodicity [114], the normalization of the distribution function [10, 20, 52], entropy evolution [42, 111], etc. have been investigated. The present section deals with the behavior of the main experimentally observed value of the kinetic temperature(s), which is proportional to the kinetic energy of chaotic particle motion.

There exist two different approaches to describe the behavior of statistical characteristics in harmonic crystals. One of them is based on the exact solution of the lattice dynamics equations to calculate the kinetic temperature as the mathematical expectation of the kinetic energy [32, 42, 52, 84]. In particular, the pioneering work of Klein and Prigogine [52] considered the transition to thermal equilibrium in an infinite harmonic chain with random initial conditions. Using the exact solution obtained by Schrödinger [106], it was shown that the kinetic and potential energies of the chain oscillate in time and tend to equal equilibrium values [52].

The present section focuses on the other approach, which uses covariances of velocities and covariances of particle motions as the main variables (the covariance

of two centered random variables is the mathematical expectation of their product). In the case of a harmonic crystal, it is possible to obtain a closed system of equations for the covariance in the stationary [50, 82, 100] and non-stationary [60, 83] cases. The solution of this system describes, in particular, the change in kinetic temperature over time. In Sects. 24.3.1.1–24.3.1.3 this idea is used to describe the transition to equilibrium in infinite crystals with monoatomic and polyatomic lattice. In particular, one-dimensional chains [5, 60, 73] and two-dimensional triangular, square, and hexagonal (graphene) lattices [70–73] are considered. Next, in Sects. 24.3.2–24.3.4 several generalizations are introduced, such as damping [23], weak interaction non-linearity [71, 75], and account for the lattice finiteness [91]. The latter is concluded by the effect of *thermal echo*.

24.3.1 Infinite Harmonic Crystal

We begin with the simplest mathematical model. Consider an infinite simple crystal lattice in the space of dimension d , which consists of identical particles. The particles positions are identified by the vectors in the undeformed state, and the nearest neighbors interact via linearized, or *harmonic*, forces. The Born-von Karman periodic boundary conditions [4] are used.

First, we formulate the *stochastic* problem. The equations of motion¹ take the form of the differential-difference equations, equivalent to the infinite² system of second-order ODEs [71]:

$$\begin{aligned} \dot{\mathbf{v}}(\mathbf{r}) &= \mathbf{D} \cdot \mathbf{u}(\mathbf{r}), & \mathbf{D} &= \omega_e^2 \sum_{\alpha} \mathbf{e}_{\alpha} \mathbf{e}_{\alpha} \Delta_{\alpha}^2, \\ \Delta_{\alpha}^2 \mathbf{u}(\mathbf{r}) &= \mathbf{u}(\mathbf{r} + \mathbf{a}_{\alpha}) - 2\mathbf{u}(\mathbf{r}) + \mathbf{u}(\mathbf{r} - \mathbf{a}_{\alpha}). \end{aligned} \quad (24.1)$$

The initial conditions are written as

$$\mathbf{u}(\mathbf{r}) \Big|_{t=0} = \mathbf{u}_0(\mathbf{r}), \quad \mathbf{v}(\mathbf{r}) \Big|_{t=0} = \mathbf{v}_0(\mathbf{r}), \quad (24.2)$$

where $\mathbf{u}_0(\mathbf{r})$ and $\mathbf{v}_0(\mathbf{r})$ are uncorrelated *random* vectors with zero mean, i.e., $\langle \mathbf{u}_0(\mathbf{r}) \rangle = 0$, $\langle \mathbf{v}_0(\mathbf{r}) \rangle = 0$.

The solution of the system (24.1)–(24.2) describes the crystal dynamics completely. Moreover, these equations can be solved analytically. However, the description of the thermal processes usually requires only the statistical characteristics, such as covariances of velocities $\varkappa(\mathbf{r}_i, \mathbf{r}_j) = \langle \mathbf{v}(\mathbf{r}_i) \mathbf{v}(\mathbf{r}_j) \rangle$ and displacements $\xi(\mathbf{r}_i, \mathbf{r}_j) = \langle \mathbf{u}(\mathbf{r}_i) \mathbf{u}(\mathbf{r}_j) \rangle$ of particles i and j . Following [71] and the references therein, we write down the *deterministic* system of second-order tensor ODEs:

¹ These equations are valid only for the simple, or *monoatomic*, lattices. The general formulae for the *polyatomic* lattices can be found in, e.g., [73], and the results are addressed in Sect. 24.3.1.3.

² For infinite crystals.

$$\begin{aligned}\ddot{\xi} &= \mathbf{D} \cdot \xi + \xi \cdot \mathbf{D} + 2\kappa, \\ \ddot{\kappa} &= \mathbf{D} \cdot \kappa + \kappa \cdot \xi + 2\mathbf{D} \cdot \xi \cdot \mathbf{D}.\end{aligned}\quad (24.3)$$

The system (24.3) yields to a single fourth-order equation which is valid both for ξ and κ :

$$\ddot{\ddot{\kappa}} - 2(\mathbf{D} \cdot \ddot{\kappa} + \ddot{\kappa} \cdot \mathbf{D}) + \mathbf{D}^2 \cdot \kappa - 2\mathbf{D} \cdot \kappa \cdot \mathbf{D} + \kappa \cdot \mathbf{D}^2 = 0. \quad (24.4)$$

The respective initial conditions will be discussed below for the particular examples. We note that Eq. (24.4) is also satisfied for harmonic crystals with arbitrary polyatomic lattice [73].

Another useful yet not inevitable assumption is the uniform initial temperature distribution. It can be demonstrated that at the time scale at which the transient processes come out and decay, the change in spatial temperature distribution is negligible (see Sect. 24.4 and the references therein). Then, the covariances depend only on the difference between the particles i and j position vectors. In this case, we can introduce a new variable instead:

$$(\mathbf{r}_i, \mathbf{r}_j) \longrightarrow (\mathbf{r}_i - \mathbf{r}_j). \quad (24.5)$$

This assumption leads to the simplification of Eq. (24.4).

Basing on the covariances, we introduce the generalized (or non-local) potential and kinetic energies, and also the generalized Lagrangian [61, 70]

$$\begin{aligned}\Pi(\mathbf{r}_i, \mathbf{r}_j) &= -\frac{m}{4} (\mathbf{D} \cdot \xi(\mathbf{r}_i, \mathbf{r}_j) + \xi(\mathbf{r}_i, \mathbf{r}_j) \cdot \mathbf{D}), \\ \mathbf{K}(\mathbf{r}_i, \mathbf{r}_j) &= \frac{m}{2} \kappa(\mathbf{r}_i, \mathbf{r}_j), \quad \mathbf{L} = \mathbf{K} - \Pi.\end{aligned}\quad (24.6)$$

If $i = j$, the traces of tensors \mathbf{K} , Π , and \mathbf{L} are equal to the respective conventional energies per particle. Note that \mathbf{K} , Π , and \mathbf{L} satisfy Eq. (24.4). As for the initial conditions, the use of the conservation laws helps to eliminate the odd derivatives (see, e.g., [71] for the details).

Next, we define the *tensor temperature* $\mathbf{T}(\mathbf{r})$ [36, 37] and *kinetic temperature* T as

$$\frac{k_B}{2} \mathbf{T}(\mathbf{r}) = \mathbf{K}(\mathbf{r}_i, \mathbf{r}_j) \Big|_{i=j}, \quad T = \frac{1}{d} \text{tr} \mathbf{T}(\mathbf{r}). \quad (24.7)$$

Here k_B is Boltzmann constant. The kinetic temperature is introduced in such a way that at the equilibrium the equipartition theorem [38] is fulfilled, i.e., kinetic energy per degree of freedom is equal to $k_B T/2$.

In the following sections, we consider several generalizations, including the influence of interaction nonlinearity and finiteness of the system. But before that, let us turn to the examples of harmonic crystals. It is noteworthy that in all examples the numerical and analytical solutions demonstrate an excellent agreement.

24.3.1.1 Hooke's Crystal

We start with the one-dimensional case ($d = 1$). Then all the vector and tensor quantities yield to their scalar equivalents. Consider one of the possible transient processes, i.e., the evolution of the generalized Lagrangian [60]. Taking the aforementioned formulae and also conservation laws into account, we get for the particle n

$$\ddot{L}_n = 4\omega_e^2 \Delta_n^2 L_n, \quad \Delta_n^2 L_n = L_{n+1} - 2L_n + L_{n-1}, \quad 0 < n < N. \quad (24.8)$$

Here the parameter $N \gg 1$ characterizes the length of the period in Born-von Karman boundary conditions. Assuming that the initial velocities of particles are uncorrelated and the initial displacements are absent, the initial conditions yield to

$$L_n \Big|_{t=0} = E \delta_n, \quad \dot{L}_n \Big|_{t=0} = 0, \quad (24.9)$$

where E is the initial energy of the instantaneous thermal perturbation, $\delta_n = 1$ for $n = 0$; otherwise $\delta_n = 0$. For $N \rightarrow \infty$ the solution yields to

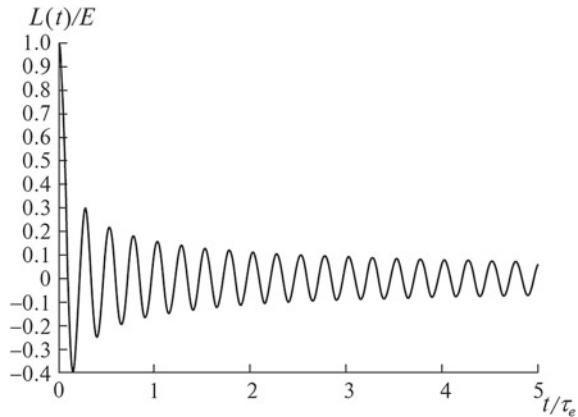
$$L_n(t) = E J_{2n}(4\omega_e t) \approx (-1)^n \frac{E}{\sqrt{2\pi\omega_e t}} \cos\left(4\omega_e t - \frac{\pi}{4}\right) + O(t^{-3/2}). \quad (24.10)$$

Recall, that if $n = 0$, L_n is equal to the conventional Lagrangian. Hence, the Lagrangian, L , satisfies the differential Bessel equation:

$$\ddot{L} + \frac{1}{t} \dot{L} + 16\omega_e^2 L = 0. \quad (24.11)$$

The oscillations occur with frequency $4\omega_e$, and the amplitude decays as the square root of time (see Fig. 24.1).

Fig. 24.1 Oscillations of the Lagrangian for the Hooke's crystal [60]



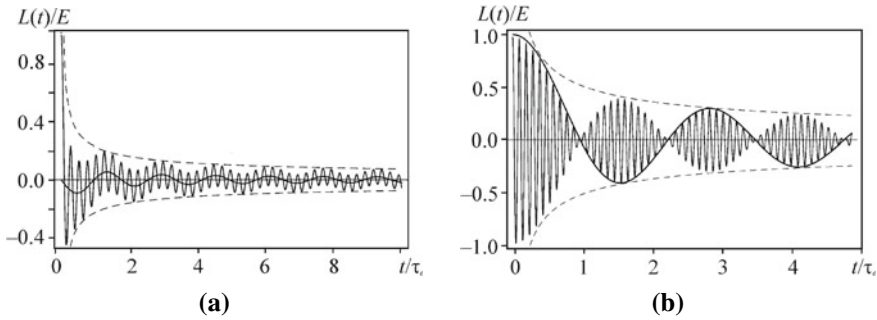


Fig. 24.2 Oscillations of the Lagrangian for (a) the soft ($\epsilon = 0.1$) and (b) the hard ($\epsilon = 24$) elastic foundations [5]. The dashed lines show the bounding functions

A similar yet essentially different result is obtained for the one-dimensional chain on the elastic foundation [5]. The introduction of the additional stiffness parameter C_1 leads to the modification of Eq. (24.8)

$$\ddot{L}_n = 4\omega_e^2 (L_{n+1} - 2(1 + \epsilon)L_n + L_{n-1}), \quad \epsilon = \frac{C_1}{C} \quad (24.12)$$

with the same initial conditions (24.9).

If the elastic foundation is soft ($\epsilon < 1$), the solution for the Lagrangian takes the form, which is proved to be valid up to $\epsilon = 1$

$$L = E \left(J_0 \left(2\sqrt{4 + \epsilon}\omega_e t \right) - \frac{1}{2}\sqrt{\epsilon}J_1 \left(2\sqrt{\epsilon}\omega_e t \right) \right). \quad (24.13)$$

The second summand in formula (24.13) gives low-frequency oscillations on which the first high-frequency summand is superimposed (see Fig. 24.2a).

For the hard elastic foundation ($\epsilon > 1$) the solution may be approximately represented as

$$L \approx E J_0(\Omega_2 t) \cos(\Omega_1 t), \quad \Omega_{1,2} = \left(\sqrt{4 + \epsilon} \pm \sqrt{\epsilon} \right) \omega_e, \quad (24.14)$$

which leads to the formations of beats: the low-frequency envelope $J_0(\Omega_2 t)$ restricts the wave packet with a high-frequency harmonic signal (see Fig. 24.2b).

24.3.1.2 Two- and Three-Dimensional Crystals

Let us pass over to two-dimensional space ($d = 2$). First, consider the so-called scalar lattices [33, 90, 104]. In this case, a scalar function of a position vector $u(\mathbf{r})$ is used to describe the system motion (24.1), i.e., each particle has only one degree

of freedom, and the temperature (24.7) is also scalar. Note that a one-dimensional chain with nearest neighbor interaction (see Sect. 24.3.1.1) is also a scalar lattice.

The exact solution for the kinetic temperature is given by [72]

$$T = \frac{T_0}{2} \left[1 + \int_{\mathbf{k}} \cos(2\omega(\mathbf{k})t) d\mathbf{k} \right], \tag{24.15}$$

where the integration is carried out with respect to components of the wave vector \mathbf{k} ; $\int_{\mathbf{k}} d\mathbf{k} = 1$. Here another important quantity is introduced: the dispersion relation $\omega(\mathbf{k})$ which is obtained from lattice dynamics Eqs. (24.1).

In 2D, the first example to be considered is the out-of-plane vibrations of square lattice [72]. In harmonic approximation, in-plane and out-of-plane vibrations of the lattice are independent. The lattice is prestrained; otherwise the oscillations would be essentially nonlinear. The kinetic energy oscillations decay, and the characteristic time of this process is of the order of several characteristic periods τ_e . The rate of decay is proportional to $1/t$ in contrast to the one-dimensional problem for which it decays as $1/\sqrt{t}$. The characteristic frequencies for both one-dimensional and two-dimensional scalar lattices are calculated in [55].

The next step is to consider in-plane vibrations of the square and triangular lattices. In this case, each particle has two degrees of freedom, and the temperature tensor (24.7) has two eigenvalues. The analytical solution of the respective equations [70, 71] clearly demonstrates that, in general, \mathbf{T} is not isotropic, and the velocity covariance for neighboring particles $\varkappa(\mathbf{r}_i, \mathbf{r}_j)$ is not equal to zero, i.e., particles' velocities are not statistically independent (see Fig. 24.3). Thus, we capture another transient process: *temperature redistribution among the degrees of freedom*.³ The characteristic frequencies for this problem are calculated in [113].

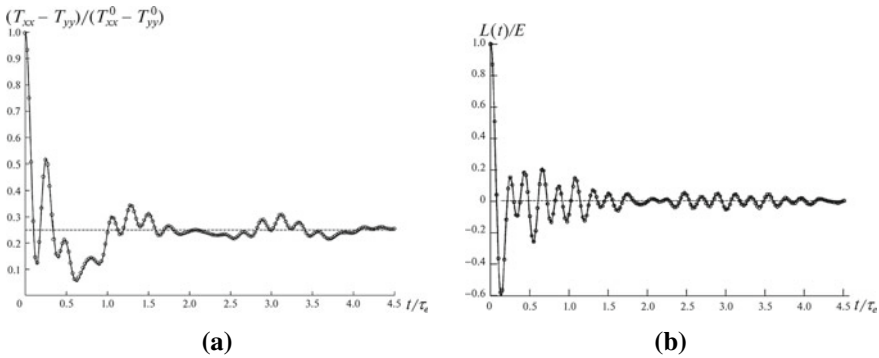


Fig. 24.3 Two transient processes associated with triangular lattice in-plane motion: (a) temperature redistribution among spatial directions and (b) oscillations of the Lagrangian [70]

³ The rate of decay for triangular lattice is again proportional to $1/t$, whereas for square lattice it decreases as $1/\sqrt{t}$. Moreover, the spatial redistribution effect doesn't appear in the square lattice.

The above derivations are valid not only for $d = 2$ but also for $d = 3$. The results similar to those shown in Fig. 24.3 are obtained in [75] for the face-centered cubic lattice.

24.3.1.3 Polyatomic Crystals

Next, we consider the effects observed only in polyatomic lattices [73].

The unit cells of polyatomic lattices are identified by their position vectors \mathbf{r} , and each unit cell has M degrees of freedom, corresponding to components of particles displacements. Hence, instead of tensor temperature (24.7), we introduce the *temperature matrix* $\mathbf{T}(\mathbf{r})$ [73, 74]. Its components are given by

$$T_{kn} = \frac{1}{k_B} \sqrt{m_k m_n} \langle v_k v_n \rangle, \quad (24.16)$$

where m_k and v_k are the masses and velocities corresponding to the k th degree of freedom. Temperature matrix is related to the *kinetic temperature* T as

$$T = \frac{1}{M} \sum_{k=1}^M T_{kk}. \quad (24.17)$$

The explicit problem statement and derivation of the formulae that describe the time evolution of the temperature matrix are given in [73]. Here we restrict ourselves by the graphic results for one-dimensional lattice with alternating masses and stiffnesses (Fig. 24.4) and for the out-of-plane vibrations of graphene (Fig. 24.5). The transient processes associated with in-plane vibrations of graphene are considered in [8].

Figure 24.4a shows that in both cases the difference between temperatures tends to the value $0.3(T_{11}^0 - T_{22}^0)$, but the shape of the curves differs. Therefore, the process of redistribution of temperature between sublattices depends on difference in the initial temperatures of the sublattices. Figure 24.4b demonstrates that for any given mass ratio, the difference between temperatures decreases with decreasing ratio of stiffnesses and tends to a limiting value corresponding to the case when this ratio tends to zero.

As for the graphene, Fig. 24.5 shows beats of difference between temperatures of sublattices. The amplitude of beats decays in time as $1/t$, so at large times, temperatures of sublattices in graphene equilibrate.

Finally, we note that the equilibrium values of kinetic temperatures in harmonic polyatomic lattices are generally different and depend on the initial value of the temperature matrix. In paper [73], the formula relating equilibrium values of kinetic temperatures with initial conditions is derived. The formula is referred to as the *non-equipartition theorem*. The theorem shows, in particular, that the kinetic temperatures

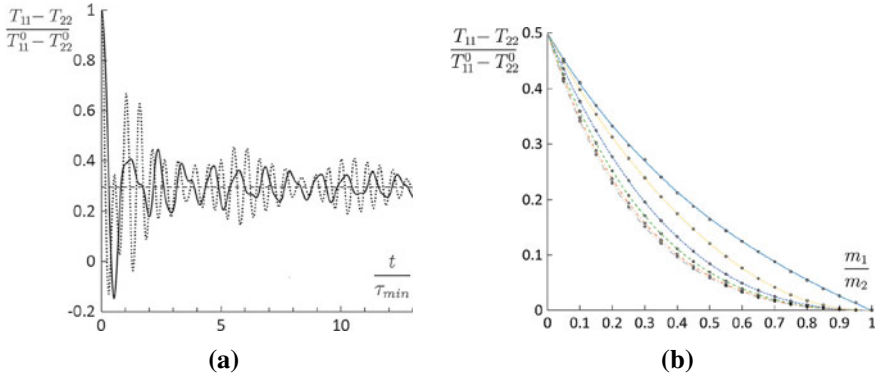


Fig. 24.4 (a) Difference between temperatures of sublattices for $T_{11}^0 \neq 0, T_{22}^0 = 0$ (solid line) and $T_{11}^0 = 0, T_{22}^0 \neq 0$ (dotted line). (b) Difference between equilibrium temperatures of sublattices for a diatomic chain with the ratio of stiffnesses equal to 1 (solid line), 1/2 (dotted line), 1/4 (short dashed line), 1/8 (dashed line), 1/16 (dash-dotted line), and 1/32 (dash-double dotted line) [73]

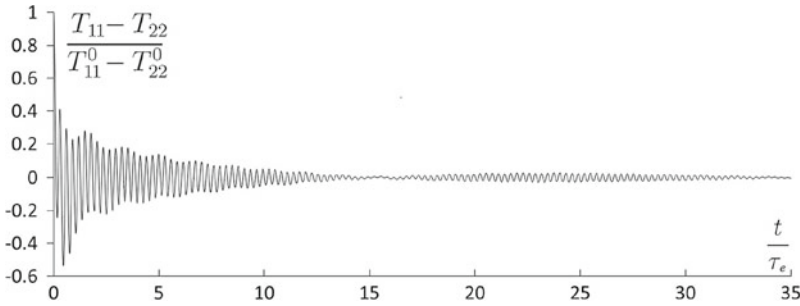


Fig. 24.5 Redistribution of kinetic temperatures among sublattices in graphene [73]

are equal at thermal equilibrium if their initial values are also equal. If initially the kinetic temperatures are different then they are usually different at equilibrium, except for some lattices.

24.3.2 The Influence of Finiteness: Thermal Echo

The account for the finiteness of the one-dimensional harmonic crystal gives rise to more phenomena and effects [91].

The infinite model predicts that the generalized energy oscillations are described by Bessel functions (24.10), and only zero-order Bessel function describes the conventional energies. In contrast, if the crystal consists of a finite number of particles, at a certain time, the amplitude decay, prescribed by the Bessel function, is replaced by a sharp short-term growth which reoccurs periodically. This phenomenon is referred

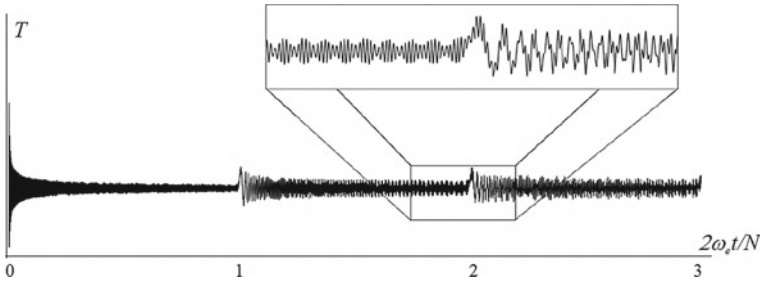


Fig. 24.6 Oscillations of temperature T in the finite Hooke’s crystal [91]

to as *thermal echo*, and the sequence of its realizations is described by a series of the Bessel functions of multiple orders. Moreover, a superposition of the temperature oscillations generated by the sequential thermal echoes results in temperature beats with each subsequent thermal echo complicating their shape (see callout in Fig. 24.6).

The solution for, e.g., temperature yields to

$$T = T_E + \frac{\delta T}{2} J_0(4\omega_e t) + \delta T \sum_{p=1}^{p=\infty} J_{2pN}(4\omega_e t), \tag{24.18}$$

$$T_E = \frac{\Delta T}{2} \left(1 - \frac{1}{N-1}\right), \quad \delta T = \Delta T \left(1 + \frac{1}{N-1}\right).$$

Here T_E is the so-called equilibrium temperature, ΔT is the temperature jump proportional to the initial energy of the instantaneous thermal perturbation E , and N is the number of particles.

Next, it can be shown that in the thermodynamic limit any thermal echo is described by the Airy function; thus formula (24.18) can be rewritten as

$$T = T_E + \frac{\delta T}{2} J_0(4\omega_e t) + \delta T \sum_{p=1}^{p=\infty} \frac{1}{\sqrt[3]{pN}} \text{Ai} \left(\frac{2pN - 4\omega_e t}{\sqrt[3]{pN}} \right). \tag{24.19}$$

So for sufficiently large N any thermal echo is shaped as an Airy function. Hence, the time, when echo p occurs, its relative “height” and “width” are estimated by

$$t_p \simeq \frac{1}{4\omega_e} \left(2pN + \sqrt[3]{pN}\right), \quad h_p \simeq \sqrt{\pi} A_1 \sqrt[6]{pN}, \quad w_p \sim \sqrt[3]{pN}, \tag{24.20}$$

where $A_1 \approx 0.53$ is the first local maximum of Airy function.

The analysis demonstrates that the maximum temperature increase caused by the thermal echo decreases as $\sqrt[3]{pN}$, and the duration of the thermal echo w_p increases with the same rate. Moreover, the amplitude of the temperature oscillations decreases as $1/\sqrt{t}$ between any two echoes. What is more the larger the crystal is, the more

noticeable become the temperature peaks h_p in comparison with the residual oscillations.

24.3.3 The Influence of Dissipation on the Transition to Thermal Equilibrium

In this section, we consider the problem of thermal equilibration in a one-dimensional *damped* harmonic crystal [23].

The problem statement remains almost the same as in Sect. 24.3.1.1. The differential-difference operator, acting on, e.g., generalized Lagrangian, takes the form

$$\frac{\partial^2}{\partial t^2} + 2\eta \frac{\partial}{\partial t} - 4\omega_e^2 \Delta_n^2, \quad (24.21)$$

which yields to (24.8) if $\eta = 0$. The characteristic frequency for this equation is $\widehat{\omega}_e = 1/4\sqrt{16\omega_e^2 - \eta^2}$. Unlike the conservative case, the solutions of this kind of equations cannot be evaluated in closed form, so only the asymptotics are estimated.

Omitting a thorough analysis given in [23], we write out the asymptotics for conventional Lagrangian L_0 , which would be determined by a waning cosine (24.10) if there was no damping:

$$\begin{aligned} L &= L^{(1)} + O(t^{-7/2}) + L^{(2)} + O\left(\frac{e^{-\eta t}}{t}\right), \\ L^{(1)} &= E \left(-\frac{t^{-3/2}}{8\sqrt{2\pi}\eta\omega_e} - \frac{t^{-5/2}(3\eta^2 + 12\omega_e^2)\sqrt{2}}{512\sqrt{\pi}\eta^{3/2}\omega_e^3} \right), \\ L^{(2)} &= E \frac{e^{-\eta t}}{2\omega_e\sqrt{2\pi}t} \left(2\sqrt{\widehat{\omega}_e} \cos\left(4\widehat{\omega}_e t - \frac{\pi}{4}\right) - \frac{\eta}{2\sqrt{\widehat{\omega}_e}} \sin\left(4\widehat{\omega}_e t - \frac{\pi}{4}\right) \right). \end{aligned} \quad (24.22)$$

Similar representations can be obtained for the rest of generalized energies. In a particular case of conservative system, the summands with superscript “(1)” disappear, because the integration is carried out over the zero-length interval. In the case of high damping $\eta \geq 4\omega_e$ the summands with superscript “(2)” vanish for the same reason.

If $\eta/\omega_e < 1$ the transient process goes in two phases. Firstly, the kinetic and potential energies oscillate approaching the asymptote $Ee^{-\eta t}/2$, whereas the Lagrangian oscillates tending to zero; their amplitudes decay as the square root of time multiplied by the respective exponent. Secondly, at very large times, the principal term of the asymptotic expansion for the kinetic energy (and, consequently, temperature) becomes proportional to $t^{-5/2}$, whereas the rest of the energies decay as $t^{-3/2}$. In the limiting case of zero dissipation this surprising second phase disappears.

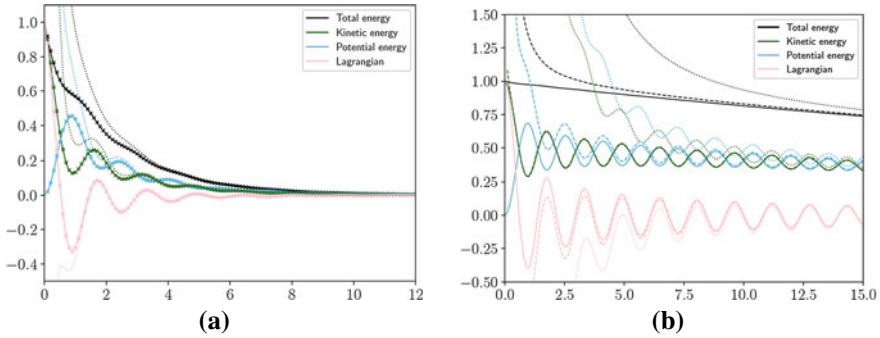


Fig. 24.7 The ratios of generalized energies to the initial value E versus dimensionless time $\omega_e t$ for (a) $\eta/\omega_e = 0.5$ and (b) $\eta/\omega_e = 0.02$: analytical solutions (solid lines), numerical solutions (crosses), asymptotic solutions (dotted lines), and approximate asymptotic solutions without power-decaying terms (dashed lines; only on the right-hand side) [23]

Note that if the damping is small, i.e., $\eta/\omega_e \ll 1$ the asymptotic formulae give wrong results at finite but not very large times (see Fig. 24.7b), so the valid approximation may be reached and the summands with superscript “(1)” are omitted.

24.3.4 The Influence of Nonlinearity on Transient Thermal Processes

In this example we present the *computational* results of the influence of a weak nonlinearity on the two transient thermal processes described above: (i) equilibration of kinetic and potential energies and (ii) redistribution of the kinetic energy among spatial directions. The account for the process (ii) is possible for both $d = 2$ [71] and $d = 3$ [75].

Let the particles interact via the Lennard-Jones potential:

$$\Pi(r) = \varepsilon \left[\left(\frac{a}{r}\right)^{12} - 2 \left(\frac{a}{r}\right)^6 \right], \tag{24.23}$$

where ε is the bond energy, and a is the equilibrium distance. In order to quantify the influence of nonlinearity, the dissociation velocity $v_d = \sqrt{2\varepsilon/m}$ is introduced. In the simulation the initial velocities are randomly distributed in a circle with radius v_0 .

Figure 24.8 shows the results for both transient processes in the triangular lattice. The curve (1) corresponds to $v_0/v_d = 0.05$, (2) is $v_0/v_d = 0.25$, (3) is $v_0/v_d = 0.5$, (4) is analytical solution for harmonic triangular lattice, and (5) is numerical solution of lattice dynamics equations. It is seen that nonlinearity increases the rate of equilibration of the system.

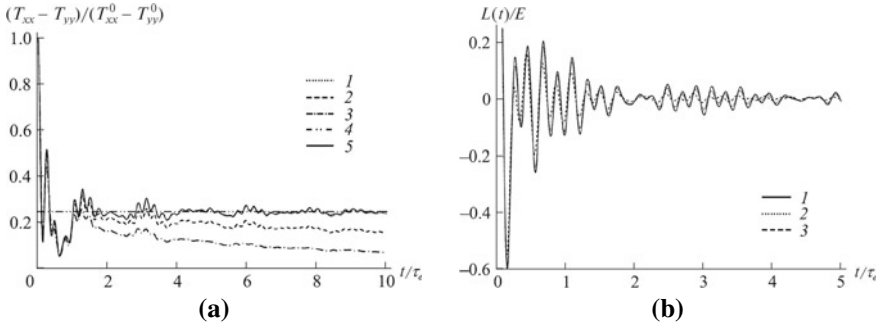


Fig. 24.8 Two transient effects in triangular lattice with Lennard-Jones interaction: (a) redistribution of temperature among spatial directions and (b) oscillations of the Lagrangian [71]

The additional analysis for FCC lattice [75] has shown that the thermal equilibration has two distinct time scales: the period of atomic vibrations τ_e and anharmonic τ_a , which depends on the initial temperature T_0 . These two scales are connected empirically by

$$\frac{\tau_e}{\tau_a} \approx \frac{k_B T_0}{\varepsilon} + 1.496 \left(\frac{k_B T_0}{\varepsilon} \right)^2 - 0.469 \left(\frac{k_B T_0}{\varepsilon} \right)^3. \quad (24.24)$$

At low temperatures $T_0 < 0.05\varepsilon/k_B$ the second time scale τ_a is almost inversely proportional to the initial temperature.

As far as the first time scale is concerned, the approach to equilibrium is accompanied by decaying high-frequency oscillations of the temperatures at times or order of several τ_e . These oscillations are caused by both transient processes, i.e., equilibration of kinetic and potential energies and redistribution of the kinetic energy among spatial directions.

At time scale τ_a , the difference of the kinetic temperatures deviates from the equilibrium value, predicted by the harmonic approximation, and monotonically tends to zero (see Fig. 24.8).

Thus, in anharmonic crystals thermal equilibration at different temperatures differs only by a time scaling. These results suggest, in particular, that, in the weakly anharmonic case, the characteristic time scales of relaxation and heat transfer may be of the same order; therefore, there may be some mutual influence between these processes.

24.4 Heat Transfer

There are several approaches to the description of heat transfer. In continuum theories, the constitutive equations are usually introduced as part of the phenomenological

approach. In particular, one of the phenomenological equations describing the wave properties of heat propagation is the Maxwell–Cattaneo–Vernotte equation [13, 115]. This equation, unlike the Fourier heat conduction equation, gives a finite speed of heat propagation. However, it still relies on the concept of the thermal conductivity coefficient, which is not a parameter of the material at the micro level. For example, it has been shown that in many materials, including nanowires [39], nanotubes [14], graphene [6, 118], silicone membranes [49], and others, the thermal conductivity depends significantly on the length of the sample on which measurements were carried out. In addition, the Maxwell–Cattaneo–Vernotte equation predicts an exponential decay of thermal perturbations, while in the ballistic regime these perturbations decay according to the power law [61, 74].

Another approach to describing heat propagation at the nanoscale is to use the kinetic Boltzmann equation [94]. This equation is usually simplified using a number of approximations for the collision term, in particular, by introducing relaxation times [9, 53]. This allows the Boltzmann equation to be solved numerically [40, 102], as well as obtaining heat propagation equations [15, 54]. In both cases, additional assumptions are often introduced [107]. In particular, the contribution of optical oscillations to heat transport is often neglected. Comprehensive literature reviews on the use of the Boltzmann equation to describe heat propagation can be found, for example, in [81, 107]. The link between the descriptions based on lattice dynamics and kinetic theory is discussed in [77, 110]. In the present section, the formulae for the heat transfer are derived either from the covariance dynamics equations or from the exact solution of the dynamics equations. This approach makes it possible to take into account all the important features of a discrete system that affect the heat propagation, in particular, to estimate the contribution of the different branches of the dispersion relation.

The analysis of heat transfer in discrete systems is usually carried out in the so-called stationary non-equilibrium state [81, 100]. In this case, the discrete system is placed between two thermostats with different temperatures. The effective heat transfer coefficient of the system is calculated for the known temperature difference, the distance between the thermostats, and the estimated heat flux. This formulation of the problem is widely used both in analytical studies [82, 100] and in computer simulations [19, 50, 81] of heat propagation. A detailed review of the results obtained in the stationary formulation is given, for example, in [18, 81]. Calculation of the effective thermal conductivity coefficient as a function of the sample length makes it possible to determine the conditions under which the ballistic, anomalous, or diffusive mode of heat propagation is realized. In the first case, the heat transfer coefficient increases linearly with length; in the second case it increases nonlinearly; and in the third case it does not depend on length at all. However, the stationary formulation does not allow determining the heat transfer law. Moreover, the results obtained in the stationary formulation may significantly depend on the choice of the thermostat [50]. Therefore, in this paper, we consider the non-stationary formulation of the energy transfer problem.

One of the problems in the study of non-stationary thermal energy transfer is to determine how the initial field of kinetic energy changes in time and space. The

initial field can be set, for example, by giving random initial velocities to particles. In this case, the use of a thermostat is not required. In the literature, such problems are usually solved numerically using, for example, the molecular dynamics method [27, 58, 79, 95]. This method makes it possible to use realistic interaction potentials and to consider the influence of nonlinearity, defects, interfaces, and other features of the real system, which are difficult to take into account analytically. However, in spite of the enormous possibilities of numerical methods, some questions are still easier to address analytically. In particular, for crystals with several branches of the dispersion relation, it is difficult to separate the contribution of different branches to the heat transfer in numerical simulations.

In this section, we continue to use an infinite harmonic crystal as the main model of a crystal. In this model, harmonic waves do not interact with each other, so the heat transfer is purely ballistic. The influence of dissipation and energy supply is regarded in Sect. 24.4.1.2. Once again, note that in all examples the numerical and analytical solutions demonstrate an excellent agreement.

24.4.1 Scalar Lattices

Let us continue the analysis of Eq. (24.4). In contrast to the previous assumption (24.5), here we carry out continualization with respect to spatial variable \mathbf{r} [61, 72], where the following change of variables is employed:

$$(\mathbf{r}_i, \mathbf{r}_j) \longrightarrow (\mathbf{r}, \mathbf{r}_i - \mathbf{r}_j), \quad \mathbf{r} = \frac{\mathbf{r}_i + \mathbf{r}_j}{2}. \quad (24.25)$$

Next, we assume that the covariances are slowly changing functions of \mathbf{r} at distances of order of a_α , then the difference operator can be approximated. Moreover, for the considered type of lattices, all the covariances become scalars (see Sect. 24.3.1.2), so Eq. (24.4) yields to [72]

$$\ddot{\varkappa} - 4D\dot{\varkappa} + 4(\mathbf{R} \cdot \nabla)^2 \varkappa = 0, \quad (24.26)$$

where ∇ is Del operator and the difference operators D and \mathbf{R} are calculated basing on the definition (24.1).

The initial conditions take the form

$$\varkappa = \frac{k_B}{m} T_0(\mathbf{r}) \delta(\mathbf{r}_i - \mathbf{r}_j), \quad \dot{\varkappa} = 0, \quad \ddot{\varkappa} = \frac{2k_B}{m} T_0(\mathbf{r}) D \delta(\mathbf{r}_i - \mathbf{r}_j), \quad \ddot{\varkappa} = 0, \quad (24.27)$$

where $\delta(\mathbf{r}_i - \mathbf{r}_j)$ is equal to 1 for $i = j$, and vanishes otherwise.

The use of discrete Fourier transform with respect to the wave vector \mathbf{k} allows to obtain the solution in the following form:

$$T = T_F + T_S, \tag{24.28}$$

where T_F is determined by formula (24.15), and it is responsible for transient processes (see Sect. 24.3.1.2). The second summand T_S describes the large-time behavior, and it is equal to

$$T_S = \frac{1}{2} \int_{\mathbf{k}} T_0(\mathbf{r} + \mathbf{c}(\mathbf{k})t) d\mathbf{k}, \tag{24.29}$$

where $\mathbf{c}(\mathbf{k}) = d\omega/d\mathbf{k}$ is the group velocity.

Thus, formulae (24.15), (24.28), (24.29) fully describe the behavior of the kinetic temperature at both short and large times. They show, in particular, that at large times the temperature field is represented as the superposition of waves traveling with group velocities $\mathbf{c}(\mathbf{k})$.

24.4.1.1 Hooke’s Crystal

As discussed before in Sect. 24.3.1.2, one-dimensional lattice is a particular case of scalar lattices, so the formula (24.29) is applicable for this case.

The solution for an infinite Hooke’s crystal is given by [61, 64]

$$T(t, x) = \frac{1}{\pi} \int_{-1}^1 \frac{T_0(x - cts)}{\sqrt{1 - s^2}} ds = \frac{1}{\pi} \int_0^\pi T_0(x + ct \cos \varphi) d\varphi. \tag{24.30}$$

This solution is analyzed in [111] for two examples of the localized ($-l \leq x \leq l$) initial temperature distribution and compared with the classical heat conduction results. The comparison for the rectangular initial perturbation is shown in Fig. 24.9. The ballistic solution has two strongly pronounced peaks traveling in the positive and negative directions with speed c , whereas the classical solution demonstrates the exponential decay of the single peak in the center.

In [65] the asymptotics for the heat wave described by the ballistic heat transfer Eq. (24.30) is analyzed for several examples of the initial temperature distribution localized in space. The solution in the vicinity of wavefront takes the simple form

$$T\left(t, \frac{x - ct}{l}\right) = \frac{\sqrt{2l}}{\pi \sqrt{ct}} \begin{cases} \int_0^{\sqrt{1-(x-ct)/l}} T_0\left(\frac{x - ct}{l} + p^2\right) dp, & -l \leq x - ct \leq l \\ \int_{\sqrt{-1-(x-ct)/l}}^{\sqrt{1-(x-ct)/l}} T_0\left(\frac{x - ct}{l} + p^2\right) dp, & x - ct \leq -l \end{cases} \tag{24.31}$$

This formula shows that the main part of the wave is located in a space region of the same size as the initial localization zone. The thermal wave shrinks vertically as

the square root of time, whereas in the horizontal direction its shape, characterized by the integral, remains unchanged. In addition, it can be demonstrated that during the wave evolution, the wavefront smoothes, e.g., for a power-law dependence, its degree increases by $1/2$.

24.4.1.2 Modifications of the One-Dimensional Crystal Model

The effect of the *elastic foundation* on the ballistic heat transfer is discussed in [66], namely, it is shown that in this case the rate of heat transfer is lower than that in the crystal without substrate.

The influence of *damping* and *energy supply* is taken into account in [24]. The respective temperature profiles are obtained analytically and analyzed, e.g. it is shown that the steady-state kinetic temperature distribution caused by a point source of constant intensity is described by the Macdonald function of zero order.

Another modification is the account for the *interaction with the second neighbors* on the crystal lattice [85, 86]. It is shown that the initial thermal perturbation evolves into two consecutive thermal waves propagating with finite and essentially different velocities (see Fig. 24.10a). The velocity of the first front corresponds to the maximum group velocity of the discrete crystalline model. The velocity of the second front is determined by the second group velocity extremum, which arises at a certain ratio between the stiffnesses of the first and second neighbor interaction in the lattice.

To conclude this section, we move away from the scalar lattices concept and mention the generalization of formula (24.29) for the case of one-dimensional crystal with alternating masses or stiffnesses [74, 86, 96] (an arbitrary polyatomic lattice is considered in Sect. 24.4.2):

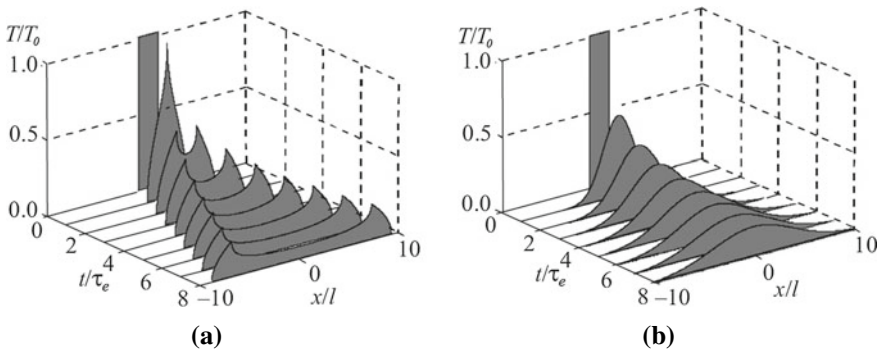


Fig. 24.9 Evolution of the solutions for a rectangular initial perturbation: (a) ballistic and (b) Fourier heat transfer [111]

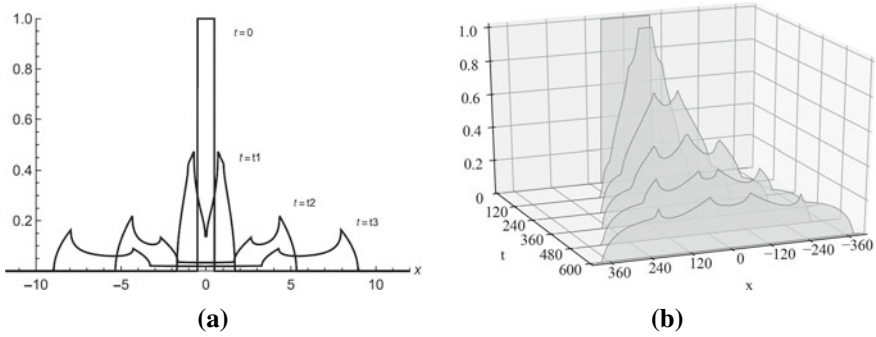


Fig. 24.10 Evolution of the solutions for a rectangular initial perturbation: (a) with regard for the second neighbor interaction [85] and (b) with alternating masses/stiffnesses [96] (for certain parameters)

$$T_S = \frac{1}{2M} \sum_{j=1}^M \int_{\mathbf{k}} T_0(x + c_j(k)t) d\mathbf{k}, \tag{24.32}$$

where M is the number of degrees of freedom in the unit cell, and c_j are the respective group velocities ($j = 1 \dots M$). Formula (24.32) is valid for all one-dimensional harmonic crystals with arbitrary M . In paper [86] it is applied to the diatomic chain. An analytical approach, that allows to identify the thermal wavefront intensity, is proposed. It is demonstrated that, for any ratios between the masses/stiffnesses, the initial thermal perturbation propagates as two successive thermal fronts having finite speeds and repeating the shape of the initial perturbation (see Fig. 24.10b). The speed of the first front corresponds to the acoustic branch of the dispersion relation, and the speed of the second front corresponds to the optical one. In the case when the particle masses differ slightly, the intensity coefficient of the acoustic front is maximum, and the optic front decays, continuing to move at non-zero speed.

24.4.1.3 Two-Dimensional Crystal

The analytical solution of the planar heat transport problem for the stretched square lattice is given in [72].

Figure 24.11a clearly shows two thermal waves traveling in the opposite directions. The peaks of the temperature distribution move with constant speed. Figure 24.11b demonstrates how the heat flows from “cold” (center) to “hot” (peaks).

The influence of the dissipation and heat supply is discussed in [25]. The differential-difference equation describing non-stationary heat propagation in the lattice and the analytical formula in the integral form describing the steady-state kinetic temperature distribution in the lattice caused by a point heat source of a constant intensity are derived.

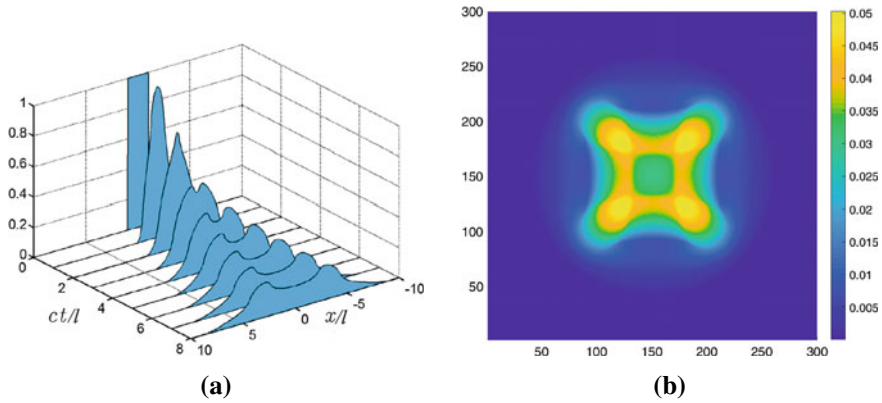


Fig. 24.11 Scalar square lattice [72]: (a) evolution of rectangular initial temperature distribution and (b) evolution of a circular initial temperature distribution (initial temperature is uniform inside a circle with radius $20a$, and the scale is normalized to the initial temperature value at the center)

24.4.2 Polyatomic Lattices

This section is concluded by the results on heat transfer in polyatomic lattices. The explicit problem statement and respective derivation are given in [74]. We write out the main result, i.e., the approximate formula for the *temperature matrix*:

$$\begin{aligned}
 T &= T_F + T_S, & T_F &\approx \int_{\mathbf{k}} \tilde{P} \tilde{T}_F P^* \mathrm{d}\mathbf{k}, & T_S &\approx \int_{\mathbf{k}} \tilde{P} \tilde{T}_S P^* \mathrm{d}\mathbf{k}, \\
 \{\tilde{T}_F\}_{ij} &= \frac{1}{2} \left\{ P^{*\mathrm{T}} T_0(\mathbf{r}) P \right\}_{ij} \left[\cos((\omega_i + \omega_j) t) + (1 - \delta_{ij}) \cos((\omega_i - \omega_j) t) \right], \\
 \{\tilde{T}_S\}_{ij} &= \frac{1}{4} \left\{ P^{*\mathrm{T}} \left(T_0(\mathbf{r} + \mathbf{c}_j t) + T_0(\mathbf{r} - \mathbf{c}_j t) \right) P \right\}_{jj} \delta_{ij},
 \end{aligned} \tag{24.33}$$

Here $\mathbf{P} = \mathbf{P}(\mathbf{k})$ is the polarization matrix which consists of normalized eigenvectors of the lattice dynamic matrix, $\mathbf{c}_j(\mathbf{k})$ is the group velocity vector which corresponds to the j th branch of dispersion relation $\omega_j(\mathbf{k})$, and $T_0(\mathbf{r})$ is the initial temperature matrix of the unit cell.

The first term, T_F , in formula (24.33) describes short-time behavior of the temperature matrix (fast process). At short times, the temperature matrix oscillates. The oscillations are caused by redistribution of energy among kinetic and potential forms and redistribution of energy among degrees of freedom of the unit cell. These oscillations at different spatial points are independent. At large time scale T_F tends to zero. The second term, T_S , in formula (24.33) describes the large time behavior of the temperature matrix (slow process). At large time scale, changes in the temperature profile are caused by ballistic heat transport. The temperature matrix is represented as a superposition of waves traveling with group velocities. Shapes of the waves are

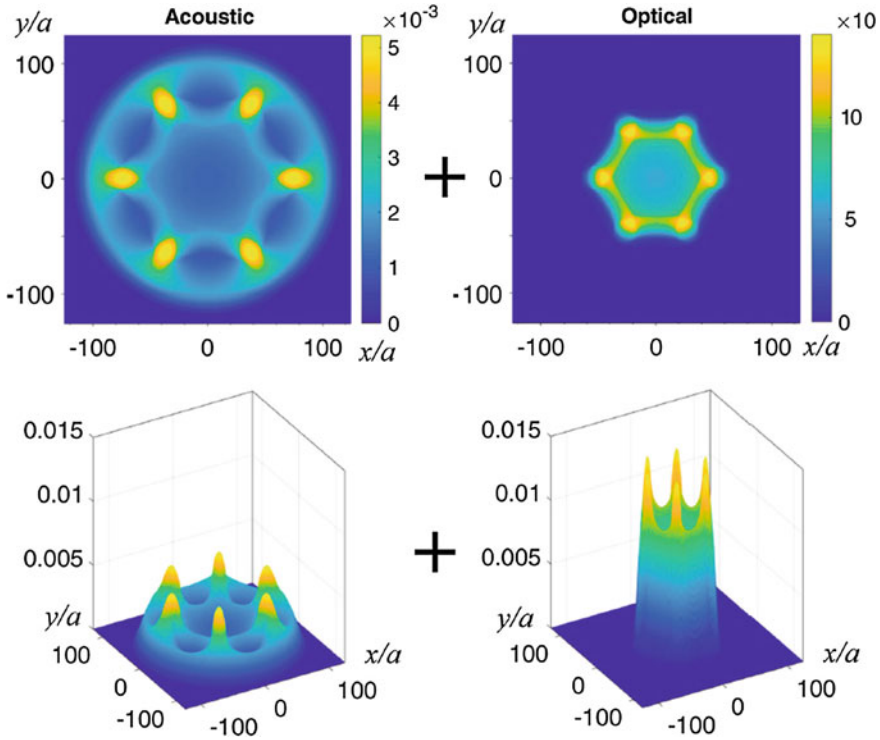


Fig. 24.12 Contributions of acoustic (left) and optical (right) vibrations to temperature profile in graphene at large time. The initial temperature is distributed inside a circle with a radius $10a$. Plus signs mean that the resulting temperature profile is equal to a sum of acoustic and optical contributions. Color bars show the ratio between current and initial temperatures [74]

determined by initial temperature profile T_0 . Note that according to formula (24.33), accurate description of ballistic heat transport requires knowledge of the dispersion relation and corresponding group velocities. It is noteworthy that the local values of temperatures, corresponding to the degrees of freedom of the unit cell, at large times are generally neither equal to each other nor equal to their equilibrium values (temperature matrix is generally not isotropic). Therefore, the thermal state of unit cells reached by thermal waves is strongly non-equilibrium. In [74] this fact is demonstrated for the chain with alternating masses.

As in Sect. 24.3.1.3, we again restrict ourselves by the graphic results for one-dimensional lattice with alternating masses and stiffnesses (Fig. 24.10) and for the out-of-plane vibrations of graphene (Fig. 24.12).

Consider the evolution of circular initial temperature profile in graphene [74]. Corresponding temperature field at $t = 20\tau_e$ is shown in Fig. 24.12. The figure shows, in particular, that the heat front is a circle as predicted by the derived formulae and the Huygens principle. At the same time, the temperature field has a symmetry of

the lattice, i.e., the heat transport is *strongly anisotropic*. Moreover, the temperature field has contributions from acoustic and optical branches of the dispersion relation. Acoustic waves have larger group velocities than optical waves; therefore, the temperature front on the left-hand side propagates faster than that on the right-hand side. We note that the temperature has a local minimum at the center. Therefore, the heat flows from “cold” to “hot”.

24.4.3 The Influence of Nonlinearity

We conclude this section by investigating the effect of anharmonicity on heat transfer. As an example, we consider equilibration of a sinusoidal modulation of temperature in the β -Fermi-Pasta-Ulam-Tsingou (FPUT) chain [57]. In this system, the particles are connected to their nearest neighbors by the potential, which includes the quadratic term with the harmonic constant C and the quartic term with the anharmonic constant β .

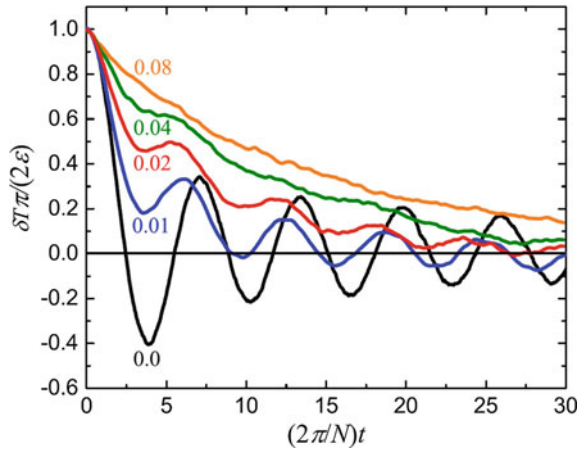
The results for different values of the anharmonicity parameter β and for different wavelengths of temperature modulation were obtained numerically and compared to the analytical solution available for the linear case, i.e., $\beta = 0$ (see formula 24.30). Also, the applicability of the linear theory to a weakly nonlinear chain was assessed for different wavelengths of temperature modulation. The initial conditions of two types were used: (i) at $t = 0$, the energy of the system is in the form of kinetic energy with zero potential energy and (ii) the other major part of the energy is initially shared between kinetic and potential energies.

Firstly, for the linear chain ($\beta = 0$), the numerical results averaged over an increasing number of realizations converged to the analytical solution. This solution predicts that equilibration of a sinusoidal modulation of temperature demonstrates oscillations with a decrease in time amplitude, following the Bessel function of the first kind. This was true for the initial conditions of both types, though convergence with an increasing number of realizations was faster for the initial conditions with nearly equal kinetic and potential energies. Convergence was also faster for a larger wavelength of temperature modulation. The kinetics of temperature equilibration, for increasing number of realizations, converges not only for the harmonic chain but also for $\beta > 0$.

Secondly, with an increase in the degree of anharmonicity, the oscillatory equilibration of temperature gradually transforms into a monotonic one. For a given temperature wavelength modulation, there exists a value of the anharmonicity parameter when the temperature equilibration occurs most rapidly. For smaller values of β , oscillations of temperature decay slowly, and for larger β , the monotonic decay is slow (see Fig. 24.13).

Thirdly, the linear theory remains informative for weakly anharmonic chains when β is smaller than a certain critical value, which decreases with increasing temperature modulation wavelength. This means that temperature modulation with short wavelength is less affected by the anharmonicity or, in other words, the linear theory

Fig. 24.13 Normalized difference between the averaged temperatures of the left and right halves of the chain, δT , as a function of normalized time for different values of the nonlinearity parameter β ; the chain consists of $N = 32768$ particles [57]



remains valid for larger values of β , as compared to the long-wavelength temperature modulation.

Overall, these results have confirmed that (i) the continuum equation derived in [61] accurately describes the temperature flow in linear chains, (ii) linear theory remains informative for weakly anharmonic chains, and (iii) short-wavelength modulations of temperature are less affected by the anharmonicity and linear theory remains valid for larger values of β , as compared to the long-wavelength modulations of temperature.

In this regard, the results presented in previous works, e.g., [27] have found their explanation. Oscillations of the short-wavelength sinusoidal temperature modulation, observed by the authors of those works, can be well explained by the linear theory [61]. The oscillations were not observed by the authors for long-wavelength temperature modulation because, in this case, the effect of anharmonicity is much stronger. The oscillations of long-wavelength temperature modulation can be observed for smaller values of the anharmonicity parameter.

24.5 Thermoelasticity: Ballistic Resonance in FPUT Chain

The previous sections dealt mostly with crystalline solids with linear interactions between the particles. The considered linear models allow an analytical description of elasticity, transient thermal processes, and heat energy transfer (thermal conduction) in crystalline solids. However, they are unsuitable for describing thermoelastic effects such as thermal expansion or the conversion of mechanical energy into thermal energy. In this section, we address some effects caused by nonlinearity of interatomic interaction.

In [63] one-dimensional chains with pair force interactions are considered. Using the approach proposed in [59], the continualization of the dynamics and energy balance equations is carried out. As a result, the coupled thermoelasticity equations for a chain are obtained. As an example, we consider the well-known α -Fermi-Pasta-Ulam-Tsingou (FPUT) model [21], a one-dimensional chain with quadratic nonlinearity. All of the aforementioned thermomechanical processes can be qualitatively described by this model. Despite the apparent simplicity of the model, the analytical description of the macroscopic thermoelastic processes, thermal conductivity, and the transition of mechanical energy into thermal energy seems to be a very difficult and yet unsolved problem. The FPUT chain demonstrates anomalous thermomechanical properties. It is shown in [16, 17, 27, 117] that the heat conduction in the FPUT chain is represented neither by the Fourier law nor by the Maxwell-Cattaneo equation. In the limiting case of large times and infinitely long chain, the heat conduction is described by the equation with fractional derivatives [89]. However, this model does not capture the quasi-ballistic heat transfer typical for small times and chains of finite length. Therefore, the results obtained in Sect. 24.4 are used to describe the quasi-ballistic heat conduction regime.

An even more complicated problem is the description of the transition of mechanical energy into thermal energy. This process is in charge, in particular, of the damping of macroscopic mechanical vibrations of the chain. The study of the decay of mechanical vibrations of the FPUT chain has a long history, beginning with the pioneering work of Fermi, Past, and Ulam [21]. In [21], the initial conditions corresponding to the excitation of the first eigenmode of the chain were considered. It was shown numerically that the oscillations damping occurs non-monotonically: the decay and growth of the energy of mechanical oscillations alternate. In the literature, this effect is often referred to as *Fermi-Pasta-Ulam-Tsingou recurrence paradox* (see, for example, [22] for the review of the works aimed at explaining this paradox). Note that in the formulation proposed in the original paper [21], the oscillations were considered at zero initial temperature. In what follows, it is shown that the introduction of a finite temperature (random particle velocities) allows us to provide a monotonic damping of mechanical energy [76].

In this section, we describe thermomechanical phenomena observed in the α -FPUT chain with a spatially sinusoidal profile of initial temperature [76]. Firstly, it is shown analytically that temperature oscillations, caused by quasiballistic heat transport, and thermal expansion give rise to mechanical vibrations with growing amplitude. This new phenomenon is referred to as *ballistic resonance* [76]. Secondly, it is demonstrated numerically that mechanical vibrations, excited by the ballistic resonance, decay monotonically in time. Therefore at finite temperatures the FPUT recurrence paradox is eliminated.

Consider the equations of motion of α -FPUT chain under periodic boundary conditions

$$m\ddot{u}_n = C(u_{n+1} - 2u_n + u_{n-1}) + \alpha \left((u_{n+1} - u_n)^2 - (u_n - u_{n-1})^2 \right), \quad (24.34)$$

where the parameter α characterizes nonlinearity. We consider initial conditions, corresponding to spatially sinusoidal kinetic temperature profile, zero initial fluxes, and no macroscopic mechanical motions

$$\begin{aligned} u_n = 0, \quad \dot{u}_n = \sigma_n \sqrt{\frac{2k_B}{m} \left(T_b + \Delta T \sin \frac{2\pi n}{N} \right)}, \\ \langle \sigma_n \rangle = 0, \quad \langle \sigma_n^2 \rangle = 1, \end{aligned} \quad (24.35)$$

where σ_n are uncorrelated random numbers with zero mean and unit variance; T_b is the average (background) temperature; ΔT is an amplitude of the initial temperature profile.

Next, we separate the motions [63]. Mechanical motion is associated with the time evolution of the mathematical expectation of particle displacement, whereas the thermal motion is defined as the difference between the total displacement and the mechanical one. Note that, in contrast to mechanical displacements, the thermal displacements are random.

We assume that the macroscopic mechanical motion of the chain is described by the equation of linear thermoelasticity, as shown in [63], while the behavior of temperature (heat transfer) is described by the ballistic heat Eq. (24.11) [61, 64]. Conversion of mechanical energy to thermal energy is neglected, then the macroscopic behavior of the chain in the continuum limit is described by the system of equations

$$\ddot{u} = c_S^2 (u'' - \beta T'), \quad \ddot{T} + \frac{1}{t} \dot{T} = c_S^2 T'', \quad (24.36)$$

where c_S is the speed of sound and β is the thermal expansion coefficient. Note that both macroscopic equations are derived from the equations of motion (24.34). Anharmonic effects are taken into account only in the equation for the displacements, whereas the second one is derived using harmonic approximation, therefore it corresponds to the purely ballistic heat transport regime.

Substituting the solution of the ballistic heat equation with initial conditions, corresponding to *sinusoidal* initial perturbation [61], into the dynamics Eq. (24.36), we obtain

$$\ddot{u} = c_S^2 u'' - \lambda c_S^2 \beta \Delta T J_0(\omega t) \cos \lambda x, \quad (24.37)$$

where $\lambda = 2\pi/L$, L is the chain length, $\omega = \lambda c_S$.

It can be seen that the temperature acts as an external force, exciting the first normal mode of mechanical vibrations. From the properties of Bessel function it follows that the external force oscillates with frequency ω and decays as $1/\sqrt{t}$. Note that the frequency coincides with the first eigenfrequency of mechanical vibrations.

The solution of (24.37) yields an exact expression for displacements

$$u(x, t) = z(t) \cos \lambda x, \quad z(t) = -\frac{\beta \Delta T \omega t}{\lambda} J_1(\omega t). \quad (24.38)$$

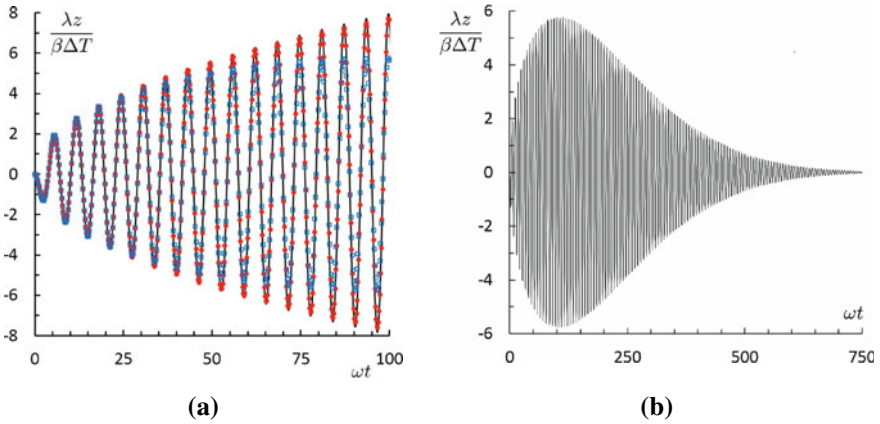


Fig. 24.14 **a** Growth of mechanical vibrations amplitude due to ballistic resonance: analytical solution (solid line) and numerical results for $\alpha a/C = -0.25$ (circles) and $\alpha a/C = -1$ (squares); **b** decay of mechanical vibrations amplitude for large times (numerical results, $\alpha a/C = -1$) [76]

At large times, the amplitude of displacement grows as a square root of time

$$z(t) \simeq -\sqrt{\frac{2}{\pi}} \frac{\beta \Delta T}{\lambda} \sqrt{\omega t} \cos\left(\omega t - \frac{3\pi}{4}\right). \quad (24.39)$$

The time dependence of the amplitude of mechanical vibrations $z(t)$ is presented in Fig. 24.14a. It can be seen that the amplitude grows in time, as described by the analytical solution (24.38). Thus the coincidence of a frequency of temperature oscillations with the first eigenfrequency of the chain leads to excitation of mechanical vibrations with growing amplitude. This phenomenon is referred to as *ballistic resonance* [76]. Note that, in contrast to the conventional mechanical resonance, the ballistic resonance occurs in the closed system without any external excitation. It is caused by conversion of thermal energy to mechanical energy.

Numerical simulations show that mechanical vibrations, excited by the ballistic resonance, decay in time (see Fig. 24.14b). The decay is caused by thermalization, i.e., conversion of mechanical energy to thermal energy. This process is not covered by our continuum model (24.36). The simulation results show that the mechanical oscillations arising at resonance decay monotonically. Therefore, the classical FPUT paradox is not observed at the finite temperature. In our calculations, the mechanical energy of the system is significantly lower than the thermal energy. It seems that this condition is necessary for monotonic decay. However, a rigorous proof of this statement requires further investigations.

24.6 Concluding Remarks

This paper summarizes the current status of research on discrete thermomechanics carried out in the Institute for Problems in Mechanical Engineering of the Russian Academy of Sciences. The main achievement is an approach for the analytical description of unsteady thermomechanical processes in perfect crystals in continuum approximation. The approach allows to describe the transition to thermal equilibrium, ballistic heat transfer, heat supply, propagation of thermoelastic waves, and other non-equilibrium processes in perfect crystals. One, two, and three-dimensional perfect crystals with arbitrary harmonic and weakly anharmonic interactions are considered. The approach predicts the existence of many peculiar thermomechanical phenomena, including but not limited to thermal waves, heat flow from cold to hot, several kinetic temperatures, thermal echo, and ballistic resonance. Still, we believe that many phenomena are yet to be discovered.

However, despite the significant progress in describing and understanding thermomechanical processes, many questions remain open. Let us briefly mention some aspects of the approach that require additional investigation.

- The relation between the kinetic temperature, defined above, and other definitions of temperature available in the literature is not straightforward. Which of these temperatures is the best parameter for the description of the thermal state of a non-equilibrium system? This question requires a separate discussion.
- Some of the presented results (e.g., heat flowing from cold to hot) seem to contradict the second law of thermodynamics. We refer to papers [62, 112] for further discussion of this important issue.
- Many of the results have been obtained for one particular type of initial conditions, namely random initial velocities and zero displacements. These initial conditions are the simplest model of a heat impact on a system. How well does this model describe the crystal heating, e.g., by a short laser pulse?
- The results have been mostly obtained in the harmonic approximation. What is the range of applicability of this approximation for real materials? To what extent can quantum effects be ignored inside this range?
- Kinetic theory is a powerful tool for the description of the thermomechanical processes in discrete systems. In some cases, the kinetic approach can be derived from the dynamical description [77]. However, in general, the establishment of this link is still connected with a number of open questions.

We are planning to address these fundamental questions in our future work.

Acknowledgements The authors acknowledge the financial support of this work by the Russian Foundation for Basic Research (A.M. Krivtsov, project No.19-01-00633; V.A. Kuzkin and E.A. Podolskaya, project No.20-37-70058).

References

1. Abramyan, A.K., Bessonov, N.M., Mirantsev, L.V., Reinberg, N.A.: Influence of liquid environment and bounding wall structure on fluid flow through carbon nanotubes. *Phys. Lett. A* **379**, 1274–1282 (2015)
2. Allen, M.P., Tildesley, D.J.: *Computer Simulation of Liquids*. Clarendon Press, Oxford (1987)
3. Anisimov, S.I., Zhakhovskii, V.V., Fortov, V.E.: Shock wave structure in simple liquids. *JETP Lett.* **65**(9), 722–727 (1997)
4. Ashcroft, N., Mermin, N.: *Solid State Physics*. Saunders College Publishing, Philadelphia (1976)
5. Babenkov, M.B., Krivtsov, A.M., Tsvetkov, D.V.: Energy oscillations in 1D harmonic crystal on elastic foundation. *Phys. Mesomech.* **19**(1), 60–67 (2016)
6. Balandin, A.A.: Thermal properties of graphene and nanostructured carbon materials. *Nat. Mater.* **10**, 569–581 (2011)
7. Barani, E., Lobzenko, I.P., Korznikova, E.A., Soboleva, E.G., Dmitriev, S.V., Zhou, K., Marjaneh, A.M.: Transverse discrete breathers in unstrained graphene. *Eur. Phys. J. B* **90**(3), 1–5 (2017)
8. Berinskii, I.E., Kuzkin, V.A.: Equilibration of energies in a two-dimensional harmonic graphene lattice. *Philos. Trans. R. Soc. A* **378**(2162), 20190114 (2020)
9. Bhatnagar, P.L., Gross, E.P., Krook, M.: A model for collision processes in gases. I. Small amplitude processes in charged and neutral one-component systems. *Phys. Rev.* **94**(3), 511–525 (1954)
10. Boldrighini, C., Pellegrinotti, A., Triolo, L.: Convergence to stationary states for infinite harmonic systems. *J. Stat. Phys.* **30**(1), 123–155 (1983)
11. Casas-Vazquez, J., Jou, D.: Temperature in non-equilibrium states: a review of open problems and current proposals. *Rep. Prog. Phys.* **66**, 1937–2023 (2003)
12. Casher, A., Lebowitz, J.L.: Heat flow in regular and disordered harmonic chains. *J. Math. Phys.* **12**, 1701–1711 (1971)
13. Chandrasekharaiah, D.S.: Hyperbolic thermoelasticity: a review of recent literature. *Appl. Mech. Rev.* **39**, 355–376 (1986)
14. Chang, C.W., Okawa, D., Garcia, H., Majumdar, A., Zettl, A.: Breakdown of Fourier's law in nanotube thermal conductors. *Phys. Rev. Lett.* **101**, 075903 (2008)
15. Chen, G.: Ballistic-diffusive heat conduction equations. *Phys. Rev. Lett.* **85**, 2297–2300 (2001)
16. Das, S.G., Dhar, A., Narayan, O.: Heat conduction in the $\alpha - \beta$ Fermi-Pasta-Ulam chain. *J. Stat. Phys.* **154**(1–2), 204–213 (2014)
17. Das, S.G., Dhar, A., Saito, K., Mendl, C.B., Spohn, H.: Numerical test of hydrodynamic fluctuation theory in the Fermi-Pasta-Ulam chain. *Phys. Rev. E* **90**(1), 012124 (2014)
18. Dhar, A.: Heat transport in low-dimensional systems. *Adv. Phys.* **57**, 457–537 (2008)
19. Dhar, A., Saito, K.: Heat Transport in Harmonic Systems. In: Lepri, S. (ed.) *Thermal transport in low dimensions. Lecture Notes in Physics* **921**, 305–338 (2016)
20. Dudnikova, T.V., Komech, A.I., Spohn, H.: On the convergence to statistical equilibrium for harmonic crystals. *J. Math. Phys.* **44**, 2596–2620 (2003)
21. Fermi, E., Pasta, J., Ulam, S.: Studies of nonlinear problems. Document LA 1940. Los Alamos National Laboratory (1955)
22. The Fermi-Pasta-Ulam problem: a status report. In: Gallavotti, G. (ed.) *Lecture Notes in Physics*, vol. 728 (2008)
23. Gavrilov, S.N., Krivtsov, A.M.: Thermal equilibration in a one-dimensional damped harmonic crystal. *Phys. Rev. E* **100**, 022117 (2019)
24. Gavrilov, S.N., Krivtsov, A.M., Tsvetkov, D.V.: Heat transfer in a one-dimensional harmonic crystal in a viscous environment subjected to an external heat supply. *Contin. Mech. Thermodyn.* **31**(1), 255–272 (2019)
25. Gavrilov, S.N., Krivtsov, A.M.: Steady-state kinetic temperature distribution in a two-dimensional square harmonic scalar lattice lying in a viscous environment and subjected to a point heat source. *Contin. Mech. Thermodyn.* **32**(1), 41–61 (2020)

26. Gendelman, O.V., Savin, A.V.: Normal heat conductivity of the one-dimensional lattice with periodic potential of nearest-neighbor interaction. *Phys. Rev. Lett.* **84**(11), 2381–2384 (2000)
27. Gendelman, O.V., Savin, A.V.: Nonstationary heat conduction in one-dimensional chains with conserved momentum. *Phys. Rev. E* **81**, 020103 (2010)
28. Goldstein, R.V., Morozov, N.F.: Mechanics of deformation and fracture of nanomaterials and nanotechnology. *Phys. Mesomech.* **10**(5–6), 235–246 (2007)
29. Golovnev, I.F., Golovneva, E.I., Konev, A.A., Fomin, V.M.: Physical mesomechanics and molecular dynamic modeling. *Phys. Mesomech.* **1**(2), 19 (1998)
30. Golovneva, E.I., Golovnev, I.F., Fomin, V.M.: Simulation of quasistatic processes in crystals by a molecular dynamics method. *Phys. Mesomech.* **6**(5–6), 41–46 (2003)
31. Guo, P., Gong, J., Sadasivam, S., Xia, Y., Song, T.-B., Diroll, B.T., Stoumpos, C.C., Ketterson, J.B., Kanatzidis, M.G., Chan, M.K.Y., Darancet, P., Xu, T., Schaller, R.D.: Slow thermal equilibration in methylammonium lead iodide revealed by transient mid-infrared spectroscopy. *Nat. Commun.* **9**, 2792 (2018)
32. Guzev, M.A.: The exact formula for the temperature of a one-dimensional crystal. *Dalnevost. Mat. Zh.* **18**, 39–47 (2018)
33. Harris, L., Lukkarinen, J., Teufel, S., Theil, F.: Energy transport by acoustic modes of harmonic lattices. *SIAM J. Math. Anal.* **40**(4), 1392–1418 (2008)
34. Hemmer, P.C.: Dynamic and stochastic types of motion in the linear chain. *Norges Tekniske Hoiskole* (1959)
35. Holian, B.L., Hoover, W.G., Moran, B., Straub, G.K.: Shock-wave structure via nonequilibrium molecular dynamics and Navier–Stokes continuum mechanics. *Phys. Rev. A* **22**, 2798 (1980)
36. Holian, B.L., Mareschal, M.: Heat-flow equation motivated by the ideal-gas shock wave. *Phys. Rev. E* **82**, 026707 (2010)
37. Hoover, W.G., Hoover, C.G., Travis, K.P.: Shock-wave compression and Joule–Thomson expansion. *Phys. Rev. Lett.* **112**, 144504 (2014)
38. Hoover, W.G.: Computational statistical mechanics. *Studies in modern thermodynamics*. Elsevier Science (1991)
39. Hsiao, T.K., Chang, H.K., Liou, S.-C., Chu, M.-W., Lee, S.-C., Chang, C.-W.: Observation of room-temperature ballistic thermal conduction persisting over 8.3 μm SiGe nanowires. *Nat. Nanotechnol.* **8**(7), 534–538 (2013)
40. Hua, C., Minnich, A.J.: Transport regimes in quasiballistic heat conduction. *Phys. Rev. B* **89**, 094302 (2014)
41. Huberman, S., Duncan, R.A., Chen, K., Song, B., Chiloyan, V., Ding, Z., Maznev, A.A., Chen, G., Nelson, K.A.: Observation of second sound in graphite at temperatures above 100 K. *Science* **364**(6438), 375–379 (2019)
42. Huerta, M.A., Robertson, M.A.: Exact equilibration of harmonically bound oscillator chains. *J. Math. Phys.* **12**, 2305–2311 (1971)
43. Indeitsev, D.A., Naumov, V.N., Semenov, B.N., Belyaev, A.K.: Thermoelastic waves in a continuum with complex structure. *ZAMM* **89**, 279–287 (2009)
44. Indeitsev, D.A., Osipova, E.V.: A two-temperature model of optical excitation of acoustic waves in conductors. *Dokl. Phys.* **62**(3), 136–140 (2017)
45. Inogamov, N.A., Petrov, Yu.V., Zhakhovsky, V.V., Khokhlov, V.A., Demaske, B.J., Ashitkov, S.I., Khishchenko, K.V., Migdal, K.P., Agranat, M.B., Anisimov, S.I., Fortov, V.E., Oleynik, I.I.: Two-temperature thermodynamic and kinetic properties of transition metals irradiated by femtosecond lasers. *AIP Conf. Proc.* **1464**(1), 593–608 (2012)
46. Ivanova, E.A., Krivtsov, A.M., Morozov, N.F.: Bending stiffness calculation for nanosize structures. *Fatigue Fract. Eng. Mater. Struct.* **26**, 715–718 (2003)
47. Ivanova, E.A., Krivtsov, A.M., Morozov, N.F., Firsova, A.D.: Description of crystal packing of particles with torque interaction. *Mech. Solids* **38**(4), 76–88 (2003)
48. Ivanova, E.A.: On a micropolar continuum approach to some problems of thermo- and electro-dynamics. *Acta Mech.* **230**(5), 1685–1715 (2019)

49. Johnson, J.A., Maznev, A.A., Cuffe, J., Eliason, J.K., Minnich, A.J., Kehoe, T., Sotomayor Torres, C.M., Chen, G., Nelson, K.A.: Direct measurement of room-temperature nondiffusive thermal transport over micron distances in a silicon membrane. *Phys. Rev. Lett.* **110**, 025901 (2013)
50. Kannan, V., Dhar, A., Lebowitz, J.L.: Nonequilibrium stationary state of a harmonic crystal with alternating masses. *Phys. Rev. E* **85**, 041118 (2012)
51. Kato, A., Jou, D.: Breaking of equipartition in one-dimensional heat-conducting systems. *Phys. Rev. E* **64**, 052201 (2001)
52. Klein, G.: Prigogine, I. Sur la mecanique statistique des phenomenes irreversibles III. *Physica* **19**, 1053 (1953)
53. Klemens, P.G.: The thermal conductivity of dielectric solids at low temperatures. *Proc. R. Soc. A* **208**(1092), 108–133 (1951)
54. Koh, Y.K., Cahill, D.G., Sun, B.: Nonlocal theory for heat transport at high frequencies. *Phys. Rev. B* **90**(20), 205412 (2014)
55. Korikov, D.V.: Asymptotic description of fast thermal processes in scalar harmonic lattices. *Phys. Solid State* **62**(11), 2232–2241 (2020)
56. Korobeynikov, S.N.: Nonlinear equations of deformation of atomic lattices. *Arch. Mech.* **57**(6), 435–453 (2005)
57. Korznikova, E.A., Kuzkin, V.A., Krivtsov, A.M., Xiong, D., Gani, V.A., Kudreyko, A.A., Dmitriev, S.V.: Equilibration of sinusoidal modulation of temperature in linear and nonlinear chains. *Phys. Rev. E* **102**(4), 062148(6) (2020)
58. Kosevich, Y.A., Savin, A.V.: Confining interparticle potential makes both heat transport and energy diffusion anomalous in one-dimensional phononic systems. *Phys. Lett. A* **380**, 3480–3484 (2016)
59. Krivtsov, A.M.: *Deformation and Fracture of Solids with Microstructure*. Fizmatlit, Moscow (2007). [in Russian]
60. Krivtsov, A.M.: Energy oscillations in a one-dimensional crystal. *Dokl. Phys.* **59**(9), 427–430 (2014)
61. Krivtsov, A.M.: Heat transfer in infinite harmonic one dimensional crystals. *Dokl. Phys.* **60**(9), 407–411 (2015)
62. Krivtsov, A.M., Sokolov, A.A., Müller, W.H., Freidin, A.B.: One-dimensional heat conduction and entropy production. *Adv. Struct. Mater.* **87**, 197–213 (2018)
63. Krivtsov, A.M., Kuzkin, V.A.: Discrete and continuum thermomechanics. In: Altenbach, H., Öchsner, A. (eds.) *Encyclopedia of Continuum Mechanics*. Springer, Berlin, Heidelberg (2018)
64. Krivtsov, A.M.: The ballistic heat equation for a one-dimensional harmonic crystal. In: Altenbach, H., Belyaev, A., Eremeyev, V.A., Krivtsov, A.M., Porubov, A.V. (eds.) *Dynamical Processes in Generalized Continua and Structures*. Springer, Berlin (2019)
65. Krivtsov, A.M., Podolskaya, E.A., Shubina, V.Y.: Asymptotics of a thermal wave in a one-dimensional harmonic crystal. *Mater. Phys. Mech.* **42**, 837–845 (2019)
66. Krivtsov, A.M., Babenkov, M.B., Tsvetkov, D.V.: Heat propagation in a one-dimensional harmonic crystal on an elastic foundation. *Phys. Mesomech.* **23**(2), 109–119 (2020)
67. Kuksin, A.Yu., Morozov, I.V., Norman, G.E., Stegailov, V.V., Valuev, I.A.: Standard of molecular dynamics modelling and simulation of relaxation. *Mol. Simul.* **31**, 1005–1017 (2005)
68. Kukushkin, S.A.: Evolution processes in multicomponent and multiphase films. *Thin Solid Films* **207**(1–2), 302–312 (1992)
69. Kukushkin, S.A., Osipov, A.V., Telyatnik, R.S.: Elastic interaction of point defects in cubic and hexagonal crystals. *Phys. Solid State* **58**(5), 971–980 (2016)
70. Kuzkin, V.A., Krivtsov, A.M.: High-frequency thermal processes in harmonic crystals. *Dokl. Phys.* **62**(2), 85–89 (2017)
71. Kuzkin, V.A., Krivtsov, A.M.: An analytical description of transient thermal processes in harmonic crystals. *Phys. Solid State* **59**(5), 1051–1062 (2017)
72. Kuzkin, V.A., Krivtsov, A.M.: Fast and slow thermal processes in harmonic scalar lattices. *J. Phys.: Condens. Matter* **29**, 505401 (2017)

73. Kuzkin, V.A.: Thermal equilibration in infinite harmonic crystals. *Contin. Mech. Thermodyn.* **31**, 1401–1423 (2019)
74. Kuzkin, V.A.: Unsteady ballistic heat transport in harmonic crystals with polyatomic unit cell. *Contin. Mech. Thermodyn.* **31**(6), 1573–1599 (2019)
75. Kuzkin, V.A., Liazhkov, S.D.: Equilibration of kinetic temperatures in face-centered cubic lattices. *Phys. Rev. E* **102**(4), 042219 (2020)
76. Kuzkin, V.A., Krivtsov, A.M.: Ballistic resonance and thermalization in the Fermi-Pasta-Ulam-Tsingou chain at finite temperature. *Phys. Rev. E* **101**, 042209 (2020)
77. Kuzkin, V.A., Krivtsov, A.M.: Unsteady ballistic heat transport: linking lattice dynamics and kinetic theory. *Acta Mech.* **232**(5), 1983–1996 (2021)
78. Lanford, O.E., Lebowitz, J.L.: Time evolution and ergodic properties of harmonic systems. In: Moser, J. (ed.) *Dynamical Systems, Theory and Applications*. Lecture Notes in Physics, vol. 38. Springer, Berlin, Heidelberg (1975)
79. Le-Zakharov, A.A., Krivtsov, A.M.: Molecular dynamics investigation of heat conduction in crystals with defects. *Dokl. Phys.* **53**(5), 261–264 (2008)
80. Le-Zakharov, A.A., Krivtsov, A.M., Porubov, A.V.: Relation between defects and crystalline thermal conduction. *Contin. Mech. Thermodyn.* **31**(6), 1873–1881 (2019)
81. Lepri, S., Livi, R., Politi, A.: Thermal conduction in classical low-dimensional lattices. *Phys. Rep.* **377**, 1–80 (2003)
82. Lepri, S., Mejia-Monasterio, C., Politi, A.: A stochastic model of anomalous heat transport: analytical solution of the steady state. *J. Phys. A* **42**(2), 025001 (2008)
83. Lepri, S., Mejia-Monasterio, C., Politi, A.: Nonequilibrium dynamics of a stochastic model of anomalous heat transport. *J. Phys. A* **43**, 065002 (2010)
84. Linn, S.L., Robertson, H.S.: Thermal energy transport in harmonic systems. *J. Phys. Chem. Solids* **45**(2), 133–140 (1984)
85. Loboda, O.S., Krivtsov, A.M., Porubov, A.V., Tsvetkov, D.V.: Thermal processes in a one-dimensional crystal with regard for the second coordination sphere. *ZAMM* **99**(9), e201900008 (2019)
86. Loboda, O.S., Podolskaya, E.A., Tsvetkov, D.V., Krivtsov, A.M.: On the fundamental solution of the heat transfer problem in one-dimensional harmonic crystals. *Contin. Mech. Thermodyn.* **33**(2), 485–496 (2021)
87. Lomakin, E.V., Lurie, S.A., Belov, P.A., Rabinskiy, L.N.: On the generalized heat conduction laws in the reversible thermodynamics of a continuous medium. *Dokl. Phys.* **63**(12), 503–507 (2018)
88. Lurie, S.A., Belov, P.A.: On the nature of the relaxation time, the Maxwell–Cattaneo and Fourier law in the thermodynamics of a continuous medium, and the scale effects in thermal conductivity. *Contin. Mech. Thermodyn.* **32**, 709–728 (2018)
89. Mellet, A., Merino-Aceituno, S.: Anomalous energy transport in FPU– β chain. *J. Stat. Phys.* **160**, 583–621 (2015)
90. Mielke, A.: Macroscopic behavior of microscopic oscillations in harmonic lattices via Wigner-Husimi transforms. *Arch. Ration. Mech. Anal.* **181**, 401–448 (2006)
91. Murachev, A.S., Krivtsov, A.M., Tsvetkov, D.V.: Thermal echo in a finite one-dimensional harmonic crystal. *J. Phys.: Condens. Matter* **31**(9), 095702 (2019)
92. Muratikov, K.L.: Theory of the generation of mechanical vibrations by laser radiation in solids containing internal stresses on the basis of the thermoelastic effect. *Tech. Phys.* **44**, 792–796 (1999)
93. Norman, G.E., Stegailov, V.V.: Stochastic theory of the classical molecular dynamics method. *Math. Models Comput. Simul.* **5**, 305–333 (2013)
94. Peierls, R.: Zur kinetischen theorie der wärmeleitung in kristallen. *Ann. Phys.* **3**, 1055 (1929)
95. Piazza, F., Lepri, S.: Heat wave propagation in a nonlinear chain. *Phys. Rev. B* **79**, 094306 (2009)
96. Podolskaya, E.A., Krivtsov, A.M., Tsvetkov, D.V.: Anomalous heat transfer in one-dimensional diatomic harmonic crystal. *Mater. Phys. Mech.* **40**, 172–180 (2018)

97. Porubov, A.V., Belyaev, A.K., Polyanskiy, V.A.: Nonlinear hybrid continuum-discrete dynamic model of influence of hydrogen concentration on strength of materials. *Contin. Mech. Thermodyn.* **33**(4), 933–941 (2021)
98. Prigogine, I., Henin, F.: On the general theory of the approach to equilibrium. I: interacting normal modes. *J. Math. Phys.* **1**(5), 349–371 (1960)
99. Psakhie, S.G., Ostermeyer, G.P., Dmitriev, A.I., Shilko, E.V., Smolin, A.Y., Korostelev, S.Y.: Method of movable cellular automata as a new trend of discrete computational mechanics. I: theoretical description. *Phys. Mesomech.* **3**(2), 5–12 (2000)
100. Rieder, Z., Lebowitz, J.L., Lieb, E.: Properties of a harmonic crystal in a stationary nonequilibrium state. *J. Math. Phys.* **8**, 1073–1078 (1967)
101. Rogers, J.A., Maznev, A.A., Banet, M.J., Nelson, K.A.: Optical generation and characterization of acoustic waves in thin films: fundamentals and applications. *Annu. Rev. Mater. Sci.* **30**, 117–157 (2000)
102. Romano, G., Grossman, J.C.: Heat conduction in nanostructured materials predicted by phonon bulk mean free path distribution. *J. Heat Transf.* **137**, 071302 (2015)
103. Saadatmand, D., Xiong, D., Kuzkin, V.A., Krivtsov, A.M., Savin, A.V., Dmitriev, S.V.: Discrete breathers assist energy transfer to AC driven nonlinear chains. *Phys. Rev. E* **97**, 022217 (2018)
104. Savin, A.V., Zolotarevskiy, V., Gendelman, O.V.: Normal heat conductivity in two-dimensional scalar lattices. *EPL* **113**, 24003 (2016)
105. Savin, A.V., Zolotarevskiy, V., Gendelman, O.V.: Heat conduction in diatomic chains with correlated disorder. *Phys. Lett. A* **381**(3), 145–152 (2017)
106. Schrödinger, E.: Zur dynamik elastisch gekoppelter punktsysteme. *Ann. Phys.* **44**, 916–934 (1914)
107. Sinha, S., Goodson, K.E.: Review: multiscale thermal modeling in nanoelectronics. *Int. J. Multiscale Comput. Eng.* **3**(1), 107–133 (2005)
108. Slepyan, L.I.: On the energy partition in oscillations and waves. *Proc. R. Soc. A* **471**, 20140838 (2015)
109. Spohn, H., Lebowitz, J.L.: Stationary non-equilibrium states of infinite harmonic systems. *Commun. Math. Phys.* **54**, 97 (1977)
110. Spohn, H.: The phonon Boltzmann equation, properties and link to weakly anharmonic lattice dynamics. *J. Stat. Phys.* **124**(2), 1041–1104 (2006)
111. Sokolov, A.A., Krivtsov, A.M., Müller, W.H.: Localized heat perturbation in harmonic 1D crystals: solutions for an equation of anomalous heat conduction. *Phys. Mesomech.* **20**(3), 305–310 (2017)
112. Sokolov, A.A., Krivtsov, A.M., Müller, W.H., Vilchevskaya, E.N.: Change of entropy for the one-dimensional ballistic heat equation: sinusoidal initial perturbation. *Phys. Rev. E* **99**(4), 042107 (2019)
113. Tsaplin, V.A., Kuzkin, V.A.: Temperature oscillations in harmonic triangular lattice with random initial velocities. *Lett. Mater.* **8**(1), 16–20 (2018)
114. Titulaer, U.M. Ergodic features of harmonic-oscillator systems. III: asymptotic dynamics of large systems. *Physica* **70**(3), 456–474 (1973)
115. Tzou, D.Y.: *Macro- to microscale heat transfer: the lagging behavior*. Wiley (2014)
116. Uribe, F.J., Velasco, R.M., Garcia-Colin, L.S.: Two kinetic temperature description for shock waves. *Phys. Rev. E* **58**, 3209–3222 (1998)
117. Xiong, D.: Heat perturbation spreading in the Fermi-Pasta-Ulam system with next-nearest-neighbor coupling: competition between phonon dispersion and nonlinearity. *Phys. Rev. E* **95**(6), 062140 (2017)
118. Xu, X., Pereira, L.F., Wang, Y., Wu, J., Zhang, K., Zhao, X., Bae, S., Bui, C.T., Xie, R., Thong, J.T., Hong, B.H., Loh, K.P., Donadio, D., Li, B., Ozyilmaz, B.: Length-dependent thermal conductivity in suspended single-layer graphene. *Nat. Commun.* **5**, 3689 (2014)
119. Ziman, J.M.: *Electrons and Phonons. The theory of transport phenomena in solids*, Oxford University Press, New York (1960)

Chapter 25

Behavior of Pipeline Steels in Gaseous Hydrogen-Containing Mixtures



Vladimir A. Polyanskiy, Ksenia P. Frolova, Yulia S. Sedova,
Yuriy A. Yakovlev, and Alexander K. Belyaev

Abstract The chapter provides an overview of the results of studying the effect of hydrogen in mixtures with gases on strength, ductility, fatigue crack growth rate, and fracture morphology of the most commonly used pipeline steels X70, X80. The main methods of testing susceptibility of pipeline steels to hydrogen following the standards are briefly discussed. The results obtained by various authors show that there is a strong influence of partial hydrogen in mixtures with gases. Fatigue crack growth rate increases many times, the fracture morphology changes, and a quasi-cleavage fracture mode is observed. At the same time, tensile strength and yield strength of smooth tensile specimens made of the base metal practically do not change. This, in turn, can lead to an incorrect interpretation of the results of testing.

Keywords Hydrogen in mixtures · Fatigue crack · Strength · Ductility · Fracture morphology · Pipeline steels · Brittle zones · Quasi-cleavage planes

25.1 Introduction

The carbon-free energy concept is faced with the problem of the lack of efficient batteries of electricity, capable of storing energy within one power plant or one region when it is sunny and windy and giving it back otherwise. One has to reserve carbon-free power generation from thermal power plants, making the whole concept meaningless and resulting in a more expensive generation. Therefore, the creation of a new energy system based on hydrogen obtained using electricity from wind and

V. A. Polyanskiy (✉) · K. P. Frolova · Y. A. Yakovlev · A. K. Belyaev
Institute for Problems in Mechanical Engineering RAS, Bolshoy pr., 61, V.O.,
St. Petersburg 199178, Russia
e-mail: vapol@mail.ru

Y. S. Sedova
Peter the Great Saint-Petersburg Polytechnic University, Polytekhnicheskaya, 29,
St. Petersburg 195259, Russia
e-mail: julka0309@mail.ru

© The Author(s), under exclusive license to Springer Nature Switzerland AG 2022
V. A. Polyanskiy and A. K. Belyaev (eds.), *Mechanics and Control of Solids and Structures*, Advanced Structured Materials 164,
https://doi.org/10.1007/978-3-030-93076-9_25

solar power plants is a promising direction for the development of modern industry [4, 58]. The Joint Technology Initiative on Fuel Cells and Hydrogen and project devoted to New Energy Externalities Development for Sustainability have been started in Europe [28]. Canada implements the project to ensure the expected level of safety in the use of hydrogen [51]. Great Britain, France, Germany, the Netherlands, and Australia implement projects to add hydrogen to existing gas pipeline networks in separate sections [10, 35]. Many other countries, as well as transnational oil and gas corporations, participate in similar projects.

It is planned to obtain hydrogen for industry from natural gas and water using various technologies (reforming, pyrolysis, electrolysis). The cost of producing hydrogen is planned to be provided by excess energy from wind and solar stations. In connection with the use of hydrogen, three main technical problems arise, namely, transportation of hydrogen, accumulation and storage of hydrogen, and generation of energy from hydrogen.

The transportation problem is proposed to be solved by injecting hydrogen into the natural gas pipelines. The network of the last ones is used for the transportation of natural gas. According to [68], it is possible to realize hydrogen injection that maintains the current safety level of gas pipeline operation. At the same time, a number of papers investigated the likely consequences of using the existing natural gas pipeline network to transport both pure hydrogen and a mixture of natural gas with hydrogen [13, 20, 32, 78, 84]. Technically, hydrogen can be added to natural gas, but it can result in a decrease in safety level [18, 39, 72]. Thus, one of the advanced problems in hydrogen power engineering is the assessment of the risks associated with the transportation of a mixture of natural gas with hydrogen.

Hydrogen-induced degradation of pipelines steels is the main problem of the addition of hydrogen to natural gas. The mechanism of destruction of pipeline walls changes in a hydrogen-containing environment [9, 33, 43, 83]. Pipeline natural gas contains not more than tenths of a percent of gaseous hydrogen.

Hydrogen degradation of metals usually results in a decrease in strength, ductility, fracture toughness, and fatigue life. A huge number of papers devoted to studying the effect of pure hydrogen on the properties of steels with different microstructures have been published. Despite the interest of the oil and gas industry in the “hydrogen problem,” a relatively small number of papers investigate the effect of a mixture of natural gas with hydrogen on the properties of the walls of gas pipelines. In particular, the topical issue of the permissible concentrations of hydrogen under operating of existing networks.

Other problems of transportation of hydrogen-containing natural gas include the likelihood of hydrogen leakage [49, 80], the likelihood of ignition due to a decrease in the minimum ignition energy with an increase in the volume fraction of hydrogen in the mixture, and the inapplicability of the detectors developed for natural gas for detecting hydrogen-initiated fires [43].

The methodological problem of material testing providing information about the behavior of metals in gaseous environments is of quite importance. In particular, there

are three fundamentally different zones in the pipeline walls: base metal, welded zone, and heat-affected zone. The mechanism of interaction of these zones with hydrogen is different, which must be taken into account.

25.2 Experimental Methods

The saturation of metals by hydrogen is the main method of studying the effect of hydrogen on the mechanical properties of the material. Usually, the following four main methods are used:

1. In gaseous hydrogen [37–86]
2. In acid solution [37, 40, 45]
3. Cathodic hydrogen charging [36, 37]
4. In electrolyte associated with near-neutral pH SCC, simulating sea or groundwater or transported natural gas [21–82].

For instance, [40] provides the standard set of test conditions for consistent evaluation of pipeline and pressure vessel steels and comparison of the test results from different laboratories on the results of absorption of hydrogen generated by corrosion of steel in wet H₂S.

All these methods or their varieties are standardized. However, the cathodic hydrogen charging is most often used because of the high degree of danger of experiments on saturation by gaseous hydrogen. It should be noted that the standard cathodic hydrogen charging method [36] allows one to saturate only flat samples that can be clamped between the seals of two adjacent vessels with electrolyte. This method involves monitoring the completeness of hydrogen saturation of samples according to the time dependence of the electric current between the electrodes, each of which is placed in its own electrolyte volume. The sample plays the role of a proton-exchange membrane between two separate electrolyte volumes. Most often, the method is modified for the cylinder-shaped samples or rectangular parallelepipeds. In this case, the specimen which must be quickly saturated with hydrogen acts as one of the electrodes.

A large number of papers referring to saturation methods are published annually. However, there are very few works devoted to the extremely important question of the distribution of hydrogen concentration inside the metal due to the hydrogen saturation, see [31–70]. As a rule, the degree of saturation and its uniformity are not checked. The amount of absorbed hydrogen is believed to be proportional to the charge passed through the electrolyte, and the average concentration of hydrogen is proportional to the cathode current density for the same charging time [77].

Mathematical modeling is the main approach used to study the distribution of hydrogen concentration [31, 67, 88].

There are only five papers [53, 70, 86, 87, 89], which present the results of direct measurements of the hydrogen concentration in titanium, copper, and steel specimens

obtained by using cathodic hydrogen charging and saturation by hydrogen in a neutral solution.

The results of direct measurements described in [53, 70, 86, 87] show that these methods do not result in the uniform hydrogen concentration under the reasonable time of charging. The difference in concentration values reaches hundreds of times. According to [53, 86], it is necessary to saturate a cylindrical steel sample with a diameter of 7 mm for 504 h to obtain a uniform distribution of hydrogen concentrations. This time is ten times greater than the average duration of cathodic hydrogen charging which is from 2 up to 20 h in the most reported experiments.

A uniform distribution of hydrogen in titanium alloys can be observed after saturation in gaseous hydrogen under pressure at temperatures above 100 °C during 100 h [89].

Thus, the available methods of saturation by hydrogen result in fundamentally different distributions of hydrogen concentrations in a metal, which depends on the saturation time and the microstructure of the alloy type. The published papers contain only incomplete data on five types of alloys, among which there are no pipeline steels. Despite the common opinion about uniform saturation, the real nonuniformity of concentrations can reach hundreds of times.

To the best of our knowledge, there are no data on the distribution of hydrogen in the walls of gas pipelines after its operation. Therefore, the comparison of different saturation methods and the choice of the most appropriate one is impossible. The question arises about the applicability of the entire set of data on the effect of hydrogen on the properties of steels to the specific problem of hydrogen degradation of pipeline metals during the transportation of hydrogen-containing gas mixtures. Additional experimental studies with specific steels under operating conditions close to real ones, as well as the development of new methods testing the resistance to hydrogen-containing mixtures under high pressure are required.

25.3 Influence of Hydrogen on the Mechanical Properties of Gas Pipelines Metals

Studies of the effect of hydrogen in mixtures with natural gas on the mechanical properties of steels are multivariable. First, the concentration of hydrogen in mixtures, pressure, exposure time, and rate of loading can take different values. Second, natural gas is multicomponent. In particular, reactions of methane with carbon dioxide and water accompanied by the release of aggressive hydrogen radicals are possible. Real natural gas usually contains other impurities that affect the mechanical properties of materials in hydrogen-containing environments [17, 63]. To minimize the effect of other constituents and focus on the influence of hydrogen, the natural gas is often simulated by nitrogen or pure methane in experiments. Various zones of a gas pipeline, namely base metal, welded zone, and heat-affected zone have different characteristics [2, 19, 48, 90]. A number of authors draw attention to the need to

conduct experiments with specimens cut from different zones of the gas pipeline. Mechanical properties are estimated on the base of tensile and fatigue tests [55, 81].

25.3.1 Tensile Tests

The tensile behavior of specimens made of steels X70 and X80 tested in the gas/hydrogen mixtures was investigated in a number of works following the procedures of American Society for Testing and Materials (ASTM) [34, 56, 64, 66, 75].

Tensile tests evaluated such mechanical properties as tensile strength, yield strength, elongation at the fracture

$$\delta = \frac{l_k - l_0}{l_0} \cdot 100\% \quad (25.1)$$

and reduction in the area

$$RA = \frac{A_k - A_0}{A_0} \cdot 100\%, \quad (25.2)$$

where l_k , A_k are the length of the specimen and cross-sectional area after testing, l_0 , A_0 are the initial length of the specimen and the cross-sectional area, respectively.

In addition, to quantify the influence of added hydrogen on the mechanical properties of the material, the following index was defined to describe the hydrogen embrittlement (HE) susceptibility:

$$RRA = \frac{RA_N - RA_H}{RA_N} \cdot 100\%, \quad (25.3)$$

where RA_H and RA_N are the reduction of area in hydrogen blends and in nitrogen gas, respectively. With this definition, $RRA = 0$ means the absence of HE, whereas $RRA = 100\%$ corresponds to the maximum HE. A similar relationship $RRA = RA_H/RA_N \cdot 100\%$ can be used instead of Eq. (25.3). In this case, $RRA = 100\%$ means the absence of HE, and $RRA = 0$, vice versa corresponds to the maximum HE.

The tensile behavior of smooth specimens is investigated using standard corset cylindrical specimens with a 6mm gauge diameter and parallel part length of 28.6mm.

In [34, 56, 64, 75], tensile tests were carried out for smooth specimens cut from the base metal of the gas pipeline.

In [56], tests were carried out for smooth specimens cut from X80 steel following Chinese standard GB/T 971 in environment of gaseous nitrogen/hydrogen mixtures containing 0, 5.0, 10.0, 20.0, and 50.0% H₂ under a pressure of 12 MPa. Similar tests were carried out in [34, 75] for specimens cut from X70 steel under a pressure

Table 25.1 Characteristics of smooth steel specimens cut from the base material of a gas pipeline under tension in a nitrogen/hydrogen mixture

Paper/Steel	Vol. % H ₂	Ultimate strength, MPa	Yield strength, MPa	Elongation at the fracture, δ , %	Reduction in the area, RA, %	HE susceptibility index, RRA, %
Meng	0	656.4	523.9	26.9	77.8	0
	5	666.0	518.6	24.6	75.1	3.4
2016/ X80	10	657.8	525.5	23.9	74.4	4.3
	20	656.1	524.8	22.2	65.4	15.9
	50	661.5	523.7	21.9	64.7	16.8
Huang 2020/ X70	0	621.8	548.9	25.4	84.9	0
	5	615.5	540.3	25.6	79.5	6.4
	10	613.2	539.7	25.5	78.9	7.1

of 10 MPa, the volume fraction of hydrogen was 0.5.0 and 10.0%. The stress–strain curves corresponding to tests in different environments coincide. Thus, there is no effect of hydrogen.

The same smooth specimens made of steel X70 were tested in an environment of CH₄/H₂ mixture containing 1% of hydrogen under a pressure of 10 MPa in [64]. To simulate the long-term operation of the gas pipeline, the test samples were saturated in the mixture for 720 h. Comparison of the stress–strain curves obtained by saturation of the specimens in five different media, namely, in ambient air, in helium, in CH₄/H₂ mixture containing 1% of hydrogen, in CH₄/H₂ mixture with 1% H₂ for 720 h, and in pure hydrogen. According to the results, the added hydrogen does not significantly affect the ultimate strength and yield strength of smooth samples. A twofold decrease in the parameter δ is observed in pure hydrogen, but the values of the ultimate strength and yield strength do not change.

The absence of the influence of hydrogen concentrations less than 100% on the ultimate strength and yield strength was confirmed in [10, 12, 61, 73]. At the same time, according to [34, 56, 75], injection of hydrogen leads to a decrease of the reduction in the area, which becomes significant when hydrogen concentrations exceed 10%. Elongation at the fracture also can be reduced (see Table 25.1).

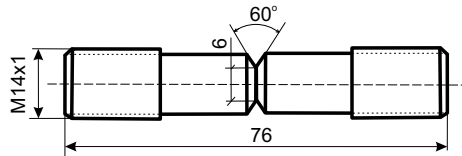
The addition of hydrogen increases the HE susceptibility since the value of the index of RRA becomes non-zero and increases with an increase in the volume fraction of hydrogen in the mixture.

The study of the effect of the added hydrogen on the mechanical properties of the weld joint of steels X70 under tension was investigated in [34, 66, 75]. The tests were carried out under a pressure of 10 MPa. A mixture of nitrogen with hydrogen was investigated in [34, 75], a mixture of methane with hydrogen was investigated at rapid and long-term (for 720 h) artificial saturation in [66]. According to the stress–strain curves presented in [75], there is no influence of hydrogen. According to [34], the addition of 5% of hydrogen results in decreasing of the elongation at the fracture from

Table 25.2 Characteristics of smooth steel specimens cut from the weld joint of a gas pipeline under tension in a nitrogen/hydrogen mixture

Paper/Steel	Vol. % H ₂	Ultimate strength, MPa	Yield strength, MPa	Elongation at the fracture, δ , %	Reduction in the area, RA, %	HE susceptibility index, RRA, %
Huang	0	639.9	573.6	22.6	78.3	0
2020/	5	659.8	570.1	20.5	69.2	11.6
X70	10	649.4	549.2	19.4	65.7	16.1

Fig. 25.1 Specimen geometry of notch tension specimen



22 to 17%, and addition of 10% of hydrogen results in a drop to 15%. The quantitative characteristics of the samples investigated in [66] are given in Table 25.2.

The added hydrogen affects the mechanical properties of the welded zone (see [34, 66] and Table 25.2). This effect is significant in comparison with the results obtained for the base metal. The ultimate strength of the welded zone slightly increases in comparison with the ultimate strength of the material tested in pure nitrogen, which indicates hydrogen strengthening. The susceptibility to HE increases with an increase of hydrogen concentration.

Tensile tests on the notch specimens were performed in [56, 64, 66, 75]. Geometry of the notch specimen is shown in Fig. 25.1. The notch models defect caused by rolling.

Notch specimens with a notch root radius of 0.1 mm made of steel X80 were tested in an argon/hydrogen mixture containing 0, 5, 10, 20, and 50% of hydrogen under a pressure of 12 MPa in [56]. Similar experiments were carried out in [75] for specimens with notch root radii $R_n = 0.083$ mm and $R_n = 0.95$ mm made of steel X70 placed in an environment of argon/hydrogen mixture containing 0, 5, and 10% of hydrogen under a pressure of 10 MPa. The values of notch root radii correspond to the values of the ratio of the maximum stress at the stress concentration region to the average applied stress at minimum cross-sectional area $K_t = 5.1$ and $K_t = 2.4$, respectively; $K_t = 1$ for a smooth specimen. The experiments were carried out for samples cut from the base metal of the gas pipeline and from the weld joint. Hydrogen was found to reduce the ultimate strength and decrease reduction in the area. Increasing the hydrogen concentration results in earlier destruction in all cases.

Comparison of the results with those obtained for smooth specimens allows concluding that notch samples are more sensitive to hydrogen added in nitrogen gas. Increasing the value of K_t results in increasing the effect of hydrogen on the tensile

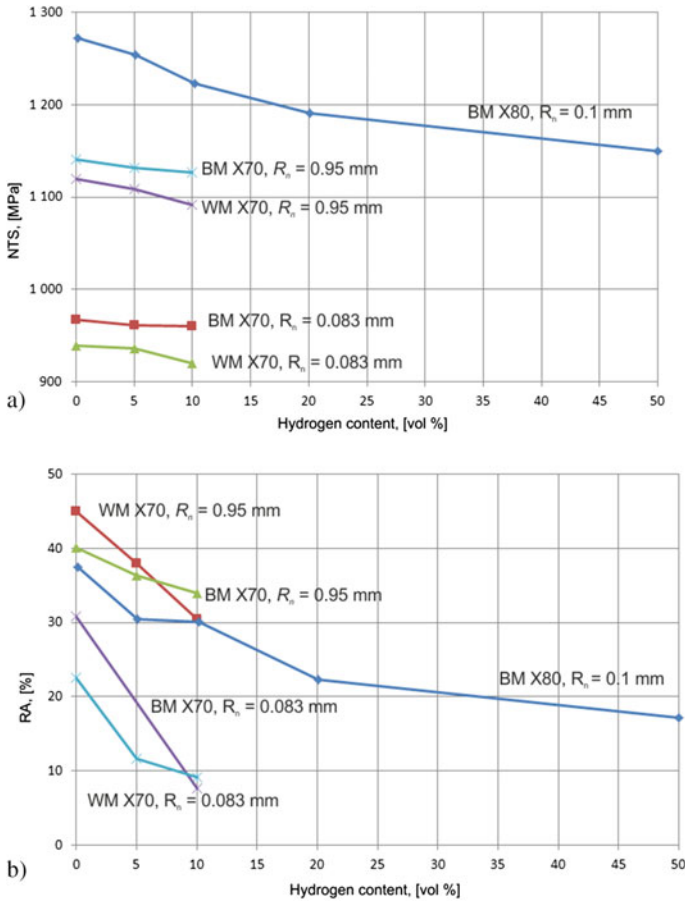


Fig. 25.2 Tensile properties of the notch specimens made of Base metal of steel X80, $R_n = 0.1$ mm [56], base metal and Weld zone of steel X70, $R_n = 0.95$ mm ($K_t = 2.4$), Base metal and Weld zone of steel X70, $R_n = 0.083$ mm ($K_t = 5.1$) [75] (NTS **a** is an ultimate strength, RA **b** is a reduction in the area)

properties of the metal. The corresponding quantitative characteristics of mechanical properties are shown in Fig. 25.2.

The reduction in the area of the specimen drops faster than ultimate strength with the increase of hydrogen content. In particular, the ultimate strength of the notch specimen with $K_t = 5.1$ decreases by 2.4% with the addition of 10% of hydrogen to argon, while the reduction in the area of the specimen decreases by 75.2% under the same conditions. Thus, the results indicate that the effect of hydrogen and stress concentration on the ultimate strength is not so great, while the effect on the plasticity of the material is significant. According to [56], the coefficient of susceptibility of

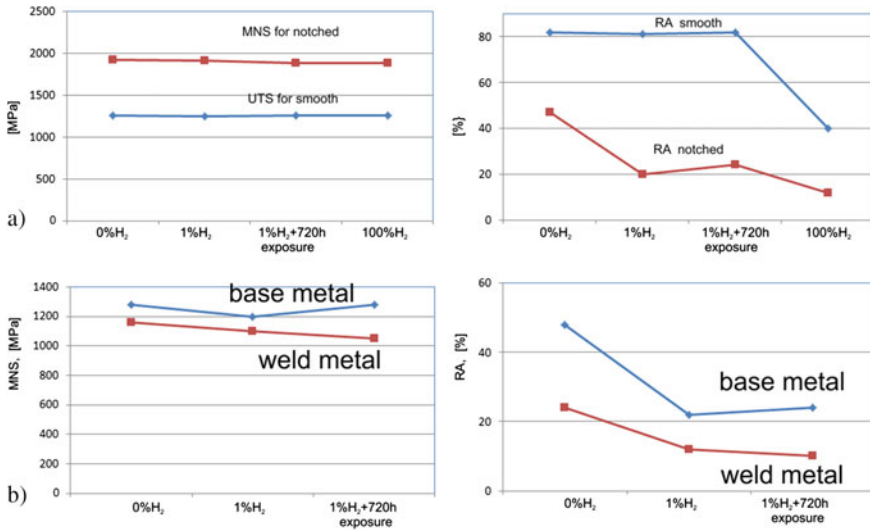


Fig. 25.3 Tensile characteristics of the notch specimens tested in pure gases and in a methane/hydrogen mixture containing 1% of hydrogen: **a** Base metal of steel X70, $R_n = 0.083$ mm [64], **b** weld zone of steel X70, $R_n = 0.083$ mm [66] (MNS/UTS is an ultimate strength, RA is a reduction in the area)

notch specimen with $R_n = 0.1$ mm to HE take values 0, 19.1, 20.5, 41.0, and 54.5% at 0, 5.0, 10.0, 20.0, and 50.0% of hydrogen, respectively.

Notch specimens cut from the base metal of a gas pipeline made of steel X70 were tested in [64] in a methane/hydrogen mixture containing 1% of hydrogen under a pressure of 10 MPa. The same tests were carried out in [66] for specimens cut from the weld joint. The notch root radius was equal to 0.083 mm. The main tensile characteristics of the specimens are shown in Fig. 25.3.

The addition of 1% of hydrogen does not change the ultimate strength of the base material, but significantly reduces the value of the reduction in the area (this effect is not observed when testing smooth samples). The ultimate strength of the welded zone slightly decreases with the increase of hydrogen concentration. As in the case of base metal, there is a drop of the reduction in the area. The quantitative values of this parameter are much lower for the weld zone than for the base metal.

Since behavior of smooth samples and notched samples is different, it is necessary to take into account the results of studies of specimens of both types to ensure the safe operation of gas pipelines.

25.3.2 *Fractography Analysis*

Microstructural analysis of the fracture surface of tensile specimens is performed in [34, 56, 64, 66, 75] using scanning electron microscopy (SEM).

According to [56], the fracture morphology of the smooth specimen made of steel X80 tested in nitrogen presents ductile fracture with numerous dimples. In the case of 20% hydrogen blend, surface cracks are found on the specimen side surface. The crack initiates near the specimen surface and secondary cracks (delamination) can occur on the fracture surface. Meng [56] suggested to relate it to the textured microstructure caused by hot rolling. A quasi-cleavage fracture mode in 20% hydrogen mixture is observed.

Analysis of the microstructure of the fracture surface of specimens made of steel X70 was carried out in a number of works [34, 64, 75]. The microstructure of the fracture surface of the specimen tested in nitrogen is found to be similar to the fracture surface observed for specimen tested in a mixture of nitrogen with 10.0% hydrogen. Necking and a ductile fracture with numerous dimples are observed in both cases. However, the dimples are smaller after the tests in the mixture. In addition, cracks propagated along the direction perpendicular to the applied stress direction appear in this case. Formation of these cracks is associated with HE.

Specimens tested in an environment of CH₄/H₂ gas mixture containing 1% H₂ exposure undergo a completely ductile fracture with microvoids coalescence [64].

Analysis of the fracture surfaces of specimens cut from the weld zone of gas pipeline made of steel X70 is presented in [34, 66].

The fracture behavior of these specimens tested in nitrogen and in 10.0% hydrogen blend is characterized by necking. In contrast to the fracture morphology in nitrogen, surface cracking can be observed around the circumference of the specimens tested in 10.0% hydrogen mixture. The hydrogen cracks exhibit the quasi-cleavage brittle fracture.

The fracture surface of specimens tested in the 1% H₂ gas mixture after 720h of exposure have ductile–brittle fracture features, which vary with distance from the edge surface with a predominantly quasi-cleavage fracture at the brittle external ring near the outer surface and fine dimples at the center (the dimples are finer than after tests in pure methane). The brittle area covered about 35% of the entire fracture surface. The side surface was covered by secondary surface cracks with two different orientations crisscrossing each other.

The influence of added hydrogen on the microstructure of the fracture surface of the notch specimens made of X70 and X80 steels was investigated in [56, 64, 66, 75].

In the absence of hydrogen, cracks initiate in the vicinity of the notch root and a shear lip is observed on the fracture surface. The ductile–dimple microscopic plasticity feature dominates. The fracture surface of specimens tested in nitrogen/hydrogen mixture reveals a quasi-cleavage fracture with brittle features. These results are consistent with the analysis carried out in the study of the quantitative characteristics of the samples under tension, namely, the ultimate strength and the value of the

reduction in the area. At the same time, according to [56], a more ductile mode of failure occurs toward the center of the specimen saturated in a hydrogen blend as an exception, which probably can be observed when the surface cracks covered a threshold area of the cross section.

The region close to the notch root of the specimen saturated in a methane/hydrogen mixture was predominantly characterized by a quasi-cleavage mode, while the inner region presented a typical ductile fracture (see [64, 66]).

The width of the brittle region is greater for specimens tested in pure hydrogen. Some secondary surface cracks can also be observed at the interface between ductile and brittle fracture zones of samples tested in a hydrogen-containing environment. The number and average length of cracks increase significantly in samples tested in pure hydrogen.

Thus, the microstructural analysis indicate that the addition of hydrogen leads to brittle fracture characterized by quasi-cleavage, while the destruction in gaseous nitrogen and pure methane are ductile.

25.3.3 Fatigue Crack Growth Test

The risk of hydrogen embrittlement of a gas pipeline depends not only on the properties of the material but also on the history of its operation, namely, the presence of pressure drops [46]. Thus, the fatigue behavior of pipeline steels in a hydrogen-containing environment must be evaluated. Fatigue tests are generally performed on specimens with the geometry shown in Fig. 25.4 which conformed to American Society for Testing and Materials (ASTM).

Kinetic diagrams representing the dependence of the fatigue crack growth per cycle on the stress intensity factor range are widely used in fatigue crack growth tests. This dependence is generally described by a power-law relationship

$$\frac{da}{dN} = C \Delta K^m, \quad (25.4)$$

Fig. 25.4 Specimen geometry of compact tension specimen

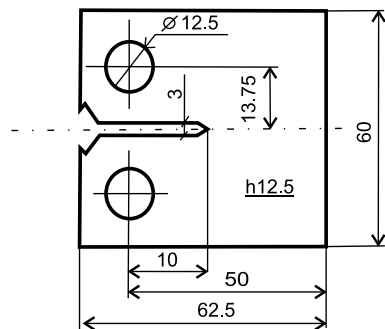
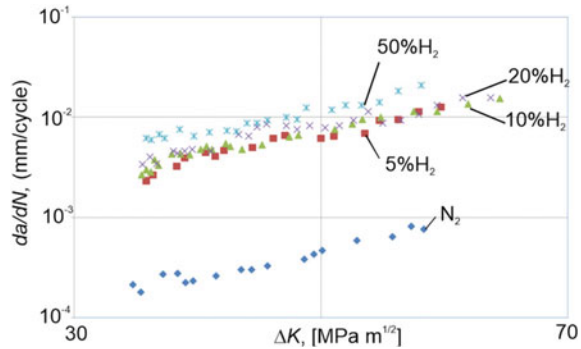


Fig. 25.5 Kinetic diagram for steel X80 [56]



where a is the length of fatigue crack, N is a number of cycles, ΔK is the stress intensity factor range, C and m are the crack growth rate factors.

Fatigue crack growth tests were carried out in [8, 34, 56, 64, 76] in mixtures with hydrogen. In [56], fatigue crack growth tests were carried out in a mixture of nitrogen with hydrogen with a frequency 1 Hz and a load ratio (the ratio of the minimum load to the maximum one) of 0.1. Kinetic diagrams obtained for steels X80 are shown in Fig. 25.5. Fatigue crack growth rate increases by at least an order of magnitude in hydrogen blends compared to nitrogen gas. In addition, fatigue crack growth rate increases with increasing hydrogen concentration.

Similar results were obtained in [34] for steels X70, where fatigue tests were carried out in mixtures of nitrogen with hydrogen with a frequency 5 Hz and the same stress factor (0.1). Kinetic diagrams obtained in [34] for the base metal, weld zone, and heat-affected zone are shown in Fig. 25.6. In particular, it is shown that for a ΔK value of 35 MPa·m^{1/2}, the crack growth increment per cycle of base metal is equal to 1.75·10⁻⁴ mm/cycle in nitrogen, 1.16·10⁻³ mm/cycle in 5.0% hydrogen mixture, and 1.47·10⁻³ mm/cycle in 10.0% hydrogen mixture. Thus, crack growth rate in hydrogen-containing environment is over eight times higher than that in nitrogen. With the stress intensity factor ranging from 35 to 100 MPa·m^{1/2}, the crack growth rate measured in 10% hydrogen mixture is 5–8 times of the crack growth rate measured in nitrogen. Same as the base metal, crack growth rate of the welded zone in 10.0% hydrogen mixture is approximately 5–10 times of that in nitrogen. Crack growth rate of the heat-affected zone is approximately 7–22 times of that in nitrogen.

Crack growth rate factors C and m corresponding to kinetic diagrams shown in Figs. 25.5, 25.6 are given in Table 25.3. These coefficients are generally determined by means of the least squares method.

Huang et al. noted that the increases in crack growth rate seem to be related to the lattice hydrogen concentration at ΔK equal to 35 MPa·m^{1/2} [34]. They suggested that there is a pressure threshold over which the crack growth rate becomes independent

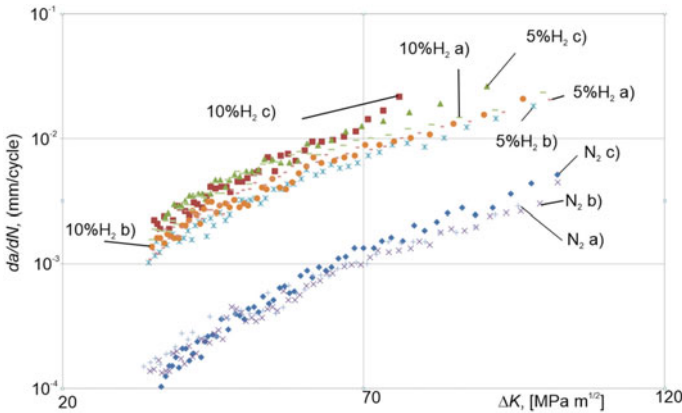


Fig. 25.6 Kinetic diagram for steel X70: **a** base metal, **b** weld zone, **c** heat-affected zone [34]

Table 25.3 Constant coefficients of kinetic fracture diagrams

Paper/Steel	Vol. % H ₂	C	m
Meng	0	$2.25 \cdot 10^{-8}$	2.59
	5	$2.57 \cdot 10^{-7}$	2.58
2016/ X80	10	$2.98 \cdot 10^{-7}$	2.58
	20	$3.51 \cdot 10^{-7}$	2.57
	50	$9.93 \cdot 10^{-7}$	2.39
Huang 2020/ X70 Base metal	0	$6.18 \cdot 10^{-9}$	2.84
	5	$1.37 \cdot 10^{-7}$	2.60
	10	$4.03 \cdot 10^{-7}$	2.38
Huang 2020/ X70 Weld zone	0	$2.63 \cdot 10^{-9}$	3.03
	5	$1.48 \cdot 10^{-7}$	2.53
	10	$1.78 \cdot 10^{-7}$	2.52
Huang 2020/ X70 Heat-affected zone	0	$3.31 \cdot 10^{-10}$	3.56
	5	$2.0 \cdot 10^{-7}$	2.53
	10	$2.0 \cdot 10^{-7}$	2.60

on gas pressure, which is probably attributed to the critical hydrogen concentration in the fatigue crack zone.

Fatigue crack growth tests on GB 20-grade steel were carried out in [76] in natural gas (88.53CH₄–6.87C₂H₆–0.0014CO₂–0.64O₂–2.41N₂-other gases)/hydrogen mixtures under a pressure of 0.4 MPa. Tests were performed at a frequency 1 Hz and a stress ratio of 0.1. Kinetic diagrams are shown in Fig. 25.7. The presence of hydrogen in natural gas increases the crack growth rate. On the one hand, there is no difference between the results obtained in natural gas and in nitrogen in a given range of stress intensity factor. On the other hand, the crack growth rate in a mixture of natural gas with hydrogen significantly exceeds the corresponding value in

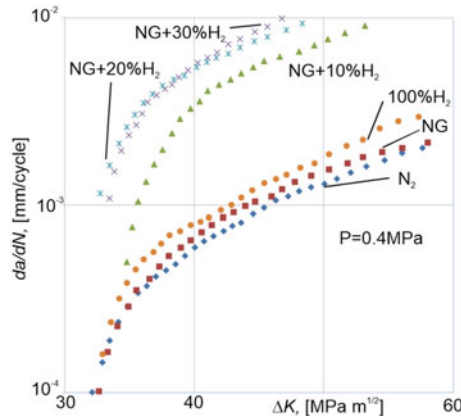


Fig. 25.7 Kinetic diagram for steel X70 tested in natural gas/hydrogen mixture [76]

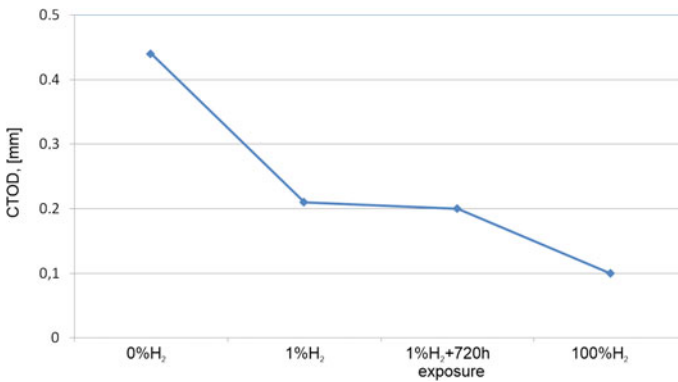


Fig. 25.8 CTOD: results for specimens made of steel X70 tested in pure gases and in methane/hydrogen mixture [64]

hydrogen. Thus, simulation of natural gas by means of nitrogen is impractical in fatigue crack growth tests. According to [76], this phenomenon can be explained by interaction of CO_2 and H_2 . It was also shown that the addition of hydrogen leads to a brittle fracture.

The crack tip opening displacement (CTOD) was determined for specimens made of pipeline steel X70 and X80 in [8, 64] (see Fig. 25.8). The fracture toughness of the specimens tested in hydrogen-containing environments is remarkably reduced. The toughness of the specimen tested in ambient air is reduced by 49% when tested in 1% H_2 gas mixture. The exposure time in CH_4/H_2 mixture does not have a noticeable effect. CTOD decreases even more in pure hydrogen. The fracture surfaces of the cracking zone ahead of the fatigue pre-crack are quasi-cleavage [64].

25.3.4 Fatigue Life

Tests with variable load allow determining the endurance limit of the material, i.e., the number of cycles at which the sample is destroyed. The effects of hydrogen on the fatigue life of the natural gas pipeline can be estimated from two aspects, namely, the residual fatigue life of pipelines with an initial flaw and the maximum allowable initial flaw size for the required fatigue life. A calculation is generally carried out in accordance with ASME Boiler and Pressure Vessel Code. The crack growth rate is estimated on the base of the kinetic diagram of material fracture. Stress intensity factor is determined in a standard way according to [69]. Fracture toughness data for steels tested in a mixture of natural gas or nitrogen with hydrogen is not measured in papers. It is assumed to be equal to which is measured in nitrogen (or in the air) and in hydrogen under a certain pressure, respectively.

Fatigue life calculations were carried out in [34, 56, 75]. The corresponding data are presented in Table 25.4. The results indicate that added hydrogen decreases fatigue life dramatically. The fatigue life of specimens with a smaller notch root radius (higher values of K_t) is much lower when compared to specimens with a larger notch root radius (lower values of K_t). Thus, the presence of a stress concentrator increases the negative effect of hydrogen on the fatigue life of the gas pipeline material.

The fatigue life of the pipeline with the initial flaw depth varied from 0.1 to 5 mm was calculated in [34]. The results are shown in Fig. 25.9. The fatigue life decreases rapidly as the initial flow depth increases in mixtures of nitrogen with hydrogen.

Dependence of the ratio of maximum allowable initial flaw depth in nitrogen to maximum allowable initial flaw depth in hydrogen mixtures on fatigue life is shown in Fig. 25.10. This ratio increases significantly with the increase in required fatigue life. Thus, the addition of hydrogen leads to a decrease in the allowable range of flow depth values.

Table 25.4 Fatigue life of pipelines (cycles)

Paper/Steel	Zone/Geometry of sample	Vol. % H ₂				
		0	5	10	20	50
Meng/X80	Base metal/smooth specimen	24431	2130	1850	1603	1073
Huang/X70	Base metal/smooth specimen	34302	3457	2442	–	–
Shang/X70	Base metal/notch specimen, $K_t = 2.4$	10134	5926	4706	–	–
	Base metal/notch specimen, $K_t = 5.1$	2547	305	75	–	–
	Weld joint/notch specimen, $K_t = 2.4$	10990	7037	4592	–	–
	Weld joint/notch specimen, $K_t = 5.1$	4273	399	98	–	–

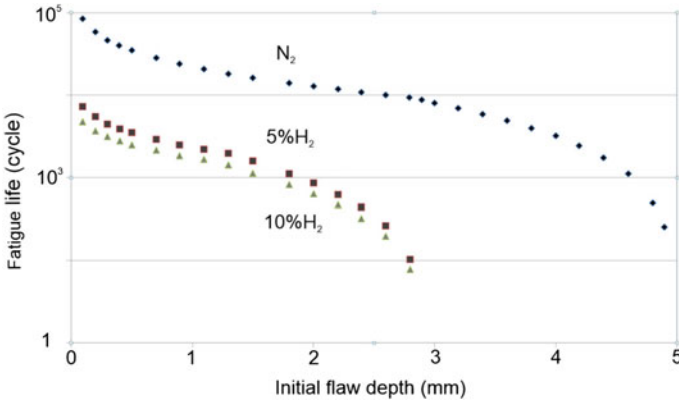
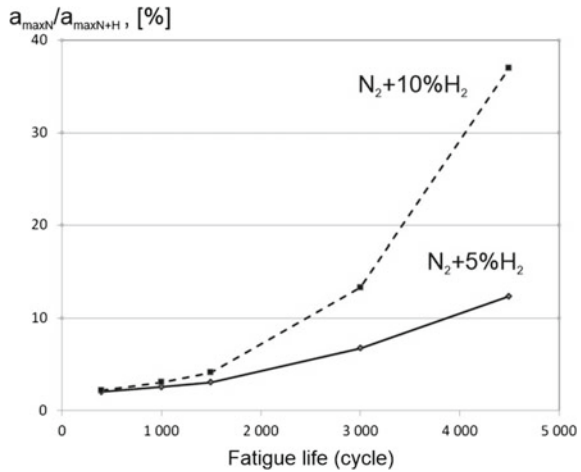


Fig. 25.9 Dependence of the fatigue life of steel X70 on the initial flaw depths [34]

Fig. 25.10 Dependence of the ratio of maximum allowable initial flaw depth in nitrogen to maximum allowable initial flaw depth in hydrogen mixtures on fatigue life [34]



The microstructure of the fracture surface after low-cycle fatigue tests performed on notched specimens made of steel X70 was analyzed in [75]. When testing specimens with $K_t = 2.4$ in nitrogen, small cracks initiate at the surface of the notch tip and then coalesce into several larger cracks propagate to the center of the specimens. After propagating for a distance in the crack growth region, these cracks progress into the fatigue rupture regions and then fracture instantaneously. The crack growth region of the specimen with $K_t = 5.1$ tested in nitrogen is characterized by intense plastic deformation, whereas the crack growth region of the same specimen tested in nitrogen/hydrogen mixtures with 10% H₂ exhibits quasi-cleavage. In addition, the fracture in the crack growth region of the specimen with $K_t = 2.4$ tested in nitrogen/hydrogen mixtures is mixed ductile–brittle.

Thus, concentration of hydrogen and stress concentration can promote the propagation of cracks in the specimen and shorten fatigue life. As a result, the fatigue life of the specimen decreases significantly with the increase of K_t and the addition of hydrogen [75].

25.3.5 Indentation Tests

An indentation test using small specimens is a promising method for monitoring and assessing the state of the metal of oil and gas equipment elements [7, 26, 27, 52]. This method also allows for the investigation of elements of weld joints. During the test process, the compressive load applied to the small specimens by a spherical or cylindrical punch and the displacement of the specimen caused by the indentation is measured.

A series of indentation tests were implemented in [65] to study the effect of a mixture of methane and hydrogen on the mechanical properties of X70 pipeline steel. The effect of 0.1, 0.5, 1, 3, and 5% of hydrogen was investigated under three values of the pressure in the pipeline, namely, 5, 7, and 10 MPa. The degree of steel susceptibility to HE was found to depend on hydrogen concentration and tends to increase with increasing concentration. As in the case of tensile tests, the composition of the gas mixture does not significantly affect the yield strength and elastic behavior, whereas the ultimate strength decreases significantly with increasing of hydrogen concentration. The influence of hydrogen concentration on the metal susceptibility to HE is more pronounced than the influence of the pressure of the gas mixture.

Investigation of the fracture surface after indentation tests under a gas mixture pressure of 7 MPa (0.1% H₂, 1% H₂, 5% H₂) and under a pressure of 10 MPa (100% H₂) shows that the fracture morphology changes under different environmental conditions [65]. The fracture surface exhibits a dimpled fracture pattern at a low partial pressure of hydrogen, which is the result of micro-void coalescence. When the partial pressure of hydrogen increases to a moderate value, the fracture surface reveals a mixed-mode fracture with some brittle features and micro-void coalescence. At higher partial pressures of hydrogen, the fracture surface of the tested specimen is characterized by quasi-cleavage planes.

25.4 Conclusions

Investigation of the problems associated with the various risks of adding hydrogen to natural gas inevitably leads to different conclusions regarding the permissible value of hydrogen concentration in the mixture. According to the published data, the problem of hydrogen degradation of metals used in gas pipelines is the most sensitive one to low hydrogen concentrations. In particular, the addition of 5–15%

of hydrogen do not increase the risks of ignition of gas pipelines, while the addition of even 5% can reduce the plasticity of material and lead to the appearance of brittle zones.

The present review shows that hydrogen embrittlement of gas pipeline metals is caused by several factors, namely, the volume concentration of hydrogen, the quality of rolling of the gas pipeline, and the specificity of zones of the gas pipeline (base metal, welded zone, heat-affected zone). The addition of hydrogen in mixtures with gas does not change significantly the ultimate strength of the material but reduces its plasticity. The negative effect is greater in the presence of defects on the walls of the gas pipelines. In addition, the weld joint is more susceptible to the presence of hydrogen in the mixture. Also, even a low concentration of hydrogen in mixtures results in a multiple decreases in the fatigue life. Thus, the same hydrogen concentrations can either lead to irreversible consequences or not cause them. However, the addition of relatively low hydrogen concentrations (about 1–5%) requires accurate investigations.

Standard methods for testing metals for hydrogen embrittlement and hydrogen cracking do not always give an unambiguous result in the case of gas/hydrogen mixtures. Additional experiments are needed to identify the most adequate methods for testing pipeline metals and to analyze the problem of adding hydrogen to the existing gas pipeline network.

Acknowledgements Support of this work by a grant No. 18-19-00160 from the Russian Science Foundation is gratefully acknowledged.

References

1. Akiyama, E., Li, S.: Electrochemical hydrogen permeation tests under galvanostatic hydrogen charging conditions conventionally used for hydrogen embrittlement study **34**(1–2), 103–112 (2016)
2. Alvaro, A., et al.: Hydrogen embrittlement susceptibility of a weld simulated X70 heat affected zone under H₂ pressure. *Mater. Sci. Eng., A* **597**, 29–36 (2014)
3. Aly, O.F., Neto, M.M.: Stress corrosion cracking. In: Aliofkhaezrai, M. (ed.) *Developments in Corrosion Protection*. IntechOpen Limited, London (2014)
4. Amoo, L.M., Fagbenle, R.L.: Hydrogen energy's key contributions to the sustainable energy mix of a low-carbon future in Nigeria. *Int. J. Sustain. Energ.* **33**(4), 742–765 (2014)
5. Austen, I.M.: Effective stress intensities in stress corrosion cracking. *Int. J. Fract.* **12**, 253–263 (1976)
6. Beavers, J.A., Harle, B.A.: Mechanisms of high-pH and nearneutral-pH SCC of underground pipelines. *Offshore Mech. Arct. Eng.* **123**, 147–151 (2003)
7. Blagoeva, D.T., Hurst, R.C.: Application of the CEN (European Committee for Standardization) small punch creep testing code of practice to a representative repair welded P91 pip. *Mater. Sci. Eng., A* **510**, 219–223 (2009)
8. Briottet, L., Ez-Zaki, H.: Influence of hydrogen and oxygen impurity content in a natural gas/hydrogen blend on the toughness of an API X70 steel. In: *Pressure Vessels and Piping Conference*. American Society of Mechanical Engineers, vol. 51685, V06BT06A036 (2018)
9. Briottet, L., Moro, I., Lemoine, P.: Quantifying the hydrogen embrittlement of pipeline steels for safety considerations. *Int. J. Hydrogen Energy* **37**(22), 17616–17623 (2012)

10. Briottet, L., et al.: Recommendations on X80 steel for the design of hydrogen gas transmission pipelines. *Int. J. Hydrogen Energy* **37**(11), 9423–9430 (2012)
11. Capelle, J., Gilgert, J., Dmytrakh, I., Pluvinage, G.: Sensitivity of pipelines with steel api X52 to hydrogen embrittlement. *Int. J. Hydrogen Energy* **33**(24), 7630–7641 (2008)
12. Capelle, J., et al.: The effect of hydrogen concentration on fracture of pipeline steels in presence of a notch. *Eng. Fract. Mech.* **78**(2), 364–373 (2011)
13. Castello, P., et al.: Techno-economic assessment of hydrogen transmission & distribution systems in Europe in the medium and long term. European Commission, Joint Research Center (2005)
14. Charles, E.A., Parkins, R.N.: Generation of stress corrosion cracking environments at pipeline surfaces. *Corrosion* **51**, 518–527 (1995)
15. Cheng, Y.: Fundamentals of hydrogen evolution reaction and its implications on near-neutral pH stress corrosion cracking of pipelines. *Electrochim. Acta* **52**(7), 2661–2667 (2007)
16. Chen, W.: Modeling and prediction of stress corrosion cracking of pipeline steels. In: *Trends in Oil and Gas Corrosion Research and Technologies*, pp. 707–748 (2017)
17. Cialone, H., Holbrook, J.: Sensitivity of steels to degradation in gaseous hydrogen. In: Raymond, L. (ed.) *Hydrogen Embrittlement: Prevention and Control*, pp. 134–152. ASTM International, West Conshohocken (1988)
18. Dagdougui, H., et al.: Hazard and risk evaluation in hydrogen pipelines. *Manag. Environ. Qual.: Int. J.* **21**(5), 712–725 (2010)
19. Davani, R.K.Z., Miresmaeili, R., Soltanmohammadi, M.: Effect of thermomechanical parameters on mechanical properties of base metal and heat affected zone of X65 pipeline steel weld in the presence of hydrogen. *Mater. Sci. Eng., A* **718**, 135–146 (2018)
20. Dickinson, R.R., et al.: Alternative carriers for remote renewable energy sources using existing CNG infrastructure. *Int. J. Hydrogen Energy* **35**(3), 1321–1329 (2010)
21. Dmytrakh, I., Leshchak, R., Syrotyuk, A., Barna, R.: Effect of hydrogen concentration on fatigue crack growth behaviour in pipeline steel. *Int. J. Hydrogen Energy* **42**(9), 6401–6408 (2017)
22. Elboudjaini, M., Revie, R.W.: Metallurgical factors in stress corrosion cracking (SCC) and hydrogen-induced cracking (HIC). *J. Solid State Electrochem.* **13**, 1091–1099 (2009)
23. Eliaz, N., et al.: Characteristics of hydrogen embrittlement, stress corrosion cracking and tempered martensite embrittlement in high-strength steels. *Eng. Fail. Anal.* **9**(2), 167–184 (2002)
24. Fang, B.Y., Atrens, A., Wang, J.Q., Han, E.H., Zhu, Z.Y., Ke, W.: Review of stress corrosion cracking of pipeline steels in “low” and “high” pH solutions. *J. Mater. Sci.* **38**, 127–132 (2003)
25. Fremy, M.E.: On the composition of cast iron and steel. *J. Franklin Inst.* **72**(5), 342–346 (1861)
26. García, T.E., et al.: Effect of hydrogen embrittlement on the tensile properties of CrMoV steels by means of the small punch test. *Mater. Sci. Eng., A* **664**, 165–176 (2016)
27. García, T.E., et al.: Estimation of the mechanical properties of metallic materials by means of the small punch test. *J. Alloy. Compd.* **582**, 708–717 (2014)
28. Gerboni, R., Salvador, E.: Hydrogen transportation systems: elements of risk analysis. *Energy* **34**(12), 2223–2229 (2009)
29. Goltsov, V.A.: Fundamentals of hydrogen treatment of materials. *Prog. Hydrog. Treat. Mater.* 3–36 (2001)
30. Gonzalez, J., Gutierrez-Solana, F., Varona, J.M.: The effects of microstructure, strength level, and crack propagation mode on stress corrosion cracking behavior of 4135 steel. *Metall. Mater. Trans. A.* **27**, 281–290 (1994)
31. Hadam, U., Zakroczymski, T.: Absorption of hydrogen in tensile strained iron and high-carbon steel studied by electrochemical permeation and desorption techniques. *Int. J. Hydrogen Energy* **34**(5), 2449–2459 (2009)
32. Haeseldonckx, D., D’haeseleer W.: The use of the natural-gas pipeline infrastructure for hydrogen transport in a changing market structure. *Int. J. Hydrog. Energy* **32**(10–11), 1381–1386 (2007)
33. Hardie, D., Charles, E.A., Lopez, A.H.: Hydrogen embrittlement of high strength pipeline steels. *Corros. Sci.* **48**(12), 4378–4385 (2006)

34. Huang, G., et al.: Mechanical properties of X70 welded joint in high-pressure natural gas/hydrogen mixtures. *J. Mater. Eng. Perform.* **29**, 1589–1599 (2020)
35. Isaac, T.: HyDeploy: the UK's first hydrogen blending deployment project. *Clean Energy* **3**(2), 114–125 (2019)
36. ISO 17081:2014. Method of Measurement of Hydrogen Permeation and Determination of Hydrogen Uptake and Transport in Metals by an Electrochemical Technique (2014)
37. ISO 16573:2015. Steel - measurement method for the evaluation of hydrogen embrittlement resistance of high strength steels. International Organization for Standardization (2015)
38. ISO 11114-4:2017. Transportable gas cylinders—compatibility of cylinder and valve materials with gas contents part 4: test methods for selecting metallic materials resistant to hydrogen embrittlement. International Organization for Standardization (2017)
39. Jo, Y.D., Ahn, B.J.: Analysis of hazard area associated with hydrogen gas transmission pipelines. *Int. J. Hydrogen Energy* **31**(14), 2122–2130 (2006)
40. Johnson, W.H.: II. On some remarkable changes produced in iron and steel by the action of hydrogen and acids. *Proc. R. Soc. Lond.* **23**(156–163), 168–179 (1875)
41. Kadhim, M.G., Albdiry, M.: A critical review on corrosion and its prevention in the oilfield equipment. *J. Pet. Res. Stud.* **14**, 162–189 (2017)
42. Kalachev, B.A.: Hydrogen Embrittlement of Metals. Metallurgy, Moscow (1985). (in Russian)
43. Kessler, A. et al.: Hydrogen safety barriers and measures. In: HySafe: Biennial Report on Hydrogen Safety (2006)
44. Kim, W.K., Koh, S.U., Yang, B.Y., Kim, K.Y.: Effect of environment and metallurgical factors on hydrogen induced cracking. *Corros. Sci.* **50**, 3336–3342 (2008)
45. Kuduzovic, A., Poletti, M., Sommitsch, C., Domankova, M., Mitsche, S., Kienreich, R.: Investigations into the delayed fracture susceptibility of 34crnimo6 steel, and the opportunities for its application in ultra-high-strength bolts and fasteners. *Mater. Sci. Eng., A* **590**, 66–73 (2014)
46. Labidine Messaoudani, Z. et al.: Hazards, safety and knowledge gaps on hydrogen transmission via natural gas grid: a critical review. *Int. J. Hydrog. Energy* **41**(39), 17511–17525 (2016)
47. Lancsater, J.: Handbook of Structural Welding: Processes, Materials and Methods in the Welding of Major Structures. Pipelines and process plant, Woodhead Publishing, Sawston (2003)
48. Lee, J.A., et al.: Hydrogen-induced toughness drop in weld coarse-grained heat-affected zones of linepipe steel. *Mater. Charact.* **82**, 17–22 (2013)
49. Lowesmith, B.J., et al.: Gas build-up in a domestic property following releases of methane/hydrogen mixtures. *Int. J. Hydrogen Energy* **34**(14), 5932–5939 (2009)
50. Maciejewski, J.: The effects of sulfide inclusions on mechanical properties and failures of steel components. *J. Fail. Anal. Prev.* **15**, 169–178 (2015)
51. MacIntyre, I., et al.: Canadian hydrogen safety program. *Int. J. Hydrogen Energy* **32**(13), 2134–2143 (2007)
52. Mao, X., Takahashi, H.: Development of a further-miniaturized specimen of 3 mm diameter for tem disk (ϕ 3 mm) small punch tests. *J. Nucl. Mater.* **150**(1), 42–52 (1987)
53. Martinsson, A., Sandstrom, R.: Hydrogen depth profile in phosphorus-doped, oxygen free copper after cathodic charging. *J. Mater. Sci.* **47**(19), 6768–6776 (2012)
54. Masouri, D., Zafari, M., Araghi, A.: Sulfide stress cracking of pipeline-case history. In: Proceedings of the NACE International. Corrosion 2008 Proceedings, New Orleans, LA (2008)
55. Matsuoka, S., Yamabe, J., Matsunaga, H.: Criteria for determining hydrogen compatibility and the mechanisms for hydrogen-assisted, surface crack growth in austenitic stainless steels. *Eng. Fract. Mech.* **53**, 103–127 (2016)
56. Meng, B., et al.: Hydrogen effects on X80 pipeline steel in high-pressure natural gas/hydrogen mixtures. *Int. J. Hydrogen Energy* **42**(11), 7404–7412 (2017)
57. Mhu, M., Du, C., Li, X., Liu, Z., Wang, S., Zhao, T., Jia, J.: Effect of strength and microstructure on stress corrosion cracking behavior and mechanism of X80 pipeline steel in high pH carbonate/bicarbonate solution. *J. Mater. Eng. Perform.* **23**, 1358–1365 (2014)
58. Midilli, A., Dincer, I.: Hydrogen as a renewable and sustainable solution in reducing global fossil fuel consumption. *Int. J. Hydrogen Energy* **33**(16), 4209–4222 (2008)

59. Mohtadi-Bonab, M.A., Szpunar, J.A., Razavi-Tousi, S.S.: A comparative study of hydrogen induced cracking behavior in API 5L X60 and X70 pipeline steels. *Eng. Fail. Anal.* **33**, 163–175 (2013)
60. Mohtadi-Bonab, M.A., Ghesmati-Kucheki, H.: Important factors on the failure of pipeline steels with focus on hydrogen induced cracks and improvement of their resistance: review paper. *Met. Mater. Int.* **25**(5), 1109–1134 (2019)
61. Nanninga, N.E. et al.: Comparison of hydrogen embrittlement in three pipeline steels in high pressure gaseous hydrogen environments. *Corros. Sci.* **59**(1–9) (2012)
62. Nelson, G.G.: Hydrogen embrittlement. In: Embrittlement of structural steels and alloys, pp. 256–333, Metallurgy, Moscow (1988) (in Russian)
63. Nelson, H.G.: Hydrogen-induced slow crack growth of a plain carbon pipeline steel under conditions of cyclic loading. In: Thompson, A.W. (ed.) *Effect of Hydrogen on Behavior of Materials*, pp. 602–611. Moran, Wyoming, USA (1976)
64. Nguyen, T.T., et al.: Effect of low partial hydrogen in a mixture with methane on the mechanical properties of X70 pipeline steel. *Int. J. Hydrogen Energy* **45**(3), 2368–2381 (2020)
65. Nguyen, T.T., et al.: Environment hydrogen embrittlement of pipeline steel X70 under various gas mixture conditions with in situ small punch tests. *Mater. Sci. Eng., A* **781**, 139114 (2020)
66. Nguyen, T.T., et al.: Hydrogen embrittlement susceptibility of X70 pipeline steel weld under a low partial hydrogen environment. *Int. J. Hydrogen Energy* **45**(43), 23739–23753 (2020)
67. Omura, T., Nakamura, J., Hirata, H., Jotoku, K., Ueyama, M., Osuki, T., Terunuma, M.: Effect of surface hydrogen concentration on hydrogen embrittlement properties of stainless steels and Ni based alloys. *ISIJ Int.* **56**(3), 405–412 (2016)
68. Öney, F., et al.: Evaluation of pipeline transportation of hydrogen and natural gas mixtures. *Int. J. Hydrogen Energy* **19**(10), 813–822 (1994)
69. Park, G.T., et al.: Effect of microstructure on the hydrogen trapping efficiency and hydrogen induced cracking of linepipe steel. *Corros. Sci.* **50**(7), 1865–1871 (2008)
70. Polyanskiy, V.A., et al.: Phenomenon of skin effect in metals due to hydrogen absorption. *Contin. Mech. Thermodyn.* **31**(6), 1961–1975 (2019)
71. Roffey, P., Davies, E.H.: The generation of corrosion under insulation and stress corrosion cracking due to sulphide stress cracking in an austenitic stainless steel hydrocarbon gas pipeline. *Eng. Fail. Anal.* **44**, 148–157 (2014)
72. Rusin, A., Stolecka, K.: Reducing the risk level for pipelines transporting carbon dioxide and hydrogen by means of optimal safety valves spacing. *J. Loss Prev. Process Ind.* **33**, 77–87 (2015)
73. San Marchi, C., Somerday, B.P., Nibur, K.A.: Development of methods for evaluating hydrogen compatibility and suitability. *Int. J. Hydrogen Energy* **39**(35), 20434–20439 (2014)
74. San Marchi, C. et al.: Fracture resistance and fatigue crack growth of X80 pipeline steel in gaseous hydrogen. *Press. Vessel. Pip. Conf.* **44564**, 841–849 (2011)
75. Shang, J., et al.: Effects of stress concentration on the mechanical properties of X70 in high-pressure hydrogen-containing gas mixtures. *Int. J. Hydrogen Energy* **45**(52), 28204–28215 (2020)
76. Shang, J., et al.: Enhanced hydrogen embrittlement of low-carbon steel to natural gas/hydrogen mixtures. *Scripta Mater.* **189**, 67–71 (2020)
77. Shi, X.B., Yan, W., Wang, W., Zhao, L.Y., Shan, Y.Y., Yang, K.: Effect of microstructure on hydrogen induced cracking behavior of a high deformability pipeline steel. *Journal Iron Steel Res. Int.* **22**, 937–942 (2015)
78. Smit, R., Weeda, M., De Groot, A.: Hydrogen infrastructure development in The Netherlands. *Int. J. Hydrogen Energy* **32**(10–11), 1387–1395 (2007)
79. Sutcliffe, J.M., Fessler, R.R., Boyd, W.K., Parkins, R.N.: Stress corrosion cracking of carbon steel in carbonate solutions. *Corrosion* **28**, 313–320 (1972)
80. Swain, M.R., Swain, M.N.: A comparison of H₂, CH₄ and C₃H₈ fuel leakage in residential settings. *Int. J. Hydrogen Energy* **17**(10), 807–815 (1992)
81. Takaki, S., et al.: Determination of hydrogen compatibility for solution-treated austenitic stainless steels based on a newly proposed nickel-equivalent equation. *Int. J. Hydrogen Energy* **41**(33), 15095–15100 (2016)

82. TM0284, NACE Standard. Evaluation of pipeline and pressure vessel steels for resistance to hydrogen-induced cracking. NACE International, Houston, TX (2011)
83. Trasatti, S.P., Sivieri, E., Mazza, F.: Susceptibility of a X80 steel to hydrogen embrittlement. *Mater. Corros.* **56**(2), 111–117 (2005)
84. Tzimas, E., Castello, P., Peteves, S.: The evolution of size and cost of a hydrogen delivery infrastructure in Europe in the medium and long term. *Int. J. Hydrogen Energy* **32**(10–11), 1369–1380 (2007)
85. Williams, D.P., Nelson, H.G.: Embrittlement of 4130 steel by low-pressure gaseous hydrogen. *Metall. Trans.* **1**(1), 63–68 (1970)
86. Wu, R., Ahlström, J., Magnusson, H., Frisk, K., Martinsson, A.: Charging, degassing and distribution of hydrogen in cast iron. Swerea KIMAB (2015)
87. Wu, T.I., Wu, J.C.: Effects of cathodic charging and subsequent solution treating parameters on the hydrogen redistribution and surface hardening of Ti-6Al-4V alloy. *J. Alloy. Compd.* **466**(1), 153–159 (2008)
88. Yagodzinsky, Y., Todoshchenko, O., Papula, S., Hanninen, H.: Hydrogen solubility and diffusion in austenitic stainless steels studied with thermal desorption spectroscopy. *Steel Res. Int.* **82**(1), 20–25 (2011)
89. Yamabe, J., Awane, T., Matsuoka, S.: Elucidating the hydrogen-entry-obstruction mechanism of a newly developed aluminum-based coating in high-pressure gaseous hydrogen. *Int. J. Hydrogen Energy* **40**(32), 10329–10339 (2015)
90. Zhao, W., et al.: Hydrogen permeation and embrittlement susceptibility of X80 welded joint under high-pressure coal gas environment. *Corros. Sci.* **111**, 84–97 (2016)

Chapter 26

Dynamic Model of Reliability and Survival in Big Data Analysis



Vladimir A. Prourzin and Sofia S. Rasova

Abstract The actual problem of estimation the indicators of reliability, survival and risk based on real operating data, characterized by different conditions and loads, is considered. A new formulation of the physical principle of reliability is proposed, and a dynamic model of reliability, analysis of survival, and risk taking into account variable loads in the form of a system of differential equations is built. A load is applied to the input of a dynamic system, and a function of the probability of failure-free functioning of the system is formed at its output. The conditions for the equivalence of dynamic models are investigated. In the presence of self-similarity of damage accumulation processes, the general dynamic model is reduced to an equivalent simplified basic dynamic model. Methods for estimating the parameters of this model based on the operating time to failure at various loading histories have been developed. To solve the problem, the maximum likelihood method was used. The results of experimental verification of the dynamic model based on the results of testing LEDs for reliability under constant and variable loading are presented. The constructed model was used to calculate a test variable load and compared with experimental data. The comparison results confirm the effectiveness of the method of dynamic models of survival and reliability under variable loading and accelerated testing. The results of the work can be used in the theory of the reliability of systems with variable loads, in the analysis of survival, the theory of accelerated and forced tests, in the construction of models of damage accumulation, and technical diagnostics.

Keywords Big data · Reliability · Survival analysis · Accelerated testing · Variable loads · Damage measure · Dynamic model · Maximum likelihood

V. A. Prourzin (✉) · S. S. Rasova
Institute for Problems in Mechanical Engineering RAS, V.O., Bolshoy pr., 61, St. Petersburg
199178, Russia
e-mail: proursin@gmail.com

S. S. Rasova
e-mail: rasova_s@mail.ru

© The Author(s), under exclusive license to Springer Nature Switzerland AG 2022
V. A. Polyanskiy and A. K. Belyaev (eds.), *Mechanics and Control of Solids and Structures*, Advanced Structured Materials 164,
https://doi.org/10.1007/978-3-030-93076-9_26

557

26.1 Introduction

Traditionally, assessments of reliability indicators are carried out using tests that are expensive and time-consuming. On the other hand, monitoring the operation of existing facilities allows you to collect a huge database of reliability indicators, in particular, data on operating time to failure. The approaches and methods of working with such huge databases constitute the content of the research area—big data [1–3]. Big data attributes are sometimes grouped together in a group called “7V”: Volume, Velocity, Variety, Veracity, Variability, Visualization, and Value. It is the variety and variability of big data that constitute the main problem of data analysis in the analysis of survival and the theory of reliability and risk. It consists in the fact that the operation of objects is characterized by various conditions and loads that change over time.

Survival analysis is a set of statistical methods for predicting the probability of an event occurring and the time before it occurs. The task of analyzing the survival rate of [4–6] is to assess the risks of disruption of this functioning using the vector of features describing the conditions of the object’s functioning. Survival analysis methods are used extensively in medicine, biology, insurance, and industry. For example, this is the loan default time, the isotope lifetime, the life expectancy of cancer patients, the failure-free operation of the technical system under the given loads.

Models of dependences of reliability indicators on loads are being developed within the framework of accelerated test methods. A fairly complete overview of modern accelerated testing methods is given in [7]. The most popular accelerated test models are the proportional intensity model and the AFT (accelerated failure time) model. An important result in the theory of accelerated tests is Sedyakin’s physical principle [8]. This principle initiated the work of other [9] researchers. In works [10] this approach is developed in relation to systems with variable loads. However, Sedyakin’s principle and its generalizations have a narrow area of rigorous application.

In this paper, a general physical principle of reliability is formulated, from which follows a dynamic model that connects the probability function of the system’s failure-free operation with the dynamics of changes in a certain measure of product damage [11–13]. Simple models with scalar loading are considered in detail and their properties are investigated. A general model with many variables is considered. The application of the dynamic model to the analysis of the reliability and survival of systems with variable load has been substantiated. Statistical methods for constructing dynamic models based on heterogeneous samples are considered.

26.2 Problem Statement

In the theory of survival, for a random variable T (the lifetime of something), the distribution function $F(t) = P\{T < t\}$ and the density $f(t) = d/dt F(t)$ are considered. Instead of the distribution function and density, in the analysis of survival,

the survival function $S(t) = 1 - F(t) = P\{T \geq t\}$ is usually used, which is equal to the probability of surviving by the time t and the risk (hazard) $h(t) = f(t)/S(t)$. In reliability theory, the survival function is called the reliability function (the probability of no-failure) $P(t)$, and the risk function is called the failure rate $\lambda(t)$. In the analysis of survival, mathematical models of the dependence of the survival and risk functions on the given θ features are of decisive importance. These features are also called covariates, loads, or stresses.

Accelerated test methods make it possible to decide on the reliability of systems during their operation under standard conditions based on the results of experiments carried out under conditions of increased loads in a shorter time. The complex of influencing factors is represented as a vector function $\theta(t)$. The set of possible loads is denoted by E , and by E_1 —is the set of loads, constant in time, $E_1 \subset E$. Let θ_0 be the load vector corresponding to normal operating conditions; $P_0(t) = P(t; \theta_0)$ and $\lambda_0(t) = \lambda(t; \theta_0)$ —reliability function and failure rate under normal load θ_0 ; $P(t; \theta)$ and $\lambda(t; \theta)$ —reliability functions and failure rate under arbitrary load. For a known failure rate $\lambda(t)$, the reliability function $P(t)$ is a solution to the differential equation:

$$\dot{P} = -P\lambda(t), \quad P(0) = 1. \tag{26.1}$$

In accelerated test models, the main issue is to build a relationship between the reliability function $P(t; \theta)$ and the reliability function $P_0(t)$ under constant loads: $\theta \in E_1$. There are two well-known accelerated test models on the set E_1 , called Lehmann models [9]. We consider a positive function $r(\theta)$ —a communication function that describes the total effect of the load influence on the duration of the system’s uptime. According to the first Lehmann model:

$$P(t, \theta) = P_0^{r(\theta)}(t), \quad \lambda(t; \theta) = r(\theta)\lambda_0(t). \tag{26.2}$$

Models of this type include, for example, the Cox proportional intensity model [14]. According to the second Lehmann model,

$$P(t, \theta) = P_0(r(\theta)t), \quad \lambda(t; \theta) = r(\theta)\lambda_0(r(\theta)t). \tag{26.3}$$

The failure rate model in the form of (26.3) is usually called the AFT (accelerated failure time) model on E_1 .

The problem of accelerated tests is to construct the coupling function $r(\theta)$. The main problems of applying the above approaches are as follows. The stress vector includes both loads and object state variables. However, the relationship between loads and state variables is not used in this case. There are problems of using the constructed models to account for variable loads.

Here we are talking about the next problem. Data on operating conditions and associated lifetimes are collected from various sources. The problem of statistical analysis of big heterogeneous data arises. Let N pairs of observations for objects of the same type be given: the lifetime t_k (time to failure) and the corresponding vector of

covariats $\theta_k(t)$, describing the operating conditions and load. It is required to construct a model that allows for an arbitrary vector $\theta(t)$ to obtain the reliability (survival) function $P(t; \theta)$. Further presentation will be carried out in terms of reliability theory.

26.3 The Dynamic Reliability Model

We consider a reliability model in which the operating load is described by the scalar quantity $\theta(t)$. One reason for failure due to a certain degradation process (mechanical, physical, chemical, etc.) is considered. We introduce a scalar value y that is a measure of damage accumulation. This parameter can have a physical meaning (for example, crack length, amount of wear, flow rate of the operating fluid, degree of corrosion, etc.) or be a generalized semi-empirical indicator [15]. A connection for the load and damage measure is introduced through the differential equation:

$$\dot{y} = F(y, \theta), \quad y(0) = y_0. \quad (26.4)$$

In general the probability of no-failure operation $P(t; \theta)$ at time t depends on the load values of $\theta = \theta(t)$ over the entire time interval $(0, t)$. This relationship can be clarified using physical considerations. The Markov property of physical systems is taken as a postulate.

The physical principle of reliability. There is a damage measure indicator $y = y(t)$ such that the failure probability on a short time interval $[t, t + \Delta t]$, provided that the system is in good operating order at time t , is determined only by the current value of $y(t)$ and does not depend on the history.

As a substantiation of the physical principle formulated, we can consider the procedure of technical diagnostics. In the process of diagnostics, it is the current values of the diagnostic parameters (damage measures) that are measured, and a conclusion about the object state and the possibility of its failure in the near future is made only based on these values. The history of the change in the damage measure is usually not considered. For example, the failure probability of a car's brakes over a short time interval depends only on the amount of brake pad wear y at the moment considered and does not depend on the history of this wear.

On the other hand, the current value of the damage measure $y(t)$ is an integral characteristic of the entire loading history. It is determined by the differential equation (26.4). The probability of failure, which is determined by the achieved value of the damage measure, thus indirectly depends on the entire loading history.

The formulated physical principle is equivalent to the condition for the existence of a non-negative coefficient D that depends only on the value of the damage measure at time t : $D = D(y(t))$, and such that

$$\frac{P(t + \Delta t; \theta)}{P(t; \theta)} = 1 - D(y(t)) \Delta t + o(\Delta t). \quad (26.5)$$

The expression to the left of the equal sign is the probability of failure-free operation of the system on a short time interval $[t, t + \Delta t]$, provided that the system did not fail on the interval $[0, t]$. The expression to the right is the value of this conditional probability linearized with respect to Δt that depends only on the current value y . The function $D(y)$ has the meaning of the hazard of failure when the damage measure reaches the value y . The transfer in expression (26.5) to the limit as Δt tends to zero gives the differential equation

$$\dot{P}(t) = -P(t)D(y(t)). \tag{26.6}$$

Comparison of Eqs. (26.1) and (26.6) implies a relationship between the failure rate and the failure danger function under load $\theta(t)$:

$$\lambda(t; \theta) = D(y(t; \theta)). \tag{26.7}$$

Combining Eqs. (26.4) and (26.6) gives a system of differential equations, i.e., a dynamic reliability model:

$$\begin{cases} \dot{y} = F(y, \theta), & y(0) = y_0; \\ \dot{P} = -PD(y), & P(0) = 1. \end{cases} \tag{26.8}$$

The load $\theta = \theta(t)$ is applied to the input of system (26.8), and the output is the dependence $y(t)$ of the damage measure on time and the reliability function $P(t)$.

Below are examples of dynamic models. For clarity, the load is assumed to be constant over time: $\theta(t) \in E_1$.

26.3.1 Example 1

Let in system $F(y, \theta) = -H(\theta)(y - R(\theta))$, $H(\theta) > 0$, $R(\theta) > 0$, $D(y) = \lambda_0 y$. The solution of the first equation of system (26.8) at $\theta(t) \in E_1$ has the form of $y(t) = R(\theta) + (y_0 - R(\theta)) \exp(-H(\theta)t)$. The damage measure $y(t)$ tends to $R(\theta)$ with increasing time, while the hazard function $D(y)$ tends to a constant value $R(\theta)\lambda_0$ of the faster, the larger $H(\theta)$. If we set $y_0 = R(\theta)$, then this constant value is reached immediately and the solution of the second equation of system (26.8) gives an exponential distribution $P = \exp(-R(\theta)\lambda_0 t)$. If $y_0 > R(\theta)$, then the case of an increased failure rate in the initial period of time (“infant mortality”) with a transition to a constant rate is modeled. If $y_0 < R(\theta)$, then there is the case of a reduced failure rate in the initial period.

26.3.2 Example 2

Let in system (26.8) $F(y, \theta) = y^{1-\alpha} R(\theta)$, $\alpha \neq 1$, $y_0 = 0$. At constant load θ , the solution to the first equation of system (26.8) is given by the expression: $y(t) = \alpha (R(\theta)t)^{\frac{1}{\alpha}}$. Let the failure hazard function have a power-law dependence on the damage measure: $D(y) = cy^\beta$, $c, \beta > 0$. Then, the solution of the second equation of system (26.8) gives a reliability function in the form of the Weibull distribution. Let in this example another failure hazard function be given: $D(y) = \exp(-f^2(y)/2) / (\sqrt{2\pi}\sigma \Phi(f(y)))$, where $f(y) = (\alpha \ln(y/\alpha) - \mu)/\sigma$; parameters $\sigma, \mu > 0$, and $\Phi(x)$ is the Laplace function. Then, at $\theta(t) \in E_1$, system (26.8) generates the lognormal distributions of the failure-free operation time.

26.3.3 Self-similarity Property

Let the hypothesis of self-similarity in accelerated tests be valid. Self-similarity is based on an assumption about the similarity of damage accumulation processes under various loads. As was shown in [6], if the hypothesis of self-similarity is valid, the Eq. (26.4) for the damage measure y must be a differential equation with separable variables; i.e., the following representation of the right-hand side must be performed: $F(y, \theta) = S(y)R(\theta)$. A dynamic model (26.8) in this case has the following form:

$$\begin{cases} \dot{y} = S(y)R(\theta), & y(0) = y_0; \\ \dot{P} = -PD(y), & P(0) = 1. \end{cases} \tag{26.9}$$

The problem of statistical analysis of big data within the framework of the model (26.9) is reduced to the construction of functions $S(y)$, $R(\theta)$ and $D(y)$.

Remark 1 According to its physical meaning, the damage measure y under constant load should change monotonically. It follows that the function $S(y)$ has constant sign.

26.3.4 Model Equivalence and the Basic Dynamic Reliability Model

Let two different measures of damage y_1 and y_2 be considered to describe a failure under load $\theta(t) \in E$, and let two dynamic reliability models be constructed:

$$\begin{cases} \dot{y}_1 = F_1(y_1, \theta), & y_1(0) = y_{10}, \\ \dot{P}_1 = -P_1 D_1(y_1), & P_1(0) = 1; \end{cases} \tag{26.10}$$

$$\begin{cases} \dot{y}_2 = F_2(y_2, \theta), & y_2(0) = y_{20}, \\ \dot{P}_2 = -P_2 D_2(y_2), & P_2(0) = 1. \end{cases} \tag{26.11}$$

The conditions for the equivalence of these models are studied. Two dynamic reliability models (26.10) and (26.11) are *equivalent* on a given set of loads E if the identity $P_1(t; \theta) \equiv P_2(t; \theta)$ is satisfied for each $\theta \in E$.

Let the ratio of the functions F_1 and F_2 be a constant sign. Further, without loss of generality, we can consider it positive. Let this ratio not depend on the load: $F_1(y_1, \theta)/F_2(y_2, \theta) = H(y_1, y_2) > 0$. Dividing the first equation of system (26.10) by the first equation of system (26.11), we obtain the differential equation $dy_1/dy_2 = H(y_1, y_2)$ with the initial condition $y_1(y_{20}) = y_{10}$. Let $y_1 = \varphi(y_2)$ be the solution to this equation. Since the function $H(y_1, y_2)$ is positive, the function $\varphi(y_2)$ increases monotonically. Let us define the system hazard function (26.11) as $D_2(y_2) = D_1(\varphi(y_2))$. Then, for all $t > 0$ and loads θ , the equivalence condition is satisfied:

$$\begin{aligned} P_1(t) &= \exp\left(-\int_0^t D_1(y_1(s)) ds\right) = \exp\left(-\int_0^t D_1(\varphi(y_2(s))) ds\right) = \\ &= \exp\left(-\int_0^t D_2(y_2(s)) ds\right) = P_2(t). \end{aligned}$$

As a result, next Statement is proved.

Statement 1. *If the ratio of functions $F_1(y_1, \theta)/F_2(y_2, \theta)$ has of constant sign and does not depend on the load, then by choosing a function $D_2(y_2)$, dynamic model (26.11) can be made equivalent to dynamic model (26.10).* The equivalence property allows substantiating the use of semi-empirical models: any damage measure even if it does not have a definite physical meaning, as long as its value monotonically depends on the amount of real damage, can be used.

Let the reliability models (26.10) and (26.11) are self-similarity (have the form of (26.9)), i.e., $F_1(y_1, \theta) = S_1(y_1) R_1(\theta)$ and $F_2(y_2, \theta) = S_2(y_2) R_2(\theta)$. By virtue of Statement 1, these models will be equivalent when the functions R_1 and R_2 coincide up to a constant factor: $R_1(\theta) = a R_2(\theta)$, $a \neq 0$. In this case, the ratio $H(y_1, y_2) = a S_1(y_1)/S_2(y_2)$ does not depend on the load. This ratio has of constant sign by virtue of Note 1.

An important conclusion follows from this: for the self-similar system (26.9) there is an infinite set of equivalent systems. All of them are determined by the same function $R(\theta)$ and any constant-sign function $S(y)$. From the set of these equivalent models, the model of the simplest form is distinguished at $S(y) \equiv 1$. Thus, for any model of the form of (26.9), there is an equivalent dynamic model that we will call the basic dynamic reliability model:

$$\begin{cases} \dot{x} = R(\theta), & x(0) = x_0; \\ \dot{P} = -P D_0(x), & P(0) = 1. \end{cases} \tag{26.12}$$

The new damage measure x is a nonlinear transformation of the initial measure y : $x = g(y)$, and $D_0(x)$ is the failure hazard function of the basic dynamic model. Without loss of generality, the function $R(\theta)$ in this model can be considered positive. The transfer from basic model (26.12) to model (26.9) with some function $S(y)$ is performed by the transformation $D(y) = D_0(g(y))$, where $g(y) = x_0 + \int_{y_0}^y dy/S(y)$ is the solution to the equation $dx/dy = 1/S(y)$, $x(y_0) = x_0$. A solution of system (26.12) in the general form is

$$x(t) = x_0 + \int_0^t R(\theta(s)) ds, \quad P(t) = \exp\left(-\int_0^t D_0(x(s)) ds\right). \quad (26.13)$$

Consider the basic model (26.12) at constant loads. Then, $x(t) = x_0 + R(\theta)t$, and the application of this equality to replace the integration variable in (26.13) gives

$$P(t) = \exp\left(-\frac{1}{R(\theta)} \int_{x_0}^{x_0+R(\theta)t} D_0(x) dx\right). \quad (26.14)$$

26.4 Multidimensional Models

A set of covariates generally includes a set of system state parameters and a set of external loads. It is convenient to divide the system state vector into two vectors: $z = (z_1, z_2, \dots, z_n)$ and $y = (y_1, y_2, \dots, y_m)$. Vector z is auxiliary variables, vector y is a set of damage measure indicators. The vector function $\theta(t) = (\theta^{(1)}(t), \theta^{(2)}(t), \dots, \theta^{(l)}(t))$ sets variable loads. The system of equations

$$\begin{cases} \dot{z} = G(z, \theta), & z(0) = z_0; \\ \dot{y} = F(y, z, \theta) & y(0) = y_0; \\ \dot{P} = -PD(y). & P(0) = 1 \end{cases} \quad (26.15)$$

is a general dynamic model of reliability, describing the dynamics of accumulation of damages and the occurrence of failure taking into account variable loads.

The first equation of the system (26.15) admits an independent solution $z(t)$. Let's substitute it in the second equation as additional loads. As a result, we get a system of the form (26.8). We write down the well-known property of risk functions as follows.

Remark 2 Let there are some independent types of failures in a system and the common failure of system occurs at approach at least one of particular failures. Let for each particular failure the hazard function is built. Then common hazard function of system is equal to the sum of particular hazard functions.

In this case it is possible to present the system failure schematically as the failure of sequentially joint elements. At least in the first approximation it is possible to consider that particular failures are independent when they have different physical

nature or when they are linked with operation of different nodes or subsystems. Let there are m types of independent failures and each one has its own damage measure indicator. A hazard function for each failure is $D_i(y_i)$. Then the hazard function of the system has the form $D(y) = \sum_{i=1}^m D_i(y_i)$ and the dynamic model is

$$\begin{cases} \dot{y}_i = F_i(y_i, \theta), & y_i(0) = y_{i0}; \quad i = 1, \dots, m \\ \dot{P} = -P \sum_{i=1}^m D_i(y_i), & P(0) = 1. \end{cases} \quad (26.16)$$

Self-similar processes of damage accumulation are considered below. Then $F_i(y_i, \theta) = S_i(y_i) R_i(\theta)$. Arguing similarly to the case of a simple system, we arrive at an equivalent basic dynamical model

$$\begin{cases} \dot{x}_i = R_i(\theta), & x_i(0) = x_{0i}, \quad i = 1, \dots, m; \\ \dot{P} = -P D_0(x), & P(0) = 1, \end{cases} \quad (26.17)$$

where $D_0(x) = \sum_{i=1}^m D_{0i}(x_i)$. The new measure of damage x_i is a nonlinear transformation of the original measure y_i : $x_i = g_i(y_i)$, functions $D(y)$ and $D_0(x)$ are related by dependency $D(y_1, y_2, \dots, y_m) = D_0(g_1(y_1), g_2(y_2), \dots, g_m(y_m))$. Here

$$g_i(y_i) = x_{i0} + \int_{y_{i0}}^{y_i} \frac{dy_i}{S_i(y_i)}. \quad (26.18)$$

The non-negative function $R_i(\theta)$ specifies the dependence of the growth rate of the generalized damage value x_i on the current load.

The system (26.17) may be reduced to m systems with a scalar load:

$$\begin{cases} \dot{x}_i = R_i(\theta), & x_i(0) = x_{0i}; \\ \dot{P}_i = -P_i D_{0i}(x_i), & P_k(0) = 1. \end{cases} \quad k = 1, \dots, m. \quad (26.19)$$

The probability of a failure-free operation of the system is equal to $P = \prod_{i=1}^m P_i$

26.4.1 Example. The Model of Failure of Electrical Machines Owing to Heat Ageing of Insulation

We will consider model of failure electrical machines owing to a heat ageing of a winding insulation of a rotor and a stator [11]. The external mechanical load on an electrical machine is set by vector-functions $\theta(t)$. The temperature vector of the machine nodes is denoted $\tau = (\tau_1, \tau_2, \dots, \tau_n)$ where the first two components are the temperatures of the rotor and stator. Rotor and stator failures are considered independent. The dynamic model of reliability is

$$\begin{cases} C\dot{\tau} = \Lambda\tau + \theta; \\ \dot{y}_1 = -R(\tau_1)y_1; \\ \dot{y}_2 = -R(\tau_2)y_2; \\ \dot{P} = -P(D_1(y_1) + D_2(y_2)). \end{cases} \tag{26.20}$$

Here the first equation describes the change in the temperature of the machine nodes under the action of the load vector θ [16], C is the diagonal matrix, Λ is a square matrix of dimension $[n \times n]$. The physical model of an ageing of insulation is set by the equations of kinetics of chemical reactions [11]: $\dot{y}_i = -R(\tau_i)y_i$, where y_1, y_2 —are specific concentrations of the initial substance in the winding insulation of the rotor and the stator. These variables are used as damage measure indicators. The equation presents the decrease of concentration of initial substance, depending on time and a temperature. The initial value of the concentration is equal 1. The hazard of failure of winding insulation grows with diminution of the concentration of initial substance. According to the Arrhenius equation the coefficient $K = A \exp\left(-\frac{E_a}{K\tau}\right)$, where E_a is the activation energy, K is the universal gas constant, τ is the Kelvin temperature.

Let the solution of the first equation $\tau(t)$ be constructed. It is also possible to consider the case where the rotor and stator temperatures are obtained from measurements. Rename $\tau_1(t), \tau_2(t)$ as new loads $\theta_1(t), \theta_2(t)$. P_1, P_2 are probabilities of no-failure of the rotor and the stator, $P = P_1 P_2$. The system (26.20) has been reduced to two simple self-similar systems of the form (26.9). Each of the two equations is written as

$$\begin{cases} \dot{y} = -R(\theta)y; \\ \dot{P} = -PD(y). \end{cases} \tag{26.21}$$

26.5 Building a Dynamic Reliability Model Based on Experimental Data

We consider the problem of constructing functions that define a dynamic model (26.17), based on the operating time to failure under various loads. An object is considered, the state of which is given by the generalized vector measure of damage $x(t)$, and the operational load is given by the vector function of time $\theta(t)$. The reliability function $P(t)$ specifies the probability of no-failure operation of the object at the moment of time t . The (26.17) system has a general solution in integrals:

$$x_i(t) = x_{i0} + \int_0^t R_i(\theta(s)) ds, \quad P(t) = \exp\left(-\int_0^t D_0(x(s)) ds\right). \tag{26.22}$$

The probability density of failure $f(t; \theta) = -dP(t; \theta)/dt$ is

$$f(t; \theta) = P(t; \theta) D_0(x(t; \theta)). \tag{26.23}$$

Remark 3 Let in the base model (26.17) the values of the function $R_i(\theta)$ are specified up to the parameters of the scale a_i : $R_i(\theta) = a_i R_i^*(\theta)$, and the function $D_0(x)$ is specified up to the parameters of the scale b_i arguments: $D_0(x) = D_0^*(b_1 x_1, \dots, b_i x_i, \dots, b_m x_m)$. It is easy to make sure that the reliability indicators, calculated by the (26.17) model will depend on the products $a_i b_i$ of the scale parameters. Two systems with the same meaning of these products will be equivalent. This means that one of the scale parameters a_i or b_i can be set arbitrarily. Then the second parameter is determined by the value of the product.

We consider the problem of constructing a dynamic reliability model of the form (26.17), in which damage measure indicators x and loads θ are vectors. Let the operating time to failure t_k and the corresponding loads $\theta_k(t)$, $k = 1, \dots, N$, are known for N products of the same type. Loads can be partially or completely different from each other. Loads can be both constant and variable over time.

Parametric families of functions $R_i(\theta; \alpha_i)$ and $D_{0i}(x_i; \beta_i)$ with vectors of unknown parameters $\alpha_i = (\alpha_i^{(1)}, \dots, \alpha_i^{(p_i)})$ and $\beta_i = (\beta_i^{(1)}, \dots, \beta_i^{(q_i)})$. The problem of estimating these parameters from known observations $t_k, \theta_k(t), k = 1, \dots, N$ is posed.

The maximum likelihood method [17] is one of the most versatile methods for estimating unknown parameters of the failure distribution directly from the available time to failure t_k sample. As an estimate of the parameters of the dynamic model, the values that maximize the probability of the appearance of this sample are taken. For this, a likelihood function is constructed—the product of the failure probability densities calculated for each value of t_k . Due to (26.22), (26.23), the logarithm of the likelihood function in this case is:

$$L(\alpha, \beta) = \sum_{k=1}^N \left[- \sum_{i=1}^m \int_0^{t_k} D_{0i}(x_i(t; \theta_k, \alpha_i); \beta_i) dt + \ln \sum_{i=1}^m D_{0i}(x_i(t_k; \theta_k, \alpha_i); \beta_i) \right]. \tag{26.24}$$

The maximum likelihood estimates $\hat{\alpha}, \hat{\beta}$ are obtained by solving the problem of unconstrained maximization of the function $L(\alpha, \beta)$.

The problem of constructing a basic model (26.17) in the case of constant values of the loads θ_k is considered separately. Then the expression for $x_i(t)$ is a linear function of time: $x_i(t) = x_{i0} + R_i(\theta_k; \alpha) t$. These expressions are used to replace a variable in each (26.24) integral. The designation is introduced: $G_i(x_i; \beta_i) = \int_0^{x_i} D_{0i}(u; \beta_i) du$. Then

$$L(\alpha, \beta) = \sum_{k=1}^N \left[- \sum_{i=1}^m \frac{G_i(x_{i0} + R_i(\theta_k; \alpha) t_k; \beta_i)}{R_i(\theta_k; \alpha)} + \ln \sum_{i=1}^m D_{0i}(x_{i0} + R_i(\theta_k; \alpha) t_k; \beta_i) \right]. \tag{26.25}$$

The solution to the problem of constructing a basic dynamic model at constant loads is to maximize the nonlinear function (26.25).

26.5.1 Example 3

Let the reliability model under the temperature load $\theta = \theta(t)$ be given by the well-known equation of the kinetics of chemical reactions (26.21). According to the Arrhenius equation, the function $R(\theta) = \exp(\alpha_1 - \alpha_2/\theta)$, where θ is the absolute temperature, α_1, α_2 —parameters to be assessed. The risk of failure increases with decreasing concentration $y(t)$ of the original substance.

The damage accumulation equation satisfies the self-similarity condition, i.e., the dynamic reliability model has the form (26.9). Here $S(y) = -y$. When passing to the equivalent base model (26.12), the new damage measure x increases from zero, $x(0) = 0$, the risk of failure grows with the growth of x . Let the failure hazard function $D_0(x)$ be constructed as a power function of the damage measure: $D_0(x) = \beta_1 x^{\beta_2}$. Let the test temperature loads $\theta_k, k = 1, \dots, N$, be constant in time. The likelihood function (26.25) takes the following form:

$$L(\alpha, \beta) = \sum_{k=1}^N \left[-\frac{\beta_1 (\exp(\alpha_1 - \alpha_2/\theta_k) t_k)^{\beta_2+1}}{(\beta_2 + 1) \exp(\alpha_1 - \alpha_2/\theta_k)} + \ln \beta_1 + \beta_2 (\alpha_1 - \alpha_2/\theta_k + \ln t_k) \right]. \quad (26.26)$$

By virtue of Remark 3, the number of independent variables of the likelihood function (26.26) can be reduced and go to the problem with three unknowns. New unknown parameters are introduced: $z_1 = \ln \beta_1 + \alpha_1 \beta_2, z_2 = -\alpha_2 \beta_2, z_3 = \beta_2$. The designation is introduced $f_k(z_1, z_2, z_3) = \ln D_0(R(\theta_k) t_k) = z_1 + z_2/\theta_k + z_3 \ln t_k$. Then $G(R(\theta_k) t_k)/R(\theta_k) = t_k \exp(f_k)/(z_3 + 1)$. Substitution of these values into the likelihood function (26.26) gives

$$L(z_1, z_2, z_3) = \sum_{k=1}^N \left[\frac{-t_k \exp(f_k(z_1, z_2, z_3))}{(z_3 + 1)} + f_k(z_1, z_2, z_3) \right].$$

Let be \hat{z}_1, \hat{z}_2 and \hat{z}_3 deliver the maximum of the constructed likelihood function. The transition to the initial parameters is carried out: $\hat{\beta}_2 = \hat{z}_3, \hat{\alpha}_2 = -\hat{z}_2/\hat{z}_3$. The parameters α_1 and β_1 are related by the equality $\hat{z}_1 = \ln \beta_1 + \alpha_1 \hat{\beta}_2$. You can take any positive value of $\hat{\alpha}_1$, for example, for physical reasons, and calculate the parameter $\hat{\beta}_1$ from it. For any such pair of values $\hat{\alpha}_1, \hat{\beta}_1$, the solution of the (26.26) system gives the same value of the required probability $P(t)$.

To return to the original dynamic model (26.21), the function $D(y)$ is constructed from the expression (26.18). Here $x = g(y) = -\ln y$ and $D(y) = \beta_1 (-\ln y)^{\beta_2}$. As a result, a dynamic reliability model has been built:

$$\begin{cases} \dot{y} = -y \exp\left(\hat{\alpha}_1 - \frac{\hat{\alpha}_2}{\theta(t)}\right), & y(0) = 1; \\ \dot{P} = -P \hat{\beta}_1 (-\ln y)^{\hat{\beta}_2}, & P(0) = 1, \end{cases}$$

which can be used to calculate the probability of no-failure operation $P(t)$ at any temperature load $\theta(t)$.

26.6 Experimental Verification of the Dynamic Reliability Model

This section analyzes the results of field tests for reliability and builds dynamic reliability models. For the experimental study, real physical objects were selected—green LEDs with a diameter of 5 mm. LEDs are a rather complex technical object, in which, during its operation, various physicochemical degradation processes occur, leading to failure. The average operating time of an LED under normal load is measured in years. In order to significantly reduce the duration of the experiment, accelerated test methods are used. For this, tests are carried out at increased electrical load.

It should be noted that the experiment was carried out in order to check the adequacy of the proposed dynamic model and methods for its construction. Here, the sampling of experimental data on the operating time of products under various loads is of importance. The specific type of the tested product itself is not important here, the specific LED model is not indicated. This work does not claim to be a comprehensive study of the reliability of LEDs.

Green LEDs with normal values of forward current $I_f = 19 - 20$ mA and forward voltage $U = 2.3 - 2.5$ V were selected as the test object. The test items are divided into 5 groups with $N_k = 31, 37, 65, 25, 28$ items in each group. Each group has its own load $\theta_k, k = 1, \dots, 5$. Reliability tests were carried out under four constant voltage and one variable load modes. The variable load was a step function with voltage values of 4.2 V (time interval 0–140 h), 4.8 V (140–260 h) and 6.6 V (from 260 h until the time of the last element failure). As a result of the tests, $r_k = 31, 36, 63, 23, 28$ values of the MTBF $t_{ki}, k = 1, \dots, 5, i = 1, \dots, r_k$ were obtained. Runtime values are sorted in ascending order. Initial data and primary test results are shown in Table 26.1.

Based on the test results, a basic dynamic model of the form (26.12) is built. For its construction, test data with four constant loads $\theta_1 = 6.6$ V, $\theta_2 = 5.9$ V, $\theta_3 = 5.4$ V and $\theta_4 = 5.0$ V are used. All functions included in the model are assumed to be exponential: $R(\theta) = (\theta/\alpha_1)^{\alpha_2}, D_0(x) = \beta_1 x^{\beta_2}, G(x) = \int_0^x D_0(u; \beta) du = \beta_1 (\beta_2 + 1)^{-1} x^{\beta_2+1}$. The parameter vectors $\alpha = (\alpha_1, \alpha_2), \beta = (\beta_1, \beta_2)$ were estimated using the maximum likelihood method.

The following estimates are obtained for $\hat{\alpha}, \hat{\beta}$. As shown above, the feature of the (26.12) model allows one to reduce the dimension and one of the coefficients, α_1 or β_1 , can be set to an arbitrary value. Then the second of them is calculated according to the experimental data. It is accepted here $\hat{\alpha}_1 = 8$. The rest of the values are obtained from minimizing the maximum likelihood function (26.26) and they are equal: $\hat{\alpha}_2 = 22.89, \hat{\beta}_1 = 0.206, \hat{\beta}_2 = 0.564$. The calculated reliability functions

Table 26.1 Initial data and reliability test results of LEDs

No	Load U, V	N_k	r_k	MTBF(h.), t_{ki}
1	6.6	31	31	4.6; 5.6; 5.8; 5.9; 6.4; 6.4; 6.9; 6.9; 7.1; 7.4; 7.7; 8.4; 8.8500; 9.6; 9.9; 11.1; 11.8; 13.3; 13.7; 15.2; 15.7; 16.7; 17.4; 17.8; 18.7; 22.7; 26.0; 29.2; 33.5; 34.6; 69.9
2	5.9	37	36	9.0; 9.9; 12.2; 14.2; 14.9; 17.6; 18.2; 20.2; 20.4; 21.6; 24.8; 25.0; 25.0; 25.0; 25.1; 28.7; 32.2; 34.0; 35.2; 36.1; 39.4; 40.1; 50.3; 50.6; 51.9; 57.1; 60.5; 61.1; 62.0; 63.3; 69.8; 70.7; 75.2; 82.5; 104.9; 129.7
3	5.4	65	63	45.9; 47.1; 50.6; 51.8; 53.5; 53.8; 54.0; 55.4; 56.2; 57.9; 61.8; 63.9; 64.0; 64.8; 65.2; 70.5; 79.9; 85.0; 85.2; 87.0; 87.3; 87.5; 90.9; 94.4; 96.3; 98.0; 101.8; 103.6; 109.8; 111.9; 113.2; 119.3; 121.0; 124.0; 125.1; 133.6; 144.8; 148.0; 150.1; 165.8; 188.0; 228.0; 250.7; 278.1
4	5.0	25	23	23.2; 41.6; 50.5; 70.8; 72.4; 76.3; 85.0; 112.0; 121.0; 136.0; 139.6; 146.0; 152.8; 164.0; 187.2; 193.2; 215.1; 263.0; 276.0; 297.7; 320.0; 340.0; 378.4
5	Variable load	28	28	97; 122.0; 174.0; 198.0; 206.0; 231.0; 242.0; 261.0; 262.0; 262.5; 264.0; 264.0; 264.5; 265.0; 265.0; 265.0; 265.5; 266.5; 268.5; 271.0; 274.5; 275.0; 277.5; 286.0; 291.0; 310.0; 313.5; 428.0

under constant loading belong to the family of Weibull distributions with an exponent of the form $\hat{\beta}_2 + 1$.

To check the adequacy and predictive ability of the constructed models, the calculated values of the reliability function according to the (26.12) model were compared with its empirical values constructed from the results of tests for variable loading. Note that the data from this experiment were not used to estimate the parameters of the model. The coefficient of determination is $R^2 = 0.9238$. This value is confirmed by the adequacy of the model.

26.7 Conclusion

A dynamic model of reliability, analysis of survival and risk under arbitrary loads was built. The model is a system of ordinary differential equations, the input of which is a load, and the output is a reliability function. In the case of self-similarity of damage accumulation processes, the general dynamic model is reduced to a simplified basic dynamic model. The model has direct application in cases where the loads are specified as deterministic functions of time. First of all, such a situation arises when

assessing the indicators of reliability and survival according to real operating data, as well as during accelerated tests. Methods for estimating the parameters of a dynamic model based on the operating time of objects to failure at various loading histories have been developed. To solve the problem, the maximum likelihood method is used. Finally, the problem is reduced to the problems of finding an unconditional extremum of nonlinear functions. The simplest case of evaluating the parameters of the dynamic model of the reliability model occurs at constant test loads. Based on experimental data obtained during accelerated tests of LEDs for reliability with various loads, the adequacy of the simplest dynamic model of survival and reliability is confirmed. After evaluating its parameters according to experimental data, this model can be used to calculate reliability indicators for an arbitrary load.

Acknowledgements The present work was supported by the Ministry of Science and Higher Education within the framework of the Russian State Assignment under contract No. FFNF-2021-0008.

References

1. Leskovec, J., Rajaraman, A., Ullman, J.D.: Mining of Massive Data Sets. Cambridge university press, Cambridge (2020). <https://doi.org/10.1017/9781108684163>
2. Hong, Y., Zhang, M., Meeker, W.Q.: Big data and reliability applications: the complexity dimension. *J. Qual. Technol.* **50**(2), 135–149 (2018). <https://doi.org/10.1080/00224065.2018.1438007>
3. Pyne, S., Rao, B.P., Rao, S.B. (eds.): Big Data Analytics: Methods and Applications. Springer (2016)
4. Kleinbaum, D.G., Klein, M.: Survival Analysis. Springer, New York (2010)
5. Klein, J.P., Moeschberger, M.L.: Survival Analysis: Techniques for Censored and Truncated Data. Springer (1997)
6. Wang, W., Lu, S.E., Cheng, J.Q., Xie, M., Kostis, J.B.: Multivariate survival analysis in big data: A divide and combine approach. *Biometrics* (2021)
7. Escobar, L.A., Meeker, W.Q.: A review of accelerated test models. *Stat. Sci.* **21**(4), 552–577 (2006)
8. Sedyakin, N.M.: On one physical principle of the theory of reliability. *Izv. AN SSSR. Technicheskaya kibernetika* **3**, 80–87 (1966)
9. Bagdonavicius, V., Nikulin, M.: Accelerated Life Models: Modeling and Statistical Analysis. Chapman & Hall, Boca Raton, Florida (2002)
10. Pavlov, I.V.: Calculating reliability indices under the conditions of an alternating operating regime. *J. Mach. Manuf. Reliab.* **41**, 431–434 (2012)
11. Novikov, P.I., Prourzin, V.A.: Dynamic model of the reliability of insulation in electrical machines. *J. Mach. Manuf. Reliab.* **1**, 106–111 (2005)
12. Prourzin, V.A.: General physical principle in dynamic model of reliability. *Int. J. Risk Assess. Manag.* **20**(4), 322–332 (2017). <https://doi.org/10.1504/IJRAM.2017.087902>
13. Prourzin, V.A.: The dynamic reliability model under variable loads and accelerated tests. *J. Mach. Manuf. Reliab.* **49**(5), 395–400 (2020). <https://doi.org/10.3103/S1052618820050118>
14. Cox, D.: Regression models and life tables (with discussion). *J. Roy. Stat. Soc. B* **74**, 187–220 (1972)
15. Bolotin, V.V.: Resurs mashin i konstruksii (Lifetime of Machines and Structures). Mashinostroyeniye, Moscow (1990)

16. Novikov, P.I., Prourzin, V.A.: A rapid method of identifying the thermal parameters of an electrical machine during heat tests. *Electr. Technol. Russ.* **1**, 22–30 (2001)
17. Myung, I.J.: Tutorial on maximum likelihood estimation. *J. Math. Psychol.* **47**(1), 90–100 (2003)

Chapter 27

Using the Wear Model of Polymer Composites Based on Polytetrafluoroethylene to Determine the Filling Efficiency of Matrix



Elena B. Sedakova and Yuri P. Kozyrev

Abstract The structural parameter of composites with dispersed filler of nano- and micro-dimensions is proposed. The derivation of the physical wear model from the empirical wear formula is considered in order to predict the wear resistance of composites at the stage of their design. The developed model allows to estimate wear resistance of composites depending on filler concentration, size and peculiarities of filler particles distribution. The validity of the wear model is shown by the results of comparing the calculated results with the experimental curves.

Keywords Friction · Wear · Polymer · Filler · Wear model · Composite

27.1 Introduction

A characteristic feature of the development of modern mechanical engineering is the variety of external conditions in which mechanisms operate. Increase of service life of machines and mechanisms in many respects depends on the solution of tribological problems of their units. One of the perspective ways of the decision of a problem of maintenance of required indicators of reliability of friction pairs is application of self-lubricating polymeric materials and composites on their basis. It gives an opportunity of replacement in friction pairs of antifriction metals and alloys that provide possibility of almost silent work of wear units in conditions without greasing, in water, in chemically active environment and in vacuum. Besides, such friction units can work rather in a wide range of changing temperatures and loads. The available wide range of application areas of polymeric materials in many respects is explained by introduction in them of various types of fillers.

The principle of obtaining polymer composite materials is to create a predetermined combination of two different phases (filler and matrix) using certain tech-

E. B. Sedakova (✉) · Y. P. Kozyrev
Institute for Problems in Mechanical Engineering RAS, V.O., Bolshoy pr., 61, St. Petersburg
199178, Russia
e-mail: ykoz2006@yandex.ru

© The Author(s), under exclusive license to Springer Nature Switzerland AG 2022
V. A. Polyanskiy and A. K. Belyaev (eds.), *Mechanics and Control of Solids and Structures*, Advanced Structured Materials 164,
https://doi.org/10.1007/978-3-030-93076-9_27

573

nological methods. As a result of filling materials are obtained, the basic physical and mechanical properties of which differ from the properties of the matrix. The strengthening mechanism depends on both the type of filler and the properties of the filler and matrix [1, 2].

Usually polymer composites are divided into three groups. The first group includes dispersion-strengthened composites. The second group includes composites reinforced by continuous fibers, fabrics of different weaves, and plates. The third group includes composites based on polymer mixtures that are not capable of mutual dissolution of each other and are characterized by a certain distribution of the polymer particles of one nature in the matrix of the other polymer.

In this work the questions connected with tribotechnical application of polymeric composites with the disperse fillers of micro and nanosize in the form of powders in various ratios with a matrix are considered. A special place among them is occupied by composites on the basis of polytetrafluoroethylene (PTFE). Low friction coefficient values, heat resistance, water, and chemical resistance higher than all other polymers contribute to their wide application in light and medium loaded friction units.

At present it is established [3–6] that three main factors influence the wear resistance of composites with disperse filler:

- the structural organization of the material at the supramolecular level;
- supporting function of the filler;
- presence of layers separating the contacting surfaces and playing the role of a solid lubricant.

The rational choice of polymer composition for obtaining the materials with the required tribological characteristics is impossible without solving the issues of creating wear models, especially involving mathematical apparatus.

27.2 Structural Model of Polymer Composites Based on Polytetrafluoroethylene

Preliminary mixing of polymer particles with disperse filler is typically used in the production of composites based on polymers such as polytetrafluoroethylene (PTFE), polyester ester ketone (PEEK), and polyphenylene sulfide [6, 7]. Given that the polymer particles are larger than the filler particles, mixing is associated with deposition of the filler particles on the polymer particles. Shaping under pressure and at elevated temperatures (up to 380 °C) leads to the formation of a structure in which each polymer particle is surrounded by filler particles [2]. If the filler particles are microscopic, the composite formed at optimal filler concentrations for tribological purposes (around 20–30 vol %) is characterized by a structure of laminar-lattice type. This structure consists of a lattice of polymer particles intersecting with a single-layer or multilayer lattice of filler particles. In terms of engineering modeling, the

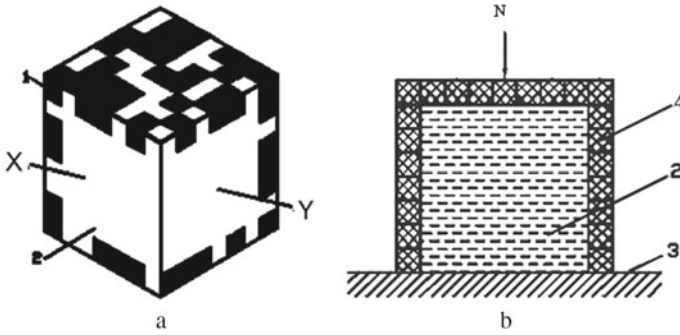


Fig. 27.1 The extraction of a unit element from the composite—composite cell. **a:** 1 is the filler particle, 2 is the polymeric matrix; (x, y) a crosscut over the boundary of filler and polymer particles; (other faces) a crosscut between filler particles and neighboring polymer particles; **b:** N is the total load superposed onto the element; 2 is the polymeric matrix; 3 is the metallic counterbody; 4 is the wall, formed by the filler particles

influence of the single-layer lattice of filler particles on the stress distribution within the composite and, indirectly, on its frictional characteristics was first considered in [7].

Figure 27.1 a gives a composite cell—an accepted shape of a unit element of a filled polymer with the spatial structure, where polymer particles (2) and filler particles (1) are cube shaped, their sizes being r_p and r_f , respectively.

It is apparent that with the growth of the filler content, it is quite possible that the surface of a PTFE particle will be filled with filler particles. One of the main features of the structure is the presence of the threshold volume concentration of the filler φ_{f0} , at which the entire surface of the polymer particle is covered by a layer of filler particles. This layer affects the strength properties of the composite as a whole. Consequently, to assess the tribological and physical-mechanical characteristics of polymer composites, it is necessary to calculate the relations that allow calculating the concentration of the filler on the faces of the polymer cube φ_{SK} for a given volume concentration of fillers [8, 9].

In deriving the relation for calculating φ_{SK} , consider the model of a single element of the composite structure shown in Fig. 27.1a. If the volume concentration of the filler is a φ_f , then the number of particles of the filler can be found from the

$$n_{fV} = \frac{\varphi_f V_C}{r_f^3}. \tag{27.1}$$

where V_C is the composite volume.

Then, by analogy, let us find the number of polymer particles in the same composite volume:

$$n_{pV} = \frac{(1 - \varphi_f)V_C}{r_p^3}. \tag{27.2}$$

To analyze one composite particle, let us assume that $n_{pV} = 1$. Then, from Eq. (27.2) we find that

$$V_C = \frac{r_p^3}{1 - \varphi_f}. \quad (27.3)$$

Substituting Eq. (27.3) into Eq. (27.1) we find the number of filler particles on the surface of one polymer particle

$$n_{fK} = \frac{1 - \varphi_f r_p^3}{(1 - \varphi) r_f^3}. \quad (27.4)$$

Knowing the value of n_{fK} , we proceed to the determination of φ_{SK} . Consider that the total area of the polymer particle is equal to $6r_p^2$, and one filler particle in this model covers two polymer surfaces at once. Then the surface concentration of the filler on the polymer cube faces [8]

$$\varphi_{SK} = n_{fK} \frac{1 - \varphi_f r_f^2}{3r_p^2}. \quad (27.5)$$

Substituting Eq. (27.4) into Eq. (27.5), we finally find

$$\varphi_{SK} = \frac{\varphi_f r_f}{3(1 - \varphi_f) r_f}. \quad (27.6)$$

Thus, for powdered PTFE we can assume that $r_p = 50\text{--}100 \mu\text{m}$; for foundry coke powder $r_f = 5\text{--}10 \mu\text{m}$ [10]. We can determine the threshold concentrations of the filler. If we denote it as φ_{f0} , it can be found based on the calculated relation [11]

$$\varphi_{f0} = \frac{3r_f r_p}{r_p^2 + 3r_p r_f}. \quad (27.7)$$

The value of φ_{f0} being known, Eq. (27.7) allows for the choosing of the size of r_p and r_f

The results of calculation of φ_{SK} values by the Eq. (27.6) are given in Table 27.1.

Table 27.1 shows that at the same number of filler particles, the filler concentration on the polymer cube faces is almost 4 times higher than the volume concentration of the filler. So, for example, for $\varphi_f = 0.2$, corresponding to concentration of industrial material $\Phi 4K 15M5$ (80 vol.% PTFE + 15 vol.% coke + 5 vol.% MoS_2), $\varphi_{SK} = 0.75$.

The frictional contact surface of the composite consists of an alternation of matrix and filler materials, as noted in [12, 13]. This is evident from scanning electron microscopy of the frictional surfaces. Under the action of an external compressive load N , the contact pressure is distributed between the matrix and the filler, while the wear resistance of the composite depends on the mechanical and frictional properties of those components. Let us examine the unit element of a polymeric composite,

Table 27.1 Calculated values of the filler concentration on the polymer cube faces depending on the volume concentration of the filler [9]

φ_f	n_{fK}	φ_{SK}
0.05	38	0.16
0.10	81	0.33
0.15	129	0.53
0.20	182	0.75
0.25	243	1.00

the spatial percent of the filling of which has a threshold value. When the element touches the moving counterbody, after a while one side of the shell will wear. After that, the face of the polymeric cube and the residual part of the shell consisting of filler particles in the form of walls normal to the contact surface start to contact the counterbody. Figure 27.1b depicts the cross section of the model cell for this case. The total load N normal to the contact surface between the composite and the counterbody is superposed onto the unit element.

Then the pressure on the contact surface p_C under the action N (Fig. 27.1b) will be distributed between the matrix and the filler structure [14]

$$p_C = p_m(1 - \varphi_S) + p_f\varphi_S, \quad (27.8)$$

where φ_S is the surface concentration of the filler in any plane parallel to the friction surface.

To determine φ_S , we first obtain, on the basis of Fig. 27.1b the relation for the threshold concentration of the filler on the friction surface φ_{S0} [8], corresponding to φ_{f0}

$$\varphi_{S0} = \frac{2r_p r_f}{r_p^2 + 2r_p r_f}, \quad (27.9)$$

where coefficient 2 reflects the fact that one filler particle overlaps two polymer surfaces at once.

Then, at concentrations of filler on friction surface less than threshold, in Eq. (27.9), it is necessary to enter φ_{SK} , determined by Eq. (27.6), which will change its value from 0 to 1 in case of using of filler of micron sizes. Considering the above, from Eq. (27.9) we obtain [8]

$$\varphi_S = \frac{2r_p r_f \varphi_{SK}}{r_p^2 + 3r_p r_f}. \quad (27.10)$$

By analogy with Eq. (27.10) let us introduce φ_{SK} into the Eq. (27.7). Then we obtain the equation for determine φ_f [8]

$$\varphi_f = \frac{3r_f r_p \varphi_{SK}}{r_p^2 + 3r_f r_p}. \quad (27.11)$$

Let's solve Eq. (27.8) taking into account equality of deformations of matrix ε_m and filler ε_f . under the action of N . Therefore, in determining the strength properties of the spatial structure of a dispersed filler, it is necessary to introduce, instead of the elastic modulus, a new characteristic of such a structure—the resistance to deformation of the dispersed medium E_f . The φ_{SK} value should influence the wall modulus of the filler particles. Then, for the case of a single-layer arrangement of dispersed filler particles of micron size [10, 15]

$$E_f = E_{f0} \varphi_{SK}, \quad (27.12)$$

where E_{f0} is the resistance to deformation of the disperse medium when the filler completely fills the layer contacting the surface of the polymer particle.

Let's assume that elastic characteristics of matrix and filler are identical under compression and tension. Then

$$p_f = \frac{p_m E_f}{E_m}, \quad (27.13)$$

where E_m is the elastic modulus of the matrix material.

After substituting Eq. (27.13) into Eq. (27.8) we obtain

$$p_C = p_m (1 - \varphi_S) + \frac{p_m E_f}{E_m} \varphi_S. \quad (27.14)$$

From Eq. (27.14) we find

$$p_m = \frac{p_C}{(1 - \varphi_S) + \frac{E_f}{E_m} \varphi_S}. \quad (27.15)$$

Substituting Eq. (27.15) into Eq. (27.14) and using the designation $\chi = E_{f0}/E_m$, we finally find

$$p_C = \frac{(1 - \varphi_S) p_C}{(1 - \varphi_S) + \chi \varphi_{SK} \varphi_S} + \frac{\chi \varphi_{SK} \varphi_S p_C}{(1 - \varphi_S) + \chi \varphi_{SK} \varphi_S}. \quad (27.16)$$

Let us introduce in Eq. (27.16) the designations

$$\beta = \frac{(1 - \varphi_S)}{(1 - \varphi_S) + \chi \varphi_{SK} \varphi_S}; \quad (1 - \beta) = \frac{\chi \varphi_{SK} \varphi_S}{(1 - \varphi_S) + \chi \varphi_{SK} \varphi_S} \quad (27.17)$$

Comparing Eq. (27.10) with Eq. (27.11) we find that $\varphi_S \approx 0.7 \varphi_f$. Taking this into account, let us rewrite Eq. (27.17) [15]

$$\beta = \frac{(1 - 0,7\varphi_f)}{(1 - 0,7\varphi_f) + 0,7\chi\varphi_{SK}\varphi_f};$$

$$(1 - \beta) = \frac{0,7\chi\varphi_{SK}\varphi_f}{(1 - 0,7\varphi_f) + 0,7\chi\varphi_{SK}\varphi_f}. \quad (27.18)$$

Taking into account Eq. (27.18) we write Eq. (27.16) in the form

$$p_C = \beta p_C + (1 - \beta) p_C, \quad (27.19)$$

where β is the loading of the composite matrix.

Obviously, when $\varphi_f = 0$, $\beta = 1$, which corresponds to the case of complete absence of filler, then $P_C = P_m$. It is known [14] that the wear of materials strongly depends on the contact pressure value. Thus, when the share of contact pressure coming to the matrix decreases, the total wear of the composite will also decrease.

If we divide Eq. (27.19) onto the contact area between the composite and the counterbody, it becomes possible to pass to the expression written for the distribution of pressures, which takes place on the contact surface between the wall and polymeric matrix. It is known [14] that the material wear greatly depends on the contact pressure. That is why if we decrease the pressure applied to the matrix, we decrease the wear of the composite material.

Let us examine of how the value of β varies under other volumetric concentrations of the filler (less than the threshold value). This is important since under the threshold concentration of the filler the strength properties can drop [16] since the cracks can proliferate over a structure of filler particles. That is why if the requirements regarding the strength and wear resistance are combined, the filler content in real composites is close to the threshold value, but nevertheless it is slightly less.

Conversely, if we introduce the filler, the value of the modulus of elasticity becomes higher and, thus, the elasticity decreases. This last phenomenon is important if the composites are used as a material for sealing elements. In this case, the filler content should be sufficiently small, but at the same time, it cannot be allowed to sharply decrease the material wear resistance in general.

Figure 27.2 a shows the relationships between β , φ_s , and φ_f , which were calculated using Eqs. (27.18) and (27.10), respectively. From Fig. 27.2 a, it is seen that if φ_f is increased up to 25%, we can observe the decreasing of the matrix loading down to $\beta = 0.09$, i.e., by approximately 10 times. At that, already at $\varphi_f = 1\%$ the value of β decreases to 0.76. Thereby, it is possible, in principal, to generate poorly filled composites with φ_f being equal to several parts of a percent [16]. Such materials are more wear resistant and, at the same time, they are elastic. From Eq. (27.19), it follows that if β is decreased, the filler loading increases simultaneously and its value can increase up to 0.91 at $\varphi_f = 25\%$. In this case, the total load is taken by the filler.

Figure 27.2 a shows the relation between φ_{fs} and φ_f (curve 2). At that, at $\varphi_s > 60\%$ the percolation of the filler particles is seen, and as a result conducting channels

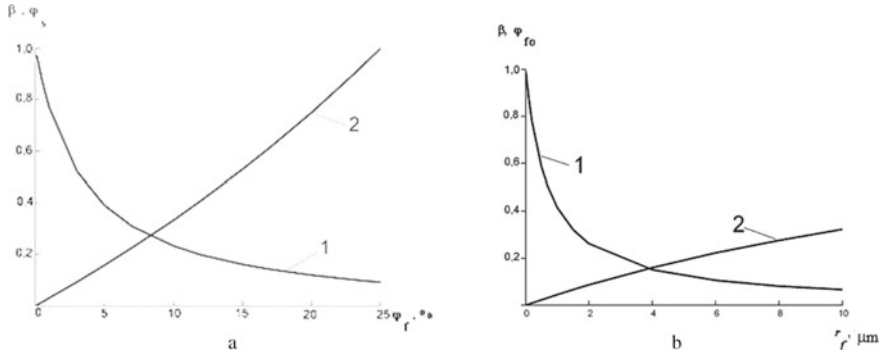


Fig. 27.2 a: The calculation dependence of the values of β , φ_{f0} on r_f for the model polytetrafluoroethylene—based composite with the foundry coke: 1— β , and 2— φ_s . **b:** The calculation dependence of the values of β , φ_{f0} on r_f , for the model polytetrafluoroethylene—based composite with the foundry coke: 1— β , and 2— φ_{f0}

are formed. Hereby, using the presented relationships it is possible to choose the volumetric concentration φ_f to insure the needed conductivity.

Let us examine how the value of β depends on φ_{f0} if r_f is varied. For this purpose, using Eq. (27.8) we calculate the value of φ_{f0} for different r_f at $r_p = 63 \mu\text{m}$. Let us examine the variant of the composite cell for the case when φ_{f0} is obtained via varying r_f from 0.05 up to $10 \mu\text{m}$. Then, by using the obtained values of φ_{f0} we find the value of β with the help of Eq. (27.18). The results of the calculations are presented in Fig. 27.2b. Let us examine how the value of β depends on φ_{f0} if r_f is varied. For this purpose, using Eq. (27.7) we calculate the value of φ_{f0} for different r_f at $r_p = 63 \mu\text{m}$. Let us examine the variant of the composite cell for the case when φ_{f0} is obtained via varying r_f from 0.05 up to $10 \mu\text{m}$. Then, by using the obtained values of φ_{f0} we find the value of β with the help of Eq. (27.18). The results of the calculations are presented in Fig. 27.2b in the form of dependencies.

From Fig. 27.2b, it is seen that if the value of r_f is increased up to $10 \mu\text{m}$, the value of β decreases continuously down to 0.07 (curve 1), since the ratio of F_c/F_m increases. At that, the value of φ_{f0} increases (Fig. 27.2 a, curve 2), since the thickness of the wall formed by the filler particles increases. All of these effects should be taken into account during the development of a composite.

Figure 27.2b, it follows that for nanosized filler particles, the matrix loading is high and the filler loading is insignificant. In this case, to increase the wear resistance of the composite, i.e., to decrease the value of β , as the fillers it is necessary to use disperse mediums whose modulus of elasticity is very high (in accordance with Eq. (27.18)). They can be media of a ceramic nature, fullerenes, or different nanomaterials.

Let as examine the natural diamond powder (NDP) crushed by a planetary mill down to r_f values of from 10 to 100nm , which is used as a filler [18]. The Table 27.2 depicts the values of β and φ_{f0} of the model polytetrafluoroethylene-based composites filled by a natural diamond powder with $E = 740 \text{GPa}$ and the respective value of

Table 27.2 Calculated values of β by Eq. (27.18), φ_{f0} by Eq. (27.7) and φ_w for the model composite PTFE + NDP at $r_p = 63 \mu\text{m}$

r_f	β	$\varphi_{f0}, \%$	$\varphi_{w0}, \%$
10	0.63	0.05	0.03
30	0.38	0.14	0.09
50	0.27	0.24	0.15
70	0.21	0.33	0.20
100	0.16	0.47	0.30

$\chi = 1644$. In practice, due to the technological peculiarities of the natural diamond powder milling process, it is accepted to characterize such composites by the values of the weight concentrations φ_w . In addition, Table 27.2 depicts the values of the respective weight threshold concentrations φ_{w0} by considering the densities of the diamond and the composition, which are 3.5 and 2.2 kg/m³, respectively.

From Table 27.2, it follows that if the value of the filler modulus of elasticity is increased in comparison with finely dispersed coke KL-1 by 7 times under r_f lying in the range of 10–100 nm, the value of β is less than 0.49. It is shown that the matrix loading decreases for such materials and verifies the correctness of the performed analytical investigations. It is necessary to point out that if the values of φ_{w0} mentioned in the table are exceeded, the strength properties of the composite drop and the wear rises.

Let us consider the features of the previously considered structural model of the composite based on polytetrafluoroethylene when using disperse nanosize filler (NF). Usually particles with sizes of 10–100 nm fall into this one. NF have a number of specific properties, such as, for example, high surface activity. This is determined by the fact that the fraction of surface atoms with uncompensated bonds increases sharply in the case of NF. For example, for particles sized 5 nm, this fraction reaches 15% [19]. As a result, the ability to adsorb, ionic and atomic exchange, and contact interactions of structural elements increases. Apparently, this allows NF to create multilayered spatial structures around the polymer particle without significant loss of composite strength [20, 21]. If the NF have dimensions of 100 nm, then, as follows from the data in Table 27.2, already at concentrations of a few fractions of percent, the number of filler particles becomes sufficient to create multilayer structures around the polymer particles—multilayer wall.

When creating a model of the multilayer structure, we give the previously introduced value φ_{SK} the additional status of the multilayer coefficient ζ_{fl} . And ζ_{fl} can take values greater than 1, i.e., by the number of available layers of the filler completely or partially filled. Substituting in Eq. (27.4) the value φ_{f0} , we find the value n_{fK0} , characterizing the number of particles of the filler at the completely filled layer. Then coefficient of multilayer wall around polymer particles [15, 22]

$$\zeta_{fl} = \frac{n_{fK}}{n_{fK0}} = \frac{\varphi_f(1 - \varphi_{f0})}{\varphi_{f0}(1 - \varphi_f)}. \tag{27.20}$$

Equation (27.20) shows the dependence of ζ_{fl} on φ_f . If the first layer is completely filled, $\zeta_{fl} = 1$. If the first and second layers are filled, then $\zeta_{fl} = 2$. Moreover, with the corresponding increments in φ_f , ζ_{fl} will take integer and intermediate values. It is obvious that these conclusions may be extended to any number of layers. In the case of nanoscale fillers, the value of φ_{f0} , is a sufficiently small value, so in expanding the Eq. (27.20) we neglect the value of the product, including φ_{f0} . Given this, the Eq. (27.20) will take the form

$$\zeta_{fl} = \frac{\varphi_f}{\varphi_{f0}} = \frac{\varphi_f r_p}{3r_f}. \quad (27.21)$$

By multiplying Eq. (27.21) by r_f we find the wall thickness of the multilayer filler structure Δw

$$\Delta w = \frac{1}{3} r_p \varphi_f. \quad (27.22)$$

Equation (27.22) shows that the value of Δw is proportional to the concentration φ_f for a polymer particle size r_p . Equations (27.21) and (27.22) are obtained under the assumption of compact packing of cubic non-fractal particles. On the other hand, it is known that nanoscale particles at different types of interaction form structures of fractal clusters (aggregates), density of which decreases with increasing of aggregate size. However, real fractals have two natural length scales, above and below which an object is not a fractal [19]. The lower limit is related to the specific size of structural elements, and the upper limit is related to the aspiration of fractal dimensionality to its limit. Thus, if an aggregate consists of particles, it can form a non-fractal aggregate of size Δw with a density and, hence, a modulus of elasticity such as the particle material. If the number of particles in the aggregate increases, it becomes a fractal aggregate whose density and hence elastic modulus will decrease. By multiplying Eq. (27.21) by r_f we find the wall thickness of the multilayer filler structure Δw

Now we assume that E_f depends on the number of layers. With a small number of layers, E_f depends on the stability of the wall, which declines with decrease in the number of layers. With a larger number of layers, E_f may decline as a function of the walls' packing density. Thus, there must be a maximum in the dependence of E_f on ζ_{fl} . This condition is satisfied by the theoretical expression for the elastic modulus of the filler

$$E_{fl} = 4 \frac{E_{f0}}{\Delta_E} \left(\exp \left[- \Delta_w / t_c \right] - \exp \left[- 2 \Delta_w / t_c \right] \right), \quad (27.23)$$

where E_{f0} is the maximum resistance to wall deformation; Δ_E is the coefficient depending on the filler particle size; t_c is the wall thickness constant.

Let us determine the value of Δ_E . In the proposed model, the wall can consist of particles of different sizes. It is known that there is a scale effect of strength. Then it is obvious that a wall composed of smaller elements will have higher strength and stiffness than a wall made of larger elements. The Weibull model [15] is most widely used to analyze the scale effect. This model is based on the concept of the weakest

link and treats the material structure as a chain whose strength is determined by its weakest link. For different volumes of material, the Weibull equation relates the ratio of their volumes to the ratio of strength. If we assume that the strength is proportional to the modulus of elasticity E , then the Weibull equation will be

$$\Delta_E = \frac{E_2}{E_1} = \left(\frac{V_1}{V_2} \right)^{\frac{1}{m_h}}, \quad (27.24)$$

where E_1, E_2 are the moduli of elasticity of the material volume V_1 and V_2 , respectively; m_h is the Weibull modulus.

Let's choose the size of particles from the nanoscale zone from 20 to 100 nm. Let's assume the value $m_h = 5$ and determine the ratio of elastic moduli of particles with dimensions from the extreme points of the range, namely, $r_{f1} = 100$ nm and $r_{f2} = 20$ nm. Since $V_1 = r_{f1}^3$ and $V_2 = r_{f2}^3$. Substituting the volumes of these particles into the Eq. (27.11) we find $\Delta_E = 2.62$. Thus, the modulus of elasticity of particles of size 20 nm is E times higher than the modulus of elasticity of particles of size 100 nm. Let's assume that in Eq. (27.22) the value E_{f0} will denote the reference modulus at 20 nm, which will decrease by the value Δ_E as the particle size increases.

The part of Eq. (27.23) in brackets is an extremum function. To find the position of the maximum, we take the derivative of this expression and equate it to zero, then

$$(\exp[-\Delta_w/t_c] - \exp[-2\Delta_w/t_c])' = \frac{2 \exp[-2\Delta_w/t_c]}{t_c} - \frac{\exp[-\Delta_w/t_c]}{t_c} = 0. \quad (27.25)$$

After reducing Eq. (27.25) by t_c , transferring the terms, and logarithmizing, we obtain an expression for determining t_c

$$t_c = \frac{\Delta_w}{\ln 2}. \quad (27.26)$$

In Eq. (27.26), the value of Δ_w represents a tightly packed wall. The thickness of such a wall will depend on the size of nanoparticles. The minimum particle size is assumed to be 20 nm. Let's take the wall thickness value at this particle size as a reference size Δ_{WE} , equal to 0.83 μm . This wall is densely packed, and such a filler structure provides the minimum wear of the composite at $\varphi_f = 0.025$. Since the elastic modulus of the particles decreases with increasing particle size, for particles with a size of 100 nm, for example, the tightly packed wall should be thicker to provide the same stability parameters. The parameter Δ_E can be used to estimate the wall thickness at different particle sizes. Then Eq. (27.26) for particles from the above-denoted nanoscale can be written as

$$t_c = \frac{\Delta_{WE} \Delta_E}{\ln 2}. \quad (27.27)$$

Let's rewrite Eq. (27.18) for the multilayer filler

$$\beta = \frac{(1 - 0.7\varphi_f)}{(1 - 0.7\varphi_f) + 2.8 \frac{\chi}{\Delta_E} (\exp[-\Delta_w/t_c] - \exp[-2\Delta_w/t_c])\varphi_f}$$

$$1 - \beta = \frac{0.7\chi\varphi_f}{(1 - 0.7\varphi_f) + 2.8 \frac{\chi}{\Delta_E} (\exp[-\Delta_w/t_c] - \exp[-2\Delta_w/t_c])\varphi_f}. \quad (27.28)$$

Substituting $\varphi_f = 0$ into Eq. (27.28), we find that $\beta = 1$. In that case, the whole load will be applied to the polymer matrix. For all other values of φ_f , we will find that $0 \leq \beta < 1$. With increase in E_f and corresponding increase in χ , we will see decline in β .

27.3 Composites Wear Model

When creating new polymer composites for frictional purposes it is required to predict their wear resistance at the initial stage of development [24, 25]. We can use the empirical wear law in terms of wear coefficient [26]

$$K = apve^{bpv} + c(e^{dpv} - 1), \quad (27.29)$$

where pv is the load (p is the contact pressure and v is the slip velocity); a , b , c , and d are dimensional coefficients specific to the material.

The empirical wear law is valid over a wide range of loads and may be used to determine K for any pv within that range, as shown in [25]. In engineering, the wear resistance of materials is often evaluated on the basis of the linear wear rate I_h . Taking into account that $I_h = Kp$, we find from Eq. (27.29) that

$$I_h = ap^2ve^{-bpv} + cp(e^{dpv} - 1). \quad (27.30)$$

However, Eq. (27.30) may only be used to estimate I_h for a finished material. To predict the properties of composites that are being developed, we need a formula that takes into account not only the wear characteristics of the components in the composite but also their mutual influence. To find the empirical wear law for a composite, it is insufficient to know the dimensional coefficients obtained individually for the matrix and the filler, since their influence on the wear resistance is not additive. That is confirmed by the significant difference in the dimensional coefficients, which is associated with both the wear mechanism and the influence of the temperature on the physicomaterial characteristics. We need to find an empirical wear law whose coefficients take account of the distribution of the total load over the frictional surfaces of the matrix and the filler. Then from Eq. (27.30), taking account of β , we

write the wear rate of the composite as the sum of the wear rates of the matrix and of the filler

$$\begin{aligned}
 I_h &= \beta^2 p^2 v a_1 e^{-b_1 p v} + \beta p c_1 (e^{d_1 p v} - 1) + \\
 &(1 - \beta)^2 p^2 v a_2 e^{-b_2 p v} + (1 - \beta) p c_2 (e^{d_2 p v} - 1) = \quad (27.31) \\
 &p^2 v (\beta^2 a_1 + (1 - \beta)^2 a_2) e^{-b_1 p v} + p (\beta c_1 + (1 - \beta) c_2) (e^{(\beta d_1 + (1 - \beta) d_2) p v} - 1),
 \end{aligned}$$

where $a_1, b_1, c_1,$ and d_1 the dimensional coefficients characterizing I_h for the matrix; $a_2, b_2, c_2,$ and d_2 the dimensional coefficients characterizing I_h for the r the filler.

In deriving the overall empirical wear law for the matrix and the filler, we need to take account of those coefficients. The coefficient b in the exponent of the first term in Eq. (27.30) is associated with the formation of secondary structures, as noted in [25]. Two diffusional processes associated with the formation of secondary structures cannot occur simultaneously in the composite. In practice, the process associated with the physicomechanical properties of the matrix will predominate. Indeed, we see that $b_1 \gg b_2$. Thus, we may adopt b_1 in the exponent of the first term for the composite as a whole. The influence of the other coefficients of the matrix and the filler on the coefficients for the composite as a whole will be determined by β . Let

$$a_e = \beta^2 a_1 + (1 - \beta)^2 a_2; b_e = b_1; c_e = \beta c_1 + (1 - \beta) c_2; d_e = \beta c_1 + (1 - \beta) d_2;$$

Then

$$I_h = a_e p^2 v e^{-b_e p v} + c_e p (e^{d_e p v} - 1). \quad (27.32)$$

We assume that the wear rate of the initial polymer corresponds to Eq. (27.30) with the dimensional coefficients $a_1, b_1, c_1,$ and d_1 . Dividing Eq. (27.32) by Eq. (27.30), we find the wear rate of the composite relative to the unfilled matrix

$$I_C^m = \frac{I_h^C}{I_h^m}. \quad (27.33)$$

The value of I_C^m allows us to estimate the tribotechnical efficiency of composite filling. Let us decompose the exponents in brackets in Eqs. (27.32) and (27.30) into a Taylor series and take only the first two terms. As a result, we obtain for Eq. (27.32)

$$e^{\beta d_1 + (1 - \beta) d_2 p v} = 1 + [\beta d_1 + (1 - \beta) d_2] p v,$$

and for Eq. (27.30)

$$e^{d_1 p v} = 1 + d_1 p v. \quad (27.34)$$

Dividing Eq. (27.34) by Eqs. (27.32) and (27.30), and considering that $b_e = b_1$, we finally find the linear wear rate of the composite relative to the unfilled matrix [26]

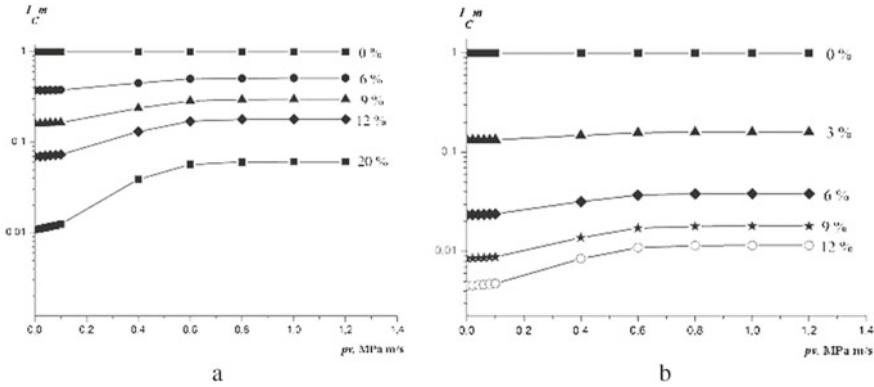


Fig. 27.3 The calculation dependences of I_C^m on the filler volume concentration and pv for model composites based on PTFE filled with AG-600 CO5: **a**—with micron-sized filler; **b**—with nanosize filler

$$I_C^m = \frac{a_e^{-b_1pv} + c_e d_e}{a_1 e^{-b_1pv} + c_1 d_1}. \tag{27.35}$$

If $pv \rightarrow 0$ and $\varphi_f = 0$, then $I_C^m = 1$, since all coefficients in Eq. (27.35) will be equal. As it follows from Eq. (27.35), the value of I_C^m depends only on pv . This makes it possible to build I_C^m dependences for different load modes: $p = var, v = const$; $v = var, p = const$.

To verify the proposed model, we plotted according to Eq. (27.35) the dependences of I_C^m on the filler volume concentration and pv for model composites based on PTFE (Fig. 27.3) filled with carbon material AG-600 CO5 with different dispersity. In Fig. 27.3a the dependences are plotted for a model composite with $r_f = 7 \mu\text{m}$. and $r_p = 63 \mu\text{m}$. In this case, the value of φ_{f0} is 20 vol.% at $\zeta_{f1} = 0.74$ and $\Delta_W = 7 \mu\text{m}$. In Fig. 27.3b for the nanoscale filler $\varphi_{f0} = 12 \text{ vol.}\%$ at $\zeta_{f1} = 50.4$ and $\Delta_W = 2.52 \mu\text{m}$. The indicated concentrations are the limits, because when they are exceeded, the strength characteristics of the composites decrease.

The concentration dependence Fig. 27.3a shows that I_C^m decreases by two orders of magnitude when a micron-sized filler is introduced with concentration $\varphi_f = 20 \text{ vol.}\%$, and in the case of application of nanosize filler (Fig. 27.3b). The same decrease in I_C^m is achieved at $\varphi_f = 12 \text{ vol.}\%$.

From Fig. 27.3 a shows that the I_C^m of the model composite based on PTFE with a microsized filler at $pv \geq 0.6 \text{ MPa m/s}$ has a noticeable dependence on pv . At the same time, the value of I_C^m , decreases monotonically with increasing φ_f and reaches a minimum value at $\varphi_f = 20 \text{ vol.}\%$. At $pv \leq 0.6 \text{ MPa}$, the decrease in I_C^m reaches 2 orders of magnitude. At the same time, when nanosize filler is used (Fig. 27.3b), the dependence of I_C^m on pv is less pronounced. From Fig. 27.2b follows that use nanosize filler already at $\varphi_f = 12 \text{ vol.}\%$ leads to an increase in the wear resistance of the composite by more than 2 orders of magnitude. The obtained calculated dependences

have good agreement with the experimental data published both by other researchers. Thus, the proposed approach to modeling the wear resistance of polymer composites makes it possible to determine by calculation the effective concentrations of dispersed filler of micro- and nanoscale, as well as to evaluate the tribotechnical efficiency of filling at the stage of designing friction units.

References

1. Vettegren, V.I., Bashkarev, A.Y., Suslov, M.A.: Kinetics of friction and wear of polymer composite materials. *Phys. Solid State* **47**(9), 1681–1686 (2005)
2. Samyn, P., Schoukens, G.: Experimental extrapolation model for friction and wear of polymers on different testing scales. *Int. J. Mech. Sci.* **50**, 1390–1403 (2008)
3. Mashkov, Yu.K., Kallistratova, L.F., Ovchar, Z.N.: *Struktura i iznosostoykost modifitsirovannogo polimera* (Structure and wear resistance of the modified polymer). Om-GTU, Omsk (1998)
4. Bahadur, S.: The development of transfer layers and their role in polymer tribology. *Wear* **245**(1–2), 92–99 (2000)
5. Fridrich, K.: *Friction and Wear of Polymer Composites*. Elsevier Science Publisher, Amsterdam (1986)
6. Aderikha, V.N., Shapovalov, V.A., Pleskachevskii, Yu.M.: Strength, structure and wear resistance of PTFE composites with carbon filler. *Tren. Iznos.* **29**(2), 160–168 (2008)
7. Sewyer, W.G., Freudenberg, K.D., Bhimara, P., Schadler, L.: A study on the friction and wear behavior of PTFE filled with alumina nanoparticles. *Wear* **254**, 573–580 (2003)
8. Kozyrev, Yu.P., Sedakova, E.B.: The effect of the structural features of polytetrafluoroethylene-based composites on the reduction of matrix loading. *J. Mach. Manuf. Reliab.* **39**(2), 131–135 (2010)
9. Kozyrev, Yu.P., Sedakova, E.B.: Application of a segregated network model to analyze the surface structure effect on the wear resistance of polytetrafluoroethylene composites with a fine filler. *J. Mach. Manuf. Reliab.* **38**(3), 259–262 (2009)
10. Kozyrev, Yu.P., Kovalenko, N.A.: Method of Calculating “Threshold $\frac{1}{2}$ Concentration for Compositions Based on of Fluoroplastic-4. *Mekhanika Kompozitnykh Materialov* **5**, 931–934 (1982)
11. Bhattacharyya, S.K., Bacu, S., De, S.K.: Effect of size, shape and oxide content of metal particles on the formation of segregated network in PYC composites. *Composites* **9**(3), 177–183 (1978)
12. Li, F., Hu, K.A., Li, J.L., Zhao, B.Y.: The friction and wear characteristics of nanometer ZnO filled polytetrafluoroethylene. *Wear* **249**(10/11), 877–882 (2001)
13. Lai, S.Q., Yue, L., Li, T.S., and Hu, Z.- M.: The friction and wear properties of polytetrafluoroethylene filled with ultrafine diamond. *Wear* **260**, 462–468 (2006)
14. Berlin, A.A., Volfson, S.A., Oshmyan, V.G., et al.: *Printsipy sozdaniya kompozitsionnykh polimernykh materialov*. (Design Principles of Composite Polymer Materials), Khimiya, Moscow (1990)
15. Kozyrev, Yu.P., Sedakova, E.B.: Antifrictional nanocomposites based on polymers with a multilayer disperse filler. *Russ. Eng. Res.* **31**(1), 22–24 (2011)
16. Kozyrev, Y.P., Sedakova, E.B.: A method to detect permissible loads under friction using empirical law of wear. *Vestnik Mashinostroeniya* **6**, 44–46 (2007)
17. Broshcheva, P.N., Okhlopko, A.A., Yuchyugyaeva, T.S., et al.: Usage of nature diamond powders as a filling for polytetrafluoroethylene. *Trenie Iznos* **22**(6), 684–688 (2001)
18. Bahadur, S.: The development of transfer films and their role in polymer tribology. *Wear* **245**, 92–99 (2000)

19. Feder, E.: *Fracnals*. Mir, Moscow (1991)
20. Shi-Quan, Lai, Tong-Sheng, Lia, Xu-Jun, Liu, Ren-Guo, Lv., Li, Yue: The tribological properties of PTFE filled with thermally treated nano-attapulgit. *Tribol. Int.* **39**, 541–547 (2006)
21. Sedakova, E.B., Kozyrev, Yu.P.: Influence of particle size on the wear resistance and strength of polymer composites. *Russ. Eng. Res.* **38**(7), 513–516 (2018)
22. Sedakova, E.B.: Structural features of composites tribotechnical purposes on a basis of polytetrafluoroethylene with nanosize fillers. *Voprosy materialovedeniya* **2**, 75–82 (2013)
23. Weibull, W.: Statistical distribution function wide applicability. *J. Appl. Mech.* **18**, 293–297 (1951)
24. Sedakova, E.B., Kozyrev, Yu.P.: Estimation of the tribotechnical efficiency of polytetrafluoroethylene filling. *J. Mach. Manuf. Reliab.* **50**(3), 235–241 (2021)
25. Kozyrev, Yu.P., Sedakova, E.B.: Wear mechanisms of polytetrafluoroethylene and its composites. *Russ. Eng. Res.* **29**(7), 674–677 (2009)
26. Sedakova, E.B., Kozyrev, Yu.P.: Predicting the behavior of the polymer composites on the basis of a physical model of wear. *Russ. Eng. Res.* **34**(2), 76–78 (2014)

Chapter 28

Hydrodynamic Mechanism of Temperature Gradient Formation in Microfluidic Nematic Devices



Izabela Śliwa and Alex V. Zakharov

Abstract The purpose of this chapter is to show some routes in describing the mechanism responsible for the formation of the temperature difference at the boundaries of the microfluidic hybrid aligned nematic (HAN) channel, initially equal to zero, if one sets up the stationary hydrodynamic flow or under the effect of an externally applied shear stress (SS) to the bounding surfaces. Calculations based on the nonlinear extension of the classical Ericksen–Leslie theory, supplemented by thermomechanical correction of the SS σ_{zx} and Rayleigh dissipation function, with accounting the entropy balance equation, show that due to the coupling among the σ_{zx} , the gradients of the temperature ∇T and the director $\hat{\mathbf{n}}$ fields in the HAN channel the horizontal nematic flow \mathbf{v} is excited. The direction and magnitude of \mathbf{v} is influenced by both the heat flux \mathbf{q} across the HAN channel and the strength of the σ_{zx} .

Keywords Liquid crystals · Hydrodynamics of anisotropic systems · Thermomechanical force

28.1 Introduction

Consisting of anisotropic molecules, liquid crystal (LC) materials were called curious soft matter until their impressive impact on modern technology. The primary technological revolution was brought by these LC materials in the field of displays. With the development of the LC display market, the question arises about the follow-

Dedicated to the memory of Professor W. Jeżewski

I. Śliwa

Poznan University of Economics and Business, Al. Niepodleglosci 10, 61-875 Poznan, Poland
e-mail: izabela.sliwa@ue.poznan.pl

A. V. Zakharov (✉)

Institute for Problems in Mechanical Engineering RAS, V.O., Bolshoy pr., 61,
St. Petersburg 199178, Russia
e-mail: alexandre.zakharov@yahoo.ca

ing areas of application of LC materials. Perhaps there is no more suitable direction for the application of LC materials than LC sensors (LCSs) and LC actuators (LCAs) [1]. They have various advantages in comparison with other types of microsensors and microactuators; simple structure, high shape adaptability, easy downsizing, and low driving voltages. This is because LC materials are extremely sensitive to external disturbances and can be used for the construction of stimuli-responsive devices, such as LCSs or LCAs [1]. Nematic liquid crystal (NLC) channels or capillaries of appropriate size are microdevices, whose molecular orientations can be manipulated by forces applied macroscopically, or can be generated locally within the microfluidic nematic channel [2] or capillary [3]. A challenging problem in all such systems is the precise handling of nematic microvolume, which in turn requires self-contained micropumps of small package size exhibiting either a very small displacement volume (displacement pumps) or a continuous volume flow (dynamic pumps). One of the pumping principles in the microsized LC channel confined between two infinitely long boundaries is based on the coupling between the tangential component of the shear stress (SS) σ_{zx} and the director field $\hat{\mathbf{n}}$, together with accounting the effect of the temperature gradient ∇T [4, 5].

It has been shown that the horizontal hybrid aligned nematic (HAN) microfluidic channel, being initially in the rest, if heated both from below or above, due to the temperature gradient ∇T , starts moving in the horizontal direction [6–8]. In the case when the director $\hat{\mathbf{n}}$ is anchored homeotropically to the cooler (T_{lw}) lower, and homogeneously to the hotter (T_{up}) upper boundaries, due to coupling between $\nabla T \sim \frac{\Delta T}{d}$ and $\nabla \hat{\mathbf{n}}$, the hydrodynamic flow $\mathbf{v} = v_x \hat{\mathbf{i}}$ [7] in the horizontal direction is excited. Here, $\Delta T = T_{up} - T_{lw}$ is the temperature difference on the HAN boundaries, d is the thickness of the HAN channel, and $\hat{\mathbf{i}}$ is the unit vector taken parallel to the horizontal boundaries of the HAN channel (see Fig. 28.1). The magnitude of the flow v_x is proportional to $\sim \frac{d}{\eta} \sigma_{zx}^{tm}$ [6–8], where $\sigma_{zx}^{tm} \sim \xi \frac{\Delta T}{d^2}$ is the tangential component of the thermomechanical stress tensor σ_{ij}^{tm} , η is the viscosity, and ξ is the thermomechanical constant [6]. The direction of the hydrodynamic flow \mathbf{v} is influenced by the character of the preferred anchoring of the average molecular direction $\hat{\mathbf{n}}$ to the boundaries of the HAN channel and the heat flux \mathbf{q} across the bounding surface [7, 8]. Measurements of temperature's induced flow have been performed on the HAN cell [9], and the main result of that experimental study is the estimation of the thermomechanical constant $\xi \sim 10^{-12}$ J/K m [9].

Despite the fact that the possibility of formation of hydrodynamic flows in nematic channels under the influence of temperature gradients has been theoretically described since [6–8], only detailed numerical simulations performed within the framework of the extended Ericksen–Leslie theory [10, 11] allowed us to recreate the complete picture of the formation of flows in nematic microchannels and capillaries. One of the aims of this chapter is to describe the various regimes of hydrodynamic flow formation due to the interaction between the temperature and director field gradients obtained by numerical modeling of these processes. This review is devoted to the latest results describing the possibilities of computational methods implemented in the framework of the nonlinear extension of the Ericksen–

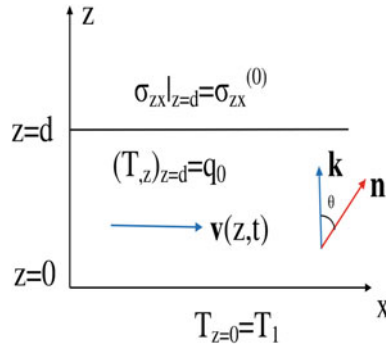


Fig. 28.1 The coordinate system used for theoretical analysis. The x -axis is taken as being parallel to the director directions on the upper surface, $\theta(z, t)$ is the angle between the director $\hat{\mathbf{n}}$ and the unit vector $\hat{\mathbf{k}}$, respectively. Both the heat flux \mathbf{q} and the unit vector $\hat{\mathbf{k}}$ are directed normal to the horizontal boundaries of the LC channel

Leslie theory, with accounting the entropy balance equation [12]. Another purpose of our chapter is to show some routes in describing the mechanism responsible for formation of the temperature difference ΔT on the boundaries of the HAN channel, being initially equal to zero, if one sets up the stationary hydrodynamic flow or under the effect of the externally applied shear stress to the bounding surfaces.

This is the first such review that describes in detail the role of thermomechanical force in formation of the hydrodynamic flow in microsized nematic channels and capillaries. It is based on the nonlinear extension of the Ericksen–Leslie theory, supplemented by thermomechanical correction of the shear stress and Rayleigh dissipation function, and also takes into account the entropy balance equation. The fact that the main results were obtained by numerical methods indicates that experimenters still have a lot of work to do in order to create a more complete picture of formation of the hydrodynamic flows in microsized nematic channels and capillaries.

The layout of this chapter is as follows. In the next section, the system of hydrodynamic equations describing both the director motion and the fluid flow in microfluidic HAN channel containing the temperature gradient, under the effect of the external shear stress, is given. Numerical results for the number of hydrodynamic regimes, caused by both the shear stress and the heat flux across the bounding surfaces of the HAN channel, describing orientational relaxation of the director, velocity, and temperature are given, in Sect. 28.3. The role of flow in a temperature gradient formation across a hybrid aligned nematic channel is given in Sect. 28.4. Conclusions are summarized in Sect. V.

28.2 Shear-Driven Flow Regimes in Microfluidic Nematic Devices: Tumbling and Laminar

In the case of the stationary shear stress flow, the director $\hat{\mathbf{n}}$ is oriented in the shear xz plane, where the xz plane, defined by the liquid crystal flow \mathbf{v} (the direction x coincides with the unit vector $\hat{\mathbf{i}}$) and the velocity gradient ∇v in the z -direction coinciding with the unit vector $\hat{\mathbf{k}}$; y is the vorticity axis coinciding with the unit vector $\hat{\mathbf{j}}$ (see Fig. 28.1). So, one deals with a twofold result. First, the hydrodynamic torque,

$$\mathbf{T}_{vis} = \frac{\gamma_1}{2} (1 + \gamma_{21} \cos 2\theta) \dot{\gamma} \hat{\mathbf{j}} = [(\alpha_3 \cos^2 \theta - \alpha_2 \sin^2 \theta) \dot{\gamma}] \hat{\mathbf{j}}, \quad (28.1)$$

exerted per unit LC volume in a shear flow, vanishes when the director $\hat{\mathbf{n}}$ aligns at a stationary angle [13–15],

$$\theta_{st} = \frac{1}{2} \cos^{-1} (-\gamma_1/\gamma_2) = \frac{1}{2} \cos^{-1} (\gamma_{21}^{-1}) = \tan^{-1} \left(\sqrt{\alpha_3/\alpha_2} \right), \quad (28.2)$$

with respect to the direction of the flow velocity $\mathbf{v} = \dot{\gamma} y \hat{\mathbf{i}}$. Second, the director $\hat{\mathbf{n}}$ continuously rotates in the shear plane. Here $\gamma_{21} = -\gamma_2/\gamma_1$, $\gamma_1 = \alpha_3 - \alpha_2$ and $\gamma_2 = \alpha_3 + \alpha_2$ are the rotational viscosity coefficients (RVC's), α_2 , and α_3 are the Leslie coefficients, and $\dot{\gamma} = \partial v_x/\partial z$ is the shear rate. It is clear from this equation that if $|\gamma_1| > |\gamma_2|$ or $\alpha_3 > 0$ (because, in practice, $\alpha_2 < 0$), than no real solution for θ_{st} exists. Physically, this means that in this case the director will tumble under the shear flow of the nematic.

In turn, in the case of the HAN microfluidic channel, when there is only a temperature difference $\Delta T = T_{up} - T_{lw}$ on the HAN boundaries, and where the director $\hat{\mathbf{n}}$ is anchored homeotropically to the lower, and homogeneously to the upper boundaries, due to the coupling between ∇T and $\nabla \hat{\mathbf{n}}$, the hydrodynamic flow $\mathbf{v} = v_x \hat{\mathbf{i}}$ [6–8] is excited. The magnitude of the flow v_x is proportional to $\sim \frac{d}{\eta} \sigma_{zx}^{tm}$, and the direction of the hydrodynamic flow \mathbf{v} is influenced by the character of the preferred anchoring of the average molecular direction $\hat{\mathbf{n}}$ to the boundaries of the HAN channel and the heat flux \mathbf{q} across the bounding surface [7, 8]. Among many questions that arise in this connection, we will be interested in two ones.

First, how the viscous torque $\mathbf{T}_{vis} = \frac{\gamma_1}{2} (1 + \gamma_{21} \cos 2\theta) \dot{\gamma} \hat{\mathbf{j}}$ effects the character of director field $\hat{\mathbf{n}}$ (or the polar angle θ) evolution to its stationary orientation $\hat{\mathbf{n}}_{st}$ with respect to the nematic flow \mathbf{v} , under the influence of the tangential component of the shear stress σ_{zx} together with accounting the temperature gradient ∇T ? It will be investigated for two types of the nematic phases; first, for the “laminar” case of nematic phase, when $\gamma_{21} > 1$, and, second, for the “tumbling” case of nematic phase, when $\gamma_{21} < 1$ [13–15], respectively. For instance, to the laminar nematic phase belongs the liquid crystal composed of 4 – cyano – 4' – pentylbiphenyl (5CB) molecules, whereas to the tumbling nematic phase belongs the liquid crystal composed of 4 – cyano – 4' – octylbiphenyl (8CB) molecules [16], respectively. Sec-

ond, is it possible to form a temperature difference ΔT across the HAN microfluidic channel, initially being equal to zero, under the action of the tangential component of the shear stress σ_{zx} applied to the boundary of the LC channel?

The answers to these questions will be given within the framework of nonlinear extension of the classical Ericksen–Leslie theory [10, 11], supplemented by thermomechanical correction of the shear stress and Rayleigh dissipation function, as well as taking into account the entropy balance equation [12]. It has recently been shown, both experimentally [17] and numerically [18], that only stationary flow v_{st} with a triangular sharp profile and position of the maximum in the vicinity of the restricted boundaries may built the highest temperature difference $\Delta T = T_{up} - T_{lw}$ in the HAN microfluidic channel of few degrees. By means of other hydrodynamic flow with profiles, which can not demonstrate the sharp growth of v_{st} across the HAN channel, one can achieve the same result only by using of the “high-speed” hydrodynamic flow $\sim 0.1 \mu\text{m/s}$ [17]. But taking into account that some LC systems driven by external SS exhibit such non-equilibrium phenomena as tumbling behavior [7, 8, 18], the mechanical description can shed some light on the problem of temperature gradient formation, when under certain conditions the thermomechanical force can overcome elastic, viscous, and anchor forces and cause a temperature gradient across the HAN channel.

28.2.1 Formulation of the Balance of the Linear Momentum, Torque, and Conductivity Equations for Microsized Nematic Fluids

We are primarily concerned with the description of the physical mechanism responsible for the shear-driven nematic flow in microfluidic hybrid aligned nematic (HAN) channels, under the effect of the external shear stress

$$(\sigma_{zx}(z))_{z=d} = \sigma_{zx}^0, \quad (28.3)$$

applied to the upper boundary of this channel (see Fig. 28.1). We consider a hybrid aligned channel composed of both the laminar and tumbling types of nematics, which is delimited by two horizontal bounding surfaces at distance d on a scale in the order of tens micrometers. According to this geometry the director is maintained within the xz -plane (or in the yz -plane), defined by the heat flux $\mathbf{q} = Q_0 \hat{\mathbf{k}}$ directed normal to the horizontal boundaries of the LC channel. Because we are dealing with the HAN channel under the influence of both the SS σ_{zx}^0 and the heat flux \mathbf{q} directed perpendicular to the HAN channel, and taking into account that the length of the channel L is much bigger than the thickness d , we can suppose that the component of the director $\hat{\mathbf{n}} = n_x \hat{\mathbf{i}} + n_z \hat{\mathbf{k}} = \sin \theta(z, t) \hat{\mathbf{i}} + \cos \theta(z, t) \hat{\mathbf{k}}$, as well as the rest of the physical quantities, also depend only on the z -coordinate and time t . Here, θ denotes the angle between the director and the unit vector $\hat{\mathbf{k}}$ (see Fig. 28.1). In order to

understand how the viscous \mathbf{T}_{vis} , elastic \mathbf{T}_{el} , thermomechanical \mathbf{T}_{tm} , and anchoring \mathbf{T}_{an} torques, as well as the tangential component of the shear stress σ_{zx} , effect the character of the director field $\hat{\mathbf{n}}$ evolution to its stationary orientation with respect to the nematic flow \mathbf{v} , we must formulate the boundary conditions for the temperature $T(z, t)$, velocity \mathbf{v} and the director $\hat{\mathbf{n}}$ fields.

We consider a hydrodynamic regime where the HAN channel is subjected to uniform heating from above, for instance by the laser irradiation [19], and the director $\hat{\mathbf{n}}$ is strongly anchored to both solid surfaces, homeotropically to the lower cooler (T_1) and homogeneously to the upper bounding surfaces, where

$$\theta(z)_{z=d} = \frac{\pi}{2}, \quad \theta(z)_{z=0} = 0, \quad (28.4)$$

whereas the boundary conditions for the temperature field are

$$\left(\frac{\partial T}{\partial z}\right)_{z=d} = -Q_0/\lambda_{\perp} = q_0, \quad T(z)_{z=0} = T_1, \quad (28.5)$$

respectively. Here, λ_{\perp} is the heat conductivity coefficient perpendicular to the director $\hat{\mathbf{n}}$, whereas Q_0 is the heat flux across the upper boundary, respectively. As a result, we obtain a picture where there is a balance between the heat flux \mathbf{q} , SS σ_{zx}^0 , viscous, elastic and anchoring forces, and, in general, the LC fluid settles down to a stationary flow regime in the horizontal direction [7, 8]. Upon assuming an incompressible fluid, the hydrodynamic equations describing the orientational dynamics induced both by SS σ_{zx}^0 and \mathbf{q} can be derived from the torque, linear momentum and the entropy balance equations for such LC system.

Taking into account the micro-size of the HAN channel, one can assume the mass density ρ to be constant over the LC volume, and thus we are dealing with an incompressible fluid. The incompressibility condition $\nabla \cdot \mathbf{v} = 0$ assumes that only one nonzero component of the vector \mathbf{v} exists, viz. $\mathbf{v}(z, t) = u(z, t)\hat{\mathbf{i}}$.

If the director is disturbed by both the shear stress σ_{zx}^0 and the heat flux \mathbf{q} , generated by the uniform heating from above, the relaxation of $\hat{\mathbf{n}}(z, t)$ to its equilibrium orientation $\hat{\mathbf{n}}_{eq}(z)$ in the HAN channel is governed by elastic $\mathbf{T}_{elast} = \frac{\delta \mathcal{W}_F}{\delta \hat{\mathbf{n}}} \times \hat{\mathbf{n}}$, viscous $\mathbf{T}_{vis} = \frac{\delta \mathcal{R}^{vis}}{\delta \hat{\mathbf{n}}_i} \times \hat{\mathbf{n}}$, and thermomechanical $\mathbf{T}_{tm} = \frac{\delta \mathcal{R}^{tm}}{\delta \hat{\mathbf{n}}_i} \times \hat{\mathbf{n}}$ torques exerted per unit LC's volume. Here, $\mathcal{R}^{vis} = \frac{1}{2}h(\theta)u_{,z}^2 - \gamma_1 \mathcal{A}(\theta)\theta_{,t}u_{,z} + \frac{1}{2}\gamma_1\theta_{,t}^2$ is the viscous, $\mathcal{R}^{tm} = \xi\theta_{,t}\theta_{,z}T_{,z}(\frac{1}{2} + \sin^2\theta) - \xi T_{,z}u_{,z}\theta_{,z}\sin^2\theta(1 + \frac{1}{2}\sin^2\theta)$ is the thermo-mechanical, and $\mathcal{R}^{th} = \frac{1}{2T}(\lambda_{\parallel}\cos^2\theta + \lambda_{\perp}\sin^2\theta)T_{,z}^2$ is the thermal contributions to the full Rayleigh dissipation function $\mathcal{R} = \mathcal{R}^{vis} + \mathcal{R}^{tm} + \mathcal{R}^{th}$ [7, 8]. The set of functions $h(\theta) = \alpha_1\sin^2\theta\cos^2\theta - \gamma_1\mathcal{A}(\theta) + \frac{1}{2}\alpha_4 + g(\theta)$, $\mathcal{A}(\theta) = \frac{1}{2}(1 + \gamma_{21}\cos 2\theta)$, $g(\theta) = \frac{1}{2}(\alpha_6\sin^2\theta + \alpha_5\cos^2\theta)$ are the hydrodynamic functions, $u_{,z} = \partial u(z, t)/\partial z$, $\theta_{,z} = \partial\theta(z, t)/\partial z$, $\theta_{,t} = \partial\theta(z, t)/\partial t$, and $T_{,z} = \partial T(z, t)/\partial z$, whereas α_i ($i = 1, \dots, 6$) are six Leslie coefficients, λ_{\parallel} and λ_{\perp} are the heat conductivity coefficients parallel and perpendicular to the director $\hat{\mathbf{n}}$. In turn, $\mathcal{W}_F =$

$\frac{1}{2} \left[K_1 (\nabla \cdot \hat{\mathbf{n}})^2 + K_3 (\hat{\mathbf{n}} \times \nabla \times \hat{\mathbf{n}})^2 \right]$ denotes the elastic energy density, K_1 and K_3 are splay and bend elastic coefficients, and $\hat{\mathbf{n}}_{,t} = \frac{d\hat{\mathbf{n}}}{dt}$ is the material derivative of the director $\hat{\mathbf{n}}$, respectively.

The hydrodynamic equations describing the reorientation of the LC phase in our case, when there exists the heat flux \mathbf{q} across the upper boundary of the HAN microfluidic channel and under the effect of the SS σ_{zx}^0 , can be derived from the torque balance equation [7, 8] $\mathbf{T}_{elast} + \mathbf{T}_{vis} + \mathbf{T}_{tm} = 0$, which has the form

$$\left[\frac{\delta \mathcal{W}_F}{\delta \hat{\mathbf{n}}} + \frac{\delta \mathcal{R}^{vis}}{\delta \hat{\mathbf{n}}_{,t}} + \frac{\delta \mathcal{R}^{tm}}{\delta \hat{\mathbf{n}}_{,t}} \right] \times \hat{\mathbf{n}} = 0. \quad (28.6)$$

The linear momentum equation for the velocity field \mathbf{v} can be written as [7, 8]

$$\rho \frac{d\mathbf{v}}{dt} = \nabla \cdot \sigma, \quad (28.7)$$

where ρ is the mass density of the nematic system, $\sigma = \sigma^{elast} + \sigma^{vis} + \sigma^{tm} - \mathcal{P}\mathcal{I}$ is the full stress tensor (ST), and $\sigma^{elast} = -\frac{\partial \mathcal{W}_F}{\partial \nabla \hat{\mathbf{n}}} \cdot (\nabla \hat{\mathbf{n}})^T$, $\sigma^{vis} = \frac{\delta \mathcal{R}^{vis}}{\delta \nabla \mathbf{v}}$, and $\sigma^{tm} = \frac{\delta \mathcal{R}^{tm}}{\delta \nabla \mathbf{v}}$ are the ST components corresponding to the elastic, viscous, and thermomechanical forces, respectively. Here, \mathcal{P} is the hydrostatic pressure in the HAN system and \mathcal{I} is the unit tensor, respectively.

When the gradient of temperature ∇T is set up across the HAN channel, we expect that the temperature field $T(z, t)$ satisfies the heat conduction equation [7, 8, 12]

$$\rho C_P \frac{dT}{dt} = -\nabla \cdot \mathbf{Q}, \quad (28.8)$$

where $\mathbf{Q} = -T \frac{\delta \mathcal{R}}{\delta \nabla T}$ is the heat flux in the nematic phase, and C_P is the heat capacity of the LC system.

To be able to observe the evolution of the director field $\hat{\mathbf{n}}$ (or the polar angle $\theta(z, t)$) to its equilibrium orientation $\hat{\mathbf{n}}_{eq}(z)$, and exciting the velocity field $\mathbf{v}(z, t)$ caused both by the heat flux \mathbf{q} and the external SS σ_{zx}^0 , we consider the dimensionless analog of the torque and linear momentum balance equations, as well as the entropy balance equation.

The dimensionless torque balance equation describing the reorientation of the LC phase can be written as [7, 8]

$$\bar{\gamma}_1(\chi)\theta_{,\tau} = \mathcal{A}(\theta)u_{,z} + (\mathcal{G}(\theta)\theta_{,z})_{,z} - \frac{1}{2}\mathcal{G}_{,\theta}(\theta)\theta_{,z}^2 - \delta_1\chi_{,z}\theta_{,z} \left(\frac{1}{2} + \sin^2\theta \right), \quad (28.9)$$

where $\mathcal{G}(\theta) = \sin^2\theta + K_{31}\cos^2\theta$, $\mathcal{G}_{,\theta}(\theta)$ is the derivative of $\mathcal{G}(\theta)$ with respect to θ , $\chi(z, \tau) = T(z, \tau)/T_{NI}$ is the dimensionless temperature, T_{NI} is the nematic–isotropic transition temperature, $\theta_{,z} = \partial\theta(z, \tau)/\partial z$, $\chi_{,z} = \partial\chi(z, \tau)/\partial z$, $K_{31} = K_3/K_1$, K_1 , and K_3 are the splay and bend elastic constants of the LC phase, $\tau = (K_{10}/\gamma_{10}d^2)t$ is the dimensionless time, $\bar{z} = z/d$ is the dimensionless dis-

tance away from the lower solid surface, $\bar{u} = \left(\frac{\gamma_{10d}}{K_{10}}\right)u$ is the dimensionless velocity, $\bar{\gamma}_1(\chi) = \gamma_1/\gamma_{10}$ is the dimensionless RVC γ_1 , $\delta_1 = \xi T_{NI}/K_{10}$ is the parameter of the nematic system, and $\xi \sim 10^{-12}$ J/mK is the thermomechanical constant [9]. Notice that the overbars in the space variable z and velocity u have been eliminated and γ_{10} and K_{10} are the highest values of the RVC $\gamma_1(\chi)$ and the splay constant $K_1(\chi)$ in the temperature interval $[\chi_1, \chi_2]$ belonging to the nematic phase. In the case of incompressible fluid, the dimensionless Navier–Stokes equation reduces to [7, 8]

$$\delta_2 u_{,\tau}(z, \tau) = \sigma_{zx,z} = \left[\bar{h}(\theta)u_{,z} - \bar{\mathcal{A}}(\theta)\theta_{,\tau} - \delta_1 \chi_{,z}\theta_{,z} \sin^2 \theta \left(1 + \frac{1}{2} \sin^2 \theta \right) \right]_{,z}, \quad (28.10)$$

$$\bar{\mathcal{P}}_{,z}(z, \tau) + \frac{\partial \mathcal{R}(z, \tau)}{\partial \theta_{,\tau}} \theta_{,z} = 0, \quad (28.11)$$

where $\bar{h}(\theta) = h(\theta)/\gamma_{10}$ and $\bar{\mathcal{A}}(\theta) = \mathcal{A}(\theta)/\gamma_{10}$, respectively, and $\mathcal{R}(z, \tau) = \frac{\gamma_{10}d^4}{K_{10}^2} \mathcal{R}(z, t)$ is the full dimensionless Rayleigh dissipation function, $\bar{\mathcal{P}}(z, \tau) = \frac{d^2}{K_{10}} \mathcal{R}(z, t)$ is the dimensionless hydrostatic pressure in the HAN channel, whereas $\delta_2 = \rho K_{10}/\gamma_{10}^2$ is an extra one parameter of the nematic system. The stress tensor component σ_{zx} is given by [9] $\sigma_{zx}(z, \tau) = \frac{\delta \mathcal{R}(z, \tau)}{\delta u_{,z}} = \bar{h}(\theta)u_{,z} - \bar{\mathcal{A}}(\theta)\theta_{,\tau} - \delta_1 \chi_{,z}\theta_{,z} \sin^2 \theta \left(1 + \frac{1}{2} \sin^2 \theta \right)$.

When the temperature gradient $\nabla \chi$ is set up across the HAN channel, we expect that the temperature field $\chi(z, \tau)$ satisfies the dimensionless heat conduction equation [7, 8]

$$\delta_3 \chi_{,\tau}(z, \tau) = \left[\chi_{,z} \left(\lambda \cos^2 \theta + \sin^2 \theta \right) \right]_{,z} + \delta_4 \left[\chi \theta_{,z} \left(\theta_{,\tau} \left(\frac{1}{2} + \sin^2 \theta \right) - u_{,z} \sin^2 \theta \left(1 + \frac{1}{2} \sin^2 \theta \right) \right) \right]_{,z}, \quad (28.12)$$

where $\lambda = \lambda_{\parallel}/\lambda_{\perp}$, and $\delta_3 = \frac{\rho C_p K_{10}}{\lambda_{\perp} \gamma_{10}}$ and $\delta_4 = \xi \frac{K_{10}}{d^2 \gamma_{10} \lambda_{\perp}}$ are extra two parameters of the nematic system. Note that the overbars in the space variable z , in the last four Eqs. (28.9), (28.10), (28.11), and (28.12) have also been eliminated.

In order to elucidate the role of both the heat flux $\mathbf{q} = q_0 \hat{\mathbf{k}}$ and the external SS σ_{zx}^0 on the reorientation process in the microsized HAN channel, we consider the hydrodynamic regime when the director $\hat{\mathbf{n}}$ is strongly anchored to both solid surfaces, homeotropically to the lower cooler (χ_1), whereas on the upper boundary it assumes that the heat flux is vanished or restricted. In this case, the boundary conditions must satisfy the following equations:

$$\begin{aligned} \theta(z)_{z=0} &= 0, \theta(z)_{z=1} = \frac{\pi}{2}, \\ \chi(z)_{z=0} &= \chi_1, \chi_{,z}(z)_{z=1} = q_0, \end{aligned} \quad (28.13)$$

where $q_0 = -\frac{Q_0 d}{T_{N1} \lambda_{\perp}}$ is the dimensionless heat flux across the upper boundary of the HAN channel.

The velocity on the lower boundary must satisfy the no-slip boundary condition

$$u(z)_{z=0} = 0, \quad (28.14)$$

whereas on the upper boundary the SS is applied as

$$(\sigma_{zx}(z))_{z=1} = \sigma_{zx}^0. \quad (28.15)$$

Now the reorientation of the director in the microsized HAN channel confined between two solid surfaces, when the relaxation regime is governed by the viscous, elastic, thermomechanical forces, and the SS σ_{zx}^0 with accounting the heat flux $\mathbf{q} = q_0 \hat{\mathbf{k}}$, can be obtained by solving the system of the nonlinear partial differential Eqs. (28.9), (28.10), and (28.12), with the appropriate boundary conditions both for the polar angle $\theta(z, \tau)$, temperature $\chi(z, \tau)$ (Eq. (28.13)) and the velocity $u(z, \tau)$ (Eqs. 28.14–28.15), as well as with the initial condition

$$\theta(z, \tau = 0) = \frac{\pi}{2}. \quad (28.16)$$

28.2.2 Numerical Results for the Relaxation Regimes in HAN Channel

First of all, we focus on the problem how much the viscous torque $\mathbf{T}_{vis} = \bar{\gamma}_1(\chi)\theta_{,\tau} - \mathcal{A}(\theta)u_{,z} = \bar{\gamma}_1(\chi)\theta_{,\tau} - \frac{1}{2}(1 + \gamma_{21} \cos 2\theta)u_{,z}$ influences the character of director field $\hat{\mathbf{n}}(z, \tau)$ (or the polar angle $\theta(z, \tau)$) evolution to its stationary $\hat{\mathbf{n}}_{st}(z)$ distribution across the microfluidic HAN channel with the temperature gradient. In our case the $\nabla\chi$ is produced by the heat flux \mathbf{q} (see Eq. (28.13)), directed across the microfluidic HAN channel.

Calculations of the temperature dependence of $\gamma_{21} = -\gamma_2/\gamma_1$, as well as a comparisons of the values of the RVCs γ_1 and γ_2 , both for 5CB and 8CB, at temperature corresponding to nematic phase, are given in Table 28.1. The rest material parameters of these 5CB and 8CB nematic crystals are: the mass density $\sim 10^3 \text{ kg/m}^3$, the experimental data for elastic constants [20] $K_1(T)$ and $K_3(T)$ vary between 6 and 13 pN, and 7 and 14 pN, respectively. So, the highest values are $K_{10} \sim 13 \text{ pN}$, $K_{30} \sim 14 \text{ pN}$, and $\gamma_{10}(5CB) \sim 0.968 \text{ Pa s}$ and $\gamma_{10}(8CB) \sim 0.86 \text{ Pa s}$, respectively. In the following, we use the measured values, obtained by the adiabatic screening calorimetry and photopyroelectric techniques, both for the specific heat $C_p \sim 10^3 \text{ J/kgK}$ [21], and the thermal conductivity coefficients $\lambda_{\parallel} \sim 0.24$ and $\lambda_{\perp} \sim 0.13 \text{ W/mK}$ [22], the calculated value of the thermomechanical constant $\xi \sim 10^{-12} \text{ J/mK}$ [9], and measured values of the Leslie coefficients $\alpha(T)$ ($i = 1, \dots, 6$) [16], respectively.

Table 28.1 The values of the RVCs γ_1 and γ_2 and their ratio $\gamma_{21} = -\gamma_2/\gamma_1$ for 5CB and 8CB nematic liquid crystals. The values of the nematic–isotropic (NI) phase transition temperatures are $T_{NI} \sim 307\text{ K}$ and $\sim 313\text{ K}$, for 5CB and 8CB, respectively. All data for RVCs are given in Pa s [16]

T/T_{NI}	0.964	0.974	0.98	0.984	0.99	0.993
$\gamma_1(5CB)$	0.968	0.78		0.61		0.45
$-\gamma_2(5CB)$	1.01	0.80		0.67		0.56
$\gamma_{21}(5CB)$	1.04	1.03		1.1		1.24
$\gamma_1(8CB)$			0.86		0.73	
$-\gamma_2(8CB)$			0.52		0.47	
$\gamma_{21}(8CB)$			0.60		0.64	

The set of parameters values, which are involved in Eqs. (28.9), (28.10), and (28.12), are thus $\delta_1 \sim 24$, $\delta_2 \sim 2 \times 10^{-6}$, $\delta_3 \sim 6 \times 10^{-4}$, and $\delta_4 \sim 10^{-10}$. Using the fact that $\delta_2 \ll 1$, the Navier–Stokes equation (28.10) can be considerably simplified as velocity follows adiabatically the motion of the director. Thus, the whole left-hand side of Eq. (28.10) can be neglected, reducing it to

$$\sigma_{zx} = \bar{h}(\theta)u_z - \bar{A}(\theta)\theta_\tau - \delta_1\chi_{,z}\theta_z \sin^2\theta \left(1 + \frac{1}{2}\sin^2\theta\right) = \sigma_{zx}^0, \quad (28.17)$$

whereas the Eq. (28.12) also can be considerably simplified, because both parameters δ_3 and $\delta_4 \ll 1$, and the whole left-hand side of Eq. (28.12), as well as the second term, can be neglected, so that Eq. (28.12) takes the form

$$[\chi_{,z}(\lambda \cos^2\theta + \sin^2\theta)]_{,z} = 0. \quad (28.18)$$

The last equation has a solution

$$\chi_{,z}(z, \tau) = \frac{q_0}{\lambda \cos^2\theta + \sin^2\theta}. \quad (28.19)$$

Physically, this means that the temperature field $\chi(z, \tau)$ across the HAN cell, under above-mentioned conditions, is proportional to the heat flow q_0 on the upper restricted surface, when the temperature on the lower surface is kept constant.

In the case when the SS σ_{zx}^0 is equal to 10 ($\sim 5\text{ Pa}$) and there is the heat flux $q_0 = 0.02$ ($Q_0 \sim 200\text{ nW}/\mu\text{m}^2$) directed to the bulk of the nematic channel, the evolution of the director field \hat{n} to its stationary orientation \hat{n}_{st} in the microsized HAN channel, which is described by the polar angle $\theta(z, \tau_k)$, for different times started from $\tau_1 = 0.001$ (curve 1) to $\tau_R = \tau_7 = 0.4$ ($\sim 0.07\text{ s}$) (curve 7), for both cases 5CB (see Fig. 28.2a) and 8CB (Fig. 28.2b), is shown in Fig. 28.2. In the calculations, by means of the numerical relaxation method [23], the relaxation criterion $\epsilon = |(\theta_{(m+1)}(z, \tau) - \theta_{(m)}(z, \tau))/\theta_{(m)}(z, \tau)|$ was chosen to be equal to 10^{-4} , and the numerical procedure

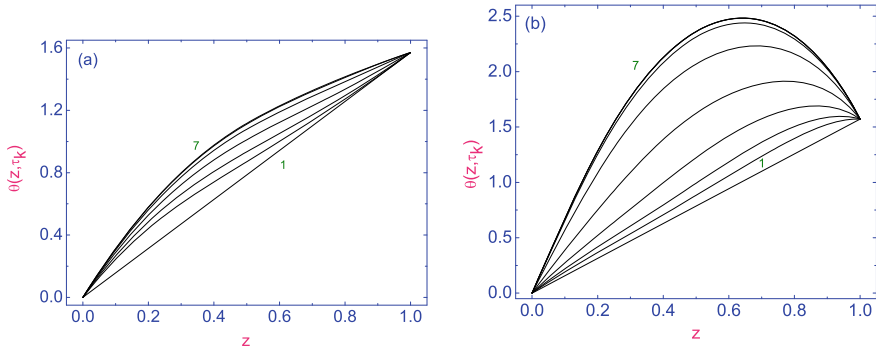


Fig. 28.2 **a** Evolution of the polar angle $\theta(z, \tau_k)(5CB)$ [in rad.] to its stationary distribution across the dimensionless (scaled by d) HAN microfluidic channel, under the effect of the SS $\sigma_{zx}^0 = 10$ (~ 5 Pa), for different times started from $\tau_1 = 0.001$ (curve 1) to $\tau_R = \tau_7 = 0.4$ (~ 0.07 s) (curve 7), respectively. **b** The same as in **a**, but the evolution of the polar angle $\theta(z, \tau_k)(8CB)$ [in rad.] to its stationary distribution across the dimensionless (scaled by d) HAN microfluidic channel. Here q_0 is equal to 0.02

was then carried out until a prescribed accuracy was achieved. Here, m is the iteration number.

In turn, the evolution of the velocity field $u(z, \tau_k)$ to its stationary distribution across the HAN microfluidic channel, under the effect of the same SS $\sigma_{zx}^0 = 10$ (~ 5 Pa), for different times started from $\tau_1 = 0.001$ (curve 1) to $\tau_R = \tau_7 = 0.4$ (~ 0.07 s) (curve 7), respectively, both for *5CB* (see Fig. 28.3a) and *8CB* (see Fig. 28.3b) nematics, is shown in Fig. 28.3. First of all, the effect of the viscous torque \mathbf{T}_{vis} , or $\gamma_{21} = -\gamma_2/\gamma_1$, on the evolution of the velocity field $u(z, \tau)$ is manifested in the qualitative difference in the velocity profiles for *5CB* and *8CB* nematics. In the case of *5CB*, we have concave profiles (see Fig. 28.3a), while in the case of *8CB*, these profiles represent, at the final stage of evolution, almost linear dependencies, where the velocity $u(z, \tau_k)$ increases from zero ($u(z = 0, \tau_k) = 0$), at the lower boundary of the channel, to the value $u(z = 1, \tau_k) \sim 22$ (~ 0.7 mm/s), at the upper boundary. In the case of *5CB*, the value of velocity $u(z = 1, \tau_k)(5CB)$ at the upper boundary is equal to ~ 23 (~ 0.73 mm/s). Second, the main effect of the viscous torque \mathbf{T}_{vis} , or $\gamma_{21} = -\gamma_2/\gamma_1$, is manifested in the character of evolution of the director field $\hat{\mathbf{n}}$ to its stationary orientation $\hat{\mathbf{n}}_{st}$ in the microsized HAN channel, which is described by the polar angle $\theta(z, \tau_k)$. Indeed, in the case of *5CB*, the polar angle $\theta(z, \tau_k)(5CB)$ increases monotonically from 0 to ~ 1.57 ($\pi/2$), whereas in the case of *8CB*, the polar angle $\theta(z, \tau_k)(8CB)$ increases monotonically from 0 to $\theta(z = 0.64, \tau_k)(8CB) \sim 2.48$, in the vicinity of the centrum of the HAN channel, with a subsequent decrease to the value of ~ 1.57 ($\pi/2$) at the upper boundary of the HAN channel. Thus, the main effect of $\gamma_{21} = -\gamma_2/\gamma_1$ affects the nature of the reorientation of the director field $\hat{\mathbf{n}}$ to its stationary orientation $\hat{\mathbf{n}}_{st}$ in the microsized HAN channel, which is described by the polar angle $\theta(z, \tau_k)$. In the case of the tumbling-type nematic phase, composed of *8CB* molecules, when $|\gamma_1| > |\gamma_2|$,

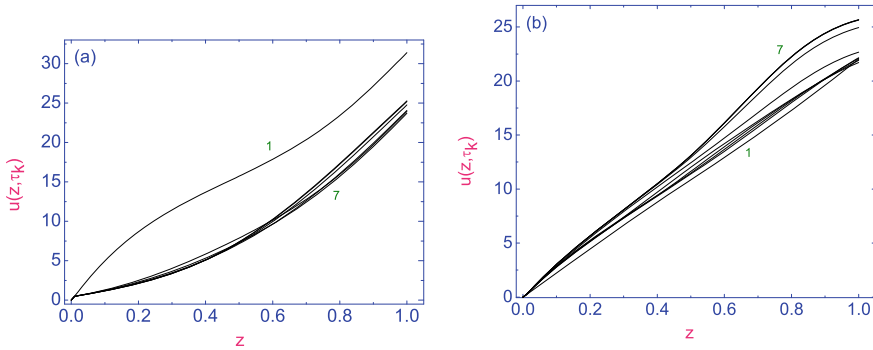


Fig. 28.3 **a** Evolution of the dimensionless velocity field $u(z, \tau_k)$ (*5CB*) (scaled by $K_{10}/\gamma_{10}d$) to its stationary distribution across the dimensionless (scaled by d) HAN microfluidic channel, under the effect of the SS $\sigma_{zx}^0 = 10$ (~ 5 Pa), for different times started from $\tau_1 = 0.001$ (curve 1) to $\tau_R = \tau_7 = 0.4$ (~ 0.07 s) (curve 7), respectively. **b** The same as in **a**, but the evolution of the dimensionless velocity field $u(z, \tau_k)$ (*8CB*) (scaled by $K_{10}/\gamma_{10}d$) to its stationary distribution across the dimensionless (scaled by d) HAN microfluidic channel. Here, q_0 is equal to 0.02

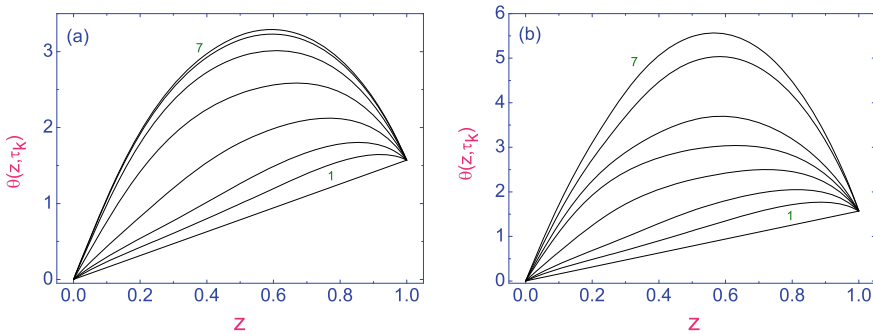


Fig. 28.4 **a** Evolution of the polar angle $\theta(z, \tau_k)$ [in rad.] to its stationary distribution across the dimensionless (scaled by d) HAN microfluidic channel, in the case of the tumbling-type nematic phase, composed of *8CB* molecules, and under the effect of the SS $\sigma_{zx}^0 = 20$ (~ 10 Pa), for different times started from $\tau_1 = 0.001$ (curve 1) to $\tau_R = \tau_7 = 0.4$ (~ 0.07 s) (curve 7), respectively. **b** The same as in **a**, but $\sigma_{zx}^0 = 30$ (~ 15 Pa) and $\tau_R = \tau_7 = 0.6$ (~ 0.1 s), respectively. Here, q_0 is equal to 0.02

the director will tumble under shear flow of the nematic, whereas in the case of the laminar-type nematic phase, composed of *5CB* molecules, when $|\gamma_1| < |\gamma_2|$, the dynamics of nematic liquid crystals produces the alignment regime.

In turn, when the SS σ_{zx}^0 is increased and equal to 20 (~ 10 Pa) (see Fig. 28.4a) and 30 (~ 15 Pa) (see Fig. 28.4b) and there is the heat flux 0.02 ($Q_0 \sim 200$ nW/ μm^2), in the case of the tumbling type nematic phase, composed of *8CB* molecules, when $|\gamma_1| > |\gamma_2|$, the evolution of the director's field $\hat{\mathbf{n}}$ to its stationary orientation $\hat{\mathbf{n}}_{st}$, in the vicinity of the centrum of the HAN channel, is undergoing a qualitative change. According to our calculations, the shear stress σ_{zx}^0 produces the velocity field $u(z, \tau)$

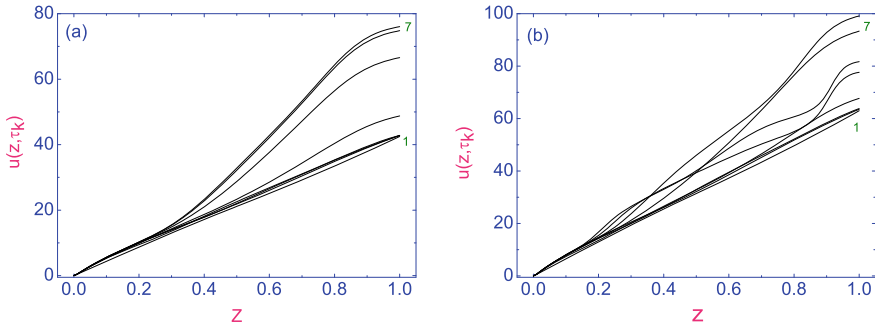


Fig. 28.5 **a** Evolution of the dimensionless velocity field $u(z, \tau_k)$ (scaled by $K_{10}/\gamma_{10}d$) to its stationary distribution across the dimensionless (scaled by d) HAN microfluidic channel, in the case of the tumbling-type nematic phase, composed of *8CB* molecules, and under the effect of the SS $\sigma_{zx}^0 = 20$ (~ 10 Pa), for different times started from $\tau_1 = 0.001$ (curve 1) to $\tau_R = \tau_7 = 0.4$ (~ 0.07 s) (curve 7), respectively. **b** The same as in **a**, but SS $\sigma_{zx}^0 = 30$ (~ 15 Pa) and $\tau_R = \tau_7 = 0.6$ (~ 0.1 s), respectively. Here, q_0 is equal to 0.02

directed in the positive direction (see Fig. 28.5), and its effects on the director distribution across the HAN microfluidic channel is so strong, that in the middle part of the nematic channel the biggest value of the polar angle $\theta(z, \tau)$ is equal to 5.5 ($\sim 315^\circ$), at $\sigma_{zx}^0 = 30$ (~ 15 Pa), and the director executes, practically, a full cycle of rotation (see Fig. 28.4b). That influence decreases with further decreasing of σ_{zx}^0 . But taking into account that the director field is strongly anchored to both boundaries of the HAN channel, homeotropically to the lower and homogeneously to the upper, the balance of the viscous, elastic, thermomechanical, anchoring forces and the SS σ_{zx} , applied to the upper restricted surface, leads to rotation of the director field mainly in the middle part of the HAN microfluidic channel.

The maximum of the absolute magnitude of the dimensionless velocity $u_{st}(z) = \frac{\gamma_{10}d}{K_{10}} v_x^{st}$ in the microsized HAN channel, at the final stage of the relaxation process is equal to ~ 75 (2.266 mm/s), at $\sigma_{zx}^0 = 20$ (~ 10 Pa) (see Fig. 28.5a), and ~ 95 (2.871 mm/s) at $\sigma_{zx}^0 = 30$ (~ 15 Pa) (see Fig. 28.5b), respectively.

In the case when the heat flux $q_0 = 0.02$ ($Q_0 \sim 200$ nW/ μm^2) across the upper boundary is directed to the bulk of the tumbling type nematic phase, composed of *8CB* molecules, whereas the SS σ_{zx} is applied to the upper restricted surface, the evolution of the temperature field $\chi(z, \tau)$ to its stationary distribution $\chi_{st}(z)$ across the HAN channel is characterized practically by linear dependence of $\chi(z, \tau)$, from the temperature on the lower boundary $\chi_{z=0} = 0.98$ (~ 307 K) to the temperature on the upper one $\chi_{z=1} = \chi_{up}$ (see Fig. 28.6). Calculations show that under the effect of the lower SS $\sigma_{zx}^0 = 10$ (see Fig. 28.6 (curve 1)) and higher $\sigma_{zx}^0 = 30$ (see Fig. 28.6 (curve 3)), the heating of the upper boundary is characterized practically same of χ_{up}^{st} : $\chi_{up}^{st}(\sigma_{zx}^0 = 10) \sim 0.995$ (~ 311.5 K) and $\chi_{up}^{st}(\sigma_{zx}^0 = 30) \sim 0.9946$ (~ 311.3 K), respectively, whereas in the case of $\chi_{up}^{st}(\sigma_{zx}^0 = 20) \sim 0.9924$ (~ 310.6 K). Note that in all these cases the dimensionless temperature on the lower boundary is kept

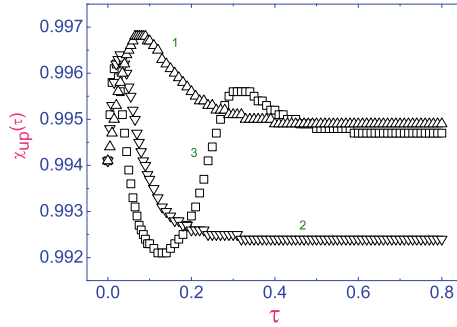


Fig. 28.6 Evolution of the dimensionless temperature on the upper boundary of the tumbling-type nematic phase $\chi_{up}(\tau)$ (scaled by T_{NI}) to its stationary value χ_{up}^{st} , for three values of the dimensionless SS (scaled by K_{10}/d^2): $\sigma_{zx}^0 = 10$ (curve 1), 20 (curve 2), and 30 (curve 3), respectively. The curves correspond to the heat flux $q_0 = 0.02$ ($Q_0 \sim 200$ nW/ μm^2), directed across the upper boundary

constant $\chi_{lw}^{st} \sim 0.98$ (~ 307 K), and across the HAN microfluidic channel the vertical temperature gradient $\nabla\chi$ directed to the warmer upper boundary is built up. So, the highest temperature difference $\Delta\chi = \chi_{up}^{st} - \chi_{lw}^{st} = 0.015$ (~ 4.5 K), which initially was equal to 0, is built up in the HAN microfluidic channel under the effect of the lower SS $\sigma_{zx}^0 = 10$, and after time $\tau_R \sim 0.4$ (~ 0.07 s).

The effects of the SS σ_{zx}^0 , directed in the negative direction, both on the evolution of director field $\hat{\mathbf{n}}$ to its stationary orientation $\hat{\mathbf{n}}_{st}$ in the microsized HAN channel, composed of *8CB* molecules, which is described by the polar angle $\theta(z, \tau_k)$ (see Fig. 28.7), and the velocity field $u(z, \tau_k)$ (see Fig. 28.8), for different times started from $\tau_1 = 0.001$ (curve 1) to $\tau_R = \tau_7 = 0.4$ (~ 0.07 s) (curve 7), are shown in Figs. 28.7 and 28.8, respectively. According to our calculations, the SS σ_{zx}^0 produces the velocity field $u(z, \tau)$ directed in the negative direction, and its effect on the director distribution across the HAN microfluidic channel is so strong, that in the middle part of the nematic channel the director field $\hat{\mathbf{n}}$ is directed, practically, orthogonal to both boundaries (the biggest value of the polar angle is equal to 3.14 ($\sim 180^\circ$)) (see, Fig. 28.7b). The relaxation process of the velocity field is characterized by the growth of $|u(z, \tau)|$ upon increasing τ , before getting to the stationary distribution $u_{st}(z) = u(z, \tau = \tau_7 = \tau_R)$ across the microsized HAN channel. This distribution is characterized by the maximum value of $u_{st}(z = 1)$ on the upper bounding surface ($z = 1$), and the hydrodynamic flow $u_{st}(z = 1)$ is directed parallel to both bounding surfaces in the negative direction. The maximum value of the dimensionless velocity $|u_{st}(z = 1)| = \frac{\gamma_{10}d}{K_{10}} |v_z^{st}(z = 1)|$ in the HAN channel, on the upper bounding surface, at the final stage of the evolution process is equal to ~ 60.4 (~ 1.9 mm/s), at $\sigma_{zx}^0 = -20$ (~ 10 Pa) (see Fig. 28.8a), and ~ 102 (~ 3.14 mm/s), at $\sigma_{zx}^0 = -30$ (~ 15 Pa) (see Fig. 28.8b), respectively. In the case when the heat flux across the upper surface is restricted ($q_0 = 0.02$ ($Q_0 \sim 200$ nW/ μm^2)), one also deals with a practically linear increase of $\chi(z, \tau)$ across the HAN channel from the temperature on

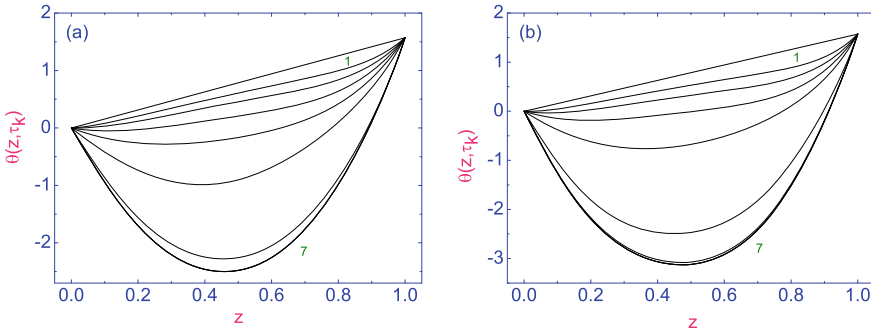


Fig. 28.7 **a** Evolution of the polar angle $\theta(z, \tau_k)$ [in rad.] to its stationary distribution across the dimensionless (scaled by d) HAN microfluidic channel, composed of $8CB$ molecules, and under the effect of the SS $\sigma_{zx}^0 = -20$ (~ 10 Pa), for different times started from $\tau_1 = 0.001$ (curve 1) to $\tau_R = \tau_7 = 0.47$ (~ 0.08 s) (curve 7), respectively. **b** he same as in **a**, but SS $\sigma_{zx}^0 = -30$ (~ 15 Pa) and $\tau_R = \tau_7 = 0.48$ (~ 0.08 s), respectively. Here q_0 is equal to 0.02

the lower ($\chi_{z=0} = 0.98$ (~ 307 K)) to the value on the upper boundary $\chi(z = 1)$. The evolution of the dimensionless temperature on the upper boundary of the HAN microfluidic channel $\chi_{z=1}(\tau)$, composed of $8CB$ molecules, to its stationary value $\chi_{z=1}^{st}$, for three values of the SS $\sigma_{zx}^0 = -10$ (curve 1), -20 (curve 2), and -30 (curve 3), is shown in Fig. 28.9. Calculations show that the relaxation process of $\chi_{z=1}(\tau)$ to its stationary value $\chi_{z=1}^{st}$, at both lower values of the SS $\sigma_{zx}^0 = -20$ (~ -10 Pa) and -30 (~ -15 Pa), is characterized by oscillating behaviour of $\chi_{z=1}(\tau)$, before getting to $\chi_{z=1}^{st}(\sigma_{zx}^0 = -20) = 0.9945$ (~ 311.3 K) and $\chi_{z=1}^{st}(\sigma_{zx}^0 = -30) = 0.993$ (~ 310.8 K), respectively, whereas $\chi_{z=1}^{st}(\sigma_{zx}^0 = -10)$ is equal to ~ 0.992 (~ 310.4 K). So, the highest temperature difference $\Delta\chi = 0.0145$ (~ 4.3 K), which initially was equal to zero, is built up in the HAN channel, under the influence of the SS $\sigma_{zx}^0 = -20$ (~ -10 Pa). Note that in all these cases the dimensionless temperature on the lower boundary is kept constant $\chi_{z=0} = 0.98$ (~ 307 K), and across the HAN channel the vertical temperature gradient $\nabla\chi$ directed to the warmer upper boundary is built up.

The effect of shear stress σ_{zx}^0 applied in both positive 10 (~ 5 Pa) (see Fig. 28.10a) (case I) and negative -10 (~ -5 Pa) (see Fig. 28.10b) (case II) directions on the evolution of the director field $\hat{\mathbf{n}}$ to its stationary orientation $\hat{\mathbf{n}}_{st}$ in the microsized HAN channel, composed of laminar-type nematic ($5CB$), is shown in Fig. 28.10. This evolution is described by the polar angle $\theta(z, \tau_k)$, and calculations are given for different times started from $\tau_1 = 0.001$ (curve 1) to $\tau_R = \tau_7 = 0.4$ (~ 0.07 s) (curve 7), respectively. First of all, the effect of shear stress on the evolution of the director field $\hat{\mathbf{n}}$ is manifested in the qualitative difference in the polar angle profiles for the cases I (see Fig. 28.10a) and II (see Fig. 28.10b), respectively. In the case I, we have convex profiles, when the polar angle $\theta(z, \tau_k)(5CB)$ increases monotonically from 0 to ~ 1.57 ($\pi/2$), whereas in the case II, the polar angle $\theta(z, \tau_k)(5CB)$ decreases

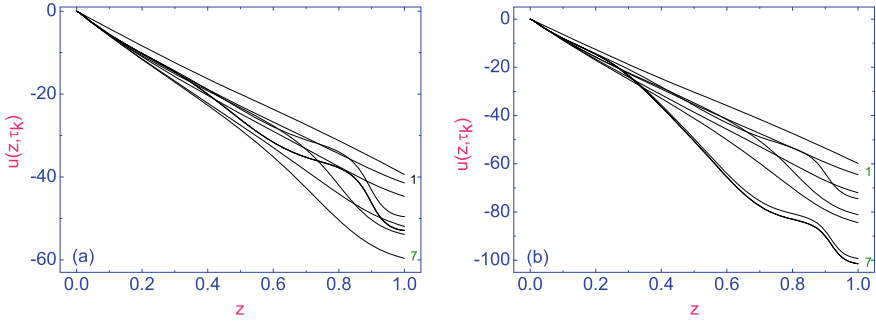


Fig. 28.8 **a** Evolution of the dimensionless velocity field $u(z, \tau_k)$ (scaled by $K_{10}/\gamma_{10}d$) to its stationary distribution across the dimensionless (scaled by d) HAN microfluidic channel, composed of $8CB$ molecules, and under the effect of the SS $\sigma_{zx}^0 = -20$ (~ 10 Pa), for different times started from $\tau_1 = 0.001$ (curve 1) to $\tau_R = \tau_7 = 0.32$ (~ 0.053 s) (curve 7), respectively. **b** The same as in **a**, but SS $\sigma_{zx}^0 = -30$ (~ 15 Pa) and $\tau_R = \tau_7 = 0.6$ (~ 0.1 s), respectively. Here q_0 is equal to 0.02

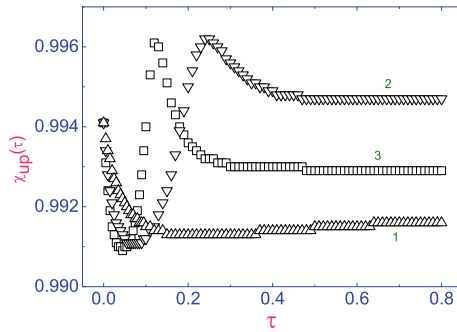


Fig. 28.9 Evolution of the dimensionless temperature on the upper boundary of the HAN microfluidic channel $\chi_{up}(\tau)$ (scaled by T_{NI}) to its stationary value χ_{up}^{st} , for three values of the dimensionless SS (scaled by K_{10}/d^2) $\sigma_{zx}^0 = -10$ (curve 1), -20 (curve 2), and -30 (curve 3), respectively. The curves correspond to the heat flux $q_0 = 0.02$ ($Q_0 \sim 200$ nW/ μm^2), directed across the upper boundary

monotonically from 0 to $\theta(z = 0.3, \tau_k)(5CB) \sim -0.28$, with a subsequent increase to the value of ~ 1.57 ($\pi/2$) at the upper boundary of the HAN channel.

Second, the effect of shear stress applied in both the positive (case I) and negative (case II) directions on the evolution of the velocity field $u(z, \tau)$ is mainly quantitative (see Fig. 28.11a, b), where the velocity $u(z, \tau_k)$ increases from zero ($u(z = 0, \tau_k) = 0$), at the lower boundary of the channel, to the value $u(z = 1, \tau_k) \sim 22$ (~ 0.7 mm/s), at the upper boundary, in the case I, and from zero ($u(z = 0, \tau_k) = 0$), at the lower boundary of the channel, to the value $u(z = 1, \tau_k) \sim -10$ (~ -0.32 mm/s), at the upper boundary, in the case II, respectively.

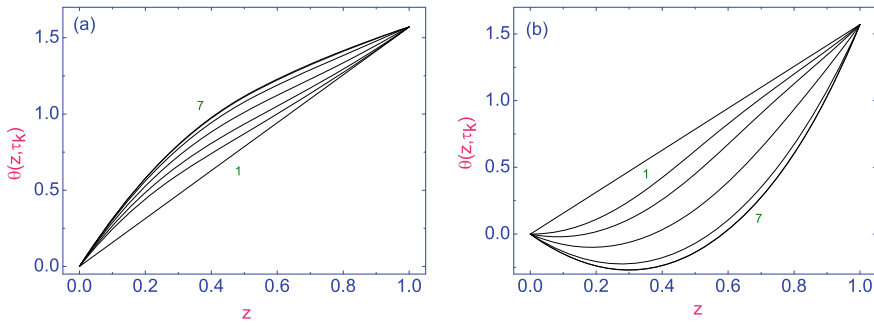


Fig. 28.10 **a** Evolution of the polar angle $\theta(z, \tau_k)$ [in rad.] to its stationary distribution across the dimensionless (scaled by d) HAN microfluidic channel, composed of *5CB* molecules, and under the effect of two values of the SS σ_{zx}^0 : **a** first is equal to 10 (~ 5 Pa), whereas **b** second is equal to -10 (~ -5 Pa), respectively. The different times started from $\tau_1 = 0.001$ (curve 1) to $\tau_R = \tau_7 = 0.47$ (~ 0.08 s) (curve 7), respectively, whereas q_0 is equal to 0.02

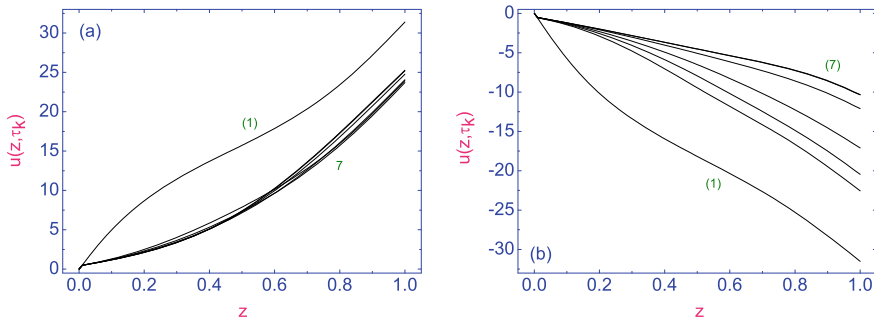


Fig. 28.11 **a** Same as in Fig. 28.10, but the curves correspond to the evolution of the dimensionless velocity field $u(z, \tau_k)$ (scaled by $K_{10}/\gamma_{10}d$) to its stationary distribution across the dimensionless (scaled by d) HAN microfluidic channel

28.3 A Role of a Flow in a Temperature Gradient Formation Across a HAN Channel

The purpose of this paragraph is to show, in the framework of the classical Ericksen–Leslie theory [10, 11], together with accounting the thermoconductivity equation for the temperature field [12], the simple way how the temperature gradient can be built up across the HAN channel under the action of the hydrodynamic flow. We consider the heat conduction regime which assumes that the temperature on the lower boundary is kept constant, whereas on the upper one, where it has been assumed that the heat flux is vanished, it must satisfy the boundary conditions

$$\chi(z)_{z=0} = \chi_1, \quad (\chi_{,z}(z))_{z=1} = 0. \tag{28.20}$$

As a result, the temperature difference, being initially equal to zero, grows up to the maximum possible value $\Delta\chi = \chi_{up} - \chi_{lw}$, corresponding to the nematic phase. The answer to the question of which restricted surfaces are cooler or warmer depends on the direction of the hydrodynamic flow \mathbf{v}_{eq} .

We consider a nematic system composed of asymmetric polar molecules, such as *cyanobiphenyl*, which are confined between two solid surfaces that impose a preferred orientation of the average molecular direction $\hat{\mathbf{n}}$ on the restricted surfaces, one, for instance, homeotropic on the lower, and, other, planar, on the upper bounding surfaces. So, we will describe the HAN channel under the influence of the temperature gradient $\nabla\chi$ directed parallel to the unit vector $\hat{\mathbf{k}}$. Here $\hat{\mathbf{k}}$ is a unit vector directed away from the lower substrate to the upper one (see Fig. 28.1).

The coordinate system defined by this task assumes that the director $\hat{\mathbf{n}}(t, \mathbf{r})$ lies in the xz plane (or in the yz plane) (see Fig. 28.1). Assuming that the temperature gradient $\nabla\chi$, due to the growth of the temperature difference on the HAN boundaries, under the action of the hydrodynamic flow, varies only in the z direction, $\nabla\chi = \frac{\partial\chi(z, \tau)}{\partial z}\hat{\mathbf{k}}$, we can suppose that the components of the director $\hat{\mathbf{n}} = \sin\theta(z, \tau)\hat{\mathbf{i}} + \cos\theta(z, \tau)\hat{\mathbf{k}}$, as well as the rest of the physical quantities also depend only on the z coordinate. Here θ denotes the polar angle, i.e., the angle between the direction of the director $\hat{\mathbf{n}}$ and the normal $\hat{\mathbf{k}}$ to the bounding surfaces. An assuming of incompressible fluid, the dimensionless hydrodynamic equations corresponding to the torque balance (see Eq. (28.9)) and the linear moment balance (see Eq. (28.10)) equations, as well as the entropy balance equation (see Eq. (28.12)) take the form [18]

$$\theta_{,\tau} = \mathcal{A}(\theta)u_{,\tau} + \mathcal{G}(\theta)\theta_{,zz} + \frac{1}{2}\mathcal{G}_{,\theta}(\theta)\theta_{,z}^2 - \delta_6\chi_{,\tau}\theta_{,\tau} \left(\frac{1}{2} + \sin^2\theta \right), \quad (28.21)$$

$$\delta_7 u_{,\tau}(\tau, z) = (\sigma_{zx})_{,\tau}, \quad (28.22)$$

$$\delta_8 \chi_{,\tau}(\tau, z) = [\chi_{,\tau} (\lambda \cos^2\theta + \sin^2\theta)]_{,\tau} + \delta_9 \left[\chi\theta_{,\tau} \left(\theta_{,\tau} \left(\frac{1}{2} + \sin^2\theta \right) - u_{,\tau} \sin^2\theta \left(1 + \frac{1}{2} \sin^2\theta \right) \right) \right]_{,\tau}, \quad (28.23)$$

where $\mathcal{A}(\theta) = \frac{1}{2}(1 - \gamma_{21} \cos 2\theta)$ and $\mathcal{G}(\theta) = \sin^2\theta + K_{31} \cos^2\theta$ are the hydrodynamic and elastic functions, respectively, $\sigma_{zx} = \frac{\delta\mathcal{R}}{\delta u_z}$ is the stress tensor component, the set of the LC parameters δ_i ($i = 6, 7, 8, 9$) is the same as in the section III, $\tau = \frac{K_1}{\gamma_1 d^2} t$ is the dimensionless time, and $\bar{z} = z/d$ is the dimensionless distance away from the lower boundary of the HAN channel. Notes that the overbars in the space variable z , in the last three Eqs. (28.21)–(28.23) have been eliminated.

Consider now the HAN system confined between two solid surfaces when the director $\hat{\mathbf{n}}$ is strongly anchored to these boundaries, homeotropically to the lower and homogeneously to the upper boundaries

$$\theta(z)_{z=0} = 0, \quad \theta(z)_{z=1} = \frac{\pi}{2}, \quad (28.24)$$

whereas the velocity on these boundaries must satisfy the no-slip boundary condition

$$u(z)_{z=0} = 0, \quad u(z)_{z=1} = 0. \tag{28.25}$$

Now the temperature field $\chi(\tau, z)$ in the HAN channel confined between two solid boundaries, when the temperature on the lower boundary is kept constant, whereas on the upper one, where it has been assumed that the heat flux is vanished, must satisfy the boundary conditions [17]

$$\chi(z)_{z=0} = \chi_1, \quad (\chi_{,z}(z))_{z=1} = 0. \tag{28.26}$$

The set of parameters, which are involved in Eqs.(28.21)–(28.23), are equal to $\delta_6 \sim 24$, $\delta_7 \sim 2 \times 10^{-6}$, $\delta_8 \sim 6 \times 10^{-4}$, and $\delta_9 \sim 2 \times 10^{-9}$. Using the fact that δ_7 , δ_8 and $\delta_9 \ll 1$, the Navier–Stokes (28.22) and the heat conduction (28.23) equations can be considerably simplified. Thus, the whole left-hand side of Eqs.(28.22) and (28.23) can be neglected and these equations take the form

$$\sigma_{zx} = h(\theta)u_{,z} - \mathcal{A}(\theta)\theta_{,\tau} - \delta_6\chi_{,z}\theta_{,z} \sin^2 \theta \left(1 + \frac{1}{2} \sin^2 \theta \right) = \mathcal{C}(\tau), \tag{28.27}$$

where $\gamma_1 h(\theta) = \alpha_1 \sin^2 \theta \cos^2 \theta - \mathcal{A}(\theta)\theta_{,\tau}u_{,z} + \frac{1}{2}\alpha_4 + g(\theta)$, $g(\theta) = \frac{1}{2}(\alpha_6 \sin^2 \theta + \alpha_5 \cos^2 \theta)$, $\mathcal{C}(\tau)$ is the function that does not depend on z and will be fixed by the boundary conditions, and

$$[\chi_{,z}(\lambda \cos^2 \theta + \sin^2 \theta)]_{,z} = 0. \tag{28.28}$$

To be able to observe the formation of the temperature difference across the HAN channel under the effect of the stationary hydrodynamic flow, it was considered the stationary analog of the Eq.(28.21), when $\theta_{,\tau} = 0$. In this case the dimensionless temperature across the hybrid aligned nematic channel is given by [18]

$$\chi(z) = \int_0^z [\mathcal{H}(\theta, u_{,z}) - (\mathcal{H}(\theta, u_{,z}))_{z=1}] / I(\theta, z) dz + \chi_1, \tag{28.29}$$

where $\mathcal{H}(\theta, u_{,z}) = h(\theta)u_{,z} - \mathcal{A}(\theta)\theta_{,\tau}$, $I(\theta, z) = \delta_6\theta_{,z} \sin^2 \theta (1 + \frac{1}{2} \sin^2 \theta)$, and $\chi_1 = T_1/T_{NI}$. The formation of the temperature difference across the HAN channel under the influence of the stationary flow with a triangular sharp profile

$$u(z, \zeta) = \begin{cases} \frac{\alpha z}{\zeta}, & (0 \leq z < \zeta), \\ \frac{\alpha}{1-\zeta}(1-z), & (\zeta \leq z < 1), \end{cases}$$

have been investigated by standard numerical relaxation method [23], and the results are shown in Fig. 28.12a and b, respectively. The relaxation criterion $\epsilon = |(\theta(\tau_R) -$

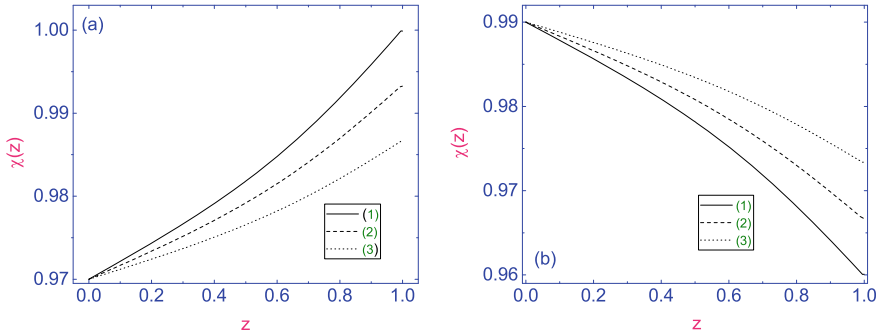


Fig. 28.12 **a** The dimensionless distance z (scaled by d) dependence of the dimensionless temperature $\chi(z)$ (scaled by T_{NI}) across the HAN channel under the effect of the stationary dimensionless flow $\mathbf{v} = u(z, \zeta)\hat{\mathbf{i}}$ (scaled by $K_{10}/\gamma_{10}d$), with a triangular profile, for a number of values of α [18]: 0.0009 (curve 1), 0.0007 (curve 2), and 0.0005 (curve 3), respectively. In this case, the vector \mathbf{v} is directed in the positive verse. **b** The same as in Fig. 28.12a, but $\mathbf{v} = -u(z, \zeta)\hat{\mathbf{i}}$ is directed in the negative verse

$\theta_{eq})/|\theta_{eq}|$ for calculating procedure was chosen to be equal to 10^{-4} , and the numerical procedure was then carried out until a prescribed accuracy was achieved.

When the stationary hydrodynamic flow $\mathbf{v} = u(z, \zeta)\hat{\mathbf{i}}$ is directed in the positive direction (see, Fig. 28.12a), the temperature on the lower boundary of the HAN channel keeps a constant value $\chi_{z=0} = \chi_1 = 0.97$ ($\sim 298\text{ K}$), and across the nematic sample the vertical temperature gradient $\nabla\chi$ directed to the warmer upper boundary is built up. The highest temperature difference $\chi_{max}(\zeta) \equiv \Delta\chi = \chi_{up} - \chi_{lw} = 0.03$ ($\sim 9\text{ K}$), which initially was equal to zero, is built up in the HAN channel, under the influence of the hydrodynamic flow $u(z, \zeta)$, where the magnitude of the factor α is equal to 0.0009 ($\sim 1.2\text{ nm/s}$) (see Fig. 28.12a, curve (1)). The rest curves (2) and (3) correspond to $\alpha = 0.0007$ ($\sim 1\text{ nm/s}$), and 0.0005 ($\sim 0.7\text{ nm/s}$), respectively. In the case of inverse direction of $\mathbf{v} = -u(z, \zeta)\hat{\mathbf{i}}$ (see, Fig. 28.12b), the temperature on the upper restricted surface keeps a constant value $\chi_{z=1} = \chi_1 = 0.99$ ($\sim 304\text{ K}$), whereas the lower surface is cooled down up to 0.96 ($\sim 295\text{ K}$), close to the nematic-solid phase transition temperature, at the value of $\alpha = 0.0009$ (curve (1)). In all these cases, ζ (~ 0.98) is located close to the upper boundary of the HAN channel. The magnitude of $\chi_{max}(\zeta)$ has a huge influence on the location of the maximum of $u(z, \zeta)$. In the case when ζ is placed in the middle part of the nematic channel $\zeta = 0.5$ (see, Fig. 28.13a), the temperature difference, which initially was equal to zero, grows up to $\Delta\chi \sim 0.0008$ ($\sim 0.3\text{ K}$), at the value of $\alpha = 0.0009$, and only with the growth of α up to a two order of the magnitude, from 0.0009 up to 0.09 ($\sim 0.1\text{ }\mu\text{m/s}$), that difference grows up to a few degrees $\Delta\chi \sim 0.02$ ($\sim 6\text{ K}$). The effect of position of ζ on the magnitude of the highest temperature difference $\chi_{max}(\zeta)$, when on the lower boundary a constant temperature is kept $\chi_{z=0} = \chi_1 = 0.97$ ($\sim 298\text{ K}$), for a number of values of the hydrodynamic velocity $u(z, \zeta)$, is shown in Fig. 28.13b. Notes that

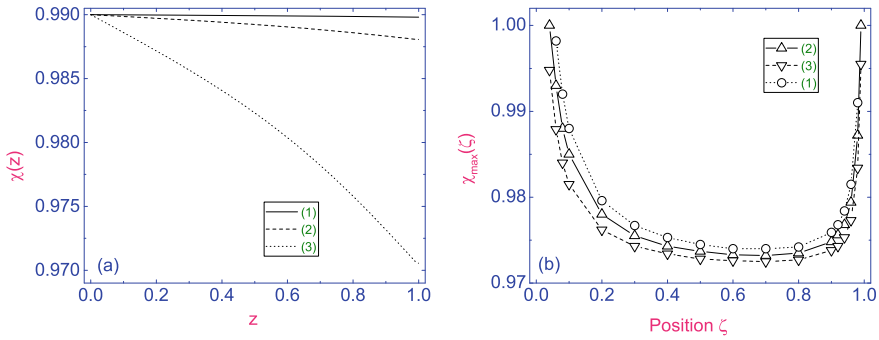


Fig. 28.13 **a** The dimensionless distance z (scaled by d) dependence of the dimensionless temperature $\chi(z)$ (scaled by T_{NI}), for the stationary dimensionless flow $\mathbf{v} = -u(z, \zeta = 0.5)\hat{\mathbf{i}}$ (scaled by $K_{10}/\gamma_{10}d$) directed in the negative x and calculated for a number of α [18]: 0.0009 (curve 1), 0.009 (curve 2), and 0.09 (curve 3), respectively. **b** Dependence of $\chi_{max}(\zeta)$ versus position of ζ for a number of α : 0.0011 (curve 1), 0.0009 (curve 2), and 0.0007 (curve 3), respectively

the velocity $u(z, \zeta)$ and temperature $\chi(z)$ on the restricted boundaries have to satisfy the boundary conditions Eqs. (28.24) and (28.25), respectively.

We have found that the quantity $\chi_{max}(\zeta)$ is sensitive to position of ζ , and demonstrates increasing of the magnitude of the highest temperature difference when ζ is close to both boundaries of the HAN channel. Such behavior of $\chi_{max}(\zeta)$ is dictated by Eq. (28.29). Indeed, in the case of stationary flow, the value of the shear rate shift $\Delta u_{,z} = u_{,z}^+ - u_{,z}^- \sim \frac{1}{\zeta(1-\zeta)}$ increases to infinity in the vicinity of the bounding surfaces, when the position of $\zeta \rightarrow 0$ or 1. Physically, this means that only stationary flow with a triangular sharp profile and position of the maximum in the vicinity of the restricted boundaries may built up the highest temperature difference in the hybrid aligned nematic channel in a few degrees. By means of other hydrodynamic flow with profiles, which can not demonstrate the sharp growth of $u_z(z)$, one can achieve the same result only by using the “high-speed” hydrodynamic flow $\sim 0.1 \mu\text{m/s}$.

It was shown by the Brewster angle spectroscopy (BAS) technique that the hydrodynamic flow of arachidic (eicosanoic) acid through the narrow channel with the width in $\sim 0.1 \mu\text{m}$, and with the triangular velocity profile at shear rate greater than 0.2 s^{-1} for various values of surface pressure might be achieved [17]. It has also been shown that as the flow rate increases, the velocity profile gradually becomes sharper, eventually becoming triangular. In a typical fluid, such a profile would indicate shear thickening. If so, we do not exclude a possible extension of the BAS technique to the case of above-mentioned nematic system.

28.4 Conclusion

This chapter discusses some recent numerical advances in predicting the structural and hydrodynamic behavior of thermally excited flow in microfluidic hybrid aligned nematic (HAN) channels. Despite the fact that certain quantitative and qualitative advances have been made in the hydrodynamic description of relaxation processes in microsized nematic channels under the effect of a temperature field, there are still a number of questions concerning the temperature gradient formation across these channels.

It has been shown that, owing to the action of a temperature gradient, a horizontal nematic layer, initially at the rest, when heated both below and above, starts moving in the horizontal direction. In the case of strong homeotropic and planar anchorings on the boundaries, the equilibrium distribution of the velocity field $v_{eq}(z)$ across the HAN channel is characterized by a sharp increase of the absolute magnitude of $v_{eq}(z)$ in the vicinity of the boundary with the planar anchoring [7]. This result, in turn, suggests a number of questions. Is it possible to produce the onset of a temperature difference ΔT between the two boundaries of the HAN microfluidic channel as a result of a stationary hydrodynamic flow distribution $v_{eq}(z)$ across the channel or by application of the shear stress (SS) σ_{zx} to the boundaries of this channel? Or, in more general terms, how does ΔT depend on $v_{eq}(z)$ or σ_{zx} ?

The above-mentioned numerical results demonstrate that both the stationary flow with a triangular velocity profile $v_{eq}(z)$ and the SS σ_{zx} , applied to the boundaries of the HAN channel may, under certain conditions, overcome the viscous, elastic, thermomechanical, and anchoring forces and cause a temperature gradient across this channel, with the maximum absolute value of the temperature difference ranging up to a few degrees.

Acknowledgements The reported study was funded by RFBR and DFG, project number 20-52-12040.

References

1. Schenning, A.P.H.J., Crawford, G.P., Broer, D.J.: Liquid Crystal Sensors. CRC Press, Taylor and Francis Group, Boca Raton (2018)
2. Zakharov, A.V., Maslennikov, P.V., Pasechnik, S.V.: Electrically driven nematic flow in microfluidic devices containing a temperature gradient. *Phys. Rev. E*. **101**, 062702-1–062702-9 (2020)
3. Zakharov, A.V., Maslennikov, P.V., Pasechnik, S.V.: Electrically driven nematic flow in microfluidic capillary with radial temperature gradient. *Phys. Rev. E*. **103**, 012702-1–012702-11 (2021)
4. Squires, T.M., Quake, S.R.: Microfluidics: fluid physics at the nanoliter scale. *Rev. Mod. Phys.* **77**, 977–1026 (2005)
5. Schoch, R.B., Han, J., Renaud, P.: Transport phenomena in nanofluidics. *Rev. Mod. Phys.* **80**, 839–883 (2008)
6. Akopyan, R.S., Zeldovich, B.Ya.: Thermomechanical effects in deformed nematics. *Sov. Phys. JETP*. **87**, 1660–1669 (1984)

7. Zakharov, A.V., Vakulenko, A.A.: Influence of the flow on the orientational dynamics induced by temperature gradient in nematic hybrid-oriented cells. *J. Chem. Phys.* **127**, 084907-1–084907-7 (2007)
8. Šliwa, I., Zakharov, A.V.: Heat driven flow in micro-sized nematic volumes: computational studies and analysis. *Symmetry*. **13**, 459-1–459-40 (2021)
9. Akopyan, A.R., Alaverdian, R.B., Santrosian, E.A., Chilingarian, Y.S.: Thermomechanical effects in the nematic liquid crystals. *J. Appl. Phys.* **90**, 3371–3376 (2001)
10. Ericksen, J.L.: Anisotropic fluids. *Arch. Ration. Mech. Anal.* **4**, 231–237 (1960)
11. Leslie, F.M.: Some constitutive equations for liquid crystals. *Arch. Ration. Mech. Anal.* **28**, 265–283 (1968)
12. Landau, L.D.: Lifshitz: *Fluid Mechanics*. Pergamon, Oxford (1987)
13. Archer, L.A., Larson, R.G.: A molecular theory of flow alignment and tumbling in shear nematic liquid crystals. *J. Chem. Phys.* **103**, 3108–3111 (1995)
14. Zakharov, A.V., Dong, R.Y.: Two shear flow regimes in nematic liquid crystals: near a charged surface and in the bulk. *J. Chem. Phys.* **116**, 6348–6353 (2002)
15. Zakharov, A.V., Thoen, J.: Pretransitional anomalies in the shear flow near a second-order nematic- smectic-A phase change. *Phys. Rev. E*. **69**, 051709-1–051709-4 (2004)
16. Chmielewski, A.G.: Viscosity coefficients of some nematic liquid crystals. *Mol. Cryst. Liq. Cryst.* **132**, 339–352 (1986)
17. Kurnaz, L.M., Schwartz, D.K.: Channel flow in a Langmuir monolayer: unusual velocity profiles in a liquid-crystalline mesophase. *Phys. Rev. E*. **56**, 3378–3384 (1997)
18. Zakharov, A.V., Vakulenko, A.A.: Temperature gradient formation across a nematic hybrid-oriented film. *Chem. Phys. Lett.* **454**, 80–84 (2008)
19. Zakharov, A.V., Maslennikov, P.V.: Laser-excited motion of liquid crystals confined in a micro-sized volume with a free surface. *Phys. Rev. E*. **96**, 052705-1–052705-10 (2017)
20. Madhusudana, N.V., Pratibha, R.P.: Elasticity and orientational order in some cyanobiphenyls: part IV. Reanalysis of the data. *Mol. Cryst. Liq. Cryst.* **89**, 249–257 (1982)
21. Jamee, P., Pitsi, G., Thoen, J.: Systematic calorimetric investigation of the effect of silica aerosols on the nematic to isotropic transition in heptylcyanobiphenyl. *Phys. Rev. E*. **66**, 021707-1–021707-8 (2002)
22. Marinelli, M., Ghosh, A.K., Mercuri, F.: Small quartz silica spheres induced disorder in octyl-cyanobiphenyl (8CB) liquid crystals: a thermal study. *Phys. Rev. E* **63**, 061713-1–061713-9 (2001)
23. Berezin, I.S., Zhidkov, N.P.: *Computing Methods*, 4th edn. Clarendon, Oxford (1965)

Chapter 29

Signatures of Transient Purely Ballistic Heat Conduction: Theory and Experimental Investigation



Aleksei A. Sokolov, Wolfgang H. Müller, Anton M. Krivtsov,
and Alexey V. Porubov

Abstract In this paper, we propose an approach to define thermal conductivity for a purely ballistic transient heat conduction and study its size dependence for two-dimensional structures in circular geometry in order to use this dependence as a purely ballistic regime signature. Then, a review of various experimental techniques by which the thermal conductivity is measured is presented. Finally, the thermal conductivity of graphene in purely diffusive regime is measured for one fixed sample size using Raman thermometry. The result of the proposed theoretical approach is a linear dependence on the sample size in the case of purely ballistic thermal conductivity. An outcome of an experimental study of graphene in a purely diffusive regime and the presented review of experimental methods are the basis for an extension of further experimental studies to the anomalous heat conduction regimes.

Keywords Ballistic heat transport · Ballistic limit · Harmonic crystal · Graphene · Raman · Transient processes · Anomalous heat transport

29.1 Introduction

In recent years, the study of anomalous thermal conductivity, i.e., processes that deviate from the classical Fourier equation, has been actively developing in the scientific community. A number of experimental studies of this anomaly in solid crystals can be found in [10, 11, 26]. A theoretical description of this phenomenon is

A. A. Sokolov (✉) · W. H. Müller
Technische Universität Berlin, Einsteinufer 5, 10587 Berlin, Germany
e-mail: sokolov@tu-berlin.de

W. H. Müller
e-mail: wolfgang.h.mueller@tu-berlin.de

A. M. Krivtsov · A. V. Porubov
Institute for Problems in Mechanical Engineering RAS, V.O., Bolshoy pr., 61, St. Petersburg
199178, Russia
e-mail: akrivtsov@bk.ru

possible by using the kinetic approach (Boltzmann equation), the Maxwell-Cattaneo model [15], the Guyer-Krumhansl model [19], lattice dynamics [20], and some other methods.

The difficulty in connecting the proposed models with processes in real materials lies in the fact that such transient processes occur at very high speeds (speed of sound in crystals, e.g., >10 km/s for graphene [7]). Moreover, since the process is fundamentally different from Fourier's law, it lacks the thermal conductivity coefficient as a material parameter. However, even when Fourier's law does not hold, in an experimental setting and molecular dynamic simulations when a steady non-equilibrium temperature gradient is applied to the specimen, it turns out that it is convenient to use the mathematical formulation of Fourier's law and to observe the size dependence of thermal conductivity as a signature of anomalous regimes [6, 20, 28, 29]. Thus, experimental methods, which have now already become a standard, have been developed to determine the thermal conductivity coefficient from Fourier's law [30]. As an alternative, for example, the thermal grating method deals directly with a non-stationary formulation [11]. However, it has some open questions to consider. For example, the measurement of the thermal process occurs indirectly, through the accompanying thermoelastic process, which, despite the fact that it does not have a significant effect in the classical regime, can become more pronounced in the ballistic regime (see so-called *ballistic resonance* [18]).

In the classical regime of heat conduction, the heat flux is proportional to the gradient of temperature. Accordingly, the coefficient of proportionality (heat conductivity κ) is a material parameter and does not depend on the system size, L . In anomalous heat conduction, the process deviates from the classical Fourier law. A number of theoretical results have shown a power divergence of heat conductivity $\kappa \sim L^\alpha$ for 1D systems [20]. This result was confirmed also experimentally [27].

Recently in the laboratory "Discrete Models in Mechanics" IPME RAS under the supervision of A.M. Krivtsov, a ballistic heat conduction model based on the analysis of crystal dynamics was developed [16, 17]. The proposed model has a number of obvious advantages (analytical description, lack of phenomenological assumptions). Despite the fact that there are also some shortcomings (harmonic approximation, lack of quantum effects description) it is undoubtedly promising for the description of ballistic heat propagation from the point of view of continuum mechanics and constitutive theory. For an experimental study of the limits of applicability of this theory and its correspondence to real materials, a joint project with W.H. Müller, Chair of Continuum Mechanics and Constitutive theory of TU Berlin was initiated. The group has extensive experience in experimental work on a micro-level and expertise in continuum mechanics [1, 21, 22].

In order to connect the two descriptions, non-stationary ballistic model and the classical Fourier thermal conductivity coefficient, a theoretical method is proposed in this work, based on a definition of thermal conductivity for transient ballistic processes originally suggested in [17]. Furthermore, experimental studies using the methods available in the laboratory of TU Berlin and a review of works on this topic are presented. Last, an experimental measurement of the thermal conductivity of graphene is performed. Graphene was chosen as the material of investigation

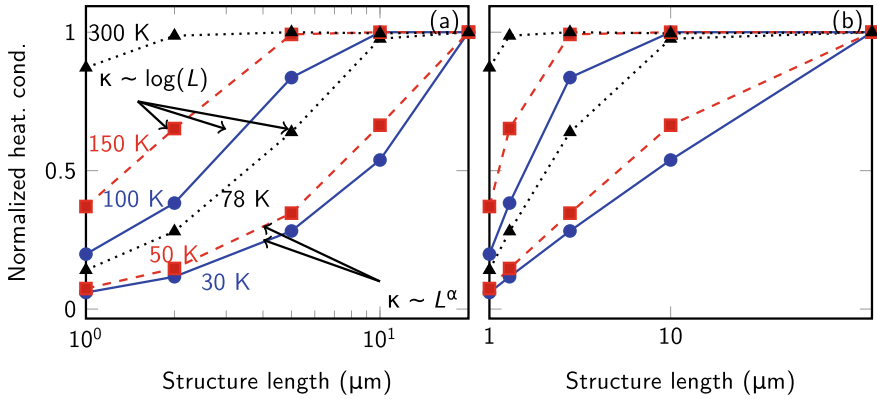


Fig. 29.1 Dependence of thermal conductivity on length of the structure at different temperatures, **a** logarithmic scale, **b** linear scale. The data for each curve is normalized to its value at $L = 20 \mu\text{m}$. Graphs are plotted using data from [29]

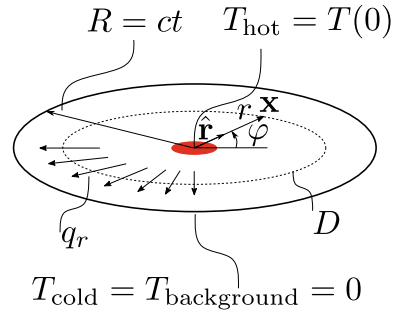
because, first, it has great potential for technological applications in microelectronic devices. Second, its greatest importance is that it is cheap to manufacture and it is possible to produce ultrapure defect-free monocrystalline samples (grain size up to $20 \mu\text{m}$). Thus, graphene appears to be a very convenient playground for experimental verification of the abovementioned theoretical predictions.

Theoretical results presented in [20] for 2D anharmonic systems show a logarithmic divergence of thermal conductivity $\kappa \sim \log(L)$. This is confirmed by experimental results with graphene for a quadrilateral over a large temperature range [32] and for circular geometries at room temperature (RT) [8, 12], and also by numerical simulation at RT for circular geometry [4]. Numerical simulations of 2D FPU systems¹ in [31] showed a logarithmic divergence for $\alpha\beta$ -FPU and purely quartic models, and a power divergence for β -FPU systems. In [29], a kinetic theory was used and third-order terms in the Hamiltonian were taken into account. The results [29] indicate a logarithmic divergence for temperatures approximately above liquid nitrogen temperatures and a power divergence below (see Fig. 29.1). These findings for 2D materials showing power divergence are of special interest, since at very low temperatures the influence of anharmonicity decreases and a purely ballistic heat conduction regime is achievable.

The rest of this paper is structured as follows. In Sect. 29.2, thermal conductivity is defined for the equations of ballistic heat conduction and its size dependence is investigated. In Sect. 29.3, a review of experimental techniques and results of measurements performed at TU Berlin are presented. The size dependence of thermal conductivity obtained theoretically from ballistic model in previous section is compared with available experimental data. Section 29.4 closes with a conclusion.

¹ FPU = Fermi-Pasta-Ulam.

Fig. 29.2 Schematic representation of the considered anomalous heat conduction process



29.2 Divergence of Heat Conductivity for Transient Purely Ballistic Heat Conduction

An engineering approach to the definition of thermal conductivity stems from the problem of two regions with temperatures T_{hot} and T_{cold} , separated at a distance L with a medium with thermal conductivity κ . In a classical diffusive heat conduction regime, a linear temperature profile results with uniform heat flux q . In this case, heat conductivity is defined as

$$\kappa = \frac{qL}{\Delta T}, \quad \Delta T = T_{\text{hot}} - T_{\text{cold}}. \quad (29.1)$$

When studying anomalous heat conduction, the heat flux is not uniform. This was observed, for example, in one-dimensional discrete systems [20]. For a one-dimensional system of N particles between hot and cold reservoirs separated by a length L , an averaged heat flux is defined as $\langle q \rangle = \sum_n q_n / N$, where q_n is a local per particle heat flux and a definition for the thermal conductivity similar to (29.1) results, $\kappa = \langle q \rangle L / \Delta T$. The same approach is possible for bulk systems [28] where a spatial average over the volume between the reservoirs is used.

Let us consider the anomalous heat flux in two-dimensional materials. It was shown in [16] that a fundamental solution for the kinetic temperature field for a purely ballistic heat conduction regime is a self-similar function, which can be represented as

$$T = \frac{1}{t^2} f\left(\frac{r}{t} \sin \varphi, \frac{r}{t} \cos \varphi\right), \quad r < R, \quad (29.2)$$

where r, φ are polar (radial and angular, respectively) coordinates, $R = ct$, and c is the fastest group velocity in the system. For $r > R$, the temperature field remains zero (we assume a background temperature of zero).

The process described by this fundamental solution has the following features. Initially, a point perturbation is applied at the point of origin. Then the heat flows from the center radially away forming a growing circle with a radius increasing at a constant speed. Outside of this circle the temperature remains zero, see Fig. 29.2.

Applying the approach subsumed in formula (29.1), the thermal conductivity can be defined as follows. Heuristically we fix the moment of observation time and restrict the considered space to the circle inside which by the moment of observation the energy has spread radially. Then the average heat flux, which is to be substituted in (29.1) and which causes the energy spread from the heated center to the colder boundary, is the average of a radial component of flux over the whole area of this circle,

$$\langle q \rangle = \frac{\int_S \mathbf{q} \cdot \hat{\mathbf{r}} dS}{S} = \frac{\int_0^{2\pi} \int_0^R q_r(r, \varphi) r dr d\varphi}{\pi R^2}, \quad (29.3)$$

where $\hat{\mathbf{r}}$ is the radial vector and S is the area of the circle.

The temperature difference in the denominator of (29.1) between hotter and colder regions will be in this axisymmetric case given by the difference between the temperature in the center, from which the heat flows radially away, and the temperature of the background toward which the heat flows. Since the background temperature is zero the temperature difference is $\Delta T = T(0)$.

As an approximation, we assume that the temperature profile can be factorized into radial and angular components,

$$T(r, \varphi) = \frac{1}{t^2} f\left(\frac{r}{t} \sin \varphi, \frac{r}{t} \cos \varphi\right) \approx \frac{1}{t^2} \Theta\left(\frac{r}{t}\right) \Phi(\varphi). \quad (29.4)$$

Although this may be not strictly true, the author believes that the main factor which contributes to the thermal conductivity within this framework is the flux in the direction of the radial component along which the heat transfers from the hotter (center) to the colder (boundary) region. The heat flux is also factorized as

$$q_r \approx \hat{q}_r(r, t) \Psi(\varphi). \quad (29.5)$$

A more precise form of heat flux function will be presented later.

Substituting the averaged heat flux (29.3) into the thermal conductivity (29.1) and taking for the length of the system the radius of the circle, $L = R$, yield

$$\kappa = \frac{\langle q \rangle R}{\Delta T} = \int_0^{2\pi} \Psi(\varphi) d\varphi \frac{\int_0^R \hat{q}_r(r, t) r dr}{\pi R T(0)}. \quad (29.6)$$

We are interested in the proportionality dependence of the thermal conductivity but not in its absolute value. Therefore, by recalling $R = ct$ and by omitting the constant arising from integration of angular component and other constants, one obtains the following proportionality:

$$\kappa \sim \frac{\int_0^R \hat{q}_r(r, t) r \, dr}{tT(0)} \sim t \int_0^R \hat{q}_r(r, t) r \, dr, \quad (29.7)$$

where the last proportionality arises, because it can be seen from (29.2) that $T(0) \sim 1/t^2$.

Let us consider the local energy balance equation,

$$\rho \dot{u} = -\nabla \cdot \mathbf{q}, \quad (29.8)$$

and integrate it over the surface of a circle $D : |\mathbf{x}| \leq r$,

$$\int_{S \in D} \rho \dot{u} \, dS = - \int_{S \in D} \nabla \cdot \mathbf{q} \, dS. \quad (29.9)$$

According to divergence theorem, the right-hand side of this equation transforms into

$$\begin{aligned} \int_{S \in D} \nabla \cdot \mathbf{q} \, dS &= \int_{l \in \partial D} \mathbf{q} \cdot \mathbf{n} \, dl = \int_0^{2\pi} \hat{q}_r(r, t) \Psi(\varphi) r \, d\varphi = r \hat{q}_r(r, t) \int_0^{2\pi} \Psi(\varphi) \, d\varphi \\ &= C_1 r \hat{q}_r(r, t), \end{aligned} \quad (29.10)$$

where ∂D is the circle boundary, normal to which is a radial unit vector $\mathbf{n} = \hat{\mathbf{r}}$, $dl = r \, d\varphi$. C_1 is the constant arising from integration of the angular part of heat flux. The left-hand side together with $u = c_V T$, where c_V is the specific heat capacity at constant volume, gives

$$\begin{aligned} \int_{S \in D} \rho \dot{u} \, dS &= \rho c_V \int_{S \in D} \dot{T} \, dS = \int_0^{2\pi} \Phi(\varphi) \, d\varphi \int_0^r \frac{\partial}{\partial t} \left[\frac{1}{t^2} \Theta \left(\frac{\tilde{r}}{t} \right) \right] \tilde{r} \, d\tilde{r} = \\ &= C_2 \int_0^r \frac{\partial}{\partial t} \left[\frac{1}{t^2} \Theta \left(\frac{\tilde{r}}{t} \right) \right] \tilde{r} \, d\tilde{r}. \end{aligned} \quad (29.11)$$

Expanding time derivative in the last equality yields

$$\frac{\partial}{\partial t} \left[\frac{1}{t^2} \Theta \left(\frac{\tilde{r}}{t} \right) \right] = -\frac{2}{t^3} \Theta \left(\frac{\tilde{r}}{t} \right) - \frac{\tilde{r}}{t^4} \Theta' \left(\frac{\tilde{r}}{t} \right), \quad (29.12)$$

where the dash (...) denotes differentiation with respect to the argument. Substituting it back to (29.11) leads to

$$\int_{S \in D} \rho \dot{u} dS = -\frac{C_2}{t} \int_0^{r/t} \left[2\Theta\left(\frac{\tilde{r}}{t}\right) + \frac{\tilde{r}}{t} \Theta\left(\frac{\tilde{r}}{t}\right) \right] \frac{\tilde{r}}{t} d\frac{\tilde{r}}{t} = -\frac{C_2}{t} \zeta\left(\frac{r}{t}\right). \quad (29.13)$$

A combination of (29.10) and (29.13) yields an expression for the radial component of the heat flux,

$$\hat{q}_r(r, t) = \frac{C_3}{rt} \zeta\left(\frac{r}{t}\right), \quad C_3 = C_2/C_1. \quad (29.14)$$

Substitution of (29.14) into the integral in (29.7) gives

$$\int_0^R \hat{q}_r(r, t) r dr = \int_0^{ct} \frac{C_3}{t} \zeta\left(\frac{r}{t}\right) dr = \int_0^c C_3 \zeta\left(\frac{r}{t}\right) d\frac{r}{t} = \text{const.} \quad (29.15)$$

Thus, from (29.15) and (29.7) it follows that

$$\kappa \sim t. \quad (29.16)$$

It is also seen from (29.15) that the average heat flux in this process is constant, $\langle q \rangle = \text{const.}$ Therefore, proportionality of thermal conductivity is determined by the ratio $R/T(0)$. Recalling that $R = ct$, and $T(0) \sim 1/t^2$ this result is directly obtained.

By using the result (29.16) and $t = R/c$ it also follows that

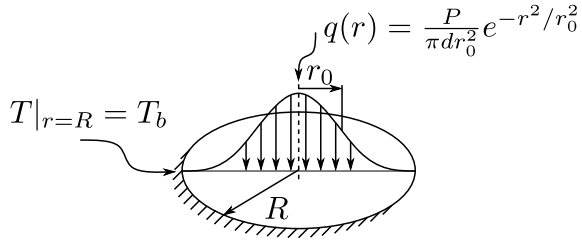
$$\kappa \sim R. \quad (29.17)$$

Formula (29.17) shows that the thermal conductivity diverges linearly with the disk radius R . Note that mostly in anharmonic systems the dependence is not of the power type but logarithmic. One of the publications [31] shows a power (but not a linear) dependence for β -FPU system.

29.3 Experimental Techniques

A conventional experimental technique for measuring a coefficient of heat conductivity κ is to apply a temperature difference on the boundaries of the system and to measure a steady heat flux. Heat conductivity is then calculated from Fourier's law. For a circular symmetry, the heating is usually applied to the center of the system under observation so that a temperature difference is established between the center and the boundary of the examined disk. We consider the following mathematical formulation of the problem. A graphene disk with radius R is heated in the center by a laser. The boundary is held at ambient temperature. The heat production $q(r)$ is assumed to be Gaussian within the plane:

Fig. 29.3 Heat production of the Gaussian type in a circular membrane



$$q(r) = \frac{P}{\pi d r_0^2} e^{-\frac{r^2}{r_0^2}}, \tag{29.18}$$

where d is the thickness of graphene, r_0 is the theoretical Gaussian spot size.

The situation is presented in Fig. 29.3. In order to describe a steady temperature profile, let us consider the diffusive Fourier equation in cylindrical coordinates with a production term $q(r)$:

$$\kappa \frac{1}{r} \frac{d}{dr} \left(r \frac{dT}{dr} \right) + q(r) = 0. \tag{29.19}$$

We introduce the dimensionless variable $\tilde{r} = r/r_0$. By integrating Eq. (29.19), we get the solution as follows:

$$T(\tilde{r}) - T(0) = \frac{1}{2} \frac{P}{\pi d \kappa} \int_0^{\tilde{r}} \frac{1 - e^{-x^2}}{x} dx = \frac{1}{2} \frac{P}{\pi d \kappa} \left(\ln \tilde{r} - \frac{1}{2} \text{Ei}(-\tilde{r}^2) + \frac{\gamma}{2} \right) \approx \frac{1}{2} \frac{P}{\pi d \kappa} \left(\ln \tilde{r} + \frac{\gamma}{2} \right), \tag{29.20}$$

where Ei is the exponential integral function, γ is the Euler’s constant. Then if the drop of the temperature between temperature in the center T_c and the boundary T_b is known one can express the heat conductivity by the formula:

$$\kappa = \frac{1}{2} \frac{P}{\pi d (T_c - T_b)} \left(\ln \frac{R}{r_0} + \frac{\gamma}{2} \right). \tag{29.21}$$

29.3.1 Raman Thermometry

Introductory Remarks

Raman thermometry was introduced in the work of Balandin and colleagues [3, 5]. The laser beam is used as a heating source in the center of a membrane and at the same time as a probe. In order to apply this technique successfully, the graphene membrane must be attached to an efficient heat sink. The temperature of a boundary can then be assumed to have ambient temperature. By knowing the laser power and a

Fig. 29.4 **a** Room-temperature Raman spectrum from single-layer suspended graphene **b** optical microscope image of the sample. The scale bar is 5 μm

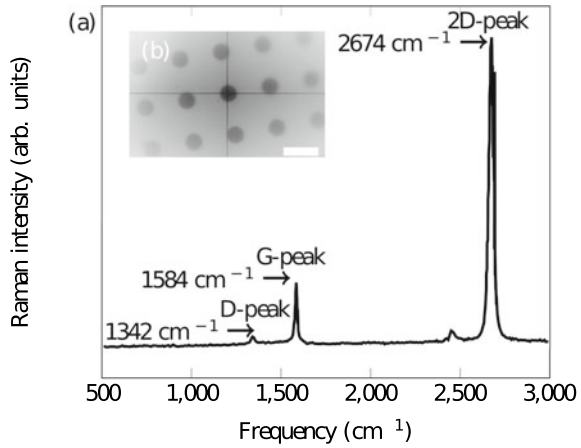
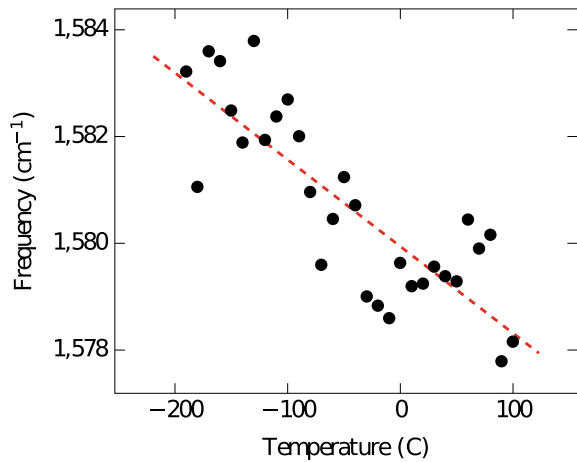


Fig. 29.5 Temperature dependence of G-peak position of a single-layer graphene (black dots) and linear fit (red dashed line). The graph is plotted using data from [3]



coefficient of absorption, and by combining it with measured temperature difference the coefficient of heat conductivity is calculated by using formula (29.21).

The spectrum of a suspended single-layer graphene at room temperature is presented in Fig. 29.4. Characteristic features are the G-peak located around ca. 1580 cm^{-1} and the D-peak located around ca. 1380 cm^{-1} . It was observed in [3] that an increase of temperature leads to a red shift of the G-peak. The dependence of the G-peak position on the temperature of a graphene on a substrate is presented in Fig. 29.5 (data taken from [3]).

The temperature dependence of a G mode can be described by the following equation (after [3]):

$$\omega = \omega_0 + \chi T, \tag{29.22}$$

Table 29.1 Temperature coefficient of single-layer graphene

Substrate	χ (cm ⁻¹ /K)	Method	Comment	Ref.
SiO ₂	-0.015	External heating	-	[3]
SiO ₂	-0.03	External heating	-	[25]
Suspended	-0.0405	External heating	-	[2]
-	-0.03	MD	AIREBO, quasilinear	[14]
-	-0.06	MD	LCBOP, quasilinear	[14]
-	-0.0517	MD	Tersoff-2010	[14]

Table 29.2 Coefficient of optical absorption of single-layer graphene

Optical absorption coefficient α	Wavelength nm	Ref.
3.4 ± 0.7%	532	[2]
2.3 ± 0.1%	500–740	[24]
2.3 ± 0.2%	1033–2479	[23]
2.9 ± 0.2%	532	[5]

where ω_0 is the frequency of the G mode when the temperature is extrapolated to 0 K, χ is the temperature coefficient, calculated from a slope of linear fit.

Temperature coefficients calculated in a number of publications are presented in Table 29.1. In numerical calculations [14], several interatomic potentials were considered. Only the Tersoff-2010 potential was able to reproduce the linear G-peak shift observed in the experiments, while LCBOP and AIREBO potentials show a nonlinear, non-monotonic behavior at low temperatures, which deviates from the experimental results. At higher temperatures, these two potentials show a quasilinear behavior with temperature coefficients presented in Table 29.1.

By applying this technique one can use the reflected laser light as a thermometer and determine the temperature difference in (29.21). When knowing the coefficient of optical absorption of graphene α and the power of incident laser P_I the absorbed power P is calculated $P = \alpha P_I$. Then κ is calculated from (29.21). The coefficients of optical absorption obtained in recent publications are presented in Table 29.2. A conventional method to measure the absorption is to measure the difference between the laser power with a power meter, first through an empty hole and then through a suspended graphene membrane [2, 5].

Coefficients of thermal conductivity from various references are presented in Table 29.6. The disadvantage of this method is that the spatial resolution is limited by the diffraction limit $\sim 1 \mu\text{m}$. Therefore, systems bigger than $1 \mu\text{m}$ do not allow to investigate ballistic transport at RT with this method since ballistic transport is observed at RT only at smaller scales. Thus, in Table 29.6, the values of heat con-

Table 29.3 Laser power in % of maximum power of source and absorbed power

% Max power	0.1	0.5	1	5	10	50
Incident power mW	39e-3	196e-3	0.36	2.69	4.91	27.46
Absorbed power mW	9e-4	4.5e-3	0.008	0.06	0.11	0.63

duction that correspond to a diffusive regime when κ is a material parameter are presented.

We assume temperature coefficient for G-peak to be equal $\chi = -0.04 \text{ cm}^{-1}/\text{K}$ [2] and an optical absorption of graphene 2.3% [24]. The power of laser can be changed with the steps of ..., 0.1%, 0.5%, 1%, 5%, 10%, 50%, 100% of the maximum working power. It gives us the following correspondence with absorbed laser power compiled in Table 29.3.

The beam power was measured by using an Edmund Optics Touchscreen Laser Power Meter with beam spread on the aperture of the sensor with a 5x magnification objective. We performed the experiments with different powers of laser excitation in order to obtain the G-peak shift as a function of absorbed laser power. By using the temperature coefficient and the relations (29.22) the corresponding temperature difference is calculated. The powers 0.1%, 0.5%, 1% do not cause any noticeable peak shift and correspond to the ambient temperature peak position. The power of 50% was excluded from the investigation because it was visually seen that illumination of the substrate occurred at this power, which could cause additional power generation at the boundary. Thus, the peak shift is calculated as difference of peak positions at powers 0.5% and 10%. $\Delta\omega = \omega_{0.5\%} - \omega_{10\%}$.

Materials and Measurement

In the experiment, TEM grids made of gold are used as a support for the substrate. The Au grid is 300 mesh with size between the bars $63 \mu\text{m}$. The grid is covered with the amorphous carbon film. The thickness of the carbon film is about 12 nm and it has 2 micron holes, see Fig. 29.4b. Monoatomic graphene layer grown by chemical vapor deposition is transferred over carbon layer (covering the holes), $d = 305 \text{ nm}$. For Raman measurements $\lambda = 532 \text{ nm}$ laser source with a 100x objective and numerical aperture $\text{NA} = 0.85$ is used, which gives theoretical Gaussian spot size used in Eq. (29.18) $r_0 = \lambda/\pi\text{NA} = 0.19 \mu\text{m}$.

In order to ensure reproducibility, we performed ten measurements of a peak shift $\Delta\omega$ with ten different graphene disks, where the presence of graphene was confirmed by obtaining the Raman spectrum of graphene. The measurements were conducted as follows. First the Raman G-peak was measured by acquisition at 0.5% for 120 s. Then spectral acquisition was done at 10% power for 120 s. This time length of spectral acquisition was chosen in order to ensure a steady state to be established in the graphene sheet, and to acquire enough intensity at low power.

Table 29.4 Peak positions at 0.5% and 10% incident beam powers and frequency shift $\Delta\omega$ (cm^{-1}) measured at ten different membranes

No.	$\omega_{0.5\%}$	$\omega_{10\%}$	$\Delta\omega$
1	1583.55	1580.95	2.6
2	1581.82	1578.94	2.88
3	1587.35	1584.25	3.1
4	1585.15	1581.89	3.26
5	1586.38	1582.24	4.14
6	1584.17	1580.84	3.33
7	1583.55	1580.35	3.2
8	1584.56	1581.9	2.66
9	1585.57	1581.96	3.61
10	1584.81	1581.26	3.55

Table 29.5 Heat conductivity κ at 10% incident beam power measured for ten different membranes

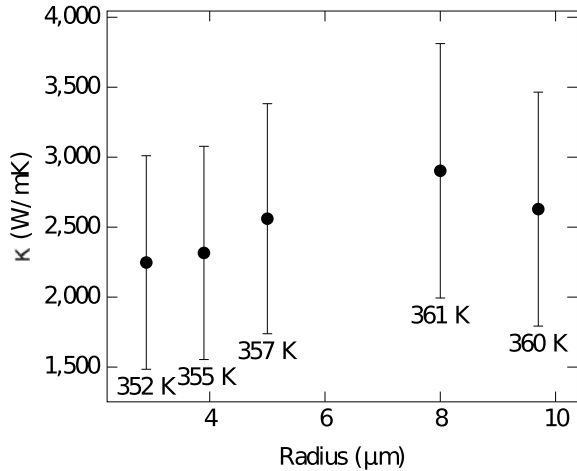
No.	κ (W/mK)	No.	κ (W/mK)
1	2292	6	2069
2	1922	7	1828
3	1439	8	1789
4	1862	9	2240
5	1651	10	1678

Table 29.6 RT heat conductivity of graphene measured using Raman thermometry and comparison with the theoretical works

κ (W/mK)	Comment	Ref
4419	0.01% ^{13}C	[5]
2792	1.1% ^{13}C	[5]
2197	50% ^{13}C	[5]
2826	99.2% ^{13}C	[5]
600	–	[9]
1877	–	This work
2622	Kinetic theory	[29]
1910	Theory, in plane graphite	[13]

The measured peak shift and the heat conductivity are presented in Tables 29.4 and 29.5, respectively. The obtained values lead to a mean value of 1877 W/mK with standard error $\sigma^{\text{std}}/\sqrt{N} = 252$ W/mK, where σ^{std^2} is the dispersion and $N = 10$ is the number of measurements.

Fig. 29.6 Dependence of heat conduction coefficient of size of graphene disks at near-RT's. The graph is plotted using data from [2]



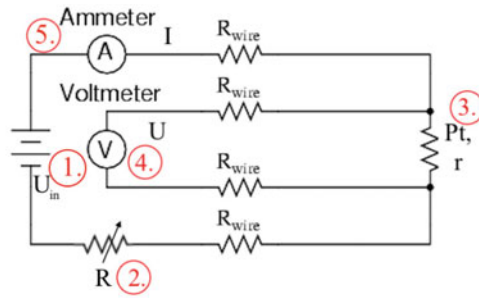
From [2] (see Fig. 29.6), it is difficult to say anything about size dependence of heat conductivity at room temperature due to the large error. It is concluded [2] that the effect of size dependence is not observed due to high uncertainty, defects, and other impurities of membranes.

29.3.2 Scanning Thermal Microscopy

Another technique to study heat conduction in materials is Scanning Thermal Microscopy (SThM), which is based on Atomic Force Microscopy (AFM). The temperature scan is achieved by measuring the changing resistance in a wire running through an AFM probe. A conventional design of the device is given as follows. A wire made of material with known thermal coefficient (e.g., platinum) is passed thorough the AFM cantilever tip and acts as a nano-thermometer (see Fig. 29.7c, d). The device consists of voltage source (1.), variable resistor (2.) with electrical resistance \mathcal{R} , platinum sensor (3.) with electrical resistance ε , digital voltmeter, which is read by a computer software, and the ammeter (5.) (see Fig. 29.7a) the output of which can be seen at the digital readout on the thermoresistor signal amplifier, Fig. 29.7b. Photos, Fig. 29.7b, c, were taken in TU Berlin, Chair of Continuum Mechanics and Constitutive Theory.

Let us consider the working principle in more detail. The goal is to measure the resistance of the platinum wire ε . A voltage source provides a constant voltage U_{in} . By using the knob (2.) the resistance \mathcal{R} in the circuit can be changed. Then the current in the system is calculated using the following formula:

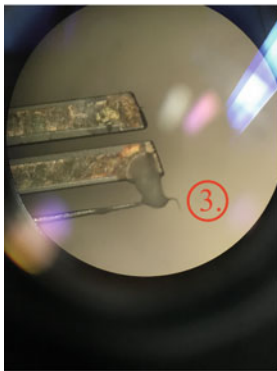
$$I = \frac{U_{in}}{\varepsilon + \mathcal{R}}. \tag{29.23}$$



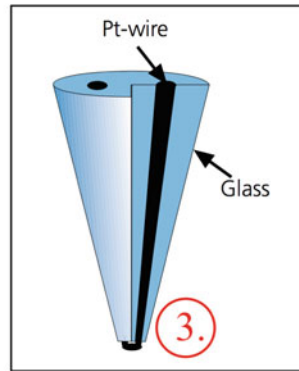
(a) Electrical scheme of thermoresistive measurement circuits.



(b) Photo of thermoresistor signal amplifier



(c) Optical microscope photo of Thermoresistive MV 2000™ AFM tip on a tuning fork.



(d) Sketch of Dual-Wire Thermoresistive Probe with fused junction whose resistance is temperature-dependent.

Fig. 29.7 Thermoresistor measurement system layout

If $\mathcal{R} \gg r$ the changes of thermometer resistance r (3.) do not affect the current I significantly. Thus by changing \mathcal{R} it is possible to control the value of the current. The voltage source (1.) and the resistance (2.) connected in series can be considered as a constant current source if the auxiliary resistance connected to the system is relatively small compared to \mathcal{R} . Thus the current in the system can be calculated using the following relation and the ammeter (5.):

$$I \sim \frac{U_{\text{in}}}{\mathcal{R}}. \quad (29.24)$$

The desired resistance r at the tip (3.) is defined by the voltage drop measured by the digital voltmeter (4.) The advantage of the scheme is that any voltage dropped across the main current-carrying wires will not be measured by the voltmeter, and so do not enter into the resistance calculation at all. The sought resistance is then measured as follows:

$$\mathcal{R} = \frac{\text{Voltmeter indication}}{\text{Ammeter indication}}. \quad (29.25)$$

One can set the current constant and monitored directly from ammeter, and map only the change of the voltage as a function of position of cantilever (x, y) . Let us indicate the voltmeter indication by $U(x, y)$ and the ammeter indication simply by I . Then the electrical resistance map across the surface is $\mathcal{R}(x, y) = U(x, y)/I$. However, one is interested in the temperature map. The temperature of the tip can be found by using the formula

$$\mathcal{R} = \mathcal{R}_0(1 + \alpha T), \quad T(x, y) = \frac{r(x, y)/\mathcal{R}_0 - 1}{\alpha} = \frac{U(x, y)/I\mathcal{R}_0 - 1}{\alpha}, \quad (29.26)$$

where \mathcal{R}_0 is the resistance at 0°C , and $\alpha = 0.0038\text{C}^{-1}$ is the thermal coefficient of Platinum.

If the applied current is low and does not cause Joule heating the device is operating in a passive mode and if tip and the surface are in thermal equilibrium the temperature of the surface is measured.

If the applied current is higher the device acts as a heat source and the heat is absorbed by the surface. Such a regime is called active. By knowing the supplied power, the theoretical model of absorption, and the read temperature of the tip, one can calculate coefficient of heat conductivity. This measurement is based on the equation

$$R^{\text{th}} \dot{Q} = \Delta T = T_p - T_{\text{amb}}, \quad (29.27)$$

where $R^{\text{th}}[\text{K}/\text{W}]$ is thermal resistivity, ΔT is the temperature difference between the point of power generation T_p and the heat sink, and \dot{Q} is the heat transfer rate or the power of heat generation. Conventionally, it is the difference between temperature of the tip, which is measured from (29.26) and the substrate, which is held at ambient temperature T_{amb} . Two techniques are used to measure R^{th} : (a) a feedback loop is used to keep T_p constant by applying different heating power \dot{Q} , and then the resistance is

inversely proportional to measured power $R^{\text{th}} = \text{const}/\Delta T$ and (b) using a constant heating power and measure temperature T_p of the probe, and then the resistance is proportional to the measured temperature difference $R^{\text{th}} = \text{const} \Delta T$.

The power of heat generation \dot{Q} is caused by Joule's heating of the tip and can be calculated directly from measurements $\dot{Q} = IU$:

$$\dot{Q} = \text{Voltmeter indication} \times \text{Ammeter indication}. \quad (29.28)$$

The measured thermal resistance usually combines contributions from several elements. For example [8], it can be

$$R^{\text{th}} = R_t + R_c + R_{\text{spr}}, \quad (29.29)$$

where R_t is thermal resistance of probe tip, R_c is the contact resistance between tip and sample, and R_{spr} is the thermal spreading resistance into the specimen. We are usually interested in R_{spr} . Difficulties can occur during the determination of R_c and R_t when the heat conduction is anomalous. The advantage of this technique is a high spatial resolution (up to 17 nm as reported in [8], 20 nm in [12]).

A correlation between thermal resistance and heat conductivity in central symmetry can be obtained from the solution of the heat conduction problem in cylindrical coordinates as a function of radial coordinate r . A thick-walled cylinder is held at temperature T_c at the inner surface, $T|_{r=r_0}$ with a heat flux q , $\partial T/\partial r = -q/\kappa$. The solution of a homogeneous Laplace equation in cylindrical coordinates

$$\frac{1}{r} \frac{\partial}{\partial r} \left(r \frac{\partial T}{\partial r} \right) = 0 \quad (29.30)$$

is

$$T(r) = -\frac{qr_0}{\kappa} \ln \frac{r}{r_0} + T_c. \quad (29.31)$$

Let us denote the temperature of the outer boundary $r = R$ by T_b , $\Delta T = T_c - T_b$. Then from (29.31) the following relation holds:

$$q = \frac{\kappa}{r_0 \ln(R/r_0)} \Delta T. \quad (29.32)$$

The heat transfer rate is then calculated as the product of the heat flux and the area of inner surface $S = 2\pi r_0 d$. This leads to

$$\dot{Q} = \frac{2\pi d \kappa}{\ln R/r_0} \Delta T = \frac{1}{R^{\text{th}}} \Delta T \Rightarrow \kappa = \frac{\ln R/r_0}{2\pi d R^{\text{th}}}. \quad (29.33)$$

In [8, 12], SThM was applied to measure heat conduction phenomena on a sub-micron scale, see Figs. 29.8 and 29.9. The presence of ballistic heat conduction was observed in both references. Both show a logarithmic trend of heat conduc-

Fig. 29.8 Dependence of thermal conductivity on radius of graphene disk at RT. Graphs are plotted using data from [4, 12]. Dashed lines were added for convenience

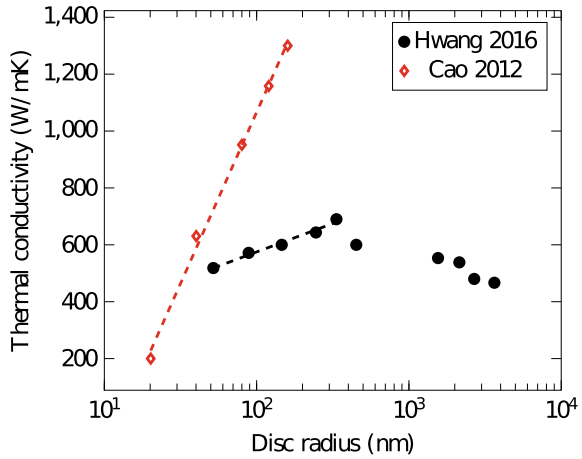
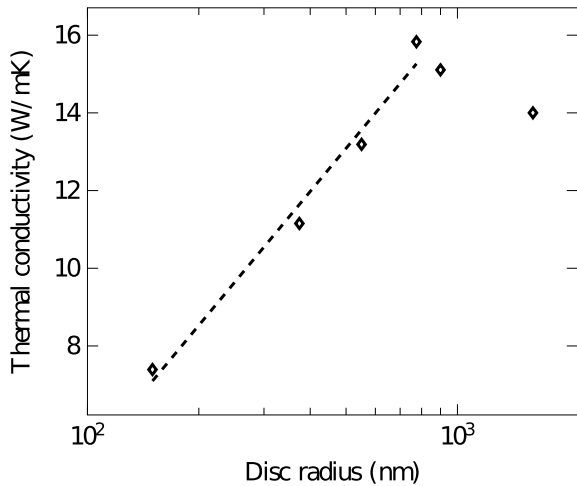


Fig. 29.9 Dependence of thermal conductivity graphene disk + probe tip at RT. Values are calculated with Eq. 29.33 with thermal resistances taken from [8]. A dashed line was added for convenience



tion divergence on scales $< \sim 800$ nm. In both papers, an interesting decrease of heat conductivity was observed at larger scales. This effect may be attributed to the very small size of the heat source. Figure 29.9 shows the values of heat conduction obtained by Eq. (29.33) with thermal resistances including all contributions as shown in Eq. (29.29) taken from [8]. It was shown in [8] that the thermal resistance of the substrate is several magnitudes lower than the measured full resistance. Thus it can be neglected. It was shown that the value of the tip-sample contact remains constant. Thus it does not influence the size dependence. Yet no absolute values were given. This explains the extremely low values obtained of heat conduction (with respect to what presented in literature for graphene) in Fig. 29.9, since it reflects the conduction of graphene membrane + tip-sample contact. The absolute values reported by [12] are about 600 W/mK, which is relatively low when compared to most results obtained

with optothermal techniques, but it corresponds to the result in [9]. A numerical study [4] confirms the logarithmic trend observed in experimental investigations [8, 12] but does not represent non-monotonic behavior since only systems smaller than 800 nm were studied. Absolute values of thermal conductivity [4] (~ 300 W/mK the largest value corresponding to largest investigated sample size) are larger than reported in [8, 12] and closer to values predicted by theory [13] and optothermal technique (see Table 29.6).

29.4 Conclusions

A scientific group from the Technical University of Berlin assessed the possibility of experimental measurement of the thermal conductivity in the case of anomalous heat transfer corresponding to the theoretical estimates of scientists from the laboratory “Discrete Models of Mechanics” IPME RAS within the framework of the international cooperation RSF-DFG. A theoretical approach which allows to define thermal conductivity in transient ballistic case and compares it with steady state measurements was proposed. The results showed that the heat conductivity is power dependent on size (in this particular case, the dependence is linear), such that $\kappa \sim R$, Eq. 29.17. This contradicts to a logarithmic dependence reported in a number of experimental and theoretical studies for anomalous heat transport. On the other hand, some studies [29, 31] also predict a power dependence of heat conductivity in 2D structures at very low temperatures and spatial scales. This raises the question as to whether a logarithmic dependence corresponds to ballistic or some intermediate (between ballistic and diffusive) quasi-ballistic regime of heat conduction. This, in principle, gives rise to further theoretical and experimental challenges.

Experimental techniques that can be used for investigation of the size dependence were also considered in this paper. Raman thermometry is a promising candidate for such studies. However, the effect of power size dependence or any size dependence was not yet observed in the reviewed literature. The difficulty lies in the relatively large minimum size of the laser spot limited by optical diffraction, which is comparable to the phonon mean free path in graphene at RT and in the low-temperature resolution, which causes high uncertainty. A value of ~ 1900 W/mK was obtained by using this method in the current work.

Scanning thermal microscopy is another suitable method. Its main advantage is high spatial and temperature resolution. Complications arise in determining additional thermal resistances contributions, along with the sought thermal resistance of the specimen, to the measured value. By using this technique a logarithmic dependence of the heat conduction coefficient on size was observed at the sub-micron scale.

The goal of further research is to measure the size dependence of heat conduction in circular graphene disks using the aforementioned methods and to compare it with the theoretical predictions presented in the current work.

Acknowledgements The proposed theoretical and experimental approaches lay the foundation for further studies of ballistic heat propagation in crystals within the framework of projects of the German Research Foundation (DFG) (Grant No. 405631704) and the Russian Science Foundation (Grant No. 19-41-04106).

References

1. Abali, B., Wu, C., Müller, W.: An energy-based method to determine material constants in nonlinear rheology with applications. *Contin. Mech. Thermodyn.* **28**(5), 1221–1246 (2016)
2. Cai, W., Moore, A., Zhu, Y., Li, X., Chen, S., Shi, L., Ruoff, R.: Thermal transport in suspended and supported monolayer graphene grown by chemical vapor deposition. *Nano Lett.* **10**(5), 1645–1651 (2010)
3. Calizo, I., Balandin, A., Bao, W., Miao, F., Lau, C.: Temperature dependence of the raman spectra of graphene and graphene multilayers. *Nano Lett.* **7**(9), 2645–2649 (2007)
4. Cao, A.: Molecular dynamics simulation study on heat transport in monolayer graphene sheet with various geometries. *J. Appl. Phys.* **111**(8), 083528 (2012)
5. Chen, S., Wu, Q., Mishra, C., Kang, J., Zhang, H., Cho, K., Cai, W., Balandin, A., Ruoff, R.: Thermal conductivity of isotopically modified graphene. *Nat. Mater.* **11**(3), 203–207 (2012)
6. Dhar, A., Kundu, A., Kundu, A.: Anomalous heat transport in one dimensional systems: a description using non-local fractional-type diffusion equation. *Front. Phys.* **7**, 159 (2019)
7. Dmitriev, S., Baimova, J., Savin, A., Kivshar, Y.: Ultimate strength, ripples, sound velocities, and density of phonon states of strained graphene. *Comput. Mater. Sci.* **53**(1), 194–203 (2012)
8. El Sachat, A., Könemann, F., Menges, F., Del Corro, E., Garrido, J., Torres, C., Alzina, F., Gotsmann, B.: Crossover from ballistic to diffusive thermal transport in suspended graphene membranes. *2D Mater.* **6**(2), 025034 (2019)
9. Faugeras, C., Faugeras, B., Orlita, M., Potemski, M., Nair, R., Geim, A.: Thermal conductivity of graphene in corbino membrane geometry. *ACS Nano* **4**(4), 1889–1892 (2010)
10. Fehér, A., Lukács, N., Somlai, L., Fodor, T., Szücs, M., Fülöp, T., Ván, P., Kovács, R.: Size effects and beyond-fourier heat conduction in room-temperature experiments (2021). [arXiv:2102.11744](https://arxiv.org/abs/2102.11744)
11. Huberman, S., Duncan, R., Chen, K., Song, B., Chiloyan, V., Ding, Z., Maznev, A., Chen, G., Nelson, K.: Observation of second sound in graphite at temperatures above 100 k. *Science* **364**(6438), 375–379 (2019)
12. Hwang, G., Kwon, O.: Measuring the size dependence of thermal conductivity of suspended graphene disks using null-point scanning thermal microscopy. *Nanoscale* **8**(9), 5280–5290 (2016)
13. Klemens, P., Pedraza, D.: Thermal conductivity of graphite in the basal plane. *Carbon* **32**(4), 735–741 (1994)
14. Koukaras, E., Kalosakas, G., Galiotis, C., Papagelis, K.: Phonon properties of graphene derived from molecular dynamics simulations. *Sci. Rep.* **5**(1), 1–9 (2015)
15. Kovács, R., Rogolino, P.: Numerical treatment of nonlinear fourier and maxwell-cattaneo-vernotte heat transport equations. *Int. J. Heat Mass Transf.* **150**, 119281 (2020)
16. Kuzkin, V.: Unsteady ballistic heat transport in harmonic crystals with polyatomic unit cell. *Contin. Mech. Thermodyn.* **31**(6), 1573–1599 (2019)
17. Kuzkin, V., Krivtsov, A.: Fast and slow thermal processes in harmonic scalar lattices. *J. Phys. Condens. Matter* **29**(50), 505401 (2017)
18. Kuzkin, V., Krivtsov, A.: Ballistic resonance and thermalization in the Fermi-Pasta-Ulam-Tsingou chain at finite temperature. *Phys. Rev. E* **101**(4), 042209 (2020)
19. Lebon, G., Jou, D., Casas-Vázquez, J., Muschik, W.: Heat conduction at low temperature: a non-linear generalization of the guyer-krumhansl equation. *Period. Polytech. Chem. Eng.* **41**(2), 185–196 (1997)

20. Lepri, S., Livi, R., Politi, A.: Thermal conduction in classical low-dimensional lattices. *Phys. Rep.* **377**(1), 1–80 (2003)
21. Liebold, C., Müller, W.: Measuring material coefficients of higher gradient elasticity by using AFM techniques and Raman-spectroscopy. In: *Generalized Continua as Models for Materials*, pp. 255–271. Springer (2013)
22. Liebold, C., Müller, W.: Comparison of gradient elasticity models for the bending of micro-materials. *Comput. Mater. Sci.* **116**, 52–61 (2016)
23. Mak, K., Sfeir, M., Wu, Y., Lui, C.H., Misewich, J.A., Heinz, T.F.: Measurement of the optical conductivity of graphene. *Phys. Rev. Lett.* **101**(19), 196405 (2008)
24. Nair, R., Blake, P., Grigorenko, A., Novoselov, K., Booth, T., Stauber, T., Peres, N., Geim, A.: Fine structure constant defines visual transparency of graphene. *Science* **320**(5881), 1308–1308 (2008)
25. Nguyen, K., Abdula, D., Tsai, C., Shim, M.: Temperature and gate voltage dependent raman spectra of single-layer graphene. *Acs Nano* **5**(6), 5273–5279 (2011)
26. Northrop, G., Wolfe, J.: Ballistic phonon imaging in solids—a new look at phonon focusing. *Phys. Rev. Lett.* **43**(19), 1424 (1979)
27. Okamoto, N., Yanagisawa, R., Anufriev, R., A., M., Sawano, K., Kurosawa, M., Nomura, M.: Semiballistic thermal conduction in polycrystalline sige nanowires. *Appl. Phys. Lett.* **115**(25), 253101 (2019)
28. Saito, K., Dhar, A.: Heat conduction in a three dimensional anharmonic crystal. *Phys. Rev. Lett.* **104**(4), 040601 (2010)
29. Saito, R., Mizuno, M., Dresselhaus, M.: Ballistic and diffusive thermal conductivity of graphene. *Phys. Rev. Appl.* **9**(2), 024017 (2018)
30. Volz, S.: *Microscale and Nanoscale Heat Transfer. Topics in Applied Physics*, vol. 107. Springer, Berlin Heidelberg (2007)
31. Wang, L., Hu, B., Li, B., et al.: Logarithmic divergent thermal conductivity in two-dimensional nonlinear lattices. *Phys. Rev. E* **86**(4), 040101 (2012)
32. Xu, X., Pereira, L., Wang, Y., Wu, J., Zhang, K., Zhao, X., Bae, S., Bui, C., Xie, R., Thong, J., et al.: Length-dependent thermal conductivity in suspended single-layer graphene. *Nat. Commun.* **5**(1), 1–6 (2014)

Chapter 30

A Randomized Approach to Estimate Acoustic Strength of Water



Grigory A. Volkov, Aleksey A. Gruzdkov, and Yuri V. Petrov

Abstract The problem of pulse-induced and acoustic cavitation of degassed water is considered within the framework of the incubation time approach. The analytical model to describe a dependency of the cavitation threshold on the pulse duration is developed and applied to experimental data in order to evaluate the main model parameter as the incubation time. The Sign-Perturbed Sums (SPS) method is used to get its estimation in the form of a confident interval. Obtained values of the incubation time are used to describe the dependency of the acoustic cavitation threshold on the ultrasonic frequency.

Keywords Pulse induced cavitation · Ultrasonic cavitation · Incubation time · Sign-perturbed sums

30.1 Introduction

The cavitation phenomenon is related to the discontinuity of liquid where small vapor bubbles grow and collapse under negative pressure. The volatile nature of liquids makes the estimation problem of cavitation limit properties difficult and stipulates the existence of a relatively wide range of strength parameters values.

The analytical approaches to estimate cavitation threshold are very useful in many practical applications where the knowledge of admissible values of ultrasound is

G. A. Volkov (✉)

Saint-Petersburg State University, Universitetsky pr., 28, St. Petersburg 198504, Russia

e-mail: g.volkov@spbu.ru

A. A. Gruzdkov

Saint-Petersburg State Institute of Technology, Moskovsky pr., 26,

St. Petersburg 190013, Russia

e-mail: gruzdkov@mail.ru

Y. V. Petrov

Institute for Problems in Mechanical Engineering RAS, V.O., Bolshoy pr., 61,

St. Petersburg 199178, Russia

e-mail: y.v.petrov@spbu.ru

necessary. For example, the onset of the process leads to the distortion and failure of acoustic signals if the frequency or the magnitude exceeds some critical values [1]. The acoustic cavitation is also applied to various medical and biological problems and it can lead to unnecessary damage of the tissue and blood cells [2]. The huge pressure caused by bubble collapses can lead to a new substance nucleation [3, 4]. These pressures also initiate damage of some solids and the wear rate depends on the type of loading, for example, pulse-induced and acoustic cavitation provide different surface loss for the same time [5]. The previous study demonstrated that the incubation time approach permits the prediction of the cavitation threshold for any frequency of the acoustic wave and for different types of pulse load [6–9]. The developed model allowed us to describe the dependency of the ultrasonic cavitation threshold on the frequency for degassed water and seawater. It also provided good results for pulsed-induced cavitation of distilled water. It should be noted that the corresponding values of incubation time were adjusted manually by fitting the model curve to experimental data. The present research is aimed to develop a standard way of data analysis to determine the model parameter values confidently. For this purpose, the randomized method of Sign-Perturbed Sums is used with the incubation time approach to have the result in the form of confident intervals involving true parameter value with a given probability [10]. This approach was successfully applied to the problem of dynamic fracture of brittle materials under constant rate of loading [11, 12].

30.2 Pulse-Induced Cavitation

The pulse-induced cavitation basically occurs under compression pulse reflection from the free surface as a tensile one.

To simplify the analysis, one of the simplest time profiles of the load is considered in the form of a triangular linearly fading pulse

$$P(t) = A \left(1 - \frac{t}{T}\right) [H(t) - H(t - T)], \quad (30.1)$$

where A is the amplitude of the pulse, T is its duration, and $H(t)$ is the Heaviside function. The time-profile of the load at some distance x from the free surface is the sum of initial and reflected pulses

$$\begin{aligned} P(x, t) = & A \left(1 - \frac{t}{T} - \frac{x}{cT}\right) \left[H\left(t + \frac{x}{c}\right) - H(t) + H\left(t + \frac{x}{c} - T\right) \right] \\ & - A \left(1 - \frac{t}{T} + \frac{x}{cT}\right) \left[H\left(t - \frac{x}{c}\right) - H\left(t - \frac{x}{c} - T\right) \right] = A f(x, t), \end{aligned} \quad (30.2)$$

where c is the sound velocity in the liquid. The lowest value of the magnitude A which leads to bubble growth and collapse at the nearest distance to the free surface

and at any time is called the cavitation threshold and notated as A^* . The next point is aimed to calculate the dependence of the threshold A^* on load pulse duration T .

30.2.1 Incubation Time Criterion

Short pulses and high frequencies of ultrasonic waves imply extremely high rates of loading, therefore, the incubation time criterion is applied as a condition of the cavitation onset. This criterion allows taking into account correctly both low quasi-static load and dynamic impacts under solving various problems of fracture.

The general form of the criterion is

$$\frac{1}{\tau} \int_{t-\tau}^t \text{sign}(P(t')) \left| \frac{P(t')}{P_s} \right|^\alpha dt' \geq 1, \quad (30.3)$$

where $P(t)$ is the load, P_s is the static threshold of cavitation that corresponds to the limit of negative pressure in equilibrium, τ is the incubation time and α is the dimensionless parameter characterizing the material sensitivity to the loading history. The substitution of the load profile (30.2) into the criterion (30.3) leads to the expression of the relative value of the threshold

$$\frac{A^*}{P_s} = \left(\frac{\tau}{I_{max}} \right)^{\frac{1}{\alpha}}, \quad (30.4)$$

where $I_{max} = \max_t \int_{t-\tau}^t \text{sign}(f(x, t')) |f(x, t')|^\alpha dt'$. It should be noted that the maximum of I is achieved at first in different cross sections x which determined by the ratio of the pulse duration and the incubation time.

If the load duration is greater than the incubation time, $T \geq \tau$, then it means that pulse is sufficiently long and the maximum of I for the first time is achieved when the reflected pulse does not intersect to the initial one. It happens in the section $x = \frac{cT}{2}$ at time $t = \frac{T}{2}$ and the only one Heaviside function $H(t - \frac{x}{c} - T)$ is equal to zero in formula (30.2) this case. Thus, the maximum I can be calculated as follows:

$$I_{max} = \int_{\frac{T}{2}}^{\frac{T}{2}+\tau} \left(\frac{3}{2} - \frac{t'}{T} \right)^\alpha dt' = \frac{T}{\alpha+1} \left(1 - \left(1 - \frac{\tau}{T} \right)^{\alpha+1} \right). \quad (30.5)$$

In the case of relatively short pulses, when $T < \tau$, the effect of the compressive pulse on the integral value has been holding on much longer than the pulse duration. Thus, the nearest cross-section where I becomes maximum is $x = \frac{cT}{2}$ at the tome moment $t = \frac{\tau}{2}$.

$$I_{max} = \int_{\frac{\tau}{2}}^{\frac{\tau}{2}+T} \left(1 - \frac{t'}{T} + \frac{\tau}{2T} \right)^\alpha dt' = \frac{T}{\alpha+1}. \quad (30.6)$$

The substitution of formulas (30.5), (30.6) into (30.4) leads to the analytical expression of the threshold amplitude versus pulse duration

$$\left(\frac{A^*}{P_s}\right)^\alpha = \begin{cases} (\alpha + 1) \frac{\tau}{T}, & T < \tau, \\ (\alpha + 1) \frac{\tau}{T} \left(1 - \left(1 - \frac{\tau}{T}\right)^{\alpha+1}\right)^{-1}, & T \geq \tau. \end{cases} \quad (30.7)$$

30.2.2 Sign-Perturbed Sums Method

The SPS method is applied to an analysis of the experimental data obtained by Besov et al. [13] in order to estimate the value of the incubation time.

The previous study showed that the SPS-procedure provides the mathematically approved result for growing monotonically model functions. To get this property, the new dimensionless variable $\xi = \frac{\tau}{T}$ is substituted into (30.7)

$$\left(\frac{A^*}{P_s}\right)^\alpha = \varphi(\xi) = \begin{cases} \frac{(\alpha+1)\xi}{1-(1-\xi)^{\alpha+1}}, & \xi \leq 1, \\ (\alpha + 1)\xi, & \xi > 1. \end{cases} \quad (30.8)$$

This variable ξ can be understood as an average rate of load pulse and the $\varphi(\xi)$ is a monotonically increasing function. Thus, the following observation model is treated by SPS-procedure

$$y_i = \varphi(\xi(T_i, \tau)) + v_i, \quad i = 1..N, \quad (30.9)$$

where $y_i = \left(\frac{A^*}{P_s}\right)_i^\alpha$ is a measured value in test, T_i is a value of the control input parameter, v_i is random noise, i is a test number and τ is the system parameter to be estimated.

The main steps of the Sign-Perturbed Sums algorithm were discussed in details in [11, 12]. It is obtained that $\tau \in [15.5; 16.8] \mu\text{s}$ under following values of static threshold $P_s = 1.0 \text{ bar}$ and $\alpha = \frac{1}{2}$. The calculation results of the cavitation threshold on the frequency are demonstrated in Fig. 30.1 while Fig. 30.2 shows its dependence on the pulse duration.

All data points are in good coincidence to theoretical curves. It should also be noted that all tests in the work [13] have been performed for short load pulses with a duration less than the incubation time. It means that the exact shape of the time profile of the load pulse does not influence much the value of threshold amplitude.

Fig. 30.1 Dependence of the threshold amplitude on the average load rate for distilled water. Comparison of theoretical curves to experimental data [13]

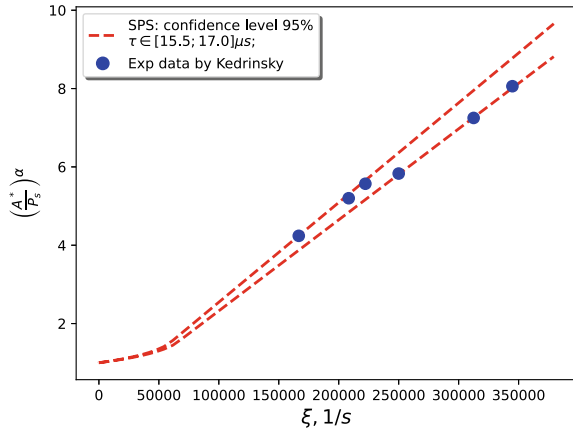
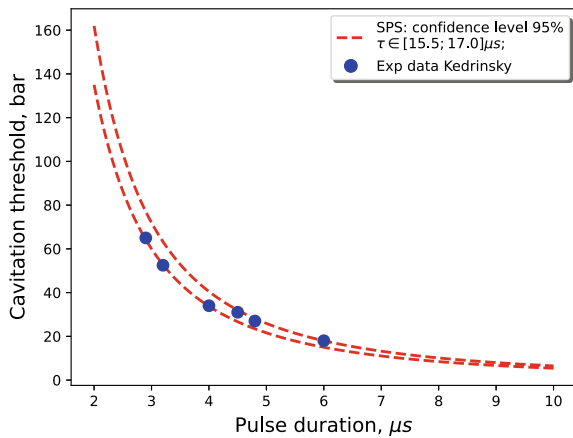


Fig. 30.2 Dependence of the threshold amplitude on the pulse duration for distilled water. Comparison of theoretical curves to experimental data [13]



30.3 Ultrasonic Acoustic Cavitation

The cavitation can also be induced by an intensive acoustic field and this part is aimed to check how the incubation time estimation obtained above corresponds to experiments on ultrasonic cavitation.

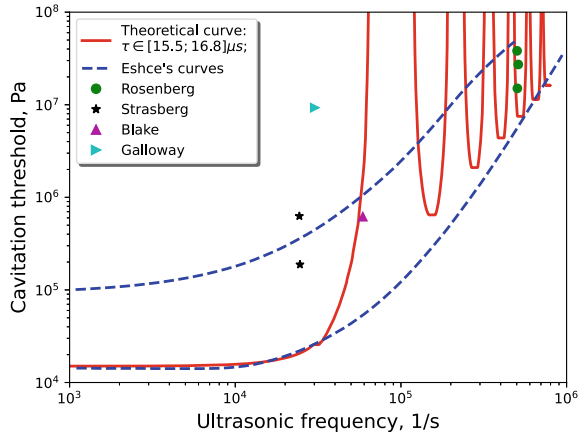
The ultrasonic wave loading can be described as follows:

$$P(t) = A \sin(\omega t) , \tag{30.10}$$

where $\omega = \frac{2\pi}{T}$ is the ultrasonic frequency and A is the wave magnitude. The incubation time criterion allows calculating the threshold amplitude A^* by

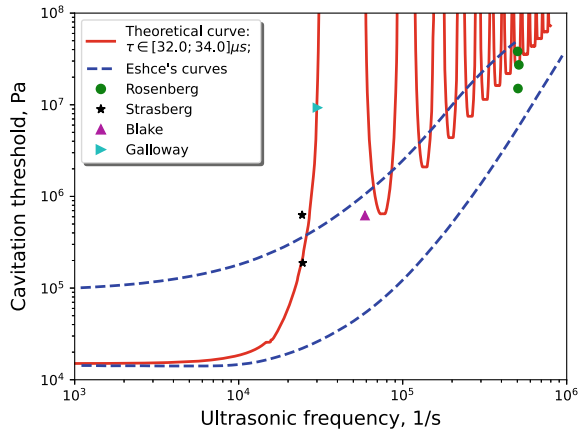
$$\left(\frac{A^*}{P_s}\right)^\alpha = \min_{\tau \in [\tau_{min}; \tau_{max}]} \left(\frac{\frac{\omega \tau}{2}}{\int_0^{\frac{\omega \tau}{2}} \psi(z) dz} \right) , \tag{30.11}$$

Fig. 30.3 Dependence of the threshold amplitude on the frequency in comparison to experimental data for degassed water [14]. Model parameters are $\tau \in [15.5; 16.8] \mu\text{s}$, $P_s = 0.15 \text{ bar}$, $\alpha = \frac{1}{2}$



where $\psi(z) = \text{sign}(\cos z)|\cos z|^\alpha$. The precise analysis of the formula (30.11) derivation is provided in [7]. It is evident that if $\tau = k \frac{4\pi}{\omega}$, where k is a whole number, then the integral of the numerator in (30.11) is equal to zero and the threshold tends to infinity. It is assumed that the incubation time can be any value from the confident interval obtained above in the Sect. 30.2 and the threshold amplitude for the certain frequency is a minimal one among all values calculated for every $\tau \in [15.5; 16.8] \mu\text{s}$. The result of modeling is compared to experimental curves by Eshce and other data points from [14] and demonstrated in Fig. 30.3. The value of the static threshold is set as $P_s = 0.15 \text{ bar}$ since the bottom Eshce's curve corresponds to the value much lower than 1.0 bar. The non-monotonic behavior of the analytical curve qualitatively corresponds to the band of Eshce's curves and also describes data points of other researchers. Figure 30.4 is plotted in an attempt to describe the first group of points by Strasberg and Galloway by adjusting the value of the incubation time scatter. Good

Fig. 30.4 Dependence of the threshold amplitude on the frequency in comparison to experimental data for degassed water [14]. Model parameters are $\tau \in [32.0; 34.0] \mu\text{s}$, $P_s = 0.15 \text{ bar}$, $\alpha = \frac{1}{2}$



coincidence for this group is achieved for $\tau \in [32.0; 34.0] \mu\text{s}$. A probable explanation is that the distilled water contained more vapor bubbles than the degassed one and its strength was lower.

30.4 Conclusions

The problem of pulse-induced and ultrasonic cavitation was studied within the framework of the incubation time approach. The Sign-Perturbed Sums method was successfully applied to estimate the incubation time value in the form of a confident interval. Taking into account the volatile structure of liquids and their non-homogeneity, the interval form of possible values of the incubation time looks more applicable to engineering practice. It was demonstrated that the obtained values for pulse-induced cavitation tests can be used in modeling ultrasonic cavitation. Comparison of analytical results with the experimental data demonstrated that the developed model is able to explain both a wide band of the cavitation threshold and its growth with the frequency increase. This model also explains qualitatively the data outliers which are not included in Eshce's band.

Acknowledgements This research was performed under support of the RSCF project No 20-79-10078.

References

1. Urick, R.J.: Principles of Underwater Sound-2. McGraw-Hill Book, New York (1975)
2. Maxwell, A.D., Wang, T.-Y., Yuan, L., Duryea, A.P., Xu, Z., Cain, C.A.: A tissue phantom for visualization and measurement of ultrasound-induced cavitation damage. *Ultrasound Med. Biol.* **36**(12), 2132–2143 (2010). <https://doi.org/10.1016/j.ultrasmedbio.2010.08.023>
3. Nigmatulin, R.I., Aganin, A.A., Toporkov, D.Y.: Possibility of cavitation bubble super-compression in tetradecane. *Dokl. Phys.* **63**(8), 348–352 (2018). <https://doi.org/10.1134/S1028335818080098>
4. Takahashi, H., Sugiyama, T., Nakabayashi, S., Yoshikawa, H.Y.: Crystallization from glacial acetic acid melt via laser ablation. *Appl. Phys. Express* **14**(4), 045503 (2021). <https://doi.org/10.35848/1882-0786/abf053>
5. Hanke, S., Kaiser, S.A.: Comparison of damage mechanisms: acoustic cavitation versus series of single laser-induced bubbles. *Wear* **476**, 203641 (2021). <https://doi.org/10.1016/j.wear.2021.203641>
6. Gruzdkov, A.A., Petrov, Yu.V.: Cavitation breakup of low-and high-viscosity liquids. *Tech. Phys.* **53**(3), 291–295 (2008). <https://doi.org/10.1134/s106378420803002x>
7. Volkov, G.A., Gruzdkov, A.A., Petrov, Y.V.: The incubation time criterion and the acoustic strength of sea water. *Acoust. Phys.* **53**(2), 119–122 (2007). <https://doi.org/10.1134/S1063771007020017>
8. Volkov, G.A., Petrov, Y.V., Gruzdkov, A.A.: Liquid-vapor phase equilibrium conditions in an ultrasonic field. *Dokl. Phys.* **60**(5), 229–231 (2015). <https://doi.org/10.1134/S1028335815050122>

9. Volkov, G.A., Petrov, Y.V., Gruzdkov, A.A.: Acoustic strength of water and effect of ultrasound on the liquid-vapor phase diagram. *Tech. Phys.* **60**(5), 753–756 (2015). <https://doi.org/10.1134/S1063784215050278>
10. Csáji, B.C., Campi, M.C., Weyer, E.: Sign-perturbed sums: a new system identification approach for constructing exact non-asymptotic confidence regions in linear regression models. *IEEE Trans. Signal Process.* **63**(1), 169–181 (2015). <https://doi.org/10.1109/TSP.2014.2369000>
11. Volkova, M., Volkov, G., Granichin, O., Petrov, Y.: Sign-perturbed sums approach for data treatment of dynamic fracture tests. In: 2017 IEEE 56th Annual Conference on Decision and Control, CDC 2017, vol. 2018-January, pp. 1652–1656 (2018). <https://doi.org/10.1109/CDC.2017.8263887>
12. Volkova, M.V., Granichin, O.N., Volkov, G.A., Petrov, Y.V.: On the possibility of using the method of sign-perturbed sums for the processing of dynamic test data. *Vestnik St. Petersburg Univ. Math.* **51**(1), 23–30 (2018). <https://doi.org/10.3103/S1063454118010132>
13. Besov, A.S., Kedrinskij, V.K., Morozov, N.F., Petrov, Yu.V., Utkin, A.A.: On analogy of first destruction stage of solid state and liquids during impulse loading. *Dokl. Akademii Nauk* **378**(3), 333–336 (2001)
14. Flynn, H.G.: Physics of acoustic cavitation in liquids. In: *Physical Acoustics: Principles and Methods*, vol. 1, Part B. Academic Press, New-York, London (1964)